

Matthias Söllner, Gerald Pirkl (Eds.)

Applied Research Conference 2021

Conference Proceedings



23rd July 2021

OTH Amberg-Weiden

(Virtual Conference)



Ostbayerische Technische Hochschule
Amberg-Weiden



HOCHSCHULE
ANSBACH



Hochschule
Augsburg University of
Applied Sciences



TECHNISCHE
HOCHSCHULE
DEGGENDORF THD



Technische Hochschule
Ingolstadt



HOCHSCHULE LANDSHUT
HOCHSCHULE FÜR ANGEWANDTE WISSENSCHAFTEN



HOCHSCHULE
FÜR ANGEWANDTE
WISSENSCHAFTEN
MÜNCHEN



GEORG-SIMON-OHM
HOCHSCHULE NÜRNBERG



OTH OSTBAYERISCHE
TECHNISCHE HOCHSCHULE
REGENSBURG

Matthias Söllner, Gerald Pirkl (Eds.)
Applied Research Conference 2021
Conference Proceedings
July 23rd, 2021
OTH Amberg-Weiden
(Virtual Conference)

Organizer:

Ostbayerische Technische Hochschule Amberg-Weiden
Hochschule Ansbach
Hochschule Augsburg
Technische Hochschule Deggendorf
Technische Hochschule Ingolstadt
Hochschule Landshut
Hochschule München
Technische Hochschule Nürnberg Georg Simon Ohm
Ostbayerische Technische Hochschule Regensburg

Bibliographic Information

Matthias Söllner, Gerald Pirkl (Eds.)

Applied Research Conference 2021

Ostbayerische Technische Hochschule Amberg-Weiden
Fakultät Elektrotechnik, Medien und Informatik
Kaiser-Wilhelm-Ring 23
92224 Amberg

Preamble of the editors

The ARC 2021 is the tenth conference of the Master of Applied Research program (MAPR). After a break due to the corona pandemic last year, this year the conference takes place as a purely virtual event on July 23rd, 2021 organized by OTH Amberg-Weiden.

Students of the master programs from nine cooperating bavarian universities present the results of their research in talks and papers printed in this publication. In ten virtual rooms sessions with different topics are organized.

In their master program every student works on his very own research topic for a period of one and a half years, which is divided in three semesters. In each of the semesters they write a thesis about the progress of their work, finishing with the master thesis in the third semester. Supervised by a professor they work in close cooperation with other researchers and have the chance to force their scientific career.

The conference and this book give a snapshot of the research going on at the nine cooperating bavarian universities of applied sciences.

We would like to thank all supporters of the conference, especially all the chairs and the BBB-supporters. A special thank goes to all colleagues who supervise a student in the MAPR program.

Despite the pandemic, research was able to continue. Hopefully we see a live conference in 2022 again.

Amberg, July 2021

Sgd.

Prof. Matthias Söllner

Prof. Dr.-Ing. Gerald Pirkl

General Chairs and Program Chairs

Prof. Matthias Söllner

OTH Amberg-Weiden

Kaiser-Wilhelm-Ring 23, 92224 Amberg

Tel.: 09621 482-3632

e-mail: m.soellner@oth-aw.de

Prof. Dr.-Ing. Gerald Pirkl

OTH Amberg-Weiden

Kaiser-Wilhelm-Ring 23, 92224 Amberg

Tel.: 09621 482-3606

e-mail: g.pirkl@oth-aw.de

Committee

General Chair

Söllner Matthias, Ostbayerische Technische Hochschule Amberg-Weiden

Pirkl Gerald, Ostbayerische Technische Hochschule Amberg-Weiden

Steering Committee

(Members of “Studiengangskommission des Studiengangs Applied Research”)

Bogner Werner, Technische Hochschule Deggendorf

Horn Anton, Ostbayerische Technische Hochschule Regensburg

Klippel Clemens, Hochschule München

Mottok Jürgen, Ostbayerische Technische Hochschule Regensburg

Pirkl Gerald, Ostbayerische Technische Hochschule Amberg-Weiden

Reichenberger Marcus, Technische Hochschule Nürnberg Georg Simon Ohm

Söllner Matthias, Ostbayerische Technische Hochschule Amberg-Weiden

Stolle Reinhard, Hochschule Augsburg

Timinger Holger, Hochschule Landshut

Uhl Christian, Hochschule Ansbach

Vaculin Ondrej, Technische Hochschule Ingolstadt

Walter Michael, Hochschule Ansbach

Contents

1	Conference Program and Timetables	11
1.1	General Timetable	11
1.2	Sessions Timetable	12
1.3	Talk Sessions	13
1.3.1	Virtual Room 1	13
1.3.2	Virtual Room 2	14
1.3.3	Virtual Room 3	15
1.3.4	Virtual Room 4	16
1.3.5	Virtual Room 5	17
1.3.6	Virtual Room 6	18
1.3.7	Virtual Room 7	19
1.3.8	Virtual Room 8	20
1.3.9	Virtual Room 9	21
1.3.10	Virtual Room 10	22
1.4	Poster Sessions	23
1.4.1	Poster Session 1	23
1.4.2	Poster Session 2	24
1.4.3	Poster Session 3	25
1.4.4	Poster Session 4	26
1.4.5	Poster Session 5	27
2	Papers: Software Engineering and Software Technologies	29
2.1	Analyzing and Rating Electric Vehicles Cyber Security Risks	30
2.2	Conception and development of a brain computer interface system as an end-user product	34
2.3	Development and Validation of a new iterative parametrization approach for Equivalent Circuit Models of Li-Ion Batteries	38
2.4	Tailor-made IT security standards for SMEs	44
2.5	A Decentralised Approach for Drive Decision Clearance of Automated Guided Vehicles at Intersections With Ambient-Approximated Traffic Control	49
2.6	Analysis of the operation of a cooling supply system for a hospital	54
2.7	Semi-automated 3D Reconstruction of Indoor and Outdoor Environments from RGB-D Data Captured by a Remote-controlled Robot	58
2.8	Development of an Open Source and Offline Voice User Interface for Blind and Visually Impaired People	64
2.9	Requirements and trends of modern Manufacturing Execution Systems in the context of Industry 4.0	70
2.10	Development of a learning platform for automotive security	73
2.11	Choosing a RISC-V Core for Implementing an FPGA-Based Security Module	76
2.12	Computational Acoustics using OpenFoam	81
2.13	Simulating realistic domestic hot water consumption of a complex apartment building in a dynamic building model in IDA ICE	87
3	Papers: Optical Technologies and Communication Networks	91
3.1	Cryptographic protection of High-Precision Clock Synchronization	92
3.2	Computational efficient noise suppression in phase-shifting holography	98
3.3	Formulas for Mutual and Self-Inductances of Multiple Coupled Loops	103

4	Papers: Materials and Manufacturing Technologies	109
4.1	Diffuse Reflectance Spectroscopy on TNT Samples With Different Carbon Contents	110
4.2	Tufting process and machine to manufacture prototypes of a tension rods supported hydrogen pressure vessel	116
4.3	A slim SLA-3D-printed bioreactor suited for multiphoton microscopy	122
4.4	Classification of the laser powder bed fusion pollution of the optical system phenomenon in optical tomography monitoring data with an analytically developed decision tree	126
4.5	Aluminium-Iron Intermetallic Metal Matrix Composites	132
4.6	Analytical evaluation of vacuum buildup concepts for aircraft structures	135
4.7	Studies on the firing behavior of bone china and the influence of raw material components on strength and translucency	141
4.8	Influence of pore geometries on the thermal shock resistance in ceramics investigated by numerical simulation	144
4.9	Comparison of a simulation-based with an analytical calculation of the temperature field of a laser process	148
4.10	Improvement of the solid-liquid separation of biogas digestate with a starch based flocculant	151
4.11	Strain-Induced Embrittlement at Elevated Temperatures of Heat-Resistant Steel 16Mo3	156
5	Papers: Power Technologies	161
5.1	Development of a calculation tool to support the planning of the utilization of hybrid emergency power generators	163
5.2	Change in the energy market - opportunities for industrial companies	169
5.3	Impact of air supply parameters on in-vehicle performance of PEMFCs used in an ultra-efficient FCEV	172
5.4	Aerodynamic design studies on new types of aircraft with vertical take-off and landing capabilities	177
5.5	Sustainable materials for insulating high-altitude rural Kyrgyz residential houses: A parametric economic study	183
5.6	Investigation of the heat transfer during condensation of wet flue gas in horizontally, corrugated tubes	189
5.7	Options on the test planning for the AC/DC-Dual Active Bridge	193
5.8	Conversion of non-existent load-profiles for PV-Systems	199
5.9	On the development of a seasonal seasonal heat storage for single-family houses: Design boundary conditions including the storage heat losses	202
5.10	Evaluation of possible charging demand of battery electric vehicles in parking garages and Park+Ride areas based on real entry and exit data	207
5.11	Modularity Analysis of Power Electronics Architectures	212
5.12	Potential of e- mobility in rural areas – Evaluation of opportunities and barriers based on literature review	216
5.13	Slip control of an induction machine in the field weakening region during six step operation	221
5.14	Influence of a novel binder material on the electro-chemical performance of silicon-containing anodes	227
5.15	Development of a Vanadium/Vanadium Redox-Flow Battery for Demonstrational Purposes	232
5.16	Development of different H ₂ -storage concepts for reduced emission shipping	238
5.17	Investigations regarding cooling of thermoelectric modules in a nano combined heat and power unit	243
5.18	Development of the control strategy for the heating system in the MAGGIE research project	248
5.19	Concept development of a hybrid ship driving system and investigation of different constellations of components and control strategies	253
5.20	Comparison of different calculation methods for the outflow from pressurized vessels	258
5.21	Potential analysis for long-term storage of a decentralized power-to-gas technology	264
5.22	Influence of Hydrogen on the combustion process of a single cylinder spark ignited gas engine	269
5.23	Determination of the restriction-free inductive and capacitive reactive power potential based on the example of a medium-voltage industrial operation	271
5.24	Development and Validation of a 3L-ANPC Bridge Type Inverter Based on GaN HEMTs	276
5.25	Chance in the energy market - opportunities for industrial companies	279
5.26	Development of a virtual fuel injector for operation with Diesel and Oxymethylenether	282
6	Papers: Car Technologies	287

6.1	Investigation of acoustic absorbing material in an impedance tube	288
6.2	Analysis of the requirements for the communication between an automated bus and the providing server needed for a booking app in the rural area	292
6.3	Asymmetric Firmware Attestation for Electronic Control Units	297
6.4	The Future of Product Development within the Context of Digitalisation - Challenges of Data Networking	303
6.5	Characterization of liner materials in terms of gas tightness and permeation for a cuboid, tension rod supported, high pressure hydrogen vessel	309
6.6	Measurement of PHEV according to WLTP	316
6.7	Method for Vehicle Crash Pulse Comparison in Pre-Crash Safety Systems	320
6.8	Analysis of Cybersecurity Vulnerabilities in Embedded Systems based on ISO/SAE 21434	325
6.9	Characterization of Object Detection Performance in an Edge Environment	330
6.10	Free Electric Vehicle Charging - A Practical Attack on Charging Systems	336
6.11	Concept and requirements for an AI-based automotive HiL-testing system	340
6.12	A Calibration Workflow for 3D Beamforming Radar for Integrated Vehicle Safety Systems	346
6.13	Development and commissioning of a component test bench for the operation of electrical machines used in EPS Applications	352
6.14	Analysis of the influence of gear blank geometry on the transmission error of cylindrical gears	356
6.15	Analysis of the required sensor range for an automated bus operating in rural areas based on a simulation	362
7	Papers: Logistics and Organization	367
7.1	Application of Lean Construction Management to sustainably increase of productivity in the construction industry	368
7.2	Structural Differences in the Higher Education Research in Germany between Universities and Universities of Applied Sciences	374
7.3	Use of Digital Assistance Systems in Production	380
8	Papers: Machine Learning	385
8.1	Applications of Robust Dynamical Component Analysis (DyCA) on simulated Data	386
8.2	Embedded Development of an Artificial Neural Network for Range Estimation on Infrared Images	392
8.3	Simulative data generation and labeling for autonomous driving specific AI models using MATLAB/Simulink, ROS and Gazebo	396
8.4	Applications and Limitations of Dynamical Component Analysis (DyCA)	401
8.5	Parameter choice for the short-time Fourier transformation in frequency-domain Blind Source Separation	407
8.6	AI-based control-algorithm for stationary batteries with regards to load-management	412
9	Papers: Robotics	417
9.1	Preliminary work on determining the global and local pose of a mobile robot in outdoor environments using proprioceptive and exteroceptive sensor technology	418
9.2	Development and construction of a Hand Exoskeleton for Virtual Reality	423
9.3	An Enhancement of Common Rail Track Detection Methods for Automatic Train Operation in Shunting Services	426
9.4	System Architecture of Autonomous Mobile Robots	431

10 Papers: Measurement Technologies	435
10.1 Hardware Setup for Three-Dimensional Acoustic Source Localization	436
10.2 Ultra Low Noise Amplifier for a Noise Measurement System	441
10.3 “Applied error analysis on a research ORC Plant at the University of Bayreuth”	445
10.4 High-speed ADC Data Acquisition with an FPGA for OTDR-based Fiber Sensors	450
10.5 Development of measuring methods for condition monitoring, fault detection and optimization of a medical angiography floor stand	454
10.6 Miniaturisation of a Sensor System Using Reflectivity Based Surface Plasmon Resonance Imaging (SPRi)	459
10.7 Investigation of the Float Current Analysis and the Float Current Settling Process via DVA on 18650 Li(NiCoAl)O ₂ /Graphite Cells	463
10.8 Theoretical and experimental investigation of code correlation methods for optical time domain reflectometry in POF	469
10.9 Method Development for the detection of filmic contaminations in additive manufacturing	474
Author’s Index	483

Chapter 1

Conference Program and Timetables

1.1 General Timetable

08:30h	Opening	Prof. Matthias Söllner
08:40h-08:50h	Begrüßung durch die Präsidentin	Prof. Dr. Andrea Klug President OTH Amberg-Weiden
08:50h-09:20h	Keynote: "Künstliche Intelligenz im Ingenieursumfeld"	Prof. Dr. Gerald Pirkl
Break		
09:30h-10:30h	Morning Session, Part 1	
Break		
10:50h-11:50h	Morning Session, Part 2	
Lunch Break		
12:30h-13:30h	Poster Sessions	
Break		
13:40h-15:00h	Afternoon Session, Part 1	
Break		
15:20h-16:40h	Afternoon Session, Part 1	
16:40h	End of the event	

1.2 Sessions Timetable

Virtual Rooms 1-5

	Virtual Room 1	Virtual Room 2	Virtual Room 3	Virtual Room 4	Virtual Room 5
Chair:	Sehr Armin	Ehrlich Ingo	Timinger Holger	Meiller Dieter	Aßmuth Andreas
BBB Support: 09:30h-10:30h Break 10:50h-11:50h	Schöler-Niewiera Florian Optical Technologies and Communication Networks Car Technologies 1	Schmidl Elisabeth Robotics	Wirth Harald Software Engineering and Soft- ware Technologies 1	- Machine Learning 1	- Measurement Technologies 1
Chair:	Vaculin Ondrej	Schmid Josef	Zatocil Heiko	Limbrunner Thomas	Dietl Guido
BBB Support: 13:40h-15:00h Break 15:20h-16:40h	Schöler-Niewiera Florian Car Technologies 2	- Car Technologies 3	- Software Engineering and Soft- ware Technologies 2	Mandel Gerd Machine Learning 2	Grüger Klaus Measurement Technologies 2

Virtual Rooms 6-10

	Virtual Room 6	Virtual Room 7	Virtual Room 8	Virtual Room 9	Virtual Room 10
Chair:	Hehenberger-Risse Diana	-	Weiß Andreas	Beer Stefan	Hauner Anton
BBB Support: 09:30h-10:30h Break 10:50h-11:50h	Chiu Tak San Materials and Manufacturing Technologies 1	-	- Power Technologies 1	- Power Technologies 2	Fersch Silke Power Technologies 4
Chair:	Reichenberger Marcus	Emmel Andreas	Wiehl Michael	Kreutzer Otto	Taschek Marco
BBB Support: 13:40h-15:00h Break 15:20h-16:40h	Oszlonyai Cornelia Materials and Manufacturing Technologies 2	- Materials and Manufacturing Technologies 3	- Software Engineering and Soft- ware Technologies 3 Logistics and Organization	Liebl Simon Power Technologies 3	- Power Technologies 5

Poster Sessions 1-5 (each session about 20 posters)

	Virtual Poster Session 1	Virtual Poster Session 2	Virtual Poster Session 3	Virtual Poster Session 4	Virtual Poster Session 5
Chair:	Walter Michael	Schindler Wolfgang	Kreutzer Otto	Sehr Armin	Hauner Anton
BBB Support: 12:30h-13:30h	Chiu Tak San Open Topic	- Open Topic	Fersch Silke Open Topic	Schmidl Elisabeth Open Topic	Liebl Simon Open Topic

1.3 Talk Sessions

1.3.1 Virtual Room 1

Morning Session:
Optical Technologies and Communication Networks
Car Technologies 1

Chair: Sehr Armin

BBB-Support: Schöler-Niewiera Florian

09:30h-09:50h	Schulitschenko Andreas: Cryptographic protection of High-Precision Clock Synchronization
09:50h-10:10h	Spellauge Tillmann: Computational efficient noise suppression in phase-shifting holography
10:10h-10:30h	Theil Markus: Formulas for Mutual and Self-Inductances of Multiple Coupled Loops
Break	
10:50h-11:10h	Acikgöz Yunus Ahmet: Investigation of acoustic absorbing material in an impedance tube
11:10h-11:30h	Babl Roman: Analysis of the requirements for the communication between an automated bus and the providing server needed for a booking app in the rural area
11:30h-11:50h	Gronau Maximilian: Asymmetric Firmware Attestation for Electronic Control Units

Afternoon Session:
Car Technologies 2

Chair: Vaculin Ondrej

BBB-Support: Schöler-Niewiera Florian

13:40h-14:00h	Heinzl Alexandra, Eursch Andreas: The Future of Product Development within the Context of Digitalisation - Challenges of Data Networking
14:00h-14:20h	Hupfeld Alexander: Characterization of liner materials in terms of gas tightness and permeation for a cuboid, tension rod supported, high pressure hydrogen vessel
14:20h-14:40h	Khan Farrak: Measurement of PHEV according to WLTP
14:40h-15:00h	Krause Robert, Sequeira Gerald Joy Alphonso: Method for Vehicle Crash Pulse Comparison in Pre-Crash Safety Systems
Break	
15:20h-15:40h	Lasow Alexander: Analysis of Cybersecurity Vulnerabilities in Embedded Systems based on ISO/SAE 21434
15:40h-16:00h	Ludwig Korbinian: Prototypical implementation of a new process and toolchain for thermal management projects
16:00h-16:20h	Maierhofer Michael: Damage Equivalent Vibration Testing
16:20h-16:40h	Prokscha Ruben: Characterization of Object Detection Performance in an Edge Environment

1.3.2 Virtual Room 2

Morning Session: Robotics

Chair: Ehrlich Ingo

BBB-Support: Schmidl Elisabeth

09:30h-09:50h	Fenn Markus: Preliminary work on determining the global and local pose of a mobile robot in outdoor environments using proprioceptive and exteroceptive sensor technology
09:50h-10:10h	Gerdts Dennis: Development and construction of a Hand Exoskeleton for Virtual Reality
10:10h-10:30h	Heuser Johanna: An Enhancement of Common Rail Track Detection Methods for Automatic Train Operation in Shunting Services
Break	
10:50h-11:10h	Jamakatel Prakash: ROS based Architecture for Optical Inspection using KUKA KR 10 Robotic Arm
11:10h-11:30h	Römmelt Lennard: System Architecture of Autonomous Mobile Robots
11:30h-11:50h	Wolf Martin: Long-term Effects of Exoskeletons on the Human Body

Afternoon Session: Car Technologies 3

Chair: Schmid Josef

13:40h-14:00h	Scheck Korbinian, Pfeffer Peter E., Aydogdu Seda, Schick Bernhard: Parking - Evaluation of Manual and Automated Parking Maneuvers with Subjective Assessment Indicators
14:00h-14:20h	Schmidt Jonas: Free Electric Vehicle Charging - A Practical Attack on Charging Systems
14:20h-14:40h	Schöniger Roland, Leidl Karl, Schramm Martin: Concept & requirements for an AI-based automotive HiL-testing system
14:40h-15:00h	Sezgin Fatih: A Calibration Workflow for 3D Beamforming Radar for Integrated Vehicle Safety Systems
Break	
15:20h-15:40h	Tunc Okan: Development and commissioning of a component test bench for the operation of electrical machines used in EPS Applications
15:40h-16:00h	Tworek Anton: Design of an innovative HiL test bench with a fully integrated brake system for automated driving
16:00h-16:20h	Wenig Alois Andreas: Analysis of the influence of gear blank geometry on the transmission error of cylindrical gears
16:20h-16:40h	Zeitler Fabian: Analysis of the required sensor range for an automated bus operating in rural areas based on a simulation

1.3.3 Virtual Room 3

Morning Session:

Software Engineering and Software Technologies 1

Chair: Timinger Holger

BBB-Support: Wirth Harald

09:30h-09:50h	Agchar Ismael: A Tokenizer for Single-Track Music
09:50h-10:10h	Albert Martin: Analyzing and Rating Electric Vehicles Cyber Security Risks
10:10h-10:30h	Beloschapkin Igor: Conception and development of a brain computer interface system as an end-user product
Break	
10:50h-11:10h	Durak Eren: Development and Validation of a new iterative parametrization approach for Equivalent Circuit Models of Li-Ion Batteries
11:10h-11:30h	Falk Maximilian: Aerodynamic CFD analysis of a ski jumper using an embedded full transient multi-body simulation
11:30h-11:50h	Fitznar Dennis: Tailor-made IT security standards for SMEs

Afternoon Session:

Software Engineering and Software Technologies 2

Chair: Zatocil Heiko

13:40h-14:00h	Krause Julia: A Decentralised Approach for Drive Decision Clearance of Automated Guided Vehicles at Intersections With Ambient-Approximated Traffic Control
14:00h-14:20h	Lamprecht Robert: Digitization in higher education
14:20h-14:40h	Mayer Florian, Bentz Jörg, Schweigler Christian: Analysis of the operation of a cooling supply system for a hospital
14:40h-15:00h	Mülbredt Natalie: Semi-automated 3D Reconstruction of Indoor and Outdoor Environments from RGB-D Data Captured by a Remote-controlled Robot
Break	
15:20h-15:40h	Münch Andreas, Mottok Jürgen: Development of a Certificate Administration for a Security Module
15:40h-16:00h	Oumard Christina: Development of an Open Source and Offline Voice User Interface for Blind and Visually Impaired People
16:00h-16:20h	Scharold Franziska: Requirements and trends of modern Manufacturing Execution Systems in the context of Industry 4.0
16:20h-16:40h	Schönhärl Stefan: Development of a learning platform for automotive security

1.3.4 Virtual Room 4

Morning Session: Machine Learning 1

Chair: Meiller Dieter

09:30h-09:50h	Anselstetter Fabienne, Schell Patricia, Warmuth Monika, Uhl Christian: Applications of Robust Dynamical Component Analysis (DyCA) on simulated Data
09:50h-10:10h	Arndt Lorin: Multicriterial optimization of a Convolutional Neural Network using the Hyper Space Exploration
10:10h-10:30h	Cevallos Gabriel: Data Workflow
Break	
10:50h-11:10h	Egeler Jonas: EEG Sound Quality Prediction with AI
11:10h-11:30h	Friedrich Sissy: Generating Trajectories for Robot Movements using Learning from Demonstration
11:30h-11:50h	Goltz Jonas: Reviewing Uncertainty Estimation in Deep Reinforcement Learning

Afternoon Session: Machine Learning 2

Chair:Limbrunner Thomas

BBB-Support: Mandel Gerd

13:40h-14:00h	Kornatzki Julia: Embedded Development of an Artificial Neural Network for Range Estimation on Infrared Images
14:00h-14:20h	Reineck Marcel: Evaluation of hyperscalability for object detection and tracking
14:20h-14:40h	Sahin Ahmet: Simulative data generation and labeling for autonomous driving specific AI models using MATLAB/Simulink, ROS and Gazebo
14:40h-15:00h	Schell Patricia, Anselstetter Fabienne, Warmuth Monika, Uhl Christian: Applications and Limitations of Dynamical Component Analysis (DyCA)
Break	
15:20h-15:40h	Vorderobermeier Tobias: Parameter choice for the short-time Fourier transformation in frequency-domain Blind Source Separation
15:40h-16:00h	Weber Georg, Theumer Philipp, Braunreuther Stefan: AI-based control-algorithm for stationary batteries with regards to load-management
16:00h-16:20h	Zeitler Sally: Realistic and efficient data generation for object detection and segmentation neural networks
16:20h-16:40h	

1.3.5 Virtual Room 5

Morning Session: Measurement Technologies 1

Chair: Aßmuth Andreas

09:30h-09:50h	Bugl Benedikt: Hardware Setup for Three-Dimensional Acoustic Source Localization
09:50h-10:10h	Heckel Robert: An active temperature control mechanism for miniaturized Pirani vacuum gauges
10:10h-10:30h	Herrmann Sven, Gleichauf Johanna, Niebler Christine: Analysis of the shape of chest movement induced by heartbeats for heart rate simulation
Break	
10:50h-11:10h	Hümmer Benedikt: A measurement setup to determine kinematic and kinetic changes of a rider-bike system after modification of geometrical aspects
11:10h-11:30h	Kögler Michael, Dendorfer Sebastian: Comparison of muscle recruitment in different muscle models following total knee arthroplasty
11:30h-11:50h	Leibold Christoph: Analysing Nitrifying Bacterial Communities in Biofilm-based Wastewater Treatment Plants Depending on Chemical Wastewater Parameters and Purification Processes

Afternoon Session: Measurement Technologies 2

Chair: Dietl Guido

BBB-Support: Grüger Klaus

13:40h-14:00h	Lukas Raphael, Kölbl Josef, Kufner Michael: Ultra Low Noise Amplifier for a Noise Measurement System
14:00h-14:20h	Mišák Jan: Applied error analysis on a research ORC Plant at the University of Bayreuth
14:20h-14:40h	Morf Fabian, Vinogradov Juri, Nopp-Nowak Flaviu, Engelbrecht Rainer: High-speed ADC Data Acquisition with an FPGA for OTDR-based Fiber Sensors
14:40h-15:00h	Riedl Thorsten: Development of measuring methods for condition monitoring, fault detection and optimization of a medical angiography floor stand
Break	
15:20h-15:40h	Schloder Benedikt: Miniaturisation of a Sensor System Using Reflectivity Based Surface Plasmon Resonance Imaging (SPRi)
15:40h-16:00h	Theiler Michael, Lewerenz Meinert, Schmid Michael: Investigation of the Float Current Analysis and the Float Current Settling Process via DVA on 18650 Li(NiCoAl)O ₂ /Graphite Cells
16:00h-16:20h	Unruh Denis, Engelbrecht Rainer, Dengler Simon: Theoretical and experimental investigation of code correlation methods for optical time domain reflectometry in POF
16:20h-16:40h	Weinmann Steffen: Method Development for the detection of filmic contaminations in additive manufacturing

1.3.6 Virtual Room 6

Morning Session:

Materials and Manufacturing Technologies 1

Chair: Hehenberger-Risse Diana

BBB-Support: Chiu Tak San

09:30h-09:50h	Bier Tobias: Feasibility study for additive manufacturing of movable step modules for a spiral escalator
09:50h-10:10h	Graml Johanna: Diffuse Reflectance Spectroscopy on TNT Samples With Different Carbon Contents
10:10h-10:30h	Guidolin Michele, Kroiß Tobias: Development of Measuring Strategies in the Free-Form Optics Manufacturing
Break	
10:50h-11:10h	Hanisch Patrick, Bischoff Sarah, Huber Robert: Adsorption of <i>Sporosarcina pasteurii</i> on quartz sand mixed with different additives
11:10h-11:30h	Heidacher Konstantin: Tufting process and machine to manufacture prototypes of a tension rods supported hydrogen pressure vessel
11:30h-11:50h	Heyder Susanne, Wieser Helmut, Burger Simon: Influence of different material grades on Urea-related corrosion phenomena in Automotive Applications

Afternoon Session:

Materials and Manufacturing Technologies 2

Chair: Reichenberger Marcus

BBB-Support: Oszlonyai Cornelia

13:40h-14:00h	Högl Christina: MEMS-based realization and characterization of dielectric barrier discharge plasma actuators for ionization applications
14:00h-14:20h	Kroiß Tobias, Guidolin Michele: Development of Grinding Strategies in the Free-Form Optics Manufacturing
14:20h-14:40h	Lichtenstern Isabella, Wucherer Stefanie: Simulation-based validation of an automated production and material flow control system
14:40h-15:00h	Lorentschk Michael, Rudolph Matthias, Bastl Daniel, Schwarz Sascha, Sudhop Stefanie: A slim SLA-3D-printed bioreactor suited for multiphoton microscopy
Break	
15:20h-15:40h	Meiser Joshua: Classification of the laser powder bed fusion pollution of the optical system phenomenon in optical tomography monitoring data with an analytically developed decision tree
15:40h-16:00h	Probst Florian: Experiments increasing the hardness of the high interstitial steel Cronidur30
16:00h-16:20h	Rauchheld Sarah, Reichstein Simon: Aluminium-Iron Intermetallic Metal Matrix Composites
16:20h-16:40h	Reitenberger Johannes, Goller Ralf: Analytical evaluation of vacuum buildup concepts for aircraft structures

1.3.7 Virtual Room 7

Morning Session:
No Talks

Afternoon Session:
Materials and Manufacturing Technologies 3

Chair: Emmel Andreas

13:40h-14:00h	Salg Manuel: Studies on the firing behavior of bone china and the influence of raw material components on strength and translucency
14:00h-14:20h	Schmid Stefanie, Lehle Karla, Schratzenstaller Thomas: Biocompatibility of Additive Manufactured and Surface Treated Cardiovascular Stents
14:20h-14:40h	Seibold Joshua, Hildebrand Jan Sebastian, Krcmar Wolfgang: Influence of pore geometries on the thermal shock resistance in ceramics investigated by numerical simulation
14:40h-15:00h	Seidel Felix: Improvement and optimization of the on-wing low-pressure-turbine repair process
Break	
15:20h-15:40h	Tröger Johannes: Comparison of a simulation-based with an analytical calculation of the temperature field of a laser process
15:40h-16:00h	Utz Elisabeth: Improvement of the solid-liquid separation of biogas digestate with a starch based flocculant
16:00h-16:20h	Whittlesey Niklas: Strain-Induced Embrittlement at Elevated Temperatures of Heat-Resistant Steel 16Mo3
16:20h-16:40h	Wrana Christian: Development and installation of a 3D-weaving machine to manufacture a strutted cuboid composite vessel

1.3.8 Virtual Room 8

Morning Session: Power Technologies 1

Chair: Weiß Andreas

09:30h-09:50h	Aleynikov Danil: Development of a calculation tool to support the planning of the utilization of hybrid emergency power generators
09:50h-10:10h	Bäuml Benedikt, Jaeger Magnus: Change in the energy market - opportunities for industrial companies
10:10h-10:30h	Baur Sebastien, Henze Diane, Limbeck Simon, Zeyer Klaus Peter: Impact of air supply parameters on in-vehicle performance of PEMFCs used in an ultra-efficient FCEV
Break	
10:50h-11:10h	Benke Lukas, Werther Martin: Aerodynamic design studies on new types of aircraft with vertical take-off and landing capabilities
11:10h-11:30h	Beringer Jakob, Mehta Kedar, Ehrenwirth Mathias, Zörner Wilfried: Sustainable materials for insulating high-altitude rural Kyrgyz residential houses: A parametric economic study
11:30h-11:50h	Böhmisch Markus: Designing the Logic Module of a Four-Mode Controlled Four Switch Buck-Boost Converter

Afternoon Session: Software Engineering and Software Technologies 3 Logistics and Organization

Chair: Wiehl Michael

13:40h-14:00h	Schubaur Philipp: Choosing a RISC-V Core for Implementing an FPGA-Based Security Module
14:00h-14:20h	Siegmüller Anna, Mottok Jürgen: Software Testing Workflow for a Multi-Controller Architecture Security Gateway
14:20h-14:40h	Sturm Elisabeth Christine: Computational Acoustics using OpenFoam
14:40h-15:00h	Toutouly Lovis, Steffens Oliver: Simulating realistic domestic hot water consumption of a complex apartment building in a dynamic building model in IDA ICE
Break	
15:20h-15:40h	Kempf Lena: Application of Lean Construction Management to sustainably increase of productivity in the construction industry
15:40h-16:00h	Kluger Felix: Structural Differences in the Higher Education Research in Germany between Universities and Universities of Applied Sciences
16:00h-16:20h	Rembold Anina: Use of Digital Assistance Systems in Production
16:20h-16:40h	Wachter Sarah Maria: Research on the Supply Chain resilience of German small and medium-sized companies

1.3.9 Virtual Room 9

Morning Session: Power Technologies 2

Chair: Beer Stefan

09:30h-09:50h	Briechle Maximilian, Raab Daniel: Investigation of the heat transfer during condensation of wet flue gas in horizontally, corrugated tubes
09:50h-10:10h	Czerwek Florian: Investigation of an innovative heat storage system with air module and ice storage
10:10h-10:30h	Fischer Maximilian Dominik, Goldmann Daniel, Schramm Simon: Options on the test planning for the AC/DC-Dual Active Bridge
Break	
10:50h-11:10h	Gegaj Lumbardh: Conversion of non-existent load-profiles for PV-Systems
11:10h-11:30h	Götz Rebekka: Techno-economic analysis of reactive power sources
11:30h-11:50h	Hanser Andreas, Dawoud Belal: On the development of a seasonal seasonal heat storage for single-family houses: Design boundary conditions including the storage heat losses

Afternoon Session: Power Technologies 3

Chair: Kreutzer Otto

BBB-Support: Liebl Simon

13:40h-14:00h	Kaiser Markus, Elias Jörg: Evaluation of possible charging demand of battery electric vehicles in parking garages and Park+Ride areas based on real entry and exit data
14:00h-14:20h	Kern Tobias: Modularity Analysis of Power Electronics Architectures
14:20h-14:40h	Knepper Karoline, Ehrenwirth Mathias, Zörner Wilfried: Potential of e- mobility in rural areas – Evaluation of opportunities and barriers based on literature review
14:40h-15:00h	Kuffer Alexander: Slip control of an induction machine in the field weakening region during six step operation
Break	
15:20h-15:40h	Lukas Sibö, Palme Frank, Pettinger Karl-Heinz: Influence of a novel binder material on the electro-chemical performance of silicon-containing anodes
15:40h-16:00h	Menne Valentina, Henze Diane, Limbeck Simon, Zeyer Klaus Peter: Development of a Vanadium/Vanadium Redox-Flow Battery for Demonstrational Purposes
16:00h-16:20h	Mutzhas Dominic: An Abstracted Process for a Prospective Energy-Demand Analysis Demonstrated on the municipality Höhenkirchen Siegersbrunn
16:20h-16:40h	Pace Dominik, Huber Lea, Heberl Michael, Dawoud Belal: Development of different H ₂ -storage concepts for reduced emission shipping

1.3.10 Virtual Room 10

Morning Session: Power Technologies 4

Chair: Haumer Anton

BBB-Support: Fersch Silke

09:30h-09:50h	Pellert Nico: Investigations regarding cooling of thermoelectric modules in a nano combined heat and power unit
09:50h-10:10h	Preis Michael, Rechenauer Christian: Development of the control strategy for the heating system in the MAGGIE research project
10:10h-10:30h	Reidl Tobias, Huber Lea, Heberl Michael, Dawoud Belal: Concept development of a hybrid ship driving system and investigation of different constellations of components and control strategies
Break	
10:50h-11:10h	Reischl Thomas: Dynamic Simulation of a HT-PEM Fuel Cell with Internal Methanol Reforming
11:10h-11:30h	Riedmaier Thomas, Bär Katharina, Zörner Wilfried: Comparison of different calculation methods for the outflow from pressurized vessels
11:30h-11:50h	Rückerl Alexander, Steffens Oliver: Potential analysis for long-term storage of a decentralized power-to-gas technology

Afternoon Session: Power Technologies 5

Chair: Taschek Marco

13:40h-14:00h	Schaller Timo: Influence of Hydrogen on the combustion process of a single cylinder spark ignited gas engine
14:00h-14:20h	Schweiberer Philipp: Determination of the restriction-free inductive and capacitive reactive power potential based on the example of a medium-voltage industrial operation
14:20h-14:40h	Starost Veit: Development and Validation of a 3L-ANPC Bridge Type Inverter Based on GaN HEMTs
14:40h-15:00h	
Break	
15:20h-15:40h	Weber Lukas, Jaeger Magnus: Chance in the energy market - opportunities for industrial companies
15:40h-16:00h	Weidlich Johanna, Reum Tobias, Schrag Tobias, Ehrenwirth Mathias: Analysis of the denomination and standard situation
16:00h-16:20h	Wopper Christoph: Development of a virtual fuel injector for operation with Diesel and Oxymethylenether
16:20h-16:40h	

1.4 Poster Sessions

Time Slot: 12:30h -13:30h

1.4.1 Poster Session 1

Chair: Walter Michael, BBB-Support: Chiu Tak San

<p>Agacdeviren, Deniz: Development of an Application for the Planning Process of Private Charging Infrastructure</p>
<p>Aleshin, Nikita: Highly dynamic real-time motion planning for flexible robot systems on the example of automotive assembly</p>
<p>Allrich, Vincent: Development of a holistic funding concept for smallest biogas plants</p>
<p>Anzenhofer, Alexander: Development of a simulation model for ultrasonic cutting tools</p>
<p>Arnold, Fabian: An Optical Method for Droplet Detection in Vapor compression Refrigeration Cycle Systems</p>
<p>Bader, Luca: Application of the fully probabilistic service life calculation in precast reinforced concrete elements with an increased proportion of reactive additives</p>
<p>Baldauf, Tobias: Modelling of biogas cogeneration units in a heat and electricity grid network</p>
<p>Barth, Tobias: Environment modeling and interaction with objects</p>
<p>Bröll, Lukas: Movement filtered heart rate variability (HRV) data from a chest-worn Sensor</p>
<p>Bruckschloegl, Jonas: Contribution to the Calculation of End Winding Inductances of Multiphase Induction Machines</p>
<p>Cameron, Emily: Possible causes of short interruptions in the high-voltage electricity network with automatic restart</p>
<p>Detling, Michael: Research into Future Strategies for the Security Testing of Embedded Systems</p>
<p>Diewald, Maximilian: Development of a Customizable Monolateral External Fixator for the Lower Extremities</p>
<p>Faust, Moritz: Development of a virtual reality simulation as a complementary approach in exposure based addiction therapy</p>
<p>Fiechtl-Otter, Georg: Analysis of company data with a focus on forecasting methods and inventory management</p>
<p>Flach, Charley Michelle: Development of concepts for direct heating of a biogas fermenter with hot product gas from methanation</p>
<p>Förster, Florian: Digital shadow of a modular production system</p>
<p>Frey, Lars: Development and simulation of business models for charging infrastructure and battery electric vehicles</p>

1.4.2 Poster Session 2

Chair: Schindler Wolfgang

<p>Fuxen, Philipp: Anomaly Detection for Automotive Cyber-Physical Systems with Deep Learning</p>
<p>Glashauser, Michael: Analysis of a multi-level battery management system with one DC-DC converter per battery cell</p>
<p>Göttling, Federica: Benchmark Analysis of the Vertical Comfort</p>
<p>Grabinger, Lisa: Causal Inference from an Engineering Perspective</p>
<p>Gremer, Michaela: Development of a gatedriver for a modular multiphase SiC inverter</p>
<p>Greve, Alina: Dimethyl Ether as a Clean Energy Source: Synthesis Routes and Catalysts</p>
<p>Guillermo, Luis: Characterisation of ultrasonic fields using quantitative schlieren imaging</p>
<p>Hansen, Philipp: AI-based expert system for project management</p>
<p>Hausmann, Philip Andrew: Image Stitching for Multi-Sensor Data Fusion on Drones</p>
<p>Heindl, Melanie: Development and experimental investigation of various hydrogen and heat storage composites</p>
<p>Hennemann, Lukas: Analysis of several state-of-the-art Convolutional Neural Networks for the Conception of a Model for the Face Detection of Neonates</p>
<p>Heusgen, Valentin: Potential Analysis of Relevant Renewable Energies in Germany</p>
<p>Hoang, Van Danny: Collaborative Robot - Pick and Place Tasks in a Household Environment</p>
<p>Hofmann, Christoph: Lifetime estimation on high-performance steels under static load</p>
<p>Husser, Evelyn: Preventing the Upper-Crossed Syndrome: a holistic approach to determine sitting positions to avoid and strength exercises to perform</p>
<p>Iberl, Andreas: Review of Water Transport in the Water-Bearing Conducting Bundles (Xylem) of Trees and Alternative Hypotheses on Their Causes</p>
<p>Ilter, Ahmet: Development of an experimental and operational modal analysis toolbox in MATLAB</p>
<p>Izycki, Thomas: Cooperative and Decentralized Path Planning with Path Optimization for a Swarm of Tiny UAVs</p>
<p>Jäck, Christian: Hot Powder Compression of FFF Components</p>

1.4.3 Poster Session 3

Chair: Kreutzer Otto, BBB-Support: Fersch Silke

<p>Joerg, Kilian: Active Noise Cancellation in glass structures with a LMS – algorithm</p>
<p>Joop, Dominik: Development of a liner integration concept for space- efficient hydrogen tanks</p>
<p>Kern, Annabelle: Concept and investigations for the development of an acoustic sensor system based on Atomic Layer Thermopiles (ALTPs)</p>
<p>Ketterle, Andreas: Effects of different PLA recipes on FDM printing results in terms of surface quality</p>
<p>Köck, Hannah: Infiltration of Hydrogel in Osteoarthritic Human Cartilage Explants</p>
<p>Kokorsch, Marcel: On a Low-Cost Flight Arena for a Quadcopter Swarm</p>
<p>König, Gabriel: Subjective and Objective Evaluation of Autonomous Driving</p>
<p>Kottre, Andreas: Towards the reduction of machine downtimes through mechanisms for automatic detection and visualization of complex fault situations</p>
<p>Kraupner, Johannes: Priliminary test for the development of approaches to reduce haemostasis in ECMO-systems according to optimized fluid mechanical operating factors and their validation</p>
<p>Kraus, Andreas: OREWA Optimization and restructuring of district heating networks including evaluation of transferability, ecology and economy</p>
<p>Krug, Niklas: Fieldbus communication for low voltage power electronics</p>
<p>Kullmann, Manuel: Design, Construction and Manufacturing of an Injection System for Liquid Rocket Engines under Consideration of Additive Manufacturing</p>
<p>Lamert, Sergej: Application of deep learning techniques for analysis of operating data of a hybrid buck converter</p>
<p>Leuze, Nico: Intelligent Robotic Systems - Perception-Based Manipulation</p>
<p>May, Fabio: Design of Percussion Robots in a Collaboration of Musicians and Engineers</p>
<p>Meisinger, Alexander: Usability of oemof to adapt an existing national energy model</p>
<p>Miedaner, Marco: Development of a modular injection mould including high-resolution 3D printed mold nests for production of economical prototypes and/or small series of parts used in medical engineering with a high level of detail (< 0.5 mm)</p>
<p>Mikschl, Manuel: Calibrated Differential Coupler Measurements on Automotive Ethernet Data Links</p>
<p>Mück, Jochen: Method for production planning and control of customer-specific products using the example of additive manufacturing</p>

1.4.4 Poster Session 4

Chair: Sehr Armin, BBB-Support: Schmidl Elisabeth

<p>Naulin, Janine: Potential of future ERP-systems</p>
<p>Neudecker, Christine: Energy management on the example HAW Landshut</p>
<p>Ott, Jonas: Design of an optimized DCDC-converter for efficient hydrogen production by electrolysis from fluctuating solar power</p>
<p>Paglia, Chiara: Identification of low-dimensional nonlinear dynamics from high-dimensional data</p>
<p>Pastore, Antonello: Industrial-grade AMR system with flexible kinematic concept and swarm capability</p>
<p>Rampl, David: Integration of the heat sector with sector coupling in a simulation model for energy cell design</p>
<p>Reindl, Thomas: Comparison of selected additive manufacturing processes in terms of dimensional accuracy, surface quality and mechanical properties</p>
<p>Rosner, Florian: Control of an Inverse Pendulum Using Deep Reinforcement Learning</p>
<p>Salzberger, Stefan: AI-supported 6 dimensional pose estimation of small load carriers in intralogistics</p>
<p>Schaeffer, Leon: Preliminary studies on a novel hand orthosis based on a prestressed compliant structure</p>
<p>Scharnagl, Tassilo: Mass surveillance of an ant colony</p>
<p>Schäufele, Thomas: Investigation of magnetic properties with iron loss separation for soft magnetic laminated ring core sample up to 250 °C</p>
<p>Scheuerer, Ralph: Speaker recognition techniques on laryngectomy voices</p>
<p>Schidek, Anna: Flexibilization of Technical Development Processes of Medical Devices</p>
<p>Schlereth, Benedikt: Suchraum für die multikriterielle Optimierung von Merkmalsberechnungen für das maschinelle Lernen bestimmen</p>
<p>Schmidt, Manuel: Construction of rhIL-4 expression vector</p>
<p>Schoplocher, Paul: Macro simulations as the basis for a dynamic building system modeling to create a digital twin</p>
<p>Shigailow, Markus: Development of a Modular Structured Model-Based Control for Determining a Distributed Energy System's Operation</p>
<p>Simon, Marvin: Deep Reinforcement Learning for Fighting Forest Fires with a Network of Aerial Robots</p>

1.4.5 Poster Session 5

Chair: Haumer Anton, BBB-Support: Liebl Simon

<p>Sparrer, Lisa Marie: Virtual vehicle test platform for human-machine interfaces</p>
<p>Stapff, Veronika: Process monitored production of multi-material components with automated integration of sensors using Additive Manufacturing</p>
<p>Straller, Armin: Automated Testing Framework for Path Planning Algorithms using Scenario Description Files</p>
<p>Swierkot, David: Transformation for video compression</p>
<p>Theen, Johannes: Development of a flying optical reconnaissance system for autonomous assistance of emergency personnel in rescue missions</p>
<p>Timur, Issayenko: Small Electric Vehicle Engineering – Model-Based Testing of Li-Ion Battery Systems</p>
<p>Urlhart, David: The Ladder of causation</p>
<p>Veitl, Jakob: Nanofibrous interlayers establishing adhesion between lithium-ion-battery components</p>
<p>Vollenbröcker, Julia: Development of an Algorithm for the Operationally Optimized Scheduling of Power Generation Plants in a Microgrid</p>
<p>von Wilcken, Jean-Luc: Development and evaluation of models for estimating the temperature loads of sounding rockets</p>
<p>Wagner, Felix: Towards efficient POSIX-compatible thread level parallelism on the ParaNut processor</p>
<p>Weber, Julia: Alternative Powertrain Concepts for Logistics Vehicles</p>
<p>Weber, Robert: Arduino-based pH Monitoring and Control for All-Iron Redox Flow Batteries</p>
<p>Weigelt, Samuel: Improved Tool-Based Collaboration between Systems Engineer and Project Manager</p>
<p>Weindler, Jeremy: Development of an innovative power-to-heat technology for the integration of renewable electricity surpluses</p>
<p>Weinzierl, Manuel: Sustainability assessment of utilization concepts for heat from biogas combined heat and power plants</p>
<p>Wendt, Thilo: Low noise actual value acquisition in power electronic devices</p>
<p>Werner, Patrick: Low temperature district heating and cooling networks</p>
<p>Zinnel, Laura: Tool Condition Monitoring</p>

Chapter 2

Papers: Software Engineering and Software Technologies

Contents

2.1	Analyzing and Rating Electric Vehicles Cyber Security Risks	30
2.2	Conception and development of a brain computer interface system as an end-user product	34
2.3	Development and Validation of a new iterative parametrization approach for Equivalent Circuit Models of Li-Ion Batteries	38
2.4	Tailor-made IT security standards for SMEs	44
2.5	A Decentralised Approach for Drive Decision Clearance of Automated Guided Vehicles at Intersections With Ambient-Approximated Traffic Control	49
2.6	Analysis of the operation of a cooling supply system for a hospital	54
2.7	Semi-automated 3D Reconstruction of Indoor and Outdoor Environments from RGB-D Data Captured by a Remote-controlled Robot	58
2.8	Development of an Open Source and Offline Voice User Interface for Blind and Visually Impaired People	64
2.9	Requirements and trends of modern Manufacturing Execution Systems in the context of Industry 4.0	70
2.10	Development of a learning platform for automotive security	73
2.11	Choosing a RISC-V Core for Implementing an FPGA-Based Security Module	76
2.12	Computational Acoustics using OpenFoam	81
2.13	Simulating realistic domestic hot water consumption of a complex apartment building in a dynamic building model in IDA ICE	87

Analyzing and Rating Electric Vehicles Cyber Security Risks

Martin Albert

Ostbayerische Technische Hochschule Regensburg

albert-martin.de

Email: martin1.albert@st.oth-regensburg.de

Abstract—The electrification of a vehicle comes along with an increased attack surface for hackers. Therefore analyzing and identifying weak points and their damage potential is essential for stakeholders of the vehicle industry.

This paper will analyze the attack points and paths of electric vehicles. Part of the investigation will be the charging interfaces, charging protocols, and charging infrastructure. Furthermore, will some interesting scenarios be proposed and rated with the ISO/SAE 21434 standard[1]. At last, the impact of such attacks will be analyzed for the financial impact of insurance companies.

I. INTRODUCTION

Digitization takes over more and more parts of our lives. The same can be said about the automotive sector as the cars not only get more connected, but the engine types also shift slowly from combustion towards electric, as more electric car models get introduced. With this move of more digitization, an increased attack surface comes along used by hackers. Therefore analyzing and identifying weak points and their damage potential is essential for stakeholders of the vehicle industry.

That is why this paper will analyze the attack points and paths of electric vehicles, and propose some interesting scenarios which will be rated with the ISO/SAE 21434 standard. Furthermore, will the impact of such attacks be analyzed, but only for the financial impact of insurance companies.

II. THREAT SCENARIOS IN ELECTRIC VEHICLES

By defining important attack paths and damage scenarios, specific for electric vehicles and their infrastructure (e.g. charging stations), threat scenarios will be defined and rated. The attack points can be taken as a starting point. Each attack point alone can be an attack path, but combinations of these can reveal even more interesting attack paths and result in more versatile damage scenarios.

The probability of these attack paths happening in the real world will not be part of this investigation, as this depends on the software/hardware implementation from each OEM and supplier for each individual vehicle.

A. Points of Attack

Electric vehicles have some differences in their points of attack compared to a conventional electric connected vehicle, as the integration of a battery, an electric motor, and the

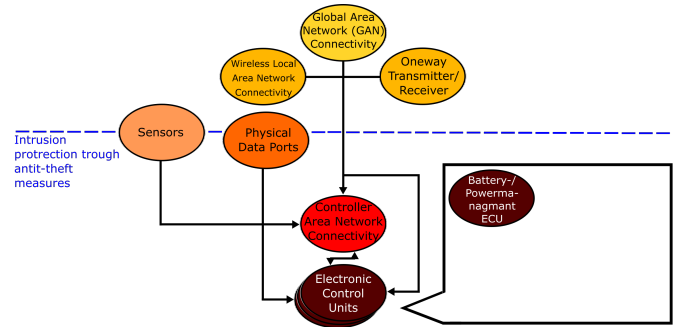


Figure 1. Attacksurface of electric cars and the resulting damage

consequential changes in charging and driving of this vehicle, results in changes of components. Since electric vehicles and the associated individual innovations of the manufacturers are still relatively new technologies (compared to the millennia of combustion vehicle distribution) in the automotive industry, the identification of security gaps is particularly important here.

Attack Point: Charging Interfaces: The charging port of an electric vehicle is one of the physical data ports, but it is also accessible from the outside of the vehicle. The access is in normal conditions, protected against unauthorized access by requiring user interaction inside the vehicle (e.g. charging port unlock by button). This is can be seen as valid until an active charging process exposes the ports and an attacker can access them. Charging is a relatively common situation in electrically powered vehicles, as the charging times are long and the capacity of the batteries is, in the current state, too low to allow for big intervals without charging. Therefore charging ports should be hardened to the same level of security as other publicly accessible interfaces (e.g. WLAN).

Attack Point: Control of charging process and battery management: Furthermore, in electric vehicles, the control of the charging process and the battery management are separated from the other components of the vehicle. This is done both when separating communication paths and control units inside the vehicle. Due to the high hazard potential of batteries, both the EV-specific communication path and the control units involved become a possible point of attack with serious

consequences.

Attack Point: The Charging infrastructure: The charging infrastructure is more important for the security in electric vehicles than it was for conventional combustion engine vehicles, as the refilling process in conventional cars relied on mechanics. Electric Vehicles require active digital communication, between vehicles and charging stations, before they can establish a safe charging process. Furthermore were management systems for the charging station implemented (e.g. Open Charge Point Protocol (OCCP)), which enables data exchange on the internet. The University of Louisiana found in an investigation, that this leads to possible attacks in vehicles. [2] The Fraunhofer research institute uncovered some vulnerabilities in charging station [3]. We, therefore, list the possible points of attack for the charging infrastructure, in the following:

- Connection to the Internet
- Authentication
- Smartphone
- Physical Access

Connection to the Internet: Since the charging stations are often connected to the Internet, the possibility to manipulate them rises. This includes manipulation of the transmitted data (e.g. through "man-in-the-middle"-attacks) or direct access to the software using maintenance access.

Authentication: Authentication during a charging process is also a target for attack. The high diversity of payment options (NFC, WLAN, apps, etc.) on these devices creates many opportunities for attackers. Research by Mathias Dalheimer showed that some charging cards are susceptible to manipulation [4].

Smartphone In addition to the hardware keys, some manufacturers also offer to start the charging process via an app. As a result, not only the app but also the operating system running on the smartphone must provide a secure environment. Some apps, therefore, require a secure element.

Physical Access Finally, the system can also be attacked via physical access to the charging infrastructure. This is more accessible with charging stations than with conventional refueling methods. Charging stations are not tied to individual filling stations with video surveillance but are widely distributed across many parking lots. This reduces the protection against physical attacks.

B. Resulting selected Attack Paths

Attack Path: Malicious battery management ECU firmware update over the air

The trend of updating the firmware of vehicles over the air gains popularity, as new features and security-related patches could be integrated without the need for a repair shop. The updates are delivered over the internet or directly over wireless technologies. But this comes with its potential security risks. Let's suppose an electric vehicle class with over-the-air updates (internet-based) allows updating the firmware of the battery management ECU. Also, suppose that a vulnerability in the communication allows to manipulate

sent updates or lets an attacker create his messages with malicious firmware updates.

Because the attack can be performed without physical access to the car, an attacker has an **Unlimited** window of opportunity. As this attack can be performed with messages sent over the internet and tools for crafting all kinds of messages can be crafted with tools freely available, no special equipment (**Standard**) is needed. As this attack would require modification to the firmware, information about the ECU (processor architecture, original firmware, functionality in the car, etc.) would be required. This means that either some **Confidential** information has been leaked or could be accessed through another attack. The confidentiality level of the required information can increase, depending on the kind of attack that allows modifying/creating malicious messages for updating the firmware of the vehicle. The attack would at least need one **Expert** as the modification of the firmware needs knowledge about the functionality of every used or attacked component in the car and how to trigger. Depending on the complexity of the attack and the firmware even **Multiple Experts** are reasonable. The time needed to prepare and perform the attack relies heavily on the underlying attacks and complexity of the firmware. Even an expert will take more than a month to find and test a vulnerability in the over-the-air communication and also get access to the firmware of the vehicle, understanding it and modifying it. A time of **<6 Months** is possible, but more is also imaginable as the complexity increases.

Depending on the real attack this results in a **Medium to Low** attack feasibility.

Attack Path: Malicious firmware updates of charging stations to attack car electronics

As of today, there have been multiple attacks on charging stations. Some involve changing the running firmware. This can be done in various ways. The OCCP 1.6 protocol is widely used and still gets integrated into modern charging stations (as of today). It norms the communication between these stations and the backend server, which enables load balancing, payment systems, authentication systems, and more. Version 1.6 of the protocol does not define necessary encryption for firmware updates. As a result, many charging points didn't integrate any security measures for this feature. Combined with general missing encryption of messages an attacker can manipulate the firmware of charging stations once he has access to the network. OCCP 2.0 requires a secure implementation of these features, but version 1.6 is still widely used. After gaining control of a charging station the communication between it and an electric vehicle can be controlled. Strong security measures may prevent attackers from interacting with the internal communications of the vehicle.

To manipulate the battery, another vulnerability in the battery management and/or power management ECU is required.

Assuming the described attack path is possible, where one or multiple charging stations get taken over (through the internet), the communication with the charging vehicle is

manipulated to grant access to the inner communication of the vehicle. A vulnerability in the power management/battery management units allows an attacker to manipulate the possible voltages, which can cause damage to electronics or the battery.

If the described management ECU would be attacked alone, a **Moderate to Easy** window of opportunity would be given as physical access would be required. But this proposed attack enables updates over the internet to create an attack chain with an **Unlimited** window of opportunity and is scalable to limitless amounts of cars. To analyze and test the attack **Specialised** equipment will be needed, as the communication and testing manipulation of firmware would at least require non-everyday tools (e.g. CAN-bus adapters, JTAG-debugger, etc.). The complexity in such an attack requires knowledge about multiple very specific topics in the vehicle and therefore not only needs **Multiple Experts** but also needs at least **Restricted** information about the inner working of the vehicle. Resulting of the complexity of this attack, and depending on the number of experts involved in this attack, it could be prepared in **less than 6 months**. A longer time is also reasonable as the attacks could be more complex and the number of people working on it can vary. This leads to **Medium** attack feasibility.

Attack Path: Taking over communication between vehicle and charging station to introduce malicious messages into the vehicle

The charging management of an electric vehicle needs to communicate with the charging station, before starting the charging process. The vehicle should handle the incoming messages isolated from the internal network of the vehicle. A vulnerability that allows introducing or reading messages in the internal network from the charging port can leak private information or enable further attacks. But also non-protected messages can be sent into the car and trigger actions in the car. For example, unlocking the car or manipulating the drive speed.

Because the attack needs to be performed with physical access to the charging port of the car, but the port can be accessed while charging the vehicle, an attacker has an **Easy** window of opportunity. As this attack can be performed with messages sent over the charging port, hardware for the underlying communication standard is needed (**Specialised**). Such attacks would require information about messages in the internal communication in the vehicle. This means that either some **Restricted** information has been leaked or could be accessed through another attack. The confidentiality level of the required information can increase, depending on the kind of attack that allows modifying/creating malicious messages for updating the firmware of the vehicle. The attack would at least need one **Expert** as the modification of messages and the used communication standard are specialized. Depending on the complexity of the attack **Multiple Experts** are reasonable. The time needed to prepare and perform the attack relies heavily on the underlying attacks and complexity of the firmware. A time of **<1 Month** is possible, but more

is reasonable as well as the complexity increases. This leads to **Low** attack feasibility.

III. DAMAGE SCENARIOS

Damage Scenarios can be separated into two categories. The first category contains connected vehicles as a whole (blue), whereas the second category focuses on electric vehicles (green).



Figure 2. Damage Scenarios of connected and electric vehicles

A. Damage Scenarios for connected vehicles

If there are vulnerabilities present at a point of attack, they can be exploited to cause damage. There are several possible types of damage, which are listed below.

THEFT: One goal of attackers can be to bypass the vehicle's anti-theft protection. If it can be bypassed (e.g. with a relay attack) then the vehicle can be stolen. In addition to the loss of the vehicle, there is also the possibility of the usage for other illegal activities, which can harm not only the owner of the vehicle but others as well. Depending on the scalability of the underlying attack, the damage can be anything for an insurance company.

PRIVACY: Due to the linking of vehicles with the internet and the use of more and more data to provide functions, a lot of private data is stored in and passed to the vehicle, including sensitive data, which is a valuable attack goal for an attacker, for example, login details. The privacy of a road user is mostly not included in insurance. That is why damage to privacy can be seen as negligible. Only a company vehicle leaking confidential information of the insurance can cause damage depending on the criticality of the information.

DENIAL OF SERVICE: A DoS attack can paralyze individual control units or the communication between systems. As a result, functions can no longer be executed. If the DoS attack is persistent, a workshop must be visited to eliminate it by installing official firmware or replacing the affected control units. Only damage with good scalability potential can cause non-negligible damage for insurance companies.

PHYSICAL DAMAGE: Physical damage can be caused by for example deploying airbags, or damaging electronics by short circuits. This can be achieved by manipulated software. As a consequence, the vehicle must be transported to the workshop to repair the damage. Just as before is the scalability of the attack and the caused damages, the decisive factors and can vary strongly.

DAMAGE TO SURROUNDINGS: The vehicle itself can also emit danger, as they can be used as weapons. They move large masses at high speeds and in the event of a control loss, can harm not only the driver and his occupants but also other road users and generally uninvolved objects. They also transport some kind of energy reservoir (fuel, batteries, hydrogen, etc) which are flammable or even explosive. This can also be used to damage surrounding objects. The potential of financial damage is enormous, as one vehicle can create chain reactions that lead to massive costs. For example, a vehicle burning down in a multistory car park starts a chain reaction of surrounding cars burning down as well. But just like in the theft case, the damage depends on the scalability of the attack. If only minor damage to one surrounding object can be done a smaller financial impact can be expected.

B. Damage scenarios for electric vehicles

The impact of security vulnerabilities on electric vehicles was studied at Carnegie Mellon University in Pittsburgh, Pennsylvania. Attacks were classified into two subgroups:

- Temporary Damage
- Permanent Damage

Generally, the impacts in electric vehicles can be seen as new subclasses of connected vehicles.

DISABLING CHARGING: A charging fault is a subclass of DoS attacks. As a result, the vehicle cannot charge power from the charging equipment. This can lead to the vehicle becoming immobile and having to be repaired in a workshop and therefore can cause a big financial impact if the attack is scalable to many vehicles.

RANGE MANIPULATION: Another scenario is range manipulation. In this case, the vehicle's software is modified, so that a different voltage is applied to the battery. This achieves the effect of either more range with less power or vice versa. This is already being done by car tuners. However, permanent damage (to the battery or other electric components) can be caused by improper settings. As this attack would shift the payment obligation from the insurance to the owner of the vehicle, at least a moderate impact can be expected. The ease and widespread of an attack causing this can increase the impact.

BATTERY ATTACK: Range manipulation, or performance tuning, can shorten battery life by operating the battery outside of specifications. While battery damage is a side effect there, malicious manipulation (e.g., constantly charging and discharging the battery) can also make the battery a direct target for attackers. By bypassing the safe parameters of the batteries (e.g. falling below the minimum charge, exceeding the maximum charge, or exceeding the maximum charging voltage), the longevity can be damaged, or the battery can even become a safety issue (e.g. fire). The direct battery damage is not covered by most insurances, while further damages to

surroundings can open up the question of who is to blame for a failed battery and therefore further surrounding damage.

FIRE: If a battery is overloaded, e.g. by operating it outside its designed safety parameters, a fire can be started. Due to the size of the battery in electric vehicles and their design, it is not possible today to extinguish every cell. Thus, a fire in electric vehicles always ends in complete burnout. This can, just like before, also damage the environment around the vehicle and a single vehicle can cause Major damage to the surroundings.

PAYMENT DETAILS: The charging station itself and its interfaces can also become the targets of attackers. Manipulation or stealing of payment data is possible and can enable fraud. Just as with the privacy details, insurances are mostly affected by these if companies' resources are in danger by this attack.

IV. CONCLUSION

Within this paper, the attack points of electric vehicles were analyzed and used to create potential attack paths. These attack paths could be rated after the ISO/SAE 21434 norm. Furthermore were the damage scenarios and their financial impact on insurance companies was discussed.

Using these information priorities in security development and insurance damage calculations can be made. The abstract form of the risk analysis allows to cover a large number of cases and can be adapted to varying situations.

Combining all of this allows an increase of security in vehicles and allows insurance companies to reevaluate current vehicle damage potentials.

REFERENCES

- [1] "Iso/sae dis 21434, road vehicles — cybersecurity engineering," ISO/SAE International, Standard, Mar. 2020, key: ISO/SAE DIS 21434:2020(E).
- [2] U. of Louisiana, R. Gottumukkala, R. Merchant, A. Tazuin, K. Leon, A. Roche, and P. Darby, "Cyber-physical system security of vehicle charging stations," Tech. Rep., 2019, https://www.researchgate.net/publication/334630130_Cyber_physical_System_Security_of_Vehicle_Charging_Stations, Last Visit: 15.04.2021.
- [3] I. B. Fraunhofer Institute, "Expert from fraunhofer itwm uncovers security vulnerabilities of charging stations," Tech. Rep., 2018, <https://www.fraunhofer.de/en/press/research-news/2018/January/security-vulnerabilities-of-charging-stations.html>, Last Visit: 15.04.2021.
- [4] M. Dalheimer, "Schwarzladen: Ladekarten manipulieren leicht gemacht," Tech. Rep., <https://gonium.net/blog/2017/10/26/schwarzladen/>, Last Visit: 15.04.2021.

Conception and development of a brain computer interface system as an end-user product

Igor Beloschapkin

Technische Hochschule Nürnberg Georg Simon Ohm
Fakultät Elektrotechnik, Feinwerktechnik Informationstechnik
90402 Nürnberg
beloschapkinig61248@th-nuernberg.de

Abstract—A Brain Computer Interface (BCI) is an interface between a computer and, in this case, the human brain. At this point in time there are many scientific solutions for the use of a BCI but none of them are practical at all. This paper is about the conception and development of a tactile BCI system for communication with the usability of an end-user product. The goal is to have a closed BCI system, which can be used by Amyotrophic Lateral Sclerosis (ALS) patients and alike, without them or their caregivers spending many hours getting into BCI software.

I. INTRODUCTION

Amyotrophic lateral sclerosis (ALS) is a group of rare neurological diseases that mainly involve the nerve cells (neurons) responsible for controlling voluntary muscle movement. Voluntary muscles produce movements like chewing, walking, and talking. The disease is progressive, meaning the symptoms get worse over time. Currently, there is no cure for ALS and no effective treatment to halt, or reverse, the progression of the disease.

Once the patient is unable to produce any eye movement, the so called totally locked-in state (TLIS) is reached and concurrent eye-tracking systems cannot be further used for communication with the outside world. Thus, the only way to communicate with the patient is a Brain Computer Interface (BCI), measuring the brainwaves using Electroencephalography (EEG). The BCI presents a stimulus to the user and the brain reacts with event related potentials (ERPs). We record that electrical brain activity and detect the ERPs through signal processing. Most BCIs use the *BCI2000* software, working with a regular A-Z, 0-9 Matrix, looking for the P300 wave in the patients brain to calibrate and configure such (reference to figure 1). The P300 wave is an ERP elicited in the process of decision making, such as *Heureka* moments, measured by an EEG. Using this data, we create commands such as spelling a letter or pressing a button. A BCI as of now is a typical research system, used and developed by scientists and engineers over the course of many years, not something for the regular user. Therefore the usability is usually very bad.

A. BCI Principles

A BCI system mainly consists of three parts:

- Recording electrical brain activity
- Analyzing the data through signal processing

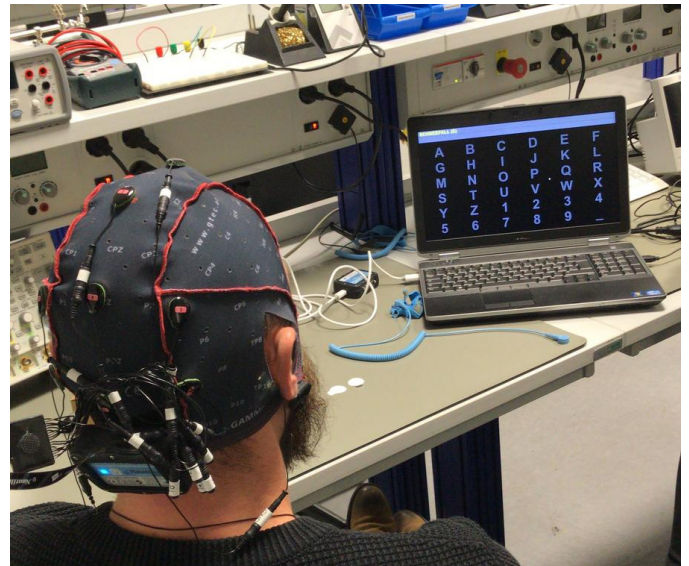


Figure 1. BCI2000 Copyspeller With A-Z, 0-9 Matrix

- Using the processed data to create commands

The *recording of electrical brain activity* can be done in an invasive and non-invasive way. At the Technische Hochschule Nürnberg we use an EEG as a noninvasive BCI. An invasive alternative would be *electrocorticography*, which is a type of electrophysiological monitoring that uses electrodes placed directly on the exposed surface of the brain. The *analyzing of the data through signal processing* and the *creation of commands* is done purely in software.

1) *EEG*: An EEG is a device to record the electrical potential of the brainwaves through the scalp [1]. The recorded signal is then processed by an amplifier and a number of filters. Further signal-processing can then extract the P300 signal from the data. For a BCI which is specialized in extracting the P300 signal, only the electrodes P08, P07, P0Z and CPZ are needed [2].

2) *P300*: The user has to focus on the target and is presented by a random order of stimuli, of which one contains the target. The P300 signal is an ERP which follows after the presentation of a rare target among nontargets (reference to figure 2). The figure shows the P300 as the red signal and

a regular EEG following nontargets as the blue signal. The

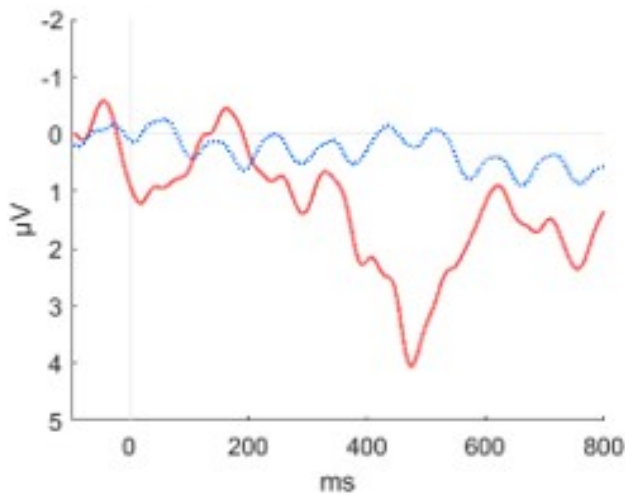


Figure 2. P300 Signal (red)

computer recognizes the P300 and thus the intention of the user. This can then be used to process another command, such as spelling a letter.

B. Tactile BCI

An ALS-patient in the TLIS, unable to move their eyes, needs another approach. The Technische Hochschule Nürnberg has developed the tactile BCI system for this particular use case. It stimulates the user not by focusing on a visual target but by focusing on a vibratory target. We have developed little stimulatory motors, which are usually used in game controllers or smartphones (reference to figure 3). These so called *Taktilos*



Figure 3. Taktilos

are attached to various areas of the human body, for example both arms and legs for a total of four *Taktilos* (reference to

Motor Number	Body Area
1	Right Arm
2	Left Arm
3	Right Leg
4	Left Leg

Table I
TACTILE 4X1 MATRIX

table I. They vibrate in a random order to present random stimuli. The user now has to focus on a single area of stimulus, which presents the target of the four *Taktilos*. Whenever the target now vibrates among the nontargets, a P300 signal is evoked. The P300 evoked by a tactile stimulation is almost as strong as a P300 evoked by visual stimulation (reference to figure 4).

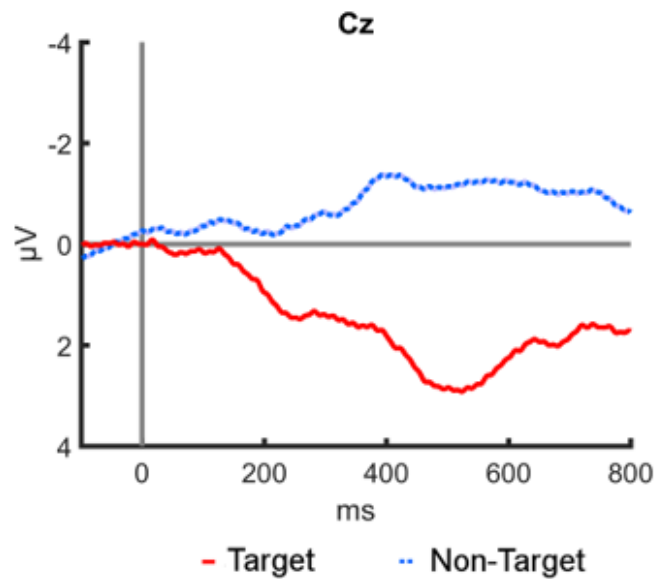


Figure 4. Tactile P300 Signal

C. Current state

The current system uses BCI2000 as the core software on a personal windows computer. The EEG hardware is connected to the computer on which BCI2000 runs. On that same computer we run our own Tactile BCI Filter software which parses the output of BCI2000 and sends it to an ESP32 mikrocomputer by UDP. The ESP32 itself drives the *Taktilos* through the General Purpose Input/Output (GPIO). Figure 5 shows the flowchart of the current system.



Figure 5. Flowchart of current tactile system

D. Concept

The goal of this project is to develop a BCI system with the following characteristics:

- Good usability
- Open Source
- Future sustainability

Our BCI system should provide the user with a tactile BCI in a closed device. It should not be installed on the private computer, as most BCIs are now. It should also automatize most of the steps needed to calibrate a P300 speller, specialized on the hardware used, instead of providing a lot of different configurations. Modern BCI software usually provides a lot of functions and configurations for being used in a lab by scientists and engineers. This makes a regular BCI system hard to use by caregivers and patients who may need it for daily communication. Furthermore it should be open source, to provide the functionality to anyone. The future sustainability is also very important for the system as not to become obsolete in the near future.

1) *OpenViBe*: OpenViBe is a software platform that enables to design, test and use BCIs. It can also be used as a generic realtime EEG acquisition, processing and visualization system. It is more modern than BCI2000, the de facto standard in BCI software, and provides a graphical user interface (GUI) for designing BCI scenarios (reference to figure 6). The current

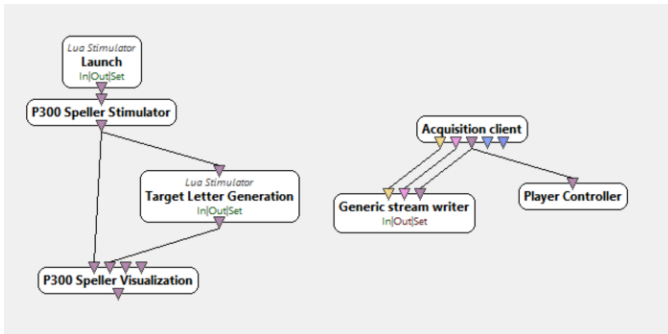


Figure 6. OpenViBe Designer

version 3.1.0 includes an XDown Filter in the P300 classification to further enhance evoked potentials[6]. For scripting, Lua can be used to automate most of the calibration. The first step in improving the usability and future sustainability is by adjusting our tactile BCI system from using BCI2000 as the core software to using OpenViBe. This includes changes in the Tactile Filter Software as well as the ESP32.

2) *Bluetooth Low Energy*: Figure 5 shows that the current connection between the computer and the ESP32 uses WIFI to transmit User Datagram Protocol (UDP) packets. The ESP32 currently opens up it's own WIFI node. Connecting the personal computer to the node ensures a direct connection between the computer and the ESP32 but it prevents the computer from using another WIFI in parallel. As with all TCP/IP protocols, UDP also has the downside that the message itself is encapsulated and passed on to the Network Layer. Therefore it provides no *congestion control* [3]. If the operating system is sending out packets in the background, for example during an update process, the messages are not transferred immediately because there may be other messages in queue first. This

can slow down the motor stimulation, and thus the P300 classification, by more than 100ms, which can make the stimulus useless. TCP on the other side does not always send out immediately, as it has to wait for ACK. Because of these reasons the WIFI connection will be replaced by a Bluetooth Low Energy (BLE) connection, which usually suffers from no such problems. The latency in BLE connections for short messages, such as in our tactile BCI system, ranges usually from 7.5ms to 22.5ms [4], which is more than enough for our P300 classification. The BLE connection itself is implemented by an already existing Game Controller Library for the ESP32, which will also provide a *GRID Interface* for setting up the communication (reference to figure 7).

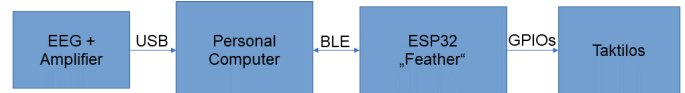


Figure 7. Flowchart of the tactile system using BLE

3) *GRID interface*: GRID is a software to assist in communication [5]. It is widely known in the medical area and used by ALS patients and alike, with, for example, an eye-tracker. The software presents graphical rows and columns which contain elements that can be programmed to activate certain buttons or functions of a computer (reference to figure 8). It can be used to control a computer and to communicate

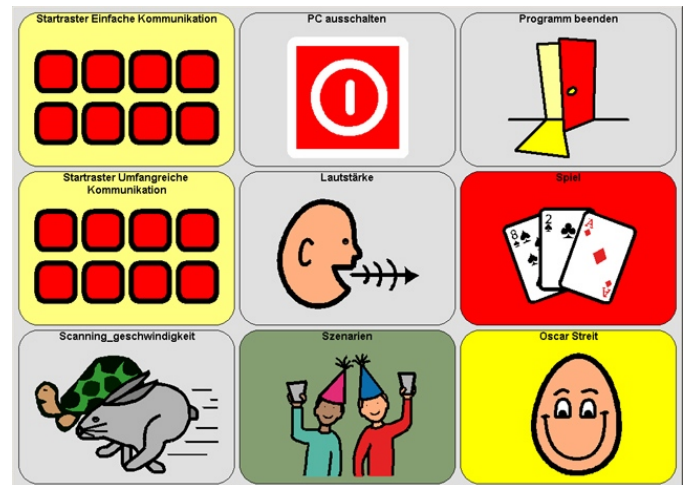


Figure 8. GRID 2 communication software

to sustain the independence of the user. The TLIS can make it impossible for an eye-tracker to be used as the hardware to control the GRID software, thus we want to enable an interface between our tactile BCI system and GRID. Users will be able to easily implement our tactile BCI system into their already running GRID configuration. The GRID software can be controlled by interfaces such as AUX input or game controller input. We are implementing a game controller emulation on the ESP32 to not only be used by the tactile BCI system as the driver for the Taktilos, but also as a feedback to give input to GRID. This way a successful P300 extraction can

trigger a function on the computer already pre-programmed by the user, such as opening a browser or communicating with the caregiver.

4) *Raspberry Pi*: After implementing all those changes to the existing system, which runs on a computer, we are working on creating another BCI system in parallel which is isolated from the main system and can be used to distribute the BCI system to the regular user. Here we are going to use a regular Raspberry Pi as the hardware core of the tactile system. It provides us with a computer with enough computing power to calculate P300 extractions, while also being cheap and small. This way we can isolate the BCI system from the personal computer of the user. Because of the complexity of a BCI software system, this provides the feature of having a complete set up operating system (OS) image which can be worked upon and then synchronized on all our tactile BCI systems. By running OpenViBe as the BCI software of choice we can

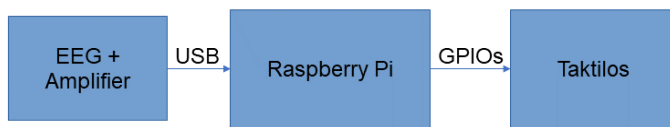


Figure 9. Flowchart of concept tactile system

also automate a lot of the setup of a communicative P300 BCI. This way we can set up a *BCI Box* that works out of the box and thus can be used by regular caregivers and patients.

5) *Unicorn BI*: The current EEG used in our tactile BCI system is the gUSBamp developed by *g.tec medical engineering*. The company itself is specialized in brain computer interface technology and neurotechnology. They produce invasive and non-invasive hardware for real-time data analysis. The g.tec EEGs, being the standard in BCI technology, are supported by most BCI software. The gUSBamp is an amplifier made for the acquisition of biosignals such as EEGs for the brain or EKGs for the heart. It's a medical product and supports up to 16 channels for signal acquisition. For a user that wants to use a BCI system for basic communication, it has a few drawbacks: It is rather hard to set up because of wet electrodes and it has a reasonably high price for an end-user. The electrodes have to be prepared with a contact gel, which can be rather messy and takes some experience. The *Unicorn Hybrid Black* on the other hand is a rather new BCI EEG for end-users developed by g.tec. It's price is less than a factor of 10 compared to the standard g.USBamp and the dry electrodes can be used without any contact gel. The cap can just be pulled over the scalp and after a check of the signals in the software, the calibration can begin (reference to figure 10). Besides having a much better usability it also has a rather modern design, which can make people using the device more comfortable.

II. CONCLUSION

Creating a closed, tactile BCI system by migrating the software core from BCI2000 to OpenViBe and setting it all

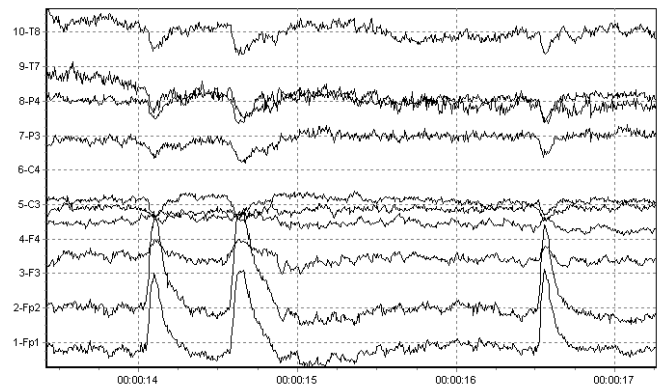


Figure 10. EEG channel signals

up on a Raspberry Pi for the system to be isolated from the private computer of the user will be fundamental steps in the direction of a BCI system directed at a regular end-user. The automation of the calibration and the setting up of a P300 speller using Lua scripting will change the way BCI systems are used and looked at by regular users and engineers alike. These steps should improve the usability of the tactile BCI system to such a degree that it can be used by caregivers and patients all around the world to enable basic communication.

ACKNOWLEDGMENT

I would like to thank Prof. Dr-Ing. Thomas Giesler for letting me work on this interesting, future-driven project. Furthermore i would like to thank the BCI Team Würzburg Prof. Dr. Andrea Kübler, Matthias Eidel and Maria Pfeiffer for collaborating in this project. Also thanks to Wolfgang Tröger, an ALS Patient who works together with the Technische Hochschule Nürnberg on testing the BCI systems we develop and the laboratory engineers Martin Wimmer and Sonja Rittmeier.

REFERENCES

- [1] Nunez, P. L. and Srinivasan (2007), R., Electroencephalogram, *Scholarpedia*, 2(2), 1348, 10.4249/scholarpedia.1348
- [2] William Speier and Aniket Deshpande and Nader Pouratian (2016), A Method for Optimizing EEG Electrode Number and Configuration for Signal Acquisition in P300 Speller Systems, *Journal of Clinical Neurophysiology*, 126(6), 1171 - 1177, 10.1016/j.clinph.2014.09.021
- [3] Ravi Kumar (2018), TCP vs UDP, *Medium*, <https://medium.com/@yoursproductly/tcp-vs-udp-38b10bb1bbf3>, accessed: 13.05.2021
- [4] Björn Schmitz (2021), Niedrige Latenzen mit Bluetooth Low Energy, *Medtech Ingenieur*, <https://medtech-ingenieur.de/niedrige-latenzen-mit-bluetooth-low-energy/>, accessed: 13.05.2021
- [5] The Grid 2, *Stiftung barrierefrei kommunizieren*, <https://www.barrierefrei-kommunizieren.de/>, accessed: 13.05.2021
- [6] Bertrand Rivet, Antoine Souloumiac, Virginie Attina and Guillaume Gibert (2009), xDAWN algorithm to enhance evoked potentials: application to brain-computer interface, *IEEE Trans Biomed Eng.* 2009 Aug;56(8):2035-43, 10.1109/TBME.2009.2012869

Development and Validation of a new iterative parametrization approach for Equivalent Circuit Models of Li-Ion Batteries

Eren Cem Durak
 Munich University of Applied Sciences
 Faculty for Electrical Engineering and
 Information Technology
 Munich Germany
 eren.durak@hm.edu

Abstract— In this paper, a brief overview of different state-of-the-art models will be presented, which are used to simulate the behavior of lithium-ion batteries. After that, a new parametrization approach for equivalent circuit models will be presented which can alter its parameters to adapt to any given load-profile. The method uses discretized versions of the differential equations which describe the battery behavior to fit its parameters. This will enable battery characterization without the need of standardized profiles. This novel parametrization method will be investigated in terms of better prediction of battery states and minimization of modeling efforts both in terms of cost and time.

Keywords— *Lithium battery, Equivalent Circuit Models, Iterative Learning, Battery Simulation, Look-Up Tables*

I. INTRODUCTION

Academic Research and applications of lithium-ion batteries have seen an increasing interest during the past decade [1]. This is mainly due to the increased use of electric applications, ranging from phones and laptops to the automotive domain. The automotive industry is investing highly in the research and development of electric vehicles (EV) due to the recent increase in the demand for such vehicles. These vehicles are mostly using electric batteries to store their energy, thus the investment in battery technology. Electric applications using a battery as their primary energy and power source will be accompanied by a battery management system (BMS) [2]. Here, the need to manage the battery performance and control its internal parameters, like the temperature, is vital to the longevity of the battery life and therefore a key component to the environmental impact of this battery. The accurate prediction of the State-of-Charge (remaining charge), State-of-Health (remaining maximum storage capacity), and other characteristics (U and I) is the main objective of a battery model, which is implemented in the BMS [3]. In this paper, a brief overview of mentioned battery models will be given. After that a novel approach to battery modeling will be presented, it uses discretized versions of differential equations that describe the dynamic behavior of such batteries. Lastly, the results will be discussed and an outlook for further research will be given.

II. STATE-OF-THE ART

Battery Models presented here can be categorized in three main topics: the physics-based electrochemical models [4], the equivalent circuit models [5] and the data-driven models, which use artificial intelligence algorithms such as neural networks for battery modeling [6].

A. Physics-based electrochemical models

The Physics-based electrochemical models use several forms of differential equations to describe and estimate the behavior of the battery. One Example is the single-particle (SP) model [7]. In this type of model, a single particle is used to represent the concentration distribution of lithium-ions in the electrode. However, the accuracy of these models is relatively low. Therefore these models are often used for investigating the primary performance and the effect of solid-phase diffusion of the electrodes but not for the dynamic behavior of the battery. Another example is the pseudo-two-dimensional model (P2D) which was presented by Doyle and Newman et al. [8]. The P2D model treats the anode and cathode of the cell as porous electrodes composed of numerous spherical particles, and the spaced between the particles are filled with the electrolyte [9]. The concentration distribution and potential distribution of the lithium-ion in the electrolyte liquid phase and the solid phase of the electrode material particles are described by several coupled partial differential equations (PDEs), to comprehensively examine the main reaction and side reaction rates inside the cell [9].

B. Electrical Equivalent Circuit Models

The equivalent circuit models have gained interest in real-time applications, especially in the automotive domain due to their simple model structure and relatively easy parametrization. They use simple electrical components such as resistors and capacitors to describe the behavior of the battery [10]. The most simple equivalent circuit model is the Rint-Model [2]. It is based on the Thevenin theorem [2] which states that any linear electric circuit can be replaced by a black box and an approximation of the steady-state behavior of the circuit with a single voltage source and an internal resistance mostly denoted as R_{int} . An extension of the Rint-Model can be achieved by simulating the ideal voltage source and internal resistance as a function of the State-of-Charge (SoC) and temperature [1]. This information can be stored in the form of lookup tables and experiments can identify the value for each component for each temperature and SoC. This aspect of the Rint-Model makes it a semi-empirical model. To overcome some of the drawbacks of the Rint-Model the RC-Model was developed [10]. These models are an extension of the Rint-Model. They use one or more resistors and capacitors circuits, which are connected in parallel to better simulate the dynamic or transient behavior of the battery. Figure 1 shows the structure of an RC-Model with one RC-Part, hence it is a first-order RC-Model. [11].

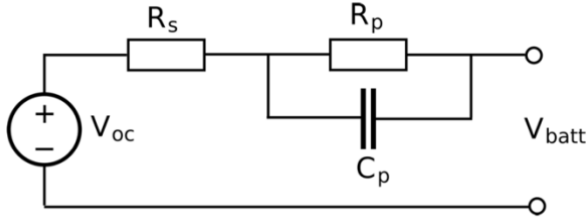


Fig. 1. RC-Circuit with one RC-Part [11]

The components R_p and C_p are also dependent on variables such as the SoC and temperature and therefore this model can also be enhanced by identifying each value experimentally and storing the data in lookup-tables. More RC-parts can be added to this circuit to improve its fidelity. However it should be stated that, with each added RC-part the model becomes more complex to solve and therefore an unambiguous parametrization is difficult.

C. Data-Driven Models

Data-Driven Models have very good performance for non-linear problems like battery simulation. However, their performance is heavily dependent on the number of datasets and their quality. This fact makes the development of such models rather expensive. Though with increased usage of battery-powered devices like phones and cars this data will become more available and therefore cheaper. In [6] Dong used a dual neural network fusion battery model to estimate the SoC. A Combination of a linear neural network with a back-propagation neural network was used [6]. In this model, the terminal voltage, discharge current, and battery temperature were used as an input vector and the output is the estimated SoC. The average error in this estimation was 1.03% with a maximum error of 4.82% [6].

III. MODEL DESIGN

An ECM with one RC-Circuit has been chosen for further investigation. High fidelity and acceptable usage of computational resources make this model type an ideal candidate for further improvement. The model has been developed in the programming language Python 3.8. The novel parametrization approach has been built into an existing battery model, which was developed by Mühlbauer et. al in reference [12]. The model has been developed in an object-orientated programming (OOP) approach, meaning the model has been structured in classes and methods. Figure 2 shows a general structure of the testing environment. The test environment is used on the top level for initializing and calling the battery model, as well as for the final evaluation and plotting of the simulation results. The SoC Estimation and the OCV Estimation have been implemented as separate methods in the ECM class and have been taken over from the model in reference [12]. The novel fitting and update algorithms are built into the “ECM” class in figure 2 as separate methods. Figure 3 shows the structure of the actual battery model. The parameter values are a function of the current SoC and temperature. Each model parameter is defined as a three-dimensional array where one axis defines the dependency of the current, one the dependency of the SoC, and one the dependency on the temperature.

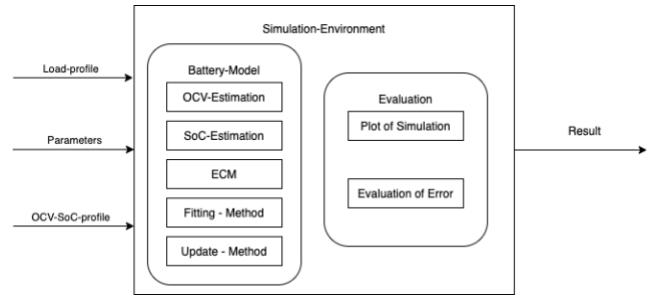


Fig. 2. Structure of Testing Environment

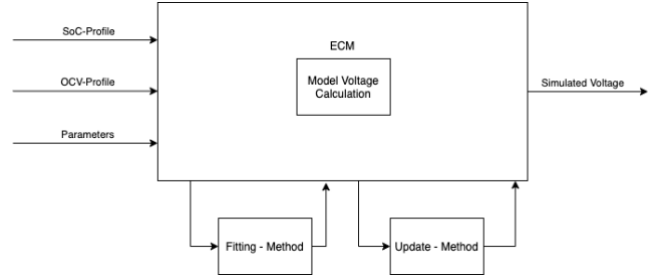


Fig. 3. Structure of ECM with novel parametrization approach

It is intended to adapt its parameters by using the error between the measured voltage and simulated voltage in an iterative manner. The model integrates the passed current to estimate the used energy and therefore the remaining SoC. It then associates the measured terminal voltage of the battery with the SoC. In this way, the model has a good estimation for SoC-OCV Relation. It takes this SoC-OCV Relation, and the measured current to calculate the simulated voltage U_{sim} . U_{sim} is calculated in two parts. First, the voltage in the serial resistance R_s is calculated using equation (1) second the voltage in the RC-part is calculated by using equation (2).

$$U_s = R_s \cdot I \quad (1)$$

$$U_{RC} = I(t) \cdot R_p - \tau \cdot \frac{dU_{RC}}{dt} \quad (2)$$

However, it can be seen that equation two is a differential equation and therefore it needs to be discretized to be used in an iterative learning manner. Equation 3 shows the discretized version of equation 2.

$$U_{(k+1)} = \left(1 - \frac{T_s}{\tau}\right) \cdot U_{(k)} + \frac{T_s \cdot R_p}{\tau} \cdot i_{(k)} \quad (3)$$

T_s equals the time step for one iteration in which the error is evaluated to update the parameters, k equals the time step numeration and τ equals the time constant for the first RC-part.

$$\tau = R_p \cdot C_p \quad (4)$$

The algorithm which is used to update the parameters were presented in [13] by Bohlen. The error will be weighted and the parameters will be updated as a function of their vicinity to the data point [13]. To obtain a global minimum of the error several different algorithms will be used, such as differential evolution to alter the parameters [14]. The algorithms minimize the squared sum of the error between the simulated terminal voltage and the measured voltage by varying the

model parameters. As previously determined the terminal voltage of the battery is therefore:

$$U_T = U_{OC} + U_s + U_{RC1} \quad (5)$$

The error is defined as:

$$F = (U_{\text{measured}} - U_{\text{simulated}})^2 \quad (6)$$

A. Fitting Method

As for the novel parametrization method, the data is being fitted to the discretized versions of the actual differential equations defining the dynamic battery behavior. The overall terminal voltage is being calculated with equation (5) but the voltage at the serial Resistance is defined in equation (1), and the voltage at the RC-Circuit in equation (3). The fitting algorithm works similar to the sliding window approach known from the machine learning domain. First, the model starts with parameters, which are not influenced by the fitting or the update algorithm. After a certain amount of time steps have been simulated, the fitting method is being called for a fixed time frame (or simulation window). Figure 3 illustrates this process.

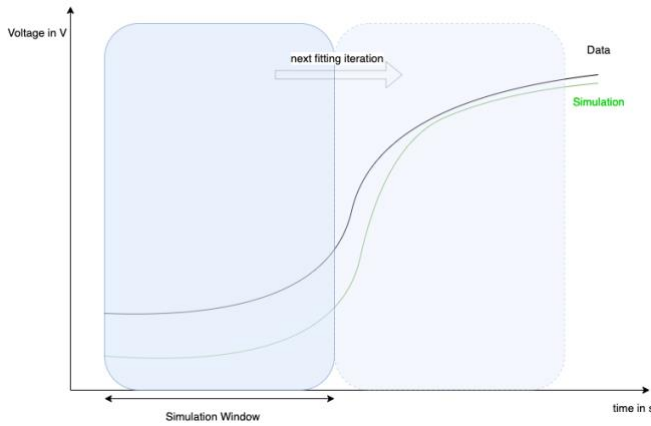


Fig. 4. Sliding window approach for fitting algorithm.

The operating point is defined by the mean value of the SoC, current, and temperature in this time frame. The fitting algorithm starts with the parameter values, which have been interpolated from the unlearned mappings. The boundaries were set as follows, R_s between 0.001 and 0.8 Ω , R_p between 0.01 and 1 Ω and τ_1 between 1 and 250 s. The fitting algorithm varies the parameter values between the boundaries to minimize the error between the simulated terminal voltage and the measured voltage, as defined in equation (6). The fitting algorithm is terminated if the convergence falls below the value of 0.01. The convergence in the differential evolution algorithm is defined as the standard deviation of the population divided by their mean [14].

$$\text{Convergence} = \frac{\text{Standard Deviation of Population}}{\text{Absolute Mean Value of Population}} \quad (7)$$

B. Update Method

In the design of the update method, special features of battery characteristics must be taken into account.

- Some operating points are accessed more often than others, for example, an SoC of 50% is going to be measured more frequently than 1% or 100% [13].
- The parameters mostly show a monotonous and smooth dependency along with the input variables, meaning e.g. SoC, current, temperature, etc. [13].
- The model parameters cannot be made dependent on all variables, which affect the battery behavior, so a certain scattering of the measurement values at the same operating point is inevitable [13].

The update algorithm will change the whole parameter mapping based on a single operating point. The influence on the vicinity of the operating point should be higher than the influence on the more distant values. As described in reference [13] the mathematical description of the update algorithm, the generalized input values are X_1, X_2, \dots, X_N , where N is the number of input variables. In the used model, the input variables are SoC, current, and temperature, so the number of input variables N is three. One example of the function value is the serial resistance of the battery model R_s . As the parameters in the used model are a function of SoC and current, the characteristic of R_s can be described by:

$$R_s = R_s(x_1, x_2, x_3) = R_s(\text{SoC}, I, T) \quad (8)$$

As described earlier, the fitted value for a specific operating point $\vec{x}_0 = (x_{1,0} \dots x_{N,0})$ is being returned and passed to the update method. With this fitted value for the parameter P the delta between the unfitted and fitted value is being calculated:

$$\Delta P(\vec{x}_0) = P_{(\text{unfitted})}(\vec{x}_0) - P_{(\text{fitted})}(\vec{x}_0) \quad (9)$$

The new parameter map $P_{\text{Map,new}}(\vec{x})$ can be calculated by adding this delta, multiplied by a smoothing function $h(\vec{x}_0)$ to the original parameter map $P_{\text{Map,old}}(\vec{x})$:

$$P_{\text{Map,new}}(\vec{x}) = P_{\text{Map,old}}(\vec{x}) + \Delta P(\vec{x}_0) \cdot h(\vec{x}_0) \quad (10)$$

As mentioned before, the values in the vicinity of the operating point should be affected more than the distant ones. This will be achieved by multiplying the delta by a smoothing function. One mathematical function, which fulfills this requirement, is the gauss error distribution curve.

$$h(\vec{x}_0) = \alpha \cdot \left(e^{-\left(\frac{x_1 - x_{1,0}}{\sigma_1}\right)^2} \cdot e^{-\left(\frac{x_2 - x_{2,0}}{\sigma_2}\right)^2} \dots e^{-\left(\frac{x_N - x_{N,0}}{\sigma_N}\right)^2} \right) \quad (11)$$

In equation (11) the factor α defines the height of the curve and therefore, the maximum amount of influence on the current operating point $\vec{x}_0 = (x_{1,0} \dots x_{N,0})$. With a high value for α , the adaptation rate would be very high and the delta would be added without any damping. Typical values for α could be between 0 and 1. For $\alpha = 1$ the parameter value would be locally set to the fitted value without any damping of measurement scattering, for $\alpha = 0$ no adaptation would occur [13]. Considering that, this method can be applied on dynamic profiles, a high dynamic current can be applied without a significant change in the SoC or temperature. As a result of that, the novel parametrization approach presented in this work influences the parameter map asymmetrical. This

means, that the influence on the SoC or temperature axis can be set independently from the influence on the current axis. In the context of the smoothing function this means, the width of the bell in the three dimensions is not symmetrical and an asymmetric gauss curve can be applied in the update method. The width of the bell is defined by the values σ_1 to σ_N . In the model the width of the smoothing function for the first dimension is defined by equation (12):

$$w(x_1) = \frac{x_{1,max} - x_{1,min}}{\sigma_1} \quad (12)$$

Figure 5 visualizes the smoothing function for the serial Resistance dependent on only the SoC and current. Figure 4 shows the asymmetric smoothing function in which the width in SoC direction is significantly larger than in current direction.

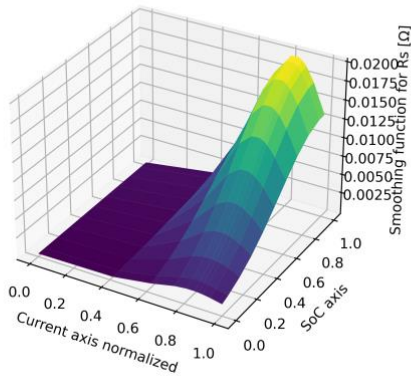


Fig. 5. Smoothing Function for a current range and the SoC range normalized, and $\alpha = 0.02$, $\sigma_{SoC} = 5$ and $\sigma_1 = 30$.

Now a guideline can be described for one iteration of the adaptation [13]:

1. Definition of the operating point by calculating the mean values for the SoC, current and temperature for the observed simulation window
2. Interpolation of the parameter values from the maps, which are not updated yet
3. Calling of fitting method, described in chapter A, to calculate the optimal parameter values for the observed simulation window
4. Calculation of the delta between the unfitted and fitted parameter values at the current operating point (\vec{x}_0) according to equation (9)
5. Calling of the update method
6. Calculation of the smoothing function h at the current operating point (\vec{x}_0) according to equation (11)
7. Update the parameter map according to equation (10)

Figure 6 shows the flowchart for the battery model outlined above. Initially, the data is transferred to the battery model. With this data, the model computes the voltage with unlearned parameter maps for each time step k . k is the iteration parameter that records the progress of the

simulation. After the simulation reaches certain progress defined by the parameter window, the operating point for that simulation window is set. The fitting method adjusts the parameters for that specific operating point using the equations stored in the battery model. Then the optimized parameter is entered into the update method, where the parameter map is updated. Subsequently, the simulation continues until it reaches the next progress point where the window fits again. Thus, the window is advanced by its length at each iteration. This iterative process continues as long as the simulation runs.

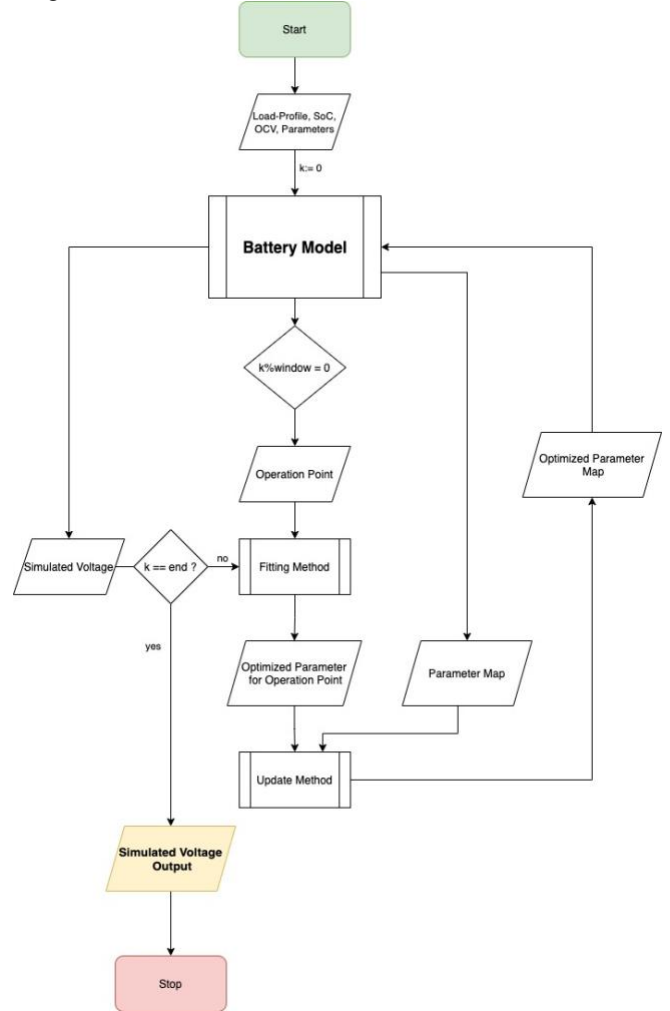


Fig. 6. Flowchart for iterative parameter learning in the battery model

IV. VALIDATION

The validation of the model has been performed as follows. First artificial parameters have been defined in the model. The load profile was carried out and the simulated voltage has been logged. Note that in this step, the parameters were not influenced in any kind. After that, it was assumed that the simulated voltage from the first step corresponds to the true behavior of the battery. Next, the simulation was started with constant parameters, and the evolution of the parameters was observed. After several iterations of the load profile, the parameters reflected the artificial true parameters. It has to be noted that the validation was carried out with parameters only dependent on SoC and current. Figure 7 shows the true parameter for the serial resistance.

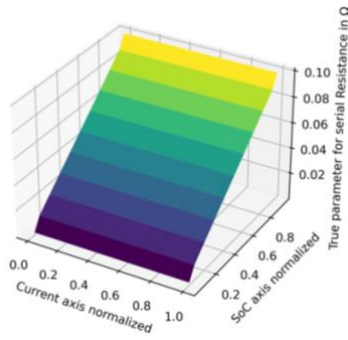


Fig. 7. True parameter for serial Resistance

Figure 8-10 shows the evolution of the parameter and as you can see it is similar to the true parameter. The delta at high SoC and low currents is due to the fact that the load profile rarely or never includes these operation points.

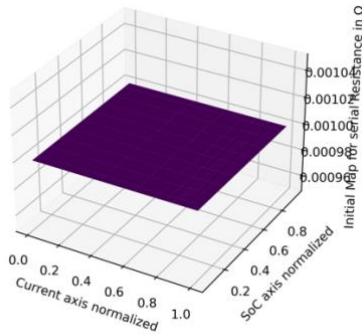


Fig. 8. Initial parameter for serial resistance

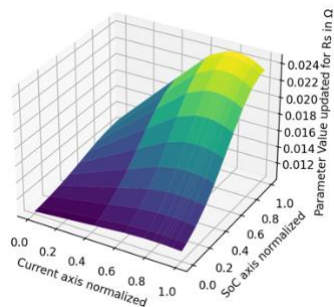


Fig. 9. Parameter for serial resistance after five iterations

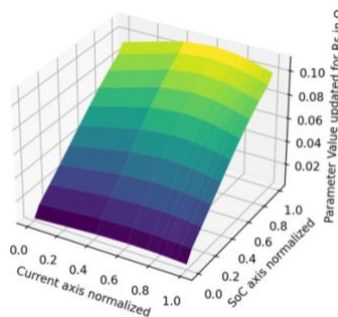


Fig. 10. Parameter for serial resistance after 15 iterations

Figure 11 shows the final simulation results in the validation result with a median error of 0.09 V.

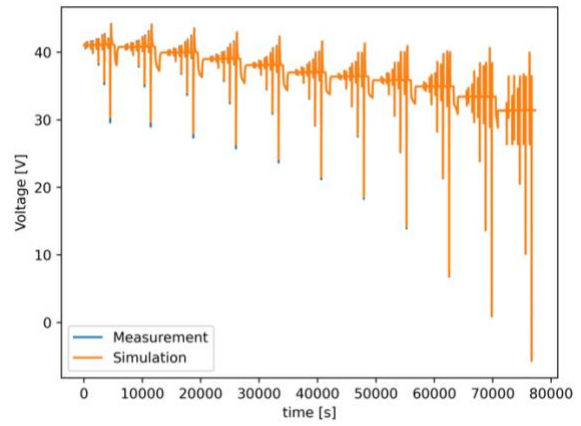


Fig. 11. Final simulation Result for validation

V. RESULTS

In this chapter, the simulation results of the model will be presented. It has to be noted that these results were conducted at a constant temperature of 22°C. The load profiles have been measured as part of [12]. “The verification and validation of the battery model is carried out on a battery test system from ScienLab (SL80/100/8BT6C) providing up to 100 A per channel and is based on an analysis of the root mean square (RMS) error of the simulated and measured voltage. The RMS error is obtained by calculating the moving RMS with the sliding window method and a window length of two. The applied battery pack (Battery 1) comprises 20 Samsung 18650 25R lithium-ion cells in a 10s2p configuration with a rated capacity of 5 Ah and a rated voltage of 36 V. Note that a measurement error of the battery test system, which was determined during calibration, is considered.” [12]. In reference [12] the same data set was used to parametrize the model with before mentioned standard method. First, the simulation has been conducted with a state-of-the-art parametrization method, described in reference [12]. The parameters were fitted to the pulse profile beforehand and after that, the model simulated the load profile. With this method, a median error value of 0.007636 V has been achieved. After the novel parametrization approach has been applied a median error value of 0.005875 V has been achieved. This results in an improvement of 23.06 %. Figure 12 shows the simulation result for the load profile with 4 pulses ranging from 2 A to -5 A .

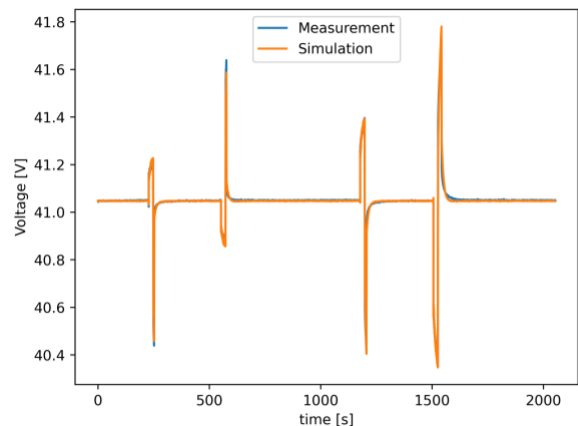


Fig. 12. Simulation result for a pulse profile with four pulses.

The parameters, which affect the behavior of the update algorithm and therefore influence the simulation performance, are called hyperparameters. The following hyperparameters have been identified.

- The height of the gauss curve α at the current operating point
- The width of the gauss curve along the SoC axis, σ_{SoC}
- The width of the gauss curve along the current axis, σ_I
- The width of the gauss curve along the temperature axis, σ_T
- The width of the simulation window frame for which the parameters are fitted, *window*
- Termination criterion of the fitting method, *convergence*, which is defined in equation (7)

These hyperparameters have a tremendous effect on the simulation performance and suitable values for them are found through a preliminary sensitivity analysis. The initial values were chosen as the standard. Then only one parameter was increased and decreased and the effect on the median was recorded. This was done for every hyperparameter. Optimal hyperparameters are defined as the ones, which result in the lowest simulation error. With this method, relatively good approximations for the ideal hyperparameters were identified. Since this process does not grant identification of optimal hyperparameters, it is possible to improve simulation performance even further. However, table 1 shows the hyperparameter values for which an improvement of 23,06 % was achieved. This analysis was conducted with the parameters only dependent on SoC and current.

TABLE I. HYPERPARAMETERS IDENTIFIED BY A PRELIMINARY SENSITIVITY ANALYSIS

Hyperparameter	Minimal Value	Optimal Value	Maximal Value
α	0.002	0.02	0.2
σ_{SoC}	5	30	100
σ_I	5	30	100
window	100	4000	20000
Convergence	0.001	0.01	0.1
median	0.035665 V	0.005875 V	0.010376 V

VI. CONCLUSION AND FUTURE WORK

In the course of this work, the structure of battery cells and storage systems were analyzed. Subsequently, a general overview of different types of battery models, which are represented in the current literature, has been created. These include the physics-based models, the data-driven models, and also the equivalent circuit models. Subsequently, the model types have been studied for their advantages and disadvantages, to iteratively adjust their parameters. It turned out that the ECM group is best suited for the aim of this work. Consequently, the model with one RC-Circuit was used to implement the new fitting and update method. After that, the model was validated by using artificial parameters. The combination of the novel fitting and update method resulted in an improvement of 23.06 % of the median simulation error,

for a pulse profile with parameters, which were already fitted with a state-of-the-art fitting method.

Future work may include an addition of a second RC-Circuit to improve the fidelity of the battery model. Also, an additional dimension for battery degradation can be appended to the model parameters. Furthermore, the novel method will be tested with a real system. In addition, the model will be combined with a SoC estimator and a Kalman filter for SoH estimation.

VII. ACKNOWLEDGEMENT

The author would like to thank Prof. Dr. Ing. Oliver Sven Bohlen, Markus Mühlbauer, and Christian Rosenmüller from MUAS for their help and support with this work.

VIII. REFERENCES

- [1] R. Xiong, *Battery Management Algorithm for Electric Vehicles*. Singapore: Springer Singapore, 2020.
- [2] A. Nikolian, J. de Hoog, K. Fleurbay, J.-M. Timmermans, P. V. de Bossche, und J. V. Mierlo, „Classification of Electric modelling and Characterization methods of Lithium-ion Batteries for Vehicle Applications“, S. 16.
- [3] G. L. Plett, *Battery management systems: battery modeling. Volume 1. Boston* : London: Artech House, 2015.
- [4] Q. Zhang, D. Wang, B. Yang, X. Cui, und X. Li, „Electrochemical model of lithium-ion battery for wide frequency range applications“, *Electrochimica Acta*, Bd. 343, S. 136094, Mai 2020, doi: 10.1016/j.electacta.2020.136094.
- [5] F. Jin, H. Yongling, und W. Guofu, „Comparison Study of Equivalent Circuit Model of Li-Ion Battery for Electrical Vehicles“, *Res. J. Appl. Sci. Eng. Technol.*, Bd. 6, Nr. 20, S. 3756–3759, Nov. 2013, doi: 10.19026/rjaset.6.3587.
- [6] G. Dong, X. Zhang, C. Zhang, und Z. Chen, „A method for state of energy estimation of lithium-ion batteries based on neural network model“, *Energy*, Bd. 90, S. 879–888, Okt. 2015, doi: 10.1016/j.energy.2015.07.120.
- [7] A. Romero-Becerril und L. Alvarez-Icaza, „Comparison of discretization methods applied to the single-particle model of lithium-ion batteries“, *J. Power Sources*, Bd. 196, Nr. 23, S. 10267–10279, Dez. 2011, doi: 10.1016/j.jpowsour.2011.06.091.
- [8] M. Doyle, T. F. Fuller, und J. Newman, „Modeling of Galvanostatic Charge and Discharge of the Lithium/Polymer/Insertion Cell“, *J. Electrochem. Soc.*, Bd. 140, Nr. 6, S. 1526–1533, Juni 1993, doi: 10.1149/1.2221597.
- [9] Y. Wang u. a., „A comprehensive review of battery modeling and state estimation approaches for advanced battery management systems“, *Renew. Sustain. Energy Rev.*, Bd. 131, S. 110015, Okt. 2020, doi: 10.1016/j.rser.2020.110015.
- [10] X. Hu, S. Li, und H. Peng, „A comparative study of equivalent circuit models for Li-ion batteries“, *J. Power Sources*, Bd. 198, S. 359–367, Jan. 2012, doi: 10.1016/j.jpowsour.2011.10.013.
- [11] F. Saidani, F. X. Hutter, R.-G. Scurtu, W. Braunwarth, und J. N. Burghartz, „Lithium-ion battery models: a comparative study and a model-based powerline communication“, *Adv. Radio Sci.*, Bd. 15, S. 83–91, Sep. 2017, doi: 10.5194/ars-15-83-2017.
- [12] M. Mühlbauer, O. Bohlen, und M. A. Danzer, „Analysis of power flow control strategies in heterogeneous battery energy storage systems“, *J. Energy Storage*, Bd. 30, S. 101415, Aug. 2020, doi: 10.1016/j.est.2020.101415.
- [13] O. S. Bohlen, „Impedance based battery monitoring“, Dissertation, Rheinisch-Westfälischen Technischen Hochschule Aachen, 2008.
- [14] „scipy.optimize.differential_evolution — SciPy v1.5.4 Reference Guide“. https://docs.scipy.org/doc/scipy/reference/generated/scipy.optimize.differential_evolution.html (zugriffen Dez. 20, 2020).

Tailor-made IT security standards for SMEs

A qualified selection

Dennis Fitznar, B.A.
 University of Applied Sciences Augsburg
 An der Hochschule 1
 86161 Augsburg, Germany
 dennis.fitznar@hs-augsburg.de

Abstract - With the advance of digitalization, the focus is increasingly on ensuring information security. SMEs are only partially prepared for the resulting challenges. The appropriate tools for realization are missing. IT security is usually only considered from the perspective of large corporations. The aim is to develop an IT-supported roadmap for the step-by-step achievement of an ISMS (Information Security Management System) for SMEs with permanent benchmarking.

Keywords - digitization, IT security, SMEs and ISMS

I. THE RESEARCH PROJECT NetDiSC

The ongoing digitization of the working world and, in particular, of value creation processes is also changing logistics and cross-company processes. Many companies are now faced with the challenge of transferring parts of their traditional service offering to digital value creation models.

After all, the core business of companies has always included not only the further development of products and services, but also the optimization of the associated organizational structures and processes. In this context, the opportunities and risks of digital transformation are increasingly coming into focus.

What is needed are practicable solutions that ensure the flow of digital processes - especially at the interfaces between companies and business partners - as well as innovative, digital value creation models that enrich companies' current service bundles. This is precisely the research area of "NetDiSC" (Network for Digital Supply Chains), which is being funded by the Bavarian State Ministry of Science and the Arts for four years.

"NetDiSC" is equally dedicated to both areas - the targeted analysis and evaluation of data along the supply chain as the basis for new, digital business processes and models, and the necessary IT security measures in the hardware and software environment.

II. SUB-PROJECT 3: EVALUATION OF IT SYSTEM LANDSCAPES

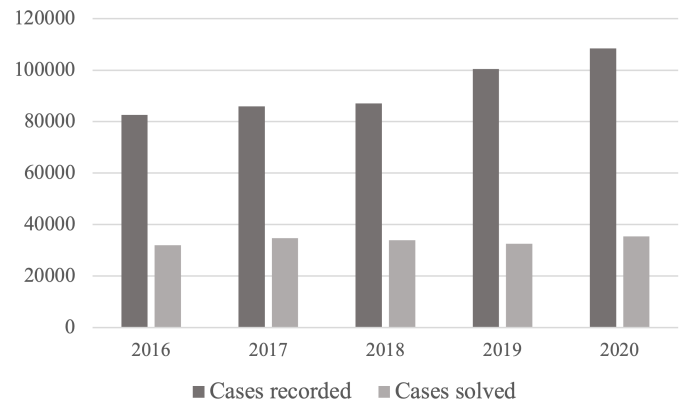
The digitization of production, logistics and administration requires a comprehensive overview and knowledge of the cross-company IT infrastructures. Under the title Evaluation of IT System Landscapes, a model for evaluating internal and

external information technology is being developed in subproject III of NetDiSC in collaboration with three practical partners from Bayerisch-Schwaben. Since a reorientation of the subproject in 2020, this has focused on the assessment and monitoring of IT security standards at SMEs.

III. PROBLEM DEFINITION AND OBJECTIVES

According to the BKA's Federal Situation Report Cybercrime from 2020, the number of cases has increased by approx. 23.8% to 108,474 since 2016. Thereof, only 35,390 are considered solved.

IMAGE 1. Case figures of the BKA

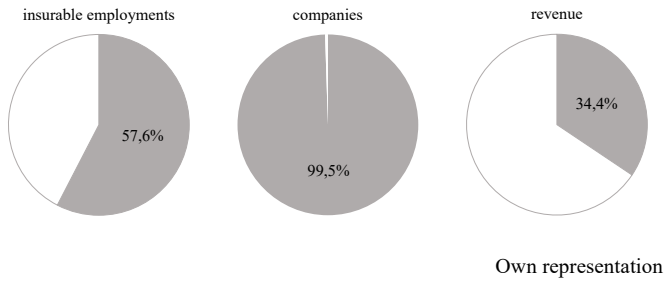


Own representation

The steady rise in the volume of cases is due to the rapid advance of digitization, the increasing professionalization of perpetrators, and rising capabilities of malware to conceal itself from security mechanisms, as well as the low barriers to entry into cybercrime.

Digitalization and networking through the Internet of Things, Industry 4.0 and smart cars are increasingly making IT security more relevant. Small and medium-sized enterprises will be part of these trends. In Germany, around 3.467 million companies (99.5 %) were classified as small and medium-sized enterprises in 2018 according to the SME definition of IfM Bonn:

IMAGE 2. Relevance of German SMEs



In contrast to large companies, SMEs have limited resources for IT security. A study conducted by WIK for the German Federal Ministry for Economic Affairs and Energy as part of the IT Security in Business initiative shows that time and costs are the biggest hurdles. In addition, there is a lack of awareness of IT security in companies despite advancing digitization. Even in high-risk areas, protection is inadequately provided. For example, two-thirds of small SMEs say that IT security is very important, but only about 20% of them have conducted an IT security analysis.

These low IT security standards of SMEs as well as the steadily increasing case volumes of cybercrime mean a high risk for companies in the SME category. Providing IT security for SMEs is not of less importance than for large corporations. Rather, the opposite can be assumed: For example, they are usually less diversified, and attacks can cause higher damage. Despite the existing knowledge about the relevance of IT security, lack of resources and knowledge often lead to neglect of the topic. The security of industrial plants and systems requires expertise from a wide variety of fields, such as automation technology, network technology, production planning and control, data analysis and much more.

IT security is usually only considered from the perspective of corporations. Some frameworks exist for the implementation of IT security standards, such as ISO/IEC 27001 or TISAX. These established frameworks are too extensive and complex for SMEs.

The aim of the sub-project is to develop an IT-supported roadmap for the step-by-step achievement of an ISMS (Information Security Management System) for SMEs with permanent benchmarking. This should result in a risk-oriented and continuous improvement of a company's information security.

IV. CONCEPT AND TOOL

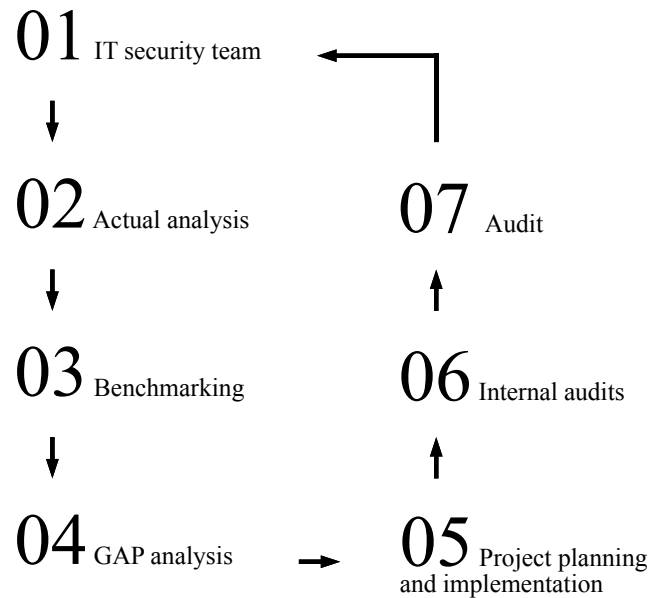
The IT-supported roadmap is based on a step-by-step approach.

The success of the concept presented below is measured by the three protection goals of information security:

- Confidentiality
- Integrity
- Availability.

The protection goal of "confidentiality" is ensured if data worthy of protection is viewed, processed, and managed exclusively by persons who have the necessary authorization. Confidentiality thus protects access to information. "Integrity" is achieved when data worth protecting remains intact and complete. So, while "confidentiality" deals with the authorization to change data, "integrity" covers the detection of data changes. The protection goal of "availability" is achieved when systems are always available to authorized persons, can be used as intended, and operational processes are therefor not disrupted.

IMAGE 3. Step-by-step procedure



Own representation

The first step, the **establishment of an IT security team**, forms the basis for the subsequent steps. This team should include, if available, the IT security officer, a member of the company management, the IT manager, the data protection officer, an occupational safety specialist, a representative of the staff council, and a representative of the building services department.

This is followed by the **actual analysis**. This includes identifying critical applications and analyzing the IT structure as well as answering a questionnaire for each application or unit of the IT structure.

The first step is to focus on the localization of all applications that support business-critical processes or process information worthy of protection. This includes information that must be protected by legal requirements regarding to the basic values of confidentiality, integrity, and availability. In each case, the need for protection must be determined based on three categories. A distinction is made between no need for protection (Z), normal need for protection (C), medium need for protection (B) and high need for protection (A).

This is followed by an analysis of the IT structure - IT systems, rooms and buildings that are necessary for the operation of the critical applications. The aim is to link the application and the IT structure and to derive the respective protection requirements.

The concept provides for the complete IT structure and all applications, including the respective protection requirements and persons responsible, to be entered into the tool. The units of the IT structure are to be categorized (IT systems, rooms, buildings). The applications can be linked to the IT structure in the database by means of an m:n relationship.

The inventory ends with the completion of a questionnaire. This must be completed in the tool for each application and unit of the IT structure depending on the respective category and only with a protection requirement of A, B, or C. The answers given define the current maturity level of IT security. Any documents, drawings or lists are to be uploaded.

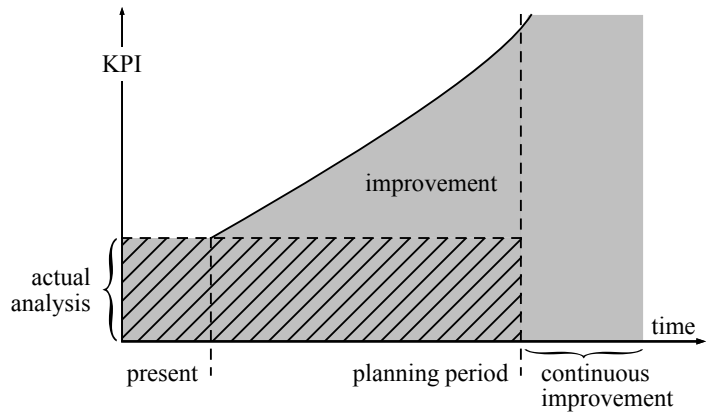
The **determination of the benchmarking** defines the later reference value for the GAP analysis. To ensure framework-independent benchmarking, the tool will contain all requirements and the relevant content of the frameworks described in the following chapter. The requirements are to be assigned to the respective certificates and categorized in the tool. The framework-dependent requirements are to be bundled individually and assigned a priority of high (a), medium (b) or low (c). When bundling the requirements, in case of combining requirements of the same framework, weightings are to be stored. For each bundled requirement, individual tasks are defined and assigned. The tasks must contain a title, a description, and an estimated indication of the expenditure in working hours. In addition, it is possible to define a responsible person as well as a start and end date.

The **GAP analysis** is carried out according to the relevant needs of the respective company and requires benchmarking. The goal of the GAP analysis is a systematic and holistic review of the network and security infrastructure. The existing IT security infrastructure (inventory) is checked against the previously defined benchmark. This enables the comparison of a company's information security with one or more standards and regulations. The procedure is described below:

The deviation - the so-called gap - results from the comparison between the actual analysis and the reference value. The deviation can be reflected in several key figures based on the data stored in the tool: Estimated effort as time and number of bundled requirements.

The gap analysis is visualized as a coordinate system. As shown in Image 4, the ordinate contains the previously defined gap indicator. The abscissa reflects the time. The present shows the result of the actual analysis. The reference value defines the planning horizon.

IMAGE 4. GAP Analysis: Example Visualization



Own representation

The prioritization of the bundled requirements (a, b or c) and the categorization of the IT structure as well as applications (A, B, C) results in an IT structure-related or application-related overall prioritization of the bundled requirement. For example, if an application has a medium protection requirement (B) and the bundled requirement that has not yet been implemented has a priority of high (a), an overall priority is obtained by adding the respective conversion factors (see Table 1):

$$2 + 3 = 5$$

protection requirement + priority = overall priority

TABLE 1. Conversion factors

Protection requirements	Priority	Conversion factor
A	a	3
B	b	2
C	c	1

Own representation

The total prioritization determines the positioning of the stored effort in time on the abscissa. This results in the curve shown in the graph. This curve represents the development of a company's information security under the assumption of the stored effort estimates.

In **project planning and implementation**, the individual tasks resulting from the GAP analysis and prioritized are processed. For each task, a responsible person, and a date for start and completion must be defined. The responsible persons as well as all other data are to be stored in the tool. The progress is visualized by means of a burn-down chart and the constantly changing GAP analysis.

The **internal audit** is the company's own responsibility and follows the realization. The audit criteria and the scope of the audit can be freely defined within the company. It provides an overview of the current degree of realization and serves as a tool for identifying potential for continuous improvement in accordance with the PDCA cycle (Plan, Do, Check, Act). If an SME wants ISO/IEC 27001 certification, this step is mandatory.

The inventory shall be conducted every three years and existing individual bundled requirements shall be reviewed for changes, adjustments, and additions.

This is optionally followed by the **audit**, which is considered the last step and is also the permanent mandate to check the ISMS for effectiveness and up-to-dateness and to adapt it if necessary. After completion of the implementation and all tasks, an SME can aim for the respective certification, depending on the chosen benchmarks. For some SMEs, obtaining a certificate is mandatory due to competitiveness. For example, car manufacturers usually require the existence of a TISAX certificate. Obtaining a certificate also has many advantages, as exemplified below:

- Anchor information and data security in the company
- Reduce process and financing costs
- Reduce business risks
- Reduce the risk of individual liability
- Some clients insist on the existence of certificates
- Improve image and competitiveness

For example, the prerequisite for the award of an ISO 27001 certificate based on IT-Grundschrift is a review of the subject of the audit by a BSI-certified auditor for ISO 27001 audits. Within the scope of the audit, reference documents prepared by the institution are examined, an on-site inspection is carried out and an audit report is prepared. For the award of an ISO 27001 certificate based on IT-Grundschrift, this audit report is checked by the certification body at the BSI. Surveillance audits are carried out annually during the validity of the certificate issued.

V. RELEVANT CERTIFICATES

The IT security certificates relevant for benchmarking are explained below:

ISO/IEC 27001 includes requirements for establishing, implementing, maintaining, and continuously improving a documented IT management system. In addition, the standard includes requirements for the assessment and treatment of information security risks according to the individual needs of the organization.

TISAX is a standard for information security defined by the automotive industry. Many automotive manufacturers and suppliers in the German automotive industry require TISAX certification from business partners. The member companies of the German Association of the Automotive Industry e. V. (VDA for short) have created their own catalog, derived from the international industry standard ISO/IEC 27001, and adapted to the requirements of the automotive world.

VdS 10000 provides specifications and assistance for the implementation of an IT management system as well as concrete measures for the organizational as well as technical protection of IT infrastructures. The aim of VdS 10000 is to define an appropriate level of protection for small and medium-sized enterprises and organizations, which can be implemented with as little effort as possible.

VI. FURTHER APPROACH

The research project is currently in the conceptual phase. This will be followed by the development of the tool as a prototype for the realization of the IT-supported roadmap. Starting with the writing of a requirements specification, followed by the creation of a relational database model and the conceptual design of the user interface and user experience. After completion, this is to be tested and validated by the practical partners involved in the sub-project. Subsequently, the optimization takes place in cooperation with a practice partner.

ACKNOWLEDGMENT

This research is generally supported by our colleagues from HSA_ops - the operational research team of our university of applied research in Augsburg - who provided expertise that greatly assisted the research, although they may not agree with all the interpretations of this paper.

REFERENCES

Bundeskriminalamt (2020). Cybercrime Bundeslagebild 2020. Abgerufen am 14.04.2021, von https://www.bka.de/SharedDocs/Downloads/DE/Publikationen/JahresberichteUndLagebilder/Cybercrime/cybercrimeBundeslagebild2020.pdf?__blob=publicationFile&v=4

Bundesamt für Sicherheit in der Informationstechnik (2019): Zertifizierung nach ISO 27001 auf der Basis von IT-Grundschutz. Abgerufen am 14.04.2021, von https://www.bsi.bund.de/SharedDocs/Downloads/DE/BSI/Grundschutz/Zertifikat/ISO27001/Zertifizierungsschema.pdf?__blob=publicationFile&v=1

C. Kraus, H. Plehn (2020): In 12 Schritten zu mehr Informationssicherheit. Ist, BoD - Books on Demand: Hamburg

Institut für Mittelstandsforschung, Unternehmensbestand (2016). Abgerufen am 14.05.2021, von <https://www.ifm-bonn.org/statistiken/unternehmensbestand/kmu-insgesamt/deutschland>

WIK Wissenschaftliches Institut für Infrastruktur und Kommunikationsdienste GmbH (2017): Aktuelle Lage der IT-Sicherheit in KMU, Bad Honnef

A Decentralised Approach for Drive Decision Clearance of Automated Guided Vehicles at Intersections With Ambient-Approximated Traffic Control

Julia Krause

Faculty of Electrical Engineering and Media Technology
Deggendorf Institute of Technology
Deggendorf, Germany
Email: julia.krause@stud.th-deg.de

Abstract—Industrial manufacturing is becoming more and more automated, among others with automated guided vehicles as transport systems. These transport systems are replacing increasingly often personal in industry, for example, to reduce costs and increase efficiency. For the use of driverless transport systems in industry, it is important that the relevant information is shared in the system. With a large number of vehicles, it is necessary to coordinate them to avoid deadlock situations and therefore is needed a scalable algorithm. There are two ways to do this: the centralized approach or the decentralized approach or a combination of both. This paper is about a decentralized algorithm with optimized traffic control to coordinate autonomous vehicles. The aim is to get a system that avoids collision and deadlock situations and having little downtime as possible because the route is not free and the condition that the goods arrive on time should also be fulfilled. In the end, this approach should lead to a system of vehicles with optimized intersection clearance and traffic flow.

I. INTRODUCTION

“Autonomous Guided Vehicles (AGVs) are more and more used for the transportation of goods in industrial warehouses” [10]. The current state is that mostly a central approach is in use in industry, in addition, centralized planning does not scale very well with a rising number of vehicles. A decentralised approach would improve resilience, because if a central server fails, the entire system is down. So, it is a single point of failure [3]. In contrast, with a decentralised system, only the affected user fails, the rest continues to function. Another advantage is: “Decentralized decision-making allows the system to react dynamically to changes in the system state and environment” [5]. But before a decentralised robot swarm can be used, the following applies. “Robustness to dynamic changes in the industrial environment and in the swarm itself, as well as guarantees of conflict and collision avoidance, are important requirements for swarm technology to mature and become established” [4]. What is more, decentralized algorithms are more complex than centralized server approaches, but the effort can be worthwhile. In related work can mostly be found central approaches. The work of [9] is about a central control strategy based on authorization tokens to avoid conflicts.

AGVs are requesting resources when these come to resource points. The AGV with the task with the highest priority gets the authorization to the requested resource. The approach in [10] is as well about a centralized control with a predefined road map. Via traffic rules collisions of the AGVs will be avoided, here, the AGVs have the same priority. A centralized zone-control model is described in [7]. The road network is split into zones, including lanes, crossings and depots. The vehicles are only moving from one zone to the other. The zones in which a vehicle can move there called neighbouring zones. In general zones have two states “available” or “occupied”. In [11] a semaphore-based model for traffic control is proposed. It consists of a centralized control architecture without the interaction of single AGVs. The central controller is responsible for the path planning and the traffic control according to priority. The semaphore is used for the access to intersections and bidirectional lanes. Both are resources that are only allocated to one AGV. In addition, there are traffic lights for each resource.

As mentioned already before most approaches to these topics are centralized approaches. But the following approach [5] is about a decentralized decision-making process for autonomous mobile robots, which are moving in a defined space. In [1] and [2] an approach with fixed map out of only unidirectional segments and firmly defined intersections is presented. There an intersection has always a cross point and attention points. The general architecture consists of two layers: the path planning layer and the route map layer. For this work the route map layer is interesting, this layer is responsible for conflict and deadlock avoidance. This happens in a decentralized process, where AGVs share information, and intersections will be allocated to a single AGV. The mechanism of prioritisation is applied in the papers [1], [2], [9] and [11] and it is also needed in this work to be able to create an efficient traffic flow.

This work is integrated into the existing C# project that currently runs as an application on the hardware. The hardware is an autonomous vehicle, which has four trailers or a vehicle

without trailers and both transport material for production with it. The vehicle is driving dynamically on an existing road network, such an environment is shown in figure 1.

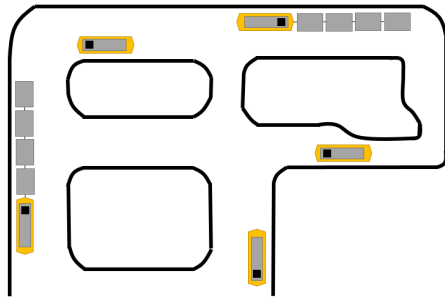


Figure 1. Example for the Environment

The vehicles are managed currently by a central server. This system is used in logistics processes, because “autonomous transport systems, i.e. a group of self-directed vehicles executing transport jobs, are able to meet the demand of flexibility in logistics” [6]. In this area of operation, the vehicle is part of a process, so it is not able to operate completely free [6]. By using a decentralized approach for intersection clearance, the system should be even more decentralised, and the traffic flow should be improved.

The paper is organized as follows: Section II presents the problem description, Section III is about the whole approach divided into: distribution of information, decision taking, traffic control and deadlock avoidance, Section IV describes the simulation and the results were discussed and finally, Section V presents the conclusions and further ideas.

II. PROBLEM DESCRIPTION

In the currently used system, the intersection clearance and the coordination of the vehicles run via a central server with a database. Every intersection is handled like a resource, which can only be used by one vehicle. Vehicles that get the driving clearance from the server can enter this area, the others stop in front of the area and wait to get the driving clearance from the server. The server issues a new driving clearance when the previous vehicle has left the area. With an increasing number of vehicles, the communication load on the central server increases. To increase the number of vehicles and the overall performance of the system solutions for road vehicles can be used [8]. On the other hand, it is costly to install a server in a system of, for example, two vehicles. The currently used system is already partially decentralized, so these methods are already robust. The main single point of this system is the central driving clearance at intersections. Without the central driving clearance, it will actually come to vehicle collisions or system deadlock.

In this use case, an intersection means an overlap of the required space of two or more vehicles. Two examples of an intersection of the planned path are shown in figure 2, the left one shows a classic intersection and the right one shows

a partial bidirectional lane, both should be handled the same way. The vehicles are currently moving on a road network, that is in some cases similar to our street road network. So, the path planner plans the path on the existing road network. It is possible that this planned path will be adapted at a later date.

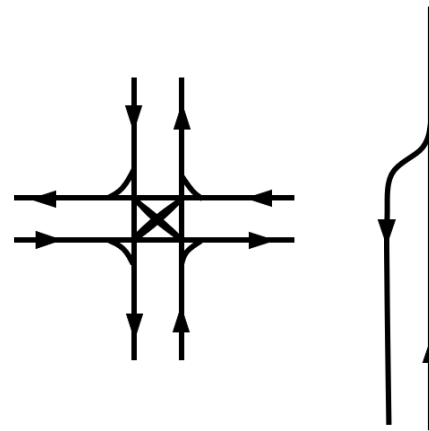


Figure 2. Examples of Intersections

If it is known where which vehicles are located, it is possible to react according to the situation that has arisen or to a situation that is about to arise, as in the case of route overlaps. In order to distribute this information, a decentralized route synchronization was implemented and evaluated. The required space is calculated every second from the planned path actual 30 meters in advance, by each vehicle. The length is adjustable. The required space is shared in the network of vehicles according to their direct distance. Thus, each vehicle receives the necessary position data of the other vehicles. Next, the required space is checked for collisions with other vehicles. The required space is shown in figure 3, the black line is the planned path where it is moving on and the green area is the required space. If a collision or a route overlap as an

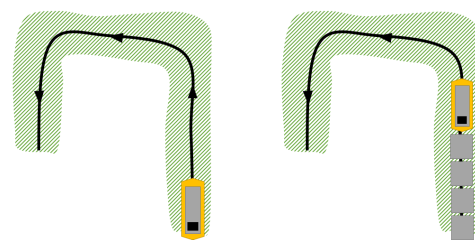


Figure 3. Required Space of a Vehicle Without and With Trailers

intersection is detected, it is necessary to react. The reaction will be that one of the two or both will stop. If space is enough for one to cross the route of the others, it will be allowed to do this, otherwise, it must stop. Added to this traffic flow is needed as well. This means that it is not enough for one of the vehicles to drive, but if traffic jam forms, it must be first be cleared, if it is still possible.

III. APPROACH FOR DECENTRALIZED DRIVE CLEARANCE DECISION

The basis of the algorithm for decentralized decision clearance in this work is the distribution of the required space and position data in the system. If the data is not available, no decision can be made. The driving clearance on this basis then results in whether a traffic flow is achieved or whether deadlock situations occur. The overlaps with [11] are that this road network also consists of intersections and bidirectional lanes. The approach with the traffic lights can be applied to this problem, not statically on the road network, but depending on the required space. A similar approach as [7] can also use for this work, the required space can be divided into zones. Before entering the next zone, the vehicle has to check the situation in the zone. The parallels from [1] and [2] to this work are it is also a decentralized system, in which vehicles share information. The difference is that there is a fixed road network with predefined points and intersections. In this work, we have a dynamic road network without any predefined intersection points.

A. Distribution of Information

The information is distributed in this system via WLAN (Wireless Local Area Network) between the vehicles via an optimized UDP (User Datagram Protocol) telegram. This telegram has different message types, to be able to process the messages in the desired module and contains the position and the required space. By distributing the data in telegrams, new vehicles can be already added to the system. Their data is shared with other participants, so that it is not possible for unknown vehicles to arrive at an intersection. This telegram is also sent dynamic according to the distance of two vehicles. With this information, a stop point will be calculated if necessary. It is necessary when there is an overlap of the required space of two or more vehicles. The stop point will be the point that is far enough away from the intersection, that crossing the intersection is still possible, an adjustable value is defined for this. If two or more vehicles will stand at a stop point, it continues with the decision taking process.

B. Decision Taking

The decision taking process becomes active when an overlap of the required space of two or more vehicles is detected and a stop point was calculated. This decision taking process is a decentralised local master vote. The winner of these process is like a short-term local master for the intersection where it is located. In this case, the local master gets the right to cross the intersection. The simplified process which expires is shown in figure 4.

The process starts when a stop point is available. If there is more than one stop point, the one closest to the vehicle is relevant. Thus, this process is only carried out once per vehicle but is restarted when the stop point has changed. If there is a stop point, the valid required space continues to the stop point and this valid one is sent in the telegram. Start decision process means that each vehicle waits and then requests clearance

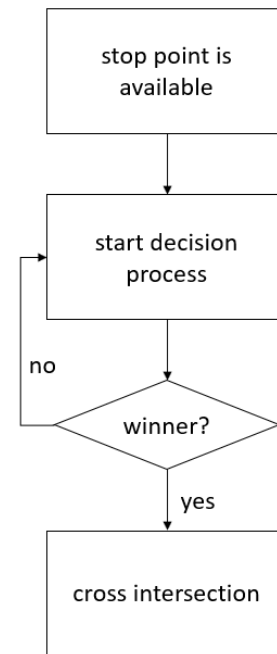


Figure 4. Flow Chart Stop Process

to drive with the full available required space. The request telegram is sent to all those for whom an overlap is detected. The fastest vehicle, that no longer calculates an intersection point or the vehicle with the highest priority is the winner and gets the clearance to drive through the area of overlap. While the winner vehicle continues to drive, the others wait until the winner has crossed the intersection. After that, the rest of the vehicles goes back to start decision process and the process runs again. This also applies to vehicles that are new to this overlap. These vehicles wait a random time and then request again. The decision taking process goes on until only one vehicle is left at an intersection and runs parallel for all other intersections.

In a second step, not only the local master should have the right to pass the intersection, but also other vehicles should be able to pass the intersection with him.

Such a solved intersection situation is shown in figure 5. In order to show this in a graphically simple way, the zones that got a drive clearance are coloured green and those that are not yet released are coloured red. In this case, the vehicle on the right has the driving clearance because its zones are green. The vehicle coming from above can drive to the end of the green zone and then stops for the moment. If there is no more overlap of the required space, it can continue to drive. For this simple use case, the Process is sufficient. In a system with more and more intersections and more and more participants, traffic control is needed.

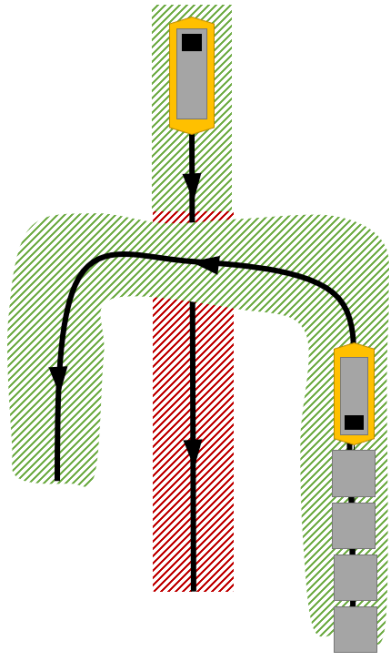


Figure 5. Intersection of Two Vehicles

C. Traffic Control

In order to guarantee the flow of traffic, frequently used routes would have to be prioritised in order to avoid congestion. If it becomes apparent that certain routes of the road are more frequented than others, a bottleneck can occur here if the flow of traffic is not further facilitated. A mechanism like traffic light control in road traffic is needed. The more traffic there is in one direction, the more vehicles should be allowed to drive in that direction when the route is free. Prioritisation then changes the decision taking process. Creating a traffic flow gets the highest priority and the highest priority will then also be the winner of the decision taking process. But that alone is not enough; there is more to efficient traffic control. To ensure that vehicles can continue their drive, the intersection zones must not be blocked. Therefore, stopping points must not be located in intersection zones. The stop point calculation must ensure that this is also the case.

D. Deadlock Avoidance

Deadlocks in this case are when vehicles can no longer drive on, which can make certain routes impassable. The number of vehicles that drive in can increase and will probably do so, if the deadlock lasts for a longer period of time. An example of such a situation is represented in figure 6. This figure shows part of a route network.

The solving of deadlock situations is problematic because of the length of the vehicle with trailers. It is easier than vehicles are small and can rotate on place. Due to the trailers, these vehicles can also not drive backward. The situation of figure 6 could still be solved. However, the aim is to prevent such situations do not occur at all. This would be possible by giving

priority to vehicles that are at risk of blocking certain areas and thus creating deadlocks.

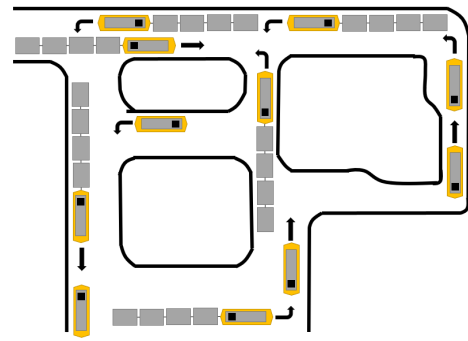


Figure 6. Deadlock Situation

IV. SIMULATION AND RESULTS

During the development process, testing is carried out in the simulation at the same time and afterward tested on the vehicle themselves. The simulation has a graphical user interface to visualize the process and the moving vehicles. It can be detected whether a code flow is present or whether errors occur. If collisions still occur in the simulation, then the algorithm must be improved again. The simulation test is more or less a test that does not cause any material damage in the event of errors. The function can therefore be sufficiently tested already before it is tried out on the vehicles themselves. It is also possible to observe the flow of traffic on different road scenes. In addition, an approximate data load that would be caused on a WLAN network is calculated. This data load gives a first rough indication of how large the data load on the WLAN network would be in practice. In general, the result of the simulation is that the algorithm fulfills the previous expectations. The tests will show whether how good the performance of this algorithm is. How much time to wait at an intersection vehicle have on average and how good traffic flow works and if the aim to minimize traffic jam is reached. Starting with a small number of vehicles and step by step minimizing the deadlock situations and simultaneously increasing the number of participants in the system, to check how well the algorithm scales.

V. CONCLUSION

This algorithm leads to a system with fewer total failures. The system can be used without additional hardware, in the form of a server, and it can also be quickly expanded to include new vehicles. The only remaining possible source of failure is the WLAN. If this fails, the system will also fail for the same period of time. The process then continues automatically when the WLAN signal is detected. Depending on how time-critical the logistics transports are, a short-term failure or signal fluctuation of the WLAN can also be tolerated. This principal cloud be used for other information or decisions as well because the whole software is constructed modularly. It is also possible to distribute a new content of a telegram via the

same way in the system. So, it is not only limited to position or space requirement information.

Although this algorithm is more complex to implement, it scales better and can be expanded more easily. The centralized approach reaches its limit at some point when communication with all participants is no longer possible. Including this decentralized approach, the system will become step by step a robot swarm with distributed intelligence, in form of information exchange for collision avoidance and traffic control. This approach can be used for all autonomous transport systems, where the path is known in advance and the system itself can run the C#-application or the code as a windows service.

REFERENCES

- [1] Digani, Valerio; Sabattini, Lorenzo; Secchi, Cristian; Fantuzzi, Cesare (2013): Towards decentralized coordination of multi robot systems in industrial environments: A hierarchical traffic control strategy. In: Ioan Alfred Letia (Hg.): 2013 IEEE International Conference on Intelligent Computer Communication and Processing (ICCP 2013). Cluj-Napoca, Romania, 5-7 September 2013. 2013 IEEE International Conference on Intelligent Computer Communication and Processing (ICCP). Cluj-Napoca, Romania, 9/5/2013 - 9/7/2013. IEEE International Conference on Intelligent Computer Communication and Processing. Piscataway, NJ: IEEE, S. 209–215.
- [2] Digani, Valerio; Sabattini, Lorenzo; Secchi, Cristian; Fantuzzi, Cesare (2014): Hierarchical traffic control for partially decentralized coordination of multi AGV systems in industrial environments. In: Robotics and Automation (ICRA), 2014 IEEE International Conference on. May 31 2014-June 7 2014 : [Hong Kong, China]. 2014 IEEE International Conference on Robotics and Automation (ICRA). Hong Kong, China, 5/31/2014 - 6/7/2014. [Piscataway, NJ]: IEEE, S. 6144–6149.
- [3] Draganjac, Ivica; Miklic, Damjan; Kovacic, Zdenko; Vasiljevic, Goran; Bogdan, Stjepan (2016): Decentralized Control of Multi-AGV Systems in Autonomous Warehousing Applications. In: IEEE Trans. Automat. Sci. Eng. 13 (4), S. 1433–1447.
- [4] Eren, Utku; Hansen, Emma (2019): Collision-Free Decentralised Density Feedback Control for Swarms. In: IFAC-PapersOnLine 52 (12), S. 364–369.
- [5] Fracapane, Giuseppe; Koster, René de; Sgarbossa, Fabio; Strandhagen, Jan Ola (2021): Planning and control of autonomous mobile robots for intralogistics: Literature review and research agenda. In: European Journal of Operational Research.
- [6] Krä, Michaela; Hörbrand, Sebastian; Schilp, Johannes (2019): Dynamic production control for flexibility in Cyber-Physical Production Systems using an autonomous transport system. In: Procedia CIRP 81, S. 1160–1165.
- [7] Li, Qin; Pogromsky, Alexander; Adriaansen, Teun; Udding, Jan Tijmen (2016): A Control of Collision and Deadlock Avoidance for Automated Guided Vehicles with a Fault-Tolerance Capability. In: International Journal of Advanced Robotic Systems 13 (2), S. 64.
- [8] Lombard, Alexandre; Perronnet, Florent; Abbas-Turki, Abdeljalil; El Moudni, Abdellah (2016): Decentralized management of intersections of automated guided vehicles. In: IFAC-PapersOnLine 49 (12), S. 497–502.
- [9] Pan, Fei; Sun, Qiyuan (2019): A Traffic Control Strategy of the Heavy-duty AGVs in a Square Topology. In: 2019 IEEE International Conference on Mechatronics and Automation. IEEE ICMA 2019 : August 4-7, 2019, Tianjin, China. 2019 IEEE International Conference on Mechatronics and Automation (ICMA). Tianjin, China, 8/4/2019 - 8/7/2019. Piscataway, NJ: IEEE, S. 263–268.
- [10] Secchi, Cristian; Olmi, Roberto; Rocchi, Fabio; Fantuzzi, Cesare (2015): A dynamic routing strategy for the traffic control of AGVs in automatic warehouses. In: IEEE Staff (Hg.): 2015 IEEE International Conference on Robotics and Automation (Icra). 2015 IEEE International Conference on Robotics and Automation (ICRA). Seattle, WA, USA, 5/26/2015 - 5/30/2015. Piscataway: IEEE, S. 3292–3297.
- [11] Shao, Shengjun; Xia, Zeyang; Chen, Guodong; Zhang, Jun; Hu, Ying; Zhang, Jianwei (2014): A new scheme of multiple automated guided vehicle system for collision and deadlock free. In: Guoqing Xu (Hg.): 4th IEEE International Conference on Information Science and Technology (ICIST), 2014. 26-28 April 2014, Shenzhen, Guangdong, P.R. China.

2014 4th IEEE International Conference on Information Science and Technology (ICIST). Shenzhen, China, 4/26/2014 - 4/28/2014. Annual IEEE Computer Conference; IEEE International Conference on Information Science and Technology; ICIST. Piscataway, NJ: IEEE, S. 606–610.

Analysis of the operation of a cooling supply system for a hospital

1st Florian Mayer

Department of Mechanical,
Automotive, and Aeronautical
Engineering

Munich University of Applied Sciences
Munich, Germany
Florian.Mayer@hm.edu

2nd Jörg Bentz

Department of Building Services
Engineering, Paper and Packaging
Technology and Print and Media
Technology

Munich University of Applied Sciences
Munich, Germany
Joerg.Bentz@hm.edu

3rd Christian Schweigler

Department of Building Services
Engineering, Paper and Packaging
Technology and Print and Media
Technology

Munich University of Applied Sciences
Munich, Germany
Christian.Schweigler@hm.edu

Abstract— Refrigeration systems play an important role in the energy transition, with 6.1 million metric tons of greenhouse gas emissions in 2019 solely in Germany. Additionally, the worldwide stock of air-conditioning units will almost triple by 2050.

In the project "ENOS" ("Energy Optimization System", funded by the BMWi) the focus lies on the development of an optimization algorithm large-scale cooling systems.

In the current phase of the project, load analyses are performed, looking for patterns to predict future load profiles, with the focus on the operating characteristic of the cold-water storage tank. In operation, due to geometric restrictions the cold-water storage offers only limited potential for reducing peak load situations in the cooling system. The contribution of external and internal loads is investigated. The outside temperature accounts for a minority of the overall energy demand.

Keywords—Cooling, Supply System, Optimization, Algorithm, Hospital, BMWi,

I. MOTIVATION AND GOAL

Energy Transition means significantly reducing greenhouse gas emissions to effectively slow the rate of global warming. The building sector is the fourth largest emitter in Germany with a share of 15.2 percent (cf. [1]). Process cooling and air-conditioning accounts for 5 percent of the building sector's emissions (cf. [2]), which is equivalent to approximately 6.1 million tons of greenhouse gases in 2019 in Germany.

Climate change is continuously increasing the frequency and intensity of summer days ($T_{max} > 25^{\circ}\text{C}$) and of hot days ($T_{max} > 30^{\circ}\text{C}$). These constantly high temperatures are accompanied by a precipitation deficit (cf. [3]). The interest in technical systems to create a good indoor climate for comfort and productivity purposes is rising in Germany. At the same time, the increased average outdoor temperature will raise the cooling load of industrial and process refrigeration systems. According to a forecast by [4], the stock of air conditioning units will almost triple worldwide by 2050.

Refrigeration systems are playing an increasingly important role in the energy transition. Advanced control technology can partially compensate for the additional energy demand of the increasing stock.

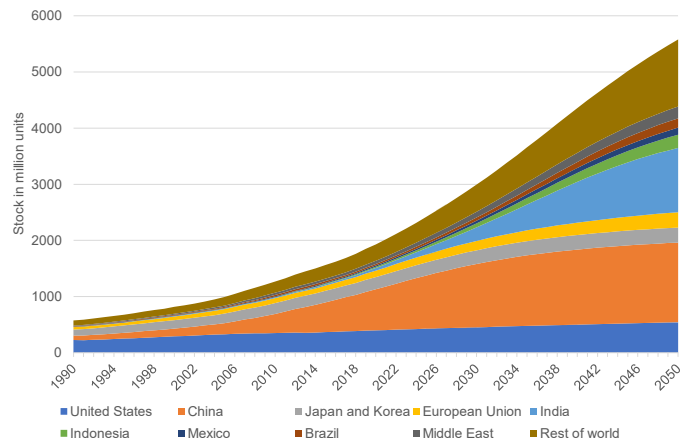


Fig. 1 Global air conditioner stock, 1995-2050 [4]

In the project "ENOS", whose name stands for "Energy Optimization System" and is funded by the BMWi, the focus is on the development of an optimization algorithm for the refrigeration system at the Großhadern Hospital. For this, various input parameters must be determined and analysed. The manual adjustment of energy supply systems is often time consuming and requires a certain technical understanding. Software-based optimization immediately establishes an optimal and efficient operating condition.

The goal of the ENOS project is to provide the plant operator with setting recommendations to achieve the most efficient operating condition possible. In perspective, these setting recommendations will be implemented to a certain extent without prior manual verification. The energy demand and the resulting emissions are to be significantly reduced. A further goal is the reduction of the personnel expenditure, which must be spent for the monitoring and operation of the refrigeration plant.

The Hospital Großhadern was completed in 1977 and is one of the largest hospitals in Germany with over 2,000 beds. Due to the increasing demand, the hospital has been continuously expanded since its completion (cf. [5]). The technical building systems were therefore not planned and built as a single unit but consist of several partly independent subsystems with different responsibilities. Among other things, this leads to more difficult operability. For example, free cooling is not used when outside temperatures are low, as manual monitoring of the parameters would be too personnel intensive. In addition, the system usually runs inefficiently for safety reasons.

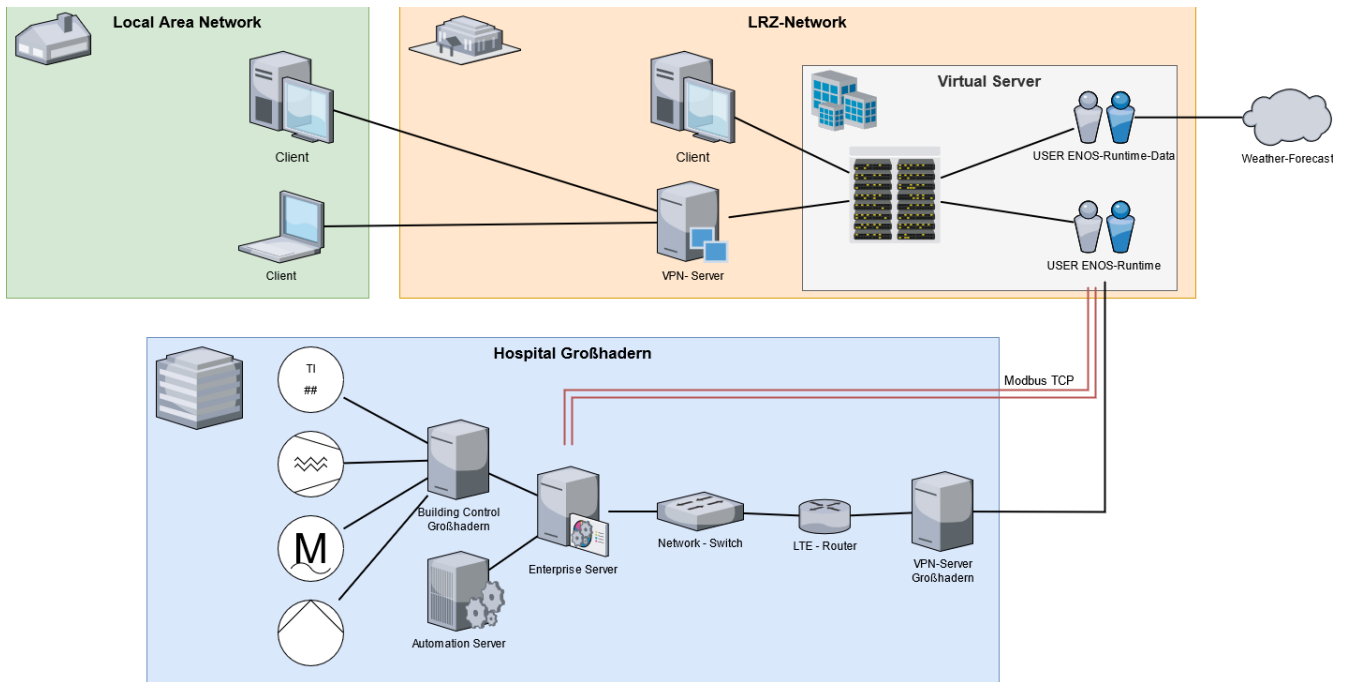


Fig. 2 Network structure of the ENOS project (Own representation with the help of the software Draw.io)

In the previous subproject, a script was written to query and store data from the local weather forecast. Subsequently, the forecast was compared with the real weather data depending on the time difference between the occurrence of the weather event and the query of the weather forecast.

The aim of this project is a load analysis of the refrigeration system of the radiology department at Max-Lebsche-Platz 34, looking for patterns to predict future load profiles.

First, the system-critical components of the refrigeration plant are identified, and their parameters defined. The central component is a load analysis and the determination of different load scenarios. The results are analysed and incorporated into the algorithm.

II. DATA ACQUISITION

Current system data and weather data are recorded in the building services of the Hospital Großhadern and transferred to the "LRZ"-Network via a Modbus. Figure 2 shows the network structure of the ENOS project. The measurement data are recorded via the building services in the clinic and transferred to a central server. This server feeds the data to various automation servers, which control the individual components of the system. Via Modbus, the recorded measurement data is transferred to a virtual server at the Leibniz Computing Centre in Garching. Current weather data and the weather forecast are also stored there.

The data is processed directly on the servers of the Leibniz Computing Centre. Access to these servers is possible via the networks of the Munich universities.

The measured data were transmitted up to the third calendar week 2021 as "Unsigned Integer" in two's complement. This allows the representation of negative numbers in the dual system. The value range of the integer is reduced by one bit,

since the first bit acts as a sign bit. If the number is positive, the sign bit is set to 0, and for negative numbers, it is set to 1. To convert the unsigned integer, the decimal number is converted to binary, the sign bit is removed, and the decimal number is converted back to binary. (cf. [5])

In this case, the measured data of the outside temperature are transmitted by the Großhadern clinical center with 16 bits. 65536 corresponds thereby to "10000000000000" and thus theoretically -0 degrees Celsius. Furthermore, the data is previously multiplied by a factor of 10 in the decimal system to be able to transmit values with one decimal place as integers and to reduce the amount of data.

III. ANALYSIS OF SYSTEM-CRITICAL PLANT COMPONENTS

The structure of various plant components is only recorded in technical plans up to a clear level of representation. To carry out more in-depth optimizations and analyses, various plant components are examined in more detail in the following chapter. The components are identified on one hand by looking at the sensor data and on the other hand by on-site inspections.

Six temperature sensors are assigned to the chiller's cold water storage tank via the data point list. The relative position of the sensors to each other can be taken from the system plan. The exact position of the sensors is determined by a sighting of the chilled water storage tank. Untypically for a storage tank, the hydraulic connection is not subordinated to any stratification. The loading is done by the supply and return of the cold-water side from the top, while the consumer side is hydraulically connected at the bottom.

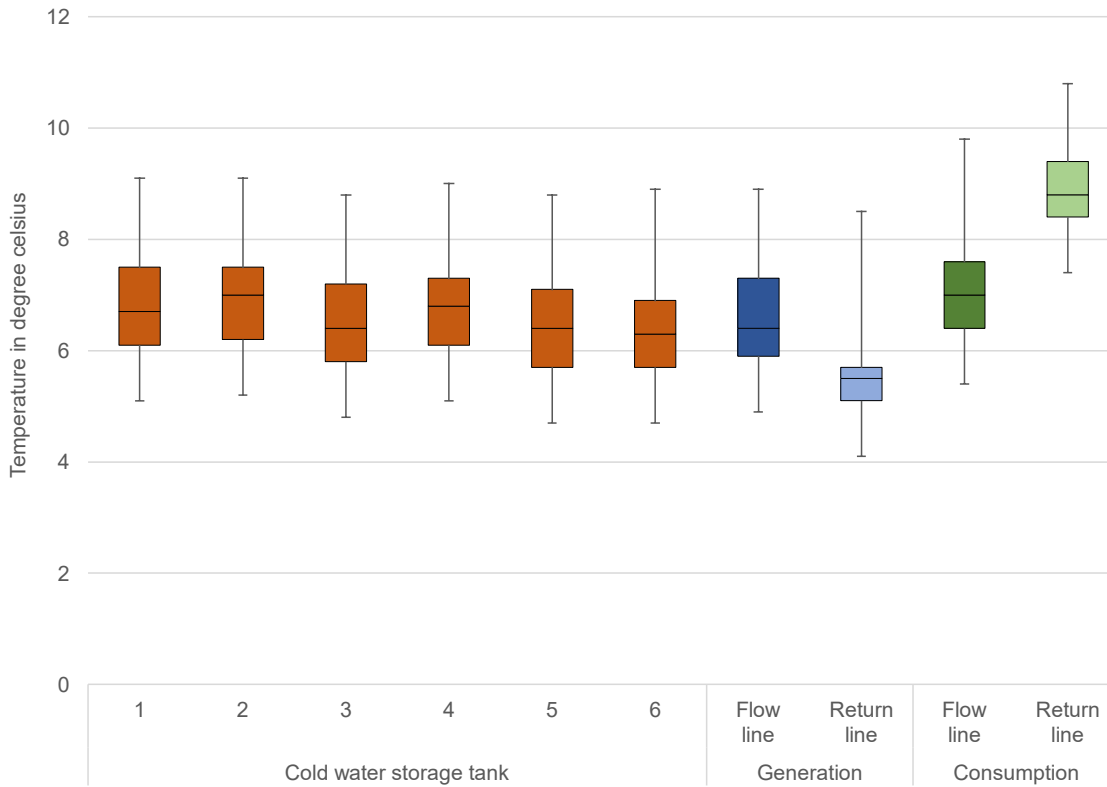


Fig. 3 Temperature data of the cold-water storage tank

According to Figure 2, all measured data are transferred to the LRZ server via a VPN and a Modbus and then saved in an xlsx file format using a Python script for processing. In the Figure 3 the distribution of the temperature data of the storage tank and the connected hydraulic system components from January 16th to March 20th, 2021 is visualized.

An ideal mapping of the state of charge of the storage would be given if the measured data of the temperature sensors 1 and 2 represent the uppermost warmest layer of the storage. In an adiabatic cold storage tank, the return flow of the consumers gives the highest temperature level. Losses to the environment can be neglected due to the high exchange rate of the storage tank. The chilled water pumps of the two chillers exchange the storage water in approximately 8 minutes. A significant increase in temperature due to transmission cooling losses requires longer idle times.

As can be seen from the Figure 3 temperature sensors 1 and 2 show on average colder measured data than the sensor in the return flow of the consumer circuit. On average, the deviation of the highest measured value of the storage tank to the temperature of the return is -1.92 degrees Celsius.

The coldest temperature level of the overall refrigeration system and, consequently, of the chilled water storage tank and the surrounding hydraulics is determined by the temperature of the supply of the chilled water circuit. The average deviation of the lowest measured temperature in the storage tank from the temperature of the flow is 2.56 degrees Celsius.

The difference of the 25% quartile of the coldest measured data to the 75% quartile of the warmest measured data in the storage tank is 1.6 degrees Celsius. Thus, the previously

calculated deviations are higher than the average ranges of variation in the reservoir. On average, the maximum temperature difference at any time is 0.64 degrees Celsius.

The temperatures of the inlet are not adequately reflected in the sensors of the tank. Either mixing occurs outside the sensing range of the temperature sensors or the entering water masses are promptly discharged from the storage tank without a storage effect

IV. LOAD ANALYSIS

All necessary input parameters are determined with the help of the data records obtained via the Modbus and plausible limit values are determined. Input parameters are then defined from the determined scenarios.

The determined load profile of the hospital is then considered in combination with the various load parameters, such as the opening hours of the businesses and possible running times of medical equipment.

With the help of a sensitivity analysis, the influence of various load parameters on the load profile is examined. The differentiation between climate and process cooling is to be considered. The logged outdoor temperature significantly influences the room cooling, while the operating schedule of the hospital largely affects the process cooling. The sensitivity analysis is performed using Microsoft programs and the Visual Basic scripting language, and then visualized for better understanding. The scenarios are determined on the one hand by the determined input parameters and on the other hand by expert interviews. The focus is placed on extreme situations in hospital operations.

To determine the load parameters, firstly the cooling load of the hospital is calculated. For this purpose, the temperatures

and the volume flow of the consumer circuit were loaded via the Modbus and saved in an .xlsx file. Using the parameters determined, (1) is used to calculate the amount of heat Q that the refrigeration system is currently discharging from the building.

$$Q = m * c * \Delta \vartheta \quad (1)$$

Figure 4 shows the hourly averaged consumer load with outdoor temperature for the first week of March 2021.

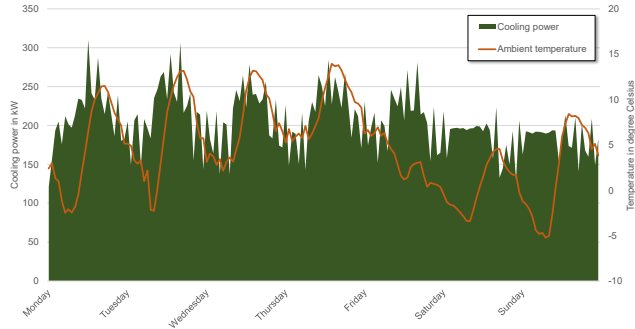


Fig. 4 Cooling power and ambient temperature in the first week of March 2021

The total cooling demand results from contribution of internal and external loads. The internal loads are dependent on heat dissipation from people and equipment, while the external loads are caused by transmission cold losses through the external wall.

The share of the external load is calculated using the correlation coefficient r between two data sets x and y via (2). Hereby, x is the cooling load and y is the outdoor temperature.

$$r = \frac{\sum[(x_i - \bar{x})(y_i - \bar{y})]}{\sqrt{\sum(x_i - \bar{x})^2 * \sum(y_i - \bar{y})^2}} \quad (2)$$

For March 2021, the cooling load is 19% dependent on the outside temperature and thus on the outside load.

V. RESULTS

In Summary, the external load, depended on the outside temperature, accounts for the minority of the overall energy demand. This may be caused by the cold weather situation in March. The ongoing analysis in the summer months will further clarify the influence of transmission heat gains from the ambient.

Due to its limited volume, the cold-water storage acts more as a hydraulic separator rather than an actual thermal buffer. Thus, peak loads cannot be absorbed reliably.

REFERENCES

- [1] Bundesministerium für Wirtschaft und Energie (BMWi), „Energiedaten: Gesamtausgabe,“ Bonn, 2019.
- [2] F. Imbery, K. Friedrich, S. Haeseler, C. Koppe, W. Janssen und P. Bissolli, „Vorläufiger Rückblick auf den Sommer 2018 –eine Bilanz extremer Wetterereignisse,“ Deutscher Wetterdienst, Offenbach, 2018.
- [3] IEA, „Global air conditioner stock, 1990-2050,“ IEA Paris, 2019. [Online]. Available: <https://www.iea.org/data-and-statistics/charts/global-air-conditioner-stock-1990-2050>. [Accessed on 06 05 2021].
- [4] Staatliches Bauamt München, „Bayern,“ 2017. [Online]. Available: <https://web.archive.org/web/20171201031225/http://www.stbam2.bayern.de/hochschulbau/projekte/Klinikum-GH.php>. [Accessed on 18 01 2021].
- [5] I. Junold, „Das negative Zweierkomplementzahlensystem,“ Friedrich-Schiller-Universität, Jena, 2010.

Semi-automated 3D Reconstruction of Indoor and Outdoor Environments from RGB-D Data Captured by a Remote-controlled Robot

Natalie Mülbredt

Nuremberg Institute of Technology

Nuremberg, Germany

E-mail: muelbredtนา67426@th-nuernberg.de

Abstract—Since the release of KinectFusion in 2011, the number of research contributions on 3D reconstruction from RGB-D images has grown rapidly. New methods and algorithms have increasingly resulted in faster and qualitatively better reconstructions of environments. Accordingly, state-of-the-art methods can be well applied in applications where many user-defined models of real-world environments are needed, such as for virtual orientation and mobility training for visually impaired people. While most publications use handheld cameras for RGB-D data acquisition, this work aims to develop a semi-automated process. Instead of a human on site, a robot equipped with a RGB-D camera will be remotely controlled to capture data of indoor and outdoor environments. This data, as well as data captured from the same environments with a handheld camera, will be processed with Open3D’s reconstruction pipeline and compared in terms of reconstruction quality. The aim of this work is to evaluate if the developed remote control of the robot is sufficient to capture adequate data for reconstruction and if the system can replace a human on site.

I. INTRODUCTION

3D reconstruction is one of the classic problems in computer vision and describes the process of creating virtual three-dimensional models by reconstructing the shape and appearance of real-world objects or scenes. The application area of 3D reconstruction is wide-ranging and covers sectors from robotics, medicine, civil engineering, archaeology, gaming or AR and VR technology. Although research in this field goes back decades, new algorithms and methods are still being investigated as the demand for photorealism and performance increases with the advancement of technology. With the launch of the Microsoft Kinect camera in 2010, RGB-D cameras became available to a larger user base. Other cameras followed soon, such as the Intel RealSense, Primesense Carmine, and Google Tango. These cameras are not only low-cost and lightweight, but also provide decent resolution at real-time rates [1], [2]. One of the first and best known - and therefore most frequently cited - approaches is KinectFusion [3], which achieves accurate reconstructions at real-time rates. The response to the KinectFusion algorithm has been tremendous and has led to a significant increase in research for novel or adapted reconstruction methods and algorithms. Thus, despite limited sensor resolution, today’s methods achieve a very high level of reconstruction detail in real time. Depth sensors have become ubiquitous and are even incorporated in mobile devices, mostly

to enhance AR applications. For example, Samsung, Huawei, and LG have equipped their devices with Time-of-Flight (ToF) cameras, while the latest Apple devices are equipped with a Light Detection and Ranging (LiDAR) sensor. In the field of 3D reconstruction of an environment, the terms Simultaneous Localization and Mapping (SLAM) and Structure from Motion (SfM) are commonly used. The term SLAM originates from robotics and is a method used for navigation in unknown environments. Its goal is to estimate the position of the robot and the map of the environment simultaneously and in real time (online). The focus is strongly on trajectory and pose optimization, while the reconstruction of the environment is often limited to a two-dimensional representation or a sparse point cloud [1]. SfM is a technique from computer vision and, similar to SLAM, estimates both camera positions and the 3D environment based on multiple images taken from different viewpoints. However, the focus in this case is on creating dense 3D reconstructions of the environment with high-quality geometry and texturing. In contrast to SLAM, SfM is mostly performed offline.

One application area where such fast 3D reconstructions are particularly useful is virtual orientation and mobility training for visually impaired people. In these applications, blind people can explore an environment in VR via auditory and haptic feedback and build a mental map without time limit or danger before visiting the location in real life. Accordingly, the demand for 3D models of real environments is very high. These could be generated rather quickly by reconstruction from RGB-D images. To eliminate the need for a human to be on site, this approach uses a remote-controlled robot to capture RGB-D images of indoor and outdoor scenes. This can save travel time and thus accelerate the process. To assess the quality of the reconstruction, the same scene will be recorded using a handheld device for comparison. The aim is to evaluate whether the remote control of the robot is sufficient for capturing appropriate data for the reconstruction and whether the system can replace a human on site.

II. RELATED WORK

Even though there are different algorithms for reconstructing static scenes (i.e. scenes without moving objects), the processing pipelines of RGB-D images are always very similar

to each other and consist of three stages: In the first stage noise reduction and outlier removal is applied on the incoming data. In the following step, the camera position of the current frame is estimated by calculating the best aligning transformation to the previous frame. In the final stage, all frames are transformed with their respective estimated transformation and merged into a common model. [1]

The following sections summarize the basic methods and problems of 3D reconstruction from RGB-D images, as well as different solution and optimization approaches for each stage. The publications cited for commonly used algorithms or methods are only a few of many available examples.

A. RGB-D cameras and Depth Map Processing

Basically, there are two different sensor types for range scanning: passive and active sensors. Passive range scanning sensors are equipped with a stereo camera system. For depth estimation, both images are used to calculate the 3D positions of corresponding points via triangulation. Passive sensors are only suitable for highly textured scenes, since only in this case enough color and intensity features are available to detect the correspondences needed for depth estimation. Active range scanning sensors, on the other hand, illuminate the scene with infrared light, allowing depth measurements even in featureless regions. There are two different principles: Structured Light and Time-of-Flight (ToF). While Structured Light cameras project a known and unique pattern onto the scene to generate artificial features for matching, ToF cameras emit an IR light pulse and measure its round-trip time. As the sun's infrared radiation can affect the IR camera's saturation, active range sensors are more suitable for indoor than outdoor applications [4], [5]. Hence, many publications [6]–[8] have focused only on indoor reconstruction. Only a few [9]–[11] have tested their methods for both indoor and outdoor environments. Dark materials pose another problem when using active sensors, as they do not reflect light [4], [5]. Another drawback of RGB-D cameras is that the spatial positions of both lenses differ and a calibrated relative pose is needed to align the color with the depth image. Inaccurate calibration, as well as missing hardware synchronization of the lenses, can lead to RGB-D misalignments [5], [12], [13]. Compared to laser scanners, RGB-D cameras have a smaller field of view, which covers about 60 degrees and are limited in depth measurement to typically less than 5 meters [6]. Furthermore, the color images suffer from optical distortions that are not accounted by the pinhole camera model [12], [13] and the depth estimations suffer from noise [6]. For this reason, the noisy depth images are usually smoothed with a bilateral filter in a preprocessing step [14]–[16].

B. Camera Pose Estimation

The goal of the Camera Pose Estimation is to determine the transformation from the current to the previous input image. The most commonly used method for this is the Iterative Closest Point (ICP) algorithm [6]–[8], [17] The ICP algorithm starts with an initial alignment estimate for the

relative transformation between the corresponding points of two frames and iteratively computes the transformation that minimizes the distance between the point pairs [6]. Instead of finding correspondences for all points, some approaches only use feature points. For feature extraction, several algorithms such as Scale-Invariant Feature Transform (SIFT) [11], [18], Speeded Up Robust Features (SURF) [17], [19] or Oriented FAST and Rotated BRIEF (ORB) [8], [17] are utilized. To achieve proper results, the initial alignment of the ICP algorithm must be close to the optimal pose [20]. For computing these initial estimates, the Random Sample Consensus (RANSAC) algorithm is typically used [6], [8], [11], [17]. The advantage of RANSAC is its robustness against outliers [21].

Tracking drift, which is reinforced by noisy input data, poses a major challenge when scanning large environments [13], [22]. Drift is caused by the accumulation of trajectory errors over time, resulting in a distortion of the reconstructed surfaces when frame-to-frame tracking is used. To reduce drift errors, some approaches use keyframe-to-frame [23], [24] or frame-to-model tracking [3], [6], [25] instead. Nevertheless, small tracking errors can usually not be avoided. These errors cause loop closure problems, so that parts of the scene that have already been scanned are reacquired and thus integrated twice. To counteract this problem, global pose optimizations are applied. The two most common methods are Pose Graph Optimization (PGO) [7], [17], [26] and Bundle Adjustment (BA) [8], [15], [27]. A pose graph represents the constraints between frames and consists of nodes and edges. A node contains a frame and its transformation into the global space. An edge represents a relative transformation between two adjacent frames. Thus, without loop closures, the pose graph would be a linear chain. Instead, loop closures are added as constraints between non-adjacent frames. PGO is the process of minimizing the conflict between the sequential and loop closure constraints. BA uses feature points as constraints to jointly optimize for feature point positions and camera poses by minimizing the reprojection error. [5], [6]

C. Model Representation and Fusion

Various dense 3D surface representations have been developed to fuse the RGB-D data into a common model. The most frequently used representations are voxel- or point-based [1]. In a voxel-based representation, the model surface is stored in a signed distance function (SDF). The SDF contains the signed distance of each point to the nearest surface along the sensor's line of sight. If a point is in front of the surface and thus outside the object, its value is positive. A point with a negative value is located behind the surface. The surface itself is therefore defined by the zero crossings. In addition to the signed distance, an integration weight and the fused color is stored for each voxel. [28]

Since in most cases only the voxels close to the surface are relevant, the truncated signed distance function (TSDF) is mainly used [3], [14], [15], [24], which updates for each incoming frame only the voxels that are within a certain

threshold around the surface. However, this not only averages noise, but also smooths surface details which are smaller than the threshold [5]. A main problem when using voxel-based representations are GPU memory limitations and the restriction to a predefined volume and resolution [2]. The maximum voxel resolution for large scenes is approximately 4 to 10 mm. Thus, the depth and color resolution of the sensors are undersampled [29]. To address this problem, voxel hierarchies [10], [30], [31] or voxel hashing [29], [32], [33] can be applied. Fusion of the model is achieved by per-voxel weighted averaging of the TSDF values, colors and weights in the voxel grid with the incoming ones [5]. The 3D mesh can be extracted either by raycasting [3], [10], [25] or via the Marching Cubes algorithm [8], [14], [24].

Another method is to represent the model by points or surfels [6], [22], [23]. Here, the 3D points of the model are stored in a list together with their associated attributes such as position, normal, radius and confidence counter. The confidence counter indicates whether the point is stable or unstable. When merging the incoming points with the model, correspondence points must first be found. If correspondents are found, the most reliable point is merged with the new point estimate using a weighted average. If no reliable corresponding point is found, the incoming point is added to the global model as an unstable point. Each time a point is merged with other incoming points, its confidence counter is incremented. Once the counter exceeds a certain number, the point becomes stable. [16]

D. Color and texture mapping

A photorealistic 3D reconstruction model should not only possess detailed geometry but also high-fidelity texture. However, the generation and mapping of high-quality textures from multiple input color images is a challenging problem. Noisy input data, optical distortions, camera drift, synchronization errors between captured color and depth frames, motion blur, and view-dependent lighting effects contribute to blur and ghosting artifacts as well as misalignments [12], [13], [34]. One method for calculating the color of a vertex is to blend multiple images using a weighted average [3], [10], [14]. However, these method often results in blurry textures, since geometric misalignments are not addressed.

Another method is projective texture mapping, where each face or vertex is associated with a single view. In order to mitigate visible seams between the boundaries of each face, a discrete labeling problem is typically solved. For example, the state-of-the-art method of Waechter et al. (2014) [35] proposes a global color adjustment strategy that solves a conditional random field energy equation consisting of a data and a smoothing term. While the data term favors views that are closer to the face and less blurry, the smoothing term penalizes inconsistencies between adjacent faces. Nevertheless, these approaches can still produce tearing artifacts when input images have large misalignments [34].

Further approaches for color and texture mapping make use of warping and are more resistant to misalignments caused

by geometric errors and camera drift [13]. While in [36] matching SIFT features are used to apply deformations on the images in order to fit them to the mesh, in [37] and [38] the optical flow between projected texture images is used. A popular approach proposed by Zhou and Koltun (2014) [12] preserves sharp textures by optimizing camera poses and non-rigid warpings on the input images simultaneously. In [13], a global-to-local non-rigid optimization method is proposed to correct camera positions and compensate the geometric error by texture coordinate warping to mitigate the seams between textures. In [34] a global patch-based image synthesize system is developed that generates aligned images from the input images in order to compensate for misalignment caused by geometric error and camera drift. Although these methods can correct only small misalignments, large misalignments can still lead to blur and ghosting artifacts [13], [34].

The latest publications employ neural rendering approaches that use deep networks to generate novel image views [39]–[41].

III. CONCEPT

A. Problem, requirements and method selection

In the research area of virtual orientation and mobility training for visually impaired people, several methods for exploring virtual environments have been developed. For example, users can either navigate through virtual indoor and outdoor environments by using a keyboard [42], [43], a controller [44], [45], force feedback devices [46], [47], walk-in-place movements [48], [49] or by real walking [50]. Thereby, they receive spatial audio and haptic feedback. The goal of these applications is to enable visually impaired people to explore an environment independently and safely, and to build a mental map in advance that they can, at best, retrieve as a navigation aid during their real visit. However, these applications can only be used if 3D models of the desired environments are available. Unfortunately, this is rarely the case. Often the 3D models are either highly simplified or they have been modeled by architects or civil engineers and are too detailed for VR simulations. In both cases, modeling by hand is time consuming and requires the right (usually purchasable) software, skill and experience.

The requirements that a 3D model must meet in order to be used for VR simulations for visually impaired people are geometric accuracy, real size scaling and - contrary to what is probably assumed - accurate appearance. Since some visually impaired people still have residual vision, it should be supported with textures that are as sharp and detailed as possible. Real-time reconstruction, on the other hand, is not required at this point. According to the requirements, offline 3D reconstruction (SfM) from RGB-D images fits well as a method to generate such models. Another advantage of meshes created from RGB-D images is that only the surface of the environment is reconstructed. Everything else is not accessible for the user in VR anyway. Compared to detailed models consisting of various individual objects, the reconstructed

meshes require less memory and computing power and are therefore more suitable for VR applications.

As introduced at the beginning, there are a lot of research papers dealing with reconstruction from RGB-D data. Most of them [3], [6], [27], [33] have used datasets captured with handheld cameras. However, this requires someone to be on site with a basic understanding of data acquisition, such as ensuring that important objects are scanned from all viewpoints to avoid the generation of holes, that areas that have already been scanned are re-scanned to provide loop closures, or that attention is paid to slow movements to avoid motion blur. For this reason, the aim of this work is to develop a semi-automated process for the reconstruction of environments. For data acquisition, it is to be examined whether the human on site can be replaced by a remote-controlled robot. The reconstruction itself is performed automatically to achieve fast and accurate results.

B. Data acquisition

In this work, two different use cases for data acquisition will be compared. The first use case describes the classical approach, where a human on site scans the environment with a handheld camera. The second use case describes the alternative in which a remotely controlled robot scans the environment via its integrated camera.

1) *Use Case 1 - iPad Pro:* For the first use case, an iPad Pro (Apple) with LiDAR sensor and the app Stray Scanner [51] is used as handheld camera. The GUI of the app is similar to a typical camera application and can be used to record a RGB video. In addition, depth images, depth confidence maps, camera position estimates for each image, and the camera calibration matrix are saved.

2) *Use Case 2 - Segway Loomo robot:* For the second use case a Segway Loomo robot (Ninebot) is used. Segway offers a SDK that allows the development of Android applications for the Loomo. Functions are provided to directly access the sensors, such as the RealSense camera or the ultrasonic sensor, and to control the base and head movement of the robot. Furthermore, connections to other Android devices can be established via WiFi to send and receive data. Accordingly, these functions will be used to develop an application to remotely control the Loomo via an Android device. To do this, the RGB image from the RealSense camera is streamed to the connected device and interaction elements are provided for motion control. For easy operation, different control modes will be tested against each other, such as control via joysticks (similar to a gaming controller) or via a simple motion field. For safety reasons, the integrated ultrasonic sensor is used to detect obstacles and to stop the robot if necessary, independently of the remote commands. The captured RGB-D images will be sent to and stored on the Android device. An advantage of the Loomo is that its RealSense camera is located at knee height and thus scans exactly the area that is important for blind people to navigate with the white stick.

C. 3D Reconstruction

For 3D reconstruction, the open source library Open3D [52] for Python is used, as it is well documented and has proven its performance in various publications [7], [20], [53], [54]. In Figure 1 the reconstruction pipeline is visualized. For the reconstruction, various parameters can be configured, such as the ICP or global registration method, the number of frames per fragment, keyframe number, voxel size, and many more. These are marked with a blue diamond. The pipeline

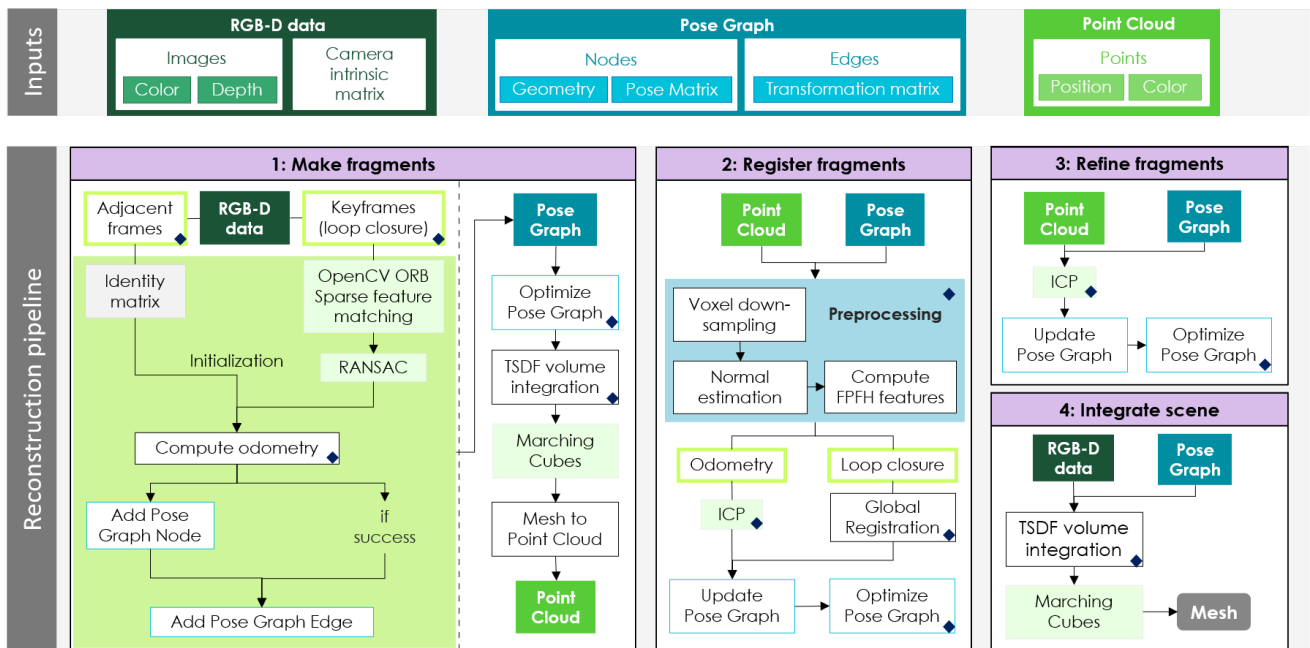


Figure 1. Reconstruction pipeline of Open3D

consists of four individual steps. In the first step, fragments are created. For this, a defined number of synchronized RGB-D images for each fragment and the intrinsic camera matrix are read in and the odometries between neighboring frames are calculated. In addition, a number of keyframes is specified. For keyframes ORB features are detected and RANSAC is used as initialization. The calculated frames and transformations are then added to a pose graph. For each fragment, the pose graph is optimized and the TSDF volume is calculated. The mesh is extracted by using the Marching Cubes algorithm and a point cloud is generated. After the fragments have been created, they are aligned in the global space in the second step. First, the point cloud of each fragment is imported and preprocessed. After that, neighboring fragments are aligned with the ICP algorithm and keyframes with a global registration method (e.g RANSAC). Thereafter, the pose graph is updated and optimized again. In the third step, the pairs detected in step two are each registered using the ICP algorithm and global optimization is performed again to refine the pose graph. The last step integrates all RGB-D images into a common TSDF volume and extracts the mesh by the Marching Cubes algorithm. If necessary, a Color Map Optimization can be performed afterwards. However, this is not integrated in the pipeline by default. Once the reconstruction is completed, the 3D model can be saved and imported into Unity3D, for example, for VR simulations.

Both the RGB-D images from the iPad and those from the Loomo will be processed with the reconstruction pipeline and compared in terms of geometric accuracy and appearance.

IV. CONCLUSION

3D reconstruction from RGB-D images offers a solution to quickly generate 3D models of real environments. This is for example necessary when many customized models are needed, such as for virtual orientation and mobility training for visually impaired people. Many publications showed that detailed reconstructions can be achieved with simple handheld RGB-D cameras. In this work, a semi-automated process will be developed, in which a human on site is replaced by a remotely controlled robot for data acquisition. It will be investigated whether accurate RGB-D images of indoor and outdoor environments can be captured via the remote control. For this, a Loomo robot will be used and different control modes will be tested against each other. For comparison, the same environments will also be captured with an iPad Pro with LiDAR sensor. The data from both systems will then be processed using Open3D's reconstruction pipeline and the resulting models will be compared in terms of geometric accuracy, scaling, and appearance in order to assess whether the robot can replace a human on site.

REFERENCES

- [1] M. Zollhöfer, P. Stotko, A. Görlitz, C. Theobalt, M. Nießner, R. Klein, and A. Kolb, "State of the art on 3d reconstruction with rgb-d cameras," in *Computer graphics forum*, vol. 37, no. 2. Wiley Online Library, 2018, pp. 625–652.
- [2] O. Yilmaz and F. Karakus, "Stereo and kinect fusion for continuous 3d reconstruction and visual odometry," in *2013 International Conference on Electronics, Computer and Computation (ICECCO)*. IEEE, 2013, pp. 115–118.
- [3] R. A. Newcombe, S. Izadi, O. Hilliges, D. Molyneaux, D. Kim, A. J. Davison, P. Kohi, J. Shotton, S. Hodges, and A. Fitzgibbon, "Kinectfusion: Real-time dense surface mapping and tracking," in *2011 10th IEEE international symposium on mixed and augmented reality*. IEEE, 2011, pp. 127–136.
- [4] M. Zollhöfer, "Commodity rgb-d sensors: Data acquisition," in *RGB-D Image Analysis and Processing*. Springer, 2019, pp. 3–13.
- [5] R. Maier, "High-quality 3d reconstruction from low-cost rgb-d sensors," Ph.D. dissertation, Technische Universität München, 2020.
- [6] P. Henry, M. Krainin, E. Herbst, X. Ren, and D. Fox, "Rgb-d mapping: Using kinect-style depth cameras for dense 3d modeling of indoor environments," *The International Journal of Robotics Research*, vol. 31, no. 5, pp. 647–663, 2012.
- [7] S. Choi, Q.-Y. Zhou, and V. Koltun, "Robust reconstruction of indoor scenes," in *Proceedings of the IEEE Conference on Computer Vision and Pattern Recognition*, 2015, pp. 5556–5565.
- [8] J. Wang, S. Huang, L. Zhao, J. Ge, S. He, C. Zhang, and X. Wang, "High quality 3d reconstruction of indoor environments using rgb-d sensors," in *2017 12th IEEE Conference on Industrial Electronics and Applications (ICIEA)*. IEEE, 2017, pp. 1739–1744.
- [9] T. Whelan, M. Kaess, M. Fallon, H. Johannsson, J. Leonard, and J. McDonald, "Kintinuous: Spatially extended kinectfusion," 2012.
- [10] J. Chen, D. Bautembach, and S. Izadi, "Scalable real-time volumetric surface reconstruction," *ACM Transactions on Graphics (TOG)*, vol. 32, no. 4, pp. 1–16, 2013.
- [11] S. Tang, Q. Zhu, W. Chen, W. Darwish, B. Wu, H. Hu, and M. Chen, "Enhanced rgb-d mapping method for detailed 3d indoor and outdoor modeling," *Sensors*, vol. 16, no. 10, p. 1589, 2016.
- [12] Q.-Y. Zhou and V. Koltun, "Color map optimization for 3d reconstruction with consumer depth cameras," *ACM Transactions on Graphics (TOG)*, vol. 33, no. 4, pp. 1–10, 2014.
- [13] Y. Fu, Q. Yan, L. Yang, J. Liao, and C. Xiao, "Texture mapping for 3d reconstruction with rgb-d sensor," in *Proceedings of the IEEE conference on computer vision and pattern recognition*, 2018, pp. 4645–4653.
- [14] E. Bylow, J. Sturm, C. Kerl, F. Kahl, and D. Cremers, "Real-time camera tracking and 3d reconstruction using signed distance functions," in *Robotics: Science and Systems*, vol. 2, 2013, p. 2.
- [15] K. Wang, G. Zhang, and H. Bao, "Robust 3d reconstruction with an rgb-d camera," *IEEE Transactions on Image Processing*, vol. 23, no. 11, pp. 4893–4906, 2014.
- [16] M. Keller, D. Lefloch, M. Lambers, S. Izadi, T. Weyrich, and A. Kolb, "Real-time 3d reconstruction in dynamic scenes using point-based fusion," in *2013 International Conference on 3D Vision-3DV 2013*. IEEE, 2013, pp. 1–8.
- [17] F. Endres, J. Hess, J. Sturm, D. Cremers, and W. Burgard, "3-d mapping with an rgb-d camera," *IEEE transactions on robotics*, vol. 30, no. 1, pp. 177–187, 2013.
- [18] P. Henry, M. Krainin, E. Herbst, X. Ren, and D. Fox, "Rgb-d mapping: Using depth cameras for dense 3d modeling of indoor environments," in *Experimental robotics*. Springer, 2014, pp. 477–491.
- [19] C. Wang and X. Guo, "Feature-based rgb-d camera pose optimization for real-time 3d reconstruction," *Computational Visual Media*, vol. 3, no. 2, pp. 95–106, 2017.
- [20] Q.-Y. Zhou, J. Park, and V. Koltun, "Fast global registration," in *European Conference on Computer Vision*. Springer, 2016, pp. 766–782.
- [21] R. Szeliski, *Computer vision: algorithms and applications*. Springer Science & Business Media, 2010.
- [22] Y.-P. Cao, L. Kobbelt, and S.-M. Hu, "Real-time high-accuracy three-dimensional reconstruction with consumer rgb-d cameras," *ACM Transactions on Graphics (TOG)*, vol. 37, no. 5, pp. 1–16, 2018.
- [23] J. Stückler and S. Behnke, "Integrating depth and color cues for dense multi-resolution scene mapping using rgb-d cameras," in *2012 IEEE International Conference on Multisensor Fusion and Integration for Intelligent Systems (MFI)*. IEEE, 2012, pp. 162–167.
- [24] F. Steinbrucker, C. Kerl, and D. Cremers, "Large-scale multi-resolution surface reconstruction from rgb-d sequences," in *Proceedings of the IEEE International Conference on Computer Vision*, 2013, pp. 3264–3271.

- [25] P. Henry, D. Fox, A. Bhowmik, and R. Mongia, "Patch volumes: Segmentation-based consistent mapping with rgb-d cameras," in *2013 International Conference on 3D Vision-3DV 2013*. IEEE, 2013, pp. 398–405.
- [26] Q.-Y. Zhou and V. Koltun, "Dense scene reconstruction with points of interest," *ACM Transactions on Graphics (ToG)*, vol. 32, no. 4, pp. 1–8, 2013.
- [27] M. Dou, L. Guan, J.-M. Frahm, and H. Fuchs, "Exploring high-level plane primitives for indoor 3d reconstruction with a hand-held rgb-d camera," in *Asian Conference on Computer Vision*. Springer, 2012, pp. 94–108.
- [28] B. Curless and M. Levoy, "A volumetric method for building complex models from range images," in *Proceedings of the 23rd annual conference on Computer graphics and interactive techniques*, 1996, pp. 303–312.
- [29] F. Reichl, J. Weiss, and R. Westermann, "Memory-efficient interactive online reconstruction from depth image streams," in *Computer Graphics Forum*, vol. 35, no. 8. Wiley Online Library, 2016, pp. 108–119.
- [30] M. Zeng, F. Zhao, J. Zheng, and X. Liu, "Octree-based fusion for realtime 3d reconstruction," *Graphical Models*, vol. 75, no. 3, pp. 126–136, 2013.
- [31] F. Steinbrücker, J. Sturm, and D. Cremers, "Volumetric 3d mapping in real-time on a cpu," in *2014 IEEE International Conference on Robotics and Automation (ICRA)*. IEEE, 2014, pp. 2021–2028.
- [32] O. Kähler, V. A. Prisacariu, C. Y. Ren, X. Sun, P. Torr, and D. Murray, "Very high frame rate volumetric integration of depth images on mobile devices," *IEEE transactions on visualization and computer graphics*, vol. 21, no. 11, pp. 1241–1250, 2015.
- [33] I. Dryanovski, M. Klingensmith, S. S. Srinivasa, and J. Xiao, "Large-scale, real-time 3d scene reconstruction on a mobile device," *Autonomous Robots*, vol. 41, no. 6, pp. 1423–1445, 2017.
- [34] S. Bi, N. K. Kalantari, and R. Ramamoorthi, "Patch-based optimization for image-based texture mapping," *ACM Trans. Graph.*, vol. 36, no. 4, pp. 106–1, 2017.
- [35] M. Waechter, N. Moehle, and M. Goesele, "Let there be color! large-scale texturing of 3d reconstructions," in *European conference on computer vision*. Springer, 2014, pp. 836–850.
- [36] E. Aganj, P. Monasse, and R. Keriven, "Multi-view texturing of imprecise mesh," in *Asian Conference on Computer Vision*. Springer, 2009, pp. 468–476.
- [37] M. Eisemann, B. De Decker, M. Magnor, P. Bekaert, E. De Aguiar, N. Ahmed, C. Theobalt, and A. Sellent, "Floating textures," in *Computer graphics forum*, vol. 27, no. 2. Wiley Online Library, 2008, pp. 409–418.
- [38] M. Dellepiane, R. Marroquim, M. Callieri, P. Cignoni, and R. Scopigno, "Flow-based local optimization for image-to-geometry projection," *IEEE Transactions on Visualization and Computer Graphics*, vol. 18, no. 3, pp. 463–474, 2011.
- [39] K.-A. Aliev, D. Ulyanov, and V. Lempitsky, "Neural point-based graphs," *arXiv preprint arXiv:1906.08240*, vol. 2, no. 3, p. 4, 2019.
- [40] V. Sitzmann, J. Thies, F. Heide, M. Nießner, G. Wetzstein, and M. Zollhofer, "Deepvoxels: Learning persistent 3d feature embeddings," in *Proceedings of the IEEE/CVF Conference on Computer Vision and Pattern Recognition*, 2019, pp. 2437–2446.
- [41] J. Thies, M. Zollhöfer, and M. Nießner, "Deferred neural rendering: Image synthesis using neural textures," *ACM Transactions on Graphics (TOG)*, vol. 38, no. 4, pp. 1–12, 2019.
- [42] J. Sánchez, M. Sáenz, A. Pascual-Leone, and L. Merabet, "Enhancing navigation skills through audio gaming," in *CHI'10 Extended Abstracts on Human Factors in Computing Systems*, 2010, pp. 3991–3996.
- [43] J. Sánchez and J. Mascaró, "Audiopolis, navigation through a virtual city using audio and haptic interfaces for people who are blind," in *International Conference on Universal Access in Human-Computer Interaction*. Springer, 2011, pp. 362–371.
- [44] O. Lahav, H. Gedalevitz, S. Battersby, D. Brown, L. Evett, and P. Merritt, "Using wii technology to explore real spaces via virtual environments for people who are blind," *Journal of Assistive Technologies*, 2014.
- [45] K. Allain, B. Dado, M. Van Gelderen, O. Hokke, M. Oliveira, R. Bidarra, N. D. Gaubitch, R. C. Hendriks, and B. Kybartas, "An audio game for training navigation skills of blind children," in *2015 IEEE 2nd VR workshop on sonic interactions for virtual environments (SIVE)*. IEEE, 2015, pp. 1–4.
- [46] O. Lahav and D. Mioduser, "Multisensory virtual environment for supporting blind persons' acquisition of spatial cognitive mapping, orientation, and mobility skills," in *Proceedings of the Third International Conference on Disability, Virtual Reality and Associated Technologies, ICDVRAT 2000*, 2000, pp. 53–58.
- [47] D. Tzovaras, G. Nikolakis, G. Fergadis, S. Malasiotis, and M. Stavrakis, "Design and implementation of haptic virtual environments for the training of the visually impaired," *IEEE Transactions on Neural Systems and Rehabilitation Engineering*, vol. 12, no. 2, pp. 266–278, 2004.
- [48] J. Kreimeier and T. Götzelmann, "Real world vr proxies to support blind people in mobility training," *Mensch und Computer 2018-Workshopband*, 2018.
- [49] Y. Seki and T. Sato, "A training system of orientation and mobility for blind people using acoustic virtual reality," *IEEE Transactions on neural systems and rehabilitation engineering*, vol. 19, no. 1, pp. 95–104, 2010.
- [50] L. Thevin, C. Briant, and A. M. Brock, "X-road: virtual reality glasses for orientation and mobility training of people with visual impairments," *ACM Transactions on Accessible Computing (TACCESS)*, vol. 13, no. 2, pp. 1–47, 2020.
- [51] K. Blomqvist, "Collecting rgb-d datasets on lidar enabled ios devices," 2021. [Online]. Available: <https://keke.dev/blog/2021/03/10/Stray-Scanner.html> (visited on May 12, 2021).
- [52] Q.-Y. Zhou, J. Park, and V. Koltun, "Open3D: A modern library for 3D data processing," *arXiv:1801.09847*, 2018.
- [53] J. Park, Q.-Y. Zhou, and V. Koltun, "Colored point cloud registration revisited," in *Proceedings of the IEEE international conference on computer vision*, 2017, pp. 143–152.
- [54] A. Knapitsch, J. Park, Q.-Y. Zhou, and V. Koltun, "Tanks and temples: Benchmarking large-scale scene reconstruction," *ACM Transactions on Graphics (ToG)*, vol. 36, no. 4, pp. 1–13, 2017.

Development of an Open Source and Offline Voice User Interface for Blind and Visually Impaired People

Christina Oumard

Nuremberg Institute of Technology

Nueremberg, Germany

Email: oumardch67627@th-nuernberg.de

Abstract—Since Blind and Visually Impaired (BVI) people lack a sensory channel to receive information, they often need additional aids, in order to carry on with everyday life. This work addresses the development of an offline Voice User Interface (VUI) framework especially for BVI people. This system consists of an Automated Speech Recognition (ASR), Natural Language Understanding (NLU), Dialog Manager (DM) and Text To Speech (TTS) component. To integrate the needs of BVI people, a questionnaire was sent out to them that gathers information about their previous experiences with voice assistants and further suggestions for new helpful features. The self determined requirements include an intuitive use and navigation through the menu with individual and barrier-free commands. It should provide features for which online variants are not customizable or suitable in terms of data security or adaptability. Additionally the request and response system should be designed to be simply expanded, changed and configured. Besides these specifications also proven principals, design patterns and guidelines from online VUIs and related studies were taken into account during the developing process. A first prototype that works completely offline has already been developed. However, after the gathered requirements have been incorporated, the usability of the system and how well the framework meets the needs of BVI people still needs to be tested.

I. INTRODUCTION

Today's common availability of technology makes our everyday life easier and easier. This is in part through the ever growing availability of smart devices which in recent years gained a significant traction in private homes and lay the foundation for smart home. These smart homes can be defined as a home that improves the comfort, convenience, safety and entertainment of its occupants through being equipped with computing and information technology [1]. They also possess ambient intelligence and automatic control for example through a set of sensors and responds to the needs and behavior of its residents [2]. Devices, that enable the control of smart homes are for example smart speaker like Google Home and Amazon Alexa. The first impression and the features these devices promise are on the one hand an increase in comfort through hands-free operation from a distance and on the other hand more safety through monitoring components like sensors. However these systems are often criticized in terms of data protection. This mistrust can be circumvented by making the system offline in order to avoid sending the recorded voice data to the provider's server for processing. Instead the processing

of the audio takes place locally e.g. on embedded devices. These solutions might not perform as good due to the lower computing power. The whole pipeline of speech recognition, processing and responses takes more time and is also more error-prone. Nevertheless these disadvantages can be partially compensated by the design of the VUI for example through an additional spellchecker or a smaller dictionary of words or intents that can be recognized. Another disadvantage of online services is that these systems cannot be customized independent of the provider. Especially for the proposed approach of an customized offline VUI for BVI this property is very deciding.

In order to make these smart home systems working offline, the VUI operations in particular must run on a local device. The VUI, defined as "a user interface that uses speech input through a speech recognizer and speech output through speech synthesis or prerecorded audio" [3], acts as an interface between the user and the smart home system. Since interaction with a VUI only relies on audio input and output (i.e. hands- and eye-free operations), they are especially suitable for BVI people. This paper proposes a VUI specifically designed for the needs of BVI people. This approach can subsequently also be extended to a smart home system for instance through additional interaction with IoT devices.

The following sections will put the approach into the context of related work, compares different engines for each integrated component, and summarizes the collected findings into an own concept.

II. RELATED WORK

Assistive technologies for BVI people is a research field of large interest. According to investigations into the research of the last two decades [4], the prior topics in this area address the issues of accessibility, independent travel, information access and indoor and outdoor navigation. Through evaluating recent patenting and innovation trends, this study also indicates that the annual growth rate in areas including 'voice and sound control associated with vision assistance' are the highest.

In the following, prior research for offline systems, systems designed for impaired people and also general design guidelines for VUI are discussed.

A. Related approaches of VUIs

The presented related approaches cover VUIs that are designed offline or especially for impaired people.

[5], [6] and [7] describe a home automation based on acoustics for the use with physically challenged people. The system works offline on a raspberry pi. A huge disadvantage is, that it only contains a query processor that returns the implemented output to a users input keyword. The multimodal system of [8] combines a voice interface with tactile gestures to allow a 2.5D representation of 3D artworks, that makes the art accessible for BVI people. [9] presents an offline and privacy-by-design speech assistant for seniors using the frameworks Kaldi, RASA and MaryTTS. Besides these custom developed systems for impaired people commercial services like Amazon also offer features that focus on impaired people. As [10] states, Amazon's voice assistant Alexa will provide better support for people with vision loss in the future. A new feature is in cooperation with the Royal National Institute of Blind People (RNIB) and establishes a direct connection to the RNIB's counseling center without using a smartphone.

The following developments were not published in a paper format but also present implementations of offline speech recognition and VUIs. [11] is named Sarah that runs on a Linux-VM, except the Speech Input. This component works with a raspberry pi 2 and a USB-Microphone (Jabra SPEAK 410). For speech recognition the service from wit.ai is used. A special feature is that it also allows text as an input and not only speech. PIPPA [12] is a completely offline smart speaker based on the technology of neuronal networks, Mozilla DeepSpeech and data storage on an private cloud. This system is already very far in the development and can manage voice control with some complexity. The project [13] introduces into a very similar technical setting as the proposal of this paper. The system is an open source voice assistant with Rasa, Mozilla DeepSpeech, Mozilla TTS and the Rasa Voice Interface. Limitation of this system is the pre-trained Speech To Text (STT), as it is trained on generic data and is not yet customized for the needed vocabulary. They also mentioned to add a spellchecker to the NLU pipeline to compensate for minor errors in the STT model. All of these approaches named similar disadvantages of online VUIs. The first and obvious topics are the voice data security and usage rights [11] due to the permanent listening and analyzing of the private conversations [14]. The second negative aspect is the inflexibility of these systems and that they are only usable as standalone solutions [11]. At least the dominant market position of Google, Amazon and Microsoft in this area is also criticized [12].

In order to give a reference for the offline approaches, the results of [15] are also mentioned. This paper investigates the usability and user experiences of the Google home smart speaker to detect usability challenges of users when interacting with it. Some issues that have been found are the dependency on a reliable internet connection, the influence of background noise while interacting with the device and capturing multiple

commands in a single transaction. Overall it was classified as a usable and user-friendly device that shows promises for international users.

B. Design Patterns and Style Guides

[16] introduces design patterns for VUIs and [17] in general audio navigation patterns. Both also provide examples implemented with VoiceXML <https://www.w3.org/TR/voicexml20/>. The main challenge for an VUI is, to provide the user an intuitive design for navigating through the required steps to achieve their purpose. Under considerations of the user's short term memory it is very important to properly dose the provided information during this navigation. The ear can not browse a set of recordings the way the eye can scan visual information. While information on screen is in most cases available during the whole interaction, the information of VUI is no longer available after being received. These problems were elaborated:

1. Speech is transient. Once you hear it or say it, it is gone.
2. Speech is invisible. The user does not see the interface.
3. Speech is asymmetric. Speaking is faster than typing, but listening is slower than reading
4. Speech is one-dimensional. The ear can not browse and depends on the output timing of the system
5. Speech is flexible. The same issue can be expressed in different ways, which affects the accuracy of the system.

To handle all these problems the following patterns are provided:

- Scripted Interaction: Guide the selection of an option with a limited vocabulary.
- Escalating Detail: Provide an error recovery strategy when the recognizer does not return a recognition hypothesis
- Index: Present a menu of options to the user
- Decoration: Present the same choices to the user with different background information.
- Detailed information: Deliver information with a different level of detail. like footnote an available link to more information
- Information Spreading: Divide the amount of information being delivered to the user at once into manageable pieces
- Active Reference: help the user stay oriented

Besides design patterns there are also style guides and principles online available from established systems like Amazon Alexa [18], Google [19] and Watson [20]. Some of these guidelines are also used for the concept of this proposal (see section III).

There are also some approaches that enriched or replaced the verbal audio feedback with sounds. For example auditory icons instead of graphical components [21], earcons as navigational cues (location) in a menu hierarchy [22], or Spearcons (Speech-based earcons) [23] and Spindex [24] are used. These extensions come with an improved usability that could already be validated within studies. Due to sound cues being shorter than spoken text, the speed of the system itself

and therefore the users search time and accuracy through the interface menu could be improved. Nevertheless for using this earcons, their language has to be learned and it might not be the same for every system. Another problem arises when the menu is expanded at a later date, as this might cause a lot of restructuring and reordering of the earcons. To avoid this issue spearcons are more useable. They are generated by speeding up the verbal menu phrase until it is no longer comprehensible as a particular spoken word. This makes them unique but also similar to similar menu actions. For example spearcons of the menu items "save" and "save as" sound similar. This characteristic contributes to a better understanding of the system by the user. Due to the fact that these cues are not related to the position in the menu hierarchy but to the specific name of the menu item, a change in the menu is a lot easier as with earcons. Spindex cues are generated similar to Spearcons, but only with the first letter of each menu item.

C. Executed Framework Comparisons

The following studies compare components that are part of VUIs. The gained insights will be used to develop a concept and select engines for a VUI specifically for BVI people. [25] compares ten, at the time, different state-of-the-art dependency parsers to support users of NLP applications when selecting a parser. Therefore their accuracy and speed are evaluated while covering a range of approaches, on a large multi-genre corpus of English. The investigations revealed that for highest speed, spaCy and ClearNLPg are good choices.

[26] compares six NLU services LUIS, Watson, APi.ai, wit.ai, Lex and Rasa. The authors give the advise to compare the different services with domain specific data, before using an NLU service. For the used corpora, LUIS showed the best results, but the open source alternative RASA could achieve similar results with their testing conditions.

[27] lists ten existing platforms for Conversational AI and evaluates the levels of conversational maturity. Classes from 1a to 4b were defined, with 1a being the worst and 4b the best class. Notable where DialogFlow and Amazon Lex, as they were assigned with the best awarded class 3b, followed by VoiceXML with 3a. RASA was also rated good with class 2b.

[28] compares dialog frameworks: RavenClaw, DialogStudio, Owlspeak (uses VoiceXML), Rasa, OpenDial, PyDial and compared them with their own framework design. This framework enables the user to effectively develop an intelligent dialog system and provides a hierarchical argument structure. The framework was tested through developers that were tasked with developing task-oriented dialog systems. The framework turned out to be easy to use and that it works effectively. But if the system is incorrectly implemented problems occurred by locating the responsible component.

III. CONCEPT

Based on the in section II introduced literature a concept for the VUI was designed. It consists of the following

components: ASR from DeepSpeech [29] (german version: [30]), NLU from spaCy [31], DM will be implemented with RASA [32] and TTS with SVOX-pico-TTS (see. Figure 1). The system runs on a raspberry pi 4 and for audio input a ReSpeaker Mic Array v2.0 is used. The pipeline starts with the users' spoken input. The ASR component converts this speech to written text. Further preparation for the DM are then carried out by the NLU component. Through interpreting the text, semantic connections, the meaning and the context of the statement can be understood. The resulting data is used as input for the DM, that generates the textual response. This text is synthesized again to speech by the TTS component and provided to the user.

In the following pros and cons of selected engines for each VUI component are summarized. For the ASR component DeepSpeech [29], [30] and pocketsphinx [33], snips [34] and snowboy are compared (see Table I). For NLU spaCy, snips and RASA [32] (see Table II), for DM RASA and VoiceXML [35] (see Table III) and for TTS Mozilla TTS and Pico2wave are compared (see Table IV).

Conclusive RASA with the SpaCy NLU backend and snips perform very similar and both can keep up very well with the online versions [37], [38]. In terms of readiness to use and language variety the decision is made for RASA NLU with SpaCy backend. This framework was also rated very good in [26]. In general, more positive than negative ratings were found, which makes the final selection much more difficult. In order to determine a final combination, at least the two DMs VoiceXML and RASA are both implemented and compared. During the implementation and use of RASA, further advantages and disadvantages could be identified. First the docs, covering among other things general instructions, examples, tutorials, best practices are very comprehensive and useful. The training of the custom model with own defined user intents, systems responses, stories and rules runs fast and easy locally. Also some configs, endpoints, credentials and further actions through python code can be added easily. Another point to highlight is the ease of testing and debugging of the trained model as performance metrics like accuracy and F1-score are made available through the provided development

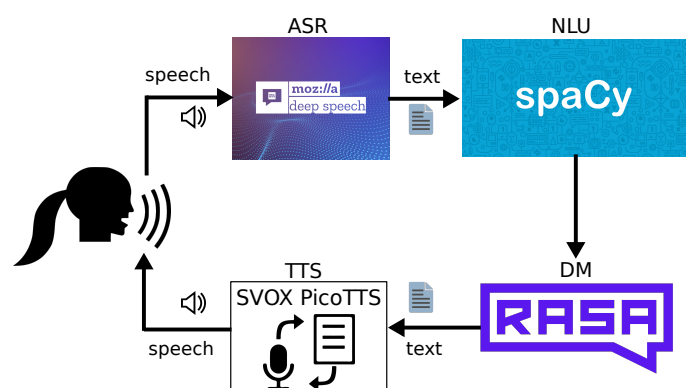


Figure 1. Concept and procedure for the VUI development

Table I
PROS AND CONS OF ASR FRAMEWORKS

ASR	Pro	Con
DeepSpeech	<ul style="list-style-type: none"> - open source, - based on deep learning - architecture is significantly simpler than traditional speech systems, through laboriously engineered processing pipeline - pretrained english and german models - transfer learning - training process with tensorflow or local - crowd-sourced approach - low Word Error Rate (WER) [36] 	huge model-size and cpu usage [36]
pocketsphinx	<ul style="list-style-type: none"> - works with Linux, Windows, on MacOS, iPhone and Android - small modelsize 	<ul style="list-style-type: none"> - uses Hidden Markov Model - high WER [36]
snips	<ul style="list-style-type: none"> - online training, offline tooling and machine learning pattern as download - domain specific ASR 	
snowboy	online training, offline tooling	hotword detection

Table II
PROS AND CONS OF NLU FRAMEWORKS

NLU	Pro	Con
spaCy	<ul style="list-style-type: none"> - high speed - 49+ languages - No vendor lock-in - applies deep learning methods by using tensorflow 	
snips	- open source	only 6 languages
RASA	<ul style="list-style-type: none"> - open source - 9 languages - offers different pipelines (one with spaCy) - can be used with a GUI - pre-defined pipelines with sensible defaults which work well for most use cases 	

Table III
PROS AND CONS OF DM FRAMEWORKS

DM	Pro	Con
RASA	<ul style="list-style-type: none"> - open source - contextual dialogs - memory for context - short conversation with context and comprehension on a intermediate level - easily competes with the other commercial products - based on machine learning - combines NLU and DM 	
VoiceXML	<ul style="list-style-type: none"> - spelling correction - small talk - long conversation with context and comprehension on an advanced level - shields application authors from low-level, and platform-specific details 	

Table IV
PROS AND CONS OF TTS FRAMEWORKS

TTS	Pro	Con
Mozilla TTS	- 20+ languages	- six times slower than real time
SVOX-pico-TTS	<ul style="list-style-type: none"> - small - sounds natural - fast synthesis - included into the 1.6 release of Android platform 	- 5 languages

tools (e.g. rasa shell). The only disadvantage is the needed training after changing the files defining the rules, stories and intents the model depends on. For using VoiceXML the assistant has to run on a server that also stores the vxml files. It is possible to link a phone number to the application and call the implemented assistant. Whereas RASA comes with a NLU component, the VoiceXML platform consists of the following partially optional elements: the VoiceXML interpreter, ASR, a TTS component, audio playback and a voice recognition system. To use the additional components, the system needs to be linked to der VoiceXML server. Since this VUI is intended to run completely offline, these components can not be used. In order to only use the standardized concept of the dialog management based on the vxml files, an own interpreter for the vxml files would have to be implemented. Since the advantages of VoiceXML can not be used due to the offline design, RASA seems to be more suitable for this application.

To adapt the VUI to BVI people, their individual experiences with existing voice assistants, suggestions for yet missing helpful features and example dialogs for the DM are gathered through a questionnaire. The questionnaire was designed with accessibility in mind and can be filled out online with a screen reader. In addition, a telephone number is provided to go through it also by telephone in case of problems or general preference.

Besides the user specifications, the general requirements are set through online available design patterns and guidelines from proven systems like Google Assistant, Alexa and Watson.

The following principle from Google (G) [19], Alexa (A) [18] and Waton (W) [20] will be integrated during the development:

- G: **"Optimize for relevance:** In conversation, saying too much is as uncooperative as saying too little. Facilitate comprehension by keeping turns brief and optimally relevant from the user's point of view."
- A: **Context carryover and pronouns:** conversations often refer to previous topics and replace nouns with pronouns such as "it" or "that".
- A: **Handle over or under-answering:** Skip questions or ask for information again, if the user over or under answers.
- A: **End the prompt in a question:** In order to guide the user and show its their turn.
- A: **Keep lists under four items:** "On average, humans can only retain four objects within their working memory at a time."

- A: **Always explicitly acknowledge a request:** Repeat the recognized text that the user can evaluate if everything was understood correctly.
- A: **Proactively offer more when a goal is completed:** Point users to features they may not know about yet.
- W: **Recipient Design:** Adapt the flow of the conversation to the user's approach and knowledge and do not prescribe a single path
- W: **Minimization:** "using the least number of words or requiring the least amount of effort".
- W: **Repair:** Relax the concern of minimization when recipient misunderstood for example by paraphrasing or elaborating.

IV. CONCLUSION

In summary this paper presents a literature research to the topic of VUIs, designed offline and/or for impaired people, their components and proven guidelines and design patterns. Based on previous research pros and cons for all components: ASR, NLU and DM and TTS are summarized and one in each category is selected for the proposed VUI. To decide which DM to use, RASA (with SpaCy pipeline) and VoiceXML are both implemented and tested. At the current time and state of the project, the selection consists of Mozilla DeepSpeech, SpaCy, RASA and Pico. Future work contains an evaluation of the received questionnaires and clustering of proposed requirements. Based on these specifications the DM will be customized and the underlying models of ASR might be trained on more needed words. After the system is developed and passes first technical tests, it will be evaluated again by BVI people.

REFERENCES

- [1] F. K. Aldrich, "Smart homes: past, present and future," in *Inside the smart home*. Springer, 2003, pp. 17–39.
- [2] L. C. De Silva, C. Morikawa, and I. M. Petra, "State of the art of smart homes," *Engineering Applications of Artificial Intelligence*, vol. 25, no. 7, pp. 1313–1321, 2012.
- [3] D. Schnelle-Walka, "I tell you something," in *Proceedings of the 16th European Conference on Pattern Languages of Programs*, 2011, pp. 1–26.
- [4] A. Bhowmick and S. M. Hazarika, "An insight into assistive technology for the visually impaired and blind people: state-of-the-art and future trends," *Journal on Multimodal User Interfaces*, vol. 11, no. 2, pp. 149–172, 2017.
- [5] M. Kamala, G. Bhanusree, M. Dullapally, P. Thakkar, and R. Patel, "Offline voice recognition with low cost implementation based intelligent home automation system."
- [6] S. Suresh and Y. S. Rao, "Modelling of secured voice recognition based automatic control system," *International Journal of Emerging Technology in Computer Science & Electronics (IJETCSE) ISSN*, pp. 0976–1353, 2015.
- [7] G. Prasanna and N. Ramadass, "Low cost home automation using offline speech recognition," *International Journal of Signal Processing Systems*, vol. 2, no. 2, pp. 96–101, 2014.
- [8] J. Iranzo Bartolome, L. Cavazos Quero, S. Kim, M.-Y. Um, and J. Cho, "Exploring art with a voice controlled multimodal guide for blind people," in *Proceedings of the Thirteenth International Conference on Tangible, Embedded, and Embodied Interaction*, 2019, pp. 383–390.
- [9] A. Seiderer, H. Ritschel, and E. André, "Development of a privacy-by-design speech assistant providing nutrient information for german seniors," in *Proceedings of the 6th EAI International Conference on Smart Objects and Technologies for Social Good*, 2020, pp. 114–119.
- [10] J. Erl, "Alexa unterstützt menschen mit sehverlust," <https://mixed.de/alex-a-unterstuetzt-menschen-mit-sehverlust/>, April 2021 (accessed May 13, 2021).
- [11] Micha, "Diy sprachsteuerung (fast) komplett offline," <https://duke.de/2017/02/diy-sprachsteuerung-fast-komplett-offline/>, February 2017 (accessed May 13, 2021).
- [12] R. Peinl, "Smart speaker ohne cloud," https://smarthome-franken.org/wp-content/uploads/2019/02/Peinl-2019-Forschungspaper_Smart-Speaker.pdf, January 2019 (accessed May 13, 2021).
- [13] J. Petraityte, "How to build a voice assistant with open source rasa and mozilla tools," <https://blog.rasa.com/how-to-build-a-voice-assistant-with-open-source-rasa-and-mozilla-tools/>, August 2019 (accessed May 13, 2021).
- [14] CS, "Sprachsteuerung auf dem raspberry pi mit jarvis – teil 3 offline spracherkennung," <https://schmidt-feldberg.de/sprachsteuerung-auf-dem-raspberry-pi-mit-jarvis-teil-3-offline-spracherkennung/>, March 2018 (accessed May 13, 2021).
- [15] A. Pyae and T. N. Joelsson, "Investigating the usability and user experiences of voice user interface: a case of google home smart speaker," in *Proceedings of the 20th International Conference on Human-Computer Interaction with Mobile Devices and Services Adjunct*, 2018, pp. 127–131.
- [16] D. Schnelle and F. Lyardet, "Voice user interface design patterns," in *EuroPLoP*, 2006, pp. 287–316.
- [17] D. Schnelle, F. Lyardet, and T. Wei, "Audio navigation patterns," in *EuroPLoP*, 2005, pp. 237–260.
- [18] Amazon.com, "Alexa design guide," <https://developer.amazon.com/de-DE/docs/alexa/alexa-design/get-started.html>, 2021 (accessed April 18, 2021).
- [19] Google.com, "Conversation design," <https://developers.google.com/assistant/conversation-design/welcome>, 2021 (accessed April 18, 2021).
- [20] B. Moore and R. Arar, "Talk meets technology - conversational design guidelines," <https://conversational-ux.mybluemix.net/design/conversational-ux/>, 2021 (accessed April 18, 2021).
- [21] E. D. Mynatt, "Transforming graphical interfaces into auditory interfaces for blind users," *Human-Computer Interaction*, vol. 12, no. 1-2, pp. 7–45, 1997.
- [22] S. A. Brewster, "Using nonspeech sounds to provide navigation cues," *ACM Transactions on Computer-Human Interaction (TOCHI)*, vol. 5, no. 3, pp. 224–259, 1998.
- [23] B. N. Walker, A. Nance, and J. Lindsay, "Spearcons: Speech-based earcons improve navigation performance in auditory menus." Georgia Institute of Technology, 2006.
- [24] M. Jeon and B. N. Walker, "'spindex': Accelerated initial speech sounds improve navigation performance in auditory menus," in *Proceedings of the human factors and ergonomics society annual meeting*, vol. 53, no. 17. SAGE Publications Sage CA: Los Angeles, CA, 2009, pp. 1081–1085.
- [25] J. D. Choi, J. Tetreault, and A. Stent, "It depends: Dependency parser comparison using a web-based evaluation tool," in *Proceedings of the 53rd Annual Meeting of the Association for Computational Linguistics and the 7th International Joint Conference on Natural Language Processing (Volume 1: Long Papers)*, 2015, pp. 387–396.
- [26] D. Braun, A. H. Mendez, F. Matthes, and M. Langen, "Evaluating natural language understanding services for conversational question answering systems," in *Proceedings of the 18th Annual SIGdial Meeting on Discourse and Dialogue*, 2017, pp. 174–185.
- [27] J. Aronsson, P. Lu, D. Strüber, and T. Berger, "A maturity assessment framework for conversational ai development platforms," *arXiv preprint arXiv:2012.11976*, 2020.
- [28] Y. Park, S. Kang, and J. Seo, "An efficient framework for development of task-oriented dialog systems in a smart home environment," *Sensors*, vol. 18, no. 5, p. 1581, 2018.
- [29] A. Hannun, C. Case, J. Casper, B. Catanzaro, G. Diamos, E. Elsen, R. Prenger, S. Satheesh, S. Sengupta, A. Coates *et al.*, "Deep speech: Scaling up end-to-end speech recognition," *arXiv preprint arXiv:1412.5567*, 2014.
- [30] A. Agarwal and T. Zesch, "German end-to-end speech recognition based on deepspeech," in *KONVENS*, 2019.
- [31] M. Honnibal and I. Montani, "Industrial-strength natural language processing," <https://spacy.io/>, 2021 (accessed May 13, 2021).
- [32] T. Bocklisch, J. Faulkner, N. Pawlowski, and A. Nichol, "Rasa: Open source language understanding and dialogue management," *arXiv preprint arXiv:1712.05181*, 2017.

- [33] D. Huggins-Daines, M. Kumar, A. Chan, A. W. Black, M. Ravishankar, and A. I. Rudnicky, "Pocketsphinx: A free, real-time continuous speech recognition system for hand-held devices," in *2006 IEEE International Conference on Acoustics Speech and Signal Processing Proceedings*, vol. 1. IEEE, 2006, pp. 1–1.
- [34] A. Coucke, A. Saade, A. Ball, T. Bluche, A. Caulier, D. Leroy, C. Doumouro, T. Gisselbrecht, F. Caltagirone, T. Lavril *et al.*, "Snips voice platform: an embedded spoken language understanding system for private-by-design voice interfaces," *arXiv preprint arXiv:1805.10190*, 2018.
- [35] J. A. Larson, "Voicexml and the w3c speech interface framework," *IEEE MultiMedia*, vol. 10, no. 4, pp. 91–93, 2003.
- [36] P. Inc., "Speech-to-text benchmark," <https://github.com/Picovoice/speech-to-text-benchmark>, January 2020 (accessed May 13, 2021).
- [37] J. Dureau, "Snips nlu is an open source, private by design alternative to dialogflow, amazon lex, and other nlu cloud services," <https://medium.com/snips-ai/snips-nlu-is-an-open-source-private-by-design-alternative-to-dialogflow-amazon-lex-and-other-nlu-a95dbe16f4a1>, July 2018 (accessed May 13, 2021).
- [38] A. Coucke, "Benchmarking natural language understanding systems: Google, facebook, microsoft, amazon, and snips," <https://medium.com/snips-ai/benchmarking-natural-language-understanding-systems-google-facebook-microsoft-and-snips-2b8ddcf9fb19>, February 2017 (accessed May 13, 2021).

Requirements and trends of modern Manufacturing Execution Systems in context of Industry 4.0

Franziska Scharold
 University of Applied Sciences
 Ansbach
 Faculty of Technology
 Ansbach, Germany
 franziska.scharold@hs-ansbach.de

Abstract—This paper aims to identify requirements and trends of modern Manufacturing Execution Systems that arise in the context of Industry 4.0, based on a literature review. The megatrend Industry 4.0 has arrived in factories several years ago. Before this term emerged, Manufacturing Execution Systems already existed. Nevertheless, heterogeneous software environments that are not integrated can be found in many factories. In addition, the demand for customized products, which require small batch sizes and claim a maximum degree of flexibility, is increasing. Thus, a Manufacturing Execution System is necessary, which makes the complexity of the production processes controllable. This paper highlights that the three requirements of unified shopfloor connectivity, cloud computing & advanced analysis and decentralization are important for modern Manufacturing Execution Systems. Furthermore, the trends of digitalization have an impact on the modules of resource and material management. This work is addressed to all interested readers from the fields of engineering, computer science and automation technology.

Keywords—*Manufacturing Execution Systems, Digital Manufacturing, Smart Factory, Industry 4.0*

I. INTRODUCTION

A Manufacturing Execution System (MES) is a production management system that operates close to the process. This system supports the MES tasks defined in the guideline VDI 5600 [1], which was defined by the Association of German Engineers (VDI). An MES monitors, plans and controls production processes in discrete manufacturing as well as in the process industry and provides relevant information for decision makers and process managers [1].

Manufacturing Execution Systems are the link between the corporate management level and the shopfloor (see Figure 1). This is referred to as vertical integration. At the corporate management level, Enterprise Resource Planning (ERP) maps commercial processes and refers to a long-term time horizon of weeks to months. The shopfloor, on the other hand, refers to the operational machine and control level, where the time horizon varies from minutes to seconds [2].

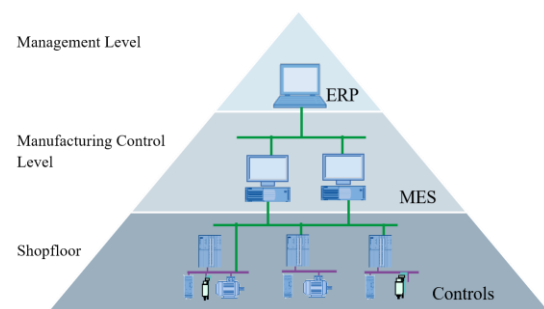


Fig. 1. Classification of a MES in the IT infrastructure of a company [1]

In recent decades, the operation and control of manufacturing systems has changed significantly. Since 2013, the concept of "Industry 4.0" has been strongly promoted by the federal government in Germany. This fourth industrial revolution subsumes the megatrend of digitalization in industry. The concept focuses on the digital model of a real factory in all areas and extends across the entire value chain. Cyber-physical production systems (CPPSs) are created by merging physical production processes with information and communication technology [3]. This creates a "Smart Factory" in which CPPSs collect information from physical production processes to make decentralized decisions with high flexibility. In addition, Industry 4.0 includes the integration of the Industrial Internet of Things (IIoT), process simulation and optimization, cloud computing, and artificial intelligence (AI) [4]. Therefore, it can be assumed that the future of MESs will be strongly influenced by the fourth industrial revolution [5].

II. REQUIREMENTS OF A MODERN MES

The paradigm of the fourth industrial revolution is also changing the requirements for MESs. Industry 4.0 assumes a fully interconnected factory. In addition to the vertical integration already mentioned, this also requires horizontal integration. This is understood to involve a complete mapping of all data that is generated during the manufacturing process. It also refers to the processes within a company as well as across company boundaries [6].

Previous requirements for an MES do not fully consider this change. Based on the concept of the Smart Factory, the following new requirements therefore arise:

A. Unified Shopfloor Connectivity

In a Smart Factory, it is assumed that a large number of different machines are involved [7]. For this reason, the use of standardized communication between the machines and the MES is necessary. UMCM (Universal Machine Connectivity for MES) can be used to connect the machines and the MES. UMCM is based on VDI Guideline 5600. In contrast to standards such as OPC, UMCM describes not only the use of a standardized transport layer (e.g. XML or OPC or OPC-UA) but also the application layer and its logical structure. The protocol of the application layer includes both the syntax and the data contents and units. This ensures that the machines and the MES speak the same language. UMCM can be used to transfer data such as time stamps, process values, counter readings and the machine status [8].

B. Cloud Computing & Advanced Analysis

A previous requirement for MESs was online capability, which enabled short-term reactions to changes in the production process. This was based on the real-time capability of the production systems [6]. In the context of Industry 4.0, the trend of cloud computing is emerging. This approach is designed to extend or replace local factory software by using software from cloud services. Both the company's own and third-party hardware can be used. If third-party hardware is used, data management and certain software logics and functions can be outsourced. This opens up new business models for MES providers. However, outsourcing the local factory software also raises questions about data security and privacy [9].

The networking of production plants to CPPSs creates large volumes of data that must be processed and stored. This data provides information about the status of the product and the overall production system. A holistic view of manufacturing processes is the vision of the Smart Factory. To achieve this goal, there must be an integration of data from different sources. Advanced analytics is used to gain a complete understanding of the production processes. For this, a real-time analysis of the data is mandatory, even before it is stored. However, an offline capability of the MES is also essential [5]. By using AI, structures of data streams in a production line can be analyzed and anomalous behavior can be identified. Early anomaly detection can prevent production disruptions and thus increase the output of the CPPSs [10].

C. Decentralization

In order to achieve a certain degree of autonomy from time-intensive, recurring processes, the fourth industrial revolution envisions a flexibilization and decentralization towards service-oriented architectures (SOA) [3]. This dissolves the previous strict separation between the levels in the IT infrastructure in companies (see Figure 2). In the future, the existing automation hierarchy will be successively dissolved by the introduction of decentralized, networked systems. This means that the existing structures for hardware and networking as well as for engineering and information processing will no longer exist. With the possibility of providing and using decentralized services in the various nodes, the automation pyramid is gradually abstracted to its functional structure by means of CPPSs. However, the real-time critical controllers will continue to be located

predominantly close to the process at the field level [11]. The first signs of this requirement can already be seen in the automotive industry. Necessary work steps are no longer planned in the work preparation department, but at various locations. This is done by collecting and aggregating data that accumulates over the entire production process [7].

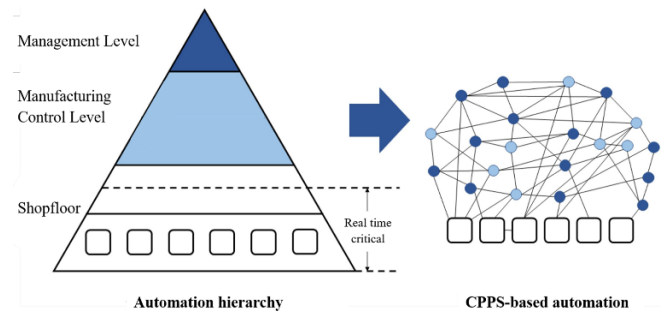


Fig. 2. Dissolution of the hierarchical automation pyramid to a CPPS-based automation [11]

III. MES TRENDS

The tasks of the MES defined in VDI Guideline 5600 simultaneously describe its modules [1]. MESs typically have a modular structure. These are, for example, data acquisition, performance analysis, and resource and personnel management. Companies using an MES can freely combine the system according to their own needs [6].

Some trends that have developed within the modules in connection with Industry 4.0 are presented below.

The module *resource management* aims to ensure that the availability and technical functionality of the resources are guaranteed on time and in line with requirements. A distinction is made between different categories of equipment, such as machines, lines, tools and NC programs. Frequently, a conflict of objectives arises between high reliability and long availability. Maintenance is thus a central aspect [1]. This resulted in the trend of smart maintenance. For this, a maintenance technician receives a message about a machine failure on his smartphone. This message contains relevant information of the affected machine. A maintenance order is generated with the smartphone. After the maintenance technician has analyzed the condition of the machine, he enters any problems discovered in the maintenance order and can also add images of the damage to the digital machine history [7].

The aim of *materials management* is to supply production with materials on time and as required and to manage circulating stocks. The latter involves materials that are outside the inventory-managed warehouses and are called work in progress (WiP). The tasks of material management include batch management, initiation of material transports and management of the WiP [1]. In the context of Industry 4.0, digital availability and networking of all information is required to achieve an effective and efficient material supply in real time. Companies often use different transport systems equipped with various degrees of automation (manual transports, driverless transport systems, etc.). In addition, different production planning and control methods are also used, e.g. supermarket, Kanban, push-pull principles. Therefore, the trend is emerging for MESs to take on the role of interoperability manager. This enables target-oriented material flows through an adapted information flow for an

efficient and dynamically adapted production flow in the company and along the supply chain [12].

IV. CONCLUSION

In this paper, the requirements and trends of new MESs in the context of Industry 4.0 were shown. Existing requirements are changing in the course of the fourth industrial revolution with regard to unified shopfloor connectivity, cloud computing & advanced analysis and decentralization. The trends of digitalization also have an influence on the modules of MESs. This is particularly evident in the modules of resource and material management. It can be assumed that the Industry 4.0 concept will also influence all other modules according to VDI Guideline 5600. The requirements and trends surveyed show that MESs are an integral part of the Smart Factory.

This work serves as a guide for interested scientists and engineers who want to understand the importance and the connection between MESs and Industry 4.0. Due to the increasing relevance of digitalization, there will be a high demand in the future for specialists who can understand and teach the connection between information technology, automation and production technologies.

REFERENCES

- [1] VDI-Richtlinie 5600 - Blatt 1: Fertigungsmanagementsysteme (Manufacturing Execution Systems - MES), VDI/VDE-Gesellschaft Mess- und Automatisierungstechnik, 2016.
- [2] J. Kletti, MES, Manufacturing Execution System: Moderne Informationstechnologie zur Prozessfähigkeit der Wertschöpfung. Berlin [u.a.]: Springer, 2006.
- [3] H. Kageramann, W. Wahlster, and J. Helbig, Recommendations for implementing the strategic initiative INDUSTRIE 4.0: Final report of the Industrie 4.0 Working Group, 2013.
- [4] M. Hermann, T. Pentek, and B. Otto, "Design Principles for Industrie 4.0 Scenarios," in 2016 49th Hawaii International Conference on System Sciences (HICSS), Koloa, HI, USA, 2016, pp. 3928–3937.
- [5] F. Almada-Lobo, "The Industry 4.0 revolution and the future of Manufacturing Execution Systems (MES)," *jim*, vol. 3, no. 4, pp. 16–21, 2016, doi: 10.24840/2183-0606_003.004_0003.
- [6] J. Kletti, MES - Manufacturing Execution System. Berlin, Heidelberg: Springer Berlin Heidelberg, 2015.
- [7] J. Kletti, Das MES der Zukunft – MES 4.0 unterstützt Industrie 4.0, 2013.
- [8] O. Brauckmann, Digitale Revolution in der industriellen Fertigung - Denksätze. Berlin, Heidelberg: Springer Vieweg, 2018.
- [9] L. Ren, L. Zhang, F. Tao, C. Zhao, X. Chai, and X. Zhao, "Cloud manufacturing: from concept to practice," *Enterprise Information Systems*, vol. 9, no. 2, pp. 186–209, 2015, doi: 10.1080/17517575.2013.839055.
- [10] S. Mantravadi, C. Li, and C. Möller, "Multi-agent Manufacturing Execution System (MES): Concept, Architecture & ML Algorithm for a Smart Factory Case," in Proceedings of the 21st International Conference on Enterprise Information Systems, Heraklion, Crete, Greece, 532019, pp. 477–482.
- [11] VDI/VDE-Gesellschaft Mess- und Automatisierungstechnik (GMA), Cyber-Physical Systems: Chancen und Nutzen aus Sicht der Automation: Thesen und Handlungsfelder, 2013.
- [12] VDI-Richtlinie 5600 - Blatt 7: Fertigungsmanagementsysteme (Manufacturing Execution Systems - MES) - MES und Industrie 4.0, VDI/VDE-Gesellschaft Mess- und Automatisierungstechnik, 2021.

Development of a learning platform for automotive security

Stefan Schönhärl

Ostbayerische Technische Hochschule Regensburg

Email: stefan1.schoenhaerl@st.oth-regensburg.de

Abstract—Vehicles went through a radical change from purely mechanical constructs to now containing a multitude of Electronic Control Units(ECU). The security of those ECUs need to be a priority to ensure cars stay safe. Since some automotive networks can be interacted with directly from the outside today, it is especially vital ECUs connected to these networks are secure. Improving the security can be done in various ways, one of which is education. Developers responsible for implementing software on these ECUs are less likely to write vulnerable code, when they know about these vulnerabilities. This can be achieved by providing them with a prepared environment, where they themselves are tasked with exploiting vulnerable code.

I. INTRODUCTION

Modern vehicles are fundamentally different compared to their predecessors. Historically vehicles were mostly mechanical constructs, but their functionality was limited to their primary use - driving. Today on the other hand vehicles fulfil a multitude of tasks, like providing information and entertainment for passengers, improve the safety of the passengers through technologies like emergency brake assistants and others. Those modern technologies are implemented upon a multitude of Electrical Control Units(ECU) with a combined 100 million lines of code [1]. Even though those technologies provide a lot of upsides to the user, there are drawbacks as well.

Since multiple of those technologies require communication with the outside world, they are liable to attacks by hackers. It follows, that if a safety-critical ECUs can be attacked, the vehicle as a whole can no longer be considered safe. Improving automotive security in general is a problem, that can be approached in various ways.

II. STATE OF SCIENCE AND KNOWLEDGE

A. Test Automation

Software development, especially in an embedded or automotive environment, is often prone to bugs. ECUs often don't offer protection from hackers, like a memory protection unit, due to their low cost. Furthermore the software often has to be coded in a lightweight programming language, such as C/C++. Possible security flaws include:

- Brute Force
- Buffer Overflows
- Format String Vulnerability
- Side Channel Attacks

To prevent those vulnerabilities, the software has to be tested extensively. Manual tests have certain drawbacks, as they are

prone to errors, because of their repetitive nature, and they are also time and cost-inefficient, compared to automated tests. By transforming these manual tests into automated ones, they become more reliable, faster and it is possible to design them according to the latest standards. Depending on the test, test automation can become difficult and expensive.

B. Side Channel Analysis

Side-channel analysis is becoming an increasingly important topic in automotive security. Various aspects contribute to this. On one hand, a side-channel analysis will be used more by hackers and researchers to discovering vulnerabilities, compared to the past, since traditional vulnerabilities, like Buffer Overflows, are becoming rarer.

Side-channel analysis however is not impacted the same way traditional vulnerabilities are. It will still be possible to analyse byproducts and get information about the inner working of the system and use those to attack it.

Furthermore, side-channel analysis has applications in machine learning. By collecting side-channel information, certain inferences can be drawn. For example, by analysing the power consumption, certain faulty states can be detected.

C. Linking of Development Cycles

According to most widely used automotive electronic system development model, the V-Model [2], software testing is typically done at the end of the software development life-cycle.

Figure 1 shows, that the left side of the V is considered the design phase, while the test phase is on the right side, with the actual implementation happening in the middle. To improve the security, the test should already be performed continually while implementing. This procedure increases the probability that a bug will be found and also simplifies fixing the bug.

D. Education

A majority of security vulnerabilities stem from mistakes the developer made while coding. Those include those presented in II-A.

Even though there are resources available about secure coding practices, it seems even third-year software development students don't adhere to these practices [3]. Therefore programmers need to be shown in-depth, what effects not adhering to these standards can have. Depending on the vulnerability, there may also exist countermeasures the developer can implement

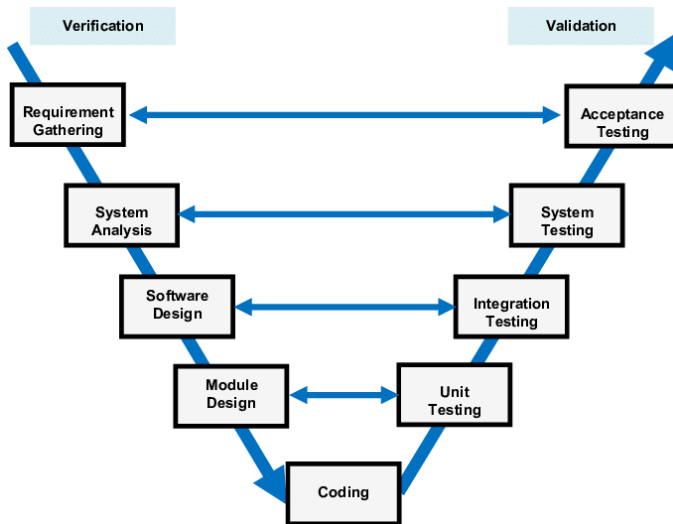


Figure 1. V-Model life cycle for the automotive software testing [2]

to prevent the vulnerability or make the exploit more difficult. Automotive network protocols specifically were not designed with security in mind, since they were not intended to be addressed from outside the car.

III. SECURITY EDUCATION PLATFORM

To improve automotive security by education, a new platform is being developed. It consists of two equal parts, the first dealing with conventional embedded security vulnerabilities, such as those listed in II-A and more advanced vulnerabilities, dealing with automotive networks.

The knowledge about the vulnerabilities is acquired by providing a prepared environment, in which participants themselves are tasked with exploiting the vulnerabilities, just like a real hacker would.

Vulnerabilities are built into so called **Challenges**, which are inspired by Capture-the-Flag events. There are lectures provided for each Challenge, introducing the topic, explaining underlying concepts and giving suggestions on how to appropriately defend against such attacks.

Not only is it possible to work on the hardware platform hands-on, but also in a virtualised form, to allow their use during the corona pandemic.

A. Embedded Security

The embedded security part consists of 6 different topics.

1) *Python Introduction*: Since the programming language Python is easy to learn and it is suitable to the following tasks, the first topic is a brief introduction to python. The main topics are lists, and how to effectively manipulate them.

2) *Brute Force*: The second topic is Brute Force attacks and their variations. A simple Brute Force attack aims at guessing a password to a service by trying combinations of a given alphabet. More sophisticated versions of Brute Force Attacks include Dictionary and Rainbow Table attacks. Finally countermeasures against such attacks, like prolonging response

time and account locking are discussed.

The challenge tasks the user with writing a script, that finds the correct password for a service, that returns the amount of correct characters to the user. This design choice was made, because this challenge still acts as an introduction.

3) *Buffer Overflows*: In the Buffer Overflow section introduces hardware specifics, like memory in Flash and SRAM, as well as Registers, like Program Counter, Link Register and Stack Pointer and how they are saved on the Stack. A Buffer Overflow can attack programs, that allows the user to write over reserved array borders. Furthermore it is discussed, how they can be prevented by using Memory Management Units, Memory Protection Units, Address Space Layout Randomisation (ASLR), or Stack Canaries.

The goal of the challenge is to log into another service without a password. To achieve this the user needs to find the successful login function in the source code and the address of the function in a screenshot of the corresponding disassembly. He then can exploit the program with a Buffer Overflow and jump to the correct address.

4) *Format String Vulnerabilities*: Topic 4 is about the `printf()` function and how it can be exploited when used incorrectly by a Format String Vulnerability. Again the first step is to explain how the `printf()` function works on the memory level and how memory can be read out by `printf()` parameters. Preventing Format String Vulnerabilities is done by using `printf()` and its parameters correctly. Using modern IDEs warns users, in case it is used incorrectly. Format String Vulnerabilities can be made harder to exploit by using similar mechanisms like in III-A3.

In the Format String Vulnerability challenge the user is able to read out the stack by using `printf()` parameters as input for the program. Users can find the flag required to solve the challenge on the stack.

5) *Use-After-Free*: The name Use-After-Free originates from the C function `free()`. It can occur when an object is deleted (`free()`'d) but a pointer to the object still exists, which is called a *Dangling Pointer*. This can be exploited by an attacker. Use-After-Free Vulnerabilities are prevented by using programming languages with garbage collection, since unused pointers are deleted at certain intervals. Exploiting them can be made harder by enabling ASLR as well.

The challenge presents the user with an interactive database based on a C *struct*. New structs instances can be created, deleted, selected, displayed and updated. To solve this challenge a user has to be selected, creating a pointer, which is dangling when deleting the struct afterwards. Creating a new user with the address of the flag as a parameter and dereferencing the struct by displaying it, outputs the required flag.

6) *Time-based Side Channel Attack*: The final Embedded Security challenge is about Side Channel Attacks. There are multiple kinds of Side Channel Attacks, like Timing, Power Consumption, Acoustic and Optical. As an introduction it is explained how the time it takes a program to answer a password input can be used to guess parts of the correct

password. Another example for a Power Consumption Side Channel Attack is given, which allows an attacker to extract parts of the secret key, used in an Advanced Encryption Standard (AES) implementation. An effective countermeasure to Side Channel Attacks is to introduce noise into the system [4].

The challenge presents the user with a similar problem to the challenge in III-A2. This time, the key can be extracted, by measuring the time it takes the program to answer a password input with a single character. This process is repeated for each element of the alphabet. The response of the program will take the longest, when the correct character is input. To acquire the whole password, this process is repeated, while taking the previously guessed characters as the starting point.

B. Automotive Security

In the Automotive Security section of the platform there are 3 topics available. Each attack is based on the CAN protocol in different OSI model layers.

1) *CAN Man-in-the-Middle*: The first topic deals with a base data transfer via CAN-bus, which implements elements of the Data Link- and Physical Layer [5]. A brief introduction to other protocols, like LIN and Automotive Ethernet is given, which is followed by an in-depth explanation of the CAN protocol. In preparation for this and the following challenge, Scapy is introduced, which acts as a package manipulation tool. The term Man-in-the-Middle (MitM) Attack is explained as well, since it is the attack users will need to perform in the challenge part.

The goal of the challenge is to decrease the mileage of a simulated car, in order to be sold at a higher price. The first step is to read out the CAN messages on the bus and identify the message containing the mileage. After it has been found, the message can be intercepted and its payload decreased.

2) *ISO-TP Relay Attack*: Modern cars often use keyless entry systems, which can be attacked by relaying the challenge - response authentication messages between the car and key. Gaining access to a locked car can furthermore be accomplished by sniffing the challenge - response message and reverse engineering the algorithm and solving it without the key present. This challenge utilises the ISO TP protocol as a transmission method between car and key, which is located in the transport layer. Finally, the ISO TP protocol, its frame types, flow control and error handling are explained.

The goal of the challenge is to unlock the simulated car by sending a self-crafted ISO-TP message. Again the CAN traffic needs to be read out and the message containing the lock/unlock signal has to be found by continually locking/unlocking the car. By examining the sniffed messages it should be clear, that the message gets slightly altered after each locking process. The solution is to apply the unlocking algorithm on the string and sending that message to the simulated car.

3) *UDS Scanning*: The final automotive security topic is about the Application Layer Protocol Unified Diagnostic Services(UDS). UDS provides functions, that allow reading

or reprogramming ECUs, which can be protected by UDS Security levels and Session Control. The protection is realised with a seed-key algorithm, which, depending on the implementation, can be broken with some effort.

To solve this challenge, the user needs to change into a different session first. Afterwards he can try using available function. Since they are protected he can request security access, which requires a security key. For simplicity sake, this key can be brute forced, since it is only has a length of 2 byte. If the security access is successful, the user can use the protected function, which completes the challenge.

IV. CONCLUSION

Security is becoming increasingly important in automotive software development. There are multiple measures, that can be taken to increase the security in this field, one of which is educating the developers. By confronting them with the challenge to exploit those vulnerabilities themselves, they are made aware of the vulnerabilities and are less likely to make those same mistakes. A learning platform has been established, which teaches users about conventional embedded security and advanced automotive network vulnerabilities. Parts of the platform have already been offered to 6 & 7th semester students as an elective course. The vast majority of students managed to solve the initial challenges, the later challenges however were solved less often. An exam at the end of the semester proved, that students were able to identify vulnerabilities by analysing source code and give suggestions on how the program can be made secure. Further work on the platform include research and subsequent implementation of new challenges. Especially challenges dealing with Automotive Ethernet are interesting. Individual challenges will also be expanded to include new aspects, like cryptography.

REFERENCES

- [1] R. Currie, "Developments in car hacking," SANS Institute, 2015.
- [2] A. Tierno, M. M. Santos, B. A. Arruda, and J. N. H. da Rosa, "Open issues for the automotive software testing," in *2016 12th IEEE International Conference on Industry Applications (INDUSCON)*, 2016, pp. 1–8. DOI: 10.1109/INDUSCON.2016.7874609.
- [3] V. Mdunyelwa, L. Fitcher, and J. van Niekerk, "An educational intervention for teaching secure coding practices," in *Information Security Education. Education in Proactive Information Security*. 2019.
- [4] D. Debayan, M. Shovan, N. Saad Bin, G. Santosh, R. Arijit, and S. Shreyas, "High efficiency power side-channel attack immunity using noise injection in attenuated signature domain," 2017, pp. 1–6.
- [5] International Organization for Standardization, *ISO 11898-1: Road vehicles - Controller area network (CAN) - Part 1: Data link layer and physical signalling*. ISO, 2015.

Choosing a RISC-V Core for Implementing an FPGA-Based Security Module

Philipp Schubaur
philipp.schubaur@hs-augsburg.de
Hochschule Augsburg

Abstract—Security in embedded devices is becoming more crucial, as the number of edge nodes, connected to the Internet, increases. To protect against attackers, security commonly makes use of expensive and additional components, such as Trusted Platform Module (TPM), crypto accelerators or secure memory.

In contrast, a security module is proposed, speaking of an encapsulated unit for a System on Chip (SoC), located on the Programmable Logic (PL), which is established as Field Programmable Gate Array (FPGA). Therefore, code execution is separated away from the connected and hence vulnerable Hard Processor System (HPS). The proposed module is supposed to be customizable, based on the specific implementation demands, realizing an efficient and suitable security level.

A soft core is the central element of the security module for replacing existing solutions for cryptography, key management or acceleration via additional hardware. On this account, the current situation of RISC-V soft core implementations is analyzed and sorted. To choose a suitable core, a filtering process is presented by using defined, strict criteria and discussion-based decision making.

In the end, only the PicoRV32 fulfills stated requirements. Afterwards, the suitability of this specific soft core is evaluated and the upcoming steps for a first prototype of the security module are proposed.

I. INTRODUCTION

As the performance gain of embedded devices stagnates by increasing the number of transistors, other ways for performance gain are utilized [1]. Therefore, System on Chip (SoC) are getting more common. Specifically speaking of a combination of Hard Processor System (HPS) and Programmable Logic (PL), commonly implemented as Field Programmable Gate Array (FPGA). To increase computing power, dedicated designs for defined processes get realized on the FPGA and therefore, accelerate the processing. But most of the time, not the entire FPGA is being used, resulting in surplus logical elements on the PL.

Detached of this development, security on embedded devices gets more important, as the number of connected devices increases. To realize 'smart' components, they commonly are attached to the internet. Either directly or via a gateway, hence are accessible and thus vulnerable via the connection.

To overcome this, state of the art development makes use of additional components, such as Trusted Platform Module (TPM), secure memory or assorted processor structures with additional low-power cores [2]. The idea of the proposed security module is to overcome the gap between, at a first glance, independent developments and align the targets.

A methodology is presented, encapsulating execution of program code away from the HPS, running Linux or Real-time Operating System (RTOS), into the FPGA, running the stated soft core.

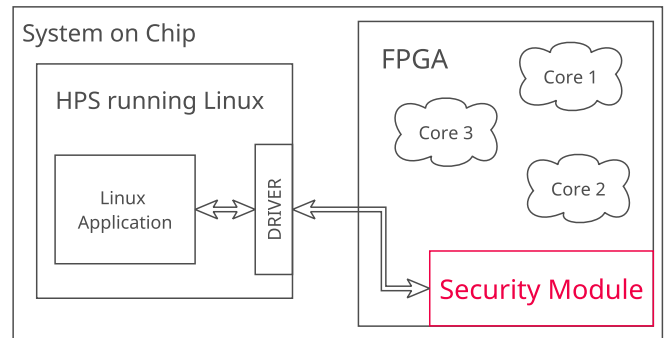


Figure 1. Block diagram

The overall concept is shown in Figure 1. On the left hand side, the HPS, consisting of a hardwired ARM [3] core, running Linux. And, connected via a system bus and a kernel driver module, the PL with the security module, running on the FPGA. It also presents the idea of the security module, being an additional part of an already existing implementation.

Encapsulation of security-critical processes into separate hardware is a proven approach for security by design. Either by additional external hardware, such as TPM. Or even a multi-core approach of hardware design directly on the die, e.g. the STM1-Series [2].

Unfortunately, both ideas demand extensive hardware or silicon design effort and therefore is not to be done during field operation. The presented security module can be freely adopted to changes, e.g. by implementing new cryptography algorithms. Furthermore, it is also possible to be a retrofit into existing designs, realizing a more secure embedded device via remote bitstream updates. Retrofit in this perspective means, the proposed module can be added into existing designs and therefore making use of the mentioned, so far unused logical elements.

Hence, by enabling security features with the proposed security module, connecting embedded devices to the internet is more secure and updatable.

To achieve this encapsulated behavior in the security module, a soft core for code execution in the FPGA is needed.

This idea is preferred over a block design or bare-metal implementation as existing software projects can be easily migrated into the security module. Thus, no complete redesign is needed and the extent for an implementation is lower.

Soft core describes the idea to embed a Central Processing Unit (CPU) into the PL. This can be done in multiple ways and configurations, mainly defined by the used Instruction Set Architecture (ISA) and peripheral environment.

To run a CPU and connect software to hardware, the ISA is key. The compiler translates high-level behavior into low-level bitwise description, which can be loaded and executed by a soft core. Recent developments in the field of soft core are heading in the direction of open source ISA.

There have been multiple attempts to propose an open, transparent and license-free architecture. Lately, publications were made by Sun Microsystems with SPARC [4] or IBM with POWER [5]. In scope of academic and industrial implementations in recent years, target moves to RISC-V [6]. It was first proposed in 2010 and is separated into different base instructions and extensions. Security benefits from open source ISA, as the code base can be reviewed and thus e.g. reveals intended vulnerabilities. Furthermore, open source ISA grants long-term support, standard language compliance with the published compiler and is furthermore open source.

The proposed security module differs from security hardware components, as it demonstrates an implementation inside of the SoC, overcoming demand of external components on the Printed Circuit Board (PCB). In harmony of objectives, the security module can be retrofitted into existing devices, increasing security of remote devices, running in the field. Coming along, the complexity in relation to a TPM is reduced for implementing only symmetrical cryptography in a first glance.

The contribution of this paper is a transparent selection process for the identification of an open source RISC-V soft core implementation that is suitable for a security module implementation in an FPGA. Following up, the current market situation around open source RISC-V soft cores gets extracted and analyzed. Based on that, a selection process is presented, to reduce the amount of cores down to the suitable ones.

The rest of the paper is structured as follows. Section II documents related work and following up, Section III examines the selection process. Section IV documents first results from the soft core implementation, before summing up the results in Section V.

II. RELATED WORK

Höller et. al. [7] observed the RISC-V soft core market in 2019 and implemented three cores on Xilinx hardware. In comparison to their work, a recheck of the available cores is done and the selection process is more specifically directed into a concrete use case. In addition, the security module implementation is targeted to different platforms, speaking of Intel (Quartus) [8] as well as Xilinx (Vivado) [9].

Heinz et. al. [10] implemented multiple cores in 2019, using the 'TaPaSCo' framework and compared them, regarding

resource usage and performance. The present paper differs, as no framework is supposed to be used for the proposed security module. The decision against a framework is based on the platform independence and long-term support. Furthermore, Heinz experienced difficulties, implementing some cores without significant change in the code base.

The proposed idea of the security module is, to be published open source, as soon as it reaches production-stable state. In comparison, closed-source solution for an encapsulated execution on FPGA is available from the commercial developer Intrinsix [11]. Their system is tape-out proven and also targets a retrofit solution, but demands licensing and is restricted to the dedicated scenarios.

III. SELECTION OF RISC-V CORE

As the selection process targets a soft core for the security module, this publication presents the procedure to obtain the most suitable core. Choosing an already implemented core is recommended, as it accelerates development of the system.

Developing a dedicated core is possible but ensuring compliance to the RISC-V standard is not granted in first place and delays development. As a result, an already published and released soft core is obtained. During the process, multiple sources are utilized. As starting point, two collections of cores [6] and [12] are advisable. Höller [7] also quotes this as his starting point of research. Furthermore, as RISC-V is an open source ISA, many cores follow up the licensing and therefore are publicly released on GitHub [13].

During research, around 45 suitable cores are localized. To choose an appropriate one, requirements and demands are defined. They get presented in the following key points as well as some example cores and explanations why the specific core was not chosen.

Starting with all 45 cores, the steps are separated into strict criteria and a discussion-based selection. The number of suitable cores gets reduced step by step, as a demand is applied to the core and verified, if it is fulfilled. This process is repeated, until only a few cores, meeting all requirements, remain. These cores get inspected in detail and discussed, prior to a final decision.

A. Proprietary Core

As already mentioned by Höller [7], there are commercial implementations of soft cores. Furthermore, there are proprietary cores, released by the silicon manufacturer itself. Namely, Intel proposes its 'NIOS II' processor [14], Xilinx the 'MicroBlaze' and, as the third notable vendor, Lattice the 'LatticeMico32' [15].

All three cores are available in different stages of complexity and capability. Starting with basic functionality and slow performance with a free-to-use but proprietary license up to complete licensing, including the code base. As all three cores rely heavily on silicon-specific behavior and as the security module joins the idea of generality, all of them get abandoned during the selection process.

B. Wrong ISA

RISC-V ISA needs to be supported by the corer, resulting in the exclusion of multiple cores. As alternative, open source ISAs, such as the Microwatt core with the POWER architecture [16] or the LEON3 [17] with the SPARC V8 architecture, are not suited. For instance, SPARC V8 got terminated by Oracle in 2017 [18] and thus, making it obsolete.

C. Only an extension

The core needs a complete support of the ISA of RISC-V regarding the official release in 2019 [19]. This is not achieved by extensions, which only expand an existing implementation of a Core, such as XCrypto [20].

D. Non-32-bit architectures or bit-serial

A central design element of soft cores is the freedom to choose the width of the used bus systems or architecture in general. Based on the powers of the number two, multiple widths are possible. The presented selection process on restricts the cores to 32-bit width. This examines the ideal trade-off between performance and space demand on the PL.

Furthermore, most of the embedded systems running Linux, rely on 32 bit. Two different data widths introduce conversion processes and therefore decrease efficiency.

This also applies to some very specific implementations. Namely, bitwise and non-parallel execution, as it is e.g. proposed by the serv core [21], are dismissed.

E. Hobby projects

In contrast to the mentioned commercial implementations, regarding professionalism and effort, multiple RISC-V soft cores are available from single developers on a private project base. As an example, Kamikaze [22] is developed by a single person, not providing any documentation, licensing regulations or support. The decision was made to abandon nearly all of such cores, as the security module is supposed to be a long-term and evolving project. An exception was made for NeoRV32 as it is outstandingly elaborated, see section III-K3.

F. Maintenance issues

Apart from being developed by a larger group, also bigger projects lack a sufficient maintenance. Mainly in discontinuing or deprecation the development. As a standout candidate, ZPU [23] was looking appropriate, claiming to be the smallest Core to consolidate GCC as compiler. In fact, development and support was discarded 6 years ago, rendering the core obsolete.

G. Documentation issues

As the publication and ratification of RISC-V is not restricted to a single area or country, open source soft cores are globally available. Pointing out the importance of the documentation, again speaking of long-term support, readability is key. Unfortunately, some cores, such as Nutshell [24] and Hummingbird [25] are mainly documented in Chinese language, thus making it unusable for the security module.

H. Uncommon programming practices

As the number of implementations of dedicated components in PL increases, new languages and approaches evolve. In the last decade, VHDL and Verilog were the way to go, regarding hardware description in software. In addition to that, High Level Synthesis (HLS) evolved and new frameworks want to gain market share. Namely, nMigen [26] or SpinalHDL [27] are proposed. But they are not suitable for a hardware independent or retrofit idea of the security module from native source files. Therefore, e.g. the cores VexRiscv [27] or Minerva [28] are filtered out.

I. GNU GPL

General Public License (GPL) represents an open source standard of licensing [29]. As already ratified, this is welcomed for the implementation of the security module. But as §6 in the license mentions, keys are also to be supplied on the publication. As the security module is supposed to handle encryption keys and therefore protect this secret, it is in contrast to the GNU GPL v3. Therefore, the cores representing this specific license, were abandoned. Namely, mor1k [30] and ReonV [31] looked promising, but got voted out.

J. General license issues

Apart from 'pure' open source licensing, some cores are available in source code and free to use for verification and education. As it comes to an industrial usage, licenses have to be purchased from the vendor. Therefore, RV12 [32] did not fulfill the requirements.

K. Discussion

After the execution of the proposed filtering process, six cores remained. As no more fixed exclusion criteria was involved, decision making from this point on might differ on a personal perspective. In best knowledge, the judgment of the cores is liable and therefore suitable for the final selection process.

1) *ParaNut*: ParaNut is a soft core, developed at the University of Applied Sciences Augsburg [33]. It mainly targets a multi-core approach, accelerating processing of algorithms via multi-cache architecture. The core was declined because of the usage of SystemC [34] as the programming language. Even though, during the automatic workflow, generated Hardware Description Language (HDL) code is human readable, the additional step reduces compliance to a hardware independent and universal idea.

2) *Ibex*: Ibex [35] is the RISC-V soft core used in Open Titan [36]. This project represents a huge collection of PL-Modules for implementing a Root of Trust (RoT). This extends the idea of the intended security module into a total utilization of the PL for security mechanisms. As this core is more powerful, it also demands more peripheral, to support all features of the core. This enables it to be used in bigger platforms, such as PULP [37]. But as this soft core is intended for bigger systems, it lacks a minimal implementation, as stated in the documentation.

3) *NeoRV32*: The NeoRV32 [38] would have been supposed to be voted out under the category of a hobby project, as it is solely developed by a single person. But it caught the attention, as it is outstandingly elaborated in regards of documentation. After contacting the developer and discussing the long term support, the core is rejected as there was no long term support granted and all knowledge about the cores rests with one person.

4) *CV32E40P and SCR1*: CV32E40P [39] and SCR1 [40] are soft cores, maintained by the OpenHWGroup respectively SyntaCore. As big vendors, they supply the industry with a wide range of different RISC-V cores. We discontinued the implementation of those cores, as they are both written in System Verilog and as no full support is given by some Integrated Development Environment (IDE).

5) *PicoRV32*: As the last contender in this election process, the PicoRV32 [41] remained. This core is widely used, both in education as well as real silicon implementations for SoC on sale. For example, the Raven SoC [42] utilizes the PicoRV32 as its core in silicon. Furthermore, the core follows the idea of a single file approach, reducing complexity of the security module and supporting the retrofit idea.

IV. EVALUATION

After election of all given RISC-V soft cores, the PicoRV32 was the privileged candidate. All requirements were met, furthermore equipped with easy configuration, an active community of developers and a successful formal verification of the core. As the chosen PicoRV32 soft core consists only of one file, a synthesis test is run with both IDEs, speaking of Quartus for Cyclone V (5CSEBA6U23I7), respectively Vivado for the ZYNQ-7020 (XC7Z020clg400). With minor additional modules, this yielded similar utilization numbers as presented in the official Git repository [41], as shown in Table I.

Table I
RESOURCE DEMANDS OF PICORV32

	Vivado	Quartus	Git
Look-Up Table (LUT)	889	872	761
Random Access Memory (RAM)	48	48	48
Flip Flop (FF)	517	517	442
Block-RAM	0.5 Block	4 Tiles	-

V. CONCLUSION

The paper presents a selection process of a RISC-V soft core for implementing an encapsulated security module on the PL of a SoC. Concept wise, a soft core is preferred over a modular approach. Thus, examining a faster and more flexible implementation as well as a retrofit ability, as already implemented algorithms in software can be easily migrated from the HPS onto the security module.

The chosen soft core relies on RISC-V as ISA. As the number of RISC-V compliant soft core rises, a market review was performed. During the process, a wide variety of soft cores was found. To choose a suitable core, a filtering and selection process was implemented and run on the list of soft

cores. Exclusion took place for the cores based on criteria such as sufficient code and documentation quality, 32-bit width, a suitable open source license and long term support. After running this criteria, the remaining cores got inspected more in detail, discussed and a final core was chosen. The soft core to be utilized in the security module is the PicoRV32. It is widely used and verified, well documented and guides are available, supporting a quick implementation.

ACKNOWLEDGMENT

The author wants to thank Dominik Merli and the team of HSA_innos for the valuable comments and suggestions. This work was partly funded by the project SIS4.0.

REFERENCES

- [1] J. Shalf, "The future of computing beyond moore's law," *Philosophical transactions. Series A, Mathematical, physical, and engineering sciences*, Mar. 1, 2020, ISSN: 1364-503X. DOI: 10.1098/rsta.2019.0061.
- [2] STMicroelectronics. (Feb. 20, 2020). First stm32 mpu: 2 cortex-a7 and 1 cortex-m4 makes 3 reasons to jump on board. STMicroelectronics, Ed., [Online]. Available: <https://blog.st.com/stm32mp1-mpu-stm32mp157a-ev1-stm32mp157c-dk2/>.
- [3] Arm. (Mar. 22, 2021). Arm instruction set architecture, [Online]. Available: <https://developer.arm.com/architectures/instruction-sets>.
- [4] Sun Microsystems. (Mar. 29, 2021). The sparc architecture manual, [Online]. Available: <https://compas.cs.stonybrook.edu/~nhonarmand/courses/sp15/cse502/res/sparcv8-manual.pdf>.
- [5] IBM. (Mar. 22, 2021). Power isa version 3.0 b, [Online]. Available: <https://ibm.ent.box.com/s/1hzcwkwf8rbju5h9iyf44wm94amnlcrv>.
- [6] RISC-V. (Apr. 16, 2021). Risc-v cores and soc overview. RISC-V, Ed., [Online]. Available: <https://github.com/riscv/riscv-cores-list>.
- [7] R. Höller, D. Haselberger, D. Ballek, P. Rössler, M. Krapfenbauer, and M. Linauer, "Open-source risc-v processor ip cores for fpgas — overview and evaluation," in *2019 8th Mediterranean Conference on Embedded Computing (MECO)*, Jun. 2019, pp. 1–6. DOI: 10.1109/MECO.2019.8760205.
- [8] intel. (Mar. 22, 2021). Intel® quartus® prime software suite, [Online]. Available: <https://www.intel.com/content/www/us/en/software/programmable/quartus-prime/overview.html>.
- [9] Xilinx. (Mar. 22, 2021). Vivado design suite, [Online]. Available: <https://www.xilinx.com/products/design-tools/vivado.html>.
- [10] C. Heinz, Y. Lavan, J. Hofmann, and A. Koch, "A catalog and in-hardware evaluation of open-source drop-in compatible risc-v softcore processors," in *2019 International Conference on ReConfigurable Computing and FPGAs (ReConFig)*, Dec. 2019, pp. 1–8. DOI: 10.1109/ReConFig48160.2019.8994796.

- [11] M. Beal, "Using risc-v as a security processor for darpa chips and commercial iot," in *7th RISC-V Workshop Proceedings*, Nov. 29, 2017. [Online]. Available: <https://riscv.org/proceedings/2017/12/7th-risc-v-workshop-proceedings/>.
- [12] RISC-V. (Apr. 5, 2021). Risc-v exchange: Cores & socs. RISC-V, Ed., [Online]. Available: <https://riscv.org/exchange/cores-socs/>.
- [13] I. GitHub. (Apr. 16, 2021). Github. I. GitHub, Ed., [Online]. Available: <https://github.com/>.
- [14] Intel Corporation. (Nov. 10, 2020). Nios ii processors, [Online]. Available: <https://www.intel.de/content/www/de/de/products/programmable/processor/nios-ii.html>.
- [15] Lattice Semiconductor. (Oct. 12, 2020). Latticemico32, [Online]. Available: <https://www.latticesemi.com/en/Products/DesignSoftwareAndIP/IntellectualProperty/IPCore/IPCores02/LatticeMico32.aspx>.
- [16] antonblanchard. (Nov. 24, 2020). Microwatt, [Online]. Available: <https://github.com/antonblanchard/microwatt> (visited on 11/27/2020).
- [17] Gaisler Research. (Mar. 29, 2021). Leon3 processor. Cobham Gaisler, Ed., [Online]. Available: <https://www.gaisler.com/index.php/products/processors/leon3> (visited on 11/27/2020).
- [18] ZDNet. (Sep. 5, 2017). Sun set: Oracle closes down last sun product lines. S. Vaughan-Nichols, Ed., [Online]. Available: <https://www.zdnet.com/article/sun-set-oracle-closes-down-last-sun-product-lines/>.
- [19] RISC-V Foundation. (Dec. 2019). The risc-v instruction set manual, Volume i: User-level isa, document version 20191214-draft. A. Waterman and K. Asanović, Eds., [Online]. Available: <https://github.com/riscv/riscv-isa-manual/releases/download/draft-20201013-51522f9/riscv-privileged.pdf> (visited on 10/14/2020).
- [20] scarv. (Nov. 20, 2020). Xcrypto, [Online]. Available: <https://github.com/scarv/xcrypto> (visited on 11/27/2020).
- [21] olofk. (Nov. 27, 2020). Serv, [Online]. Available: <https://github.com/olofk/serv> (visited on 11/27/2020).
- [22] rgwan. (Mar. 4, 2017). Kamikaze, [Online]. Available: <https://github.com/rgwan/kamikaze> (visited on 11/27/2020).
- [23] zylin. (Apr. 21, 2015). Zpu, [Online]. Available: <https://github.com/zylin/zpu> (visited on 11/27/2020).
- [24] OSCPU. (Sep. 17, 2020). Nutshell, [Online]. Available: <https://github.com/OSCPU/NutShell> (visited on 11/27/2020).
- [25] SI-RISCV. (Nov. 26, 2020). E200-opensource, [Online]. Available: https://github.com/SI-RISCV/e200_opensource (visited on 11/27/2020).
- [26] m-labs. (Jan. 22, 2020). Nmigen, [Online]. Available: <https://github.com/m-labs/nmigen> (visited on 04/22/2021).
- [27] SpinalHDL. (Apr. 19, 2021). Vexriscv, [Online]. Available: <https://github.com/SpinalHDL/SpinalHDL> (visited on 04/22/2021).
- [28] lambdaconcept. (Sep. 9, 2020). Minerva, [Online]. Available: <https://github.com/lambdaconcept/minerva> (visited on 11/27/2020).
- [29] I. Free Software Foundation. (Mar. 22, 2021). Gnu general public license, [Online]. Available: <https://www.gnu.org/licenses/gpl-3.0.en.html>.
- [30] openrisc. (Jul. 26, 2020). Mor1kx, [Online]. Available: <https://github.com/openrisc/mor1kx> (visited on 11/27/2020).
- [31] lcbcFoo. (Oct. 7, 2018). Reonv, [Online]. Available: <https://github.com/lcbcFoo/ReonV> (visited on 11/27/2020).
- [32] RoaLogic. (Sep. 27, 2018). Rv12, [Online]. Available: <https://github.com/RoaLogic/RV12> (visited on 11/27/2020).
- [33] A. Bahle and G. Kiefer, "The paranut/risc-v processor - an open, parallel, and highly scalable processor architecture for fpga-based systems," in *embedded-world2020*, 2020. [Online]. Available: <https://www.embedded-world.de/de/events/vortrag/the-paranutrisc-v-processor--an-open-parallel-and-highly-scalable-processor-architecture-for-fpga-based-s/742766>.
- [34] S. I. Accellera. (Mar. 22, 2021). Systemc, [Online]. Available: <https://www.accellera.org/downloads/standards/systemc>.
- [35] lowRISC. (Nov. 27, 2020). Ibex, [Online]. Available: <https://github.com/lowRISC/ibex> (visited on 11/27/2020).
- [36] lowRISC contributors. (Nov. 12, 2020). Opentitan, [Online]. Available: <https://opentitan.org/> (visited on 11/27/2020).
- [37] pulp-platform. (Feb. 24, 2020). Pulp, [Online]. Available: <https://github.com/pulp-platform/pulp> (visited on 04/22/2021).
- [38] stnolting. (Nov. 27, 2020). Neorv32, [Online]. Available: <https://github.com/stnolting/neorv32> (visited on 11/27/2020).
- [39] openhwgroup. (Nov. 27, 2020). Cv32e40p, [Online]. Available: <https://github.com/openhwgroup/cv32e40p> (visited on 11/27/2020).
- [40] syntacore. (Nov. 14, 2020). Scr1, [Online]. Available: <https://github.com/syntacore/scr1> (visited on 11/27/2020).
- [41] cliffordwolf. (Apr. 27, 2020). Picorv32, [Online]. Available: <https://github.com/cliffordwolf/picorv32> (visited on 11/27/2020).
- [42] efabless. (Oct. 19, 2019). Raven, [Online]. Available: <https://github.com/efabless/raven-picorv32> (visited on 11/27/2020).

Computational Acoustics using OpenFOAM

Elisabeth Christine Sturm
 Faculty of Mechanical Engineering
 University of Applied Sciences Ingolstadt
 Ingolstadt, Germany
 ORCID: 0000-0002-7113-6242

Abstract— With the ever-increasing computational power of modern computer systems, complex and fine-grained simulation models can be applied to a wide range of application domains such as Computational Fluid Dynamics (CFD). Until now, CFD is mainly used for fluid problems but rarely used for acoustic problems even though some methods are suitable for aeroacoustics simulations. In this paper, the general possibility of calculating acoustic waves with a CFD tool is evaluated. The problem here lies in the huge difference of the atmospheric or reference pressure compared to the pressure leading to an acoustic significance. For a general understanding of the simulation details for acoustics problems and validation, Kundt's tube is investigated in more detail. For calculation of the physics including the speed of sound, the open-source tool OpenFOAM will be used. OpenFOAM is capable of solving smaller acoustics problems with the provided solvers. For more complex problems and with the usage of hybrid methods, external solvers are better suited. In this paper, the focus is on a direct, laminar simulation of Kundt's tube with OpenFOAM, computed by the solver rhoPimpleFoam.

Keywords—CFD, Computational Acoustics, Kundt's tube, OpenFOAM

I. INTRODUCTION

For a general understanding of the simulation details for acoustics problems, Kundt's tube is used, which will be described later in section III. This tube was named after the German physician August Kundt, who studied sound waves within a tube to identify the nodes of a resulting standing wave and absorption characteristics of materials. The phenomenon of standing waves is also known from musical instruments like the flute or an organ, where the sound is generated by the resulting waves. To validate the speed of sound calculated by the simulation as well as the general principles applied within the tube, the open-source tool OpenFOAM will be used. The knowledge about fluid dynamics principles and the governing equations will be applied to the Kundt's tube by simulating the speed of sound in the fluid air.

II. THEORETICAL BACKGROUND

A. Fluid Dynamics

In this paper, the focus will be on Newtonian fluids such as air. Newtonian fluids consist of simplifications and were named after Isaac Newton, who described them with a linear association between the stress and the rate of strain.

The governing equations for simulations describe the balance of mass, momentum, and energy with five equations and six variables ρ, u, v, w, p, e .

For more information see the references [1], [2], [3], or [4], where this section is based on.

1) Mass balance

The Mass Conservation (or Equation of Continuity) focuses on a specific control volume. Within this volume, the creation and destruction of mass must equal the mass flow rate on the surfaces of this volume. Shortening the equation by the division of dV and writing out the mass flow rate, the Equation of Continuity is defined as:

$$\frac{\partial \rho}{\partial t} + \frac{\partial(\rho v_1)}{\partial x_1} + \frac{\partial(\rho v_2)}{\partial x_2} + \frac{\partial(\rho v_3)}{\partial x_3} = 0, \quad (1)$$

with v_1, v_2, v_3 being the velocity in the x, y, z -direction. Using the Nabla-Operator the generally known equation is:

$$\frac{\partial \rho}{\partial t} + \rho \nabla \cdot \vec{v} = 0 \quad (2)$$

where \vec{v} is the velocity vector. For incompressible fluids, this equation could be simplified as the density does not differ over time leading to the omission of the first quotient. The density is also equal in all three dimensions, so it can be written in front of the sum.

2) Momentum balance

The Navier-Stokes equations (NSE) are based on the Euler equation, which itself does not include the viscosity of fluids (inviscid fluids). This viscosity results in frictional forces, which are part of the NSE. The NSE are known as

$$\underbrace{\frac{\partial(\rho \vec{v})}{\partial t}}_{\text{local acceleration}} + \underbrace{\rho \vec{v} \cdot \nabla \vec{v}}_{\text{convective acceleration}} = \underbrace{-\nabla p}_{\text{pressure force}} - \underbrace{\nabla \tau}_{\text{frictional force}} + \underbrace{\rho \vec{g}}_{\text{body force}} \quad (3)$$

where τ is the second-order stress tensor and \vec{g} being the gravitational force vector. The last vector depending on the simulation problem can also be a magnetic or electrical force.

For acoustic calculations and sound propagation, the bulk viscosity has to be considered. In the stated NSE above, the loss of compression and dilatation in the fluid is not included. As the propagation of acoustic signals is in the longitudinal direction, only the viscous stress in these directions needs to be evaluated. The bulk viscosity λ is therefore the second coefficient of viscosity and given as:

$$\lambda = -\frac{2}{3}\mu \quad (4)$$

, where μ is the molecular viscosity.

3) Total energy balance

The first law of thermodynamics states that the rate of change within equals the sum of the heat transfer (in- and outside) and the work (body and surface forces). For the change of energy, it will be differentiated between the

mechanical (kinetic) and thermodynamic (internal) energy. The heat-transfer is described by the heat of the control volume (absorption or emission of radiation) as well as the transfer through the surfaces (temperature gradients like thermal conduction). This thermal conduction has a linear relation to the local temperature gradient and is given by Fourier's law for thermal conduction. The total energy balance can be described with the formula:

$$\rho \frac{D}{Dt} \left(e + \frac{V^2}{2} \right) = \rho \dot{q} + \frac{\partial}{\partial x_j} \left(\kappa \frac{\partial T}{\partial x_j} \right) - \frac{\partial}{\partial x_j} (p u_j) + \frac{\partial}{\partial x_j} (u_i \tau_{ji}) + \rho F_j u_j \quad (5)$$

B. Computational Fluid Dynamics

Computer-based simulation is increasingly used for solving fluid flow problems and is part of the term *Computational Fluid Dynamics* (CFD). Additionally, to normal fluid mechanics problems, nowadays even electronic or heat transfer problems can be solved. This leads to widespread usage of CFD, which is reflected in the many industry sectors and companies using CFD.

As explained in the last section, a flow of a fluid can be described with equations. In more complex situations such as turbulent flow, combustion, or even multiphase flows it is not possible to solve these equations analytically, therefore a discretization method is applied instead. Often the finite volume (FV), finite element (FE), or finite difference (FD) methods are used. For validation, it is necessary to compare the results with experimental data, as concrete descriptions are often not available.

For further information, see references [5] and [6], the fundamental information for this part.

1) Laminar and Turbulent Flow

To identify a laminar or turbulent flow, the Reynolds Number is normally considered. This number describes the relation from the inertial force to the friction forces and results in:

$$\text{Re} = \frac{\rho v d}{\mu} \quad (6)$$

where d is the diameter of the sphere, which e.g., equals the diameter for a cylindrical flow. Depending on the value of this Reynolds Number it is possible to differentiate between laminar and turbulent flows and even say, that two flows are physically similar. The dividing value of 2300 is often called the critical Reynolds Number.

The laminar flow is determined by separate layers of fluid with different velocities. Being above the critical Reynolds Number, the flow gets irregular and often random with three-dimensional turbulences.

The information about the Reynolds Number is based on reference [7].

Centered on the critical Reynolds Number, the different methods used for turbulent and laminar flow will be described, which refer to [5]. The first approach is the direct numerical simulation (DNS), where the NSE are solved for every volume and every time without any turbulence models. As a result, a

dense mesh is needed to resolve all small turbulences. The second method is called large-eddy simulation (LES) and is based on a mesh with fewer elements because very small turbulences are modeled. The last approach, the Reynolds-averaged Navier-Stokes method (RANS), defines the equations for means of pressure and velocity and therefore does not calculate the turbulences in detail.

The computing time increases from RANS, LES to DNS, while the last one is more exact than the other methods.

2) Boundary Conditions

Besides initial values, it is also necessary to define boundary conditions for the end faces of the simulation space. These are mainly divided into no-slip, far-field boundary conditions, or periodic restrictions with reference to [1].

The no-slip boundary condition has the restriction, that the relative velocity between wall and fluid is zero, which often results in a boundary layer. [8] The far-field boundary is used in cases, where the simulation space is too small compared to the real problem. In this case, it is necessary, that the boundary has nearly no influence on the result. Periodic boundaries can describe pressure or velocity and define a periodic change of the value (e.g., sine). Sometimes even a displacement is used as this boundary condition (e.g., membrane). Additional to these boundary conditions, it is also possible to define a specific value or normal gradient. A zero gradient is often used when either pressure or velocity is defined so that the other value can be extrapolated.

3) CFD and Aeroacoustics

Acoustic is based on two main field sizes, the dynamic pressure, and the velocity of the molecules (vector). The dynamic pressure is defined as the subtraction of the total pressure with the reference pressure.

Another important value is the speed of sound a , which depends on the fluid as well as the temperature and can be calculated with the following equation [1]:

$$a = \sqrt{\gamma R T}, \quad (7)$$

with γ being the ratio of specific heats or isentropic expansion factor, R the specific gas constant, and T the temperature. For air at room temperature (293 K), the speed of sound is $343,1 \frac{m}{s}$ [1].

4) Aeroacoustics Simulation Methods

The direct method for simulations with a very dense mesh as well as high calculating times is the most exact methodology. Without using any simplifications, the governing equations are solved for every part of the model.

In contrast to solving the governing equations in every region of the simulation space, it is also possible to rely on hybrids methods, especially when the simulation space is comparable large. Here the regions are divided into a source region, a near-field, and a far-field. Hybrid methods are based on a control surface, against which the normal CFD is calculated. Acoustic analogies describe the propagation from the control surface in the near field to the far-field. More information about these Integral methods can be found in [9].

C. Simulation Workflow

The workflow of a simulation can be easily split up into different sections, which are defined differently according to literature. Nevertheless, all of them combine at least three steps, which are pre-processing, processing, or solving, and post-processing. In this paper, two more steps will be included. This leads to the following 5-tier simulation workflow:



Figure 1: Simulation Workflow

This chapter is based on references [5] and [10].

1) General Settings

The first step is to identify the problem itself and the resulting physical questions. This includes the identification of the material or fluids, the geometry, which is used, and general boundary conditions as well as an approximation of the result, if possible. Also, the numerical method and discretization method (FE, FV, FD) need to be selected. Depending on this general information like stationary/non-stationary and laminar/turbulent, the solver can be chosen.

2) Pre-processing

Preprocessing steps focus on the generation of all the information needed to simulate the model by a solver. This includes the geometry as well as mesh generation, with e.g., consideration of element types and mesh density. Then the boundary conditions need to be defined as well as the initial conditions for pressure, velocity, and temperature. The fluid characteristics and optional turbulence treatment are defined. As the last step, it is necessary to select the specific parameters for the simulation (e.g., starting time, end time, time step).

3) Processing

The solving is mainly characterized by the execution of several iterative steps. This includes solving the system of equations, which leads to calculated pressure, velocity, and temperature. This is done for all elements as well as all time steps, where the solution is found by iterative calculations steps. The next step is made when the current step reaches a specific convergence criterion.

4) Post-processing

After the simulation, the results can be displayed in different ways: e.g., evaluation within one plane (distribution of pressure, velocity), streamlines in a 3D or 2D-plot, or colored plots like surfaces for pressure or velocity or temperature, and more.

5) Control & Documentation

After plotting and displaying the results, it is necessary to compare these results with the assumption made in the first step and to verify, whether the result is realistic or not.

To save the outcome of the simulation and possible errors for further investigations, it is useful to use a documentation.

D. Software

1) OpenFOAM

OpenFOAM is a Linux-based open-source CFD software with no direct graphical user interface. Having a large user base, *OpenFOAM* offers many features including complex

fluid flows, chemical problems, turbulence flow as well as heat transfer, electromagnetics, and acoustics. For more information about *OpenFOAM*, see their website [11].

OpenFOAM offers a wide range of different solvers, in total up to 100. These can be grouped into solvers for e.g., incompressible, compressible, or multiphase flow, heat transfer and combustion. Another difference lies in the capability to solve laminar or turbulence problems. All solvers as well as a short description are listed in reference [12].

To view the results or the mesh generated by *OpenFOAM*, additional programs can be used. *ParaView* is one possibility.

2) ParaView

ParaView is an open-source data analysis and visualization tool, which is capable of many different platform inputs. It gives the possibility to quickly load in the data and access is with different techniques. E.g., it is possible to evaluate simulations over time, which are used in the CFD simulation. This information as well as more detailed explanations can be found on the website of *ParaView* [13].

III. MODELLING KUNDT'S TUBE

Kundt's tube is a famous example of the propagation of sound waves. It exists of one long tube, where the diameter is small compared to the wavelength. On the inlet side, a speaker or membrane initiates a plane acoustic wave in the axial direction, which is then propagated to the other side, where it is possible to have a closed or open end (reflective or transmissive). Setting the right input frequency, it is possible to get a standing wave, which is a superposition of the forward and backward travelling wave. Alternatively, the length of the tube can be adjusted to the frequency.

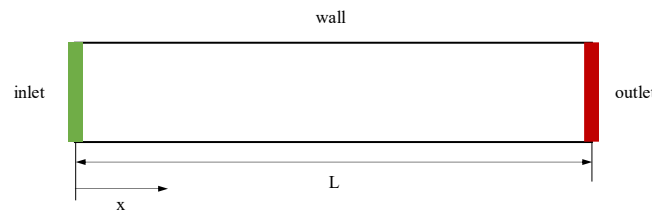


Figure 2: Kundt's tube

Kundt's tube is often used to evaluate the absorption of the material at the end of the tube. One big advantage lies in the reproduction and steadiness of all environmental conditions. With some restrictions, the tube describes the one-dimensional propagation of sound waves. In general, the resulting field containing the initial and reflected wave is:

$$p(x) = \bar{p}(e^{-jkx} + re^{jkx}), \quad (8)$$

where r is the pressure reflective coefficient. Because the pressure p and velocity v are dependent on each, only one is directly calculated during the simulation.

The theoretical background can be found in the references [14] and [15] in more detail, where this section is based on.

A. General Settings

The fluid is air with the properties as described in section III.B.2). As air is a compressible fluid, the general solver *rhoPimpleFoam* is used. This is a transient solver capable of

solving turbulent compressible problems. The finite volume method will be used, where algebraic equations for each element are used. The differential equations are integrated and therefore lead to face fluxes. The calculation of the faces also offers more boundary options. Both these advantages are the reason the FV method is often used in CFD simulation. This information and further details can be found in reference [6].

B. Pre-processing

1) Mesh generation

For the simulation, a cylindrical tube is needed. As *OpenFOAM* is text-based it is necessary to understand the parameters and syntax used to define a mesh. First, it is necessary to define outer points (vertices), which will then form a hexahedron, where it is also essential to define the number of volumes in each direction. The outer faces can then be divided into several boundary conditions sets. The tube will have the dimensions 1 m \times 0.02 m.

For the x-direction (sound propagation) the tube will be divided into several discs with a specific thickness. The discretization of the frontal area is more complex. It is possible to have a rectangular shape in the middle and triangles next to the edges or to use wedges. Both versions are inconvenient for this case, as they consist of triangle shapes and there is a huge difference in the sizes of the volumes. Therefore, a grid combining both advantages is taken. This includes rectangular shapes in the middle and round shapes in the edges (see Figure 3). The usage of variables (e.g., length l , radius r) was implemented, so all points are generated automatically.

s was specified as 0.001 m for all simulations, as it is perpendicular to the direction of wave propagation. For comparison, three different values for s_2 were used (in x -direction): 0.01 m | 0.005 m | 0.001 m. The mesh for the general documentation is based on $s_2 = 0.001$ m. The mesh is generated by giving the command *blockMesh*.

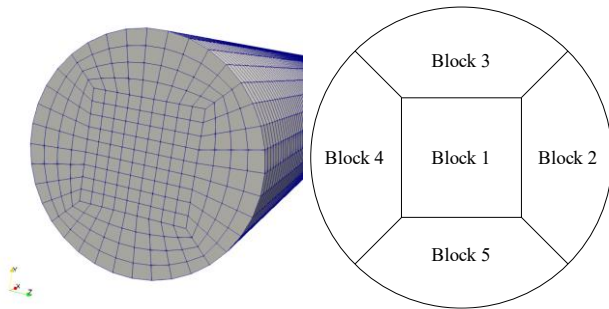


Figure 3: Frontal Area Mesh

2) Control and fluid parameters

The start ($t = 0$ s) and end time ($t = 6.6 \cdot 10^{-3}$ s) are defined. The time step for a first calculation is set to $\Delta t = 3 \cdot 10^{-6}$ s, which can be calculated by a formula recommended by *OpenFOAM* [16]. The Courant Number is allowed to reach a maximum of 1, which is taken for the conservative selection of the time step. With an approximate mesh length from 0.001 m and the speed of sound, the time step can be calculated.

The write interval is set to a different time interval ($\Delta t = 3 \cdot 10^{-5}$ s), as the time step used for the calculation would lead to too many results for plotting. As the atmospheric pressure is already stated with six digits, it is

important to increase the default write precision to at least twelve digits.

The thermophysicalProperties file was adjusted to air parameters. The physical properties of air, the number of moles, and the molecular weight [17], are:

$$\begin{aligned} nMoles &= 1 \\ molWeight &= 28.965 \frac{\text{g}}{\text{mol}} \end{aligned} \quad (9)$$

For the transport model, the dynamic viscosity μ and Prandtl number will be needed. For the fluid air with room temperature ($T_K = 293$ K) the calculation is simplified due to experimental data [18]:

$$\mu = \frac{1.458 \cdot 10^{-6} T_K^{1.5}}{T_K + 110.4} = 1.8 \cdot 10^{-5} \frac{\text{kg}}{\text{m} \cdot \text{s}} \quad (10)$$

$$Pr = 0.68 + 4.69 \cdot 10^{-7} (T_K - 540)^2 \approx 0.7 \quad (11)$$

The specific heat c_p and heat of formation H_f are the following [18], where the specific heat is calculated as an empirical expression:

$$c_p = 1002.5 + 275 \cdot 10^{-6} (T_K - 200)^2 = 1004.9 \frac{\text{J}}{\text{kgK}} \quad (12)$$

$$H_f = \Delta H_f^\theta \{O_2\} + \Delta H_f^\theta \{N_2\} + \Delta H_f^\theta \{Ar\} = 0 \frac{\text{J}}{\text{mol}} \quad (13)$$

Then the Reynolds Number has to be calculated:

$$Re = \frac{\rho v l}{\mu} \ll 1.3 \quad (14)$$

where the velocity is lower than $10^{-3} \frac{\text{m}}{\text{s}}$ as the simulation will show. As the number is severely below 2300 for this case, the flow can be assumed to be laminar. Consequently, no parameters for turbulence modeling need to be set.

3) Boundary Conditions

The internal pressure field is set to the atmospheric pressure. For the pressure inlet, a periodic condition was chosen, which is implemented by the parameter *uniformFixedValue* in combination with the sine function. The frequency was set to $f = 343.1$ Hz, which leads to one complete wavelength within the tube. As the pressure leading to acoustic realization is comparable small, the value for the amplitude is set to 0.1 Pa. The outlet as well as the walls have the *zeroGradient* boundary condition.

As an internal field value, the velocity is set to zero. The inlet is calculated regarding the definition of the pressure leading to the *pressureInletOutletVelocity* boundary condition. For the outlet, the *inletOutlet* condition is used, where the velocity equals zero. The wall is described with a *no-slip* boundary condition.

The field temperature is set to 293 K, which equals room temperature. All boundary conditions are set to *zeroGradient*. This means, that the wall is adiabatic. In acoustic simulations, there is a small heat transfer, but this is not significant for the simulation.

C. Processing

Firstly, the mesh is created, and the initial values as well as fluid data and control settings are loaded for the model. While solving, the values for every time step and every key variable are calculated. If the mesh is not dense enough to dissolve the physical conditions or the time step is too big, the iteration will reach the termination criterion and therefore exit, as the convergence criterion cannot be met.

D. Post-processing

Starting *ParaView*, it is necessary to load the model. Then there are several possibilities to plot the calculated data.

1) Animation

In *ParaView*, it is possible to show the pressure amplitude or difference with colors. Running through all times steps, an animation will be seen. For one time step it can look like:



Figure 4: Colored plot for $t = 0.0029$ s

2) Line Plot

For analyzing the propagation of the wave, the time is chosen, where the wave first reaches the outlet. This is at approximately $t = 2.9 \cdot 10^{-3}$ s and should show a sinus wave, which has the relative negative pressure next to the inlet and the relative positive pressure next to the outlet.

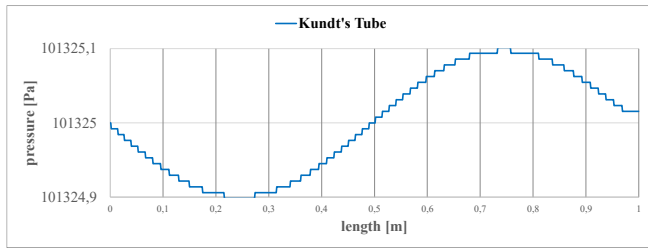


Figure 5: Wave Propagation

3) Point over time

Another possibility is to evaluate the values at one specific point over time. First, a point close to the inlet is evaluated to see, whether the correct inlet pressure is applied. Additionally, the points at 25%, and close to the end of the tube are evaluated to control the forming of a standing wave as well as the speed of sound.

IV. VALIDATION

A. Reasonability and Control

Figure 6 shows, that the initial periodic pressure is applied correctly, as the sin wave matches the period of $2.9 \cdot 10^{-3}$ s as well as the amplitude of 0.1 Pa.

Looking at the evaluation of the point next to the outlet (Figure 8), the first increasing value is found at $t = 2.8 \cdot 10^{-3}$ s, which means that the speed of sound within the simulation ($351 \frac{m}{s}$) differs with a relative error of 2.3%. This can also be seen in Figure 5, where the value at the outlet is above the atmospheric pressure. The higher value results in the superposition with the start of the reflecting wave.

Also, in Figure 8 the amplitude of the standing wave approximately reaches the doubled value of the initial wave, as the reflecting coefficient equals 1 (due to boundary cond.).

Figure 7 shows the node of the standing wave leading to amplitudes close to zero, which is reached as soon as the reflective wave meets the forward travelling wave.

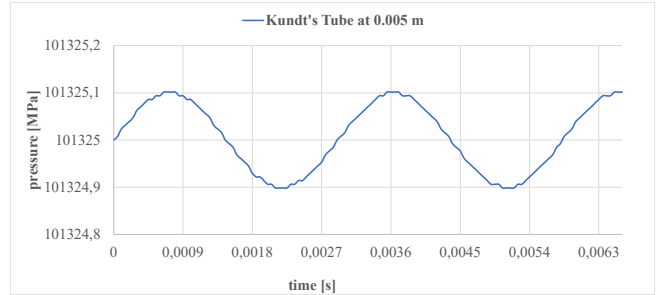


Figure 6: Point pressure over time ($x = 0.005$ m)

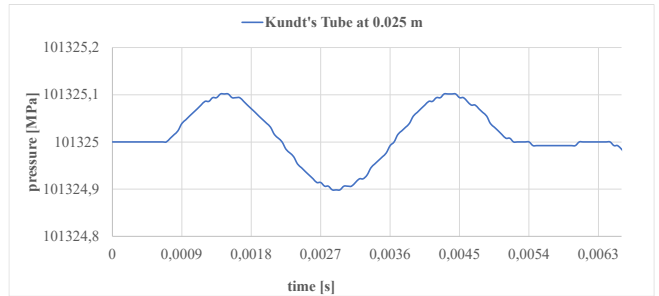


Figure 7: Point pressure over time ($x = 0.25$ m)

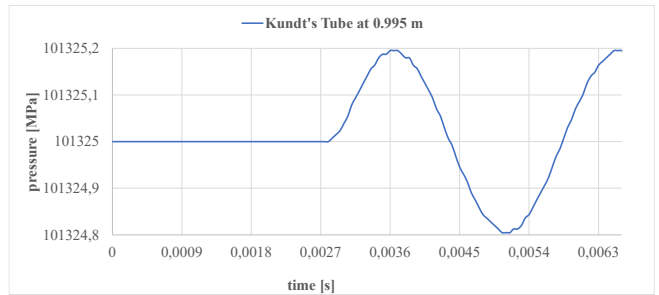


Figure 8: Point pressure over time ($x = 0.995$ m)

B. Change in Simulation Parameters

1) Differences in mesh density

While simulating Kundt's tube, different mesh densities were used. The size was only varied in the direction of sound propagation (x-axis). The 1 m tube was meshed with an edge length of 0.001 m (reference mesh density), 0.005 m (reduced mesh density), and 0.01 m (further reduced mesh density). The difference can be seen in the amplitude of the progressing pressure wave (see Figure 9). As a result of these simulations, the reference variant results in a simulation, where the results sufficiently meet the expectations.

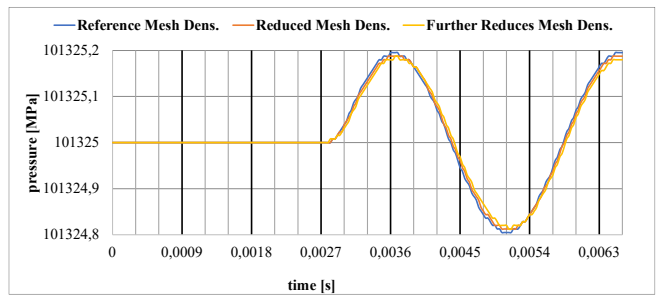


Figure 9: Different Mesh Density

2) Differences in time steps

Additionally, the influence of the time steps was examined. The time step was varied between $3 \cdot 10^{-6}$ s and $3 \cdot 10^{-5}$ s. In Figure 10 the results are shown as a line plot. The time step has a huge influence on the resulting speed of sound. For further research, an even smaller time step could be used to achieve slightly better results. It must be considered that reducing the time step has a huge impact on the computing times. Therefore, an appropriate compromise between accuracy and time efficiency has to be made.

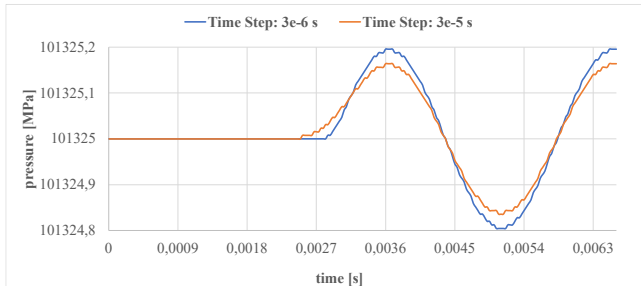


Figure 10: Different Time Steps

3) Different boundary conditions

In *OpenFOAM*, it is also possible to change the pressure boundary conditions at the inlet to velocity boundary conditions. This can be done by changing the pressure to a *zeroGradient* condition and applying a sinusoidal velocity. The same physical phenomena can be found in this simulation.

V. CONCLUSION

To calculate acoustic problems in *OpenFOAM*, the offered standard solvers are capable of simple and laminar flows. With an error of 2,3% to the real sound of speed, the simulation can be called realistic. From the findings in section 0, it can be presumed, that a reduction of the time step would result in even better results. Looking at specific points in the tube, it can also be seen that a standing wave is formed (see $x = 0.25$ or $x = 0.75$ m). Also, the summation of the values in the forming standing wave is doubled, which equals the conclusions of the theoretical background.

VI. FUTURE WORK

A. Far-Field condition

In many acoustics' problems, it is also necessary to calculate a far-field or have non-reflective boundaries simulating the far-field. This can be achieved by using a specific boundary condition, which is called *waveTransmissive*. For more information about the behavior of boundary conditions, the research of Poinso and Lele will give a good overview [19].

B. Acoustics solvers

In this paper, a direct calculation method with a solver for compressible flows was used. This solver is part of the standard solvers in *OpenFOAM* and not specialized for acoustic calculations but is acceptable due to the comparatively simple problem. If more complex simulations should be calculated, it will be better to use specified acoustic solvers or even hybrid methods to save calculation time.

An example is a specific solver for weakly compressible flows with low Mach numbers, which is distributed by the Swedish Chalmers University of Technology. This solver (*rhoPimpleAdiabaticAcousticFoam*) is based on hybrid methods and calculates the CFD problem for each time step, then determines the acoustic source terms, which are then evaluated by the acoustic solver. All this information as well as a test case can be found in reference [20].

ACKNOWLEDGMENT

I thank the University of Ingolstadt in cooperation with other Universities in Bavaria for the opportunity of the "Applied Master in Engineering Sciences". Especially I want to thank Prof. Dr.-Ing. Jörg Bienert (THI) for being my tutor.

REFERENCES

- [1] T. K. Sengupta and Y. G. Bhumkar, *Computational Aerodynamics and Aeroacoustics*. Singapore: Springer Singapore, 2020.
- [2] J. D. Anderson, "Governing Equations of Fluid Dynamics," in *Computational Fluid Dynamics*, J. F. Wendt, Ed., Berlin, Heidelberg: Springer Berlin Heidelberg, 1992, pp. 15–51.
- [3] J. H. Spurk and N. Aksel, *Fluid Mechanics*. Cham: Springer International Publishing, 2020.
- [4] Z. Zhai, *Computational Fluid Dynamics for Built and Natural Environments*. Singapore: Springer Singapore, 2020.
- [5] J. H. Ferziger, M. Perić, and R. L. Street, *Computational Methods for Fluid Dynamics*. Cham: Springer International Publishing, 2020.
- [6] F. Moukalled, L. Mangani, and M. Darwish, *The Finite Volume Method in Computational Fluid Dynamics*. Cham: Springer International Publishing, 2016.
- [7] H. Schlichting and K. Gersten, *Boundary-Layer Theory*. Berlin, Heidelberg: Springer Berlin Heidelberg, 2017.
- [8] H. J. Aguerre, S. M. Damián, J. M. Gimenez, and N. M. Nigro, Eds., *Modeling of Compressible Fluid Problems with OpenFOAM Using Dynamic Mesh Technology*, 2013.
- [9] A. S. Lyrantzis, "Surface Integral Methods in Computational Aeroacoustics—From the (CFD) Near-Field to the (Acoustic) Far-Field," *International Journal of Aeroacoustics*, vol. 2, no. 2, pp. 95–128, 2003, doi: 10.1260/14754720322775498.
- [10] A. Datta and V. Rakesh, *An Introduction to Modeling of Transport Processes*. Cambridge: Cambridge University Press, 2009.
- [11] OpenCFD Ltd (ESI Group), *About OpenFOAM*. [Online]. Available: <https://www.OpenFOAM.com/>
- [12] OpenCFD Ltd (ESI Group), *Standard Solvers*. [Online]. Available: <https://www.OpenFOAM.com/documentation/user-guide/standard-solvers.php>
- [13] Kitware, *Welcome to ParaView*. [Online]. Available: <https://www.paraview.org>
- [14] M. Möser, *Engineering Acoustics*. Berlin, Heidelberg: Springer Berlin Heidelberg, 2004.
- [15] E. Macho-Stadler and M. J. Elejalde-García, "Experiments with Kundt's tube," *J. Phys.: Conf. Ser.*, vol. 1287, p. 12022, 2019, doi: 10.1088/1742-6596/1287/1/012022.
- [16] OpenCFD Ltd (ESI Group), *Tutorial Guide: Decompression of a tank internally pressurised with water*. [Online]. Available: <https://www.OpenFOAM.com/documentation/tutorial-guide/tutorialse7.php>
- [17] D. Gatley, S. Herrmann, and H.-J. Kretschmar, "A Twenty-First Century Molar Mass for Dry Air," *HVAC&R Res.*, vol. 14, no. 5, pp. 655–662, 2008, doi: 10.1080/10789669.2008.10391032.
- [18] "Appendix B: Properties of Air," in *Wiley-Professional Engineering Publishing Series, The Shock Absorber Handbook*, J. C. Dixon, Ed., Chichester, UK: John Wiley & Sons, Ltd, 2007, pp. 375–378.
- [19] T. Poinso and S. Lele, "Boundary conditions for direct simulations of compressible viscous flows," *Journal of Computational Physics*, vol. 101, no. 1, pp. 104–129, 1992, doi: 10.1016/0021-9991(92)90046-2.
- [20] H. Nilsson, *CFD with OpenSource Software*: Chalmers University of Technology.

Simulating realistic domestic hot water consumption of a complex apartment building in a dynamic building model in IDA ICE

Lovis Toutouly and Oliver Steffens
 OTH Regensburg
 Regensburg, Germany
 Email: lovis1.toutouly@st.oth-regensburg.de

Abstract—This document describes the process of simulating a hot water system used in an intricate multi-family housing complex. At first a political motivation for the background of this research topic is elaborated. After analysing state-of-the-art heat generator and piping systems, the theoretical background for calculating the most crucial aspect, their heat losses due to domestic hot water (DHW) distribution, is discussed. This knowledge is used for calculating steady-state heat losses of both a novel advanced and a state-of-the-art piping system, using an Excel-sheet. Then, the simulation software 'IDA ICE' is used to create a model of a demonstration building.

Looking at upcoming tasks the use of the innovative heat generation and distribution system and the implementation of a complex control system will be implemented into the model. Subsequently, the pipe system's heat losses will be analysed and validated with the steady-state Excel-sheet calculation method. In the last step, the control scheme is optimised in order to minimise these heat losses.

First results using the steady state calculation already show a reduction in distribution losses of 15 % from the advanced pipe system, compared to state-of-the-art distribution systems.

I. INTRODUCTION

A. Political Statement

In order to counteract climate change, representatives of all countries met at the 2015 World Climate Conference in Paris, 197 of which committed themselves to limiting global warming to well below 2 °C and if possible to 1.5 °C, and to achieving greenhouse gas neutrality worldwide by the second half of the century at the latest. Within this context, Germany has set itself the goal of reducing greenhouse gas emissions by 55 % by 2030 compared to 1990 [1]. The long-term goal for 2050 is to achieve the greatest possible greenhouse gas neutrality. To achieve this, the building sector - like all sectors - must make an appropriate contribution. With around 35 % of the entire final energy consumption (in 2016), there is enormous potential here to reduce energy consumption and to use renewable energies for the generation of heating and cooling in buildings in an energy-efficient manner [2]. The German government, for example, plans to exploit this enormous energy-saving potential and reduce the primary energy demand of buildings by a full 80 percent by 2050 compared to 2008 [3]. If this demand is examined closely, it can be seen that through the application purposes of ambient heating, hot water, air conditioning and lighting, over 90 percent is consumed

for ambient heating and hot water [4]. While energy losses through the outer shell of newly built apartment buildings have been under a process of steady reduction, the energy demand of DHW has not changed significantly over the last decade. Therefore, looking at a building's total energy consumption, DHW production, provision and its distribution, depending on the users' expectation of comfort, is going to be of greater importance than ever before [5].

B. State-of-the-art heat generators & distribution systems

The following figure was created by analysing data from the German federal statistic office, regarding heating types used in German buildings between the years of 2015 and 2019. It shows, that since 2016, there has been a slow increase of

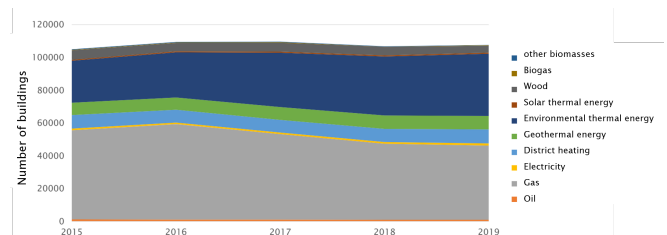


Figure 1. Completed buildings in Germany according to the type of heating energy predominantly used ranging from years 2015 to 2019 [6]

environmental thermal energy being used and an equally slow decrease in gas heating systems.

While there are a number of different heating generators, distribution systems can be divided into three different basic systems. Figure 2 shows systems in similar design, ranging from two to up to four pipes being used for providing a three-storey house with DHW and hot drinking water. The 4-pipe system has the most technical freedom of different party being used and has generally the lowest energy losses but is also the highest in building costs. Whereas the 2-pipe system has the most energy losses but is the cheapest in acquisition.

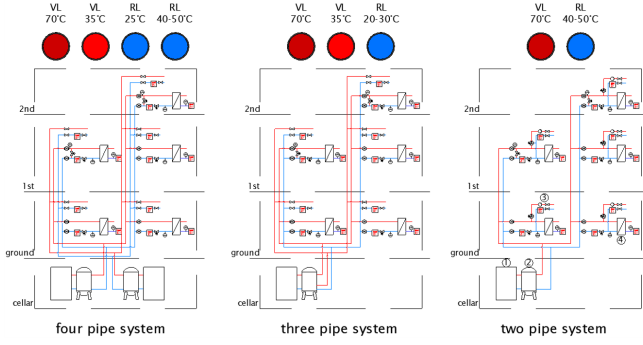


Figure 2. Basic distribution systems can be divided into three different kinds

C. Theoretical physical principles

As mentioned before, by distributing water from a heat generator to the consumers tap always leads to heat losses. There are no ideal heat generators. At the same time energy is also lost during distribution. Although a distinction must be made between the two conditions of standstill and operation, the types of heat transfer remain the same. This is shown in figure 3. Fluids, when in contact to a surface, transfer heat

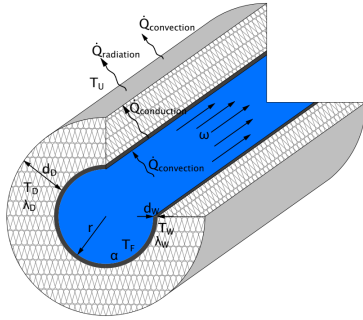


Figure 3. Varying stages of a heat transfer between a flowing liquid inside an insulated pipe

by convection $\dot{Q}_{\text{convection}}$, where α_i is the inner heat transfer coefficient between fluid and the pipe's surface, A_i is the pipe's inner surface and T are present thermal conditions of the pipe's surface and the fluid [9].

$$\dot{Q}_{\text{convection}} = \alpha_i \cdot A_i \cdot (T_p - T_f) \quad [W] \quad (1)$$

Through the layers of the pipe's wall and the insulation it travels using conduction $\dot{Q}_{\text{conduction}}$. This law is defined by the fluids and the environment T_e and the arising heat conducting resistances R_{th} [10].

$$\dot{Q}_{\text{conduction}} = \frac{T_f - T_e}{R_{\text{th},\alpha_i} + \sum_{i=1}^n (R_{\text{th},i}) + R_{\text{th},\alpha_o}} \quad [W] \quad (2)$$

From the outer surface of the insulation, it is delivered to the environment by radiation $\dot{Q}_{\text{radiation}}$ and convection [10].

$$\dot{Q}_{\text{radiation}} = \alpha_{\text{radiation}} \cdot A \cdot (T_s - T_e) \quad [W] \quad (3)$$

II. METHODS AND PROCEDURES

A. Calculation using Excel-sheet

Following the analysis, we compare the calculated heat losses from a basic distribution system to an advanced, 'pulsating', novel system from the OTH Regensburg's research project 'MAGGIE'. Figure 4 shows a schematic of how the system works: While DHW is produced in a high-tech heating center, the distribution happens via a three-pipe system, entering each of the six houses. From here on a 4-pipe system feeds the floor heating and, in combination with a 560 litre hot water tank in each house, for hot drinking water [8]. The innovation

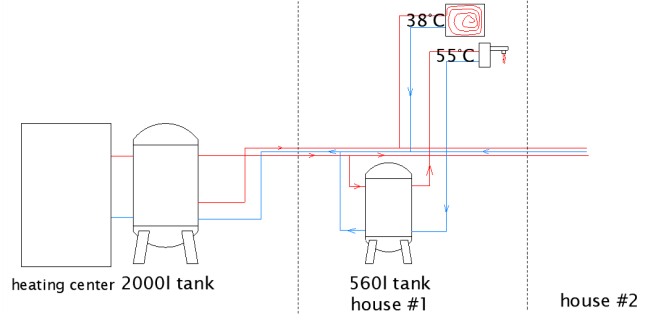


Figure 4. Schematic illustration showing a novel system with intermittent 'pulsating' operators from OTH Regensburg's research projekt 'MAGGIE'

lies in loading these six hot water tanks in a controlled scheme. This leads to times, where the distribution to the tanks is able to be in a state of rest, hence leading to reduced heating losses in these supplying pipes.

B. Simulating using IDA ICE

For the calculations with Excel, parameters such as pipe-length, diameter, isolation-thickness and ambient temperatures had to be entered by hand. The next step is to recreate the distribution system as it is shown schematically in figure 5 using the simulation software IDA ICE.



Figure 5. Demonstration building, rebuilt using IDA ICE with visualised pipe-system

Figure 6 shows a portion of this model. The purple rectangle represents one of the six hot water tanks as mentioned before. To the right of it, the blue lines picture pipes leading to the consumer's tap. To the left of it, these lines form the inflow and reflux of the water tank. All the other modules on the left build up the control scheme for loading the tank.

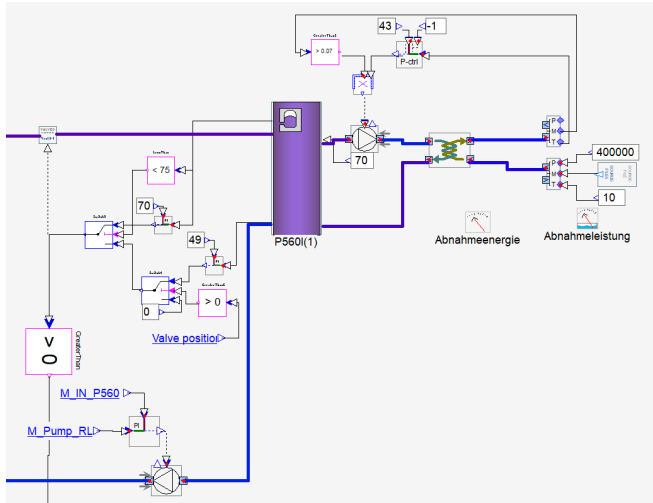


Figure 6. Building model section from IDA ICE picturing one of the six hot water tanks with consumer (right side) and controlling scheme (left side)

III. RESULTS

For a detailed comparison of the advanced, novel 3-pipe system with the state-of-the-art 2-pipe system, variations in the pipe insulation coating were considered. Version 1 has a standard insulation while version 2 has double insulation. All other margin conditions were left unchanged. The chart in

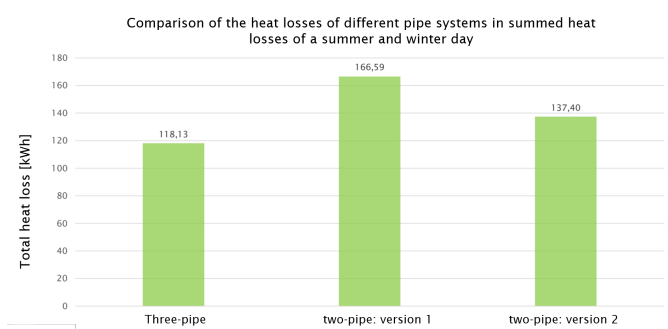


Figure 7. Total heat losses as sum of a summer and winter day regarding the advanced 3-pipe system and two versions of the 2-pipe system

figure 7 shows that total heat losses regarding the sum of a winter and a summer day from the novel 3-pipe system, are reduced by 15%. In the span of a year this leads to an energy equivalent of 3.5 MWh.

Furthermore, recreating the simulation of a pipe section in IDA ICE showed a deviation of only 3.1% between the two simulation methods.

IV. CONCLUSION

Recreating hot water distribution systems may become a bigger share in designing buildings. While their outer shells experience a steady process of reducing energy losses, the next step is looking at the inside of buildings. One of the easier, but on the other hand most promising prospects may be simulating such models. An advantage of the novel system could already

be proven by calculating its heat losses using a steady-state Excel-sheet. To validate this reduction, the distribution system is being recreated in IDA ICE. Furthermore this simulation method is able to represent real conditions more closely.

REFERENCES

- [1] Hendrick Kafsack, Frankfurter Allgemeine Zeitung, *EU einigt sich auf höheres Klimaziel*, Brüssel, 2021
- [2] Bundesministerium für Wirtschaft und Energie (BMWi), *Energieeffizienzstrategie 2050*, 2019
- [3] Bundesministerium für Umwelt, Naturschutz und nukleare Sicherheit (BMU), *Klimaschutz in Zahlen - Fakten, Trends und Impulse deutscher Klimapolitik*, 2018
- [4] Bundesministerium für Wirtschaft und Energie, *Energieeffizienz in Zahlen - Entwicklungen und Trends in Deutschland*, 2018
- [5] Shell Deutschland und Bundesindustrieverband Deutschland, *Klimaschutz im Wohnungssektor - Wie heizen wir morgen?*, 2014
- [6] Statistisches Bundesamt, *Bauen und Wohnen: Baugenehmigungen/Baufertigstellungen von Wohn- und Nichtwohngebäuden (Neubau) nach Art der Beheizung und Art der verwendeten Heizenergie*, Lange Reihen ab 1980
- [7] Richard Heimrath, Andreas Heinz, Thomas Mach, Wolfgang Streicher, Christian Find and Richard Riva, Arbeitsgemeinschaft Erneuerbare Energie, Institut für Nachhaltige Technologien, *Solarunterstützte Wärmenetze: Technologie und Komponentenentwicklung*, 2002
- [8] Tobias Saller, Andreas Schnabl, Thomas Mühlberger, Felix Meier and Stefanie Huthöfer, *Energetische Stadtanierung - Integriertes Quartierskonzept-Margaretenau*, 2016
- [9] Isaac Newton, *Scala graduum caloris: calorum descriptiones & signa*. In *Philosophical Transactions, volume 22*, pages 824-829, 1701
- [10] Hans Dieter Baehr, Karl Stephan, *Wärme- und Stoffübertragung*, 2019

Chapter 3

Papers: Optical Technologies and Communication Networks

Contents

3.1	Cryptographic protection of High-Precision Clock Synchronization	92
3.2	Computational efficient noise suppression in phase-shifting holography	98
3.3	Formulas for Mutual and Self-Inductances of Multiple Coupled Loops	103

Cryptographic protection of High-Precision Clock Synchronization

Andreas Schulitschenko
 Deggendorf Institute of Technology
 Autonomous Systems / Driver Assistance Systems
 Deggendorf, Germany
 Email: andreas.schulitschenko@live.de

Abstract—Clock synchronization has become an essential feature for the autonomous vehicle, as many ECUs (electronic control unit) depend on a precise idea of time. These ECUs make objects with precise time stamps available to others, e.g. via V2X communication. To secure these timestamps, the actual protocol must be secured. This paper analyses security features of existing IEEE standards to create a security concept, how the IEEE 802.1AS standard can be secured. In addition, a proof of concept is created and the time delays involved are measured and evaluated.

I. INTRODUCTION

The automobile of tomorrow is in a constant exchange of information with itself and its environment. Data provided by external communication partners is used in the vehicle for safety-critical decisions, among other things. This type of information exchange is also referred to as V2X communication. Furthermore, collected data is generated and evaluated directly in the vehicle. Detected objects from a camera, for example, are forwarded to a powerful control unit. This control unit receives further messages with objects from other sensors, such as RADAR and LiDAR. The algorithm used puts the objects into a temporal relation and, based on this fused data, makes a decision as to whether to display a warning message to the driver or even intervene in the driving process itself. The necessary temporal relation can only be calculated if the control units used have been synchronized via a time synchronization protocol, such as IEEE 1588 or IEEE 802.1AS.

Due to the strong networking of different communication partners, it is important that the common time base is trustworthy and has not been modified by third parties. To this end, the source, content and sequence of the individual PTP messages must be verified.

The focus of this work is to find methods to cryptographically secure the IEEE 802.1AS standard, to show the feasibility with the help of a prototypical implementation, and to show the delay caused. Different IEEE standards are examined and a security concept is presented that secures IEEE 802.1AS against certain attacks. The prototype implementation is intended to demonstrate the feasibility of the proposed concept.

II. BACKGROUND

PTP is one of the most widely used protocols for time synchronization. A number of research activities have been

undertaken to evaluate and improve the security of these protocols. This section reviews some of the efforts in the literature. The growing popularity of IEEE 1588 PTP for synchronization in critical infrastructure has led to concerns about its security [1] [2]. Threats to IEEE 1588 can be broadly divided into data plane attacks (e.g., message modification) and physical plane attacks (e.g., replay and delay attacks). While cryptographic protocols are able to thwart data plane attacks against realistic adversaries, some signal plane attacks, such as those of delay attacks, remain open vulnerabilities. In [3], the researchers conclude that time synchronization can be either highly accurate or secure against delay attacks. They encrypt PTP using IEEE standard 802.1AE (MACsec), but can identify individual packets using statistical network analysis. This allows PTP to be targeted with a message delay attack. The researchers show that this delay attack can only be prevented in trusted environments. Such an environment is given in the vehicle, the topology and all device are known and coordinated during installation.

Even in the recently published IEEE 802.1AS-2020 standard, no security functions are adopted from the IEEE 1588-2019 standard. For this reason, the standard is cryptographically secured with proprietary extensions in the course of this work.

A possible way to secure the time synchronization protocol is discussed in the paper [4]. The researchers show that all possible one-way time synchronization protocols are vulnerable to replay attacks. Further, they demonstrate that with a set of conditions, two-way synchronization can be protected against this type of attack. [4]

- Condition 1 Both communication partners must use an authenticated encryption scheme to prevent third parties from generating valid messages.
- Condition 2 Both communication partners must communicate via the shortest possible path.
- Condition 3 The packet transmission time (path delay) must be measured in advance and compared with the currently measured time.

III. CONCEPT OF IEEE 1588-2019

IEEE 1588 introduces a multi-pronged approach that leads to a range of security mechanisms and configuration options that meet different security objectives.

A. Integrated safety mechanisms of IEEE 1588-2019

The first method (Prong A) is directly integrated into the PTP protocol and has been designed to be used by any PTP system regardless of the underlying transport layer. It provides both authentication of the PTP instance and integrity protection of the PTP message. This approach does not aim to protect the confidentiality of the PTP message itself, since the timestamps it contains are not secret. The mechanism can be processed in two ways. [5] Figure 1 shows the arrangement of TLVs in a PTP message. In the first type, the PTP message k is received and temporarily stored in a queue. Only after receipt of another message $k+x$, which contains the associated key for the message k , can k be checked for integrity. Only when the integrity check passes may the PTP message be passed to the PTP instance and processed. This approach is referred to as 'Delayed Processing' and is not considered in the rest of the process. [5] In the second type, the PTP message is checked immediately after receipt and processed further in the PTP instance if the integrity check passes. This concept is called 'Immediate Processing' and requires some preconditions. Before sending the PTP message, all communication partners must be authenticated and have the symmetric key. [5]



Figure 1. PTP message with the TLV extensions for delayed and immediate processing [5]

B. External safety mechanisms of IEEE 1588-2019

The second method (Prong B) deals with security mechanisms that are outside of PTP but may already be present in the system and therefore can also be used to improve security in the time synchronization infrastructure. Currently there are two options for this approach, MACsec and IPsec. IPsec is not considered further because this protocol operates at OSI Layer 3 and therefore cannot be used to deploy IEEE 802.1AS, which is defined at OSI Layer 2. [5] The second approach, IEEE 802.1AE (MACsec) [6], is specified for use in OSI Layer 2. When using this mechanism, a secure connection is established between two link partners. All exchanged data or messages, including PTP messages, are provided with integrity protection. It is also possible to encrypt the transmitted data to obtain confidentiality.

IV. SAFETY CONCEPT

The mechanisms described above are combined in a security concept. The 'Immediate Processing' concept is used for end-to-end (E2E) protection. IEEE 802.1AE (MACsec) is used for peer-to-peer (P2P) protection.

Figure 2 shows how both concepts E2E and P2P merge. The PTP message is first protected with the TLV authentication presented. The resulting message is seen by MACsec as user data. 'User Data' and 'EthernetType' form the 'Secure Data'.

A cipher suite is used to cryptographically secure the entire message, starting at the first byte of the destination MAC address and ending at the last byte of the 'Secure Data'. The ICV calculated from this is inserted after the 'Secure Data'. The ICV is also secured by this procedure. Such a secured message has authentication, authorization, sequence numbering and integrity protection as security properties.

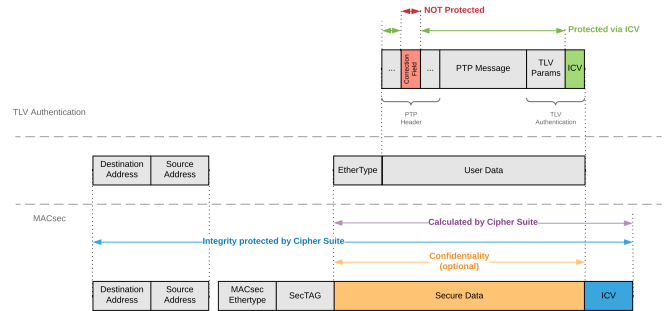


Figure 2. Concept of a cryptographically secured time synchronization protocol [6] [5]

Condition 1 is satisfied by both concepts, E2E and P2P. Condition 2 is ensured by a fixed defined topology of devices and PTP instances. By using the IEEE 802.1AS standard, a path delay (PDelay) measurement is performed cyclically by each PTP instance and checked whether the threshold of 800 nanoseconds is met. With the help of the PDelay measurement the (Condition 3) can be fulfilled.

A. End-to-End (E2E) protection

The TLV authentication concept is used to secure the PTP message from the grandmaster to the slaves. It does not matter how many interconnecting partners sit between these two entities and forward the PTP message. With E2E protection, integrity protection is maintained over the entire transmission path between master and slave.

The PTP message is processed and forwarded by every PTP relay instance, but the ICV in the TLV Authentication may only be generated and entered in a message by the master. The receiving PTP instance verifies the message, caches the ICV, generates the new message to be sent, and then reinserts the cached ICV into the PTP message. The fact forwards the PTP message is regenerated depends on the implementation of the PTP instance and must therefore be taken into account.

Possible manipulation by third parties can be detected by this mechanism. Only the previously defined master and the authenticated slaves have the corresponding keys. Key management and distribution are discussed in more detail in the chapter V.

A vulnerability in this type of protection are the 'Correction Field', 'Source Port Identity' and 'Sequence ID' in the PTP header (Figure 2). These fields cannot be secured with the ICV because they are modified by devices such as bridges during forwarding. These particular fields are secured using the P2P concept.

B. Peer-to-Peer (P2P) protection

The P2P concept is implemented with the IEEE 802.1AE standard. With P2P protection, the path between the individual link partners is secured. Only the correct link partner can verify the message and decrypt it if necessary. A third party that is not registered in the defined network topology cannot re-authenticate or re-encrypt the data.

V. KEY MANAGEMENT

Some form of key management is required to establish a secure connection between the two ports. This can be done by manual key configuration or by using the EAPoL (Extensible Authentication Protocol over Local Area Network) protocol. This protocol is used to distribute the necessary keys to the devices and instances involved. It further authenticates the devices and enables the corresponding port upon successful authentication. The port can now participate in the secured or encrypted communication. A RADIUS (Remote Authentication Dial-In User Service) server is used as the key server. This generates the necessary keys, such as CAK (Connectivity Association Key) and SAK (Secure Association Key). At least one instance of a KaY (Key Agreement Entity) is required on each device. Such a KaY controls the exchange and storage of keys on the devices.

Figure 3 shows on which device and in which software the required KaYs and their keys are located. Each PTP instance has an E2E KaY which is used for E2E security. Each instance of this E2E KaY has the same SAK, as this is used to authenticate the PTP message. Further, a P2P KaY is instantiated in pairs on the directly connected devices. These P2P KaYs provide the SAK for the encryption and decryption of the time synchronization packets. For example, the grandmaster P2P KaY and the P2P KaY of Bridge 1, form such a pair. Bridge 1 and slave 1 are another pair. Bridge 1 has several P2P KaYs, but only the KaY that is responsible for the respective physical Ethernet port can decrypt the communication of the remote station.

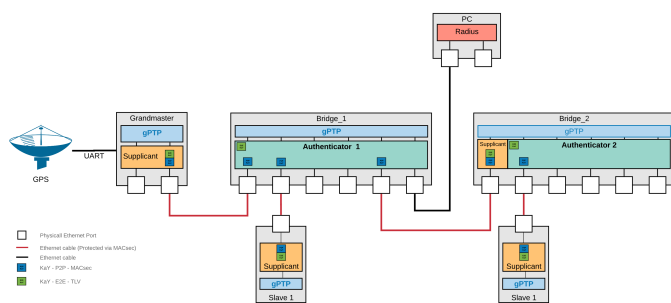


Figure 3. Storage concept of the keys used in the test system

If a second bridge is required in the network, an authenticator is also installed and configured on it. It must be ensured that the port which represents the connection to the first bridge is not managed by the authenticator, but by a supplicant. Only a supplicant can authenticate with an authenticator and enable

the port there. This makes it imperative that a supplicant is also present on the second bridge.

VI. LAYOUT OF PTP MESSAGES

The E2E and P2P concept can only be applied to certain PTP messages. The authenticator listens for all packets that are encrypted or secured. It checks if the PacketNumber (PN) of the sent message is still in the set window. If the authenticator determines that the PN of the message does not match its stored PN or is not within the defined interval, it concludes that the connection is faulty and terminates the CA (Connectivity Association). As a result, the individual partners can no longer communicate over a secure connection and must re-authenticate. This behavior applies in the time synchronization context for some messages, as these are only exchanged between the individual link partners and the authenticator cannot receive them. Thus, these particular PTP messages cannot be secured using the E2E concept. Table I shows which messages are suitable for E2E protection.

PTP message type	Applied concept	PTP message length	
		unprotected	protected
Announce	P2P + E2E	90 Bytes	144 Byte (Special case)
Sync	P2P + E2E	60 Bytes	114 Bytes
Follow UP	P2P + E2E	90 Bytes	144 Bytes
Pdelay Request	P2P	68 Bytes	100 Bytes
Pdelay Response	P2P	68 Bytes	100 Bytes
Follow UP			
Signaling	P2P	74 Bytes	106 Bytes

Table I
PTP MESSAGES WITH APPLIED PROTECTION CONCEPT AND LENGTH IN BYTES

A. PTP messages without E2E protections

The PDelay request message serves as an example for a PTP message without E2E protection. This is only secured with the P2P concept. Figure 4 shows the structure of the PDelay request message. The ICV secures the entire message, starting with the destination MAC address and ending with the reserved bytes.

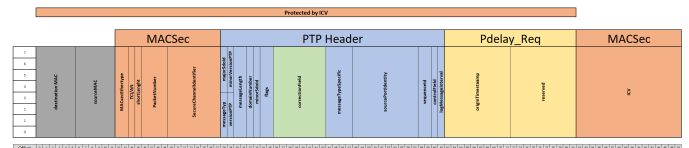


Figure 4. Example of a PTP message secured only via P2P concept

B. Special case - Announce message

The Announce message must be considered as a special case, because the TLV extension 'PathTrace' (IEEE 1588 - chapter 16.2) grows with each forwarding to the next PTP instance. With this extension the route of the PTP message is

recorded. Each PTP instance receiving this message can check how many PTP instances have already processed and forwarded this message. The structure of the Announce message is shown in Figure 5, other optional TLVs are not considered. The offset at the bottom describes the current byte in the message. The upper bar, which is marked 'Protected by ICV (MACsec)' and in orange color, marks the bytes protected by MACsec. In this case MACSec protects every single byte of the message. The bar below (red + 'Protected by ICV (TLV)) marks the bytes that can be protected by the E2E concept via TLV. The individual elements of the PathTrace extension are marked in purple.



Figure 5. Special case: The Announce message with its components

Before sending, the PTP instance enters its own identity (clock identity) into the so-called 'pathSequence' list. This list is represented by the elements 'clockidentity[0]', '...' and 'clockidentity[N]'. Due to this behavior the sequence of clock identities cannot be secured with the E2E concept. Only the PTP master is allowed to generate the checksum (ICV) of the E2E concept and this master cannot predict which PTP instances will be traversed on the way to the PTP slave. The PathTrace extension is not completely excluded from the E2E concept, but only the static entries, 'tlvType' and 'clockIdentity[0]', are secured.

VII. EXPERIMENTAL RESULTS

A. Test setup

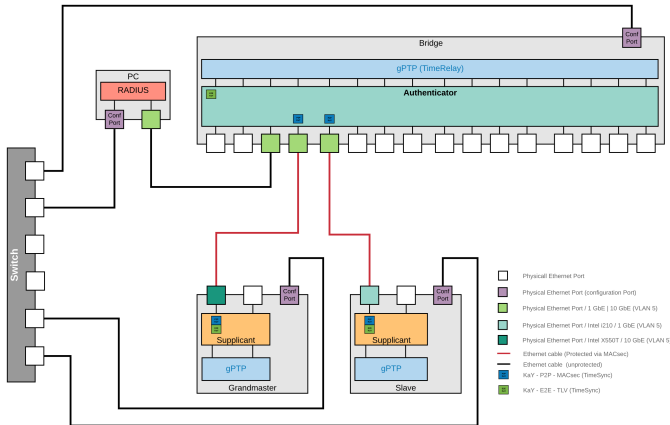


Figure 6. Test setup for the functional test of the safety concept

The grandmaster has a powerful CPU with 12 logical cores and a network card with two 10GbE ports. A slightly lower performance platform is used as the slave. These Ethernet ports have the ability to capture hardware timestamps for received messages. Each hardware component has an explicit configuration port that can be used to establish a SSH or

RemoteDesktop connection. These ports are connected to a dedicated switch. The bridge connects the grandmaster, slave and key server (RADIUS) with each other. All protocols required for the following tests are sent via this bridge. There is a gPTP instance that has also implemented these security features (P2P and E2E). This test setup, as well as the test cases defined below, are only intended to measure the additional time required to authenticate, encrypt and decrypt individual messages. It follows that the security of the concept is not evaluated.

B. Testcase Definition

For test cases 1 and 2, one measurement is performed on the grandmaster and one on the slave. A measurement takes about 2 minutes. In this time, enough measurement points are generated to be able to make a representative statement. Subsequently, two test cases are defined, which are again divided into two measuring points. Each PTP message that is sent or received is measured. Test case 3 is only measured on the slave.

- **Message generation**
 - P2P protection
 - E2E protection
- **Message verification**
 - P2P protection
 - E2E protection

1) *Testcase: Message generation:* In this test case, the generation of the individual PTP messages is measured. Sending of the message via socket is not measured. Two measurement points are defined here. The first measuring point 'Tx_P2P' measures the time required for P2P protection. This includes tasks like preparing the socket to send a new message, memory reservation of this, generating the whole Ethernet message, and encrypting the whole message with MACsec.

Measurement point two is called 'Tx_E2E' and measures the time required for E2E protection. This measurement point is a subset of the 'Tx_P2P' measurement. The tasks measured include generation of the PTP header, generation of the PTP payload, and securing the PTP message with TLV authentication. These two measurements must be performed in two different functions, otherwise not every PTP message to be sent can be measured. The exact measurement points and sequence of measurement points are shown in Figure 7.

2) *Testcase: Message verification:* In the second test case, the time required for verification of the received PTP messages is to be evaluated. Similar to testcase 1 a distinction is made between the two types of protection. Measurement point one (Rx_P2P) measures the P2P protection in the same way as the first test case. Here, the reception of the message is not measured, but only the verification of the message. This includes the time it takes to perform tasks such as checking the SectAG of MACsec, decrypting the message, and copying the decrypted data to the message store.

The verification of the PTP message is done at the second measuring point 'Rx_E2E'. The verification time of the PTP header and the attached TLVs, as well as the authentication of the PTP message is measured. The exact measuring points and sequence of the measuring points are shown in Figure 8.

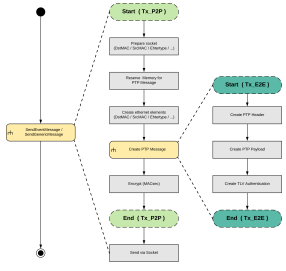


Figure 7. Measuring points for the Tx path

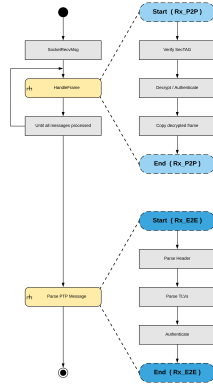


Figure 8. Measuring points for the Rx path

3) *Testcase: Residence time:* In this testcase, the residence time of the bridge is measured. The safety concept is also implemented on the bridge and is activated for the respective testcase. The residence time indicates how much time elapses between receiving a PTP message on a PTP port and sending the corresponding PTP message on another PTP port. This measured time is added to the correction field of the PTP message by the executing PTP instance.

VIII. DISCUSSION OF THE RESULTS

A histogram was created for each of the individual measurement scenarios, which shows the time required for execution in microseconds. The X axis of the diagrams represent a time slice. The Y axis indicates the frequency with which the task could be executed in this particular time slot. Three measurement series were measured in each case. Once with the P2P protection active, this is labeled 'P2P' and plotted with the color red. On the other hand, only the E2E protection is active. This case is called 'E2E' and plotted with the color green. 'Origin' is the case where neither E2E nor P2P protection is active, i.e. no security features are active. This case serves as a reference and is intended to show the actual difference to the concept used. A distinction is also made as to which device (grandmaster or slave) the measurement was performed on.

A. Measurements of a P2P and E2E secured message

The Announce, Sync and FollowUp messages are available for selection. The Announce message is chosen as an example for this type of protection because it is the longest message. This makes possible differences between the individual test scenarios stand out better. When analyzing the message generation, the diagram (Tx_P2P) from the grandmaster is compared with the corresponding diagram (Rx_P2P) from the slave. Measurements were made for Rx_P2P at the grandmaster, but since the slave does not send any announce messages, these measurements, as well as the counterparts (Tx_P2P) at the grandmaster, can be neglected.

1) *Evaluation of the message generation (Tx_P2P):* Figure 9 shows the measurement results of P2P protection on the

master. It can be seen that P2P protection is more time-consuming than E2E protection. This can be justified by the encryption of the message, as well as the larger number of bytes that have to be processed. E2E protection also takes more time to secure than generation without protection (Origin). This can be attributed to the authentication of the PTP post-run and the generation of the ICV. The measurement covers the P2P as well as the E2E protection.

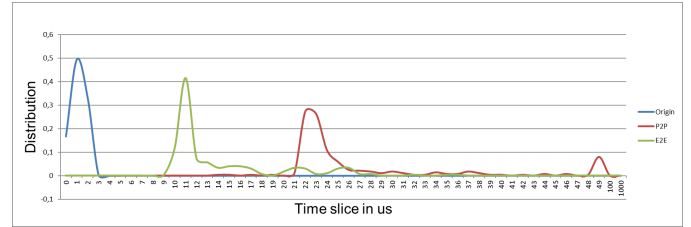


Figure 9. Tx_P2P: Histogram of the measured times of the Announce message at the grandmaster

2) *Evaluation of the message verification (Rx_P2P):* Only the measurements on the slave are considered here, since the slave does not send any announce messages to the master, but only receives them. Figure 10 shows the results of the measurement point Rx_P2P. It can be seen that the E2E protection and the Origin case do not increase the delay in this case. If the time required for P2P protection on the master and slave is considered, it can be seen that encryption on the master is more time-intensive than decryption on the slave.

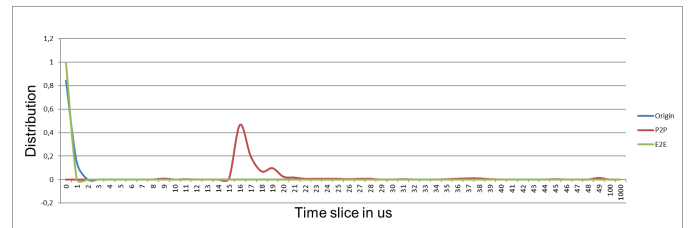


Figure 10. Rx_P2P: Histogram of the measured times of the Announce message at the slave

In the Rx_E2E measurement, only the E2E protection is measured. Compared to the master, the slave may take about 5 microseconds longer on average to authenticate the PTP message. This can be attributed to the slightly weaker processing power of the slave. The effort for the generation and verification of the TLV should be on average be very similar.

B. Measurements of a pure P2P secured message

The PDelay Request, PDelay Response, PDelay Response Follow Up and Signaling messages are available for selection. The PDelay Request message is selected as an example of this type of protection. Measurements for E2E protection of this message type were performed, but do not provide any relevant information, since E2E protection is not used for this message type. Furthermore, the measurements for which E2E protection is active can also be neglected in the following diagrams.

1) *Evaluation of the message generation (Tx_P2P)*: In Figure 11 it can be seen that the P2P protection has two larger accumulations, range between 10 and 13 microseconds and the range from 24 to 29 microseconds, in the time required. This distribution of measurement results across these ranges can be attributed to thread shedding from the operating system.

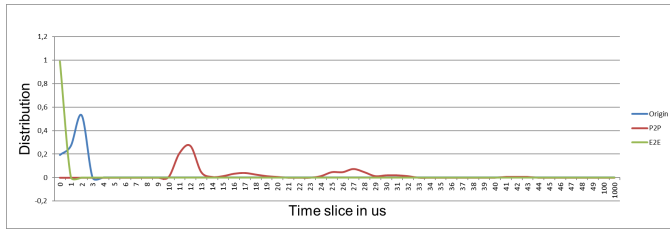


Figure 11. Tx_P2P: Histogram of the measured times of the PDelayRequest message at the grandmaster

Compared to the grandmaster, the slave in the Tx_P2P measurement takes on average 5 microseconds longer for encryption. The weaker computing power of the slave may be a reason for this.

2) *Package verification evaluation (Rx_P2P)*: No particular anomalies are visible when evaluating the reception path. As with the previous measurements, the slave takes about 5 microseconds longer to decrypt the message. If the time required for encryption and decryption is compared on the grandmaster or slave in each case, it can be seen that encryption and decryption on the same hardware do not show any major differences. Thus, it can be claimed that encryption and decryption are equally computationally intensive.

C. Residence Time measurement

For this measurement the FollowUP message is considered more closely. When the message is sent from the grandmaster, the correction field has the value 0. The bridge receives a message and forwards it to the slave. During this forwarding step the bridge adjusted the correction field and adds the measured residence time. The correction field of the FollowUP message is now recorded and evaluated at the slave. Figure 12 shows, that an active P2P protection does not have a significant impact on the residence time. Only an increase up to 2 milliseconds can be seen. It is worth mentioning that the bridge does not comply with IEEE 802.1as, as it exceeds the 10 millisecond limit for the residence time. However, this circumstance cannot be linked to the security concept.

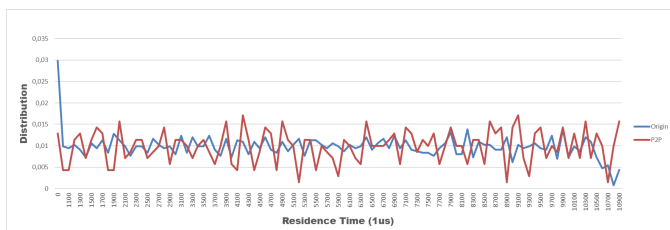


Figure 12. Histogram of the measured residence times of the bridge

The goal of this work was to find methods for cryptographically securing the IEEE 802.1AS standard, to create a concept from this, and to demonstrate the execution of this with the help of a prototypical implementation. The results of this work show that an implementation is not only possible, but can also be computed with a reasonable amount of time. For example, a PTP message could be secured in less than 50 microseconds using the presented concept. The residence time required by the standard of less than 10 milliseconds on a PTP instance can be met. The disadvantages of this type of protection are the high configuration effort and the partly rigid network topology. These disadvantages could be reduced using configuration tools such as NetConf. The concept protects the PTP message against some types of attack, but not yet against all. Here the further approaches (Prongs C and D) in the ANNEX S of the IEEE 1588 standard could support and further increase the security. Approach (Prong) D provides for the use of monitoring and management methods. For this purpose, each PTP instance stores relevant time synchronization parameters, which are then used as history and check the current time synchronization. Architecture based mechanisms such as redundancy are also proposed.

REFERENCES

- [1] M. Ullmann and M. Vögeler. "Delay attacks — Implication on NTP and PTP time synchronization". In: *2009 International Symposium on Precision Clock Synchronization for Measurement, Control and Communication*. 2009, pp. 1–6.
- [2] T. Mizrahi. "A game theoretic analysis of delay attacks against time synchronization protocols". In: *2012 IEEE International Symposium on Precision Clock Synchronization for Measurement, Control and Communication Proceedings*. 2012, pp. 1–6.
- [3] Robert Annessi, Joachim Fabini, Félix Iglesias, et al. "Encryption is Futile: Delay Attacks on High-Precision Clock Synchronization". In: *CoRR abs/1811.08569* (2018). arXiv: 1811.08569. URL: <http://arxiv.org/abs/1811.08569>.
- [4] Lakshay Narula and Todd E. Humphreys. "Requirements for Secure Clock Synchronization". In: *CoRR abs/1710.05798* (2017). arXiv: 1710.05798. URL: <http://arxiv.org/abs/1710.05798>.
- [5] "IEEE P1588™/D1.5 Draft Standard for a Precision Clock Synchronization Protocol for Networked Measurement and Control Systems". In: (2019), pp. 1–530.
- [6] "IEEE Standard for Local and metropolitan area networks—Media Access Control (MAC) Security". In: *IEEE Std 802.1AE-2018 (Revision of IEEE Std 802.1AE-2006)* (2018), pp. 1–590.

Computational efficient noise suppression in phase-shifting holography

Tillmann Spellauge

Multiphoton Imaging Lab

Department of Applied Sciences and Mechatronics

Munich University of Applied Sciences

Lorthstraße 64, 80335 Munich

Email: tspellau@hm.edu

Abstract—In this paper we give a comprehensive description of the influences of both detector noise and phase-shifting errors on the calculation of complex valued interference terms in phase-shifting interferometry. To our knowledge, the theory presented here is the first that addresses not only the noise suppression capability in phase-shifting as reported in literature but in addition is capable of quantifying the influences of phase-shifting errors. This is of particular interest in low cost phase-shifters such as home-built piezo-electric stages. Furthermore, a computational efficient method for the calculation of such interference terms is developed. Its noise suppression capability is experimentally confirmed by measurements based on incoherent holographic microscopy.

I. INTRODUCTION

Holographic imaging enables the compressed capturing of three dimensional object information in a two dimensional hologram [1]. Commonly this is done by measuring the intensity distribution of the interference between two optical fields [2]. Digital holography systems have allowed for the convenient storage and processing of the 2D hologram [3]. However in digital holography, the presence of incoherent background as well as the twin image in the intensity measurements can lead to artifacts being introduced into the reconstructed 3D object. Further artifacts can be introduced by detector noise. A common technique for the removal of the background, the twin image, as well as detector noise suppression is phase-shifting [4], [5]. For this purpose one of the interfering fields is shifted by global phase terms for at least three times with intensity measurements being taken for each phase-shift. From this set of measurements the background and twin image free complex valued interference term can be recovered. While phase-shifting is well documented [6], the influence of phase-shifting errors has received little attention. These influences are of particular interest in low cost phase-shifting implementation, which make use of home-built piezo-electric stages for example. In such systems the presence of friction, the absence of position feedback and other adverse factors can lead to significant phase-shifting errors, which in turn negatively influence the calculation of the complex valued interference term.

In this work a computational efficient method for the calculation of complex valued interference terms will be given. Next a theoretical framework for the description of the influences of

both detector noise and phase-shifting errors on the calculation of the complex valued interference term is derived. The noise suppression capability of the calculation methods will be experimentally confirmed by measurements using an incoherent holographic microscope.

II. THEORY

All interference based digital holographic methods have in common, that real valued intensity distributions of interference patterns, resulting from the superposition of two mutually coherent light fields E_1 and E_2 , are measured:

$$\begin{aligned} I(x, y) &= |E_1(x, y) + E_2(x, y)|^2 \\ &= I_b(x, y) + IF(x, y) + c.c. \end{aligned} \quad (1)$$

where I is the intensity of the interference pattern, x and y are the lateral coordinates and $c.c.$ denotes the complex conjugate of the previous term. I_b is the combined intensity of the two fields and does not contain any information about the interference other than ensuring positive intensity values. In the case of incoherent holography I_b can contain additional background, resulting from the incoherent overlap of the fields from neighboring object points. The amplitude and phase information of the object is solely contained in the complex valued interference term $IF(x, y) = \overline{E_2(x, y)} \cdot E_1(x, y)$, which is not directly accessible by intensity measurements. In order to recover IF and remove its complex conjugate (its twin image), the phase-shifting method can be used [4], [5]. For this purpose one of the fields is shifted step by step by increasing global phase factors $\alpha^{(n)}$:

$$E_2^{(0)}(x, y) \rightarrow e^{i\alpha^{(n)}} E_2^{(0)}(x, y) = E_2^{(n)}(x, y) \quad (2)$$

where n is an integer. Since the same phase-shift is applied to each detector pixel, from here on out the coordinates x and y will be dropped. Initially the phase-shifts are chosen to uniformly fill the interval $[0, 2\pi[$:

$$\alpha^{(n)} = \frac{2\pi}{N_\alpha} n \quad (3)$$

with n being an integer in the interval $[0, N_\alpha[$ and N_α being the total number of phase-shifts. The problem at hand is to recover IF from a series of measurements $I^{(n)}$ with:

$$\begin{aligned} I^{(n)} &= |E_1 + E_2^{(n)}|^2 \\ &= |E_1|^2 + |E_2^{(n)}|^2 + \overline{E_2^{(n)}} \cdot E_1 + c.c. \\ &= I_b + IF \cdot e^{-i\alpha^{(n)}} + c.c. \end{aligned} \quad (4)$$

Equation 4 can be regarded as a linear system of n equations, with every equation corresponding to a single measurement. It can be seen, that the second term in Equation 4 is equal to the discrete inverse Fourier vector corresponding to the relative frequency of -1 , except for the complex scalar factor IF . In Dirac notation the discrete inverse Fourier vectors is written as:

$$|m\rangle = \frac{1}{\sqrt{N_\alpha}} e^{i\alpha^{(n)}m} \quad (5)$$

with the norm $\| |m\rangle \| = 1$ and m being an integer corresponding to the relative frequency. By inserting Equation 5 into Equation 4, the linear system of equations representing the measured intensities is rewritten to:

$$|I\rangle = \sqrt{N_\alpha} I_b |0\rangle + \sqrt{N_\alpha} IF |-1\rangle + \sqrt{N_\alpha} \overline{IF} |+1\rangle \quad (6)$$

with $|I\rangle$ being a Dirac-vector containing all measurements. The measured intensities can be fully described by three frequencies with suitable amplitude and phase. Furthermore it can be seen, that the frequencies $|-1\rangle$, $|0\rangle$ and $|+1\rangle$ are needed to represent any possible measurement. Therefore, at least three measurements have to be taken.

In order to extract IF from the measured data, the linear system of n equations in Equation 6 has to be inverted. The solution to this problem is a linear functional F_{IF} . By use of the standard scalar product $\langle a|b\rangle = \sum a_n b_n$ the functional F_{IF} is found to be:

$$F_{IF} := \frac{1}{\sqrt{N_\alpha}} \langle -1| \quad (7)$$

F_{IF} is parallel only to the vector containing IF and is orthogonal to the vectors containing I_b and \overline{IF} . Thus, IF can be recovered by calculating the scalar product of the functional and the measured intensities:

$$F_{IF}(|I\rangle) = \frac{1}{\sqrt{N_\alpha}} \langle -1|I\rangle = IF \quad (8)$$

$IF(x, y)$ is determined by applying the functional to each pixel in the recorded data: in detail, $IF(x, y)$ can be recovered by calculating a single inner product for each pixel in $|I\rangle(x, y)$. Compared to other methods, such as the Fourier transformation methods by Morimoto and Fujisawa [7] or by singular value decomposition [8], this method offers a reduced computational complexity, resulting in shorter computation times.

Up to this point ideal noise free intensity measurements have been assumed. In real measurements however, there is always additive detector noise present. It is introduced by read-out noise, photon-shot noise and thermal noise. These

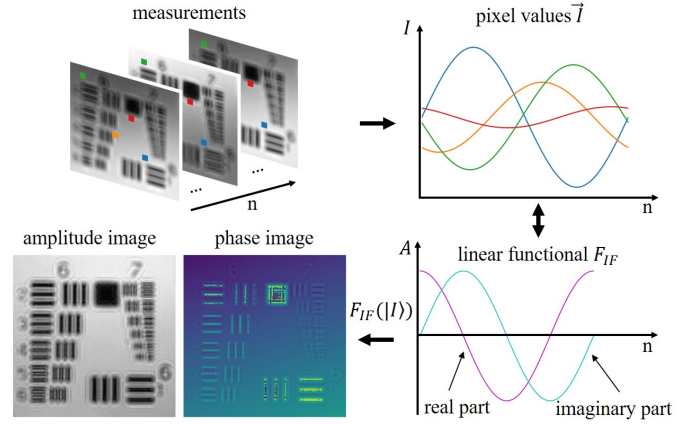


Figure 1. Schematic depiction of the calculation of the complex valued interference term. Upper left: Three exemplary measurements with phase-shifts in the range $[0, 2\pi[$. Upper right: Exemplary intensity modulation of single pixels in the phase shifting data. Lower right: Amplitude A of the real and imaginary part of the linear functional. Lower left: IF depicted as its amplitude and phase image.

detector noise contributions can be combined to a single noise component:

$$|N\rangle = \sum \tilde{N}_m |m\rangle \quad (9)$$

where \tilde{N}_m is the value of the noise amplitude spectrum at frequency m and $|N\rangle$ is a vector containing the noise contributions of each measurement. For the sake of simplicity the noise is considered to be white uncorrelated noise, i.e. the amplitude of the noise spectrum is independent of the frequency:

$$N_0 = \tilde{N}^{(i)} = \tilde{N}^{(j)} \quad (10)$$

with N_0 being the constant noise amplitude and i and j being arbitrary integers. As before F_{IF} is applied to the measured data in order to calculate IF . However in the present of noise F_{IF} is not only parallel to $IF |-1\rangle$ but also to $\tilde{N}_{-1} |-1\rangle$ leading to a noisy version of IF :

$$\begin{aligned} F_{IF}(|I\rangle + |N\rangle) &= \\ &= F_{IF}(\sqrt{N_\alpha} I_b |0\rangle + \sqrt{N_\alpha} IF |-1\rangle + \sqrt{N_\alpha} \overline{IF} |+1\rangle \\ &\quad + \sum \tilde{N}_m |m\rangle) \\ &= IF + \frac{1}{\sqrt{N_\alpha}} \tilde{N}_{-1} = IF + \frac{1}{\sqrt{N_\alpha}} N_0 \end{aligned} \quad (11)$$

Even though noisy measurements always lead to a noisy IF , the detector noise in IF can be reduced by increasing the number of intensity measurements.

Besides detector noise, error in the phase-shifting can introduce further noise. Therefore, the influence of randomly non uniformly spaced phase-shifts is considered. In this case F_{IF} is no longer orthogonal to $|m\rangle$ for $m \neq -1$:

$$F_{IF}(|m\rangle) = \epsilon_m \quad (12)$$

This leads to contributions of all non-orthogonal frequency components in $|I\rangle + |N\rangle$:

$$F_{IF}(|I\rangle + |N\rangle) = IF + \epsilon_1 \overline{IF} + \epsilon_0 I_b + \frac{1}{\sqrt{N_\alpha}} N_0 + \frac{1}{\sqrt{N_\alpha}} \sum \epsilon_m \tilde{N}_m \quad (13)$$

The random nature of the phase-shifting errors allow the introduction of: $\sum \epsilon_m \tilde{N}_m = \sqrt{N_\alpha} \epsilon N_0$, where ϵ is the typical value of the ensemble of all ϵ_m . Thus, Equation 13 is rewritten to:

$$F_{IF}(|I\rangle + |N\rangle) = IF + \epsilon \overline{IF} + \epsilon I_b + \frac{1}{\sqrt{N_\alpha}} N_0 + \epsilon N_0 \quad (14)$$

This formula gives a comprehensive description of the influences of both detector noise and random phase-shifting errors on the calculation of IF , with the three key features being:

- 1) Errors in the phase-shifting lead to cross-talk between IF , its complex conjugate and the background.
- 2) Errors in the phase-shifting lead to a constant noise term which can not be reduced by taking more measurements.
- 3) The influence of the detector noise can be reduced by increasing the number of phase-shifts.

III. METHODS

In order to demonstrate the noise suppression capability of the scalar product method, measurements are taken with an incoherent holography microscope. Phase-shifting is performed by a home-built piezo-electric actuator.

A. Optical setup

Digital holography with spatially and temporally low coherent fields, like those emitted by LED's or fluorescent objects, is challenging since no external reference can be found which is mutually coherent with the object field. However, the object field is always coherent to itself. Even though the object field can interfere with an unchanged version of itself, no additional information is contained in such interference patterns. This problem can be solved by inducing a change between the two versions of the object field while maintaining mutual coherence. The highest degree of coherence can be achieved by propagating the two fields against each other, i.e. inducing an axial shear. In this way each object point is interfering with a propagated version of itself. Some mutual coherence is lost since neighboring de-focused object points can overlap resulting in a non-coherent superposition. However compared to other methods such as lateral shear interferometry [6] this effect is small. One example of such a system is Fresnel incoherent correlation holography (FINCH) [9]. Commonly it is implemented in an in-line configuration by the use of a spatial light modulator [10]. A low cost alternative is the implementation as a Michelson type interferometer as demonstrated by Cossairt et al. [11]. A similar system is used for the experiments presented here. The Michelson type interferometer is shifting the image planes of the two interferometer arms axially by Δz against each other, while keeping their optical path lengths equal. A CMOS detector is placed between the

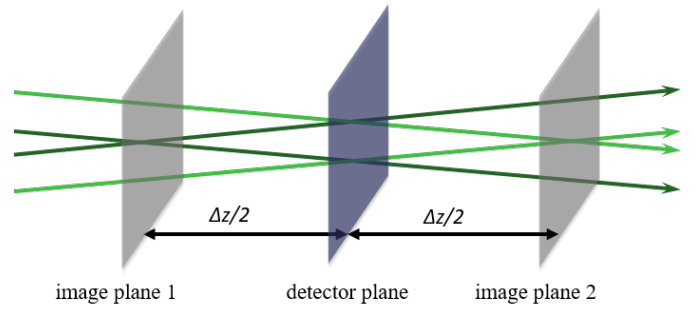


Figure 2. Schematic of the hologram formation in a focal shear interferometer.

two image planes as shown in Figure 2. The interferometer is used as the detector in a telecentric microscope consisting of a 4x 0.13 NA infinity corrected objective lens and a 200 mm tube lens. The theoretical transverse resolution of the microscope is $2.41 \mu\text{m}$. Phase-shifting is done by a home-built piezo-electric stage. For the low coherence illumination, a consumer LED emitting at 515 nm with a spectral bandwidth of 40 nm is used. Its Gaussian spectral intensity distribution leads to a coherence length of approximately $3 \mu\text{m}$. The light emitted by the LED is coupled into a multimode optical fiber. The output of the fiber is collimated onto the sample in a transmission configuration by use of a fiber collimator.

B. Piezo-electric stage characterization

The piezo-electric stage introduces global phase-shifts into one of the interferometer arms by shifting a mirror. To avoid hysteresis, the phase-shifts are done in one direction only and the stage is returned to its zero position after each measurement cycle. Each cycle consists of 40 phase-shifts with one intensity measurement after each shift. In order to characterize the phase-shifts, measurements are taken without an object in the microscope. The phase-shifts are quantified on a pixel basis according to the method by Takeda et al. [12]. The initial phase of each pixel is set to zero, thus accounting for slight tilts of the mirrors in the Michelson interferometer. The mean phase-shifts of all pixels are regarded as the exact phase-shifts of the piezo-electric stage in one measurement cycle. This procedure is repeated for ten cycles. The mean and standard deviation for all 40 phase-shifts across the ten cycles is calculated. The results are shown in Figure 3. The mean phase-shifts are used to choose the measurement interval used for the calculation of IF when the object is introduced. The interval boundaries are indicated by the two green dashed lines in Figure 3.

C. Image reconstruction

If the object is situated in the front focal plane of the objective lens, the propagation distances from the two image planes to the detector plane are $\Delta z/2$ but with opposite sign. Thus, the two fields E_1 and E_2 are complex conjugates of each other:

$$E_2(x, y) = \overline{E_1(x, y)} \quad (15)$$

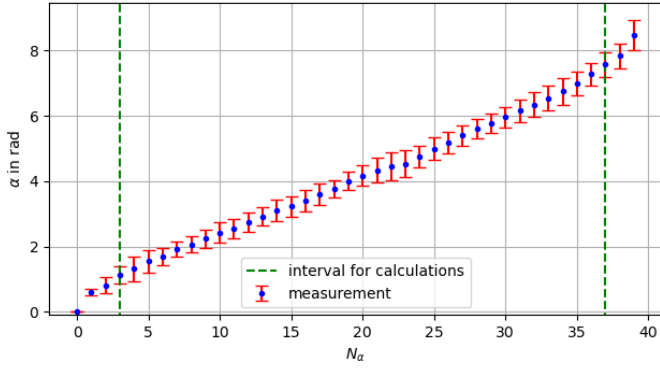


Figure 3. Mean (blue dots) and standard deviation (red bars) of the phase-shifts introduced by the home-built piezo-electric stage. The interval used for the calculation of IF is indicated by the green dashed lines.

IF then becomes:

$$IF = \overline{E_2(x, y)} \cdot E_1(x, y) = E_1(x, y)^2 \quad (16)$$

By decomposing the field $E_1(x, y)$ into its amplitude and complex phase, $IF(x, y)$ is written as:

$$\begin{aligned} IF(x, y) &= (A(x, y) \exp(-i\Phi(x, y)))^2 \\ &= A^2(x, y) \exp(-i2\Phi(x, y)) \end{aligned} \quad (17)$$

with $A(x, y)$ being the amplitude and $\Phi(x, y)$ being the phase. $IF(x, y)$ is thus equal to one of the fields but with squared amplitude and twice its phase. Therefore, IF can be treated as an ordinary light field. In a microscope the angular magnification is one over the image magnification; big angles in the object space are converted to small angles in the image space. Since IF is captured in the image space, the small angle approximation can be assumed. This allows IF to be propagated using the Fresnel propagator [13] in order to calculate the in-focus image.

D. Noise analysis

For the characterization of the noise present in IF , an USAF 1951 resolution test chart is placed in the front focal plane of the objective lens and ten measurement cycles are taken. In this configuration the proper calculation of IF can easily be checked by digitally propagating it and visually inspecting the in-focus image. Since the phase of IF is showing a 2π ambiguity the noise in the phase is not easily definable. Thus, only the noise in the amplitude of IF is considered. The amplitude of IF is normalized to one and the amplitude noise is defined as the standard deviation in a sufficiently large area of uniform illumination. This value gives the amount of noise as a fraction of the maximum amplitude of IF .

IV. RESULTS AND DISCUSSION

Figure 4 shows the mean noise level of $|IF|$ for increasing numbers of independent measurements. The noise is evaluated in the green marked areas shown in Figure 5 and Figure 6. A decrease in the noise level is clearly visible. To validate the theoretically derived inverse square root dependence between

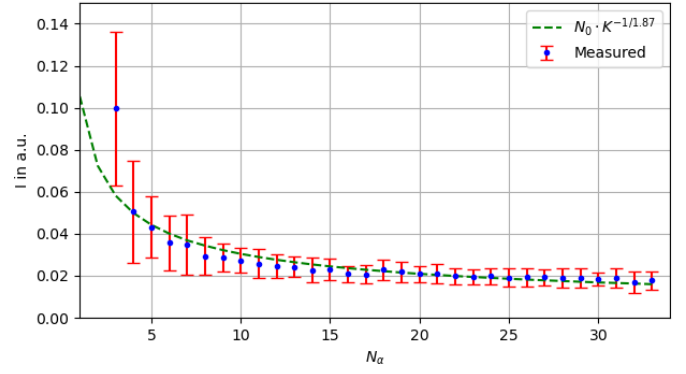


Figure 4. Mean relative noise level of the complex valued interference terms (blue dots) and their standard deviation (red bars), as well as a least mean square error fit of a root function (green dashed line).

the number of measurements and the noise level, a root function is fitted to the measured mean noise levels. The free parameters are the initial noise level N_0 and the order of the root function. The order of the best mean square error fit is determined to be -1.87 , which is slightly lower than the theoretical value of -2 , meaning that the achieved noise reduction is nominally worse than theoretically predicted. This however is to be expected and can be explained by the presence of correlated noise and influences of phase-shifting errors. The initial noise is determined to be 10.5% of $|IF|$. The noise level in a single intensity measurement can

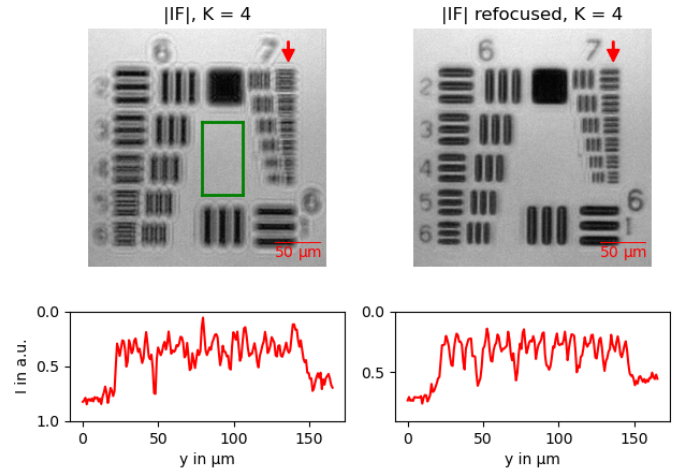


Figure 5. Top left: $|IF|$ of a USAF 1951 resolution test chart calculated from four interferograms. The green rectangle shows the area for the noise characterization. Top right: Digitally re-focused version of $|IF|$. Bottom left: Intensity profile along the red arrow in $|IF|$. Bottom right: Intensity profile along the red arrow in the re-focused $|IF|$. The effect of digital refocusing is clearly visible in the images as well as in the profiles. The limited noise suppression leads to poorly defined small structures in the re-focused image.

be calculated from N_0 by multiplying the initial noise with the maximum visibility of the measured interferograms. The maximum visibility is determined to be 54.3% leading to a noise level in the intensity measurements of 5.7% which is in

good agreement with the manufacturer specifications.

Noticeable is the high noise level for the reconstruction from three interferograms. This is due to bad matching between the global phase factors of the measurements and the functional. As discussed before, such mismatches can lead to slow varying modulations being introduced due to cross-talk between IF and its complex conjugate. Because of this systematic error this value is not used for fitting.

Figure 5 and Figure 6 show $|IF|$ and its digitally re-focused version calculated from four respective 33 interferograms. In Figure 5 the presence of noise is clearly noticeable. In Figure 6 the noise reduction is apparent even by visual inspection. The

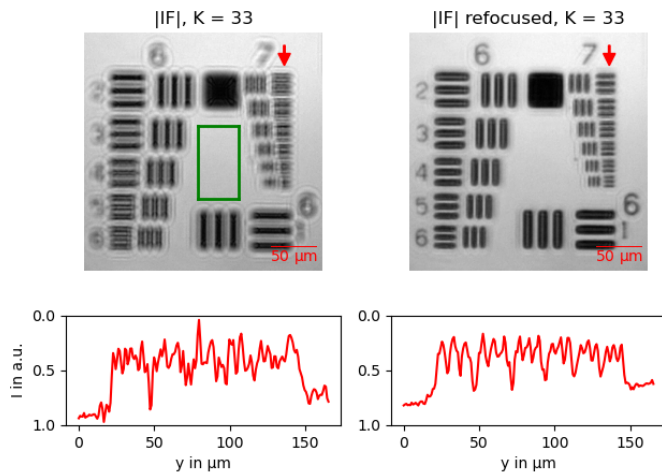


Figure 6. Top left: $|IF|$ of a USAF 1951 resolution test chart calculated from 33 interferograms. The green rectangle shows the area for the noise characterization. Top right: Digitally re-focused version of $|IF|$. Bottom left: Intensity profile along the red arrow in $|IF|$. Bottom right: Intensity profile along the red arrow in the digitally re-focused $|IF|$. The effect of digital refocusing is clearly visible in the images as well as in the profiles. The noise suppression leads to well defined small features in the re-focused image.

noise reduction becomes especially apparent when comparing the intensity profiles across the group seven elements of the USAF target. The noise reduction leads to better defined features, thus increasing the perceived resolution of the digitally re-focused image. According to the Rayleigh criterion element 4 of group 7 of the USAF target is still resolved, corresponding to a resolution of $2.46 \mu\text{m}$. This is in excellent agreement with the theoretical resolution of the microscope of $2.42 \mu\text{m}$.

V. CONCLUSION

We derived a comprehensive analysis of the influences of detector noise and phase-shifting errors on the calculation of complex valued interference terms from phase-shifting measurements. It could be shown that random errors in the phase-shifting lead to cross talk between the complex valued interference term, its complex conjugate (its twin image) and the background. This cross talk introduces undesirable artifacts into holographic data, which can not be avoided employing low cost phase-shifters. To our knowledge, the influences of these errors on the calculation of complex valued

interference terms can be quantified for the first time with our theory. In this work the detector noise and the phase-shifting errors are described by white uncorrelated noise. However, the theory can easily be modified to incorporate more accurate descriptions of the detector noise, as well as non-linearities in the phase-shifting.

Furthermore, a computational efficient way of calculating the complex valued interference term from phase-shifting data has been developed. By applying it to incoherent holographic microscopy, its validity and detector noise suppression capability has been confirmed experimentally.

ACKNOWLEDGMENT

The author would like to thank Dr. Martin Berz for the ongoing cooperation and the many fruitful discussions, Prof. Dr. Thomas Hellerer for the opportunity to publish this work and the continuous support, Patrick Byers, Thomas Kellerer, Melina Lobenhoffer, David Redka and Maximilian Spellaue for their useful input.

REFERENCES

- [1] D. Gabor, "A new microscopic principle," *Nature*, vol. 161, no. 4098, pp. 777–778, 1948.
- [2] T.-C. Poon, Ed., *Digital Holography and Three-Dimensional Display*. Boston, MA: Springer US, 2006. [Online]. Available: <http://link.springer.com/10.1007/0-387-31397-4>
- [3] U. Schnars and W. Jüptner, *Digital Holography*. Berlin/Heidelberg: Springer-Verlag, 2005. [Online]. Available: <http://link.springer.com/10.1007/b138284>
- [4] I. Yamaguchi and T. Zhang, "Phase-shifting digital holography," *Optics Letters*, vol. 22, no. 16, p. 1268, aug 1997. [Online]. Available: <https://www.osapublishing.org/abstract.cfm?URI=ol-22-16-1268>
- [5] S. Lai, B. King, and M. A. Neifeld, "Wave front reconstruction by means of phase-shifting digital in-line holography," *Optics Communications*, vol. 173, no. 1-6, pp. 155–160, 2000.
- [6] J. Gresty, "Optical Shop Testing," *Optica Acta: International Journal of Optics*, vol. 26, no. 7, pp. 836–836, jul 1979. [Online]. Available: <https://www.tandfonline.com/doi/full/10.1080/716099479>
- [7] M. Fujisawa, "Fringe pattern analysis by a phase-shifting method using Fourier transform," *Optical Engineering*, vol. 33, no. 11, p. 3709, nov 1994. [Online]. Available: <http://opticalengineering.spiedigitallibrary.org/article.aspx?doi=10.1117/12.181923>
- [8] B. Katz, D. Wulich, and J. Rosen, "Optimal noise suppression in Fresnel incoherent correlation holography (FINCH) configured for maximum imaging resolution," *Applied Optics*, vol. 49, no. 30, pp. 5757–5763, 2010.
- [9] J. Rosen and G. Brooker, "Digital spatially incoherent Fresnel holography," *Optics Letters*, vol. 32, no. 8, p. 912, 2007.
- [10] —, "Fresnel incoherent correlation holography (FINCH): A review of research," *Advanced Optical Technologies*, vol. 1, no. 3, pp. 151–169, 2012.
- [11] O. Cossairt, N. Matsuda, and M. Gupta, "Digital refocusing with incoherent holography," in *2014 IEEE International Conference on Computational Photography (ICCP)*. IEEE, may 2014, pp. 1–9. [Online]. Available: <http://ieeexplore.ieee.org/document/6831819/>
- [12] M. Takeda, H. Ina, and S. Kobayashi, "Fourier-transform method of fringe-pattern analysis for computer-based topography and interferometry," *Journal of the Optical Society of America*, vol. 72, no. 1, p. 156, jan 1982. [Online]. Available: <https://www.osapublishing.org/abstract.cfm?URI=josa-72-1-156>
- [13] J. W. Goodman, *Introduction to Fourier Optics*, ser. McGraw-Hill physical and quantum electronics series. W. H. Freeman, 2005. [Online]. Available: <https://books.google.de/books?id=ow5xs{ }Rtt9AC>

Formulas for Mutual and Self-Inductances of Multiple Coupled Loops

Markus Theil

University of Applied Science Augsburg
 Department of Electrical Engineering
 Germany, Augsburg 86161
 Email: markus.theil@hs-augsburg.de

Abstract—Formulas for the determination of mutual and self-inductances of coaxial loops are presented in this work. The described formulas are based on simplification of magnetostatic fields. Due to this, exact solutions can be given for infinitely thin conductors of any shape by the Neumann formula. However, the evaluation of this solution is quite difficult and can only be solved with high mathematical effort. Therefore, approximation formulas are presented as well, which allow the determination of mutual inductances in different applications, e.g. for large and small distances between the coils. For the self-inductance, a boundary value approximation of the Neumann formula is performed which provides an overall exact solution. The basic principles of these approximations are described as well. The formulas are compared with the results of a field simulation and analyzed regarding to their ranges of validity and accuracy.

May 06, 2021

I. INTRODUCTION

One of the major problems of conventional wireless power transmission systems is the reduced efficiency with increasing distance. The method first presented in [1] can improve the efficiency at higher transmission distances by using an additional oscillating circuit (resonator) on the transmitter and receiver side. Accordingly, there is a resonator in front of the source and load loop, Fig. 1 (a). The geometry of the resonators is designed so that the coils have the maximum quality (Q -factor) at the resonance frequency. This system is often referred to *strongly coupled magnetic resonance* (SCMR). The disadvantage of this technique is that twice the number of the loops are needed and the resonators have to be placed at a certain distance t in front of the source and load loop.

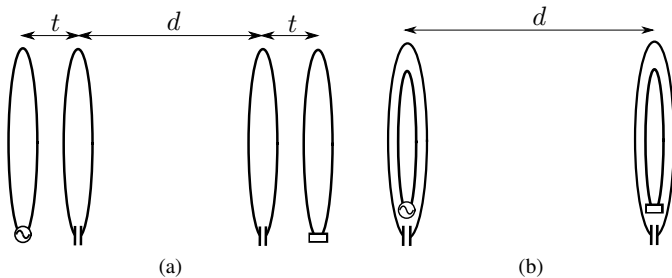


Figure 1: Comparison between (a) SCMR and (b) CSCMR

A related work [2] avoids the latter problem by placing the resonant circuits around the source and load loop. Thus, the loops on the transmitter and receiver side can be placed in one plane, Fig. 1 (b). The authors call their method *conformal strongly coupled magnetic resonance* (CSCMR). Further analysis showed that additional resonators can increase the transmission bandwidth. From the results of their study, the authors conclude that the relative bandwidth of a system with two resonators per transmitter and receiver side is about 23%. In contrast, with a comparable arrangement according to Fig. 1 (a) and (b), the relative bandwidths are about 2,5% and 12,2%. Because of this potential to increase the bandwidth of an inductive coupling by additional resonators makes this technology very interesting for wireless data transmission. However, for an accurate description of the transmission characteristics it is necessary to know all mutual and self-inductances of the system.

In this study, formulas for the determination of mutual and self-inductances are presented and evaluated according to their validity ranges and accuracy, which allows the development of a transmission model for an arbitrary number of coupled loops. In particular, coaxial loops are considered here. Approximation formulas are presented for different applications, e.g. for large and small distances between the coils. Also, the exact solutions to the problems are given for all cases. The formulas are verified with the results of a field simulation. Therefore, the finite element program Comsol Multiphysics is used.

II. DETERMINATION OF MUTUAL AND SELF-INDUCTANCES

A general expression for the determination of mutual and self-inductances of an infinitely thin wire is given by the Neumann formula

$$L_{ij} = \frac{\Phi_{ij}}{I_j} = \frac{\mu_0}{4\pi} \oint_{C_i} \oint_{C_j} \frac{d\vec{s}_j d\vec{s}_i}{|\vec{r}_j - \vec{r}_i|}. \quad (1)$$

Due to the restriction to very thin wires, the condition $R \gg r$ must be satisfied such that the approximation of a line integral is approximately given, where R corresponds to the radius of the loop and r to the radius of the wire. Thus, the volume of the wire is negligible and equation (1) can be used to determine the inductances of arbitrarily but closed guided wires. The vectors \vec{r}_j and \vec{r}_i of the integral are to be interpreted as follows. The

vector \vec{r}_i points to the contour formed by the field generating wire, \vec{r}_j to the enclosed area of the second wire.

However, a problem comes up when the Neumann formula is used for the determination of self-inductances. In this case the vectors \vec{r}_j and \vec{r}_i are identical. Thus, the paths of the line integrals are equal as well and would therefore lead to a singular integral value. So the Neumann formula can normally not be used to calculate self-inductances. However, if the finite but small thickness of the wire is taken into account, one of the location vectors can be displaced by this thickness in the z -direction [3]. In general, the mutual inductance close to the wire is being calculated. But as will be shown in section III, the deviations caused by this are negligible.

An important property of mutual inductances that can be obtained from the Neumann formula is the reciprocity of the magnetic coupling. For double integrals it is permitted to swap the integration variables. Consequently, for mutual inductances follows

$$\frac{\mu_0}{4\pi} \oint_{C_i} \oint_{C_j} \frac{d\vec{s}_j d\vec{s}_i}{|\vec{r}_j - \vec{r}_i|} = \frac{\mu_0}{4\pi} \oint_{C_j} \oint_{C_i} \frac{d\vec{s}_i d\vec{s}_j}{|\vec{r}_i - \vec{r}_j|}$$

$$\Rightarrow L_{ij} = L_{ji} =: M. \quad (2)$$

Due to this theorem, the number of mutual inductances that have to be determined for transfer networks consisting of an arbitrary number of coupled loops is halved.

The Neumann formula is the exact solution for mutual and self-inductances of thin wires of arbitrary shape. The solution of the integral is explained shortly. In the following sections, it will be shown which simplifications can be made in the specific cases. For the general consideration of the solution, one of the two location vectors is arbitrary at first, i. e. $\vec{r}_j = \vec{r}$. Therefore, the general solution is given by [4]

$$L_{ij} = \mu_0 \sqrt{R\varrho} \left\{ \left(\frac{2}{k} - k \right) K(k) - \frac{2}{k} E(k) \right\} \quad (3)$$

with the module k according to

$$k = \frac{2\sqrt{R\varrho}}{\sqrt{(R+\varrho)^2 + z^2}}. \quad (4)$$

$K(k)$ and $E(k)$ are complete elliptic integrals of the first and second kind. For $0 \leq k \leq 1$, the elliptic integrals provide a real solution and can then be evaluated via a power series expansion. However, for numerical calculations, algorithms like the *arithmetic-geometric mean* (AGM) are preferred, since they provide super-linear convergence [5]. Nevertheless, an evaluation of these functions is difficult unless it is possible to use algorithms that are already implemented. Therefore, simpler approximation solutions for different applications are presented in the following sections.

A. Formulas for Self-Inductances

In order to use the Neumann formula for the determination of self-inductances, the finite radius r of the wire is taken into account. Thus, z gets an offset by r . For ϱ , the radius R of the

loop is chosen. With these definitions for z and ϱ , equation (3) and (4) become

$$L = \mu_0 R \left\{ \left(\frac{2}{k} - k \right) K(k) - \frac{2}{k} E(k) \right\} \quad (5)$$

with

$$k = \frac{2R}{\sqrt{4R^2 + r^2}}. \quad (6)$$

Generally, for the determination of the self-inductance, the case $r \rightarrow 0$ has to be considered. In the case $r \rightarrow 0$, the module $k \rightarrow 1$. However, from the definition of K and E it follows

$$\lim_{k \rightarrow 1} K(k) = \infty$$

$$E(1) = 1.$$

Therefore, the complementary module k' can be introduced

$$k' = \sqrt{1 - k^2}. \quad (7)$$

The introduction of the new module avoids the difficulties of evaluating K when the module converges to one. The elliptic integrals K and E can be developed into a power series of k' according to [4]

$$K(k') = \ln \left(\frac{4}{k'} \right) + \frac{1^2}{2^2} k'^2 \left(\ln \left(\frac{4}{k'} \right) - \frac{2}{1,2} \right)$$

$$+ \frac{1^2 3^2}{2^2 4^2} k'^4 \left(\ln \left(\frac{4}{k'} \right) - \frac{2}{1,2} - \frac{2}{3,4} \right)$$

$$+ \frac{1^2 3^2 5^2}{2^2 4^2 6^2} k'^6 \left(\ln \left(\frac{4}{k'} \right) - \frac{2}{1,2} - \frac{2}{3,4} - \frac{2}{5,6} \right) + \dots \quad (8)$$

and

$$E(k') = 1 + \frac{1}{2} k'^2 \left(\ln \left(\frac{4}{k'} \right) - \frac{1}{1,2} \right)$$

$$+ \frac{1^2 3}{2^2 4} k'^4 \left(\ln \left(\frac{4}{k'} \right) - \frac{2}{1,2} - \frac{1}{3,4} \right)$$

$$+ \frac{1^2 3^2 5}{2^2 4^2 6} k'^6 \left(\ln \left(\frac{4}{k'} \right) - \frac{2}{1,2} - \frac{2}{3,4} - \frac{1}{5,6} \right) + \dots \quad (9)$$

This series converges strongly when k' is small, i.e. when $k \rightarrow 1$. With the module from equation (6) it follows

$$k' = \sqrt{1 - k^2} = \sqrt{1 - \frac{4R^2}{4R^2 + r^2}}$$

$$\Leftrightarrow \frac{r}{2R} \sqrt{\frac{1}{1 + \frac{r^2}{4R^2}}}.$$

Since $R \gg r$, k' can be expressed as

$$k' \approx \frac{r}{2R}. \quad (10)$$

If $k \rightarrow 1$ and consequently $k' \rightarrow 0$, only the first term of the series (8) and (9) provides a contribution [6]. For K and E follows

$$K = \ln \left(\frac{4}{k'} \right) = \ln \left(\frac{8R}{r} \right)$$

$$E = 1.$$

These expressions can now be substituted into (5) and taking into account that $k \rightarrow 1$. Thus, the final solution is

$$L = \mu_0 R \left[\ln \left(\frac{8R}{r} \right) - 2 \right]. \quad (11)$$

Interestingly, Maxwell derived the same formula by geometrical consideration in his work „*A Treatise on Electricity and Magnetism*“ [7] without dealing with elliptic integrals.

In general, a further distinction for self-inductances can be made between an external L_o and internal inductance L_i . The total inductance of a geometrical arrangement is then the sum of both components

$$L = L_i + L_o. \quad (12)$$

The solutions presented so far consider just the outer inductance. L_i takes all flux components into account that are enclosed by the contour of the inner radius R , Fig. 2. However, if the wire has a finite thickness, a field distribution also occurs over the cross section. The flux components through the wire are taken into account by L_i . Depending on the thickness, this makes a significant contribution to the self-inductance.

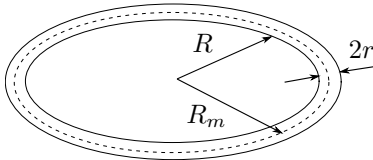


Figure 2: Illustration of the concept of the inner and outer self-inductance

Assuming that $R \gg r$, the magnetic field strength \vec{H} inside the wire corresponds to the field strength of an infinitely long wire [8]. Therefore, \vec{H} is known as

$$\vec{H} = \frac{I}{2\pi r^2} \vec{e}_\phi. \quad (13)$$

Thus, L_i can be determined via the stored energy in the wire

$$W = \iiint_V \frac{1}{2} \mu_0 H^2 dv = \frac{1}{2} L_i I^2 \quad (14)$$

$$\Rightarrow L_i = \frac{\mu_0 l}{8\pi} \approx \frac{\mu_0 R}{4}. \quad (15)$$

Strictly speaking, to calculate the length l of the loop, the mean radius, i.e. $R_m = R + r$, must be used. Since $R \gg r$, the length of the wire can be given in a good approximation as $2\pi R$. Extending equation (11) by L_i gives the following solution

$$L = \mu_0 R \left[\ln \left(\frac{8R}{r} \right) - 1,75 \right]. \quad (16)$$

B. Formulas for Mutual Inductances

In contrast to the determination of the self-inductance, a distinction is made here between two cases. The first case considers the coupling of two coils that lie in different planes, Fig. 3 (a). The first case thus considers the coupling between transmitter and receiver side. The second case analyzes the

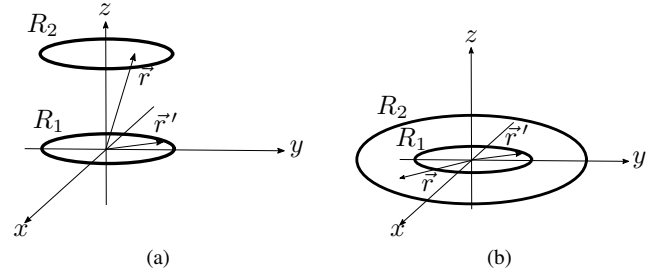


Figure 3: Two coupled loops at (a) different level (b) the same level

coupling between two coils that are in the same plane, Fig. 3 (b). In both cases the exact solution is given by

$$M = \mu_0 \sqrt{R_1 R_2} \left\{ \left(\frac{2}{k} - k \right) K(k) - \frac{2}{k} E(k) \right\} \quad (17)$$

with

$$k = \frac{2\sqrt{R_1 R_2}}{\sqrt{(R_1 + R_2)^2 + z^2}}. \quad (18)$$

However, the evaluation of elliptic integrals is difficult, as already mentioned in the previous section. Therefore, alternative approximation formulas for different applications are now presented.

1) *Mutual Inductances for loops at different levels:* When determining mutual inductances according to Fig. 3 (a), an analytical evaluation via Biot-Savart's law is often found in the literature. In the one-dimensional case it is

$$\vec{B} = \frac{\mu_0}{4\pi} \int_C I(\vec{r}') \frac{d\vec{s}' \times (\vec{r} - \vec{r}')}{|\vec{r} - \vec{r}'|^3}. \quad (19)$$

Misunderstandings can arise if it is not known which restrictions apply here. A simple analytical evaluation of the integral is only possible under the restriction that the magnetic flux density \vec{B} only depends on z , i.e. $\vec{B} = B_z \vec{e}_z$. If the radial dependence is also taken into account, elliptic integrals must again be evaluated. For the simplified case the solution is

$$\begin{aligned} \vec{B} &= \frac{\mu_0 I}{4\pi} \int_0^{2\pi} \frac{d\phi' (zR_1 \cos \phi' \vec{e}_x + zR_1 \sin \phi' \vec{e}_y + R_1^2 \vec{e}_z)}{(R_1^2 + z^2)^{3/2}} \\ \Rightarrow \vec{B} &= \frac{\mu_0 \pi I}{2} \frac{R_1^2}{(R_1^2 + z^2)^{3/2}}. \end{aligned}$$

Evaluating the flux through the second loop gives a final expression for M

$$M = \frac{\Phi}{I} = \frac{\iint \vec{B} d\vec{a}}{I} \quad (20)$$

$$\Rightarrow M = \frac{\mu_0 \pi}{2} \frac{R_1^2 R_2^2}{(R_1^2 + z^2)^{3/2}}. \quad (21)$$

As will be shown later, due to the neglect of the radial dependence, this solution is accurate for very large distances, only. Since at large distances the flux density is approximately

constant at the second loop, it does not further depend on the radius.

A simplified solution for mutual inductances at large distances can also be determined from the Neumann formula. This can be done by an expansion of the integrand and taking into account that the distance is large. Therefore, the following solution is found [9]

$$M = \frac{\mu_0\pi}{2} \frac{R_1^2 R_2^2}{(R_1^2 + R_2^2 + z^2)^{3/2}} \left[1 + \frac{15}{32}\gamma^2 + \frac{315}{1024}\gamma^4 \right] \quad (22)$$

with

$$\gamma = \frac{2R_1 R_2}{R_1^2 + R_2^2 + z^2}. \quad (23)$$

For large distances ($z \gg R_{\min}$), the contributions due to γ^2 and γ^4 are neglectable. In this case, both equations (21) and (22) are identical except for the radius of the second coil in the denominator of equation (22). As the simulation results will show, equation (22) thus converges faster against the simulated curve than (21).

The approximation formulas presented so far are well applicable for large distances between the coils, since here a radial dependence of the flux density is neglectable. However, the smaller the distance becomes the more the flux depends on the radial component. For this case, Maxwell presented a series formula in [7] that provides very exact results if the distance between the two loops is small

$$M = \mu_0 R_1 \ln \left(\frac{8R_1}{r} \right) \Lambda + \mu_0 R_1 \Omega \quad (24)$$

with

$$\Lambda = 1 + \frac{c}{2R_1} + \frac{c^2 + 3z^2}{16R_1^2} - \frac{c^3 + 3cz^2}{32R_1^3} + \dots \quad (25)$$

$$\Omega = -2 - \frac{c}{2R_1} + \frac{3c^2 - z^2}{16R_1^2} - \frac{c^3 - 6cz^2}{48R_1^3} + \dots \quad (26)$$

$$c = R_2 - R_1 \quad , \quad R_2 > R_1 \quad (27)$$

and

$$r = \sqrt{c^2 + z^2}. \quad (28)$$

The series formula is derived from the self-inductance of a loop from equation (11). This relation can be seen by considering the case that $R_1 = R_2$ and $z \rightarrow 0$. Thus, only the first term of Λ and Ω will contribute and equation (11) is found again. The accuracy and the range of validity of the formula can be extended as desired by adding more terms. More terms for Λ and Ω can be found in [4].

2) *Mutual Inductances for loops in the same level:* For the determination of the mutual inductance of two loops lying in the same plane, a neglect of the radial component of the flux density is in general no longer valid. In this case the flux density is primarily dependent on ϱ while a dependence on z no longer exists. The validity range of the solutions explained here is in general strongly limited. First, a solution with Biot-Savart's law is being determined. For this purpose, the mutual

inductance at the origin, i.e. $z = 0$, can be evaluated with the already known equation (21). Consequently, the mutual inductance is

$$M = \frac{\mu_0\pi}{2} \frac{R_2^2}{R_1} \quad , \quad R_1 > R_2 \quad (29)$$

or

$$M = \frac{\mu_0\pi}{2} \frac{R_1^2}{R_2} \quad , \quad R_1 < R_2. \quad (30)$$

When applying this formula it is important to note that useful results can only be expected if one of the two loops is significantly larger. In this case it can be assumed that the flux density caused by the larger loop is approximately constant within the smaller loop at the origin. Thus, to a first approximation the radial dependence of the flux density is negligible. However, this is only appropriate for radii of strongly different sizes.

The same approximation just mentioned can also be applied to equation (22). Here as well, useful values can only be expected if the radii are of different size. Thus, the approximation for (22) is

$$M = \frac{\mu_0\pi}{2} \frac{R_1^2 R_2^2}{(R_1^2 + R_2^2)^{3/2}} \left[1 + \frac{15}{32}\gamma^2 + \frac{315}{1024}\gamma^4 \right] \quad (31)$$

with

$$\gamma = \frac{2R_1 R_2}{R_1^2 + R_2^2}. \quad (32)$$

The series formula by Maxwell can be used here as well. In this case, even a simplified form can be given, since the dependence on the z -component does not longer exist. Thus, Λ and Ω are given by

$$\Lambda = 1 + \frac{c}{2R_1} + \frac{c^2}{16R_1^2} - \frac{c^3}{32R_1^3} + \dots \quad (33)$$

$$\Omega = -2 - \frac{c}{2R_1} + \frac{3c^2}{16R_1^2} - \frac{c^3}{48R_1^3} + \dots \quad (34)$$

with

$$r = c. \quad (35)$$

As already noted, the series formula is derived from the self-inductance according to equation (11). Therefore, very accurate solutions are given when the radii of the loops are almost equal.

III. VERIFICATION

A. Self-Inductance

The formulas for the determination of the self-inductance of a coaxial loop are now compared with the results of a field simulation. As an example, a wire with a radius of $r = 1$ mm was modelled, while the radius R of the loop has been stepwise increased up to 100 mm. Fig. 4 shows the plots for the selected geometry. The solutions with the inner inductance L_i are practically identical to the simulation results. The relative error δ_{rel} in Fig. 5 shows that the error is far below 1%, as long as the ratio R/r is greater than 10. The error without the inner inductance is much higher but decreases with increasing ratio. At small ratios, the error is pretty high

in both cases, since here, the approximation by a line integral becomes no longer valid. The finite thickness of the wire must then be taken into account and the Neumann formula must be extended to a double volume integral over the current density. The exact solution with the elliptic integrals and the formula derived from it are identical. Therefore, an evaluation of elliptic integrals would not be necessary in this case to achieve reliable results. Overall, equation (16) can be considered as an exact solution, if the geometrical boundary conditions are satisfied.

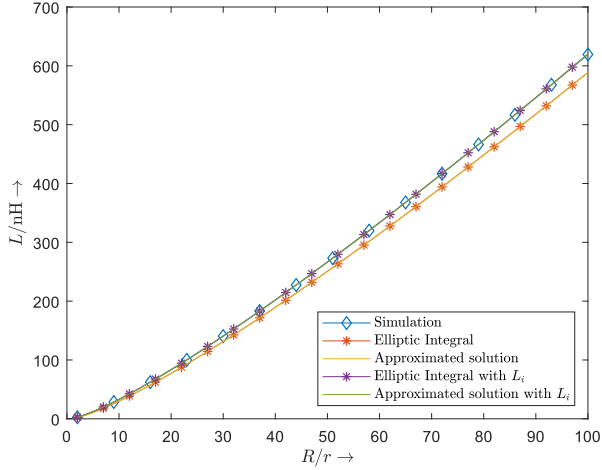


Figure 4: Comparison of the simulation results and the formulas with and without L_i

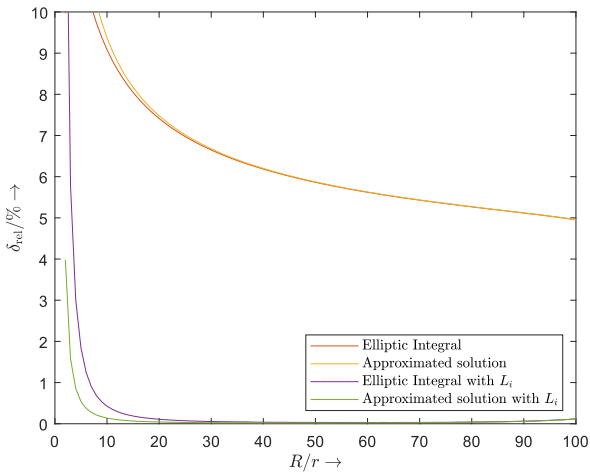


Figure 5: Comparison of the relative errors

B. Mutual Inductance

First, the dependence of the mutual inductance on the distance is analyzed. Therefore, two equal loops with a radius of $R_1 = R_2 = 10$ mm are assumed while the distance z has been stepwise increased. The radius of the wire has been chosen as 0,1 mm. Fig. 6 shows the approximation formulas

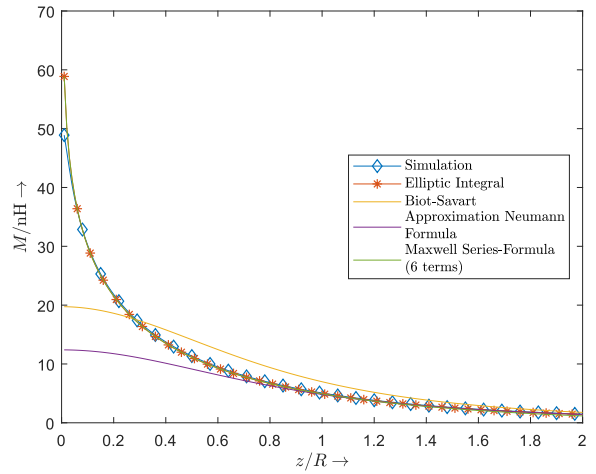


Figure 6: Mutual inductance as a function of the distance z

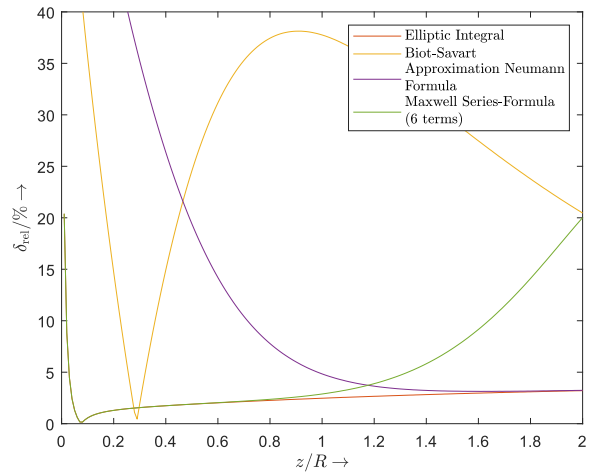


Figure 7: Relative error of mutual inductance at different levels

in comparison to the simulation results. The solution with the elliptic integrals has a nearly constant error below 5%, Fig. 7. Both equations (21) and (22) showing a decreasing error at large distances whereby (22) converges faster against the simulated curve. Maxwell's series formula shows nearly no deviations from the exact solution with elliptic integrals for small distances ($z < R$). The relative error is always below 5% here, except for the deviations at very small ratios. With increasing distance the error increases, since the series only includes a finite number of terms. Six terms are included here for the evaluation, since most of the remaining terms do not contribute because $c = 0$. If $R_1 \neq R_2$, more terms can be included for more accurate results at larger distances, whereby here, the equation derived from the Neumann formula provides reliable results.

Next, the mutual inductance of two loops that lie in the same plane are evaluated. Therefore, the radius of the smaller loop R_1 has been increased up to the larger radius $R_2 = 100$ mm.

As before, the plot with the elliptic integrals is almost identical with the simulation results, Fig. 8. The relative error is $< 1\%$, Fig. 9. Maxwell's series formula converges strongly to the simulated plot for large ratios ($R_1/R_2 > 0,6$), i.e. when R_1 approaches the size of R_2 . The relative error is then less than 5% . For small ratios, no useful results are obtained. In general, for small distances and equally large radii the first two terms of Λ and Ω are already sufficient to obtain satisfying results. However, the range of validity can be increased by adding further terms as can be seen in the error analysis. If the ratio of $R_1/R_2 < 0,45$ the radial dependence of the flux density seems to be neglectable and the approximation formulas (30) and (31) obtain useful results. The error is less than 10% in this range.

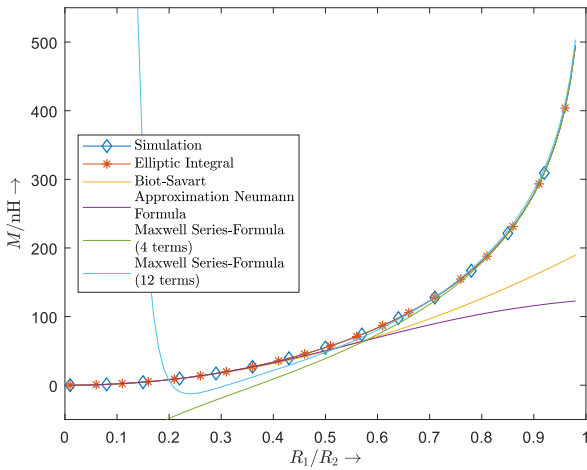


Figure 8: Mutual inductance as a function of the radius

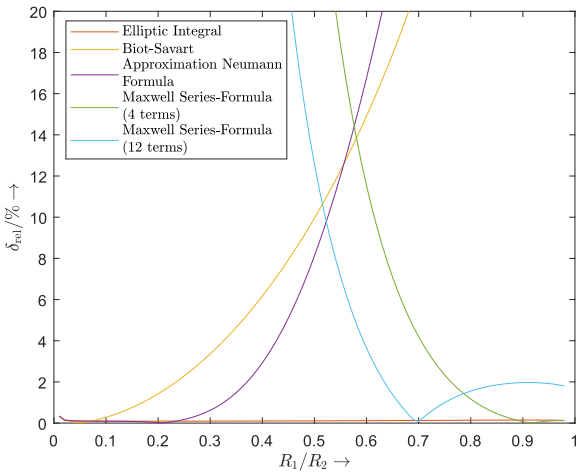


Figure 9: Relative error of mutual inductance at the same level

IV. CONCLUSION

Various formulas for the determination of mutual and self-inductances have been presented. Even for the simplest geome-

try of a circle with only one turn, an exact solution can only be given with high mathematical effort. Therefore, it is important to verify the validity of simplifications or alternative solutions in order to avoid errors. With the error analysis worked out here, it can be estimated under the given boundary conditions, in which cases reliable results can be expected from these formulas. When determining self-inductances, an evaluation of elliptic integrals is not necessary. The limit value consideration of the exact solution led to a simpler relationship, whose courses do not differ much from each other. It is important to note that all calculations here are based on the evaluation of line integrals. If such an approximation of the geometrical dimensions of the coil is not possible, i.e. $R \gg r$, major errors are to be expected.

When determining mutual inductances, a distinction can be made between two cases, if an evaluation of elliptic integrals should be avoided. In the first case, the coupling between two loops located at distance z was determined. Here, for small distances the series formula by Maxwell should be used up to the range $z \approx R_{\min}$. At larger distances the approximation of the Neumann formula is preferred, since it converges faster than the formula derived from Biot-Savart's law. Due to this range splitting, the expected error should be always below 5% . The same separation can be applied to the second case as well. However, the expected error is higher as in the first case, up to 10% .

Of course, the solutions with the elliptic integrals have the highest accuracy but also a high implementation effort. If this solution is preferred, it is recommended to choose ready-to-use algorithms for elliptic integrals to ensure that K and E converge, e.g. the function $[K,E] = \text{ellipke}(m)$ in Matlab. It must be noted that the argument m does not correspond to the module k . The relation $m = k^2$ has to be applied.

REFERENCES

- [1] Kurs, A., Karalis, A., Moffatt, R., Joannopoulos, J. D., Fisher, P. and Soljacic, M., „Wireless power transfer via strongly coupled magnetic resonances,“ *science*, 317(5834), 83-86, Jul 2007.
- [2] H. Hu and S. V. Georgakopoulos, „Multiband and Broadband Wireless Power Transfer Systems Using the Conformal Strongly Coupled Magnetic Resonance Method,“ in *IEEE Transactions on Industrial Electronics*, vol. 64, no. 5, pp. 3595-3607, May 2017.
- [3] Küpfmüller, Karl, Wolfgang Mathis, and Albrecht Reibiger. *Theoretische Elektrotechnik: Eine Einführung*. Springer-Verlag, 2013.
- [4] Rosa, Edward Bennett, and Frederick Warren Grover. *Formulas and tables for the calculation of mutual and self-inductance*. No. 169. US Government Printing Office, 1948.
- [5] ARNDT, Jörg. *Matters Computational: ideas, algorithms, source code*. Springer Science & Business Media, 2010.
- [6] Leone, Marco. *Theoretische Elektrotechnik*. Springer Fachmedien Wiesbaden, 2018.
- [7] Maxwell, James Clerk. *A treatise on electricity and magnetism*. Vol. 2. Oxford: Clarendon Press, 1873.
- [8] Henke, Heino. *Elektromagnetische Felder: Theorie und Anwendung*. Springer-Verlag, 2011.
- [9] S. Raju, R. Wu, M. Chan and C. P. Yue, „Modeling of Mutual Coupling Between Planar Inductors in Wireless Power Applications,“ in *IEEE Transactions on Power Electronics*, vol. 29, no. 1, pp. 481-490, Jan. 2014.

Chapter 4

Papers: Materials and Manufacturing Technologies

Contents

4.1	Diffuse Reflectance Spectroscopy on TNT Samples With Different Carbon Contents	110
4.2	Tufting process and machine to manufacture prototypes of a tension rods supported hydrogen pressure vessel	116
4.3	A slim SLA-3D-printed bioreactor suited for multiphoton microscopy	122
4.4	Classification of the laser powder bed fusion pollution of the optical system phenomenon in optical tomography monitoring data with an analytically developed decision tree	126
4.5	Aluminium-Iron Intermetallic Metal Matrix Composites	132
4.6	Analytical evaluation of vacuum buildup concepts for aircraft structures	135
4.7	Studies on the firing behavior of bone china and the influence of raw material components on strength and translucency	141
4.8	Influence of pore geometries on the thermal shock resistance in ceramics investigated by numerical simulation	144
4.9	Comparison of a simulation-based with an analytical calculation of the temperature field of a laser process	148
4.10	Improvement of the solid-liquid separation of biogas digestate with a starch based flocculant	151
4.11	Strain-Induced Embrittlement at Elevated Temperatures of Heat-Resistant Steel 16Mo3	156

Diffuse Reflectance Spectroscopy on TNT Samples With Different Carbon Contents

Johanna Graml

Dept. of material engineering
Nuremberg Institute of Technology
 Nuremberg, Germany
 gramljo67567@th-nuernberg.de

Abstract—The following thesis aims to develop a method for spectroscopic investigation of titanium oxide materials. It is to be used as a novel catalyst support in polymer exchange membrane fuel cells (PEM-FC). For analysis of the band gap, powders were prepared with three different preparation methods and measured with diffuse reflectance spectroscopy (DRS) using a UV/VIS/NIR spectrometer. It could be shown that band gap determination on carbon-doped titanate nanotubes is possible with DRS. For undoped titanate nanotubes, a value of 3,5 eV was measured for the band gap of the titanium dioxide. For carbon-doped titanate nanotubes, values of 3,12 to 3,35 eV could be measured, depending on the carbon content.

I. INTRODUCTION

The use of proton exchange membrane fuel cells (PEM-FC) is gaining more and more attention which is especially important for automotive industry because it is one of the interesting alternatives to combustion engines [1]. Hydrogen powered fuel cell cars would enable zero emission and reduce environmental and geopolitical impacts [1], [2]. Like combustion engines PEM fuel cells need also some sort chemical fuel as energy source [2]. They require the use of hydrogen and oxygen as chemical fuel which is converted to electrical energy and water [2], [3]. With almost 40 % the efficiency of a fuel cell is higher than gasoline (22 %) or diesel engines (25 %). Other advantages include lower noise emission as well as less abrasion and a lower maintenance interval because of the less moving mechanics [1]. The PEM fuel cell consists of a proton exchange membrane with an ion conducting electrolyte and an anodic and cathodic electrode on each side. The electrolyte separates anode and cathode and serves as barrier, through which only ions can migrate [2], [4]. The catalyst material supports the electrochemical reaction of hydrogen and oxygen [4]. The hydrogen is dissociated at the anode and oxidized by the release of electrons to protons which then diffuse through the membrane. On the cathode side, oxygen is reduced through electronic current via the load [2]. Several researchers are trying to improve the efficiency and lifetime of PEM fuel cells. According to the current state of technology, the electrodes consist of carbon black. During operation of the fuel cell carbon black materials are degraded by carbon corrosion, which is caused by two mechanisms [5]. On the one hand, this could be caused by an uneven distribution of fuel on the

anode and transfer of oxygen through the membrane, which can occur during startup and shutdown cycles of the PEM fuel cell. On the other hand, insufficient fuel supply may occur in individual cells due to ice formation if the fuel cells operate at temperatures below freezing. In both cases, the anode electrode is only partially covered with hydrogen. The hydrogen depletion drives the anode potential negative until water and carbon oxidation occurs. The corrosion of carbon black as support for the catalyst results in agglomeration of catalyst material as well as in reduction of the conductivity. This has a negative effect on lifetime and performance of the fuel cells and should be avoided. Due to the aforementioned aspects, the requirements for catalyst support materials are a high surface area, conductivity and chemical stability [5]. Since the discovery by Kasuga et al., titanate nanotubes are tested and modified for different applications [6]. Doping those titanate nanotubes with carbon [7], [8] has increased in popularity. Especially carbon-doped titanate nanotubes (C-TNTs) is a novel material that is expected to optimize the function of fuel cell electrodes due to its high surface area, conductivity and estimated stable incorporation of carbon inside the nanotube structure.

To gain a better understanding of the conduction mechanism we attempt to determine the band gap using diffuse reflectance spectroscopy (DRS). The main objective of the following thesis is to investigate the influence of carbon doping on the band gap of titanate nanotubes in order to draw conclusions on the effects of conductivity. For this purpose, a method was developed which allows to determine the band gap of high absorption samples. Three different sample preparation methods, pellets and two different types of cuvettes, were tested. Their advantages and disadvantages were worked out.

II. LITERATURE REVIEW

A. Properties of titanate and carbon-doped titanate nanotubes

Titanates are a versatile family of titanium-oxygen modifications with one or more single-valued ions. They have a layered structure, with the TiO_6 octahedra arranged in a chain in one spatial direction. The linkage of these octahedral chains ensures a two-dimensional arrangement of the basic units. Cations, protons and water molecules can be intercalated between the individual octahedral planes, promoting ion and

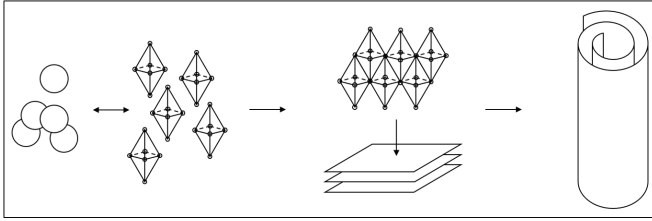


Figure 1. Schematic representation of the formation mechanism of titanate nanotubes after [9]

proton conductivity [9]. Titanate nanotubes can be synthesized via hydrothermal route first described by Kasuga, who treated TiO_2 powder for 20 hours at 110°C with a 10 molar sodium hydroxide solution [6]. The formation mechanism is still under discussion. Dissolution of TiO_2 , rearrangement to titanate nanosheets and subsequent scrolling to nanotubes as shown in Fig. 1 is widely accepted [9]. The nanotubes have an inner diameter in the range of 4-10 nm and an outer diameter of 10-25 nm. H-TNTs as well as C-TNTs can reach specific surface area up to $400 \frac{\text{m}^2}{\text{g}}$ [8], [9]. The conductivity of the C-TNTs is about $10^{-2} \frac{\text{S}}{\text{cm}}$ and exceeds the conductivity of the H-TNTs with $10^{-6} \frac{\text{S}}{\text{cm}}$ by four orders of magnitude [9]. Since their discovery, great efforts have been made to analyze the properties of TNTs and to specifically improve them by doping with various elements. The influences of doping elements such as nitrogen [10] or carbon have been investigated [7], [8]. In the case of nitrogen doping, the atoms can either occupy the oxygen sites in the lattice or cause a lattice distortion due to the corporation as interstitial nitrogen. Doping with carbon has not been studied as thoroughly. Carbon can have both negative and positive oxidation states and can be deposited on interstitial sites as a result of its atom radius. Furthermore, carbon can substitute the oxygen atoms on regular lattice sites [11].

B. Diffuse reflectance spectroscopy

To gain better understanding of the conduction mechanism we attempt to determine information about the band gap using diffuse reflectance spectroscopy (DRS). In this process, the radiation reflected from a surface in terms of its spectral composition compared to the composition of the incident primary radiation is investigated [12]. Only the diffuse part of radiation is relevant. When the beam hits the sample, it is reflected by the material in all directions with equal probabilities. Part of the radiation is absorbed and the rest is reflected. The specular reflected part of the incident beam is captured by a light trap. The diffuse reflected beam is sent to the detector. The main factor for diffuse reflection is a mat surface because a reflective surface would cause the extinction to be too high and therefore falsify the measurement results [13]. It is assumed that the angular distribution of the diffuse reflection is isotropic [12]. In addition, the sample must be thick enough so all incident light is absorbed or scattered before it reaches the back surface of the sample. A thickness

between one and three millimeters is required [14]. The measured spectra is evaluated with the theory of Kubelka and Munk.

C. Theory of Kubelka and Munk

The band gap can be determined via the Kubelka-Munk method. This theory only applies to diffuse reflection and even small amounts of regular reflection can cause deviation. This problem can be avoided by diluting the powder under investigation with a non-absorbing standard [13]. For example, magnesium oxide (MgO), barium sulfate (BaSO_4), or titanium dioxide (TiO_2) can be used [15]. The theory of Kubelka and Munk is based on Eq. (1) [16].

$$F(R) = \frac{(1 - R)^2}{2 * R} \quad (1)$$

R represents the reflectivity and $F(R)$ is proportional to the extinction coefficient. The extinction coefficient is a dimension for the attenuation of electromagnetic radiation by a medium. The attenuation occurs by absorption [17]. Eq. 1 is usually applied to strongly light-scattering materials and absorbing particles in a matrix. The basic Kubelka-Munk model assumes diffuse illumination of the sample [18]. A modified Kubelka-Munk function can be obtained by multiplying the $F(R)$ function by $h\nu$, where the corresponding coefficient n associated with the electronic transition [18].

$$(F(R) * h * \nu)^n \quad (2)$$

The coefficients h and ν represent Planck's constant with $6,626 * 10^{-34}$ Js and the frequency of light with $300 \frac{\text{m}}{\text{s}}$ dependent on the wavelength. By using this equation as a function of energy, the nature of the band gap of semiconductors can be obtained.

A distinction is made between indirectly allowed with $n=2$, indirectly forbidden with $n=3$, directly allowed with $n=\frac{1}{2}$ and directly forbidden transition with $n=\frac{3}{2}$. The use of $n=2$ for an indirectly allowed transition is suggested for titanium dioxide [18]. For graphic analysis, a straight line can be fitted on the absorption band of the spectra. The so obtained values for slope and intercept can be set into Eq. (3) to calculate the band gap energy [18].

$$E_g = \frac{1239,84 * m}{-b} \quad (3)$$

E_g is the band gap specified in electron volt (eV). The parameter m is the slope of the straight line and the parameter b corresponds to the y-axis intercept. The parameters m and b are obtained by linear fitting $y=m*x+b$ [18]. The value 1239,84 results from the multiplication of Planck's constant with the speed of light in vacuum in terms of electron volt, consequently 1 nm wavelength has an energy of 1239,84 eV.

D. TiO_2 modifications and their band gap energies

Several researchers have already investigated the electronic structure of various titanium dioxide materials [11], [14], [19], [20]. The band gap energies of titanium dioxide as well as carbon-doped titanium dioxide are influenced by the charge properties, the electronic structure, the crystalline phase, the composition as well as surface conditions [19]. For amorphous titanium dioxide, Valencia [19] determined a band gap of 3,40 eV. Aronne [20], on the other hand, referred to a band gap of 2,5 eV for the amorphous material. For crystalline titanium dioxide the modifications anatase and rutile were considered individually. Valencia [19] gave an indirect band gap of 3,23 eV for pure anatase and 3,10 eV for rutile. Jafry [21] published a band gap energy of 3,42 eV for titanium dioxide (P25). Di Valentin and Murphy [11], [14] only considered carbon-doped titanium dioxide and not titanate nanotubes. Di Valentin [11] reported for undoped titanium dioxide 4,20 eV (anatase) and 4,20 eV (rutile), respectively. Murphy [14] has analysed the band gap of carbon-doped titanium dioxide. The band gap energies here are 3,14 eV for anatase and 2,45 eV for rutile, respectively. Di Valentin [11] additionally distinguishes between interstitial and substitutional position of atoms. For anatase band gap energies of 3,4 eV for the presence of interstitial carbon and 1,9 eV for substitutional carbon was measured. Other results were obtained with 2,4 eV for both substitutionally and interstitially incorporated atoms for the carbon-doped materials of rutile [11].

At the current state, only band gap energies of undoped titanate nanotubes were reported. Yoo [22] gave band gaps between 3,3 and 3,5 eV and Mendez-Galvan [23] a value of 3,3 eV for H-TNTs. For carbon-doped titanate nanotubes band gap energies have not yet been published.

III. EXPERIMENTAL

A. Synthesis of C-TNTs and H-TNTs

1) *Carbothermal treatment of precursor powders:* Prior to hydrothermal synthesis of the carbon-doped species the TiO_2 precursor powder was modified by incorporating carbon. The precursor powder was prepared in a Carbolite HTR 11/75 rotary tube furnace using a fused silica reactor tube. 4,5 g of TiO_2 Aeroxide P25 (Evonik®) were heated under acetylene/nitrogen (1:9) gas flow. A heating rate of 68°C/min, a dwell time of 15 minutes at a temperature of 750°C and a gas flow rate of 2 l/min were set. The resulting carbon-doped precursor powder was used for synthesis of C-TNTs.

2) *Hydrothermal synthesis of C-TNTs and H-TNTs:* The synthesis steps were identical for C-TNTs and H-TNTs. For the C-TNTs, the previously prepared C-doped precursor powder was used. The synthesis of H-TNTs was performed using TiO_2 Aeroxide P25 from Evonik® as precursor powder. For the synthesis, 2,00 g of precursor powder was dispersed in 277,5 g deionized H_2O and stirred with a magnetic stir bar for two minutes at 500 rpm. Then, the suspension was treated

with ultrasonic for 15 minutes at 600 rpm with 64 W, which corresponds to 80% of constant power of the ultrasonic. In the following step, 120 g of sodium hydroxide beads (NaOH) was added to the suspension, which was transferred into a polytetrafluoroethylene (PTFE) bottle together with the magnetic stir bar, followed by two minutes of stirring. The covered bottle was connected to a silicon hose and was mounted inside a beaker filled with thermo oil. The mixture was treated for a duration of 24 hours at a constant temperature of 130°C. The temperature inside the bottle was measured by a thermocouple. While the suspension has sedimented, the supernatant were decanted and refilled with deionized H_2O . The procedure was repeated until the supernatant reached a conductivity below 50 $\mu S/cm$. For ion exchange of the intercalated Na^+ ions with protons, the supernatant was decanted and refilled to 1977,2 g with deionized H_2O and 22,8 g of 32-% hydrochloric acid was slowly pipetted. The suspension was gently stirred for 15 minutes with a magnetic stirrer. Sedimentation and decantation were repeated until the supernatant had a conductivity below 2 $\mu S/cm$. The sediment filtered by vacuum and dried at 60-80°C in a incubator for 24 h or until constant weight. Finally, the product was crushed using a mortar.

B. Diffuse reflectance spectroscopy

1) *Preparation of the samples:* C-TNTs are of a blackish color. For that reason, the samples were diluted to improve the signal to noise ratio. For dilution, TiO_2 Aeroxide P25 was used. Different concentrations of C-TNTs 750, 1 wt.-%, 5 wt.-%, 10 wt.-% and 25 wt.-% C-TNTs respectively, were prepared. The materials are mixed to a homogeneous powder in the SpeedMixer DAC 150.1 FVZ-K from FlackTek Inc. To ensure better homogenization, 20 ceramic grinding beads of type ZY-S 3,0 - 3,3 mm from Sigmund Lindner GmbH were added. The powder was mixed for 30 seconds at 1500 rpm with three repetitions. After the mixing process, the ceramic balls were removed. Three different preparation methods were used. On one hand pellets were pressed, on the other hand two different cuvettes were applied, a powder and a liquid one. Powder cuvettes slightly compress the powder. Liquid cuvettes only had to be filled with the powder and could be measured without compression. Pellets were pressed with 2 g of powder mixture in a matrix with a diameter of 32 mm and put into manual press from Fluxana GmbH & Co. KG and compacted with a pressure of 30 MPa. After that the sample was fixed on a microscope slide and inserted into the sample holder. By means of the steady decrease of the dilution medium, it could be determined, that undiluted samples are also measurable. Therefore, the pure powders were measured. For this, only powder cuvettes were used. No special sample preparation was necessary. In Table I all samples are listed.

2) *Measurement:* For measurements UV/VIS/NIR spectrometer Lambda 19 by Perkin Elmer was used with an integrating sphere with a diameter of 60 mm. A light trap was attached to cut off specular reflection to measure

Table I
SAMPLES

Sample	Dilution	Standard	Preparation
C-TNTs 750	1 wt.-%	TiO ₂	Pellets
C-TNTs 750	1 wt.-%	TiO ₂	Powder cuvette
C-TNTs 750	1 wt.-%	TiO ₂	Liquid cuvette
C-TNTs 750	1 wt.-%	BaSO ₄	Pellets
C-TNTs 750	1 wt.-%	BaSO ₄	Powder cuvette
C-TNTs 750	1 wt.-%	BaSO ₄	Liquid cuvette
C-TNTs 750	5 wt.-%	TiO ₂	Pellets
C-TNTs 750	5 wt.-%	TiO ₂	Powder cuvette
C-TNTs 750	5 wt.-%	TiO ₂	Liquid cuvette
C-TNTs 750	5 wt.-%	BaSO ₄	Pellets
C-TNTs 750	5 wt.-%	BaSO ₄	Powder cuvette
C-TNTs 750	5 wt.-%	BaSO ₄	Liquid cuvette
C-TNTs 750	10 wt.-%	TiO ₂	Pellets
C-TNTs 750	10 wt.-%	TiO ₂	Powder cuvette
C-TNTs 750	10 wt.-%	TiO ₂	Liquid cuvette
C-TNTs 750	10 wt.-%	BaSO ₄	Pellets
C-TNTs 750	10 wt.-%	BaSO ₄	Powder cuvette
C-TNTs 750	10 wt.-%	BaSO ₄	Liquid cuvette
C-TNTs 750	25 wt.-%	TiO ₂	Powder cuvette
C-TNTs 750	25 wt.-%	TiO ₂	Liquid cuvette
C-TNTs 750	25 wt.-%	BaSO ₄	Powder cuvette
C-TNTs 750	25 wt.-%	BaSO ₄	Liquid cuvette
C-TNTs 750	70 wt.-%	BaSO ₄	Powder cuvette
C-TNTs 750	80 wt.-%	BaSO ₄	Powder cuvette
H-TNTs	-	BaSO ₄	Powder cuvette
C-TNTs 725	-	BaSO ₄	Powder cuvette
C-TNTs 750	-	BaSO ₄	Powder cuvette
C-TNTs 775	-	BaSO ₄	Powder cuvette
C-TNTs 800	-	BaSO ₄	Powder cuvette

only diffuse reflection. Here the wavelength λ was plotted on the x-axis and the function of reflection $F(R)$ on the y-axis. Sample and standard were fixed to the two corresponding slots. On the standard slot P25 as well as barium sulfate were tested. The spectra are recorded with scan speed 120 nm/min and a slit width of 4 nm. Detector change is at 860,8 nm and lamp change at 319,2 nm. All measurements were recorded in a range from 200-2500 nm. The fitting of the straight line for evaluation of the band gap energy was done with the Gnuplot software. The straight line is plotted together with the associated spectrum. The band gap energy is estimated from the intersection with the x-axis.

IV. RESULTS AND DISCUSSION

A. Diluted samples

1) *Reference materials:* First step was the investigation of the influence of the standard. For the comparison between Aeroxide TiO₂ P25 and BaSO₄, an amount of 10 wt.-% C-TNTs 750 was selected because the carbon influence can be best seen here. Fig. 2 and 3 shows spectra using different

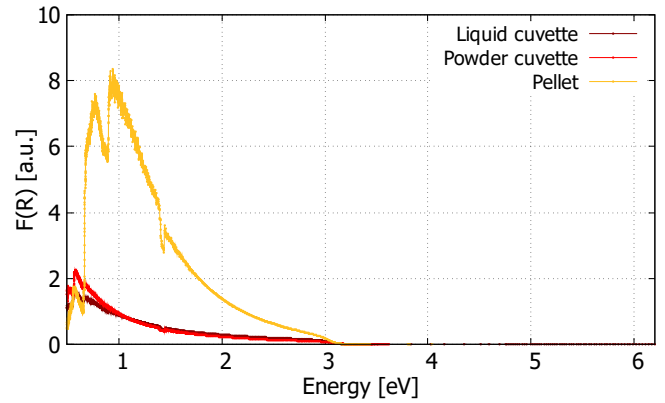


Figure 2. 10% C-TNTs 750 with reference titanium dioxide

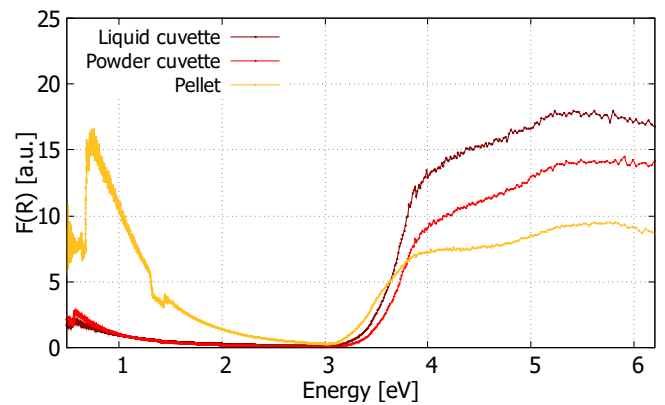


Figure 3. 10% C-TNTs 750 with reference barium sulfate

standards and sample preparation methods. It can be seen that there is almost no difference in the spectra between the types of cuvettes. In contrast, the pellets showed a much more pronounced band in the low energy range. Furthermore, it is clear that the increase in $F(R)$ in the high energy range is not present for all preparation types when titanium dioxide is used as standard. A comparison of the two standards shows that the slope in the higher energy range results from the titanium dioxide. This curve is not visible in the measurements with the titanium dioxide standard because these reflectance values have been factored out by the standard. In summary two conclusions can be taken from this experiment. On the one hand, the measured peak in the high energy range fits the documented band gap energies of the titanium oxide. On the other hand, the measurements show that the peak in the low energy range results from carbon. This is also confirmed by the fact that the peak is visible with both standards.

2) *Sample preparation:* The next step was to investigate the sample preparations. Both standard and samples were prepared in the same way. Fig. 2 shows the three methods of 10% C-TNTs 750 referenced against Aeroxide TiO₂ P25. It was discovered that with increasing C-TNT content, it was no longer possible to press pellets, because the compression during the pressing process has significantly darkened the

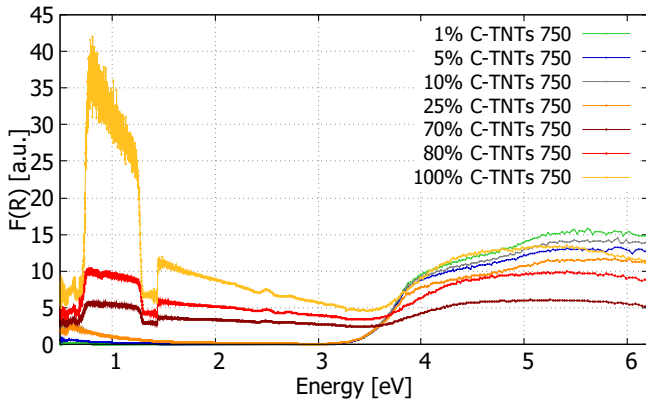


Figure 4. Different dilutions of C-TNTs 750 prepared in powder cuvettes. Standard: BaSO₄

color of the sample, which made reflectance measurement impossible. Fig. 3 shows the same samples measured against standard BaSO₄. It can be seen that the method with the highest compression of the powder results in the lowest reflectance in the high energy range. The other way around the most compressed powder shows the highest reflectance in the low energy range. Additionally a higher content of C-TNTs 750 results in a increased peak in the low energy range. Fig. 2 shows that the peak in the low energy range is most pronounced with the pellet method, followed by the powder cuvette. During sample preparation, it was found that the powder mixture became darker due to compression during the pressing process. Because the powder cuvette also uses a slight compression on the sample by screwing the stamp into the holder, it is obvious that this also leads to darkening of the sample. With the liquid cuvette, the powder is merely filled in, but the sample is not additionally compressed. Fig. 3 shows that the plateau in the high energy range decreases with increasing degree of compression. As already mentioned in the previous section, this peak results from the titanium dioxide. Because the compression makes the sample appear optically darker, it is clear that the influence of the white powder titanium dioxide is reduced and therefore also the plateau becomes less pronounced. The plateau could also be caused by the compression resulting in a smoother surface. This could cause more specular reflection.

Already during sample preparation, it became clear that the powder cuvettes offers several advantages. On the one hand, very small amount of sample material is required, on the other hand, the purity of the integration sphere can be ensured, because unlike the pellet, no pollution of the measuring gap by powder is possible. Therefore, the powder cuvette was selected as the best measurement method. Because the influence of carbon on the band gap structure of TiO₂ is of interest in this investigation, measuring against barium sulfate as a standard was chosen. In the following figure the graphs of different levels of dilution are shown (see Fig. 4). Tab. II shows the band gap energies in the high and low energy range from the

Table II
BAND GAP ENERGIES OF DILUTED C-TNTs 750

C-TNT 750 content [wt.-%]	1. band gap energy [eV]	2. band gap energy [eV]
1	-	3,52
5	-	3,50
10	0,55	3,49
25	0,55	3,47
70	0,64	3,17
80	0,66	3,25
100	0,70	3,11

Table III
CARBON CONTENT AND BAND GAP ENERGIES OF PURE TNTs

TNT sample	Carbon content [wt.-%]	1. band gap energy [eV]	2. band gap energy [eV]
H-TNTs	-	-	3,50
C-TNTs 725	4,88	0,69	3,35
C-TNTs 750	6,44	0,70	3,31
C-TNTs 775	7,92	0,70	3,28
C-TNTs 800	8,60	0,71	3,12

highest dilution with 1% to the pure sample of 100% C-TNTs 750. For the samples with 1% and 5% C-TNT content, the peak in the low energy range is too small to be fitted with a tangent over the linear area. Taking a look on the values it became clear, that both band gap energies change with the degree of dilution. Additionally, it was visible that it is possible to measure pure C-TNT powder. To obtain information about the pure material, following all C-TNT samples and the white colored H-TNTs were measured without any dilution.

B. Pure samples

For pure samples, four different C-TNTs and undoped H-TNTs were investigated. The carbon contents of the respective TNTs are shown in Tab. III. The different contents result from the production process of the precursor powder. The carbon content increases with a higher treatment temperature. If the band gaps of the diluted samples (Tab. II) are compared with the pure samples (Tab. III), a difference in the band gap values can be seen. For the first band gap, the value decreases with increasing dilution. In contrast, the value of the second band gap increases with increasing dilution. Because P25 is added as dilution material, the proportion of carbon in the structure changes, which results in a change of the band gap. When looking at the spectra, two areas are of interest. First, a peak in the range of 0,5 to 1,5 eV can be seen in all C-TNT samples. In contrast, this peak cannot be seen in the spectra of H-TNTs, which indicates that this peak is caused by carbon.

Fig. 5 shows the H-TNTs and C-TNT 725 samples plotted individually as example. The other C-TNT samples can be plotted simultaneously like the C-TNT 725 graph. By taking a look at Tab. III, it can be seen that the 1. band gap with a slope of only 0,02 eV has no significant dependence. It can

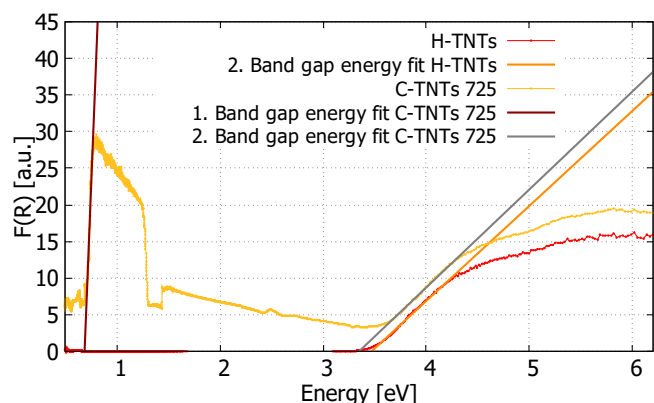


Figure 5. Low energy fit C-TNTs 725

be assumed that even with a higher carbon content in the C-TNT powder, there is no significant change in the band gap. Second, for all TNT samples, a 2. band gap located between 3,10 and 3,50 eV is visible, which is caused by the titanium/oxygen back bone. The band gap energy is determined to identify whether the carbon influences the band gap of titanium dioxide. It indicates that the band gap energy of the titanium/oxygen back bone decreases with increasing carbon content. As more and more carbon is inserted, the structure is probably also changing more and more. It can be assumed that a distortion of the lattice has a significant influence on the band gap.

V. SUMMARY AND OUTLOOK

In summary, the blackish colored C-TNT powders as well as the H-TNTs can be measured with a suitable measuring method via UV/VIS spectrometry. The samples are preferably prepared by using a powder cuvette. The use of BaSO₄ as standard material has proven to be the most useful for this type of application. It was found that the carbon in the C-TNTs influences the band gap of the titanium dioxide to a certain extent. The more carbon is in the sample, the smaller the band gap energy becomes. The values for the C-TNTs are located in a range from 3,12 to 3,35 eV. For the undoped nanotubes, a value of 3,50 eV was determined. It is important to mention that the band gaps were determined based on F(R). The type of the band gap transition has not yet been considered here. Further evaluations of the spectra with taking the type of transition into account are necessary. This may cause the bandgap values to change slightly. Also the band gaps of the precursor powders have to be investigated in order to be able to evaluate the influence of the carbothermal treatment.

REFERENCES

- [1] M. Weider, A. Metzner, and S. Rammler, "Das brennstoffzellen-rennen: Aktivitäten und strategien bezüglich wasserstoff und brennstoffzelle in der automobilindustrie," 2004.
- [2] S. M. Haile, "Fuel cell materials and components," *Acta Materialia*, vol. 51, no. 19, pp. 5981–6000, 2003.
- [3] C. Frahm, "Brennstoffzellentechnologie: Was dem wunderantrieb wasserstoff zum durchbruch fehlt," 2020.
- [4] P. Zihrl, *Untersuchungen zur Aktivität und Stabilität von Membran-Elektroden-Einheiten für PEM-Brennstoffzellen*. Dissertation, Technische Universität München, München, 22.08.2018.
- [5] J. Wu, X. Z. Yuan, J. J. Martin, H. Wang, J. Zhang, J. Shen, S. Wu, and W. Merida, "A review of pem fuel cell durability: Degradation mechanisms and mitigation strategies," *Journal of Power Sources*, vol. 184, no. 1, pp. 104–119, 2008.
- [6] T. Kasuga, M. Hiramatsu, A. Hoson, T. Sekino, and K. Niihara, "Formation of titanium oxide nanotube," *American Chemical Society*, no. 14, pp. 3160–3263, 1998.
- [7] M. Abdullah, S. K. Kamarudin, and L. K. Shyuan, "TiO₂ nanotube-carbon (tnt-c) as support for pt-based catalyst for high methanol oxidation reaction in direct methanol fuel cell," *Nanoscale research letters*, vol. 11, no. 1, p. 553, 2016.
- [8] U. Helbig, K. Herbst, J. Roudenko, J. Helbig, B. Barton, and U. Kolb, "Carbon-doped titania as a precursor for titanate nanotubes," *Journal of Materials Research*, vol. 33, no. 9, pp. 1288–1300, 2018.
- [9] K. Herbst, *Elektrisch leitfähige Ti-O-C-Nanotubes mit hoher spezifischer Oberfläche*. Dissertation, Friedrich-Alexander-Universität Erlangen-Nürnberg, Erlangen, 2015.
- [10] Y.-P. Peng, S.-L. Lo, H.-H. Ou, and S.-W. Lai, "Microwave-assisted hydrothermal synthesis of n-doped titanate nanotubes for visible-light-responsive photocatalysis," *Journal of hazardous materials*, vol. 183, no. 1-3, pp. 754–758, 2010.
- [11] C. Di Valentin, G. Pacchioni, and A. Selloni, "Theory of carbon doping of titanium dioxide," *Chemistry of Materials*, vol. 17, no. 26, pp. 6656–6665, 2005.
- [12] G. Kortüm, *Reflexionsspektroskopie: Grundlagen, Methodik, Anwendungen*. Springer-Verlag Berlin Heidelberg GmbH, 1969.
- [13] G. Kortüm and G. Schreyer, "Über die gültigkeit der kubelka-munkfunktion für reflexionsspektren an pulvern," *Zeitschrift für Naturforschung*, pp. 1018–1022, 10. Oktober 1956.
- [14] A. Murphy, "Band-gap determination from diffuse reflectance measurements of semiconductor films, and application to photoelectrochemical water-splitting," *Solar Energy Materials and Solar Cells*, no. 14, pp. 1326–1337, 2007.
- [15] H.-H. Perkampus, *UV-VIS-Spektroskopie und ihre Anwendungen*, vol. 21 of *Anleitungen für die chemische Laboratoriumspraxis*. Berlin and Heidelberg: Springer, 1986.
- [16] P. Kubelka and F. Munk, "The kubelka-munk theory of reflectance: An article on optics of paint layers," *Zeitschrift für Technische Physik*, no. 12, pp. 593–601, 1931.
- [17] K. Lüders and R. O. Pohl, *Pohls Einführung in die Physik: Band 2: Elektrizitätslehre und Optik*. Berlin, Heidelberg: Springer-Verlag Berlin Heidelberg, 23., neu bearb. und mit kommentaren und aufgaben vers. aufl. ed., 2010.
- [18] R. López and R. Gómez, "Band-gap energy estimation from diffuse reflectance measurements on sol-gel and commercial tio₂: a comparative study," *Journal of Sol-Gel Science and Technology*, vol. 61, no. 1, pp. 1–7, 2012.
- [19] S. Valencia, J. M. Miran, and G. Restrepo, "Study of the bandgap of synthesized titanium dioxide nanoparticles," *The Open Materials Science Journal*, no. 4, pp. 9–14, 2010.
- [20] A. Aronne, M. Fantauzzi, C. Imparato, D. Atzei, L. de Stefano, G. D'Errico, F. Sannino, I. Rea, D. Pirozzi, B. Elsener, P. Pernice, and A. Rossi, "Electronic properties of tio₂-based materials characterized by high ti³⁺ self-doping and low recombination rate of electron-hole pairs," *RSC Advances*, vol. 7, no. 4, pp. 2373–2381, 2017.
- [21] H. R. Jafry, M. V. Liga, Q. Li, and A. R. Barron, "Simple route to enhanced photocatalytic activity of p25 titanium dioxide nanoparticles by silica addition," *Environmental science & technology*, vol. 45, no. 4, pp. 1563–1568, 2011.
- [22] J. E. Yoo, A. A. Alshehri, S. Qin, S. M. Bawaked, M. M. M. Mostafa, N. Katabathini, D. Fehn, J. Schmidt, A. Mazare, N. Denisov, G. Cha, K. Meyer, and P. Schmuki, "Establishing high photocatalytic h₂ evolution from multiwalled titanate nanotubes," *ChemCatChem*, vol. 12, no. 11, pp. 2951–2956, 2020.
- [23] M. Méndez-Galván, C. A. Celaya, O. A. Jaramillo-Quintero, J. Muñoz, G. Díaz, and H. A. Lara-García, "Tuning the band gap of m-doped titanate nanotubes (m = fe, co, ni, and cu): an experimental and theoretical study," *Nanoscale Advances*, vol. 3, no. 5, pp. 1382–1391, 2021.

Tufting process and machine to manufacture prototypes of a tension rods supported hydrogen pressure vessel

Heidacher Konstantin

Munich University of Applied Sciences

Department of Mechanical, Automotive and Aeronautical Engineering

Email: heidache@hm.edu

Abstract—This publication covers the development of a semi-automated tufting system for a tension rod supported hydrogen vessel including the manufacture of first prototypes and ideas for industrialization. It could have been shown that the tufting process with the high structural-mechanical quality of the fiber rod insertion could be verified. A first analysis show the high potential of the tufting process for industrialisation.

I. INTRODUCTION

Due to the current shift in the automotive industry from combustion engines using fossil fuels to renewable energies, in particular electric mobility with batteries or hydrogen/fuel cells, new space-optimized hydrogen composite tanks are required. [1] These tanks have a cuboid shape to install it in the battery housing of a car and tensile rods to prevent the tank from buckling of the flat surfaces. Two different manufacturing concepts for tension-braced hydrogen tanks are currently being developed at the Munich University of Applied Sciences in the scope of the BRYSON project. The integral design concept is 3D-weaving of the tank. Here, the tension rods and the woven structure are built in one single process. [2] On the other hand the discrete manufacturing concept is used. The winding of the tank wall and the insertion of the tension rods using the tufting process take place in two separate steps. In a final step, resin impregnation takes place in both designs. Basically, the development follows the requirements of DIN 17268 and SAE 2601 (700bar tank technology). In this publication the discrete manufacturing method is presented. The basis is a 3D printed core made of PLA. On top of this core the winded carbon structure is built. [3] [4] Following this, the tufting process is used to integrate the tension rods made out of aramid fibers. A prototype machine has been developed for the manufacture of these prototype tanks.

Tufting describes a textile process to insert thread loops in a structure in the textile industry e.g. carpet production. The loop is formed by the friction between the yarn and the material base. For most of the tufting machine the sewing thread that penetrates the base material is held with a tufting foot to prevent the contraction of already manufactured loops. [5] Another component of state of the art tufting machine is the looper which align the loops. Tufting machines for rug production offer more than 12 needle bars, witch results in a total number of 900 to 2300 needles with a stitching length

of 3 to 8 mm. Also hand-tuft gun are used for individual production. [6] One example for a rug tufting machine is shown in Fig.1.



Figure 1. Rug tufting machine Tuftco iTron 2.0 [7]

Tufting process is also know for composite materials for out-of-plane fiber reinforcement. [8] State-of-the-art is the tufting head from KLS, model RS 522 Fig.2.

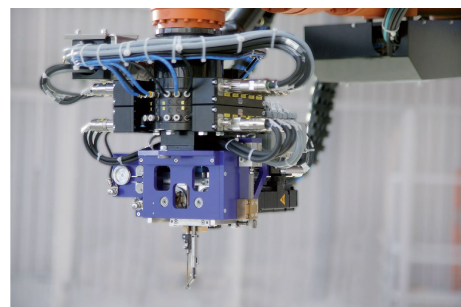


Figure 2. Tufting head KSL RS 522 for composite materials [9]

This is developed to be mounted on a standard multi-axis robot arm [10] [9] or integrated in a gantry machine to manufacture preforms with a 3D reinforcement. [11] Only one needle can be used and the roving thickness is limited to 2K filaments. The stitching length is 3-18 mm and the max.

material thickness is 35 mm for a needle size NM 250. [9] For the preform the needle insert a yarn in z-direction to fix the layers. The stitch can be free [12] or on a support material. [13] [9] The loop can be formed in the preform or outside the fiber material. [14] The process can also be used to build sandwich structures. [15] Thickness differences of the material can be specifically compensated by a variable needle stroke. [16]

In the scope of this work the prototype machine for the tufting of composite material was developed using a multi-needle system (Fig. 3). The machine is used to manufacture specimens for new hydrogen pressure vessels. Actual is a semi-automated scale model tufting machine for a vessel thickness of 33 mm. The machine works with 16 needles (size NM 250) in one needle bar including a guidance system to support the needles. Actual the machine can perform rovings with 2K Filaments. With this tufting machine, tensile rods and loop deflectors can be integrated to the pressure vessel.



Figure 3. Needle bar from HM

II. TANK PROTOTYPE

The hydrogen tank is developed on a scale model. The dimensions of the finished prototype are 91 x 91 x 31 mm. The rod spacing of 4 mm results in a pattern of 16 x 16 tension rods. [17]

A. Core

The basis of the hydrogen vessel is a 3D printed PLA core which consists of two parts (tub and cap). Grids on top and on the bottom orientate the tufting needles and provide a guidance of the needle. Support walls are inserted in the area of the grids to prevent deformation of the core during the tufting process. The core defines the tank volume and consists of one chamber.

B. Boss

An aluminium tube with a flange fused with the core serves as a tank nozzle (boss). The boss is firmly seated to the core by a material-locking joint (temp. 200 °C). The boss is also necessary as inlet for the liner integration and to perform bursting tests.

C. Winding structure

Carbon fiber bandages are wound around the core. These carbon layers take the horizontally acting forces of the tank. The carbon fibre used is: Type T700 from Toray, filament count 24 k. The stacking of the winding layers:

[0°; 0°; 90°; 90°; -45°; +45°; 90°; 90°; 0°; 0°]

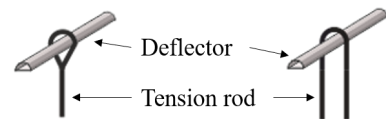
The +45° are used to seal the corners. The circumferential layers (0°, 90°) create a biaxial layer structure. The winding process is not considered further here.

D. Tension rods

The aramid fiber (Twaron type 2200 from Teijin with 2k filaments) tension rods are inserted using the tufting process in a rectangular pattern with a spacing of 4 mm and start directly at the rounding of the side walls. Two different loop shapes are formed by the tufting needles, the sewing stitch and the tufting stitch.

1) *Tufting stitch*: The needle is moved vertically to the prototype (z-direction). The needle pierces the prototype tank and is then withdrawn a bit. Now the loop tunnel is formed, and the metal deflector is inserted. During the upward movement of the needle, the fibre pulls the deflector to the tank wall. Fig. 4 a) shows the tufting stitch.

2) *Sewing stitch*: The feed in horizontal direction positions the needle bar above the next tufting row. The deflector is inserted after the feed movement and integrated firmly with the next stitch. Fig. 4 b) shows the sewing stitch.



(a) Tufting stitch (b) Sewing stitch

Figure 4. Loop shapes of the tension rods

III. TUFTING MACHINE

The tufting machine Fig. 5 is built using the following components:

A. Spindle drive

The force- and time-controlled spindle drive of a tensile testing machine (Zwick 1465) is used to realize the needle feed. Automation is time-controlled and controls the path of the needle bar. A force monitoring system is set up to control the needle bar movement. The needle is advanced via the transverse direction (z-axis). The setup is extended by further components of a tufting machine.

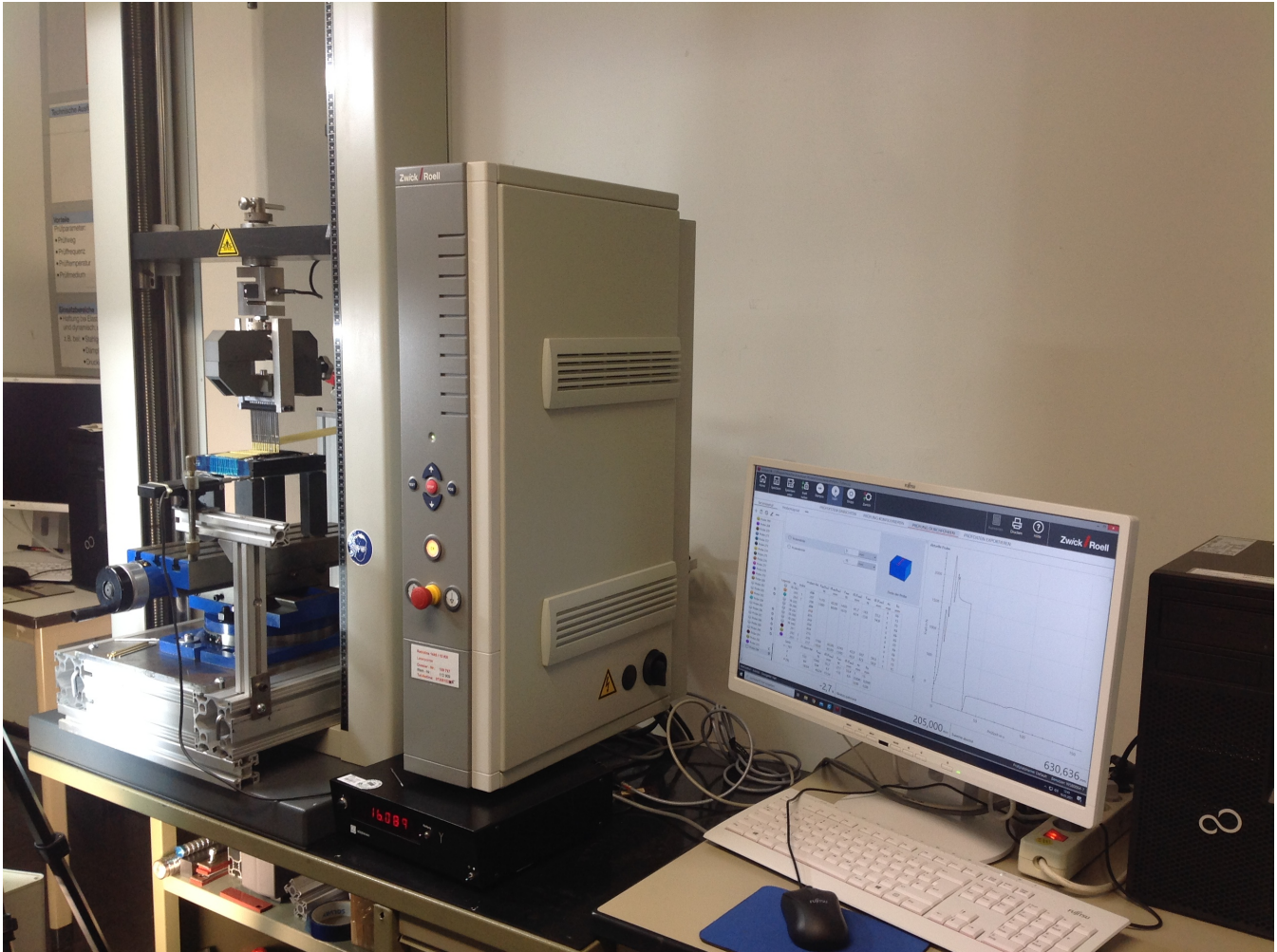


Figure 5. Tufting machine

B. Cross table with support for prototypes and measuring system

A cross table is used to realize the feed in the x - y -plane. The axes are moved with a hand wheel. The y -axis is necessary for the prototype feed. The x -axis is only needed for fine positioning of the prototype. The support device for the prototypes consists of two half's and is mounted on the cross table. The core is fixed by clamping the two halves together using screws. For a precise position of the core a glass measuring system with digital display from Heidenhain is attached.

C. Needle, needle bar

An aluminium block with holes and clamping screws represents the needle bar and is mounted to the load cell of the cross beam.

Two rails are attached to the sides of the needle bar to stabilize the needles during tufting. The needles are guided by a beam attached between the two rails. The needle currently used is from company Schmetz (type: 1000H, size: NM 250)

D. Fiber feeding system

The complete fiber feeding system is shown in Fig.6. On the left side are the creels and one fiber guidance to the fiber tension system with one clamping system. Next is the fiber tension system. In the middle is the process clamping system with the fiber guidance for the needle bar. From here the fiber runs to the needle bar on the right side of the figure. The individual components are described in more detail below:

1) *Fiber guidance*: A central component of the tufting machine is the fiber guidance. The roving is made available via a creel. From the creel, the roving passes via a fibre guidance to the rear clamping unit. From here, up to the needle bar the fiber tension system is acting. The force of the tension system can be unloaded by a clamping unit.

2) *Creel*: The roving for each needle is wound onto spools and provide a roving supply for approximately five prototypes. The 16 spools are held in place by bearing blocks and an axle.

3) *Clamps*: The clamps are made with horizontal toggle clamps, metal rails and silicone strips. A pocket is milled into the metal plates, in which a silicone strip is inserted. The metal rail is also covered with silicone. For clamping, the horizontal

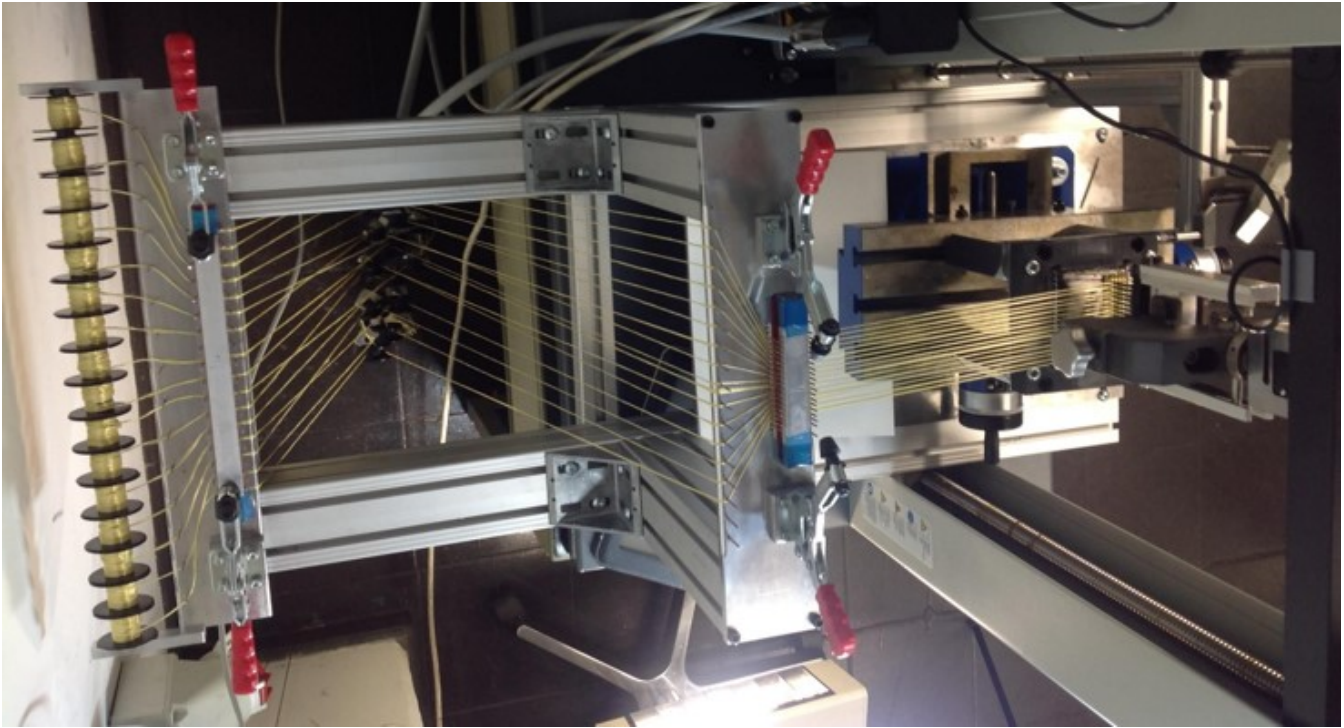


Figure 6. Fiber feeding system

toggle clamps press on the metal rail and thus squeeze the roving between the silicone strips. The silicone is needed to avoid damages of the roving. For the rear clamping unit, the roving spacing is 15 mm. For the process clamping unit, 4 mm to guide the rovings optimally to the needle bar.

4) *Fiber tensioning*: Individual fiber tensioning is implemented. Tensioning is supported with a deflection roller and an attached weight (350 g). This tension system provide a fiber reserve for one prototype.

5) *Focusing*: The correct spacing of the rovings is arranged by two focusing devices, positioned near the clamping systems (Fig. 6).

IV. TUFTING OF THE PROTOTYPE

Tension rods and deflector are insert through the tufting process using up to 16 needles.

The needle bar moves to the lower position, the needles pierce the core and the two carbon tank walls. The process clamping unit is closed to unload the roving.

The needles are pulled back by 10 mm and the loop tunnel is formed Fig. 7 a). The deflector is inserted into the tunnel. By opening the process clamping unit, the rovings are loaded again and the rovings are withdrawn, the loop tunnel closes and the deflector is pressed against the needle Fig. 7 b).

The needle bar moves to the start position. The lower deflector is pressed against the carbon tank wall.

A. Force monitoring

Based on the force monitoring, the process can be controlled. In Fig. 8 the force acting is recorded for one needle and a tank



(a) Loop tunnel (b) Closed loop with deflector

Figure 7. Loop tunnel to insert deflector

wall thickness of 2 mm. The maximum force is 115 N recorded for the penetration for the lower tank wall. Furthermore, the data can be used for dimensioning the needles for the industrial process.

V. LINER INTEGRATION AND PRESSURE TEST

Liner integration and pressure test are not part of this paper.

VI. INDUSTRIALISATION

To manufacture larger hydrogen pressure vessels there are critical technical points to be verified concerning the tufting process (e.g. needle design, looper). Overall an assessment of an economic production should be performed including production speed, out put rate, machine costs etc..

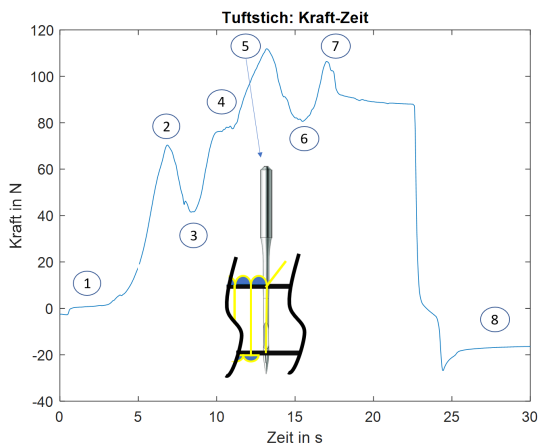


Figure 8. Force monitoring

Based on the actual status the tufting process itself and the needle design can be assessed.

A. Final aramid fiber

The stress calculation shows that a 5 k aramid roving should be used for the original vessel. The final yarn twisting of this roving has to be defined. It can have a strong influence on the needle design.

B. Needle

With an assumed tank height of 130 mm, a needle length of approximately 180 mm is required. The needle length is composed as follows:

$$\begin{aligned}
 & \text{Needle support (15 mm)} \\
 & + \text{ safety distance to the tank (5 mm)} \\
 & + \text{ installation height (130 mm)} \\
 & + \text{ max. piercing for loop formation (30 mm)} \\
 & \underline{\underline{= \text{ minimum length of the needle (180 mm)}}}
 \end{aligned}$$

The Euler buckling is critical for the stability of the needle. [18] The needle material is steel. Euler buckling case 1 (one side firmly clamped) and case 4 (one side firmly clamped, second side displaceable mounted) were examined in more detail. Relevant for further considerations is Euler buckling case 4 with a possible needle cross-section (tube) outer diameter 2.5 mm and inner diameter 1.5 mm. The finally fiber for the tension rods is a 5K filaments aramidfiber. The expected force acting on the needle comes from the experiment Section IV-A. For multidimensional force measurement with the tufting needle, the needle can be equipped with sensors. [19] As a tuft needle with a length of 180 mm, a hollow shank needle similar to utility model document DE 203 10 571 U1 is conceivable. Like the actual system, the needle must be firmly clamped on the piston and guided on the shank. With such a tank height, the distance between the grids of the core becomes larger. Therefore, it can be used a washout core for needle guidance, as well as for stabilization in the manufacturing processes. Core materials can be salt,

bismuth or Styrofoam. Salt is dissolved with water, bismuth is melted out, and Styrofoam is dissolved with acetylene. Washing out the cores is not inspected now and can cause significant difficulties because the tank is pierced with tension rods. The friction between the core and the needle still needs to be investigated.

C. Tufting machine

One aspect concerning the tufting machine is the contribution of a looper. For a better creation of the loop tunnel, it can be used a looper to perfectly open the loops. The looper is state of the art in the rug production [20]. An other aspect is the support feed, it can be done by a linear drive. [21]

VII. PROJECT RESULTS

The developed semi-automated tufting machine is essential for the quality of the insertion process of tension rods and their mechanical strength. The quality was analysed by visual inspection and microscopy: Solid integration of the tension rods into the prototypes. The fibre pre-load provides that the tension rods are stretched tautly and there is no fray along the tension rod. The loop deflector fits exceptionally with the wrapped carbon fibre layers. The prototype is shown in Fig.9. A first analysis show the high potential of the process for industrialization.

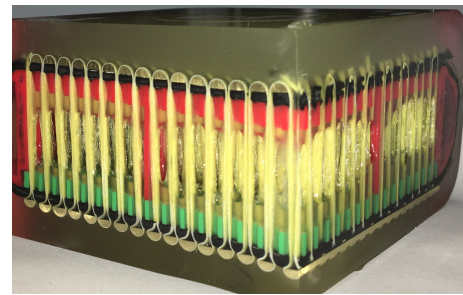


Figure 9. Prototype

Acknowledgements. The BRYSON project is funded by the German Federal Ministry for Economic Affairs and Energy.

REFERENCES

- [1] P. Jochem, *Alternative Antriebskonzepte bei sich wandelnden Mobilitätsstilen*. KIT Scientific Publishing, 2013.
- [2] A. R. Labanieh, X. Legrand, V. Koncar, and D. Soulat, "Development in the multiaxis 3d weaving technology," *Textile Research Journal*, vol. 86, no. 17, pp. 1869–1884, 2016.
- [3] A. Horoschenkoff, M. Huber, and A. Hupfeld, "Bauraumoptimierter wasserstoff tank mit innerer zugverstrebung," in *Proceedings of the Munich Symposium on Lightweight Design 2020: Tagungsband zum Münchner Leichtbauseminar 2020*. Springer Berlin Heidelberg, 2021, pp. 86–89.
- [4] M. Ruf, H.-U. Stahl, K. Kunze, S. Zaremba, A. Horoschenkoff, T. von Unwerth, and K. Drechsler, "Neue bauweisen von wasserstoffdruckbehältern für die integration in zukünftige fahrzeugarchitekturen," in *Proceedings of the Munich Symposium on Lightweight Design 2020: Tagungsband zum Münchner Leichtbauseminar 2020*. Springer Berlin Heidelberg, 2021, pp. 74–85.
- [5] T. Gries and K. Klopp, *Füge- und oberflächentechnologien für textilien: Verfahren und anwendungen*. Springer, 2007.
- [6] A. Ciechomska, "Colour in loops: Exploring colour perception in relation to lightin weaving and hand-tufting technique," 2017.

- [7] "Tuftco corp. tufting machine," <https://www.tuftco.com/tufting-2/contract-hospitalityv>, viewed on 18.04.2021. [Online]. Available: <https://www.tuftco.com/tufting-2/contract-hospitality>
- [8] C. Sickinger, H. Wilmes, L. Herbeck, A. Herrmann, B. Köhnke, and R. Wockatz, "Strukturelles nähen, eine maßnahme zur realisierung von hochleistungsfaserverbundstrukturen." *DGLR Jahrbuch 2000 Band I+II*, vol. 2, pp. 1–10, 2000.
- [9] K. K. S. GmbH, "Datasheet RS 522 Tufting head, year ="
- [10] D. Lombetti, "Tufting of complex composite structures," 2015.
- [11] L. Liu, P. Wang, X. Legrand, and D. Soulat, "Investigation of mechanical properties of tufted composites: Influence of tuft length through the thickness reinforcement," *Composite Structures*, vol. 172, pp. 221–228, 2017.
- [12] J. W. Treiber, "Performance of tufted carbin fibre/epoxy composites," 2011.
- [13] M. ÇETİN, S. SCHOFER, and T. GRIES, "Development of an inline quality measurement system for tufting process," *Marmara Fen Bilimleri Dergisi*, vol. 27, pp. 1–4.
- [14] G. Dell'Anno, J. Treiber, and I. Partridge, "Manufacturing of composite parts reinforced through-thickness by tufting," *Robotics and Computer-Integrated Manufacturing*, vol. 37, pp. 262–272, 2016.
- [15] J. W. Hartley, J. Kratz, C. Ward, and I. K. Partridge, "Effect of tufting density and loop length on the crushing behaviour of tufted sandwich specimens," *Composites Part B: Engineering*, vol. 112, pp. 49–56, 2017.
- [16] C. Cherif *et al.*, *Textile Werkstoffe für den Leichtbau*. Springer, 2011.
- [17] M. Huber, "Entwicklung eines textilen fertigungsprozesses zur herstellung zugverstreuter tankprototypen aus faserverbundwerkstoffen," 2021.
- [18] V. Läßle, "Knickung von stäben," in *Einführung in die Festigkeitslehre*. Springer, 2011, pp. 154–170.
- [19] E. Chehura, G. Dell'Anno, T. Huet, S. Staines, S. W. James, I. K. Partridge, and R. P. Tatam, "On-line monitoring of multi-component strain development in a tufting needle using optical fibre bragg grating sensors," *Smart Materials and structures*, vol. 23, no. 7, p. 075001, 2014.
- [20] E. Wood, "22. wool carpet manufacture," 2009.
- [21] "Liner drive," <https://www.igus.de/info/linearachsen-mit-antrieb>, viewed on 18.04.2021. [Online]. Available: <https://www.igus.de/info/linearachsen-mit-antrieb>

A slim stereolithography 3D-printed bioreactor suited for multiphoton microscopy

Michael Lorentschk¹, Matthias Rudolph¹, Daniel Bastl¹, Sascha Schwarz^{1,2,3}, and Stefanie Sudhop^{1,3}

¹Center for Applied Tissue Engineering and Regenerative Medicine – CANTER, Hochschule München, Lothstrasse 34, 80335, Munich, Germany

²Chair of Applied Mechanics, Department of Mechanical Engineering, Technical University of Munich Boltzmannstr. 15, 85748 Garching, Germany

³Center for NanoScience – CeNS, Schellingstraße 4, 80799 Munich, Germany

Email: lorentsc@hm.edu

Abstract — In this work, a 3D-printed bioreactor that is imageable from both sides in a regular laboratory microscopy setup is demonstrated. A biofabricated tubular vessel-like cell construct containing human mesenchymal stem cells embedded in collagen type I as extracellular matrix (ECM) is inserted into the inner chamber. Ultimately, multi-photon imaging is applied: Two-photon excited fluorescence (TPEF) for the cells and second harmonic generation (SHG) for the ECM. Subsequently, 3D reconstruction of a part of the cell construct is performed via Z-stacking of consecutive focal planes (X/Y). The bioreactor can be sealed and contacted with microfluidic tubing, which is the prerequisite for leakage-free long-term (7d+) perfusion experiments in an incubation chamber (37 °C).

I. INTRODUCTION

Biofabricated three-dimensional (3D) cell constructs that mimic only certain aspects of native tissue are suited as model systems for clinical and pharmaceutical research to partly substitute both 2D cell culture and animal testing [1].

To assess the quality of a 3D cell construct, the structure of the extracellular matrix (ECM) can be visualized via multi-photon imaging. Two-photon excited fluorescence (TPEF) and second harmonic generation (SHG) are powerful and cell-friendly multi-photon imaging techniques [2] that enable visualization in the optical focal plane only. 3D reconstruction is possible via Z-stacking of consecutive focal planes.

Stereolithography (SLA) is a laser-based photopolymerization 3D-printing process that can produce very fine features in liquid resin (methacrylated acid esters + photoinitiators) with a minimum feature size of 150 μm in X/Y and a minimum layer thickness of 25 μm in Z direction [3]. For their material properties to become hard and brittle, parts must be fully polymerized under UV light. Using SLA, microfluidic devices such as small-scale bioreactors can be produced.

II. MATERIALS AND METHODS

A. Design and fabrication of microfluidic devices

All 3D parts are designed using computer-aided design (CAD) software SolidWorks 2020 (Dassault Systèmes, FR). The design aims at the feasibility of sealed containing and contacting to perform long-term vessel perfusion experiments. Outer X/Y-dimensions of the main body match a standard

microscope slide (76 mm x 26 mm). The Z-height (3.2 mm) is kept as slim as possible while being wide enough to accommodate the 3D cell construct (1.8 mm inner diameter) fixed in a plastic holder (2.6 mm Z-height), see fig. 1A.

The main parts of the bioreactor are 3D-printed using a desktop SLA printer (Form2, Formlabs, US). Clear resin v4 (prod.nr. RS-F2-GPCL-04, Formlabs, US) is used as material. Long-term cytocompatibility of fully polymerized clear resin was shown by Moreno-Rivas et al. [4]: In a live/dead assay over 5 days, HeLa cells on clear resin performed significantly better than on other resin types (e.g. Dental LT).

After the printing process, the parts are washed in isopropyl alcohol for 5 min and post-cured with UV light (405 nm)

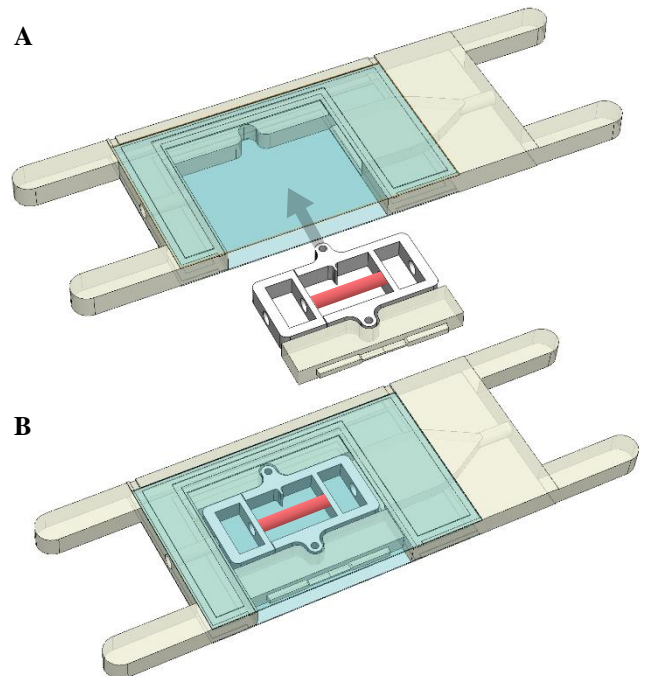


Fig. 1. CAD rendering of the SLA-3D-printed bioreactor core unit with glued cover glass slides (blue) and inserted PLA holder (white), containing a tubular vessel-like cell construct (red). (A) Assembly state. (B) Final state.

using accessory devices (Form Wash and Form Cure, Formlabs, US). Curing time for the bioreactor's main body is 15 min at 60 °C, as according to the manufacturer, complete crosslinking can only be ensured at 60 °C. Clear resin reaches 96% of its maximum elastic modulus after 15 min at 60 °C [5]. Additionally, the bioreactor is exposed to more UV radiation during the following assembly steps, which amounts to a total of 35 min.

The plastic holder (white object in fig. 1A) which is used as basis for the biofabrication of tubular cell constructs (red object in fig. 1 and central white tubular structure in fig. 3), is fabricated using fused deposition modelling (FDM) 3D-printing. The part is printed using high-temperature polylactic acid (PLA) through a 0.25 mm extrusion nozzle on a FDM printer (Ultimaker 3, Ultimaker, NL). High-temperature PLA (Volcano, FormFutura, NL) is used in this process for its improved thermostability under long-term (14d+) incubation.

A stainless-steel nozzle with an outer diameter of 1.8 mm is inserted in this PLA holder to constitute the central object that the cells will form the ECM around into a tubular shape.

B. Assembly of bioreactor core unit

24 mm x 40 mm x 170 μ m thin cover glass slides (Carl Roth, DE) are integrated in the bioreactor's design due to their optimized refraction index for microscopy. They constitute the walls of the inner chamber where the PLA holder containing the cell construct will be placed in step (E). Clear resin is used as adhesive in this assembly step. For optimal adhesive distribution, the bioreactor's design features grooves next to the cover glass slides' edges to help excessive adhesive (i.e. clear resin) to be wiped off the edges. Curing time under UV light for the gluing of the bioreactor's glass walls is two times 10 min at 60 °C (from each side). To avoid susceptibility to fracturing due to inner tensions between glass slides and gluing, heating and cooling must be conducted in a smooth manner, meaning that the non-crosslinked glue should be placed in the Form Cure device already during the heating phase (25 - 60 °C) and should be left in the device after crosslinking to cool down to room temperature slowly.

C. Cell culture

Human mesenchymal stem cells (hMSC) are used in this experiment due to their high resilience, their low contractility and the fact that this specific cell line (SCP-1) [6] is genetically modified to produce green fluorescent protein (GFP) in the cytoplasm and is therefore inherently labelled. Cells were used up to passage 8 for this experiment. As cell culture medium, Dulbecco's Modified Eagle Medium (DMEM) is supplemented with 10% fetal bovine serum (FBS) and 1% glutamine and 0.5% penicillin and 0.5% streptomycin.

D. Biofabrication of tubular cell construct

The poloxamer Pluronic F-127 (Sigma Aldrich, DE) is mixed 1:4 in deionized water to produce a thermoreversible hydrogel. With this hydrogel, a sacrificial casting form is fabricated around the PLA holder mentioned in (A) via extrusion-based bioprinting according to a standard protocol [7]. A 0.5%-solution of bovine collagen type I (prod.nr. 50105, Matrix BioScience, DE) is mixed 4:1 with a

neutralization buffer following the manufacturer's protocol [8]. Then, cells are counted, centrifuged and added to the buffer solution to obtain an effective cell concentration of 5 million cells per mL casting volume. 900 μ L of the mixture between collagen, buffer and cells is pipetted into the sacrificial casting form. For full collagen crosslinking, the cell construct is placed in 37 °C incubation for 1 h. Afterwards, 9 mL of DMEM is added and the construct is statically cultured at 37 °C and 5% CO₂ atmosphere. A complete medium change for this specific construct was performed every 7 days.

E. Final assembly of cell construct into bioreactor core unit

All bioreactor parts are sterilized in 80% EtOH for 5 min. This specific hMSC cell construct was removed from incubation at day 53 and fixated by soaking it in 4% paraformaldehyde solution for 15 min. The stainless-steel needle is removed from the PLA holder (fig. 3). Still within the PLA holder, the vessel-like construct is inserted into the bioreactor's inner chamber (fig. 1A). The whole structure is then embedded in cover medium with optimized refraction index (Eukitt, O.Kindler, DE) for multi-photon imaging.

The chamber is sealed with liquid cyanoacrylate glue that has been classified as biocompatible in contact with human osteoblasts and fibroblasts by Damate et al. [9]. However, the bioreactor's design includes a minimized contact area between glue and cell culture medium through a form-fitting lid part (shown next to the white PLA holder in fig. 1A).

F. TPEF and SHG imaging

Using TPEF, the inherent GFP in these modified hMSC can be excited and therefore made visible. GFP produces fluorescence with an intensity maximum at $\lambda = 485$ nm in response to excitation at $\lambda = 515$ nm. An excitation requires the energy levels of two photons and therefore the chance of fluorescence is primarily given within the focal plane. This limits photobleaching and toxicity to cells in the focal plane [10], making TPEF suited for live-cell imaging as well.

SHG is a non-linear and label-free imaging process that highlights non-centrosymmetric structures (particularly helices such as collagen). Unlike fluorescence, SHG does not require exogenous labels and does not apply cell damage to living cells [11]. It can be combined with TPEF in the same microscopy setup using the same laser light source [2].

The microscopy setup for SHG+TPEF imaging features a near infrared (NIR) ($\lambda = 1030$ nm) femtosecond pulsed laser source with 100 fs pulse width and a laser power of 100 mW. SHG signal is received by two detectors: one behind the specimen to receive the transmitted SHG signal ("forward") and one reverted of the specimen (epidetection) to receive the reflected SHG signal ("backward"). Channel 1 shows backward directed SHG signal, Channel 2 shows SHG signal in forward direction, Channel 3 shows TPEF signal (GFP).

A water-immersed 20x objective with a numerical aperture (NA) of 0.95 (Nikon, JP) was used in this experiment. This aims at capturing only a part of the tubular structure but at improved spatial resolution in the X/Y-plane due to the 20-fold magnification and good spatial resolution in Z-direction due to a balanced dimension of NA.

G. Coloring of imaging channels and 3D reconstruction

Raw image sequences of all three channels are separately added into stacks, using the software Fiji that is based on ImageJ 2.1 (National Institute of Health, US). An overlapping Z-area that contains relevant pixel values in all three stacks was identified and saved as substack. The maximum value of each histogram was set to 'auto' for each stack, the minimum value and contrast curve were not altered. Subsequently, the three spatially coherent substacks were color-merged: Channel 1 in blue, Channel 2 in red and Channel 3 in green. The volume of imaging voxels equals $0.36 \mu\text{m} \times 0.36 \mu\text{m} \times 5 \mu\text{m}$ in X-, Y-, and Z-direction.

With the Fiji plugin "3DViewer", a 3D reconstruction of the spatial volume part of the tubular cell construct that was captured in a certain Z-stack can be created. The resulting graphics were rendered using the following settings: [Image = Substacks-Colormerged & Display as = Volume & Color = None & Threshold = 0 & Resampling factor = 1].

The procedure is repeated for each Z-stack that is captured.

III. RESULTS

A. Fabrication and assembly process

After all fabrication and assembly steps and after disinfection with EtOH, the bioreactor was able to hold deionized water in its chamber (tested under still condition, i.e. no perfusion). Furthermore, the dimensions of the interior space were large enough to accommodate the PLA holder including the biofabricated vessel-like cell construct, which – owing to the cell-anchoring grown around the PLA holder – adds 0.3-0.6 mm to the required space in Z-direction.

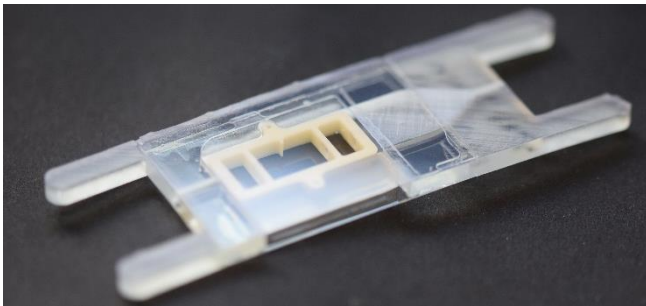


Fig. 2. Cured and assembled state of the bioreactor's core unit. The main body was SLA-3D-printed using Formlabs clear resin. Cover glass slides were glued with clear resin and cured with UV light (405 nm) as well. The PLA holder, containing the 3D cell construct in the final use case, was inserted into the inner chamber afterwards.

B. Biofabrication and cultivation of cell construct

The cell construct showed strong shrinkage, mostly along the Y-axis (indicated with bars in fig. 3). From 7.4 mm Y-height of the sacrificial casting volume (orange bar) to 2.3 mm Y-height of the final state after 53 days of incubation (red bar). The stainless-steel needle in the middle, which the vessel-like structure wraps around, represents an unalterable Y-height of 1.8 mm. Hence, when deducted from the values, the actual shrinkage of the cell construct is from 5.6 mm to 0.5 mm, which corresponds to a shrinkage factor of 91%, leaving the cell construct with 9% of its initial Y-height. This indicates an average wall thickness of $250 \mu\text{m}$.

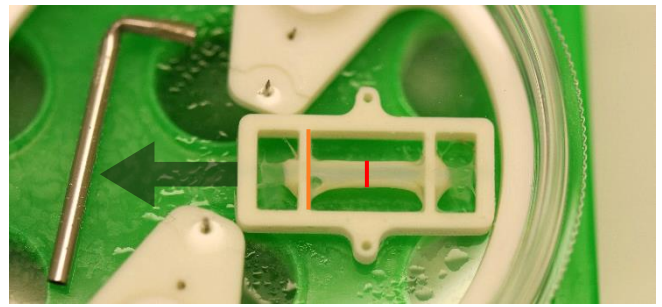


Fig. 3. Biofabricated vessel-like cell construct in PLA holder. Image shows the state after fixation with paraformaldehyde and after removal of the 1.8 mm stainless-steel needle (black arrow). Duration of static cultivation was 53 days. Along cultivation, the Y-height of the tubular cell construct (as seen from top view) decreased from 7.4 mm (orange bar) to 2.3 mm (red bar). Hence, the wall thickness around the 1.8 mm needle is $250 \mu\text{m}$ in average.

C. Multi-photon imaging and 3D reconstruction

Two spatially adjacent Z-Stacks were captured in the multi-photon (TPEF+SHG) setup and processed into 3D reconstructions, see fig. 5. The curvature of the vessel-like cell structure was successfully visualized.

The inside of the tubular construct (vessel lumen) is clearly distinct from the outside area, textually labelled in fig. 4 / 5. Overly bright spots occur due to cured resin residues on the cover glass slide surface.

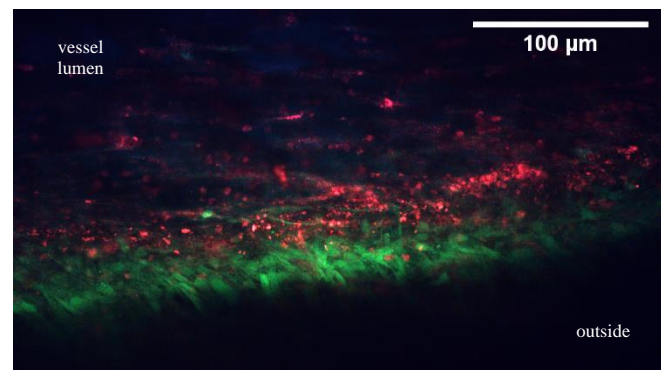


Fig. 4. Single X/Y-plane of vessel-like cell structure imaged with TPEF+SHG. Backward SHG signal (channel 1) is shown in blue, forward SHG signal (channel 2) is shown in red and GFP signal (channel 3) is shown in green. The outer vessel wall as a distinct boundary area is clearly visible.

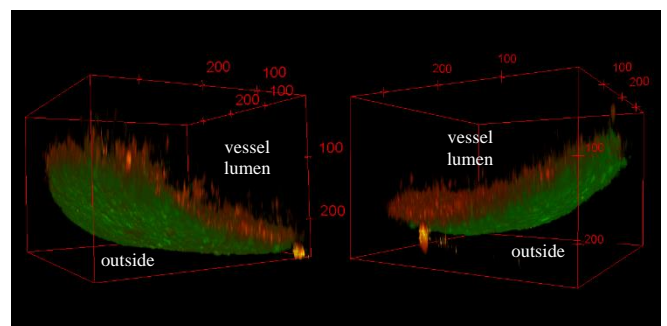


Fig. 5. 3D reconstruction of two spatially adjacent Z-stacks. The volume views are tilted towards each other for better clearness of view. Hence, the front view plane is coherent. SHG signal (channel 1 and 2) is shown in red, GFP signal (channel 3) is shown in green. Axis scales are in μm .

IV. DISCUSSION

A. 3D-printing and fabrication process

The 3D-printing process of SLA is suited for fabrication of delicate parts for microfluidics and microscopy. Using clear resin as gluing for thin glass slides works well in this design.

The bioreactor is robust in the case of exposure to moderate mechanical strain in form of pressure, whereas it is not robust if exposed to mechanical strain in form of bending and torsion along any axis.

A perfectly aligned rectilinear main body is essential for all further assembly steps of the bioreactor, especially the robust bonding of the 170 μm thin cover glass slides that have limited bending capacity (i.e. they fracture easily or otherwise produce gaps in bonding if bended after curing of the resin if the main body's surface is not completely planar). This implies high risk of leakage if not handled carefully.

B. Optical setup and light penetration depth

This work shows imaging of a fixated (i.e. dead) specimen, but TPEF+SHG are suited for live-cell imaging as well, which is going to be examined in further experiments. Prerequisite for this are genetically modified cell lines that produce and contain fluorophores (e.g. GFP) within the living cells, in order to avoid cell-toxic manual fluorescent staining.

In terms of imaging quality, using refraction-optimized cover glass slides and embedding cover medium is essential to maximize the quality and light penetration depth of TPEF and SHG signals. For live-cell perfusion experiments, an optically clear cell culture medium (without pH indicator) is an alternative to embedding cover medium (Eukitt).

In the results of this work (fig. 4), it is noticeable that the signal intensity in all three channels decreases with increasing Z-depth into the specimen. This finding aligns with multi-photon imaging literature [2, 10, 11]. The calculated wall thickness of 250 μm (chapter III.B) is not fully visible in the 3D reconstructions. Using a microscopy objective with lower NA, which implies a wider distance of possible focus points, light penetration depth could be increased. At the same time, signal intensity might be decreased in total and the focal volume would be longer in Z-direction, which would lead to lower Z-resolution of stacks.

However, as the bioreactor's design includes axisymmetric reversibility along the Y-axis (i.e. the specimen can easily be flipped), a lower NA might not be necessary. Instead, digital image stitching techniques that combine Z-stacks in the X/Y-plane and even stitching in Z-direction could be considered.

Dot-like structures in channel 1 / 2 (displayed in blue / red in fig. 4) could in a large part be autofluorescence of the cells mixed with the intended SHG signal. A validation with Hoechst 33342 staining (live-cell specimen) or DAPI (fixated specimen) staining could provide valuable insights on what structures appear in which channel (and at which λ).

C. Biocompatibility

The biocompatibility of fully cured (i.e. crosslinked) clear resin (Formlabs, US) has been shown prior to this work, but only using HeLa tumor cells, however in direct contact [4]. Biocompatibility of liquid cyanoacrylate glue has only been shown for fibroblasts and osteoblasts for indirect contact [9]. Ongoing live-cell experiments including incubated perfusion with DMEM will yield further data on the performance and live/dead quota of hMSC in collagen type I under indirect contact with cured resin, partly cured resin and cyanoacrylate.

V. CONCLUSION

It has been shown that an SLA-3D-printed bioreactor design with cover glass slides as walls can be fabricated and sealed. Furthermore, it has been shown that multi-photon imaging of a 3D cell construct located within the interior space of this bioreactor is feasible and 3D reconstruction via Z-stacking of consecutive focal planes (X/Y) can be applied, which visualizes the curvature of the vessel-like cell structure.

ACKNOWLEDGMENT

The authors thank Hauke Clausen-Schaumann for helpful discussions and Thomas Kellerer from the Multiphoton Imaging Laboratory at Hochschule München for providing TPEF and SHG images.

REFERENCES

- [1] Y. Fang and R. M. Eglén, "Three-Dimensional Cell Cultures in Drug Discovery and Development," *SLAS discovery : advancing life sciences R & D*, vol. 22, no. 5, pp. 456–472, 2017, doi: 10.1177/1087057117696795.
- [2] K. König, "Multiphoton tomography for tissue engineering," in *Optics in Tissue Engineering and Regenerative Medicine II*, San Jose, CA, 2008.
- [3] Formlabs Inc., "3D printing resolution: Understanding the results," 2018. [Online]. Available: <https://formlabs.com/blog/3d-printer-resolution>
- [4] O. Moreno-Rivas, D. Hernández-Velázquez, V. Piazza, and S. Marquez, "Rapid prototyping of microfluidic devices by SL 3D printing and their biocompatibility study for cell culturing," *Materials Today: Proceedings*, vol. 13, pp. 436–445, 2019, doi: 10.1016/j.matpr.2019.03.189.
- [5] Formlabs Inc., "Whitepaper: Post Cure Guide," 2018. [Online]. Available: <https://3d.formlabs.com/white-paper-post-curing-formlabs-resins-guide/>
- [6] W. Böcker *et al.*, "Introducing a single-cell-derived human mesenchymal stem cell line expressing hTERT after lentiviral gene transfer," *Journal of cellular and molecular medicine*, vol. 12, no. 4, pp. 1347–1359, 2008, doi: 10.1111/j.1582-4934.2008.00299.x
- [7] M. Schmid, "Optimierung und Evaluierung des generativen Biomolding Prozesses und von zellbeladenen 3D-Kollagen-Strukturen," Bachelorarbeit, Hochschule München, 2018.
- [8] Matrix Bioscience GmbH, "Preparation of Collagen Gel for Cell Culture: 2-dimensional and 3-dimensional," 2020. [Online]. Available: http://www.matrixbioscience.com/uploads/media/MATRIX_Anwendungshinweise_Kollagen_2-D_3-D_Gel_v200225.pdf
- [9] C. Andreotti Damante *et al.*, "Evaluation of Regular Market Ethyl Cyanoacrylate Cytotoxicity for Fibroblasts and Osteoblasts," *Surgical infections*, vol. 21, no. 1, pp. 29–34, 2020, doi: 10.1089/sur.2019.141.
- [10] W. Denk, J. H. Strickler, and W. W. Webb, "Two-photon laser scanning fluorescence microscopy," *Science (New York, N.Y.)*, vol. 248, no. 4951, pp. 73–76, 1990, doi: 10.1126/science.2321027.
- [11] P. J. Campagnola, A. C. Millard, M. Terasaki, P. E. Hoppe, C. J. Malone, and W. A. Mohler, "Three-Dimensional High-Resolution Second-Harmonic Generation Imaging of Endogenous Structural Proteins in Biological Tissues," *Biophysical Journal*, vol. 82, no. 1, pp. 493–508, 2002, doi: 10.1016/S0006-3495(02)75414-3

Classification of the laser powder bed fusion pollution of the optical system phenomenon in optical tomography monitoring data with an analytically developed decision tree

Joshua Meiser
 Department of Mechanical,
 Automotive and
 Aeronautical Engineering
 Munich University MUAS
 Munich, Germany
 EOS GmbH Electro Optical Systems
 Krailling, Germany
 E-mail: meiser@hm.edu or Joshua.Meiser@eos.info

Abstract—A pollution of the optical system of a laser powder bed fusion machine has the potential to influence the quality of the additive manufacturing process as well as to damage elements of the machine’s optical system. Hence this work develops an approach how to detect and identify such pollution automatically in the EOSTATE Exposure Optical Tomography (Exposure OT) monitoring data with an analytically developed decision tree.

I. INTRODUCTION

Alongside the collection and analysis of data of the laser powder bed fusion process, the monitoring system of the future should also provide a decision about the process quality and ultimately about the part quality [4]. So far, over 20 process phenomena of the laser powder bed fusion process are known. Each has its individual characteristics. Some are just normal process behavior detected by the monitoring systems, others are process instabilities caused by operator errors or by coincidence. [20] In order to provide a decision about the process quality, a process phenomenon must first be detected and classified. This classification is already possible for three relevant process phenomena [19, 21, 18]. Aim of this work is to develop the decision tree for a newly appeared phenomenon. It should be able to automatically classify the pollution of the optical system process phenomenon in the Exposure OT monitoring data.

II. MATERIALS AND METHODS

The optical system of an EOS GmbH laser powder bed fusion machine consists of multiple elements. From the laser, the light passes through the optical fiber, the collimator, the beam extender, the F-theta-lens, one or two protection glasses (which separate the optical system from the build chamber) and through the atmosphere down to the powder. It must be assumed that every pollution in the optical path of the laser beam has the potential to influence the properties of the beam

and the energy it transports. However, relevant are only those types of pollution which lead to a process instability. [17]



Figure 1. Polluted protection glass of a developed machine from the EOS GmbH (M290). Left: Normal image of the pollution of the glass. Right: Image of the pollution taken under a microscope. The protection glass separates the process chamber from the optical system. The pollution is caused by an particle emitted from the process during parameter studies for a copper alloy. [1]

A. Previous approaches to automatically classify laser powder bed fusion process phenomena

Previous approaches mainly tried to find 1:1 correlations between a part defect e.g. detected in computer tomography monitoring data and process monitoring data of the laser powder bed fusion process. While some of the approaches were unsuccessful [14], others were more successful [3] [6]. Further approaches tried to identify and recognize the patterns in the monitoring data which lead to defects in the parts. Therefore, different machine learning methods were used. One of the teams claims to be able to recognize defects such as delamination and splatter with an accuracy of 96.80%. [5] [2] Another possible approach is the simulation of the monitoring data based on the information and parameters the machine receives to build a part. The underlying machine learning

method compares the real monitoring data to the simulated monitoring data. So far, this works well for the standard process. [14]

B. Approach of this work

With the approach of this work, a process instability must first be detected and classified as a certain process phenomenon before its influence on the process and the part quality can be evaluated. Therefore, an analytically developed decision tree has proven to be a suitable method. However, it also turned out that the classification only via the Exposure OT data is not sufficient enough. Thus, if necessary, this approach uses additional available job specific data to classify a phenomenon. [19, 21, 18]

C. Decision Tree

There are various types of decision trees. In this approach, a classification tree is used. According to the classic machine learning method, a decision tree is trained by splitting up the data branch node after branch node until a stopping criteria is reached. The approach of this work deviates from the classic decision tree. [16] It is built up analytically by describing the characteristics of the perceptible and definable process phenomena on the process and on the monitoring side. [21, 16]

D. Job-specific data and data sources

The job-specific data includes all data generated by the monitoring systems as well as the information included in the task file. There are multiple different data sources which provide job specific data. Relevant for this study are the data generated by EOSPRINT, EOSTATE Base, PowderBed and Exposure OT [11].

EOSPRINT is a data preparation and process management software for additive manufacturing. In it, the building process of the job is prepared and sent to the machine as a file. That file, the task file, contains all information required by the machine to build the job, e.g. the layer thickness, the exposure parameters such as the laser power or the exposure type (inskin, downskin, upskin, contour, edges, support) as well as the orientation of the stripes and hatch vectors, etc. If required, information included in a task file can be extracted and used later to classify a deviation. [12]

EOSTATE Base monitors all sensor data of the machine by constantly checking their status, e.g. the build platform temperature or the filter pressure. If a value deviates from a predefined range, the manufacturing process is stopped. [11]

EOSTATE PowderBed takes an image of the powder bed after each layering and exposure phase. It has a built in algorithm to detect irregularities such as an incomplete powder layer, groves or cavities. [11]

Exposure OT captures the entire build space and measures

the process light emission in the near infrared range. The resulting gray value images contain information about the emitted light in this range during the exposure of a complete layer. There is one integrated gray value image created per job layer. During the exposure stage of a job layer, the camera of the system takes ten gray scale images per second with a resolution of 2000 x 2000 pixels for an EOS M290 machine. All the images taken during the exposure stage of a layer are continuously stacked and the gray value is integrated per pixel. The result is the integrated gray value image. [11, 13, 15] The Exposure OT software has built-in algorithms. 'Part Statistics' calculates the mean gray value per part layer and other statistical values. The 'simple indications detector' works similar to OpenCV's 'Simple Blob Detector' [22]. With the help of various parameters, it can be adjusted when to detect a bright or a dark spot as indication. The indication is then listed on the indication list. Additional information is added to the indication on the list. e.g. the layer height, the part identification number, the x, y position of the indication center, the indication area, etc. [11]

E. Method

Based on two use cases, the pollution of the optical system phenomenon is described and characterised on the process and on the monitoring side as well as delimited from other phenomena. As a result, the branch of the decision tree is developed.

F. Use case I, pollution of the protection glass by an ejected particle from the process

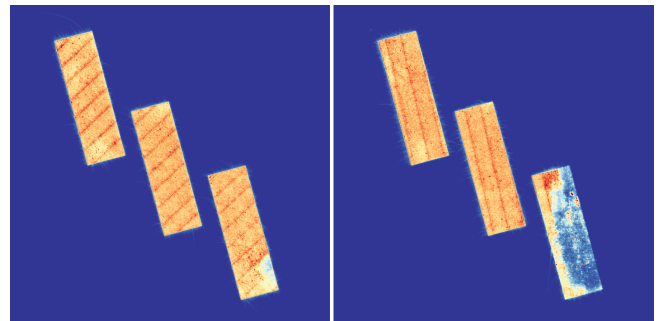


Figure 2. Recorded Exposure OT integrated gray value images of the job in which the protection glass was polluted by the ejected particle shown in figure 1. Left: Image of the layer 128. The affected area with the low gray value intensity is relatively small in the bottom right part. Later, the affected area with the low gray value intensity is relatively large in the bottom right part as can be seen in the right image. Right: Image of the layer 137. (representation: lower gray value = 0, upper gray value = 5.000, color map = red-yellow-blue).

During the build of a job, a particle was emitted from the process and landed on the protection glass of the optical system. The protection glass separates the process chamber from the optical system. As can be seen in figure 1, the protection glass is not only affected at the particle landing spot but also in its surroundings. [1]

In the Exposure OT images, the phenomenon is visible for the first time in layer 114 as an area with low gray value intensity in the bottom right part. From layer 114 to layer 133, the appearance of the phenomenon is relatively similar. However, there seems to be a dependency of the size and shape of the affected area from the stripe direction. The normally very bright areas of stripe overlaps are nearly invisible as well. (see figure 2)

The size of the affected area increases from layer 134 on. The majority of the part surface has a lower gray value intensity from layer 134 to layer 138 (=job end). The appearance of the phenomenon is again quite alike. A dependency of the affected area from the stripe exposure direction is indicated. The normally very bright areas of stripe overlaps are nearly invisible as well. Additionally, the area with the low intensity is interrupted by smaller spots with a higher gray value intensity.

Based on the evaluation of the Exposure OT data together with the micrograph of the pollution, the following theory results for describing the situation that led to the phenomenon (compare figure 1 and 2). First, a particle was ejected from the process and landed on the bottom of the protection glass. The particle landed on the glass on axis with a part area and was therefore in the path of the laser beam over multiple consecutive layers. The particle is shading the laser beam in the projected area. In this area the energy input into the part layers is reduced. That leads to the lower gray value intensity in the Exposure OT images (layer 114 – 133). Because the particle is in the path of the laser beam, the particle and the glass heat up over time. With the exposure of layer 133 or 134 a level is reached, in which the pollution spreads, the glass is tarnished, melted or similar. With that, also the surroundings of the particle are shading the laser beam in the projected part area. That area is now larger as can be seen from layer 134 on. (compare figure 2)

G. Use Case II, pollution due to a dust particle on the surface of the F-theta-lens

A pollution on the top surface of the F-theta-lens of an EOS M400-4 influenced the process behavior (see figure 3) of the entire job (446 layers). Unfortunately, there is no micrograph of the pollution available as in the first use case. According to the service engineer who changed the polluted F-theta-lens, it was a dust particle lying on the surface of the lens. Once the laser hits the particle, the laser burns it and soot is produced, which is deposited on the lens. The heat generated due to the energy input of the laser can also damage the coating of the lens. However, this is not visible on the lens. In extreme cases, also the glass can be melted and damaged. [9]

It is known that optical systems have a thermo-optical-focus shift. The focal position moves with increasing thermal load in the direction of the lens (= upwards). This is also

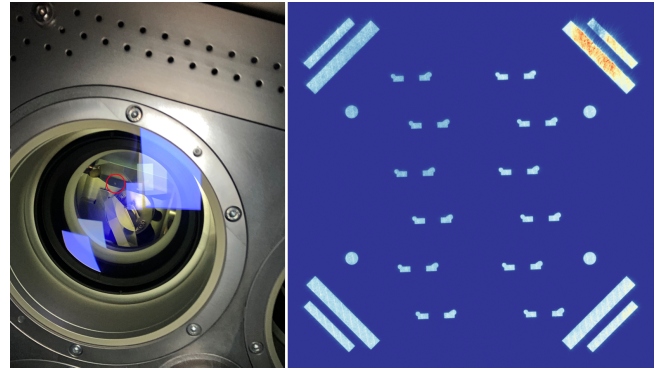


Figure 3. Left: Pollution of the F-theta-lens of an EOS M400-4 [8]. Right: Integrated Exposure OT gray value image of the layer 249 of the job with the pollution. With the exception of a smaller part area, the two parts in the top right corner show a higher gray value intensity. The job was built in an aluminium alloy. (representation: lower gray value = 0, upper gray value = 5.000, color map = red-yellow-blue).

known as z-shift. [10] As can be seen in figure 3, the two parts in the top-right corner show areas with a very unstable process behavior. There is a high density of different kinds of bright spots. Also, the smaller of the two parts shows an area with low gray value intensity (see figure 3). The affected areas stay mostly the same over the full length of the job. Similar to the first use case, the stripe orientation seems to have an influence on the characteristics of the phenomenon. The averaged image of the layers 150-250 shows a lower gray value intensity in an area of the top right part (see figure 4).

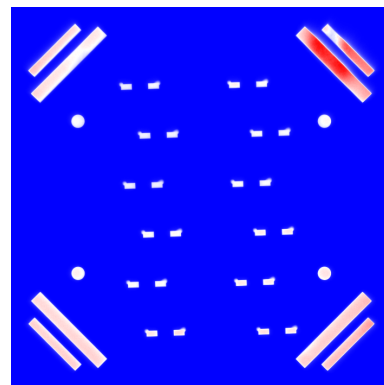


Figure 4. Averaged integrated gray value Exposure OT image of the job with the polluted F-theta-lens from layer 150-250. The part in the top right corner has an area with a low gray value intensity (representation: lower gray value = 0, upper gray value = 3018, color map = blue-white-red).

H. Pollution of the Optical System Phenomenon

Although the pollution of the protection glass and the pollution of the f-theta-lens did not lead to the exact same process behavior, they share some common characteristics. Hence for now, they are summarized as pollution of the optical system phenomenon which summarizes all process phenomena caused by a pollution of the optical system perceptible and definable in the Exposure OT data.

Derivation of the decision tree based on the characteristics of the phenomenon

As described before, a process phenomenon of the direct metal laser melting process can be classified by a decision tree using its unique characteristics [21, 18]. However, it should be mentioned that these unique characteristics can also result through comparison and differentiation from other process phenomena.

III. RESULTS

Based on the characteristics and demarcations, the branch of the decision tree to detect the polluted optical system phenomenon results (see figure 5).

Once an indication is detected by the Exposure OT analysis algorithm, the classification process is triggered (see section II-D). If a classification is not possible due to a lack of information or the current level of knowledge, it is classified as 'unknown'.

Currently only two other process phenomena are known to have a spot-like appearance and a lower gray value intensity at once [20]. The use cases show that one option to distinguish the pollution of the optical system phenomenon from the other two phenomena is by using the characteristic that the spot with lower gray value intensity occurs in multiple successive layers in the same area. Thus the process behaviour is at least as long influenced as the pollution is present or on axis with the laser beam. (see node 2 in figure 5)

There is a larger amount of process phenomena that have a spot-like appearance with a high gray value intensity. However, currently there are four other types of phenomena known that could potentially influence the process behaviour in the same area in multiple consecutive layers.

The first type are geometry-related overheatings. These can either be excluded via the geometry of the part and the exposure interval between the part layers or more clearly via the exposure strategy in the layers below. A part overheats over time if the energy input per time is higher than the energy output per time [20]. So it is at first tested whether or not there is a relevant thermal bottleneck below the affected part layer. Then it is tested whether the exposure interval is low enough for the part to overheat. (see node 9 and 10 in figure 5) Overheatings in the layers above downskins are easier to distinguish. If a part has a geometry-related overhang that is flatter than a certain number of degrees, the first layers above this area are exposed with a special exposure strategy called downskin. There is usually powder or support underneath a downskin, so the heat conduction is poor. The job-specific information can be used to check whether there is a downskin in the layers below an indication. (see node 8 in figure 5) [20, 18]

The second type is caused by ejected particles from the

process that have landed on a part area. Up to a certain level, these emitted glowing particles are part of the normal process behavior and are ejected randomly. Therefore it is unlikely that they will end up in the same area over and over again to a relevant extent over several layers. However, if the powder layer is too thick in an area, the process becomes very unstable and a large number of particles is ejected in this area. [20] It is known that the process normally levels out powder layer thickness variations automatically within a couple of layers. If the powder layer is thick, the part layer will also be a little thicker, because there is more volume to melt. The next powder layers will then be a bit thinner, till the powder layer thickness is back to normal. [7] If the sensor of the machine responsible for the powder layer thickness does not show a deviation and there are spot-like areas with a high gray value intensity over a certain number of consecutive layers, it is unlikely that the spot is caused by a too thick part layer. (see node 7 in figure 5)

The third type are spot-like phenomena with a high gray value intensity which is caused by an interaction between the laser beam and substances ejected from the process. They seem to be strongly dependent on the stripe exposure direction. The exact position is also rather coincidental. As long as the sensors responsible for the shielding gas flow do not show any deviations, it is unlikely that the effect will occur over several layers in the same area. [16] (see node 6 in figure 5)

The fourth type is caused if a part area does not receive any powder during the layering stage. The consequence is a high gray value intensity in the areas in which the powder is missing. Because powder is missing, there is less volume to melt. As soon as re-coating is back to normal, this results in a higher layer thickness, which ultimately leads to the same phenomenon as the too thick powder layer already described. The phenomenon is a little easier to percept and define in the EOSTATE PowderBed data. [21]

IV. DISCUSSION

Before a process instability can be classified as a certain process phenomenon with the developed decision tree, it must be detected by the process monitoring systems. Although it is not the focus of this work, the parameterisation of the algorithms responsible for the detection should not be disregarded.

Caused by the current nature of the tree, only unique classifications are possible. In practice, however, it is possible that various phenomena superimpose each other. A suitable solution must be found for this.

Since the tree was developed through the characterization and demarcation of known phenomena, there is a risk that there is another unknown phenomenon with very similar characteristics. For example it is not known how the pollution

of the protection glass of the Exposure OT camera looks like in the monitoring data.

The nodes 9 and 10 basically test the possibility of an overheating of the part area in which the indication is detected. This is similar to a process simulation. It is also noticeable that the classification is more likely to result from differentiation from other already known phenomena than truly from its own characteristic. Whether those are a suitable methods remains to be seen as soon as the branch of the decision tree is implemented and tested in software.

A very small data set consisting only of two use cases was used to characterize and develop the classification tree. It cannot be excluded that other types of pollution lead to process instabilities with different characteristics.

V. CONCLUSION AND OUTLOOK

Even with a small amount of data, a method can be developed to classify a process phenomenon of the laser powder bed fusion process in Exposure OT monitoring data. The better the characteristics of the phenomenon are known and described, the better it can be classified. It is also advantageous to know the characteristics of the other existing phenomena and to incorporate further job-specific information into the classification process. This for example separates this approach from a classic pattern recognition in images.

The next step is the software implementation to further test, improve and optimize the developed tree. A suitable quality criterion for the classification result must be defined and a training data set as well as a test data set must be created.

ACKNOWLEDGEMENT

This paper was created as part of the Master of Applied Research in Engineering Sciences at the Munich University of Applied Sciences and at EOS GmbH.

The author would like to thank Prof. Dr. Marc Lotz as supervising professor at Munich University of Applied Sciences, Marek Listl, Dr. Klaus Neumaier and all the others from EOS and AMCM who contributed their knowledge or support and had an open ear for the questions and ideas.

REFERENCES

- [1] AMCM GmbH. *Division Application & Innovation: Expert Interview*. Starnberg, 16. April 2021, 11-12 a.m., 2021.
- [2] Hermann Baumgartl et al. "A deep learning-based model for defect detection in laser-powder bed fusion using in-situ thermographic monitoring". In: *Progress in Additive Manufacturing* 5.3 (2020), pp. 277–285. ISSN: 2363-9512. DOI: 10.1007/s40964-019-00108-3.
- [3] Manisha Bisht et al. "Correlation of selective laser melting-melt pool events with the tensile properties of Ti-6Al-4V ELI processed by laser powder bed fusion". In: *Additive Manufacturing* 22.2 (2018), pp. 302–306. ISSN: 22148604. DOI: 10.1016/j.addma.2018.05.004.
- [4] Keith Bowers, Volker Buscher, and Ross Dentten. *Smart Infrastructure, Getting more from strategic assets*. Ed. by University of Cambridge. 2021. URL: <https://www-smartinfrasturcture.eng.cam.ac.uk/system/files/documents/the-smart-infrasturcture-paper.pdf>.
- [5] Alessandra Caggiano et al. "Machine learning-based image processing for on-line defect recognition in additive manufacturing". In: *CIRP Annals* 68.1 (2019), pp. 451–454. ISSN: 00078506. DOI: 10.1016/j.cirp.2019.03.021.
- [6] Sam Coeck et al. "Prediction of lack of fusion porosity in selective laser melting based on melt pool monitoring data". In: *Additive Manufacturing* 25 (2019), pp. 347–356. ISSN: 22148604. DOI: 10.1016/j.addma.2018.11.015.
- [7] EOS GmbH. *Division Additive Minds and Business Development: Expert Interview*. Kailling, 19. April 2021, 10-11 a.m., 2021.
- [8] EOS GmbH. *Division Application Engineering Metal: Expert Interview*. Kailling, 16. April 2021, 2-3 p.m., 2021.
- [9] EOS GmbH. *Division Central Service Operations: Expert Interview*. Kailling, 19. April 2021, 10-11 a.m., 2021.
- [10] EOS GmbH. *Division Innovation Management: Expert Interview*. Kailling, 13. April 2021, 11-12 a.m., 2021.
- [11] EOS GmbH. *EOS Monitoring & Quality Assurance: for production with Additive Manufacturing*. Ed. by EOS GmbH. online, 2021. URL: <https://www.eos.info/en/additive-manufacturing/software-3d-printing/monitoring-software>.
- [12] EOS GmbH. *EOSPRINT 2: Data Preparation & Process Management for Additive Manufacturing (AM)*. Ed. by EOS GmbH. online, 2021. URL: <https://www.eos.info/en/additive-manufacturing/software-3d-printing/data-preparation-3d-printing>.
- [13] Lukas Fuchs and Christopher Eischer. *In-process monitoring systems: for metal additive manufacturing*. Ed. by EOS GmbH. 2018.
- [14] EOS GmbH. *Division Innovation Management: Expert Interview*. EOS GmbH Krailling, 15. March 2021, 11-12 a.m., 2021.
- [15] A. Gögelein et al. "Process Monitoring of Additive Manufacturing by Using Optical Tomography". In: *14th Quantitative InfraRed Thermography Conference* (2018).
- [16] Ameet V. Joshi. *Machine learning and artificial intelligence*. Cham, Switzerland: Springer, 2020. ISBN: 9783030266219.
- [17] Marek Listl. *Specialist Data Analysis: Expert Interview*. EOS GmbH Krailling, 12. January 2021, 09-12 a.m., 2021.
- [18] Joshua Meiser. "Classification of relevant laser powder bed fusion process phenomena in optical tomography monitoring data with an analytically developed decision tree". Project Report II. Munich: Munich University of Applied Sciences, 2021.
- [19] Joshua Meiser. "Concept creation for an in-situ quality assurance system for serial additive manufacturing." Project Report I. Munich: Munich University of Applied Sciences, 2020.
- [20] Joshua Meiser. "Development of generic process situations to trigger relevant and with online process monitoring detectable process effects of the DMLS process". Bachelor Thesis. Munich: Munich University of Applied Sciences, 2020.
- [21] Joshua Meiser. "Identification of the laser powder bed fusion-incomplete powder layer phenomenon in opticaltomography monitoring data with an analyticallydeveloped decision tree". In: *Interne Forschungskonferenz an der Hochschule München - Paper zur Projektarbeit II* (2021).
- [22] opencv.org. *cv::SimpleBlobDetector Class Reference*. online, 2021. URL: https://docs.opencv.org/3.4/d0/d7a/classcv_1_1SimpleBlobDetector.html.

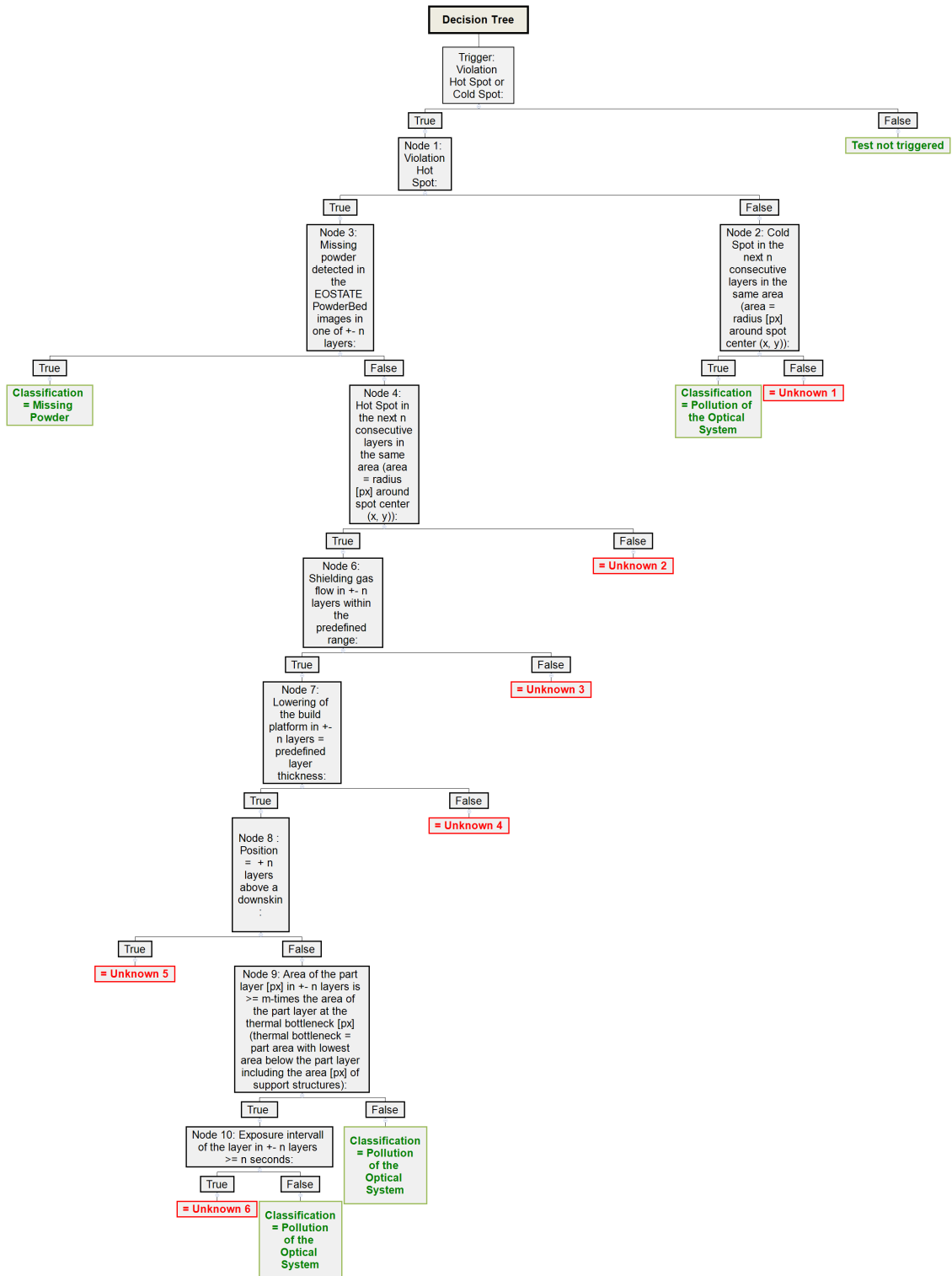


Figure 5. Analytically developed branch of the decision tree to classify the pollution of the optical system phenomenon in the Exposure OT monitoring data.

Aluminium-Iron Intermetallic Metal Matrix Composites

1st Sarah Rauchheld
Faculty of Materials Engineering
Georg Simon Ohm University of
Applied Sciences Nuremberg
 Nuremberg, Germany
 rauchheldsa74602@th-nuernberg.de

2nd Simon Reichstein
Faculty of Materials Engineering
Georg Simon Ohm University of
Applied Sciences Nuremberg
 Nuremberg, Germany
 simon.reichstein@th-nuernberg.de

Abstract—This paper describes examinations on formation kinetics of Fe-Al intermetallics in Al-Fe melt. Aim is to find solidification parameters resulting in a new Al-Fe_xAl_y metal matrix composites (MMC).

Keywords—Intermetallics, MMCs, aluminium, iron, DSC analysis, metallography

I. INTRODUCTION

Normally iron is regarded as a common impurity in aluminium because of its ability to decrease the protecting oxide layer of Al₂O₃ which develops on technically pure aluminium. The lack of an oxide layer weakens the aluminium's corrosion resistance and reduces the level of wear resistance typically offered by an Al₂O₃ layer. At first glance, the iron's negative impact on material properties does not seem to merit a detailed study of aluminium-iron intermetallic metal matrix composites. Its future technical potential, however, is high, as are its application opportunities. For example, the material could be used for components where conventional intermetallic materials would be too expensive. The advantages of combining of aluminium and iron are a lower density and correspondingly higher efficiency of the component in the installed condition. In the following paper this intermetallic material is examined regarding the development of the phase.

II. EXPERIMENTAL WORK

A. Specimen production

The material used contains 3.5 wt. % iron, about 1.0 wt. % of Ni and also 8-12 wt. % silicon in an aluminium matrix. The material for the creation of the specimen was heated in a furnace to 950 °C and held there for about 30 minutes before it was cast on a plate and then cut into pieces with a size of 2 mm x 5 mm x 2 mm. The specimens generated were then subjected to differential scanning calorimetry (DSC) analysis.

B. Specimen preparation

After the first analysis in the DSC instrument the specimen was embedded in a bakelite block using an Ecopress 100 press by meltkon. The settings were adapted to the specific parameters required for the Bakelite to melt and solidify properly. The material was heated to 190 °C, the pressure was increased to 270 bar and then these settings were held for 3:30 min. The stamp transferring the pressure was allowed to cool down until it reached a temperature of 45 °C. After the embedded specimen had been removed from the specimen

chamber and allowed to cool down to room temperature, the grinding process was started. Owing to the specimen separation method selected, a grit size of 600 could be used from the start, followed by grit sizes of 1200 and 2400 after a suitable period. As the material prepared was aluminium, no further polishing was performed, to avoid the risk of scratching the finely ground surface. After the preparation steps the microstructure was investigated under the microscope.

C. Specimen examination

After the preparation required for the respective examinations, the specimens were analysed. Two different approaches were considered for the DSC. The first hypothesis was that the microstructure changes with the temperature the specimen is heated to. So, the first set of investigations was made with different maximum temperatures at the same heating rate. The second hypothesis assumed a relationship between cooling rate and microstructure and was therefore also examined. All DSC analyses were made using the Pegasus DSC 404 F3 by Netzsch. Its SiC furnace can provide a heating rate of 50 K per minute. The specimen is positioned on the sample table (as shown in Figure 2) and heated under an argon atmosphere to minimise the influence of oxygen and prevent the formation of an oxide layer. After these examinations the specimen is prepared for subsequent observations under the optical microscope. The microscope used was the Axio Imager A2, from the Zeiss line of optical stereo light microscopes, with associated software.

III. RESULTS

The analyses performed led to different results that are presented in the following chapter. According to the differences in the origin and treatment of the specimens their respective results are separated in different sections for a better overview.

A. DSC specimens with variable maximum heating temperature

The first approach was to examine the effect of different maximum heating temperatures on microstructure formation. For this purpose, the specimens were placed in the DSC instrument. The chosen temperatures were 750 °C, 850 °C, 950 °C and 1050 °C, and the heating and cooling rate was set to 10 K per minute. Overheating was necessary to ensure that the whole volume would melt. The differences in the set

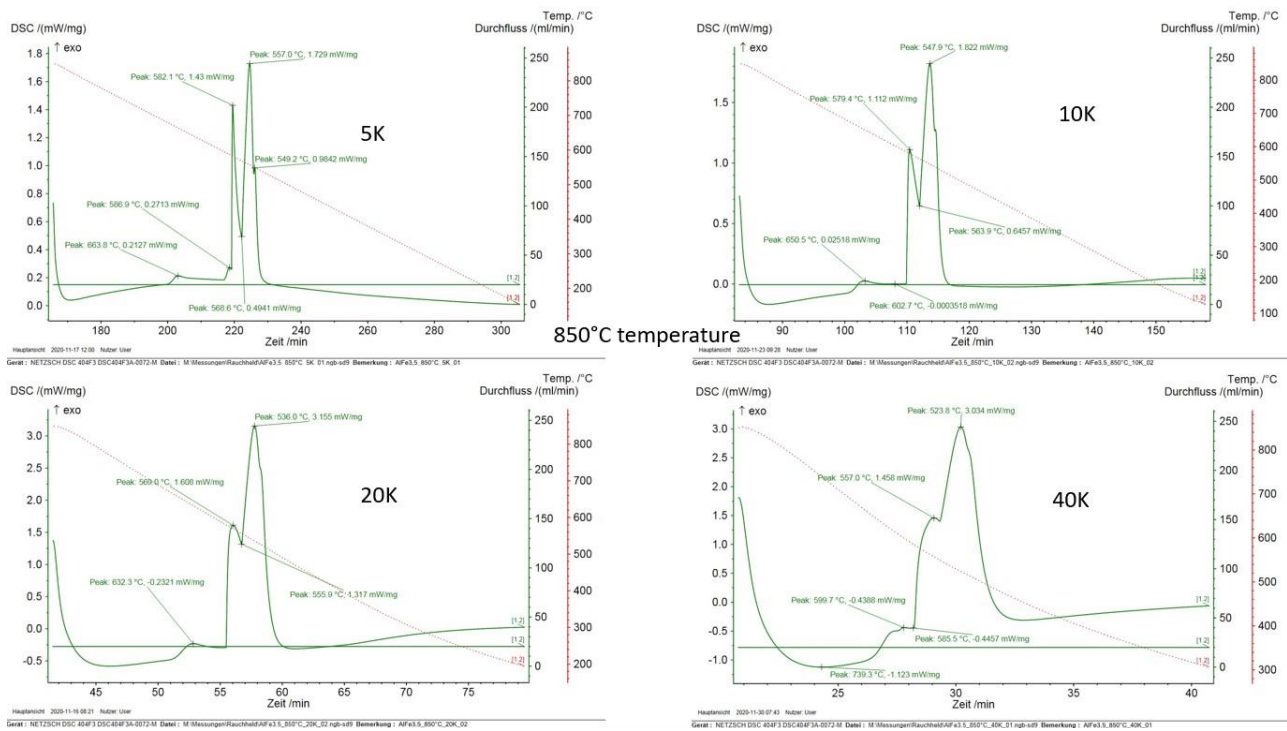


Figure 1: DSC diagrams with heating/cooling rates of 5K/min, 10K/min, 20K/min and 40K/min and a constant melt temperature of 850°C

overheating temperatures were chosen because it was not clear which temperature would be necessary to avoid impact of nucleation history on the resulting microstructures in the molten matrix. The diagrams of the DSC analysis show only minor differences between all four of the analyses as far as can be visualised in the graphs. When comparing the position of the peaks they differ in a range of about 5 °C so the results seem to be reliable and comparable. To complete the observation these specimens were also investigated under the light microscope to make sure that there were no visible differences either. The optical images from the optical microscopy show that the microstructure for a maximal heating temperature of 750 °C differs from the other three microstructures. The main difference consists in the plates going through the matrix in addition to the more globular phases, which are the only phases found in the other specimens. The conclusion drawn from this series of experiments was that plate formation ceases once the specimen is overheated sufficiently, nor do further increases in temperature result in any changes in the microstructure. All following experiments was conducted at a heating temperature of 850 °C.

B. DSC specimens with variable cooling rate

The next parameter to be investigated was the cooling rate. After finding out that the maximum melt temperature had no significant influence on the microstructure, the next step was to examine the heating and cooling rate. The parameter limits were set by the DSC instrument used, as the furnace can only provide rates between 1 K/min and 50 K/min. In the first investigation four cooling and heating rates were examined: 5 K/min, 10 K/min, 20 K/min and 40 K/min, as shown in figure 1. This overview indicates a great variance in the individual graphs. The first peak in the diagram, in particular, is a lot more pronounced in the 5 K/min graph than in the 40 K/min graph. The next step was to check if these

differences in the diagrams correlate with changes in the microstructure of the material. Therefore, the specimens were prepared for optical microscopy.

All images shown in figure 2 were acquired using the same magnification so that the sizes of the intermetallic phases can be compared. Leaving aside the differences in the shape of the phases for the moment, the first thing to note is the difference in the size of the individual phases. The possible explanation here is that with the lower cooling rate the intermetallic phases have more time to form and because of that the iron in these phases has more time to bond into the phase. That would lead to the possibility of a purer aluminium matrix with less impurities resulting from the iron. As the cooling rate increases, the matrix solidifies earlier and more quickly and the intermetallic phase forms within a shorter period, crystallising in a noticeably different metallographic phase. Another distinctive feature is the formation of different shapes. The lower the cooling rate the more cubic is the formation of the phase, and the higher the cooling rate the more pronounced the formation of more needle-shaped intermetallic phases appears to be.

Next, a DSC analysis was performed at the cooling rate of 1 K/min (as shown in figure 3). The DSC analysis of the specimen examined at a cooling rate of only 1 K/min revealed some very obvious differences compared to the diagrams in figure 1. The underlying course of the curve is caused by the instrument not being calibrated for the heating rate used, so the information on the heating energy cannot be used to draw conclusions from it. The main focus lies on the position of the peaks as they are reliable information. When comparing the temperatures, it was noted that the crystallisation temperatures decrease as the cooling rate increases. The crystallisation temperature of the first peak starts at 587.6 °C in the diagram of the 1 K/min cooling rate and continuously decreases for the temperatures of 582.1 °C at 5 K/min, 579.4 °C at 10 K/min and 569.0 °C at 20 K/min, down to a

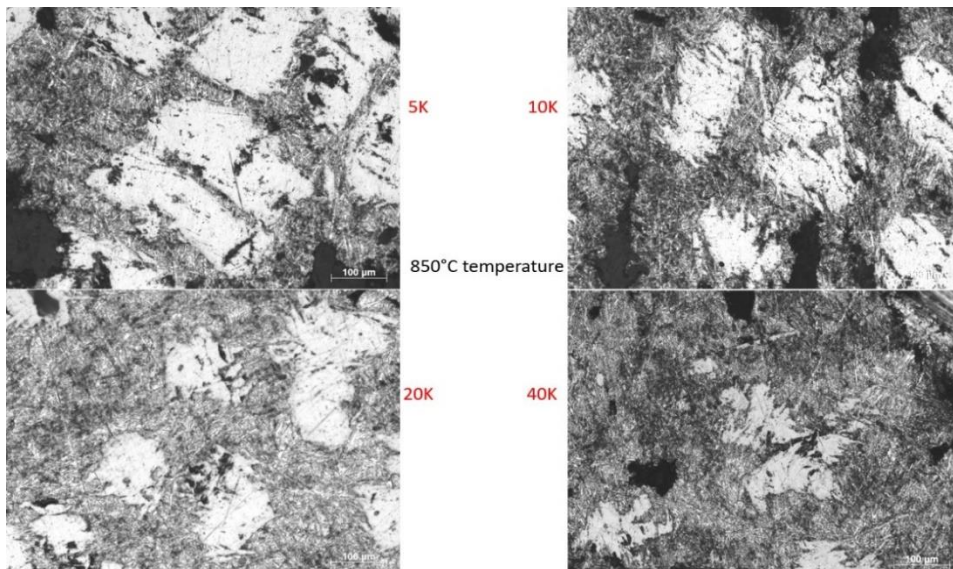


Figure 2: Microscopic images of the microstructure related to the different heating/cooling rates

final temperature of 557.0 °C at a cooling rate of 40 K/min. The same behaviour can be observed for the second peak, where the temperature starts at 563.4 °C at 1 K/min and the crystallisation temperatures drop to 557.0 °C at 5 K/min, 547.9 °C at 10 K/min and 536.0 °C at 20 K/min, until the lowest crystallisation point is measured at 523.8 °C and 40 K/min. Another noticeable difference concerns the third peak in the diagrams of figure 3 and figure 1. This peak is only measurable in the graphs with cooling rates of 1 K/min, 5 K/min and 10 K/min. These third peaks show the same decrease in temperature over the different cooling rates. The lack of the third peak at 20 K/min and 40 K/min could either originate in the higher cooling rate, where the small peak is just not visible because the measuring points of the software were set too far from each other, or the rapid cooling process prevents this intermetallic phase from forming as it needs more time to develop.

IV. CONCLUSION AND OUTLOOK

Having completed this set of experiments two main conclusions can be drawn: Firstly, the lack of impact of the

highest heating temperature of the specimen, with only the slightest differences observed in the diagram. And with virtually no visible differences in the DSC analysis the expected similarities in the metallographic observations are found. Therefore, it can be concluded that heating the melt up to temperatures of 850 °C or higher removes possible melt history nucleation effects. Contrary to the result from chapter III.A, the experiments described in chapter III.B demonstrated a connection between cooling rate, peak temperature and formation of the intermetallic phase. For these specimens, noticeable differences in microstructure were identified. Apparently, the size of the intermetallic phases is the larger the lower cooling rates are applied. Also, formation of intermetallic phases starts at higher temperatures for lower cooling rates. Finally, some indication of suppression of intermetallics formation for higher cooling rates is found. Further experiments will be carried out using samples from furnace cooling to either confirm or question comparability to the well-controlled and protected environment of a DSC instrument. The parameters influencing the possible formation of the microstructure could completely change the outcome.

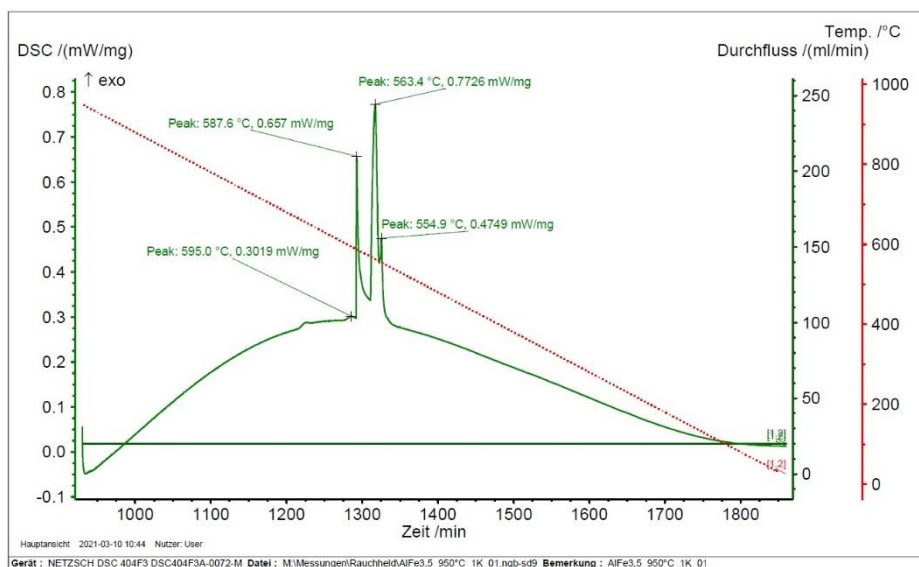


Figure 3: DSC analysis of specimen AlFe3,5_950°C_01K_01

Analytical evaluation of vacuum buildup concepts for aircraft structures

1st Johannes Reitenberger
 Faculty of Mechanical and Process Engineering
 Hochschule Augsburg
 Augsburg, Germany
 Johannes.Reitenberger@HS-Augsburg.de

2nd Prof. Dr.-Ing. Ralf Goller
 Faculty of Mechanical and Process Engineering
 Hochschule Augsburg
 Augsburg, Germany
 ralf.goller@hs-augsburg.de

Abstract— In order to be able to substitute the low-cost material aluminum for the significantly lighter but more expensive fiber-reinforced plastics in the manufacture of aircraft panels, the production of these composites must be optimized. Due to the high proportion of manual activities involved, the production of these components from composite materials has so far resulted in relatively high manufacturing costs. If the processes can be designed in such a way that manual work is eliminated as far as possible, profitability can be significantly increased. In the course of this work, concepts are developed and evaluated that can make this possible.

I. INTRODUCTION

High fuel consumption and the associated costs, but also the ever-increasing pressure from the general public to reduce CO₂ emissions in order to protect the climate, are prompting the aerospace industry to constantly explore and develop ways to save weight. The focus is on innovations that enable higher payloads to be carried with a lighter and therefore more efficient design. To meet these requirements, the trend is toward fiber-reinforced composite materials that combine low weight with high load-bearing capacity. The use of components made of fiber-reinforced plastics has increased significantly in aircraft construction in recent years. For example, the current passenger jet of the European aircraft manufacturer Airbus, the A350XWB, has a 50% share of composite materials in its primary structure [1].



Figure 1: Fuselage shell of the Airbus A350 made of carbon fiber reinforced plastic [2]

Fiber composite materials such as carbon fiber reinforced plastic (CFRP) are used, among other things, for the fuselage shell (see Figure 1) and for the wings of the A350XWB. In aircraft construction, various production methods are used to manufacture aircraft components from fiber-reinforced plastics. Despite various partially automated processes, many

manual processes are required for the production of composite components in aircraft construction, which take up a lot of time. To reduce production costs, the proportion of manual manufacturing steps must be reduced in order to be able to significantly shorten the manufacturing time. Only the resulting reduction in labor costs makes composite manufacturing more economical than metal versions. The manufacturing process for fiber composite components is described in more detail below.

II. BASICS OF THE MANUFACTURING PROCESS

CFRP materials belong to the class of composite materials. These materials are composed of two or more bonded materials. In the case of CFRP, these are unidirectionally oriented carbon fibers embedded in a polymer matrix. CFRP has the greatest mechanical strength in the direction of the fibers. Accordingly, the fibers in CFRP laminates are aligned along the main load direction. The A350XWB fuselage shell is composed of multiple layers of unidirectional fiber matrix laminates, which are stacked and aligned at individual angles according to mechanical load requirements (see Figure 2).

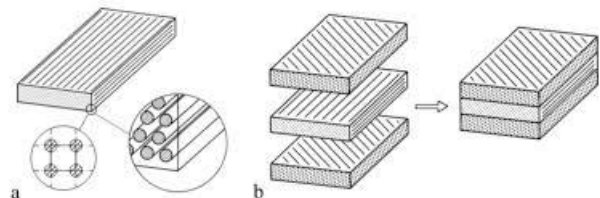


Figure 2: CFRP laminate structure with several unidirectional fiber layers embedded in an epoxy matrix [3]

CFRP components can be manufactured with either a thermoplastic or a duroplastic polymer matrix. The fuselage shell of the A350XWB has a duroplastic matrix.

The production of the fuselage shells is divided into the following steps:

1. placing the pre-impregnated fibers into the tool
2. placing the stringers (longitudinal stiffeners)
3. creation of the vacuum structure
4. curing and demolding

Before going into the development of a new vacuum setup, the manufacturing steps are briefly described.

A. Fiber placement process

Automated CFRP depositing processes are mostly used for the production of aircraft shells.

The basic principle of fiber placement processes is the automated depositing of pre-impregnated textile semi-finished products, so-called prepregs, along programmed tool paths [4].

With the aid of the AFP process used here, the individual layers are deposited in a concave mold, the so-called tool (cf. Figure 3). The tool has the negative shape of the outer contour of the aircraft shell to be achieved.



Figure 3: AFP Process for Panel production (picture PAG)

B. Stringer placement process

At the next station, the "Stringer Placement Tool", the stringers, which are also made of CFRP and are sourced from a manufacturer in the USA, are inserted (see figure 4).

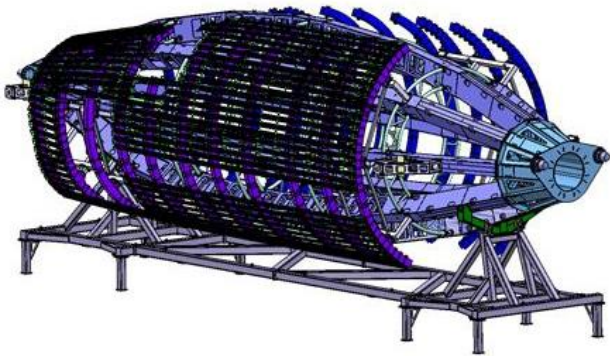


Figure 4: CAD model of the stringer placement tool (PAG)

After a protective layer has been removed from the so-called omega stringers, an adhesive film is applied and heated. A special film tube is then inserted into each one, which ensures that the pressure is distributed evenly to the last corner during curing. This ensures that the stringers adhere strongly to the laminate. For this reason, the tubes are even offset with fine metal plates so that magnets in the setting tool can hold the parts firmly together. [2]

Figure 5 shows how the stringers are placed on the laminate using the stringer placement tool.



Figure 5: Positioning the stringers on the aircraft panel (picture PAG)

C. Vacuum build-up

In order to avoid air inclusions inside the laminate, which reduce component quality and strength, a vacuum is created above the panel, which compacts the laminate. So-called auxiliary materials are laid on top of the laminate. The auxiliary materials consist of a layer of fleece and a layer of peel-ply. The release fabric ensures that the aircraft shell can be detached from the overlying layers after curing and does not stick. Excess resin is absorbed by the fleece layer above. The schematic lay-up is shown in Figure 6.

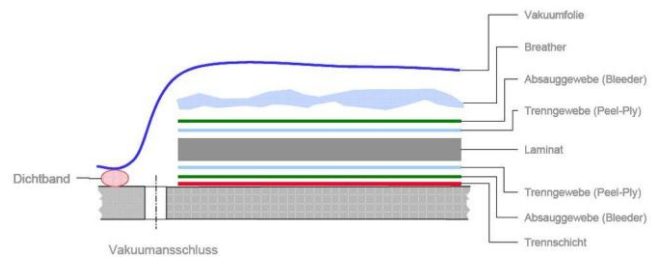


Figure 6: Vacuum buildup for autoclave cycle [6]

A sealing tape is then applied around the laminate structure. The vacuum film is applied manually to the sealing tape. To ensure that the vacuum bagging film adheres to the laminate everywhere without tension after evacuation of the sealed area, the film must be draped into folds by hand at the stringer positions (see figure 7).

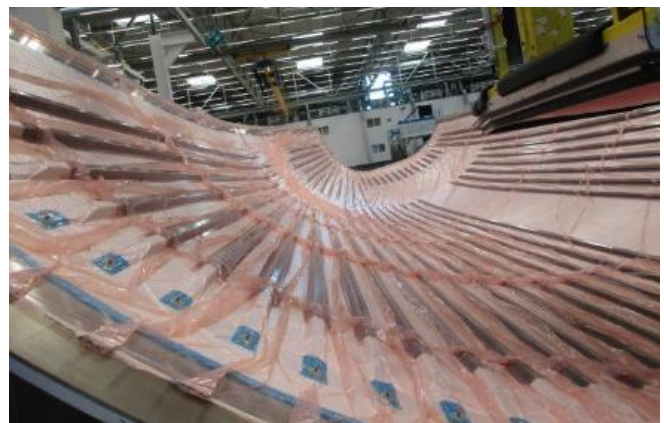


Figure 7: Aircraft shell with finished vacuum build-up (picture PAG)

During the following evacuation process, the air is almost completely pumped out of the area to be vacuumed. To ensure that there are no leaks in the vacuum setup, a so-called leak test must be performed. This involves disconnecting the vacuum assembly from the vacuum pump. After several hours, it is checked whether the vacuum is still present. If this is the case, the panel can be taken further into the autoclave. An autoclave is a heatable pressure vessel with precise control that allows reproducible temperature, pressure and vacuum cycles during the consolidation and curing of composites [7]. But if the vacuum has escaped due to leakage, the complete vacuum assembly must be checked and replaced if necessary, otherwise defective components will be produced that can no longer be used. A leak test must then be carried out again. This process is repeated until there are no more leaks.

Due to the complex manual processes, the vacuum process is very error-prone. In addition, the elimination of leakages significantly increases the production time. As a result of the many manual operations and the long process time, high costs are incurred in this manufacturing stage. In order to make this production step more economical and reliable in the future, alternatives to the current vacuum setup are being developed in this work.

D. Curing and demolding

After the vacuum build-up is created, the duroplastic matrix of the laminate is cured in an autoclave.

When the autoclave cycle is completed, the cured aircraft shell is taken to the so-called "demolding" station. There, the vacuum bag is removed and all auxiliary substances and materials are removed. This finishes the CFRP manufacturing process.

The shell is then examined ultrasonically for inclusions in the laminate. This is followed by the installation of transverse stiffeners, so-called bulkheads, and other elements. All these components, are connected to the aircraft shell by riveted joints.

III. PROBLEMS WITH THE VACUUM BUILD-UP

Largescale structural components are manufactured in the aircraft industry with the aid of flat tape layers and structural elements such as the stiffening profiles (stringers for example). Both the joining of these elements and the following vacuum build-up currently involves a very high proportion of manual operations.

When considering manufacturing costs, this stage of production is the most labor-intensive and therefore contains approximately 2/3 of the total costs. If this process can be automated for an industrial application, not only a more economical production method, but also a higher process stability can be achieved. [7]

Before a new concept for an error-minimized and more economical vacuum assembly can be created, it must first be clarified exactly which requirements it must meet.

In addition to the qualitative requirements, the production of an aircraft panel must also meet ecological, economic and process-related demands.

In the course of a brainstorming session and scientific research, a list of various requirements was drawn up to guide

the new development. The following technical boundary conditions must be fulfilled:

- 1) Temperature resistance of the materials used up to at least 200 °C for the autoclave cycle
- 2) Absolute tightness of the vacuum assembly
- 3) Easy detectability of occurring leakages
- 4) No inclusions in the vacuum buildup
- 5) Possibility of uniform pressurization of the complete component geometry
- 6) No reduction in laminate quality, e.g. due to rough surface or sharp edges on the vacuum build-up
- 7) No damage to the laminate when creating and removing the vacuum setup
- 8) Good reproducibility of the vacuum setup
- 9) Use of certified materials for vacuum build-up

Each of the developed concepts must fulfill all technically necessary framework conditions. If this is not the case, the corresponding concept is excluded. In order to determine which of the remaining concepts is most suitable, the various processes must be evaluated on the basis of an analytical, hierarchical process using evaluable requirements. This is done by means of a so-called AHP diagram (see figure 8)

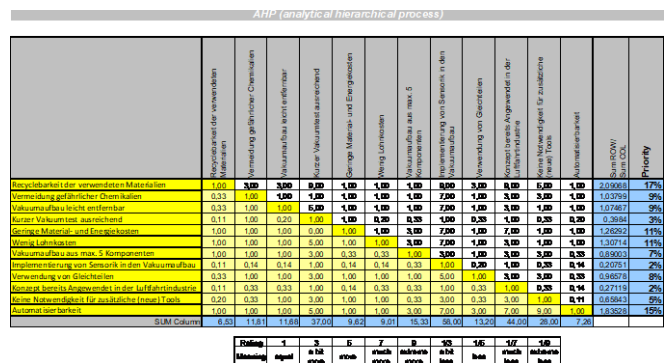


Figure 8: AHP-diagram

The AHP diagram compares all of the listed requirements in pairs. Since many different departments and areas are involved in the production of aircraft shells, it is important to evaluate the requirements from as many perspectives as possible in order to obtain an optimal solution. For this purpose, the evaluation of the individual requirements was carried out in close coordination between the people involved in this project from Premium Aerotec and from the Augsburg University of Applied Sciences.

It turns out that recyclability is the most important requirement and the implementation of sensors in the vacuum build-up is the least important.

IV. ALTERNATIVE PROCESSES

In addition to the vacuum process described above, there are already alternative processes currently used in composite manufacturing. Due to the high quality requirements and the enormous component size of aircraft shell components, it is necessary to investigate in advance which of the currently

widespread processes are suitable for aircraft construction. To begin with, we will look at a process that has already been used for aircraft panels in prototype status, the so-called "AutoVac" process.

A. „AutoVac“ Procedure

The principle of this process is based on the scientific concept of preparing the vacuum buildup not on the real component, but in a preliminary stage prior to the actual production of the component. [7]



Figure 9: Demonstrator with foil and auxiliary material (picture PAG)

For this purpose, all components required for the vacuum buildup must be positioned one process step earlier together with the stringers on the previously deposited CFRP laminate of the aircraft panel. This is therefore to be done with the aid of the stringer placement tool, which is first wrapped with the vacuum bag. The vacuum foil is held to the tool with small suction cups. The auxiliary material packages (fleece and peel-ply) required to create a vacuum build-up are then positioned above the vacuum film. The complete vacuum build-up is then placed on the aircraft panel with the stringers.

This process has already been tested using a smaller wood model of the stringer placement tool (see figure 9). The same components (stringers, auxiliaries, etc.) were used for the implementation as for the components from regular production.

The complete structure on the wooden demonstrator is then transferred to a prepared CFRP structure. The tests showed that the stringers shift during the positioning process due to the complex setup with the auxiliary materials. Therefore, this process had proven to be rather unsuitable.

B. „PapaVac“ concept

As the "AutoVac" process requires all the tools needed for vacuum build-up to be integrated into the stringer placement tool, this creates a complex system in which stringers can easily slip during positioning. To avoid this, a process is being developed in which the vacuum build-up is created independently of the stringer placement tool in a separate tool.

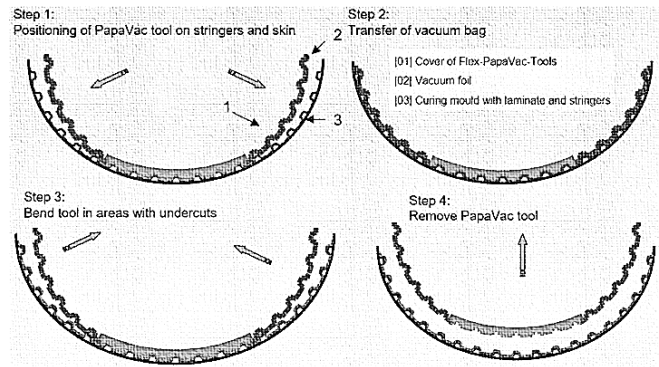


Figure 10: System view on the „PapaVac“ concept (PAG)

For such a process, the so-called "PapaVac" concept was created (see Fig. 10). In this process, the vacuum bagging film is draped into the desired geometry in advance with the aid of a tool, while the stringers continue to be positioned as is currently customary with the aid of the stringer placement tool. However, when creating the vacuum assembly, the time-consuming manual draping of the vacuum foil is avoided by pressing it into an appropriate shape in advance. In order for the tool to pass the film to the panel with the stringers, it must be made of a flexible, silicone-like material. This ensures that the flexible tool can be easily transferred over the stringer. The flexibility allows the tool to be released afterwards by simply bending it open at the edges. However, this concept has never been pursued beyond the concept level. The main reason for this is that no flexible material that is both suitable from a technical point of view and certified for aircraft construction has yet been found. Residual silicone, for example, can easily adhere to the CFRP component and must therefore be removed at great expense after curing before it diffuses into the component, thus impairing quality [8].

In order to be able to implement the "PapaVac" process in practice in the future, many material and process-related investigations must be carried out.

However, before a concept can be developed to the point of series application, it must be examined in detail which of the previous concepts are the most promising. In addition, other concepts from other industries are considered which are also suitable.

C. Vacuum film spraying

In order to dispense with the cumbersome draping of the vacuum bagging film, a liquid elastomer is to be applied to the prepared laminate and auxiliary material structure with the aid of a spray gun (see figure 11).

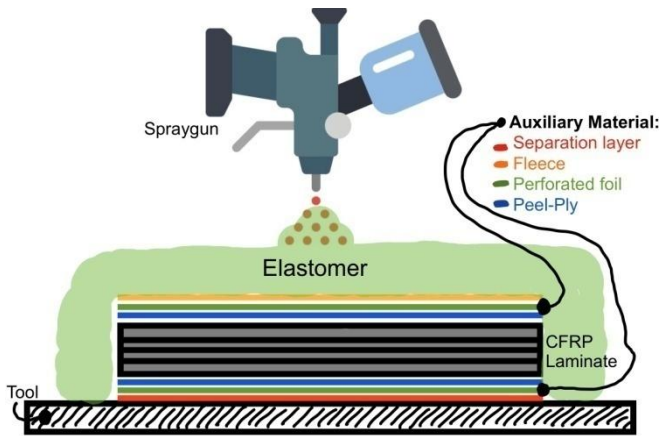


Figure 11: Spraying vacuum film concept sketch

This technology is currently already used in boat building, among other things. [9]

The advantages of the system are the short process time and the reusability of the vacuum hood produced. A disadvantage of this process is that liquid silicone elastomers have always been used up to now. However, silicones may not be used in the production of CFRP aerospace components. Alternative elastomer materials must therefore be sought.

D. Use of a "Negative Tool form"

In this process, the vacuum bag is replaced by a tool which reproduces the negative shape of the CFRP part to be produced. This negative tool is placed over the laminate and auxiliary material structure (see figure 12).

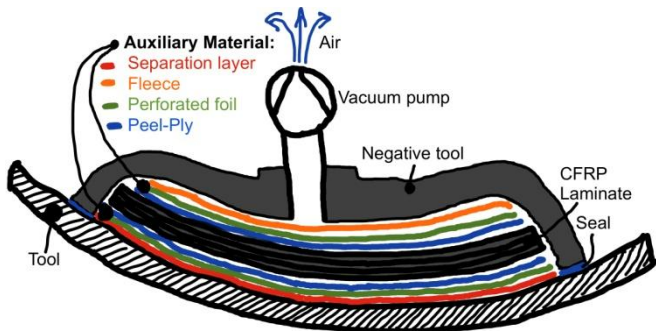


Figure 12: "Negative Tool form" concept sketch

The advantages of this system are mainly the short process time and the reusability of the tool.

The disadvantage of this concept is the high tooling costs required. These are due to the fact that the negative tool must be manufactured from very expensive metallic materials with an extremely high dimensional accuracy, as well as being equipped with connections and valves.

V. EVALUATION OF THE INDIVIDUAL CONCEPTS

Since it is not possible in reality to develop concepts that meet all requirements 100 percent, it is important to evaluate all requirements quantitatively in terms of their relevance in order to obtain a concept that best meets expectations. With the evaluation of the AHP diagram, a weighting is defined for the various requirements. The concepts are then eva-

luated taking into account the previously determined weighting factors. This is done with the help of the concept evaluation matrix (see figure 13).

To do this, the various requirements and the column with the percentage weightings are first transferred to the new table. Along the top row, all concepts with names are first lined up next to each other. The concepts are now evaluated individually within the group with regard to all requirements. The evaluation, the so-called rating, takes place in the team after majority agreement of all participants. The concepts are evaluated individually with regard to each requirement. The rating is determined by a graduated point system. The concepts are rated with one point for insufficient fulfillment of the requirement up to nine points for very good fulfillment of the requirement. The points awarded are divided into the following levels: 1 point, 3 points, 5 points, 7 points and 9 points.

In order to be able to take the importance of the individual requirements into account in the overall evaluation, the weightings must be offset against the rating. To do this, the score assigned to the concept in the points field (Pkt.) is multiplied by the percentage weighting of the evaluated requirement. The result is entered in the adjacent field in the "Wert" column. The value takes into account both how well the concept meets the requirement and how important the requirement is in the overall context.

Konzeptbewertung							
		Anforderung		Pegel 100		Gesamtwert	
		Pkt.	Wert	Pkt.	Wert	Pkt.	Wert
Anforderungen							
Reichhaltigkeit der verwendeten Materialien	17%	1	0,17	1	0,17	5	0,87
Vermeidung gefährlicher Chemikalien	9%	3	0,26	3	0,26	3	0,26
Vakuumaufbau leicht entfernbar	9%	7	0,63	7	0,63	7	0,63
Kurzer Vakuumzeit ausreichend	3%	3	0,10	3	0,10	3	0,10
Geringe Material- und Energiekosten	11%	5	0,53	3	0,32	5	0,53
Geringe Luftkosten	11%	3	0,33	3	0,33	3	0,33
Vakuumaufbau max. max. 5 Komponenten	7%	1	0,07	1	0,07	3	0,22
Implementierung von Sensoren in den Vakuumaufbau	2%	1	0,02	1	0,02	1	0,02
Vermeidung von Glasfasern	8%	3	0,24	5	0,40	3	0,24
Konzept bereits Angewendet in der Luftfahrtindustrie	2%	9	0,20	5	0,11	7	0,16
Keine Notwendigkeit für zusätzliche (hohe) Tools	5%	7	0,35	1	0,05	3	0,16
Aufwandlos herstellbar	10%	5	0,26	3	0,16	5	0,26
Rating (Bewertung jedes Konzepts bezüglich Erfüllung der Anforderungen)		Summe	3,70	2,92	4,28	7	5,95
Rating (Bewertung jedes Konzepts bezüglich Erfüllung der Anforderungen) von 9 Pkt. für sehr gut bis 1 Pkt. für nicht erfüllt in Spalten (S1/S3,1)							
		Ranking	3	4	2	1	1

Figure 13: Concept Evaluation Matrix

When the rating of a concept has been completed and all values for the associated requirements have been determined, the sum of the individual values can be calculated. The sum of the values of the individual requirements is entered in the sum field below. The higher the sum is, the better the concept is. The ranking number in comparison to the other concepts is stored in the field below the sum.

In order to additionally visually emphasize the evaluation of the concepts, the ranking list is highlighted with a graduated traffic light color format (see figure ui). The best concepts are shown in a green to yellow color range. The less suitable concepts are highlighted in orange to red. This evaluation system makes it possible to filter out the best from many proposed solutions.

It can be seen that the concept with the "Negative Tool" performs best, followed by the sprayed vacuum build-up and the "AutoVac" process.

The final solution selection can be directly taken from the list as the evaluation winner. Alternatively, the participants can decide to combine aspects of the best solutions, or, in the case of a decision, to select the final solution concept by means of a vote.

VI. SUMMARY

The production of aircraft fuselage shells from carbon fiber reinforced plastics is divided into various process steps. First, the CFRP laminate is produced by an automated AFP lay-up process. Stringers are then placed on the panel using the stringer placement tool. Then, the vacuum build-up is created and the prepared panel is transferred to the autoclave for curing. Finally, all auxiliary materials are removed on the "demolding" station. Due to the many manual operations, the vacuum build-up offers the most potential for optimization in order to make the manufacturing process more economical. Before starting to develop new concepts for an improved vacuum setup, it is first necessary to define which technical framework conditions and requirements the new system must fulfill. The requirements were compared with each other using an analytical procedure within the AHP diagram. It turns out that recyclability is the most important requirement. Weighting factors are calculated from this. Four different concepts were presented below. The "AutoVac" method was already tested in the experimental stage, but had functional deficiencies due to its high complexity. In the other so-called "PapaVac" concept, an attempt was made to reduce the complexity by using a separately generated auxiliary structure. However, this concept was not pursued beyond the concept level. Therefore, some development work is still required for this concept. The sprayed vacuum bagging process has been used in other industries, but for this application the appropriate material selection still needs to be defined. The "Negative Tool" offers many process advantages, but a large amount of development and component costs are required for its introduction. In the concept evaluation, the concept with the "Negative Tool" performed best. However, the final concept selection has yet to take place.

VII. OUTLOOK

In the further course of the project, other concepts, also from other sectors, must first be investigated to determine whether they are suitable for simplifying the vacuum setup. These will then also be evaluated using the concept evaluation matrix. Subsequently, the best processes will be elaborated to such an extent that the processes can be tested at trial level. Finally, the most suitable process is to be found by the following evaluation of the individual test results. Particular attention will be paid to the component quality and practicality of the concepts. The coordination and selection of the process to be pursued further will be closely coordinated with the responsible employees at Premium Aerotec. Once the final concept has been determined, it can be worked out for implementation within series production. This requires further tests at model level. Subsequently, a full-scale aircraft

shell is produced. After further successful investigations and tests, the new process can finally be used for series production.

REFERENCES

- [1] M. Hinsch und J. Olthoff, *Impulsgeber Luftfahrt*. Berlin, Heidelberg: Springer Berlin Heidelberg, 2013.
- [2] M. Gründer, *Airbus-Zulieferer: A350-Rumpfschalen aus Augsburg*. [Online]. Verfügbar unter: <https://www.flugrevue.de/airbus-zulieferer-a350-rumpfschalen-aus-augsburg/> (Zugriff am: 16. Februar 2021).
- [3] *images (JPEG-Grafik, 395 × 127 Pixel)*. [Online]. Verfügbar unter: <https://encrypted-tbn0.gstatic.com/images?q=tbn:ANd9GcQNoeDQAemwQAFX5a93jSONPDNcFL-FIH9rPQ&usqp=CAU> (Zugriff am: 12. April 2021).
- [4] H. Lengsfeld, F. Wolff-Fabris, J. Krämer, J. Lacalle und V. Altstädt, *Faserverbundwerkstoffe: Prepregs und ihre Verarbeitung*. München: Hanser, 2015.
- [5] Reinhard Krammer, „Prozessschritte AutoVac“. Augsburg, 6. Apr. 2021.
- [6] Andreas Nussberger, *Composite Technologies - Zusammenfassung*. [Online]. Verfügbar unter: <https://forum.fsmb.de/forum/index.php?thread/7923-faserverbundwerkstoffe/&pageNo=19> (Zugriff am: 3. Mai 2021).
- [7] Dieter Meiners, „Beitrag zur Stabilität und Automatisierung von CFK-Produktionsprozessen“. Dissertation, Natur- und Materialwissenschaften, Technische Universität Clausthal-Zellerfeld, Clausthal-Zellerfeld, 2007.
- [8] Birgit Niesing, „weiter.vorn: Das Fraunhofer-Magazin 3 / 12“, *Forschung, Technik und Innovation*, 2012.
- [9] LOFT48°, *Prospekt Vakuumbauben VAKUUMHAUBEN – PASSGENAU UND MEHRFACH VERWENDBAR: Die innovative Systemlösung bringt frischen Wind in die Leichtbau-Fertigung* (Zugriff am: 27. März 2021).

Studies on the firing behavior of bone china and the influence of raw material components on strength and translucency

Manuel Salg
 Faculty of Materials Engineering
 Georg Simon Ohm Institute of
 technology Nuremberg
 Nuremberg, Germany
 salgma62300@th-nuremberg.de

Abstract—In this work, the effects of modifying a standard bone china formulation on strength and translucency were investigated. 3 compositions were prepared, the standard formulation for comparison, one with increased cornish stone content and another with increased kaolin content. Test specimens were pressed from each composition. They were fired at 1230°C and tested for strength by 4-point bending, additionally the Weibull modulus was determined. The transmission was measured using a spectrometer. The strengths of the standard composition were 87,7 N/mm², and 89,3 N/mm² with increased cornish stone content. The transmission increased from 4,20% to 5,06%. With higher kaolin content, the strength decreased to 61,88 N/mm² and the transmission to 1,18%

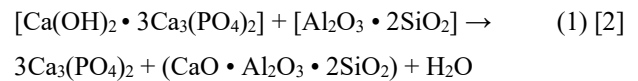
Keywords—bone china, composition, strength, transmission, translucency

I. INTRODUCTION

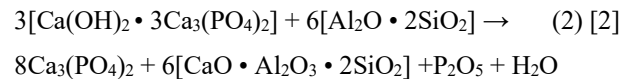
In 1794 Josiah Spode Jr. started the production of bone china as it is known today. The typical mass composition is 50% bone ash, obtained from calcining bovine bones, 25% china clay (kaolin) and 25% cornish stone, a feldspar rich mineral. Due to its small sintering range, sometimes small amounts of quartz are added to reduce warping or shrinking during the firing process. Bone china is mainly known for its translucency and white color, but also has very high resistance to impact and chipping. [1] These properties result from the composition of crystalline phases in the sintered bodies. The main phases are crystals of β -tricalcium phosphate (β -TCP), anorthite and sometimes small amounts of quartz that can be found in a complex glass-matrix. There is still no consent in the literature to the formation of these crystalline phases, as some studies were able to detect phosphorus in the glass matrix, whereas others could not find any. There are two theses by Roberts and Beech that describe the reaction between hydroxyapatite of the bone ash and the kaolin to form β -TCP and anorthite. It was mentioned that these reaction equations are only simplifications. The actual reaction behavior takes place somewhere in between those two. [2]

The first hypothesis is called “the non-phosphate glass equation”. It says anorthite is formed entirely from the excess calcium in the bone ash surplus to the amount needed to combine with the phosphorus pentoxide in the bone ash to form β -TCP. The excess clay transforms into mullite, which is believed to eventually be built into the glassy phase with the

other raw materials. The reaction takes place as the following [2]:



The second reaction is called “the phosphate glass equation”. In this all the calcium oxide in the bone ash is provided for the formation of anorthite by reaction with the alumina and silica from the china clay. It is assumed that the actual amount of anorthite formed depends on the amount of alumina in the china clay. All remaining calcium oxide in the body that is not depleted is assumed to form β -TCP and all other components, including the excess phosphorus pentoxide from the bone ash, react to form the glassy phase. The reaction is described as the following [2]:



Due to these reactions, bone china shows a significant crystalline content. It consists of 70% crystalline phases and 30% glass. Other porcelain types show the reverse: 30% crystalline phases and 70% glass. This contribution would explain the higher resistance to impact and chipping. [1] The high translucency results from the low difference in the refractive indices “n” of the different phases in the sintered bone china bodies. Anorthite has a refractive index of 1,58, the value of β -TCP lies between 1,59 and 1,62 and the of the glass phase is 1,56. This results in a very low Δn of 0,07 at most. Due to the small deviations, the incoming light is barely scattered at the grain boundaries, loses hardly any intensity and is therefore more translucent than conventional hard porcelain. [3]

The goal of this study is to modify the typical composition of bone china and therefore to influence the properties such as translucency or strength. For the following experiments 3 mixtures are prepared. Series A is the typical recipe and serves as a reference. Series B has an increased cornish stone content by reduced parts of bone ash. Similar to series B, series C has an increased china clay content due to a reduction of bone ash. You can see the different compositions in Table 1.

Table 1: Planned Bone China Compositions

Series	Bone Ash [wt.-%]	Kaolin [wt.-%]	Cornish stone [wt.-%]
A	50	25	25
B	40	25	35
C	40	35	25

II. EXPERIMENTAL PROCEDURE

For a qualitative analysis of the crystalline phases, the raw materials are examined with X-ray diffraction. The sample is prepared by the backloading method. The measurements are carried out on the powder diffractometer “XpertPro” from the company “PANalytical”. A copper anode is used for the measurement, the tube voltage is 45 kV and the tube current 40 mA. The measuring range is between 5° and 80°2θ.

For mixing and homogenizing the different batches A, B and C were each placed in a container together with ceramic balls of different diameters and rotated over a period of 24 hours. From the homogenized mixtures, beams are pressed for strength measurement. A dry uniaxial press from “Weber” was used for this purpose. 15 beams with a mass of 1,5 g are pressed out of each composition under 15 kN. The beams are sintered at 1230°C. The heating rate is 5 K/min and the maximum temperature is maintained for one hour. Testing of the bending tensile strengths of the sintered specimens is carried out according to the standard DIN EN 843 [4]. The bending strength [N/mm²] of the specimens is calculated from the mean values of the specimen dimensions [mm] and the maximum test load [N] using the following formula:

$$\sigma_f = \frac{3 \cdot F \cdot l}{b \cdot d^2} \quad (3)$$

- σ_f : Stress in outer fibers at midpoint [N/mm²]
- F : Maximum recorded force (N)
- l : Quarter length of lower support rollers [5 mm]
- b : Width of test beam [mm]
- d : Depth or thickness of test beam [mm]

After measuring the strengths, the Weibull modulus of the test series is determined to the standard DIN EN 843-5 [5]. From the Weibull distribution, the fracture probability of the specimens can be interpreted.

In order to be able to make a statement about translucency, samples are measured on the Lambda 1050 spectrometer from the “PerkinElmer” company. Therefore, platelets with a diameter of 40 mm and a thickness of 2,3 mm are prepared. Through shrinkage during the sintering process, the thickness of the specimens should be around 2,0 mm. To measure the transmission of the samples, an integrating sphere is used. The specimens are examined over a wavelength range from 350 nm to 800 nm. Using the standards DIN EN 167 [6], 169 [7], 170 [8] a mean transmittance is given.

III. RESULTS

A. Raw material XRD analyses

The XRD spectra showed that the raw materials used are of high purity. In addition to the main component oxyapatite, small amounts of albite, an Na-feldspar, were detected in the bone ash. The kaolin has a very high degree of purity, only small amounts of quartz could be detected incidentally. The cornish stone consists of albite, a Na-feldspar, biotite, a layered silicate, microcline, a K-feldspar and small amounts of quartz. The results confirmed that with the selected raw materials all conditions are met to be able to manufacture a bone china ceramic.

B. Composition preparation and strength measurements

During the homogenization process, the high plasticity of the Kaolin posed a problem. The homogenization was

prevented by the fact that the compositions stuck together in the mixing container. The poor distribution of the raw materials was clearly reflected in the strengths determined (Fig. 1). Series A had an average strength of 25,9 N/mm². The strength of series B was 26,5 N/mm² and series B was found to have a strength of 24,4 N/mm². The similarly low strength values prove that there was an inhomogeneous distribution of the raw materials in all series. The low Weibull modulus indicates the same result. Typical values for the Weibull modulus for technical ceramics are between 10 and 20 [9]. From the strengths determined for the bone china series resulted in a Weibull modulus of between 5,13 and 5,93. Based on these results, a different route of homogenization was selected. The formulations were newly prepared and processed into slip with the addition of 50 wt.-% water. The slip was poured into the mixing container with the ceramic balls and rotated for 24 hours. The slip was then dried at 100°C and ground up. The samples showed significantly better values with this homogenization method (Fig. 2). The strength of the A series increased to 87,7 N/mm². Series B went up to a strength of 89,3 N/mm². The value of series C was slightly lower at 61,9 N/mm². In addition to the increase in strength, there was also an improvement in the Weibull modulus. Series A increased to 12,62 and Series B up to 18,76. The high values of series B could be due to the increased glass content. As a result of the high cornish stone content, more glass phase is formed during the sintering process and the residual porosity is largely reduced. The Weibull modulus of series C increased to 6,9, which is still relatively low by comparison. The lower results of the C series can possibly be explained by the increased kaolin content. The increased alumina content should lead to a higher sintering temperature, since the reaction between alumina, silica and highly reactive calcium oxide requires a high temperature to form anorthite. [10] For this reason, the specimens from this composition may not yet be densely sintered and therefore have lower strength values and Weibull modulus.

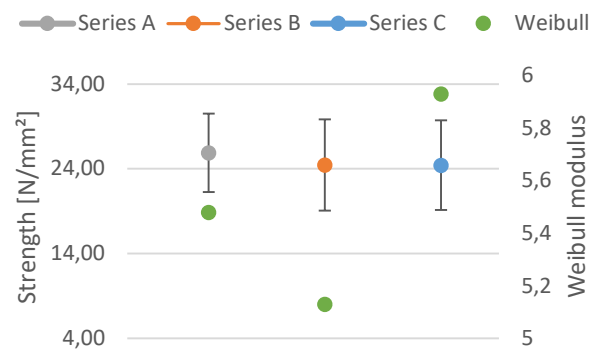


Fig. 1: Determined strengths and Weibull modulus of the dry homogenised compositions

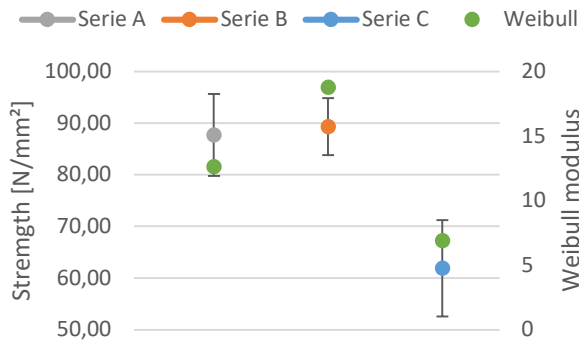


Fig. 2: Determined strengths and Weibull modulus of the wet homogenised compositions

C. Transmission measurements

Due to the different behavior of the formulations during the sintering process, difference in the thicknesses can be observed. The thickness of the specimens influences the light transmission, but the results can be compared with each other, as the deviations are only minor. Compared to the standard composition, the translucency in series B could be increased with a higher cornish stone content as described in [11]. Due to the increased glass phase content, there should be less residual porosity and fewer grain boundaries in the bone china bodies at where the light is refracted. Series C shows by far the lowest transmission. The reason for this could again be the increased kaolin content. This is due to the fact, that the ceramic may not yet be densely sintered at 1230°C and there are still air pores left which provide locations for light scattering. The kaolin additionally brings an increased content of quartz into the ceramic. If the glass melt cannot dissolve the quartz grains so that they cannot pass into the glass phase, the grains also represent interfaces for light scattering. [12] Fig. 3 shows the recorded transmission versus the wavelength. The graphs show that the ceramic absorbs almost all the light intensity at lower wavelength. On higher wavelengths it shows an increase in transmission. This would explain why a warm light is emitted when a bone china ceramic is shined through (Fig. 4).

Table 2: Sample thickness and calculated transmittance of platelets specimens

	Series A	Series B	Series C
Thickness sample [mm]	2,022	1,985	2,080
Calculated transmittance [%]	4,2	5,06	1,18

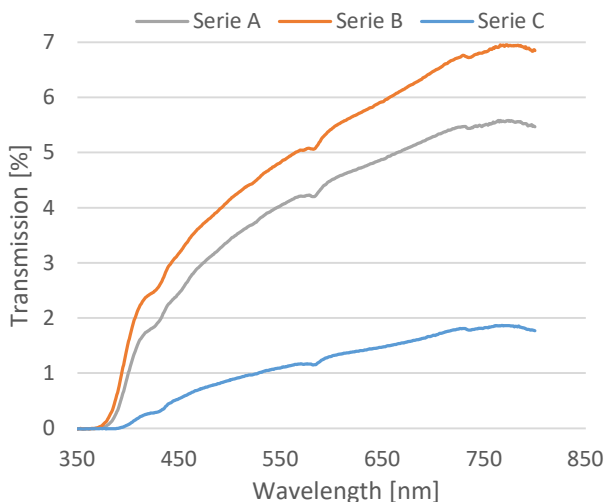


Fig. 3: Recorded transmission versus the wavelength



Fig. 4: Translucency of a bone china lamp

IV. CONCLUSION

Compared to the standard formulation of bone china, the strength and translucency could be increased with higher cornish stone content. An increased kaolin content had a negative effect on strength and transmission under the conditions of this work. The results could possibly be improved by increasing the sintering temperature. Another way to improve the results overall would be to produce a spray granulate from the formulations. However, the production is very complex and requires certain equipment. Furthermore, a density determination and phase analysis of the fired samples would be interesting in order to be able to make a more precise statement about the processes during firing.

V. REFERENCES

- [1] S. Bragança und C. Bergmann, „A comparative study between bone china and hard porcelain,“ *Industrial Ceramics*, 2008.
- [2] A. Kara und R. Stevens, „Characterisation of biscuit fired bone china body microstructure. Part II: Transmission electron microscopy (TEM) of glassy matrix,“ *Journal of the European Ceramic Society* 22, pp. 737-743, 2002.
- [3] H. Salmang und H. Scholze, *Keramik* ISBN- 10 3-540-63273-5, Berlin Heidelberg: Springer, 2006.
- [4] „DIN EN 843-1:2008-08 Hochleistungskeramik - Mechanische Eigenschaften monolithischer Keramik bei Raumtemperatur - Teil 1: Bestimmung der Biegefestigkeit“.
- [5] „DIN EN 843-5:2007-03 Hochleistungskeramik - Mechanische Eigenschaften monolithischer Keramik bei Raumtemperatur - Teil 5: Statistische Auswertung“.
- [6] „Persönlicher Augenschutz - Optische Prüfverfahren; Deutsche Fassung EN 167:2001“.
- [7] „Persönlicher Augenschutz - Filter für das Schweißen und verwandte Techniken - Transmissionsanforderungen und empfohlene Anwendung; Deutsche Fassung EN 169:2002“.
- [8] „Persönlicher Augenschutz - Ultraviolettschutzfilter - Transmissionsanforderungen und empfohlene Anwendung; Deutsche Fassung EN 170:2002“.
- [9] „Technische Keramik,“ Brevier, [Online]. Available: http://www.keramverband.de/brevier_dt/5/3/3/5_3_3_4.htm. [Zugriff am 14 Mai 2021].
- [10] Y. Zhang, Y. Y. a. W. Li und Y. Ren, „Effect of Al₂O₃ Addition on the Flexural Strength and Light Transmission Properties of Bone China,“ *Int. J. Appl. Ceram. Technol.* 12 [4], p. 875-884, 2015.
- [11] F. Singer und S. S. Singer, *Industrielle Keramik*, Berlin Heidelberg: Singer, 1969.
- [12] Y. Zhang und N. Zhou, „Fabrication and characterization of bone china using synthetic bone,“ *Ceramic International* 42, pp. 14910-14917, 2016.

Influence of pore geometries on the thermal shock resistance in ceramics investigated by numerical simulation

1st Joshua Seibold

Faculty of Materials Engineering
Georg Simon Ohm University of
Applied Sciences Nuremberg
Nuremberg, Germany
seiboldjo67703@th-nuernberg.de

2nd Jan Sebastian Hildebrand

Faculty of Materials Engineering
Georg Simon Ohm University of
Applied Sciences Nuremberg
Nuremberg, Germany
jansebastian.hildebrand@th-nuernberg.de

3rd Wolfgang Krcmar

Faculty of Materials Engineering
Georg Simon Ohm University of
Applied Sciences Nuremberg
Nuremberg, Germany
wolfgang.krcmar@th-nuernberg.de

Abstract—The thermal optimisation of ceramic building materials for electrically heated, dynamically storing steam generators is to be carried out by means of thermal simulation calculations. In particular, transient quenching processes with different structural properties of the ceramic materials are to be investigated with finite element simulations and thermal stresses derived from them. For this purpose, a cuboid specimen with a side length of 33.16 mm is simulated, which is quenched abruptly at a temperature of 720 °C in water at a temperature 20 °C. The body was created with uniformly and non-uniformly distributed pores in order to investigate their influence on the thermal properties in more detail. It was found that ceramics with pores can reduce the maximum main stress compared to the zero sample without pores. The zero sample had a maximum occurring main stress of 16.4 MPa. The spherical pore geometry had the strongest effect reducing the maximum main stress to a value of 11.5 MPa.

Keywords— thermal main stress, pore geometry, FEM simulation, thermal shock, cordierite

I. INTRODUCTION

Ongoing climate change is a major challenge for our society. For this reason, the Federal Government of Germany presented an energy concept in autumn 2010, which contains the guidelines for future energy and climate policy [1]. The energy concept is intended to fulfil the energy policy target triangle of climate protection, price stability and, above all, security of supply. By developing new and more effective energy generation processes and energy storage systems, Germany is to be led into the age of renewable energies in the long term. A coherent overall strategy is to be developed by 2050 and replace fossil energy sources in Germany [2]. Thermal energy storage (TES) units in particular are needed for heating and cooling from renewable energies. TES can be heated by electrical energy or industrial waste heat. For this purpose, surplus generated energy must be stored temporarily so that it can be made available afterwards [3]. Heat storage systems in particular offer potential savings at high temperatures. However, the materials used as storage medium must fulfil certain requirements at high storage temperatures. In this work, cordierite ceramics are examined with these requirements using simulations based on the finite element method (FEM) and thus the best possible pore geometry of the storage material is determined. For this purpose, a thermal shock test is simulated on porous cordierite ceramics. The ceramic is heated to 720 °C until thermal equilibrium is reached at this final temperature. The

sample is then abruptly placed in a defined volume of water at a temperature of 20 °C and the temperature profiles and the resulting stresses in the workpiece are analysed.

II. FINITE-ELEMENT-SIMULATION

The ANSYS 2019 R3 software from ANSYS was used for the numerical investigations. The FEM is basically used to solve differential equations. Here, the body to be measured is covered with a grid. With so-called iterative equation solvers, the displacement of the individual nodes of the grid is calculated. Schematically, the real component is broken down into many small virtual elements. Depending on the simulation, this is followed by a mathematical description of the interaction between these elements. The next step is to set up and solve the resulting system of equations. Finally, the results for each element are interpreted and read out [4].

A. Modelling of thermal shock tests on porous cordierite ceramics

Before the simulation of the thermal shock test of cordierite can be started, some presettings have to be defined. The first step is the creation of the virtual bodies. On the one hand, the solid cordierite-sample body in the form of a cube with a defined edge length of 33.16 mm and water as the fluid, which surrounds the sample body with a volume of 127.35 litres. In addition, different types of pores are inserted into the created test specimens. Subsequently, the created bodies are defined as volume bodies and additionally the contact surfaces are set. Finally, the solid and liquid bodies are defined.

TABLE 1. Material Data of cordierite, water and air

Material Data	Density [kg/m ³]	C _p (Specific Heat Capacity) [J/(kgK)]	Thermal Conductivity [W/(mK)]
Cordierite	2130	1000	0.708
Water	997	4184	0.600
Air	Ideal gas	1012	0.026

B. Pore Geometry

To investigate the influence of different pore geometries on the thermal shock resistance, three different pore types were chosen. The total pore volume of 20 % as well as the volume of each individual pore was kept constant in order to determine only the influence of the geometry. The volume of each individual pore is 10 mm³. Spherical, cuboidal and cylindrical macro pores were inserted into the body with the ANSYS 2019 R3 software.

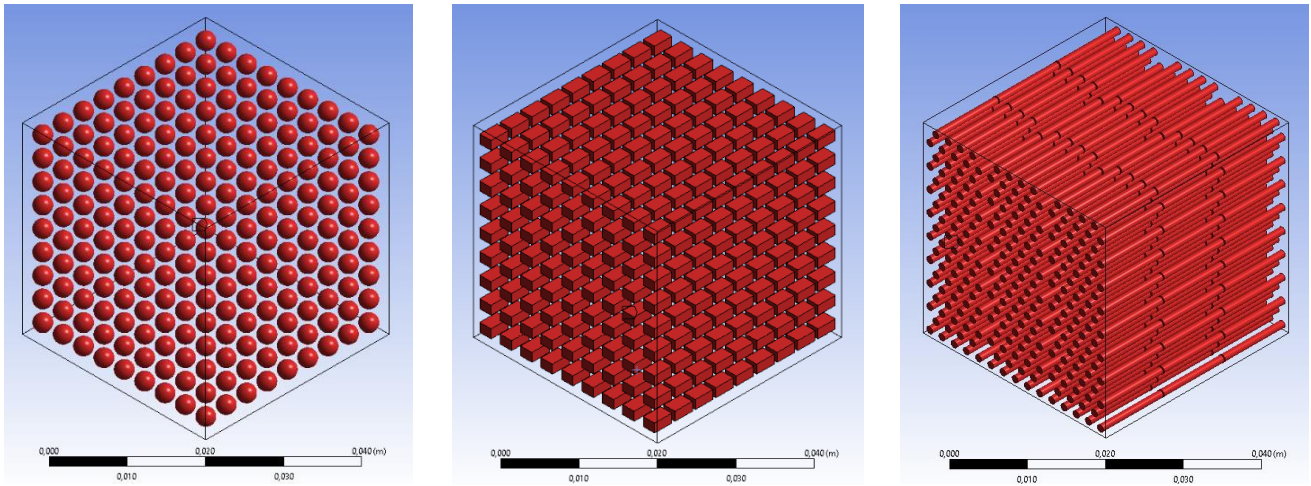


Fig. 1. Spherical (left), cuboid (middle) and cylindrical (right) pores aligned in their longest lateral expansion

For this purpose, the influence of porosity in general on the thermal shock properties will be investigated. The pore-specific influence and the orientation of the pores in the test specimen will also be determined

Figure 1 shows the three different pore geometries. As an example, these are only shown here in their longest lateral extension. The cuboid and cylindrical pore cubes were not only constructed in their lateral longest orientation, but also in all three spatial directions (xyz) in order to simulate the influence of the pore orientation. This was not necessary for the spherical pores, as they have the same properties in every spatial direction. A cube without pores was additionally simulated as a reference sample.

III. RESULTS AND DISCUSSIONS OF THE FLUID MECHANICS SIMULATIONS ON THERMAL SHOCK PROPERTIES

The simulation of the thermal shock treatment was carried out in the Fluent sub-programme of the simulation software. The temperature profile of the specimen was calculated as a function of time. The temperature distribution was simulated within 180 s in 1 s-intervals. The temperature profile of the specimens over time and the average tensile stresses that occur in the ceramic body during thermal shock were investigated.

A. General influence of the pores

In order to investigate the general influence of pores on the thermal shock resistance, temperature profiles of the differently porous samples were carried out over time during the thermal shock test. These were then compared with the non-porous zero sample (Fig. 2). The zero sample and the spherically porous sample are shown here as examples. A plane cut was made through the centre of the sample to see how the temperature profile inside the observed volume behaves during quenching. Figures 2 and 3 show the temperature profile inside the sample after 60 s. It is shown that there is hardly any difference at this time step in the temperature profile of the two samples.

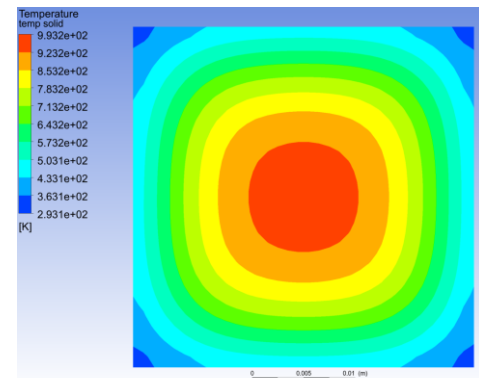


Fig. 2. Temperature profile at the time step of 60 s of the cordierite zero sample during the thermal shock test (720 °C)

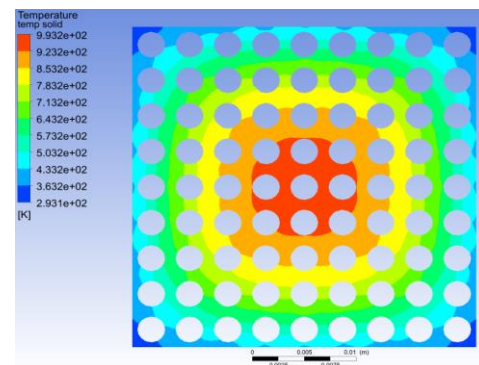


Fig. 3. Temperature profile at the time step of 60 s of the spherically porous cordierite sample during the thermal shock test (720 °C)

The maximum principal stresses in the workpiece were considered in order to demonstrate the more precise influence of pores. Figure 4 shows the maximum principal stresses of the porous samples compared to the zero sample. The exact maximum principal stresses can be found in Table 2. The largest maximum principal stress occurs in the zero sample.

TABLE 2. Maximum main tension of porous specimens with different percentages of orientation of the largest lateral expansion in each of the three spatial directions

Sample	zero-sample	cyl_xyz33	cyl_z100	cyl_z100_rad	cub_xyz33	cub_z100	cub_z100_rad	sph	sph_rad
Max. main tension [Pa]	1,64E+07	1,51E+07	1,56E+07	1,56E+07	1,18E+07	1,16E+07	1,15E+07	1,27E+07	1,28E+07
Percentage of largest lateral expansion aligned in axis x [vol.-%]	0,00	33,33	0,00	0,00	33,33	0,00	0,00	[-]	[-]
Percentage of largest lateral expansion aligned in axis y [vol.-%]	0,00	33,33	0,00	0,00	33,33	0,00	0,00	[-]	[-]
Percentage of largest lateral expansion aligned in axis z [vol.-%]	0,00	33,33	100,00	100,00	33,33	100,00	100,00	[-]	[-]

B. Specific pore influence

In order to compare the three types of pores with each other, they were each simulated with and without radiation in the body.

The samples with cylindrical pores have the highest value of 15.6 MPa among the porous samples. The cubic samples have the lowest maximum stress of 11.5 MPa. Figure 4 shows that the samples with and without radiation hardly differ from each other. Figure 4 shows all simulated results of the main stresses graphically. Among the porous samples, the samples with cylindrical pores generally have the worst properties. The cuboid pores with the lowest measured main stresses perform the best.

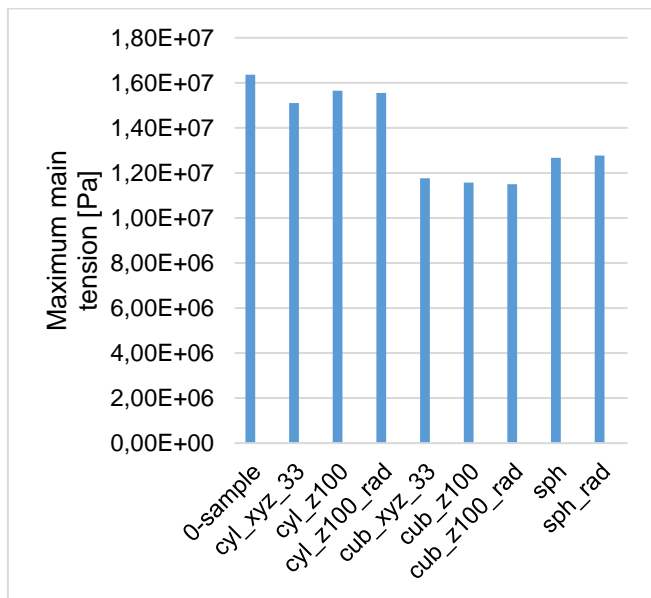


Fig. 4. Maximum main tension of specific pores and the zero-sample

The difference in maximum principal stress between the two specimens is 4.1 MPa and thus the cuboid pores withstand 26.28 % more thermal stress. Compared to the zero sample, they even perform better by 29.88 %.

The maximum main stresses occurring in the samples with radiation over the time course of 240 s are shown graphically in Figure 5. The zero sample has the highest peak and thus the highest stresses in the workpiece. In addition, the zero sample builds up and releases the stresses more quickly. The greatest stress occurs here after only a few seconds. The zero sample reaches this fastest after 8 s and the spherical sample the slowest after 16 s.

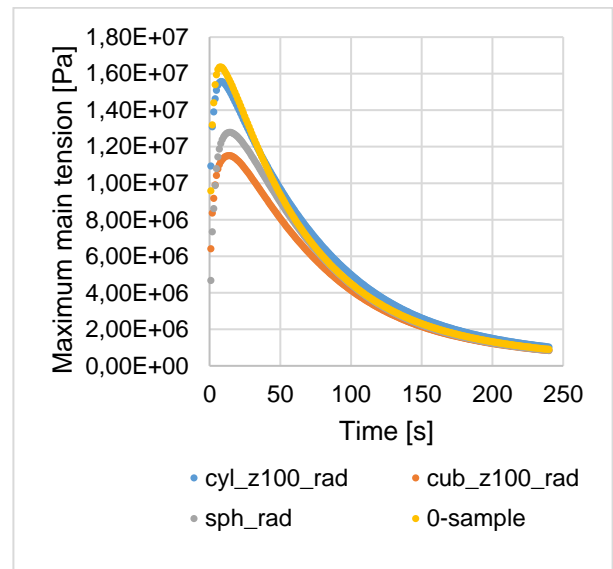


Fig. 5. Maximum main stresses occurring on the workpieces with radiation over time

C. Influence of pore orientation

Porosification particles can arrange themselves in a preferential orientation i.e. when extruding ceramic materials. Due to a possible preferential orientation and a targeted alignment of pores after firing, the material properties of the ceramic sample can differ from a sample with randomly aligned pores. For this purpose, only the cylindrical and cubic ones were investigated. Therefore, the pores were not only oriented in their longest lateral extension in one spatial direction, but equally distributed in all three spatial directions (Fig. 6 and 7).

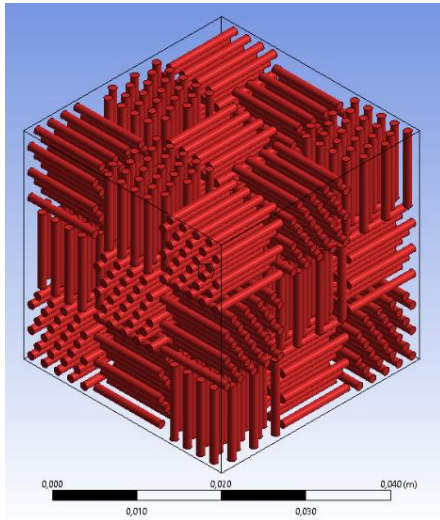


Fig. 6. Cylindrically aligned pores in all spatial directions

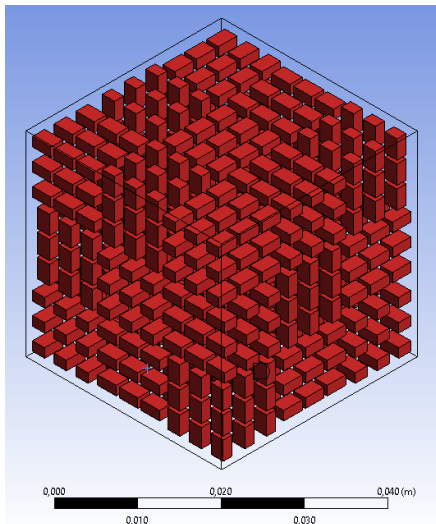


Fig. 7. Cuboidal aligned pores in all spatial directions

Due to the simulation results, there is no clear influence of the pore orientation on their maximum main stress. The differences in the resulting stresses due to the orientation of the pores are negligible concerning the test conditions.

IV. CONCLUSIONS

Based on the simulations, it can be seen that highest main stress during the thermal shock test occurs within the zero sample without pores. High stresses in the sample can cause cracks that can have a negative effect on the mechanical properties of the ceramic. Since these ceramics are to be used

as heat storage materials and are thus constantly exposed to high thermal stresses, the minimizing of thermal stress through specific porosity is a suitable method. All pores inserted into the ceramic result in an improvement of the thermal shock resistance. However, there are also differences between the individual pore geometries and their respective orientation. The samples with cubic and spherical pores have significantly lower stresses and are therefore more suitable than samples with cylindrical pores considered within this investigation. The radiation that only occurs in the pores is very low and therefore negligible. In summary, it can be said that pores in cordierite ceramics can lower the maximum principal stresses in the thermal shock test and can therefore be better suited as thermal storage materials than solid ceramic bodies.

REFERENCES

- [1] Federal Environment Agency Germany: <https://www.umweltbundesamt.de/themen/klima-energie/klimaschutz-energiepolitik-in-deutschland/szenarien-konzepte-fuer-die-klimaschutz>; 01.05.2021; 11:00
- [2] Federal government germany: [https://forschung-energiespeicher.info/footer/foerderinitiative-energiespeicher/](https://www.bundesregierung.de/statisch/jb11-12/Webs/Breg/DE/Themen/Jahresbericht_2011_2012/03_Energie/1_Energiewende/_node.html#:~:text=Nach%20der%20Reaktorkatastrophe%20von%20Fukushima%20hat%20die%20Bundesregierung,bis%20Ende%202022%20schrittweise%20aus%20der%20Kernenergie%20; 01.05.2021; 13:00
[3] Energy storage funding initiative, „forschung-energiespeicher.info,“ April 2011. Available: <a href=); 02.05.2021; 10:00
- [4] C. Gebhardt, Praxisbuch FEM mit ANSYS Workbench, Hanser-Verlag, 2018.

Comparison of a simulation-based with an analytical calculation of the temperature field of a laser process

Johannes Tröger

Ostbayerische Technische Hochschule Regensburg
Labor Lasermaterialbearbeitung
Technologie Campus Parsberg-Lupburg
Am Campus 1, 92331 Parsberg
johannes.troeger@st.oth-regensburg.de

Abstract—In laser processes, specific heat input into the workpiece is required. The prediction of the process-determining temperature field is helpful to estimate the influence of process parameters and material properties on the process sequence. The analytical calculation of the temperature distribution during the laser process considering real geometries and boundary conditions is possible only to a limited extent. Therefore, the temperature field, which is mainly influenced by the energy input due to laser radiation and heat conduction, is calculated using the finite element method. In this article, a calculation using FEM in COMSOL Multiphysics is compared to an analytical solution.

I. INTRODUCTION

The knowledge of the spatial and temporal temperature distribution in the workpiece is of central importance for all laser material processes, which basically only differ in the laser intensity used and the duration of laser material interaction. Knowledge of the temperature field is fundamental for analyzing the physical correlations in the workpiece. Thus, residual stresses, microstructure and distortion can be predicted and favorable process parameters can be derived [1].

Since the interplay of process and material parameters in laser processing is complex, the analytical calculation of the temperature field considering real geometries and boundary conditions is possible only to a limited extent. Therefore, the temperature field is calculated using the finite element method. In this work, the temperature distribution during welding is calculated by FEM simulation and compared to an analytical solution of the temperature field afterwards.

II. FUNDAMENTALS

The laser beam is defined in the global coordinate system with the beam propagation in the z -direction and a constant forwarding speed in the x -direction (see Figure 1). The workpiece is stimulated by the energy input of the laser beam locally, causing the material to heat up. The applied beam energy depends primarily on the feed rate of the laser v_x , the focus diameter of the laser beam d_f , as well as on the absorbed laser power P_{abs} , and the intensity distribution I . Especially when

processing metals, the absorbed power is strongly reduced by the reflectance at the workpiece surface. According to ISO 11146, the diameter of a laser beam is defined by the second momentum of the beam profile corresponding to four times the standard deviation ($d_f = 4\sigma$) of the intensity distribution along the major and minor axis of the beam [2].

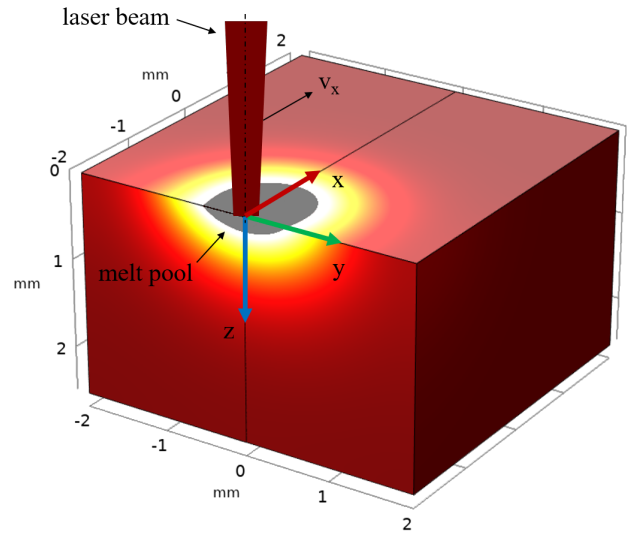


Figure 1. Schematic illustration of the laser process

The power density distribution \dot{Q} is calculated with the laser power P_{abs} absorbed at the component surface by Equation 1.

$$\dot{Q}(x, y, t) = \frac{P_{abs}}{2\pi\sigma^2} \cdot \exp\left(-\frac{(x - v_x \cdot t)^2 + y^2}{2\sigma^2}\right) \quad (1)$$

The heat flux arising from a beam source is dominated by the heat conduction in the solid, which depends on the thermal diffusivity with the thermal conductivity κ , the specific heat per unit volume c_p and the density ρ (see Equation 2).

$$D = \frac{\kappa}{c_p \cdot \rho} \quad (2)$$

Neglecting thermal radiation and convection, the temperature distribution T in the material is given with \dot{Q} by the following diffusion equation (see Equation 3) [3].

$$\frac{\partial T}{\partial t} - D\nabla^2 T = \frac{\dot{Q}}{c_p} \quad (3)$$

III. ANALYTICAL SOLUTION OF THE TEMPERATURE FIELD

The laser focus position is located on the workpiece surface ($z = 0$). With Green's function for the diffusion equation at the surface, the analytical solution of temperature distribution (Equation 1 - 3) is simplified by integration over time and volume (see Equation 4) [3].

$$T(x, z) = \frac{P_{abs}}{c_p} \times \int_0^\infty \frac{\exp\left[-\left\{\frac{[(x - v_x \cdot t)^2 + y^2]}{4D \cdot t} + \frac{z^2}{4D \cdot t}\right\}\right]}{\sqrt{\pi^3 D \cdot t} (2\sigma^2 + 4D \cdot t)} dt \quad (4)$$

Figure 2 shows the analytical solution of the temperature distribution (Equation 4) in the x-z-plane for a moving laser beam with the laser feed in x-direction and a Gaussian intensity distribution. The material chosen is aluminum.

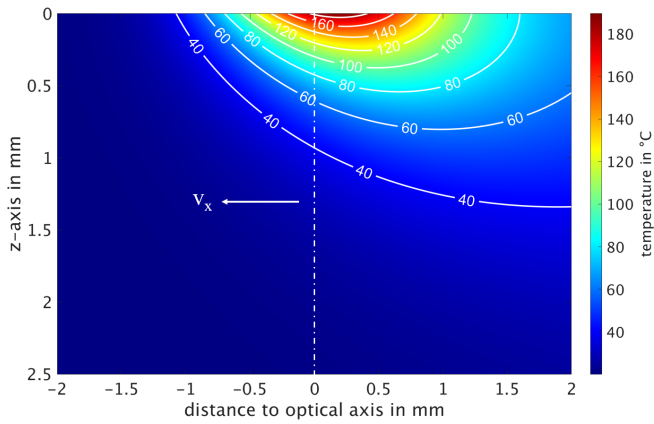


Figure 2. Analytical solution of the temperature distribution (absorbed laser power: $P_{abs} = 150 W$; feed rate: $v_x = 18 \frac{m}{min}$; laser focus position: $z = 0 mm$; spot radius: $\sigma = r/2 = 0.5 mm$; thermal conductivity: $\kappa = 238 \frac{W}{m \cdot K}$; specific heat capacity: $c_p = 900 \frac{J}{kg \cdot K}$; density: $\rho = 2700 \frac{kg}{m^3}$)

IV. FEM-SIMULATION OF THE TEMPERATURE FIELD

A. Geometry and Discretization

The simulation is based on a 3D model, since the temperature field depends on the x-axis, the y- and the z-direction. The model geometry is given by the component thickness (z-axis) assuming a weld specimen with a thickness of 2.5 mm. The width (y-axis) and the depth (x-axis) of the three-dimensional model are set to 2 mm, each.

Due to symmetry, only a half-model is simulated for more efficient calculation, where the plane of the mirror symmetry is defined by the x-z-plane and the optical axis of the laser beam is located at the origin of the coordinate system.

Due to the simple geometry of the workpiece, a mapped hexahedral meshing can be used. To be able to resolve the energy coupling of the laser beam into the material with sufficient accuracy, even for materials with high absorption coefficients, a graded mesh is applied for a higher mesh density at the surface region.

B. Material and Physics

For defining the material properties of the workpiece, the following values are assumed for an aluminum sheet:

- Thermal conductivity: $\kappa = 238 \frac{W}{m \cdot K}$
- Specific heat capacity: $c_p = 900 \frac{J}{kg \cdot K}$
- Density: $\rho = 2700 \frac{kg}{m^3}$

The simulation approach of the temperature field inside the workpiece is based on the physics "heat transport in solids" combined with the material properties and its geometric dimensions. Additionally, the initial temperature of the study is set to a constant value of 293 K as a boundary condition. By implementing the heat source as a surface boundary condition via a generally valid source term (see Equation 1), it is possible, to calculate the temperature for the focal laser position on the workpiece surface. Due to the neglect of heat radiation and convection at the component boundaries, all planes were defined as "thermal insulations". For discretization of the physical model, the biquadratic serendipity approach was preferred ensuring a fast convergence of the solution.

C. Solution of the Simulation Model

Figure 3 shows the resulting half model of the simulation study as a 3D temperature distribution of the laser process with the laser feed in the x-direction and the Gaussian intensity distribution.

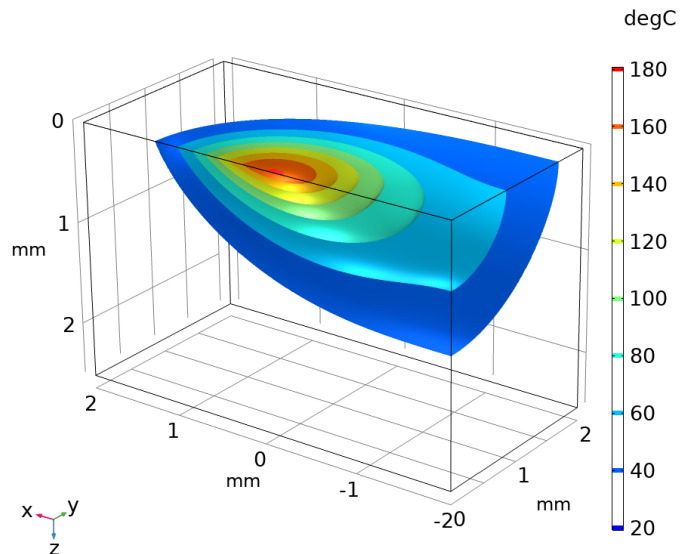


Figure 3. Temperature distribution of the FEM simulation (laser feed in x-direction, beam propagation in z-direction)

V. RESULTS

Figure 4 gives the relative error of the calculated heat amount compared to the analytical solution according to Equation 5 and shows that the simulation converges well against the analytical solution. The convergence time strongly depends on the choice of discretization, where the scaling factor sf is the number of elements of the mesh per unit length of 1 mm.

$$rel. error = \frac{|solution_{FEM} - solution_{analytical}|}{solution_{analytical}} \quad (5)$$

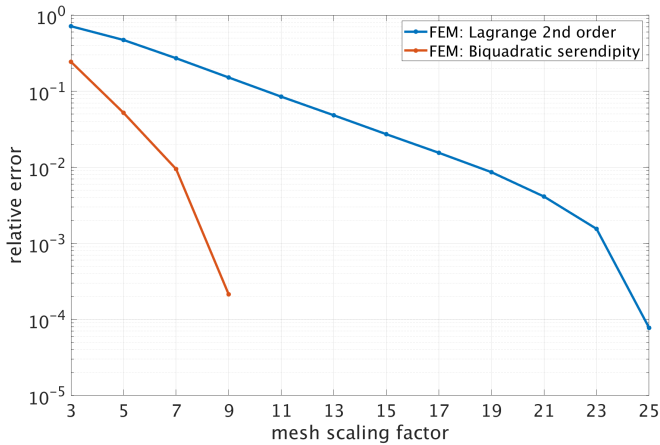


Figure 4. Relative error of the simulation as a function of the mesh size in a semi-logarithmic plot

Figure 5 shows the normalized total amount of heat deposited by the laser at the surface ($z = 0$). The biquadratic serendipity method converges with the analytical result (dotted line) already after the fourth iteration step of the mesh study. With the 2nd order Lagrangian discretization, a comparable result is achieved only after 12 iteration steps. This means that for the Lagrange 2nd order method, due to the simpler discretization approach, a much finer mesh is required to obtain comparable results.

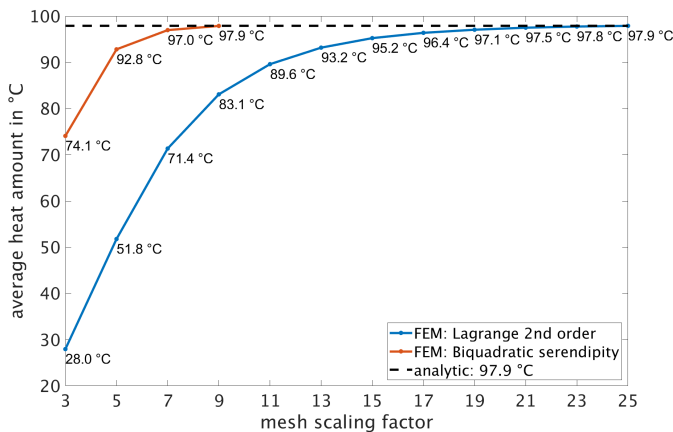


Figure 5. Total amount of heat deposited by the laser (normalized)

The temperature distribution along the laser feed direction also corresponds well with the calculated solution if the meshing is sufficiently accurate.

To compare the simulation result with the analytical solution, the temperature distribution at the component surface in the laser feed direction was evaluated for different levels of mesh discretization and plotted in comparison with the analytical solution (see Figure 6). Particular attention was paid to the temperature distribution at the surface of the solid, since this is the area where the process of heat coupling into the material takes place. In the remaining part of the body, only heat conduction takes place, which results in much lower temperature gradients compared to energy coupling. Analytical and simulation-based results coincide well for volume elements above 28000.

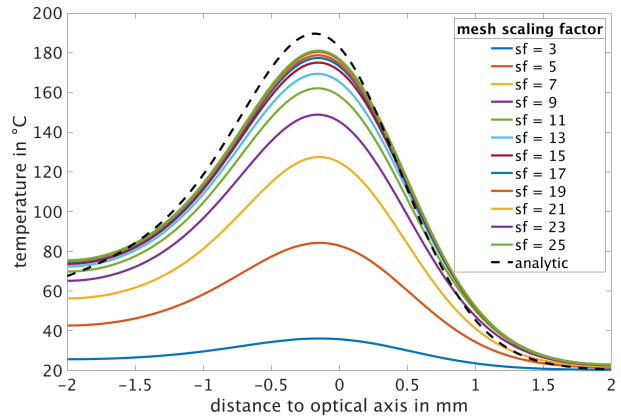


Figure 6. Temperature of the plane from laser propagation and laser feed at the specimen surface (discretization: Lagrange 2. order)

VI. SUMMARY AND OUTLOOK

To predict the spatial and temporal temperature distribution in laser material processing, a 3D FEM process simulation was set up. The computed temperature field coincides well with the analytic solution. For further verification, the surface temperature will be compared to pyrometer and infrared camera measurements, qualifying the model for simulation-based process layout.

By evaluating the simulation results at different feed rates, findings relating to the temperature gradient in front of the focal spot and the course of isotherms in the material can be obtained in the future. In addition, the model will be enhanced to develop a computer-aided method for process design and optimization for laser-based hot-melt bonding to allow a systematical identification of suitable process parameters with minimal experimental effort.

REFERENCES

- [1] H. Hügel, T. Graf, Laser in der Fertigung, Vieweg Teubner, Wiesbaden, 2009.
- [2] ISO 11146, Lasers and laser-related equipment - Test methods for laser beam widths, divergence angles and beam propagation ratios - Part 1: Stigmatic and simple astigmatic beams, 2005.
- [3] H. E. Cline, T. R. Anthony, „Heat treating and melting material with a scanning laser or electron beam” in Journal of Applied Physics 48, General Electric Research and Development Center, New York, 1977.

Improvement of the solid-liquid separation of biogas digestate with a starch based flocculant

Elisabeth Utz

Ostbayerische Technische Hochschule Amberg-Weiden
 Faculty of Mechanical Engineering / Environmental Technology
 Kaiser-Wilhelm-Ring 23, 92224 Amberg
 E-Mail: e.utz@oth-aw.de

Abstract—It was tried to improve the solid-liquid separation of an energy crop based biogas digestate. The aim was to get a dry matter (DM) rate ≤ 1.5 % (w/w) in the liquid fraction by a simple press separation. Without optimization, the liquid fraction had an average DM rate of 3.6 %. To improve this result, the separation pressure was reduced from 10 to 3 bar and a cationic polymer flocculant based on pea starch was added. A very high amount of 85 g polymer per kg DM was needed to sufficiently lower the DM rate. More preferable results were obtained at a dosage of 100 g polymer per kg DM. The previous addition of a $\text{Ca}(\text{OH})_2$ solution lowered the electrical conductivity from 23 to < 10 mS/cm but did not improve the flocculant efficiency. The diminution of the separation mesh size from 0.5 to 0.3 mm led to clogging and hardly affected the DM rate of the liquid fraction.

I. INTRODUCTION

Biogas digestate is the remaining from anaerobic digestion of manure and plants. Due to its partial resemblance to mineral fertilizers, especially regarding the amount of nitrogen, phosphorus and potassium it contains, it is often spread on the fields [12]. But since the plant availability of the nutrients is difficult to calculate, mineral fertilizers are additionally applied. In consequence, unused nitrogen is converted into nitrate and pollutes the groundwater [18], [11]. The excess of nitrogen also increases greenhouse-gas emissions, particularly nitrous oxide (N_2O), nitric oxide and nitrogen dioxide (NO_x) and ammonia (NH_3) [15]. According to the German Federal Environmental Agency, these emissions increase not least because of the increasing storage and spreading of biogas digestate [14]. Besides, if nitrate is leached out of the soil, it is no longer available to neutralize the protons of the nitrification [1]. As a result, the buffering capacity of the soil decreases until, finally, the soil is not able to resist pH change any longer and turns acidic.

With the amendment of the Fertilizing Ordinance from 2017, which entered into force on May 1st 2020 [2], the agricultural application of fertilizers, especially nitrogen and phosphorus, has been more severely restricted to prevent further groundwater pollution. In order to still agriculturally apply manure and biogas digestate, it is now often necessary to previously remove nitrogen.

Another problem is the uneven local distribution of manure and digestate. While animal farming leads to a high amount of manure and digestate in certain regions, areas where cultivation predominates depend on the application of

mineral fertilizers. The base chemical for nitrogen fertilizers is in the main ammonia, which is gained from atmospheric nitrogen with the energy-intensive Haber-Bosch-process. But due to the high water content of > 90 %, the transport of the digestate overage from one region to another is uneconomic as well. The nitrogen should therefore not only be removed from the digestate but also be recovered as a concentrated and better manageable mineral fertilizer. This way, it could be used in cultivation regions and the nitrogen cycle within the agriculture could be closed. Moreover, the energy for the Haber-Bosch-process could be saved.

II. DIGESTATE PROCESSING TREATMENTS

There are already some treatments to remove nitrogen from manure and digestate, the most established of which were analyzed in the research project 'GÄRWERT – GÄRprodukte ökologisch optimiert und WERTorientiert aufbereiten und vermarkten' [8], [9], [5]. All regarded treatments have the first step in common: a screw press separation. This leads to a fractionating not only of solid and liquid phase but also of nutrients: most of the phosphorus and the organic nitrogen remain in the solid fraction while the ammonium-nitrogen can be found predominantly in the liquid fraction [4]. The results of this study show that hardly any treatment is economically feasible. Technologies that require heat, e.g. drying and vacuum evaporation, are only profitable if the heat is free. That means the biogas has to be used in a local thermal power station and the resulting heat is not used otherwise. Ammonia stripping is financially attractive only if the processing objective is to remove nitrogen but not to reduce the volume. Moreover, the stripping process is here assumed to work at low pressure conditions and a temperature about 80 °C and is therefore also dependent on thermal energy. The volume reduction and nitrogen removal of the liquid phase by membrane technology (i.e. ultrafiltration and reverse osmosis) is the only process that is independent of heat. However, it is only profitable for high transport and distribution costs of the digestate because of the extremely high energy consumption of the ultrafiltration.

The development of a new membrane treatment that manages without ultrafiltration is assumed to improve the profitability of digestate processing. To ensure a high mass transfer and to prevent the membrane from fouling and scaling,

Table I
PARAMETERS OF THE DIGESTATE

Parameter	Digestate	Liquid fraction	Unit
ρ	1,025	1,001	kg/m ³
pH	7.7	7.8	
σ	22.7	22.7	mS/cm
DM rate	6.6	3.6	% (w/w)
TN _b	4.9	4.6	g/l
NH ₄ -N	–	2.31	g/l
COD	70.5	47.0	g O ₂ /l

however, the DM rate of the liquid fraction must not exceed 1.5 % (w/w). The aim of this work is to optimize the solid-liquid separation mechanically as well as chemically provided that the DM rate of the liquid fraction does not exceed 1.5 % and both fractions can basically still be used in agriculture. The reduction of the DM rate should ideally be obtained by screw press separation, since it is a simple, cheap and already current treatment method for biogas plants in Germany [19].

III. MATERIALS AND METHODS

A. Substrate analysis

To determine the DM rate referring to [3], the analyzed substrates were dried for 24 hours at 105 °C. The electrical conductivity of the liquid fraction and the pH value were measured with a WTW measuring station *inoLab® Multi 9620 IDS* using the *TetraCon® 925* measuring cell and the *SenTix® 980* electrode, respectively. The total nitrogen concentration (total nitrogen bound, TN_b) was measured in a 1:100 solution by cuvette test (*Hach® LCK 338 LATON* and *DR6000 UV-VIS Benchtop* Spectrophotometer). Likewise the ammonia-nitrogen (NH₄-N) was determined with the cuvette test *LCK 303* and the chemical oxygen demand (COD) with *LCK 014*.

B. Digestate

The digestate was collected from a mesophilic energy crop based biogas plant and was removed between secondary digester and storage tank. It is mainly composed of maize silage (85 %), whole-crop cereal (WCC) silage (12 %) and whole grain (3 %) and does not contain manure or biowaste. It has a fibrous consistency and a DM rate of approximately 6.3 %. A simple press separation with a mesh size of 0.5 mm and a pressure of 3 bar leads to a DM rate of still 3.6 % in the liquid fraction. The collected samples were kept in a refrigerator at 4 °C. For the experiments, the samples were warmed up to 20 °C in a water bath. Table I shows the relevant parameters of the raw digestate and the separated liquid fraction at 20 °C.

C. Flocculant

The majority of preliminary findings related to the flocculation of manure and digestate are based on polyacrylamide flocculants (PAM) [16], [10]. Although the biodegradability of these flocculants allows the application on agricultural fields,

their preparation requires acrylamide which is environmentally harmful. For that reason, the flocculant *Emfloc® ECG 750* by the *Emsland Group®* used in this case is based on pea starch. The polymer was received as an approximately 25 % solution that was diluted to a 2.5 % solution with purified water.

D. Flocculation process and press separation

The mixing process took place in a 2000 ml beaker filled with 600 g digestate at room temperature. The polymer was stirred in for 15 seconds with a near-wall, trapezoidal stirrer (*EKATO HOLDING GmbH*) to achieve a high contact rate. The stirring speed for the mixing process was 350 rpm, which corresponds to a torsional moment of approximately 4 Ncm. For the flocculation process itself, the mixture was stirred for 15 minutes with a speed of 30 rpm and a corresponding torsional moment of approximately 1 Ncm.

Between 200 and 250 g of the flocculated digestate were then separated in a laboratory Jar test press from *Afmitech Friesland B.V.™* with a mesh size of 0.5 mm and a pressure of 3 bar, maintained for 10 minutes. For comparison, a mesh size of 0.315 mm and a pressure of 10 bar were also tested. To further examine the impact of the separation mesh size, the digestate has been screened with different mesh sizes. Therefore, the sieve stack was shaken for 5 minutes on a screening machine with an amplitude of 0.3. This was done for the original digestate and a sample that was flocculated with 50 g of polymer per kg DM. 100 g of sample were taken for each screening.

E. Pretreatment with lime slurry

Since the flocculant efficiency was much lower than expected, it was tried to increase the efficiency by decreasing the electrical conductivity σ [7], [10]. This was achieved by adding a 10 % (w/w) lime slurry (Ca(OH)₂) solution, which was stirred in for 90 seconds at 350 rpm before the flocculant was added. The calcium was assumed to precipitate CaCO₃ and thus reduce σ . The electrical conductivity could also be reduced by acidification. Since this would lead to foaming on the one hand and would on the other impair the conditions for the further membrane treatment of the liquid fraction though, this option was not tested.

IV. RESULTS AND DISCUSSION

A. Flocculant dosage

As it can be seen in Figure 1, a reduction of the DM rate ≤ 1.5 % by means of a polymer flocculant and press separation is basically possible with at least 85 g polymer per kg DM. But despite this already high amount of flocculant, the liquid fraction was still opaque and contained visible particles that did not noticeably sediment within 24 hours. When 98 g polymer per kg DM were added, an obvious separation of solid and liquid fraction could already be observed during the flocculation process. The specific values for viscosity and turbidity of the liquid fractions have not been measured so far, but the liquid fraction was visibly sheerer and less viscous than for the former dosages. This could also be the reason

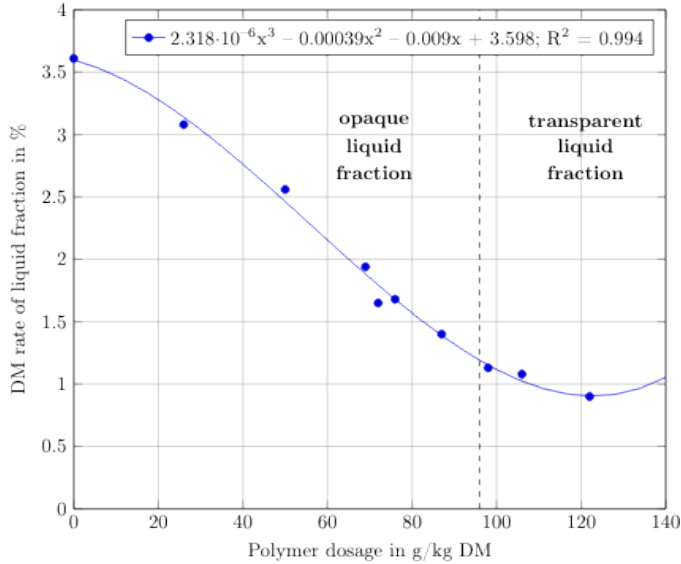


Figure 1. DM rate of liquid fraction dependent on polymer dosage

why particles that remained in the liquid fraction settled down quite quickly. The DM rate decreased to 1.13 % and could probably have been further reduced by sedimentation. The severely different liquid fractions have to be further analyzed and compared.

A further increase of the polymer dosage up to 122 g polymer per kg DM again lowered the DM rate to 0.9 %. Higher dosages have not been tested. The plot in Figure 1 implies that this may have been the highest dosage before the flocculation results get worse with increasing dosage. Even disregarding the costs for the flocculant, however, the required amount of at least 85 g polymer per kg DM leads to an excessive volume increase (55 l of 2.5 % polymer solution per m³ digestate). Furthermore, polymer flocculant remaining in the liquid phase will quite likely have a detrimental effect on membranes [17]. A reduction by press separation after a simple flocculation with Emfloc[®] ECG 750 is therefore not recommendable.

B. Calcium addition

As predicted, the addition of Ca(OH)₂ decreased σ . However, to remain under the value of 10 mS/cm that is mentioned as a threshold in [7], a high amount was needed. As Figure 2 and Figure 3 illustrate, a dosage of 7.7 g Ca²⁺ per liter digestate decreased σ to about 10 mS/cm and raised the pH value up to 10.3. But despite the much lower conductivity, the efficiency of the flocculant was even worse when Ca(OH)₂ was added. This could perhaps be explained by the high amount of Ca²⁺ which may already have changed the surface charge. In this case, an anionic flocculant would have been needed. With increasing lime dosage, a decline of the water content in the solid fraction was observed.

The high amount of Ca(OH)₂ needed to decrease σ and increase the pH value is explained by the extremely high buffering capacity of the digestate. Due to the anaerobic milieu during the digestion, the digestate is saturated with carbon

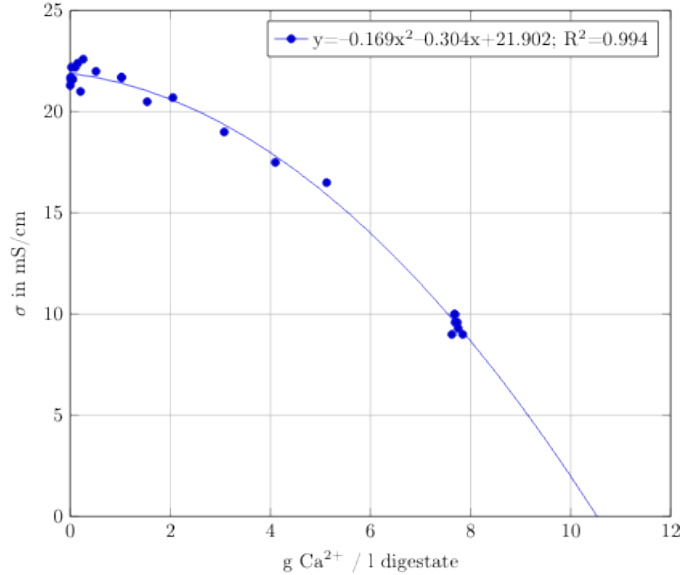


Figure 2. Dependence of σ on lime dosage

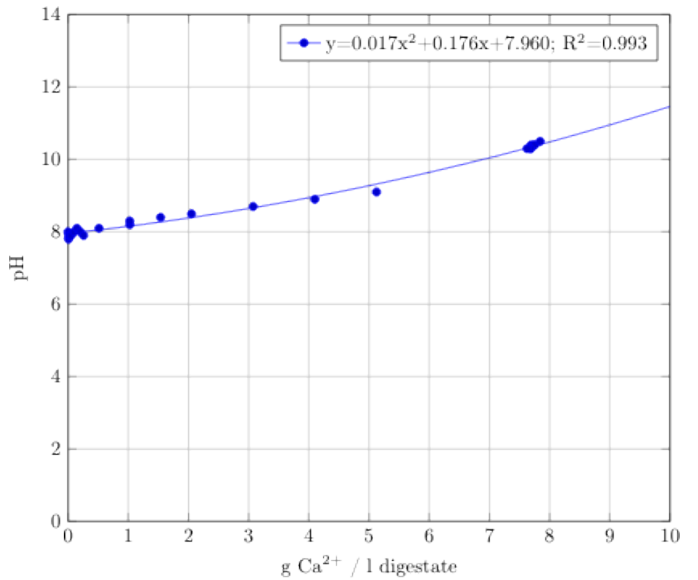


Figure 3. Dependence of pH on lime dosage

dioxide and has therefore a bicarbonate buffer. Since the carbonate was precipitated by calcium, the buffer was eliminated which can explain the flat incline of the pH-curve until the addition of 5 g Ca²⁺ per l digestate and the steeper increase afterwards. The ammonia-ammonium-equilibrium acts as an additional buffer because of its dependence on the pH value.

C. Separation parameters

The pressure increase up to 10 bar reduced the water content of the solid fraction, but it had negative effects on the DM rate of the liquid fraction. The separation with a mesh size of only 0.315 mm led to clogging and thus a high weight proportion caused by a high water content of the solid fraction. When separating with both, a 0.500 and a 0.315 mm sieve

in succession, clogging could be prevented and the smaller sieve restrained few additional solids, but the flocculant dosage could not be distinctly reduced to get similar results.

Figure 4 and Figure 5 show the results of the screening experiment with different mesh sizes. With the same mesh size, the DM rate of the fine fraction – original as well as flocculated – is about 1 % higher than that one of the liquid fraction after press separation. This can be explained by the missing pressure. A large part of the liquid did not pass the sieve but was held back in the coarse fraction so that the solids in the fine fraction are less 'diluted'. The absence of pressure also explains the low weight proportion of the liquid fractions in Figure 5 which is not even half of the liquid weight proportion after press separation. Figure 5 illustrates that there seem to be at least two 'peaks' for mesh sizes in the original digestate: one for $d = 1$ mm and one for $d = 0.25$ mm. Varying the mesh size in between these values did not particularly affect the weight proportion of the separated fractions for the original digestate. This is explained by the degradation processes in the biogas reactor that leave decomposition products of certain similar sizes. A strong impact of the flocculant could be regarded for the mesh sizes 2 and 0.25 mm. In both cases, the weight proportion of the flocculated digestate was about 15 % lower than for the untreated digestate. It is assumed that loose flocks with a high water content were built and held back by the sieve. It is not clear, why the flocculated digestate passed the 0.125-mm-sieve better than the untreated substrate. Maybe, particles in this size have been agglomerated by the flocculant and did not retain the water any longer. Since the difference is only about 7 g, it could also be due to the heterogeneity of the digestate that makes it difficult to always take similar samples.

In general, the impact of flocculation is higher than the impact of the mesh size. Probably the press cake acts as an additional filter that approximately corresponds to the tested smaller mesh size of 0.315 mm. With a sieve of this mesh size, the press cake became so dense that a part of the digestate could not pass and was therefore not separated.

V. CONCLUSION

The demanded reduction of the DM rate of digestate by flocculation with a starch based flocculant and subsequent press separation is possible, but can not be recommended because of the high amount of polymer solution. The addition of $\text{Ca}(\text{OH})_2$ decreases the electrical conductivity but simultaneously impairs the flocculant efficiency. A smaller mesh size would either hardly cause any improvement or cause technical problems such as clogging. Therefore, a two-step-separation, as it was performed for example in [6], may be necessary to preprocess the digestate. If the first separation step focuses on dewatering the solid fraction, the addition of lime could, on one hand, improve the separation and even remove some phosphorus from the liquid fraction. On the other hand, this addition may impair the flocculant efficiency and therefore the separation result of the decantation as second step. To clarify these presumptions, the impact of lime on several separation

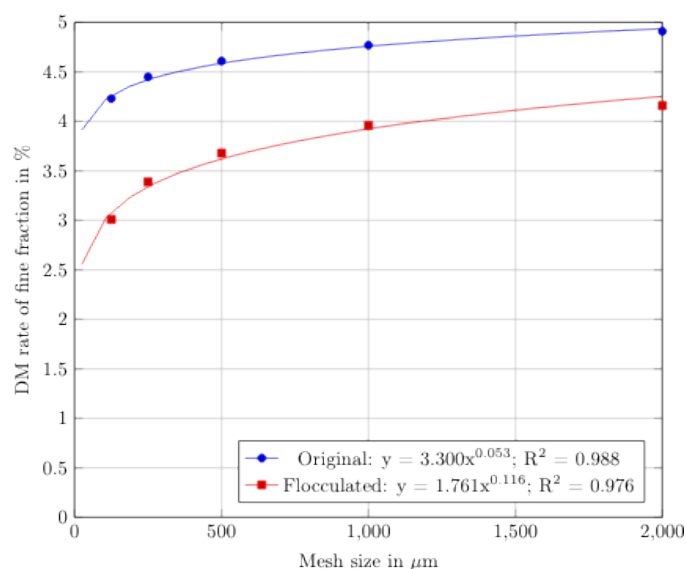


Figure 4. DM rate of fine fraction dependent on mesh size

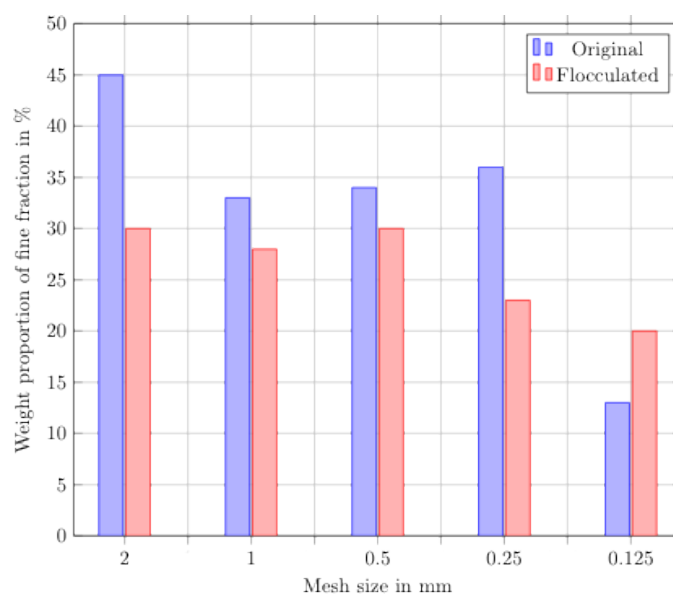


Figure 5. Weight proportion of fine fraction dependent on mesh size

factors has to be further examined. Another approach could be a combination of anionic and cationic flocculants as it is proposed in [13].

ACKNOWLEDGMENT

The author would like to thank the Emsland Group® for supplying the flocculant Emfloc® ECG 750.

REFERENCES

- [1] N. Bolan, M. Hedley, and R. White, "Processes of soil acidification during nitrogen cycling with emphasis on legume based pastures," *Plant and Soil*, vol. 134, pp. 53–63, 1991.
- [2] Bundesministerium für Ernährung und Landwirtschaft, "Verordnung zur Änderung der Düngeverordnung und anderer Vorschriften vom 28.04.2020," *Bundesgesetzblatt*, pp. 846–861, 2020. [Online]. Available: https://dejure.org/BGBl/2020/BGBl_I_S_846

- [3] Deutsches Institut für Normung e.V., Ed., *DIN EN 12880:2001-02, Characterization of sludges – Determination of dry residue and water content; German version EN 12880:2000*. Berlin: Beuth Verlag, 2001.
- [4] Fachagentur Nachwachsende Rohstoffe e.V., *Leitfaden Biogas*, 7th ed., Gülzow, 2016. [Online]. Available: https://www.fnr.de/fileadmin/allgemein/pdf/broschueren/Leitfaden_Biogas_web_V01.pdf
- [5] M. Fechter and M. Kraume, “GÄRWERT Teilvorhaben 2: Großtechnische Messdatenerfassung und -evaluation,” Fachagentur Nachwachsende Rohstoffe e.V., Tech. Rep., 2017. [Online]. Available: blob:resource://pdf.js/e5531844-cf6b-43d0-b979-e7927d559550#filename=Schlussbericht_TV2_Messdatenerfassung.pdf
- [6] T. Gienau, “Energieeffiziente Gärrestaufbereitung – Auswirkung verschiedener Vorbehandlungen auf die Ultrafiltration und Umkehrosmose von Gärresten,” Ph.D. dissertation, Technische Universität Berlin, 2018. [Online]. Available: https://depositonce.tu-berlin.de/bitstream/11303/7780/4/gienau_tobias.pdf
- [7] J. Gregory, *Particles in water : properties and processes*. Boca Raton, FL London: Taylor & Francis IWA, 2006.
- [8] C. Herbes, J. Dahlin, S. Wulf, U. Roth, M. Kraume, M. Fechter, K. Möller, and I. Petrova, “GÄRWERT – GÄRprodukte ökologisch optimiert und WERTorientiert aufbereiten und vermarkten,” Fachagentur Nachwachsende Rohstoffe e.V., Tech. Rep., 2017. [Online]. Available: blob:resource://pdf.js/d5d734dc-a44d-4621-821c-0b79fc078200#filename=Schlussbericht_gemeinsamer_Teil.pdf
- [9] C. Herbes, U. Roth, S. Wulf, and J. Dahlin, “Economic assessment of different biogas digestate processing technologies: A scenario-based analysis,” *Journal of Cleaner Production*, vol. 255, no. 120282, 2020.
- [10] M. Hjorth, K. V. Christensen, M. L. Christensen, and S. G. Sommer, “Solid—liquid separation of animal slurry in theory and practice. a review,” *Agronomy for Sustainable Development*, vol. 30, no. 1, pp. 153–180, 3 2010.
- [11] I. Jakobs, F. Grimm, L. Keppner, and F. Hilliges, “Nitratbericht 2020,” Bundesministerium für Ernährung und Landwirtschaft (BMEL) and Bundesministerium für Umwelt, Naturschutz und nukleare Sicherheit (BMU), Tech. Rep., 2020. [Online]. Available: https://www.bmu.de/fileadmin/Daten_BMU/Download_PDF/Binnengewasser/nitratbericht_2020_bf.pdf
- [12] M. Koszel and E. Lorencowicz, “Agricultural use of biogas digestate as a replacement fertilizers,” *Agriculture and Agricultural Science Procedia*, vol. 7, pp. 119–124, 2015.
- [13] G. Petzold, S. Schwarz, and K. Lunkwitz, “Flockungsmittelkombinationen zur Steigerung der Effektivität von Flockungsprozessen,” *Chemie Ingenieur Technik*, vol. 74, pp. 438–442, 2002.
- [14] Umweltbundesamt, “Daten zur Umwelt 2018,” 2018. [Online]. Available: www.umweltbundesamt.de/publikationen/daten-zur-umwelt-2018-umwelt-landwirtschaft
- [15] United Nations Framework Convention on Climate Change, “Estimation of emissions from agriculture,” 2004. [Online]. Available: <https://unfccc.int/resource/docs/2004/sbsta/inf04.pdf>
- [16] United States Department of Agriculture, *Environmental Engineering*, 2019, ch. 4. [Online]. Available: https://www.nrcs.usda.gov/wps/portal/nrcs/detail/?cid=nrcs141p2_024573
- [17] J. Wagner. Membrane filtration handbook. [Online]. Available: <http://www.wagnerdk.dk/Downloads.htm>
- [18] L. Wang, A. S. Butcher, M. E. Stuart, D. C. Gooddy, and J. P. Bloomfield, “The nitrate time bomb: a numerical way to investigate nitrate storage and lag time in the unsaturated zone,” *Environmental Geochemistry and Health*, vol. 35, no. 5, pp. 667–681, 6 2013.
- [19] D. Wilken *et al.*, “Digestate as fertilizer,” 2018. [Online]. Available: https://www.biogas.org/edcom/webfbvnsf/id/BJHCPA-DE-Digestate-as-Fertilizer/protect\T1\textdollarfile/Digestate_as_Fertilizer.pdf

Strain-Induced Embrittlement at Elevated Temperatures of Heat-Resistant Steel 16Mo3

Niklas Whittlesey

Department of Mechanical, Automotive and
Aeronautical Engineering
Munich University of Applied Sciences
Munich, Germany
Email: whittles@hm.edu

Abstract—The heat-resistant material 16Mo3 was investigated with respect to its strength at room temperature, 300 °C and 500 °C. The microstructure and chemical composition were evaluated. Fracture surfaces of all test samples were observed by using SEM. The tensile tests showed embrittlement at 300 °C, which can be explained by the formation of blocks at strain-induced dislocations. The blockages are caused by the sufficiently high diffusion rate of nitrogen at elevated temperatures to dislocation sites of the microstructure. Fracture surfaces present a reduction of dimples at 300 °C. In addition, the Portevin-Le Chatelier phenomenon was observed. The effect of dynamic strain ageing was discussed and related. Especially for heat exchangers and steam generators, the embrittlement range of 300 °C can be relevant, as embrittlement can reduce the service life.

I. INTRODUCTION

The ferritic steel 16Mo3 1.5415 is commonly used for heat exchangers and steam generators. The temperature loading conditions for these applications typically range from 200 to 500 °C. Since the low-alloy steel is low-cost, it is widely used. In addition, wall thickness allowances are very conservative and are often simply assessed. This shows the demands of the steel, which are very low. Nevertheless, fatigue failure due to cyclic temperature changes has become increasingly apparent in recent years. The behaviour of 16Mo3 is largely unexplored in comparison to higher-grade high-temperature materials such as P91, which has been researched in detail in the context of the matter project. One reason for the lack of information is certainly the price of the material, as safety allowances can be given very generously.

For the material 16Mo3, the cyclic behaviour at elevated temperatures could be investigated. At 200 °C, an initial softening and softening process is followed by a softening until failure of the sample. At 500 °C, the steel shows a continuous softening process after a short softening [1, 2].

In the further course of this work, the static strength at elevated temperatures is to be verified. It is suspected that strain-induced embrittlement takes place in the temperature range relevant to practical use. For this purpose, the uniaxial tensile test is carried out.

II. MATERIAL AND EXPERIMENTAL DETAILS

The material investigated was analysed using optical emission spectrography, and the composition is shown in following

table. The microstructure can be seen in fig. 1 where clearly the ferritic and bainitic grains can be seen. Due to low carbon content bainitic grains occur more less than ferritic. Furthermore appear large and small ferritic grains which were measure from 10 to 50 µm in size. It is suspected that a poor manufacturing process is the cause of this. Due to high ferrite content this steel is highly prehaustinated for welding processes.

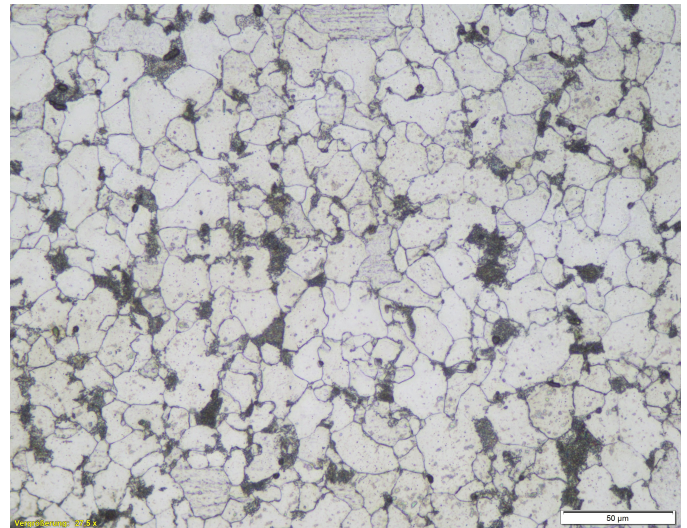


Figure 1: Ferritic-bainitic microstructure

Table I: Chemical composition of studied steel 16Mo3 in wt.%

C	Si	Mn	P	S	N	Cu	Cr	Ni	Mo
0,2	0,22	0,74	0,008	0,003	0,01	0,16	0,1	0,11	0,26

The heat treatment of high-temperature steels is mainly aimed at the formation of a ferritic-bainitic structure. This is characterised by a low carbon, solid solution, the bainitic ferrite, in acicular or plate form. The transformation from austenite produces a high dislocation density with an arrangement in dislocation cells. Furthermore, finely distributed carbides are present, either between the needles of the bainitic ferrite or within the plates [3].

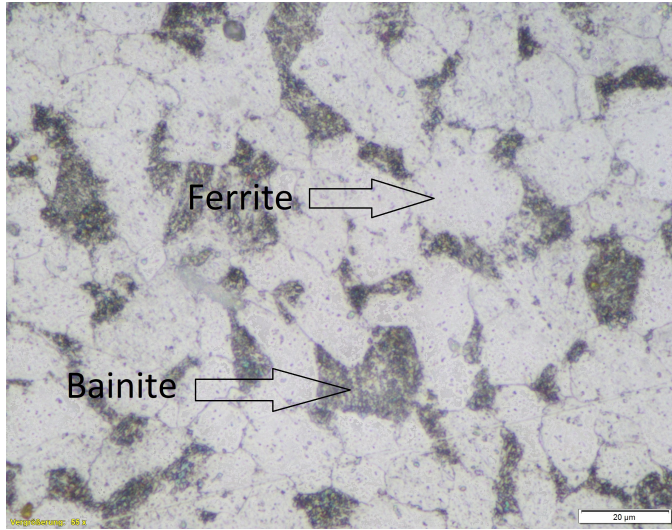


Figure 2: Ferritic-bainitic microstructure with detailed bainitic grains

The tensile specimens were taken from a seamless tube by machining. The orientation of the specimen is in axial direction to the tube. The wall thickness corresponding to the sample thickness was left in its original state. The following studies refer to the material 16Mo3 (1.5415). The tensile test was carried out according to DIN EN ISO 6892-2 and was performed at room temperature, 300 and 500 °C. A strain rate of $7 \cdot 10^{-6} s^{-1}$ were used till yield point, after $1,4 \cdot 10^{-3} s^{-1}$. For each experiment sample were 3 measured and the mean value given. Finally, the fracture surfaces of the tensile specimens are examined under the scanning electron microscope (SEM). In particular, the fracture behaviour is assessed.

In order to assess the fracture behaviour the tested samples are examined by using SEM. The formation of dimples is examined.

III. RESULTS AND DISCUSSION

The results of the tests carried out are presented and discussed in the following. The table below shows the results of the tensile tests. Clear embrittlement at 300 °C was observed. The increase in hot strength and the decrease in elongation at break are the indicators for this.

Table II: Results of tensile tests

	$R_{p0,2}$ [MPa]	R_m [MPa]	A [%]
20 °C	359,11	547,89	11,87
300 °C	402,11	623,32	9,58
500 °C	269,22	325,05	8,01

In fig. 3, the stress-strain diagram is discussed in which all tests are shown for better comparability. The tension profiles

of the respective temperatures are marked accordingly. In addition, detailed sections at 300 and 500 °C are inserted. In the area of the elastic range, a decrease of the Young's modulus with increasing temperature can be observed, this is in line with expectations and corresponds to the theoretical principles [1, 2, 3].

The results show maximum strength at 300 °C. The lowest tensile strength was found at 500 °C. Compared to room temperature, the elongation at break decreased at 300 °C. The lowest elongation at break was measured at 500 °C. From the results, it can be concluded that embrittlement occurs at 300 °C, as an increase in strength and decrease in elongation at break was observed. A closer look at the stress curves revealed the Portevin-Le Chatelier effect at 300 and 500 °C, see detailed sections. The stress oscillation occurs periodically on the graph line after the yield point [4]. In the literature [5, 6, 7], the mechanism of plastic instability phenomenon associated with the Portevin-Le Chatelier effect in Fe-Mn alloys at an elevated temperature is generally attributed to a dynamic strain aging effect.

The increase in strength in the range of 300 °C is known as blue brittleness and can be explained as follows. If there is enough dissolved nitrogen in the steel, it diffuses into the dislocation areas and blocks the dislocations. The steel becomes brittle. Between 200-300 °C, the diffusion speed of the N atoms is so high that embrittlement occurs in such steels during deformation. Nitrogen has been detected, see chemical composition. This leads to an increase in tensile strength and hardness with a simultaneous decrease in ductility. A further increase in temperature also causes increasing softening here. Furthermore the diffusion rate of nitrogen atoms in steel is so high that they can immediately follow a deformation. Due to their small size, the nitrogen atoms accumulate in the tensile stress area of the dislocation and block it. The result is increased strength with greatly reduced ductility [8, 9, 10, 11].

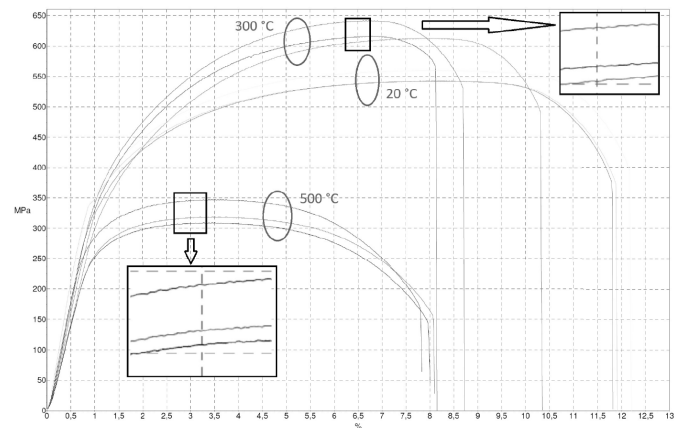


Figure 3: Stress-strain diagram at different temperatures. Detailed cuttings are presenting the Portevin Le Chatelier phenomenon.

In the following, the results of the SEM investigations are shown and discussed.

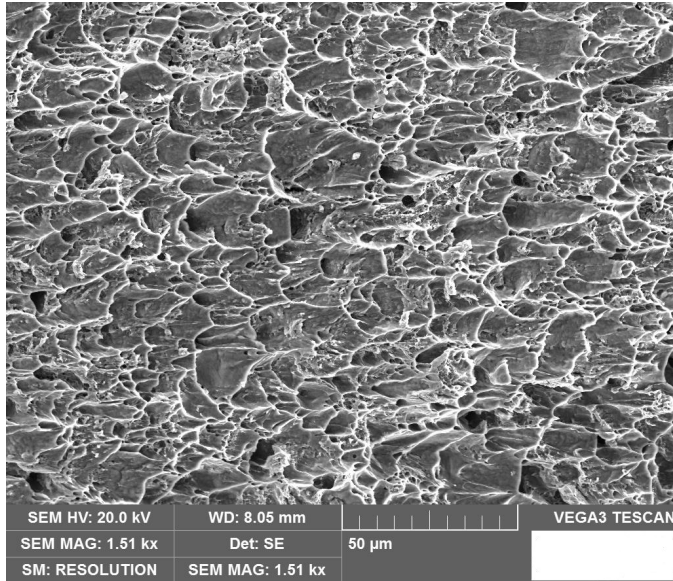


Figure 4: Fracture surface at 20 °C

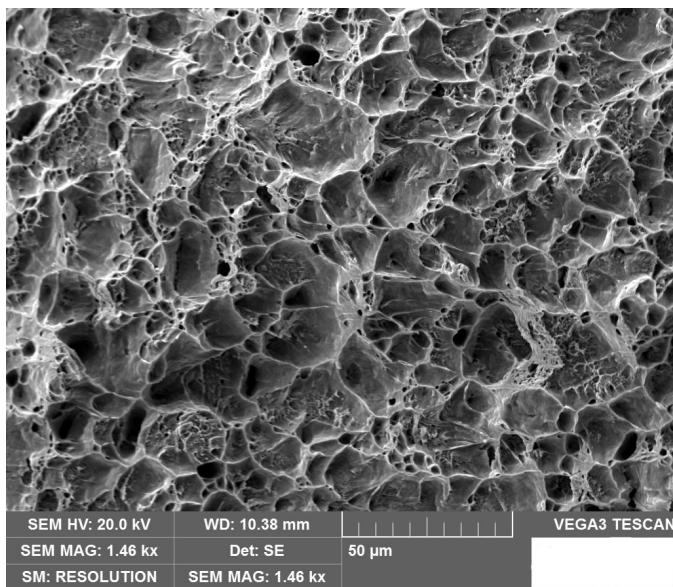


Figure 5: Fracture surface at 300 °C

Fig. 4 presents the fracture surface at 20 °C. Numerous and strong dimples formations can be seen which indicate a ductile behaviour. Fig. 5 presents the fracture surface at 300 °C. There are significantly fewer dimples than in Fig. 4 and the formation is also less extensive. The result of the embrittlement previously described in tensile tests can also be observed here. Fig. 6 shows the fracture surface at 500 °C which is accompanied by a strong decrease in strength, which can be observed in the microstructure.

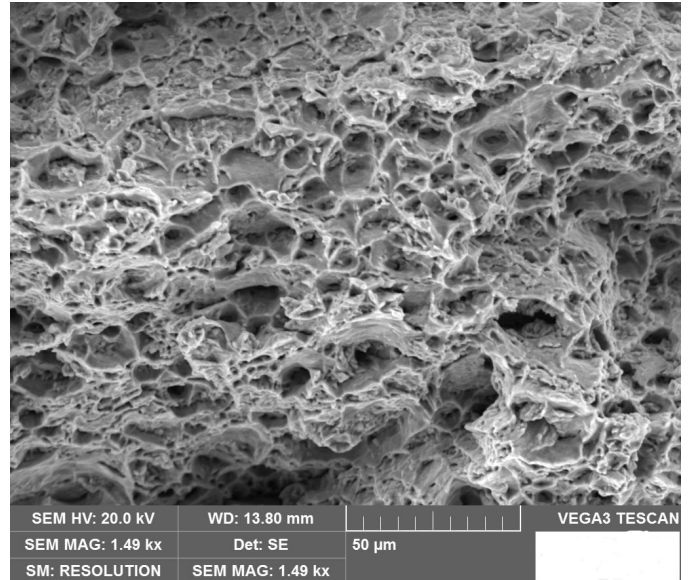


Figure 6: Fracture surface at 500 °C

IV. SUMMARY AND CONCLUSIONS

Tensile specimens in the axial direction were taken from a seamless tube of the material 16Mo3. Microstructural analyses, chemical composition and tensile properties were tested at room temperature, 300 °C and 500 °C. The microstructure and chemical analysis did not show any irregularities. The tensile tests demonstrated the Portevin-Le Chatelier phenomenon. Furthermore, an embrittlement in the range at 300 °C could be determined, which can be described by the diffusion of nitrogen at dislocations. For heat exchangers and steam generators, the range at 300 °C should be particularly limited. The tensile tests demonstrated the Portevin-Le Chatelier phenomenon. Furthermore, an embrittlement in the range at 300 °C could be determined which can be described by the diffusion of nitrogen at dislocations. Fracture surfaces of different test temperatures were evaluated by using SEM. Test specimen at 300 °C indicate a decrease of dimples which accompanied with decrease of ductile behavior.

For heat exchangers and steam generators, the range at 300 °C is particularly relevant. In addition relevant components must endure frequent changes in expansion. Embrittlement of the material can lead to a reduction in service life with regard to cyclic strain.

For future components made of 16Mo3 the temperature area of 300 °C with cyclic strain behavior should be avoided.

REFERENCES

- [1] Markus Hoffmann and Horst Biermann. “Static and Cyclic Deformation Behavior of the Ferritic Steel 16Mo3 Under Monotonic and Cyclic Loading at High Temperatures”. In: *steel research international* 83.7 (2012), pp. 631–636. ISSN: 16113683. DOI: 10.1002/srin.201100238.
- [2] D. Kulawinski et al. “Fatigue behaviour of 16Mo3 steel at elevated temperatures under uniaxial as well as biaxial-planar loading”. In: *Fatigue & Fracture of Engineering Materials & Structures* 40.6 (2017), pp. 909–923. ISSN: 8756758X. DOI: 10.1111/ffe.12551.
- [3] Hans Jürgen Maier, Thomas Niendorf, and Ralf Bürgel. *Handbuch Hochtemperatur-Werkstofftechnik: Grundlagen, Werkstoffbeanspruchungen, Hochtemperaturlegierungen und -beschichtungen. 5., überarbeitete und erweiterte Auflage.* Wiesbaden: Springer Vieweg, 2015. ISBN: 978-3-658-10590-7. DOI: 10.1007/978-3-658-10591-4. URL: <http://search.ebscohost.com/login.aspx?direct=true&scope=site&db=nlebk&AN=1071178>.
- [4] Barbara Grzegorzczuk et al. “Effect of Deformation Temperature on the Portevin-Le Chatelier Effect in Medium-Mn Steel”. In: *Metals* 9.1 (2019), p. 2. DOI: 10.3390/met9010002.
- [5] X. G. Wang, L. Wang, and M. X. Huang. “Kinematic and thermal characteristics of Lüders and Portevin-Le Châtelier bands in a medium Mn transformation-induced plasticity steel”. In: *Acta Materialia* 124 (2017), pp. 17–29. ISSN: 13596454. DOI: 10.1016/j.actamat.2016.10.069.
- [6] Binhan Sun et al. “Discontinuous strain-induced martensite transformation related to the Portevin-Le Chatelier effect in a medium manganese steel”. In: *Scripta Materialia* 133 (2017), pp. 9–13. ISSN: 13596462. DOI: 10.1016/j.scriptamat.2017.01.022.
- [7] Michael Callahan et al. “Coincidence of strain-induced TRIP and propagative PLC bands in Medium Mn steels”. In: *Materials Science and Engineering: A* 704 (2017), pp. 391–400. ISSN: 09215093. DOI: 10.1016/j.msea.2017.08.042.
- [8] Eckart Doege and Bernd-Arno Behrens. *Handbuch Umformtechnik.* Berlin, Heidelberg: Springer Berlin Heidelberg, 2016. ISBN: 978-3-662-43890-9. DOI: 10.1007/978-3-662-43891-6.
- [9] I. E. Dolzhenkov. “Influence of deformation rate on the blue brittleness temperature and dislocation density of carbon steel”. In: *Metal Science and Heat Treatment* 9.6 (1967), pp. 423–426. ISSN: 0026-0673. DOI: 10.1007/BF00657585.
- [10] I. E. Dolzhenkov. “Elongation and reduction of carbon steels at blue brittleness temperatures”. In: *Metal Science and Heat Treatment* 11.4 (1969), p. 321. ISSN: 0026-0673. DOI: 10.1007/BF00653207.
- [11] I. E. Dolzhenkov. “The nature of blue brittleness of steel”. In: *Metal Science and Heat Treatment* 13.3 (1971), pp. 220–224. ISSN: 0026-0673. DOI: 10.1007/BF00652795.

Chapter 5

Papers: Power Technologies

Contents

5.1	Development of a calculation tool to support the planning of the utilization of hybrid emergency power generators	163
5.2	Change in the energy market - opportunities for industrial companies	169
5.3	Impact of air supply parameters on in-vehicle performance of PEMFCs used in an ultra-efficient FCEV	172
5.4	Aerodynamic design studies on new types of aircraft with vertical take-off and landing capabilities	177
5.5	Sustainable materials for insulating high-altitude rural Kyrgyz residential houses: A parametric economic study	183
5.6	Investigation of the heat transfer during condensation of wet flue gas in horizontally, corrugated tubes	189
5.7	Options on the test planning for the AC/DC-Dual Active Bridge	193
5.8	Conversion of non-existent load-profiles for PV-Systems	199
5.9	On the development of a seasonal seasonal heat storage for single-family houses: Design boundary conditions including the storage heat losses	202
5.10	Evaluation of possible charging demand of battery electric vehicles in parking garages and Park+Ride areas based on real entry and exit data	207
5.11	Modularity Analysis of Power Electronics Architectures	212
5.12	Potential of e- mobility in rural areas – Evaluation of opportunities and barriers based on literature review	216
5.13	Slip control of an induction machine in the field weakening region during six step operation	221
5.14	Influence of a novel binder material on the electro-chemical performance of silicon-containing anodes	227
5.15	Development of a Vanadium/Vanadium Redox-Flow Battery for Demonstrational Purposes	232
5.16	Development of different H ₂ -storage concepts for reduced emission shipping	238
5.17	Investigations regarding cooling of thermoelectric modules in a nano combined heat and power unit	243
5.18	Development of the control strategy for the heating system in the MAGGIE research project	248
5.19	Concept development of a hybrid ship driving system and investigation of different constellations of components and control strategies	253
5.20	Comparison of different calculation methods for the outflow from pressurized vessels	258
5.21	Potential analysis for long-term storage of a decentralized power-to-gas technology	264
5.22	Influence of Hydrogen on the combustion process of a single cylinder spark ignited gas engine	269
5.23	Determination of the restriction-free inductive and capacitive reactive power potential based on the example of a medium-voltage industrial operation	271

5.24	Development and Validation of a 3L-ANPC Bridge Type Inverter Based on GaN HEMTs	276
5.25	Chance in the energy market - opportunities for industrial companies	279
5.26	Development of a virtual fuel injector for operation with Diesel and Oxymethylenether	282

Development of a calculation tool to support the planning of the utilization of hybrid emergency power generators

Danil Aleynikov
 Faculty of Electrical Engineering
 Augsburg University of Applied
 Sciences
 Augsburg, Germany
 danil.aleynikov@hs-augsburg.de

Abstract — This paper describes a methodological approach to the investigation of aspects of the isolated grid, such as forecasting the power consumption, as well as the analysis of important participants, which arise in case of maintenances in the grid. This paper gives an input for the creation of a calculation tool, which enables an operation of an isolated grid in a more efficient way.

Keywords—power generator, solar energy, standard load profile, renewable energy, isolated network, efficiency, energy consumption, forecasting, software, battery, state of charge.

I. PROJECT DESCRIPTION

During the LINDA project ("Local isolated grid supply and accelerated network restoration with decentralized generation systems in case of large-scale power outage"), a concept was developed to set up a local isolated network to supply critical infrastructures. With the help of a decentralized generating unit, an isolated grid is built up step by step, that also allows solar plant systems to feed in. The principle of using solar plant systems during emergency power operation (during troubleshooting or maintenance work in the grid) is also to be applied in the LINDA 2.0 research project for emergency power generators in order to reduce fuel consumption and emissions during emergency power supply. In the LINDA 2.0 project, a hybrid power supply unit, consisting of a battery storage system, a grid-forming inverter and a diesel engine as "range extender" is designed. Since the emergency power supply provides the energy predominantly by the battery, it is important, to determine the best possible state of charge of the battery for the further deployment and thus to allow a usage of the renewable energy for the network supply. It is necessary to find out, whether there are possibilities to forecast the amount of energy needed during the maintenance period. the maintenance period.

II. INTRODUCTION

Electricity generation is the main cause of CO₂ emissions in Germany. These emissions could be lowered in the last years due to a growing share of renewable energy sources. However, the use of renewable energy places new demands on the structure and stability of the grid. [1] Today, the issue of security of electricity supply is a very important aspect for the consumer. To ensure the performance of the network, it is necessary to carry out appropriate maintenance or troubleshooting work on the system. Also, municipal services must be prepared for accidents which can occur unforeseen at any time. All these cases require the disconnection of a certain area from the general power grid. In these cases a connection to an emergency power system

is necessary. An example of an emergency power generator is a mobile generator, used when the public power grid is not accessible to consumers, or when a failure of the power grid would lead to supply problems for critical infrastructure such as in hospitals or in nuclear power plants. The unit usually consists of an internal combustion engine and a generator. The engine draws fuel from a tank that is permanently available and thus converts chemical energy into kinetic energy. This kinetic energy in turn drives a generator, which feeds the generated electricity directly into the network of the system to be supplied. The schematic representation of an isolated grid supplied by a power generator can be seen in the Fig. 1.

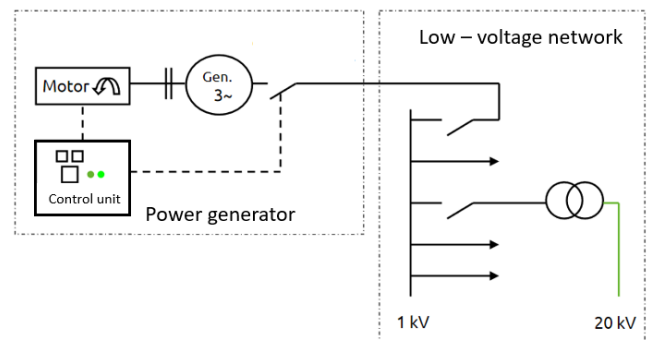


Fig. 1. Isolated grid, supplied by a power generator

III. QUALITY OF SUPPLY

Ensuring a high quality of supply - in particular high security of supply and low fluctuations in network voltage and frequency - is technically much more complex in a small isolated network than in a large interconnected grid.[2]

Power generation and power consumption must be exactly in balance at all times. The index for the quality of this equilibrium and thus for the quality of supply for end consumers is the network frequency. In Germany power supply networks are operated - regardless of the voltage level - at a frequency of 50 Hz. This means that the electrons make 50 complete pendulum movements in one second. It is very important that this frequency is always strictly adhered to. If there is an imbalance between generation and consumption, the grid frequency fluctuates, this would have fatal consequences for households, since all electrical and electronic devices are designed for these uniform voltage and frequency specifications. In the case of large power transmissions, frequency deviations can lead to undesirable current flows, which can potentially also have a high destructive power to the infrastructure.

Usually, it is controlled by the frequency converter. This is an electronic device that allows to regulate the speed of a three-phase motor. Background: If electrical machines or three-phase motors are operated directly on the AC voltage network, only a fixed speed is available to them - depending on the number of poles and the fed-in frequency of the local electricity network. However, if an application or a production process requires a variable AC voltage, i.e. a controllable speed, frequency converters are used. From a constant alternating voltage, these can generate an alternating voltage with variable amplitude (level of the output voltage) and frequency. A frequency converter is therefore connected upstream with a motor in order to generate a needs-based, changeable alternating voltage. The power grid no longer generates the frequency and voltage level with which the motor works, but the frequency converter takes over this task and regulates the output frequency and the output voltage.

IV. PHOTOVOLTAICS IN AN ISOLATED GRID

In 2020, nine percent of the electricity generated was generated by photovoltaics. The use of photovoltaic systems became more and more important over the years. The share of the energy generated by the sun, has increased continuously since 2003. This also increases the total number of small roof systems with a size of up to 30 kWp. This means that when hybrid power generators are used in an isolated grid, there will be not only energy consumers, but also decentralized energy resources (DER).

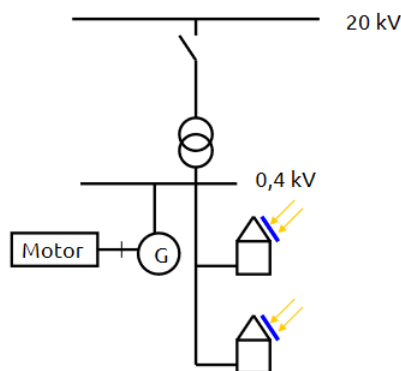


Fig. 1. Isolated grid with connected DER

This generates some difficulties, since electrical energy cannot be stored for a short time in interconnected networks, it can only be distributed between generator and consumer. [3] In the case when the generated energy exceeds the consumption energy, the frequency increases. Nowadays, only the old solar modules stop their production between 50.2 Hz and 51.5 Hz, whereas newer ones only gradually reduce their production. From the new upper frequency limit of 51.5 Hz, however, all solar systems switch off without exception. [4]

Excess energy leads to a reverse power on the generator, if the permissible reverse power of the generator is exceeded, the protection unit is triggered, which can lead to a power failure.

This forces a grid operator to certain measures, such as the separation of the solar system from the network, to avoid strong frequency fluctuations.

There are two possibilities to switch of the solar panels:

- Manual separation of solar panels
- Changing of the generator frequency to 51.7 Hz. This leads to an automatic, permanent separation of the solar panels from the grid

Both of them lead to a loss of energy generated by solar panels, which could supply the grid and, as a consequence, increased fuel costs.

Generally, the usage of the conventional generator in an isolated grid has the following disadvantages:

- Inability of usage of solar systems
- Noise development, approx dB (A) 66 at 7 m
- High CO₂ emissions
- High usage and maintenance costs

V. HYBRID POWER GENERATOR

For this reason, a hybrid power unit is being developed by the University of Applied Sciences Augsburg and Technical University of Munich. It consists of a battery as the main energy source, a diesel generator, which acts as a range extender in case of deviations from the predicted energy consumption or generation, or when maintenance has to be carried out for a longer period of time as planned and inverter, that is responsible for correct charging or discharging process of the battery. Fig. 3 shows, the isolated grid supplied by the hybrid generator.

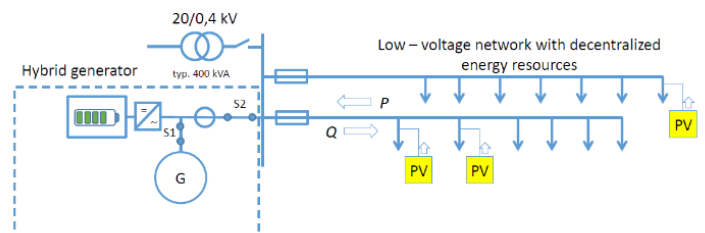


Fig. 3. Scheme of the hybrid generator connected to the isolated grid

A. Advantages of the hybrid generator:

- Ability of usage of generated energy solar panels
- It is a system in which the energy is drawn most of all from the battery. This leads to a considerable reduction in the operating hours of the diesel generator set.
- Reduced fuel consumption leads to a reduction in exhaust emissions and less pollution.
- Less maintenance costs and labor.
- Reduced noise development

B. Hybrid generator functionality

The hybrid generator arrives at the facility and continuously supplies the isolated grid uninterrupted with energy, while there is no connection to the public grid.

During the maintenance period, energy in the required amount will be taken from the battery. Produced solar energy, covers at first an ownconsumption of consumers in an isolated grid, all excesses of this energy have to be stored by the hybrid generator and can be used later. If the charge level reaches a predefined minimal value, the diesel generator starts automatically, for topping up the battery.

To avoid unnecessary starting the generator and ensuring secure supply of the energy, it is important to determine the state of charge of the battery before operating.

This value is very important to ensure that the hybrid generator works in the correct ranges, as an incorrectly estimated amount of energy can lead to a power failure, if there is too little charge. If the battery is full, it can not store any energy anymore. The produced energy will be lost and at the same time it can lead to an undesired increase in the frequency in the network and further shutdown of solar systems and as well to possible network failure.

Since the battery is a very expensive part of the hybrid generator, the further important aspect is, that the level of charge should always be on the optimum value, according to the battery type. By a storing of the hybrid generators, batteries should also have a charge level between 40% - 80%. [5] Under no circumstances should completely discharged batteries be stored. Otherwise, self-discharge of the batteries can lead to deep discharge. All this factors can lead to rapid battery wear, reducing battery life and capacity.

VI. ENERGY BALANCE

Energy balance has an important role for determination of optimum state of charge. To determine the balance, two main factors must be taken into account, namely:

- How much energy will be consumed.
- How much energy will be generated.

For the beginning it is important to analyse energy consumers and producers of the isolated grid.

A. Consumers

For the study case, in general, the private household that needs to be supplied with electricity is considered to be a consumer. The amount of energy consumed can vary strongly. There are standardized values depending on the size of the household (Table 1). The consumption data is presented in terms of kWh per year. This gives an understanding, that households with two adults, according to statistics, will consume 2500 kWh per year. These values show the average annual values, which of course will differ

in reality. So it is important to know to forecast the energy consumption.

TABLE I. ENERGY CONSUMPTION ACCORDING THE SIZE OF THE HOUSEHOLD [6]

Number of people in the household	Electricity consumption per year in kWh
1	1500
2	2500
3	3500
4	4500

Since a typical maintenance in average is performed only during one day, it is important to know the approximated daily energy consumption in the grid.

For this purpose, there are so-called standard load profiles (SLPs) which are used by the energy supplier for electricity consumers without a recorded power measurement. These SLPs replace the non-existent load profile curve of the end user with a calculated, reasonably accurate forecast of the electricity consumption for every 15 minutes.

SLPs are representative load profiles that are used for different consumer groups for example households, agriculture and retail, for each of which a similar consumption behavior can be assumed.

There are several load profiles according to type and activity, such as:

- H0 - Household, private consumption, possibly minor commercial needs
- G0 - Industry in general, mean of the entire group
- G1 - Commercial, weekdays 8 a.m. to 6 p.m. (offices, medical practices, workshops, administrative facilities)
- G2 - Commercial, predominant consumption in the evening hours (evening restaurants, leisure facilities, sports clubs, fitness studios, solariums)
- G3 - Continuous business (refrigerated storage building, pumps, community facilities, forced ventilation ...)
- G4 - Commercial, all kinds of shops, hairdresser
- G5 - Commercial, e.g. bakery

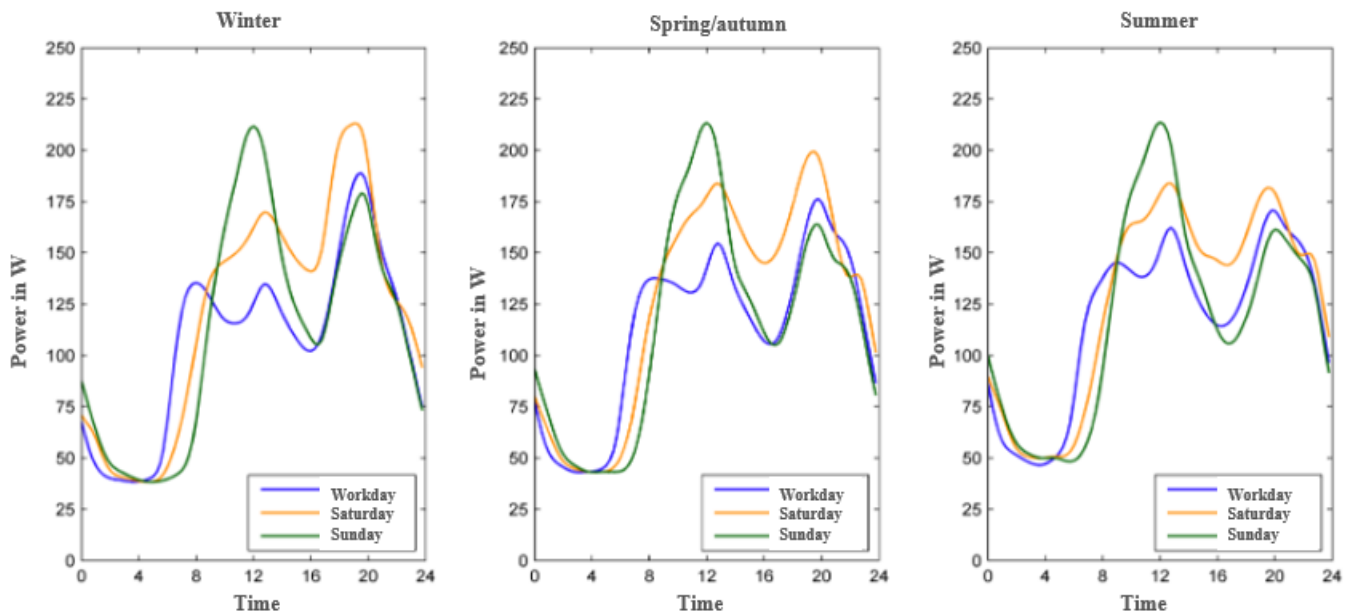


Fig. 2. H0 standard load profile

- G6 - Business, weekend operations (focus) (e.g. restaurants, tourist bars, cinemas, sports facilities)
- L0 - Agriculture in general, mean of the entire group [7]

The standard load profile H0 is shown in Fig. 4. It displays nine types of days: winter, spring/autumn and summer in bundle with a typical working day, Saturday and Sunday. It is noticeable, that each variant has a different load consumption behavior over the time. However the largest differences are to be seen between working day, Sunday and Saturday. The detailed values with the 15 - minute intervals are provided by BDEW (Bundesverband der Energie- und Wasserwirtschaft e.V.), which contains accurate values of the forecasting.

All values are standardized to the consumption of 1000 kWh per year, therefore it is necessary to re-scale those profiles to the individual annual consumption of each consumer in the network.

B. Generation (Photovoltaics)

In photovoltaics, the solar radiation energy is converted into electrical energy by the usage of the photovoltaic effect. Single solar cells generate only low voltages and currents. Only when the cells are connected to form modules and the modules are interconnected they produce technically usable voltages and currents. [8]

There are several factors which influence the amount of the produced energy by the solar panels. These are discussed below.

Season

In summer the days are longer and there are more hours of sunshine. Therefore, the photovoltaic yield in summer is significantly higher than in the winter months. In total, around 70% of the yield of a photovoltaic system is generated in summer and only 30% is generated in the winter months.

Course of the day

Photovoltaic systems generate the most electricity in the midday, since at midday the sun is highest in the sky and the sunlight can hit the module surface perpendicularly. However, considerable yields are also achieved at other times of the day, such as in the afternoon or late morning. When the sun has set, however, no more electricity is generated. Since the electricity demand of a household does not adapt to the electricity production of the photovoltaic system and load peaks are reached especially in the morning and evening hours, the combination of photovoltaic systems and electricity storage can be appropriate. Electricity storage systems simply store excess electricity generated at for example midday and make it available for consumption at other times in the evening or morning. [9]

For a detached house with a 4-person household and an electricity consumption of 4,500 kWh per year, the typical size of a photovoltaic system is around 6 kilowatt peak or 36 square meters. [10]

There is an opportunity to forecast the possible yield of the solar panels during the day in a certain period of time. The load profile of EnBW for photovoltaics is used to determine the load contribution. In order to calculate the load occurring at the respective point in time, it is necessary to multiply the value at the respective point in time and month by the total installed solar panel power. The following Fig. 5 shows the characteristic hourly load profile for a day in

spring/autumn and winter. It can be seen that there is usually no power feed-in from photovoltaic systems before 6:30 a.m. and after 9:30 p.m.. Similar to the case of an energy consumption SLP, all values are standardized to a solar panel power of 1 kWp per year, therefore it is necessary to re-scale those values to the individual annual total power of DER in the respective grid.

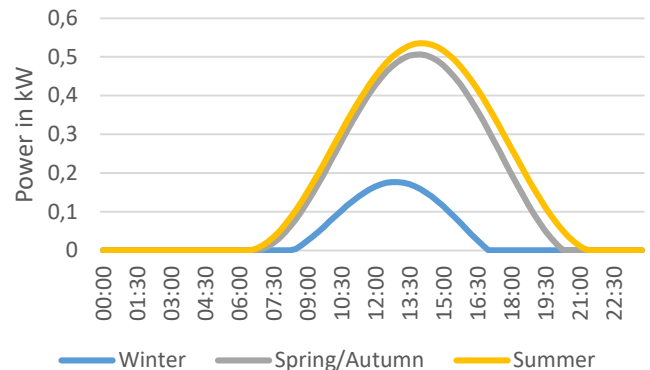


Fig. 5. Hourly load profile of the PV systems

C. Energy balance tool

More than 1.7 million PV roof systems with a nominal output of up to 30 kWp had a total output of around 18.4 GWp at the end of 2020. [11] According to the population in Germany there are 83 million people, that gives an understanding, that the average value of performance of a photovoltaic system per inhabitant equals 0,2216 kWp.

Let's assume, that a household with four persons have an installed PV power of 0,8864 kWp and will as well consume 4500 kWh annually. With the SLP described before it is possible to calculate, that in summer on a working day, the daily consumption of the household would be 12,6629 kWh and the generation is about 3,68 kWh. It means, that a usage of generated energy by the solar panels can cover about 30% of a daily consumption. It is important to mention, that these calculations are based on generalized statistics and can not be applied for the usage of the hybrid generators. For the more exact values, the data about the isolated grid is to be provided by the distribution network operator. This calculation can be anticipated manually by utilizing load profiles.

Since a manual calculation is very time-consuming, and should as well take into consideration a time period of the planned maintenance there is a need to create a special tool for calculating the energy balances depending on the season, the connected loads and the installed power of the PV systems. The tool contains the SLP for the households and solar panels. Based on this data and detailed district characteristics, the energy balance between consumption and generation is to be calculated in following steps:

1. The dataset of the isolated grid to be analysed shall be selected by the user
2. Number of energy consumers and producers will be distinguished
3. User have to choose a day type (summer, winter, spring/autumn)
4. The start and end time of the maintenance shall be chosen.

5. After all necessary parameters are selected, the tool calculates the sum of the consumption and generation of the grid over the time period for the selected type of the day.
6. As result, the tool returns the energy balance between generation and consumption.

Month	Summer
Type of day	Sunday
Stat time	08:00:00
End time	18:00:00
Number of households	
Ø-Energy consumption per household in kWh	
Sum of the energy consumption of all households in kWh	
Ø-Annual energy generation per PV system	
Sum of the energy production for all PV in kWp	
Energy balance	

Calculate

Select dataset

Fig. 6. Energy balance tool

A graphical user interface ensures to make the tool easy to use. The implementation takes place in programming language VBA in Microsoft Excel, in view of the fact that, this is a very widespread and frequently used program and thus the applicability of the tool outside the university (e.g. at the distribution network operator) can be guaranteed.

VII. CONCLUSION AND OUTLOOK

Energy suppliers are responsible to supply power uninterrupted. To ensure, that the network is in operation at all times, it is necessary to ensure that all elements of the grid are in a preferably optimal state. With regular inspections, the utilities have the opportunity to reliably maintain the power grid and repair damage at an early stage. [12]

In times of rapidly developing technologies, it is no longer enough to simply carry out this work. Nowadays efficiency as well as minimizing costs and disruptive factor of the maintenance have also a great importance. According to all data described in this paper, such as all the advantages of a hybrid generator, it is possible to significantly improve quality of the maintenance processes in the network.

The developed tool, provides transparency for the effective planning of a maintenance process with new developed hybrid generators. Once the main parameters of the hybrid generator are defined, the tool helps to forecast the required number of mobile generators and their exact state of charge of batteries. This ensures high quality of a grid supply as well as a usage of the generator in best conditions and prevents to reach the dangerous level of discharge or overcharging. This in turn helps to extend the battery life. Nevertheless, more detailed development is necessary. For example the influence of abnormal outside temperatures on the user's electricity consumption, as long as it directly affects the use of heating facilities should be considered. Also, the degree of cloudiness plays an important role concerning the yield of the PV systems. It will also be taken into account in the further course of this research study.

According to meteorological data, cloud parameters will be included:

- clearly
- cloudy
- overcast

The direct dependence of these parameters on the level of electricity generation by solar panels will be studied in more detail and introduced into the system as a coefficient.

In a future outlook, the functionality can be extended as well, for example, that tool becomes an automatic planner for a maintenance date, so-called "Smart planner", which can analyse input grid parameters in order to suggest the best date for a maintenance of an isolated grid.

After determining of the type and capacity of the battery, it could be another improvement to forecast the state of the battery automatically, by taking battery self-discharge rate into consideration.

Last but not least, a possible increase in the complexity of the tool, suggests utilizing a more powerful programming languages, for example Python, since it is more flexible, functional and has a large number of libraries.

REFERENCES

- [1] W. der Physik, *Stromerzeugung und Stromverbrauch in Deutschland*. [Online]. Available: <https://www.weltderphysik.de/gebiet/technik/energie/strom/erzeugung-und-verbrauch/> (accessed: May 10 2021).
- [2] *Netzfrequenz - Netzfrequenz.info*. [Online]. Available: <https://www.netzfrequenz.info/wissenswertes/netzfrequenz.html> (accessed: May 12 2021).
- [3] R. Upmann, "PowerPoint-Präsentation," [Online]. Available: https://www.solarwirtschaft.de/fileadmin/media/pdf/BSW_50Hz_Erlauterung_der_Problematik_Intersolar2012.pdf
- [4] GmbH, Next Kraftwerke, "49,5-Hertz-Problematik," *Next Kraftwerke GmbH*, 16 Dec., 2016. <https://www.next-kraftwerke.de/wissen/495-hertz-problematik> (accessed: May 17 2021).
- [5] *Battery State of Charge Determination*. [Online]. Available: <https://www.mpoweruk.com/soc.htm> (accessed: May 17 2021).
- [6] *Stromverbrauch im Haushalt: Vergleich & Übersicht*. [Online]. Available: <https://www.co2online.de/energie-sparen/strom-sparen/strom-sparen-stromspartipps/stromverbrauch-im-haushalt/> (accessed: May 12 2021).
- [7] Bdew, *Standardlastprofile Strom*. [Online]. Available: <https://www.bdew.de/energie/standardlastprofile-strom/> (accessed: May 10 2021).
- [8] SOLARWATT GmbH, *Wie funktioniert eine Photovoltaikanlage? Strom aus Sonnenlicht*. [Online]. Available: <https://www.solarwatt.de/photovoltaikanlage/photovoltaik-know-how/wie-funktioniert-eine-pv-anlage> (accessed: May 11 2021).
- [9] Wegatech, *So viel Ertrag bringt Ihnen Photovoltaik | Wegatech*. [Online]. Available: <https://www.wegatech.de/ratgeber/photovoltaik/grundlagen/ertrag/> (accessed: May 11 2021).
- [10] P. Kloth, "Photovoltaik: Größe und Ausrichtung," *Energieheld GmbH*, 14 Mar., 2019. <https://>

www.energieheld.de/solaranlage/photovoltaik/dimensionierung (accessed: May 10 2021).

- [11] Prof. Dr. Henrik te Heesen, Prof. Dr. Volker Herbort, and Prof. Dr. Martin Rumpler, “Studie zum Ertrag von Photovoltaikdachanlagen 2018,” [Online]. Available: https://www.umwelt-campus.de/fileadmin/Umwelt-Campus/User/HteHeesen/research/pv/Ertragsstudie_2018.pdf
- [12] *Inspektionen in Energieversorgungsunternehmen - TROTEC*. [Online]. Available: <https://de.trotec.com/anwendungen/inspektionen-motoren-und-karosserie/inspektionen-in-energieversorgungsunternehmen/> (accessed: May 11 2021).

Change in the energy market - opportunities for industrial companies

Benedikt Bäuml

Technical University of Applied Sciences Amberg-Weiden
Faculty of Electrical Engineering Media and Computer Science
Kaiser-Wilhelm-Ring 23, Amberg, 92224, Germany
Email: ben.baeuml@googlemail.com

Supervising Professor: Prof. Dr.-Ing. Magnus Jaeger
Technical University of Applied Sciences Amberg-Weiden
Faculty of Industrial Engineering and Health
Hetzenrichter Weg 15, Weiden, 92637, Germany
Email: m.jaeger@oth-aw.de

Abstract—The German government's goal of becoming climate-neutral by 2045 will lead to a major change in the energy market. At the moment, this is particularly noticeable in the form of a rising CO₂ tax as well as the increasing volatility in electricity generation from renewable energies. In order to ensure grid stability in the future as the expansion of renewable energies continues, the European Commission is setting incentives for companies to adapt their load to the respective generation.

Against this background, the research question is: "To what extent can industrial companies benefit from the expected changes in the energy market through dynamic energy management?"

This research question is exemplified by the analysis of a medium-sized industrial company that processes raw materials. The focus is on the development of an energy forecasting tool to plan energy quantities for the production programme, under the aspect of cost and CO₂ emission optimisation.

The energy forecasting tool aims to achieve a prediction accuracy of 10 percent for the expected performance curve for the energy sources used for heat and electricity supply. Its goal is to propose a production scenario, in which the economic and ecological objectives are optimised while considering the customer's requirements.

The first investigations confirm that in the future companies will be able to profit from the changes in the energy market through dynamic energy management. Decarbonisation in the production process and the flexible adjustment of the loads used in the company, adapted to the renewable energies currently available in the grid, can be a key for success.

Keywords— dynamic energy management, energy forecasting tool, load management, load shifting potential, CO₂ tax, decarbonisation

I. INTRODUCTION

The growing consumption of our societies with the beginning of industrialisation and the continuously increasing world population lead to a strong rise in the emission of climate-damaging greenhouse gases.

The associated anthropogenic temperature increase of the earth is now generally seen as a serious threat to humanity. Floods, droughts, famines, water shortages or the melting of the polar ice caps and the resulting rise in sea levels are some of the main problems of our time. Global warming and the associated shift from fossil fuels to renewable energies has now become the central challenge of the 21st century.

Four years after the Paris Climate Agreement, the European Commission drafted the "European Green Deal".

This stipulates that Europe reduces its net greenhouse gas emissions to zero by 2050 [1].

At an online congress of the CDU/CSU parliamentary group, Angela Merkel recently affirmed that she wants to achieve the goal of climate neutrality no later than 2045. That would be five years earlier than currently planned. In addition, 65 percent less greenhouse gases need to be emitted by 2030 than in 1990, compared to the previous target of 55 percent. For 2040, a reduction target of 88 percent is set. In 2020, Germany was already able to achieve its climate target of a 40 percent reduction in greenhouse gases compared to 1990 [2].

Due to the new, even more ambitious goals of the German government, the energy industry is facing a serious change. This is reflected on the one hand by a CO₂ tax and on the other hand by the increasing volatility of electricity generation due to the expansion of renewable energies. Up to now, electricity generation has been adjusted to the electricity load. This is becoming increasingly difficult due to the expansion of renewable energies.

Therefore, attempts are being made to adapt the load to the generation as far as possible in order to ensure grid stability. Due to the increasing volatility of electricity generation, the exchange electricity price is subject to ever greater fluctuations.

So far, these fluctuations have not been passed on to the consumer. However, in order to control the consumption behaviour of consumers, the European Commission is presenting a new directive for the internal electricity market [3]. This directive provides that price fluctuations are passed on to consumers in order to give them an incentive to consume electricity at precisely the time when there is a high share of renewable energies in the grid.

The electricity price for industry is made up of electricity generation, grid fees and state taxes/levies and surcharges, as can be seen in Fig. 1.

State taxes/levies and surcharges are the fixed part of the electricity price. Grid charges can be influenced by companies themselves by trying to smooth their electricity consumption

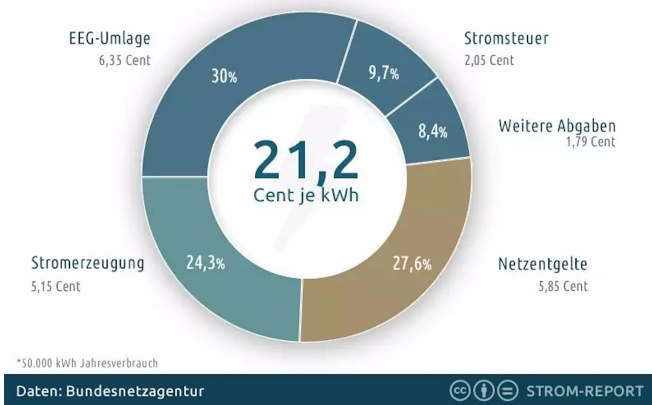


Figure 1. Average composition of the commercial electricity price

without significant peaks. The electricity generation sector is variable, which is reflected in the exchange electricity price. The electricity supplier sells the electricity to the customer at a fixed agreed price. Therefore, the customer cannot profit from price fluctuations on the exchange.

Electricity is traded on the intraday and dayahead markets. These markets reflect the current ratio of electricity supply to electricity demand. One of the main factors influencing the exchange electricity price is the weather, which leads to even higher exchange price fluctuations with the further expansion of renewable energies.

Due to the high regulations and access requirements, less-consuming companies cannot participate in these markets and profit from the price fluctuations by adjusting their load.

This is to be changed by a new directive on the internal electricity market. In the near future, industrial companies will therefore be able to participate in this market. Against this background, the research question is: "To what extent can industrial companies benefit from the expected changes in the energy market through dynamic energy management?"

May 17, 2021

II. MATERIALS AND METHODS

The clarification of the research question is based on the example of a medium-sized industrial company. It will be analysed to what extent the company can benefit from dynamic energy management.

The focus is on the development of an energy forecasting tool to plan energy quantities for the production programme, under the aspect of cost and CO₂ emission optimisation. As future energy costs increasingly change through a variable electricity price and CO₂ taxes, companies inevitably have to decarbonise and try to adapt their electricity load to electricity generation.

For the research question, a representative industrial company was chosen. The main requirements were a highly

variable electricity consumption and the consumption of fossil fuels such as gas and/or heating oil.

Strobel Quarzsand GmbH is the leading producer of high-quality quartz sands in Bavaria and is an ideal company to investigate the research question because of its energy use. The medium-sized company with about 70 employees is located in Freihungsand in the Oberpfalz. The core competence lies in the processing of quartz sands, which are used internationally as high-quality products, mainly in the glass industry, construction chemistry and the foundry industry. The products are defined by the different sand types, essentially described by grain sizes and purity content. The raw material is extracted by the company itself in various open-cast mines in the Oberpfalz.

The production in Freihungsand is roughly divided into the process stages sand feeding, wet classification, drying, dry classification, storage and loading. For about 10 years, the company has already been using combined heat and power to optimise the cost of energy supply. In wet classification, the sand is cleaned of unwanted residues and divided into different grain sizes. This process takes up most of the electricity consumption. Drying takes place through water pre-separation during storage of the sand followed by further drying in a gas-fired drum dryer. This is a process stage that is decisive in terms of process heat. During dry classification, the various sands are further subdivided into different grain sizes and then stored in silos for upcoming loading to customers.

The energy forecasting tool has the objective of predicting the company's energy consumption based on the specific production programme and making adjustments where necessary to optimise energy costs and emissions in the future. It represents the basic element of the investigations.

In order to be able to make a forecast the sand types to be produced must be assigned their specific energy consumption. The consumption by sand type differs essentially in the process steps used, which require the use of "energy consumers".

For the forecasting tool, the production process with the required "consumers" must be described for each sand type. Consequently, the production is divided into different plant groups, which in turn contain the associated consumers. Each sand type passes through different plant groups. For each plant group, the power is calculated as a function of the mass flow rate. In this way, conclusions can be drawn about the power consumption according to the respective sand type. The same applies to natural gas consumption in drying.

To check the validity of the energy forecast tool, the production programme and the energy data recorded and stored at the company are compared with the forecast. This quickly reveals the extent to which the energy consumption forecast matches the available energy data.

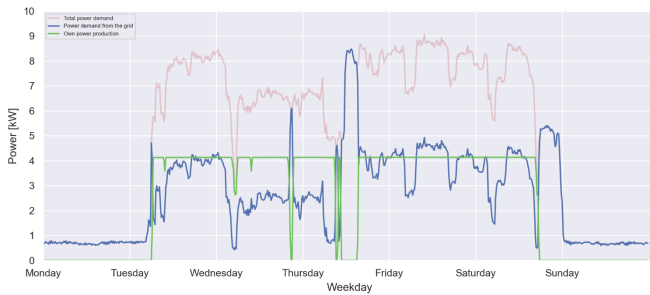


Figure 2. Electrical power curve over one week of Strobel Quarzsand (no real power data)

III. RESULTS

Fig. 2 shows the company's real electricity power curve over a production week that includes a public holiday on Monday. The red characteristic curve represents the total power demand. The blue characteristic curve is the power curve of the electricity purchased from the grid and the green characteristic curve is the power curve of the company's own electricity production through a block-type thermal power station.

The high volatility of the entire power curve is immediately apparent. This is due to the different production methods of the sand types as well as production changes and respective maintenance work.

It is planned that the energy forecasting tool which is currently being developed will predict the power curve with an accuracy of about 10 percent on the basis of a few key figures and the production programme.

Through the precise prediction of energy consumption, load peaks can be recognised at an early stage and shifted through production interventions.

The load shifting potential is also clearly visible in Fig. 2. The company's production flexibility plays an important role here, because it determines the extent to which it can choose between different production scenarios. In the company examined, short-term delivery orders are mostly relevant (1-3 days); long-term production programme planning is only possible to a limited extent.

Nevertheless, energy-intensive sands can be produced precisely at the time when there is a high proportion of renewable energies in the grid. If the price fluctuations on the power exchange which are caused by supply and demand in the grid are passed on to the consumers, companies can benefit by adjusting their load.

The CO₂ tax introduced in Germany in 2021 will make the drying of sands with natural gas in drum dryers increasingly uneconomical. In the medium term, alternative processes must be examined. As a result, the energy forecasting tool will gain additional importance and benefit.

IV. CONCLUSION

The study shows that in the future, companies will be able to benefit from the changes in the energy market through dynamic energy management. Essentially, companies must try to decarbonise and adapt their load to electricity generation from renewable energies.

Studies show that many companies have load shifting potential, which is already being used to some extent as balancing power [4].

How big the profit for companies will be depends above all on the extent to which the price fluctuations on the exchange are passed on to companies.

The federal government could, for example, hold out the prospect of tax relief in the area of electricity tax or the EEG levy as an incentive to additionally motivate companies to use variable electricity tariffs. Grid stability could thus be significantly improved, which would allow a faster expansion of renewable energies.

In the future, companies should use the right energy at the right time.

REFERENCES

- [1] o. V., The European Green Deal, Brüssel : European Commission, 2019.
- [2] o. V., „ZEIT ONLINE,“ 05.05.2021. Available: <https://www.zeit.de/politik/deutschland/2021-05/klimaschutz-bundesregierung-klimaziele-co2-ausstoss-treibhausgase>. www.google.com [Zugriff am 07.05.2021].
- [3] EU, „RICHTLINIE 2019/944 DES EUROPÄISCHEN PARLAMENTES UND DES RATES,“ Brüssel, 2019.
- [4] T. Ladwig, „Demand Side Management in Deutschland zur Systemintegration erneuerbarer Energien,“ Dresden, Technische Universität Dresden, 2018, pp. 41-43.

Impact of air supply parameters on in-vehicle performance of PEMFCs used in an ultra-efficient FCEV

Sebastien Baur
University of Applied Sciences Munich
Department of Mechanical, Automotive
and Aeronautical Engineering
 Munich, Germany
 Email:sebastien.baur@hm.edu

Diane Henze
 Simon Limbeck
University of Applied Sciences Munich
Department of Mechanical, Automotive
and Aeronautical Engineering
 Munich, Germany
 Email:diane.henze@hm.edu

Klaus Peter Zeyer
University of Applied Sciences Munich
Department of Applied Sciences and
Mechatronics
 Munich, Germany
 Email:klaus_peter.zeyer@hm.edu

Abstract—This paper explores the effects of air-supply parameters on low temperature polymer electrolyte membrane fuel cells. To study in-vehicle performance, tests were conducted in a laboratory. Additional tests in the student built ultra-efficiency vehicle are planned. The change in fuel cell efficiency and power caused by the variation of different air parameters inside the vehicle are investigated. It was experimentally determined that short time in-vehicle performance of the fuel cell is improved when inside the fuel cell compartment within the vehicle. Long-term effects have to be examined further, as the causes for an incremental decrease in stack voltage at constant power draw are not completely understood yet.

Keywords—fuel cell, PEMFC, FCEV, air, performance, impact.

I. INTRODUCTION

Fuel cells are continuously supplied electrochemical converters. The chemical energy of the reactants oxygen and hydrogen is converted into heat and creates an electrical potential between the fuel cell anode and cathode that can be used to generate an electrical current. Polymer Electrolyte Membrane Fuel Cells (PEMFCs) are low temperature fuel cells that are used in a broad range of application such as backup power supply, in aerospace, powertrains of vehicles and for portable power generation. Thanks to their compact size, good dynamic properties including fast start-up and no moving or fluid parts, PEMFCs are the fuel cells of choice for the mobility sector [1-3].

Fuel cells are made by building a stack of multiple cells in series to reach desired voltage and power. The individual cells consist of the eponymous polymer membrane, usually made of Nafion [4], that lies between catalyst layers (CL) of anode and cathode. The membrane-electrode assembly (MEA) is constructed with the porous gas diffusion layers (GDL) on both sides. The bipolar plates (BPP), the definition of which often encompasses the GDL, supply the reactants, connect two neighbouring cells and conduct the electric current. Fig. 1 illustrates the different parts of a PEMFC cell.

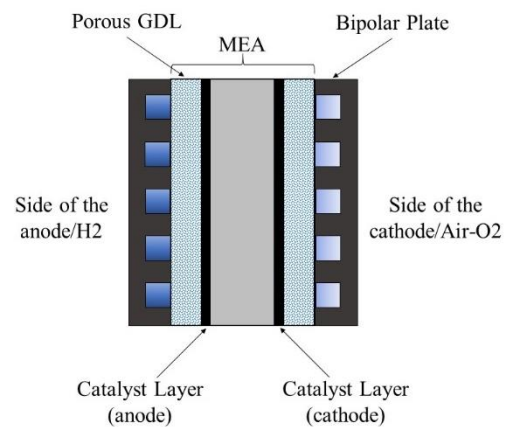


Fig. 1 Components of a single PEMFC cell

Despite the big steps undertaken in PEMFCs development and research in the last few years, the technology is still advancing/evolving and the effects of various parameters on fuel cell performance are not completely understood. A significant factor pertaining to fuel cell efficiency is the inlet air. Open cathode PEMFCs like the one described in this paper, are mostly supplied with oxygen from the surrounding air. The temperature, humidity and pressure of the air and the control of these factors and their effects on fuel cell efficiency will be discussed in this paper.

This paper was written in cooperation with the Hydro2Motion (H2M) student team, focusing on developing the most efficient FCEV possible, with the goal of competing in the shell eco marathon efficiency challenge [5]. The fuel cell powers supercapacitors that are used to supply an electric motor. The fuel cell used in the laboratory and the efficiency vehicle is a PEMFC from Baltic Fuel Cells “Susy 450” with 45 cells with 44 mm² active cell area each and a peak power of 450 W [6].

II. STATE OF THE ART

The efficiency of PEMFCs is usually around 50 % [7]. This indicates that around half of the released energy of the redox reaction is released as heat. Main losses are due to:

- Activation losses
- Ohmic losses
- Mass transport losses

The released heat has to be managed as Nafion membranes can only be used below 90 °C [8]. The influence of temperature on PEMFCs has been investigated by multiple papers.

A. Temperature and cooling of PEMFCs

The quotient $\eta_{th} = \frac{\Delta G}{\Delta H}$ defines the thermodynamic energy conversion efficiency η_{th} . The molar free Gibbs Energy ΔG of the reaction and the molar free enthalpy ΔH depend on temperature and pressure. In contrast to the efficiency of heat engines undergoing the Carnot cycle, higher temperature does not lead to higher theoretical efficiency in fuel cells. The theoretical efficiency curve of hydrogen oxygen fuel cell (H₂/O₂-Zelle) and of the Carnot cycle are depicted in Fig. 2.

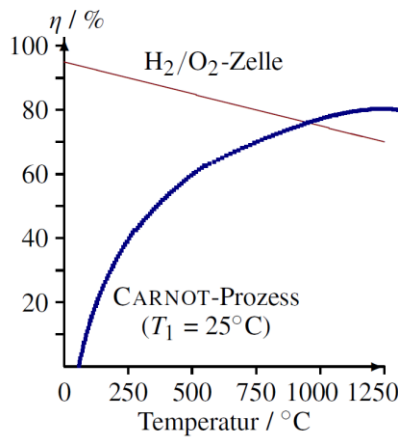


Fig. 2 Effect of temperature on efficiency [7]

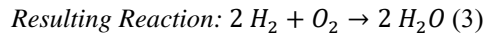
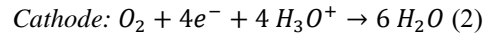
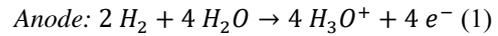
To determine the effect of temperature on fuel cell efficiency further factors beyond the thermodynamic efficiency have to be explored.

The manufacturer of the fuel cell described in this paper specifies an optimal operating temperature of 55 °C [5]. Similar results can be found in the study of the German Aerospace Center, that showed an optimal operating temperature of 52.9 °C for low temperature PEMFCs [9].

Some studies show an improvement of cell power at higher temperatures through higher electrocatalytic activity [10], although the studies do not explicitly show that this effect is related to temperature and not caused by parameters like relative humidity. Another study by Sahu et al. [11] found higher cell voltage but lower efficiency. A higher cell temperature leads to more evaporation of the water on the cathode side which leads to a natural balancing effect of the temperature since a higher power draw results in higher water production and the evaporation of water is highly endothermic [12].

B. Humidity

A wide range of papers and studies have focussed on water management, since it is a major factor for fuel cell performance and longevity, often focusing on flow channel designs [13-15]. The product of the chemical reaction in the cell is water:



This water is produced on the cathode side of the cell. But water is required on the anode side, as “the proton formed in the oxidation reaction of hydrogen gas at the anode adheres to water molecules and forms provisional hydronium ions” [16]. A higher water content therefore leads to better ionic conductivity. Since the Nafion used in membranes is hydrophilic and permeable [17], Gittleman [18] examined the ionic conductivity of Nafion at different humidity levels and found a clear correlation. His results are listed in Table 1.

TABLE I. MEMBRANE PROTON CONDUCTIVITY

Membrane Proton Conductivity	
Relative Humidity [%RH]	Conductivity [S]
30	0.025
50	0.04
60	0.06
70	0.08
80	0.125
90	0.18

Table 1 Conductivity of Nafion membranes at different relative humidity [18]

Membrane drought or “dry out” leads to a disproportionate increase of ohmic resistance [19]. Dry out is more likely at higher temperatures which underlines the difficulty in determining effects of temperature and humidity independently [20].

Lee and Hwang [21] looked at performance characteristics at different cathode humidity levels and found the maximum power density at around 60 % relative humidity. The reason for this optimum to be lower than the relative humidity leading to higher conductivity, is most likely due to effects in fuel cell like flooding. Flooding describes the process of fluid water forming in the gas channels of the fuel cell. This has adverse causes, since especially in low temperature fuel cells, liquid water can form and stop reactants, in this case oxygen from the air, of reaching the place of reaction. Humidity cycling between low and high humidity leads to degradation of the MEA [22].

Another factor that should be considered is the change of oxygen concentration depending on humidity, since in dry air the oxygen content is typically around 20.9 vol.-%, but at 100 % relative humidity the content is only 20.4 vol.-% oxygen.

C. Oxygen

Optimal oxygen stoichiometry of the inlet air is crucial for optimal fuel cell operation. Studies show that an air excess ratio (AER) between 1.5 and 2.5 is to be desired [23-24]. This is especially important as the oxygen reduction reaction (ORR) is significantly slower compared to oxidation on the cell anode [25].

D. Air pressure

Relevant literature determines that inlet air pressure (cathode pressure) correlates positively with cell performance. Löhn [3] finds an increase in air pressure from 1 to 1.5 bar at constant current density of 0.6 A/cm² resulting in a cell voltage increase of 100 mV from 0.5 V to 0.6 V. The study used a PEMFC with Nafion membrane and a similar active cell area as the Baltic fuel cell, with a size of 45.16 cm².

Fig. 3 shows the results of Monem et al. [1] only observed small increases from air pressure increase. A 18.2 % increase in pressure resulted in 0.5 % cell voltage increase.

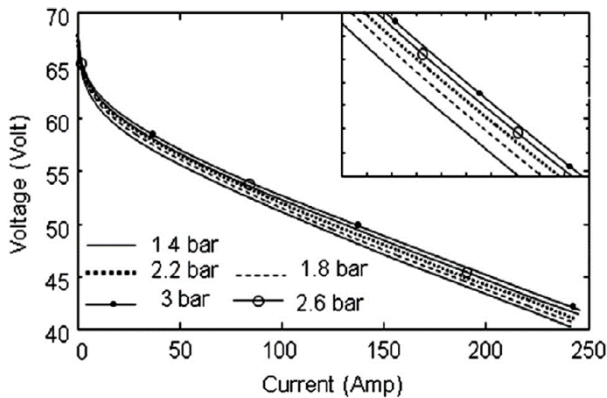


Fig. 3 Cell characteristic curve depending on air pressure [1].

In summary different findings regarding the impact of air parameters can be found in these studies, especially regarding the effects of air pressure.

III. EXPERIMENTAL SET UP

The fuel cell manufacturer is Baltic Fuel Cells. Two identical fuel cells are used in the laboratory and the vehicle. Fig. 4 depicts the fuel cell in the laboratory. The stack of individual cells is visible, the electrical contacts at the bottom of the stack as well as the valves and hydrogen pipe on the top left.



Fig. 4 Close up of the Baltic fuel cell stack

In Fig. 5 the experimental set-up in the laboratory is visualized. The Baltic fuel cell is connected to an electronic load. Multiple sensors for cell voltage, current, temperature, relative humidity, hydrogen mass flow and others are read out by an Arduino microcontroller. The microcontroller additionally controls the hydrogen valves and the fuel cell fan. A 12 V AC adapter provides power to fan and valves as well as providing measurements for the calculation of system efficiency. Hydrogen is provided by a 200-bar cylinder, this pressure is reduced by a hydrogen pressure regulator (not depicted) to 0.3 bar.

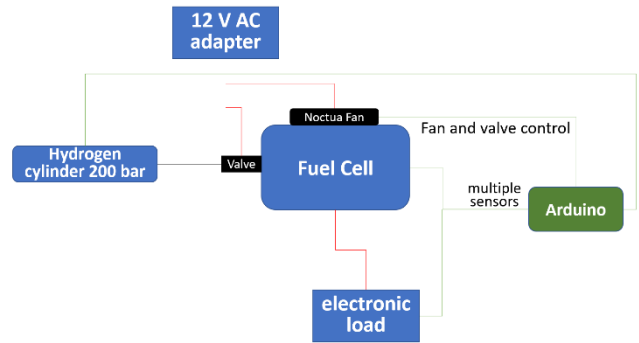


Fig. 5 Schematic view of the lab unit

Measurements were conducted by saving the sensor input values to a SD card connected via SPI to the microcontroller. For each measurement point the average of at least 15 values was taken. The electronic load was set in constant current mode (CC). Fan and purge control were held constant.

IV. ULTRA-EFFICIENT FUEL CELL VEHICLE

In the ultra-efficient vehicle, the fuel cell is located at the back of the vehicle in a compartment separate from the driver compartment, as well as the supercapacitor, the electric engine, and the single rear driven wheel. To simulate in-vehicle operation, tests within a closed space with similar volume of 0.105 m² and similar opening size to the vehicle drivetrain compartment were conducted in the laboratory.

One defining factor in the geometric integration of the fuel cell is the air flow. Depending on the positioning of the compartment openings and the compartment size, the air flow changes air parameters. Additionally, the necessary fan power to cool the fuel cell and provide it with oxygen is impacted. In Figure 6 the fuel cell compartment of the vehicle is depicted in orange.

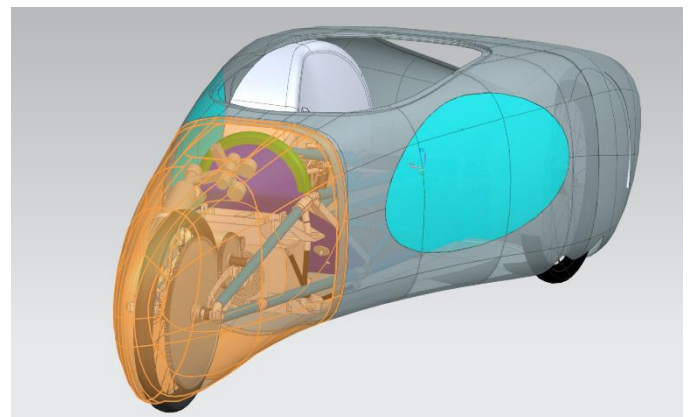


Fig. 6 Rear isometric CAD view of the H2M vehicle

The outlet air can impact the air parameters of the fuel cell inlet air. In the small powertrain compartment of the ultra-efficient vehicle a part of the air is recirculated as the compartment openings are kept to a minimum for aerodynamic reasons. As such the hotter and humid outlet air causes these parameters to be higher in the inlet air and can therefore improve fuel cell performance. As this air has a lower oxygen content, the stoichiometry may be lower than optimal lowering fuel cell performance.

V. RESULTS

The characteristic curve of the fuel cell stack in Fig. 7 results from measurements recorded with the fuel cell in the compartment (orange curve) and outside of the compartment (blue curve).

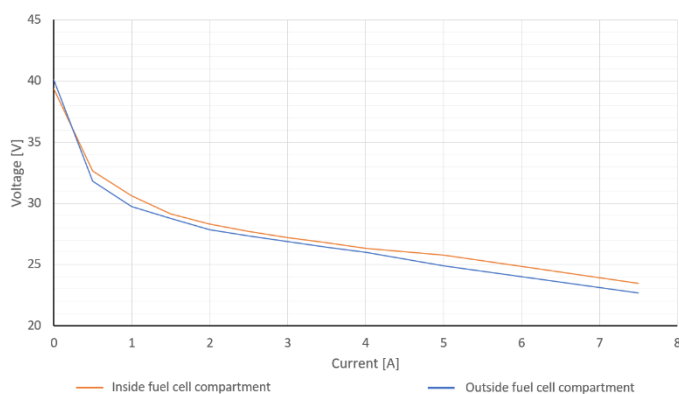


Fig. 7 Characteristic curve of the fuel cell in and outside of test compartment

Below 4 A fuel cell performance is similar, with performance in the compartment being slightly higher, at 3 A the stack voltage is higher by 0.3 V. Above 4 A the difference is more pronounced, at 5 A the average stack voltage in the compartment is 25.76 V and 24.89 V without it, i.e., almost 1 V lower. This measurement is significant since the accuracy of the measurement is around ± 50 mV. At a constant current of 3 A the temperature of the fuel cell in the compartment is constantly ca. 3 degrees higher.

The relative humidity of the cathode side is 2-5 % higher in the “compartment” but decreases after 10 min. The cell voltage of the closed room also decreases after approximately 10 min. The reason for this decrease is unclear, since it can also be observed in the open room measurement but on a much smaller scale. Further tests will have to be conducted to explore the causes of this slow but continuous decrease.

VI. CONCLUSION AND OUTLOOK

At required vehicle power the Baltic fuel cell operates at lower operating temperature and relative humidity than the optimal ranges given in the literature. Nonetheless at a maximum of over 50 % at 3 A the system efficiency of the fuel cell stack is located in the operating range given by the vehicle design.

In a next step, measurements with a humidifier will be performed, so that the impact of inlet air humidity can be explored more clearly, and other interfering factors can be excluded experimentally. In that way further possible improvements of fuel cell system efficiency through better water management in the cell can be explored.

The operation of the fuel cell in a closed environment leads to minimally higher cell performance but worsens performance on test with long constant loads. This time-dependent effect has to be confirmed in longer measurements of the fuel cell system.

Additional variables for fuel cell efficiency are the power draw of further auxiliary devices, such as the normally closed valves and the purge process. Purge interval timing and purge duration determine the loss of hydrogen as well as the positive effect of reducing gradual voltage drop caused by the accumulation of impurities. Experiments were carried out showing the possible improvement in hydrogen consumption without fuel cell performance changes leading to higher efficiency.

A new fan control was implemented and leads to improved efficiency of the fuel cell in laboratory settings. Further improvements and refinements of the fan control and air flow will have to be developed to reach optimal efficiency of the fuel cell system while powering the vehicle. As soon as the construction of the vehicle is completed, a full vehicle test should be conducted to validate the findings inside the vehicle in “real-world driving” conditions.

ACKNOWLEDGMENT

The authors thank G. Löbl for his valuable technical support and his willingness to help and answer questions.

REFERENCES

- [1] A. A. Monem, A. Azmy, and S. A. Mahmoud, “Effect of process parameters on the dynamic behavior of polymer electrolyte membrane fuel cells for electric vehicle applications,” *Ain. Shams Eng. Journal* London, vol. (2014)5, pp. 75–84, 2014.
- [2] J. Garche, L. Jörissen, “Übersicht und Einführung zur Technik der Brennstoffzelle” Zentrum für Sonnenenergie- und Wasserstoff-Forschung Baden-Württemberg, 2002.
- [3] H. Löhn, “Leistungsvergleich von Niedertemperatur PEM Brennstoffzellen – Experimentelle Untersuchungen, Modellierung und numerische Simulation” Dissertation, Technische Universität Darmstadt, 2010.
- [4] K.A. Mauritz, and R. B. Moore, “State of understanding of Nafion” *Chem. Rev.*, vol. (2004)104, 10, pp. 4535–4586, 2004.
- [5] Hydro2Motion, www.hydro2motion.com, 2021.
- [6] Baltic Fuel Cells, “Susy 450 technical data”, 2021.
- [7] P. Kurzweil, „Brennstoffzellentechnik. Grundlagen, Komponenten, Systeme, Anwendungen“, 2. Edition Springer Vieweg, Wiesbaden, 2013.
- [8] M. Casciola, G. Alberti, M. Sganappa and R. Narducci, “On the decay of Nafion proton conductivity at high temperature and relative humidity,” *Journal of Power Sources*, 162, pp. 141-145, 2006.
- [9] C. Werner, F. Gores, L. Bussemeyer, J. Kallo, S. Heitmann and M. Griebenow, “Characteristics of PEMFC operation in ambient- and low-pressure environment considering the fuel cell humidification”, *CEAS Aeronautical Journal*, vol. 6, pp. 229-243, December 2014.
- [10] N. Nachiappan, G. Paruthinmal and G. Sasikumar, “Effect of nitrogen and carbon dioxide as fuel impurities on PEM fuel cell performances”, *Ionics*, vol. 19, pp. 351-354, 2013.
- [11] I. P. Sahu, G. Krishna, M. Biswas and M. K. Das, “Performance study of PEM fuel cells under different loading conditions” 4th International Conference on Advances in Energy Research 2013, ICAER 2013, *Energy Procedia*, vol. 54, pp. 468-478, 2014.
- [12] S. M. Hashmi, “Cooling strategies for PEMFC stacks”, Dissertation, Universität der Bundeswehr Hamburg, 2010.
- [13] X. R. Wang, Y. Ma, J. Gao, T. Li. G. Z. Jiang and Z.Y. Sun, “Review on water management methods for proton exchange membrane fuel cells”, *International Journal of Hydrogen Energy*, vol. 46, pp. 12206-12229, 2021.

- [14] S. Jung, J. Deliang-Yang and C. King, "Water management along the flow channels of PEM fuel cells", *AIChE Journal*, vol. 50(10), pp. 2594-2603, 2004.
- [15] T. Tran, S. Huang, D. Ha Vu and V. N. Duy, "Effects of Gas channel Design on Water Management and on the performance of PEMFCs: A review", *Int. J. Electrochem. Sci.*, vol. 13, pp. 10480-10495, 2018.
- [16] J. Walkowiak-Kulikowska, J. Wolska and H. Koroniak, "Polymers application in PEMFCS", *Physical sciences reviews*, De Gruyter, 2017
- [17] O. M. Osamudiamen, "Assessment of humidity management effects on PEMFC performance", Master thesis KTH Ind. Eng. and Mgmt. Stockholm, 2010.
- [18] C. Gittleman, "Automotive perspective on PEM evaluation", General motors fuel cell research lab, New York, 2019.
- [19] A. Sorrentino, K. Sundmacher and T. Vidakovic-Koch, " Polymer electrolyte fuel cell degradation mechanisms and their diagnosis by frequency response analysis methods: a review", *energies*, vol. 13(21), p. 5825, 2020.
- [20] K. Abrosimov, A. Ustinov and A. Khayrullina, "effect of ambient air condition on PEMFC performance", *Journal of Renewable and Sustainable Energy*, vol. 9, 2017.
- [21] P. H. Lee and S. S. Hwang, "performacne characteristics of a PEMFC with parallel flow channels at different cathode relative humidity levels", *Sensors*, vol. 9, 2009.
- [22] A. Kusoglu, A. M. Karlsson, M. H. Santare and S. Cleghorn, "machanical behavior of fuel cell membranes under humidity cycles and effect of swelling anisotropy on the fatigue stresses", *Journal of Power Sources*, vol. 170, pp. 345-358, 2007.
- [23] K. Bosung, C. Dowon and K. Yongchan, "The Effects of Air Stoichiometry and Air Excess Ratio on the transient response of a PEMFC Under Load Change Conditions", *app. Energy Journal*, vol. 138, pp. 143-149, 2015.
- [24] P. Štekl and P. Kadlec, "Influence of Oxygen Content at the PEM Fuel Cell Cathode", *Adv. Methods of Theory of Elec. Eng.*, pp. 4-6, 2015.
- [25] L. Lux, K. Williams and S. Ma, "Heat-treatment of metal-organic frameworks for green energy applications", *Cryst. Eng. comm.*, vol. 1, 2015.

Aerodynamic design studies on new types of aircraft with vertical take-off and landing capabilities

Benke Lukas

Faculty of Electrical Engineering and Information Technology
Technische Hochschule Ingolstadt
Ingolstadt, Germany
lub5410@thi.de

Werther Martin

Faculty of Mechanical Engineering
Technische Hochschule Ingolstadt
Ingolstadt, Germany
maw3232@thi.de

Abstract—Targeting a more efficient use of the air jet induced by a traditional propeller – as used on helicopters and quadcopters – different air guidance strategies were studied. By means of computational fluid dynamics 4 significantly different geometries were investigated and compared to a simple propeller without air guidance. The strategies for an increased lift are: 1) creating aerodynamic lift using a wing shaped body, 2) increasing mass flow, 3) increasing and decreasing air velocity and 4) enlarging the area for momentum transfer. As for the tested configurations, the lift force of a simple propeller was not topped by any of these. A major advantage though is the improved opportunity for passenger or cargo space without disturbing the air flow any further.

Keywords—computational fluid dynamics (CFD), vertical take-off and landing (VTOL), helicopter, propeller, ring wing, bladeless fan, thrust nozzle, ducted fan.

I. INTRODUCTION

Except for lighter than air aircraft, almost any aircraft with vertical take-off and landing capabilities produces its lift using some sort of propeller. As a propeller pushes air from above e.g. a helicopter underneath it, the flow gets very turbulent and much energy is lost as vortices dissipate into heat. Consequently, it can be assumed, that the efficiency of a propeller can be significantly improved by guiding the air jet in a suitable way.

In order to find an adequate method for the efficient air guidance 4 significantly different geometries were created and studied. All of them apply varying strategies of producing or improving the lift created by the same propeller.

The studied geometries are named:

- ring wing
- bladeless fan
- ducted fan
- ring nozzle

II. NUMERICAL SIMULATION

The study was performed by computational means. Therefore, a digital model was created using CATIA V5. Then a mesh – required for computing the flow field – was derived from it with the program ICEM CFD to discretize the

geometrical computing space. The air flow and the forces acting on the geometries were calculated by one of the two available computational fluid dynamics (CFD) solvers OpenFOAM or TAU-code. Further evaluation of the flow field was conducted using the open-source software ParaView.

A. Solvers

Both used flow solvers (OpenFOAM and TAU-Code) are built around the Reynolds-averaged Navier-Stokes (RANS) equations describing the physical behavior of fluids. These are solved in a stationary way iteratively for every configuration. In case of the Solver used with OpenFOAM the RANS equations were simplified for an incompressible fluid flow – which is applicable for air in case of speeds lower than 30 % of the speed of sound. With calculated velocities far below this value, all simulated configurations can be treated as incompressible. The turbulences of the flow were simulated using the standard single equation Spalart-Allmaras turbulence model.

B. Setup

1) Fluid

The operating fluid for all studied geometries is air according to the international standard atmosphere (ISA) at sea level. Consequently, the specific gas constant of air is defined as $R = 287 \text{ J/kgK}$, the temperature at sea level is $T = 288.15 \text{ K}$ and the pressure $p = 101325 \text{ Pa}$. Using the ideal gas law

$$p = \rho \cdot R \cdot T \quad (1)$$

the density ρ results in 1.225 kg/m^3 .

2) Boundary conditions

For the simulations, all geometries are positioned with the 256 mm diameter propeller approximately in the center of a cylindrical computing space with 2875 mm radius (22.5x propeller radius), 2300 mm (18x propeller radius) above and 5750 mm (45x propeller radius) below the studied geometries (see Fig. 1). The computing space was chosen this big to minimize effects of the boundary definition of the outer boundary – where all gradients are assumed to be zero [1] – on the investigated geometry.

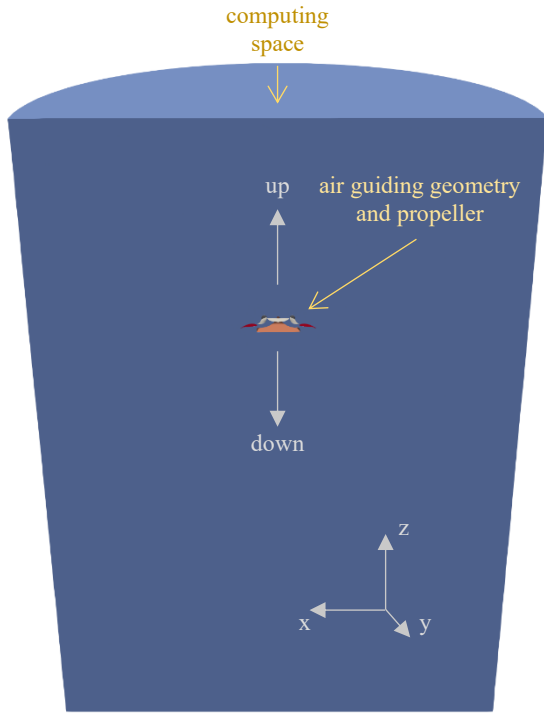


Fig. 1. Qualitative overview of simulated computing space

All surfaces of the geometries are taken as “viscous walls” with a fully turbulent flow on their surfaces to allow the simulation of viscous effects on the boundary. Only the propeller consists of two coincident discs that are defined as “actuator inlet” and “actuator exhaust” respectively. The forces transferred from the propeller to the air are calculated by the solver according to the 2-dimensional blade element theory based on predefined propeller parameters [1].

3) *Grid independency*

To allow for a realistic simulation the discretization of the computing space i.e. the mesh needs to be fine enough. Thus, a grid independency study was conducted with a geometry different from the models named before, but with similar scales and the same propeller. Thereby a mesh with roughly 10 million elements turned out to be good in terms of accuracy and duration of calculation.

C. *Validation of propeller model*

The 5-bladed propeller used for every geometry was modelled according to data derived from physical experiments by the aerodynamics laboratory of Technische Hochschule Ingolstadt. The total diameter of the physical propeller and the modelled one is 256 mm and its hub diameter is 38 mm. Both CFD solvers provide the possibility of simulating a propeller disc using the 2-dimensional blade element theory of aerodynamics. Therefore, pitch angle, cord length, lift and drag coefficients (dependent from the actual angle of attack) were defined for various sections of the blades from hub to tip as well as the number of blades and the rotational velocity.

As can be seen in Fig. 2 the modelled propeller matches the real one good enough to allow for an appropriate simulation of the air jet.

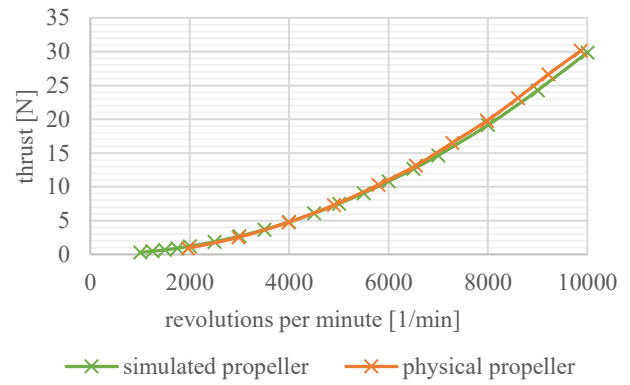


Fig. 2. Thrust comparisson of simulated and physical propeller

III. GEOMETRY DESCRIPTION

The investigated geometries and the corresponding ideas of how lift should be created are described individually for each air guidance strategy.

A. *Ring wing*

5 versions of the ring wing configuration (see Fig. 3 for version 3) were simulated. They mainly differ by the way air is guided to the ring wing.

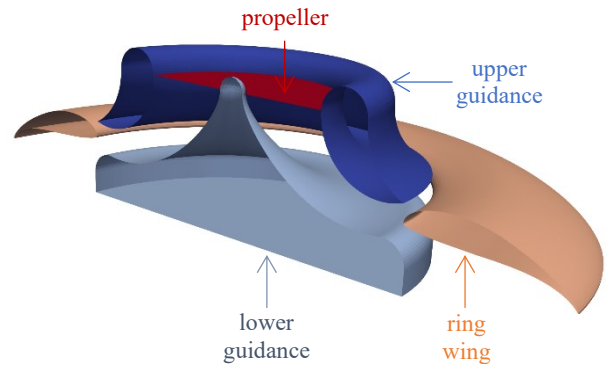


Fig. 3. Overview of simulated ring wing configurations (cross-sectional view of version 3)

The idea behind this geometry is to produce aerodynamic lift by a ring wing based on the Selig S1223 profile [2]. The profile is logarithmically scaled in horizontal direction to compensate for the radially increasing circumference of the circular geometry. In order to make the flow approach the wing in the usual horizontal way, the propeller sucks in air from above the geometry and pushes it through the upper and lower guidance bodies towards the wing nose. The upper and lower guidance bodies were designed to keep the cross-sectional area – through which the air flows – constant.

1) *Version 1*

The 1st simulated version is formed with a round shape on the outer end of the upper guidance body. The lower guidance body has a sharp edge guiding the air to the ring wing with an angle of attack of 8°. The ring wing itself is defined with an inner diameter of 221 mm and a cord length of 200 mm. This results in the ring wing’s nose being positioned right at the end of the guidance channel in the middle between upper and lower guidance bodies.

2) Version 2

In this version the angle of attack of the ring wing profile was increased to 14° to produce a higher lift. In addition, it was moved up by 5 mm (relative to the guidance bodies) and out by 30 mm to reach an inner diameter of 251 mm. This should allow for an easier air outflow from the guidance channel. Furthermore, the lower guidance body was caved to keep the momentum transfer away from the surface and to more evenly spread the higher pressure caused by the propeller.

3) Version 3

Version 3 is almost equivalent to version 2 except for the existence of a cave and the design of the guidance exhaust. Here the upper guidance was adapted to form a nozzle with the ring wing, which should result in a decreased static pressure on the ring wing's upper surface. The lower guidance's outer edge was formed to build a diffuser with the ring wing to increase the static pressure underneath the ring wing and thus create more lift.

4) Version 4

This version is based on the previous one but with sharp edges on the guidance exhaust to prevent the flow from following the guidance bodies. This should improve how the incoming flow approaches the ring wing body.

5) Version 5

Version 5 is identical to version 4 but without the upper guidance body.

B. Bladeless fan

The bladeless fan was designed with the study by M. Jafari, H. Afshin, B. Farhanieh and A. Sojoudi [3] in mind. The propeller sits inside the shaft and sucks air from above the geometry as can be seen in Fig. 4. Then the flow is pushed into the bladeless fan ring from where it leaves downwards through the gap following the bladeless fan ring using the Coandă effect.

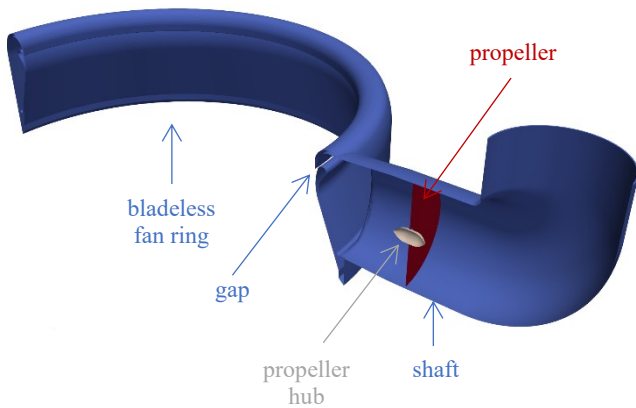


Fig. 4. Overview of simulated bladeless fan configurations (cross-sectional view of version 2)

The main idea behind this geometry is to increase the total mass flow by not only emitting air through the small gap in the profile but also a lower pressure in the center of the bladeless fan ring due to the wing shaped profile (induced flow) and entrained flow from outside the ring (see Fig. 9 for reverence). Thereby the total momentum should increase and consequently push up the bladeless fan.

1) Version 1

Version 1 provides an internal shaft diameter of 260 mm which is only slightly bigger than the propeller's outside diameter. The bladeless fan ring has an outer diameter of 2100 mm and a gap size of 2 mm resulting in a cross-sectional area for the air to leave the bladeless fan ring of about 13000 mm^2 . Compared to the larger propeller disc area of 50000 mm^2 a higher pressure inside the bladeless fan (between propeller and gap) as well as an increased outflow velocity (to keep the mass flow constant) should appear.

2) Version 2

The 2nd version of the bladeless fan is very similar to the 1st version. Only the bladeless fan ring diameter was decreased to 1217 mm while the gap size was increased to 6 mm. This results in an outflow area of about 23000 mm^2 which should allow for a more continuous airflow compared to version 1.

C. Ducted fan

The ducted fan is mainly a de Laval nozzle consisting of two convergent shaped parts followed by a diffuser (see Fig. 5). At the transition between the first ("nozzle") and the second ("jet") convergent part of the de Laval nozzle, the propeller is located. It is a sharp-edged transition, whereas the jet continuously merges into the diffuser so that the guidance allows the flow to follow its shape to ensure an adjacent flow.

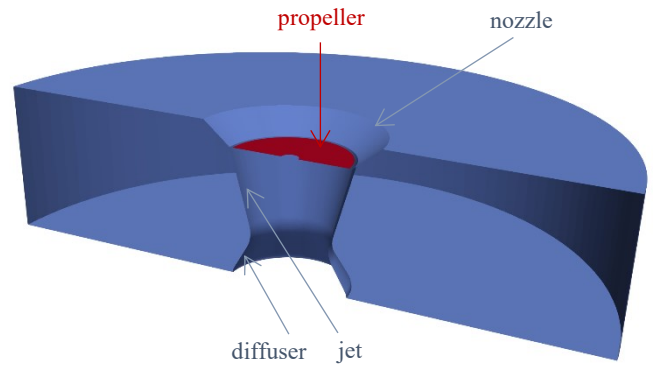


Fig. 5. Overview of simulated ducted fan configurations (cross-sectional view of version 3)

Compared to the other investigated configurations, the advantage of the design depicted in Fig. 5 lies in the fact that no redirection of momentum takes place. Instead, favorably generated forces that act on the geometric parts plus the lift produced by the propeller fully contribute to the overall lift force as no further losses occur. Design point for the shape is 7000 revolutions per minute (RPM). Thus, an adjustable de Laval nozzle design may be required for propeller speeds that differ from the above.

1) Nozzle

As a reference, the geometry of a simple nozzle with a curved guidance was analyzed. The total height measures 368 mm with the propeller located 45 mm underneath the uppermost point. The diameter is 490 mm at the top and tapers to 52 mm in the narrowest cross-section right at the bottom end. Furthermore, it measures 349 mm at the point where the propeller is situated.

2) Version 1

The 1st version of a de Laval nozzle has a total height of 220 mm which is divided by the parts nozzle, jet and diffuser in sections of 50, 55 and 115 mm respectively. The nozzle is designed with an angle of 50° to the vertical with the jet following at only 5°. The diffuser continues with an edge radius of 55 mm followed by a straight section at 45° to the vertical. It ends orthogonally to the horizontal bottom of the fuselage with an edge radius of 25 mm. The diameter is 389 mm at the top of the nozzle, 270 mm at the point where the propeller is situated, 260 mm in the narrowest cross-section and 414 mm at the bottom end.

3) Version 2

Compared to version 1, the jet now shows an angle of 10° to the vertical and is 165 mm high. The diffuser connects with an edge radius of 65 mm followed by a straight section at 30° to the vertical. Consequently, the diameter measures 210 mm in the narrowest cross-section and 300 mm at the bottom end.

4) Version 3

Version 3 differs from 2 in that the jet has an angle of 15° to the vertical and therefore, the diameter at the bottom end is 263 mm and 177 mm in the narrowest cross-section.

5) Version 4

Version 4 differs from 2 in that the diffuser is 345 mm high. It connects to the jet with an edge radius of 260 mm followed by a straight section at 10° to the vertical, ending orthogonally to the horizontal bottom of the fuselage with an edge radius of 375 mm. Thus, the diameter at the bottom end is 290 mm and 204 mm in the narrowest cross-section.

D. Ring nozzle

The ring nozzle consists of an upper and lower guidance body next to the propeller at the top of the geometry as Fig. 6 shows. The upper and lower guidance bodies are engineered to keep the flow through cross-sectional area constant starting from the propeller plane down till a nozzle facing downwards in the last section of the flow tunnel. This nozzle is designed according to the findings from the ducted fan geometries. The outwards bending section of the upper and lower guidance bodies is equivalent to the guidance bodies used for the ring wing. The geometry's outer surface is cylindrical with 673 mm in diameter.

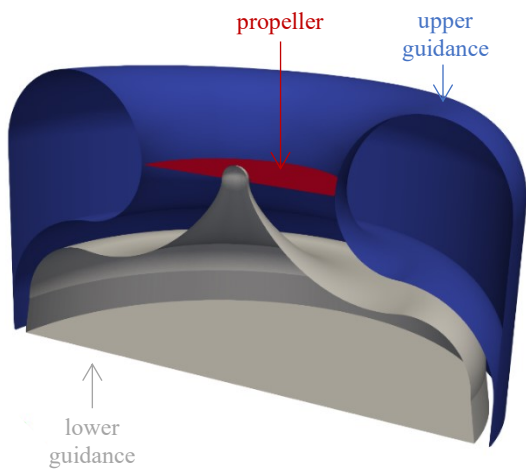


Fig. 6. Simulated ring nozzle configuration (cross-sectional view)

The ring nozzle should accelerate the flow velocity and as a result increase the total momentum. Simultaneously the area for momentum transfer is enlarged. This is achieved by forming the cylindrical jet of a usual propeller to a ring with a significantly bigger circumference to allow for an intense interaction between air jet and the surrounding air.

IV. RESULTS AND DISCUSSION

The simulations of the 4 geometries and all their versions were conducted for various propeller speeds ranging from 2000 RPM up to 9000. The different resulting velocities affect the production of lift according to the Bernoulli equation and the law of conservation of momentum. Depending on the applied lift creation mechanism the effective lift force varies widely as shown in Fig. 7.

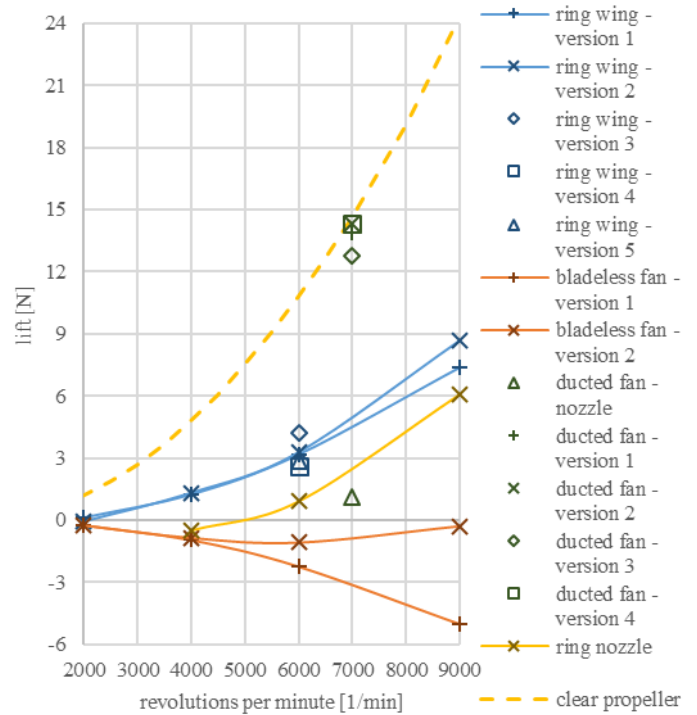


Fig. 7. Lift comparison of the simulated geometries and their versions

The TAU-code was used for simulating the ring wing, bladeless fan and ring nozzle, while the ducted fan was studied using OpenFOAM.

A. Ring wing

The forces acting on the bodies of the ring wing geometry spread in a similar way for versions 1, 2, 4 and 5 as shown in Table I. Most of the air is pushed down by the propeller and guided outwards by the lower guidance body resulting in it being pushed down as the momentum needs to be conserved. Upper guidance and ring wing in contrast produce lift. A higher velocity on the upper guidance's upper surface leads to a lower static pressure compared to the slightly lower velocity on its lower surface. In addition, the total pressure on the body's lower surface is increased by the propeller and thereby leads to some lift. The ring wing works just like a normal wing with its suction side being the upper surface and the pressure side being the lower one.

TABLE I. COMPARISON OF LIFT PRODUCED BY INDIVIDUAL BODIES OF THE RING WING GEOMETRIES

Produced lift	Bodies of the ring wing geometry		
	Ring wing	Upper guidance	Lower guidance
Version 1	10,28 N	5,93 N	-24,37 N
Version 2	7,21 N	0,33 N	-15,97 N
Version 3	-4,65 N	-3,45 N	0,49 N
Version 4	3,79 N	10,26 N	-22,64 N
Version 5	5,56 N	–	-13,36 N

Version 3 of the ring wing geometry works differently compared to the others (see Fig. 8). Here the air doesn't flow round the ring wing but follows the convex curvature of the lower guidance body. There, an accelerated flow results in a very low pressure on the outer convex part of the lower guidance which significantly increases its lift compared to any other ring wing geometry and even compensates for the high pressure on the inner concave part.

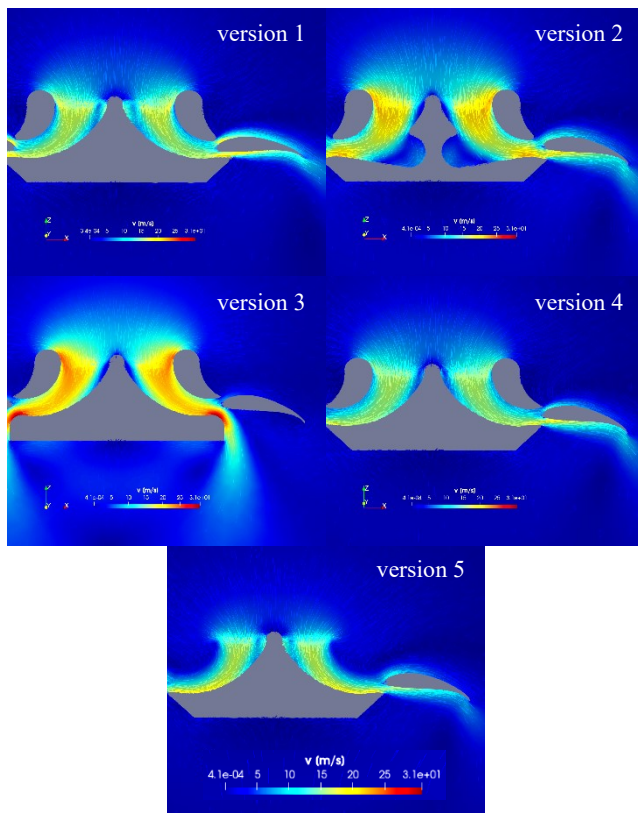


Fig. 8. Overview of velocities of the studied ring wing configurations (cross-sectional view)

B. Bladeless fan

The effective lift achieved by the geometry depends on a force resulting from the surface pressure on the bodies and a viscous force dependent from the wall shear stress resulting from the velocities close to the surface. In case of most simulated configurations of the bladeless fan, the viscous forces as well as the pressure part are sucking the geometry downwards. The major viscous portion results from the thin layer of air streaming downwards from the gap with high

velocity. This results in significantly higher viscous forces than on any other geometry simulated.

For version 2 the mass flow through a disc under the bladeless fan ring with slightly bigger diameter was increased to over 600 % – when compared to the mass flow through the propeller disc in the shaft of version 2 at 6000 RPM – and to over 800 % at 9000 RPM. This is achieved by sucking in air from above and entraining air from the surrounding as it can be seen in Fig. 9.

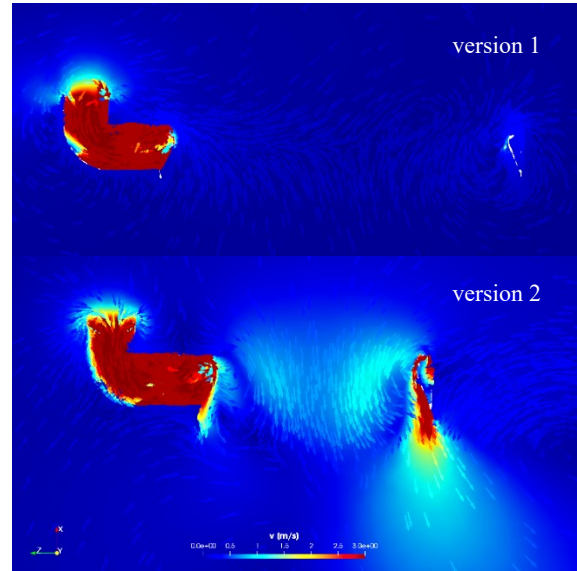


Fig. 9. Overview of velocities of the studied bladeless fan configurations (cross-sectional view)

Even though the downwards facing viscous force grows with increasing propeller speed, the pressure force starts to act in upwards direction starting from 9000 RPM at version 2. This might be due to a bigger pressure difference between the inside of the bladeless fan ring and the surrounding fluid. Probably an even higher pressure inside the bladeless fan ring and/or a bigger gap could help overcome the viscous force and achieve a positive total lift force. However, this might require an optimized impeller to efficiently increase the pressure.

C. Ducted fan

The pure nozzle causes a propeller lift which is 1.24 times higher than the clear propeller's one. As Fig. 10 shows, positive static pressure is acting on almost all the inner area facing upwards. Thus, the total lift force is just above zero.

Version 1 of the de Laval nozzle generates 80 % propeller lift compared to the clean propeller but also negative static pressure acting on the nozzle and jet parts as the flow induced by the propeller increases the velocity above and below the propeller plane. Therefore, the total lift reaches a value of 96.5 % of the clean propeller's lift. The diffuser, however, is not effective at all.

The propeller of version 2 produces only 75.5 % of the clean propeller's lift, whereas Version 3 reaches 85.5 %. However, the generated forces acting on the geometry effect a total lift which is 99.3 % of the clean propeller's lift at version 2, while version 3 lands at 88.9 % due to the excessive constriction. Obviously, an optimum exists between nozzle jet

effect on the one hand and static pressure distribution on the other.

Version 4 reaches only 60.7 % propeller lift compared to the clean propeller but generates the most lift force on the geometry so that the total lift is the same as with version 2. The core jet is not just passing through the diffuser but starts to follow the contour now. Further optimization may lead to hoped-for pressure recovery in the entire diffuser area which makes it work more effectively.

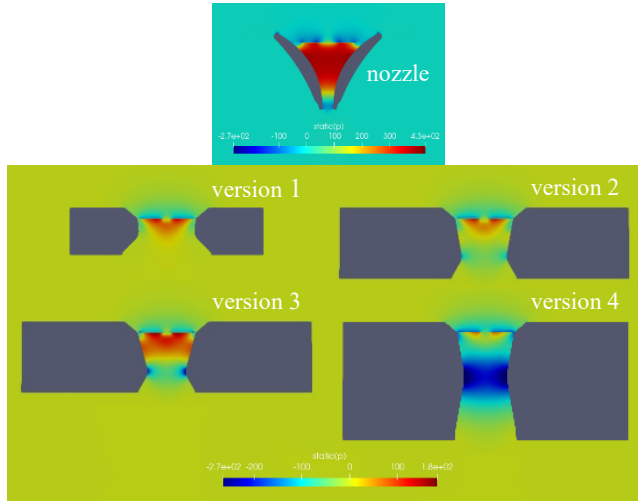


Fig. 10. Overview of static pressure relative to the reference state (101325 Pa) of the studied ducted fan configurations (cross-sectional view)

D. Ring nozzle

At the bottom of the lower guidance body low pressure that is induced by a big vortex ring (see Fig. 11) appears and sucks down the body. Consequently, the conducted ring nozzle simulations show a lower guidance body that overcomes the lift of the upper guidance body by 23 to 29 % but in opposite direction. As a result, the two bodies combined produce a downwards force that first needs to be compensated by the propeller before creating any lift.

Since the effective lift increases drastically with higher propeller speeds (see Fig. 7), it can be assumed that a higher pressure makes the configuration more effective. Therefore, an optimized impeller might be required.

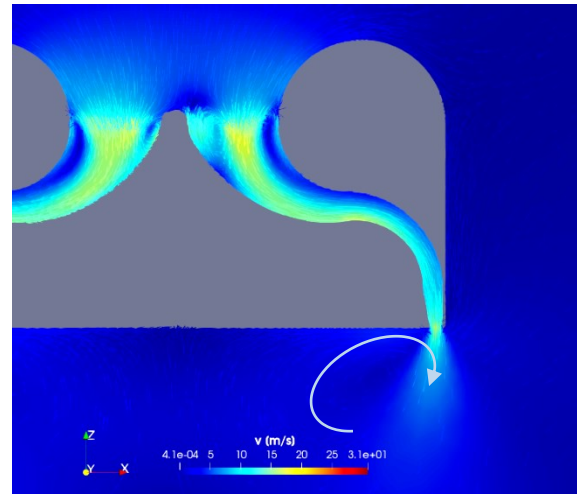


Fig. 11. Velocities of the studied ring nozzle configuration (cross-sectional view)

V. CONCLUSION

When compared to the clear propeller, most of the configurations produce significantly less lift. Only some of the ducted fan geometries get very close. With further optimization they could even produce more lift than the corresponding propeller without air guidance geometry.

In addition, it should be noted, that a helicopter's fuselage disturbs a propeller's air jet in a considerable way and thereby reduces the effective lift. Thus, any results of the studied geometries that are within reach of the clear propeller's lift indicate a promising strategy for producing lift. This is because for all 4 geometries the fuselage could easily be integrated into the air guidance bodies without disturbing the air jet any further.

In general, this study is by no means final and there is still room for geometry improvements with all studied designs.

REFERENCES

- [1] *TAU-Code User Guide*, Release 2018.1.0, DLR, Cologne, Germany, 2018.
- [2] University of Illinois at Urbana-Champaign. (n.d.). *UIUC Airfoil Coordinates Database* [Online]. Available: https://m-selig.ae.illinois.edu/ads/coord_database.html
- [3] M. Jafari, H. Afshin, B. Farhanieh, A. Sojoudi, „Numerical investigation of geometric parameter effects on the aerodynamic performance of a Bladeless fan,“ *Alexandria Engineering Journal*, vol. 55, pp. 223–233, 2016.

Sustainable materials for insulating high-altitude rural Kyrgyz residential houses: A parametric economic study

Jakob Beringer
Institute of Energy Systems (InES)
Technische Hochschule Ingolstadt
 Ingolstadt, Germany
 jakob.beringer@thi.com

Kedar Mehta
Institute of Energy Systems (InES)
Technische Hochschule Ingolstadt
 Ingolstadt, Germany
 kedar.mehta@thi.com

Mathias Ehrenwirth
Institute of Energy Systems (InES)
Technische Hochschule Ingolstadt
 Ingolstadt, Germany
 mathias.ehrenwirth@thi.com

Wilfried Zörner
Institute of Energy Systems (InES)
Technische Hochschule Ingolstadt
 Ingolstadt, Germany
 wilfried.zoerner@thi.com

Abstract — The heat demand for residential households in cold-climatic environments such as high-altitude rural Kyrgyzstan can be 300 kWh/(m²·a) or above. It has been identified that leakages and a lack of insulation are the main reasons for this high heat demand. Typically, insulation materials, compounded of oil-based plastics and foams (like extruded polystyrene or polyurethane foam), are mainly industry processed and rarely exist in rural regions. The isolated location and low-income scenario of Kyrgyz remote settlements are considered as key hurdles for availability of such insulation materials. In that case, sustainable fabrics like straw, reed or sheep wool from agricultural activities can play a role. These materials are widely and locally available and can be used for insulation, too. In this paper, the effect of different materials and their thicknesses on heat demand is analysed. Therefore, a building simulation model of an uninsulated rural Kyrgyz house was developed in the software *EnergyPlus*. Various combinations of insulation material and thicknesses are simulated in a study to optimize heat demand. Additionally, the study was concluded by presenting the economic feasibility of the presented sustainable insulation materials. The results indicate that typical payback periods between 4 and 7 years can be achieved.

Keywords—Central Asia, building technology, thermal envelope, heat demand, insulation, sustainable material

I. IMPORTANCE OF INSULATION FOR RURAL HIGH-ALTITUDE KYRGYZ RESIDENTIAL HOUSEHOLDS

Most rural houses in Kyrgyzstan are earthen buildings typically constructed with soil, clay-straw, or adobe. The majority of the building stock in Kyrgyzstan was constructed during the Soviet period roughly 35-60 years ago [1]. So, age and building characteristics lead to a high space heating demand, particularly in rural regions where around 66 % of the Kyrgyz population lives [2, p. 10]. Further to this, long and harsh winters intensify space heating demand.

However, the most relevant factor for this high demand is the lack of insulation in most rural Kyrgyz houses. The widespread low-income scenario. The current buildings in Kyrgyzstan are often poorly insulated, which results in a high heat flow rate out of the building. Therefore, the application of suitable insulation material is the most promising solution to overcome this problem. From a thermal point of view, it can

be obtained that the lower the thermal conductivity of the layer is, the less heat is going to be lost. In that context, insulation is considered as a material with low thermal conductivity or a high thermal resistance. Typically, insulation materials cannot be used for structural applications due to their limited or insufficient structural resistance. Therefore, additional more rigid layers are required to provide stability. In the best case, walls are capable of both, able to hold the roof construction and creating a thermally sealed envelope. As a result, heat losses can be minimized, and less heat is required to hold temperature on a constant level. Unfortunately, typical residential houses in Kyrgyzstan are built with poor or even without insulation [3, 4].

Sustainable insulation materials are considered as by-products from agricultural activities. Almost 55 % of the Kyrgyz total land area are used for agricultural activities, so it is one of the most important economic sectors in Kyrgyzstan [5]. Especially pasture for livestock (mainly sheep, goats, and cattle), which is the traditional profession of the Kyrgyz people, is practiced. Due to the specific geographical conditions of the country, most of the farms are located in mountainous regions at high altitudes. Because of the active agricultural and livestock activities, several materials are available as a side-product and can be used as insulation materials. On the one hand, due to their unstable income and poverty in rural Kyrgyzstan, the application of thermal insulation to their homes is not considered as being practical by most rural householders [6, p. 3]. On the other hand, the active agricultural and livestock sectors provide an opportunity to use sustainable materials such as straw bale, sheep wool and reed panel for house insulation. These materials can be potentially considered economically feasible as they are available locally from agricultural waste. Hence, the presented study performed an economic evaluation on locally available sustainable insulation materials to assess the economic viability as well as the impact of such materials to reduce high domestic heat demand of rural Kyrgyz houses.

II. OVERVIEW OF THE AVAILABLE MATERIALS AND TECHNOLOGIES

In the following sections, different insulation materials, which are locally available in Kyrgyzstan, are analysed regarding their origin and thermal properties. They are divided

into two classes, non-renewable and renewable materials. Oil-based plastics and foams are considered as non-renewables. Examples for renewable materials are sustainable fabrics like wool, straw or reed.

A. Oil-based plastics and foams

In Kyrgyzstan, “Penoplex” is a widely accepted material for insulation [7]. Penoplex is an insulation material created by extruding polystyrene. It is sold from a Russian company, which has production lines in Central Asia, too [8]. According to different sources, the price for a 40 mm thick insulation layer of Penoplex is around 2.70 €/m² [9, 10]¹.

Furthermore, a common technology for insulating a house is polyurethane (PU) foam. This special kind of polymeric material can be sprayed on various surfaces such as walls or roofs and even around corners [11, p. 1]. It is very adhesive, so that the structure where the foam is applied on is of minor importance. The chemical reaction of two liquids is utilized on site to create a foam which is then pumped through a pipe to spray it on surfaces. This reaction is also called curing. According to [12, p. 243] PU foam is toxic during the manufacturing (mixing and installation) and curing process. Spray application generates isocyanate vapours and aerosols which are harmful to skin, eyes and respiratory tracts [13] which can be considered as a huge disadvantage in this context. The foam may appear hardened after a few minutes. Nevertheless, for about 24 hours unreacted chemicals can be detected which created toxic gases.

The technologies presented above can reduce heat demand significantly despite comparatively low investment costs. But these materials show disadvantages as well. On the one hand, they are based on plastics derived from crude oil. Hence, such materials are non-sustainable and finite. On the other hand, the impact on health has not been fully investigated. In rare cases buildings can get inhabitable after distributing such a foam [14]. However, most important in this context is the lack of availability of conventional insulation materials in Kyrgyz remote settlements in the rural highlands. Alternatively, sustainable insulation materials can be used. They are often based on plants and fibres and will be described in the following chapter.

B. Sustainable and renewable insulation materials

Previous research identified that sustainable insulation materials can reduce domestic space heating demand considerably [1]. This makes sustainable insulation materials significantly more environmentally friendly. According to [1], there are three most commonly available natural insulation materials (sheep wool, straw bales and reed panel) in Kyrgyzstan which are described in the following section.

Sheep wool is a lightweight by-product of the sheep pasture. The quality of wool, which often plays a role in the textile market, does not affect the material performance for insulation applications [15]. Shorter wool yarns are also suitable as the material is not woven. So, for insulation purposes wool can be used, which is not suitable for the fabric industry. The wool can simply be stuffed into prepared cut-outs in the facade construction. Nevertheless, a pilot study

[15] showed that its usage should not be exaggerated, and the volume of production needs to be carefully considered to ensure long-term sustainability of the operation.

Another widely available material is straw. Straw is an often-unused by-product of agricultural activities. Around two tons per ha of agricultural areas in Kyrgyzstan are currently unused and could be utilized for different applications like power generation or insulation [16]. Formed to bales, it can be used for insulation purposes. There are two widespread straw bale insulation techniques available. These bales can either be used as filling material in a beam structure or as load bearing structure itself. This benefits in a reduced demand of building materials as [17]. Especially for the second option, straw bales are applied in thicknesses of 45 cm or more to withstand the loads. The high thickness turns out as positive outcome to reduce the heat loss through the building envelope and recommended to withstand extremely low temperature in winters. Unfortunately, the comparability with other methods is then rather difficult as the standard model (described in chapter III) can no longer be applied. A low moisture content (less than 15 %) is necessary to use straw as an insulation material.

The third insulation material analysed in this study is reed which is common construction material for roofs and walls [18]. However, the use of reed panels is mainly dependent on the availability of it in Kyrgyzstan. As reed especially grows in swamplands or shores, the availability is not very widespread. Similar to straw bales, reed can be either used as the main construction material by forming bales or by creating panels to put onto the existing wall made from e.g. bricks [19].

To measure the effectiveness of the different materials on heat demand, the material properties need to be analysed. Tab. 1 offers a parameter overview of the three sustainable materials which are considered in this study as sustainable insulation materials for rural Kyrgyz houses.

Tab. 1. Overview of the selected sustainable insulation materials

Material	Thermal and Mechanical Properties ^a		
	Conductivity in W/(mK)	Density in kg/m ³	Specific Heat in kJ/(kgK)
Sheep wool	0.04	26	1.7
Straw bale	0.045	95	2.1
Reed panel	0.065	225	1.2

^a All material properties are from [20]. According to this source, the data represent a conservative average of common products. In any case, the installation process has an influence, too. The determined values are in accordance with other sources used in this paper, e.g. [21].

III. METHODOLOGY

To determine the effectiveness of the presented insulation materials, it is necessary to identify heat demand of an uninsulated rural Kyrgyz house.

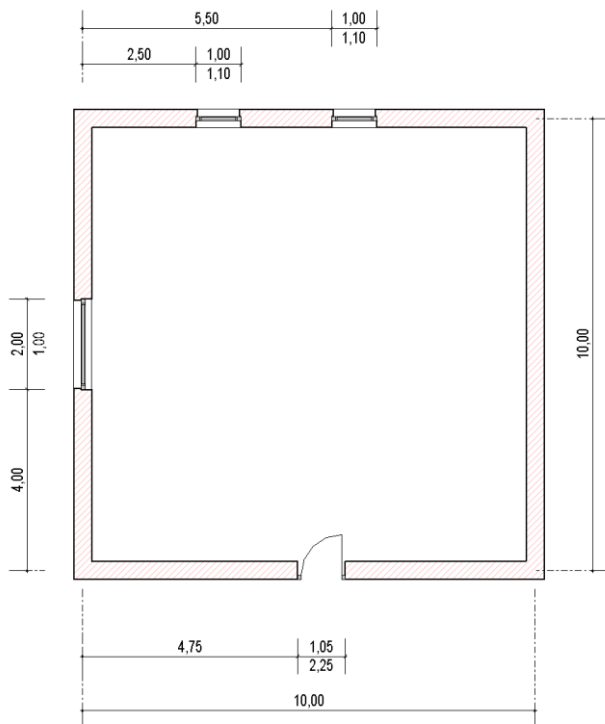
One approach to determine a building's heat demand is the open source software *EnergyPlus* [22]. In a simplified description, a local weather profile and a target temperature are required to determine the temperature difference between interior and exterior. Heat losses are derived by multiplying the temperature difference with the surface area of the

¹ In the sources, the Kyrgyz currency KGS (Kyrgyz Som) is used (270 KGS/m²). 1 € equals 100 KGS.

building and the U-value of the area. The used model of the building is based on a literature review [1, 3, 23, 24]. The simulation is based on the model from the “American Society of Heating, Refrigerating and Air-Conditioning Engineers” (ASHRAE). For a precise simulation result a weather file based on data from the software *Meteonorm* is imported into *EnergyPlus*. In this case weather data from the city of *Naryn* is used as these are the closest available to rural areas in Central Kyrgyzstan.

To develop a base case scenario, a standard rural residential Kyrgyz house model was created in *EnergyPlus*, which is briefly described in the following paragraph. The house is built with adobe bricks, a common wall material. Often, multiple generations share one building which is represented by an occupancy profile with high fluctuation of inhabitants over the day. The size the building is considered 10 meters (length) and 10 meters (width), therefore yielding 100 m² floor area, which can be considered as typical value. An estimated room height of 2.3 meters and a total building height up to the ridge of 6.5 meters is applied. This is necessary to define the surface sizes of walls and roof as surface is part of the calculation for the heat flow. The window configuration is kept simple (three larger windows, see also in floor plan in Fig. 1), but they must be included to generate reasonable and realistic results as they need to be considered as heat bridges due to their poor conditions (U-value of the window including frame is around 3 W/(m²·K)). But even more important, these windows lead to solar gains in the heat balance of the building. General inaccuracies by aging and weathering of the building leads to additional heat bridges.

Fig. 1. Floor plan of the model used for the standard house (calculating uninsulated heat demand)



Rural Kyrgyz houses often have an open roof construction (no sidewalls to close gables), which has a negative impact on heat demand (up to 300 kWh/(m²·a)) [1]. Previous investigation showed that closing the sidewalls of the roof construction can reduce heat demand by about 20 % without any need of insulation materials [1]. Before thinking about insulating building components, it is recommended to close these open gables due to the low investment costs and benefit of this measure. However, this is not considered in the framework of this paper. The standard model already uses a closed roof, which results in a heat demand of 207 kWh/(m²·a). Nevertheless, this is still high for a residential home. The following chapter evaluates different measures to reduce heat demand. Furthermore, these actions are related to their investment costs. Due to their possible implementation in older existing buildings, wall and ceiling insulation is the focus of this study.

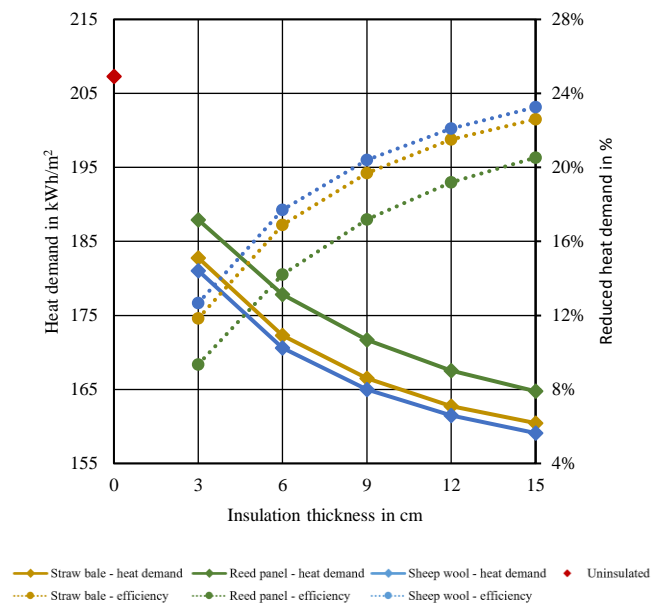
IV. EVALUATION OF THE SUITABLE SUSTAINABLE MATERIALS IN *ENERGYPLUS*

A. Wall insulation

Insulating walls is a common method to insulate the house as it is probably the most known approach. According to the material analysis in chapter II, an additional layer is placed on all four outer walls of the model. The insulation material is attached on the outside of the wall.

A parametric study is performed by varying materials and thicknesses. The three materials sheep wool, straw and reed with a thickness of 3 to 15 cm (increment of 3 cm) are projected. Of course, the thicker the layer of insulation material, the less heat demand is evaluated (see Fig. 2). Depending on material and thickness, the building’s heat demand can be reduced by 9 to 23 % compared to the reference design (displayed in red as uninsulated house, which

Fig. 2. Simulation results for various thicknesses and different insulation materials when insulating the four outer walls of the standard house



equals the standard base case model). As expected, a correlation to the conductivity of each material is noticeable, i.e., the lower a material’s heat conductivity, the higher its contribution to minimizing the building’s heat demand.

Using sheep wool with the lowest thermal conductivity will reduce heat demand further than using reed panels or straw bales with the same thickness.

When using whole (straw) bales as insulation material, the bricks used for the structural support of the building are not necessary anymore. Due to the complexity of such applications and poor comparability to the other analysed insulation configurations, such constructions are not considered here.

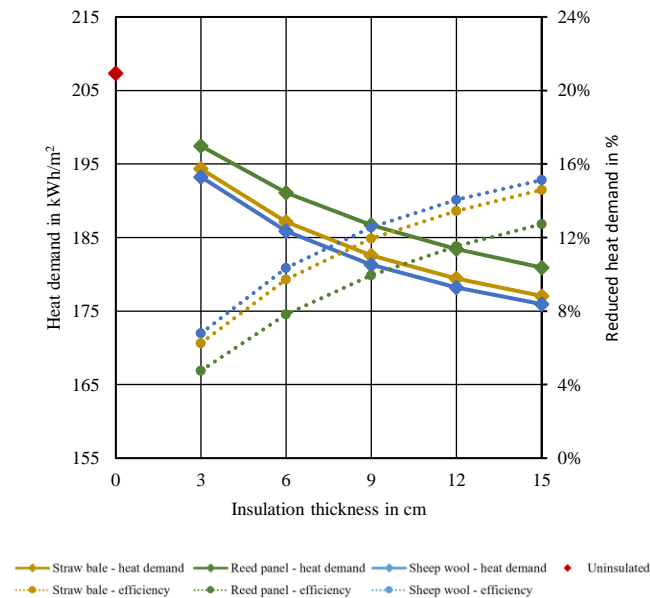
B. Ceiling insulation

In a second step, the ceiling insulation is observed to evaluate the effectiveness of the selected materials on the ceiling surface. Generally, the procedure is similar to the wall insulation. The thickness of the insulation is again varied in steps from 3 cm to 15 cm. According to their material properties, again reed brings the lowest decrease in heat demand considering the same thickness for all materials (c.f. Fig. 3). In comparison to wall insulation, the energy savings are generally lower. A reason here is the smaller surface of the ceiling (100 m²) compared to the sum of all outer walls (129 m²).

C. Combination of wall and ceiling insulation

Combining insulation of wall and ceiling will reduce heat demand further. A maximum of 35-40 % reduction can be achieved by using the maximum thickness on both

Fig. 3. Simulation results for various thicknesses and different insulation materials when insulating the ceiling of the standard house



² Around 0.065 US\$/kWh_{th} are stated for a house boiler powered with coal for an individual household in the urban environment [28, iv]. This equals around 0.055 €/ kWh_{th}.

components wall and ceiling. In this scenario, a minimum heat demand of 126 kWh/(m²·a) can be reached. However, taking European standards into account this value is still high [25]. This may be due to poor building conditions and poor window quality.

V. ECONOMIC EVALUATION BASED ON PAYBACK PERIOD

The aim of this section is to find the most economically reasonable level of sustainable thermal insulation of a rural building in Kyrgyzstan. Therefore, costs for materials and installation processes must be defined. Tab. 2 shows estimated rough numbers for material cost in m³ without any installation efforts. Moreover, this shows the raw material price per volume. This is necessary to display the different amounts of material needed to cover the whole surface with insulation material. As an example, assuming an insulation thickness of 3 cm, 1 m³ of material is enough for around 33 m² of surface area. But when using a thickness of 15 cm, the same amount of material would only be sufficient for around 7 m². In some cases, calculations were necessary, to determine a value for a volumetric unit. Considering different thicknesses is only reasonable if the material costs are significant. Otherwise, the costs for the installation process define the investment of these measures.

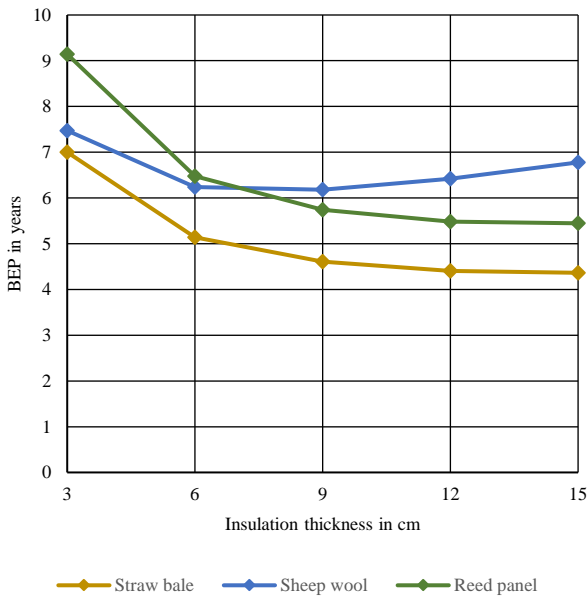
Tab. 2. Overview of the selected sustainable insulation materials

Material	Cost in € per m ³	Remarks
Sheep wool	60	chance to open a new market for shrinking fibre processing market; fibre quality less important; based on [26]
Straw bale	15	hard to validate; straw as waste product; comparable low price; based on own evaluation
Reed panel	25	Only building material; based on [27]

It can be estimated that the installation price is approximately 9 €/m². Own evaluations showed that these are roughly costs for insulating a house with sustainable insulation material in an urban context. This value can be considered as a careful (and probably to high) calculation for rural regions.

To identify the time until the investment has returned, the total costs for installation are divided by the cost savings of each year, which describes the break-even point or short BEP. In this case, these cost savings equal the amount of money, which can be saved by a reduced heat demand as for generating heat a fuel is needed. In this study, average fuel costs of 0.055 €/kWh_{th} are estimated. Unfortunately, estimating these costs for one kWh is difficult, especially for the rural Kyrgyz region due to a lack of information. Nevertheless, for urban areas approximations for the levelized cost of heat, as this price per kWh is also called, exist². Possibly these levelized costs of heat are higher compared to rural regions due to the unequally split of wealth in the country

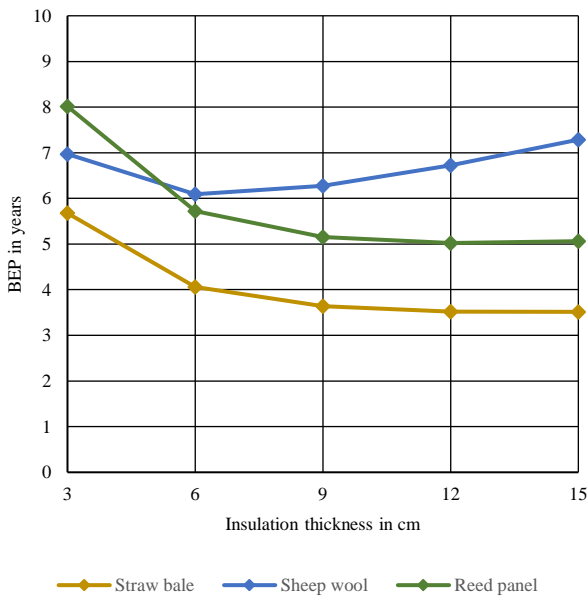
Fig. 5. Break-even point (BEP) for various thicknesses and different insulation materials when insulating the four outer walls of the standard house



[29]. In absence of any more precise data, 5.5 KGS are considered as price for one kWh_{th} even in rural areas.

When plotting the BEPs over thickness (see Fig. 5), it is visible, that installation costs are the driving component of this investment as utilising more material by increasing thickness is beneficial. However, for reed panels due to low material costs, the BEP is still decreasing with an increasing thickness. Hence, an even thicker insulation layer can make sense, if increasing the thickness does not affect the installation costs.

Fig. 4. Break-even point (BEP) for various thicknesses and different insulation materials when insulating the ceiling of the standard house



Analysing the BEP of insulating the ceiling, the results differ (see Fig. 4). In this case it is a horizontal area, which makes the installation process easier. The material can just be placed on top of the existing roof structure, which is required to withstand load-bearing forces from roof. This results in lower installation costs. So, material costs have a bigger impact on the BEP when insulating the ceiling. Consequently, it is more interesting when planning to insulate existing houses. If the space in the attic is not needed for any other purpose, the material will be simply laid out on top of the existing structure. In this case no special constructions or tools are required, which makes it possible to implement without help of any third party. Hence, installation costs can be neglected, which impacts the economic evaluation in a positive way. Nevertheless, this study assumes a price of 4 €/m² for installing the ceiling insulation. Otherwise, this would lead to a distortion of the result as for material costs a significant price is estimated.

Combining the measures for ceiling and wall shows that from an economic point of view insulating the wall is more expensive as there is more material necessary and the installation costs are higher. But even when considering all 256 combination of the four materials (none, straw, sheep wool and reed) in six different thicknesses on two different building components ((4×6)² = 256), the BEPs are reasonable. Nearly 80 % of the combinations have a break-even point within less than 7 years, around 15 % of the possible combinations in less than 5 years, which is considered as an attractive payback period [30]. But it is questionable if the poor income of rural Kyrgyz households is sufficient for such measures as the cold climatic conditions and snowfall in the mountain regions slow down the agricultural activity during the winter in Kyrgyzstan. Grazing animals cannot find enough fodder in the snow-covered terrain. Therefore, the rural population struggles to generate a constant income from their occupation in agriculture. This is one of the reasons for the high poverty rate in rural Kyrgyzstan [31, p. 459]. Appropriate governmental funding schemes can be helpful here.

VI. CONCLUSION

This parametric study showed the economic potential of sustainable materials for rural Kyrgyz houses. When upgrading the thermal shell of the building, material and insulation costs can be considered as key parameters. If the insulation material can be used free of charge, the time until break-even will be reduced or, in case no extra costs for installation occur, the measures will pay off from the first day onwards. This key lesson should be disseminated among rural communities in Kyrgyzstan to increase the awareness.

Unfortunately, all the listed insulation materials in the paper are still not acknowledged as insulation materials in Kyrgyzstan. Hence, it is necessary to make the local residents aware of the enormous potentials by using such materials. As an additional positive outcome, greenhouse gas emissions from households will decrease due to a low heat consumption.

A further heat demand reduction can be achieved by optimizing the windows and frame material or thermal sealing of the roof construction but require a higher investment. A case-by-case decision is necessary here. It is recommended

that heat demand reduction measures can be implemented sequentially by considering the income scenario of rural Kyrgyz settlements to make them viable.

REFERENCES

- [1] K. Mehta, M. Ehrenwirth, C. Trinkl, W. Zömer, and R. Greenough, "Impact of Locally Available Thermal Insulation Structures on Space Heating Demand of High-altitude Rural Buildings: A Case Study of Kyrgyzstan," in *International Solar Energy Society Hg - Eurosun 2020*. Accessed: (Publication in progress).
- [2] Food and Agriculture Organization of the United Nations (FAO), *National gender profile of agricultural and rural livelihoods - Kyrgyz Republic: Country gender assessment series*, 2016. Accessed: Dec. 17 2020. [Online]. Available: <http://www.fao.org/3/a-i5763e.pdf>
- [3] R. Botpaev, J. Orozaliev, and K. Vajen, "Economically optimal level of thermal insulation for single-family houses in Kyrgystan," Sep. 2011. Accessed: Sep. 21 2020. [Online]. Available: https://www.uni-kassel.de/maschinenbau/fileadmin/datas/fb15/110912_Paper_Thermal_Insulation_for_single-family_houses_in_Kyrgyzstan_rb.pdf
- [4] K. Mehta, M. Ehrenwirth, C. Trinkl, W. Zömer, and R. Greenough, "A Parametric Study on the Feasibility of Solar-thermal Space Heating and Hot Water Preparation under Cold Climates in Central Asian Rural Areas," in *International Solar Energy Society (Hg.) - Eurosun 2020*. Accessed: (Publication in process).
- [5] N. Komendantova, N. Atakanov, and U. Chekirbaev, "Industrial Development of Kyrgyzstan: Required Infrastructure and Priority Industrial Sectors," Oct. 2018.
- [6] K. Hall, "Supporting Energy Efficiency and Renewables Uptake in Rural Communities in Mountainous Kyrgyzstan," Mountain Societies Research Institute (MSRI), Bishkek (Kyrgyzstan), 2018. Accessed: Apr. 29 2021. [Online]. Available: <https://www.ucentralasia.org/Research/Item/1711/EN>
- [7] B. Aypov, *Building Construction Techniques in Ak-Tal, Kyrgyzstan*. Interview. Accessed: Sep. 25 2020.
- [8] Penoplex, Ed., "PENOPLEX® FASSADE," Accessed: Nov. 2 2020. [Online]. Available: <http://penoplex.com/penoplex-fassade-2/>
- [9] Пеноплекс Комфорт (1185x585x40 мм). [Online]. Available: <https://td-pzsp.ru/teploisolyaciya/penopolistrol/tproduct/196333959-918159259104-penopleks-komfort-1185h585h40-mm> (accessed: Jan. 25 2021).
- [10] Пеноплекс | Пеноплекс - создан дарить тепло, "ПЕНОПЛЕКС (ПЕНОПЛЕКС) КОМФОРТ купить в Москве," Accessed: Jan. 25 2021. [Online]. Available: <https://www.kupi-penoplex.ru/uteplitel-plity-penoplekskomfort>
- [11] Center for the Polyurethanes Industry, "Guidance on Best Practices for the Installation of Spray Polyurethane Foam," 2012. Accessed: Apr. 27 2021. [Online]. Available: <https://polyurethane.americanchemistry.com/Spray-Foam-Coalition/Guidance-on-Best-Practices-for-the-Installation-of-Spray-Polyurethane-Foam.pdf>
- [12] J. C. Harris, "Toxicology of Urea Formaldehyde and Polyurethane Foam Insulation," *JAMA*, vol. 245, no. 3, p. 243, 1981, doi: 10.1001/jama.1981.03310280019020.
- [13] US EPA, *Potential Chemical Exposures From Spray Polyurethane Foam | US EPA*. [Online]. Available: <https://archive.epa.gov/epa/saferchoice/potential-chemical-exposures-spray-polyurethane-foam.html> (accessed: Apr. 27 2021).
- [14] M. Griffith-Greene, "Spray foam insulation can make some homes unlivable," 25 Oct., 2013. <https://www.cbc.ca/news/spray-foam-insulation-can-make-some-homes-unlivable-1.2224287> (accessed: Apr. 27 2021).
- [15] K. W. Corscadden, J. N. Biggs, and D. K. Stiles, "Sheep's wool insulation: A sustainable alternative use for a renewable resource?," *Resources, Conservation and Recycling*, vol. 86, pp. 9–15, 2014, doi: 10.1016/j.resconrec.2014.01.004.
- [16] L. Rocha-Meneses, T. F. Bergamo, and T. Kikas, "Potential of cereal-based agricultural residues available for bioenergy production," *Data in brief*, vol. 23, p. 103829, 2019, doi: 10.1016/j.dib.2019.103829.
- [17] T. Ashour, H. Georg, and W. Wu, "Performance of straw bale wall: A case of study," *Energy and Buildings*, vol. 43, no. 8, pp. 1960–1967, 2011, doi: 10.1016/j.enbuild.2011.04.001.
- [18] F. Asdrubali, F. D'Alessandro, and S. Schiavoni, "A review of unconventional sustainable building insulation materials," *Sustainable Materials and Technologies*, vol. 4, pp. 1–17, 2015, doi: 10.1016/j.susmat.2015.05.002.
- [19] M. Miljan, K. Akermann, and K. Karja, *Thermal transmittance of reed-insulated walls in a purpose-built test house*, 2014. Accessed: May 1 2021. [Online]. Available: https://www.researchgate.net/profile/matis_miljan/publication/292874395_thermal_transmittance_of_reed-insulated_walls_in_a_purpose-built_test_house/links/58c68fc8a6fdce648ec7e93/thermal-transmittance-of-reed-insulated-walls-in-a-purpose-built-test-house.pdf
- [20] Plag Ralf, *ubakus*: u-wert.net GmbH. Accessed: Apr. 29 2021. [Online]. Available: <https://www.ubakus.com/en/r-value-calculator/>
- [21] K. Zwiebauer, "Insulation Materials - Product groups," Learning unit funded by European Commission, 2015. Accessed: May 3 2021. [Online]. Available: https://www.e-genius.at/fileadmin/user_upload/lernfelder/daemmstoffe/alt/daemmstoffe_praxis/en/Insulation%20Materials_Product%20Groups.pdf
- [22] Lawrence Berkeley National Laboratory, *Energy Plus: Version 9.4.0*: U.S. Department of Energy's (DOE), 2021. Accessed: Apr. 27 2021. [Online]. Available: <https://energyplus.net/>
- [23] E. Boronbaev, "Energy saving Architecture: Background, Theory and Practice in Kyrgyzstan," *E3S Web Conf.*, vol. 172, 2020, doi: 10.1051/e3sconf/202017219010.
- [24] International Business Council, Ed., "Kyrgyzstan Construction Materials Value Chain Stakeholder Analysis: Final Report," Mar. 2016. Accessed: Dec. 18 2020. [Online]. Available: http://ibc.kg/en/analysis/surveys/1866_results_of_a_survey_on_kyrgyzstan_construction_materials_value_chain_stakeholder_analysis
- [25] *Zweite Verordnung zur Änderung der Energieinsparverordnung, BGBl I Seite 3951 vom 18.Nov.2013: EneV*, 2014. Accessed: May 4 2021. [Online]. Available: https://www.bmwi.de/Redaktion/DE/Downloads/Gesetz/zweite-verordnung-zur%20aenderung-der-energieinsparverordnung.pdf?__blob=publicationFile&v=1
- [26] Информационное Агентство Кабар, *Kyrgyzstan exports lamb to Iran, wool to China*. [Online]. Available: <http://en.kabar.kg/news/kyrgyzstan-exports-lamb-to-iran-wool-to-china/> (accessed: May 3 2021).
- [27] CEEBA, *Info thermohouse insulation*. [Online]. Available: <http://www.ceeba.kg/index.php?ln=en&pg=svr> (accessed: May 3 2021).
- [28] A. Balabanyan, K. Hofer, J. Finn, and D. Hankinson, "Keeping Warm: Urban Heating Options in the Kyrgyz Republic: Summary Report," May. 2015. Accessed: Jul. 9 2020. [Online]. Available: <https://documents.worldbank.org/en/publication/documents-reports/documentdetail/555021468011161504/keeping-warm-urban-heating-options-in-the-kyrgyz-republic-summary-report>
- [29] A. Sultanov, O. Ojielo, C. Jaulmes, N. Chuykov, and A. Orosbaev, *Monitoring of the Sustainable Development Goal Indicators in the Kyrgyz Republic: 2014-2018*. A Statistical Compendium, 2020. Accessed: Dec. 8 2020. [Online]. Available: <http://www.stat.kg/media/files/Odf67c73-a648-4c10-a6b5-c4df2311cac7.pdf>
- [30] O. Kaynakli, "Parametric Investigation of Optimum Thermal Insulation Thickness for External Walls," *Energies*, vol. 4, no. 6, pp. 913–927, 2011, doi: 10.3390/en4060913.
- [31] L. Sagynbekova, "Environment, Rural Livelihoods, and Labor Migration: A Case Study in Central Kyrgyzstan," *Mountain Research and Development*, vol. 37, no. 4, pp. 456–463, 2017, doi: 10.1659/MRD-JOURNAL-D-17-00029.1.

Investigation of the heat transfer during condensation of wet flue gas in horizontally, corrugated tubes

Maximilian Briechle

Nuremberg Institute of Technology

Faculty of Process Engineering

Kesslerplatz 12, Nürnberg

Email: briechlema59305@th-nuernberg.de

Daniel Raab

APROVIS Energy Systems

Ornbauer Str. 10, Weidenbach

Email: daniel.raab@aprovis-gmbh.de

Abstract—Due to its low efficiency, condensation with a high amount of inert gas is not very well investigated. However, as the demand for efficiency rises, this phenomenon gets more interesting. The goal of this paper is to evaluate the predictability of the heat transfer coefficient during condensation of flue gas in corrugated tubes. For this, corrugated tubes with 3 different diameters were investigated. 3 different initial dew points were investigated to match industry relevant applications. For every dew point and diameter combination a range of Reynolds-numbers were investigated. The measured heat transfer coefficients are compared with a correlation found by Gundermann [1] in a previous work for smooth tubes. The used correlation showed a good fit for the measured corrugated tubes, however not all questions regarding the comparability between smooth and corrugated tubes could be answered.

I. INTRODUCTION

Highly efficient use of energy in industrial applications gets more critical as the demand for the reduction of greenhouse gases rises. Therefore previously less interesting potential energy savings become more interesting. One such energy saving potential is the use of condensing boilers. Contrary to conventional boilers, condensing boilers not only use the heat generated by burning fuel, but also utilize the latent heat trapped in the generated flue gas. The most interesting component regarding latent heat in flue gas is water, which is formed during the burning of any hydrocarbon such as Methane:



While the condensation of single substance gases is well investigated and understood, the condensation of gas mixtures with a large share of non-condensable gas is not. Therefore empirical approaches are commonly used. For smooth tubes, Gundermann [1] was able to generate a correlation using such an empirical approach. With this correlation he was able to describe the heat transfer during condensation of wet flue gas based on the corresponding heat transfer without condensation, as well as the flue gas parameters. This Paper will investigate whether the correlation found by Gundermann is suitable for corrugated tubes as well.

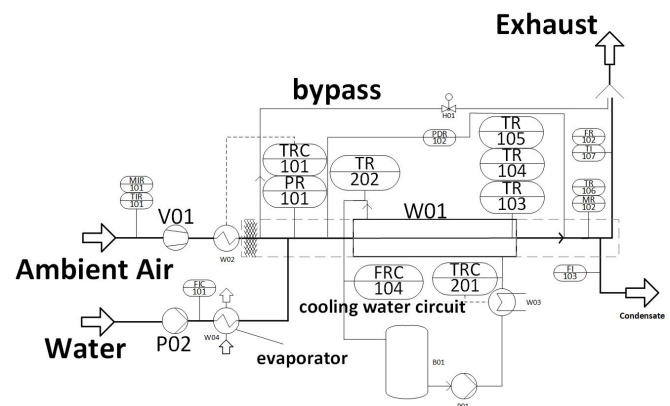


Figure 1: Process flow sheet of the experimental setup

Corrugated tubes in heat exchanger are used when the naturally induced turbulence in smooth tubes is not big enough. This is either the case when the fluids are highly viscose, which is often found in the food industry, or when the available space is not sufficient for smooth tubes. However, in addition to the heat transfer, the pressure drop is also increased compared to smooth tubes. As both effects can not be described analytically and not much literature on the topic is available, this paper aims to partially fill this gap.

II. EXPERIMENTAL SETUP

A. Experimental apparatus

To investigate the heat transfer, a double-tube heat exchanger with countercurrent flow setup was used (W01). The flowsheet of the used heat exchanger is shown in figure 1. For the inner tubes, different corrugated tubes were used, while smooth PVC-tubes were used for the outer tubes. The diameter for the outer tubes were adjusted for each diameter of the different inner tubes.

The measurements were done with synthetic flue gas. The synthetic flue gas consists of ambient air and water vapor. The water molar fraction and thus dew point of the flue gas can



Figure 2: All three used corrugated tubes for the experiments

be adjusted by setting the Water pump (P02). The ambient air and water vapor are both heated separately and before mixing. The temperature of the synthetic flue gas is monitored before entering the inner tube. The synthetic flue gas flows through the inner tube. Water flows through the annular gap of the heat exchanger. The total amount of flue gas flowing through the inner tube can be set by adjusting the ambient air fan (V02), as well as adjusting the bypass valve (H01). The cooling water is supplied via the laboratory cooling water loop. The temperature can be adjusted and the flow rate is controlled by valves at the shell side of the heat exchanger.

B. Data acquisition

Control and monitoring of the heat exchanger is done via a LabView interface. To evaluate the heat transfer, the temperature of the flue gas and the cooling water is measured at the beginning and end of the corrugated tube segment using thermocouples (TRC 101, TR 103 - 105, TRC201, TR 202). To assess the temperature of the exiting gas, the method described by Mac Nelly et al. [2] is used. According to their findings, the mean temperature can be measured at the radial coordinates of $r_i \cdot 0.25$ and $r_i \cdot 0.75$. In addition, the temperature at the center of the tube is also measured. The condensed water vapor is collected at the end of the measuring length and collected in a container. The flow rate of the condensed water is calculated by measuring the change in mass of the container water in a given time (FI103).

To ensure accuracy, the measurements are only started when the heat exchanger shows a stationary state. To further minimize any error, 10 measurements over a span of 10 minutes are taken for each data point.

C. Corrugated tubes

Corrugated tubes are tubes with augmented surfaces. The tubes used in this paper are spirally corrugated tubes. They are produced by cold forming smooth tubes with specialized tools. Three different spirally corrugated tubes of different initial smooth diameters were used to investigate the heat transfer. The original outer diameters of the Tubes were 18 mm, 22 mm and 28 mm. The Tubes were selected to fit industrial applications. The used corrugated tubes are shown in figure 2.

III. DATA REDUCTION

A. Heat transfer without condensation

With the used experimental setup, temperature changes of all involved fluids are measured. From this measured temperature change, a total heat flux is calculated using the change in enthalpy of the flue gas as well as the produced condensate:

$$\dot{Q} = \dot{H}_{gas,in} - \dot{H}_{gas,out} - \dot{H}_{condensate,out} \quad (2)$$

From this heat flux, a overall heat transfer coefficient can be calculated:

$$kA = \frac{\dot{Q}}{\Delta T_{log}} \quad (3)$$

Where ΔT_{log} is the mean logarithmic temperature difference. This can be used to calculate a mean inner heat transfer coefficient

$$\alpha_{i,mean} = \frac{1}{A_i \cdot \left(\frac{\Delta T_{log}}{\dot{Q}} - \frac{1}{A_o \cdot \alpha_{o,mean}} - \frac{s}{A_m \cdot \lambda_W} \right)} \quad (4)$$

Where s is the wall thickness of the used tube, A_m is the average surface area of the Tube and λ_W is the thermal conductivity of the tube material. To further increase comparability, the heat transfer coefficient $\alpha_{i,mean}$ is converted to the corresponding Nusselt number:

$$Nu = \frac{\alpha_{i,mean} \cdot d_i}{\lambda_{gas,mean}} \quad (5)$$

To calculate the mean inner heat transfer coefficient from equation 4, the mean outer heat transfer coefficient $\alpha_{o,mean}$ must be known. While the heat transfer in the annular gap of two smooth tubes is well known, the heat transfer in the annular gap within an corrugated inner tube and a smooth outer tube is not. However, as the outer heat transfer coefficient gets bigger, its influence in equation 4 decreases. Therefore, the outer heat transfer coefficient is increased by increasing the flow rate of the cooling water and the outer heat transfer coefficient is calculated with equations from the literature for smooth annular gaps.

IV. VALIDATION WITHOUT CONDENSATION

To validate the experimental setup, measurements with predictable results are done. Two such measurements were done. The first experiment was measuring the Nusselt number without any condensation. APROVIS generated specific equations to calculate the Nusselt number for each of the tested tubes. The equations were evaluated for two diameters with 22 data points in total. The comparison of measured Nusselt numbers and calculated Nusselt numbers is shown in figure 3.

A second validation was done on the measured pressure drop over the measuring length. To validate the measurements a correlation for the fanning friction factor by Vicente [3] was used.

$$f = 1.47 (h/d)^{0.91} (p/d)^{-0.54} Re^{-0.16} \quad (6)$$

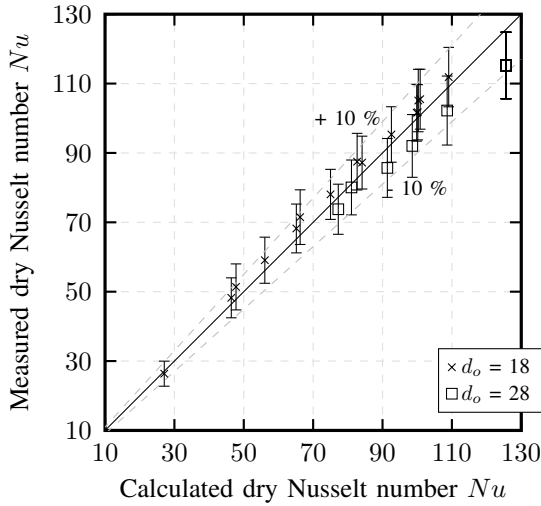


Figure 3: Comparison of the measured Nusselt number and the calculated Nusselt number without condensation

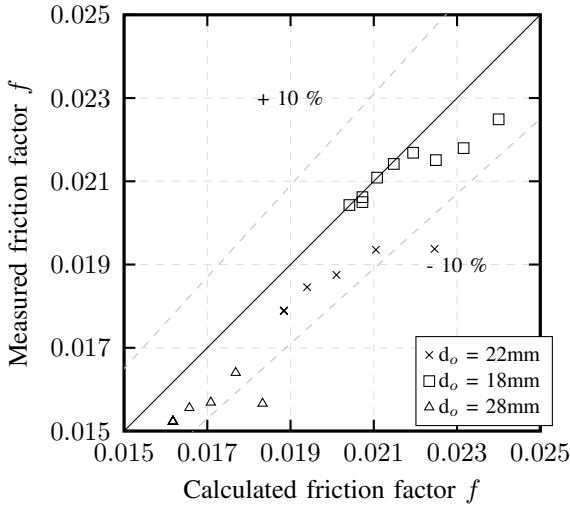


Figure 4: Comparison of the measured fanning friction factor and the calculated fanning friction factor without condensation

Where h is the depth, and p is the distance between the grooves. The measured friction factor and the calculated friction factor are shown in figure 4. Both validations show a good fit.

V. RESULTS WITH CONDENSATION

To evaluate the heat transfer during condensation, the heat transfer in three different corrugated tubes were measured. To include the influence of the Reynolds number in the measurements, 4 different mass flow rates (\dot{M}) were investigated for each tube. To further increase the coverage of different industrial applications, 3 different dew points (ϑ_τ) and 4 different cooling water temperatures (ϑ_{KW}) have been investigated. However, not all combinations have been tested. Figure I shows all the measured points. In total 71 data points have been generated.

Table I: Measured tubes and thermodynamic conditions - 71 Measured points in total

$d_o = 22 \text{ mm}, \vartheta_{in} = 120 \text{ }^\circ\text{C}$			
L	\dot{M}	ϑ_τ	ϑ_{KW}
1.85 m	2.5 g/s	42 °C	10 °C
	3.5 g/s	48 °C	35 °C
	4.5 g/s	54 °C	45 °C
	5.5 g/s		
$d_o = 22 \text{ mm}, \vartheta_{in} = 120 \text{ }^\circ\text{C}$			
L	\dot{M}	ϑ_τ	ϑ_{KW}
1.85 m	2.5 g/s	42 °C	25 °C
	^a 3.2 g/s	48 °C	
	3.9 g/s	54 °C	
	4.6 g/s		
<i>a</i> : This point was not measured for $\vartheta_\tau = 54 \text{ }^\circ\text{C}$			
$d_o = 28 \text{ mm}, \vartheta_{in} = 120 \text{ }^\circ\text{C}$			
L	\dot{M}	ϑ_τ	ϑ_{KW}
1.85 m	5 g/s	42 °C	35 °C
	7 g/s	48 °C	
	8.5 g/s	54 °C	
	10 g/s		
$d_o = 18 \text{ mm}, \vartheta_{in} = 120 \text{ }^\circ\text{C}$			
L	\dot{M}	ϑ_τ	ϑ_{KW}
1.89 m	1 g/s	42 °C	35 °C
	2 g/s	48 °C	
	3 g/s	54 °C	
	4 g/s		

A. Condensation in corrugated tubes

Figure 5 shows the mass flow rate and cooling water dependent measured heat transfer coefficient. The measured heat transfer coefficient in corrugated tubes showed the same behavior as known from smooth tubes. The heat transfer coefficient increased with higher mass flow rate and with lower cooling water temperature. The effect of the cooling water temperature decreased with lower temperatures.

B. Test of the Correlation

No analytical method to calculate the heat transfer during condensation with a high volume of inert gas is known in the literature. However, through a large amount of measurements, Gundermann [1] was able to generate a correlation to describe the heat transfer during condensation in smooth tubes:

$$f_c = \frac{\alpha_i}{\alpha_{i,dry}} = 20.22 \cdot y^{1.093} \cdot Gz^{0.0193} \quad (7)$$

Where y is the molar fraction of water vapor and Gz is the Graetz number, both at the beginning of the measured length. With this correlation, the heat transfer coefficient with condensation can be calculated as a function of the flue gas parameters and the dry heat transfer coefficient.

The goal of this paper is to evaluate the fit of this for corrugated tubes. So far this correlation has only been tested

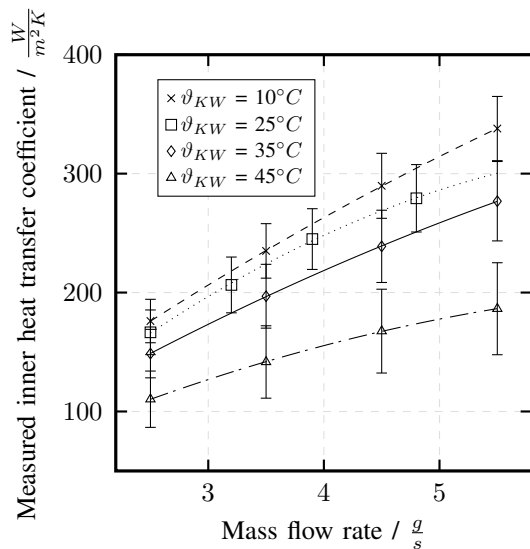


Figure 5: Measured inner heat transfer coefficient at $d_o = 22 \text{ mm}$, and $\vartheta_\tau = 48 \text{ }^\circ\text{C}$ at 4 different cooling water temperatures (ϑ_{KW})

for smooth tubes. The heat transfer coefficient is calculated with the correlation found by Gundermann. The dry heat transfer coefficient needed to calculate the heat transfer with condensation is calculated with the equation provided by APROVIS. Figure 3 shows sufficient fit of this equation. The measured and calculated heat transfer coefficients are shown in figure 6. The measured data scatters evenly around the correlated data. 89% of the measured Data is within 15% of the correlated data. This is in line with what Gundermann found for smooth tubes, where 95% of the measured data was predicted within an uncertainty of 15%. Therefore, the factor f_c calculated by equation 7 is sufficient in describing the effect of condensation with high amounts of inert gas.

VI. DISCUSSION

The measurements show, that condensation is not influenced by the corrugation of the tested tubes. The difference between the smooth and the tested corrugated tubes is mainly in the dry heat transfer. This result is unexpected, as the higher turbulence induced by the corrugation increases the radial mass transport inside the tube and should therefore lower any water vapor fraction gradient inside the tube.

A possible reason for this result was stated by Ren et al. [4]. There it was found that the main heat transfer resistant is in the liquid condensate film. As the corrugation does not induce much turbulence into the liquid film, this might be the reason for the similarity. However, as Ren et al. used a minimum initial vapor fractions of 60 %, these results might not be applicable to experiments done here, as the maximum initial vapor fraction used is only 15 %. As the vapor fraction for the experiments done by Ren et al. is much higher, the amount of condensate is likely higher as well.

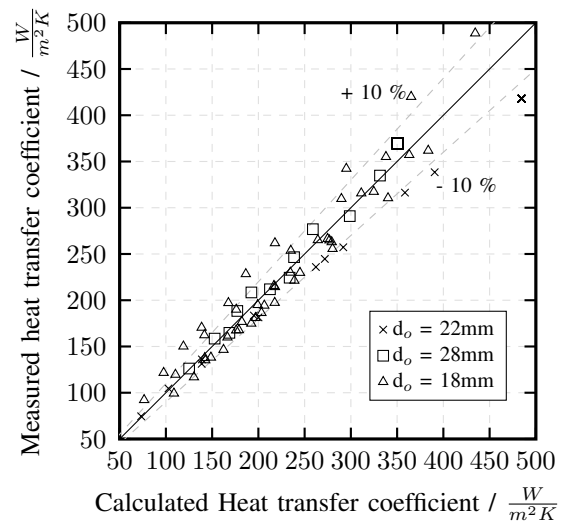


Figure 6: Comparison of the heat transfer coefficient calculated with correlation 7 and the measured heat transfer coefficient. Sorted by outer tube diameter

VII. CONCLUSION AND FUTURE WORK

The experiments done in this paper show, that the heat transfer coefficient during condensation in corrugated tubes can be described with the correlation found by Gundermann. However, the reason why the correlation developed for smooth tubes also fits corrugated tubes could not be fully answered. Further work will tackle this problem.

In addition to the here investigated heat transfer, pressure drop is a necessary parameter when designing a heat exchanger. Future work will address this problem with the goal of describing the pressure drop during condensation in a similar way the heat transfer coefficient was described in this paper.

REFERENCES

- [1] M. Gundermann, F. Raab, D. Raab, and T. W. Botsch, "Investigation of the heat transfer coefficient during the condensation of small quantities of water vapour from a mixture with a high proportion of non-condensable gas in a horizontal smooth tube," *International Journal of Heat and Mass Transfer*, vol. 170, p. 121016, May 2021. [Online]. Available: <https://www.sciencedirect.com/science/article/pii/S0017931021001198>
- [2] S. M. Nelly, W. Nieratschker, M. Nadler, D. Raab, and A. Delgado, "Experimental and Numerical Investigation of the Pressure Drop and Heat Transfer Coefficient in Corrugated Tubes," *Chemical Engineering & Technology*, vol. 38, no. 12, pp. 2279–2290, 2015. [Online]. Available: <https://onlinelibrary.wiley.com/doi/abs/10.1002/ceat.201500160>
- [3] P. G. Vicente, A. Garcia, and A. Viedma, "Experimental investigation on heat transfer and frictional characteristics of spirally corrugated tubes in turbulent flow at different Prandtl numbers," *International Journal of Heat and Mass Transfer*, vol. 47, no. 4, pp. 671–681, Feb. 2004. [Online]. Available: <https://www.sciencedirect.com/science/article/pii/S001793100300454X>
- [4] B. Ren, Z. Pu, X. Tang, J. Wang, A. He, and H. Lu, "Mechanism of Condensation Enhancement by Corrugated Low Finned Tubes in Presence of Noncondensable Gas," *IOP Conference Series: Earth and Environmental Science*, vol. 513, no. 1, p. 012009, Jun. 2020, publisher: IOP Publishing. [Online]. Available: <https://iopscience.iop.org/article/10.1088/1755-1315/513/1/012009/meta>

Options on the test planning for the AC/DC-Dual Active Bridge

Maximilian Dominik Fischer

Department of Electrical Engineering
and Information Technology

University of Applied Sciences Munich

Email: maximilian.fischer0@hm.edu

Daniel Goldmann

Department of Electrical Engineering
and Information Technology

University of Applied Sciences Munich

Email: daniel.goldmann@hm.edu

Simon Schramm

Department of Electrical Engineering
and Information Technology

University of Applied Sciences Munich

Email: simon.schramm@hm.edu

Abstract—As part of the development of the AC/DC-Dual Active Bridge, an efficient, fast and structured test procedure is required. It is important that as many relevant aspects of the system as possible are covered by the tests. This paper deals with different test design procedures that could be considered for this process.

At first the specifications of the AC/DC-Dual Active Bridge will be shown. Afterwards the different planning methods are compared and the decision for “Design of Experiments” (DOE) is explained. In addition, it is explained why the extensive tests of the converter are required.

At the end of the paper, it is shown how the method “Design of Experiments” is applied to the AC/DC-Dual Active Bridge.

I. THE AC/DC-DUAL ACTIVE BRIDGE

The development of electric vehicles is increasingly important, as they form the link between the sectors "mobility" and "electricity". In contrast to combustion vehicles, "refueling" is not quite as simple for an electrical vehicle and complex charging systems are required. The AC/DC-Dual Active Bridge (AC/DC-DAB) represents such a system. The chosen topology is shown in figure 1.

The converter features inbuilt galvanic isolation, while the transformer can be kept very compact due to the high switching frequency of the two full bridges. This is an essential feature, especially for use as an onboard charger, because it means that the vehicle does not become unnecessarily weighted.

The power is bidirectionally set to single phase 7.5 kW, with connection to the low voltage grid [1]. This means that the grid voltage has a nominal effective value of 230 V and a nominal frequency of 50 Hz. A total charging power of about 22 kW is thus achieved with three converters, as it is usual in many charging solutions ([2], [3]).

Furthermore, a power factor ($\cos(\varphi)$) of 0 overexcited to 0 underexcited is specified. The converter can thus be operated in a grid-supporting mode. The DC-voltage is in the range of 300 V to 400 V, and the switching frequency of the two full bridges is set to be 100 kHz.

These specifications serve as the basis for the test planning, as they provide the corresponding parameters for various tests. In addition, the specification defines the operating limits of the system. For example, looking at the AC-side, there is a normative range in which operation must be possible. While

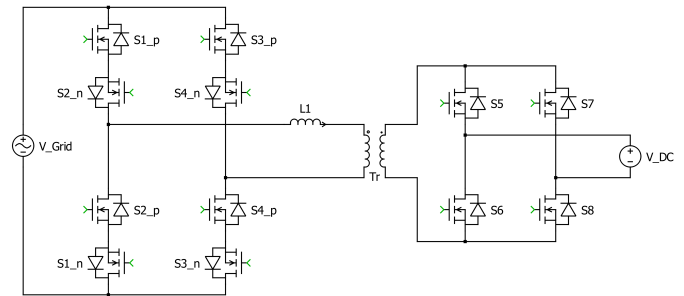


Figure 1. Topology of the AC/DC-DAB [4]

the nominal frequency is 50 Hz, the frequency could drop to 47.5 Hz. The maximum frequency is 52.2 Hz. This is specified in the grid connection specifications for the low voltage grid [5]. It is also possible that the voltage can differ slightly from its nominal value. In the low voltage grid, a tolerance of the voltage amplitude of $\pm 10\%$ is allowed [5].

Based on these maximum and minimum operating limits, a test plan can be designed.

II. THE NEED FOR STRUCTURED TEST PLANNING

As mentioned at the beginning, an experimental design will be created to test the functions of the AC/DC-DAB. This chapter will explain why a design of experiments is necessary at all.

The scope of influencing factors, disturbance factors and output variables is very large for a complex system such as the AC/DC-DAB. Examples of influencing factors are the AC-voltage, the DC-voltage and the operating point itself. In addition, there are influences such as the ambient temperature, air humidity, material differences, disturbances in the AC-voltage or ripple in the DC-voltage and many more.

As output variables, the efficiency is a good quantity, but there are other variables here, such as the current waveform (harmonics, etc.).

In addition to these static values, there are also dynamic values. Since the converter must also handle load steps, voltage changes or voltage errors (e.g. short circuit) correctly,

this should also be included in the tests.

Here, the main focus is on dynamic tests, which make the input variables even more diverse. It is possible, for example, that an input factor does not remain constant permanently, but changes suddenly. Here it is important how fast the value changes and to which value this value rises or falls. So there are numerous additional factors that can influence the experiment.

The large number of parameters shows, that a structured test sequence is required. At the same time the test should offer the possibility to draw conclusions from the measured values.

It is also extremely important to have a traceable test procedure so that changes to the system can be tested in the same way each time. Another point is that the scope of the tests must not be too large, so that not too much time is lost with the system test.

Once this test plan has been created, it can be used within an automatic test sequence so that the entire test plan can be executed automatically and evaluated at the end. This saves additional time and gives the possibility that even smaller system changes can be tested in the same full test-plan like bigger system changes.

III. OPTIONS FOR A TEST DESIGN

After the need for a systematic experimental design was explained in the previous chapter, this chapter will present various tools and procedures for creating an experimental design.

Relevant aspects are mainly the required time, which can be represented by the number of necessary experiments, and the added value that the corresponding measurement results will provide.

This is valid for any system test regardless of whether it is a hardware or a software test. There are certain input factors for each test that are specifically adjustable. In addition, there are disturbance factors, whereby these are factors that can not be controlled. The results are corresponding output variables. In the following, the input factors are simply referred to as factors.

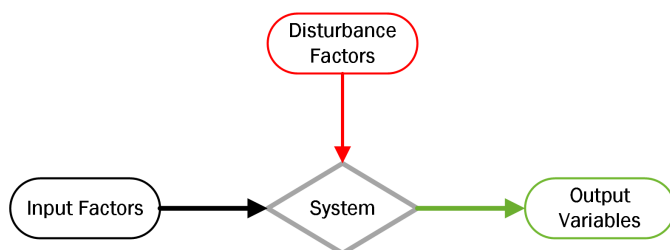


Figure 2. System structure [6]

A. Try and Error

The first and simplest method for executing the necessary experiments is the so-called "Try and Error-method". The various influencing factors of the system are changed in a more or less structured way. These changes are continued until an error occurs. Further tests are then conducted around the working area of this error so that the reason for the error can be identified and resolved.

The advantage of this method is the little preliminary work, since no detailed planning of the process is needed. This is mainly caused by the "looking for an error" method, where it is not clear from the beginning at which factor settings an error will occur. It is not possible to plan the complete tests in advance.

A major disadvantage is, that individual aspects can be forgotten during testing. In addition, it is difficult to introduce an end criteria, which defines at which point enough test runs have been carried out, if no error occurs. This decision is therefore up to the persons performing the test and not necessarily up to the developers of the system.

The most important disadvantage is the cost factor. The test equipment, prototypes as well as the time for the evaluation of the test results are expensive and should therefore be used very efficiently [7, p. 28]. Especially in the case of suddenly necessary retesting, there is a big cost factor.

With the "Try and Error-method" the number of required tests can be very high, because it is not clearly defined when enough tests have been performed.

B. One Factor at the Time

In contrast to the "Try and Error-method" explained above, the "One Factor at the Time" (OFAT) method runs in a more structured way. Nevertheless, it is also difficult to plan the entire course of the experiment in detail beforehand, since the execution depends in parts on the results of the tests.

In general, only one factor is changed at a time when running the tests, while the other factors remain constant. The point of this procedure is that the influence of this factor is so easily recognizable. If the test results do not change at all, even though one factor is changed, it is clear that this factor has no impact.

If the entire test series has been performed, the next factor is changed in the second step. For this step, the first factor is set to the value that caused the best initial values. The same procedure is then followed with the third factor until all factors have been tested.

A short example, shown in figure 3, will show the procedure accordingly.

For example, a system has two input factors (P1 and P2), the input voltage and the output voltage of the system, and the efficiency as output. First, the input voltage (P1) is continuously increased, while the output voltage remains

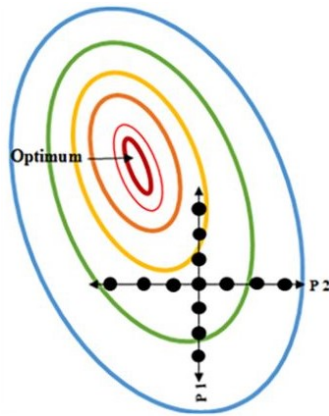


Figure 3. Possible test procedure with OFAT [8]

constant. In the next step, the output voltage is increased continuously, whereby the input voltage is set to the value at which the resulting efficiency is highest.

The optimum can now be easily read off. It is located at the selected input voltage and the output voltage with the corresponding highest efficiency.

The problem with this is, that it is not absolutely necessary that this value really represents the optimum. It is quite possible that this value only represents the optimum of the tested factor values and that the absolute optimum of the system is somewhere else. As shown in the figure it is not possible to reach the real system optimum with the selected values.

So, in order to really recognize the system optimum, several iterations are needed. This leads to a larger experimental workload as soon as the system has more than about three input factors. In addition, the changes of the factors have to be adjusted more and more finely, so that an approximation to the optimum can be ensured.

In general with OFAT it is not possible to get conclusions about the relations of the factors to each other ([7, p. 30]). Only the influence of each factor on the system behavior will be recognized.

C. Full Experimental Plan

The most complete way to test a system is the “Full Experimental Plan”. Here all factor levels are combined so that in the end every possible combination is tested.

The number of tests (n_{Tests}) can therefore be calculated in the planning phase using equation 1. It depends on the number of factors and the number of factor levels.

$$n_{Tests} = levels^{factors} \quad (1)$$

The great advantage of this procedure is that at the end it is sure that no effect has been missed. In addition, it is possible to determine exactly how many tests must be performed before the start of the experiment. This means that

it is also clear how much time is required. In many areas this is an important information, because especially for hardware tests it is important to plan exactly when laboratories, test equipment etc. are needed.

The key disadvantage is the large amount of time needed, especially for complex systems that have many influencing factors. Equation 1 shows that the number of necessary tests becomes extremely large very quickly. While a test with two factors and three stages each requires only nine runs, a test with four factors and three stages each already requires 81 tests.

In addition, it is difficult to cover input ranges such as the DC-voltage of the AC/DC-DAB. There are no clear values here, but everything in the range from 300 V to 400 V is a possible value. So, theoretically, there would already be an infinite number of stages in this case. Since this is not possible, intermediate stages, such as 5 V steps, would have to be introduced.

By doing this, a complete test plan is theoretically not 100% reached. Nevertheless, the results would probably be sufficient.

D. Design of Experiments

Each of the three methods shown above have advantages, but all of them have also significant disadvantages. Especially with regard to the development of the AC/DC-DAB, it is necessary to use the test times as efficiently as possible, since these are recurring tests that are intended to validate system modifications.

The fourth method is “Design of Experiments” (DOE), a statistical test design. Basically, statistical methods are used to reduce the experimental effort without losing relevant knowledge. In addition, a randomized experimental sequence is used to ensure that disturbance factors have as little influence as possible on the system and thus on the experimental results.

In contrast to some other methods, DOE allows correlations between different influencing factors to be identified.

Basically, there are different types of test plans used in DOE. Depending on the knowledge of the system parameters, so-called screening plans are initially created, which serve to identify individual influencing factors and to make an initial estimate of the direction in which these factors influence the target variable.

Basically the following two types of experimental design are possible. One is a full factorial design and the other is a fractional factorial design. In the last case, the correlation of individual factors is used to reduce the number of experiments.

1) *Factorial Design*: First, the full factorial experimental design will be examined. In a full factorial experimental design, all possible corner points of the experimental field are tested.

Figure 4 shows an example of an experiment with three influencing factors.

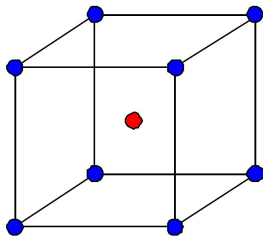


Figure 4. Three factor factorial design with center point [9]

The blue points are the corner points resulting from the minimum and maximum of the different factors. The "cube" lies in a coordinate system with three dimensions, the three factors.

In this example, each of the three factors has two levels, so it is a so-called 2^k -experiment. The number of tests can be calculated according to equation 2.

$$n_{Tests} = 2^{factors} \quad (2)$$

The red point in the middle is the so-called central point, which can be introduced optionally, so that nonlinearities in the interrelations of the factors can be recognized better. For this measuring point all parameters are set to a mid value (between maximum and minimum). By using the central point the needed tests are increased by one.

In principle, it is also possible to use more than two levels per factor, as figure 5 shows with three levels each. Here, the number of tests increases accordingly, as already shown by equation 1. The figure shows again a central point, which this time is shown in blue. The reason is that this measuring point does not act as a central point, but results automatically from the three levels of factors.

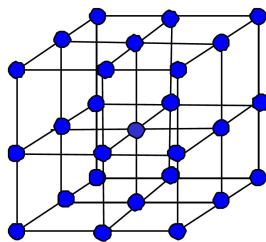


Figure 5. Three factor factorial design with different value steps [9]

If the levels are increased until all possible values are covered, this is again a complete experimental design, as presented in section III-C.

2) *Fractional Factorial Design:* As mentioned at the beginning, correlations between the factors should help to reduce the number of experiments. For this it is necessary, to know the system in more detail, because the probability

is higher that unknown correlations between factors are forgotten.

In principle, the corner points are used again in a fractional factorial design, but only half of them. Figure 6 shows the used measuring points again in blue.

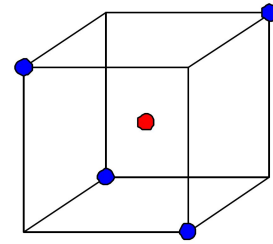


Figure 6. Three factor fractional factorial design with center point [9]

Also in this case it is possible to introduce the central point additionally.

With the choice of the corner points to be excluded it is important that furthermore each factor is varied.

In the example (figure 6) it is not possible to test only the right side of the cube, which would mean, that the first factor is never changed. Instead it is necessary that every factor is changed at least once. The result are exactly the shown measuring points in figure 6. Alternatively, it is of course possible to choose exactly the other four corner points.

The presented fractional factorial experimental design is a so-called $\frac{1}{2}$ -factorial experimental design, since the number of experiments was reduced to half. As the number of influencing factors increases, $\frac{1}{4}$ -factorial experimental designs can also be used. Similarly, there are other levels. Nevertheless, it must be clear that as the number of tests decreases, the risk of overlooking effects increases.

IV. APPLICATION OF DOE FOR THE AC/DC-DAB

After presenting different tools for experimental design, this chapter will describe the specific application of DOE to the AC/DC-DAB.

First, the different factors have to be identified and defined. A structure-model of the different factors at the AC/DC-DAB is shown in figure 7.

Basically, there are different output parameters for a converter, with the most common parameter being the efficiency. In addition, the current shape will be analyzed, whereby the focus is here on the current harmonics. Both values are interesting and it may helps in the development, if there are correlations with the input factors.

The two voltages are obvious as input factors. On the one hand the secondary voltage, the DC-voltage, can be varied and on the other hand the primary voltage can change. Since the primary voltage is an AC-voltage, it can change

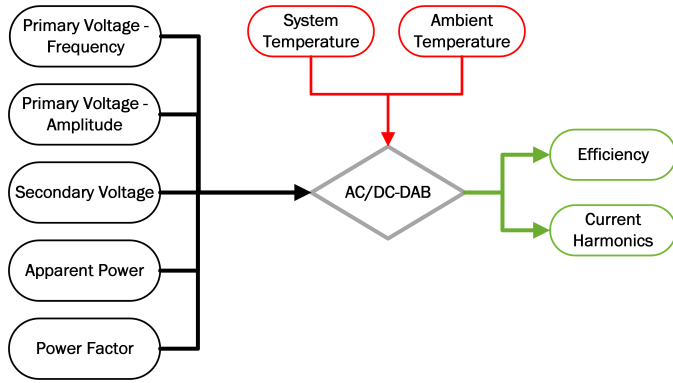


Figure 7. Different input and output factors for the AC/DC-DAB

in frequency as well as in its amplitude. It is important that the voltage specification is always within the low voltage standards that apply to the European grid (chapter I). Both voltages can additionally have disturbances. In case of the DC-voltage, this is primarily a possible voltage ripple while for the AC-voltage, e.g. harmonics can also cause a kind of ripple. This is indicated by the so-called “Total Harmonic Distortion” (THD). For the system tests, both voltages are assumed to be ideal, since effects arising from this will not be investigated until a further step.

Other factors are the active power (P) and reactive power (Q), which are relevant for the momentary operating point. A converter, like the AC/DC-DAB, is usually designed for a maximum apparent power (S), which results from both values according to equation 3.

$$S = \sqrt{P^2 + Q^2} \tag{3}$$

To ensure that this apparent power can not be exceeded during the test planning, the operating point must be expressed differently. Otherwise, a measuring point at which the active and also the reactive power is at a maximum may occur. This would lead to exceeding the maximum apparent power of the system.

Here the apparent power in combination with the power factor ($\cos(\varphi)$) is suitable. The calculation of the active power in dependence of these two values is shown in equation 4.

$$P = S * \cos(\varphi) \tag{4}$$

In addition to the intended values, there are other factors, as already shown in figure 7. Above all, the ambient temperature and the system temperature can be identified as disturbance variables.

The ambient temperature can not be specifically adjusted at the actual test set-up for the AC/DC-DAB, so that the temperature is dependent on the laboratory temperature. Nevertheless, it is measurable and can thus be included in the test protocol.

The system temperature is also difficult to influence and depends on the one hand on the ambient temperature but also

on the time that has already been tested. A further influence on the system temperature is probably given by the actual operating point, since the current increases at high power and with this also the losses in the semiconductors increase. This leads to a higher heat loss.

To minimize these two interferences it is possible to randomize the test order.

When creating the test plan, the factors are changed by default one after the other, so that, for example, the frequency of the AC-voltage remains constant for some runs at the beginning. Supposing that all the runs are made one right after the other, it can be assumed that the system temperature will be much higher in the second half of the experiments than in the first tests. The influence of the frequency can in this way hardly be differentiated from the influence of the system temperature. If, on the other hand, the tests are performed in random order, all parameters are also changed at the beginning and the influence of the system temperature plays a minor role.

Table I
FULL FACTORIAL TEST PLAN FOR THE AC/DC-DAB

Run	A	B	C	D	E	Run	A	B	C	D	E
1	-	+	-	-	-	18	+	+	+	+	-
2	+	+	-	+	+	19	+	+	-	+	-
3	+	-	+	-	-	20	-	+	-	+	+
4	+	+	-	-	-	21	0	0	0	0	0
5	-	-	-	-	-	22	-	-	-	-	+
6	+	-	+	+	+	23	+	-	-	-	+
7	+	+	+	-	+	24	+	-	-	-	-
8	-	-	+	+	-	25	-	+	+	+	-
9	-	+	-	+	-	26	+	+	-	-	+
10	+	-	+	+	-	27	+	-	-	+	-
11	-	-	-	+	-	28	-	-	+	-	-
12	-	+	-	-	+	29	+	+	+	+	+
13	-	-	-	+	+	30	-	+	+	-	-
14	-	+	+	-	+	31	-	+	+	+	+
15	-	-	+	+	+	32	-	-	+	-	+
16	+	-	-	+	+	33	+	-	+	-	+
17	+	+	+	-	-						

Table I shows the two stage full factorial experimental design of the AC/DC-DAB, with the influencing factors generally represented here as A, B, C, D and E. The values of the individual factors are represented by + and - each, representing the maximum and minimum values, in each case.

It can be seen that the factors are changed randomly, so randomization has already been performed here.

In addition, in run 21 a line with only zero can be seen, which increases the number of tests to 33 instead of the 32, which would be expected according to equation 2. This is the central point. This central point is supposed to help to recognize nonlinear properties better, because otherwise only two levels would be set for each factor (compare section III-D).

In principle, it would be better to set three levels directly for each factor, but the number of necessary tests would be 243 (equation 1), which is much higher than with two levels. This

case would be less practicable.

In addition to the full factorial experimental design, a fractional factorial experimental design was also created, which is shown in table II.

Table II
FRACTIONAL FACTORIAL TEST PLAN FOR THE AC/DC-DAB

Run	A	B	C	D	E	Run	A	B	C	D	E
1	+	-	-	-	-	10	-	-	-	+	-
2	-	+	+	+	-	11	+	-	+	-	+
3	+	+	-	-	+	12	+	-	-	+	+
4	-	+	-	-	-	13	-	-	+	+	+
5	-	-	-	-	+	14	-	+	-	+	+
6	0	0	0	0	0	15	+	+	+	+	+
7	+	+	-	+	-	16	+	-	+	+	-
8	+	+	+	-	-	17	-	-	+	-	-
9	-	+	+	-	+						

This experimental design has also a central point in run number six.

It is a $\frac{1}{2}$ -factorial experimental design, which means that the number of runs can be reduced to the half (central points are not considered). The required number of runs is therefore 16 plus the additional central point.

For the AC/DC-DAB the full-factorial experimental design is used first, since the AC/DC-DAB system is known in principle, but individual correlations are still open and can thus be better analyzed. The number of experiments is also moderate with this experimental design, so that it can be executed.

V. CONCLUSION AND OUTLOOK

The paper has shown the topic of designing experiments. Different methods for the experimental planning have been explained and compared to each other. Especially the application of DOE on the AC/DC-DAB was taken up in chapter IV.

In the further course of the project, the experimental designs will be implemented in practice and applied to the AC/DC-DAB. The results obtained from this can then be used for further development.

The first step will be that the test set-up is taken into operation with the help of a conventional inverter. This has the advantage that the focus is on the test set-up and the converter itself is already functional.

The next step will be to perform the tests on the AC/DC-DAB, initially observing the time required for one test. This can be used to calculate whether 33 necessary test runs are a reasonable value in practice. Depending on the result, it is possible that the effort for 33 tests is too great or that far more tests would be possible.

At the end, the measurement data should be evaluated and analyzed according to the DOE-methods.

In addition a kind of benchmark of the two systems can be made out of the test results. This helps to detect weaknesses of the AC/DC-DAB, which then could be eliminated.

REFERENCES

- [1] M. Fischer, "Comparison of the Operating Mode of different DAB-based AC/DC-Converters with Integrated Galvanic Isolation," Poster for the ARC in the summer term 2020, University of Applied Sciences Munich, Munich, 2020.
- [2] EVBox Manufacturing B.V., "EVBox Elvi: The charging solution at home: Data sheet," Online, 2019. [Online]. Available: https://www.mobilityhouse.com/media/productattachments/files/DE_Product_Brochure_Elvi_5.pdf
- [3] SMA Solar Technology AG, "SMA EV CHARGER 7.4 / 22: Charging electric vehicles with solar power – intelligent, fast, cost-effective," 2020. [Online]. Available: <https://files.sma.de/downloads/EVC-10-DS-de-10.pdf>
- [4] M. Wang, S. Guo, Q. Huang, W. Yu, and A. Q. Huang, "An Isolated Bidirectional Single-Stage DC-AC Converter Using Wide-Band-Gap Devices With a Novel Carrier-Based Unipolar Modulation Technique Under Synchronous Rectification," *IEEE Transactions on Power Electronics*, vol. 32, no. 3, pp. 1832–1843, März 2017.
- [5] VDE, "VDE-AR-N 4105: Generation systems on the low-voltage grid," 2020-10.
- [6] M. El Ghazi, "Statistical Design of Experiments for Beginners," 2019. [Online]. Available: https://www.researchgate.net/publication/336286514_Statistische_Versuchsplanung_fur_Einsteiger
- [7] Robert Bosch GmbH, "11. Experimental Methodology (DoE): Quality Management in the Bosch Group | Technical Statistics: Employee training," 2010. [Online]. Available: https://assets.bosch.com/media/global/bosch_group/purchasing_and_logistics/information_for_business_partners/downloads/quality_docs/general_regulations/bosch_publications/booklet-no11-versuchsmethodik_DE.pdf
- [8] A. Uhoraningoga, G. K. Kinsella, G. T. Henahan, and B. J. Ryan, "The Goldilocks Approach: A Review of Employing Design of Experiments in Prokaryotic Recombinant Protein Production," *Bioengineering*, vol. 5, no. 4, 2018. [Online]. Available: <https://www.mdpi.com/2306-5354/5/4/89>
- [9] Beat Giger, "Design of Experiments: Full and fractional factorial tests," Ulm, 2005. [Online]. Available: <https://docplayer.org/20587774-Design-of-experiments.html>

Conversion of non-existent load-profiles for PV-Systems

Lumbardh Gegaj
*Ostbayerische Technische Hochschule
 Regensburg (OTH-Regensburg)
 Forschungsstelle für Energienetze und
 Energiespeicher (FENES)*
 Regensburg (Bavaria), Germany
 lumbardh1.gegaj@st.oth-regensburg.de

Abstract—When there are multiple PV-Systems in a low voltage network, but not all load profiles are available, they must be determined. This is done using a python-program which takes an existing load-profile and converts it according to the respective orientation angle and insurrection angle. This is necessary so that network simulations, in the Network-simulation-program “Digsilent Powerfactory”, can be carried out.

Keywords—*nonexistent load-profile, PV-Systems, conversion of load-profiles, python program, powerfactory*

I. INTRODUCTION

The Research-work was carried out in the framework of the Project “Netzdienliches integrales Elektromobilitäts-Energiemanagementsystem für dezentrale Energieversorgung” (short: NiEMob, eng.: Grid-serving, integral electromobility energy managementsystem for decentralized energy supply systems) in cooperation with the „OTH-Regensburg“ and „Consolinno Energy GmbH“. Here Consolinno deals with the measurement-hardware (Energy-manager) and the OTH-side is responsible for the network-modelling and the associated computing and simulation tasks(Network-manager). The endgoal of the project is the intelligent use of the grid so that a grid expansion is delayed as much as possible. To accomplish that it is planned that Consolinno provides the real-time load data of the corresponding network resources (Household loads, PV-Systems, Charging stations, Voltage, Current) via database, so the OTH-side can use those in the network-simulations. The results coming from the simulations will then be sent back to the database so the Energy-manager can adjust the respective loads. Since there is no real-time measurement-data available yet, the respective load data must be determined otherwise.

The load data for households and charging stations are simulated with own programs. The not present load-profiles of the PV-Systems will be attained through the conversion of an existing load-profile of a known PV-System.

II. PREPARATIONS

First all PV-Systems in the network under consideration must be located and noted.

Secondly, the respective orientation and elevation angel must be found out. Due to lack of accuracy, those are largely estimated using 3 dimensional maps.

Third, the grid model is searched PV-Systems with existing load data. Since in this case there weren't any, another PV-Systems load-profile was used. It is necessary that there is a geographical proximity to the network under consideration.

Fourth, a csv file with the “source” load data and one with the names and angles of all the PV-Systems in the network must be created, so the python-program can “read” its input information.

III. GENERAL IDEA AND FORMULA-DETERMINATION

Owing to the fact that no load profile data is available for the PV-Systems located in the grid area, existing load profile data from other PV-Systems located in the vicinity are used. Due to the improbability that all PV-Systems have the same orientation and elevation, a conversion factor is required, which can convert the respective angles into the respective PV-Systems position independently of each other. It should be noted that an orientation of 0 degrees (south orientation) and an elevation of 20 degrees was chosen as a reference.

To generate a conversion factor there are four steps necessary, as shown in the following example.

At the beginning there is a load profile of a “spring”-PV-System with an orientation of 45 degrees (south-west) and an elevation of 13 degrees. A load profile for a PV-System with -23 degrees (south-southeastern) orientation and an elevation of 30 degrees is to be generated.

Step 1: A conversion factor for the elevation to reference-elevation is determined. After multiplication of the original load profile with the gained factor, a load profile for 45 degrees orientation and 20 degrees elevation exists.

Step 2: Now the load profile for the reference-PV-Systems is calculated. Here first the conversion factor for orientation is calculated and then multiplied with the previously determined load profile. The result is load profile of the reference system at 0 degrees orientation and 20 degrees elevation.

Step 3: Now Step 1 and 2 essentially have to be repeated, just backwards. The new conversion factor for -23 degrees orientation is calculated. Then the reference load profile is divided with said factor. As an intermediate result there is the load profile for an orientation of -23 degrees and an elevation of 20 degrees.

Step 4: To get the final result the conversion factor for 30 degrees elevation is calculated. The load profile from Step 3 is then divided by that factor which results in the final load profile of the PV-System with -23 degrees orientation a 30 degrees elevation.

The total conversion factor therefore consists of the for factors from steps 1 to 4.

$$TotalFctr = Fctr_{St1} \cdot Fctr_{St2} \div Fctr_{St3} \div Fctr_{St4} \quad (1)$$

With the total conversion factor all that has to be done is to multiply the source load profile with that factor from “(1)” and the load profile of the desired PV-System has been calculated.

IV. DETERMINING THE CONVERSION FORMULAS

Now it is shown how the conversion factors are determined. The conversion requires two different factors for the alignment and elevation according to the 4 Steps above. How the necessary formulas were determined shall be briefly discussed. More detailed information on this can be found in L. Gegaj’s project work entitled “Verteilung von Elektroauto-Ladesäulen und Umrechnungsfaktor-Bestimmung für PV-Anlagen entsprechend ihrer Ausrichtung und Aufständerrung” (eng.: Distribution of electric car charging stations and Conversion factor determination for PV-Systems according to their orientation and elevation) from March 2021.

A. Conversion factor for the elevation angle

If a graph is drawn over the relationship between the elevation under consideration and the reference elevation, one recognizes that the course is similar to a straight polynomial function, which is limited by a parabola, as shown in Figure 1.

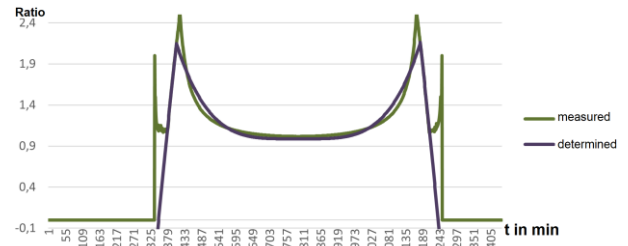


Figure 1: Graph of the relationship between the elevation under consideration and the reference elevation

Using Matlab one can recreate the Graph. The formula of the enveloping parabola is:

$$f_{Prbl}(x) = -4,57 \cdot 10^{-5} \cdot x^2 + 0,073 \cdot x - 19,81 \quad (2)$$

For x in “(2)” the respective minutes of the day must be inserted (0-1440).

To get the ratio in the middle one has to use the following Equation:

$$f_{Ratio}(x) = p1 \cdot \left(\frac{(x - 794)}{1440}\right)^4 + p2 \quad (3)$$

For x in “(3)” again the respective minutes of the day must be inserted. But since the result of “(3)” depends on the original elevation of the “source”PV-System, the two parameters “ $p1$ ” and “ $p2$ ” must also be reproduced as a function of the angle using Matlab. Since the roof pitch in Germany is a maximum of 60 degrees, the elevation angle has been limited to between 0 and 60 degrees. The respective formulas are:

$$f_{P1}(x) = 0,1619 \cdot x^2 + 1,6 \cdot x - 100,7 \quad (4)$$

$$f_{P2}(x) = 2,658 \cdot 10^{-06} \cdot x^3 - 7,992 \cdot 10^{-05} \cdot x^2 - 0,003445 \cdot x + 1,08 \quad (5)$$

In “(4)” and “(5)” the desired elevation angle has to be inserted in x .

B. Conversion factor for the orientation angle

Here the same procedure as in “A” has to be repeated.

$$f_{Prbl}(x) = -4,4 \cdot 10^{-5} \cdot x^2 + 0,06989 \cdot x - 19,13 \quad (6)$$

$$f_{Ratio}(x) = -0,6 \cdot \left(\frac{\text{orientation angle}}{90^\circ}\right) \cdot \tan\left(p1 \cdot \left(\frac{(x - 794 - p2)}{1440}\right)\right) + 1 \quad (7)$$

In “(6)” and “(7)” the respective minutes of the day must be inserted for x .

$$f_{P1}(x) = 5,05 - 0,2972 \cdot \left(\frac{x}{90}\right)^4 - 0,4417 \cdot \left(\frac{x}{90}\right)^2 \quad (8)$$

$$f_{P2}(x) = 90 \cdot \sin\left(2,658 \cdot \left(\frac{x}{180}\right)\right) \quad (9)$$

In the parameter functions of “(8)” and “(9)” the desired orientation angle (+90 degrees (west) to -90 degrees (east)) must be inserted.

V. EXECUTION OF PROGRAMMING

Once the conversion factors have been determined (See “IV”), they must be placed in python program so that all load profile values are converted automatically in Powerfactory.

A. Preparation of the csv files

The goal of the python program is the creation of load profiles for the required PV-Systems, therefor the respective csv file layout has to be identical to the one of the “source” load profile.

Additionally a new csv file must be created which includes the names of all PV-Systems in the network and their respective orientation and elevation angles.

B. Python programming

The calculations are carried out using functions as seen in Figure 2.

```

19 ##Funktionen
20 ##Faktor fuer Aufstaenderung
21 #def AUFSTAENDERUNG():
22 def AUFSTAENDERUNG(aufwinkl, aufmts):
23     #aufwinkl=0 #Aufstaendigungswinkel (max 60°)
24     #aufmts=0 #Minuten des Tages
25     aufParab1=-4.565*(10**(-5))*(aufmts**2)+0.07252*aufmts-19.81
26     aufP1=0.1619*(aufwinkl**2)+1.6*aufwinkl-100.7
27     aufP2=2.658*(10**(-6))*(aufwinkl**3)-7.992*(10**(-5))*(aufwinkl**2)-0.003445*aufwinkl+1.084
28     ausVrhlt=aufP1*((aufmts-794)/1440)**4+aufP2
29     ERGEBNIS=0
30     if ausVrhlt < aufParab1:
31         if ausVrhlt >= 0:
32             ERGEBNIS=aufVrhlt
33         #return("Parabel:", aufParab1, "P1:", aufP1, "P2:", aufP2, "Verhaeltniss:", ausVrhlt , "Er
34         #return("Faktor:", ERGEBNIS)
35     return(ERGEBNIS)
36
37 ##Faktor fuer Ausrichtung
38 #def AUSRICHTUNG():
39 def AUSRICHTUNG(auswinkl, ausmts):
40     #auswinkl=0 #Ausrichtungswinkel (-90 bis 90°)
41     #ausmts=0 #Minuten des Tages
42     ausParab1=-4.4*(10**(-5))*(ausmts**2)+0.06989*ausmts-19.13 #Einhullende Para
43     ausP1=-0.29722*(auswinkl/90)**6)+0.4417*((auswinkl/90)**2) #Parameter 1
44     ausP2=90*math.sin(2.658*(auswinkl/180)) #Parameter 2
45     ausVrhlt=-0.6*(auswinkl/90)*math.tan(ausP1*((ausmts-794-ausP2)/1440))+1 #Verhaeltnisskurve
46     ERGEBNIS=0
47     if ausVrhlt < ausParab1:
48         if ausVrhlt >= 0:
49             ERGEBNIS=ausVrhlt
50         #return("Parabel:", ausParab1, "P1:", ausP1, "P2:", ausP2, "Verhaeltniss:", ausVrhlt , "Er
51         #return("Faktor:", ERGEBNIS)
52     return(ERGEBNIS)

```

Figure 2: Functions of the conversions described in Section IV

The functions in Figure 2 take the respective angle and a point in time as input and return a result for each point in time. In lines 22 and 39 the functions are defined. In lines 25 and respectively 42 the enveloping parabolas are calculated. In lines 26, 27 and respectively 43 and 44 the necessary Parameters are calculated. The mentioned calculations must be calculated first. At last the ratios are calculated in line 28 and respectively line 45. In the if queries in lines 30 and 47 those results that are not enveloped in the respective parabolas are discarded. Those functions then return a result for each considered minute of the day.

```

139 if Tageszahl<=(Tage*196):
140     Umrechnungsfaktor_m1=AUFSTAENDERUNG(QuelleAufstand, Minutenzahl)
141     Umrechnungsfaktor_m2=AUSRICHTUNG(QuelleAusrichtung, Minutenzahl)
142     Umrechnungsfaktor_g3=AUFSTAENDERUNG(Aufstand, Minutenzahl)
143     Umrechnungsfaktor_g4=AUSRICHTUNG(Ausrichtung, Minutenzahl)
144
145     Wirk=0
146     Blind=0
147     if not P1==0:
148         Wirk=P1*Umrechnungsfaktor_m1*Umrechnungsfaktor_m2/Umrechnungsfaktor_g3/Umrechnungsfaktor_g4
149
150     if not Qvar==0:
151         Blind=Qvar*Umrechnungsfaktor_m1*Umrechnungsfaktor_m2/Umrechnungsfaktor_g3/Umrechnungsfaktor_g4

```

Figure 3: Calculation of the converted values of the load profile

Figure 3 shows the usage of the previously created conversion functions. In lines 140 to 143 each conversion is calculated, in lines 148 and 151 each point of the new load

profile is calculated using the 4 conversion parameters as described in section III. Finally the now fully calculated new load profile is exported into a new csv file. This is automatically repeated for each necessary PV-System.

C. Execution of the program in powerfactory

The program is executed in powerfactory, so the new csv files are actually calculated. In figures 4 and 5 the respective load profiles from one day can be seen.

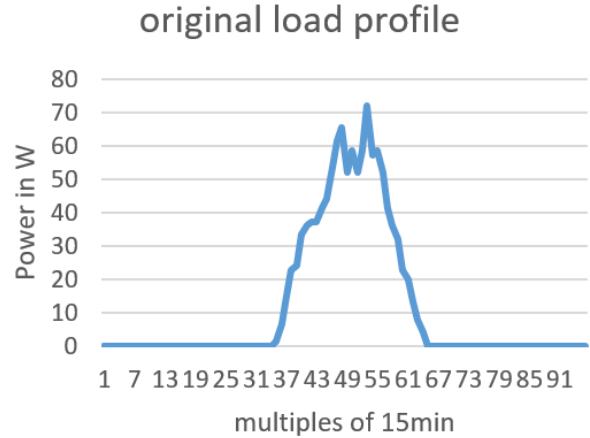


Figure 4: load profile of the source PV-System

In Figure 4 the load profile of the source PV-System with 0 degrees orientation and 20 degrees elevation on 01/01/2019 is shown.

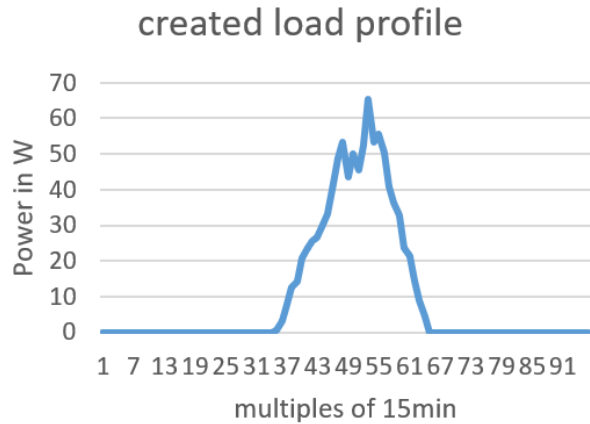


Figure 5: new calculated load profile of a PV-System

In Figure 5 the calculated load profile of a PV-System with 64 degrees orientation and 30 degrees elevation on 01/01/2019 is shown.

ACKNOWLEDGMENT

The support and aid of Mr. Markus Henneke, M.Sc. is gratefully acknowledged. Furthermore, the FENES team receives further recognition, in particular for cross-project support.

On the development of a seasonal seasonal heat storage for single-family houses: Design boundary conditions including the storage heat losses

Andreas Hanser
(Laboratory of Sorption Processes)
Master Applied Research
Ostbayerische Technische Hochschule
Regensburg
Regensburg, Germany
andreas.l.hanser@st.oth-regensburg.de

Belal Dawoud
(Laboratory of Sorption Processes)
Ostbayerische Technische Hochschule
Regensburg
Regensburg, Germany
belal.dawoud@oth-regensburg.de

Abstract—This paper deals with the establishment of basic conditions for a seasonal heat storage for single-family houses. For this purpose, the heat demand of a single-family house in Regensburg is considered, as well as the possible yield from a solar thermal system at the same location. A storage application is implemented to compensate for the temporal discrepancy between demand and solar availability. After the description of the basics, the process parameters are presented in detail. In addition to the consideration of an ideal system, different heat loss rates of the storage unit and their effects on the solar coverage rate, the necessary collector area and the necessary storage capacity are estimated and discussed.

Keywords—seasonal heat storage, heat demand, solar coverage rate, solar thermal system

I. INTRODUCTION

The biggest challenge of our time is global warming and accordingly its unpredictable consequences if we do not react. Besides the use of renewable energies, increasing the efficiency of energy usage is the most important tool in the fight against climate change. Alongside industry and commerce, private residential buildings are an important part of energy consumption. In Germany, the fraction of space heating in the overall demand of residential buildings was almost 68%, in 2018 [1]. This fact shows a high potential for savings in this area. In the field of sustainable heating of residential buildings solar thermal systems are well known and frequently used. The biggest issue with solar heating is the temporal discrepancy between solar supply in and heat demand of the building. A long-term storage system could transfer the excess heat gained during summer into the high consumption winter months. This increases the energy efficiency of the building significantly [2]. This paper addresses the boundary conditions for seasonal heat storage in single family houses with the main energy supply by a solar thermal system. These boundary conditions include primarily the heat load of the building. The possible heat generation of a solar thermal system is also important. These two main factors result in a heat comparison over a period of one year, from which the properties of a storage tank can be derived. Furthermore, different efficiencies of the storage process and their influence of factors like solar coverage rate, solar collector area and needed storage capacity were considered.

II. CALCULATION AND INPUT PARAMETERS

One of the most important elements in designing a seasonal storage unit is to take a close look at the heat demand of the building and the supply of heat that is available. In the following section properties of the building and the solar thermal system are presented and the made assumptions are explained.

A. Building properties

The building is a detached single-family house located in Regensburg, Germany. The living space is 137 square meters divided over two floors with a floor height of 2.60 meters. The outer shell of the building includes a window area of 20 percent of the living space which is equivalent to 27 square meters. The heat demand of buildings mainly depends on the thermal losses to the environment. The driving source of these losses is the temperature difference between inside the building and the ambient. The losses are countered by the thermal resistance of the building components such as walls, windows, the roof and so on. Equation (1) shows that the thermal resistance is a combination of the layer thickness d and thermal conductivity λ of the different layers. A wall for example is built with several layers. On the outside some kind of finish like exterior plaster followed by insulation, the structural element like brickwork and the interior plaster. Each part has its own thermal resistance which, when added together, results in the total thermal resistance of the wall. In addition, the effects of convection on the inside R_{si} and on the outside R_{se} are also part of the total thermal resistance [2,3]. Fig. 1 shows an example of a structural construction of a wall with three layers with different thicknesses and thermal conductivities and the temperature curve through it.

$$R = \frac{d}{\lambda} \quad (1)$$

$$U = \frac{1}{\Sigma R_n + R_{si} + R_{se}} \quad (2)$$

The reciprocal value of the total thermal resistance of a construction part is called heat transfer coefficient or U-value whose unit is $W/m^2 \cdot K$ as seen in (2). This value gives the amount of heat which transfers per square metre and Kelvin. temperature difference.

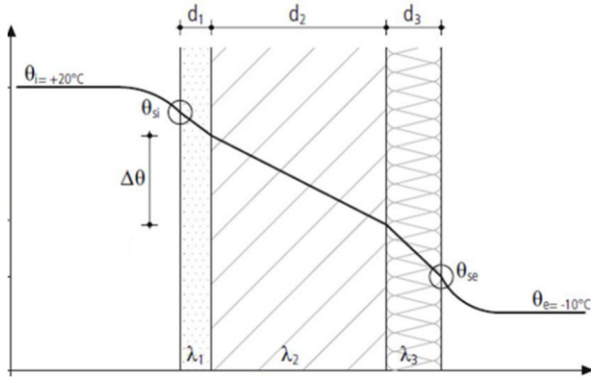


Fig. 1. Temperature curve through a wall with different layers with different thicknesses and thermal conductivities. [2]

As seen in (3) the transmission heat loss Φ is the result of the outside touching surface area A and the U-value of the respective construction element depending on the temperature difference between inside T_{in} and ambient T_{amb} . The room temperature is set to 20 °C. The outside temperature depends on the temperature data. This calculation has to be done for every building element with a different thermal resistance and therefore a different U-value. The sum of all results in the total transmission heat loss [2,4].

$$\Phi = A * U * (T_{in} - T_{amb}) \quad (3)$$

Buildings are divided into different categories based on their thermal properties. The recent standard for highly efficient residential buildings is the passive house standard. It is assumed that the simulated building was built according to this standard. In order for a building to achieve this, limits for the U-values of construction parts must be complied and thermal bridges must also be avoided. The U-value for walls, the roof and the base plate are set to 0.10 W/(m²*K). For windows and doors the U-value is set to 0.80 W/(m²*K) [6]. These buildings are suitable for seasonal thermal storage because its overall heat demand is already relatively low. This results in a smaller amount of storage heat [6,7].

Alongside transmission heat losses there are also ventilation heat losses that have to be considered. To preserve the air quality in living rooms it is necessary to exchange the air on a regular basis. The easiest way is to open a window again and again. But this is neither energy efficient nor does it ensure sufficient ventilation. A better solution is a central ventilation system with heat recovery. These systems guarantee the right amount of fresh air according to the air change rate n (4). This exchange rate determines how much of the total air volume of the building must be exchanged every hour. It is set to 0.5 1/h for residential buildings [4]. This system uses a heat exchanger to heat up the incoming fresh air with the outgoing air. Although this works very well there is still some external heat needed, depending on the efficiency of the air heat exchanger η_{hx} . According to the passive house standard which the building is built after, the heat exchanger has a heat recovery efficiency of 80 percent [7]. This heat is also part of the total heat demand of a building. The required heat to compensate the ventilation heat losses is calculated as shown in (5) [2,4]. The heat demand Q_{air} depends on the Volume V_{air} and the properties of the air ρ_{air} (density) and c_{air} (specific heat capacity). As at the transmission heat the

Temperature difference is the key parameter of the calculation.

$$V_{air} = V_{built} * n \quad (4)$$

$$Q_{air} = V_{air} * \rho_{air} * c_{air} * (T_{in} - T_{out}) * (1 - \eta_{hx}) \quad (5)$$

B. Solar thermal system

The heat to cover the demand caused by transmission and ventilation is generated by a solar thermal system. Solar collectors are able to collect the solar radiation and transform it into thermal energy. A heat transfer fluid is heated inside the collectors. The heated fluid links the collectors with the building's heat distribution system via pipes and a pump. The amount of generated heat depends mostly on the incoming solar radiation and the collector area. The efficiency of the collectors is determined by the ambient T_{amb} and the collector temperature T_{col} as well as product specific characteristics α_1 , α_2 , and η_0 as shown in (6). E is the value of solar radiation [8].

$$\eta_{col} = \eta_0 - \frac{\alpha_1 * (T_{col} - T_{amb}) + \alpha_2 * (T_{col} - T_{amb})^2}{E} \quad (6)$$

The model collectors are flat plat collectors with an optical efficiency η_0 of 0,81 and the factors α_1 of 3.8 W/(m²*K) and α_2 of 0.009 W/(m²*K) [8].

III. PROPERTIES OF THE SIUMULATION MODEL

In this section the properties of the simulation model are described. At first the structure of the building and solar system part and after that the storage unit.

A. Simulation structure of the building and the solar system

As mentioned before many parameters such as the transmission and ventilation heat losses but also the efficiency of the solar collectors depend on the ambient temperature. The used temperature data are from 2010 for Regensburg and contains hourly measured values of the entire year [9]. The hourly basis enables to consider not only the difference between months but also the difference between day and night. Which makes the model more detailed. Fittingly, the radiation data is also from 2010 from the nearest available radiation measurement station in Weihenstephan, Germany and also based on hourly measurements [10]. The year 2010 was chosen because of the high quality of both data sources. In the event of an error, the data errors are corrected by averaging directly preceding and following measured values.

During the simulation, every value that is based on the ambient temperature or the radiation data is calculated for every hour in the period of the year. This means the heat demand of the building with both parts transmission and ventilation is known for every hour. The solar heat supply by the thermal collectors is determined based on the collector efficiency which is also calculated for every temperature and radiation value. The result is a comparison of heat demand and heat supply for every hour.

B. Simulation structure of the Storage Unit

The storage Unit in this work is not tied to any particular storage technology. It is just a unit which stores heat if there

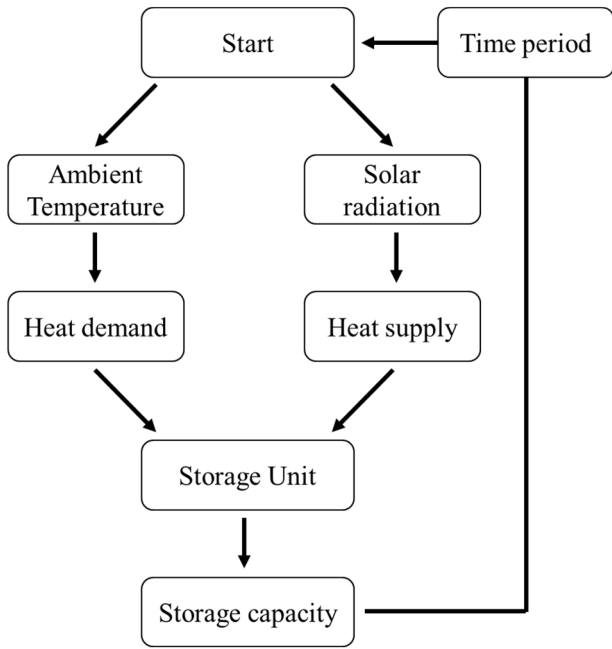


Fig. 2. Basic process flow chart for the storage unit

is a surplus and releases heat if the demand is higher than the supply. The storage capacity is not fixed. In fact there are the three following operating cases. First, the heat delivery from the solar thermal system and the heat demand are equal. In this case, the storage tank has no task, the supplied heat is used directly to cover the demand of the building. Second, the heat supply exceeds the demand. Here, the surplus energy that is not directly used is added to the storage. Third the heat demand is higher than the heat supply. In this case the missing heat to cover the demand is used from the storage. The latter

is only possible if there is enough heat available in the storage. These calculations are made for every hour of a year. The result of each hour is the starting point and thus the current storage status for the following hour. The storage heat calculation first starts at zero and is not able to be negative. Fig. 2 shows a simply process flow chart for the storage unit. This leads to a diagram of heat surpluses and furthermore to a maximum point of stored heat. This maximum amount of stored heat is equal to the storage capacity needed in the considered situation. The heat supply and thus the storable heat depends highly on the solar fraction. This fraction is determined by the percentage of solar energy used to meet the demand. The demand also includes possible heat losses.

IV. PARAMETRIC SIMULAITONS AND DISCUSSION

A. Building heat demand and solar heat supply

The upper part of Fig. 3 displays the development of heat demand values over the period of the year. The fluctuations are caused by the hourly data especially by the temperature difference between day and night. As expected, the heat loss reaches its high in the winter months. During summer there are some negative heat losses which means there is heat entry into the building. This happens when the ambient temperature exceeds the nominal inside temperature of 20 °C. Depending on the amount of incoming heat this could require some kind of house cooling. The bottom part of Fig. 3 shows the heat supply from one square meter of solar thermal collector surface. As before, the expected results are visible here. The heat yield increases form the beginning of the year until July and then falls down till the end of the year. In May and June there are some events with lower values. The reasons for smaller heat generation are for example cloudy days with little sunshine. The comparison of these two graphs clearly shows the temporal discrepancy between demand and supply which was mentioned before Especially in July when the heat

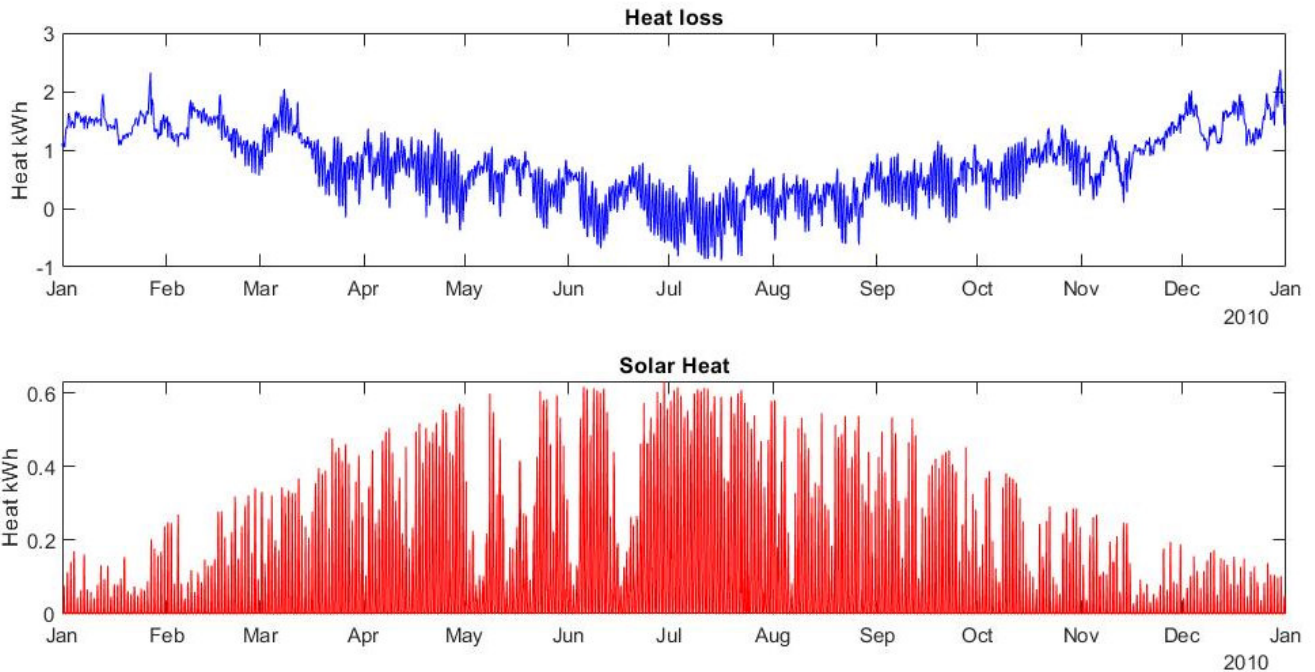


Fig. 3. Heat loss curve of the building during a year (top part) and solar heat supply over the year (bottom part).

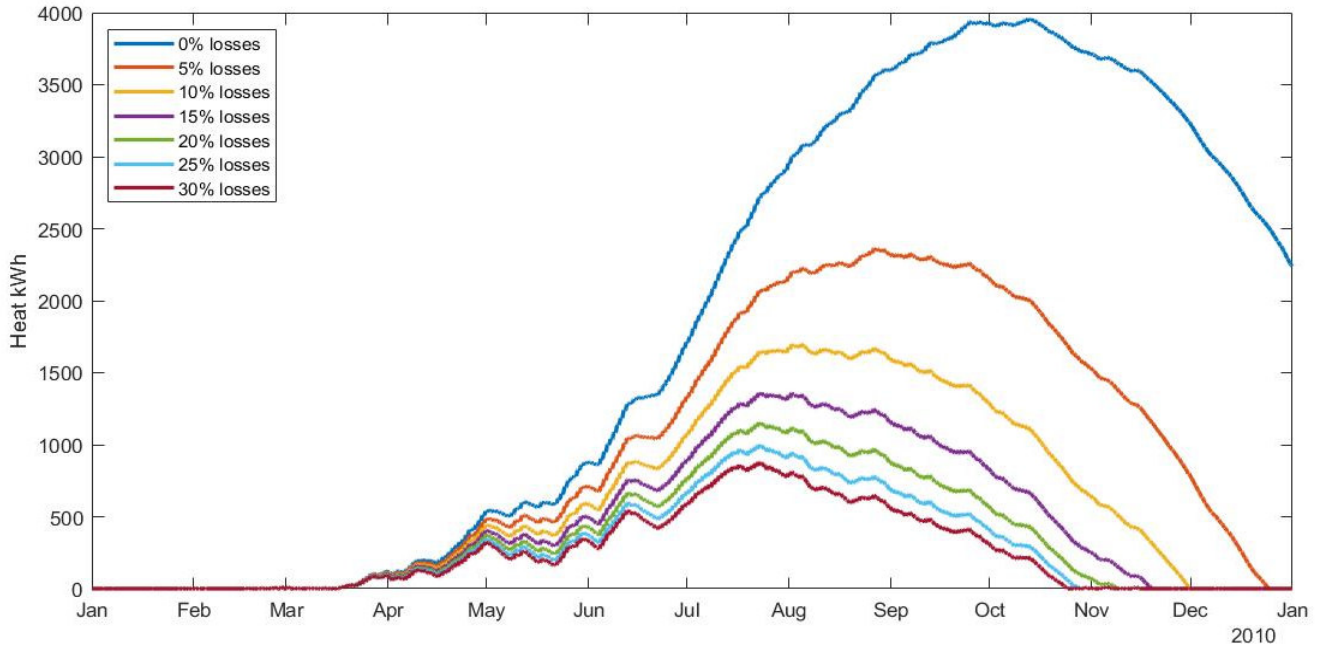


Fig. 2. State of charge throughout an entire year with different heat loss rates from loss-free to 30 percent of storage heat losses.

demand is negative and at the same time the heat supply reaches its peak. In contrast, the opposite is the case in the December, when demand is highest and supply lowest.

The total amount of heat losses of the considered year is 6553.8 kWh. This is divided into transmission heat loss of 5309.9 kWh per year and 1244.8 kWh of ventilation heat loss per year. The proportion of transmission is therefore significantly bigger than ventilation. There is a negative energy balance on 7852 hours which means that there is a heat demand for the most part of the year. The overall heat generation of one square meter of collector surface is 722.68 kWh per year. The comparison of these two results for heat demand and heat supply shows that it is theoretically possible to cover the whole heat losses of the considered building with 9.08 square meters of solar collector area. This results in a 100 percent solar coverage.

Based on the difference between heat demand and heat supply a storage unit is calculated. The total storage capacity needed to cover all surpluses and give the opportunity to cover the overall demand completely is 3402 kWh. This result is the maximum value of the storage unit over the period of one year.

B. Considering storage heat losses

The previous calculations were made for an ideal system which means apart from the efficiency of the solar thermal collectors and the ventilation system heat exchanger there were no consideration of efficiency rates. The storage unit offers a high potential for energy losses due to the increasing storage content and the long storage period. In Fig. 4 the curves of the storage level over the considered year are displayed. Each of the seven different lines stands for a heat loss rate from 0% up to 30% heat losses over a period of one week. The calculations were made with a solar collector area of 10 square meters which is approximately the needed area for a 100% solar coverage. The start of the calculation was with a storage level at zero. About at the middle of march the solar heat exceeds the heat losses of the building and the storage level increases. It becomes clear that the curve of the

ideal assumed storage unit is markedly different from the others. Especially in the further course of the year when the storage level continues to grow the maximum of 3959 kWh is significantly higher than the others. For example, the curve which represents heat losses of five percent has a maximum value of 2364 kWh. The remaining heat at the end of the year enables to cover the heat demand of the first few months of the following year and therefore the entire heating period. Just the loss-free application has heat remaining at the end of the year. The others are getting to zero before the end of the year which means there is no heat left in the storage.

The data in Fig. 4 are based on collector area for an ideal system to reach 100% solar coverage. The solar fraction with storage heat losses decreases to 79.7% with 5% losses and 70.8% with 20% losses. This results in a bigger need of collector area to cover the losses. The needed collector areas to reach 100% solar fraction with the different storage heat loss rates are summarised in Table 1. As seen on the curves in Fig. 4. The step from without losses to five percent is quite big. A loss-free system needs 9.08 m² of as mentioned before,

TABLE 1 COLLECTOR AREA AND STORAGE CAPACITY AT DIFFERENT STORAGE HEAT LOSS RATES.

Heat Loss Rate	Collector Area m ²	Storage Capacity kWh
0%	9.08	3402.7
5%	16.64	4417.3
10%	27.72	5510.0
15%	39.69	6253.2
20%	48.83	6360.3
25%	56.40	6236.1
30%	61.68	5928.0

with five percent the needed area increases to 16.64 m². The required area becomes larger and larger with increasing losses. If the storage has a loss of 30% per week, 61m² are needed to achieve a solar coverage rate of 100%. With an unlimited storage capacity in this case.

Table 1 also gives a look at the storage capacity which is needed in every heat loss scenario. The capacity needed increases with bigger heat losses, too. In contrast to the collector area the capacity reaches a maximum and decreases afterwards. The capacity to cover all heat surpluses and reach a complete solar coverage is in an ideal system 3402.7 kWh. With 20% losses it is 6360.3 kWh and then at 30% it is 5928.0 kWh. The peak is around 18% with about 6384 kWh.

This happens because of the increasing collector area. If the solar fraction is fixed and the storage heat losses are increasing as it is in this scenario, the heat source must generate more energy. This means the collector surface must get bigger. At some point the heat supply is so big that the directly used heat gets a bigger impact. When this state is reached, the heat storage gets less important. With a big collector area there is even with low solar radiation enough heat generation to cover most parts of the demand. With enough collector area it is theoretically possible to reach a full solar coverage without any kind of heat storage. But this is very inefficient and and very expensive.

V. CONCLUSION

This paper has presented a single-family house located in Regensburg, Germany and its thermal balance. Including the heat demand and the yield of a solar thermal system over the period of one year. The passive-house building with a living space of 137 square meters has a transmission heat loss of 5309 kWh and a ventilation heat loss of 1244 kWh per year. To compensate the losses the solar thermal system is able to deliver 722 kWh per square meter collector area and year. The storage capacity to enable a fully solar heated building depends strongly on the storage losses and ranges from 3402 kWh under ideal conditions to about 6384 kWh at the maximum. The following conclusions can be drawn from this work:

- Buildings with high efficiency standards are better suited for seasonal storage due to the already lower heat losses.
- There is a temporal discrepancy between the peaks of solar heat supply and heat demand of a building. This requires a long-term heat storage system.

- In a loss-free storage even a collector area of 9.08 m² is enough to reach full solar thermal coverage in a passive house building with 137 m² living space.
- Increasing the heat loss percentage from 5% to 30% results in increasing the required collector area from 16.64 m² to 61.68 m² to maintain a 100% solar fraction.
- With increasing heat losses the storage capacity increases, too. With a loss percentage of about 18% the increasing collector area causes a higher heat supply and thus a lower demand for storage capacity.

The used calculation model has some opportunities to improve. The model of the building will be more detailed. For example, the heat storage ability of construction parts or the gain of heat due to solar radiation on parts of the building or through windows could be considered. Furthermore, this work only looks at one particular year. Average climate data would make the results more reliable. In the next phase, the model will be further developed and a thermochemical storage technology will be integrated.

REFERENCES

- [1] Umweltbundesamt, Anteile der Anwendungsbereiche am Endenergieverbrauch der privaten Haushalte 2008 und 2018, 2020
- [2] M. Sterner and I. Stadler, *Energiespeicher – Bedarf, Technologien, Integration*, 2. Auflage, Berlin, Heidelberg:Springer Berlin Heidelberg, 2017
- [3] D. Bohne, *Technischer Ausbau von Gebäuden: Und nachhaltige Gebäudetechnik*, 11. Auflage, Wiesbaden: Springer Vieweg, 2019
- [4] DIN EN 12831-1, *Energy performance of buildings – Method of calculation of the design heat load – Part 1: Space heating load Module M3-3 german version EN12831-1*, 2017
- [5] T. Laasch and E. Laasch, *Haustechnik: Grundlagen – Planung – Ausführung*, 13. Auflage, Wiesbaden: Springer, 2013
- [6] M. Pehnt, *Energieeffizienz: Ein Lehr- und Handbuch*, Berlin, Heidelberg: Springer Berlin Heidelberg, 2010
- [7] H. Frey, *Energieautarke Gebäude: Auf dem Weg zu Smart Energy Systems*, Berlin, Springer Vieweg, 2019
- [8] V. Quaschnig, *Regenerative Energiesysteme: Technologie – Berechnung – Simulation*, 10. Auflage, München: Hanser, 2019
- [9] DWD, Climate Data Center: Hourly station observations of air temperature for Regensburg, last accessed 27.11.2020
- [10] DWD, Climate Data Center: Hourly station observations of radiation for Weihnstephan-Dürmast, last accessed 26.11.2020

Evaluation of possible charging demand of battery electric vehicles in parking garages and Park+Ride areas based on real entry and exit data

Markus Kaiser
University of Applied Sciences
Munich, Department of Engineering
and Management
Munich, Germany
mkaiser@hm.edu

Jörg Elias
University of Applied Sciences
Munich, Department of Engineering
and Management
Munich, Germany
joerg.elias@hm.edu

Abstract— The aim of this paper is to estimate the charging requirements of BEVs in parking garages and P+R facilities. For this study, real entry and exit data from parking facility providers in Munich are evaluated. The parking behaviour of the customers derived from this data, is used to evaluate the customer charging demand. For the investigation, the parking behaviour was combined with estimates of the city of Munich on future penetration rates of BEVs. These penetration rates are used to assess the number of BEVs in parking facilities. The charging requirements were calculated with the electric vehicles data currently available on the market.

Keywords—*Parking garage, Park+Ride, BEV, Charging infrastructure, Urban mobility*

I. INTRODUCTION

The shift towards electromobility can bring opportunities for parking facility operators to expand their business activities. Through this transformation, customers who previously only wanted to pay for the parking space offered, can turn into customers with an interest in charging offerings. But how large can this share of new customers become in the next five to ten years and what does this mean from today's investor perspective? An investment in charging infrastructure should be based on prior research, preferably in the context of an economic and technical study. Key questions such as the expected demand from customers and aspects regarding the selection of hardware should be answered. It is essential to answer these questions, to ensure a profitable business development in the future. In this work, the methodology and data used to answer the mentioned issues are described. The results presented in this paper are part of a guideline for parking facility operators that is being developed during my research at the University of Applied Sciences in Munich.

To evaluate the behaviour and requirements of drivers of BEVs, simulation models in MATLAB were used. The models combine available and validated data on penetration rates and charging demand of BEVs with real customer behaviour in parking garages and P+R facilities. Primarily, these surveys are intended to evaluate the charging needs regarding quantity, timing and required infrastructure. The

estimates of future BEV penetration rates come from the "integrated action program for the promotion of electromobility in Munich". This program is maintained and financed by the city of Munich's Department for Climate and Environmental Protection. The data basis for modelling the charging demand is taken from 40 BMW i3 60 Ah electric vehicles with a usable battery capacity of 18.8 kWh, a maximum AC charging power of 7.4 kW and a DC charging power of 50 kW. The data was collected using a data logging system from January 19 to November 14 in 2015 inclusive, and thus covers a period of 300 days. 17 of the 40 vehicles were equipped with a range extender (REX). The mobility behaviour of the vehicles is discussed in the publication [1] and [2]. Entry and exit data representing parking behaviour are taken from a parking garage in Munich's city centre and from a P+R facility, 11 km away from the city centre.

II. METHODOLOGY

The data of the facilities are used to reflect a customer behaviour in the parking areas. This mobility behaviour, produced by conventional cars, is combined with findings and assumptions from studies in the field of electromobility. First, the difference in the customer behaviour of both parking facilities is described.

A. Parking behaviour in city centre parking garage

Figure 1 shows the parking behaviour of customers in the city centre parking garage. It shows the distribution of the parking times for the defined periods. 18.662 parking processes were evaluated for this analysis. All operations come from the months of August to September 2020.

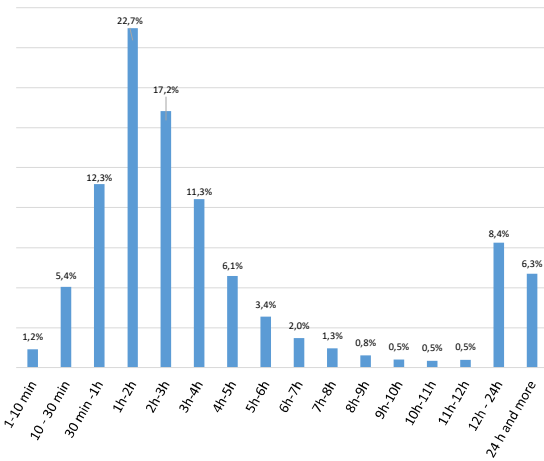


Figure 1 Duration in city centre parking facility

The largest share of parking processes has a duration between one and two hours. Parking between two and five hours represents more than one third of all parking processes. Just under 15 percent of transactions last longer than 12 hours. On the other hand, the proportion of short-term parking, i. e. less than one hour, is 19%. Figure 2 shows customer behaviour regarding entries and exits over the course of the day.

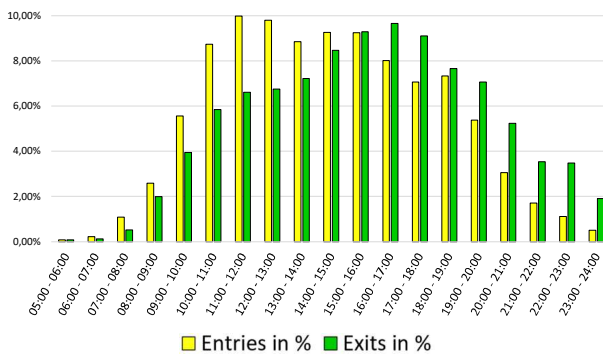


Figure 2 Entries and exits over the course of one day

This graph shows the highest percentage of entries between 11 and 12 am. A peak of exits is shown in the period between 4 and 5 pm. Time periods that stand exclusively for entries or exits cannot be seen in this chart. In short, it can be concluded for this urban parking garage, that entries and exits occur in every time slice with minor deviations in percentual distribution. With a maximum difference of 3.7% between 11 and 12 am. This behaviour is reflected in the results that follow later in the paper.

B. Customer behaviour in Park+Ride facility

Representing P+R, the customer behaviour of the facility in Fürstenried-West was examined. The linear distance to the city centre of Munich (Karlsplatz Stachus) is 11 km. The “Ride” factor for this facility is ensured by a connection to the line U3 of Munich’s public transportation network. The distribution of parking durations shown in figure 3 represents 19.041 parking operations from the months May to December 2020.

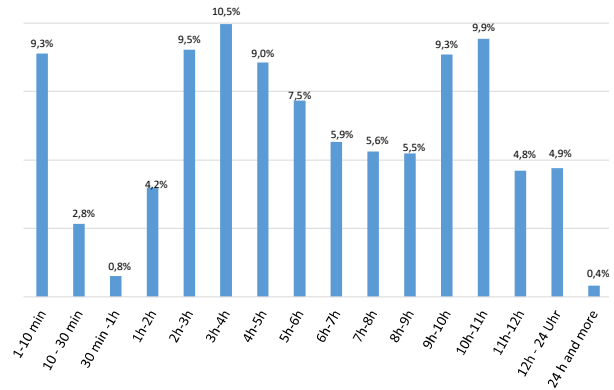


Figure 3 Parking durations of P+R Fürstenried-West

There are significant differences compared to the inner-city parking garage. Short-term parking has a share of nearly 13%, compared to 19% in the city centre facility, of which the largest part consists of 1-10 minutes. Parking times of more than 12 hours represent slightly more than 5% of the total. Just over 40% of the parking actions have a parking duration between 6 and 12 hours. Figure 4 represents the entries and exits over the course of the day.

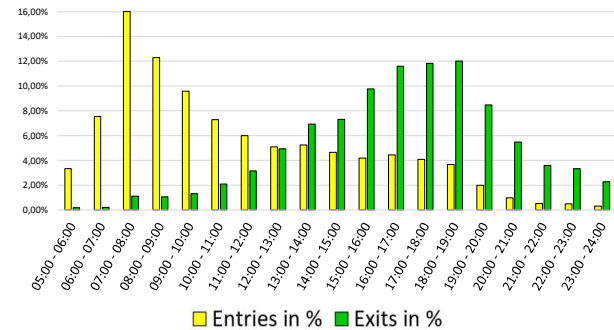


Figure 4 Entries and exits Fürstenried-West

The behavioural patterns of customers also differ in this diagram. At P+R, there is a concentration of entries in the morning, with a peak from 7 to 8 am. In the evening, from 4 to 7 pm, there is a peak in the number of exits. The presented analyses regarding customer behaviour are fundamental for calculations of charging requirements of the customers. The parking duration influences the customer requirement for charging in terms of time available for a charging process. The distribution of entries and exits places demands on the charging infrastructure with respect to the number of chargers and the required power at the same time.

The patterns will be needed to develop economic viable recommendations for parking facility operators, moreover, to promote the expansion of charging infrastructure in the urban sector.

C. Assumptions of Munich's authorities

At the current state, the evaluated parking activities are not linked to a certain vehicle, neither conventional nor battery electric. To enable this distinction, assumptions from the "integrated action program for the promotion of electromobility in Munich" are accepted. Within the framework of this work, estimations regarding penetration rates of BEVs within the whole vehicle fleet are taken on. Those are available for the years 2020 to 2027 and charted in table I. Four defined segments from the Kraftfahrt-Bundesamt (KBA) allow a classification of the BEVs on the market. Factors such as the battery capacity or the vehicle range are considered. A deviation into segments allows to implement categories of BEVs with different needs, concerning charging demand resulting from battery capacity. The share of the segments in the entire BEV fleet can be seen in this table as well. This distribution is also an estimation of the municipal authority.

TABLE I. IHFEM FORECAST

IHFEM forecast	Years under consideration							
	2020	2021	2022	2023	2024	2025	2026	2027
	Share of BEVs (entire vehicle fleet)							
[%]	0,8	2,5	4,1	6,0	7,9	10,0	12,3	15,1
	KBA segment (share in BEV fleet)							
small	30%	30%	27%	28%	28%	27%	28%	29%
compact	30%	30%	31%	31%	30%	30%	30%	30%
mid-size	30%	30%	31%	31%	30%	30%	30%	30%
large	10%	10%	12%	11%	13%	14%	12%	11%

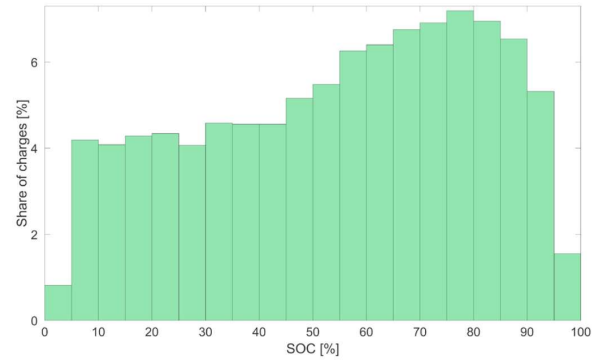
Publication [3] is dealing with these estimations in detail. The average growth rate between the years is 2%. Beginning with an increase of 1.7% from 2020 to 2021 and rising to 2.8% from 2026 to 2027. Based on the BEVs shares in the entire vehicle fleet, it is possible to implement prospects into the MATLAB simulations. Combined with the gateway-data from parking facilities of last year, estimations are made for customer charging needs in the near future.

D. Approach for estimating the charging demand

The penetration rate used, according to the year chosen, enables to classify certain vehicles entering the parking garage as BEVs. However, it is not known how high the charging demands of the individual customers are. The data base used for assigning the customer needs, is taken from the publication [2]. Around 11.000 charging processes of 40 vehicles were analysed. The SOC_{start} of each charging process was documented, the resulting distribution can be seen in figure 5.

The distribution in figure 5 is implemented into the MATLAB simulation and reproduces values for the SOC_{start}

which are needed for every charging operation. Each of the vehicles declared as BEVs are classified according to table I. For the investigations in this paper, 68 BEVs were classified into the four segments. In this, vehicles with net capacities from 16.7 up to 95 kWh are represented. A randomised chosen vehicle with an associated net battery capacity, serves as the basis to calculate the charging demand. A value for SOC_{start} according to the distribution from figure 5 and the BEVs net capacity are used to generate the charging need in kWh.



(a) Start of charging

Figure 5 Distribution of SOC_{start} from BMW i3 fleet [2]

E. Modelling of charging processes

The required amount of energy, that is calculated individually for every vehicle declared as BEV, according to the chapters C. and D., is charged when the driver places his car in the lot. The charging process of the BEVs lithium-ion battery was modelled according to the formulas and parameters of [4]. The SOC value 75% was defined as the charge changeover point. This changeover point is used for lithium-ion batteries. The required low end-of charge voltage can be achieved by this exponential reduction of the charging power. Figure 6 represents a randomly chosen charging event.

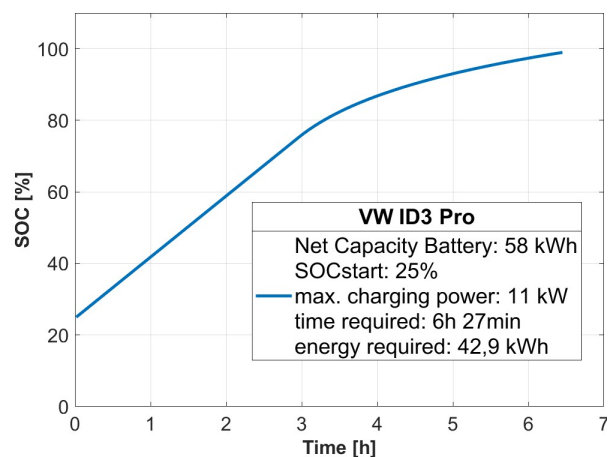


Figure 6 Exemplary AC charging process

All simulated charging events used for the investigations and results in this paper are not limited by available power or chargers from facility side. The required energy and charging infrastructure were given at any time during the simulation. If the required charging time is longer than the cars parking duration, the process is interrupted when the customer leaves the car park.

It should be noted that the calculated charging needs are based on a dataset from the year 2015. The low battery capacity of these first-generation electric vehicles influences the SOC_{start} and therefore the calculated needs used for the simulations. An SOC_{start} of 50% from the study can be equated with an SOC_{start} of 84% for a state-of-the-art BEV like the VW ID 3 Pro. The calculated charging needs have therefore to be critically assessed.

III. RESULTS

The acquired parking data will serve as a real-life basis to estimate charging requirements of future car park customers. At this state, requirements from the customers in charging quantity and infrastructure can be evaluated.

To understand the customer requirements mentioned, the customer charging need and the parking duration is compared to the required duration for charging processes. Thereby takes place a division between charging technologies, whether AC or DC charging is in the focus of evaluation. Table II shows the parameters used for the charging processes.

TABLE II. CHARGING PARAMETER

Charging parameter	Type of charging method	
	AC	DC
Max. output power	22 kW	50 kW
$\eta_{charging\ process}$	90%	90%
SOC changeover point	75%	75%
Min. parking duration for charging	30 min	30 min

A. Inner-city parking facility

Table III represents charging with AC in the city centre facility. The results come from a period of two months and 18.662 parking operations. The actual charged quantity is the amount that could be charged during the simulation. The theoretical demand is the sum of the energy amounts calculated according to chapter II, before the charging processes started.

TABLE III. CITY PARKING AC

AC Charging	Type of charging method			
	Number of BEVs	Share of completed charging processes	theoretical charging demand [kWh]	actual charged quantity [kWh]
2020	165	38%	3.623	2.230
2021	415	35%	9.956	6.427
2022	750	34%	19.484	11.506
2023	1.039	38%	24.080	15.727
2024	1.292	36%	32.270	20.460
2025	1.813	39%	43.965	27.969
2026	2.179	37%	52.289	33.079
2027	2.640	37%	63.903	40.542

The simulation shows that only 37% of the charging instances end with 100% SOC. This is also reflected in the actual charged quantity. Around 63% of the theoretical demand was charged in the simulation runs. Decisive factors are the charging durations that go along with AC charging and the mostly short parking durations shown in figure 1.

DC charging with a maximum power output of 50 kW reduces the required charging time. The influence of this advantage is reflected in table IV.

TABLE IV. CITY PARKING DC

DC Charging	Type of charging method			
	Number of BEVs	Share of completed charging processes	theoretical charging demand [kWh]	actual charged quantity [kWh]
2020	149	63%	3.729	3.345
2021	433	65%	10.392	9.264
2022	755	63%	18.482	16.423
2023	1.020	63%	23.425	20.794
2024	1.378	64%	34.369	30.796
2025	1.811	62%	42.180	37.778
2026	2.113	63%	51.854	46.282
2027	2.608	61%	63.866	56.896

The average share of charging processes completed in time is 63%. Overall, 89% of the customer demand was charged within the simulation runs. The shorter charging times favour an earlier end of the charging process, resulting in a higher chargeable amount of energy.

B. Park+Ride facility

Table V represents charging with AC in the P+R facility. The results come from a period of eight months and 19.041 parking operations.

TABLE V. P+R AC

AC Charging	Type of charging method			
	Number of BEVs	Share of completed charging processes	theoretical charging demand [kWh]	actual charged quantity [kWh]
2020	113	65%	2.873	2.364
2021	442	66%	10.625	9.051
2022	643	69%	17.354	14.813
2023	1.071	67%	26.000	22.400
2024	1.287	68%	31.469	27.276
2025	1.799	69%	43.302	37.041
2026	2.016	69%	48.538	42.346
2027	2.554	68%	62.816	54.484

The results clearly reflect the customer behaviour from figure 3. Charging with AC reaches a share of completed charging processes of 68% in average. The proportion of actual charged energy is around 86%.

Longer durations of parking leads to a high chargeable amount with AC charging technology. Also in this consideration, a change of technology to DC was implemented in the simulation.

TABLE VI. P+R DC

DC Charging	Type of charging method			
	Number of BEVs	Share of completed charging processes	theoretical charging demand [kWh]	actual charged quantity [kWh]
2020	120	92%	3.216	3.100
2021	412	91%	9.912	9.514
2022	661	92%	15.740	14.903
2023	1.030	92%	25.909	24.676
2024	1.300	91%	31.651	30.166
2025	1.693	91%	43.040	41.139
2026	2.080	92%	49.294	46.950
2027	2.538	92%	62.039	59.092

The share of completed charging processes rises to 92%. Also, the actual charged amount goes up to an average value of 95% with respect to the theoretical demand. The different charging technologies have a smaller influence on the chargeable quantity of energy, compared to the city centre facility. This is favoured by the parking behaviour shown in figure 3.

How far the share of completed charging processes serves customer requirements cannot be answered at this point. So far, there is no information on how the state of charge at the end of the process influences the customer satisfaction. From the investor's point of view, the focus is most likely on a high energy turnover, that would result in a higher turnover in sales. This assumption must be weighed against the additional costs of a DC infrastructure, which is characterised by higher CAPEX and OPEX costs.

C. Demand per customer

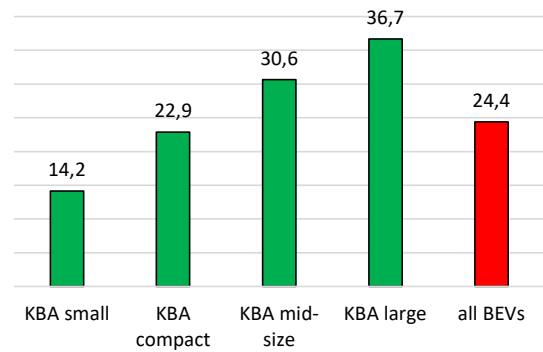


Figure 7 Average charging demand per segment [kWh]

Figure 7 shows the average charging demand per segment and for all BEVs entering the parking facilities during the simulation. The simulated vehicles from the segments have different charging needs, significantly influenced by the size of the batteries. The SOC_{start} values from figure 5 apply for all the segments without any adjustment. The average demand of the customers is about 24.4 kWh.

IV. CONCLUSION

The results presented for both facilities and charging technologies (AC and DC) make it clear, that a general recommendation for parking facility operators can't be given at the current time. Big differences concerning the customer behaviour require a separate analysis of the circumstances. An outlook towards creating profitable business models is not possible at the actual state. But it can already be said that various charging technologies might be suitable to meet customer need.

For the city centre facility, a major task will be, to figure out if it could be profitable to sell more energy with DC chargers, despite its significantly higher CAPEX and OPEX costs. A focus on AC charging might not meet the customer requirements in this context, if it is the customer request to charge up to 100% SOC. In any case it must be evaluated if the available power from facility site prevents or limits the usage of DC or AC charging. Fundamentally, the actions for P+R facilities are the same. Also, for this case, investigations to figure out the right number of chargers are needed, to give parking operators recommendations if investing in charging infrastructure makes sense from an economic perspective.

V. REFERENCES

- [1] Kessler, L., Bogenberger, K.: 'Mobility patterns and charging behavior of BMW i3 customers', 2016 IEEE 19th International Conference, 2016, pp. 1994–1999
- [2] Kessler, L., Bogenberger, K.: 'Dynamic traffic information for electric vehicles as a basis for energy-efficient routing', Transportation Research Procedia, V. 37, 2019, pp. 457–464
- [3] Fischer, M.: 'Entwicklung von Geschäftsmodellen für Ladekonzepte und Ladestationen im hochverdichteten öffentlichen Raum', München, 2020
- [4] Schuster, A.: 'Batterie- bzw. Wasserstoffspeicher bei elektrischen Fahrzeugen', Wien, 2008

Modularity Analysis of Power Electronics Architectures

Tobias Kern
 University of Applied Sciences
 Ingolstadt
 Ingolstadt, Germany
 Email: tok4623@thi.de

Abstract—For different applications different voltage and power levels are needed. Therefore power electronics are used to control and supervise the desired voltage levels. Also for different environments the operating conditions are changed. Because of this the need for a modular power electronic architecture is needed. For this purpose, the structure of various common con-/inverter topologies are examined in more detail. Afterwards the electrical stresses of each con-/inverter component is compared against each other. As result modules are proposed. With these it is possible to build up most power electronics. To maintain efficiency with the opposing physiology of the components for different voltage and power levels the parts has to be reevaluated.

I. MOTIVATION

Power electronics today are used in many applications like smartphone chargers, electric kettles, audio amplifiers, electronic control units, traction systems of cars and trains. All of those controlling their power output by switching currents of one ore more phases, which afterwards get filtered. For each application the electrical stresses have to be considered individually. For household application in Europe the mains voltage is 230 V [1]. In North and South America it is mostly 110 V. Besides private households the industry widely uses three-phase systems to power the devices to minimize losses. The three-phase system voltage also differs across the world. The power consumption of private household devices reaches up to 15 kW, whereas the industrial power consumption reaches MW to GW. To create a universal kit for power electronics architectures, the electrical stresses will be analyzed for different converters and the B6-inverter. Since household appliances are produced for the masses, cost optimisation is a relevant point. The advantage of a modular system is therefore not given.

II. ANALYSIS OF POWER ELECTRONICS ARCHITECTURES

Modern power electronics utilize switch-mode converter instead of linear regulators. Switching converters chops the current instead to continuously decrease it. Because of that the transistor is in its fully turned-on state and has a much higher conductivity against the transistor in the linear voltage regulator and therefore a higher efficiency. Also it is possible with inductive components to boost the voltage. For motor control inverters are used as variable speed drive. To find common parts between different power electronic architectures

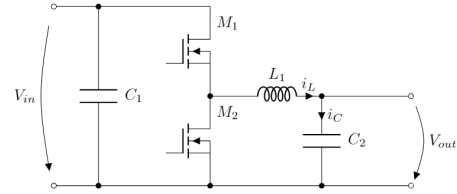


Figure 1. synchronous buck-converter topology

Table I
 VOLTAGE AND CURRENT RATING OF BUCK-CONVERTER COMPONENTS [2], [3]

voltage rating	current rating
Component: C_1	
V_{in}	$i_{out} \sqrt{\frac{V_{out}}{V_{in}} \left(1 - \frac{V_{out}}{V_{in}}\right)}$
Component: M_1, M_2	
V_{in}	i_{out}
Component: L_1	
$\max(V_{in}, V_{in} - V_{out})$	i_{out}
Component: C_2	
V_{out}	$\Delta i_L \frac{\sqrt{3}}{6}$

following voltage converters are analyzed beside the B6-inverter:
 buck-, boost-, buck-boost-, cuk-, flyback, and full-bridge-converter.

A. buck-converter

The buck converter steps the input voltage down to a lower level. It can be built in two main topologies. The difference between the synchronous and the asynchronous topology is, that an active half-bridge instead of a combination of an active switching device, like a transistor, and a diode is used as a switch. In figure 1 the synchronous buck converter is shown. It consists of an input capacitor, a half-bridge, an inductor and an output capacitor. The voltage and current ratings of each component is listed in table I

B. boost-converter

Like the buck-converter, the boost converter also exists in a synchronous and asynchronous topology. The synchronous

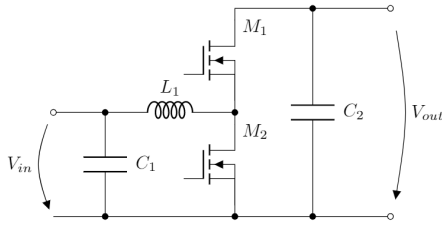


Figure 2. synchronous boost-converter topology

Table II
VOLTAGE AND CURRENT RATING OF BOOST-CONVERTER COMPONENTS [3]

voltage rating	current rating
Component: C_1	
V_{in}	$\Delta i_L \frac{\sqrt{3}}{6}$
Component: M_1, M_2	
V_{out}	i_{out}
Component: L_1	
$\max(V_{in}, V_{in} - V_{out})$	i_{out}
Component: C_2	
V_{out}	$i_{out} \sqrt{\frac{V_{out}}{V_{in}} - 1}$

topology (figure 2) consists also of an input and output capacitor, a half-bridge and an inductor. Opposite to the buck-converter the boost converter increases the input voltage to a higher level. The corresponding ratings are listed in table II.

C. buck-boost-converter

The buck-boost-converter (figure 3) is a concatenation of the buck- and boost-converter. It can decrease as also increase the voltage. Likewise the previous two it also can be built in a synchronous and asynchronous converter. But different than the buck and boost converter the buck-boost-converter can also be built in an inverting architecture, so that the output voltage is negated. The benefit of the inverting architecture is that it needs fewer components, but with higher stress limits.

D. Ćuk-converter

The Ćuk converter (figure 4) can also decrease as increase the input voltage. The Ćuk-capacitor blocks the input current to flow to the output. Also this topology has a continuous input current flow, which leads to lower distortion on the input network. Since the output current has to flow over the Ćuk-capacitor, the synchronous variant of this converter is rarely used.

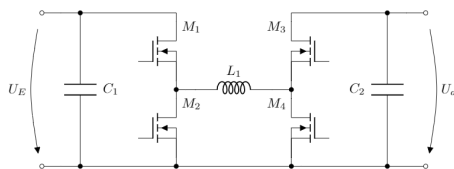


Figure 3. Non inverting buck-boost-converter

Table III
VOLTAGE AND CURRENT RATING OF BUCK-BOOST-CONVERTER COMPONENTS [3]

voltage rating	current rating
Component: C_1	
V_{in}	$\Delta i_L \frac{\sqrt{3}}{6}$
Component: M_1, M_2	
V_{in}	i_{out}
Component: M_3, M_4	
V_{out}	i_{out}
Component: L_1	
$\max(V_{in}, V_{in} - V_{out})$	i_{out}
Component: C_2	
V_{out}	$i_{out} \sqrt{\frac{V_{out}}{V_{in}} - 1}$

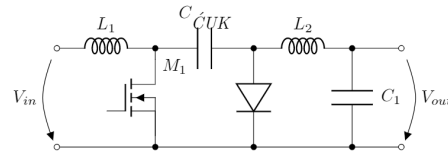


Figure 4. Ćuk-converter

E. flyback-converter

The flyback converter (figure 5) consists of just one active switching component. The main differences between different topologies are the snubber network around the transformer (e.g. RD-snubber) and the rectifier on the output side (active, passive, half-wave, full-bridge).

F. phase-shift-converter

The phase-shift converter (figure 6) is a full-bridge converter, which makes use of the phase delay of an additional inductance to enable low voltage switching.

G. B6-inverter

The B6-inverter consists of an input capacitor and three half-bridges. The input or dc-link capacitor reduces the current ripple on the input, if the source is far away. Whereas the half-bridges serve either as rectifier or inverter.

Table IV
VOLTAGE AND CURRENT RATING OF ĆUK-CONVERTER COMPONENTS [4]

voltage rating	current rating
Component: L_1	
V_{in}	$i_{out} \frac{V_{out}}{V_{in}}$
Component: M_1, D_1	
$V_{in} - V_{out}$	$i_{L1} - i_{L2}$
Component: C_{uk}	
$V_{in} - V_{out}$	$\max(i_{L2} , i_{L1})$
Component: L_2	
V_{out}	i_{out}
Component: C_1	
V_{out}	Δi_{L2}

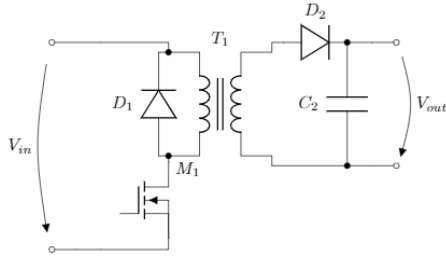


Figure 5. flyback-converter

Table V
VOLTAGE AND CURRENT RATING OF FLYBACK-CONVERTER COMPONENTS [5]

voltage rating	current rating
Component: $T_{1,prim}$	
V_{in}	$V_{in} \frac{D}{L_{pri} f_s}$
Component: $T_{1,sec}$	
V_{out}	$i_{out} + \frac{\Delta i_{Lsec}}{2}$
Component: M_1	
$V_{in} + V_{out} \frac{N_{pri}}{N_{sec}}$	$\sqrt{D \left(\left(\frac{V_{out} i_{out}}{V_{in} D} \right)^2 + \frac{(K_L I_{LM})^2}{3} \right)}$
Component: D_1	
V_{in}	$\sqrt{D' \left(\left(\frac{V_{out} i_{out}}{V_{in} D'} \right)^2 + \frac{(K_L I_{LM})^2}{3} \right)}$
Component: D_2	
$V_{out} + V_{in} \frac{N_{sec}}{N_{pri}}$	i_{out}
Component: C_2	
V_{out}	Δi_{sec}

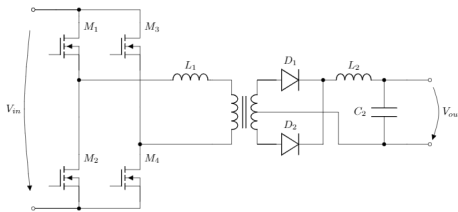


Figure 6. phase-shift-converter

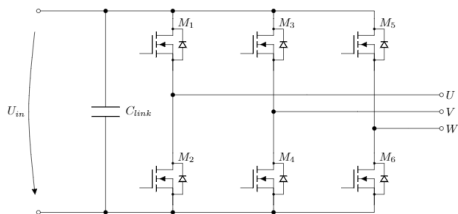


Figure 7. B6-inverter

Table VI
VOLTAGE AND CURRENT RATING OF PHASE-SHIFT-CONVERTER COMPONENTS [6]

voltage rating	current rating
Component: $M_1 - M_4$	
V_{in}	$\left(i_{out} + \frac{\Delta i_{Lout}}{2} \right) \frac{N_{sec}}{N_{prim}} + \frac{V_{in} D_{max}}{2 L_1 f_{sw}}$
Component: $L_1, T_{1,prim}$	
$2 V_{in}$	$\left(i_{out} + \frac{\Delta i_{Lout}}{2} \right) \frac{N_{sec}}{N_{prim}} + \frac{V_{in} D_{max}}{2 L_1 f_{sw}}$
Component: $T_{1,sec}$	
$2 V_{out}$	$i_{out} + \frac{\Delta i_{Lout}}{2}$
Component: D_1, D_2, L_2	
V_{out}	$i_{out} + \frac{\Delta i_{Lout}}{2}$
Component: C_2	
V_{out}	Δi_{sec}

Table VII
VOLTAGE AND CURRENT RATING OF B6-INVERTER COMPONENTS

voltage rating	current rating
Component: $M_1 - M_6$	
$\max(V_{in}, V_{UVW})$	i_{out}
Component: C_{link}	
V_{in}	

III. STRUCTURAL ANALYSIS OF POWER ELECTRONICS ARCHITECTURES

Every converter shown above consists of capacitors, inductors and switching devices, which can be active or passive. First the electrical stresses will be analyzed. Afterwards common modules are derived.

A. Capacitor stresses

As shown in the tables I - VI the input capacitors have to be rated for the input voltage as the output capacitors are rated for the corresponding output voltage. The current ratings are proportional to the inductor ripple current or the output current. For different voltage and power levels the capacitors have to be adjusted. Higher voltage rated capacitors can also be used in lower voltage applications, but their build volume is higher. The same assumption and correlation is valid for the current rating. [7]

B. Transistor stresses

Each transistor has the same ratings in current and voltage. It has to be rated for the maximum of the input or the output voltage and has to carry the whole inductor current. As in figure 8 shown, the higher the voltage the higher the on-state resistance of the transistor. Also it is visible, that the higher the on-state conductance, the higher the gate charge of the transistors. The higher voltage rated transistors may be used for lower voltage operation, but with disadvantages in efficiency. For synchronous topologies also half-bridges are commonly used.

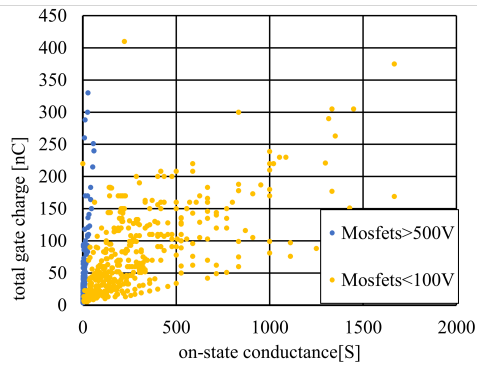


Figure 8. Correlation on-state-conductance to gate-charge in different voltage levels [8], [9]

C. Inductor/transformer stresses

The voltage rating of the inductors must fulfill the maximum voltage difference across them. Mostly the input or output voltage. Critical is here the insulation between the windings. The build volume is not getting that much greater with rising voltage. The situation is different for the current rating of the coil. With rising current the windings need a wider cross-section to handle the current. Therefore their volume rises.

D. Driver stage stresses

The gate driver, as shown in figure 9, for the active switching device only need different voltage ratings. To minimize the switching losses the source and sink current of each driver should be maximized to reduce the switching duration of the switching device.

Two types of gate drivers exists. The galvanic non isolated driver uses a bootstrap circuit consisting of capacitor, diode and resistor to supply a floating voltage for the high side switch. The galvanic isolated driver uses an isolated supply for the high and low side switch. Both driver stages, isolated and non-isolated, need a supply voltage. In low voltage applications the input voltage of the main converter can be used. At higher voltages the input voltage has to be stepped down to match the requirements of the driver. This can be handled with isolated or non isolated step-down-converters. An other possibility is to use an auxiliary voltage source.

E. Proposal of power electronic modules

If the same topology is used for different voltage and power classes, capacitors and switches need to be changed. Transformers may be changed if the winding turns ratio is not matching any more. For different current classes the inductors, switches and transformers need to be changed, whereas the capacitors may remain the same. The driver stages for the active switching devices may remain the same, if the switch type stays the same.

This concludes to different independent modules, which are shown in figure 9.

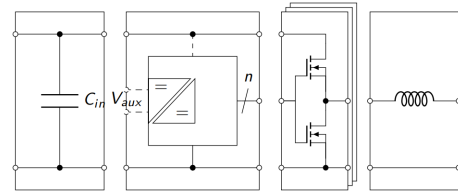


Figure 9. proposal of powerelectronics modules

IV. CONCLUSION

To conclude the architecture of power electronics can be partitioned in smaller modules, which can or must be replaced for other voltage and power classes. The first module is the capacitor module, which can mostly be found at the input and the output of a converter. Depended on the requirements (e.g. size, voltage and allowable ripple) this module must be exchanged. The coils or inductances are the second module, which depends on the carried current and the allowable current ripple of the converter. Also a half bridge module was introduced, which must be paired with a driver module. With these four modules nearly every converter type can be reassembled. Also are these modules universal and can be arranged to match different other topologies like n-phase inverter. This allows to create a universal and basic platform for all power electronics.

REFERENCES

- [1] "Din en 50160:2020-11, merkmale der spannung in öffentlichen elektrizitätsversorgungsnetzen; deutsche fassung en_50160:2010_+ cor.:2010_+ a1:2015_+ a2:2019_+ a3:2019," Berlin.
- [2] Texas Instruments and Incorporated [SLVA057], "Understanding buck power stages in switchmode power supplies," 1999. [Online]. Available: <https://www.ti.com/lit/an/slva057/slva057.pdf>
- [3] Texas Instruments and Incorporated [SLUP346], "Under the hood of a noninverting buck-boost converter," 2016. [Online]. Available: <https://www.ti.com/seclit/ml/slup346/slup346.pdf>
- [4] C. Nelson, "5 - It1070 design manual," in *Analog Circuit Design*, B. Dobkin and J. Williams, Eds. Oxford: Newnes, 2011, pp. 59–123. [Online]. Available: <https://www.sciencedirect.com/science/article/pii/B9780123851857000056>
- [5] Texas Instruments, Incorporated [SNVA761, and A], "Lm34xx how to design flyback converter with lm3481 boost controller (rev. a)," [Online]. Available: <https://www.ti.com/lit/an/snva761a/snva761a.pdf>
- [6] Texas Instruments, Incorporated [SLUA107, and A], "Phase shifted full bridge, zero voltage transition design considerations (rev. a)," 08-2011. [Online]. Available: <https://www.ti.com/lit/an/slua107a/slua107a.pdf>
- [7] T. Nakanishi and J.-i. Itoh, "Capacitor volume evaluation based on ripple current in modular multilevel converter," in *2015 9th International Conference on Power Electronics and ECCE Asia (ICPE-ECCE Asia 2015)*. Piscataway, NJ: IEEE, 2015, pp. 815–822.
- [8] Infineon Technologies AG, "20v-800v automotive mosfet - infineon technologies," 2021-05-05. [Online]. Available: [https://www.infineon.com/cms/en/product/power/mosfet/20v-800v-automotive-mosfet/?filterValues=~\(473_max~\(leftBound~-150~rightBound~100\)\)&visibleColumnIds=name,productStatusInfo,orderOnline,opn,551,packageName,473_max,559_93_max,559_93_nom,559_90_max,451_154_max,451_154_nom,547_136_nom,830,529,284_min,284_max,478_min,478_max,478_nom,618#!products](https://www.infineon.com/cms/en/product/power/mosfet/20v-800v-automotive-mosfet/?filterValues=~(473_max~(leftBound~-150~rightBound~100))&visibleColumnIds=name,productStatusInfo,orderOnline,opn,551,packageName,473_max,559_93_max,559_93_nom,559_90_max,451_154_max,451_154_nom,547_136_nom,830,529,284_min,284_max,478_min,478_max,478_nom,618#!products)
- [9] —, "500v-950v coolmos™ n-channel power mosfet - infineon technologies," 2021-05-05. [Online]. Available: <https://www.infineon.com/cms/en/product/power/mosfet/500v-900v-coolmos-n-channel-power-mosfet#!products>

Potential of e- mobility in rural areas – Evaluation of opportunities and barriers based on literature review

Karoline Knepper
Institute for new Energy Systems
Technische Hochschule Ingolstadt
Ingolstadt, Germany
karoline.knepper@thi.de

Mathias Ehrenwirth
Institute for new Energy Systems
Technische Hochschule Ingolstadt
Ingolstadt, Germany
mathias.ehrenwirth@thi.de

Prof. Dr.-Ing. Wilfried Zörner
Institute for new Energy Systems
Technische Hochschule Ingolstadt
Ingolstadt, Germany
wilfried.zoerner@thi.de

Abstract— In order to reduce the greenhouse gas emission in the transport sector, electric vehicles and electric mobility concepts were developed and driven forward by industry, research institutes and governments all over the world within the last years. But there are still challenges in the transition process of mobility sector. This paper aims to focus on the opportunities and barriers of e- mobility especially in rural areas and show the benefits that can be achieved, if e- mobility development considers regional impacts.

Keywords— e- mobility, individual transport, rural, urban

I. BACKGROUND AND MOTIVATION

The effect of climate change from greenhouse gas emissions is diverse and has a global footprint. To combat climate change, most countries have signed the Paris Agreement since 2015 [1]. The Paris Agreement aims to keep the increase in average global temperature below 2 °C (cf. Art. 2.1a). In addition, it aims at pursuing efforts to limit the temperature increase to 1.5 °C in order to reduce the risks and impacts of man-made climate change. This includes a low greenhouse gas emission development and a reduction of greenhouse gas emissions as soon as possible (cf. Art. 4.1).

The mobility and transport sector was responsible for approximately 15 % of global greenhouse gas emissions in 2020 [2]. This corresponds to around 22 % of the current global energy-related greenhouse gas emissions worldwide. In comparison to emissions in 2015, they decreased by only 1 % [3]. Additionally, the transport sector is growing faster than other end-energy-use sectors. In order to reduce the anticipated rise of emissions from transport by almost 20 % until 2030, several changes must be initiated. These contain the development of an integrated (electro-)mobility system including different modes of transport as well as low-carbon electricity production. The International Energy Agency (IEA) is more precise in its requirements. According to the IEA it is necessary that at least 20 % of all road transport vehicles must be driven by electricity by 2030, in order to keep global warming below 2 °C [3]. Consequently, governments, businesses, research institutes and others have to increase their activities to accelerate the development of electro-mobility (further e- mobility) to enable a large-scale roll-out.

This paper is intended to cover current gaps regarding the development of e- mobility. In a first step, the gaps will be identified with the help of a literature study. In the second step,

a detailed literature review will focus on e- mobility in rural areas to identify gaps and potentials.

It has been observed from the carried-out literature review that there are growing number of research publications in the field of electric mobility, in the last ten years (cf. Tab. I). To evaluate the recent theoretical and practical development in the electric-mobility field, key words were collected and research articles were searched using key words linked by Boolean operators, for instance: electric mobility AND urban. Regarding the last ten years, it is visible that more than 80 % of the research articles containing the analyzed key words were published since 2015. In order to show the impact of the Paris Agreement and the Paris Declaration on Electro-Mobility and Climate Chang, and since most publications were published after 2015, the considered time period for a further literature review ranges between 2015 and April 2021 (cf. Tab. II). As a result, following conclusions can be drawn from the literature analysis:

- Electric-mobility related research projects are mainly focused on urban areas, compared to rural regions
- Only 30 % of electric-mobility projects in both urban and rural areas are dealing with public transport as a mode of transportation, the rest is mostly directed at individual e- mobility

Tab. I Yearly amount of research articles in *Science Direct* containing “electric mobility AND urban/rural”

<i>Year</i>	'11	'12	'13	'14	'15	'16
<i>Amount</i>	258	352	392	503	564	798
<i>Year</i>	'17	'18	'19	'20	'21	
<i>Amount</i>	880	1,029	1,338	1,827	1,236	

Tab. II *Science Direct* literature review results regarded period 2015 to 2021

Research articles containing the following key words	Electric mobility	
	Urban	Rural
	5,516	2,072
<i>Public transport</i>	1,809	636

Furthermore, a lack of research addressing electric mobility in rural context can be identified. This paper lines out reasons why it is important to focus research projects concerning e- mobility more on rural areas.

II. DEFINITION OF SCIENTIFIC TERMS

A. Rural and urban areas

Depending on the region, various definitions are available to cluster areas based on their population density. The present article follows the definition recommended by the United Nations, which is briefly explained as follows [4]:

- Urban areas are densely populated areas with at least 1,500 inhabitants per km²,
- Suburban or peri-urban are a moderate density area with at least 300 inhabitants per km²,
- Rural areas are low density areas with mostly less than 300 inhabitants per km².

B. E- mobility

E- mobility will be referred in the presented paper to vehicles that rely on electricity for their primary energy consumption [5]. E- mobility is not limited to cars, but embraces different kinds of transportation:

- Individual transport like two- or three-wheelers, bikes or cars,
- Public transport such as trains or buses,
- Shared mobility like car-sharing or large capacity taxis.

III. LITERATURE REVIEW - POTENTIAL OF E- MOBILITY IN RURAL REGIONS

This section provides an overview regarding the potential of e- mobility based on selected surveys and research papers considering the different aspects of e- mobility (cf. Tab. II). This bundle includes socio-economic analysis of potential users [6, 7], a technical assessment of electric vehicles [8] as well as research project results which focus mainly on clustering e- mobility in rural and urban application fields [9–13]. Almost all data within this review was based on studies in the European context.

In a first step, opportunities and barriers of e- mobility are considered from a general perspective. In the next step the focus is placed on these aspects in the context of rural areas.

Tab. III Literature overview

Author (year)	Title	Aim	Method	Key findings
Agerskov, M. et al. (2014) [13]	Lessons Learned from the Danish EV Living Lab	Identification of problems faced during usage and benefits of electric vehicles, investigate potentials of e- mobility in Danish municipalities	Case study including a living lab in Denmark	Electric vehicles cover demand of users mostly, but range of EV's is important for potential users
Breuil, D. et al. (2016) [9]	Electromobility in rural and peri urban areas	Point out aspects of e- mobility that can satisfy some aspects of the specific demand in rural and peri urban areas	European case study	Mobility is a key stone to develop rural areas, Electromobility combined with new information technologies can support the sustainable revitalization of rural regions
Chachdi, A. et al. (2017) [7]	Socio-economic Analysis of Electric Vehicles in Morocco	Investigation of possible options to integrate e- mobility in Morocco	Survey in Morocco	92 % of daily travel distance < 60 km, user required range ≥ 200 km, necessary to popularize e- mobility projects
Dütschke, E. et al. (2013) [6]	Who will use electric vehicles?	Identification of possible private users of electric vehicles	Results of studies in model regions in Germany	Potential buyers: male, highly educated, middle-aged Higher feeling of dependency on car → early purchasers
Gautama, S. et al. (2015) [12]	Cohousing and EV Sharing: Field Tests in Flanders	Investigation of potential of electric vehicles in Belgium	Pilot test in small communities	Interim results: Urban population used shared EVs as an alternative to biking or walking not to private car Semi-urban population replaced private car with shared EVs
Kester, J. et al. (2020) [11]	Rethinking the spatiality of Nordic electric vehicles and their popularity in urban environments: Moving beyond the city?	Exploration of the perception within rural-suburban-urban categories by users and potential users	Surveys, interviews, in Denmark, Finland, Iceland, Norway, Sweden	Acceptance primarily takes place in (sub)urban regions, EVs are used in rural environments
Newman, D. et al. (2014) [10]	Urban, sub-urban or rural: Where is the best place for electric vehicles?	Questions the assumption that urban setting is most appropriate for electric vehicles	Case study in UK	In urban areas difficult to match electric vehicle characteristic with functional user trips and behavioral preferences
Wilken, D. et al. (2020) [8]	Multidimensional assessment of passenger cars: Comparison of electric vehicles with internal combustion engine vehicles	Build up a base to identify specific aspects influencing the overall performance of each vehicle technology	Combination of existing studies	Electric vehicles charged with renewable electricity are more sustainable than internal combustion engine vehicles, electric vehicles charged with electricity from current mixed sources are even worth

A. Opportunities and barriers of e-mobility

This part is dealing with ecological, technical, economical as well as infrastructural aspects connected to e-mobility. They are described and illustrated with examples subsequently.

Due to the fact that a reduction of greenhouse gas emissions is forced in the transport sector as mentioned before, e-mobility seems to be a suitable solution, as electric vehicles have zero emissions at least from an operational perspective [10]. This aspect is not referring to global emissions in general. In particular, it can have a positive effect on highly populated areas by reducing traffic causing local air pollution. While political frameworks mainly support e-mobility due to its low emissions, the ecological factor additionally motivates potential users to buy an electric vehicle [7]. However, as outlined in the assessment of [8], it is also necessary to consider the energy source for power production. Accordingly, power has to be generated completely or at least mainly by renewable energies, otherwise e-mobility just shifts its emissions from transport into the energy sector. Furthermore, in regard to densely populated regions with a high traffic load, electric vehicles operate less noisy than conventional powered vehicles. Moreover, they do not require power in a stationary mode, e.g. within congestion [10].

Regarding the user demand, the limited range of electric vehicles is often criticized [6–8, 10, 11]. Besides, this can be connected to psychological thoughts like fear of an empty battery. Due to this, e-mobility is considered most suitable for operation in urban regions, hence people travel mainly in limited areas and are not imperiled by range issues [6, 10]. Depending on their living conditions users require real ranges between 150 and 200 km if they own a second conventionally powered car [13]. According to the analyzed studies, in case only one car is available in a household a range of least 200 km is necessary to cover the mobility demand [7, 13]. In addition to the limited range, the limited speed is also a disadvantage mentioned by potential users [7, 12].

To stay in the user's perspective, another barrier has to be mentioned: Investment costs. Referring to survey results high investment costs are the main obstacle for buying an electric vehicle [7, 10, 12, 13]. Comparing different Volkswagen Golf types from 2019, the electric Golf costs almost 7,000 € more than the diesel engine Golf and around 9,500 € more than the gasoline-powered Golf [8]. Moreover, people are mostly not aware of lower maintenance and fuel costs [7, 8, 12, 13]. But maintenance costs are an important aspect, as depending on the daily driving distance an electric vehicle can be described as "a more expansive car to buy and a cheaper car to drive" [11, p. 10]. Hence, it can be assumed, that for a daily driving distance of 50 km or more higher investment costs are equalized by lower operational costs like fuel and maintenance costs.

Furthermore, the availability of infrastructure is also an important aspect influencing the acceptance of e-mobility [11, 12]. This includes, inter alia, the availability of reliable charging infrastructure providing energy at the moment the demand for energy arises. In densely populated urban areas, public charging infrastructure is necessary to push forward e-mobility, due to a lack of private parking spaces for

residents. In general, urban environments space is becoming an increasing issue as city centers get more dense, therefore also affecting other future mobility concepts [11].

B. Opportunities and barriers of e-mobility in a rural context

While analyzing several studies, it became clear that it is necessary to subdivide the evaluation of results depending on the population density of a region. However, the different countries, where these studies were conducted, have no influence the main results.

As mentioned in the previous part, the range of electric vehicles is a major issue for potential users. Regarding the technical aspects, a limited real range does not affect the daily life of rural inhabitants. With reference to this, the typical daily traveled distance in sub-urban or rural areas is between 25 km and 30 km [10–12]. Therefore, the range of the current electric vehicles should be sufficient to meet the requirements of rural users. Furthermore, longer distances in rural regions require more energy than shorter rides in urban regions. Thus, a higher state-of-charge difference is recognized which allows a more effective usage of discharge-charge cycles [10]. Additionally, due to the high travel demand in rural areas, lower operational costs of electric vehicles can compensate higher investment costs after a shorter time period compared to electric vehicles used in urban regions [10, 11].

Criticism of potential users about the limited speed of electric vehicles represents may be no major obstacle for the potential of e-mobility in the countryside, as the most common national and regional roads in sub-urban and rural areas have speed limits compared to motorways [10, 14]. Regarding the road network on the countryside, it is more essential to consider local road conditions as well as weather conditions, that may affect the road properties [11].

Concerning the necessary infrastructure, living conditions in rural areas offer more flexibility as well as possibilities to kick-off regional e-mobility as compared to urban areas. For example, in 2019, more than 80 % of the European rural population lived in single-family detached houses. On the other hand, in urban areas the major part (70 %) of population lived in flats [15]. The private house arrangements may result in more frequent opportunities to install private charging infrastructure in rural areas [11]. Furthermore, private charging stations can be supplied by the electricity grid or by a private photovoltaic system. This reduces emissions during power production process and is an important point to reduce the greenhouse gas emissions [16]. Moreover, an ownership of a private charging infrastructure can contribute to buy an electric vehicle for remote areas where the next service station is far away [11]. The charging option at home also allows electric vehicle owners a high degree of self-sufficiency. Additionally, with an increasing number of private charging stations, the demand for public charging infrastructure may decrease and thus enable the deployment of e-mobility more independently of local authorities.

Another point connected to infrastructure in many rural regions is a higher dependency of citizens on individual mobility due to a lack of public transport [9–11]. This gap can be an opportunity for electric vehicles, because potential users with a high environmental awareness prefer more sustainable modes of transport like bikes, public transport or even

alternative vehicle technologies [6]. Moreover, there is no competition between individual mobility and public transport, if there is no reliable public transport existing [11].

The literature review shows that e-mobility has high potential for rural areas compared to urban areas due to several reasons. First of all, the inhabitants of rural areas are dependent on individual mobility due to a lack of alternatives. As a result, they are more willing to invest in their individual mobility, e.g. in a car. In addition, the distances to be covered are greater than in urban areas, which means that the average distance travelled is higher. This puts the high acquisition costs and low maintenance costs, as well as the benefits of the vehicle, into relation. Secondly, the mobility needs and requirements of a vehicle fit with the technical aspects of an electric vehicle. In addition, private charging options for electric vehicles create even more independence from the local infrastructure.

IV. CONCLUSION

As outlined in the previous chapter, the development of e-mobility involves different opportunities and challenges depending on the regional context. However, the influencing attributes are similar between rural and urban areas, but their impact has to be evaluated separately. Hence, as a result of this article, the potentials of rural e-mobility are identified as well as the most important factors influencing e-mobility are derived.

The presented work attempted to structure the influencing factors in the major categories such as environmental aspects (emissions), technology requirements (range, speed), economical aspects (investment/maintenance costs) and infrastructure (charging infrastructure, public transport). Further to this, the impact factors are divided into motivator

(+), barrier (-) and motivator as well as barrier (o) for a general perspective as well as focusing on urban and rural areas. The synthesized observation of the results from the considered literature of the aspects that influence the development of e-mobility is presented in Tab. IV.

Tab. IV Assessment of the considered literature regarding the influence of the attributes on e-mobility

Factors	General				Urban		Rural		
	7	8	12	13	10	11	9	10	11
Emissions	+	+	+	+	+	+		+	+
Range			-	-	-	o	-	+	o
Speed					-			+	
Investment costs	-		-	-	-		-	+	
Maintenance cost	-								+
Private charging infrastructure									+
Public charging infrastructure			-		+				
Public transport					-	-			

In order to visualize the influence of the factors considered, the findings of the relevant papers are processed and compared against each other. Therefore, it is essential to consider: If two paper identify high investment costs as an obstacle, but a third paper concludes that investment costs can be a driver, these are subtracted, following the overall influence is reduced. The result of the processed data is illustrated in Fig. 1. The positively assessed influences are displayed as motivators above the black axis. In contrast, the rather negatively classified factors are shown as barriers.

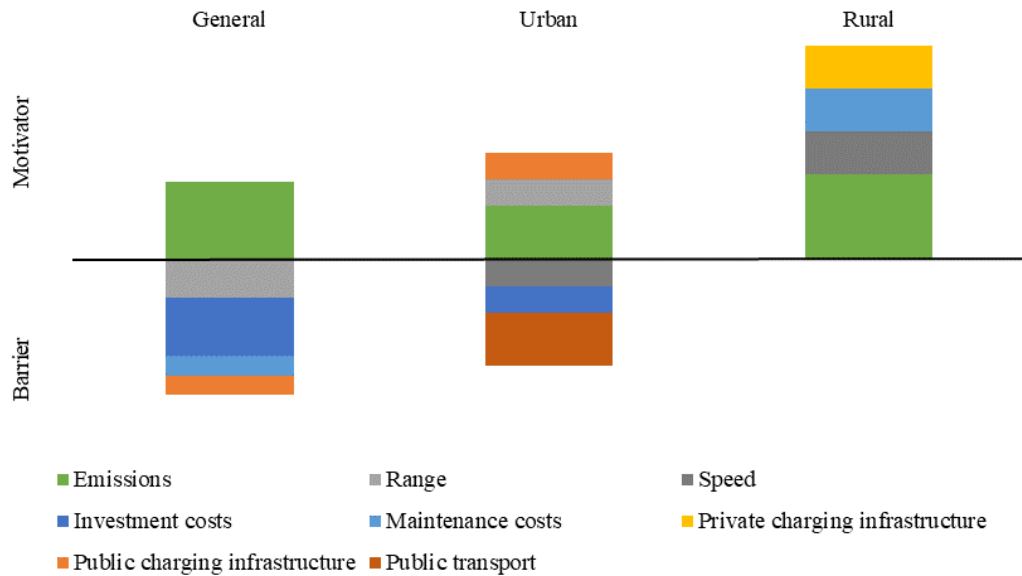


Fig. 1 Aspects influencing the development of e-mobility, divided into drivers and barriers based on the articles considered as part of the literature review

It can be observed from Fig. 1, from a general and urban perspective, both motivators and barriers have to be considered, while in a rural context, more motivators can be identified. One common aspect independent of the regarded area is, that reduced greenhouse gas emissions are the main driver for e- mobility.

Regarding the economic aspects, on the one hand, the main barrier mentioned in a general context are investment costs. On the other hand, in rural areas, this effect is not present anymore, due to different results within the considered papers. Thus, it is balanced. Consequently, the impact of purchasing cost on the development of e- mobility can be estimated as minor.

Moreover, the influence of charging infrastructure appears to be dependent on the regarding perspective. From a general point of view, it is categorized as a barrier, while in an urban and rural context it is classified as motivator. This illustrates the importance of considering regional conditions. Whereas public charging stations promote the expansion of e- mobility in urban areas, private charging stations are a driver in rural areas. Due to the fact, in rural areas, there are more possibilities available to install private charging stations individually at home. Additionally, the availability of a reliable public transport has an effect on the potential of e- mobility, as it can provide an ecological alternative for private vehicles. However, if there is no public transport existing, as in most rural areas, more individual ecological alternatives will be necessary, for instances, electric vehicles.

In order to support the development of e- mobility in rural areas, it is primarily important to create awareness for alternative mobility options. Furthermore, rural living conditions offer in some aspects a higher potential for e- mobility compared to urban areas. To wrap it up, rural areas should be given more consideration by research, local authorities, investors as well as legislators to utilize their potential.

REFERENCES

- [1] *Paris Agreement*, 2015. Accessed: Jul. 15 2020. [Online]. Available: https://unfccc.int/sites/default/files/english_paris_agreement.pdf
- [2] R. Hannah, *Sector by sector: where do global greenhouse gas emissions come from?* [Online]. Available: <https://ourworldindata.org/ghg-emissions-by-sector> (accessed: Apr. 27 2021).
- [3] United Nations Framework Convention Climate Change, *Paris Declaration on Electro-Mobility and Climate Change & Call to Action: Lima - Paris Action Agenda*. [Online]. Available: <https://unfccc.int/news/the-paris-declaration-on-electro-mobility-and-climate-change-and-call-to-action> (accessed: Apr. 27 2021).
- [4] United Nation Statistical Commission, Ed., "A recommendation on the method to delineate cities, urban and rural areas for international statistical comparisons," 2020.
- [5] Fédération International de L'Automobile, Ed., "TOWARDS E-MOBILITY THE CHALLENGES AHEAD," Brussels, 2011.
- [6] Elisabeth Dütschke, Uta Schneider, and Anja Peters, "Who will use electric vehicles?," Working Paper Sustainability and Innovation, Karlsruhe S6/2013, 2013. Accessed: May 1 2021. [Online]. Available: <http://hdl.handle.net/10419/83048>
- [7] A. Chachdi, B. Rahmouni, and G. Aniba, "Socio-economic Analysis of Electric Vehicles in Morocco," *Energy Procedia*, vol. 141, pp. 644–653, 2017, doi: 10.1016/j.egypro.2017.11.087.
- [8] D. Wilken, M. Oswald, P. Draheim, C. Pade, U. Brand, and T. Vogt, "Multidimensional assessment of passenger cars: Comparison of electric vehicles with internal combustion engine vehicles," *Procedia CIRP*, vol. 90, no. 6, pp. 291–296, 2020, doi: 10.1016/j.procir.2020.01.101.
- [9] D. Breuil, M. Khafallah, and A. Hassoune, "Electromobility in rural and peri urban areas," Belgrade, 2016. Accessed: Apr. 26 2021. [Online]. Available: https://www.researchgate.net/publication/323971543_Electromobility_In_Rural_and_Peri_Urban_Areas
- [10] D. Newman, P. Wells, C. Donovan, P. Nieuwenhuis, and H. Davies, "Urban, sub-urban or rural: where is the best place for electric vehicles?," *IJATM*, vol. 14, 3/4, p. 306, 2014, doi: 10.1504/IJATM.2014.065295.
- [11] J. Kester, B. K. Sovacool, L. Noel, and G. Zarazua de Rubens, "Rethinking the spatiality of Nordic electric vehicles and their popularity in urban environments: Moving beyond the city?," *Journal of Transport Geography*, vol. 82, November, p. 102557, 2020, doi: 10.1016/j.jtrangeo.2019.102557.
- [12] S. Gautama, D. Gillis, G. Pace, and I. Semanjski, "Cohousing and EV Sharing: Field Tests in Flanders," in *Green Energy and Technology, E-mobility in Europe: Trends and good practice*, W. Leal Filho and R. Kotter, Eds., Cham: Springer, 2015, pp. 209–235.
- [13] M. L. Agerskov and J. C. L. Hoj, "Lessons learned from the Danish EV living lab," in *2013 World Electric Vehicle Symposium and Exhibition (EVS27)*, Barcelona, Nov. 2013 - Nov. 2013, pp. 1–7.
- [14] European Commission - Mobility and Transport, *Urban and rural networks - Mobility and transport - European Commission*. [Online]. Available: https://ec.europa.eu/transport/road_safety/specialist/knowledge/road/designing_for_road_function/urban_and_rural_networks_en (accessed: May 3 2021).
- [15] eurostat, *Housing in Europe - House or flat – owning or renting*. [Online]. Available: <https://ec.europa.eu/eurostat/cache/digpub/housing/bloc-1a.html?lang=en> (accessed: May 3 2021).
- [16] J. Vopava, U. Bergmann, and T. Kienberger, "Synergies between e-Mobility and Photovoltaic Potentials: A Case Study on an Urban Medium Voltage Grid," *Energies*, vol. 13, no. 15, p. 3795, 2020, doi: 10.3390/en13153795.

Slip control of an induction machine in the field weakening region during six step operation

Alexander Kuffer
 Faculty of Electrical Engineering
 and Information Technology
 Ostbayerische Technische Hochschule Regensburg
 Regensburg, Germany
 Email: alexander1.kuffer@st.oth-regensburg.de

Abstract—In this paper an induction machine control strategy for six-step operation is proposed. Six-step operation, also called block-commutation provides one major advantage compared to the more commonly used modulation techniques(2), by making use of the maximum output inverter voltage. Especially in the field weakening region, six-step operation provides a higher torque and power output of the machine. Modulation techniques like SVPWM, DPWM have a lower reactive power in the linear operating region, where field oriented control is widely used for example. The proposed control strategy is verified by a simulation model in Matlab/Simulink.

Index Terms—Induction motor, six-step operation, block commutation, slip control, field weakening control

I. INTRODUCTION

Combustion engines are creating environmental problems due to the generation of carbon dioxide during the fuel burn process [1]. Not only because of global warming but also by reason of rising prices of petrol owing to the exhaustion of resources an eco-friendly alternative are hybrid and electrical vehicles. Required are electrical machines with a high starting torque, constant torque over a wide speed region and a high power factor at low costs.

Due to its high performance the permanently excited synchronous machine is majorly used in electrical or hybrid drives [16]. However, there is a huge ambition to use squirrel cage induction machines due to its lower production costs, its higher robustness and fewer safety problems [1]. The output torque of the induction machine drops in the first field weakening region proportional to $1/n$ and in the second field weakening region by $1/n^2$ [17]. There is huge interest to increase the output torque in this operation area by operating with the maximum dc-link voltage.

Three-phase voltage-source pulse width modulation (PWM) inverters are used for dc/ac power conversion since they can produce a variable voltage and variable frequency power [3], [4]. Six-step operation increases the output voltage by 10 percent and the electrical torque by up to 20 percent compared to conventional modulation techniques assuming a maximum modulation factor of 1 [3]. In this paper a six-step operation slip-control structure is proposed for induction machines.

In chapter II basics of the six-step operation and its control structure for induction machines are presented. Required formulas to validate the torque increase are considered.

Chapter III comprises a simulation model in Matlab/Simulink of the proposed control technique and its results. Finally, chapter IV gives a conclusion.

II. SIX-STEP OPERATION

A. Basic configuration

Figure 1 shows the three phase inverter hexagon with its space vectors A-F in the stationary α - β frame.

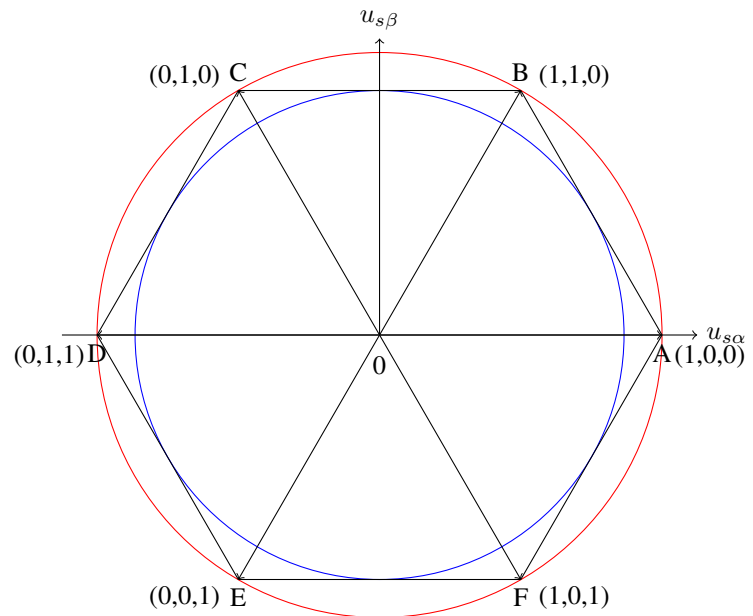


Figure 1. Three phase inverter hexagon (5)

The modulation factor M is used to measure the dc-link voltage utilization of PWM inverters and is defined here as [3], [5]

$$M = \frac{U^*}{\frac{\sqrt{3}}{3} \cdot U_{dc}} \quad (1)$$

U^* is the phase voltage reference and U_{dc} is the inverter input voltage.

Commonly used modulation techniques can reach a maximum modulation factor M of 1 in the overmodulation region II [3] for the desired fundamental voltage.

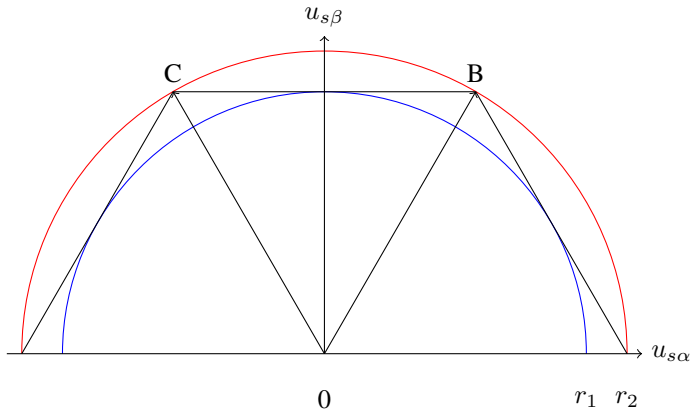


Figure 2. Three phase inverter hexagon with inscribed and circumscribed radius

According to [5], [8] $r_1 = \sqrt{3}/3 = 1/\sqrt{3}$ is the radius of the inscribed circle, $r_2 = 2/3$ the radius of the circumscribed circle. The fundamental wave of $r_2 = \pi/3$.

In the linear modulation regions and overmodulation regions I and II, the voltage vector remains in the inscribed circle of the hexagon [3], [5]. During the switching periods between the vertices zero vectors are switched [10], [3]. For example symmetrical distributed on the beginning and on the end of a switching cycle at SVPWM. During six-step operation the voltage vector jumps from one vertex to the other [18]. No zero pointing vectors are used during this operating mode [5].

The modulation factor during six-step operation results from the fundamental wave:

$$M = \frac{2 \cdot U_{dc}}{\sqrt{3} \cdot U_{dc}} = 1.10 \quad (2)$$

Required on and off times for the upper half bridge Mosfets are calculated by the duty cycles of the phase voltages. These are transformed from the rotating d,q-frame to the stationary α,β -frame to the phase voltages. The rotating angle in the α,β -frame is calculated by integrating the stator field angular velocity ω_s . Depending in which sector of the hexagon the vector currently is and on the vector components in the d- and q- axis [2], [5], on times and off times of the Mosfets are calculated by modulation techniques like SVPWM. The Mosfets which are on in which sector are defined by the vertices: for example B (1,1,0), so the upper Mosfet of the 1st half bridge is switched on and the other half bridges are switched off [11].

Since no zero vectors are being switched during six-step operation, an angle has to be calculated in which sector of the hexagon the output voltage vector in the α,β -frame is currently located. Sectors in the hexagon have to be defined in which angle, which vertices have to be switched on [2], [5].

Six sectors with an angle of $\pi/3$ radian have to be defined around the vertices. $-\pi/6$ to $\pi/6$ is sector I, $\pi/6$ to $\pi/2$ is sector II and so on [5], [15]. Depended on the requested torque, a slip frequency

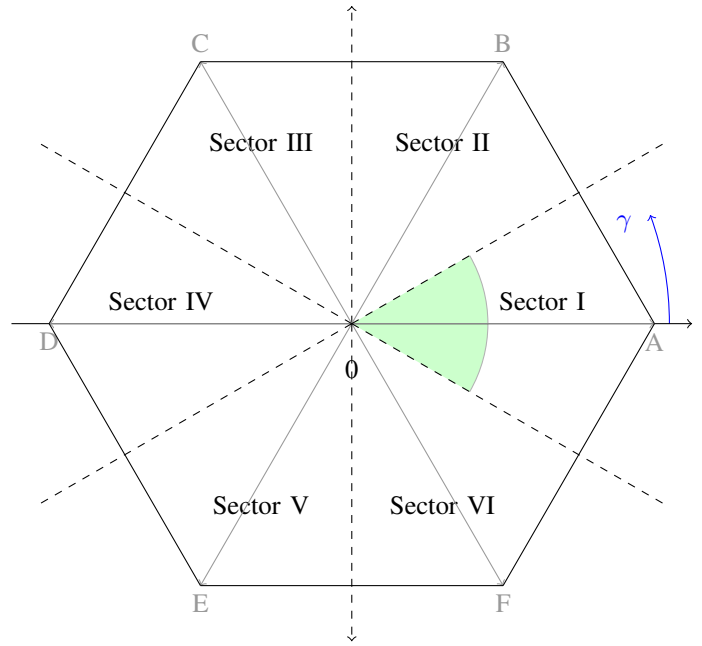


Figure 3. Six space vector sectors in the three phase hexagon

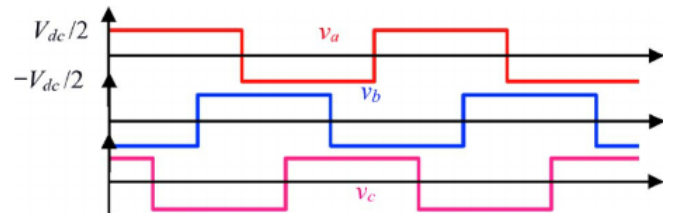


Figure 4. Six-step operation inverter output voltages

ω_r has to be calculated. Block commutation voltage looks like shown in figure 4.

B. Theory of induction machine field weakening operation

The stator voltage equations in the d,q- reference frame are defined in [4]:

$$u_{sd} = R_s i_{sd} - \omega_e \sigma L_s i_{sq} + \sigma L_s \frac{di_{sd}}{dt} + \frac{L_m}{L_r} \frac{d\lambda_r}{dt} \quad (3)$$

$$u_{sq} = R_s i_{sq} + \omega_e \sigma L_s i_{sd} + \sigma L_s \frac{di_{sq}}{dt} + \omega_e \frac{L_m}{L_r} \lambda_r \quad (4)$$

where u_{sd} , u_{sq} are the stator voltages and i_{sd} , i_{sq} the stator currents in the d,q-frame. R_s is the stator resistance, L_s , L_r and L_m the mutual stator, rotor and main field inductances. σ is the stray factor, defined as: $\sigma = 1 - L_m^2/(L_s L_r)$. ω_e is the angular velocity of the rotating stator field, λ_r the rotor flux.

The output torque equation with d,q-currents is defined as [2], [4], [12]:

$$T_{el} = \frac{3}{2} \cdot p \cdot \frac{1}{\sigma_r} \cdot L_m \cdot i_{sd} \cdot i_{sq} \quad (5)$$

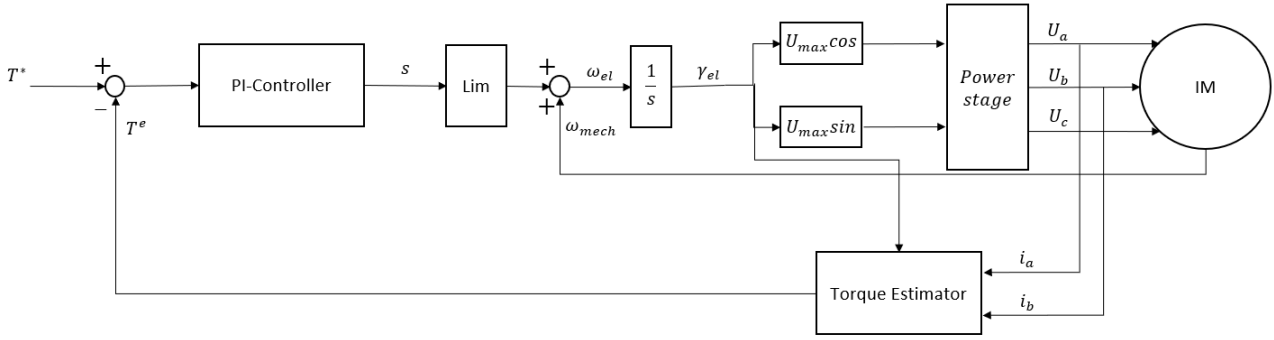


Figure 5. Block diagram of the proposed torque controller [6], [7]

where $\sigma_r = L_{r,\sigma}/L_m$ is the rotor stray factor. Assuming stationary operation and by neglecting the stator resistance R_s at high frequencies, the stator voltage equations can be simplified in [5]:

$$u_{sd} = -\omega_e \sigma L_s i_{sq} \quad (6)$$

$$u_{sq} = \omega_e \sigma L_s i_{sd} \quad (7)$$

The voltage dependent torque equation results then to:

$$T_{el} = \frac{3}{2} \cdot p \cdot L_m^2 \cdot \frac{u_{sd} u_{sq}}{\sigma L_r L_s^2 \omega_e^2} \quad (8)$$

The stator voltage constraint for the d and q voltages is given as [11], [14]:

$$u_{sq}^2 + u_{sd}^2 \leq u_{s,max}^2 \quad (9)$$

Increasing the modulation factor M, the maximum available dc-link voltage is also increased by the factor M.

$$(M \cdot u_{sq})^2 + (M \cdot u_{sd})^2 \leq (M \cdot u_{s,max})^2 \quad (10)$$

Substituting the voltage dependent torque equation by the modulation factor increased d,q voltages, the modulation factor squares:

$$T_{el,M} = \frac{3}{2} \cdot p \cdot L_m^2 \cdot M^2 \frac{u_{sd} u_{sq}}{\sigma L_r L_s^2 \omega_e^2} \quad (11)$$

Assuming a modulation factor of 1 in the linear control region [3], [13] and a modulation factor of $M = 1.10$ during six-step operation, due to equation 9 the torque increases by the square of the increased modulation factor M. In this example by 21%. In practical a modulation factor of 1 is barely reachable regarding current measurements and other death time causing components in the overall system. The benefit of the torque gain is even higher at this point.

C. Proposed control structure

Figure 5 shows the proposed voltage angle control structure. The torque reference T^* is compared to the current estimated torque T^E . The torque error is fed to a PI-Controller with the machine slip or the fundamental wave of the rotor frequency ω_r as its output. To ensure a stable operation, the slip has to be limited to the break-down slip [6], [7]. By adding the mechanical angular velocity, measured by a speed sensor, to the slip, the transformation angle between alpha and beta coordinates is obtained. Applying sin and cos functions to this angle, the maximum dc-link voltage is split up to these parts. The power stage including the inverter applies the phase voltages to the machine.

D. Torque estimation

Torque can be estimated by measuring two of the three-phase currents and transforming them with the stator angle to d,q-coordinates. The torque equation with i_d and i_q is given in [4].

E. PI-Controller

An investigation about this control method has already been made in [6], [7]. The required PI-Controller gain can be calculated by the transfer function of the induction machine.

$$K_{PI}(s) = K_c \cdot \left(\frac{1}{\omega_c} + \frac{1}{s} \right) \quad (12)$$

with ω_c as the desired closed-loop bandwidth:

$$\omega_c = \frac{\omega_b}{2T_{rpu}} \quad (13)$$

and K_c as the regulator gain to reach it:

$$K_c = \frac{\omega_b (\sigma L_{r,\sigma})^2}{2k_s T_{rpu} (V^*)^2 \omega_{el}^2} \quad (14)$$

ω_b is the base speed of the machine, $T_{rpu} = \omega_b \cdot \sigma \cdot L_r / R_r$ the rotor transient time constant in [p.u] and $k_s = L_m / L_s$ the stator coupling coefficient.

III. SIMULATION RESULTS

To validate the control structure a simulation model in Matlab/Simulink was implemented. The machine model was created in Dymola/Modelica. In order to verify the increase of output power during six-step operation a comparison with SVPWM has been made. The modulation factor M of SVPWM can ideally be assumed as 1. In this paper one operating point is validated at 5500 rpm. A DC-link voltage of 48V is used. Block-commutation should only be utilized by torque required, which is higher than torque reached by using modulation techniques in the inscribed circle. A high reactive power is produced due to the maximum voltage inverter output and a high slip frequency is provided to the machine. Primarily, the machine is controlled by a time discrete field oriented control. The d-current is kept at a constant level, whereas the q-current is risen by a ramp to its desired value. Figure 7 shows the d- and q-currents. A maximum electrical torque of 19Nm can be generated by the machine during field oriented control, no matter how high the q-current is risen. Figure 6 shows the electrical torque generated by FOC, figure 7 the torque dependent q- and d-currents.

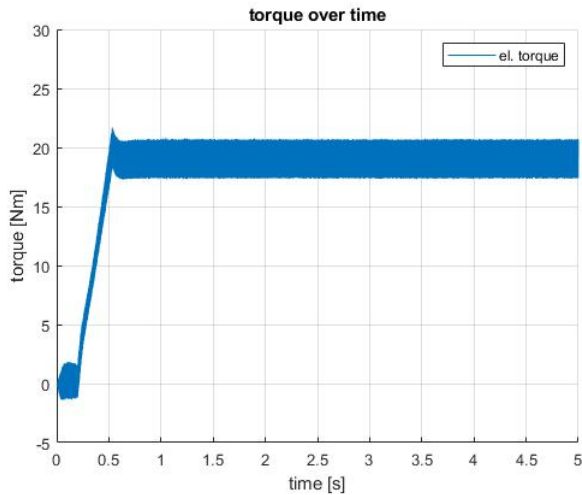


Figure 6. 19Nm motor torque with field oriented control

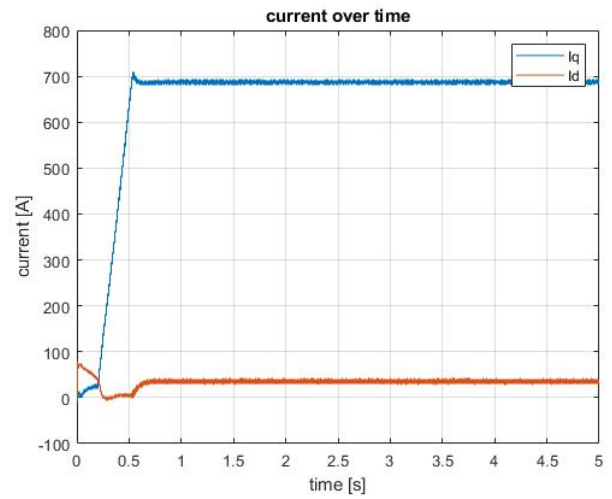


Figure 7. d- and q-currents FOC

The voltage utilization is saturated, so no matter how high the q-current for a higher torque is set, the output torque maintains the same. Figure 8 shows the generated torque by a q-current of 870A and a d-current of 35A. Figure 9 shows the currents with its oscillations.

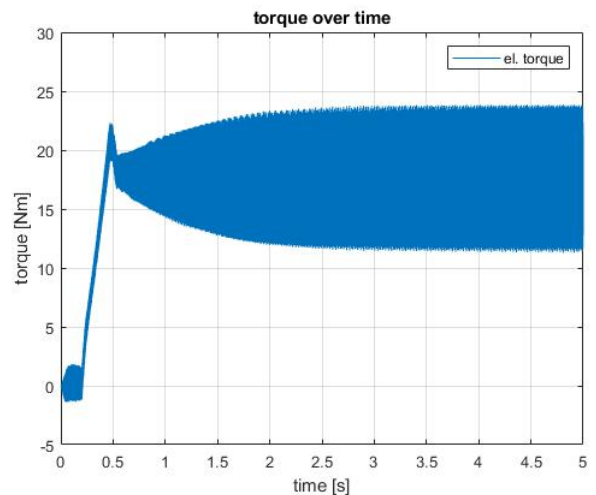


Figure 8. 19Nm maximum torque with field oriented control

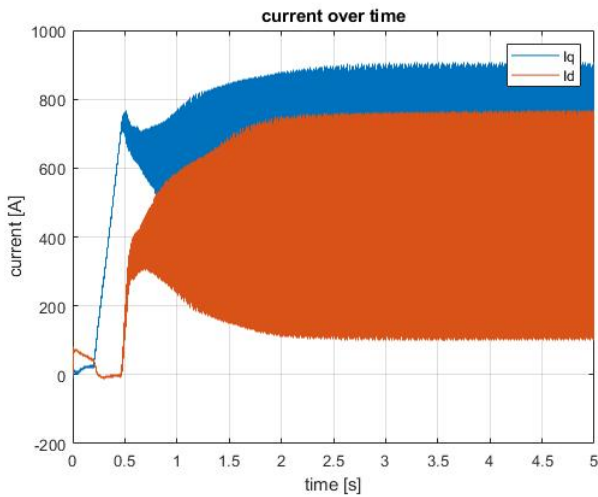


Figure 9. Saturated d- and q-currents with field oriented control

To validate the torque increase by 21 % at this operation point, 23Nm torque should be generated by the machine. Figure 10 shows the torque generated by slip control during six-step operation.

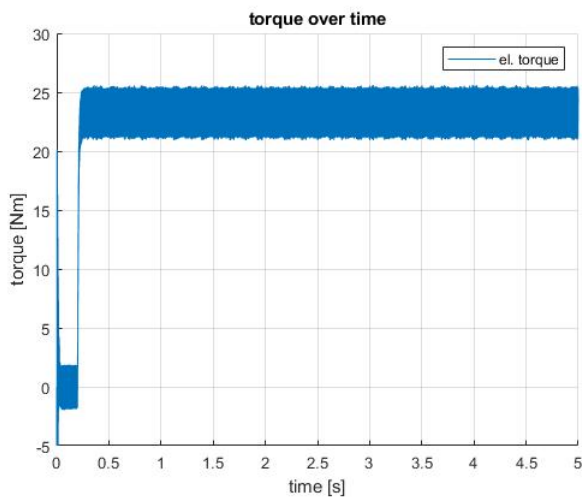


Figure 10. Slip control 23Nm output torque

IV. CONCLUSION

A higher voltage output during six-step operation to increase the output machine torque was proven successfully. The overall torque using block commutation could be increased by 21% compared to a modulation index of 1. Therefore, a specific torque higher than the maximum one using common modulation techniques can be achieved, by utilizing the proposed control structure during six-step operation of the induction machine. The overall power output could be increased by implementing this method. The machine parameters used in this paper are property of Vitesco Technologies GmbH and cannot be provided. This has no influence on the simulation

results and the proven theory. Measurement results will be obtained in summer with a prototype machine.

ACKNOWLEDGMENT

The author would like to thank the Laboratory of Electrical Machines and Drive Systems of the Ostbayerische Technische Hochschule Regensburg and especially Prof. Dipl.-Ing. Anton Haumer and Prof. Dr. Bernhard Hopfensperger who are supervising the project. In addition, the author would like to thank Vitesco Technologies GmbH for sponsoring tools and equipment such as Josef Laumer and Michael Wiesinger for their support.

REFERENCES

- [1] Aliakbar Kakouei1, Ali Vatani, "An estimation of traffic related CO2 emissions from motor vehicles in the capital city of, Iran", IRANIAN JOURNAL OF ENVIRONMENTAL HEALTH SCIENCE ENGINEERING, 2012
- [2] Zhen Dong, Wenshuang Li, "Flux-Weakening Control for Induction Motor in Voltage Extension Region: Torque Analysis and Dynamic Performance Improvement", IEEE TRANSACTIONS ON INDUSTRIAL ELECTRONICS, 2018
- [3] Dong-Choon Lee, G-Myoung Lee, "A Novel Overmodulation Technique for Space-Vector PWM Inverters", IEEE TRANSACTIONS ON POWER ELECTRONICS, 1998
- [4] Uwe Nuss "Hochdynamische Regelung elektrischer Antriebe", 2nd Edition, Eittlingen 2017, VDE Verlag, p. 9-12
- [5] Bo Wang, Xu Zhang, "Maximum Torque Analysis and Extension in Six-Step Mode-Combined Field-Weakening Control for Induction Motor Drives", IEEE TRANSACTIONS ON INDUSTRIAL ELECTRONICS, 2019
- [6] Petar Matic, Aleksandar Rakić, "Induction Motor Torque Control in Field Weakening Regime by Voltage Angle Control", Faculty of Electrical Engineering, Banjaluka, RS, Bosnia and Herzegovina, 14th International Power Electronics and Motion Control Conference, 2010
- [7] P. Matic S.N. Vukosavic, "Voltage angle direct torque control of induction machine in field-weakening regime", Faculty of Electrical Engineering, Banjaluka, Republic of Srpska, Bosnia and Herzegovina, Published in IET Electric Power Applications, 2010
- [8] Gerhard Clos, "Novel Torque Angle Control Method for the Induction Motor at the Voltage Margin", Karlsruhe Institute of Technology (KIT) Elektrotechnisches Institut (ETI) - Electrical Drives and Power Electronics
- [9] Siddavatam Ravi, Prakash Reddy, Umanand Loganathan "Improving the Dynamic Response of Scalar Control of Induction Machine Drive using Phase Angle Control", Department of Electronic Systems Engineering Indian Institute of Science, IEEE 2018
- [10] Auzani Jidin, Md. Zarafi Ahmad, "A Simple Overmodulation Strategy in Direct Torque Control of Induction Machines", The 5th Student Conference on Research and Development, 2007
- [11] Saroj Kumar Sahoo and Tanmoy Bhattacharya, "Field Weakening Strategy for a Vector-Controlled Induction Motor Drive Near the Six-Step Mode of Operation", IEEE TRANSACTIONS ON POWER ELECTRONICS, 2016
- [12] Ping-Yi Lin Yen-Shin Lai, "Voltage Trajectory Control for Vector-Controlled Induction Motor Drives to Achieve Six-Step Operation", Center for Power Electronics, National Taipei University of Technology, 2013
- [13] A. Tripathi, A. Khambadkone, S. Panda: "Dynamic Control of Torque in Overmodulation and in the Field Weakening Region, IEEE Transactions on Power Electronics, Vol. 21, No. 4, pp. 1091-1098, July 2006.
- [14] P. Matic, B. Blanuša, S. N. Vukosavić, "A Novel Direct Torque and Flux Control Algorithm for the Induction Motor Drive", IEEE International Electric Machines and Drives Conference, IEMDC'03, Proceedings, Vol. 2, pp. 965-970, 1-4. June 2003.
- [15] A. Jidin, N. Idris, A. Yatim, M. Elbuluk: "A Novel Overmodulation and Field Weakening Strategy for Direct Torque Control of Induction Machines", The Forty-Third IAS Annual Meeting, Conference Record, pp.1-8, 5-9. October 2008.

- [16] Paolo Di Barba¹ , Michal Bonislawski: “Design of Hybrid Excited Synchronous Machine for Electrical Vehicles”, University of Pavia, 2015.
- [17] Aswathy M S ,M Waheeda Beevi : “High Performance Induction Motor Drive in Field Weakening Region ”, Department of Electrical and Electronics College of Engineering, Trivandrum, 2015.
- [18] K. Vinoth Kumar, Prawin Angel Michael : “SIMULATION AND COMPARISON OF SPWM AND SVPWM CONTROL FOR THREE PHASE INVERTER ”, School of Electrical Sciences, Karunya University, 2010.

Influence of a novel binder material on the electrochemical performance of silicon-containing anodes

Sibo Lukas
 HM Hochschule München
 University of Applied Sciences,
 Technology Centre Energy,
 94099 Ruhstorf an der Rott, Germany
 Email: sibo.lukas@hm.edu

Prof. Dr. Frank Palme
 HM Hochschule München
 University of Applied Sciences
 Dachauer Str. 98b, 80335 Munich,
 Germany

Prof. Dr. Karl-Heinz Pettinger
 University of Applied Sciences
 Landshut,
 Am Lurzenhof 1, 84036 Landshut,
 Germany

Abstract— Silicon-containing anodes have been in demand in lithium-ion battery technology for many years. Using silicon on the anode side, significantly higher capacities can be achieved compared to commercially used materials. The choice of binder is highly significant to solve the problems associated with capacity fading observed along cycling. In this work a novel water-based fluorothermoplastic binder was investigated that is combined in four different formulations with a commercially used carboxymethyl cellulose binder and the prepared electrodes characterized in half cell technology. The resulting capacity characteristics are analyzed. Comparing the results with the previously used binder system of SBR and CMC, the capacity of the half cells was significantly improved.

April 26, 2021

Keywords—Lithium-Ion batteries, silicon-containing anodes, binder materials, THV, CMC, SBR

I. INTRODUCTION

To enhance the suitability of electric cars for everyday use, higher ranges as well as fast-charging capabilities are to be realized. This requires an increase in the energy density of fast-charging rechargeable accumulators is required [1]. A great potential is offered by the use of alternative anodes (traditionally graphite) in today's lithium batteries. Especially the use of water-based silicon/graphite composite anode (theoretical capacity $\text{Li}_{22}\text{Si}_5$ with $4200 \text{ mAh} \cdot \text{g}^{-1}$ approx. eleven times higher than commercial graphite) could enormously increase the energy density and environmental compatibility of the anodes [2].

Challenging in this regard is that the load capacity of the cells decreases with increasing energy density and the use of Si anodes leads to disadvantageous properties especially volume expansion during cycling and subsequent capacity fading compared to the traditionally used graphite anodes [2].

To reduce the volume expansion and increase cycle stability, novel binder materials are to be used and their suitability and combination with conventional binder materials will be investigated. The following work deals with an initial electrochemical characterization of a novel flour thermoplastic binder (THV 221). This is processed in combination with a commercially used binder (CMC) to form a silicon/graphite composite anode and analysed under different current rates in half cells. The results are compared in the second part of the work with those of a silicon/graphite anode based on a conventionally used binder system (SBR-CMC) in order to determine a possible improvement in cycle stability and service life due to the novel THV binder.

II. THEORETICAL BASIS

A. Lithium-Ion batteries

1) *Construction*: A lithium-ion battery consists of at least one Li-ion cell. In principle, this cell consists of two electrodes. These electrodes consist of a current conductor, which is coated with corresponding active materials. Between the two electrodes there is an ion-conductive electrolyte and a porous membrane as separator. The electrolyte, which contains a dissociated lithium salt, ensures a flow of ions between the electrodes during charging and discharging. The separator ensures electrical insulation between the two electrodes [3].

2) *Function*: If the electrodes are now connected between the current collectors by means of an external electrical connection to a current sink (discharging) or a current source (charging), individual positively charged lithium ions move back and forth between the electrodes. In addition to the flow of ions in the electrolyte, electrons move between the electrodes via the external wiring, thus completing a circuit. In the process, the lithium ions are deposited in or removed from the active materials, taking up or releasing an electron. Figure 1 shows the basic structure of a conventional lithium-ion accumulator and its processes in the discharge direction. As

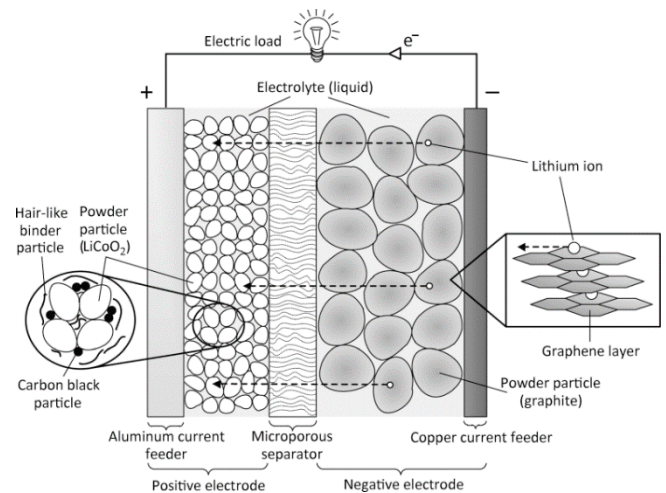


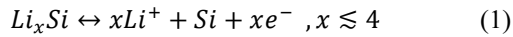
Fig. 1. Basic structure of a conventional lithium-ion accumulator and its processes in discharge direction [4]

shown in the example, lithium ions are removed from the negative electrode (deintercalation) when the battery is discharged. Graphite or amorphous carbon compounds are usually used for this purpose. The electron flow that takes place starts from the active material of the negative electrode via its

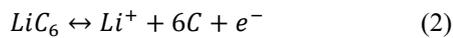
current conductor (copper) and the external electrical connection to the positive active material, again via its current conductor (aluminum) [3].

B. Silicon as anode material

Silicon offers enormous potential for increasing the energy density of future lithium-ion batteries. Compared to commercial graphite, the theoretical specific capacity of silicon is $4200 \text{ mAh}\cdot\text{g}^{-1}$, about eleven times higher [2]. This large difference in capacitance compared to commercial graphite electrodes ($372 \text{ mAh}\cdot\text{g}^{-1}$ [5]) results from the fact that silicon is capable of binding more lithium ions per atom than carbon. Around one silicon atom can intercalate up to about four lithium ions.



In graphite, on the other hand, six carbon atoms are needed to bond one lithium ion.



In addition to its electrochemical potential, silicon, as the most common element in the earth's crust, offers enormously high availability and is correspondingly more environmentally compatible than other alternatives. In addition, the production of silicon-containing anodes is solvent-free. However, the use of silicon-containing anodes also entails disadvantageous properties. In particular, the problem of extreme volume expansion during cycling has preoccupied researchers for decades and has so far hindered commercial use. Lithiation of silicon in the charging process causes a silicon atom to expand in volume by 400 percent in all spatial directions. Delithiation in the discharge step reduces the volume again to different sizes [6]. Due to the extreme volume expansion in the charging process, extreme stresses are generated, which result in contact losses, pulverization of the silicon particles, and/or unstable solid electrolyte interfaces (SEI) [7]. On the one hand, this reduces the capacity and cycle stability of the cells and, on the other hand, creates safety risks.

C. Binders

Binders must perform a variety of tasks in the electrode material of a Li-ion battery. On the one hand, binders help with the processability of the anode materials by ensuring good particle dispersion in the solvent or water. This contributes to a good distribution of the electrode material in the coating process, enabling homogeneous coatings on the ar-

rester foil. Secondly, the binder holds the coating particles together and ensures good adhesion of the coating to the surface of the arrester [8]. This is of great importance for the lifetime of the cell. Especially when using silicon-containing anodes, a suitable binder is important to counteract the problem of volume expansion described above.

In order to reduce volume expansion and increase cycle stability, a novel binder material will be used in this work and their suitability and combination with conventional binder materials will be investigated.

III. ELECTROCHEMICAL CHARACTERIZATION

A. Assessment criteria

For the electrochemical evaluation of the anodes, the Coulombic efficiency and the performance in terms of the specific capacity related to the weight fraction of the active material are considered in this work. Good performance of the anode means that the specific capacity during discharge/charge is close to the theoretical specific capacity of the active material. In addition, the capacity should be maintained as far as possible over several charge and discharge cycles. The Coulombic efficiency (CE) describes the specific discharged and charged capacity ratio. Due to parasitic reactions, the discharge capacity is lower than the charge capacity. For lithium-ion batteries, the Coulombic efficiency after several initial cycles is above 0.99 [9].

B. Test procedures

- **Wetting process:** During the wetting process, the cells are stored without current load so that the electrolyte can be homogeneously distributed between the porous surfaces of the electrode and the separator. If the electrolyte is incompletely distributed, there is a risk of dendrite formation during cycling, which in the long term can lead to an internal short circuit and thus increased self-discharge of the cell [10].
- **Cell formation:** The cell formation is performed at low currents to build the Solid-Electrolyte-Interface (SEI). This is a layer built up on the active material of the negative electrode in the first cycles of the cell. This layer protects the active material from direct contact with the electrolyte. Direct contact would lead to decomposition of the electrolyte. To build up the layer, some of the lithium ions in solution in the electrolyte are irreversibly consumed. This leads to initially low capacities in the battery during the cell formation process [3].
- **C-rate test:** To test, analyse and evaluate the electrochemical reaction of the cells two test procedures are applied. On the one hand a C-rate test is performed. In this, the cells are charged and discharged under different current rates (C-Rates). The C-rate is the normalization of the charge and discharge current (I) related to the nominal capacity (C_n) [11]:

$$C\text{-Rate} = I / C_n \quad (3)$$

- **Cycling stability:** On the other hand a cycling test is applied to analyse the long-term performance of the cells. In this, the cells are charged and discharged from 0 percent state of charge (SOC) to 100 percent SOC.

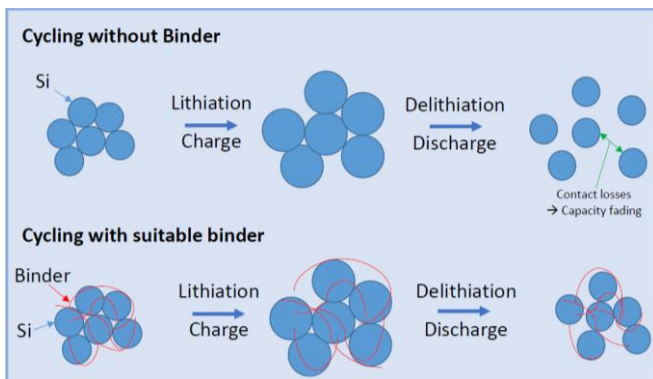


Fig. 2. Effect of Binder to avoid Silicon cracks

Both steps are performed in CCCV charge. Here the charging step is split up into two phases. The first phase is the constant current (CC) phase: Charge at a given current rate to a specific maximum voltage U_{\max} .

This is followed by the constant voltage (CV) Phase: Keep the cell on floating condition at U_{\max} until a fixed cut-off value is reached (typically current drops to $C/20$) [9].

C. T-cell measurement setup

The measurement is performed in a 3-electrode half-cell measurement setup using Lithium as counter and reference electrode. This allows the exclusion of disruptive effects from cathode materials such as aging. The anode to be tested (10 mm circularly punched out) is placed opposite the lithium metal counter electrode (12 mm circularly punched out) in the T-shaped setup. The anode and counter electrode are separated by an electrolyte impregnated (100 μ l) separator (12 mm circular punched out). A mixture of 98 wt. % LP57 and 2 wt. % vinylene carbonate is used as the electrolyte. The lithium metal reference electrode placed upright on top is also separated from the other electrodes by an electrolyte-impregnated (60 μ l) separator (10 mm circular punched out).

IV. EXPERIMENTAL SECTION

A. Chemicals

TABLE I. LIST OF USED MATERIALS

Material	Function
SUNROSE® MAC200HC	Conventional Binder I
3M™ Dyneon™ THV 221AZ	Novel Binder II
xGnP® Graphene Nanoplatelets M25 XGSciences™	Conductive additive
NMSiQC99@75 Nanomakers SA	Active material
Cu-ETP / E-Cu58	Collector foil
LP57 Selectilyte BASF	Electrolyte
Vinylene carbonate BASF	Electrolyte
VWR™ Fiberglass tissue	Separator

B. Production of the anodes

The anodes are prepared and manufactured in four formulations. In a first step, the materials consisting of water, binder, conductive additive and active material (Si-C) are mixed and dispersed in a dissolver (Dispermat CV3 Plus). The total mass fraction of active material (30 wt. %), conductive additive (40 wt. %) and binder (30 wt. %) remains the same for each formulation. The proportion of the binder itself is determined by the ratio between the novel binder and the commercial binder. This quantity ratio is varied for each batch. The gradually changed mass fractions of the binders in the total solids mass are listed in Table II. Subsequently, a thin film (140 μ m coating gap) of the dispersion is applied by means of a casting tool (Doctor Blade) onto the arrester foil (Cu). Then the coating is step-dried in a drying channel with four temperature chambers (drying temperatures: 80 °C, 90 °C, 110 °C and lastly 100 °C).

TABLE II. OVERVIEW OF THE BINDER FORMULATIONS

	Proportion novel binder [wt. %]	Proportion conventional binder [wt. %]
Formulation 1	6	24
Formulation 2	12	18
Formulation 3	18	12
Formulation 4	24	6

C. Measurement setup

The T-Cells are linked to a battery cycler (BaSyTec) in a measurement chamber. Three cells are manufactured and measured for each formulation. The measuring chamber is located in a closed room with a temperature control at 25 °C. The cells are measured according to a test plan. It consists of charge and discharge currents, cycle numbers, time parameters and the voltage range. The maximum voltage is implemented to the test plan with 1.2 volts [V] and the minimum voltage with 0.01 V. Based on the nominal capacity of the anode the current is calculated by the software according to the set C-rate. The nominal capacity here represents the theoretical specific capacity of the anode. This is calculated from the theoretical capacity of the active material silicon (3600 mAh·g⁻¹ for Li₁₅Si₄ [12]) and the weight proportion of the active material of the anode. The test of the C-rate stability is completed by charging and discharging with the C-rates: 0.2, 0.5, 1.0, 2.0, 3.0 and 5.0. Each C-rate is tested three times. Before the test procedure begins, a 12-hour break is scheduled to ensure complete wetting of the electrolyte. A formation step is also scheduled between the pause and the test run. In this step the cells are cycled five times at 0.1 C.

After the c-rate test, a cycling test is performed to analyse the cycling stability of the cell. The cell is subjected to 100 cycles at 1C.

V. RESULTS AND DISCUSSION

A. Formulation 1 CMC24/THV6:

In the test series of the first Formulation 1 (CMC/THV proportion 24/6 percent), one of the three half cells built partially failed. In the C-rate test, this only responded to high current flows (3C and 5C). In the cycling test, the cell only reacted from the 65 cycle. Therefore, it is not considered further in the evaluation. The SEI formation of the other two cells can be clearly recognized in the cell formation by the asymptotic course of the Coulombic efficiency. The Coulombic efficiency increased from 57 to 91 percent on average over the first five formation cycles in the two cells. Since the formation of the SEI layer consumes lithium ions, solvents and salts during formation and the cell resistance increases during this process, the observed cell capacity losses and thus reduced Coulombic efficiencies occur [13]. These losses decrease with the formation of the SEI layer, resulting in the asymptotic curve. From the begin of the C-rate test the Coulombic Efficiency is above 0.99 for all functional cells in each formulation.

In the following C-rate test, the cells reached a specific capacitance close to the theoretical capacitance of silicon under moderate conditions (Li₁₅Si₄ 3600 mAh·g⁻¹ [12]) at C/5. An overview of the specific capacities during the C-rate test is shown in Table III for all formulations. With increasing current rates, the capacities of the cells dropped. After the high current loads, the initial capacities of the cells could be provided again under C/5 and even slightly exceeded (compare Table III).

In the subsequent cycling test under a current rate of 1C, the capacities of the two cells behaved very similarly. An overview of the specific capacities during the cycling test are shown in Table IV for all formulations. Within the first approximately 20 cycles, the capacities increased slightly and then dropped over the remaining cycles (compare Table IV).

Overall, the capacities of the two cells faded by 10 percent (cell 1) and 14 percent (cell 2) over the 100 cycles.

B. Formulation 2 CMC18/THV12:

In the test series of the second Formulation 2 (CMC/THV proportion 18/12 percent), none of the three cells failed, but the measured capacitances scatter considerably more here. The Coulombic efficiencies, on the other hand, are close to each other and the typical asymptotic curve has again been observed. The Coulombic efficiencies increased over the five formation cycles averaged from 58 to 89 percent.

In the C-rate test the specific capacities of the cells are scattered around the theoretical $3600 \text{ mAh}\cdot\text{g}^{-1}$. The scatter of the values is a problem for reproducibility. Since the measurements and the production of the half cells are quite time consuming, the evaluation will continue at this point with the existing values. For good reproducibility, further measurements should be made in any case. As the current rate increased, the capacities of the cells dropped and after the high current load, the initial capacities of the cells could be provided again under C/5 and in some cases slightly exceeded (compare Table III).

TABLE III. SPECIFIC CAPACITIES DURING C-RATE TEST

		Specific capacity in $\text{mAh}\cdot\text{g}^{-1}$			
		C/5	1C	5C	C/5 ^a
CMC24/THV6	Cell 1	3372	2510	743	3743
	Cell 2	3782	2940	947	3894
CMC18/THV12	Cell 1	2671	1608	511	2625
	Cell 2	4320	3526	1112	4369
	Cell 3	3414	2192	618	3941
CMC12/THV18	Cell 1	4441	3599	1161	4463
CMC6/THV24	Cell 1	3627	2696	669	4090
	Cell 2	4071	3323	848	4146

^a after increased C-rates

In the subsequent cycling test, the capacity curves of cell 2 and 3 behaved quite stably. The capacity of cell 1, whose capacity was measured to be significantly lower in comparison, was less stable and fluctuated slightly up and down between cycles. Compared to the other two cells, there was also a slight increase in capacity over the 100 cycles. The capacities of the other cells dropped over the cyclization (compare Table IV).

Overall, the capacity of cell 1 increased by 14 percent over the 100 cycles and the capacity of the other cells faded by 17 percent (cell 2) and 8 percent (cell 3).

C. Formulation 3 CMC12/THV18:

In the test series of the third Formulation 3 (CMC/THV proportion 12/18 percent), one of the three half-cells built failed partially, a second failed completely. Therefore, these are not further considered in the evaluation. This is again a problem in terms of reproducibility of the results. For good reproducibility, further measurements should be made at this point as well. The SEI formation of the third cells can again be seen in the cell formation by the asymptotic course of the

Coulombic efficiency. This increased over the first five formation cycles of the cell from 62 to 90 percent.

In the following C-rate test, the cell reached a specific capacitance beyond the theoretical $3600 \text{ mAh}\cdot\text{g}^{-1}$ by far. With increasing current rates, capacities of the cell dropped (compare Table III). After the high current loads, the initial capacity of the cell under C/5 was again slightly exceeded.

In the subsequent cycling test, the cell's capacity curve behaved quite stably. The capacity of the cell faded over the 100 cycles by 15 percent (compare Table IV).

TABLE IV. SPECIFIC CAPACITIES DURING CYCLING TEST

		Specific capacity in $\text{mAh}\cdot\text{g}^{-1}$		
		Cycle 1	Cycle 100	Alteration
CMC24/THV6	Cell 1	3019	2711	-308
	Cell 2	3202	2765	-437
CMC18/THV12	Cell 1	1652	1882	230
	Cell 2	3815	3169	-646
	Cell 3	3024	2784	-240
CMC12/THV18	Cell 1	3900	3322	-578
CMC6/THV24	Cell 1	3228	2568	-660
	Cell 2	3596	2629	-967

D. Formulation 4 CMC6/THV24:

In the test series of the fourth Formulation 4 (CMC/THV proportion 6/24 percent), one of the three half cells built failed. Therefore, this is not considered further in the evaluation. The SEI formation of the other two cells can again be seen in the cell formation by the asymptotic course of the Coulombic efficiency. Coulombic efficiencies increased from 54 to 93 percent averaged over the five formation cycles.

In the C-rate test the capacities of the cells scatter slightly above the theoretical $3600 \text{ mAh}\cdot\text{g}^{-1}$. As the current rate increased, the capacities of the cells dropped. After the increased current load, the initial capacities of the cells were again slightly exceeded under C/5 (compare Table III).

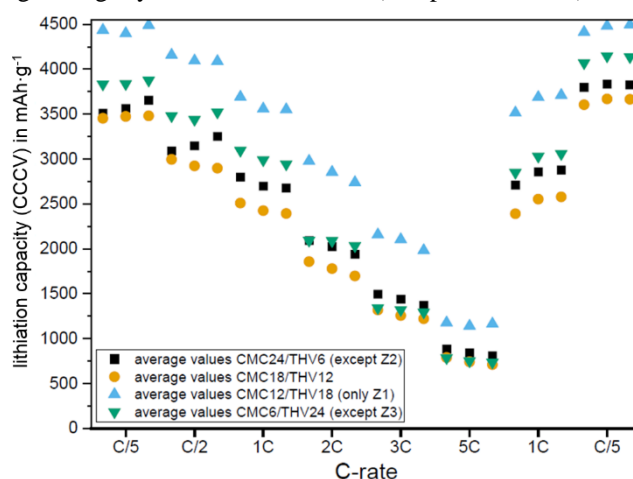


Fig. 3. Overview of the averaged lithiation capacities during C-rate test

In the subsequent cycling test under a current rate of 1C, the capacities of the two cells behaved very similarly. The capacitances dropped fairly consistently over the cycles (compare Table IV).

Overall, the capacity of the two cells faded by 20 percent (cell 1) and 27 percent (cell 2) over the 100 cycles.

An overview of the averaged courses for the C-rate test and the cycling test are shown in Figure 3 and 4 for the four formulations. The Coulombic Efficiency is about 90 percent for all formations after the five forming cycles and then continues to increase at the start of the C-rate test. From a load of 1 to 2 C, the Coulombic Efficiency of the cells is then above 99 percent. This is an indication that the SEI layer is not fully formed after the five formation cycles and more formation cycles possibly should be scheduled for future testing.

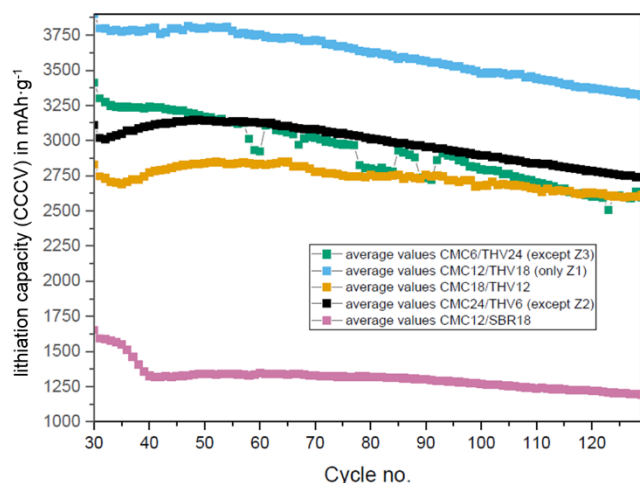


Fig. 4. Overview of the averaged lithiation capacities during cycling test

However, the five formation cycles are still justifiable at this point because the cells are only loaded with small current rates at the beginning in the C-rate test. This allows sufficient time for the SEI layer to form before loading at high current rates.

Figure 4 additionally shows the course of another anode produced according to the above-mentioned conditions. For this anode a mixture of 12 wt. % CMC-MAC 200 and 18 wt. % SBR (Zeon BM-451B) was used as binder system.

VI. CONCLUSION

Overall, it can be summarized that the use of the novel THV binder, instead of conventional SBR, in combination with the CMC binder tends to slightly increase capacity fading about 10 to 20 percent. But in return significantly higher capacities by a factor of 2 to 3 can be achieved. The combination of CMC6/THV24 achieved the most unstable capacity curve in the comparison and tended to the highest capacity fading while cycling. Nevertheless, an evaluation of which formulation achieved the most stable capacity curve cannot be clearly determined at this point, due to the very poor reproducibility in particular for the formulations 2 and 3. Further tests are necessary to gain a representative statement concerning the formulation in this respect.

REFERENCES

- [1] D. Andre, S.-J. Kim, P. Lamp, S. F. Lux, F. Maglia, O. Paschos, B. Stiaszny, *J. Mater. Chem. A* 2015, 3, 6709–6732.
- [2] F.-H. Du, K.-X. Wang, W. Fu, P.-F. Gao, J.-F. Wang, J. Yang, J.-S. Chen, *J. Mater. Chem. A* 2013, 1, 13648–13654.
- [3] S. Leuthner, in (Ed.: R. Korthauer), Springer Berlin Heidelberg, Berlin, Heidelberg, 2013, 13–19.
- [4] K. Vuorilehto, in (Ed.: R. Korthauer), Springer Berlin Heidelberg, Berlin, Heidelberg, 2018, 21–28.
- [5] N. Nitta, F. Wu, J. T. Lee, G. Yushin, *Mater. Today* 2015, 18, 252–264.
- [6] A. Casimir, H. Zhang, O. Ogoke, J. C. Amine, J. Lu, G. Wu, *Nano Energy* 2016, 27, 359–376.
- [7] C. Popsel, „Silicon based high performance Anode Materials for Next Generation Li-Ion Batteries“, *Research Paper, Nanoscience*, 2018.
- [8] L. P. C. Team, „The Role of Binders in Lithium Battery Electrodes“, The Lubrizol Corporation, 2020.
- [9] E. Redondo-Iglesias, P. Venet, S. Pelissier, *IEEE Trans. Veh. Technol.* 2018, 67, 104–113.
- [10] A. Kampker, C.-R. Hohenthanner, C. Deutschens, H. H. Heimes, C. Sesterheim, *Fertigungsverfahren von Lithium-Ionen-Zellen und -Batterien BT - Handbuch Lithium-Ionen-Batterien*, Springer Berlin Heidelberg, 2013.
- [11] C. Nebl, F. Steger and H.-G. Schweiger, *Int. J. Electrochem. Science* 2017, vol. 12, no. 6, 4940 – 4957.
- [12] N. Wagner, A. Tron, J. Tolchard, G. Noia, M. Bellmann, *J. Power Sources* 2019, 414, 486–494.
- [13] S. J. An, J. Li, C. Daniel, D. Mohanty, S. Nagpure, D. L. Wood, *Carbon N. Y.* 2016, 105, 52–76.

Development of a Vanadium/Vanadium Redox-Flow Battery for Demonstrational Purposes

Valentina Menne

Department of Mechanical, Automotive
and Aeronautical Engineering
Department of Applied Sciences
and Mechatronics
Hochschule München
University of Applied Sciences
Munich, Bavaria
Email: valentina.menne@gmx.de

Diane Henze

Simon Limbeck
Department of Mechanical, Automotive
and Aeronautical Engineering
Hochschule München
University of Applied Sciences
Munich, Bavaria
Email: diane.henze@hm.edu
Email: simon.limbeck@hm.edu

Klaus Peter Zeyer

Department of Applied Sciences
and Mechatronics
Hochschule München
University of Applied Sciences
Munich, Bavaria
Email: klaus_peter.zeyer@hm.edu

Abstract—Because of their high flexibility, robustness and longevity, vanadium redox-flow batteries are accounted as a highly promising alternative for stationary electrical energy storage. However, there is still little knowledge within the industry, and most of the existing models are prototypes or have been built as part of scientific projects. This study aims to increase knowledge and to give recommendations and guidelines in how to make this technology more accessible to students. A vanadium redox-flow battery has been designed that can be used for demonstrational purposes within laboratory experiments. Single components have been tested for their applicability within this set-up. This paper sums up the project work and retrospects the results regarding prospective flow battery system design.

I. INTRODUCTION

Along with the increasing use of volatile renewable energy sources, the need of shifting energy amounts in spatial and time dimensions rises. Therefore, energy storage technologies have experienced a growth in attention lately, both entrepreneurial and academic. Because of the efforts in these fields, the existing storage technologies improve and diversify. Different energy storage applications can have a variety of different requirements in terms of power, capacity, reaction time, weight, costs and durability. For usage within the energy transition, namely for storing varying amounts of energy, redox-flow batteries (RFB) have a high potential due to their long cycle life and their high flexibility. They can be scaled up to a power of 10 MW and several hundred MWh in capacity without self-discharge or a significant loss of efficiency, [1] with comparatively low investment costs [2] and extraordinarily low operation costs [3]. This is not possible when using common battery technologies. Currently, RFB mostly exist in the form of prototypes or integrated in long-term scientific projects. For a wide commercial and industrial use, one of the main challenges to overcome is the difficulty of an integrated system design, because of a lack of consciousness and expertise with RFB systems. This study sums up a project work at Munich University of Applied Sciences, which aims to increase knowledge and to

give recommendations and guidelines in how to make this technology more accessible for students.

II. TECHNICAL BACKGROUND

A. Electrochemical basics

Because of their similar cell structure, RFB are often classified as fuel cells. In both technologies, the electrodes do not participate in the electrochemical reaction, and active elements can be stored spatially separated from the cell. Regarding the chemical system, RFB rather resemble secondary battery elements (accumulators), because in their chemical systems, the same electroactive material is used in multiple charging and de-charging cycles. RFB differ from both fuel cells and batteries in that they cyclically pump the electroactive substances, which are dissolved in electrolytes, through the cell. Overall, they can be classified as in between battery (closed system) and fuel cell (open system) technology (figure 1).

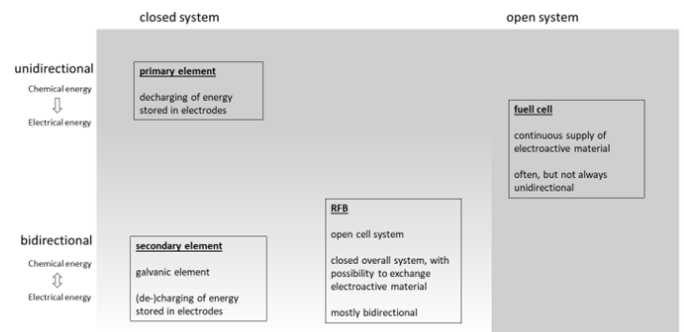
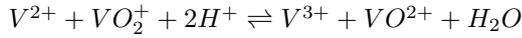


Figure 1: Classification of RFB within different electrical energy storage technologies.

A variety of different electrochemical combinations can be used within RFB. The most common cell chemistry uses all-vanadium active elements, dissolved in a sulphuric acid and water solution [4]. As can be seen in the equation below, the

main advantage of using vanadium for the redox reaction is that it is chemically stable in oxidation states II to V, and anolyte and catholyte consist of the same chemical elements. Therefore, cross-contamination and small leakages within the cell can be tolerated as they only effect short-term loss of efficiency, instead of long-term loss of capacity [5].



The composition of a typical all-vanadium RFB (VRFB) is shown schematically in figure 2. Core elements of the VRFB are the membrane-electrode-assembly (MEA) where the redox-reaction takes place, two tanks as well as two hydraulic pumps. As a particularity of RFB systems, the electrolyte is stored externally and cyclically pumped through the cell halves. Anode and cathode in the MEA only serve as electron collector and conductor and often are made out of graphite felt in combination with graphite and copper plates. In most cases, a cation exchange membrane is implemented, where H^+ -ions pass through for equalisation of state of charge. [5]

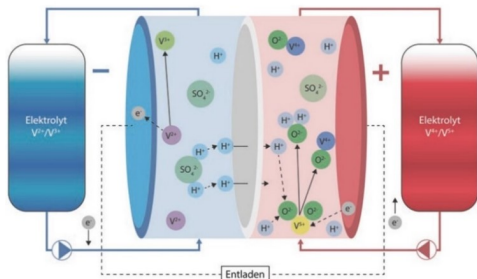


Figure 2: Composition of a typical all-vanadium RFB [4].

B. Comparison to other power storage technologies

In the field of stationary energy storage, there are several technologies that are already in use. Comparing to conventional power storage devices like pumped hydroelectricity, electrochemical energy storage technologies like those shown in figure 1 are considered as more mature because they are known for a high level of modularization, rapid response, flexible installation and short construction cycles [3]. In this chapter, some of these technologies and their performance indicators will be compared to those of VRFBs.

The main criteria for evaluating large-scale energy storage devices are rapid response time, long cycle life and low costs [3]. Response time is within milliseconds for almost all battery types, which makes this kind of energy storage eligible for stationary applications. With its favourable electrochemical configuration (as explained in the previous chapter) and, associatively, the high chemical durability and robustness against misuse, VRFB exceed many other batteries regarding cycle life (see Table I).

When regarding costs of battery applications, the whole industry is struggling with one major competitor: Currently, electricity can be produced very cheaply, and in many cases

Table I: Durability of some storage technologies [3].

Power storage technology:	cycle life (cycles)
RFB, all-vanadium:	12000-14000
RFB, zinc/bromine:	> 2000
Lithium-ion Carbon Anode:	> 1000
Lead-acid accumulator:	500-1000

it is cheaper to produce electricity in a conventional way (e.g. with coal-fired steam power plants) than to temporarily store it [6]. Therefore, costs of battery systems have to be lowered, and technologies that are already industrialized are at an advantage [7]. Depending on the application, either the power-related or the capacity-related costs (in \$/kW or \$/kWh) are decisive, whereby these two are interconnected in normal battery storage systems. With flow cells, performance and capacity are not dependent on one another and can be freely scaled based on the requirements, which is one of their most important characteristics [1]. In addition to this flexibility in investment costs, VRFB have comparatively low maintenance costs because of their high durability and reliability [3].

Another important indicator for characterizing batteries is their energy density. It is either defined by capacity per weight (which is important for mobile applications) or by capacity per volume (which is often used for stationary applications). At 10-50 Wh/L, the energy density of VRFBs is rather low compared to other RFBs (e.g. V/Br), see Table II. This means that more electrolyte has to be pumped through the cell than with other RFBs in order to achieve comparable performance. Other electrochemical energy storage devices also have significantly higher energy densities, so that the space required by VRFBs is comparatively high. [8]

Table II: Energy density of some storage technologies.

Power storage technology:	Energy density
RFB, all-vanadium:	10-50 Wh/L [3]
RFB, vanadium/bromine:	35-70 Wh/L [1]
RFB, Li-based slurry electrolyte:	up to 500 Wh/L [9]
Lithium-ion Carbon Anode:	> 200 Wh/L [10]
Lead-acid accumulator:	40 Wh/kg [11]

C. Advantages and disadvantages of RFB technology

Overall, flow cell technology, especially the all-vanadium flow cell, complements the solutions that are currently on the market for stationary energy storage. The decoupling of energy and power, as well as the many possibilities of creating them in a modular design, are the ones most mentioned. The system can therefore also be adapted for installation at a later date. These factors make the flow cell a very flexible energy source [1]. The outstanding longevity of VRFBs makes them interesting for long-term investments and further extends the range of applications. The safe and straightforward handling and operating processes make it accessible to many different industrial sectors. Because the materials used are widely

available and do not form unresolvable chemical compounds within parasitic side reactions (contrary to many other battery technologies), VRFBs can easily be recycled [3].

Despite these advantages, VRFB technology has not yet been intensively used in industrial context. Contrary to Li-Ion technology, the energy density is not very high and can only be increased in nuances. Therefore, RFB with electrolytes that are known today will not be eligible for standard mobile applications. In addition, many components from other battery applications are used (e.g. membrane) that have to be and are currently further optimized for flow cell technology. Another disadvantage is the lack of profitability that is still valid for most applications. However, due to an increased order volume, there will be a price drop for several components, especially those also used in other applications such as membranes. Even though the material costs are very low compared to other power storage systems, operators still have to put a relatively high effort in designing VRFBs to their needs. The interactions within the cell structure as well as the influence of different component combinations have to be further investigated. So far, there is little experience with the design of entire systems, which is not least due to the low level of awareness of the technology within the industry. This study aims on improving knowledge of this technology through education. [12]

III. PREPARATIONS

A. Aim of this study

This study comprises designing a prototype flow cell battery, procuring the parts needed and testing single components and, if possible, the assembled battery altogether. The so-called "demo-RFB" should serve as a demonstrator for the functionality of this type of energy storage and can be used in laboratory exercises. This structure can provide an introduction to the topic of stationary energy storage for students working on it. The demonstrator can then serve as a basis for further laboratory exercises, project works or theses. In parallel to the construction of the flow cell battery, a practical experiment can be designed in which the students can put the battery into operation and examine it. In addition, charging with the help of renewable energies should be discussed (e.g. photovoltaic modules of the Laboratory for Energy and Process Engineering at the Department of Mechanical, Automotive and Aeronautical Engineering) and the importance of stationary energy storage systems for the energy transition should be emphasized.

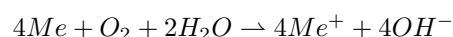
B. Constraints and preliminary considerations

The main requirements of the demonstrator differ from requirements of usual RFB because of the focus on pedagogic value and are namely:

- safety of operators
- safety of components
- transparency and appropriate presentation of RFB technology
- illustration of flexibility of RFB systems
- reliability of the test setup

Because of the critical electrolyte material in terms of acidity, the main priority was laid on the first two requirements regarding safety. For the construction of conventional flow cell batteries, metals are widely used for different parts (e.g. steel screws for screw connections of the MEA, or copper for collector plates). Since the electrolyte of the RFB is based on sulfuric acid, the use of metals is only possible to a limited extent, or it must be ensured that there be no contact between the electrolyte liquid and the corrosive media. The latter is not possible in this project due to the special set-up (see next chapter). Therefore, materials that do not react with the electrolyte liquids must be used.

Corrosion can have various causes. The most common corrosion reaction, which is also known as "rusting", is the so-called oxygen reaction. Free electrons in the electron gas of non-noble metals react in a neutral environment (e.g. H_2O) with water and oxygen [13]:



Another form is acid corrosion, which occurs mainly in solutions with a low pH value. The hydronium ions present in the acid take up free electrons from the metals and are reduced to hydrogen. The metals are oxidized and form salts. If salts are already present in the acid, this reaction is accelerated as they increase the conductivity of the liquid and can even override the passive corrosion protection of the metals. [13]

In principle, both corrosion reactions can occur in the RFB when electroactive liquid comes into contact with metals, since the electrolyte fluid is an aqueous and acidic solution. The vanadium ions can further accelerate this effect. Therefore, materials that are used should either have no free electrons or already be in an energetically favorable state so that the corrosion reactions do not take place under normal conditions.

Out of these considerations, acrylic glass was chosen for structure components because of its high chemical resistivity and because it is transparent, so the students will be able to examine the inside of the demonstrator. Also, the electrode design was adjusted, so that no metal components would come into contact with electroactive substances.

C. Design

From previous research and interviews with experts, it was concluded that the aspects sealing, flexibility and transparency should have the greatest relevance for this project. A leakage of electrolyte fluid is particularly critical for this demonstrator setup, since there is a risk of injury from chemical burns for inexperienced participants. Therefore, a set-up with least possible leakages was constructed. A sealed container is used, that is made out of glued acrylic glass and was fabricated by an experienced manufacturer. The container consists of one chamber for the MEA and two chambers for two electrolyte tanks. By this measure, hose connections were reduced from twelve to eight. An additional advantage of this set-up is that the flexibility of the RFB can be highlighted, because MEAs can be exchanged very easily and safely.

To make use of this flexibility, two types of MEAs were designed. The main challenge was that the whole MEA would be submerged into the container, and every part would be exposed to the corrosive electrolyte fluid. As explained in the previous chapter, metal materials (which are commonly used in battery current collector plates [12]) would trigger oxidation reactions and therefore de-charge the electrolyte. In one version, electrons are collected and transported by a graphite electrode plate. This leads to a higher electrical resistivity compared to conventional cell design (see figure 3). The other version copes with that by implementing graphite bars that directly lead the current upwards to metal current collectors outside the battery case (see figure 4). This comes with the disadvantage of a more complex assembly process.

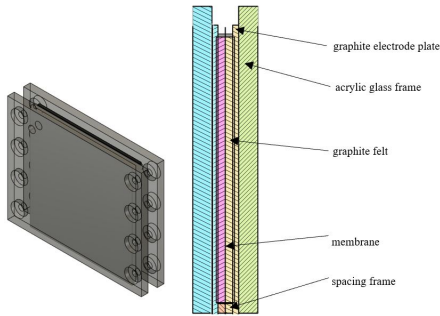


Figure 3: MEA with electrode plate.

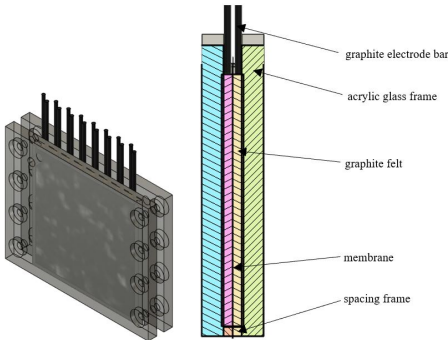


Figure 4: MEA with electrode bars.

Another large influence on the overall ohmic resistance is the compression of the graphite felts, and the resulting resistivity of contact areas. The more the components are pressed together, the higher is the contact area and the bigger is the current transfer from felt to electrodes. This can be described by the compression rate [14]

$$CR = 1 - \frac{t_c}{t_i}$$

where t_c represents the compressed, and t_i represents the initial thickness of the carbon felt. The compression rate CR is given in percentage. The CR for the two different MEAs can be seen in Table III.

The hydraulic periphery of the battery consists of two peristaltic pumps with direct current motor. Those can be

Table III: Graphite felt thicknesses and compression rates.

MEA version	t_c	t_i	CR
Electrode plate	5 mm	6 mm	83 %
Electrode bars	3,8 mm	4,7 mm	81 %

adjusted precisely, also to low volume flow rates, and are economically affordable. Also, peristaltic pumps are low-maintenance, and the highly corrosive electrolyte is not in contact with any critical parts, only with the silicone hose. For completing the electrical circuit of the cell, a laboratory power supply for charge mode and an electrical load for de-charge mode are provided. In a first step, the peristaltic pumps are controlled by the programmable power supply. For further investigations and when more measuring devices are to be integrated into the system, it could be beneficial to replace this power supply by a microcontroller-based control unit.

To sum up, the demo-RFB consists of the following setup: Two different pumps can be connected to the acrylic glass container via a total of four hose connections, which ensure that the electrolyte circulates. Between the two inner walls separating the tank from the cell area, varying MEAs can be inserted. As an example, two different MEAs are designed, which consist of different components and have different electrical resistances. The amount of exchangeable MEAs can be expanded as required, as long as the dimensions for length, width, height and the connection holes are compatible. The MEAs do not have to be sealed individually because of similar electrolyte composition in both cell halves. Figure 5 shows the acrylic glass container as well as one of the MEAs.

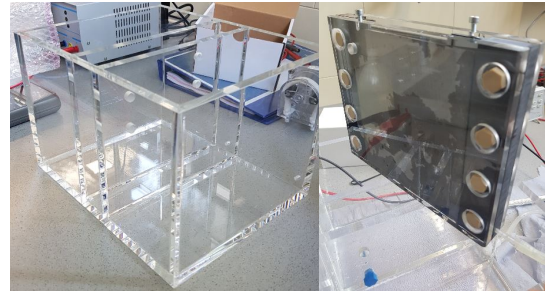


Figure 5: Container (left) and one MEA (right).

IV. PROOF OF CONCEPT-EXPERIMENTS

A. Peristaltic pump throughput

Because of the high variety of flow cell designs and the low awareness in the industry, there are no clear directives yet to be followed when dimensioning the electrolyte throughput. Even for one single design, electrolyte flow rates could vary as much as in between 200 ml/s and 200 ml/min [15]. However, it is important to know which range is possible within each setup. The peristaltic pumps chosen for this demo-RFB have a maximum flow rate of 396 ml/min, but because of other design constraints, connecting hoses have a smaller core diameter

than recommended. Therefore, the maximum flow rate is expected to be lower.

In order not to exceed the maximum nominal voltage, 23 V was specified as the maximum input voltage during operation. The actual maximum volume flow was to be determined in a tube with a 4 mm inner diameter for this voltage. In addition, further measuring points were recorded to assess the behavior of the pump at lower voltage values. At the maximum operating voltage, a volume flow of approx. 310 ml/min was measured. Applied to the flow cell structure with the MEA, this means that the pump would be able to exchange the electrolyte within the cell about 3.5 times per minute (without taking into account the flow resistances in the cell and in the container).

B. Ohmic resistance

In contrast to standard RFB applications, the demo-RFB uses plastic parts instead of metal elements for assembling the MEAs. Due to a possibly insufficient contact pressure when using plastic parts, the electrical resistance for current transfer between graphite electrodes and felts could be very high. That would lead to a low current flow and very long charging times, which would be inconvenient for a live presentation. To prevent this, an experiment was conducted, in which the electrical (ohmic) resistance of the electronic components of the cell should be roughly estimated in the dry state.

The measurement setup basically followed an indirect resistance measurement using a current-voltage measurement. During the measurement, the voltage was specified and the current was measured. According to the assumption of an ohmic resistance, the I-U characteristic curve would have to be a straight line through the origin so that one point would be sufficient to define the curve. In order to rule out measurement errors, fluctuations or other deviations with certain voltages, several current-voltage pairs were recorded. The measurement was repeated several times in the same setup and the values did not differ significantly from one another. The situation was similar when the measurement was started with the highest voltage, so no hysteresis could be observed.

Figure 6 shows the course of the current as a function of the specified voltage. In the range from 0.3 V upwards, the resistance levels off as expected with an ohmic resistance which is around 1.3 Ohm in this set-up. In the case of lower voltages, a different behavior is observed that cannot be explained by Ohm's law. This has to be due to another effect, whereby there is a high resistance at low voltages and the flow of electric current is prevented. Contact resistance is generally influenced by the three parameters surface quality, contact force and pollution layers. The resulting ohmic resistance is the sum of the foreign layer resistance and the so-called narrow resistance, which describes the contact areas. It is likely that at the measuring points with low voltage, the foreign layers cover a large part of the contact areas and only a very low current flow is possible. If the current flow continues and a certain voltage is reached, the potential barrier between the conductor and the foreign layer can be broken and the foreign layer

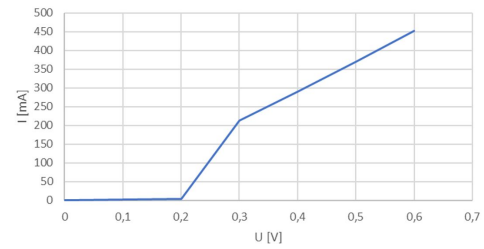


Figure 6: Measured current-voltage curve.

resistance drops to a significantly lower value R_S (see figure 7). This behavior is called "contact fritting", and the transition voltage is called "fritt voltage" U_F . This would explain the initially high resistance in the presented measurements. [16]

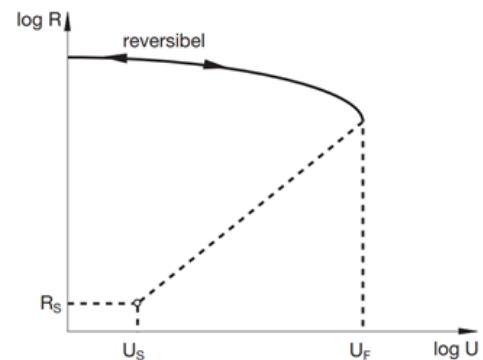


Figure 7: Ohmic resistance during fritting [16].

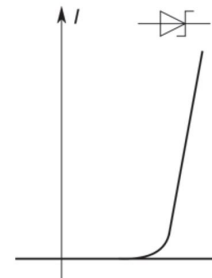


Figure 8: Current-voltage curve of a Schottky diode [17].

However, this behavior should only occur during the initial build-up of the current flow. Starting over at higher voltages, a current according to Ohm's law should be observed. This could not be examined within the first measurements. A mechanism, in which an initially high resistance becomes small at higher voltages, could also be explained by a diode characteristic, where reverse current faces a very high resistance [17]. It is possible that a kind of Schottky contact occurs at the transition between the graphite surfaces and the foreign layers. The characteristic curve of such Schottky diodes also shows a very low current flow at the beginning (see figure 8). Then the current increases exponentially until the resistance of the diode contact is very low, which could explain the subsequent ohmic

course. However, the occurrence of Schottky diodes within VRFBs is not well documented yet. For a final explanation of the observed behavior, further research and a repeated and more precise measurement in the range of 0.2-0.3 V would be necessary.

C. Argon as oxidation protection

Because the MEAs should be interchanged easily, the demo-RFB will not be sealed to be completely gas-tight. In order to prevent oxidation of the anolyte with atmospheric oxygen, a medium must be inserted that prevents it from mixing with air. In usual test stands, nitrogen is often used for this matter. The problem is that it has to be constantly refilled because of its high volatility. For this demo-RFB, experiments were carried out in order to investigate the applicability of argon for this sealing purpose.

With a density of around 1.7 kg/m^3 , argon is a particularly heavy inert gas and almost 50 % heavier than air. In this study, preliminary tests were carried out to determine whether it can remain permanently in the acrylic glass structure during the duration of the live experiment (too rapid volatilization would lead to high costs and more refilling steps). It was tested with a glowing splint test, because the heavy gas is able to displace air and oxygen which is needed for the splint to smoulder. The result was that there was no high volatility of argon within a duration of two hours, even with enforced air circulation around the experiment set-up. Therefore, argon can be investigated further as an oxidation protection for VRFBs.

V. CONCLUSION

A vanadium redox-flow battery has been designed that can be used for demonstrational purposes within laboratory experiments. Single components have been tested for their applicability within this set-up. The premises and the derived constraints for design and experiments are described in this paper.

The difficulties encountered while building this RFB for demonstrational use partly represent the main drawbacks of this technology. The hydraulic circuit of flow batteries requires mechanical components that are more complex and need more maintenance than the ones that are used for conventional electrochemical battery systems. To cope with that, more pilot projects will help gaining experience and recognizing optimized configurations for different use cases. Along with more research activities regarding optimized hardware and electrolyte materials, resistances can be minimized and efficiencies maximized. Enhanced RFB technology with optimized parameters could therefore become an important asset in the market of stationary energy storage.

ACKNOWLEDGMENT

The authors would like to thank G. Lößl for his valuable technical support.

REFERENCES

- [1] A.Z. Weber, M.M. Mench, P.N. Ross, J.T. Gostick and Q. Liu (2011), *Redox flow batteries: a review*. Journal of Applied Electrochemistry; 41: S. 1137–1164. doi:10.1007/s10800-011-0348-2.
- [2] X. Luo, J. Wang, M. Dooner and J. Clarke (2015), *Overview of current development in electrical energy storage technologies and the application potential in power system operation*. Applied Energy; 137: S. 511–536. doi:10.1016/j.apenergy.2014.09.081.
- [3] X. Fan, B. Liu, J. Liu, J. Ding, X. Han, Y. Deng et al. (2020), *Battery Technologies for Grid-Level Large-Scale Electrical Energy Storage*., Trans. Tianjin Univ.; 26: S. 92–103. doi:10.1007/s12209-019-00231-w.
- [4] M. Sterner, I. Stadler (2014) *Energiespeicher. Bedarf, Technologien, Integration*. Springer Vieweg, Berlin. ISBN: 9783642373794.
- [5] H. Prifti, A. Parasuraman, S. Winardi, T.M. Lim and M. Skyllas-Kazacos (2012), *Membranes for redox flow battery applications*. Membranes (Basel); 2: S. 275–306. doi:10.3390/membranes2020275.
- [6] C. Menictas, M. Skyllas-Kazacos, T.M. Lim (2015), *Advances in batteries for Medium- and Large-scale energy storage*., Woodhead Publishing, Sawston, Cambridge, UK. ISBN: 978-1-78242-022-4.
- [7] R. Huggins (2016), *Energy Storage. Fundamentals, Materials and Applications. 2nd ed.*, Springer International Publishing; Imprint: Springer, Cham. ISBN: 978-3-319-21239-5.
- [8] K. Lourenssen, J. Williams, F. Ahmadpour, R. Clemmer, S. Tasnim (2019), *Vanadium redox flow batteries: A comprehensive review*., Journal of Energy Storage; 25. doi:10.1016/j.est.2019.100844.
- [9] X. Wang, J. Chai, J. Jiang (2021), *Redox flow batteries based on insoluble redox-active materials. A review*., Nano Materials Science 3 (1), S. 17–24. DOI: 10.1016/j.nanoms.2020.06.003.
- [10] Y. Jiang, H. Zhao, L. Yue, J. Liang, T. Li, Q. Liu et al. (2021), *Recent advances in lithium-based batteries using metal organic frameworks as electrode materials*., Electrochemistry Communications 122, S. 106881. DOI: 10.1016/j.elecom.2020.106881.
- [11] J. Winsberg, T. Hagemann, T. Janoschka, M.D. Hager, U.S. Schubert (2017), *Redox-Flow-Batterien: von metallbasierten zu organischen Aktivmaterialien*., Angew. Chem.; 129: S. 702–729. doi:10.1002/ange.201604925.
- [12] L.F. Arenas, C. Ponce de León, F.C. Walsh (2017), *Engineering aspects of the design, construction and performance of modular redox flow batteries for energy storage*., Journal of Energy Storage; 11: S. 119–153. doi:10.1016/j.est.2017.02.007.
- [13] K.H. Tostmann (2017), *Korrosionsschutz. Theorie und Praxis*., 1st ed. Leuze Verlag, Bad Saulgau. ISBN: 978-3-87480-304-5.
- [14] R. Gundlapalli, S. Jayanti (2021), *Dataset on performance of large-scale vanadium redox flow batteries with serpentine flow fields*., Data Brief; 35: S. 106835. doi:10.1016/j.dib.2021.106835.
- [15] A.T. Glazkov, A.E. Antipov, D.V. Konev, R.D. Pichugov, M.M. Petrov, N.V. Kartashova et al. (2020), *Dataset of a vanadium redox flow battery 10 membrane-electrode assembly stack*., Data Brief; 31: S. 105840. doi:10.1016/j.dib.2020.105840.
- [16] E. Vinaricky (2002), *Elektrische Kontakte, Werkstoffe und Anwendungen. Grundlagen, Technologien, Prüfverfahren*., 2nd ed., Berlin, Heidelberg, Springer Berlin Heidelberg. ISBN: 978-3-642-56237-2.
- [17] M. Reisch (2007), *Halbleiter-Bauelemente*., Springer Berlin Heidelberg, Berlin Heidelberg. ISBN: 978-3-540-73200-6.

Development of different H₂-storage concepts for reduced emission shipping

Dominik Pace, Lea Huber, Michael Heberl, Belal Dawoud

Laboratory of Sorption Processes

East bavarian Technical University (OTH Regensburg),

93053 Regensburg, Germany

Email: Dominik1.pace@st.oth-regensburg.de

Abstract—Fossil fuels such as marine diesel can be replaced by emission-free energy carriers without losing performance. A suitable substitute is hydrogen with its gravimetric energy density of 33.33 kWh/kg H₂ [2], which has an energy density three times higher than marine diesel (11.9 kWh/kg [3]). However, the low volumetric energy density of hydrogen is a consistent challenge for the mobile sector to overcome in today's world. In addition, the high thermal energy input needed for chemical storage is another challenge that needs to be solved to pave the way for the emission-friendly energy carrier to achieve a breakthrough in the mobile sector. In this work, four storage concepts are discussed and modeled that could be considered for ocean shipping.

I. INTRODUCTION

Most ships are powered by heavy fuel oil or marine diesel. These fuels emit carbon dioxide (CO₂), sulfur oxides (SO_x) and particulate matter when burned, which can lead to increased lung and cardiovascular disease. [1]. In particular, residents near coastal regions are severely affected. For example, in the North Sea, up to 90 percent of ship emissions escape within just 90 kilometers of the coast [1]. Therefore, researchers conducted a study to investigate the effect of aerosol particles from a ship's diesel engine exhaust on human lung cells. The result showed that heavy fuel oil is richer in organic compounds, sulfur oxides and metal oxides than marine diesel, which in turn is richer in elemental carbons (soot). As a result, the international Convention for the Prevention of Pollution from Ships (MARPOL) created Annex VI, a directive that sets stricter air pollutant requirements for ocean-going vessels. Since January 1, 2020, the global sulfur limit has been reduced from 3.5 percent to 0.5 percent. Even this significantly reduced sulfur content is still 500 times higher than the permitted sulfur content in road traffic of 0.001 percent [20]. Furthermore, filters are only occasionally installed on seagoing vessels and can cause additional environmental pollution by cleaning the filters if they are not disposed in accordance with regulations. [1, 19]. Due to the economic burden of reducing emissions by burning fossil fuels, for example CO₂-taxes, as well as political measures to reduce emissions, a restructuring of ship propulsion is inevitable. Hydrogen, with its high gravimetric energy density (33.33 kWh/kg H₂ [2]) and with its global accessibility, is a suitable substitute for fossil fuels (11.95 kWh/kg and 10 kWh/L [2]). Furthermore, hydrogen can be produced with renewable energies and does not produce any CO₂ during combustion. However, the volumetric energy density of hydrogen under

normal conditions (0.003 kWh/L H₂ [2]) is the real problem. Which is why different technologies have been developed to increase the volumetric energy density (for example, storage of compressed hydrogen). With the current state of the art, it is not yet possible to store the entire gravimetric energy density of hydrogen. Currently, hydrogen is stored either physically, in pure form, or chemically, with a storage carrier. Chemical storage systems can store the largest proportion of hydrogen. However, they have the disadvantage that high temperatures are required for storage and retrieval. Therefore, an intelligent thermal management system for these technologies is necessary to make them suitable for the drives of the future. The question is therefore to what extent the technology can be used efficiently in the mobile sector. Furthermore, it will be a challenge to make the thermal management both efficient and compact to be able to use it for the mobile sector. The most promising technologies are discussed below.

II. HYDROGEN STORING METHODS AND MECHANISM

In physical storage, the hydrogen is stored in its pure form in different phases. In this process, the hydrogen is either compressed in its gaseous state or liquefied by cooling it down (temperature at - 240 °C), which has a detrimental effect on the overall storage. For example, the liquefaction of hydrogen requires about 46 percent of the stored energy of hydrogen [4]. Likewise, physical storage is not loss-free, since hydrogen in its pure form can diffuse through all conceivable materials. Chemical storage does not have this disadvantage, since the hydrogen is stored in a storage medium. As a result, the hydrogen can be stored safely and without loss. However, the high temperatures for storage and retrieval are to be seen as a disadvantage.

A. Compressed hydrogen

The most proven storage technology for hydrogen is gas storage in pressure tanks. According to the current state of the art, pressure tanks up to 700 bar are commercially available. Compression to seven hundred times atmospheric pressure increases the energy density of hydrogen to 37 kg H₂/m³ [4], which corresponds to a volumetric energy density of 1.2 MWh/m³. However, the energy requirement for compression consumes by about 13% from the stored energy by 700 bar [4].

B. Liquid hydrogen

In this storage variant, the hydrogen is cooled down to a very low temperature (-240 °C) and stored in vacuum-insulated cryotanks. Using the Linde process, the hydrogen is liquefied by expansion [22]. With these methods, high volumetric storage densities of 70.8 kg H₂/m³ are possible, corresponding to a volumetric energy density of 2.36 MWh/m³. However, achieving the high volumetric storage density is associated with a disadvantage. The process requires almost half of the stored energy (46%) for hydrogen liquefaction and temperature maintenance. The evaporation effect (1%) and the cooling during a refuelling process (5%) increase the total loss to 52% [4]. Although the losses are high, liquid hydrogen storage is preferred for transport.

C. LOHC - Liquid organic Hydrogen carrier

Liquid organic hydrogen carriers (LOHC) store hydrogen reversibly and store it safely in liquid form under normal conditions. This compound is characterized by high specific storage densities of 5.7% - 7.3% or 50 -60 kg H₂/m³ [2]. Storage (hydrogenation) occurs through a chemical bond between the hydrogen and the organic carrier. The hydrogen is stored (hydrogenated) in the storage medium at moderate temperatures (up to 220 °C) and high pressure (up to 50 bar) and is expelled from the storage medium again by means of dehydrogenation under atmospheric pressure and high temperatures (up to 330 °C). [5, 6, 7].

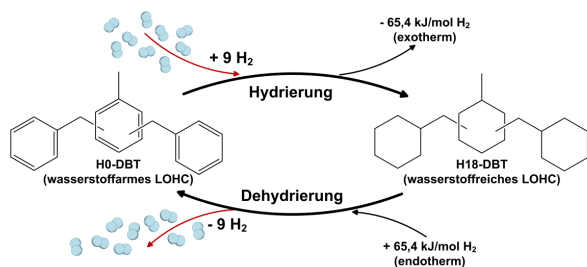


Figure 1. Reversible storage of hydrogen with liquid organic hydrogen carriers using the example of the dibenzyltoluene/perhydro dibenzyltoluene substance system [4]

A chemically reversible process includes an exothermic and an endothermic process (Fig.1). For example, in a vehicle/ship transport, only the expulsion process is of interest and thus only includes the endothermic process step, which increases the thermal energy demand of the process. In addition, the process requires a catalyst and the expelled hydrogen must be purified before it can be converted into electricity in the fuel cell. These aspects cause costs and have a negative effect on the energy balance, but the high storage densities are an enormous advantage when choosing a suitable storage medium.

D. Metal hydride

The reversible storage of hydrogen in metals takes place partly via physisorption and chemisorption. In this process, the

hydrogen atoms are stored in the intermediate lattices of the metal lattice. The compounds include binary, ternary (complex metal hydrides) and quaternary (e.g. potassium hydrogen carbonate) hydrides, with binary hydrides receiving the most attention in the literature reviewed [8, 9, 10, 11, 12, 13]. This is due to their high thermal as well as electrical conductivity, but they can also be brittle. Light metals such as lithium (Li), sodium (Na), magnesium (Ma) and aluminum (Al) are particularly interesting and allow a wide variety of metal-hydrogen mixtures. One of the advantages is that two hydrogen atoms are stored or rather adsorbed on one metal atom [14].

The charging can be done with molecular hydrogen gas or hydrogen atoms from the electrolytes. Molecular hydrogen is dissociated on the surface before adsorption, i.e. two H atoms recombine during the desorption process to form H₂. The thermodynamic aspects of hydride formation from gaseous hydrogen are described by pressure-composition isotherms (Fig.2). The host metal initially dissolves some hydrogen as a solid solution (α phase).

When the hydrogen pressure is increased along with the H concentration in the metal, interactions between the local hydrogen atoms begin. This leads to nucleation and growth of the hydride (β -phase). In the pure β phase, the hydrogen pressure increases steeply with concentration. The phase transition range ends at a critical point T_c (concentration temperature), where the transition from the α -phase to the β -phase shows a continuous course. The plateau or equilibrium pressure is strongly temperature-dependent and is related to the changes in enthalpy H and entropy S , respectively. The operating temperature (up to 350 °C) of a metal hydride system is determined by the plateau pressure in thermodynamic equilibrium (up to 10 bar) and by the overall reaction kinetics.

The highest storage densities are achieved with complex metal hydrides in combination with light elements, such as MgH₂FeH₆ with 150 kg/m³ [16], but their strong bonds to each other are a major disadvantage for their use as hydrogen storage.

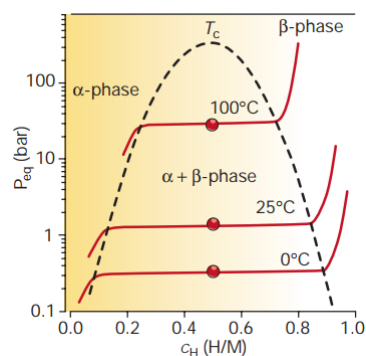


Figure 2. Pressure-concentration-temperature plot and a van't Hoff curve (logarithm of the equilibrium or plateau pressure against the reciprocal temperature) [9]

E. Metaloxid

The redox process usually consists of a two-stage process [16]. In the first stage, the metal oxide is heated to high temperatures (up to 800 °C, atm) and wetted with hydrogen. In the process, the lattice oxygen in the metal is reduced by hydrogen. Vacancies are created in the host metal and at the same time the hydrogen binds with the dissolved oxygen to form water vapour. In the reverse process, the hydrogen can be dissolved from the vapour again by the water vapour wetting the pure metal. The oxygen then replaces the oxygen vacancies in the metal and dissolves from the steam. The hydrogen that is released again is conducted out of the system. The process can be expressed with the following chemical formula.



The advantages of this process are the purity of the hydrogen obtained and the exothermic process during oxidation (hydrogen production). Due to the increase in thermal energy during oxidation, the operating temperature can be reached partly through the exothermic process. Likewise, high volumetric storage densities are achieved, as in the case of $Cu_{0,5}Co_{0,5}Fe_2O_4$ with 73.25 g/L.

III. CONCEPT DEVELOPMENT

The following concept will be simulated in Modelica. For the chemical storage technologies, the distribution of thermal energy will play a relevant role, since the processes require high temperatures and the energy input for out-storage should be kept low. Furthermore, in all concepts, the storage tanks have been defined for 100 kW gross power to make them scalable for different power classes.

In the chemical storage concepts, a pressure tank is also taken into account to bring the reactor tank to operating temperature in the event of a cold start. A hydrogen porous burner is used for this purpose. The amount of energy stored in the pressure tank is limited to heating the reactor tank or until the start of a constant hydrogen flow, so that the system can operate independently.

In all concepts using the PEM fuel cell, the waste heat from the PEM fuel cell is used for the hot and heating water supply. The product water from the fuel cell is to be used in part for the drinking and hot water supply, with the product water being temporarily stored in a water tank. A photovoltaic system on the ship is also being considered in order to charge the accumulators on board with electricity.

A. Concept 1 - Compressed hydrogen

Starting from the pressure tank (700 bar), the hydrogen feed runs directly to the PEM fuel cell (Fig.3). The initial product water, from the power generation of the fuel cell, is partly stored in a water tank and partly directly transferred to the lake water. The stored water in the tank will be used for drinking water and hot water supply. The waste heat from the power generation is to be used to heat the water in the buffer tank. If the waste heat from the PEM fuel cell is not sufficient for the

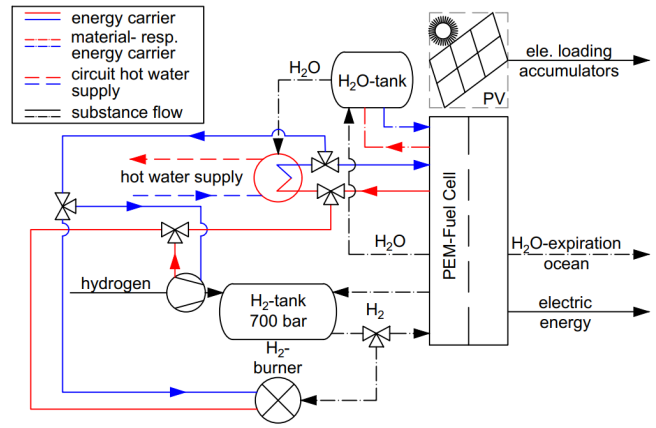


Figure 3. Concept 1 - storage system of a hydrogen pressure tank (700 bar) with thermal management and PV system

hot water or heating supply, the hydrogen burner can help out thermally. The burner is also supplied from the pressure tank.

B. Concept 2 - LOHC

The substance dibenzyltoluene is used for modeling because it has good global availability (it is also used as a heat carrier in heating technology) and high gravimetric energy density (2.07 MWh/ton_{H₁₈-DBT} (H₁₈-DBT → hydrogen loaded dibenzyltoluene) [5]. Furthermore, the simulation will be based on the LOHC plant engineering data from H₂ – Industries DBT is applied as the storage medium. The LOHC vessel is labeled "H₂ – release" in the model (Fig.??) and has a hydrogen flow of $m_{H_2} = 43$ kg/h [18]. The H₂ – release contains the loaded H18-DBT (hydrogen-loaded dibenzyltoluene) and is heated to a temperature of about 280 °C at atmospheric pressure. After purification the hydrogen mass flow is split in the system using a 3-way valve. Part of the mass flow is required for the

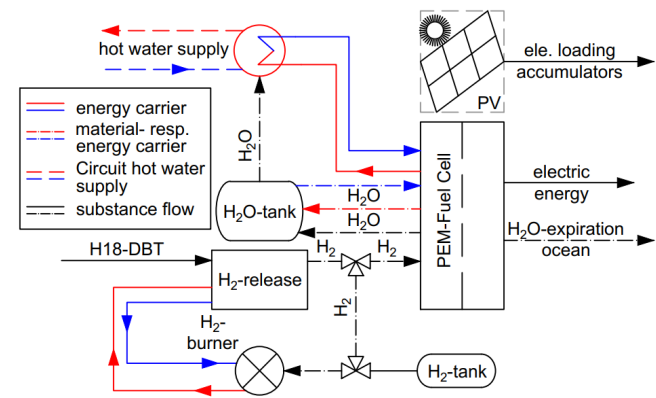


Figure 4. Concept 2 - LOHC - storage and with thermal management and PV system

continuous heat supply of the reactor tank (H_2 - release), the remaining hydrogen is fed directly into the PEM fuel cell.

C. Concept 3 - Metal hydride

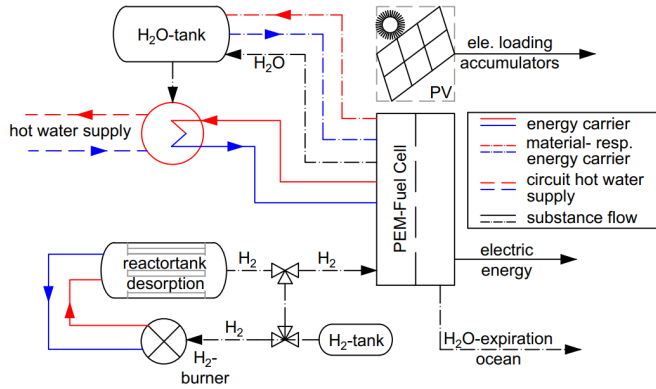


Figure 5. Concept 3 - Metal hydride - storage and with thermal management and PV system

The simple metal hydride magnesium (MgH_2) is chosen for this concept. It has a good gravimetric energy density of $2.00 \text{ MWh/ton}_{\text{MgH}_2}$ and is available worldwide. In addition, 5% natural graphite to increase thermal conductivity and a chromium-titanium-vanadium alloy (to improve sorption kinetics) are added to the magnesium [11]. The loaded magnesium hydride (MgH_2) is heated at a temperature of 340°C under atmospheric pressure (Fig.5). The dissolution of hydrogen from the magnesium is an endothermic process and extracts additional energy from the system. Therefore, some of the released hydrogen is used to power a porous burner. The porous burner is intended to contribute to temperature continuity in the reactor tank. The remaining hydrogen is fed directly into the PEM fuel cell.

D. Concept 4 - Metaloxid

For the last concept, iron oxide Fe_3O_4 is used as the oxygen carrier. Due to its worldwide availability and its good gravimetric energy density $1.60 \text{ MWh/ton}_{\text{Fe}}$, the material is ideally suited. The iron oxide is used in the form of brittle iron pellets which have a volumetric energy density of 2.60 MWh/m^3 Bulk [17]. The fourth concept is a combination of physical storage and iron Fe_x (Fig.6). The pressure tank (700 bar) is used to supply the Solid Oxide Fuel Cell (SOFC) with hydrogen during a cold start of the ship. As soon as the reactor tank with the iron pellets (Fe_x - Pellets) has reached its operating temperature (up to 700°C) due to the waste heat from the SOFC. By directing the water vapor from the SOFC into the reactor tank, with the reaction between the iron and the water vapor, iron oxide and hydrogen are produced. The hydrogen is fed directly into the SOFC, whereupon new heated water vapor is produced as feedstock for renewed hydrogen production. Furthermore, a membrane desalination plant is planned to compensate for possible bottlenecks in the water

supply. This will also be fed from the waste heat of the SOFC, as will the hot and heating water supply. If the plant requires additional steam, the steam generator will be thermally supplied by the porous burner.

IV. CONCLUSION

In this work, the best-known hydrogen storage systems were presented and discussed. The most promising hydrogen storage systems will be simulated for use in maritime shipping to form a driving scheme in the area of storage. The described concept will serve as the basis for a subsequent simulation. In the simulation, it is to be investigated to what extent thermal management can be optimised, especially in chemical storage systems, in order to find the optimum efficiency for power generation. In the following simulation, for example, the extent to which the efficiency can be optimised by equipping the systems with a solid oxide fuel cell (SOFC) will be investigated. So far, the SOFC is only intended for concept 4, as very high operating temperatures are used. In addition to thermal management, space utilisation and the maximum cargo weight of the ship will also play a decisive role, as the volumetric and gravimetric storage densities of the systems are only about one sixth of the storage densities of marine diesel. It will also be examined whether a combination of two different hydrogen storage systems is more efficient. A combination of metal oxide and LOHC or metal hydride is conceivable due to the different temperatures, as metal oxides have an operating temperature between 600°C and 800°C . It is therefore conceivable to use the waste heat from the metal oxide process for the dehydrogenation of the LOHC or metal hydrides.

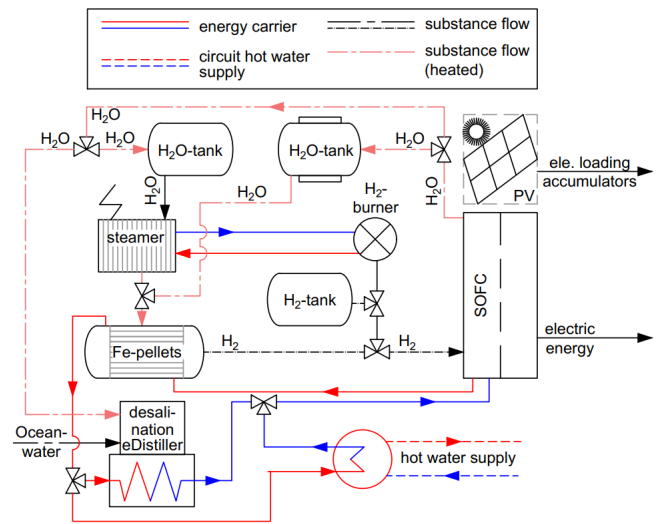


Figure 6. Concept 4 - Metaloxide - storage and with thermal management and PV system

REFERENCES

- [1] **C. Brüninghaus**, Gesundheitsgefahr durch Schiffsdiesel-Abgase, Verlag Springer, **2015**
- [2] **C. Krieger**, Verfahrenstechnische Betrachtung und Optimierung der Freisetzung von Wasserstoff aus organischen Trägermaterialien (LOHC), Dissertation - TU Erlangen-Nürnberg, **2019**
- [3] **Magazin Wissenschaft**, www.wissenschaft.de, **2017**
- [4] **K. Jorschick**, Ein-Reaktor-Konzept und Mischgashydrierung als Verfahrensvarianten zur Effizienzsteigerung in der LOHC-basierten Wasserstoffspeicherung, Dissertation TU Erlangen-Nürnberg, **2019**
- [5] **M. Müller**, Entwicklung und Betrieb einer Anlage zur kontinuierlichen Hydrierung von flüssigen organischen Wasserstoffträgern im Technikumsmaßstab, Dissertation TU Erlangen-Nürnberg, **2018**
- [6] **K. Obesser**, Synthese und Charakterisierung von heterogenen Katalysatoren zur Wasserstofffreisetzung aus Dodecahydro-N-Ethylcarbazol, Dissertation TU Erlangen-Nürnberg, **2016**
- [7] **H. Jorschik, M. Geißelbrecht, M. Ebl, P. Preuster, A. Bösmann, P. Wasserscheid**, BT/DBT-based mixtures as suitable LOHC systems for low temperature applications, *Int. Journal of Hydrogen energy*, **2020**, 45, 14897-14906
- [8] **T. Sinigaglia, F. Lewiski, M. Santos Martins, J. Cezar Mairesse Siluk**, Production, storage, fuel stations of hydrogen and its utilization in automotive applications a review, *Int. Journal of Hydrogen energy*, **2017**, 42, 24597-24611
- [9] **A. Züttel, L. Schlapbach**, Hydrogen-storage materials for mobile applications, *Nature*, **2002**, 414, 353-358
- [10] **S. Niaz, T. Manzoor, A. Pandith**, Hydrogen storage: Materials, methods and perspectives, *Renewable and Sustainable Energy Reviews*, **2015**, 50, 457-469
- [11] **A. Chaise, P. de Rango, Ph. Marty, D. Fruchart**, Experimental and numerical study of a magnesium hydride tank, *Int. Journal of Hydrogen energy*, **2010**, 35, 6311-6322
- [12] **T. Güney**, Auslegung eines Metallhydrid-Wirbelschichtreaktors zur Speicherung von Wasserstoff und Durchführung einer Wirtschaftlichkeitsanalyse, Diplomarbeit – TU Wien, **2016**
- [13] **L. Lemmerz**, Molekulare Magnesiumhydride und bimetallische Lithiumhydridoaluminat, Dissertation – RWTH Aachen, **2019**
- [14] **J.O. Abe, A. Popoola, E. Ajenifuja, O. Popoola**, Hydrogen energy, economy and storage: Review and recommendation, *Int. Journal of Hydrogen energy*, **2019**, 44, 15072-15086,
- [15] **L. Schlapbach**, Hydrogen in intermetallic Compounds I. Electronic, Thermodynamic, and Crystallographic Properties, Preparation, *Topic in Applied Physics*, Vol. 63, Springer Verlag, **1988**
- [16] **D. Zeng, M. Li, Y. Qiu, L. Ma, D. Cui, S. Zhang, R. Xiao**, A High-performance ternary ferrite-spinel material for hydrogen storage via chemical looping redox cycles, *Int. Journal of Hydrogen energy*, **2019**, (Article in Press)
- [17] **B. Gamisch, M. Gaberer, B. Dawoud**, An Experimental Study on the Kinetics of the Redox Reactions and Mechanical Stability of Iron Oxide Pellets, *Journal of Chemical Engineering of Japan*, 99, 9, 1-9, **2020**
- [18] *H₂ – Industries*, Datasheet *H₂ – release*, **2020**
- [19] **International Maritime Organization**, Prevention of Air Pollution from Ships - Annex VI, www.imo.org **Stand Mai 2021**
- [20] **Umweltbundesamt**, Seeschifffahrt, www.umweltbundesamt.de **Stand Mai 2021**
- [21] **B. Gamisch, M. Gaberer, B. Dawoud**, The kinetics of lightweight solid-state hydrogen storage materials: A review, *Int. Journal of Hydrogen energy*, **2016**, 41, 13131 - 13151
- [22] **R. Ayber**, Thomson-Joule-Effekt von Methan-Wasserstoff- und Äthylen-Wasserstoff-Gemisch, VDI-Verlag Band 511 **1965**

Investigations regarding cooling of thermoelectric modules in a nano combined heat and power unit

Nico Pellert
 department of process engineering
 Technische Hochschule Georg Simon Ohm
 Nürnberg, Deutschland
 pellertni67685@th-nuernberg.de

Abstract— The efficient cooling of thermoelectric modules (TEM) is very important for the yield of electrical energy. In this research work, water coolers with different cooling structures are investigated. The examined coolers can basically be divided into the categories single cooler and multiple cooler. The aim is to find out whether water-guided cooling is suitable for thermoelectric modules when they are exposed to a heat flux density of 10 W/cm^2 . For this purpose, the operating parameters are defined by the thermoelectric modules and used for an initial, theoretical design in the first phase of research. The surface temperature on the cold side of the thermoelectric modules must not exceed a maximum temperature of $80 \text{ }^\circ\text{C}$. The water coolers and the thermoelectric modules are used to equip a gas condensing boiler in order to convert it into a nano combined heat and power unit (CHP). The coolers are therefore supplied with heating water, which is circulated by the integrated heating pump. Another aspect of this research work is thus the investigation of the pressure loss generated by the water coolers. This additional pressure loss must not exceed 20 mbar per cooler to avoid reinvesting the gained electrical energy in the system via the heating pump. To verify the theoretically designed water coolers, they are manufactured using the selective laser melting process (SLM) and mould casting. This paper summarises the findings from two previous project works and presents the measurement results for the cooling water mass flows of 26.9 g/s and 42.1 g/s. It turns out that the surface temperature is not the limiting factor. In the worst case, this is $80 \text{ }^\circ\text{C}$ for cooler V5oR and in the best case $29 \text{ }^\circ\text{C}$ for cooler V1. The maximum estimated pressure loss of 20 mbar can only be maintained if the lowest cooling water mass flow of 26.9 g/s and a straight type of connection are selected. For the single coolers, the best solution is the cooler V1M with a pressure loss of 19 mbar and a surface temperature of $58 \text{ }^\circ\text{C}$. In the case of the multiple cooler, the variant V5mR is the best solution. This variant causes a maximum pressure loss of 20 mbar and a surface temperature of $66 \text{ }^\circ\text{C}$.

Keywords— water cooler, thermoelectric generators, thermoelectric modules, TEM, TEG, CHP-unit

I. INTRODUCTION

In the research project "Development of a nano-CHP unit based on thermoelectric modules (TEM) for combined heat and power generation in single family homes", a condensing gas boiler is modified. In addition to the hot water and heating water that is normally produced, it is also possible to obtain electrical power. The combined use of gas as a fuel for heat and electricity turns the gas condensing boiler into a nano CHP-unit. The compact system aims at an electrical output of 300 Watts and uses therefore 20 TEMs. This classifies the system as a nano-CHP unit [1]. In this research work, water coolers are designed for the cold side of the thermoelectric modules. These designs are based on the approaches of the "VDI-Wärmeatlas" [2] and served as an initial assessment of the properties of the various cooler structures.

The main purpose of this research work is to find out whether thermoelectric modules can be cooled economically and sufficiently well with water coolers. In addition, it is to be determined whether the different cooling structures differ significantly in their properties with regarding to heat transfer and pressure loss. As shown in the first phase of the research work, the connection type of the coolers for a series connection poses a problem in terms of space management and pressure loss [1]. A further goal is therefore to quantitatively estimate how great the influence of the connection type is on the performance of the coolers.

For the reasons mentioned above, the water coolers are made from aluminum AlSi10Mg using the SLM process and mould casting. The manufactured coolers are then examined on a test stand.

A. Boundary conditions of the system

The TEMs are subjected to a heat flux density of 10 W/cm^2 and thus absorb a heat flux \dot{Q} of 160 W per TEM over a surface A_{TEM} of 16 cm^2 during operation. This heat flux must be taken up by the cooler so that the TEM does not overheat. In the research work, it is specified that the temperature difference between the cooling water inlet ϑ_{in} and the cooling water outlet ϑ_{out} should only be 1 K. With (1), this results in a design cooling water mass flow \dot{M}_{cw} of 42.1 g/s.

To avoid damage, the surface temperature ϑ_{sur} of the TEM on the cold side must not become too high during operation. Based on empirical values from the involved project partners, a maximum value of $80 \text{ }^\circ\text{C}$ results for this temperature [1].

The water coolers represent an additional flow resistance, which would not be existent with a conventional gas boiler. In order not to reinvest the electrical energy gained by the TEMs via the heating pump, a pressure loss Δp of 20 mbar per water cooler must not be exceeded [1]. This pressure loss is calculated in (2) via the roughness of the inner surface of the coolers λ_i , the hydraulic diameter d_{hyd} , the pressure loss coefficient of the flow path deflections ζ_d , the density of the cooling water ρ_{cw} and the velocity of the cooling water w_{cw} .

With the boundary conditions set, it is possible to determine the geometry of the coolers. For this it is necessary to establish a second relationship between the transferred heat flux and the surface temperature of the TEM, see (3). The heat transfer capacity of the water cooler is represented by the product $k \cdot A$ in (4). The heat transfer surface A_{ht} and the heat transfer coefficient α_{cw} of the cooling water are influenced by the hydraulic diameter. The geometric determination of the coolers is thus an iterative process that continues until all boundary conditions are met.

$$\dot{Q} = \dot{M}_{cw} \cdot c_{p,cw} \cdot (\vartheta_{out} - \vartheta_{in}) \quad (1)$$

$$\Delta p = \left(\lambda_l \cdot \frac{l}{d_{hyd}} + \zeta_d \right) \cdot \frac{\rho_{cw}}{2} \cdot w_{cw}^2 \quad (2)$$

$$\dot{Q} = k \cdot A \cdot \frac{(\vartheta_{sur-in} - \vartheta_{sur-out}) - (\vartheta_{sur-out} - \vartheta_{out})}{\ln\left(\frac{\vartheta_{sur-in} - \vartheta_{in}}{\vartheta_{sur-out} - \vartheta_{out}}\right)} \quad (3)$$

$$k \cdot A = \left(\frac{1}{\alpha_{cw} \cdot A_{ht}} + \frac{s_{CB}}{\lambda_{AL} \cdot A_{TEM}} \right)^{-1} \quad (4)$$

The thickness of the cooler base s_{CB} , the thermal conductivity of the aluminum λ_{AL} and the contact surface A_{TEM} of the TEM also play a role in heat transfer but are not directly related to the pressure loss.

II. STRUCTURE OF THE EXAMINED COOLERS

During the design phase in the first project work, six different cooling structures were created, see Fig. 1. These structures can be divided into the main categories of single coolers and multiple coolers. The water coolers V1, V1M, V2, V3, V4-3D and V4 are single coolers. This means that only one TEM per cooler can be cooled. The single coolers can be described as aluminum cubes with an internal cooling structure. The cubes have an average edge length of 50 mm. As an example of the dimensions, cooler V1 is shown in Fig. 2. The cooler V4 is the only non-printed cooler with a copper helix cast in aluminum. The cooler V4-3D also has a helix structure on the inside and was printed, but a manufacturing error occurred here, which meant that this cooler had to be eliminated for investigation. The cooler V5 in its original form is a multiple cooler that can cool five TEMs simultaneously, see Fig. 3. For the measurement experiments, the cooler V5 is modified so that it only cools one TEM. This makes it easier to handle and increases the comparability to the single water coolers. With the cooler V5, the TEM can be supplied with fins (mR) or without fins (oR). The fins are increasing the heat transferring surface of the TEM and achieve a better cooling effect. The single water coolers can only be operated without fins on the TEM.

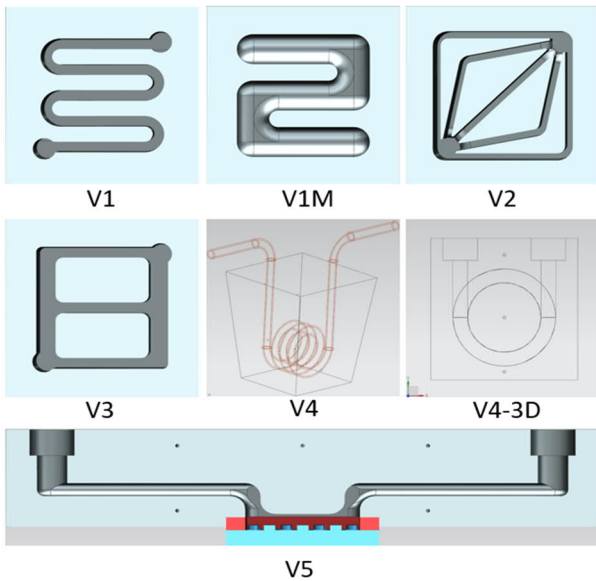


Fig. 1. Different cooling structures

To state out the small size of the flow channels Table I shows the geometric data of the water coolers. In this table the wetted surface describes the contact area between the cooling water and the aluminum body of the water coolers. Therefore, the wetted surface equals the heat transferring surface A_{ht} .

The concept of cooler V5 differs considerably from the others. To demonstrate the functioning of this cooler more clearly, Fig. 4 shows the path of the cooling water. The cooler V5 seals directly on the TEM with a gasket. Therefore, the cooling water is in direct contact with the TEM. This means that great care must be taken when mounting the cooler V5, otherwise the cooler will leak. This is a major disadvantage of the multiple cooler concept. The required seal takes up surface area on the TEM and thus impairs heat transfer compared to the single coolers. However, thermal expansion and stress can be absorbed by the seal, which is again an advantage. The attachment of the cooler V5 to the gas condensing boiler can thus be kept much simpler.

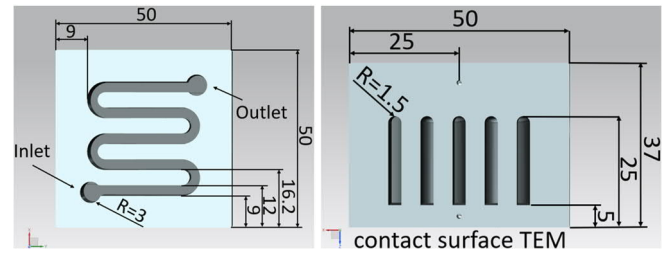


Fig. 2. Sectional view of cooler V1

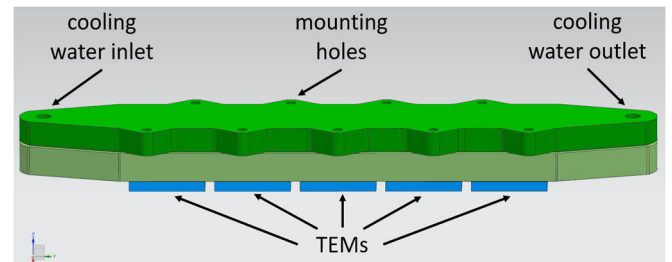


Fig. 3. Original design of the cooler V5

TABLE I. SUMMARY OF THE GEOMETRIC DATA OF THE WATER COOLERS

	channel width	channel depth	flow cross section	wetted surface
	[mm]	[mm]	[mm ²]	[mm ²]
V1	3	20	60	70.9
V1M	8	10	66.3	29.1
V2	2	20	184.4	94.9
V3	3	20	180	67.0
V4	-	-	19.6	58.2
V5mR	30	4	72	1350
V5oR	30	4	120	900

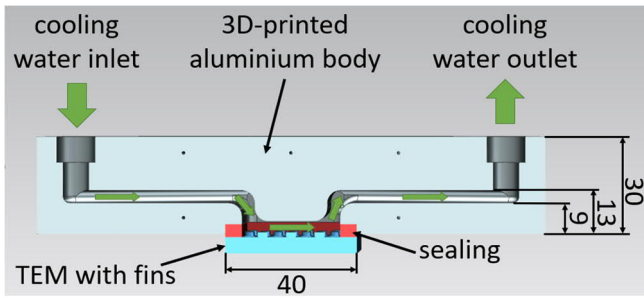


Fig. 4. Sectional view of cooler V5mR

III. DESIGN OF THE TEST STAND

To be able to correctly measure the pressure loss generated by the water coolers, the hydraulic circuit of the test stand in Fig. 5 is set up according to the specifications of DIN EN 1267:1999-11. The cooling water flows through a coriolis sensor to determine the mass flow. The valves are used to regulate the flow continuously. A pressure measuring point and a temperature measuring point are located before and after the respective water cooler. This allows the measurement of the absorbed heat flux of the cooling water and the generated pressure loss. To create a high confidence basis for the measured values, class A PT100 sensors are used for the temperature measurements in the cooling water. The pressure loss is recorded by a diaphragm differential pressure meter.

The heat source is temperature controlled and operated with two 160 W heating cartridges. A measuring block is connected between the heat source and the water coolers to even the resulting temperature profile. This ensures that the water coolers are exposed to a homogeneous temperature over the entire TEM contact surface [4].

A. Definition of the tests

The measurements are carried out at two different cooling water temperatures, 22 °C and 50 °C. At first, a cooling water temperature of 22 °C is assumed, which corresponds to the room temperature of the laboratory. This will limit heat losses from the cooling water to the environment. The temperature of 50°C represents the typical averaged level of a heating return in a single family household [1]. The way the coolers are connected to the cooling water supply is also changed. On the one hand, a 90° plug-in bow and on the other hand a straight plug-in connector is used. This makes it possible to point out the influence of the way the coolers are connected. The cooling water mass flow is varied around the operating point of 42.1 g/s in 12 % steps. The variation enables the measurement data from this work to be used for later interpolations. By varying the cooling water mass flow, it is also possible to determine if the operating point has been correctly selected. The temperature of the heat source is adjusted during the measurements so that a heat flux of 160 W is absorbed by the cooling water. Due to thermal length expansions, the contact pressure changes during the measurements. It is ensured that the surfaces relevant for heat conduction are pressed together with a minimum force of 320 N [4]. The average contact force during the measurements lies between 500 N and 550 N. However, the maximum contact force of 2 kN is caused by the limit of the load cell and must not be exceeded. The conditions of the measurement tests are summarized in Table II.

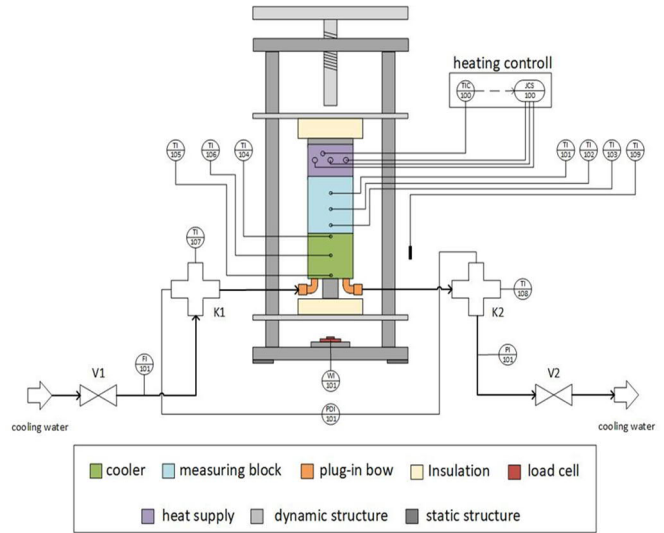


Fig. 5. Design of the test stand

TABLE II. DEFINITION OF THE TESTS

connector	[-]	90°-bow; straight
inlet temperature cooling water	[°C]	22; 50
mass flow cooling water	[g/s]	26.9-57.3
heat flux cooling water	[W]	160
contact force min/max	[N]	320/2000

IV. RESULTS

A. Surface temperature TEM

Fig. 6 shows the surface temperature of the TEM for two different cooling water mass flows and connection types for the respective water cooler. The surface temperature of the TEM at the design mass flow of 42.1 g/s is well below 80 °C for all investigated coolers. It can be stated that the basic temperature level is raised by increasing the cooling water temperature. It is noticeable that the different cooling structures have only a minor influence on the surface temperature of the TEM. However, the variants of the cooler V5 are an exception here. Due to the special sealing of this cooler, the heat transferring surface of the TEM is reduced. This results in a higher surface temperature compared to the single coolers.

The type of connection also has only a small influence on the surface temperature of the TEM. If the cooling water mass flow is reduced to 26.9 g/s, the surface temperature rises. Here, the maximum permissible temperature of 80 °C is reached by the water cooler V5oR.

Regarding the surface temperature of the TEM, the single cooler V1 with bows performs best. Here, a maximum surface temperature of 29 °C is achieved at a cooling water mass flow of 42.1 g/s and a cooling water temperature of 22 °C. In the case of the multiple cooler, the variant V5mR with bows also performs best at a cooling water mass flow of 42.1 g/s and a cooling water temperature of 22 °C. In this case, the surface temperature does not exceed 37 °C.

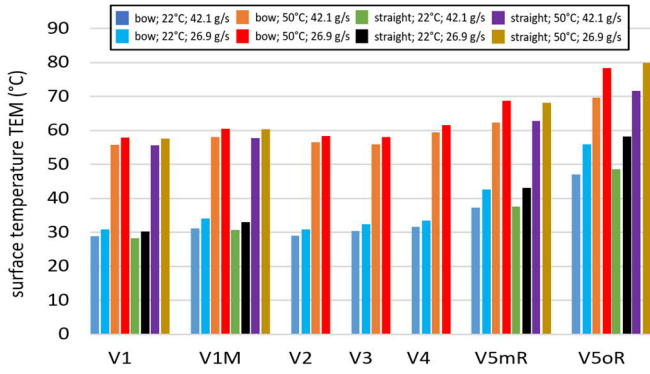


Fig. 6. Surface temperature of the TEG at a cooling water mass flow of 26.9 g/s and 42.1 g/s

B. Pressure loss

Fig. 7 shows the pressure loss generated by the water coolers for two different cooling water mass flows and the different connection types. It turns out that the different cooling structures have little influence on the pressure loss. The change in the type of connection has a far greater influence. The pressure loss is also reduced at a higher cooling water temperature. This effect is due to the reduced viscosity of the cooling water and is relatively small compared to the change of connection type.

Even with an optimal configuration of 50 °C cooling water temperature and straight connection plugs, the maximum pressure loss of 20 mbar is exceeded at a cooling water mass flow of 42.1 g/s. Only with the smallest investigated cooling water mass flow of 26.9 g/s it is possible to maintain the specified maximum pressure loss. The cooling water mass flow of 42.1 g/s was chosen to ensure that the TEM does not overheat. Since a maximum surface temperature of the TEM is maintained on the cold side even with a much lower cooling water mass flow of 26.9 g/s, this can be permanently reduced.

In the case of the single coolers, the cooler V1M with straight connections performs best in terms of pressure loss. At a cooling water mass flow of 26.9 g/s and a cooling water temperature of 50 °C, this cooler causes a pressure loss of 19 mbar. With the multiple cooler, the V5oR variant has a slightly advantage compared to the cooler V5mR. At a cooling water mass flow of 26.9 g/s and a cooling water temperature of 50 °C, the cooler V5oR produces a pressure loss of 20 mbar.

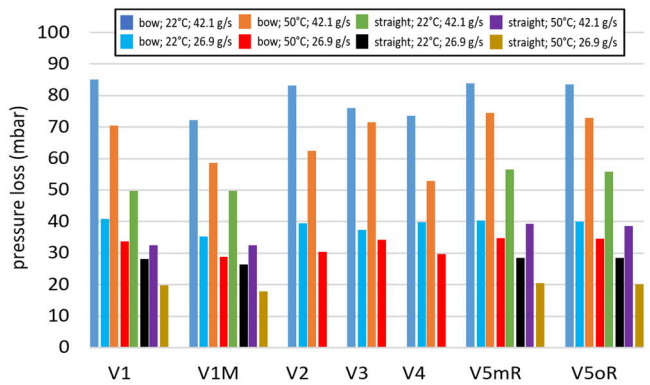


Fig. 7. Pressure loss at a cooling water mass flow of 26.9 g/s and 42.1 g/s

V. COMPARISON OF THE PREVIOUS CALCULATED DATA WITH THE EXPERIMENTAL DATA

The water coolers are designed for a cooling water mass flow of 42.1 g/s. The question now is how well this design reflects the measurement results. The error calculation during the evaluation of the measurement data showed that the measurements have a very high accuracy. The measured surface temperature of the TEM can be given with a maximum uncertainty of ±0.19 K. The measured pressure loss has a maximum uncertainty of ±0.42 mbar. Due to this high measurement accuracy, the recorded measurement data should be considered as a true value.

Fig. 8 shows the deviation between the calculated and the measured surface temperature of the TEM. The surface temperature can be predicted to an average of ±3.5 K using the relevant calculation methods. For a first rough interpretation, this deviation can be rated as very good. With the data now available, the calculations can be adjusted. The main causes of the deviations of the surface temperature of the water cooler base lie in the assessment of the flow in the respective water cooler. For more precise results, the calculation should take a closer look at whether laminar or turbulent flow is present.

Fig. 9 shows the calculated and measured pressure loss of the water coolers. Most of the deviations between the calculated and measured data are in the range of ±8.7 mbar. This is a very good result. The pressure loss of the single water coolers tends to be calculated too high. The reason for this could also be the wrong estimation of the present flow characteristics in the fluid. The narrow dimensions of the fluid channels lead to the flow being assumed to be laminar in the calculation. The inflow and outflow conditions are also taken into account when calculating the pressure loss. These inflows and outflows are considered with too much turbulence. However, this assumption is incorrect according to the measurement results.

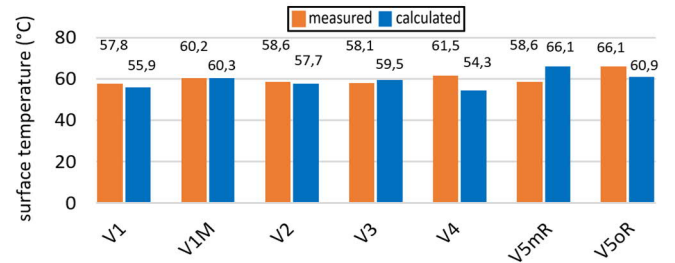


Fig. 8. Calculated an measured surface temperature at a cooling water mass flow of 42.1 g/s

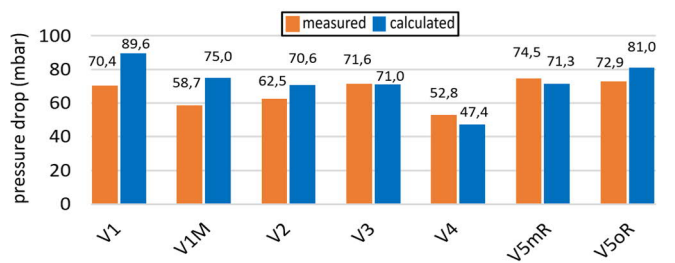


Fig. 9. calculated and measured pressure loss at a cooling water mass flow of 42.1 g/s

VI. LATER CONFIGURATION OF THE SYSTEM

During the research work, it became apparent that the limiting factor is not the surface temperature of the TEM but the pressure loss [4]. In the future nano CHP-unit, 20 TEMs will be used. The coolers are connected in parallel and in series for later use. Five coolers are connected in series to form a cooling row, resulting in 4 rows. To emphasize the advantage of the multiple cooler, the pressure losses of the final configuration are shown in Table III at a cooling water mass flow of 26.9 g/s. The measurements with straight connectors were not carried out for every cooler. For this reason, not all coolers are listed in Table III. The individual pressure losses of the single coolers can be easily added up, as they are in series. The multiple cooler in its original form can supply 5 TEMs. The research work shows that the pressure loss is mainly generated by the joints of the water coolers. In their installation situation, the single coolers have ten connection points, the multiple cooler only two. This means that the pressure loss can be reduced even further.

The cooler V1M has the lowest pressure loss of the individual coolers and falls below the maximum permissible pressure loss of 100 mbar. For this reason, the V1M cooler is the best solution for the nano CHP when it comes to choosing a single cooler. Since there is no significant difference in the pressure loss of the variants V5mR and V5oR, the lower surface temperature is used as the decisive criterion. The variant V5mR is therefore selected for the category of the multiple coolers. The cooler V5mR also falls below the maximum permissible pressure loss of 100 mbar.

TABLE III. PRESSURE LOSS AND SURFACE TEMPERATURE OF A COOLER ROW WITH STRAIGHT CONNECTORS

$M_{cw} = 26.9 \text{ g/s}$	Δp_s	ϑ_{sur}
	[mbar]	[°C]
V1	98.7	55.8
V1M	89.2	58.4
V5mR	77.6	66.3
V5oR	77.6	74.6

VII. CONCLUSION

One of the most important results of the two project works of this research is the influence of the different cooling structures on the surface temperature of the TEM and the pressure loss. Regarding the surface temperature, the cooling structure and the way the water coolers are connected have only a slight influence. The surface temperature is significantly influenced by the cooling water mass flow and the temperature level of the cooling water. The best cooling effect is achieved by the single coolers. The investigated variants of the multiple cooler V5 are also significantly influenced by the cooling water mass flow and the temperature level of the cooling water, but here it also plays a very important role whether the TEM is equipped with or without fins. Considering the pressure loss, the different cooling structures and cooling water temperatures have only a minor influence. The situation is similar for the multiple coolers. It is almost irrelevant whether the cooler V5 is operated with or without fins on the TEM. It has been shown that the connection type of the water cooler has a very large influence on the pressure loss. Therefore, care should be taken that the water coolers are connected with straight connectors. The single coolers cannot be reduced in the number of

connections they require, here the concept of the multiple cooler clearly has an advantage. The multiple cooler offers the greatest potential for reducing the pressure loss and ensuring energy-saving operation of the nano-CHP unit.

Through the results obtained, it turns out that there is no perfect cooler. The ratio between cooling capacity and pressure loss should therefore be balanced. For the individual coolers, the best solution is the cooler V1M. In the case of the multiple cooler, the variant V5mR is selected.

The cooling water mass flow can be reduced from the design point of 42.1 g/s to 26.9 g/s through the results of this research. With this lower mass flow, a sufficient cooling effect is achieved and the required electrical energy input for the heating pump is reduced.

The measured and processed data in this research work have a very high accuracy due to the use of DIN EN 1267:1999-11. The measured surface temperature can be given with an uncertainty of $\pm 0.19 \text{ K}$, the measured pressure loss with an uncertainty of $\pm 0.42 \text{ mbar}$. These small inaccuracies contribute to a very high confidence level of this work. This research also shows that the methods from the “VDI-Wärmeatlas” [2] are suitable for an initial design of water coolers with a complex cooling structure. For the next step, the water coolers should be examined regarding their inlet flow conditions. This is where the greatest potential lies to reduce the pressure loss and thus the operating costs for the nano-CHP unit.

The key findings are:

- thermoelectric modules can be operated with water-guided coolers without exceeding a maximum pressure loss of 20 mbar per cooler.
- The different cooling structures of the water coolers have a negligible influence regarding surface temperature of the TEM and generated pressure loss.
- The type of connection to the cooling water supply has a major influence on the pressure loss.
- Single coolers achieve a better cooling effect but generate more pressure loss
- The multiple cooler produces less pressure loss, but causes a higher surface temperature on the TEM.
- The methods of the “VDI-Wärmeatlas” are suitable for an initial design of complex flow geometries.

REFERENCES

- [1] Nico Pellert, “Entwicklung eines elastischen Wasserkühlers zur Kühlung thermoelektrischer Module (TEM) und Warmwassererzeugung in einem Nano-Blockheizkraftwerk”, Projektbericht 1, Nürnberg, 2020
- [2] VDI-Gesellschaft, “VDI-Wärmeatlas”, 12. Aufl., Darmstadt, 2013.
- [3] Deutsches Institut für Normung, “DIN EN 1267:1999-11”, Berlin, 2012
- [4] Nico Pellert, “Validation of the design of different concepts for cooling thermoelectric modules (TEM) in a nano combined heat and power unit”, Projektbericht 2, Nürnberg, 2021

Development of the control strategy for the heating system in the MAGGIE research project

Author: Michael Preis
 Master Applied Research in Engineering Sciences
 OTH Regensburg
 Germany
 Email: michael.preis@st.oth-regensburg.de

Supervisor: Prof. Dr.-Ing. Christian Rechenauer
 Faculty of Mechanical Engineering
 OTH Regensburg
 Germany
 Email: christian.rechenauer@oth-regensburg.de

Abstract—This electronic document describes the basic control strategy for the heating system in the MAGGIE research project, which is responsible for an efficient and reliable operation of this heating system. The functionality still has to be validated during normal operation.

I. INTRODUCTION

Germany just reached its climate goals for 2020. With a decrease of 8.7% in greenhouse gas emissions compared to 2019, the reduction in comparison to the year 1990 is 40.8%. However without the corona pandemic, Germany would have probably missed its 40% goal [1]. The constitutional court also put the German government under pressure claiming that the climate goals are not sufficient. In reaction to that the government tightened the climate protection act. The new goals are as follows [2]:

- 2030: Reduction in greenhouse gas emissions by 65% in comparison to 1990
- 2040: Reduction in greenhouse gas emissions by 88% in comparison to 1990
- 2045: Climate neutrality

Essentially this means that the reduction in greenhouse gas emissions must be accelerated. This is only possible if the use of fossil fuels is drastically reduced. Apart from the industrial and the transportation sector, which are highly dependent on fossil fuels and thus offer opportunities for reduction, the building sector in Germany has also huge potential for a decrease in greenhouse gas emissions. This is due to the rather poorly insulated building stock. On the other hand the regulations for new buildings are rather strict. The goal for old buildings now is to reach the high efficiency standards of new buildings. For further improvement in the use of energy, the use of new technologies for heating systems is currently being researched in the MAGGIE project. To reach a higher efficiency, the control strategy of such complex systems must be matched to perfectly fit the requirements. The aim of this paper is to present the developed control strategy of the heating system which represents the basis for further improvements and additions, such as the implementation of an artificial intelligence.

II. THE MAGGIE RESEARCH PROJECT

MAGGIE is a building refurbishment project. The building itself is shaped like a „U“, located in Regensburg, Bavaria, Germany and belongs to the building cooperative Margaretenau EG. It essentially consists of six linked houses. What makes it special is the variety of technologies being used. With MAGGIE the aim is to drastically increase the energy efficiency, decrease energy losses and thus decrease the running costs which effectively will lower the warm rent.

The project started with a structural stocktaking followed by conversion measures. These measures included the renovation of the basement, the first and the second floor whereas the attic was completely rebuilt. Thereby the first and second floor reached a KfW efficiency house standard of 70 and the attic even reached 55.

At first glance the technology seems rather basic due to the fact that most of the components are well known. The challenge is to combine everything to one system. The roof has a photovoltaic system installed which generates electric power for the residents. The hybrid heating system consists of three heat generators. The heat pump provides heating water at lower temperatures up to 62°C. The combined heat and power plant (CHP) simultaneously produces heating water at high temperatures of at least 80°C and electric power for the residents. The gas boiler is mainly used for emergencies in case that one of the other two heat generators is being maintained. In this case the gas boiler has enough heating power to supply the whole building with heating water up to temperatures of 95°C. The artificial intelligence combines data from the electricity market forecast, the user forecast and the weather forecast to find the most cost and energy efficient operation point for the MAGGIE system. Figure 1 shows the building after refurbishment.

III. THE CONTROL STRATEGY

The hybrid heating system is responsible for the provision of heating water. On the one hand this water is used for the heating of the building. On the other hand it is also used to generate hot drinking water in the fresh water station of each apartment. The aim of the control strategy is to guarantee a reliable as well as a efficient operation of the system.



Figure 1. The U-shaped building for the MAGGIE research project after the refurbishment [3].

A. System requirements and structure of the hybrid heating system

Figure 2 shows a very simplified hydraulic scheme of the hybrid heating system. The heating water is heated in the heating center. For the heating of the building the heating water is directly transported to the radiators or the underfloor heating system. For the hot water generation the heating water is first transported to the house heating center, which essentially consist of a buffer and a couple of valves, and then transported to the fresh water station. The system can be described as a three pipe system since it has one supply pipe for the heating of the building, one supply pipe for the hot water generation and one joint return pipe. In total there are six house heating centers and thirty fresh water stations.

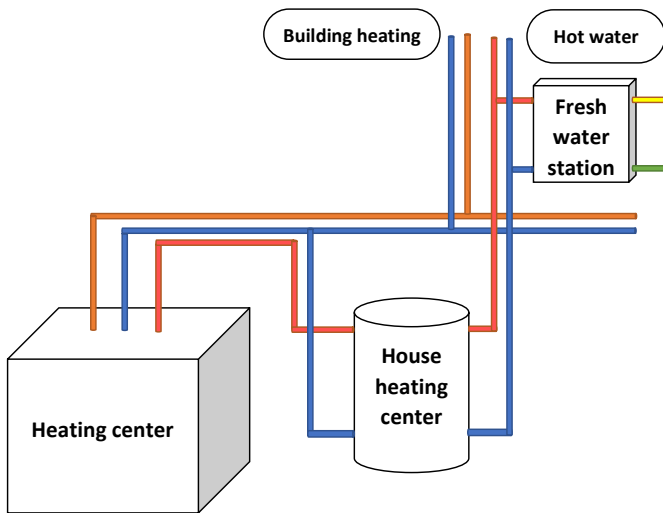


Figure 2. A simplified hydraulic scheme for the hybrid heating system with one of six house heating centers and one of thirty fresh water stations.

For the generation of hot drinking water in the fresh water stations, a heating water temperature of 70°C is required. The drinking water will be heated with the flow-through principle in a plate heat exchanger. This means, that the heating water

enters the heat exchanger on one side and transfers its heat to the drinking water, which enters the heat exchanger on the other side. After the heat exchange the heating water leaves the heat exchanger at a lower temperature whereas the drinking water leaves at a higher temperature of 50°C. Figure 3 displays the hydraulic scheme for the fresh water station in an apartment.

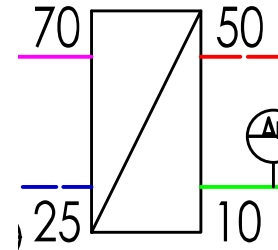


Figure 3. The hydraulic scheme for the fresh water stations [4].

The apartment heating consists of two different systems. Five out of the six houses have underfloor heating systems installed whereas one house has radiators. The heating water for the heating of the building needs temperatures up to 55°C. This temperature is required to supply the radiators. The underfloor heating system only needs temperatures up to 42°C. While lower temperatures are better for the efficiency of the heat pump, the purpose of the radiators is to investigate the behavior of named heat pump at higher temperatures. The control strategies can be separated into three different modes. Each mode can be again separated into three partial states. The heating mode requires the least heating power whereas the combined heating and hot water mode requires the most heating power. Figure 4 displays the simplified hydraulic scheme for the heating center. The components are:

- Heat generators: Heat pump, CHP, Gas boiler
- Mixing valves: M1, M2, M3
- Pumps: Building heating pump P_HZ, Hot water pump P_PWH

It should be noted that even so one pump is named hot water pump, this pump still only circulates heating water for the fresh water stations in the apartments and not the hot drinking water itself. The different control strategies and their partial states including the operating status of each component are summarized in Table I. For simplicity the heat generators and the pumps are only described as „on“and „off“.

For the mixing valves on the other hand the valve position or the temperature according to which the control is performed is indicated. Only exception is the mixing valve M2 during the partial state A2 in which the valve is controlled according to a special table. This is necessary to avoid oscillations in the control circuit. The possible positions for a mixing valve are shown in Figure 5. The mixing mode is a controlled operation in which a temperature target value shall be reached. The passageway positions let water path through to gate AB from only one gate, either A or B.

The target temperature TVLCSoll is the required temperature for the heating water to heat the building. TVLCSoll is regulated according to the heat curve in Figure 6. TVLASoll is the target temperature for the heating water to generate hot drinking water. TVLASoll thus corresponds to a temperature of 70°C. Table II summarizes the most important technical data.

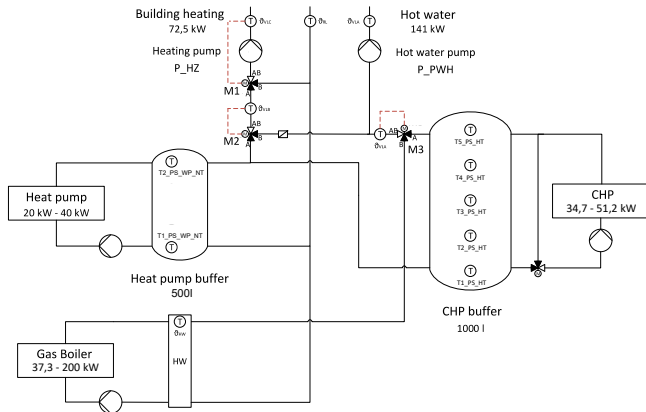


Figure 4. The simplified hydraulic scheme for the heating center [5].

Table I
OVERVIEW OF THE CONTROL STRATEGIES

Component	A Heating mode		
	1	2	3
Heat pump	on	on	malfunction
CHP	off	on	malfunction
Gas boiler	off	off	on
P_HZ	on	on	on
P_PWH	off	off	off
M1	TVLCSoll	TVLCSoll	TVLCSoll
M2	A-AB	table	B-AB
M3	-	-	B-AB
Component	B Hot water mode		
	1	2	3
Heat pump	on	on	malfunction
CHP	on	on	malfunction
Gas boiler	off	on	on
P_HZ	off	off	off
P_PWH	on	on	on
M1	-	-	-
M2	-	-	-
M3	TVLASoll	TVLASoll	TVLASoll
Component	C Combined heating and hot water mode		
	1	2	3
Heat pump	on	on	malfunction
CHP	on	on	malfunction
Gas boiler	off	on	on
P_HZ	on	on	on
P_PWH	on	on	on
M1	TVLCSoll	TVLCSoll	TVLCSoll
M2	B-AB	B-AB	B-AB
M3	TVLASoll	TVLASoll	TVLASoll

Table II
MOST IMPORTANT TECHNICAL DATA

		Unit
Heat pump power	20 - 40	kW
CHP heating power	34.7 - 51.2	kW
Gas boiler power	37.3 - 200	kW
Building heating load	72.5	kW
Hot water heating load	141	kW
TVLCSoll: Supply temperature heating	Heat curve, max. 55	°C
TVLASoll: Supply temperature hot water	70	°C

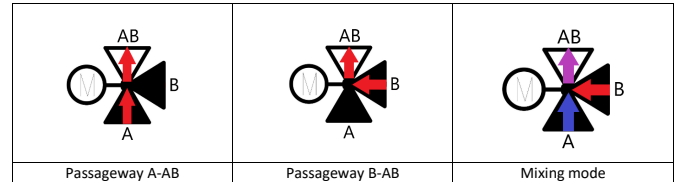


Figure 5. Valve positions of a three-way mixing valve

B. Heating mode

The heating mode is denoted with the letter A. In general only the heat pump and the CHP is operating during this mode. The gas boiler is only in operation as soon as there is a malfunction with one of the other heat generators. The heating mode is activated as soon as the average ambient temperature falls below the heating limit temperature which is set at 12°C. Then the supply temperature TVLCSoll is being regulated according to the heat curve meaning that at higher ambient temperatures, the supply temperature is lower and at lower ambient temperatures the supply temperature is higher. The heating water is being circulated by the building heating pump P_HZ. The hot water pump P_PWH is not in operation. During the partial control state A1 the heating power of the heat pump is higher than the required heating power for the building. Therefore only the heat pump is in operation. The heating water temperature is measured with a temperature sensor in the supply pipe. As soon as TVLCSoll is no longer reached for about 15 minutes the system changes to the partial control state A2.

Now in addition to the heat pump, the CHP unit is also in operation. With a combined heating power of 91.2 kW the two heat generators are powerful enough to cover the heating load of 72.5 kW. In case of a malfunction there is also the control state A3.

Now the gas boiler takes over the entire supply with heating water. For a simpler control of the system the other two heat generators are no longer providing heating water for the building. This means that even if only the heat pump has a malfunction but the CHP could be operating, all the CHP unit is doing is heating the CHP buffer. If the buffer is fully heated the CHP unit is switched off. The same goes for the heat pump if the CHP has a malfunction. The mixing valves are controlled according to Table I.

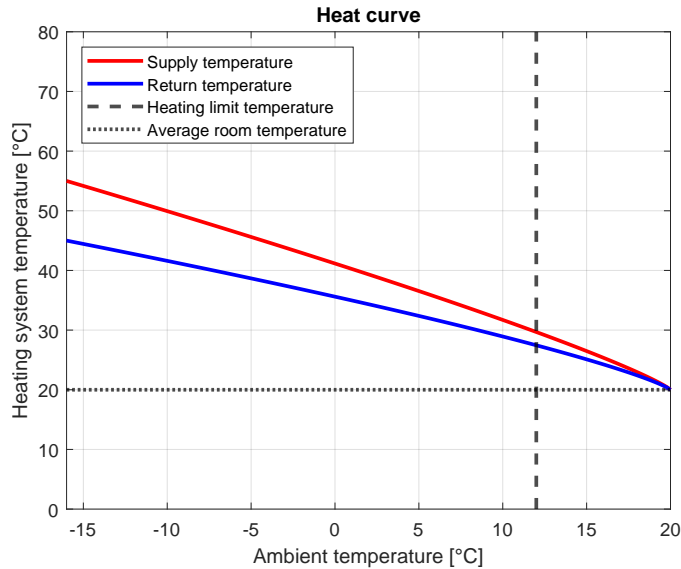


Figure 6. The heat curve for the hybrid heating system.

C. Hot water mode

The hot water mode is denoted with the letter B. During this control states the heat pump is never operating on its own due to the fact that it is impossible to heat the heating water up to 70°C. The maximum possible temperature with the heat pump is 62°C. Therefore, in the B1 control state, the heat pump and the CHP unit are operating simultaneously. The building heating pump P_HZ is not in operation. The heating water for the hot water generation is being circulated by the hot water pump P_PWH. The mixing valve M3 is regulated so that at gate AB the temperature of the heating water conforms with TVLAsoll. The heating water temperature is measured with a temperature sensor in the supply pipe for the hot water generation. As soon as TVLAsoll is no longer reached for about 15 minutes the system changes to the control state B2. This means that the heating power needed for the hot water generation exceeds the heating power provided by the heat pump and the CHP unit.

In addition to those, the gas boiler is now also operating. The combined heating power of all three heat generators is sufficient to cover the hot water heating load. The system only goes into the control state B3 if there is a malfunction with the heat pump or the CHP unit.

In B3 the gas boiler covers the whole hot water heating load. Just as in the heating mode the other two heat generators are no longer providing heating water for the hot water generation but the one without a malfunction can still heat up its buffer until it is fully heated.

D. C: Combined heating and hot water mode

The combined heating and hot water mode is denoted with the letter C. In these control states both pumps are operating. The mixing valves are controlled according to Table I. Just like in the hot water mode the heat pump is never operating on its own since the heating water temperature needs to reach

70°C.

So during C1 the heat pump and the CHP unit is in operation. The temperature of the heating water for the hot water generation is again measured with the temperature sensor in the supply pipe for the hot water generation. As soon as TVLAsoll is no longer reached for about 15 minutes the system changes to the control state C2. Since the temperature for the heating of the building TVLCSoll is lower than TVLAsoll, it is not decisive for the change of the control state.

For C2 the gas boiler goes additionally in operation so that this control state is the only one in which all the components are operating. The hybrid heating system is now capable to provide the building with enough heating power for both heating and hot water generation. If the heat pump or the CHP unit now has a malfunction the control state C3 is activated. Now the gas boiler has a good chance to operate at its highest possible power. Just like in the control states before, the other two heat generators are no longer providing heating water for the system other than for the heating of its own buffer. This is of course only possible for the heat generator without a malfunction.

IV. CONCLUSION

The control strategy for the hybrid heating system can be broken down into three categories. Each of these categories has three control states so that a total of nine partial control states can be defined. For the programming each component has its own flow chart so that the control states can be set.

The control states form the base for the operation of the hybrid heating system and for further additions or changes.

Firstly the artificial intelligence will be added so that the running cost can be minimized.

Secondly the temperature of the heating water for the hot water generation will be reduced so that a better efficiency can be reached whilst maintaining a high hygienic standard for the drinking water. What temperature for the heating water this corresponds to must still be investigated.

Last but not least the remaining radiators will be replaced with an underfloor heating system so that the temperatures for the heating of the building can be reduced and the heat pump can operate at a higher efficiency.

While simulations promise a very successful operation the real system still needs to be tested with this control strategy.

REFERENCES

- [1] Bundesministerium für Umwelt, Naturschutz und nukleare Sicherheit, "Treibhausgasemissionen sinken 2020 um 8,7 Prozent", Germany, Pressemitteilung Nr. 042/21, 16.03.2021. Accessed: 11.05.2021. [Online]. Available: <https://www.bmu.de/pressemitteilung/treibhausgasemissionen-sinken-2020-um-87-prozent/>
- [2] ZEIT ONLINE, Reuters, gra, "Bundesregierung erhöht Klimaziele", Germany, 05.05.2021. Accessed: 11.05.2021. [Online]. Available: https://www.zeit.de/politik/deutschland/2021-05/klimaschutz-bundesregierung-klimaziele-co2-ausstoss-treibhausgase?utm_referrer=https%3A%2F%2Fwww.ecosia.org%2F
- [3] Tobias Saller, "MAGGIE Gesamttreffen - AP 1.4 - Umsetzungsfahrplan", 11.02.2021, unpublished
- [4] TGA Projektierung GmbH, "Ausführungsplanung - Anlagenschema Heizung", private communication, 24.11.2020

[5] Matthias Giebisch, "Hydraulikschema", private communication,
09.11.2020

Concept development of a hybrid ship driving system and investigation of different constellations of components and control strategies

Tobias Reidl, Lea Huber, Michael Heberl and Belal Dawoud

Laboratory of Sorption Processes
East Bavarian Technical University (OTH Regensburg)
93053 Regensburg Germany
Email: tobias1.reidl@st.oth-regensburg.de

Abstract—In order to achieve the international goal of minimizing the environmental impact of energy production, the transport sector must also look for an alternative to burning conventional fuels such as heavy oil and diesel. Hybrid drive systems containing fuel cells, accumulators and photovoltaics are a promising way to achieve this in inland waterway shipping. Since green hydrogen is still more expensive compared to fossil energy sources, a major goal is to reduce fuel respectively energy consumption as much as possible. For the recent investigation, the inland push boat *ELEKTRA*, a project by *e4ships*, is considered. The methodological procedure of generating a MATLAB®/Simulink model to investigate different combinations of energy management strategies and components already available on the market, is presented. In this paper a concept of a hybrid drive system, comprising fuel cells, photovoltaics and a battery pack is presented, and the theoretical background necessary for the modelling is described.

I. INTRODUCTION

The growing demand for energy and the increase in international trade are leading to ever higher emissions of pollutants and the associated global warming. In international contracts, such as the Paris Climate Agreement, almost 190 countries have committed to reducing their pollutant emissions in the next decades keeping the global warming below 2 °C [5]. In addition to substituting conventional energy production with renewable energies in the electricity sector, greenhouse gas emissions in the heat and transport sectors have to be reduced as well.

It is mandatory to reduce the environmental impact of all energy sectors. This decarbonisation is leading to a seek for alternative driving systems in the transport sector. While it is relatively easy to electrify automobiles, planes and vessels turn out to be more difficult as there is a huge demand of power and energy. To reduce global emissions in shipping the International Maritime Organisation (IMO) stipulates that certain regulations for emission-reduction must be complied with [1]. Furthermore, the incentive for substitution of conventional fuels is the ongoing increase in the CO₂ tax per tonne emitted conducted by the German government, which continuously drives up the price of diesel and heavy oil [16]. Since 80 % of all seagoing vessels are equipped with so-called diesel-electric

drivetrains, their operational costs will also further rise with this tax increase [7]. This will make alternative propulsion systems more attractive, not only in terms of environmental protection, but also economically.

Especially fuel cell applications in shipping have already been investigated in various studies and projects as there is a range of benefits, e.g., zero local emissions, high energy and power density and low noise pollution [15]. The most promising fuel cell technologies are high and low temperature polymere electrolyte membrane (PEMFC), solid oxide (SOFC) and molten carbonate (MCFC), depending on the circumstances of the application. Currently the main challenge of these technologies is to increase their lifetime and make them economically competitive with conventional drives [12, 15].

At present, the production of green hydrogen[†] is more expensive compared to conventional fuels [13, 8]. Furthermore the hydrogen processing components including fuel cell and storage are high-priced compared to combustion engines and their components. Due to the currently high costs of green hydrogen, the system must be as efficient as possible in order to save fuel or rather costs and to be economically competitive with combustion engines.

This paper presents the theoretical basis for the creation of a ready-to-use simulation model for various investigations of power flows in the driving system. The model will enable an energetic and economic evaluation of a hybrid ship driving system that includes fuel cell (FC), battery pack and photovoltaics (PV) as energy sources. Based on the work of Bassam et al. [4] different energy management strategies will be used to find a minimum of energy consumption and energy costs. Also the dynamics of the driving system referred to load bank level variations will be considered. Subsequently, various fuel cells and accumulators available on the market can be embedded in the model.

First of all, the considered ship and the routes to be investigated are presented. Afterwards, the procedure for creating the model, including the selected components and their characteristics, are presented in section III. Based on the

[†]hydrogen obtained from renewable energy sources without CO₂ emissions

work of Bassam et al. [4] the best fitting energy management systems (EMS) for this model will be chosen in section IV. The theoretical basics for embedding the datasheets of these components will be given in V. Finally, in chapter VI an overview of the following actions in preparation for the model is shown.

II. DESCRIPTION OF THE CONSIDERED SHIP

The inland push boat ELEKTRA of the e4ships project RiverCell will be used for this examination, as an emission free driving system has already been designed for it. Also load profile data has been collected for the two main modes of operation: a regional operation in the area of Berlin/Brandenburg and a supraregional operation from Berlin to Hamburg with ranges of 65 km and 520 km. RiverCell was a pilot project to define framework conditions in the use of hydrogen or methanol as fuel. An inland waterway vessel was developed that contains a lithium-ion battery to mainly supply regional operations. For longer voyages, a polymer electrolyte fuel cell (PEMFC) is used for additional power supply, while a photovoltaic system has the task of maintaining the state of charge (SOC) of the emergency battery at 100%. In Table I an overview of the main components and their specifications is given. This represents

Table I
SPECIFICATIONS OF THE ELEKTRA PUSH BOAT

Component	Specifications	Weight [kg]
PEM Fuel Cell	2 x 96 kW	3.600
Li-ion Accumulator	2 x 1.250 kWh	35.000
Photovoltaic	2,5 kW	—
Electric Motor	2 x 200 kWp	2.400
Hydrogen Tanks	250.000 kWh / 750 kg H ₂	15.500 kg

the fundamentals for the investigation and will be adapted to the model set up in section III. [6] As shown in Tab. I, the components were dimensioned considering a real existing push boat carrying non-motorised barges with 1,400 tonnes of cargo at an average speed of 8 to 8.5 $\frac{km}{h}$. This results in an average power requirement of 165 kW. However, the maximum speed to compensate for delays is set at 10 $\frac{km}{h}$, resulting in a maximum power requirement of 400 kW. The vessel is equipped with DC/DC converters to stabilise the output voltage of the fuel cell and three-phase inverters to adjust the energy of the DC busbar to supply the two asynchronous electric motors.

Since the exact load bank curve of the ship under consideration has not been published, a performance curve of the electrical power demand must be reproduced. Figure 1 a) shows the electrical power demand by the motors depending on the vessels speed. Figure 1 b) shows the measurements of the ships' speed in regional operation. In order to develop a continuous time-function, that approximates the regional operation as precisely as possible, distinctive points in Fig. 1 b) are worked out and approximated with a polynomial of the n-th degree. Subsequently, the power value is assigned to each of these approximated velocities according to Fig. 1 a). This results in a power characteristic curve over time, which can later be integrated into the simulation model.

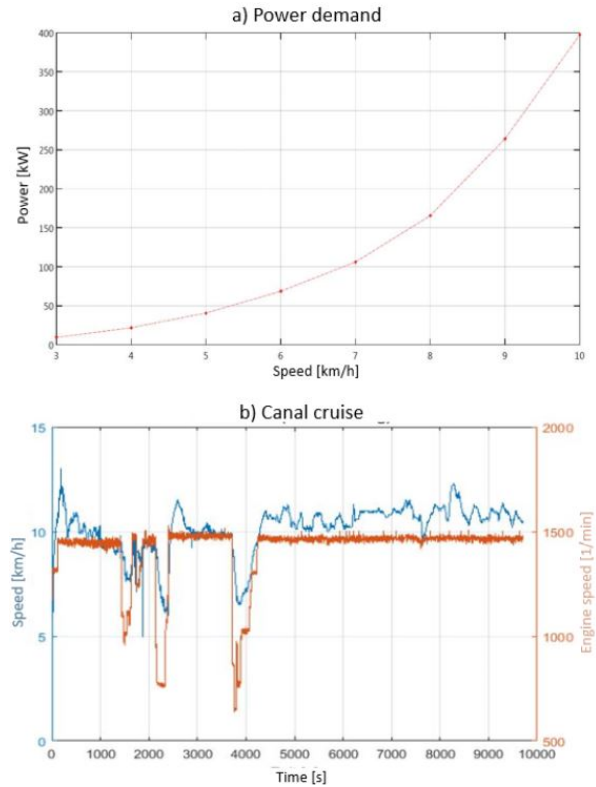


Figure 1. a) Power demand as a function of cruising speed; b) measurement of linear driving speed and engine speed of a canal cruise in the area of Brandenburg, Germany (translated from German) [6]

III. MODEL DEVELOPMENT

Figure 2 displays a parallel hybridisation of the driving system for the MATLAB[®]/Simulink implementation. The arrangement of the components for building the model is slightly different to the RiverCell study. Instead of using the photovoltaic power solely for the on-board power supply busbar, it is for the propulsion supply. The quick-charge plug (I) and the on-board power network (II) are not part of the simulation model, but the last named is included in the data of the drive load bank. Both the fuel cell and the propulsion battery are connected to a DC/DC converter to adjust their output to a suitable voltage level. The two three-phase inverters are necessary to convert the direct current (DC) into alternating current (AC).

At the beginning the fuel cell block represents the PEMFC technology. As SOFC and MCFC are considered to be the next generation technologies, at first the focus is on the PEMFC technology as it is technologically sophisticated and offered by many manufacturers already, e.g., *Ballard Power Systems*, *PowerCell* and *Plug Power Inc* [12]. The main advantages of the PEMFC system are high efficiencies regardless of the size of the system, low system complexity and high reliability [2, 14]. Nevertheless, MCFC and SOFC technologies have many benefits in terms of applicability, as it is possible to directly use short-chain hydrocarbons as an alternative such as methane without the need for reforming to high purity hydrogen.

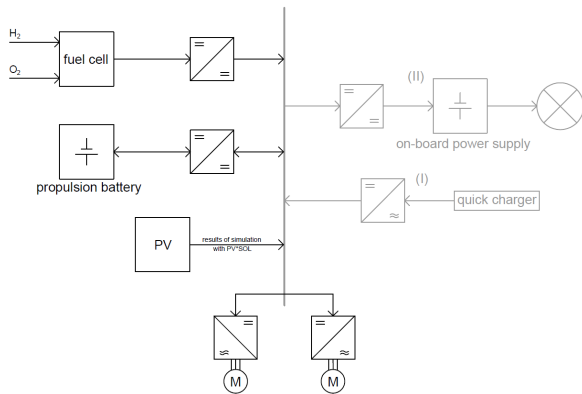


Figure 2. Template of the hybrid driving system for implementation

As this option is not CO₂-free, it may be a possibility for the transitional phase of the decarbonisation of energy systems to reduce emissions, or to generally use green methane instead, which offers storage advantages over hydrogen and still is CO₂-neutral.

Lithium-ion battery technology will be used for implementation. Due to the increasing demand for lithium-ion batteries (e.g. through their use in e-cars), production costs have fallen in relation to the number of units produced. The electrical connection between the busbar and the battery is bidirectional to allow charging and discharging of the battery. For example, if the energy demand is low and there is a high proportion of surplus energy, this energy can be temporarily stored in the battery.

The photovoltaic system is examined in an external software called PV*SOL®. In this simulation programme, the energy generated is calculated using Meteonorm’s meteorological database. The result is a detailed database of energy production with hourly values depending on the time of day and season. It is possible to export the data for a following input as load profile data into the simulation model. Instead of assuming a PV system with 2.5 kWp installed power only on the roof of the push boat, which is just sufficient to supply the emergency battery, it is presumed that the space on the pushed barge can be used. Assuming the surface is 35 m by 10 m, an area of 350 m² results. The specific power density of mono-cristalline pv-modules is about $p_{PV} = 223 \frac{Wp}{m^2}$ [17]. Therefore, an installed capacity of about 78 kWp is considered.

IV. ENERGY MANAGEMENT STRATEGY

For a further optimisation in energy use Bassam et al. [4] investigated four different energy management systems and their combination (multi-scheme EMS) using the example of the hydrogen and battery-powered passenger ship *FSC Alsterwasser*. The realised EMS of the ship is state-based. Depending on the power demand of the system P_{load} and the battery SOC the fuel cells output power level is set.

The EMS considered were equivalent fuel consumption minimisation strategy (ECMS), charge-depleting charge-sustaining (CDCS) and the classical PI EMS. In terms of minimising total

energy consumption, the multischeme and the classical PI EMS strategies are the most efficient ones. In terms of minimising hydrogen consumption, the CDCS was remarkably better than the others.

Therefore, three EMSs to be implemented and investigated in this study were chosen. The classical PI-EMS for the most efficient driving mode and the CDCS for minimising hydrogen consumption. Also a modified form of the state-based EMS, in which the ship’s power curve is divided horizontally into three ranges (low-power, cruising and high-power mode) will be examined. Figure 3 shows the different parameters which have to be monitored and given to the EMS algorithm.

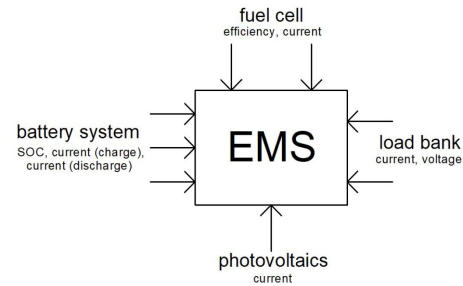


Figure 3. Basic scheme for monitored parameters of the EMS

V. THEORETICAL BASICS FOR IMPLEMENTATION

For the implementation the model in section III is consulted containing a fuel cell subsystem including DC/DC converter, a battery subsystem, a photovoltaic subsystem as inserted load bank and a load bank subsystem. These are embedded in each case and filled with information from the previously mentioned data sheets.

A. Fuel cell

A model of a fuel cell stack was developed by Njoya et al. [10] and implemented in MATLAB®/Simulink as presented in figure 4. The prefabricated fuel cell block, included in MATLAB®/Simulinks Simscape toolbox, was designed to be handled both in a simplified and a detailed version. For both of them a preset of different fuel cells (PEMFC, SOFC and alkaline fuel cell AFC), peak powers and operating voltages exist. For editing, the simplified version offers the possibility of adjusting the following parameters:

V_{0A}, V_{1A}	Voltage at 0 A and 1 A
I_{nom}, V_{nom}	Nominal operation point
I_{end}, V_{end}	Maximum operation point

Therefore, this data must be extracted from the fuel cell data sheet. For example *Horizon Fuel Cell Technologies* provides the characteristic curves of power and voltage as a function of current, which can be used.

The detailed model can additionally be fed with the following parameters:

In this paper, the theoretical background and the methodology for implementation in a simulation environment were presented. The model includes different energy sources that can be utilized and investigated. The energy management strategies are also implemented in order to increase the performance of such hybrid driving system.

VII. FURTHER RESEARCH

The next step is to contact some manufacturers to get detailed information about fuel cells and accumulators. Then the model is built and validated using the data sheets. Once this effort is done, different components can be compared and the energy management strategies can be applied to find an optimum in the operation of this model in terms of efficiency, fuel consumption and costs. As part of this research, scalability to larger power classes of vessels will also be investigated.

REFERENCES

- [1] Seeverkehr. <https://www.bmu.de/themen/luft-laerm-verkehr/verkehr/seeverkehr/#:~:text=Die%20IMO%20hat%20sich%202018,50%20Prozent%20gegen%20C3%BCber%202008%20sinken.,> 2020. 02.05.2021.
- [2] D. Akinyele, E. Olabode, and Amole Abraham. Review of Fuel Cell Technologies and Applications for Sustainable Microgrid Systems, 2020.
- [3] L. Barelli, G. Bidini, and A. Ottaviano. Optimization of a PEMFC/battery pack power system for a bus application. *Applied Energy*, 97:777–784, 2012. ISSN 03062619. doi: \url{10.1016/j.apenergy.2011.11.043}.
- [4] A. M. Bassam, A. B. Phillips, S. R. Turnock, and P. A. Wilson. Development of a multi-scheme energy management strategy for a hybrid fuel cell driven passenger ship. 42(1):623–635, 2017. doi: \url{10.1016/j.ijhydene.2016.08.209}.
- [5] Europäische Kommission. Übereinkommen von Paris. https://ec.europa.eu/clima/policies/international/negotiations/paris_de, 2020. 26.11.2020.
- [6] M. Fiedler, R. Kutz, and G. Metropoulos. Schlussbericht Demonstrationsprojekt RiverCell/ELEKTRA: Schubschiff mit Brennstoffzellen-Hybridanlage, 2017.
- [7] Infineon Technologies AG. Warum das Schiff der Zukunft elektrisch fährt. <https://www.infineon.com/cms/de/discoveries/elektrische-schiffe/>, 2020. 19.11.2020.
- [8] C. Krieger. Verfahrenstechnische Betrachtung und Optimierung der Freisetzung von Wasserstoff aus organischen Trägermaterialien, 2019.
- [9] MathWorks. Battery: Generic battery model. https://de.mathworks.com/help/physmod/sps/powersys/ref/battery.html?searchHighlight=battery&s_tid=srchtitle, 2021. 06.01.2021.
- [10] S. M. Njoya, O. Tremblay, and L.-A. Dessaint. A generic fuel cell model for the simulation of fuel cell vehicles. pages 1722–1729, 2009. doi: \url{10.1109/VPPC.2009.5289692}.
- [11] T. O. and L.-A. Dessaint. Experimental Validation of a Battery Dynamic Model for EV Applications, 2009.
- [12] J. Töpler and J. Lehmann, editors. *Wasserstoff und Brennstoffzelle: Technologien und Marktperspektiven*. Springer Vieweg, Berlin, 2014. ISBN 978-3-642-37415-9.
- [13] J. Töpler and J. Lehmann, editors. *Wasserstoff und Brennstoffzelle: Technologien und Marktperspektiven*. Springer Vieweg, Berlin, 2014. ISBN 978-3-642-37415-9.
- [14] Y. Wang and D. F. Ruiz Diaz. Materials, technological status, and fundamentals of PEM fuel cells - A review, 2020.
- [15] Y. Wang, K. S. Chen, J. Mishler, S. C. Cho, and X. C. Adroher. A review of polymer electrolyte membrane fuel cells: Technology, applications, and needs on fundamental research. 88(4):981–1007, 2011. doi: \url{10.1016/j.apenergy.2010.09.030}.
- [16] ZDF. Bundestag beschließt CO2-Abgabe: Sprit, Heizöl und Erdgas ab 2021 teurer. <https://www.zdf.de/nachrichten/politik/bundestag-co2-abgabe-benzin-heizoel-100.html>, 2020. 28.11.2020.
- [17] Y. Zhang, B. Wang, X. Li, Z. Gao, Y. Zhou, M. Li, D. Zhang, K. Tao, S. Jiang, H. Ge, S. Xiao, and R. Jia. A novel additive for rapid and uniform texturing on high-efficiency monocrystalline silicon solar cells. *Solar Energy Materials and Solar Cells*, 222:110947, 2021. ISSN 09270248. doi: \url{10.1016/j.solmat.2020.110947}.

Comparison of different calculation methods for the outflow from pressurized vessels

Thomas Riedmaier
Institute of new Energy Systems
Technische Hochschule Ingolstadt
Ingolstadt, Deutschland
thomas.riedmaier@thi.de

Katharina Bär
Institute of new Energy Systems
Technische Hochschule Ingolstadt
Ingolstadt, Deutschland
katharina.baer@thi.de

Wilfried Zörner
Institute of new Energy Systems
Technische Hochschule Ingolstadt
Ingolstadt, Deutschland
wilfried.zoerner@thi.de

Abstract—The demand for renewable energies in the last few years increased significantly, in order to reduce greenhouse gas emissions in the energy sector. As a result, especially volatile energy generators such as photovoltaic (PV) and wind power plants have skyrocketed. To stabilize the grid, flexible power generation is necessary. Solid biomass combined heat and power plants (CHP) are used for baseload operations nowadays. For a more flexible operation, the steam generation and consumption must be decoupled. Therefore, a prototype storage system consisting of a concrete storage and a steam accumulator will be built in the biomass CHP plant in Pfaffenhofen, Germany. This paper focuses on the discharge valve of the steam accumulator. Three different calculation methods, which are used to calculate the discharge mass flow from pressurized vessels, will be compared concerning their mass flow trend as a function of the valve position. This will give a first impression about the mass flow in the test bed in Pfaffenhofen.

Keywords— flexible power generation, steam accumulator, solid biomass, steam storage, CHP

I. INTRODUCTION

In the last few years the amount of volatile renewable energy generators such as photovoltaic and wind power plants have increased. For balancing demand and supply in the electricity grid constantly, flexible power generation is necessary to compensate the volatile power generation of PV and wind [1]. Due to the extensive installation of renewable generators, this especially applies to the German electricity grid and three main approaches to overcome those difficulties are:

- (1) Demand side management of consumers (optimisation of consumers' energy consumption).
- (2) Implementation of energy storage technologies [1].
- (3) Flexible operation of power plants [2].

Compared to other renewable energy technologies, biomass and biogas plants can generate electricity independently from weather conditions, which represents a major competitive advantage. While biogas plants can be used to produce electricity dependent on the electricity grid demand, biomass CHP plants can not, due to slow load change dynamics [3]. This paper focuses on biomass CHP plants with steam cycles, which have three main processes.

- a. Generating steam at high pressure and temperature through conversion of heat released from combustion of wood chips.
- b. Generating electrical power through expansion of steam through a turbine.
- c. Condensation of the exhaust steam from the turbine in a heat exchanger.

There are different solutions for increasing the flexibility of biomass CHP plants, following the aim to expand their field of application within the electricity supply.

One solution is the storage of steam, in order to decouple the steam generation and consumption. In times of low electricity demand (high availability of PV/wind power), the steam can be stored in a storage system and the turbine in the CHP plant produces less electricity. During periods of high electricity demand, the stored steam can be used to generate additional electricity in the turbine. As part of the research project "KomBio" (Fachagentur Nachwachsende Rohstoffe; 22025517), a prototype storage system will be implemented in the biomass CHP plant in Pfaffenhofen, Germany. It consists of a steam accumulator, which will store most of the steam's energy latently and a concrete storage, which will store some of the steam's heat sensibly.

This paper focuses on the discharge valve of the steam accumulator. Therefore, three different calculation methods will be compared concerning their mass flow trend as a function of the valve position. In a first approach, the valve position and its corresponding output area are specified over the discharge period. Additionally, the mass flow is calculated for each calculation method. In the second approach the mass flow is determined and the valve position is calculated. This approach provides information of how the valve must be opened over the discharge process to keep the mass flow constant. Overall, the calculations will give a first impression about the expected mass flow trend as a function of the valve position of the prototype in Pfaffenhofen.

II. OPERATION MODE OF STEAM ACCUMULATORS

Steam from the power plant is injected into the liquid phase of the accumulator. They do not store steam directly and rather store the energy in form of water. Accordingly, 50 to 80 percent of the volume of the storage system is filled with water. The operating range of the investigated steam storage is 5 to 30 bar.

The characteristics of steam and water, e.g. evaporation temperature or density are dependent on the pressure of the steam accumulator. The evaporation temperature of water is higher, when the pressure inside the steam accumulator is high (max. 30 bar). As the steam accumulator is discharged, the evaporation temperature drops from about 234 °C (30 bar) to 152 °C (5 bar). The steam accumulator is charged in times of low energy or rather low steam consumption. The steam parameters in the investigated power plant are 470 °C and 60 bar. Steam with these parameters is called ‘superheated steam’ and is needed to produce electricity in turbines. During times of low consumption, the superheated steam heats a before installed concrete storage and afterwards is injected into the steam accumulator.

When the consumption is high, the stored steam is extracted through a control valve. When the control valve is opened, the pressure in the accumulator decreases and therefore the evaporation temperature drops. Thus, the water temperature inside the accumulator rises above its evaporation temperature and water evaporates into saturated steam. Saturated steam is not usable for electricity generation. Hence, the saturated steam is routed through the concrete storage. Due to the heat stored inside the concrete storage, the steam overheats into superheated steam, which is suitable for electricity generation again.

III. THEORETICAL CALCULATION OF THE VALVE CONTROL

To estimate the mass flow behaviour of the steam accumulator in Pfaffenhofen, theoretical calculations are necessary in advance. The mass flow depends on parameters like pressure, density and cross-sectional area. The flow area can be changed by opening the valve. Three different calculation methods will be reviewed and compared in the upcoming chapters. All calculation methods will be used in two different approaches. The first approach includes three different cases (constant, linear, exponential) and the mass flow is calculated based on given valve positions. The second approach includes only a constant case (constant mass flow), where the valve position will be calculated for a given mass flow. In Tab. 1, an overview of the reviewed results is shown.

Tab. 1. Overview of the reviewed results

Cases	Approaches	
	Approach 1: Valve position given	Approach 2: mass flow given
1	Constant	Constant
2	Linear	
3	Exponential	

A. Definition of the valve position

Goal of the following calculation methods is the determination of the mass flow trend as a function of the cross-sectional area. The cross-sectional area depends on the valve position. The wider the valve is opened, the higher the area where the steam escapes the accumulator is. In this chapter the valve position as well as the linear, exponential and constant opening characteristics are defined. This definition of the valve position applies to all calculation methods. The valve position x depends on the flow area A . As the steam flows through a round pipe, the maximum cross-sectional area A_{max} can be calculated with (2). Therefore, d_{max} as the pipe diameter is needed. When closing the valve, this can be interpreted as a decrease in diameter as defined in (1).

$$x = \frac{d}{d_{max}} \tag{1}$$

The maximum pipe diameter d_{max} is given at 35,9 mm. The valve position x can take values between 0 and 1, where 0 defines the valve as fully closed (no flow diameter) and 1 as fully opened (flow diameter equals pipe diameter)

$$A_{max} = \left(\frac{d_{max}}{2}\right)^2 * \pi \tag{2}$$

The maximum cross-sectional area A_{max} for the given pipe diameter is 10.12 cm². By transforming (1) to the diameter d , the cross-sectional area A is obtained as a function of the valve position x according to (3).

$$A = \left(\frac{x * d_{max}}{2}\right)^2 * \pi \tag{3}$$

1) Approach 1: Calculation of the mass flow

Different valve positions over the discharge period will be tested in Pfaffenhofen. There are two different approaches for the calculations. Considering the first approach, the valve position is given, which allows the calculation of the corresponding cross-sectional area. In this approach, three different cases will be tested. In case 1 the valve position x remains constant over the discharge period. In case 2 and 3 the valve is opened linear and exponential over the discharge period. The pressure p_0 at the beginning of the discharge process is known. Thereby, the evaporation temperature T_s , the isentropic exponent κ , the sonic velocity w_s and the density ρ can be determined. These parameters are determined by using the Excel Add-in ‘FluidEXL’ [4]. This Add-in accesses the thermophysical-properties-library LibIF97, where the parameters named above and many other variables are stored in steam tables. The steam mass inside the steam accumulator at 30 bar, which can be extracted from previous simulations inside the project framework, amounts to 280.56 kg. This value applies for a charging efficiency of 80 %. Through discharge with a constant mass flow of 1 t/h, the steam mass inside the storage is reduced to 52.78 kg at 5 bar. Assuming that the pressure and steam mass inside the steam accumulator are directly proportional, a linear equation can be set up, which results in (4), where m is the steam mass and p the pressure inside the steam accumulator.

$$p = 0,11 * m - 0,79 \tag{4}$$

The result of this equation is followed by an iterative calculation of the steam mass inside the accumulator. Considering the mass flow at time $n-1$ m_{n-1} , the steam mass inside the accumulator at point n m_n can be calculated at any given time step t .

$$m_n = m_{n-1} - \dot{m}_{n-1} * t \tag{5}$$

After the calculation of the remaining steam mass inside the accumulator through (5), the pressure at point n can be determined. Following, parameters mass flow, steam mass inside the accumulator and pressure until the lower pressure limit (5 bar) can be calculated in an iterative procedure.

Considering case 1, valve position x is defined as constant. In case 2 (linear) and 3 (exponential), the valve position can be considered as a function over time. The time until the final value is reached influences the incline of the opening behaviour. The linear opening (case 2) is calculated with (6).

$$x_{linear} = \frac{x_{end} - x_{start}}{t_{end} - t_{start}} * t + x_{start} \quad (6)$$

t_{start} is the time at the start of the discharge process and defined as 0 seconds. The values x_{end} (end value of the valve position), x_{start} (start value of the valve position) and t_{end} are given as input parameters and are variable. With the help of time step t , the valve position at any given time can be calculated.

The exponential valve opening (case 3) can be determined with (7) and (8).

$$x_{exponential} = x_{start} * e^{k*t} \quad (7)$$

$$k = \frac{\ln(\frac{x_{end}}{x_{start}})}{t_{end}} \quad (8)$$

2) Approach 2: Calculation of the valve position

In the second approach, the mass flow serves as an input parameter and the valve position will be calculated. The equations for the calculation of the mass flow (dependent on the respective calculation method) are transformed after the cross-sectional area A . After the determination of the flow area, the valve position can be calculated with (3). With (4) and (5), an iterative calculation can be carried out until the lower threshold (5 bar) is reached.

B. Calculation Method 1: Schmidt [5]

The first method was published by [5]. The investigation was prompted by a safety concern in the nuclear power plant in Grundremmingen. It had to be clarified, how fast a gas filled vessel with high pressure can be discharged through a given opening. The calculations in this literature were done with air. However, a calculation with different gaseous mediums is also possible. Input parameters are the volume V of the vessel (in this case of the steam accumulator), the starting pressure p_0 (max. 30 bar; depends on the state of charge) and the cross-sectional area of the output valve A . The equations are based on the ideal gas law. The specific gas constant R_s and the isentropic exponent κ are constant in the calculations of [5].

A distinction has been made between a discharge in supersonic and a discharge in subsonic conditions. The distinction can be made with the critical pressure ratio in (9). If the pressure ratio is lower than the critical pressure ratio, steam flows out of the accumulator in supersonic condition.

$$\left(\frac{p_a}{p_0}\right)_{crit} = \left(\frac{2}{\kappa + 1}\right)^{\frac{\kappa}{\kappa - 1}} \quad (9)$$

The back pressure p_a equals the ambient pressure and may be considered as constantly 1 bar, as the steam is routed to the environment while discharging. The pressure p_0 depends on the state of charge of the steam accumulator and can take values between 5 bar and 30 bar. The isentropic exponent is subject to the pressure of the accumulator and varies between 1.27 (30 bar) and 1.30 (5 bar). This results in a critical pressure ratio between 0.551 at 30 bar and 0.546 at 5 bar. Because the back pressure p_a is constant, the distinction between supersonic or subsonic flow is contingent upon the pressure p_0 inside the accumulator.

Fig. 1 shows the correlation between the pressure ratio and mass flow. In case, the pressure inside the accumulator equals the ambient pressure (pressure ratio = 1), the mass flow is zero, because no pressure difference exists.

By decreasing the pressure ratio, the mass flow increases until the maximum point at the critical point (0.546 at 5 bar). In theory, the mass flow should increase, when further decreasing the pressure ratio.

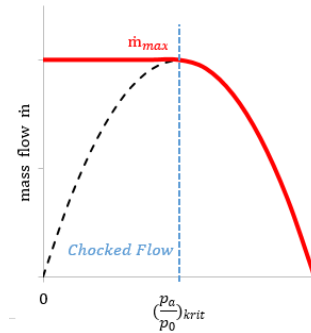


Fig. 1. Correlation between pressure ratio and mass flow [6]

However, experiments showed, that the mass flow remains the same, when decreasing the pressure ratio after the critical point has been reached. The pressure ratio falls below the critical point, if the starting pressure p_0 is high enough. In this case, the velocity of the steam at the valve equals the sonic velocity [6]. Equation (9) can therefore be transformed after p_0 , which results in (10).

$$p_0 > \left(\frac{\kappa + 1}{2}\right)^{\frac{\kappa}{\kappa - 1}} * p_a \quad (10)$$

To create a supersonic flow out of the accumulator under the conditions stated in this study, the pressure p_0 needs to be at least 1.83 bar (for κ at the lower pressure limit of the accumulator – 5 bar). This criterion is guaranteed, because the range of steam usage within the accumulator lies between 30 and 5 bar. Concluding that, in any case the steam flows out of the accumulator in supersonic condition. In [5], the ideal gas law (11) is assumed.

$$p * V = m * R_s * T \quad (11)$$

Through transformation of (11), the steam mass at the start of the discharge period m_0 can be calculated with (12).

$$m_0 = V * \frac{p_0}{R_s * T_0} \quad (12)$$

Through discharge of steam over time, while the valve is opened, the mass inside the accumulator decreases (13).

$$m = V * \frac{p}{R_s * T} \quad (13)$$

As the amount of steam inside the accumulator decreases, the pressure and evaporation temperature diminish, too. The change of steam mass over time is defined in (14).

$$-\frac{dm}{dt} = A * \Psi_{max} * p * \sqrt{\frac{2}{R_s * T}} \quad (14)$$

with (15)

$$\Psi_{max} = \left(\frac{2}{\kappa + 1}\right)^{\frac{1}{\kappa - 1}} * \sqrt{\frac{\kappa}{\kappa + 1}} \quad (15)$$

Ψ_{max} is the outflow function and summarizes the isentropic exponent κ . Because κ is pressure dependent, the values for this outflow function vary between 0.468 for 30 bar and 0.472 for 5 bar.

C. Calculation method 2: TLV [7]

The second used source is from the company TLV Euro engineering. Equations for the calculation of the steam flow rate through valves and screens are published by the company. For those equations, a case distinction is necessary (16).

$$\frac{p_1 - p_2}{p_1} \geq F_y * x_T \quad (16)$$

The differential pressure ratio x_T is assumed with 0.72 and has to be experimentally determined for each armature [8]. x_T only applies to air, which has a κ of 1.4. For different mediums, a conversion with (17) or rather the scaling factor F_y is necessary [8].

$$F_y = \frac{\kappa}{1,4} \quad (17)$$

The product of F_y and x_T lies between 0.653 (30 bar) and 0.669 (5 bar). The pressure ratio $\frac{p_1 - p_2}{p_1}$ is minimal at 5 bar with a value of 0.800. Thereby, p_2 corresponds with the ambient pressure and p_1 the pressure inside the storage. Over the whole pressure range of the accumulator, the here considered pressure ratio is higher than the product of F_y and x_T . In this case, the mass flow is calculated with (18).

$$\dot{m} = 0,66 * 2,73 * C_v * \sqrt{F_y * x_T * p_1 * \rho} \quad (18)$$

Because (18) gives no conclusion about the cross-sectional area A and for the determination of C_v , the mass flow must be known beforehand, the equation for the mass flow of screens according to (19) is used.

$$\dot{m} = 0,66 * 2,73 * C * \left(\frac{d}{4,654}\right)^2 * \sqrt{F_y * x_T * p_1 * \rho} \quad (19)$$

C is defined as the flow coefficient and is a correction factor, which represents occurring losses during discharge. As method 1 uses no correction factor, C will be set to 1 to make the results between the calculation methods more comparable.

D. Calculation method 3: Bohl/Elmendorf [6]

In chapter 5.6 from [6], the mass flow out of pressure vessels is defined. The derivation of the theoretical mass flow out of pressure vessels, results from the continuity equation, the isentropic relation and the inviscid outflow velocity after Saint-Venant and Wantzel. The equation from [6] uses the same outflow function ψ as [5]. In Fig. 2, the outflow function over the pressure ratio is plotted. The graph shows similarities to Fig. 1. The outflow function is maximized, similar to the mass flow, at the critical point and stays steady, even when the pressure ratio decreases further.

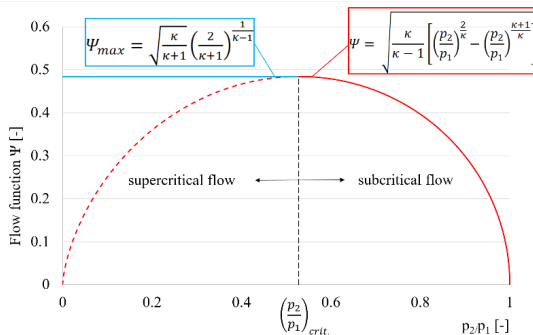


Fig. 2. Outflow function ψ plotted over the pressure ratio [9]

For outflow in supersonic condition, ψ is maximized and can be calculated according to (15).

The mass flow in supersonic outflow condition according to [6] is illustrated in (20).

$$\dot{m} = \mu * A * \Psi_{max} * \sqrt{2 * p * \rho} \quad (20)$$

As above, A is the cross-sectional area, p the current pressure inside the accumulator, ρ the current density depending on the pressure and Ψ_{max} the outflow function. Additionally, the outflow coefficient μ , which includes the velocity factor and the Poisson's ratio, are required to calculate the mass flow. As described in the chapter before, the correction factor (in this method μ) will be set to 1 for a better comparison between the methods. A value of 1 equals a loss-free discharge.

IV. RESULTS

Following, the results of the three presented calculation methods are compared in this chapter. All shown results represent a discharge of the steam accumulator from 30 bar to 5 bar, as this will be the most used discharge strategy for the test bed in Pfaffenhofen.

A. Approach 1 – Case 1: Results for a constant valve position

First, the results for a constant valve position will be presented. As an example, Fig. 3. shows the mass flow over time for a constant valve opening of 25 %. All three calculation methods show the same pattern in their trend. Method 2 has the shortest discharge period, which is about 200 to 300 seconds lower than the other two methods.

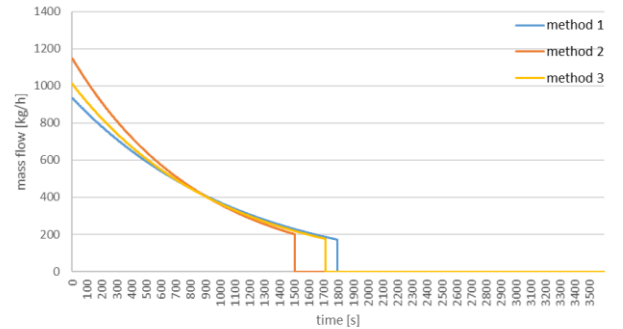


Fig. 3. mass flow with correction factors set to 1

Method 1 and 3 are almost identical in their discharge period. Reason for this behavior may be, that the equations used in those methods are both based on the same outflow function. Each method has its own simplification. Method 1 is based on the ideal gas law and uses a fixed value for the gas constant. In contrast, method 2 uses the equations for screens, whereas in reality a discharge valve is applied. In the tests in Pfaffenhofen the accuracy of the methods for this specific application will be assessed.

Overall, a decrease of mass flow over the discharge period can be seen. This is caused by the changing steam parameters. While steam is released from the accumulator, the pressure and with it the density and evaporation temperature of the steam inside the accumulator lowers. Due to the correlation $\rho = \frac{\dot{m}}{\dot{V}}$, either the mass flow must be decreased or the volume flow has to increase, when the density declines due to a pressure reduction inside the accumulator. The volume flow is defined as $\dot{V} = w * A$. The area A varies as a function of the valve position. Nevertheless, in this case it is constant, thus the velocity w during discharge must increase.

Because the steam flows out of the accumulator in supersonic condition, the velocity equals the sonic velocity and a further increase at the discharge valve is physically not possible [6]. Therefore, a heightening of the volume flow is not feasible. Consequently, the mass flow must decrease while discharging due to a density decline. At certain points (depending on the calculation method), the mass flow decreases abruptly to 0. At this point, the steam accumulator reached its lower pressure limit (5 bar). In theory, a further decrease would be physically possible, but lower pressures are not intended at the prototype and therefore are not investigated in this paper.

B. Approach 1 – Case 2 and 3: Results for a linear and exponential valve opening

The second and third presented case includes a linear and exponential opening of the valve for a chosen example. The given input parameters are the start and end values of the valve position as well as the time until the end value is reached (corresponds to the incline). For the chosen example, the start and end values are set to 10 % and 60 % respectively and the time until the end value is reached amounts to 1 hour. The trend of mass flow in comparison to the constant valve opening is different. The mass flow in the constant scenario decreased continuously, while in the exponential and linear case, which is shown in Fig. 4. and Fig. 5., it increases at the beginning.

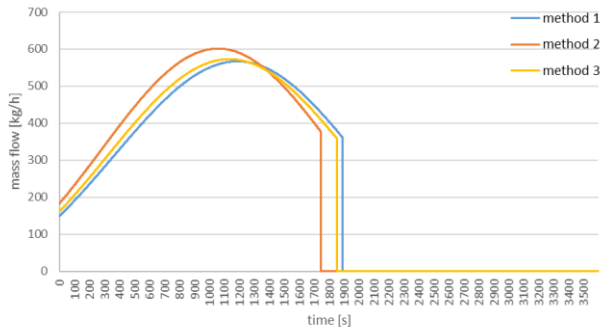


Fig. 4. mass flow - linear valve opening

The reason for this is, that the flow area increases, which counteracts the physical principle, that is responsible for the decline of the mass flow described in the chapter before. The flow area increases faster than the pressure and its corresponding density decreases, which raises the mass flow up until the turning point. Because the mass flow increases, the accumulator is discharged faster, which results in a faster decline of pressure and density inside and reduces the mass flow increase or rather the incline of the graph over time. After the turning point, the incline of the graph is negative and the mass flow decreases. At this point, the raise of the flow area is too slow to counteract the mass flow reduction.

When comparing the exponential and linear graph, it is noticeable, that the exponential graph looks drawn-out and has overall higher discharge periods. Fig. 6. compares the linear and exponential opening directly. A linear graph is the shortest way between two points, in this case the start and end value of the valve position. Due to the exponential behaviour, the exponential graph has lower values between start and end value and therefore a lower mass flow due to a smaller flow area. The peak mass flow is approximately 100 – 150 kg/h lower than in the linear case.

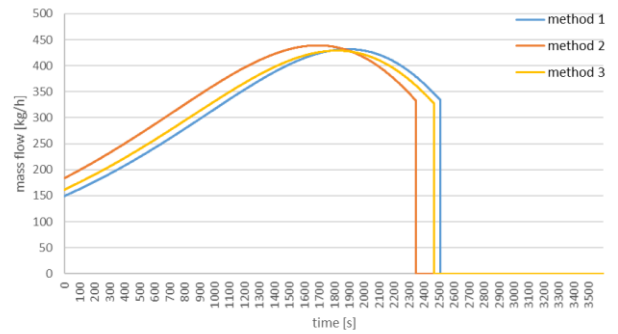


Fig. 5. mass flow – exponential valve opening

The discrepancies between the methods is independent from the type of valve opening. The discharge period for method 2 is 100 – 150 seconds lower in the linear and exponential case than the other two methods. The order of the methods in the discharge period is similar to the simulation result of the constant valve position

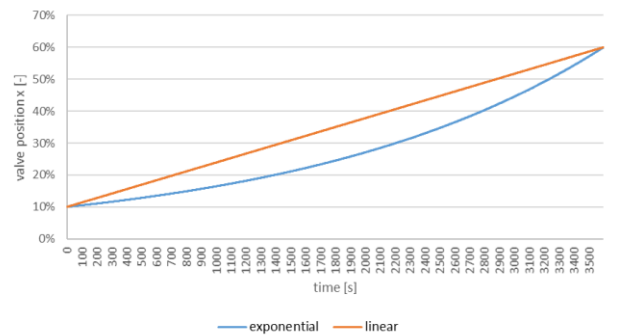


Fig. 6. Comparison of the valve position - exponential and linear

C. Approach 2: Results for a constant mass flow

In the second approach, the mass flow is given as an input parameter. The flow area A is calculated for a specific mass flow. The equations for the calculation of the mass flow for each method are transformed after the cross-sectional area. Goal of this approach is to identify, how the discharge valve must be controlled, so that the mass flow remains unchanged. In the test bed in Pfaffenhofen, a discharge mass flow between 250 – 500 kg/h is planned. Higher mass flows would result in exponential higher losses, as the velocity of steam would increase significantly with higher mass flows and the pipe diameters used at the prototype are small. The chosen example in this paper has a mass flow of 250 kg/h. The resulting valve position trend can be seen in Fig. 7.

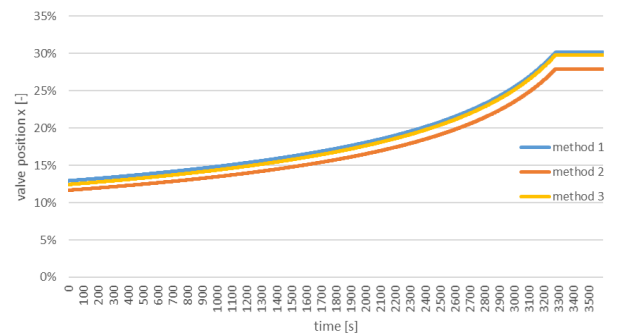


Fig. 7. Resulting valve position for a constant mass flow of 250 kg/h

The trend for each method over the discharge period is identical. The difference lies in the magnitude. The deviation between method 1 and 2 lies approximately at 2 – 3 %. Method 2 has the lowest valve position. In the results before, method 2 had the highest mass flow for given valve positions, which resulted in the shortest discharge period. Conversely, method 2 must have an overall lower valve position for a given mass flow. At around 3.200 to 3.300 seconds, the valve position remains the same. At this point, the steam accumulator is considered as fully discharged (5 bar). At first glance, the valve position for a fixed mass flow is similar to an exponential opening. In Fig. 8., an exponential trend line for method 1 is illustrated. Discrepancies occur especially at the end of the discharge period.

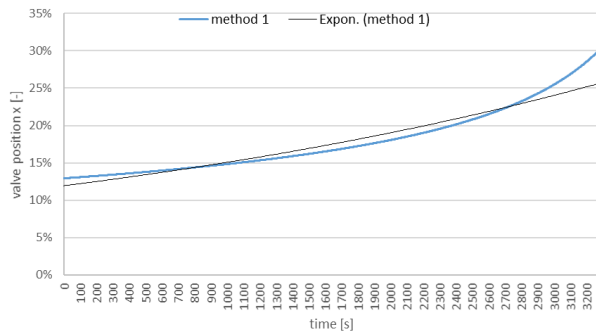


Fig. 8. Comparing valve positions – constant mass flow and exponential

For a constant mass flow, the valve needs to be opened faster and faster over time. This can be seen in Fig. 9., where in the first 1.000 seconds the valve position only changes approximately 2 – 3 %. For the same variation of the valve position at the end of the discharge period, only 100 – 200 seconds are needed. The valve position trend for a given mass flow has especially deviations at the end of the discharger period compared to the exponential behaviour.

V. CONCLUSION

In this paper, different calculation methods for an outflow of steam from a pressurized vessel were compared. Two different approaches were represented. In the first approach, the valve position and its corresponding flow area were given as input parameters. Three different versions (constant valve position; linear and exponential valve opening) and their results were presented. In the second approach the mass flow was given as an input parameter. Here, the result was the valve position over the discharge period. This approach gave information, how the valve had to be controlled, so that the mass flow remains constant. For a better comparison of the methods, the correction factors in method 2 and 3 were set to 1, which represents a loss-free outflow. Method 1 did not include a correction factor.

The results of the three methods only had small deviations. Method 2 had the highest mass flow for given valve positions independent of the discharge version. In the constant valve position case, the mass flow continuously decreases over the discharge period. When the steam accumulator is discharged, the pressure and with it the density inside decreases, which impacts the mass flow. For the linear and exponential valve opening, the mass flow increases in the beginning of the discharge phase. Because the valve in these cases is opened, the flow area increases, which counteracts the mass flow

reduction, that is caused by a decline of the density of steam. The incline of the mass flow decreases over time. At the turning point, the incline is negative and the mass flow falls off like in the constant case. In the second approach, the valve position over time conditional upon the mass flow was calculated. At first glance, the resulting valve position was similar to an exponential opening. However, especially at the end of the discharge period, deviations could be seen. To remain a constant mass flow, the valve had to be opened rapidly at the end of the discharging phase.

The results of all three calculation methods are similar even though they all have their nuances in their calculation. This leads to the assumption, that the measured mass flow in the tests in Pfaffenhofen is not too far off the theoretical mass flow. Every calculation method has its own simplifications. In the tests, the accuracy of the methods must be evaluated for the application at hand. As the correction factor for methods 2 and 3 were set to 1, the calculated mass flow is expected to be higher than in the tests. The correction factor has a huge impact on the results and can only be assumed beforehand. Method 1 does not include any correction factor and has similarities with method 3. Therefore, it is recommended to include the same correction factor in method 1.

VI. REFERENCES

- [1] A. Castillo and D. F. Gayme, *Grid-scale energy storage applications in renewable energy integration: A survey*, 2014.
- [2] A. Purkus *et al.*, “Contributions of flexible power generation from biomass to a secure and cost-effective electricity supply—a review of potentials, incentives and obstacles in Germany,” (in En;en), *Energy Sustain Soc*, vol. 8, no. 1, pp. 1–21, 2018, doi: 10.1186/s13705-018-0157-0.
- [3] E. Billig and D. Thraen, “Renewable methane – A technology evaluation by multi-criteria decision making from a European perspective,” *Energy*, vol. 139, pp. 468–484, 2017, doi: 10.1016/j.energy.2017.07.164.
- [4] *Wasserdampf, Wasser, Eis, Meerwasser - KCE Thermodynamics*. [Online]. Available: <https://thermofluidprop.com/stoffwertbibliotheken/wasserdampf-wasser-eis-meerwasser> (accessed: Mar. 1 2021).
- [5] E. Schmidt, “Ausströmen von Gasen aus Behältern hohen Innendruckes,” (in de), *Chemie Ingenieur Technik*, vol. 37, no. 11, pp. 1091–1094, 1965, doi: 10.1002/cite.330371103.
- [6] W. Bohl and W. Elmendorf, *Technische Strömungslehre: Stoffeigenschaften von Flüssigkeiten und Gasen, Hydrostatik, Aerostatik, Inkompressible Strömungen, Kompressible Strömungen, Strömungsmesstechnik*, 15th ed. Würzburg: Vogel Buchverlag, 2014.
- [7] *TLV Euro Engineering GmbH (Deutschland) - Der Dampfspezialist*. [Online]. Available: <https://www.tlv.com/global/DE/> (accessed: Mar. 8 2021).
- [8] B. Glück, “Anmerkungen zum Standard MAN 803.07/(IEC 534-2-2) Durchflußmengenermittlung für kompressible Fluide bei Stellarmaturen,” *Stadt- und Gebäudetechnik*, vol. 42, no. 3, pp. 77–80, 1988.
- [9] L. Pasięka, *The applicability of the mass-flow-model according to iso 6358 with the parameter critical conductance c and critical pressure ratio b for gases in high-pressure range up to 300 bar*, 2020.
- [10] W. Goldstern, *Steam storage installations; construction, design, and operation of industrial heat accumulators: Construction, design and operation of industrial heat accumulators*, 2nd ed. Oxford, New York: Pergamon Press, 1970.
- [11] M. Stark, F. Conti, A. Saidi, W. Zörner, and R. Greenough, “Steam storage systems for flexible biomass CHP plants - Evaluation and initial model based calculation,” *Biomass and Bioenergy*, vol. 128, p. 105321, 2019, doi: 10.1016/j.biombioe.2019.105321.
- [12] M. Stark, C. Trinkl, W. Zörner, and R. Greenough, “Methodological Evaluation of Storage Systems for Flexible Power Generation from Solid Biomass,” *Chem. Eng. Technol.*, vol. 41, no. 11, pp. 2168–2176, 2018, doi: 10.1002/ceat.201800099.

Potential analysis for long-term storage of a decentralized power-to-gas technology

Alexander R uckerl and Oliver Steffens
Ostbayerische Technische Hochschule (OTH) Regensburg
Regensburg, Germany
alexander1.rueckerl@st.oth-regensburg.de

ABSTRACT — In future energy systems with high shares of fluctuating renewable energies the power-to-gas (PtG, P2G) technology will become increasingly important for the utilization of surplus energy. Usually, such a conversion would be tied to a specific location, since a reliable CO₂ source such as the emission from an industrial facility is needed to produce and store the methane (CH₄). The focus of this research work is about an emission-free decentralized power-to-gas technology for the energy supply of buildings. With this technology the carbon dioxide produced during combustion is not released into the environment but is returned to the system cycle to produce methane. In this way, the power-to-gas plant functions as a cycle and is therefore environmentally friendly across the board. Thus, the carbon dioxide is transformed from a "climate killer" into a raw material for energy supply. Based on building performance simulation, using the software IDA ICE, a thermodynamic simulation model is created to analyse the power-to-gas system in terms of potential for seasonal storage and flows of energy and material within the plant. As IDA ICE does not contain any useable modules for the PtG components, the methodology of how a possible implementation of the PtG components in the simulation program can take place, by using Neutral Model Format (NMF) modules and existing IDA ICE modules, is described.

Keywords: Power-to-Gas, long-term energy storage, methane, IDA ICE, Neutral Model Format (NMF)

1. INTRODUCTION

In view of declining oil reserves and increasing environmental problems caused by emissions of greenhouse gases, the reduction of energy supply by fossil fuels in favor of regenerative fossil fuels in favor of regenerative energies is a major challenge for building and challenge for building and energy supply planners. In addition, the climate policy of the European Union aims to reduce greenhouse gases by 2050 by 80% compared to 1990 levels [1]. Already today, the electric power supply system is characterized by a high share of renewable energies, which is expected to increase further in the future. However, fluctuating renewable energy generation is also creating more and more unused electricity surpluses and the associated energy curtailments. The concept of power-to-gas offers considerable potential in this regard and could make a promising contribution to increasing energy

efficiency, reducing greenhouse gas emissions, and storing energy in the future.

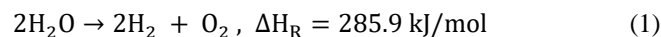
2. FUNDAMENTALS

The company Exytron Ltd. developed the SmartEnergy-Technology (SET), which is a decentralized carbon-based power-to-gas system. The fundamentals of the PtG technology and an CO₂ supply circle, which is used in the SET, are described below.

2.1. Alkaline electrolysis (AEL)

The splitting of water with excess electrical energy to produce hydrogen and oxygen is done by water electrolysis. Three different electrolysis technologies are of interest for PtG process chains: alkaline electrolysis (AEL), polymer electrolyte membranes (PEM), and solid oxide electrolysis (SOEC). Hydrogen by itself also offers good potential as a regenerative energy carrier and storage. As part of the German energy transition, a very strong expansion of installed electrolysis capacity in double digit gigawatt range is expected for Germany by 2050 [2]. The SET operates with an alkaline electrolyser, which is the most proven and well understood technology out of the three types of electrolysis considered for PtG plants [3].

The separation of hydrogen and oxygen runs under the following chemical reaction:



The AEL electrolyser can be operated between 20 and 100% of its design capacity with an electrical efficiency up to 82% [4]. This operation window makes the AEL a good choice for PtG systems as they are tied to a fluctuating and intermittent power supply.

2.2. Methanation

For the production of regenerative methane, the methanation or catalysis is necessary as an additional process step after the electrolysis. Especially as an energy storage medium, the production of methane has a great advantage, as the

volumetric energy density (calorific value in relation to volume) is three times greater than that of hydrogen (table 1).

	Calorific value [MJ/m ³]
Hydrogen	10,80
Methane	36,00

Table 1 - Calorific value of hydrogen and methane at 1 bar and 0 °C [5]

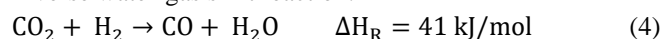
Sabatier reaction:



CO-Methanation:



Inverse water-gas shift reaction:



From the Sabatier reaction, an H₂/CO₂ ratio of 4/1, i.e. 80% hydrogen and 20% carbon dioxide, is derived as the ideal ratio for an optimal reaction process. A direct reaction of hydrogen with carbon dioxide occurs in rather rare cases, since the CO₂ is only weakly reactive. However, in most chemical methanation plants, gases with a very high CO₂ content or even pure CO₂, as in the SET, are available. Hence, a separation into carbon monoxide (CO), which is described by equation (4) the water-gas shift reaction, takes place in order to set optimal conditions for the reaction.

For the methanation of CO₂, catalysts are necessary, by which the activation energy is lowered, and the inhibited reaction is accelerated. The SET uses a nickel-based catalyst, which is an optimal catalyst material for methanation due to its high selectivity to methane. In addition, nickel is very well researched and has a very low material price, which is why it has gained good acceptance in practice [6]. However, nickel-based catalysts require very pure reactant gases to avoid poisoning. Catalyst poisoning is the strong adsorption or chemical binding of reactants, products or impurities on active sites that are otherwise available for catalysis. Catalysts are highly sensitive to sulfur or sulfur compounds (e.g. H₂S or COS) [7]. A single strongly adsorbed sulfur atom can thereby block access to several active sites of the catalyst, which ultimately leads to a deactivation of the catalyst. The data in Figure 1 indicates that the materials nickel (Ni), ruthenium (Ru), cobalt (Co), iron (Fe), suffer a loss of activity of about 3 to 4 orders of magnitude at a concentration of 15-100 ppb. Consequently, their tolerances to hydrogen sulfide are extremely low.

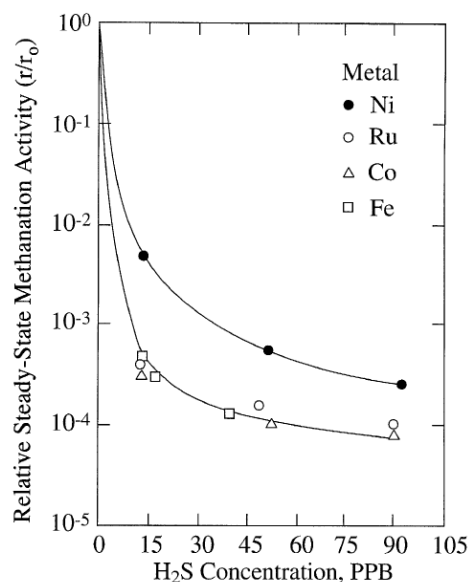
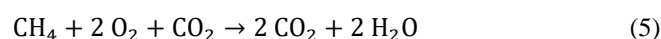


Figure 1 - Behavior of different catalyst materials towards H₂S during methanation. Reaction conditions: 100 kPa; 400 °C [7]

For this reason, high requirements are necessary for upstream gas treatment and purification of the reactants before the reaction.

2.3. CO₂ supply

In the case of power-to-gas, CO₂ is used as a raw material for methane production and is converted to the more reactive carbon monoxide by the water gas shift reaction. The product obtained via the Sabatier reaction has at most the same concentration of methane as the CO₂ concentration from its source [8]. Consequently, it is important that the supplied CO₂ has a high degree of purity as well as a reliable availability. Also, to ensure a temporal independence in CO₂ use, storage facilities are required. The SET uses a CO₂ recycling, which is a form of the so-called oxyfuel process. This process is based on very clean combustion with only carbon dioxide and water as the end product. The water can be easily separated and pure CO₂ remains, which can then be stored. Since combustion with pure oxygen involves extremely high flame temperatures, CO₂ must be added to the oxygen to achieve a cooling effect. As this mixed gas is free of nitrogen, no nitrogen oxides are formed during combustion and the highest possible CO₂ concentration can be ensured in the recycled exhaust gas. Consequently, the reaction equation (5) is obtained for combustion in the combined heat and power (CHP) plant:



A storage facility is necessary to ensure that a supply for methanation and combustion is provided as needed. In addition, storage can completely prevent the release of the climate-damaging gas. To achieve a high density and suitable conditions for loading and unloading, the CO₂ must be compressed and liquefied. For the liquefaction of a gas with

90% CO₂ concentration using a multi-stage compression with intercooling, an energy input of 0.12 kWh_{el}/kg CO₂ is required [9].

2.4. SNG-Storage

For decentralized energy supply, storage facilities, usually in the form of pressure tanks, must be provided. If Synthetic Natural Gas (SNG) is stored under compression at the usual pressures of 200 and 300 bar, it is referred to as Compressed Natural Gas (CNG).

	State	Calorific value [MJ/kg]	Calorific value [MJ/m ³]
Methane	1 bar	50	36
CNG (Methane)	200 bar, 25 °C	50	8105

Table 2 – Energy densities in comparison. Conversion with 1 MJ/m³ = 2.778 · 10⁻⁴ kWh/l [10] [11]

When methane is compressed to 200 bar, about 2% of the energy content is lost during the gas compression.

2.5. Efficiency

Figure 2 below shows the operating principle or the SET with its theoretical efficiencies given by Exytron Ltd. The amount of generated PV power that is not required for direct use and consequently fed into the PtG system is 40%. An additional 7.5% of the remaining 40% is required for the power supply of other components such as the reactor and the compressors. This ultimately leaves 32.5% of the electricity generated to operate the electrolyser. The efficiency factors of the PtG components are 0.69 for the electrolysis, 0.78 for the catalysis are also given by Exytron and coincide with the literature. Assuming an electrical efficiency of 0.36 for the CHP unit that will be used results in a rather poor overall efficiency for a re-conversion into electric power of only 15.74%.

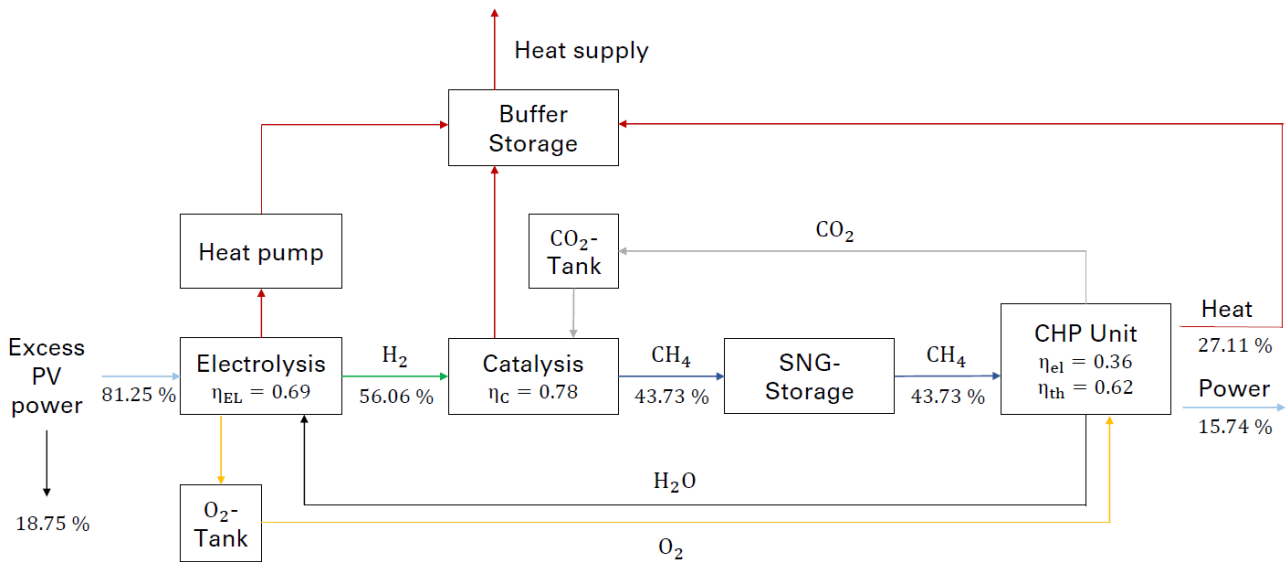


Figure 2 - Operating principle and efficiency of the SET (Source of the data: [12])

3. IMPLEMENTATION IN IDA ICE

To create an optimal simulation model, all the above-mentioned key parts of the PtG process have to be implemented in the building simulation software IDA ICE in order to analyse the potential for long-term storage. The initial goal of the simulation is to see how much methane can be produced and how much methane is consumed by the CHP unit in one year. IDA ICE is an equation-based software in which the source codes of the modules can be adapted or rewritten as desired. However, the standard modules in IDA ICE do not offer any suitable modules for the PtG components illustrated in figure 2. For this reason, the approach to the simulation is a complete re-creation or re-programming of existing modules.

3.1. Methodology

For the implementation of the components, a combination of existing modules and new NMF modules is the optimal approach. Mathematical IDA ICE modules are used to visualize the energy and material flow by using a calculative approach. Based on the degrees of efficiency, the amount of energy contained in the various substances can be calculated. Subsequently, the enthalpies given in the reaction equations (1) and (2) can be used to calculate the amount of substance produced. For instance, with an enthalpy of 285.9 kJ/mol for the separation of water, an energy of 571.8 kJ (≈ 0.16 kWh) is required to split water into two mol hydrogen and one mol oxygen. With a molar

mass of 2 g/mol for H₂, a minimum of 143 kJ is required for 1 g H₂.

In this way the amount of produced hydrogen and methane based on the generated surplus PV power can be calculated and analysed. Also, the calorific value from table 2 can be used to calculate the amount of methane produced and stored in m³. At last, the CHP unit with its associated control logic is then simulated over the same simulation period to see how much methane is consumed in one year. This is primarily existing IDA ICE modules and the generated methane can be described via a calculatory assessment.

3.2. Neutral Model Format (NMF) Modules

Another approach which will be pursued is the creation of new modules in IDA ICE via the Neutral Model Format (NMF) modules. This path is more complex than a calculative approach, however, after successful programming, usable modules for the representation of the components can be integrated into IDA ICE. The creation of NMF modules is done via text files, in which the source code is entered and are structured according to the following main sections: Equations, links, variables, parameters. Each NMF module must be designed with one or more input and output links, where the relationship

```
LINKS
/* type      name      variables      description */
  ELPROD     Term_a     Tpa, POS_IN   Qa      "PV Production [Wh] surface A";
  TQ         Term_b     Tpb, POS_OUT  Qb      "Hydrogen [Wh] surface B";
  TQ         Term_c     Tpb, POS_OUT  Qc      "Hydrogen [m³] surface B";

PARAMETERS
/* type      name      role  def    min    max    description */
  Factor     cvH2      S_P   12.70  SMALL  BIG   "calorific value H2 [MJ/m³]"
  Factor     convMJ    S_P   0.2778 SMALL  BIG   "conversion kWh/m³"
```

Figure 3 - Excerpt of a first approach possible source code for an electrolysis module

As mentioned above, the module is defined with one input, the PV power, and two outputs, hydrogen as energy content in Wh and as quantity in m³. With a planned maximum electrolyser power of 320 kW and the conversion of 1 MJ/m³ into 0,2778 kWh/m³ the hydrogen production rate is determined with the above equations as follows:

$$Q_c = \frac{320 \text{ kW} \cdot 0.69}{(12.70 \frac{\text{MJ}}{\text{m}^3} \cdot 0.2778)} = 62.50 \text{ m}^3/\text{h} \quad (6)$$

4. CONCLUSION AND OUTLOOK

In this paper, the basic principles and two approaches for incorporating the power-to-gas concept into IDA ICE in the future were described. The realisation of the simulation model will be addressed in the next steps of the research work. Also, the SET simulation model will be connected to

between input and output is described by mathematical equations. For example, in electrolysis, water and PV electricity are considered input links whereas hydrogen and oxygen are considered output links. The variables of the code do not have to be created. They are existing variables from the software, which are necessary to describe heat flow and power flow in the module. Ultimately, any factor that appears in the equations of the source code has to be defined with the respective numerical values in the parameters section. The following are excerpts from a source code that may be part of a possible solution for the electrolysis module at the current time. In the equation, the correlation between incoming PV electricity and outgoing hydrogen is shown via the efficiency degree:

```
EQUATIONS
Qa = Qb
Qa = ELPROD*0.69
Qc = Qa/(cvH2*convMJ)
```

All terms that appear in the equation are defined in the link and parameter section shown in figure 3 below. In the description column the respective link or parameter is described in words. Qa is defined as the input “PV production” whereas Qb and Qc are the outputs “hydrogen in Wh” and “hydrogen in m³.”

a building model to analyse correlation of solar gains, the building with its heat capacity, heat and power loads, the SET system and energy storage. The purpose of the simulation will be to form a basis for economic considerations of the SET in the future with the intention to provide an initial analysis of how much methane is stored and consumed over a year. The results of the efficiency analysis show that only a relatively poor efficiency of 15.74% with a re-conversion into electrical power and 27.11% heat usage is achieved at the end of the process chain. Whether it is worth working with this degree of efficiency will be shown in an economic efficiency calculation in further steps of the research. However, the power-to-gas technology should certainly be further developed for the future. A rising CO₂ price and rising natural gas costs are essential prerequisites in this respect,

which would push on the economic viability of the regenerative system.

REFERENCES

- [1] European Commission, Directive 2009/28/EC of the European Parliament and of the Council on the Use of Energy from Renewable Sources and Amending and Subsequently
- [2] T. Smolinka, N. Wiebe, P. Sterchele, A. Palzer, F. Lehner, M. Jansen, S. Kiemel, R. Mische, S. Wahren, F. Zimmermann: Studie InWEde: Industrialisierung der Wasserelektrolyse in Deutschland: Chancen und Herausforderungen für nachhaltigen Wasserstoff für Verkehr, Strom und Wärme. Bundesministerium für Verkehr und digitale Infrastruktur (BMVI). Berlin, 2018.
- [3] M. Götz, J. Lefebvre, F. Mörs, A. McDaniel Koch, F. Graf, S. Bajohr, R. Reimert, T. Kolb: Renewable Power-to-Gas: A technical and economic review. *Renewable Energy* 85 (2016), 2015. URL: <https://www.sciencedirect.com/science/article/pii/S0960148115301610> (23.04.2021)
- [4] M. Sterner, I. Stadler: *Energiespeicher – Bedarf, Technologien, Integration*. 2. Auflage, Berlin: Springer Vieweg, 2017.
- [5] G. Cerbe, B. Lendt, K. Brüggemann, M., Dehli, F. Gröschl, K. Heikrodt, T. Kleiber, J. Kuck, J. Mischner, T. Schmidt, A. Seemann, W. Thielen: *Grundlagen der Gastechnik. Gasbeschaffung – Gasverteilung – Gasverwendung*. 8. Auflage, München: Hanser, 2017.
- [6] M. Götz, J. Lefebvre, F. Mörs, A. McDaniel Koch, F. Graf, S. Bajohr, R. Reimert, T. Kolb: Renewable Power-to-Gas: A technical and economic review. *Renewable Energy* 85 (2016), 2015. URL: <https://www.sciencedirect.com/science/article/pii/S0960148115301610> (27.04.2021)
- [7] C. H. Bartholomew: *Mechanisms of catalyst deactivation*. *Applied Catalysis A: General* 212. Provo, 2001. URL: <https://www.sciencedirect.com/science/article/pii/S0926860X0008437> (27.04.21)
- [8] F. Rachow: *Prozessoptimierung für die Methanisierung von CO₂ – Vom Labor zum Technikum*. Dissertation, Technische Universität Cottbus-Senftenberg, 2017. URL: <https://opus4.kobv.de/opus4-tbtu/frontdoor/index/index/docId/4262> (20.04.2021)
- [9] O. Mayer-Spohn, M. Blesl, U. Fahl, A. Voß: *Logistik der CO₂-Sequestrierung – Optionen für den CO₂-Transport*. *Chemie Ingenieur Technik* 2006, 78, No. 4, Weinheim: Wiley-VCH Verlag GmbH & Co. KGaA, 2006.
- [10] R. van Basshuysen: *Erdgas und erneuerbares Methan für den Fahrzeugantrieb. Wege zur klimaneutralen Mobilität*. Wiesbaden: Springer Vieweg, 2015.
- [11] P. Kurzweil, O. K. Dietlmeier: *Elektrochemische Speicher. Superkondensatoren, Batterien, Elektrolyse-Wasserstoff, Rechtliche Rahmenbedingungen*. 2. Auflage, Wiesbaden: Springer Vieweg, 2018.
- [12] Eytron Vertrieb Ltd. Augsburg, 2019.

Influence of hydrogen on the combustion process of a single cylinder spark ignited gas engine

B.Eng. Timo Schaller
 OTH Amberg-Weiden
 University of applied research
 Email: t.schaller@oth-aw.de

Abstract—In the course of climate change, energy suppliers worldwide are under pressure to abolish fossil fuels and develop the technical usability of renewable energies. This change places particular demands on new storage technologies. In recent years, processes have been developed to temporarily store renewable energies in gases. One product of this CO_2 neutral conversion is hydrogen, which can be stored in large quantities and be reconverted to electricity, if required. As an application of the "Gas to Power" concept, the combustion process in a spark-ignited single cylinder engine with a variable mixture of natural gas and hydrogen is investigated. In this paper, special attention is given to the influence of hydrogen on the rate of heat release and further combustion parameters.

I. INTRODUCTION

Due to the abolition of fossil fuels in the future, renewable energies will become more and more important [1]. With the potential of a sustainable production, hydrogen is an ideal alternative to conservative sources. Furthermore hydrogen is suitable for most internal combustion engines and has the potential to significantly reduce emissions [2]. Within the scope of this work, the effects of hydrogen on several combustion parameters will be analyzed. Based on the in-cylinder pressure, a real time calculation of the energy release in the closed combustion chamber will be analyzed. The test engine is a spark-ignited single cylinder gas engine fueled with a variable mixture of natural gas and hydrogen, which is mixed in the intake manifold. This allows a first investigation of the burn process and based on this the influence of different hydrogen ratios can be carried out. The ignition timing is adjusted to keep the center of combustion (AI50) constant. However various hydrogen ratios are suitable to compensate the disadvantages from the natural gas combustion, such as the slow burning velocity and the relatively large cycle-by-cycle variations. This work will enhance the understanding of the influence of different hydrogen ratios on the energy release.

II. METHODS

The specifications of the engine are shown in table I. The high pressure cycle lasts as long as both the inlet and the exhaust valves are closed from -134 degCA to 125 degCA. The hydrogen fraction can be adjusted between 0 % and 100 %. The cylinder pressure is recorded by a piezoelectric transducer for every 0,5 deg and triggered with the crank angle (CA) signal. Every recording comprises 200 complete cycles and the averaged values of these cycles are evaluated.

Table I
ENGINE SPECIFICATIONS

cylinder bore / stroke	90 mm / 91 mm
con-rod	155,5 mm
combustion ratio	13
inlet valve closed (IVC)	-134 degCA
exhaust valve open (EVO)	125degCA
rated speed and power	2500 rpm / 6 kW

To calculate the rate of heat release for the high pressure cycle, the first law of thermodynamics for closed systems (valves closed) is written as follows [3], [4]:

$$\Delta U = Q_B - W_V - Q_L - Q_W \quad (1)$$

For the real time investigation of the combustion process, both the loss of leakage through the piston rings Q_L and the wall heat Q_W are neglected. As a result of this simplification the absolute value of the rate of heat release is lower by this amount. Nevertheless the curve of the energy release, especially the center of combustion (AI50) can be investigated. The variation of the gas-state equation with the crank angle is:

$$p \frac{\partial V}{\partial \phi} + V \frac{\partial p}{\partial \phi} = mR \frac{\partial T}{\partial \phi} \quad (2)$$

With reference to equations 1 and 2 the rate of heat release Q_B with the simplification mentioned at the beginning can be derived:

$$\frac{\partial Q_B}{\partial \phi} = \frac{1}{\kappa - 1} \left[\kappa p_i \frac{\partial V_i}{\partial \phi} + V_i \frac{\partial p_i}{\partial \phi} \right] \quad (3)$$

The measurement system delivers both the cylinder pressure p_i and the current volume of the combustion chamber V_i .

III. RESULTS AND DISCUSSION

Figure 1 shows the in-cylinder pressure for 0, 10, 60 and 100% hydrogen related to the supplied energy. The further calculation takes place when the valves are closed. Variations in the curve of cylinder pressure are near the top dead center, because the ignition timing is adjusted with rising hydrogen. The maximum pressure decreases with higher hydrogen fractions because the volumetric lower heating value of the mixture decreases and it can be seen, that the late ignition timing avoids a large rising of the pressure. With a hydrogen

fraction less than 10%, the influence of the heating value has a smaller impact than the effect of the increasing flame propagation speed, so that the cylinder pressure of this curve is higher [5].

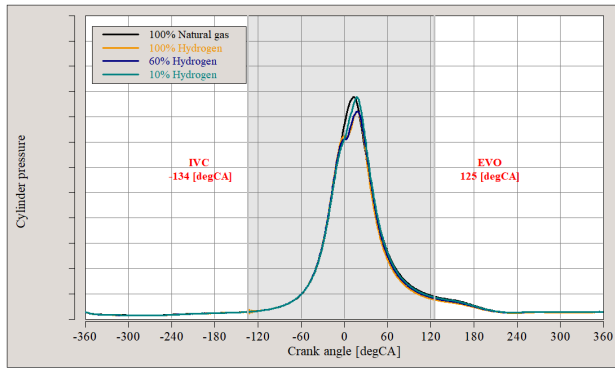


Figure 1. In-cylinder pressure for different hydrogen fractions at 2500 rpm

The rate of heat release (ROHR) is the differential curve of the energy conversion versus crank angle. With regard to equation 3 the ROHR for the in-cylinder pressures are displayed in figure 2. Due to the retarded ignition timing, the AI50 (the crank angle of 50% energy release shown in figure 2) remains stable. The hydrogen combustion takes less time than the combustion of natural gas and so the rate of heat release in the center of combustion is higher.

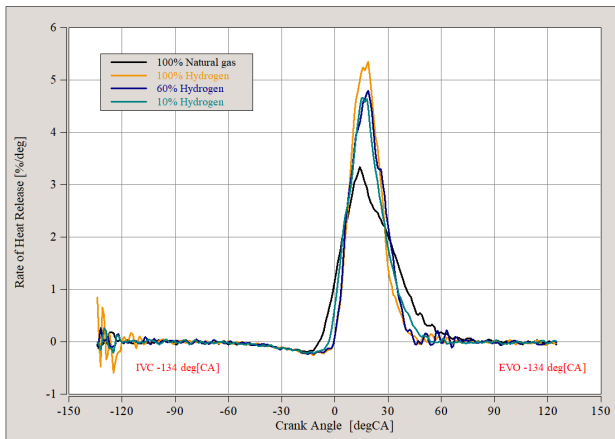


Figure 2. Rate of heat release for different hydrogen fractions at 2500 rpm

Figure 3 shows the accumulated curve of ROHR, so that the released energy reaches 100% at the end of the combustion. Due to the high burning velocity of hydrogen, the combustion duration decreases with increasing hydrogen fractions and thus the curve gets steeper. For a given AI50, the combustion duration of an increasing hydrogen fraction gets shorter and thus a loss of power can be prevented. The ignition delay is the sum of the ignition crank angle (before top dead center BTDC) and the AI5 (5% of energy release). According to table II the ignition crank angle has to be retarded to obtain constant AI50 and thus the ignition delay for increasing hydrogen fractions gets lower.

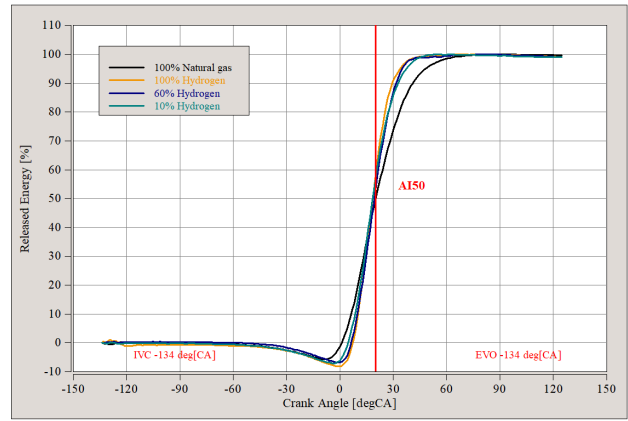


Figure 3. Released energy at 2500 rpm

Table II
ENGINE OPERATING PARAMETERS

H_2 rate	ignition CA	Δ AI50 %	deviation pressure	λ
0 %	-22	0	3,00 %	1,6
10 %	-10	3,5	1,120 %	1,6
60 %	-7	3,8	0,983 %	1,8
100 %	-3,5	2,9	0,958 %	2,0

The deviation of the in-cylinder pressure decreases, because the responsive burn characteristics and higher mass heating value of hydrogen stabilizes the combustion.

IV. CONCLUSION

The real time analysis of the burn process for a first investigation of the rate of heat release with different hydrogen fractions was carried out. Hydrogen has a significant influence on the combustion time and the ignition delay, although the ignition timing has to be retarded with increasing hydrogen ratios. Hydrogen combustion achieves a high degree of constant volume even under retarded spark ignition timing conditions because of the short combustion period. The accumulated energy release gets steeper with increasing hydrogen fractions and so the loss due to real heat releases is lower. Hydrogen stabilizes the combustion so that the (cycle-to-cycle) deviation of the in-cylinder pressure decreases with increasing hydrogen fractions.

REFERENCES

- [1] M. Zapf, *Stromspeicher und Power-to-Gas im deutschen Energiesystem*, Mönchsberg, Germany: Springer Vieweg, 2017.
- [2] Z.Huang and B. Liu, "Combustion characteristics and heat release analysis of a spark-ignited engine fueled with natural gas-hydrogen blends", in *energy and fuels*, Xi'an, China, 2007, pp.2594-2599.
- [3] A. Witt, "Analyse der thermodynamischen Verluste eines Ottomotors unter den Randbedingungen variabler Steuerzeiten", Dissertation, techn. Univ. Graz, Austria, 1999.
- [4] R. Pischinger, *Thermodynamik der Verbrennungskraftmaschine*, 2nd ed. Graz, Austria: Springer-Verlag Wien GmbH, 2002.
- [5] S. O. Akansu and Z. Dulger, "Internal combustion engines fueled by natural gas-hydrogen mixtures", *International journal of hydrogen energy* vol. 29, pp.1527-1539, Dec 2004.

Determination of the restriction-free inductive and capacitive reactive power potential based on the example of a medium-voltage industrial operation

Philipp Schweiberer

Ostbayerische Technische Hochschule Regensburg
Forschungsstelle für Energienetze und Energiespeicher (FENES)
Regensburg, Germany
philipp1.schweiberer@st.oth-regensburg.de

Abstract—Since conventional large-scale power plants provide a considerable share of reactive power, but are being eliminated in the course of the energy transition, a new concept for the provision of reactive power must now be developed. Within the scope of the Q-Integral project, a holistic view of the topic "reactive power" is to take place in order to analyze and evaluate the potentials of the various reactive power provisions with regard to economic and technical aspects both on the distribution level and on the transmission level. Industrial plants, whose reactive power potentials should contribute to voltage maintenance and thus to a grid- or system-serving behavior, are considered as one possibility of reactive power provision. In this paper, the determination of the restriction-free reactive power potential is presented. In this context, the term "restriction-free" describes the exclusion of limits resulting from the maximum utilization of operating resources. The procedure is applied to an industrial operation with three installed industrial compensation systems (ICS) in the distribution network to investigate the reactive power behavior on weekdays and weekends. From this, the secured potential is to be determined and day dependencies shall be identified, which provide information about the occurrence of inductive and capacitive potentials. The aim of the further project is to determine the secured restriction-related reactive power potential with consideration of the resource utilization in order to develop adequate regulation strategies for the internal reactive power management.

Keywords—Voltage Maintenance, Reactive Power, Industrial Operations, Energy Transition

I. INTRODUCTION

In the course of the energy transition, a change in the structure of the electricity supply network is taking place. The shift of generation capacity in the higher grid levels by conventional large-scale power plants to the lower grid levels to decentralized renewable energy plants has resulted in both bidirectional load flows and fluctuating feed-in characteristics. Hence, new challenges have emerged regarding a safe and reliable operation of power grids. Since conventional large-scale power plants provide a considerable amount of reactive power, a new concept for the provision of reactive power has to be developed now. Therefore, the reactive power potential of industrial plants in the medium-voltage grid is investigated as a possibility for voltage maintenance [1].

A. Motivation

Within the project Q-Integral, the topic "reactive power" is investigated holistically. For this purpose, various options for the provision of reactive power are being examined with regard to their technical and economic potential, which will be incorporated into a functional and efficient reactive power management system. The approaches to the investigation are both cross-voltage level and cross-grid operator. One approach of the project is the consideration of the reactive power supply of industrial operations [2]. For this purpose, the potential of plants connected to the distribution grid that can provide reactive power through industrial compensation systems (ICS) or generation plants is investigated. The objective is to determine the secured and maximum inductive as well as capacitive potential. The secured capacitive potential can be used to make statements about the extent to which the voltage drop in the upstream grid can be counteracted at times of heavy load. The secured inductive potential can be used to compensate for a voltage increase during off-peak periods. In order to be able to make statements about the reactive power potential, measurements must be carried out at relevant points on the industrial operations and considered over a period of time that allows dependencies on seasons, days of the week and times of day to be taken into account.

B. Objective

The aim of the paper is to present the determination of the restriction-free reactive power potential. In this context, the term "restriction-free" describes the exclusion of limits resulting from the maximum utilization of operating resources. The determination of the reactive power potential is shown using the example of an industrial plant in the distribution network on which measurements are carried out. The reactive power behavior on weekdays and weekends is to be investigated. From this the secured reactive power potential is to be determined as well as day dependencies are to be recognized, which give information about the occurrence of inductive and capacitive potentials. In this work the reactive power potential of ICSs is discussed. Other

potentials, provided by generation plants such as generators, are not considered further in this work.

II. TECHNICAL BASICS

A. Fundamental reactive power

Since the ICSs used in the industrial plant have an influence on the fundamental oscillation, the fundamental reactive power is considered for the calculation of the reactive power potential. The fundamental reactive power results from the phase shift of the fundamental oscillations of current and voltage and can be determined by (1) [3].

$$Q_1 = U_1 \cdot I_1 \cdot \sin(\varphi_1) \quad (1)$$

Since harmonics are measured in addition to the fundamental oscillations when measuring voltages and currents, the fundamental oscillations must be calculated using the total harmonic distortion factor (THD), which is specified via the producer of the measuring equipment and is defined according to (2) [4].

$$THD_U = 100\% \cdot \sqrt{\frac{U^2 - U_1^2}{U_1^2}} \quad (2)$$

From (2) the RMS-value of the fundamental voltage can now be calculated:

$$U_1 = \frac{U}{\sqrt{\left(\frac{THD_U}{100\%}\right)^2 + 1}} \quad (3)$$

In the same way, the RMS-value of the fundamental phase currents can be calculated (4).

$$I_1 = \frac{I}{\sqrt{\left(\frac{THD_I}{100\%}\right)^2 + 1}} \quad (4)$$

The fundamental reactive power can be calculated with (5):

$$Q_1 = \frac{U}{\sqrt{\left(\frac{THD_U}{100\%}\right)^2 + 1}} \cdot \frac{I}{\sqrt{\left(\frac{THD_I}{100\%}\right)^2 + 1}} \cdot \sin(\varphi_1) \quad (5)$$

B. Reactive power potential of industrial compensation systems

For each ICS, the input data shown in Table I is needed to calculate its reactive power potential. For the industrial plant considered in this work, there are three stations with one ICS connected.

Based on the full-uncompensated and full-compensated operation, the inductive and capacitive reactive power potential of

Table I
INPUT PARAMETER FOR THE CALCULATION OF THE REACTIVE POWER POTENTIAL

Notation	Description
$Q_{ICS,i}(t)$	Provided compensation power of the ICSs dependent on time
$Q_{ICS,inst,i}$	Installed compensation power of the respective ICS
$Q_{1,i}(t)$	Reactive power behavior of the potential-relevant station

the individual stations with a connected ICS can be calculated and thus also of the entire industrial operation [5].

$$Q_{full-uncomp} = \sum_{i=1}^n Q_{1,i}(t) - \sum_{i=1}^n Q_{ICS,i}(t) \quad (6)$$

$$Q_{full-comp} = Q_{full-uncomp} + \sum_{i=1}^n Q_{ICS,inst,i} \quad (7)$$

1) *Inductive reactive power potential*: By switching off all stages of the ICSs, the maximum inductive potential of the operation is retrieved and determined according to (8) [5].

$$\begin{aligned} Q_{pot,inductive} &= Q_{full-uncomp} - \sum_{i=1}^n Q_{1,i}(t) \\ &= - \sum_{i=1}^n Q_{ICS,i}(t) \end{aligned} \quad (8)$$

The inductive potential represents the step powers of the respective ICSs that were switched at the corresponding points in time.

2) *Capacitive reactive power potential*: By switching on all stages of the ICSs a capacitive behavior is achieved. The maximum capacitive potential is thus retrieved and can be determined according to (9) [5].

$$\begin{aligned} Q_{pot,capacitive} &= Q_{full-comp} - \sum_{i=1}^n Q_{1,i}(t) \\ &= \sum_{i=1}^n Q_{ICS,inst,i} - \sum_{i=1}^n Q_{ICS,i}(t) \end{aligned} \quad (9)$$

A graphical illustration of the inductive and capacitive reactive power potential can be seen in Figure 1. The two types of reactive power potential are indicated by black arrows and describe the extent to which the reactive power behavior can be changed around a given operating point.

III. DETERMINATION OF THE REACTIVE POWER POTENTIAL

A. Reactive power potential of the individual potential-relevant stations

1) *Reactive power potential at station S1*: Figure 2, in which the inductive and capacitive reactive power potential of station 1 is shown, shows that there is a minimum inductive

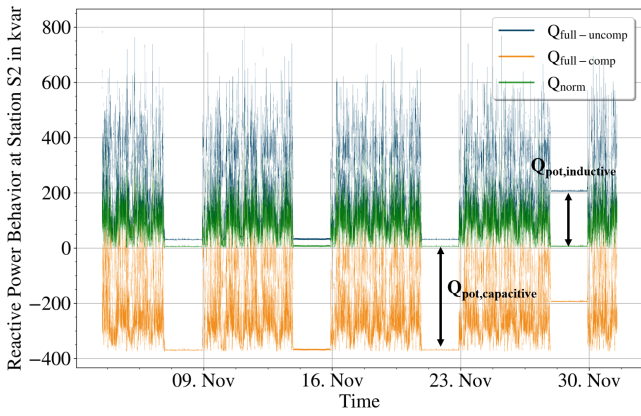


Figure 1. Reactive power behavior of the operation for normal (green), full-uncompensated (blue) and full-compensated (orange) operation at Station S2 for the month of November 2020 in second-resolution

reactive power potential unequal to 0. This fact results on the one hand from the consumer at station S1, which draws inductive reactive power, and on the other hand from the ICS, whose first stage is permanently switched in.

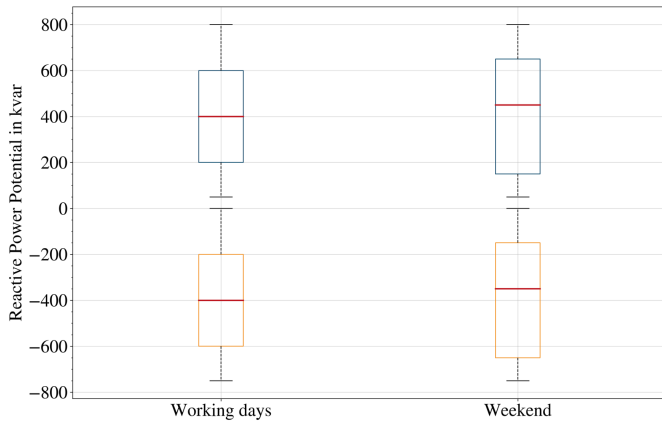


Figure 2. Inductive (blue) and capacitive (orange) reactive power potential at station S1 for the month of november

Since at least one stage of the ICS is switched at any time, the secured inductive change potential is 50 kvar. This means that the maximum inductive change potential is 750 kvar, or 93.75% of the total compensation power at station S1. The maximum capacitive potential that can be retrieved is -850 kvar. The minimum inductive potential and also the maximum inductive and capacitive potential can be retrieved both on working days and on weekends. As the distribution of the reactive power potentials in Figure 3 indicates, there are more inductive and capacitive reactive potentials on working days during heavy load times than on weekends during low load times.

2) *Reactive power potential at station S2:* For station S2 the same conditions apply as for station S1. There is a

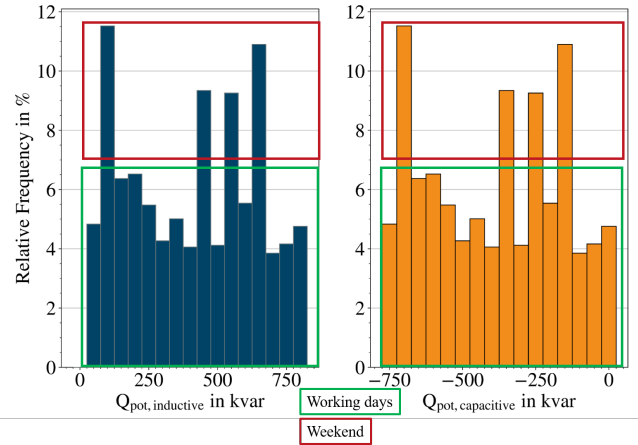


Figure 3. Distribution of inductive and capacitive reactive power potential at station S1 for the month of november

minimum inductive reactive power potential unequal 0, which results from the inductive consumer and from the operation mode of the ICS, whose first stage is permanently switched on (Figure 4). The secured inductive potential is 25 kvar. This means that a total of 375 kvar of the installed compensation power of 400 kvar can be considered as the maximum inductive change potential. Furthermore, here it is also evident that there is no secured capacitive potential.

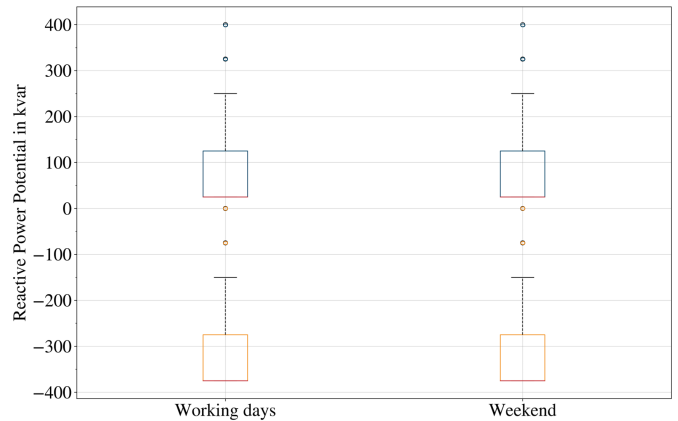


Figure 4. Inductive (blue) and capacitive (orange) reactive power potential at station S2 for the month of november

The secured inductive potential can be retrieved during working days and weekends. For working days and weekends, the maximum capacitive potential of 375 kvar can be retrieved. The distribution in Figure 5 shows that the inductive and capacitive potential is lower on weekends than on weekdays

3) *Reactive power potential at station S3:* For station S3, Figure 6 shows that the first stage of the ICS is permanently switched in, as in the two stations S1 and S2 mentioned above, and thus a secured inductive change potential of 25 kvar can be retrieved out of a total compensation power of 400 kvar. The maximum retrievable inductive potential is 375 kvar.

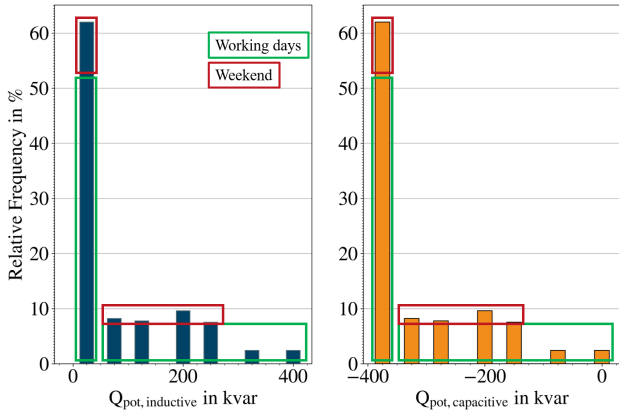


Figure 5. Distribution of inductive and capacitive reactive power potential at station S2 for the month of november

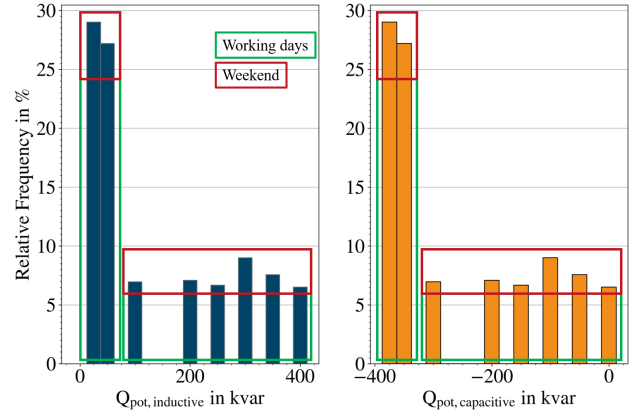


Figure 7. Distribution of inductive and capacitive reactive power potential at station S3 for the month of november

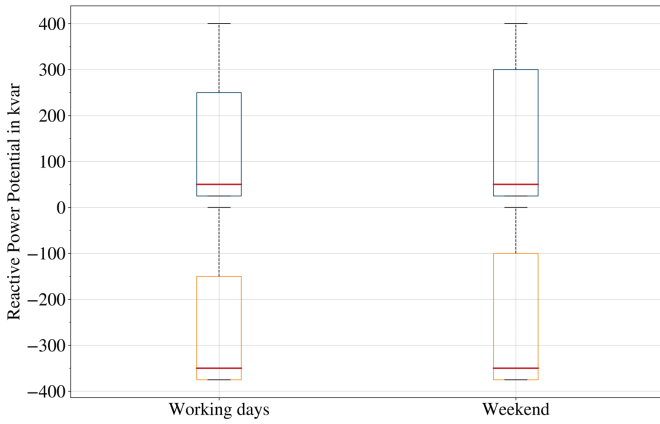


Figure 6. Inductive (blue) and capacitive (orange) reactive power potential at station S3 for the month of november

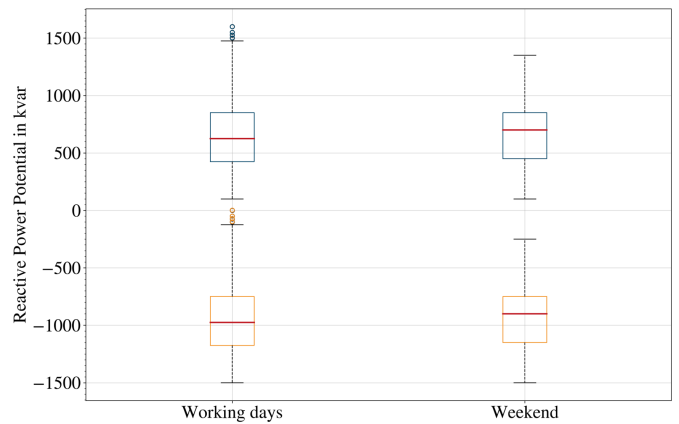


Figure 8. Entire inductive (blue) and capacitive (orange) reactive power potential for the month of november

Comparing the inductive change potential of station S2 with that of station S3, to each of which a load and an ICS are connected, the differences can be seen especially in the distributions on weekends, since especially two stages (25 kvar and 200 kvar) are used at station S2, while more stages are used at station S3 as shown in Figure 7. It can be seen further that the step power of 150 kvar at station S3 is not activated on working days and weekends. The maximum capacitive potential is -375 kvar and can be accessed on weekends and weekdays. As with the previous stations S1 and S2, there is no secured capacitive potential.

B. Reactive power potential of the entire industrial operation

Figure 8 shows that a minimum non-zero inductive reactive power potential is present and can always be retrieved, since at all the above stations the first stage of the ICSs is always switched during the period under consideration. The secured inductive potential is 100kvar. Thereby station S1 with a secured inductive potential of 50 kvar has a share of 50% and stations S2 and S3 with 25 kvar each have a share of 25%

of the total secured inductive potential. The total available compensation power of all ICSs is 1600 kvar. Out of this power, a maximum of 1500 kvar can be retrieved as maximum inductive reactive power potential. The secured capacitive potential is -250 kvar on weekends. This situation is shown again in Figure 9. It shows for each reactive power compensation system the maximum switched compensation power, the permanently switched compensation power and the average switched compensation power during normal operation, which were taken from the time series of the individual ICSs.

IV. SUMMARY AND CONCLUSION

The calculations of the reactive power potentials have shown that the inductive potential and the capacitive potential as well are larger on working days than on weekends at all potential-relevant stations. Moreover, it has been shown that the first stage is permanently switched on at all ICSs, resulting in a secured inductive potential equal to the sum of the first stage powers of the ICSs (total 100 kvar).

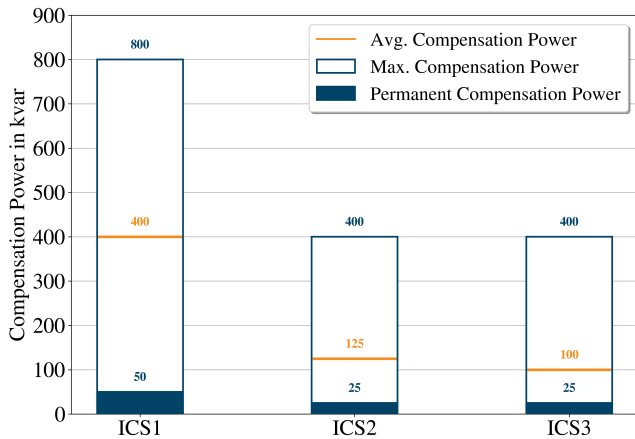


Figure 9. Average switched compensation power, maximum switched compensation power and permanently switched compensation power of the individual compensation systems for the month of November 2020

$$\min(Q_{\text{pot,inductive},S_i}(t)) \neq 0, \quad i = \{1, 2, 3\} \quad (10)$$

Furthermore, it has been shown that there is no secured capacitive potential on working days, since for each potential-relevant station the following applies:

$$\min(Q_{\text{pot,capacitive},S_i}(t)) = 0, \quad i = \{1, 2, 3\} \quad (11)$$

In the investigated industrial plant with the existing inductive loads, an inductive reactive power potential can be provided at any time by always providing compensation power through at least one ICS.

Table II and Table III show the minimum and maximum reactive power potentials. They are divided into the individual stations and the sum of the stations as well as into weekdays and weekends.

Table II

MINIMUM INDUCTIVE AND CAPACITIVE REACTIVE POWER POTENTIAL OF STATIONS S1, S2, S3 AS WELL AS THE SUM OF THE EXAMINED POTENTIAL RELEVANT STATIONS FOR WEEKDAYS AND WEEKENDS

Station	Min. ind. Potential in kvar		Min. cap. Potentia in kvar	
	Working days	Weekend	Working days	Weekend
S1	50	50	—	—
S2	25	25	—	—
S3	25	25	—	—
S1 + S2 + S3	100	100	—	-250

The next step of the project is to determine the restriction-free potential of further measurements in order to investigate the dependence on times of day as well as on seasonal influences and also on public holidays or bridging days. Furthermore, the restriction-related reactive power potential is

Table III

MAXIMUM INDUCTIVE AND CAPACITIVE REACTIVE POWER POTENTIAL OF STATIONS S1, S2, S3 AS WELL AS THE SUM OF THE EXAMINED POTENTIAL RELEVANT STATIONS FOR WEEKDAYS AND WEEKENDS.

Station	Max. ind. Potential in kvar		Max. cap. Potential in kvar	
	Working days	Weekend	Working days	Weekend
S1	800	800	-750	-750
S2	400	400	-375	-357
S3	400	400	-375	-375
S1 + S2 + S3	1600	1350	-1500	-1500

to be determined on the basis of the load profiles in addition to the restriction-free potential. This is to be realized with the help of a simulation in which the utilization of other resources such as lines and cables can be calculated. Based on the calculation, statements can then be made as to whether the restriction-free potential can be retrieved or not.

REFERENCES

- [1] Forschungsstelle für Energienetze und Energiespeicher, *-Integral – Aktives Blindleistungsmanagement mit dynamischen Blindleistungsquellen an der Schnittstelle Verteilungsnetz und Übertragungsnetz*, OTH Regensburg, [Online]. Available: <https://www.fenes.net/forschung/energienetze/laufende-projekte/q-integral/>
- [2] Technische Universität Braunschweig (2018), *Q-Integral: Aktives Blindleistungsmanagement mit dynamischen Blindleistungsquellen an der Schnittstelle Verteilungsnetz und Übertragungsnetz*, (unpublished).
- [3] W. Weißgerber, *Elektrotechnik für Ingenieure 3: Ausgleichsvorgänge, Fourieranalyse, Vierpoltheorie*, 10. ed. Springer Vieweg, Wiesbaden, 2018. [Online]. Available: <http://www.springer.com/de/book/9783658218249>
- [4] Chauvin Arnoux Group (2017, May), *PEL 102 PEL 103: Leistungs- und Energieregistriergerät*, [Online]. Available: https://www.chauvin-arnoux.com/sites/default/files/D00ZWN82_0.PDF
- [5] J. Rauch and O. Brückl, *A Reactive Power Control Strategy based on Linear Programming for Medium Voltage Distribution Grids using the Reactive Power Potential of Industrial Compensation Systems*, OTH Regensburg, FENES: (unpublished).

Development and Validation of a 3L-ANPC Bridge Type Inverter Based on GaN HEMTs

Veit Starost
TH Nürnberg
Institut ELSYS
90489 Nürnberg

Email: starostve69748@th-nuernberg.de

Abstract—This paper gives a short overview of the GaN-inverter project of the Institute ELSYS. The wide bandgap material as well as the chosen design aims at high efficiency and a desired peak output power of 25 kW. The inverter is designed for grid application, like solar grid feed-in.

I. INTRODUCTION

In the course of the energy revolution, DC power is gaining in importance due to photovoltaic and battery systems. Inverters are needed to feed excess power into the AC grid. For the development of inverters, efficiency is a crucial point. New semiconductors and circuit designs are frequently researched to improve efficiency. Following, the development of an inverter on a GaN semiconductor basis, with a peak output power of 25 kW is presented. The first chapter will explain the topology and how it affects an inverter. A short insight into the development of hard- and software is given later on. The section of the hardware is limited to the difficulties in the design process and how they are overcome. To explain the software, UML diagrams are used. This section is mainly focused on the hardware-dependent part of the software.

II. 3L-ANPC BRIDGE TYPE AND GAN HEMTs

1) *GaN HEMTs*: GaN is a semiconductor, which is currently advancing in power electronic products. It is capable of switching fast and efficiently. The transistor type HEMT is a special type of field-effect transistor whose structure is optimized for fast switching. An additional advantage of GaN is the capability of reverse conduction, which eliminates the need for a reverse diode. The reverse voltage drop behaves resistive, but with an offset of the inverse gate voltage. While switched on, the GaN HEMT acts solely resistive in both directions. Switched off, it is acting as a diode. [1]

2) *3L: three level design*: A three-level bridge type is capable of setting the output to three different voltage levels. Usually $DC+$, $DC-$ and a *neutral*-level are used. The *neutral*-level can be created by splitting the intermediate circuit voltage over two serially connected capacitors.

The first advantage of this design is a smaller ripple of the output current, as the difference between the voltage levels is lower. In addition, the maximal voltage every single transistor has to block is only half of the complete DC voltage. Especially the GaN MOSFETs profit from this advantage, as they are currently only available with up to 650 V rated

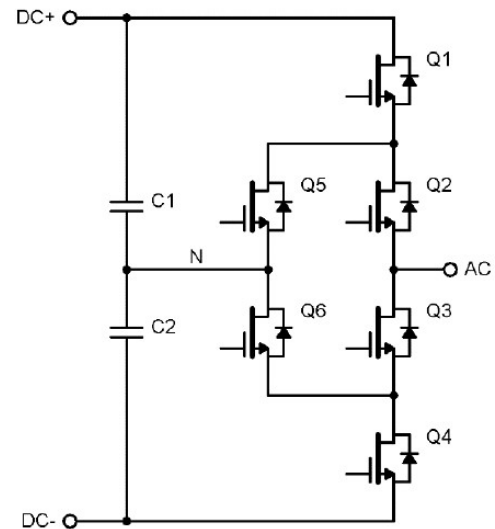


Figure 1. 3L-ANPC Topology [3]

blocking voltage. With the 3L design the GaN inverter can be used in an 800 VDC system. This voltage level is important as large batteries operate at this level. Therefore the possible uses for the inverter get extended to *Battery to Grid* and *Vehicle to Grid (V2G)*. Furthermore, the control of the whole inverter by the space vector modulation method is getting more precise with three possible output levels per phase [2]. The disadvantage is the need for more parts compared to the traditional two-level design, resulting in higher production costs.

3) *The ANPC topology*: The active neutral point clamp (ANPC) is a certain structure to realize a 3L design. It is shown in fig. 1. This topology has two possible ways to clamp the neutral-point to the output as well as one way for each, positive and negative. The similar neutral point clamp (NPC) topology has diodes in place of $Q5$ and $Q6$, which slightly reduces the cost for parts but also increases losses due to the diodes forward voltage.

III. HARDWARE DESIGN

1) *Difficulties with GaN*: The low threshold voltage, as well as the low gate capacity, lead to the fast switching capability of the GaN HEMTs. But on the other hand, it also

creates the problem of a higher risk for parasitic turn-on. To ensure safe operation, the switching time could be increased, which would be contra-productive, as this leads to increased switching losses. Another option is to improve the turn-off path of the drivers. This is achieved by a low resistance as well as a low inductance. Therefore the parasitic values of the PCB traces must be taken into account. Minimizing the current commutation loop from gate to source has the highest priority when designing a layout with GaN HEMTs. This rule is based on experience gained from tests of the preceding project theses in which the gate circuit was optimized. It is contrary to the recommendations from the manufacturer, who gives the power commutation loop a higher priority than the gate loop. In general, it can be expected that these two loops are of similar importance. [4]

A. Inverter design rules

Furthermore the usual aspects which have to be taken care of must be considered like in a conventional inverter. This includes e.g. the parasitic inductance in the power commutation loop, which can cause significant over-voltages if it is too high. Therefore, a short path with a high cross-section to the intermediate circuit capacitors is necessary [5]. To prevent interference, the routing of the AC output lines should be routed separately from the control signals. This is usually posing no problem in the design process of a conventional inverter, but with six bridges and six transistors per bridge on a single PCB, the separated routing gets more challenging.

B. Output quality improvements for grid feed-in

To feed power into the European 50 Hz grid, the transmission grid provider specifies minimal quality requirements for the current. The main requirement is a good interference immunity and therefore a small amplitude of the harmonics (EN 61000-6). A simple solution is to use a mains filter, which can be very space inefficient. Most space is usually occupied by the cooling system of an inverter, but with higher efficiency, there are fewer thermal losses that have to be cooled. Therefore the whole inverter is more space-efficient and should not be enlarged with a big filter circuit.

To archive a more compact design, three components are used to minimize the harmonics: Firstly the already mentioned 3L design, which produces lower amplitude harmonics than a 2L design, is used. For the next step, two bridges are used per phase. They work in parallel but are not switched simultaneously. Rather they are offset by half of the duty cycle to one another. This leads to different current ripples, which are opposing each other and therefore cancelling themselves partially out. This is called interleaved operation [6]. As the current ripple, which is occurring in switching frequency, is the largest share of the harmonics, the reduction increases the output quality significantly. The last step is also a current filter circuit as a mains filter, but after the previous steps, it can be designed much smaller.

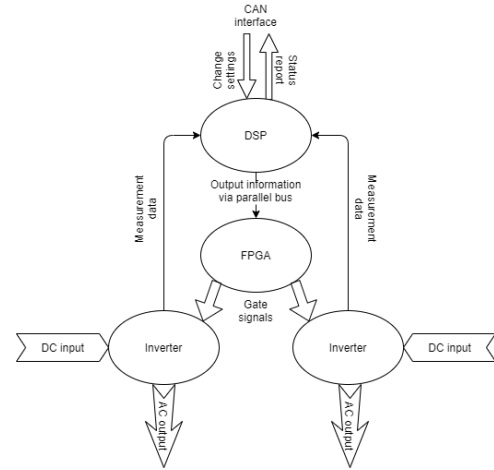


Figure 2. Data-flow diagram for the inverter control

IV. SOFTWARE STRUCTURE

The control of the inverter structure is split among three devices. The time-precise control of the 36 transistors per inverter is done by an FPGA, whereas the macro control for the desired output is calculated by a DSP. The FPGA and DSP are capable of controlling two inverters at once. Furthermore, the general settings can be changed over a CAN connection to the DSP, but this connection is not mandatory.

A. Control flow

The data flow is visualized in fig. 2. The diagram is structured as the highest level is the closest to the user and the lowest level is closest to the single transistors. The highest control level is the CAN connection, where the user can access measurement data and set general settings like desired output power and frequency. The next level is the DSP, which receives the measurement results from the inverter. They include phase currents and voltages as well as the intermediate circuit voltage. These are used to calculate the output PWM patterns for the bridges, which are then sent to the FPGA. Moreover, the DSP controls the speed of the cooling fans according to the temperature of the heat sinks. The FPGA on the lowest control level uses the bridge output PWM information from the DSP to translate it into input PWM patterns for the transistors.

B. FPGA code structure

The VHDL code is structured into three entities. Entities can be considered equivalent to classes in object-orientated programming. The dependencies of the entities are depicted in fig. 3. The *DSP Connection* handles a 16 bit parallel bus connection between DSP and FPGA. One bit is for differentiating the two inverters that can be connected. The remaining 15 bit are handed over to the *Inverter* entity. Here, the message gets decoded to change the settings of one of the inverters *3I-ANPC Bridges*. The message contains three bits to determine the destination *3I-ANPC Bridge*, four bits to define the variable for which the payload is meant and eight bits

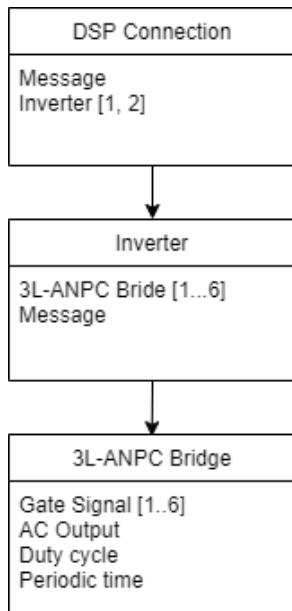


Figure 3. Structure of FPGA Entities

for the payload itself. Some synchronisation settings can be changed for all bridges at once. Every *3L-ANPC Bridge* Entity processes its settings to switch its six transistors accordingly. This entity is also responsible for keeping the bridges in safe states. This is achieved through intermediate switching steps and short dead times to ensure, that there is always at least one transistor turned off between two DC voltage levels.

As there are two ways to switch the *neutral*-level to the output, various switching strategies can be used to alternate the output voltage level. The different switching orders of the transistors can affect the switching-losses. Therefore, some of the strategies from J. Dodge (UnitedSiC) [3] are implemented and will be tested with the GaN setup.

V. CONCLUSION

The currently developed GaN inverter of the Institute ELSYS uses several hard- and software elements to aim for high efficiency. As a side effect, the design is getting more compact. With the designed peak output power, a mid-scale photovoltaic system can be connected to the grid. As a next step, a prototype has to prove the theoretical advantages in practice. The effects of the software are important to be investigated with the prototype. Moreover, the maximal continuous output power and the optimal switching frequency have to be investigated with testing.

LIST OF ABBREVIATIONS

GaN gallium nitride
HEMT high-electron-mobility transistor
ANPC active neutral point clamp
3L three level
FPGA field programmable gate array
DSP digital signal processor

NPC neutral point clamp
UML Unified Modeling Language
PWM puls width modulation
VHDL VHSIC hardware description language
PCB printed circuit board
CAN Controller Area Network
V2G Vehicle to Grid

REFERENCES

- [1] G. Systems, *GS66516B Datasheet*, 2019. [Online]. Available: <https://gansystems.com/wp-content/uploads/2019/01/GS66516B-DS-Rev-190121-1.pdf>
- [2] F. Sebaaly, H. Vahedi, H. Kanaan, N. Moubayed, and K. Al-Haddad, "Design and implementation of space vector modulation based sliding mode control for grid-connected 3l-npc inverter," *IEEE Transactions on Industrial Electronics*, vol. 63, pp. 1–1, 12 2016.
- [3] J. Dodge, "3l-anpc vs. 3l-npc inverters," Feb 2020. [Online]. Available: https://unitedsic.com/appnotes/UnitedSiC_AN0023_inv_comp.pdf
- [4] G. Systems, "Gn009 pcb layout considerations with gan e-hemts," Jan 2019. [Online]. Available: https://gansystems.com/wp-content/uploads/2019/01/GN009-PCB-Layout-Considerations-with-GaN-E-HEMTs_20190118.pdf
- [5] H. A. Fahel, "Evaluate power device efficiency with double-pulse testing using an afg," Dec 2019. [Online]. Available: <https://www.powerelectronics.com/technologies/power-management/article/21864518/evaluate-power-device-efficiency-with-doublepulse-testing-using-an-afg>
- [6] M. Florides, "Interleaved switching of dc/dc converters," Ph.D. dissertation, 01 2010.

Change in the energy market - opportunities for industrial companies

Lukas Weber

Technical University of Applied Sciences Amberg-Weiden
Faculty of Electrical engineering, media and computer science
Kaiser-Wilhelm-Ring 23, Amberg, 92224, Germany
Email: l.weber@oth-aw.de

Supervising Professor: Prof. Dr.-Ing. Magnus Jaeger
Technical University of Applied Sciences Amberg-Weiden
Faculty of Industrial Engineering and Health
Hetzenrichter Weg 15, Weiden, 92637, Germany

Abstract—In 2017, the European Parliament published the "European Green Deal," which describes a gradual reduction in net greenhouse gas emissions down to zero by 2050. The more ambitious Federal Republic of Germany target implies achieving climate neutrality by 2045. These targets require a significant increase of renewable energy production within the entire energy production market. This will increase the volatility in their supply and will result in growing fluctuations in the exchange electricity price. Against this background, the research question at hand can be formulated as "To what extent industrial companies can profit from the expected changes in the energy market through dynamic energy management?"

The research question is illustrated based on a medium-sized, raw material processing industrial company. The focus is on the development of an energy forecasting tool for the forward planning of the energy demand required because of the partly dynamically changing production, taking into consideration the aspects of cost and carbon dioxide emission optimization. The goal of this research project is to propose the production scenario for an average production day, which will then be optimized to meet customer requirements as well as economic and ecological objectives. As a first step essential production data, and framework conditions such as sales, energy demand, energy supply contracts, energy load profile data, production key figures and mass flows had to be reviewed and analyzed, to allow for a dedicated mapping of the production processes.

Initial analyses indicate that in the future, it will be possible for companies to benefit from short term changes in the energy market through dynamic energy management. This will be economically feasible as soon as energy price fluctuations are going to be passed on to the end customer. Decarbonization in the production process and flexible adjustment of the loads used in the company, adapted to the renewable energies currently available in the grid, can be a recipe for success here.

Keywords— dynamic energy management, energy forecasting tool, load management, load shifting potential, Carbon dioxide tax, decarbonization

I. INTRODUCTION

Climate change is one of the most important challenges of the 21st century. Due to the growing energy consumption of our society and the increasing world population, the emission of climate-damaging greenhouse gases is rapidly increasing, which causes an anthropogenic temperature increase [1].

Therefore, by means of long-term regulations, the emission of carbon dioxide must be regulated by transnational regulations to reduce global warming. Consequently, a joint action plan is needed.

On 12 December 2015, it was agreed at the international climate conference in Paris that global warming must be limited to a maximum of two degrees by 2100, compared to pre-industrial levels. For the first time in history, this agreement requires the signing nations, based on international law to combat climate change and mitigate its effects [3]. Four years after the Paris Climate Agreement was signed, the European Commission presented a new concept for combating climate change, the "European Green Deal". This stipulates that Europe must reduce net greenhouse gas emissions to zero by 2050 [2]. Following the ruling of the German Federal Constitutional Court against the proposed climate protection law, the government is struggling to amend the law in a timely manner.

The law, recently drafted by Federal Environment Minister Svenja Schulze (SPD) now includes stipulations on how much greenhouse gases are to be saved each year, starting in 2030. In addition, the targets for the period prior to 2030 have been increased in the various energy sectors. The energy sector is required to save one-third of the current energy consumption by 2030 than what was stipulated in the previous climate protection law. Accordingly, by 2030 it will be necessary to emit 65 percent less carbon dioxide (CO₂) compared to 1990. By 2040, the reduction has to be 88 percent, and from 2045 on, only the amount of climate-damaging gases are to be emitted that the environment can reabsorb [4].

The ambitious target is to be achieved by means of a significant increase in the expansion of renewable energies and an increase in the CO₂ tax. The CO₂ tax was introduced in Germany on January 1, 2021 and taxes the emission of climate-damaging CO₂. The CO₂ tax is currently 25 Euros per ton of CO₂. Annually, the price increases by 5 Euros per ton of carbon dioxide [5].

Due to the legally required increase of renewable energy in power generation, the volatility in the supply is constantly increasing. Renewable power generation is largely dependent on environmental factors.

Increasing fluctuations in the exchange electricity market price are the result, because the exchange electricity price reflects the relationship between supply and demand. The power exchange is divided into two markets, the forward market, and the spot market [6]. Due to the feed-in obligation for renewable energies, existing generators, such as coal-fired power plants and gas-fired power plants, must be switched on and off to keep the grid frequency balanced. Currently, the generation of electricity follows the load-following mode. In this process, power plants adjust their electricity generation to meet electricity demand.

Against the backdrop of increasingly unstable grids, the European Commission is trying to develop solutions for adjusting the electricity demand to the generation. As a result, the European Commission will continue to liberalize the internal electricity market by removing regulations so that end customers can benefit from fluctuating electricity exchange prices. Soon, industrial companies will therefore be able to participate in this market. Against this background, the research question is: "To what extent can industrial companies, through dynamic energy management, benefit from the expected change in the energy market?"

May 17, 2021

II. MATERIALS AND METHODS

To answer the research question, a quantitative field study will be conducted in cooperation with a medium-sized industrial company. The cooperation investigates to what extent it is possible for industrial companies to profit from the expected changes in the energy market through dynamic energy management.

For the field study, a representative industrial company was chosen, which has a highly variable electrical consumption as well as a high thermal energy consumption. Quarzsand GmbH is the leading producer of high-quality quartz sand in Bavaria. The potential of a dynamic energy management at the company Quarzsand GmbH is estimated as high, since for the cleaning, preparation as well as drying of sands high energy quantities are necessary. The core competence of the company is the preparation of quartz sands, which are used internationally in the construction, chemistry as well as in the glass industry. The product portfolio is defined by different sand types, which are essentially defined by the grain size and their purity content. The raw material extraction takes place in different opencast mines in Bavaria.

The production is divided into the process stages sand feeding, wet classification, drying, dry classification, storage, and loading. The Strobel Quarzsand GmbH has already been using a combined heat and power plant for about 10 years to optimize costs. To enable an exact allocation of the energy consumption, the consumers with their load curve data are recorded for each plant group. In the wet classification, the sand is separated from impurities and sorted into different grain sizes.

Drying takes place via water pre-separation during storage of the sand and subsequent drying in drying kilns, which are operating with natural gas. Drying is largely responsible for the company's high natural gas consumption. In the dry classification, the dried sand is further sorted, based on specific composition, and then stored in silos, with a view to upcoming loading to customers.

For a possible optimization of the energy purchase, it is necessary to be able to forecast the energy demand by means of an electricity consumption forecasting tool, based on a specific production program. The goal is to allow for proper adjustments, if necessary, to achieve the most economical and ecological production scenario. In order to be able to forecast the energy consumption, it is necessary to define the specific energy consumption rates based on the different sand types produced. Since the respective sand types differ in the processing steps and consequently in the energy consumption incurred by each sand type, it is first necessary to record and analyze the required production steps with the individual machines operated for each sand type. Each sand type passes through different groups of equipment during the course of the production. For each of these groups of equipment, the output can be determined as a function of mass flow and capacity utilization. This makes it possible to draw conclusions about the power consumption in relation to the respective sand types. The same applies to the natural gas consumption in the drying process.

Based on the aforementioned parameters, it is possible to draw conclusion about the respective energy demand with an underlying production program. In order to verify the predicted data, a comparison is made utilizing an underlying production program using historical data. In addition, it will then be possible to allow for factual statement about the extent to which the forecasting tool can actually help forecasting the energy demand for Strobel Quarzsand GmbH.

III. RESULTS

Figure 1 illustrates the electricity power curve of the company Strobel Quarzsand GmbH over an exemplary week. The blue curve illustrates the electricity purchased based on a one week production cycle. The green line represents the power provided by the internal combined heat and power plant and the red graph illustrates the overall power consumption of the company.

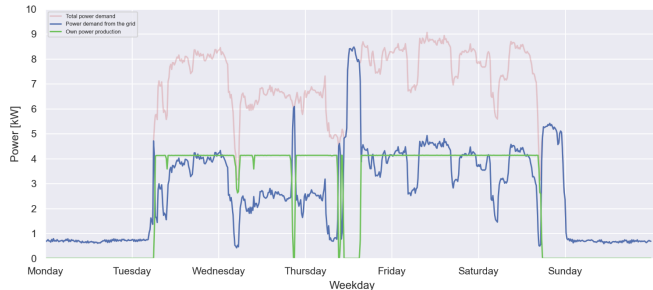


Figure 1. Electrical power curve based on a one week production cycle from Strobel Quarzsand GmbH

The very low electricity demand on Monday and Sunday is due to the fact that production has been paused. The fluctuations in the total electricity demand suggest that different sand types entail different energy demands. It is assumed that the energy forecasting tool under development will have an accuracy in consumption forecasting of over 90 percent based on a few key parameters, given knowledge of the production program. This can only be determined exactly after completion of the program. In order to achieve an increase of the prognosis quality, the prognosis tool could be amended by means of artificial intelligence.

The consumption forecast model, will enable the company to recognize load peaks at an early stage and to also implement load shifting potentials. Unfortunately, because Strobel Quarzsand schedules the production programs at a relatively short notice (one to three days in advance), a permanently optimized production program is not possible. However, the production program can be designed in such a way that sand types with a high energy demand are produced at times when the share of renewable energies in the grid is high.

As soon as the price fluctuations in the electricity grid are passed on to the end customer, the price decreases at the times when the share of renewable energies is high. Thus, it is possible to partially adjust the electricity demand to the electricity generation. Due to the increasing CO₂ tax, drying, using natural gas is deemed not to be economically feasible in the long term. The natural gas consumption can be significantly reduced by substituting the gas burners with low-temperature heat exchangers.

However, this will lead towards an increase of the electrical demand, which amplifies the importance of the electricity forecasting tool. Thus, the electricity forecasting tool allows to effectively and efficiently design the production scenario in the best possible ecological as well as economical way.

IV. CONCLUSION

The study shows that companies can benefit from the change in the energy market through dynamic energy management concepts. For this, it is necessary that companies prepare for the upcoming change and optimize the production processes towards a high percentage of decarbonization. A company's cost savings depend largely on the degree of decarbonization and the extent to which price fluctuations on the energy exchange market are passed on to industrial companies. For companies to adapt to the change at an early stage, it is necessary for the government to continue to create incentives for change and rethinking.

For companies, this means using the right type of electricity at the right time in the future.

REFERENCES

- [1] Statista, „CO₂-Emissionen: Größte Länder nach Anteil am weltweiten CO₂-Ausstoß im Jahr 2018,“ 2018. [Online]. Available: <https://de.statista.com/statistik/daten/studie/179260/umfrage/die-zehn-groessten-co2-emittenten-weltweit/>. [Zugriff am 25 12 2020].
- [2] United Nations, „Paris Agreement,“ Paris, 2015.
- [3] Endt, Chrisitan und E. Erdmann, „Zeit,“ 06 05 2021. [Online]. Available: <https://www.zeit.de/wissen/umwelt/2021-05/klimaschutzgesetz-klimaneutralitaet-paris-abkommen-klimaziele>. [Zugriff am 10 05 2021].
- [4] S. von Wirth, „Handelsblatt,“ 15 01 2021. [Online]. Available: <https://www.handelsblatt.com/finanzen/steuern-recht/steuern/co2-preis-was-die-neue-co2-steuer-fuer-verbraucher-bedeutet/26228322.html?ticket=ST-2679444-jJbFpIR2FXt9K9I1u2Zg-ap3>. [Zugriff am 10 05 2021].
- [5] H.-W. Schiffer, „Aufbau der Elektrizitätswirtschaft nach Wertschöpfungsstufen,“ in *Energiemarkt Deutschland*, Wiesbaden, Springer Fachmedien Wiesbaden GmbH, 2020, pp. 192-196.

Development of a virtual fuel injector for operation with Diesel and Oxymethylenether

Christoph Wopper
 University of Applied Sciences
 Regensburg
 Regensburg, Bayern
 Email: christoph1.wopper@st.oth-regensburg.de

Abstract—Reducing CO₂-emissions is one of the major goals in development of most vehicles and construction equipment as well as any other kind of self-propelled devices. Since battery powered electric motors are not suitable for every application, CO₂-neutral alternatives to fossil fuels have to be found. One candidate as an alternative to diesel fuel is oxymethylenether (OME). It is potentially CO₂-neutral and also has other advantages in terms of combustion and emissions behavior like very low soot formation[1]. To develop an engine running on diesel as well as OME, a lot of injection test bench measurements have to be carried out. The problem is, that injection systems like a pump-line-nozzle type system are very sensitive to influences like pre-supply pressure. Furthermore the design of the high pressure pump needs to be adapted for OME operation. All these influences would require a new mapping of the injection characteristics of the whole system, every time components are adapted during a development process. This leads to long development cycles and produces high costs. To solve this issue, a simulation model has been developed, that represents the fuel injector by itself. This model is able to predict injection rates of a previously investigated fuel injector using only the pressure signal of the high-pressure injection line, the engine speed as well as the pre-supply pressure. With this, the simulation model is the link between injection test bench and engine test bench. The model developed in this paper shows very good correlations between measured and simulated injection rates for diesel operation. The correlation for OME operation is slightly worse but still usable. The reason for the worse performance in OME operation is most likely the very limited knowledge of fuel properties like for example viscosity at different temperatures and pressures. Future additions to this model will be the modeling and calibration of the high pressure pump to aid and simplify the development of an optimized fuel injection system.

I. INTRODUCTION

Reducing global CO₂ emissions is one of mankind's greatest goals in the 21st century. To achieve this, new technologies and regulations are necessary in all areas. One example is the electrification of all possible types of drives. These are then to be operated with regeneratively produced electricity in a CO₂-neutral manner. The most prominent example of this is probably the electric car, but other areas from aircraft and ships to construction machinery and tractors also need to be electrified. The problem for aircrafts is that batteries cannot provide the energy density required for aviation. Commercially available kerosene for example has an energy density of about 42 MJ/kg [2], while the latest batteries developed by Tesla have an energy density of 0.936 MJ/kg [3].

Another problematic area is construction equipment, such as excavators. Because they often operate in areas without access to the power grid combined with the low energy density of batteries, they probably won't be battery-powered in the foreseeable future.

So-called power-to-liquid (PtL) fuels, also known as eFuels, provide a solution for these examples. They are synthesized from water and CO₂ using electrical energy. That makes them CO₂-neutral, as long as renewably generated electricity is used. This means that fuel-based drive systems can be indirectly electrified. For this reason, countries such as Germany are investing in research and development of PtL based fuels[4].

But it is not only aviation that needs eFuels. Construction machinery and tractors for example, most of which are powered by diesel engines, won't be CO₂-neutral without a CO₂-neutral power source. One candidate for a PtL diesel replacement fuel is oxymethylene ether, or short OME. This eFuel is not only potentially CO₂-neutral, but also features very low-soot combustion, which also enables further NO_x-emissions reduction.[1].

In general, internal combustion engines can be operated with a wide variety of fuels. Nevertheless, the engines and the combustion processes must be adapted to the respective fuel. OME, for example, has a significantly lower calorific value than diesel and thus requires a higher injection quantity to achieve the same performance values. The investigated engine in this study is an air-cooled, single-cylinder diesel engine with an electronically controlled, cam-driven pump-line-nozzle injection system. Tests already carried out on this engine at the engine test bench and injection test bench of the OTH Regensburg have revealed various problems. On the one hand, different examples of the same injection system have different volume behavior. The reason for this may be manufacturing tolerances of the injection nozzle and high-pressure pump. Secondly, the injection system itself reacts sensitively to changes in the pre-feed pressure. This opens up a multidimensional investigation space that cannot be satisfactorily investigated on a test bench, without a massive effort.

The aim is therefore to make measurements of the injection rate curve on the injection test bench transferable to a running engine on the engine test bench. Both in diesel and OME operation. The OME used in this study is a blend of the

Table I: Comparison of Diesel and OME properties

	Unit	OME-Mix[5]	Diesel EN590
Lower heating value	MJ/kg	19.21	42.6
Density @ 15°C	KG/m ³	1057.1	0.82
Boiling point	C	145-242	170-390
Cetan-number	-	68,6	>51
Lubricity @ 60°C	microm	320	<460
Kin. viscosity	mm ² /s	1.082	2@25 °C

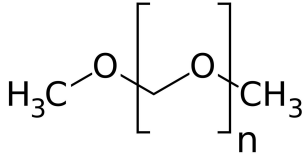
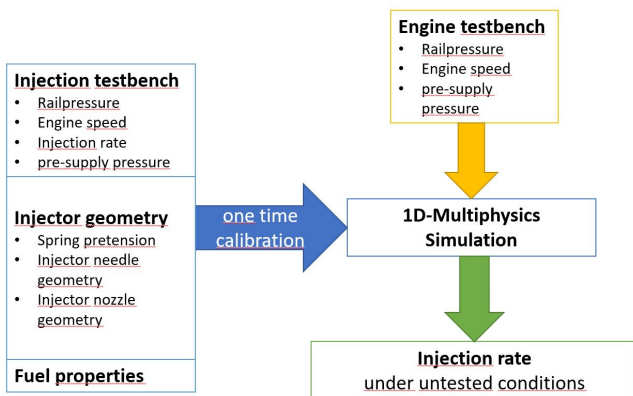
Figure 1: Chemical structure of OME_n[6].

Figure 2: Virtual injector functional scheme

OMEs with n 3-5 (see figure 1). The tool to link these two test benches is 1D simulation. A schematic of the workflow can be seen in Figure 2. Here, a simulation model of an injector, which has been tested on the injection test bench, is created and calibrated. This simulation model makes it possible to calculate the injection rate using only the engine speed and the measured pressure in the high-pressure fuel line. Provided that the same injector that was initially measured is also used on the engine test bench. The advantage is, that the injector only has to be measured with a handful of loadpoints, even though the simulation model will be able to display all normal operating points, independently from the high-pressure pump design or pre-feed pressures that are being used.

II. STRUCTURE OF THE INJECTION SYSTEM

The injection system under investigation is a so-called pump-line-nozzle system and thus consists functionally of three parts:

- The high-pressure pump: Here, driven by a cam, the fuel is sucked in and compressed to injection pressure. Normally the solenoid valve that connects the high pressure and low pressure side of the fuel system is open. As soon as the solenoid valve closes, the pressure rises and the fuel can only flow towards the injector under high pressure.



Figure 3: Moehwald HDA Injection rate analyzer[7].

- The injection line delivers the fuel from the high-pressure pump to the injector
- The injector: As soon as the pressure built up by the high-pressure pump exceeds the opening pressure of the injector, fuel gets injected into the engine. Injection continues until the injection pressure falls below the opening pressure again. This is usually achieved by opening the solenoid valve in the pump, which allows the fuel to flow back into the low pressure system, which consequently drops the pressure in the injection-line below the injector opening pressure.

III. INJECTION TEST BENCH MEASUREMENTS

The measurement of the injection system took place at the injection test bench of the OTH Regensburg. Here, the engine and the associated injection system were driven by an asynchronous machine. Instead of injecting into the engine, the injector thereby injects into a closed fuel filled chamber of an injection rate analyzer from Moehwald GmbH (see figure 3).

This works according to the hydraulic pressure rise method. The volume V_c of the aforementioned chamber is known. As soon as fuel is introduced into it, the pressure Δp changes. In addition to the chamber pressure, the sound velocity of the fluid c is determined via ultrasonic measurements. From this, the injection rate Δm is calculated using equation 1.[7]

$$\Delta m = V_c * \frac{\Delta p}{c^2} \quad (1)$$

In addition to the injection rate and the quantities required for this, such as the pressure or the engine position, the pressure in the injection line and other relevant engine parameters, such as the oil temperature, were also measured.

IV. STRUCTURE OF THE SIMULATION MODEL

The fuel injector is simulated using the 1D multiphysics simulation platform GT-Suite. The developed model describes everything from the center of the injection line - where the rail pressure sensor is located - to the tip of the injector or the connection of the leakage pipe. The goal with this model is to keep it as simple as possible and as complex as necessary. This allows sufficient accuracy to be achieved with acceptable

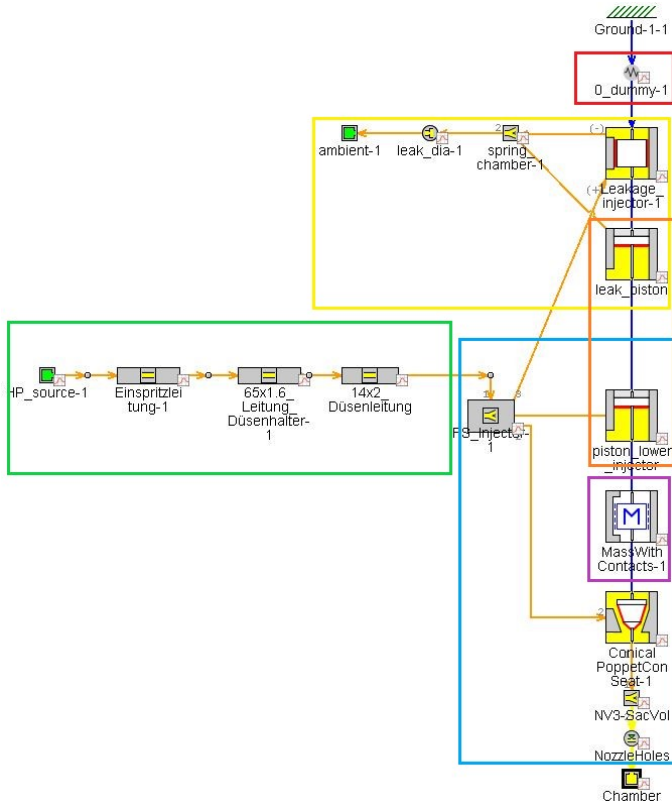


Figure 4: Structure of the simulation model

computational time. The structure of the model can be seen in figure 4. It consists of the second part of the high pressure line after the pressure measuring point (green box), the leakage path (yellow box), as well as the nozzle needle with valve seat and spray holes itself (blue box). Furthermore, the spring that preloads the nozzle is modeled (marked red), a mass that represents the mass of the needle (pink box) and two pistons (orange box) that represent the surfaces of the nozzle needle. If a pressure acts on these surfaces and the valve seat, a force is generated in the opposite direction to the spring force. If this force and thus the injection pressure is high enough, the injection valve opens.

V. CALIBRATION AND MODEL PERFORMANCE

A. Calibration

The model is calibrated using several diesel measurements. The goal is to calibrate the model with one fuel, based on a few measurements and then predict the injection rates in Diesel and OME operation without any change, except for the fuel properties.

The model is adjusted using the following three set screws:

- Length high pressure path
- Spring pretension
- Nozzle hole diameter

First of all, the length of the high pressure line is varied around the measured value to compensate for possible measurement errors in the length of the high pressure path.

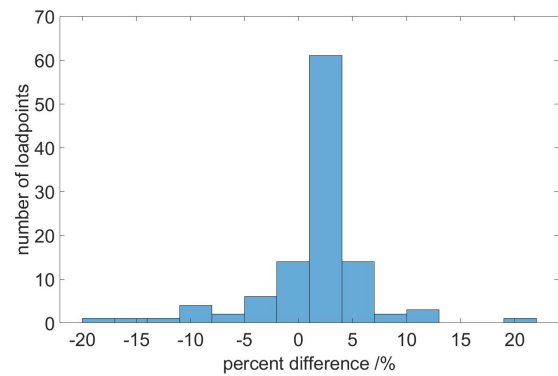


Figure 5: Distribution of injected mass deviation simulation vs. measurement for diesel operation.

Errors of this type can be caused by inaccurate measurement of the position of the pressure measuring point, or inaccurate specifications of the lengths within the injector.

If the simulated injection rate is within the range of the measured one, the spring preload can be varied to set the correct injection duration. Differences in preload between different nozzles are due, to material and manufacturing defects and tolerances, as well as errors in the assembly of the nozzle. An example of this would be incorrect spring compression due to incorrect torque when assembling the nozzle.

As soon as this corresponds to the measurement, it may be necessary to correct the length of the injection line once again so that the start and end of injection match the measurement.

Finally, the diameter of the nozzle holes is adjusted. Any differences can be easily seen in the maximum flow rate of simulation and measurement.

B. Diesel operation

After the model was calibrated, it was checked with 110 measured diesel load points. The model was found to have satisfactory accuracy. The injected mass was represented with an error of -6.5% to $+5.5\%$ in about 86% of the load points (see Figure 5). The injection start was predicted, in about 97% of the load points, with an error in the range -0.57° to $+0.48^\circ$ degrees crankangle. The maximum deviation is 2° crankangle and the mean deviation is 0.14° crankangle. Thus, the accuracy of the injection start can be rated as very good. The duration of injection has also been predicted very good. In 90% of the investigated loadpoints, the error is between -0.8° and $+0.51^\circ$ crankangle. The maximum error is 0.5° crankangle and the mean error is -0.24° crankangle.

An example of a simulated and a measured injection rate can be seen in figure 6.

C. OME operation

For OME operation, only the fuel was changed and the data from the 71 OME measurements was loaded into the simulation model. No other changes were made to the model. This showed that the model calculates the injected mass with a lower accuracy compared to diesel operation. The injected

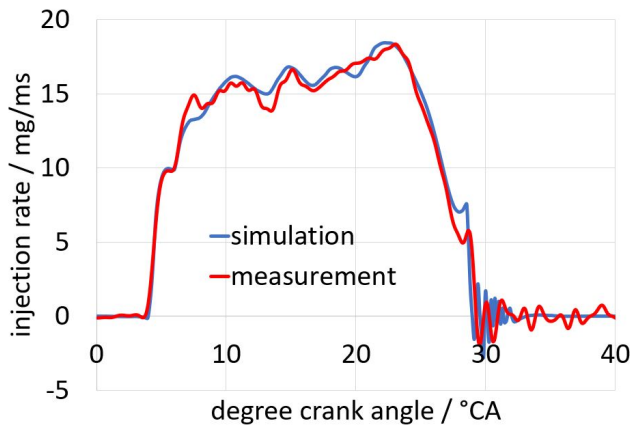


Figure 6: Comparison of simulated and measured injection rate in Diesel operation.

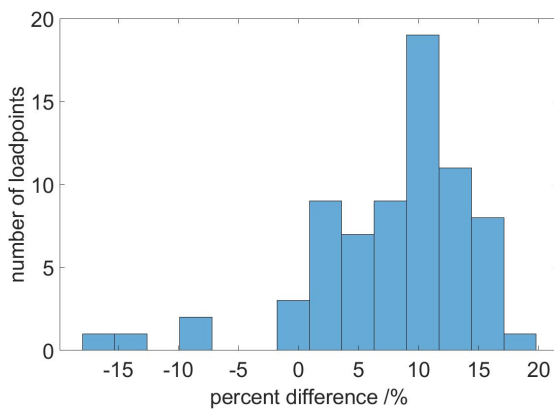


Figure 7: Distribution of injected mass deviation simulation vs. measurement for OME operation.

mass was represented with an error of +6% to +18% in about 66% of the load points (see figure 7). On average, the error is about +8%. This shows that the model generally overestimates the injected mass for OME operation. The calculation of the start of injection has an error range of -0.75° and $+1.2^\circ$ crankangle in 91% of the loadpoints. The maximum error is 2.2° crankangle and the mean error is 0.48° crankangle. Generally the model presents a good performance in calculating the start of an injection event. The duration of an injection pulse has been simulated with an error range of -2° to $+0.7^\circ$ crankangle in 85 % of the cases. The maximum observed error in injection duration is 2° crankangle and the mean error is 0.73° crankangle.

An example of a simulated and a measured injection rate is shown in figure 8.

VI. CONCLUSION

The developed simulation model can represent, both in operation with diesel and with OME, all the load points investigated in good approximation. It is noticeable that the model is significantly more accurate in diesel operation than

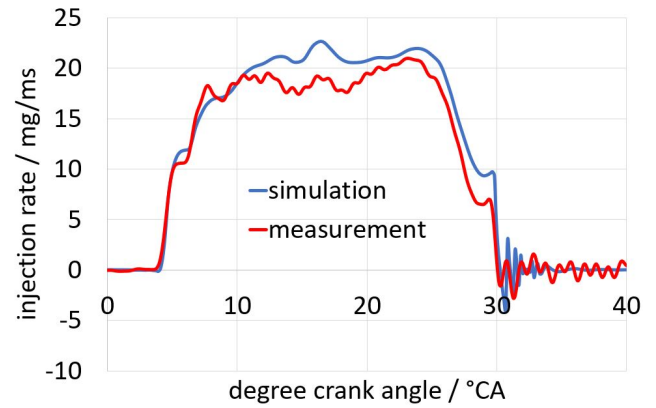


Figure 8: Comparison of simulated and measured injection rate in OME operation.

in OME operation. This can be attributed to the low availability of OME properties at the time of the study. For example, the database supplied with GT-Suite has 136 map points for the relationship between density, temperature and viscosity for diesel, whereas only one single point was available for this relationship for the experimental OME fuel used here, which is not included in this database. The situation is similar for other relevant fuel characteristics. Even though the injected mass is overestimated most of the time for OME operation, the start and duration of injection seem to be fitting. Therefore it might be applicable to scale the injection rates of the simulation to the measured amount of fuel injected on the engine test bench to create a more accurate result. Considering the limitations in terms of OME properties, the simulation model works very well.

VII. OUTLOOK

The next step is to extend the model to include the high-pressure pump. This will allow the injection system to be perfectly adapted to the use of OME and diesel in conjunction with a predictive combustion model.

REFERENCES

- [1] M. Härtl, D. Pélerin, K. Gaukel, P. Dworschak, and G. Wachtmeister, "OME als Reinstoff: Emissionsreduktion bei Dieselmotoren durch sauerstoffhaltige synthetische Kraftstoffe," 2019, pp. 799–813.
- [2] "ExxonMobil Jet A-1," 2021-05-15T16:37:51.000Z. [Online]. Available: <https://www.exxonmobil.com/en/aviation/products-and-services/products/exxonmobil-jet-a-1>
- [3] R. Staff, "Tesla's Musk hints of battery capacity jump ahead of industry event," *Reuters Media*, 25.8.2020. [Online]. Available: <https://www.reuters.com/article/us-tesla-batteries-idUSKBN25L0MC>
- [4] Publisher, "BMVI - Bund, Länder und Industrie vereinbaren Fahrplan für den Markthochlauf klimafreundlicher PtL-Flugkraftstoffe," 2021-05-14T16:07:48.000Z. [Online]. Available: <https://www.bmvi.de/SharedDocs/DE/Pressemitteilungen/2021/044-scheuer-roadmap.html>
- [5] ASG Analytik-Service Gesellschaft mbH, *Prüfbericht: 2802110-1*, 2020.
- [6] "Polyoxymethyldimethylether - Wikipedia," 2021-05-02T15:50:46.000Z. [Online]. Available: https://de.wikipedia.org/wiki/Polyoxymethyldimethylether#/media/Datei:Polyoxymethylene_dimethyl_ether.svg
- [7] moehwald GmbH, *Handbuch HDA Einspritzanalysator*, 2008.

Chapter 6

Papers: Car Technologies

Contents

6.1	Investigation of acoustic absorbing material in an impedance tube	288
6.2	Analysis of the requirements for the communication between an automated bus and the providing server needed for a booking app in the rural area	292
6.3	Asymmetric Firmware Attestation for Electronic Control Units	297
6.4	The Future of Product Development within the Context of Digitalisation - Challenges of Data Networking	303
6.5	Characterization of liner materials in terms of gas tightness and permeation for a cuboid, tension rod supported, high pressure hydrogen vessel	309
6.6	Measurement of PHEV according to WLTP	316
6.7	Method for Vehicle Crash Pulse Comparison in Pre-Crash Safety Systems	320
6.8	Analysis of Cybersecurity Vulnerabilities in Embedded Systems based on ISO/SAE 21434	325
6.9	Characterization of Object Detection Performance in an Edge Environment	330
6.10	Free Electric Vehicle Charging - A Practical Attack on Charging Systems	336
6.11	Concept and requirements for an AI-based automotive HiL-testing system	340
6.12	A Calibration Workflow for 3D Beamforming Radar for Integrated Vehicle Safety Systems	346
6.13	Development and commissioning of a component test bench for the operation of electrical machines used in EPS Applications	352
6.14	Analysis of the influence of gear blank geometry on the transmission error of cylindrical gears	356
6.15	Analysis of the required sensor range for an automated bus operating in rural areas based on a simulation	362

Investigation of acoustic absorbing material in an impedance tube

Yunus Ahmet Acikgöz

Munich University of Applied Science

Faculty of Mechanical Engineering

y.acikgoez@hm.edu

Abstract— Acoustics in vehicles is becoming increasingly more importance in today's world. The most important parameter in acoustic is the absorption coefficient. To improve the acoustics in vehicles, absorption material is used. For example, under the carpets, seats and plastic trim this material is used. BMW has developed a process to produce components with excellent absorption coefficients. This paper includes a potential investigation of the parts produced by this technology and solving problems that came up in the course of the project. The project is divided into two areas. A fault analysis on the Kundt tube is discussed. In the second part a potential investigation is carried out. Geometrically different parts are measured for acoustic properties by different measurement methods. The results are evaluated and compared.

Keywords—acoustic, reflection, sound absorption, impedance tube, BMW additive manufacturing

I. INTRODUCTION

Acoustic properties of compounds are an important consideration application. Over the last years, addition to driving dynamics, design and technical data, vehicle users also pay attention to the acoustics in a vehicle. Especially in the premium segment, it is therefore all the more important to protect the customer/driver of the vehicle from disturbing noises, such as a creaking noise, in every driving situation. A large number of acoustics engineers carry out component tests during development [1]. To improve the acoustics in vehicles, absorption material is used. For example, under the carpets, seats and plastic trim this material is used [2]. In vehicles, fleece material is used to achieve the required sound absorption. The exact name of this material is "Basotect". But the problem is that this material leads to additional weight in the vehicle, and this is an important factor in today's electrified vehicles. The classic combustion engine continues to be used as a vehicle drive but manufactures like Toyota use hybrid vehicles [3]. Noise becomes even louder because of the failure of the combustion engine. The target of research and development of automobile manufactures is light weight and best possible acoustics. Another problem of this fleece absorber material is the non-freedom of geometry. In vehicle it cannot be completely involved in free spaces. This leads to acoustic problems. The Company BMW has developed in the

"Additive Manufacturing Center" a process that produces a material with a very good absorption coefficient in all frequency ranges in which are noises in vehicles. The material has a low weight and is absolutely geometry-free. The process is like a 3D prototype printing process which is used [4].

II. CONTEXT

The acoustic behavior of materials in a measurement environment, has been analyzed in various works. The testing of Polymer Compounds analyzed in the scientific work from P. Allan. He uses acoustics test tubes from "Bruel&Kjaer" to measure the absorptions coefficient[2]. A research project is written by V. Wottstock and D. Sgriess. They researched on acoustic insulating material made from renewables [4]. The absorption coefficient of foams was measured in the work A. Grebel, J. Bös and T. Melz. They used the 2-microphone method for analytical models were created for modeling and of foams [5]. This material is very similar with the material which used from us. The absorption coefficient of some local building materials is researched in the Kundt tube from M. Sylvain, C. Houngan, M. Anjorin and A.Vianou. They measured stabilized earth, mortar and concrete material[8]. The same test method is also used by A. Piana, B. Roozen and C. Scrosati to measure glass wool [9].The difference from other works is achieved by the first analysis of the innovative material, which is manufactured by BMW. This material has not been studied in any research project. Reference values from the literature specifically for this case cannot be used. After the literature review all results must be compared with each other in order to make a statement about the material at the end. The method used to measure the acoustic properties has become clear through the literature research.

With a failure analysis on a Kundt tube there have been only a few publications so far. In a dissertation "Unsicherheit bei der Bestimmung der Schallabsorption mithilfe des Kundt'schen Rohres" [4], Grebel focused with the reasons for uncertainty and describes how to proceed these methodically. Furthermore Brunnader deals with the troubleshooting of Kundt tubes in his dissertation "Aufbau und Programmierung der 2p Messmethode im Impedanzrohr für die Messung

akustischer Materialparameter" [13]. At the University of Applied Sciences in Munich, Mr. Wimmer worked on error analysis and this was published in a thesis „Further investigations on the impedance tube for the determination of acoustical properties“ [12].

According to literature, the sources of error can be divided into two categories. Systematic and random errors. Systematic errors include possible errors due to either measurement or analysis, such as effects due to incorrect sampling, leakage, and errors in measuring length. But also, the measuring signal causes such errors. These result from the random amplitude and phase characteristics of the signal. Random errors result from the measurement and are usually unavoidable. It may be due to insufficient signal-to-noise ratio of the microphones. To minimize the noise signal, it is necessary to have a high coherence between the two microphones. Also, incorrect installation of the sample in the tube can lead to errors. By averaging and applying deterministic signals, random errors can be kept small [12].

III. METHOD

To be able to carry out the measurements in the acoustics laboratory at the Munich University of Applied Sciences, the impedance tube method (also known as Kundt tube) according to DIN EN ISO 10534-2 was used [9]. For other methods, an acoustic room with large dimensions must be organized. Because of vibrations the Kundt tube is coupled out from the environment for determining the acoustic absorption coefficient of a test sample. The data is recorded and evaluated via LabView software. The excitation by sound waves is performed by a loudspeaker at the end of the tube. The absorption coefficient of an absorber depends on the angle of sound waves. In the tube, it is measured under a 90-degree sound incidence. In reality, the waves do not always hit the materials in this way [6].

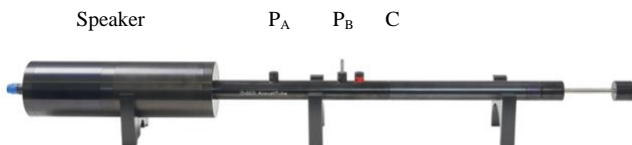


Fig. 1: AcustiTube@ AED 1000 [8]

The material sample which will be measured is located in position C to see on the Fig.1. The sound pressure at two positions (P_A/P_B) is measured by calibrated microphones from “Bruel & Kjaer”. It is also possible to use a four-microphone method but for our use the two-microphone method is enough. The speaker at the end of the tube generates a constant noise signal. The measured sound pressure is overlay at microphone positions. Because of reflections it comes to a reduction of amplitudes of the signal. Based on these values, the reflection coefficient R is determined at the measurement location.

This formula is used to convert this:

$$R = |r| = \left| \frac{\left[1 - \frac{p_A}{p_B} \cos(k\Delta x) \right] - j \frac{p_A}{p_B} \sin(k\Delta x)}{\left[1 - \frac{p_A}{p_B} \cos(k\Delta x) \right] + j \frac{p_A}{p_B} \sin(k\Delta x)} \right|$$

The absorption coefficient α is calculated like this:

$$\alpha = 1 - R$$

Sound absorption describes the reduction or loss of sound energy by hitting objects. In case of complete reflection this value is 0 in case of complete absorption equal to 1. In the literature, porous materials are described with a value of 0.6 [4] [5]. The Basotect material has a value of approx. 1 [11]. About 800 test parts from BMW manufacturing with different geometric properties are to be measured in the project. The differences between these parts are recorded in an Excel list and plot in diagrams, for a better/faster overview in the later evaluation. To ensure reproducibility of the measurement, each test is repeated three times and is archived.

IV. EXPERIMENTALS

First results show the absorption values of the different parts. BMW's technology has very good absorption skills in many frequency ranges, similar to the reference part called Basotect. The results show that the acoustic values depend on the material thickness and size and that very thin components lead to incorrect vibrations in the result. In physics the effect is named “plate oscillator”. The energy in the sound wave is converted into kinetic energy and causes disturbing noise [11]. The values are in a good range like the Basotect material but have some interferences. The measuring system has some failures and was analyzed.



Fig. 2: Impact hammer test - Air and structure-borne sound excitation

There are two possible types of excitation of the system, airborne and structure-borne sound. An impulse hammer measurement was performed using three accelerometers and a microphone. The method of moving hammer and accelerometer was used. Here, the structure-borne sound excitation by the loudspeaker, the Basotect rings and the sliding plunger. As shown in the figure 2, the system was disassembled piece by piece in order to filter out the influence of the individual elements.

V. RESULTS

Through a fault analysis, the following fault causes could be determined.

- Microphone slots
- Placement of the Basotect-rings
- Legs of the System
- Sliding Plunger
- Bolting and model of Speaker
- Preparation of the Sample

After performing the test series. The following can be said when considering the different frequency ranges:

- Basotect rings in Kundt's tube have an influence in the range 200-1600Hz
- The legs in the range in the low-frequency range up to 200-300Hz
- The sliding plunger in the range of 600-700Hz

All other defects of Kundt's tube mentioned had no influence on this case or were no reason for the unsteadiness. However, they can occur with great probability in other cases.

The exact improvement of the curve of the absorption coefficient over the frequency of the measured components cannot be shown here because of the blocking notice from BMW. However, the improvement of the measurement system during the project is easily seen in the figure 3. The absorption behavior of a Basotect sample from the beginning of the project (orange curve) and the current result (black curve) were placed on top of each other in the figure. The improvement in the range of 600-700Hz and 2600-2700Hz is quite obvious here. These areas are the proof that the points described above have a structure-borne sound (vibrations) influence on the entire system. The tube is excited, and this leads to defects in these areas.

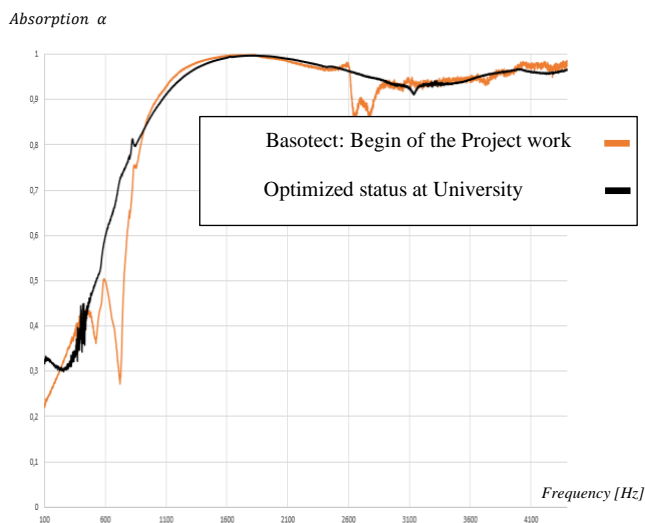


Fig. 2: Absorption level of Basotect material after all improvements

After checking all components of the system, a satisfactory result was achieved. The test bodies manufactured by BMW can be measured in the next section, without the influence of errors, and a safe result can be achieved.

VI. FUTURE WORK

A combination of Basotect and test material could lead to an improvement of his acoustic properties. It would combine the advantages of both materials to create a unique final product. The Basotect material leads to better acoustic properties the innovative material for the lightness and stiffness of the parts. To exhaust the full potential, the innovative material must first be analyzed for all its characteristics. For this purpose, a complete analysis of the components will be carried out in the second part of the project and any unusual findings will be documented. A table could therefore be drawn up for the absorption behavior with different geometric properties for different frequency curves. The material could then be used specifically for each specialist area in vehicle development.

The implementation with the software LabView is only conditionally suitable. Although results are delivered, the measurement is time-consuming, and many errors could occur. The PAK measuring software is with a license key fully automated and works with the Kundt tube as well. This system change would lead to time and cost savings. Finally, the measurement could be carried in a calibrated reverberation room (acoustic room).

The measurement can no longer be carried out at the university, but this would achieve further optimization. For external influences are excluded in the room. External influences are excluded in the room.

ACKNOWLEDGMENT

The author would like to thank Prof. Dr. Stefan Sentpali and Matthias Miltenberger from the Munich University of Applied Science for their help and support with this work. I would also like to thank BMW for their trust in me. Last but not least, I would like to thank Lukas Knorr from BMW for producing the components that were measured.

REFERENCES

- [1] S. Sentpali, R. Sinambari, "Ingenieurakustik", Springer Vieweg, Bd. 6, S.409-440, Juli 2019
- [2] P. Allan, A. Ahmadr, R. Withnall, J. Silver, Paper "Sound Transmission Testing of Polymer Compounds"
- [3] N.N (2020, Jul) [Online] Available: <https://www.toyota.de/hybrid/so-funktioniert-hybrid>
- [4] J. Steckenleiter, "Untersuchung von 3D-Druck-Absorbern im Impedanzrohr", student research project, Munich University of Applied Science, 2019
- [5] V. Wittstock, D. Sgriess, "Experimental characterisation of absorbing materials", ICA 2019 Aachen
- [6] A. Grebel, J. Bös, T. Melz, „Schaumstoffe im Kundtschen Rohr – Modelle und Einflussparameter“, TU Darmstadt, DAGA 2015 Nürnberg
- [7] M. Sylvain, C. Houngan, M. Anjorin, A.Vianou, "Measurement of the acoustic absorption coefficient of some local building materials for residential buildings using the Kundt tube method", Aug. 2018
- [8] A. Piana, B. Roozen, C. Scrosati, "Measurement of the acoustic absorption coefficient of some local building materials for residential buildings using the Kundt tube method", Jul. 2019
- [9] Gerriets(2017, Jul), partly modified, [Online] Available: <https://www.gerriets-acoustics.com/wp-content/uploads/2017/07/g-impedanzrohr-umkirch-207-freisteller.jpg>
- [10] N.N., (2020, Jul), [Online] Available: <https://www.din.de>
- [11] S. Sentpali (2020, Dez): Slides for the Course "Ingenieurakustik"
- [12] D. Wimmer, „Further investigations on the impedance tube for the determination of acoustical properties“, Bachelorarbeit, München, 2016.
- [13] R. Brunnader, „Aufbau und Programmierung der 2p Messmethode im Impedanzrohr für die Messung akustischer Materialparameter“, TU Graz, Graz, 2002.
- [14] A. Grebel, „Unsicherheit bei der Bestimmung der Schallabsorption mithilfe des Kundt'schen Rohres“, TU Darmstadt, Darmstadt, 2019.

Analysis of the requirements for the communication between an automated bus and the providing server needed for a booking app in the rural area

Roman Babl

Ostbayerische Technische Hochschule Amberg-Weiden
92224 Amberg, Deutschland
r.babl@oth-aw.de

Abstract—Innovative mobility concepts for rural areas are increasingly urgently needed. The use of automated on-demand shuttles could be one way to implement such. The purpose of this paper is to discuss the connectivity requirements for communication between an automated bus operating in a rural area and a provisioning server. Especially for the use case of a booking app for getting information as well as providing data the needed requirements are defined. This will include a look at existing related research projects. An overview of a possible model for communication is given. Based on measurements performed in previous work, the defined requirements for the selected test track are evaluated. Finally, an outlook is given on how the project will proceed.

I. INTRODUCTION

As recent studies show, the rural exodus in Germany is still an ongoing trend, which is unlikely to end by itself in the near future [1]. On the one hand, one reason for this is that the occupational field of the people living there is still changing and it is therefore more practical to live in the city. The poor or difficult to reach infrastructure also plays a role here. The low density of shopping facilities, doctors, pharmacies and other public facilities in combination with a poorly developed public transport system usually forces the citizens living there to get their own car, otherwise it is difficult to reach the mentioned. Especially for older people this is a problem because they are sometimes for health reasons no longer able to drive a motor vehicle. Therefore, they also increasingly move to the city. In order to stop or even reverse this trend, one way to make life in the countryside more attractive again is to develop a new form of passenger transport in these regions. The vision here would be an automated bus which could be ordered on demand by means of an app on the smartphone of the citizen. The bus could act like a regular bus and drive along fixed routes or, like a cab, stop only at the pick-up points booked by the users.

This paper will focus on the communication of such a described autonomous bus and the providing server which is needed for the booking app.

Hereinafter chapter II will take a closer look at the overall requirements for the communication of a self-driving vehicle to a server and presents related projects. Chapter III will describe and present a model of the system architecture of the communication. Section IV will than focus on measurements

of network coverage, throughput and other physical parameters on a test track in the rural area which were carried out in previous work and can be viewed in [2]. Also chapter IV will evaluate and review the results of the measurements in consideration of the use cases of communicating to a app. Finally, chapter V gives a conclusion of the written and presents an outlook how the project will continue.

II. OVERALL REQUIREMENTS FOR THE COMMUNICATION OF A SELF DRIVING VEHICLE TO A SERVER

In this chapter the requirements for the communication should be described. Therefore the use cases communication to the booking app is explained and estimations about the requirements are made. For each use case the requirements are based on the following physical parameters.

- *ASU*: The ASU value, which stands for Arbitrary Strength Unit, is a possible variant for representing the reception level or signal quality of a mobile radio signal. It provides a standardized, uniform representation of the signal quality of a wide variety of mobile radio standards. The value of the ASU is proportional to the measured received signal strength and its output is an integer value without a measurement unit. It is possible to calculate the received signal level in dB from the ASU. Therefore, in most standards, the conversion is from Received Signal Strength Indicator (RSSI) to ASU. Only in LTE is the conversion based on the Reference Signal Received Power (RSRP) as shown in the following equation.[3]

$$ASU = RSRP[dBm] + 140 \quad (1)$$

- *Throughput*: The throughput describes how much data can be transferred in a given time.
- *Latency*: The Latency regarding a mobile communication describes the time which is needed to transfer data packages from the source to the target.
- *Round Trip Time*: The Round Trip Time, or RTT for short, describes the bidirectional travel time of a data packet, i.e. how long the process of sending and returning it to its initiator takes. The RTT is not necessarily twice as large

as the latency, since the travel time can vary depending on the direction.[4]

- *Jitter*: The variation in latency is described by the value of the jitter.

A. Communication to booking app

Since the booking of the autonomous guided bus shall be on demand, meaning that there is no fixed timetable for it driving, a possible passenger has to be able to order the bus via app on their smartphone. Thereafter the app has to send and receive data from the bus about its status and availability. During the ride communication is necessary for monitoring the position of the vehicle. Status information about where the bus is right now, how long the ride will take as well as other general notifications for the passengers might be transferred. For the mentioned predictions the information which has to be provided by the vehicle are the geographic coordinates latitude and longitude as well as the altitude. With this information estimations on the remaining waiting time for the bus or the left time to travel can be executed by the server and then be sent to the user's smartphone. In case of a booking not only the estimated waiting time but the general availability of the shuttle has to be ensured. Therefore the "status" of the bus has to be communicated to the server which tells if the bus is ready for an operation, the state of an ongoing operation or that the service can not be provided at the moment. In the other direction the bus also has to get information by the booking app and therefore from the server. The information should include the number of passengers who have to be picked up. This is important in case more people are picked up during the same ride at different places to calculate and tell if there are still enough seats to carry another. To drive either to the current pickup location or the booked destination these locational data has to be transmitted. If there are more than only one booking, stopovers should be able to be included. Since it must be assumed that the service of the bus is not used continuous a standby command to turn of the engine and other driving relevant systems is necessary. The counterpart to this is the wake-up message which reactivates all the needed systems. Arrival and departure messages will be sent as well to the server to inform the passengers that entering or leaving the bus is now possible.

For all of the mentioned information which has to be transferred only a low amount of data should be required.

For the estimation of the size of the message which has to be transferred between the server and the vehicle a closer look is taken on the amount of the above mentioned data. For the geoinformational data the accuracy and therefore resolution of the recording GPS-Module used is decisive. The GPS-Module which will be used in the planned bus is the RT3000 v3 which is a high resolution inertial navigation system (INS) with a positional accuracy of 1cm. Due to this high accuracy also the amount of data recorded for longitude, latitude and altitude in comparison to normal GPS modules is high. Latitude and longitude are recorded with a *8 bytes* resolution and the altitude with *4 bytes*. The other data which

has to be transferred should be very low in size. Shuttle status should be describable with *1 byte* and the status of the infrastructure with only *2 bits*. The request for the next action and information about orders is estimated with *6 bytes* for locational data for start and stop location, because this is enough to match the actual accuracy of regular GPS modules like they are built into smartphones the app will run on [5]. So for a rough estimation a total of around *27 bytes* is needed to be send from the shuttle to the server. The transferred data also has no time critical aspects, therefore the periodicity of *1 s* should be enough to keep the server and the app updated. Thus the resulting needed throughput would be *27 B/s*. Latency, RTT or Jitter can also be fairly high but the overall delay shouldn't extend the generation time of the data elements, so that packages received by the server stay in the correct order. This could be important for estimation of travel and waiting time. Therefore the overall latency including jitter shouldn't extend one second.

B. Related Projects

In other similar research project communication is done with different technologies.

For instance the joint projects "KoMoD" and its follow-up project "KoMoD next" define in their interface documents two standards used for communication[6], [7]. For the use case of "V2X" (vehicle to everything) communication to a server is done via the mobile network[8]. Via this connection emergency call information is transmitted at the moment, but also traffic light switching forecasts, information about tunnels, parking information or traffic sign information could be sent via this connection. In an other documents the used mobile network standard is defined as the LTE-standard [9]. For the communication between road side units and the vehicle ITS G5 (IEEE 802.11p) a WLAN standard is used [10].

In the project U-shift the communication approach is a so called "Multi-access Edge Computing" where the communication to the vehicle is done via the roadside units which then communicate to the global backend. Communication between vehicle and roadside unit is planned to be done over G5 like in the before described projects. The connection between global backend and road side units can then be realized via fiber optic or 5G the newest mobile network standard. Also it is mentioned that a different approach could be a global communication for booking and routing like in the use case described in chapter II-A. For this communication where no realtime capability is needed U-shift would tend to try LTE as the communication technology and plans to upgrade to 5G when the availability of it is given [11].

"ICT4CART" is a project to develop versatile ICT infrastructure to enable the transition towards higher levels of automation with the help of it. In this project the communication is also done over the two technologies, WLAN and cellular network communication. Not all use cases of this project need both technologies but communication between vehicles and infrastructure and among themselves is done via G5. Services like the OEM backend or other service providers are connected

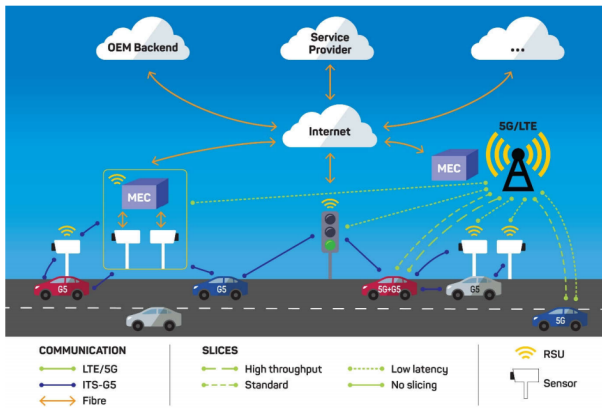


Figure 1. High-Level Overview of the communication between vehicles and the cloud, according to the project ICT4CART [12].

via LTE or 5G with the vehicles and the infrastructure [12], [13]. A Overview of this approach can be seen in figure 1. As the communication to the infrastructure shall not be discussed in this paper no technology is chosen for this use case. Like in the other shortly mentioned research projects, for the communication to the server in the first steps LTE is the technology of choice. A upgrade to 5G is considered if mobile network provider can provide this technology over, for the later in chapter IV-A described, track. A more detailed discussion of the anticipated technology for data transfer is done in chapter III-C.

III. MODEL OF A COMMUNICATION ARCHITECTURE BETWEEN VEHICLE AND SERVER

A. Data for transfer

The model of the communication architecture describes detailed how communication works between vehicle and the other parts of the system needed to provide the service of the self driving bus. One of them is also the server or respectively the application which runs on the smartphone of the user. The definition of the data which has to be transferred was done in the first step of architecture development. Which data has to be transferred is already mentioned in chapter II-A for data size estimations but shall be listed clearer here.

- *Position of the bus:*
 - Latitude
 - Longitude
 - Altitude
- *Status:*
 - Shuttle bus is ready for operating mobility service
 - Shuttle bus is no longer available for mobility service
 - Trip status:
 - * Wake-up
 - * Arrival
 - * Departure
 - * Stand-by
 - * End of service
- *Status of infrastructure:*

- Ready
- Not ready
- *Order request:*
 - Number of passengers
 - Pickup location
 - Destination
 - Standby instruction

B. Process of transfer

The next step was the description of the procedure of communication. Here customer, application(app) and bus are the three instances which have to be considered in the communication process. A exemplary process can be seen in figure 2. Here the rough process from booking the service by the customer till reaching the destination is shown. This includes also passing the data of the route to the bus, the boarding and deboarding of the passenger as well as a description of the needed communication while driving. This last point is done in a loop because data has to be sent periodically here the also already in chapter II-A described data like position and the status of the vehicle is transferred constantly to keep the app and therefore the customer updated. Also it can be thought of transferring a heartbeat from vehicle to server to let each other know that the connection is still active.

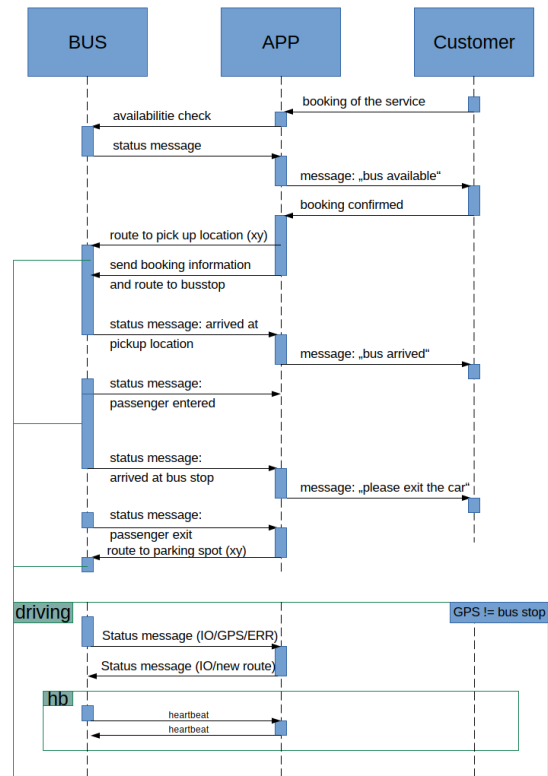


Figure 2. Exemplary process of communication between the three instances, bus, app and customer from ride booking to the pickup driving and arrival at the destination

C. Anticipated technology for data transfer

As already mentioned in chapter II-B the used technology for data transfer should be LTE. Long Term Evolution short LTE is technically a collection of standards out of the third and fourth generation of mobile communication[14]. Looking deeper into the Open Systems Interconnection model (OSI model), Transmission Control Protocol (TCP) will be the transport technology, and IP the used network protocol. What comes along with using this protocol stack shall be discussed, it can be seen starting with TCP and therefor layer 4 in Figure 3. Also the overhead data from needed headers of these protocols are mentioned and added up to calculate the additional needed throughput.

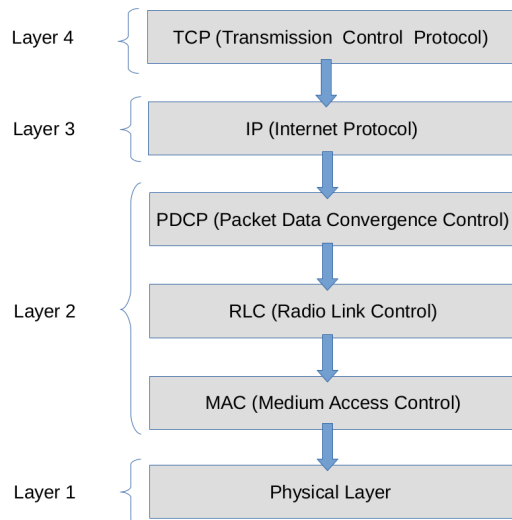


Figure 3. Overview of the last OSI model layers of the anticipated technology for data transfer from TCP over IP and LTE-Stack for data transfer to the physical layer

Going through the Layer the first is TCP. TCP is a reliability orientated transport internet protocol, where connection is established and terminated via three way handshakes[15]. These handshakes were also used while measuring the Round Trip Time. For the protocol the reliability of the connection and package delivery is highly important, therefore the positive acknowledgement function ensures that. The header size for TCP is normally 20 bytes [15]. In the next layer IP is used as the network protocol, which performs the routing between server and client. Here maximum header size is 60 bytes [16]. Layer two is defined by using LTE and three protocols PDCP, RLC and MAC are carried out, it shall not be the purpose of this paper to look deeper into what is concretely done in this layer but it can be read in [17], [18] and just the header size of the protocols will be considered. The sum of additional header data from layer 2 is rounded up 17 bytes (PDCP: 12 bit [19]+ RLC: 10 bit [20]+ MAC: 14 bytes [21]). From the last the physical layer no additional data is added, thus the maximal

additional data that is generated due to headers is 97 bytes which is over three times the amount of data to be transferred for the communication to the booking app. Therefore also the plan like described in chapter III-B sending a heartbeat so that not always the whole status message has to be sent is obsolete because the headers are needed here as well and so differences in size are negotiable.

IV. MEASUREMENTS OF NETWORK COVERAGE AND THROUGHPUT ON A TEST TRACK IN THE RURAL AREA

A. Execution of measurements

The measurements used in this paper were carried out on a test track in Neubäu am See, a district of the eastern Bavarian town of Roding. Neubäu am See can be considered rural due to its low population density as well as a low total population of 950 inhabitants[22]. The investigated route has a length of about 1.3 km and extends from the train station slightly outside Neubäu to the "Seepark Neubäu", a local recreation area. Both at the beginning and at the end of the route there are parking lots where the turning maneuver of the bus is carried out. The route can be divided into different parts due to the road conditions and the maximum allowed driving speed. From the train station, the road is narrow and lacks median lane markings. It ends in a well-built country road with a maximum speed of 80 km/h , which changes to 50 km/h at the official entrance to Neubäu. After one kilometer, a right turn follows into a road with a lower speed of 30 km/h and no median marking, which is followed to the destination. The measurement data were taken on September 30, 2020 and October 16, 2020 under different weather conditions which were not noticeably reflected in the results. The data was recorded by driving 10 laps each. The exact explanation of the measurement results can be found in the previous paper [2]. In this paper, only a summary of these will be presented and the results will be used as well as to test the use case of communication to the booking app for feasibility.

B. Summary of the measurements

The measurements which can be viewed in detail in the related work [2] showed the coverage, connection loss, throughput values, and RTT over the tested track. A clear difference regarding the network provider showed up for the driven test track, so results showed that a stable lossless connection can be established with Vodafone, there the ASU value was in the range of 21 to 57 this indicates a connection which should be stable most of the time but critical weather condition could lead to dropouts. This is completely different with Telekom here on the first day connection couldn't be established at all and results of the coverage on the second day of measurements indicated a bad connection. The ASU value for Telekom laid in the range of 0 which occurred very often and 46. Connection loss occurred as well just with Telekom as the provider. The throughput measurements where after experiencing the bad connection with Telekom just carried out for Vodafone. Results in the throughput measurements ranged from 258 kB/s to a partial maximum of 3.8 MB/s . But most of the values were

between 1 MB/s and 2 MB/s. The round trip time had its average value with 34ms and a maximum mean value of 51ms.

C. Evaluation for the Communication to booking app

The results from the measurements are now taken to evaluate if the communication to a booking app is possible in that area at the moment. Even though RTT, like mentioned in chapter II, is not necessarily twice the latency, this is now estimated for the use case evaluation.

Because of the low requirements in that use case these are more than fulfilled. The needed throughput was estimated with 27 B/s so still the lowest measured mean throughput is about 9000-times higher. But it has to be considered that additional the size of the headers from the protocol stack needs to be added. So absolute amount of data to transfer is 124 B/s but also this is still extremely low. Therefore regarding the amount of exchanged data no problems should occur. Latency was defined with 1s which is also easily fulfilled when looking at the maximum mean RTT which is 51 ms and results in a latency of 25.5 ms.

V. CONCLUSION AND OUTLOOK

In the beginning of the paper the topic of a communication from a automated bus to a providing server was described for the use cases of "communication to a booking app". There was a look into this use case given and the requirements needed to fulfill it were defined. Also three already existing project were described and in conclusion LTE or in the future 5G was defined as the used technology for data transfer. A overview of the transferred data for the communication as well as the process how data transfer should look like in the project was given. Measurements which led to the evaluation if the defined use cases are achievable with the available network infrastructure were carried out in a related work. These measurements were shortly described and summarized. In conclusion every requirement for communicating to a server for a booking app is fulfilled.

Overall the results show that for the communication to a booking app communicating via LTE on the given test track is feasible. In the next steps the communication interface has to be defined on basis of the data that has to be transferred and the system architecture. For this communication also hardware equipment like a LTE module which communicates to the infrastructure of the bus research has to be done.

ACKNOWLEDGMENT

This paper is an outcome from the joint project AUTBUS – Entwicklung eines autonomen Kleinbusses für den ländlichen Raum (engl. Development of an autonomous bus for the rural area) which was funded by the Bavarian State Ministry for Economic Affairs, Regional Development and Energy (funding code DIK-2006-0016// DIK0233/02).

For the exceptional cooperation as well as the valuable suggestions the Author would also like to thank the project partner AVL Software and Functions GmbH.

REFERENCES

- [1] F. Rösel, T. Weishaupt, "Städte quellen über, das Land dünnt sich aus: Anteil der Landbevölkerung auf niedrigstem Stand seit 1871", ifo Dresden berichtet, 2020
- [2] R.Babl, J. Schmid, A. Höß, "Analysis and evaluation of the communication requirements for remote operating an automatedbus in rural areas", unpublished
- [3] LTE-Anbieter.info, "ASU - Arbitrary Strength Unit", , 2021. [Online]. Accessible: <https://www.lte-anbieter.info/technik/asu.php> (accessed on 05/03/2021)
- [4] wikipedia.org, "Round-trip delay", 2021. [Online]. Accessible: https://en.wikipedia.org/wiki/Round-trip_delay (accessed on 05/03/2021)
- [5] Arjan, "Best practices when sending GPS location data [How To]", The Things Network, [Online]. Accessible: <https://www.thethingsnetwork.org/forum/t/best-practices-when-sending-gps-location-data-howto/1242> (accessed on 04/03/2021)
- [6] KoMoD-Projektbüro, "KoMo:D", 2021, [Online]. Accessible: <https://www.komod-testfeld.org/> (accessed on 03/03/2021)
- [7] Weisenheit, Offermann, "KoMoD Dokumentation HAV-Schicht", Digitales Testfeld Düsseldorf, 2018
- [8] K. Strehl, "KoMoD Schnittstellendokumentation C-V2X-Server", Digitales Testfeld Düsseldorf
- [9] Weisheit, "KoMoD Schnittstellendokumentation HAV / FZG Zentrale Schaltzeitprognose, Knotentopologie", Digitales Testfeld Düsseldorf, 2018
- [10] K. Altun, A. Denson, T. Hilgers, J. Weingart, "KoMoD Schnittstellendokumentation RSU / FZG CAM/DENM Positionsmeldung/Warmmeldung", Digitales Testfeld Düsseldorf, 2018
- [11] M. Grünhäuser, A. Wiemer, A. Brunßen, M. Zofka, T. Fleck, M. Conzelmann, C. Ulrich, M. Brost, I. Österle, M. Münster, J. Weimer, "U-Shift MAD Managed Automated Driving für U-Shift Machbarkeitsstudie Zulassungsfähigkeit und Wirtschaftlichkeit", Deutsches Zentrum für Luft- und Raumfahrt e.V. (DLR) (Koordinator), Institut für Fahrzeugkonzepte (DLR-FK), Institut für Verkehrssystemtechnik (DLR-TS), FZI Forschungszentrum Informatik (FZI), 2020
- [12] A. Adaktylos, G. Allmer, M. Buchholz, B. Hätyy, Y. Lassoued, G. Massot, J. Strohbeck, F. Vogl, M. Wimmer, "ICT Infrastructure for Connected and Automated, ICT4CART Reference Architecture", ICT4CART ,2019
- [13] M. Buchholza, J. Strohbecka, A.-M. Adaktylosb, F. Voglb, G. Allmerb, S. C. Barrosc, Y. Lassouedc, M. Wimmerd, B. Hätyyd, G. Massote, C. Ponchele, M. Bretine, V. Sourlasf, A. Amdititf, "Enabling automated driving by ICT infrastructure: A reference architecture", Buchholz et al. / TRA2020, Helsinki, Finland, April 27-30, 2020
- [14] wikipedia.org, "LTE (telecommunication)", 2021. [Online]. Accessible: [https://en.wikipedia.org/wiki/LTE_\(telecommunication\)](https://en.wikipedia.org/wiki/LTE_(telecommunication)) (accessed on 04/03/2021)
- [15] wikipedia.org, "Transmission Control Protocol", 2021. [Online]. Accessible: https://en.wikipedia.org/wiki/Transmission_Control_Protocol (accessed on 04/03/2021)
- [16] wikipedia.org, "IP-Paket", 2021. [Online]. Accessible: <https://de.wikipedia.org/wiki/IP-Paket> (accessed on 04/03/2021)
- [17] Alexey Anisimov, "How data is transmitted in LTE", 2019. [Online]. Accessible: http://anisimoff.org/eng/data_transmission_in_lte.html (accessed on 04/03/2021)
- [18] tutorialspoint.com, "LTE Protocol Stack Layers", 2021. [Online]. Accessible: https://www.tutorialspoint.com/lte/lte_protocol_stack_layers.htm (accessed on 04/03/2021)
- [19] wikipedia.org, "Packet Data Convergence Protocol", 2021. [Online]. Accessible: https://en.wikipedia.org/wiki/Packet_Data_Convergence_Protocol (accessed on 04/03/2021)
- [20] Prashant Panigrahi, "LTE RLC PDU Headers for AM, UM & TM – Detail Overview", 2021. [Online]. Accessible: <https://www.3glteinfo.com/lte-rlc-pdu-headers-for-am-um-tm-detail-overview/> (accessed on 04/03/2021)
- [21] wikipedia.org, "Ethernet frame", 2021. [Online]. Accessible: https://en.wikipedia.org/wiki/Ethernet_frame (accessed on 04/03/2021)
- [22] wikipedia.org, "Neubäu am See", 2021. [Online]. Accessible: https://de.wikipedia.org/wiki/Neubäu%20am_See (accessed on 04/03/2021)
- [23] google maps, [Online]. Accessible: <https://www.google.com/maps/dir/49.2367523,12.4201833/49.2394527,12.4357465/@49.2372273,12.4247531,1286m/data=!3m1!1e3!4m2!4m1!3e0> (accessed on 09/03/2021)

Asymmetric Firmware Attestation for Electronic Control Units

Maximilian Gronau

Research Group "Security in Mobility"

CARISSMA Institute of Electric, Connected, and Secure Mobility(C-ECOS)

Technische Hochschule Ingolstadt, Germany

Email: mag6802@thi.de

Abstract—Firmware updates are a well-known practice to mitigate vulnerabilities in vehicles. However, firmware updates also increase the risk that an adversary changes the firmware of an Electronic Control Unit (ECU). Remote Attestation is a promising security mechanism to detect altered firmware and unauthorized equipment. Previous works have already investigated its deployment in vehicles. However, the proposed schemes do not address the challenges of initial key distribution, firmware updates, and ECU replacement sufficiently. Asymmetric attestation schemes enable a practical solution to these challenges. Hence, this paper explores their benefits and drawbacks in connection with their deployment in vehicles. For this purpose, an asymmetric firmware attestation scheme is proposed that constitutes a practical solution to the named challenges. Afterwards, its evaluation suggests that the asymmetric firmware attestation scheme simplifies software updates and ECU replacement at the expense of performance.

I. INTRODUCTION

Modern vehicles face a serious risk of cyber-attacks. In order to address this risk, new standards as the ISO/SAE DIS 21434 [1] or the regulation on cybersecurity of the United Nations (UN) [2] have been developed. They describe the required processes and practices to ensure the security of a vehicle throughout its life cycle. For instance, the UN regulation on cybersecurity requires sufficient processes to address vulnerabilities in vehicles [2]. Firmware updates are a well-known practice to mitigate vulnerabilities [1]. For this purpose, the firmware of an ECU must be stored in modifiable memory, e.g. flash memory. However, this poses the threat that an adversary changes the firmware. This might be achieved by successfully exploiting a memory error or the update process [2]. An ECU executing manipulated firmware may harm people or properties. Therefore, the UN regulation on cybersecurity requires techniques limiting the access to the flash-memory [2]. But an adversary can circumvent this measure, if he replaces the original ECU with equipment running a modified version of the firmware. Hence, the UN regulation on cybersecurity also requires measures to prevent and detect the use of unauthorized equipment [2].

Remote Attestation is a promising security mechanism to achieve the quoted requirements. Generally, Remote Attestation (RA) denotes the activity where a device – the prover – provides evidence about some of its properties (e.g. loaded firmware) over a network to convince another device – the verifier – of its trustworthiness [3] [4]. RA is typically obtained

via a challenge-response protocol: The verifier initiates the attestation by sending an attestation challenge. After receiving the challenge the prover creates the attestation token. In the case of a symmetric attestation scheme, this is often a Hashed-Message-Authentication-Code (HMAC) calculated with the symmetric attestation key over the concatenation of the challenge and the measurement of the relevant properties (e.g. a hash-value of its firmware). The verifier also computes the attestation token. Hence, the verifier must know the symmetric attestation key and the expected measurement of the properties. The prover is assumed trustworthy, if it delivers an attestation token that is equal to the expected one. Thus, RA is suitable to detect altered firmware, if the measurement is a hash of the loaded firmware. Moreover, RA can be used to authenticate the proving device, as only the prover – besides the verifier – knows the attestation key. Consequently, the quoted requirements from the previous paragraph can be achieved with RA. [5]

Multiple works have already proposed attestation schemes for ECUs [6]–[11]. But the author found out (cf. II-A) that these works do not address initial key provisioning, firmware updates, and ECU replacement sufficiently. Furthermore, all these works require a database at the verifier that contains the attestation keys and the valid measurements for all ECUs. Such a database complicates the implementation of routines for initial key provisioning, firmware updates, and ECU replacement. However, it can be eliminated by using an asymmetric attestation scheme. It may also provide a practical solution to the aforementioned issues. Therefore, this work explores the benefits and drawbacks of asymmetric attestation schemes in connection with its deployment in vehicles. All in all, this work makes the following contributions:

- **Asymmetric Firmware Attestation Scheme:** In this work an Asymmetric Firmware Attestation Scheme (AFAS) for ECUs is proposed that simplifies firmware updates and ECU replacement in comparison to the existing attestation schemes.
- **Evaluation:** The evaluation of the design of the proposed AFAS demonstrates some of its benefits and drawbacks.

II. BACKGROUND & RELATED WORK

The current section provides necessary background information about attestation schemes for ECUs (II-A) and asymmetric

attestation schemes (II-B) by reviewing related works.

A. Attestation Schemes for ECUs

Oguma et al. [6], [7] are the first who suggest the use of RA in the automotive domain. They use RA as part of a security-architecture, that guarantees authentic and encrypted communication between ECUs with authentic software configurations. The authors suggest a symmetric attestation scheme similar to the one described in section I, where a specific Master ECU verifies the authenticity and integrity of all other ECUs in the vehicle. The implementation of this concept is accomplished with the help of a Trusted Platform Module (TPM). However, TPMs – even when compliant to TPM 2.0 Automotive Thin Profile [12] – increase the size, the costs and the complexity of ECUs to a degree, that is not practical for most ECUs [9]. Therefore, researchers have developed attestation schemes that do not require secure co-processors such as TPMs [8], [9]. The solution proposed by Kohnhäuser, Püllen and Katzenbeisser can even be implemented on commodity ECUs [9].

Recent works suggest new architectures for in-vehicle RA. Rawat et al. [10] propose a decentralized RA scheme, that enables each ECU in a vehicle to verify the others. This approach is superior to the one with a single Master ECU, as it offers more robustness, less latency and does not have a single point of failure. In order to derive the required symmetric attestation keys, the authors suggest the Double-Ratchet key derivation protocol. However, they do not explain how to provision the initial root keys for Double-Ratchet. Alladi et al. [11] present an attestation scheme where the authentication and attestation of ECUs is conducted by an edge server and Road Side Units (RSUs). The aim of this architecture is to offload the task of attestation to the edge server and the RSUs.

Initial key provisioning, firmware updates, and ECU replacement appear as a major challenge for ensuring the security of an attestation scheme in practice. However, a closer look revealed that none of the previous works elaborates on all three issues (cf. Table I). It was further noted that in all published RA schemes for ECUs the verifier has a database containing the attestation keys and the valid states of the attested ECUs [6]–[11]. This property complicates the processes responsible for initial key distribution, firmware updates, and ECU replacement. The reason is that an issuing party must always update the ECU and the database at the verifier(s). This must also include adequate error handling to keep the vehicle operational, if one of the updates fails. This paper aims to overcome the shortcomings of previous works with the help of an asymmetric attestation scheme that does not require a database at the verifier(s) and simplifies the processes responsible for firmware updates as well as ECU replacement.

B. Asymmetric Attestation Schemes

The use of asymmetric cryptography for attestation is already suggested in previous works [4], [13]–[16]. This stems from the insight that symmetric attestation schemes are not suitable for use cases, where a device is attested by an untrusted verifier [16]. The reason is that a symmetric key

Table I

	[6]	[8]	[9]	[10]	[11]
Initial Key Provisioning	✓	✓	✓		✓
Software Updates				✓	
ECU Replacement	✓	✓		✓	

must not be shared with an untrusted verifier [16]. The main difference of asymmetric attestation schemes in comparison to symmetric ones is that the prover creates a signature with its private key instead of a MAC with the shared attestation key. Furthermore, an additional Certificate Authority must provide a certificate that assures the authenticity of the associated public key. Hence, any device possessing the public key of the prover and the associated certificate can verify the signature in the attestation token. Consequently, any device can verify the authenticity and integrity of the prover without knowing the secret attestation key. Unlike previous works, this paper explores a new use case of asymmetric attestation schemes by investigating their potential with respect to initial key distribution, software updates, and ECU replacement.

III. ANALYSIS

This section defines the problem space of firmware attestation schemes for ECUs and provides the baseline for the evaluation in section V. It starts with a description of the system model (III-A) and the adversary model (III-B). Afterwards the requirements for firmware attestation schemes are presented in subsection III-C.

A. System Model

As explained in subsection II-B, asymmetric attestation schemes enable any device with the public key to be the verifier. This work wants to make use of this property by aiming for an attestation scheme that can be adapted to different architectures. This principle is captured as a requirement in subsection III-C and will be evaluated in section V. Consequently, no specific network configuration or topology is considered in the following. Thus, it is only for the sake of clarity that the following graphics always depict a setup, where the verifier interacts with the prover directly. Last but not least, this paper considers the Original Equipment Manufacturer (OEM) to be the certificate authority.

B. Adversary Model

In this work we assume an adversary with the following capabilities:

(A1) Arbitrary Code Execution at Runtime: The adversary can execute arbitrary instructions at runtime. These privileges might be gained via a successful exploitation of software vulnerabilities. Because of this capability, one must expect that the adversary reads and writes arbitrary memory at runtime. However, it is not assumed that the adversary can circumvent hardware protections or exploit the secure bootloader in Read-Only Memory (ROM). [5]

(A2) Arbitrary Load of Firmware: Furthermore, an adversary can load arbitrary firmware on an ECU. This privilege might be gained when there is a vulnerability in the update validation procedure as discovered in previous studies, e.g. in [17]. However, it is worth noting that not all software of an ECU is changed during a firmware update, e.g. the code of the secure bootloader stored in ROM.

(A3) Control over Communication Medium: Moreover, the adversary has control over the communication medium (Dolev-Yao Model [18]). Consequently, the adversary can eavesdrop messages, perform replay attacks, initiate new conversations or act as a man-in-the-middle.

On the other hand, it is assumed that the adversary cannot access the private key of the OEM, that is used to sign the certificates. This appears reasonable as the key is not stored on any ECU and attacks against the factory of the OEM are beyond the scope of this paper.

C. Requirements

In order to get deployed in vehicles, a firmware attestation scheme for ECUs shall fulfill the following requirements:

(R1) Hardware Authorization: A firmware attestation scheme for ECUs shall allow a trusted verifier to assess whether the firmware was loaded on authorized equipment. This requirement is necessary in order to fulfill the equivalent one stated in the UN regulation on cybersecurity [2].

(R2) Firmware Integrity: A firmware attestation scheme for ECUs shall enable a trusted verifier to assess whether an unaltered and updated version of the firmware has been loaded into the RAM. Therefore, the verifier must be able to detect firmware manipulated through a runtime-attack (cf. (A1)) or an erroneous update (cf. (A2)). Moreover, it must contain a mechanism in order to prevent an adversary from loading obsolete firmware with known vulnerabilities (cf. (A2)). This requirement is important to prevent the execution of manipulated or obsolete firmware in safety-critical settings and to fulfill the equivalent requirement in the UN regulation on cybersecurity [2].

(R3) Performance: The performance impact of the firmware attestation scheme for ECUs should be imperceptible for the user [9]. This requirement is necessary in order to achieve user acceptance.

(R4) Firmware Updates & ECU Replacement: The firmware attestation scheme shall support firmware updates and ECU replacement natively. In other words, the vehicle shall always be operational right after a firmware update or an ECU replacement. This requirement is necessary in order to deploy firmware attestation in vehicles successfully.

(R5) Adaptability: The firmware attestation scheme for ECUs should be adaptable to various architectures. An attestation scheme fulfilling this requirement has a greater chance of being deployed in practice. However, this requirement is optional, as a firmware attestation scheme may also be deployed, if it only suits a specific architecture.

(R6) Commodity ECUs: The proposed firmware attestation scheme shall be applicable to commodity ECUs with only a

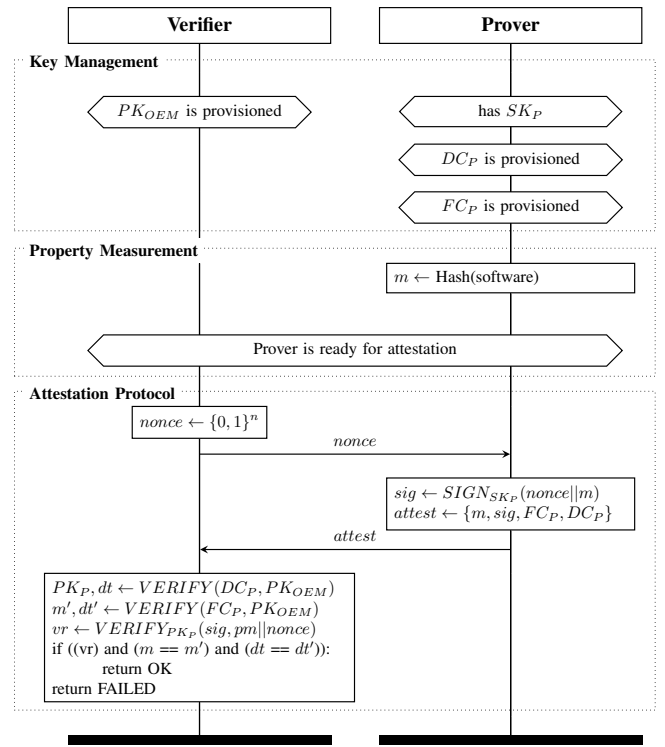


Figure 1. Firmware Attestation Protocol with Asymmetric Attestation Key.

secure storage and a protected bootloader [9]. Thus, the attestation scheme should not require additional hardware such as TPMs or Hardware Security Modules (HSMs). The attestation scheme should also work without a Protected Module Platform (PMA) such as Arm's TrustZone. This requirement ensures the suitability of the firmware attestation scheme for various ECUs.

IV. ASYMMETRIC FIRMWARE ATTESTATION SCHEME FOR ECUS

In this section, the AFAS for ECUs (cf. Figure 1) is presented. It starts with a description of the key management (IV-A) and the creation of the measurement for attestation (IV-B). Then, the attestation protocol is specified in subsection IV-C, before we elaborate on initial key distribution, firmware updates and ECU replacement (IV-D). Finally, we collect all security assumptions underlying the proposed AFAS in subsection IV-E.

A. Key Management

It is a major goal of this work to eliminate the database at the verifier(s). Therefore, it must be possible to assess the authenticity of the proving device (cf. (R1)) without knowing the device-specific attestation key. The attestation scheme of the Trusted Computing Group already provides a solution to this problem [13]: The idea is that each ECU has its secret attestation key SK_P and a device certificate DC_P authenticating the associated public key. In this work, we further demand that the certificate contains information

regarding the device type dt , e.g. the part number of the ECU. Each device certificate shall be signed with the private key of the OEM. Hence, if a prover includes its device certificate DC_P into the attestation token, any verifier can check its authenticity with the public key of the OEM. Thus, there is no need to store the attestation keys of an ECU in a database at the verifier.

In order to eliminate the database, the verifier must further be able to assess the integrity of loaded firmware (cf. **(R2)**) without knowing the valid measurement of the properties m' . A solution to this issue is the use of a firmware certificate FC_P as suggested by Kohnhäuser and Katzenbeisser in [15]. This certificate should contain a firmware identification number, the valid firmware measurement m' , the suitable devices types st' and a signature of the OEM, that ensures the integrity and authenticity of the previous data. If a prover includes this certificate in the attestation token, any verifier can assess the integrity of the loaded firmware with the public key of OEM. Thus, there is no need to store the valid firmware measurement m' for an ECU in a database at the verifier. All in all, the proposed AFAS does not need a database at the verifier(s) at all.

B. Property Measurement

The goal of the proposed AFAS is to provide evidence that an unaltered and up-to-date version of the firmware has been loaded on suitable hardware (cf. **(R1)** and **(R2)**). Generally speaking, the measured property is the firmware loaded from flash memory into the RAM. Thus, the boot process is the most reasonable time to measure the integrity of the firmware. The corresponding security mechanism is called authenticated boot or measured boot. One approach for implementing authenticated boot is the use of additional hardware modules such as TPMs [13] or Hardware Security Modules [19]. However, as this work aims for an attestation scheme applicable to commodity ECUs (cf. **(R6)**), their use is not appreciated. Instead, the proposed AFAS builds upon the work of Kohnhäuser, Püllen and Katzenbeisser [9], who suggest two implementations to measure the firmware on commodity ECUs (cf. **(R6)**) during the boot-process. The first approach uses the bootloader kept in ROM to compute a Hashed-Message-Authentication-Code (HMAC) over the hash-value of the firmware in the flash memory and the previous attestation challenge with the symmetric attestation key [9]. The authenticated measurement is then used as the key to create a HMAC over the identifier of the ECU and the current attestation challenge [9]. However, this scheme cannot be reused with asymmetric cryptography, as the verifier(s) cannot determine the authenticated measurement. Instead the current attestation token must also be signed with SK_P . Consequently, SK_P must be accessible after the execution of the bootloader. However, if SK_P is accessible for the attestation routine at runtime, also the adversary can read it (cf. **(A1)**). Therefore, the implementation of the proposed AFAS requires additional hardware support in order to guarantee that only the attestation routine can access SK_P .

PMAs such as Arm's TrustZone technology provide this hardware support. Arm's TrustZone technology [20] offers two execution environments, specifically a secure and a non-secure one. Hardware mechanisms isolate the two worlds from each other. The TrustZone technology allows to store sensitive data such as the secret attestation key or the firmware measurement in the secure execution environment in order to protect it from memory accesses by the regular applications running in the non-secure world or the adversary. This shall be used for the attestation of ECUs without an Operating System (OS) in the following way: A bootloader stored in the ROM performs a secure boot of the secure and the non-secure execution environment. At the same time the bootloader calculates a hash-value over data in the flash memory that belongs to the non-secure execution environment. Afterwards, this measurement is stored in the secure execution environment. At runtime, the attestation routine in the non-secure world calls a function in the secure world that can access the attestation key as well as the measurement and returns the attestation token. For the attestation of ECUs with a Linux-based OS running in the non-secure world, we refer the reader to the measurement approach for advanced ECUs described in [9].

C. Attestation Protocol

The verifier starts the attestation by creating an attestation challenge or *nonce* (cf. Figure 1). The *nonce* is an arbitrary number with a length of n bits. Its purpose is to prevent replay attacks (cf. **(A3)**) by guaranteeing the freshness of the attestation response. Consequently, n shall be sufficiently large to ensure that nonces are not reused accidentally. The *nonce* is sent to the prover who concatenates it with the measurement m and signs the result with SK_P . Then, the prover creates the attestation token that consists of the measurement m , the signature sig , the device certificate DC_P and the firmware certificate FC_P . It is worth noting that the attestation token must be created in the secure execution environment of the ECU. The prover then sends the attestation token to the verifier, who checks both certificates with the public key of the OEM PK_{OEM} . Afterwards, the verifier can check the signature that was provided by the prover. The attestation succeeds, if the signature is valid, the provided measurement m is equal to the expected one m' from the certificate and the actual device type dt is included in the set of authorized devices dt' . The attestation fails otherwise.

D. Initial Key Distribution, Software Updates, ECU Replacement

Initial Key Distribution: The device shall create the key pair for device attestation itself. This requires appropriate hardware support to guarantee the randomness of the secret key. Then the device sends its public key to the OEM that creates the device certificate DC_P and sends it to the device. During the installation of DC_P one must ensure that an adversary, that may reside in the network or on the device, cannot act as a man-in-the-middle. It is therefore recommended that the installation of DC_P is performed in a secure environment at

the factory, where the device authenticity can be assured. The public key PK_{OEM} shall also be installed in the factory to ensure its integrity and authenticity.

Software Updates: It is assumed that each firmware update contains its associated firmware certificate FC_P . Consequently, the proposed AFAS is operational right after an update and stays operational after a failed one.

ECU Replacement: A new ECU shall contain SK_P and the corresponding device certificate DC_P when leaving the factory. Hence, if the ECU has recent firmware installed, the vehicle is operational right after the ECU replacement. However, if the installed firmware is obsolete, then there must be a firmware update before the vehicle is operational.

E. Security Assumptions

The proposed AFAS is based on the following security assumptions:

(SA1) Secure Storage of SK_P : This work is based on the assumption that an adversary cannot access SK_P . Therefore, it must not be possible that an adversary can read memory of the secure execution environment. This further includes that the key is not leaked directly via registers or indirectly via a side-channel.

(SA2) Secure Computation and Storage of m : One must be aware, that the adversary can extract the valid measurement from the firmware certificate. Therefore, the adversary must not be able to modify the measurement of the firmware. Therefore, the computation of the measurement must not be interfered by the adversary. Furthermore, the adversary must not be able to overwrite the original measurement. Otherwise the adversary might be able to hide the presence of manipulated firmware.

(SA3) Secure Storage of PK_{OEM} : This work is based on the assumption that an adversary cannot manipulate the public key stored at the verifier(s). Otherwise an adversary may be able to install his own public key. In this case, the adversary will always be able to create valid attestation tokens by creating messages (cf. (A3)) that contain valid measurements with respect to certificates signed with the adversary's private key. An adversary may use this to evade detection after introducing unauthorized equipment or manipulated firmware.

(SA4) Secure Storage of SK_{OEM} : It is further assumed that an adversary cannot leak the secret signing key of the OEM. Otherwise the adversary may be able to create new certificates for unauthorized equipment or manipulated firmware.

V. EVALUATION

In this section the requirements from subsection III-C are used to evaluate AFAS by comparing it to existing attestation schemes for ECUs:

(R1) Hardware Authorization: The proposed AFAS fulfills (R1), if an authorized device only can create a valid signature with a secret attestation key, whose associated public key is authenticated by the OEM. This requires the secure storage of SK_P (SA1) and PK_{OEM} (SA3). The design of the proposed AFAS fulfills this requirements as it demands

that SK_P and PK_{OEM} are stored in the secure execution environment of the ECU. SK_{OEM} must also be stored securely (SA4). However, as it is stored on a device in the factory of the OEM, its security is beyond the scope of this paper and is therefore assumed as true (cf. III-B). Consequently, the design of proposed AFAS fulfills (R1) likewise the existing attestation schemes for ECUs [6]–[11]. In the future, it would be further interesting to assess, whether (SA1) and (SA3) hold in practice.

(R2) Firmware Integrity: The verifier checks the integrity of the firmware by comparing the prover's measurement m with the expected one m' from the firmware certificate. This requires that the prover's measurement is honest (SA2). Thus, the design must assure that an attacker cannot interfere with the computation of the measurement. The design of the proposed AFAS acknowledges this as it requires that the measurement is conducted by the bootloader, whose integrity is ensured by a secure boot technology. Hence, one can assume the calculation of the measurement as honest, if one trusts the implementation of the bootloader. Afterwards, the measurement must be stored in memory that protects it from malicious modifications, while it is not signed. The design of the proposed AFAS fulfills this requirement, because it demands that the measurement is stored in the secure execution environment of the PMA. Nevertheless, the design of the proposed AFAS does not support the detection of obsolete firmware yet. The reason is that the information regarding newer versions cannot be obtained from the firmware certificate. A simple solution would be the extension of the firmware certificates with a maximum lifetime. A more precise solution would be the introduction of a revocation scheme that enables the OEM to revoke certificates for firmware with known vulnerabilities. However, as the design of the proposed AFAS does not specify such a solution yet, it does not fulfill (R2) requirement. In contrast, existing attestation schemes can detect obsolete firmware, if the database at the verifier is up-to-date. However, only Rawat et al. present a procedure for updating the database at the verifier [10]. In the future, it would be further interesting to assess, whether (SA2) hold in practice.

(R3) Performance: The proposed attestation scheme has not been implemented yet. As a consequence it is not possible to compare its performance with the performance of existing attestation schemes quantitatively. Qualitatively, one can expect that the AFAS offers less performance in comparison to its symmetric counterparts. One reason is that the attestation tokens are longer and therefore have longer transmission times. Moreover, the creation of digital signatures is known to be slower than creating an HMAC [4]. Last but not least, the verifier must additionally verify two certificates. Thus, the price of eliminating the database at the verifier is an increased execution time and therefore less performance. However, without the quantitative measures it cannot be determined whether the performance might still be acceptable.

(R4) Firmware Updates & ECU replacement: As illustrated in subsection IV-D the proposed attestation scheme supports firmware updates and ECU replacement natively. This

is a major advantage of the proposed AFAS in comparison to existing attestation schemes for ECUs [6]–[11].

(R5) Adaptability: It is a major benefit of the proposed attestation scheme that any device possessing PK_{OEM} can act as a verifier. This makes the scheme adaptable to different architectures and is an advantage of the proposed AFAS in comparison to existing attestation schemes for ECUs [6]–[11].

(R6) Commodity ECUs: The proposed AFAS requires a PMA such as Arm’s TrustZone. Consequently, (R6) is not fulfilled and its applicability is limited in comparison to the attestation scheme for simple ECUs suggested in [9]. However, Arm’s TrustZone is available for commodity micro-controllers such as the Cortex-M23/M33/M35P. Hence, the proposed AFAS is more or equally applicable than most of the other attestation schemes for ECUs [6]–[10].

All in all, the evaluation of the design shows that the proposed AFAS overcomes the shortcomings of previous works with respect to firmware updates and ECU replacement. However, the evaluation also revealed open issues that should be tackled in the future. One aspect is the introduction of a revocation scheme and its evaluation. This will show whether a verifier can detect obsolete firmware. The other aspect is the implementation of the proposed AFAS in order to compare its performance to the performance of existing attestation schemes for ECUs. Moreover, one can assess whether the security assumptions (SA1), (SA2) and (SA3) also hold in practice.

VI. CONCLUSION & FUTURE WORK

This work reveals that initial key distribution, firmware updates and ECU replacement are a major challenge for firmware attestation for ECUs. Moreover, an AFAS is proposed that simplifies firmware updates and ECU replacement in comparison to the existing symmetric attestation schemes. The evaluation of its design suggests that AFAS simplifies software updates and ECU replacement at the expense of performance. Future work will focus on improving and implementing the proposed AFAS. Furthermore, the definition of a revocation scheme is planned so that obsolete firmware can be detected in the future.

REFERENCES

- [1] Vehicle Cybersecurity Systems Engineering Committee, “Road Vehicles - Cybersecurity Engineering,” 400 Commonwealth Drive, Warrendale, PA, United States, 12/02/2020. [Online]. Available: <https://www.sae.org/standards/content/iso/sae21434.d1/>
- [2] United Nations Economic Commission for Europe, “ECE/TRANS/WP.29/2020/79: Proposal for a new UN Regulation on uniform provisions concerning the approval of vehicles with regards to cyber security and cyber security management system,” 02/04/2020. [Online]. Available: <https://undocs.org/ECE/TRANS/WP.29/2020/79>
- [3] G. Coker, J. Guttman, P. Loscocco, A. Herzog, J. Millen, B. O’Hanlon, J. Ramsdell, A. Segall, J. Sheehy, and B. Sniffen, “Principles of remote attestation,” *International Journal of Information Security*, vol. 10, no. 2, pp. 63–81, 2011.
- [4] A. Francillon, Q. Nguyen, K. B. Rasmussen, and G. Tsudik, “A Minimalist Approach to Remote Attestation,” in *Proceedings of the Conference on Design, Automation & Test in Europe*, G. Fettweis, Ed. Leuven, BEL: European Design and Automation Association, 2014. [Online]. Available: <https://dl.acm.org/doi/abs/10.5555/2616606.2616905>
- [5] F. Kohnhäuser, “Advanced Remote Attestation Protocols for Embedded Systems,” Ph.D. Thesis, Technische Universität, Darmstadt, 2019. [Online]. Available: <http://tuprints.ulb.tu-darmstadt.de/8998/>
- [6] H. Oguma, A. Yoshioka, M. Nishikawa, R. Shigetomi, A. Otsuka, and H. Imai, “New Attestation Based Security Architecture for In-Vehicle Communication,” in *IEEE GLOBECOM 2008 - 2008 IEEE Global Telecommunications Conference*. IEEE, 2008, pp. 1–6. [Online]. Available: <https://ieeexplore.ieee.org/document/4698144>
- [7] G. Lee, H. Oguma, A. Yoshioka, R. Shigetomi, A. Otsuka, and H. Imai, “Formally verifiable features in embedded vehicular security systems,” in *2009 IEEE Vehicular Networking Conference (VNC)*. IEEE, 2020, pp. 1–7. [Online]. Available: <https://ieeexplore.ieee.org/abstract/document/5416378>
- [8] J. van Bulck, J. T. Mühlberg, and F. Piessens, “VulCAN: Efficient Component Authentication and Software Isolation for Automotive Control Networks,” in *Proceedings of the 33rd Annual Computer Security Applications Conference*. New York, NY, USA: ACM, 2017, pp. 225–237. [Online]. Available: <https://dl.acm.org/doi/abs/10.1145/3134600.3134623>
- [9] F. Kohnhäuser, D. Pullen, and S. Katzenbeisser, “Ensuring the Safe and Secure Operation of Electronic Control Units in Road Vehicles,” in *2019 IEEE Security and Privacy Workshops (SPW)*. IEEE, 2019, pp. 126–131. [Online]. Available: <https://ieeexplore.ieee.org/document/8844627>
- [10] A. Rawat, M. Khodari, M. Asplund, and A. Gurtov, “Decentralized Firmware Attestation for In-Vehicle Networks,” *ACM Transactions on Cyber-Physical Systems*, vol. 5, no. 1, pp. 1–23, 2020. [Online]. Available: <https://dl.acm.org/doi/10.1145/3327961.3329529>
- [11] T. Alladi, S. Chakravarty, V. Chamola, and M. Guizani, “A Lightweight Authentication and Attestation Scheme for In-Transit Vehicles in IoV Scenario,” *IEEE Transactions on Vehicular Technology*, vol. 69, no. 12, pp. 14 188–14 197, 2020. [Online]. Available: <https://ieeexplore.ieee.org/document/9261991>
- [12] Trusted Computing Group, “TCG TPM 2.0 Automotive-Thin Profile: For TPM Family 2.0; Level 0,” 31/05/2018. [Online]. Available: https://trustedcomputinggroup.org/wp-content/uploads/TCG_TPM_2.0_Automotive_Thin_Profile_v1.1-r15.pdf
- [13] —, “Trusted Platform Module Library: Part 1: Architecture,” 2019. [Online]. Available: <https://trustedcomputinggroup.org/resource/tpm-library-specification/>
- [14] E. Brickell, J. Camenisch, and L. Chen, “Direct anonymous attestation,” in *Proceedings of the 11th ACM conference on Computer and communications security - CCS ’04*, V. Atluri, B. Pfizmann, and P. McDaniel, Eds. New York, New York, USA: ACM Press, 2004, p. 132. [Online]. Available: <https://dl.acm.org/doi/abs/10.1145/1030083.1030103>
- [15] F. Kohnhäuser and S. Katzenbeisser, “Secure Code Updates for Mesh Networked Commodity Low-End Embedded Devices,” in *Computer Security – ESORICS 2016*, ser. Lecture Notes in Computer Science, I. Askoxylakis, S. Ioannidis, S. Katsikas, and C. Meadows, Eds. Cham: Springer International Publishing, 2016, vol. 9879, pp. 320–338. [Online]. Available: https://link.springer.com/chapter/10.1007%2F978-3-319-45741-3_17
- [16] S. Schulz, A. Schaller, F. Kohnhäuser, and S. Katzenbeisser, “Boot Attestation: Secure Remote Reporting with Off-The-Shelf IoT Sensors,” in *Computer Security – ESORICS 2017*, ser. Lecture Notes in Computer Science, S. N. Foley, D. Gollmann, and E. Sneekenes, Eds. Cham: Springer International Publishing, 2017, vol. 10493, pp. 437–455. [Online]. Available: https://link.springer.com/chapter/10.1007%2F978-3-319-66399-9_24
- [17] S. Nie, L. Liu, and Du Yuefeng, “Free-Fall: Hacking Tesla from Wireless to CAN Bus,” in *Black Hat USA 2018*, 2018. [Online]. Available: <https://www.blackhat.com/docs/us-17/thursday/us-17-Nie-Free-Fall-Hacking-Tesla-From-Wireless-To-CAN-Bus-wp.pdf>
- [18] D. Dolev and A. Yao, “On the security of public key protocols,” *IEEE Transactions on Information Theory*, vol. 29, no. 2, pp. 198–208, 1983. [Online]. Available: <https://ieeexplore.ieee.org/abstract/document/1056650>
- [19] M. Wolf and T. Gendrullis, “Design, Implementation, and Evaluation of a Vehicular Hardware Security Module,” in *Information Security and Cryptology - ICISC 2011*, H. Kim, Ed. Berlin, Heidelberg: Springer Berlin Heidelberg, 2012, pp. 302–318. [Online]. Available: <https://www.evita-project.org/Publications/WG11.pdf>
- [20] Arm Limited, “TrustZone technology for the ARMv8-M architecture,” Cambridge, England. [Online]. Available: <https://developer.arm.com/documentation/100690/0201/>

The Future of Product Development within the Context of Digitalisation - Challenges of Data Networking

Alexandra Heinzl, Andreas Eursch
University of Applied Sciences Munich
Faculty of Mechanical Engineering, Automotive Engineering and Aircraft Engineering
Dachauer Straße 98b, 80335 Munich
aheinzl@hm.edu, andreas.eursch@hm.edu

Abstract—The current global megatrends, and especially digitalisation, are leading to a further increase in the complexity of products and the development processes of manufacturing companies, especially in the automotive industry. However, the new digitalisation technologies also offer many opportunities to master these challenges and to take product development to a new level, making it fit for the future. The possibilities are so diverse that a big picture first had to be created in order to find the most important and promising points of attack. This paper aims to present an overview of the challenges of data networking in the context of digitalisation in the future of product development. For a better understanding of the challenges to be overcome, basics on the layer model of product data, the forms of product information and the definition of non-CAX product information are explained. Since the challenges and the associated problems, also in relation to the amount of data, are only clearly visible in many product development situations, mainly in large companies, this paper also presents the factors influencing the product development process in more detail with a focus on large companies. Furthermore, the huge opportunities that arise with intelligent data networking in product development will be highlighted.

I. INTRODUCTION

During the last few years, global megatrends such as digitalisation, individualisation, sustainability and connectivity have posed ever greater challenges to mobility and thus to manufacturing companies [1, p. 21]. In the process, products are to be developed ever faster and more innovatively. There is also a demand to react more flexibly to constant changes and external influences. This results in an increasing number of new requirements that have to be met and thus also makes the products, their components and their functions more complex. Consequently, the product development process becomes more extensive due to the data to be processed and thus also considerably more difficult. It therefore requires companies to bring the use of intelligent, computer-aided methods and technologies to the next level. Only companies that are able to deal with the enormous and still increasing complexity of the development process will have a chance in the international competition. In order to be able to reduce and control this complexity in product development, the use of networked systems is playing an increasingly important role. The net-

working of data and information offers enormous potential for the development process at a very early stage in product development. The earlier access to all relevant development data is possible and these can also be used and exploited, the faster a high-quality development status of a component is achieved. This allows designers to react more flexibly to geometric changes at an early stage. In addition, development loops are reduced through fast and early defect detection and correction.

During the last few years, the term "digitalisation" in product development has also changed significantly. Nowadays, digitalisation in particular has clearly brought its significance and the resulting opportunities into focus as an essentially important point. From IT innovations and the digitalisation of products, development processes, services and data processing, digitalisation is now seen as fully supporting the development of new approaches for the future of product development. The sophisticated and highly complex products in the automotive industry in particular are increasingly difficult to realise in the mass market. Technologies such as automated or autonomous driving and communication between vehicles, as well as the supporting technology provided by sensors, radars and special cameras, play an enormously important role here. But that is not the only thing that has made digitalisation possible. Big Data stands for enabling the company, if desired even in real time, to structure, analyse and process enormous amounts of data consistently and correctly and to make quick decisions on the basis of this [2, p. 25 f.]. As another important point, this also includes data continuity for transparency and facilitated processing of data. Furthermore, with the help of information and communication technologies, the Internet of Things enables unlimited possibilities for interacting and networking physical and virtual information and objects [3, p. 29]. Digitalisation enabled innovations, complete reorientations and designs of products, for example through disruptive technologies, to gain enormous importance in international competition. Digitalisation made these exemplary developments possible during the last few years. This is the beginning of the potential and opportunities for the future, especially the networking of data in product development.

In the meantime, several methods and tools have been developed to capture the relevant knowledge for geometric design and integrate it into the CAD system. The so-called "knowledge-based engineering" (KBE) supports the designer in the product development process to meet the challenges of increasing product requirements and the coordination of the relevant data and information for the geometric design of the product. Knowledge-based engineering is based on VDI Guideline 5610 [4], which describes a procedure and technical solutions for implementing the method. Furthermore, the guideline describes information as structured and categorised data (relevance, relationships, temporal) that can be used in a certain context. Knowledge is, in effect, networked information that establishes links and relationships and enables this knowledge to be used [4]. A contribution by Luft et al. [5] from the Stuttgart Symposium for Product Development takes another closer look at VDI Guideline 5610 and presents an applied approach and concrete recommendations with the help of an example. In addition to knowledge-based design, there are many other approaches to networking data and information in the literature, such as model-based systems engineering (MBSE), connected engineering (CE), the use of AI and PDM systems, and even graph databases.

In the following, the enormous potential in the product development process through the early and continuous networking of data and information as well as the currently existing problems and obstacles in large companies (OEM) will be further discussed. First, the basics are explained in more detail, which serve for a deeper and comprehensive understanding of the topic.

II. BASICS

In the automotive industry, companies can basically be divided into the two categories of hardware and software companies. Especially the large OEMs such as BMW, Audi and Mercedes-Benz, are referred to as producing hardware companies, as their products are one of the most important access points for people's individual mobility. However, today's products and vehicles are constantly becoming smarter, more connected and more innovative, which means that software development also plays a major role in this respect. Thus, the geometry of a product is the main access point in every phase of product development and in almost all business areas. The reason for this is the unambiguity and consistency of the geometry, data and information available.

A. Level Model of Product Data

Product description and geometry generation are among the OEMs' core tasks, which is also their greatest competence. These core tasks can be realised more productively, in higher quality and, above all, in less time through the use of knowledge-based CAD systems (Computer Aided Design). In order to be able to react flexibly in this currently highly dynamic competitive environment and to develop innovative, intelligent and individualised products, product development

must have comprehensive requirements and framework conditions at its disposal. For a better understanding of the following relationships, an analogy was first formed based on a representation of Gapingvoid [6] from psychology and linguistics. The facts are presented in the context of the future in product development and the challenges of data networking, driven by digitalisation, as a level model related to product data (see figure 1).

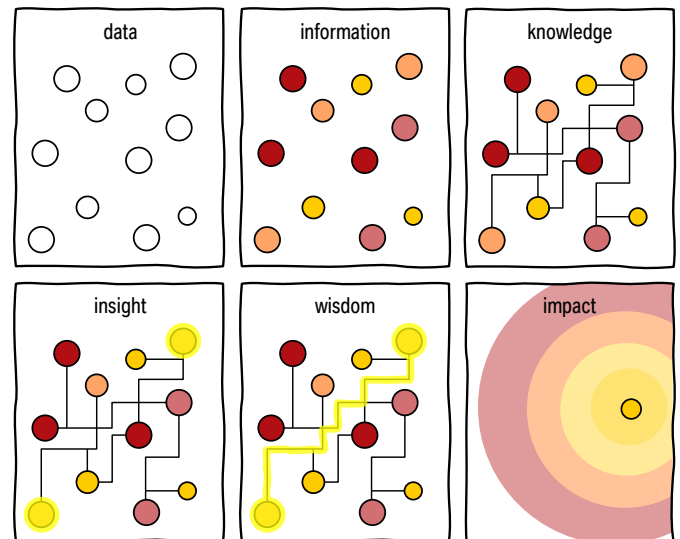


Figure 1. Level model based on [6]

At the beginning of every new vehicle project, the company has a large amount of unorganised data. This can, for example, come from a previous project or a project based on the same vehicle architecture. The data can be essential for subsequent product development if, for example, a bottleneck in the installation space has been intelligently solved with a special technical solution. However, the designer sees only limited added value in the available data for his development work, as he must first find this technical solution, based on the specific framework conditions and compromises or decisions made, in the unordered data set.

At the moment, the available data must be sorted, categorised and subsequently analysed. In this way, the designer gains a deeper insight into the data and accesses the relevant product information (reference information) for the project. This can include specifications for defined driving situations, the configurations in the vehicle as an overall vehicle plan or standards and design guidelines. In order to be able to use the available, structured information for the project, the designer establishes the connections and dependencies between the information. According to the current state of knowledge in psychology and computer science, for example, as well as in other interdisciplinary fields, this networking of information in a specific context is referred to as knowledge. This facilitates the understanding of the information at hand, which makes it possible, for example, to establish correlations or conditions through a vehicle configuration. This leads to the next step,

knowledge. This way, the designer is aware of what information he has available at one point and what information he still needs. This could be, for example, the configuration of a vehicle door. In the present overall vehicle plan, for example, a coupé is envisaged, so the question is whether it will be a 2 or 4-door. Accordingly, the designer knows what information he needs for an initial state of geometry generation, for example, the available installation space for the package. Wisdom then describes the final aspect by finding the direct path from the first information to the required information. With this wisdom and insight, especially in product development, it has an enormous impact on saving time in the search for the right information and on the effectiveness of geometry generation.

B. Forms of Product Information

The product information is available in different forms due to the complexity of the vehicle and the resulting extensive amount of data to be processed. Three main categories can be defined: *product information in the form of objects, parameters or values or in context*. The triangle of product information in figure 2 visualises these three main categories, making clear that each category has a connection to and is dependent on the other two categories.

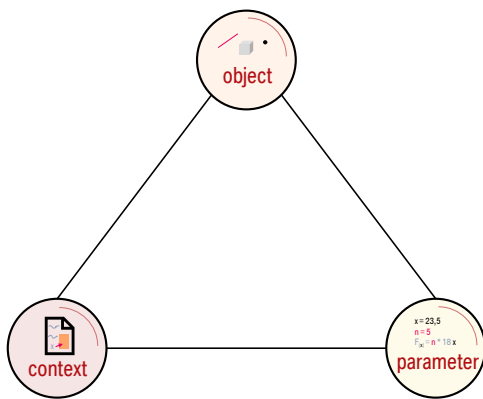


Figure 2. Triangle of product information

An object is information that can exist as a geometric element such as a point, curve or 3D geometry. For example, the course of a seal or the trim edge of a side glass can be clearly defined in this way. An object can be unambiguously assigned in space through the pictorial representation and the geometric definition. A parameter, on the other hand, is either variable depending on the application or defined as a fixed value. For example, standards or design guidelines usually define which welding pinole and the associated spacing of the welding points must be used for certain sheet thicknesses and materials. But curves can also be variably changed by parameters and rules. Context information is largely present as a description of a use case or as information between the lines. However, the correct understanding of contextual information also depends strongly on the formulation of the author and the level of knowledge of the reader or designer.

If the categories of the available product information are examined more closely, it can be established that there is a dependency. Accordingly, an object is clearly defined by values and parameters as well as the associated context information in the application. A parameter is assigned to a direct object and the context information defines in which use case this parameter changes. The context information thus influences an object in its geometric uniqueness with the help of parameters and values that are defined in the context. At this point, special attention also seems to be paid to the consumability of information. For example, a 3D geometry such as a line in space can be understood by a person much more quickly and clearly than its mathematical description using parameters and formulae. The choice of the information category that is easiest for the recipient to understand represents a decisive influence.

The product information required for vehicle development, before it is transferred to a CAx system, can generally also be referred to as so-called *Non-CAx product information*. A detailed definition follows in the next section.

C. Definition of Non-CAx Product Information

"Non-CAx product information" is the term used to describe data, information and values that are essentially required during the geometry generation of a component and support the designer in this process without there being a direct link to a CAx system (e.g. CATIA V5). This information is available in various document formats such as a PDF document, an Excel spreadsheet or a PowerPoint slide set. The information contained therein can be, for example, values from a standard or a design guideline for installation and screw clearance of a component. It can also be specified, for example, that a clearance of a few millimetres must be maintained between surrounding components in each positive and negative axis direction of the coordinate system in order to avoid acoustic noise generation due to vibrations of the components during driving operation. In addition, further information is available as context information in text form and as objects in geometry form or as an image. This available information are conditions and requirements that the geometry of the component must fulfil. However, the information suitable for the application cannot be accessed directly in CAD, except by manually transferring and defining parameters and rules. Today, there is still no compatible format for loading data or information from a PDF document, for example, easily and automatically into a CAD programme. This means that there is also no link to the relevant data source. The up-to-dateness of the documents and the information used from them must therefore be constantly checked manually. This includes direct requirements on the component such as material properties, load cases or objects. But indirect requirements also have an influence on geometry generation. These can be, for example, customer feedback on the force required to open and close a vehicle door or the acoustics in the passenger compartment.

III. CHALLENGES OF DATA NETWORKING

A. Opportunities and Challenges of the Intelligent Use of Connected Product Data in Large Companies

The challenges of data networking in product development described below are transferable to almost all companies from all branches of industry, with different product portfolios and a variable company size. Since the challenges and associated problems are only clearly visible in many situations in the product development phase, mainly in large companies, the focus of the research work is initially placed on this.

Due to the existing data and information, large companies have a great treasure that can be used and turned into a competitive advantage through intelligent networking against the background of digitalisation. In the automotive industry in particular, numerous companies have existed for almost more than 100 years and have generated an enormous amount of knowledge during this time. This industry is also dominated by the OEMs. These are large companies whose size makes the realisation of such complex products as automobiles possible in the first place. Since their foundation, they have grown steadily in terms of quality and quantity to their current size. They have managed to grow by expanding and acquiring a special core competence, by expanding their internal know-how, their corporate and competitive strategy and by creating popular, high-quality and individual products with special characteristics. The OEMs differentiate themselves mainly through their know-how in engine construction, vehicle design and their corporate values as well as their positioning in the market. The current highly dynamic market development and the megatrends are driving the companies to expand their competences and know-how, especially with regard to the new digital possibilities, in order to be able to respond even more individually to the needs of the customer. This requires an enormous amount of data and information, such as customer feedback on the force required to open the doors, target group and competitor analyses, product data from similar vehicles or previous projects, product requirements, the drive strategy and framework conditions from standards and laws. But it also offers enormous potential if this knowledge can be harnessed. Computer-aided tools and PDM systems are already being used to organise, structure and provide these data volumes, which have accumulated over time and continue to grow, and to link them together in the right places. A data backbone was developed early on with the start of digitalisation and has continued to grow. It comprises a large part of the company's internal know-how and would have the potential to offer companies an enormous advantage in product development, as this data is available in its entirety and can be used at any time. However, this potential is currently not being used, or the possibilities are only opening up with the current achievements of digitalisation, such as the use of artificial intelligence or Big Data, which is made possible by intelligent technologies for processing and evaluating huge amounts of data. The PDM systems used are already at their functional limits and deficits have been found in the applications. Therefore, in some cases,

completely newly developed or already existing tools were used only for the company or by various specialist departments for special use cases, which support the developer and make his daily business more effective. However, the use of new technologies, methods and the IT infrastructure can only be implemented slowly in companies of this size because the decision-making paths are very long and clearly defined.

With the help of new tools, it was possible, for example, to realise the workflows in the publication process of new components, extended communication methods with integrated data storage, the control and organisation of daily business and the respective task packages, as well as the initial networking of design data. The tools have a great benefit for the companies and provide individual solutions for use cases, departments and different employee roles. Due to the constant growth of the company and the requirements for the products, as well as the advancement of digitalisation in product development, the number of supporting tools is continuously increasing. Accordingly, problems are compensated and bridged for a certain time by the use of further tools. Countless new documents, data sources, access points and ways or possibilities to process a workflow are created. A holistic solution is needed here, which in turn requires a holistic approach to networking the data in order to make it usable.

B. Data Networking to Support the Designer

There are several important reasons why the networking of product and design information is so important for the large companies. In product development, as mentioned before, the main access point is the geometry of a product. The uniqueness and consistency of the data and information lies in the product design. However, a lot of information and geometric solutions are also realised and mapped with the help of a designer's experience. This is why an experienced designer is much faster in geometric design than a new employee, since he is not, or only to a limited extent, dependent on the expert knowledge of a colleague, for example. Viewed in the level model, he is already on the wisdom level, since he knows exactly what information he has available, what he still needs and how to find it. However, it is not always immediately obvious where to find the right information, which costs the designer a lot of time during work. Currently, companies have all this data and information available but do not use it or use it too little because the current digital tools are still too inefficient. This is either because the information sought cannot be found or access to it is denied to a new employee, for example, or because an experienced employee does not use the information because it takes too long and may be too inconvenient to find the information. In addition, there is the question of the timeliness and usefulness of the available information, as well as whether the benefit of the information justifies the effort of obtaining it. An enormous increase in effectiveness and efficiency in the future of product development in the context of advancing digitalisation can be achieved through the intelligent networking of product and design information. This increase is achieved by providing every authorised employee

with the information they are looking for at any time in the correct, most up-to-date data in the shortest, most suitable way. For a better understanding of the current difficulties of the topic, the challenges of data networking are presented below.

C. Influencing Factors

1) *Tool Landscape*: Today, OEMs have countless different tools. In an overarching view, these tools can be assigned to different categories. Some of them, for example, are only used by certain departments. These include various calculation and simulation tools for a complete vehicle simulation under the loads of the Euro NCAP as well as flow simulations to design the vehicle outer skin or cooling systems according to defined criteria. But tools for the design and visualisation of products as well as PDM applications are also included. These and countless other tools are available to the developers to support them in the category of operative day-to-day business. Furthermore, control and organisation tools are used, for example, for process handling and task distribution in the respective project phase or the production release of components to the supplier. For general communication within the company or with external partners and to support the personal exchange of employees, Skype for Business or tools from Microsoft are used, for example. However, since some tools cannot be clearly defined in which category they can be classified, there are intermediate categories. Applications that are both a communication tool and a control and organisation tool, or that serve to support both control and operative day-to-day business, are classified in these fields.

2) *Data Sources*: Non-CAx product information can also be stored in different data sources. This can be, for example, on the desktop, a file path on a server drive or in a cloud or a SharePoint site. This creates many storage locations where, for example, the information is not necessarily up to date. But access to individual pieces of information is also made more difficult if the path where the information is stored is moved and can therefore no longer be easily found. Accordingly, two essential questions arise: Is the right information from the right data and at the most up-to-date level available at this location? Where and how can the relevant information be found?

3) *Roles and Access Rights*: Especially in large companies, there are countless different and clearly defined roles for employees, which are assigned to them when they start their employment or change their position. Depending on the department and function in the company, there are different roles, which means that employees have different responsibilities, accountabilities and task packages. In general, each role can be assigned to a category: a department-specific role such as a designer or a simulation specialist for aerodynamics on the outer skin, a project-specific role such as the head of the front light assembly, process partners from other departments such as production or purchasing, or external partners as development service providers or suppliers. As a result, each individual role in the company only has limited access rights to a small number of defined tools that are intended for support in day-to-day business and support the employee in

the process flow. The consequence of this is that in some places the employees are denied access to relevant non-CAx product information for the geometric design of the product, and in some cases this information is only stored in the tools. Accordingly, employees who have been assigned a department-specific role, for example, cannot access any information that is accessible to a person in a leading position.

4) *Information Procurement*: The geometric design of a product often requires countless different non-CAx product information and design information that is already available in a CAx system. In order to be able to obtain and use this information, the designer is forced to walk long distances due to the large tool landscape, the lack of access rights or the lack of empirical knowledge of where and in which access point or on which interface the information is located. This costs the designer an enormous amount of his productive working time and also makes geometric design and day-to-day business more difficult.

IV. CONCLUSION

In general, from the present overview of the challenges of data networking, it can be stated that there are several influencing factors from different perspectives that make efficient networking of data difficult today against the background of digitalisation, especially in large companies. A key factor for success is the intelligent handling of data in product development. In addition to the increasing complexity of products in the area of mobility, the tool landscape, the various roles and access authorisations, as well as the different data sources and the sometimes cumbersome ways of obtaining information, make data networking enormously difficult. This takes the complexity of product development to a new level. In order to make this complexity manageable in many dimensions, measures are needed to support the designer in geometric design. Digitalisation in product development offers enormous opportunities to overcome the challenges and, in particular, to support the user in reducing complexity, while at the same time making the development process more efficient. This can be made possible, for example, through intelligent networking of knowledge with the help of machine-readable interfaces, the use of artificial intelligence and Big Data technologies, as well as data consistency and information flow tracking with a focus on the user. Many interesting approaches can be derived from this for further consideration of the research topic. The presentation of the challenges and the influencing factors on data networking should make an important contribution to the future of product development in the context of digitalisation.

REFERENCES

- [1] S. Tewes, B. Niestroj, and C. Tewes, *Geschäftsmodelle in die Zukunft denken*. Wiesbaden: Springer Fachmedien Wiesbaden, 2020.
- [2] A. E. Hassanien and A. Darwish, *Machine Learning and Big Data Analytics Paradigms: Analysis, Applications and Challenges*. Cham: Springer International Publishing, 2021, vol. 77.
- [3] F. Abolhassan, *Was treibt die Digitalisierung?* Wiesbaden: Springer Fachmedien Wiesbaden, 2016.
- [4] Verein Deutscher Ingenieure - VDI, "Wissensmanagement im ingenieurwesen, wissensbasierte konstruktion (kbe): Vdi 5610 blatt 2," 2017.
- [5] T. Luft, D. Roth, S. Wartzack, and H. Binz, "Die neue vdi-richtlinie 5610 blatt 2 "wissensbasierte konstruktion"," in *Stuttgarter Symposium für Produktentwicklung SSP 2017*, H. Binz, B. Bertsche, W. Bauer, D. Spath, and D. Roth, Eds., 2017, pp. 287–297.
- [6] Gapingvoid, "Semiotic management systems | gapingvoid," [Online]. Available: <https://www.gapingvoid.com/semiotic-management-systems/>, 20.04.2021.

Characterization of liner materials in terms of gas tightness and permeation for a cuboid, tension rod supported, high pressure hydrogen vessel

Alexander Hupfeld

Munich University of Applied Sciences

Department of Mechanical, Automotive and Aeronautical Engineering

Email: Alexander.Hupfeld@hm.edu

Abstract— To adapt the hydrogen tank design to modern automotive installation space architectures, i.e. the battery housing of current battery electric vehicle a cuboid, tension rod supported, type IV hydrogen vessel design is developed. The present work addresses possible variations of materials and their properties for the sealing liner and the tension rod. The interfacial area of tension rod and sealing liner is considered critical in terms of gas tightness. The ongoing research analyses this interface by using a sensitivity analysis and additionally approach it with hardware testing. The objective of this paper is to verify the analytic design approach and give a design target corridor with respect to the specific design of the pressure vessel.

I. INTRODUCTION

Due to climate change, political decisions are demanding zero emission vehicles regarding the mobility sector [1], [2]. Rising battery electric vehicles (BEV) registrations may show, that customers have a distinctive environmental awareness without relinquishing their individual mobility [3]. Due to long charging time combined with a short driving range of a BEV, this technology can not substitute the market of internal combustion engine vehicles (ICEV) when looked at the needs of every customer [4]. Fuel cell electric vehicles (FCEV) are a good zero emission alternative to BEV with its short refuelling duration of 3-5 minutes and its minimum range of ≈ 450 km [5]. Therefore hydrogen, as carbon-free energy source, is at the focus of research activities worldwide [6]. But in terms of modern automotive mass production it is crucial to be able to apply a modular design to manage the variant diversity and complexity in order to be cost efficient. By using synergy effects and economies of scale, the overall vehicle costs of BEV and FCEV can be lowered effectively [7]. Therefore the automotive industry is interested to define the cuboid battery installation space of modern BEV in the vehicles under body (s. Fig. 1) as storage compartment of its hydrogen storage systems for FCEV.

II. DEVELOPMENT OF DESIGN PRINCIPALS

A. General Design

The current state of technology for hydrogen tanks systems are 700 bar type IV storage systems to achieve a sufficient energy density. These high pressure type IV tanks are commercially available at a reasonable cost range [6], [9]. These high pressure hydrogen tanks are shaped cylindrical

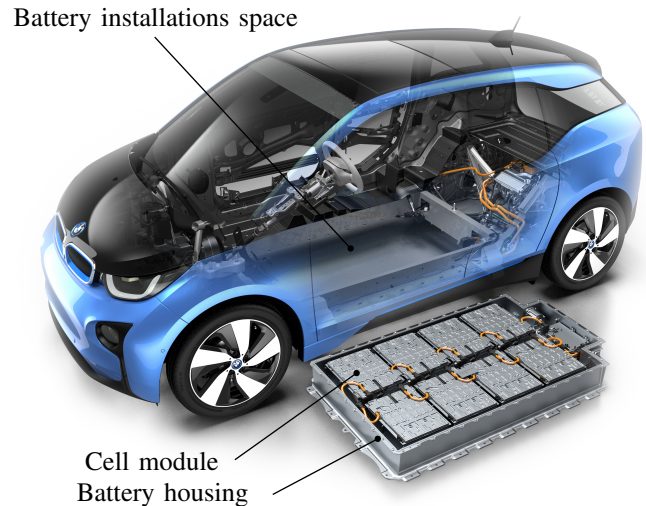


Figure 1. Battery installation space exemplified by the BMW i3 [8].

because it is favorable in terms of mechanical strength of the tank structure. In addition its manufacturing processes, i.e. winding of thermoset or thermoplastic matrix composite materials are well developed. They are integrated into existing ICEV architectures along the center tunnel and/or traverse behind the back seats. But when modern BEV architectures with a flattened vehicle floor are approached, limitations arise with regard to an advantageous vehicle package nor can any scale effects or synergies between BEC and FCEV be used to reduce manufacturing costs [9], [10]. In order to make those synergies viable and be able to make the battery housing (s. Fig. 1) accessible for high pressure hydrogen tanks, a cuboid, tension rod perforated design approach is applied. The overall tank layout follows state of technology type IV tanks designs (fully wrapped CFRP hull with polymer sealing liner) [9]. The ongoing research uses an exemplary design space of $1800 \times 1300 \times 140 \text{ mm}^3$ (s. Fig. 2) with a minimum of 45% usable volume of hydrogen [11]. Furthermore the design is carried out under consideration of the UN ECE 134. The standard sets the minimum burst pressure (BP_{\min}) to 1575 bar and the nominal working pressure (NWP) of the hydrogen tank

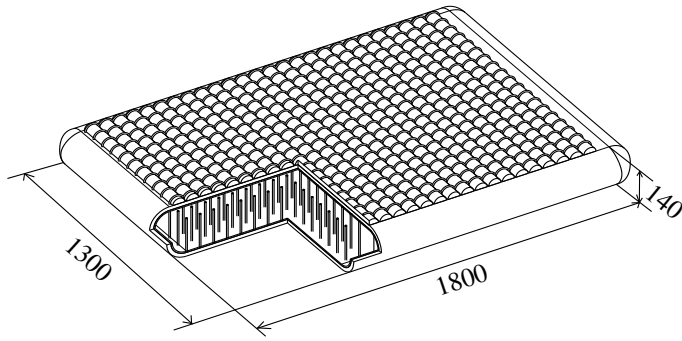


Figure 2. Cuboid, high pressure, tension rod supported hydrogen tank concept study with exemplary design space dimensions and cut out.

to 700 bar. The proof pressure testing procedure according to the UN ECE 134 requires certain load cycles within a range of up to 180% of NWP. Therefore the ongoing research uses cyclic loading within this range when it comes to hardware testing. In this first approach temperature profiles as given by the standard will not be taken into consideration during hardware testing but is respected in terms of material choice [12]. With regards to the boxed shaped tank layout, the large plane parallel opposite layers need to be reinforced by tension rods according to the load induced by the internal pressure, so no deformation of the outer carbon fibre reinforced polymer (CFRP) hull occurs. To provide a viable industrial feasibility a textile manufacturing process like weaving or tufting is necessary due to the high density of integrated tension rods [13].

B. Analytic Design Approach

Via an analytical approach a tension rod diameter to spacing ratio is determined (s. Fig. 3) for the force equivalent of BP_{min} . For a rod density below 5 to 6 struts/cm² the shear stress within the outer CFRP tank hull exceeds the interlamnari shear strength limit of ≈ 80 MPa when BP_{min} (1575 bar) is applied which may result in substantial structural damage [13]. The global properties regarding the tension rod must meet a minimum breaking tenacity of 2600 MPa and a thickness of ≈ 1.5 mm resulting in a tension rod spacing a of ≈ 4 mm (s. Fig. 4, Eq. 3). Aramid can compensate different pre-tensioning caused by manufacturing tolerances better than rods made of carbon fibres due to their lower Young's modulus [13]. The ongoing research sees industrial feasibility when textile manufacturing processes (like tufting or weaving) are applied (s. Chpt. II-A). Therefore the fibres are twisted for better processability due to lower sensitivity to frictional stresses as result of an optimized filament incorporation and an ideal packaging format, which will result in less snagging while processed.

Twisting of the fibers will also raise the elasticity and due to compacting the tank capacity will rise accordingly [14], [15]. But a twisted yarn is more difficult to fully saturate with

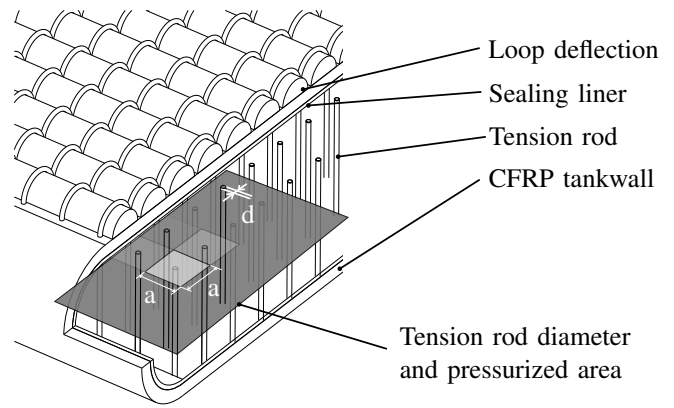


Figure 3. Detail tank concept study with tension rod diameter and pressurized area elements with side length a .

matrix material to ensure full matrix penetration of the tension rod and thus achieve gas tightness (s. Chpt. IV-B).

$$A_{rod} \times \sigma_{fibre_{min}} = A_{pressured\ area} \times p_{BP_{min}} \quad (1)$$

$$\frac{a_{pressured\ area}^2}{d_{Rod}^2 \times 0.25 \times \pi} = \frac{\sigma_{fibre_{min}}}{p_{BP_{min}}} \quad (2)$$

$$a_{rod\ spacing} = 3,6 * d_{rod} \quad (3)$$

If a force equilibrium for a spacing of 4mm is set up between the pressurized surface (minus the cross section of the tension rod) and the tension rod a force equivalent of ≈ 2200 N is determined. A test campaign was performed to determine the influence of the loop deflector with respect to the strength determined for an industry standard aramid fibre, the tension rod needs ≈ 5000 filaments to be able to withstand the load of BP_{min} without breaking [16].

C. Impermeability Analysis

According to the UN ECE R134 regulation, the allowed hydrogen discharge limit for a pressurized hydrogen vessel is set to 46 ml_{H₂}/h/l_{tank capacity} at 55°C [12]. The ongoing research is testing and analyzing liner made of epoxy resin (EP) and castable polyamide (PA6G). Referring to the new, cuboid and tension rod perforated design of the tank general gas tightness is taken into account in terms of hardware testing. Permeation is covered by an analytic approach regarding the liner thickness. In the following the theoretic permeation properties are compared and discussed.

Permeation is described as the penetration of solid bodies by gases [17]. The permeation properties of the presented hydrogen tank is determined by the liner material, the tension rod fibre material and the interphase of tension rod and sealing liner assuming complete roving penetration with sealing liner matrix. The influence of the CFRP tank wall is not considered. At a temperature of 55°C and an internal pressure of 805 bar, the hydrogen permeation shall be less than 46 ml per hour

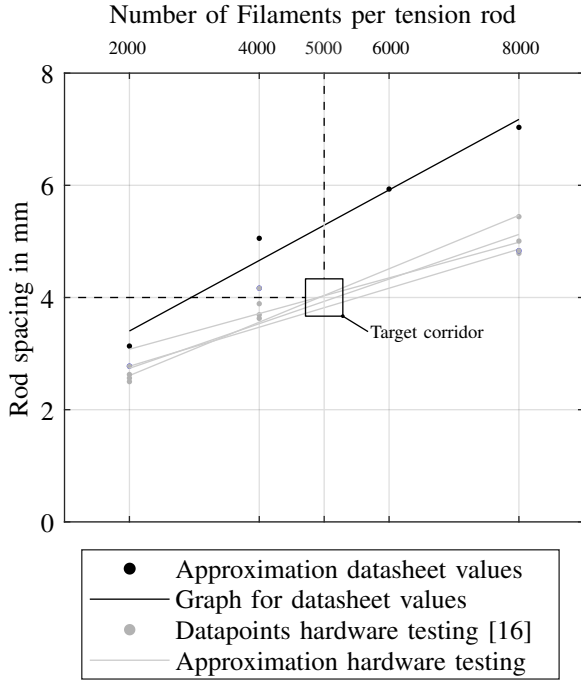


Figure 4. Overview rod spacing over filaments per tension rod.

per liter of storage volume [12]. Polyamide is current state of technology in terms of liner material in type IV tanks due to its high permeation barrier which results in a liner thickness of 1.6mm as shown in Table I [9]. But EP shows a comparable performance when used as liner material and assigned a factor of ≈ 5 in terms of liner thickness. In addition the permeation barrier of EP may be improved by adding silicate clay or by using graphene EP [10], [18].

The leakage flow rate Q for flat surfaces is calculated corresponding to Eq. 4, in which p is set to 805 bar as given by the UN ECE 134 standard as permeation approval pressure. The hydrogen exposed surface is described as A and t is the liner thickness [10].

$$Q = P(T) \times \Delta p \times \frac{A}{t} \quad (4)$$

In order to adapt it to the requirements of the R134 of 46 ml per hour per liter of storage volume, the equation is modified.

$$Q = P(T) \times \Delta p \times \frac{A}{t} \times \frac{3600 \times 10^6}{V_{H_2}} \quad (5)$$

With the given installation space (s. Fig. 2) the maximum permeation effective surface (PES) is 4,916 m² with a volume of 314 l. The measurements are taken from a computer-aided design model. As depicted in Fig. 2 the edges of the cuboid tank are shaped as half cylinders and the corners are formed as quarter spheres. The maximum tank volume is reduced by 60%, taking the outer CFRP hull, liner and fuelling connectors and tension rods into account resulting in a tank volume of ≈ 138 l which results in 5,52 kg at a hydrogen density of 40

Table I
HYDROGEN PERMEATION RATE FOR DIFFERENT LINER MATERIALS AND THICKNESSES [10], [17]

Materials	E_p^a (kJ mol ⁻¹)	P^b at 55°C (m ² s ⁻¹)
PA	26	1.0×10^{-12}
EP	28	5.0×10^{-12}
Resulting liner thickness at 50% storage volume		
Materials	d (mm)	
PA	1,56	
EP	7,35	

^a Permeation Barrier

^b Permeation Coefficient

kg/m³ at 700 bar [4]. The reduced tank volume results in a PES of 3,22m² excluding the surface area of the tension rods which results in liner thicknesses shown in Table I.

D. Rod and Liner Interface

In terms of gas tightness the interface between tension rod and sealing liner is identified as critical area. CFRP specimen which are exposed to 80 bar on a pressure testing bench show intralaminar cracks which will result in enhanced leakage rates [13], [19]. To ensure gas tightness up to 180% NWP during proof pressure testing loads must be transferred effectively between the fibre and liner interphase which demands a strong fibre-liner interface. The adhesion can be controlled via fibre surface treatment and fibre sizing. Optimized adhesion can also be achieved by modifying the polymer with functional groups that will provide an improved bonding of fibre or fibre surface coating to the matrix [20].

Loads induced by the internal pressure are not exclusively transferred to the tension rods but will cause shear stress to the interface along the tension rod (s. Fig. 5). The force distribution can be expressed as follows.

$$F_1 = F_2 - F_{liner} - F_{CFRP} - F_{rod deflector} - F_{deflector} \quad (6)$$

$$F_{liner} = 2\pi r_{rod} \int \tau_{liner} dx$$

$$F_{CFRP} = 2\pi r_{rod} \int \tau_{CFRP} dx \quad (7)$$

$$F_{rod deflector} = 2\pi r_{rod} \times r_{deflector} \int \tau_{rod deflector} d\varphi$$

The exact stress distribution along the tension rod can not be approached analytically because the interaction between the different material lay-up requires a finite element analysis which is addressed in the ongoing research but is not part of this paper since the final results are still pending. The analytical approach (s. Eq. 6) gives the spectrum of adaptable areas in the assembly of tension rod, loop deflector, liner and tank wall. The load share indication shown in (Fig. 8) gives a

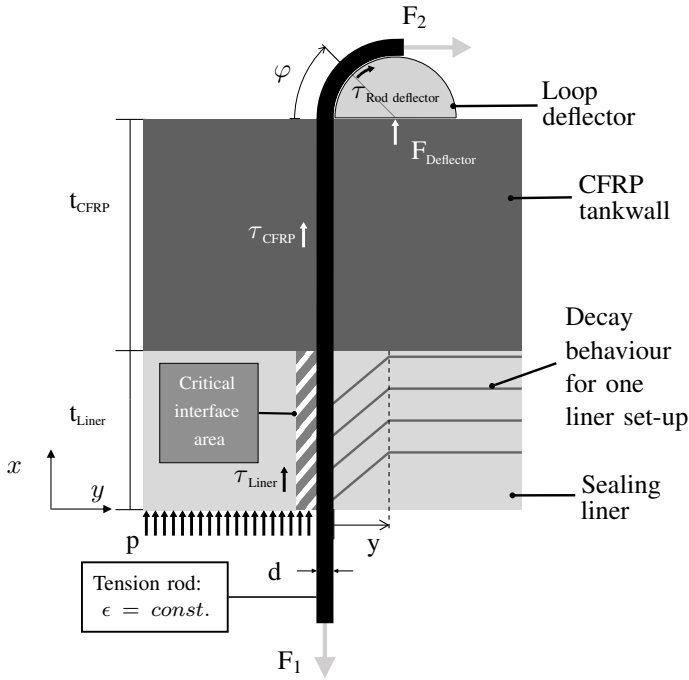


Figure 5. Schematic cross section of an embedded fibre loop.

better overall summary of the load transfer capacities regarding the remaining adaptable areas.

But to have a better understanding for different hardware testing the critical interface between rod and sealing liner is approximated analytically to provide a sensitivity analysis and get first results concerning pullout, cyclic loading and gas tightness tests. Assuming that the elongation of the tension rod is constant (s. Fig. 5), the shear stress in the critical interface of tension rod and liner (s. Fig. 4) can be described as follows:

$$\tau(y)_{Interface\ Liner}^{max} = \frac{G_{Liner} \times F_1 \times t_{Liner}}{E_{Rod} \times 2\pi \times r_{Rod}^2 \times y} \quad (8)$$

$$G_{Liner} = \frac{E_{Liner}}{2 * (1 - \nu)} \quad (9)$$

The decay behaviour of the shear stress is described by y and is varied from 0,5 to 2 mm (s. Fig. 6). Due to the described design criteria in Chpt. II-A the variations within Eq. 8 are limited. Rod spacing and the direct proportional rod diameter is limited by the shear stress within the outer CFRP skin of the tank and is additionally linked to the hydrogen storage volume. The rod force F_1 is determined by the given proof pressure load of 180% NWP and the liner thickness by the permeation coefficient (s. Tab. I). The tension rod Young's modulus is also fixated referring to the use of aramid fibres (s. Chpt. II-A). Only the shear modulus of the liner can be varied significantly. The maximum shear stress must not exceed 50 MPa to avoid interfacial failure between rod and liner. This can be obtained by lowering the Young's modulus of the liner material while maintaining its adhesion properties.

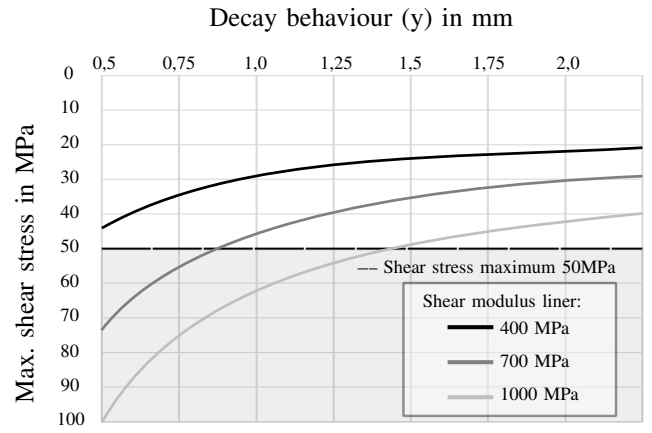


Figure 6. Influence of the decay behaviour and shear modulus on the maximum shear stress.

The lowered Young's modulus of the liner will increase the decay behaviour affected area (s. Fig. 5) and will also lower the maximum shear stress inflicted to the area. It is possible, that this behaviour will interact with surrounded tension rods, which can be tolerated if it ensures the adhesion between tension rod and liner.

III. HARDWARE TESTING

A. Tension Rod Construction

As described in Chpt. II-B the tension rod needs to be manufactured with a yarn consisting of $\approx 5k$ filaments of industry standard aramid in order to withstand the mechanical load of BP_{min} . In addition the tension rod construction needs to be suitable for textile manufacturing processes therefore a standard spin finish is applied. The yarn for the manufactured specimen are twisted using two different configurations (s. Fig. 7). Each is fabricated of three 2K rovings.

Type (A) is a cabled yarn which is also used for tire manufacturing. This type of tension rod construction ensures a parallel fibre orientation in the direction of the yarn axis thus a very good utilization of the filaments substance strength while its volume will remain constant [15]. The three filaments are fixated on one end, the other end is then twisted with ≈ 123 turns per meter (T/m).

Type (B) is a flat twisted yarn which are used for weaving or sewing processes. This yarn construction is suitable for very high stresses during textile processing. In addition the cabled yarn will have a higher strength, elasticity and a higher density [15]. For this yarn construction each roving is subjected separately to a rotation around the roving axis of $\approx 100T/m$ while one side of the yarn is bundled and fixated. The twisted rovings are then rotated around the yarn axis until the snarling tendency is subsided.

B. Epoxy Liner Characterization

The target range in terms of temperature occurring during quick ventilation and refuelling is set between $-40C^\circ$ and

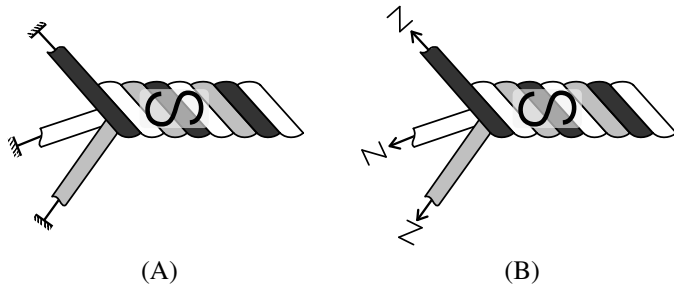


Figure 7. Yarn construction: (A) Cabled Yarn (B) Flat twisted yarn

+85C° given by the SAE J2601 standard [21]. As described in Chpt. II-D the liner material is to be adjusted by the shear modulus. To meet the criterion of 50 MPa shear stress maximum within the interface of liner and tension rod (s. Fig. 6) while burst pressure is applied, the shear modulus of the EP liner needs to be adjusted to ≈400 MPa. The lowered shear modulus is obtained by adding polyaminoamide in the corresponding weight ratio to a mixture of room-cure epoxy resin and hardener.

The presented test series (s. Tab. II) shows that a possible target corridor for an optimized EP liner is to be found between 20% and 30% added flexibilizer. The same batch of epoxy material was tested using a dynamic mechanical thermal analysis (DMTA) to analyze the influence of the modification on the temperature behaviour. It can be stated that the T_g matches the optimized target corridor for flexibilized EP liner material between 20% and 30% added flexibilizer. The tension tests to determine the Modulus of the specimen are performed in accordance to ISO 527 at room temperature.

Table II
LINER MATERIAL CHARACTERIZATION

Material	Glass Transition Temperature in °C ^a	Elastic Modulus in MPa ^b
EP without Flexibilizer	95,6	3186
EP with 20% Flexibilizer	98,2	2093
EP with 30% Flexibilizer	72,3	272
EP with 40% Flexibilizer	50,4	44

^a n=1
^b n=3

C. Interphase Specimen

For interphase characterization of composite materials pull out tests and their corresponding specimen become a standard. To test the influence of the two yarn construction (s. Chpt. III-A) on the matrix/tension rod interphase and gas tightness (described in [13]) specimen with type A and B yarn constructions are manufactured. The test series is performed with a flexibilized/non-flexibilized liner attachment. To be able to vary the liner thickness a 3d-printed cavity (40×40×20mm) is used. Dry fibres are then passed through a silicone layer. The cavity is then clamped with an according aluminum cover to seal the cavity. The liner material is then inserted and the

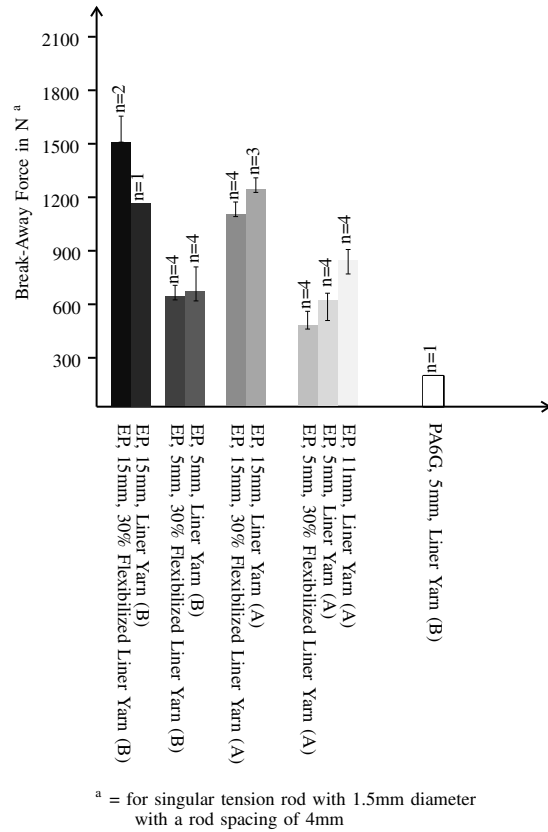


Figure 8. Results of pullout testing with different liner and yarn setups.

fibres are impregnated with the same liner material the cavity is filled with. All specimen are tempered at 60C° for 6 hours in order to let the resin fully cure.

IV. RESULTS

A. Pull-Out Test Series

A pullout test series is performed to test the influence of the different yarn constructions, flexibilized liner and thicknesses.

A corresponding liner is attached to the tension rod (s. Chpt. III-C). A single tension rod pullout test is performed. It should be noted that the presented testing results can not be directly transferred to the entire tank (s. Fig. 5) since different shear forces are acting along the rod (Eq. 6).

The determined pullout forces show, that the flexibilization of the liner attachment has a relatively small influence on the interfacial properties of tension rod and matrix. It can be observed, that the influence of tension rod construction will result in an increased break-away force this is due to undercut sections of the flat twisted yarn (s. Fig. 7). In addition the measure of dispersion with this tension rod construction is higher, because the exact positioning within the liner is not addressed while manufacturing the specimen. It can be stated, that a target corridor for liner thickness and tension rod construction is set-up to further investigate on.

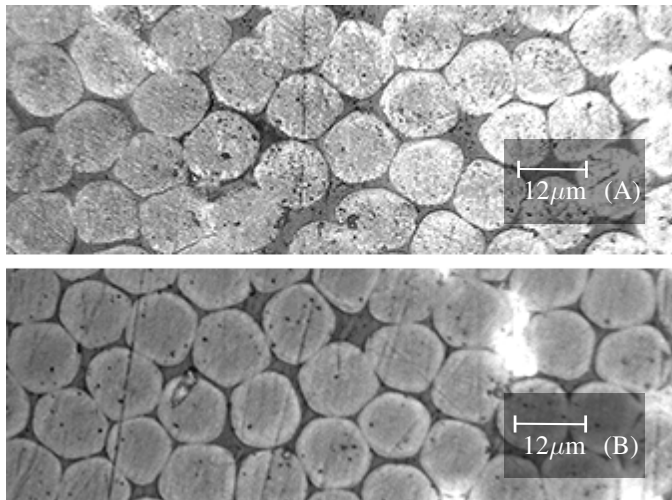


Figure 9. Optical microscope end face cut of industry standard aramid yarn type (B) in (A) room cure EP resin (B) castable polyamide.

B. Penetration and Adhesion Analysis

In the following a morphological analysis of the fractured surfaces and end face cuts are evaluated to analyse the adhesion and saturation of matrix and tension rods with respect to permeation.

A penetration analysis of the tension rod is carried out using an optical microscope. The cabled yarn type (B) specimen (s. Chpt. III-A) for this analysis are extracted from the matrix embedded areas of the interphase specimen. The circular areas mark aramid filaments, the dark gray color represents matrix saturated areas (s. Fig. 9). The specimen show good matrix penetration (EP and PA6G) for this industry standard aramid fibre despite the high compacting due to yarn processing. The white marks within the PA6G matrix are still under investigation since it is not clear whether they are imperfections due to manufacturing or due to processing of the specimen. Additionally twisting of the fibre show some matrix saturation imperfections of the yarn core. They may be caused due to the hand lay-up laminating process which is used to manufacture the EP specimen.

To evaluate the fiber/matrix adhesion a scanning electron microscope (SEM) analysis is carried out in addition to the pullout testing (s. Chpt. IV-A). As well as for the optical microscope analysis the cabled yarn type (B) specimen are extracted from the matrix embedded area. Specimen (A) (non flexibilized EP liner) shows "hackles", a characteristic for tough resin and shear failure which occurs due to tension rod pullout (s. Fig. 10 (A)) [22]. Specimen (B) with 30% added flexibilizer shows a ductile matrix behaviour as well, the filaments are still very much embedded into the matrix. The fiber matrix interphase seems to be stronger when compared to the flexibilized matrix (s. Fig. 10 (B)). Specimen (C) shows very good saturation with PA6G since the fibres are fully integrated into the the polyamide. If the saturation level of the end face cut is additionally taken into account PA6G shows

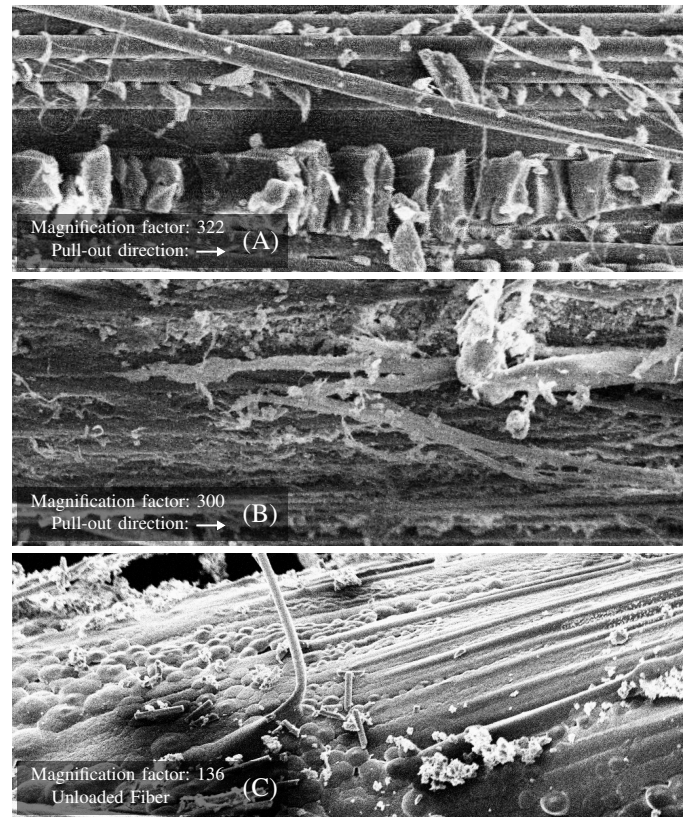


Figure 10. SEM fiber/matrix adhesion analysis:
 (A) Pullout aramid yarn type (A) non flexibilized EP liner material
 (B) Pullout aramid yarn type (A) 30% added flexibilizer EP liner material
 (C) Pullout aramid yarn type (A) PA6G liner material

very promising interaction with aramid fibers. This would allow very small liner thicknesses compared to EP as liner material which will result in increased hydrogen capacity (s. Tab. I).

C. Conclusion

Based on a general design analysis for a cuboid, tension rod supported, type IV hydrogen tank the interfacial area of tension rod and sealing liner was analysed to give a target range in terms of material choice, and gas tightness. Interface specimen with a single twisted aramid fibre (tension rod) were manufactured and subjected to a pullout test series. In addition a microscopic analysis was carried out to evaluate fibre adhesion and roving penetration with matrix material.

The investigation yielded the following conclusions:

- Aramid fibres for the tension rods of this new hydrogen high pressure vessel concept could be specified. A tension rod consisting of ≈ 5000 filaments with a spacing of $\approx 4\text{mm}$ is sufficient to mechanically withstand BP_{\min} and reduce the induced load on the tank wall.

- By applying a sensitivity analysis for the interface of tension rod to liner the material variation for the liner narrows

down to adjusting its shear modulus to maintain gaseous tightness.

– Epoxy is a compatible liner material in terms of permeation barrier and coefficient and its sealing properties can be optimized by adding resin additives. By using PA6G a standard liner for type IV vessels could be validated for the sealing liner in combination with aramid fibres.

- This approach was verified by hardware testing and a target corridor to further optimize liner thickness with respect to the hydrogen storage volume was obtained.

REFERENCES

- [1] V. Masson-Delmotte, V. P. Zhai, H.-O. Pörtner, D. Roberts, J. Skea, P. Shukla, A. Pirani, W. Moufouma-Okia, C. Péan, R. Pidcock, S. Connors, J. Matthews, Y. Chen, X. Zhou, M. Gomis, E. Lonnoy, T. Maycock, M. Tignor, and T. Waterfield, “Global Warming of 1.5°C. An IPCC Special Report on the impacts of global warming of 1.5°C above pre-industrial levels and related global greenhouse gas emission pathways, in the context of strengthening the global response to the threat of climate change, sustainable development, and efforts to eradicate poverty,” in *Summary for Policymakers*, ser. World Meteorological Organization, Geneva, Switzerland, 2018, p. 32 pp.
- [2] United Nations, *Paris agreement*. UNTC XXVII 7.d, 2015.
- [3] Zentrum für Sonnenenergie- und Wasserstoff-Forschung Baden-Württemberg, “Datenservice Erneuerbare Energien,” 2020, Accessed: December 03, 2020. [Online]. Available: <https://www.zsw-bw.de/mediathek/datenservice.html>
- [4] P. Jochem, *Alternative Antriebskonzepte bei sich wandelnden Mobilitätsstilen*. KIT Scientific Publishing, 2013.
- [5] K. Reddi, A. Elgowainy, N. Rustagi, and E. Gupta, “Impact of hydrogen SAE j2601 fueling methods on fueling time of light-duty fuel cell electric vehicles,” *International Journal of Hydrogen Energy*, vol. 42, no. 26, pp. 16 675–16 685, 2017.
- [6] H. Eichlseder and M. Klell, *Wasserstoff in der Fahrzeugtechnik*. Vieweg+Teubner Verlag, 2012.
- [7] I. Renner, “Methodische Unterstützung funktionsorientierter Baukastentechnikentwicklung am Beispiel Automobil,” Ph.D. dissertation, Technische Universität München, 2007.
- [8] BMW AG, München.
- [9] P. A. Rosen, *Beitrag zur Optimierung von Wasserstoffdruckbehältern*. Springer-Verlag GmbH, 2018.
- [10] M. Ruf, “Unpublished dissertation,” Ph.D. dissertation, Technische Universität München, 2020.
- [11] Horizon 2020, “Development of hydrogen tanks for electric vehicle architectures,” 2020, Accessed: December 07, 2020. [Online]. Available: <https://ec.europa.eu/info/funding-tenders/opportunities/portal/screen/opportunities/topic-details/fch-01-1-2020>
- [12] UN ECE R134, “Uniform provisions concerning the approval of motor vehicles and their components with regard to the safety-related performance of hydrogen-fuelled vehicles (HFCV),” 2015.
- [13] M. Huber, A. Hupfeld, M. Ruf, and A. Horoschenkoff, “Bauraumoptimierter Wasserstofftank mit innerer Zugverbreitung,” *10. Munich Lightweight Symposium*, Springer Verlag, 2020.
- [14] J. W. Treiber, “Performance of tufted carbin fibre/epoxy composites,” Ph.D. dissertation, Cranfield University, 2011.
- [15] C. Chokri, *Textile Werkstoffe für den Leichtbau Techniken - Verfahren - Materialien - Eigenschaften*. Berlin, Heidelberg: Springer Berlin Heidelberg, 2011.
- [16] D. Joop, “Auslegung eines zugverbreiteten Wasserstofftanks anhand experimenteller Werte aus Zugversuchen an Faserproben,” BA Thesis, Hochschule München. 2021.
- [17] J. Humpenöder, “Gas permeation of fibre reinforced plastics,” *Cryogenics*, vol. 38, no. 1, pp. 143–147, 1998.
- [18] T. Ogasawara, Y. Ishida, T. Ishikawa, T. Aoki, and T. Ogura, “Helium gas permeability of montmorillonite/epoxy nanocomposites,” *Composites Part A: Applied Science and Manufacturing*, vol. 37, no. 12, pp. 2236–2240, 2006.
- [19] M. Flanagan, D. Grogan, J. Goggins, S. Appel, K. Doyle, S. Leen, and C. Ó. Brádaigh, “Permeability of carbon fibre PEEK composites for cryogenic storage tanks of future space launchers,” *Composites Part A: Applied Science and Manufacturing*, vol. 101, pp. 173–184, oct 2017.
- [20] A. Takaku and R. G. C. Arridge, “The effect of interfacial radial and shear stress on fibre pull-out in composite materials,” *Journal of Physics D: Applied Physics*, vol. 6, no. 17, pp. 2038–2047, 1973.
- [21] SAE J2601, “Fueling protocols for light duty gaseous hydrogen surface vehicles,” 2020.
- [22] K. G. Schmitt-Thomas, *Integrierte Schadenanalyse*. Springer-Verlag GmbH, 2016.

Measurement of PHEV according to WLTP

Farrak Khan
 Department of Mechanical, Automotive
 and Aeronautical Engineering
 Munich University of Applied Sciences
 Munich, Germany
 fkhan@hm.edu

Abstract— In the following project work, measurements of fuel consumption, electric range and recharged energy were carried out on a plug-in hybrid. The implementation of the measurements is described in the legally prescribed procedure WLTP. These were analysed and implemented from the regulation (EU) 2017/1151. In particular, the calculation of the utility factor and the measurements at full and flat battery, which are necessary for each overall measurement, are part of the implementation. Based on a load adjustment, the chassis dynamometer was adapted to the test vehicle in order to subsequently retrace a driving profile. The measurements led to the result that the electric range and fuel consumption are dependent on the temperature and the usage behaviour.

Keywords— vehicles, Hybrid, CO₂, climate change

I. INTRODUCTION

The effects of climate change are affecting people and the environment. The average temperature on earth is rising continuously, and this increase is mainly due to the greenhouse effect. This prevents part of the heat from escaping into space, leading to a warming of the earth. The greenhouse effect is due to the greenhouse gases, which include carbon dioxide (CO₂). In 2016, transport was responsible for almost 30% of total CO₂ emissions in the EU. Of this, 72% is attributable to road transport. Cars accounted for 60.7% of the 72% of CO₂ emissions [1].

II. HYBRID ELECTRIC VEHICLES

Vehicles generate CO₂ by burning fossil fuels (diesel, petrol). Battery electric vehicles (BEV) are to be used to prevent these emissions. Since electric vehicles have not yet penetrated the mass market, hybrid vehicles are more in demand than ever. Hybrid vehicles are defined as vehicles that have at least two different energy converters (e.g., combustion engine and electric motor) and two different energy storage systems (e.g., tank and battery) [2]. When the drive is provided by the electric motor, no CO₂ is locally emitted. This means that CO₂ emissions can be avoided locally, e.g., in cities.

III. REGULATION (EU) 2017/1151 [3]

In order to measure vehicles certain procedures must be followed. In Europe the WLTP (worldwide harmonized light vehicles test procedure) is used. This procedure ensures equal conditions for all measurements to provide comparability. It is described in detail in the regulation (EU) 2017/1151. This chapter is based on this regulation [3].

A. Worldwide light-duty test cycles (WLTC)

The cycle is part of the WLTP and specifies a driving profile that must be reproduced on the chassis dynamometer. A speed profile must be followed. Depending on the vehicle mass (m) and power (P), the cycle varies. This is based on the power-to-mass-ratio (PMR).

$$PMR = \frac{P}{m} \quad (1)$$

The PMR is subdivided into three classes. Class three is also separated according to the maximum speed (v_{max}).

- Class 1: $PMR \leq 22$ W/kg
- Class 2: 22 W/kg $> PMR \leq 34$ W/kg
- Class 3: $PMR > 34$ W/kg
 - Class 3a: $v_{max} < 120$ km/h
 - Class 3b: $v_{max} \geq 120$ km/h

Most vehicles are covered by class 3b. The driving profile is determined by the class. The WLTC for class 3b has four phases: Low₃, Medium₃₋₂, High₃₋₂ and Extra High₃, see Figure 1. The WLTC for class 3b lasts 1800 s and has a range of 23.266 km. The maximum speed is 131.3 km/h [3].

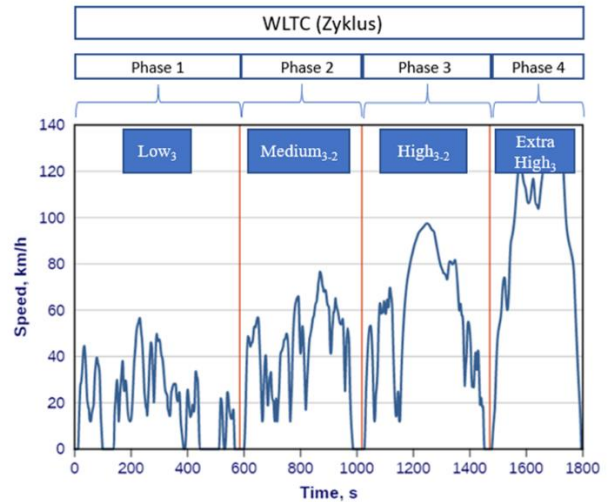


Figure 1: WLTC Class 3b [4]

B. Measurement of OVC-HEV

OVC-HEV (Off-vehicle charging hybrid electric vehicle) are also known as PHEV (Plug-In-Hybrid-Electric Vehicle). These vehicles allow the battery to be charged from the grid.

OVC-HEV drive the WLTC several times. The entire measurement is divided into two parts. The first part is the CD measurement (charge depleting) and the second part is the CS measurement (charge sustaining).

In the CD test, the power is provided by the electric motor, unless the specified vehicle speed cannot be achieved. In this case the combustion engine gets switched on. Several WLTC are run until the electrical storage is exhausted. This is followed by the CS test. Here, the propulsion is only provided by the combustion engine. The WLTC is driven once. After that, the electric storage tank gets completely charged.

Figure 2 shows a measurement sequence adapted for measurement in the vehicle laboratory.

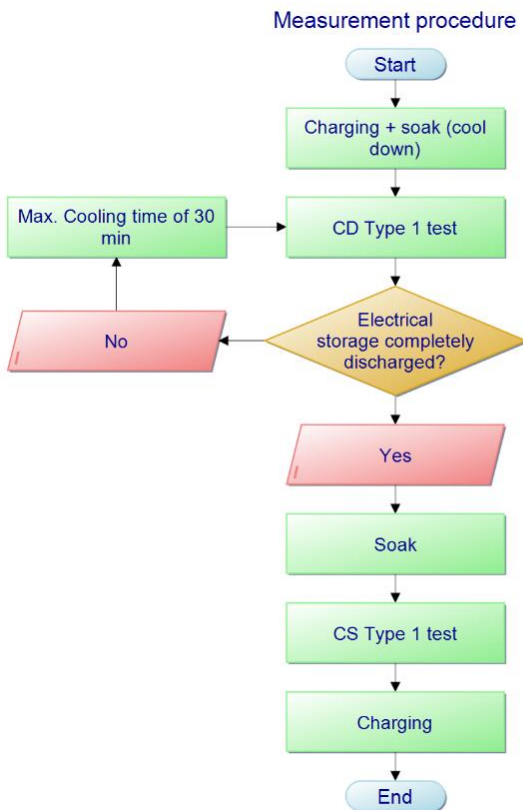


Figure 2: Measurement procedure

C. Measured values and calculations

Among others the regulation (EU) 2017/1151 sets the framework to determine the following values for PHEVs:

- All Electric Range AER (km)
- The utility factor-weighted mass emission of gaseous compounds (e.g., CO₂) (g/km)
- Utility factor-weighted fuel consumption for OVC-HEVs (l/100 km)

The utility factors (UF) for OVC-HEVs are particularly important, as they play a key role in the calculation. They are used for example for fuel consumption and CO₂ emissions. The utility factors are ratios based on driving statistics and

ranges to electrical discharge and charge conservation for OVC-HEVs.

$$UF_i(d_i) = 1 - e^{-(\sum_{j=1}^k c_j \cdot (\frac{d_i}{d_n})^j)} - \sum_{l=1}^{i-1} UF_l \quad (2)$$

Where:

- UF_i Utility factor for phase i
- d_i Distance driven to the end of phase i
- C_j j coefficient (see table 1)
- d_n Normalized distance (see table 1)
- k Number of terms and coefficients in the exponent
- i Number of the considered phase
- j Number of the considered term/coefficient
- $\sum_{l=1}^{i-1} UF_l$ Sum of the calculated utility factors up to phase (i-1)

The parameters C_j , d_n and k are defined, see table 1. The calculation is based on a database that mainly contains data (e.g., daily distance driven) of conventional vehicles (diesel, petrol). As soon as there are enough hybrid vehicles on the European market and thus enough data on hybrid vehicles available, the utility factor will be updated.

Defined parameters	
	Value
C_1	26,25
C_2	-38,94
C_3	-631,05
C_4	5964,83
C_5	-25094,60
C_6	60380,21
C_7	-87517,16
C_8	75513,77
C_9	-35748,77
C_{10}	7154,94
d_n [km]	800
k	10

Table 1: Defined parameters [[3], p. 634 – 635]

The utility factor depends on the range covered during the CD test until the electrical storage is empty. It can be seen that the first WLTC has a larger share of the utility factor than the second WLTC, see Figure 3. This means that the following WLTC has a lower proportion of the utility factor than the one before it.

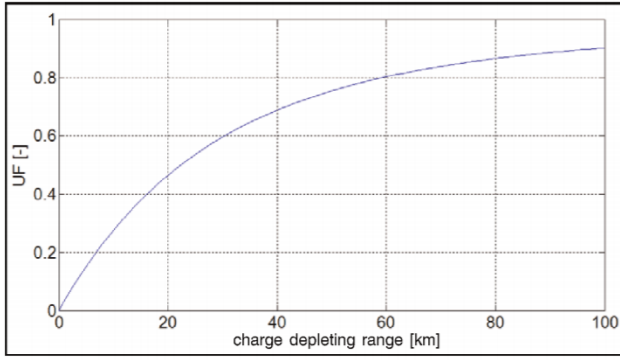


Figure 3: Utility factor [[3], p. 635]

The Utility factor-weighted fuel consumption for OVC-HEVs is calculated according to equation 3. The utility factor plays an important role here. The share of the Fuel consumption from CS-test decreases as the utility factor increases.

$$FC_{weighted} = \sum_{j=1}^k (UF_j \cdot FC_{CD,j}) + (1 - \sum_{j=1}^k UF_j) \cdot FC_{CS} \quad (3)$$

Where:

$FC_{weighted}$	Utility factor-weighted fuel consumption (l/100 km)
UF_j	Utility factor for phase j
$FC_{CD,j}$	Fuel consumption of phase j (CD-test) (l/100 km)
FC_{CS}	Fuel consumption (CS-test) (l/100 km)
j	the index of the considered phase
k	The number of phases run until the end of the transition cycle

The utility factor-weighted mass emission of gaseous compounds (e.g., CO₂) is calculated according to equation 4. The share of CO₂ emissions, which were generated during the CS test, in the overall result decreases when the utility factor increases. CO₂ emissions correlate with fuel consumption. As fuel consumption increases, so does CO₂ emissions.

$$M_{i,weighted} = \sum_{j=1}^k (UF_j \cdot M_{i,CD,j}) + (1 - \sum_{j=1}^k UF_j) \cdot M_{i,CS} \quad (4)$$

Where:

$M_{i,weighted}$	Utility factor-weighted mass emission compound i (g/km)
i	Index of the considered gaseous emission compound
$M_{i,CD,j}$	Mass emission of the gaseous emission compound i (CD-test) (g/km)
$M_{i,CS}$	mass emission of gaseous emission compound i (CS-test) (g/km)

If the combustion engine is not switched on during the CD test, then both fuel consumption $FC_{CD,j}$ and CO₂ $M_{i,CD,j}$ emissions during the CD test are zero.

IV. VEHICLE AND MEASUREMENT SETUP

The test vehicle was a BMW 745e. It is a PHEV with an electric motor and a petrol engine. The petrol engine has a power of 210 kW and a torque of 450 Nm. The electric motor has a power of 83 kW and a torque of 265 Nm. The system power is 290 kW and the system torque has a value of 600 Nm [5]. The official values such as fuel consumption and electric range are shown in the table 2.

	BMW 745e
	<i>Value</i>
All Electric Range AER [km]	48 - 55
The utility factor-weighted mass emission of gaseous compounds (CO ₂) [g/km]	41 - 49
Utility factor-weighted fuel consumption for OVC-HEVs [l/100 km]	1,8 - 2,1

Table 2: BMW 745e technical data [6]

The measurement is performed on a chassis dynamometer. The chassis dynamometer simulates real driving conditions. For this purpose, the chassis dynamometer is adapted to the vehicle and it's driving resistances. Figures 4 and 5 show the BMW 745e fixed on the chassis dynamometer.



Figure 4: BMW 745e on the chassis dynamometer



Figure 5: BMW 745e on the chassis dynamometer

V. MEASUREMENT RESULTS

Tables 3 and 4 show the measured values and the calculations for two complete measurements.

	BMW 745e
	1. Measurement
Temperature average/ start temperature 1.CD-test [° C]	19,3/18,1
Temperature average/ start temperature 2.CD-test [° C]	20,1/19,9
Temperature average/ start temperature CS-test [° C]	18,2/17,2
All Electric Range AER [km]	41,79
Fuel consumption CS-test [l/100 km]	8,53
Utility factor UF Total	0,702
Utility factor-weighted fuel consumption for OVC-HEVs [l/100 km]	2,54
Recharged energy [kWh]	11,36

Table 3: BMW 745e - 1. Measurement

	BMW 745e
	2. Measurement
Temperature average/ start temperature 1.CD-test [° C]	15,6/14,2
Temperature average/ start temperature 2.CD-test [° C]	17,5/17,1
Temperature average/ start temperature CS-test [° C]	17,6/16,1
All Electric Range AER [km]	41,33
Fuel consumption CS-test [l/100 km]	8,48
Utility factor UF Total	0,699
Utility factor-weighted fuel consumption for OVC-HEVs [l/100 km]	2,55
Recharged energy [kWh]	11,42

Table 4: BMW 745e - 2. Measurement

It is noticeable that the utility factor weighted fuel consumption is higher than the official value and the electric range is lower than the official value. Contrary to the regulation the ambient temperature during the test was lower. The test cell must have a value of 23 °C. Lower temperatures have a negative effect on the battery and therefore on the electric range. The utility factor-weighted fuel consumption increases as a result. Furthermore it has to be noted that there were also other deviations regarding the required test conditions like humidity or measuring equipment.

VI. CONCLUSION AND OUTLOOK

The work done to measure a PHEV reveals the following points. Fuel consumption, electric range and CO₂ emissions depend on:

- Environmental conditions (especially the temperature)
- Usage behaviour: how often and for how long is the electric drive used? How often is the vehicle charged?

If the required conditions are not met perfectly the changes in the test results are astonishingly high compared to the official values. This means in everyday driving consumption and electric range will change just the same.

Therefore it does make sense to check the measurement results and test on the road. For this purpose, the RDE (Real Driving Emissions) tests shall be carried out and critically analysed. The aim of the project is to show the weaknesses of the measurement methods and to find solutions to get realistic measurement results.

- [1] <https://www.europarl.europa.eu/news/de/headlines/society/20190313STO31218/co2-emissionen-von-autos-zahlen-und-fakten-infografik>, CO₂-Emissionen von Autos: Zahlen und Fakten (Infografik), [Accessed 11.03.2021]
- [2] RICHTLINIE 2007/46/EG DES EUROPÄISCHEN PARLAMENTES UND DES RATES vom 5. September 2007, zur Schaffung eines Rahmens für die Genehmigung von Kraftfahrzeugen und Kraftfahrzeuganhängern sowie von Systemen, Bauteilen und selbstständigen technischen Einheiten für diese Fahrzeuge (Rahmenrichtlinie), p. 10, 5. September 2007
- [3] Verordnung (EU) 2017/1151 der Kommission vom 1. Juni 2017 zur Ergänzung der Verordnung (EG) Nr. 715/2007 des Europäischen Parlaments und des Rates über die Typgenehmigung von Kraftfahrzeugen hinsichtlich der Emissionen von leichten Personenkraftwagen und Nutzfahrzeugen (Euro 5 und Euro 6) und über den Zugang zu Fahrzeugreparatur- und -Wartungsinformationen, zur Änderung der Richtlinie 2007/46/EG des Europäischen Parlaments und des Rates, der Verordnung (EG) Nr. 692/2008 der Kommission sowie der Verordnung (EU) Nr. 1230/2012 der Kommission und zur Aufhebung der Verordnung (EG) Nr. 692/2008 der Kommission (Text von Bedeutung für den EWR), 001.003, 27.07.2017
- [4] <https://dieselnet.com/standards/cycles/wltp.php>, Worldwide Harmonized Light Vehicles Test Cycle (WLTC), [Accessed 02.02.2021]
- [5] Technische Daten. Die neue BMW 7er Reihe. BMW-Medieninformation, 02/2019
- [6] <https://www.bmw.de/de/topics/faszination-bmw/elektromobilitaet/plug-in-hybride.html>, BMW PLUG-IN-HYBRIDE, [Accessed 16.02.2021]

Method for Vehicle Crash Pulse Comparison in Pre-Crash Safety Systems

Robert Krause

Research and Test Center CARISSMA
Technische Hochschule Ingolstadt
85049 Ingolstadt, Germany
Email: Robert.Krause@thi.de

Gerald Joy Alphonso Sequeira

Research and Test Center CARISSMA
Technische Hochschule Ingolstadt
85049 Ingolstadt, Germany
Email: Gerald.Sequeira@carissma.eu

Abstract—Use of environmental sensors in vehicles enable new driver assistance systems and form the basis for automated driving. In addition to comfort functions, information about the vehicle environment is the basis for new safety systems. Today's safety systems work in the area of active safety (accident avoidance) and automatically intervene in cases where the driver no longer reacts in time to avoid a collision with another road user. But not every accident is avoidable. Further enhancing vehicle safety is possible by linking active safety systems with passive safety systems (reducing the severity of accidents). In the event of an inevitable collision, based on information from predictive sensor technology (radar, camera, and LiDAR), irreversible safety actuators, such as new, larger airbags, should be triggered before the collision time t_0 , thus providing the best possible protection for the vehicle occupants. The relevant crash parameters, such as collision velocity, collision angle, and contact point are predicted using special vehicle dynamics models. From this information, an estimation of the expected crash severity can be made the basis for this are various crash severity prediction models. Since safety actuators are irreversible systems, the prediction must be extremely reliable. By independently calculating the crash severity using different approaches, the reliability and fault tolerance of a system can be increased through redundant prediction. This paper presents a method to compare the crash pulse predicted use different models.

I. INTRODUCTION

In recent years, the number of traffic fatalities has stagnated at a high level. Around 3,300 deaths in Germany and 26,000 deaths in Europe are reported annually in road traffic [1]. These are mainly due to human factors, such as limited performance in terms of perception and responsiveness. This is compounded by driver misconduct and distraction [2]. The proportion of fatalities and serious injuries is particularly pronounced in frontal accidents. This can be attributed to the combination of high speeds and high frequency of occurrence of this type of accident. Driver assistance systems can detect critical scenarios at an early stage. The triggering of safety systems in the right time window in case of a collision significantly reduces the consequences of the accident [3], [4]. Here, the triggering time depends on the installed safety actuators and the prevailing collision type. In order to be able to determine the crash constellation and the time of occurrence in advance, the parameters (e.g. width, length, and direction of travel) are extracted for objects in the vehicle environment using the environment sensor system. This makes

it possible to identify critical situations at an early stage and to describe inevitable collisions. The parameters required for a precise description are generated in an inevitability module by special vehicle dynamic models. All physically possible driving changes of both vehicles are taken into account at the respective time step. Each combination of driving paths is checked for contact. Thus, possible changes in the vehicle dynamics between the prediction time and the collision time t_0 can be taken into account for the correct triggering of the restrain systems. The relevant crash parameters are calculated for the expected crash constellations. These include in particular the parameters collision angle, the relative position of the vehicles to each other, and speeds. This forms the basis for determining the crash severity. For a robust estimation of the crash severity, different approaches for crash pulse prediction are pursued. One approach is based on physical models and uses them to model the crash pulse [5]–[8]. Furthermore, there are approaches based on machine learning and AI, where algorithms based on learned FEM crash simulations or real crash data can output a crash severity prediction for the corresponding vehicle constellation [9]–[16]. The combined use of both methods allows an increase in reliability, since the methods have different advantages and disadvantages depending on the scenario. For example, effects such as vehicle sliding during crashes can be represented more accurately in AI methods than in physical mass-spring-damper (MSD) models [5]. Nevertheless, a physical computation can be used here for validation.

II. STATE OF THE ART

Automated driving interventions are essentially based on the perception and processing steps Sense, Think and Act. The signal chain describing the sequence in the pre-crash can be assigned to these. This is shown schematically in Fig. 1. In the first step, the vehicle environment is perceived via the attached environment sensors. This generates data on objects in the vehicle environment. In this way, a detailed map of the vehicle environment can be created in which the objects are described with their respective position and driving speed. If critical situations are identified, possible driving paths for the ego and bullet vehicle are projected and the expected crash constellation is derived from them.

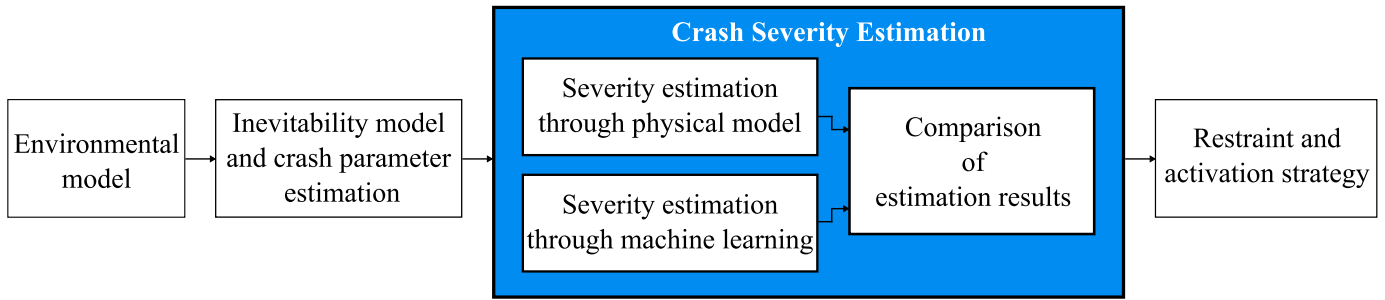


Figure 1. Generic system architecture for inevitability modelling and crash severity estimation in pre-crash safety systems

A. Vehicle motion and crash constellation prediction

The investigation of crash inevitability is carried out using information from the environment model described above. The parameters object type, velocity, position, size / geometry, etc. are exchanged between the environment model and the inevitability model in a defined cycle. These parameters are determined within the environment model from the surrounding sensor data (distance, azimuth angle, radial velocity, and intensity). This description is done either for the previously identified most critical object or for several detected objects. From this the current driving conditions are derived and based on this the possible vehicle movements are projected. This can be done by different methods, which in pre crash applications are based on simplified vehicle dynamics models. For example, such a model has been researched and published by R. Lugner [17], [18]. In his approach, the resulting driving paths (trajectories) are generated by the individual combination possibilities of steering and braking interventions. The

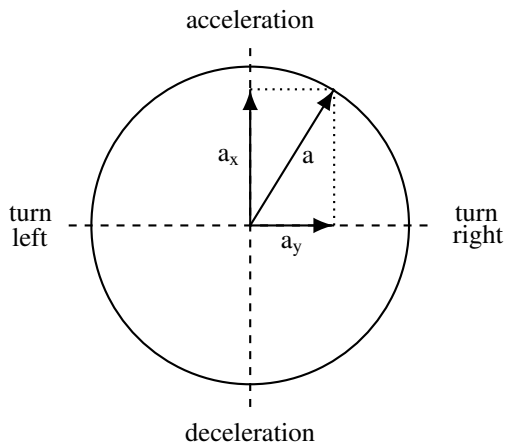


Figure 2. Representation of physically possible combinations of acceleration based on circle of forces (Kamm's circle).

boundary condition is formed by a vehicle dynamics model and respecting the limitation by Kamm circle. This is shown in Fig. 2. The bundling of the individual travel paths corresponds to a trajectory fan for the vehicle. By considering two vehicles, intersection-free trajectory combinations (collision-free) and intersecting trajectories (with collision sequence) can arise. For trajectory combinations which result in a collision, the

collision is described by crash parameters with their respective tolerances. For a complete description of the crash situation, the parameters collision angle, collision point, ego velocity, bullet velocity, time-to-collision, and some others are generated [18]. These parameters are given as input to the crash severity estimation module.

This forms the basis for the crash severity estimation.

B. Crash Severity Estimation

In crash severity estimation, predictive severity is to be estimated for the previously determined collision scenario. Based on the predicted collision and the respective driving velocities at that time, the expected acceleration curves are generated for the time period starting from the collision point t_0 . Due to the time criticality in real pre-crash situations and the limited computational power in the vehicle, models that work under these constraints must be used. Classical methods of crash analysis, such as FEM, cannot meet these requirements. Therefore, special methods have been researched that can be used to model crash severity under the given conditions in the vehicle. Two possible methods that have been published by researchers is modeling by physical mass-spring-damper (MSD) models or alternatively prediction by Artificial Intelligence (AI) algorithms.

1) *Physical MSD models*: The absorbed energy in a vehicle collision can be represented with mass spring damper models. The input variables and the underlying structure are used to model a realistic velocity reduction of the vehicles. The models can have different numbers of springs, masses and dampers and can also be combined with each other in different ways. Thus, the complexity and the required accuracy can be adapted to the respective application. Various crash severity estimations based on physical models in different complexities have been published [5]–[8].

2) *Databased AI algorithms*: Data-based models are based on machine learning algorithms, applied on the data collected through simulation, crash test, or real-crash. Based on a broad scenario variance, machine learning methods can be taught schematic correlations. The algorithm then generates new output values for similar scenarios. Various approaches from the field of AI can be considered for this purpose. Comprehensive investigations regarding the current state of

research and the performance of AI methods in the area of crash severity estimation have been published [9]–[16].

III. METHODOLOGY

The crash severity can be described by the progress of the acceleration. Plotting the integral of its curve over time, the graph of velocity is obtained. Parameters exist for both the acceleration curve and the velocity curve that classify them according to certain criteria. For the description of the crash severity, parameters like the Delta-V, ASI or A-32 Moving Window are usually used. For example, the ASI represents the maximum value of the moving average over a $\delta = 50 \text{ ms}$ time period. This value is normalized on a direction-dependent threshold \hat{a}_t with $t = x, y, z$. As an outcome, the ASI is a unit-less value [19]. As shown in Fig. 3, the same ASI can be assigned to different acceleration curves, provided that the maximum mean value over 50 ms is identical. Furthermore, it is also not evident from the value at which time the maximum acceleration was applied and in which direction it acted.

Other parameters are applied according to similar principles

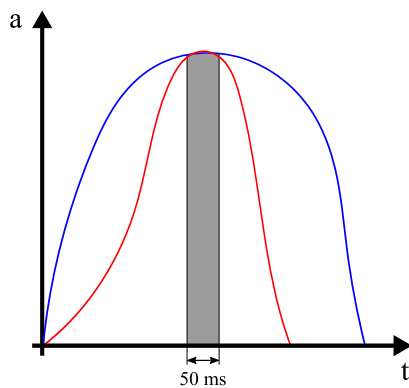


Figure 3. Representation of different acceleration curvatures with the same crash severity parameter ASI

and may show comparable problems. By describing the crash pulse by a single parameter, certain information about the pulse gets lost. In order to be able to compare the outputs of crash severity estimations in the pre-crash, further information on the progress of the crash pulse shall be used. The parameters described below make it possible to obtain further information on the curve progression in addition to the established crash severity parameters.

A. Crash Pulse Description with a Set of two Parameters

The time progression of the acceleration should be considered as the whole. This can be done by the area enclosed by the curve and the x-axis. In addition to the area, the position of the centroid of this area in x, y is used.

B. Make Pulses comparable through Normalization and Resampling

In order to make the crash sequences comparable with each other, resampling is first performed. In this process, the time steps are adapted to each other and intermediate steps are

interpolated. The starting point for this is the signal with the lower sampling frequency. This results in the same distance between the acceleration values and the same step size for both signals to be compared.

Subsequently, the crash pulse curves are normalized. This enables the direction-independent consideration of the centroid of area shift. Otherwise, a centroid of area shift in the time dimension as a function of the unit would have a significantly smaller influence than a shift of the centroid of area in the direction of the amplitude values. The normalization is carried out with respect to the time steps as well as with respect to the maximum amplitude. For this purpose, two factors are generated according to the principle shown in eq. 1. The first scale factor is for the normalization of the time steps. Starting from the last curve intersecting the zero crossing, the factor is determined so that this point is equal to one. All further values of both curves for the time axis are multiplied by this factor. The same procedure is also applied in the value range. Here the scale factor is selected so that the maximum of the curve with the higher amplitude is equal to one.

$$\text{scale factor} = 1/\max(\text{abs}(\text{value})) \quad (1)$$

Based on the then normalized crash pulses, the centroid of area and the area of the enclosed surface are calculated. Under parallel execution for both curves to be compared, the different positions of the centroid of area can be evaluated individually in x - and y - direction or absolutely by the amount of displacement. The described steps 1. resampling, 2. normalization, and 3. centroid of area and area calculation are shown schematically in Fig. 4.

IV. TEST DATASET FOR COMPARISON

A test scenario was used to evaluate and compare the introduced methods. The output of a spring-mass damper model was compared with the crash data of the FEM simulation. The scenario was a full-frontal collision of two equal vehicle at a velocity of 50 kmh^{-1} each. There is no crash angle between the vehicles. The collision point corresponds to an overlap of 100% of the width of the vehicles.

For the FEM simulation of the described scenario, a Toyota Yaris model provided for research was used. The boundary conditions, as well as the model setup for generating the data set have already been published in [20]. The sampling rate used for sampling the acceleration signal corresponds to 10 kHz.

For the application of the method, a comparison data set was generated using an MSD model. The operation of the used model is based on publications by Kilian Schneider and is described there [5]. As with the FEM model, 10 kHz was selected for sampling the acceleration curve generated in this process. Thus, no resampling is necessary in this case.

V. RESULTS AND SUMMARY

For verification, the method shown was used to compare the outputs of the FEM simulation and the MSD model. The starting point is the scenario described in sec. IV. The

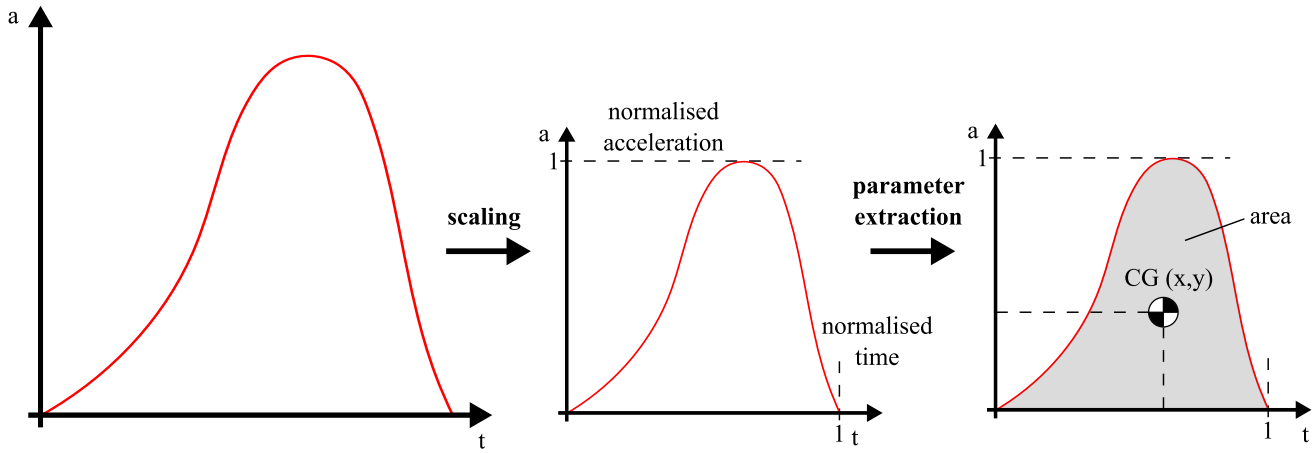


Figure 4. Overview of steps for parameter extraction and comparison of the progressions

curves as well as their calculated centroids are illustrated under fig. 5. The corresponding area enclosed by the curve as well as the exact positions of the centroids are listed in table I. Furthermore, the distance of the centroid of area to each other is described with ΔCG .

The maximum amplitude is represented by the FEM accel-

Table I
CALCULATED SEVERITY INDEX PARAMETERS FOR THE TEST DATASET

Dataset	Area	CG _x	CG _y	ΔCG
FEM	0.3275	0.3950	0.3385	-
MSD-Model	0.4566	0.4294	0.2896	0.0597

eration curve. This represents the basis for the normalization of the value range. In the time domain, however, the acceleration curve of the FEM model intersects the x-axis before the output of the MSD model. Thus, here the MSD output is the basis for normalization. The deviation of the curves from each other becomes clear by the different area contents. The area of the MSD curve is about 40 % larger compared to the FEM output. The difference in amplitude becomes clear by the shift of the centroid of area in x-direction by about 8.5 % and in y-direction by -14.5 %, starting from the FEM simulation. As a single parameter, this can be represented by the normalized distance of the centroid of area $\Delta CG = 0.0597$.

VI. CONCLUSION AND FUTURE WORK

In this paper, a method is presented, which allows to describe the crash pulse during a vehicle collision in more detail. The special conditions for the use in vehicle pre-crash safety systems are taken into account. In addition to the already existing crash severity parameters, which consider only the value level, the crash pulse can be described more precisely by respecting the complete region. For this purpose, the parameters area under the acceleration curve and its corresponding centroid are used.

The described approach is to be verified with further data sets.

Further it is to be examined whether the application of the method in the velocity course in addition to the acceleration course brings advantages. Finally, boundary parameters and permissible centroid of area displacements shall be defined to perform the comparison of different crash severity estimation methods in vehicle pre crash safety systems. Finally an implementation on a prototype vehicle is planned to test and validate this approach under realistic conditions.

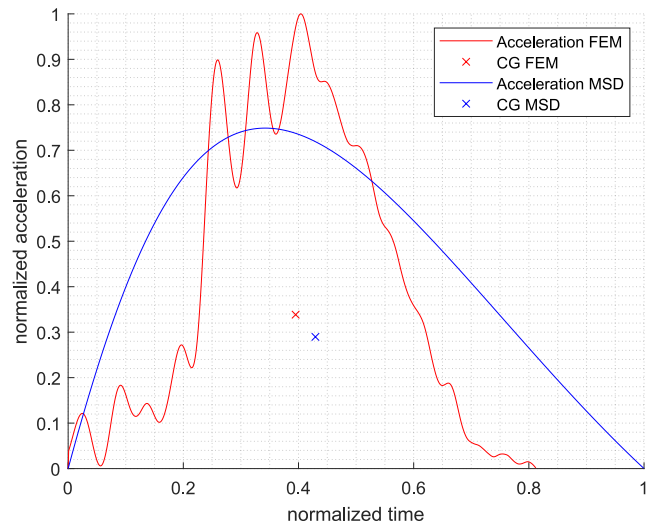


Figure 5. Representation of acceleration graphs based on FEM (red) and MSD-Model (blue) with its calculated centroid of area

REFERENCES

- [1] World Health Organization WHO, "Global status report on road safety 2018," Geneva.
- [2] Deutscher Verkehrssicherheitsrat, "Vision zero: Grundlagen & strategien," in *Schriftenreihe Verkehrssicherheit*, vol. 16, 2012.
- [3] B. Fildes, M. Keall, P. Thomas, K. Parkkari, L. Pennisi, and C. Tingvall, "Evaluation of the benefits of vehicle safety technology: The munds study," *Accident Analysis & Prevention*, vol. 55, pp. 274–281, 2013.
- [4] B. Fildes, M. Keall, N. Bos, A. Lie, Y. Page, C. Pastor, L. Pennisi, M. Rizzi, P. Thomas, and C. Tingvall, "Effectiveness of low speed autonomous emergency braking in real-world rear-end crashes," *Accident Analysis & Prevention*, vol. 81, pp. 24–29, 2015.

- [5] K. Schneider, M. Inderst, and T. Brandmeier, "Hybrid model based pre-crash severity estimation for automated driving," in *2020 IEEE 3rd Connected and Automated Vehicles Symposium (CAVS)*. IEEE, 2020, pp. 1–6.
- [6] M. Müller, X. Long, M. Botsch, D. Böhmländer, and W. Utschick, "Real-time crash severity estimation with machine learning and 2d mass-spring-damper model," in *2018 21st International Conference on Intelligent Transportation Systems (ITSC)*. IEEE, 2018, pp. 2036–2043.
- [7] B. B. Munyazikwiye, D. Vysochinskiy, M. Khadyko, and K. G. Robbersmyr, "Prediction of vehicle crashworthiness parameters using piecewise lumped parameters and finite element models," *Designs*, vol. 2, no. 4, p. 43, 2018.
- [8] B. B. Munyazikwiye, H. R. Karimi, and K. G. Robbersmyr, "Optimization of vehicle-to-vehicle frontal crash model based on measured data using genetic algorithm," *IEEE Access*, vol. 5, pp. 3131–3138, 2017.
- [9] G. J. Sequeira, A. Patel, S. Afraj, R. Lugner, and T. Brandmeier, "Fem-based methodology for crash severity estimation in frontal crash scenarios," in *IOP Conference Series: Materials Science and Engineering*, vol. 831, no. 1. IOP Publishing, 2020, p. 012019.
- [10] A. Abdulhafedh *et al.*, "Incorporating the multinomial logistic regression in vehicle crash severity modeling: a detailed overview," *Journal of Transportation Technologies*, vol. 7, no. 03, p. 279, 2017.
- [11] M. Zheng, T. Li, R. Zhu, J. Chen, Z. Ma, M. Tang, Z. Cui, and Z. Wang, "Traffic accident's severity prediction: A deep-learning approach-based cnn network," *IEEE Access*, vol. 7, pp. 39 897–39 910, 2019.
- [12] F. Zong, X. Chen, J. Tang, P. Yu, and T. Wu, "Analyzing traffic crash severity with combination of information entropy and bayesian network," *IEEE Access*, vol. 7, pp. 63 288–63 302, 2019.
- [13] C. M. Hruschka, D. Töpfer, and S. Zug, "Risk assessment for integral safety in automated driving," in *2019 2nd International Conference on Intelligent Autonomous Systems (ICoIAS)*. IEEE, 2019, pp. 102–109.
- [14] R. Lugner, K. Schneider, and T. Brandmeier, "Early activation of passive safety actuators by forward-looking crash parameter estimation," *crash. tech 2018*, 2018.
- [15] A. Iranitalab and A. Khattak, "Comparison of four statistical and machine learning methods for crash severity prediction," *Accident Analysis & Prevention*, vol. 108, pp. 27–36, 2017.
- [16] J. Zhang, Z. Li, Z. Pu, and C. Xu, "Comparing prediction performance for crash injury severity among various machine learning and statistical methods," *IEEE Access*, vol. 6, pp. 60 079–60 087, 2018.
- [17] R. Lugner, D. Vriesman, M. Inderst, G. J. A. Sequeira, N. Pasupuleti, A. Zimmer, and T. Brandmeier, "Evaluation of sensor tolerances and inevitability for pre-crash safety systems in real case scenarios," in *2020 IEEE 3rd Connected and Automated Vehicles Symposium (CAVS)*. IEEE, 2019, pp. 1–6.
- [18] R. Lugner, M. Inderst, G. Sequeira, K. Schneider, and T. Brandmeier, "Collision prediction for irreversible pre-crash safety measures," *FISITA World Congress*, 2020.
- [19] A. Burbridge and R. Troutbeck, "A model for predicting acceleration severity index in impacts with road safety barriers," *International Journal of Crashworthiness*, vol. 24, no. 4, pp. 442–452, 2019.
- [20] G. J. Sequeira and T. Brandmeier, "Evaluation and characterization of crash-pulses for head-on collisions with varying overlap crash scenarios," *Transportation research procedia*, vol. 48, pp. 1306–1315, 2020.

Analysis of Cybersecurity Vulnerabilities in Embedded Systems based on ISO/SAE 21434

Alexander Lasow

Faculty of Electrical Engineering and Information Technology

Technical University of Applied Sciences Regensburg

Regensburg, Germany

Email: alexander1.lasow@st.oth-regensburg.de

Abstract—In the future, ECU manufacturers will be obliged to develop according to the ISO/SAE 21434 security standard so that their devices are protected against currently known cyber attacks. Therefore, it is important to implement security measures reliably and then test them for functionality.

The goal of this work is to show different approaches to cyber attacks on a charge controller, how existing security vulnerabilities are detected, and subsequently how they can be avoided. Communication channels such as CAN, but also analog inputs are analyzed and examined with every possible input.

The tests have shown that despite implemented security, vulnerabilities still exist that can be exploited to cause physical or economic damage. Vulnerabilities were found that made it possible to gain UDS security access to get to the controller and thus read out sensitive data.

This shows that penetration tests are indispensable for ensuring security. For this reason, long and intensive testing of every function of an ECU is necessary to guarantee that gaps in the system are closed before release.

I. INTRODUCTION

Due to the steadily increasing digitization in automobiles, more and more powerful control units are required, which are responsible for the interaction between man and machine. Today, there are up to 100 different control units in a modern vehicle, which are connected with more than 1.5 km of cable. This transforms the former mechanical transport construct into a heterogeneous high-performance computer that makes the journey as pleasant as possible for the driver and his passengers with the help of comfort features.

Since the faultless operation of these devices is a prerequisite, it must not be possible for an attacker to impair the vehicle and thus harm the occupants. For this reason, an automotive security standard is being developed that will provide ECU manufacturers with a guideline for implementing security, ISO/SAE 21434. This standard is expected to be published in the course of 2021, and some manufacturers are already working with the early draft.

A major component of ISO/SAE 21434 is the Threat Analysis and Risk Assessment (TARA). In this, all possible points of attack on a system are to be analyzed to create a risk assessment of each weak point in this regard. Depending on how severe the risk turns out to be, a penetration test must be performed on the associated object and, if vulnerabilities are found, the software must be adapted.

II. ISO/SAE 21434

With ISO/SAE 21434 "Road vehicles - Cybersecurity engineering" a new standard for cybersecurity is being developed. Committee Draft status was achieved in September 2018, which means some details will be changed over time. Publication of the final standard was originally planned for November 2020 but was postponed until mid-2021. The designation indicates that the standard is to be jointly developed by a working group from "Internationale Organisation für Normung" (ISO) and "Society of Automotive Engineers" (SAE) and then approved by both organizations.

As vehicles provide new attack surfaces due to the increasing risks of cyberattacks and as infrastructure for online vehicle updates, fleet management, vehicle-to-vehicle (Car2X) communications, and other requirements, the standard should propose measures for development. The standardization is related to the currently developed European Union (EU) cybersecurity regulation. In coordination with the EU, the United Nations Economic Commission for Europe (UNECE) is developing a certification for a "Cyber Security Management System" which, according to the current proposals, should be mandatory for the type of approval of vehicles. With ISO/SAE 21434, a technical standard for automotive development is to be created to be able to, at least partially, prove compliance with the expected regulations[1].

This standard focuses on the definition of common terminology and the most important aspects of cybersecurity. The application of the standard is intended to make it easier for companies to demonstrate that they are acting responsibly and carefully in the development of vehicles and the prevention of cyber-attacks. The activities in product development according to the standard are controlled based on a risk assessment, and measures for organizational anchoring are required. Processes are required, but the standard only describes the task of a process and leaves the design to the users. Special technologies or solutions are not suggested, and autonomous vehicles are not given a special status in the recommendations of the standard.

A. Threat Analysis and Risk Assessment

A central point of ISO/SAE 21434 is the Threat Analysis and Risk Assessment (TARA). The concept phase consists of the definition of the object of investigation, the finding

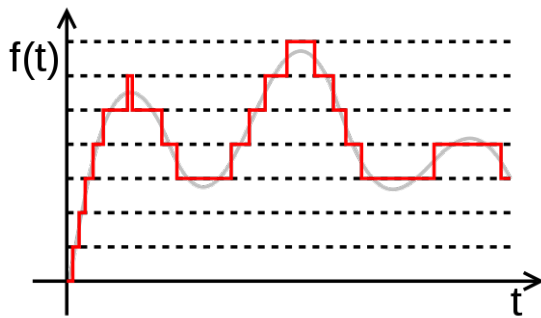


Figure 2. Sampling from Analog to Digital Values [5]

The higher the sampling interval of the incoming signal, the more precise values can be determined. Nevertheless, in most cases, it is not advisable to sample exactly, since pinpoint values are not always needed and this operation also requires more computing power. In the case of a temperature sensor in a vehicle, updating every ten seconds would be completely sufficient, since outside temperatures usually behave stably and do not change every second.

IV. PENETRATION TESTS

A penetration test, or pentest, is the technical term for a comprehensive security test of individual computers or networks of any size. In information technology, a penetration test is the test of the security of all system components and applications of a network or software system using the same methods that an attacker would use to penetrate the system without authorization. The penetration test thus determines the sensitivity of the system to be tested for such attacks. An essential part of a penetration test is tools that help to reproduce as many attack patterns as possible that arise from the numerous known attack methods.

The type of security test is based on the risk potential of a system, network, or application at risk, which means that a web server, for example, has a higher risk priority than a simple word processor. The auxiliary tools for penetration tests are correspondingly numerous and accordingly, such comprehensive security tests should only be carried out by security researchers who know what they are doing, what events they are causing, and what results they want to achieve with them.

The term penetration test is occasionally used incorrectly for an automatic vulnerability scan. While this is largely automatic, a real penetration test requires manual preparation in the form of viewing the test item, planning the test procedures and goals, selecting the necessary tools, and finally carrying out the test. The security scan, in turn, differs from the vulnerability scan in that it manually verifies the test results[6].

A. Types of Penetration Tests

After the risk level is known, it must be decided whether a penetration test is necessary. This information can be found in the automotive security standard ISO/SAE 21434[7]. After

it has been determined that a pentest should be carried out, it must be decided how much knowledge the tester should have[8]. There are three different types of pentesting, as seen in Figure 3.



Figure 3. Different Knowledgelevel of Pentests

Black-Box: With black box pentest, the inspector has no internal knowledge of the device. The only thing he knows is the data that can be found publicly, so he has the same conditions as a malicious attacker. The advantage of this method is that hidden vulnerabilities can be found that would otherwise be overlooked. The disadvantage is that deep-seated vulnerabilities are harder to find, and it takes a lot of time to find them.

Gray-Box: With gray box pentest the tester has more information than with black box. He has company-internal access and knows, e.g., the connections of the ports to the outside world. This has the advantage that weak points can be found more quickly and easily since more information is known about the control unit. However, it is not clear yet, which functions the device has.

White-Box: With white box the tester has all the information that is available about the control unit. Both the connections of the ports and the access to the firmware. This way, the pentester can examine the code for weaknesses or errors which could not be found with black/gray box. The disadvantage here is that attack methods differ greatly from those of a hacker, which is why some vulnerabilities may be overlooked or not found.

B. Denial-of-Service

A Denial-of-Service-Attack (DoS) is an attack on the availability of a system caused by overloading the connection medium. In this attack, a specific component in the system is attacked in a concentrated manner to put it out of operation and thus block other devices. This can lead to security gaps an attacker can exploit to his advantage[9].

A Dos attack can look very different on various platforms and therefore requires other methods of approach. A constant message exchange must take place on the CAN bus so that the entire channel is overflowed with packets. Since a CAN connection has a certain baud rate, which determines the speed of the data exchange of the bus, accordingly that number of CAN messages must be sent so that the channel is fully utilized. Assuming a CAN message is 120 bits in size and the baud rate is 500 Kb/s, a total of $500Kb/s/120b \approx 4167$ messages per second must be sent to utilize the entire bus. If more messages are sent now, it can result in lower priority

messages being allowed to send infrequently, if at all. Thus, a Dos attack was performed on low-priority packets.

However, if no messages should reach the recipient at all, the easiest and fastest method is to overflow the channel with at least 4167 own messages, which all have the priority '0'. Since '0' is the dominant bit in the CAN protocol and thus has the highest priority on the bus, these are preferred. Therefore the baud rate is overloaded to its limit and no more messages arrive that have a higher priority than '0'.

C. Bruteforce UDS-Security Access

Unified Diagnostic Services (UDS) is a diagnostic communication protocol in the ECU environment within automotive electronics and is used in almost all new developments by vehicle manufacturers and is not a company-specific standard. The concept of the protocol is to be able to contact and maintain all ECUs installed in a vehicle with the help of UDS. Modern vehicles have a diagnostic interface for off-board diagnostics that allows a client or tester, to be connected to the vehicle's bus system. This permits the messages defined in UDS to be sent to the ECUs, which must provide the specified UDS services. This makes it possible, for example, to query the fault memory of the individual ECUs or to update them with new firmware.

So that not all services can be performed by everyone, a security query can be performed with this service. For this purpose, the tester sends a request to the control unit. The control unit then generates a random number (seed) and sends it back. The tester uses a secret function to calculate a key, which it sends back to the ECU. The control unit checks whether the number was calculated correctly and can then enable security-critical services[3].

To gain access to this service, the correct key must be calculated. This means that the random seed with the correct password must be generated. Since the seed is random, brute-forcing is difficult, if not impossible. Through self-performed tests, a vulnerability was found that the same seed is sent after each restart of the existing load communication controller. This made it possible to implement a brute force attack.

In the course of the test, however, it turned out that a delay of ten seconds must be observed after each restart of the device before a UDS request is allowed to be sent. With a further waiting time of 200 milliseconds, until the control unit has booted up, the combined waiting time is 10.2 seconds. With a key length of 4 bytes, i.e. 32 bits, a waiting time of more than 1000 years is required to find the correct keyword, see Figure 4.

Attempts	Probability	Seconds	Minutes	Hours	Days	Years
1	0,00000002%	10,2	0,2	0,0	0,0	0,0
10	0,0000002%	102,0	1,7	0,0	0,0	0,0
100	0,000002%	1.020,0	17,0	0,3	0,0	0,0
1.000	0,00002%	10.200,0	170,0	2,8	0,1	0,0
10.000	0,0002%	102.000,0	1.700,0	28,3	1,2	0,0
100.000	0,002%	1.020.000,0	17.000,0	283,3	11,8	0,0
1.000.000	0,02%	10.200.000,0	170.000,0	2.833,3	118,1	0,3
10.000.000	0,23%	102.000.000,0	1.700.000,0	28.333,3	1.180,6	3,2
100.000.000	2,33%	1.020.000.000,0	17.000.000,0	283.333,3	11.805,6	32,3
1.000.000.000	23,3%	10.200.000.000,0	170.000.000,0	2.833.333,3	118.055,6	323,4
4.294.967.296	100%	43.808.666.419,2	730.144.440,3	12.169.074,0	507.044,8	1.389,2

Figure 4. Bruteforce Attack Duration

For this reason, this attack was unsuccessful on this device. However, this brute force attack can easily be performed on other devices that do not have a waiting period after each reset.

D. Fuzztesting

Fuzztesting, or Fuzzing, is an automated software testing technique in which the program under test is repeatedly fed random data at different input interfaces. Random data can usually be used to create situations in the operation of the program that cannot be achieved with other testing methods. Programs are often not designed for random input data and can then crash unintentionally with non-plausible data and thus also reveal vulnerabilities. Therefore, fuzzing is one of the most important techniques to detect weaknesses in the system.

Fuzzing is usually performed in software development projects and the IT security area as part of a black-box test to check new software for error vulnerability as well as to detect any security vulnerabilities. If the program reproducibly causes a problem with certain data generated by the fuzzer, white-box testing can be used to investigate the exact cause.

Fuzz testing is quite effective because the testing process is usually automated and without a termination criterion, which is why it is often used as part of the testing phase. Once a basis for fuzzing exists, already implemented fuzz tests can be extended very quickly and easily during development. Fuzzing is a method for the quality assurance of software, especially to uncover still unknown vulnerabilities and robustness problems in software[10].

1) *CAN-Bus Fuzzing*: A fuzztest on the CAN bus can look very different since either the black-box or white-box principle is used. In a black-box test, the entire data bytes of the CAN frame are randomly selected and then sent to the channel. This has the advantage that data packets can be misinterpreted at the receiver and thus the device delivers unpredictable events or crashes. To test stability, a random black box test is sufficient. However, the disadvantage here is that if an unpredictable event occurs, tracing the error is very difficult or impossible.

In a white box test, on the other hand, not only random data packets can be sent, but specific values of a CAN frame can be changed. This is the case as all information of the device is available and therefore all existing signals are present for the tester. The data of the CAN frame are usually divided into sections to assign a certain value range to each necessary signal. These signals can then be individually adapted and thus only one concrete system variable of the device can be changed. Compared to the black-box test, it is possible to trace why the ECU behaves incorrectly and then find out in which value range these problems occur.

2) *Analog Input Fuzzing*: Fuzzing with analog inputs is slightly more difficult than with a CAN frame since sensor values must be manipulated here to change the state in the ECU. The remedy here is the Hardware in the Loop (HIL) method, in which the embedded system is connected to an adapted counterpart via its inputs and outputs. This allows any value to be applied to the analog input by software, for example by adjusting the applied resistance.

Here it is possible to test in different ways with the help of the software. In the example of the temperature sensor, it is useful to find out how the control unit behaves when an exaggerated value is applied, such as $\pm 100^{\circ}C$. If the device shuts down or goes into sleep mode, it would be possible for an attacker to create a Denial of Service and thus it is a vulnerability in the system.

Another way of testing is the fuzzing of different inputs at the same time. It can happen that by a certain combination of applied values the device shows unpredictable events, which were not considered in advance. This can also be done in different ways because there is various combinatorics. The best way would be to test x different signals with y different values. However, the problem here is that a total of y^x iterations are necessary and thus the runtime is enormous. A good alternative for this would be the pairwise method, which does not test every signal with every value, but picks one signal and matches it with others. Therefore, the runtime is only $y \cdot x$ and a good mixture of values is caught.

V. CONCLUSION

With ISO/SAE 21434, an automotive security standard now exists that provides OEMs with a guideline for implementing security. This allows vulnerable points in the system to be found and assigned to a certain risk level. Depending on how high the risk is, penetration tests must be carried out, which reveal unexpected vulnerabilities so that these can be fixed before publication. This is a major advance in automotive security, as devices and systems are now protected from known attacks, and thus safety in vehicles is increased.

Nevertheless, the tests show that even though security has been implemented and tested, there are still vulnerabilities in systems that were not known before. For this reason, it is important to conduct further penetration tests even after the release of the product to detect and close newly emerging problems as quickly as possible.

REFERENCES

- [1] D. M. Tschersich. "Cybersecurity in the automotive domain." [accessed 11.05.2021]. (Jan. 2018), [Online]. Available: <https://www.m-chair.net/images/documents/lectures/2017WS/PWIN/Slides/Lecture/Continental.pdf>.
- [2] B. Kruck. "What's technically inside the iso/sae 21434?" [accessed 11.05.2021]. (), [Online]. Available: <https://www.security-analyst.org/inside-the-iso-sae-21434>.
- [3] W. Zimmermann, *Bussysteme in der Fahrzeugtechnik: Protokolle, Standards und Softwarearchitektur*. Nov. 2010, ISBN: 9783834809070.
- [4] "Lernmodul einführung in can." [accessed 07.05.2021], Vector Informatik GmbH. (Mar. 2020), [Online]. Available: <https://elearning.vector.com/mod/page/view.php?id=111>.
- [5] Minorax. "Quantized.signal." [accessed 08.05.2021]. (Jun. 2019), [Online]. Available: <https://commons.wikimedia.org/wiki/File:Quantized.signal.svg>.
- [6] B. für Sicherheit in der Informationstechnik. "Praxisleitfaden: It-sicherheits-penetrationstest." [accessed 07.05.2021]. (Nov. 2016), [Online]. Available: https://www.bsi.bund.de/SharedDocs/Downloads/DE/BSI/Sicherheitsberatung/Pentest_Webcheck/Leitfaden_Penetrationstest.html.
- [7] *Iso/sae dis 21434 - road vehicles — cybersecurity engineering*, 1st ed., Under development, Internationale Organisation für Normung, p. 108.
- [8] C. Sentinel. "Black box vs. white box testing: Key differences every organisation should know." [accessed 11.05.2021], Core Sentinel Pty Ltd. (Jun. 2017), [Online]. Available: <https://www.coresentinel.com/black-box-vs-white-box-testing>.
- [9] S. Albrecht. "Denial of service." [accessed 12.05.2021]. (Jun. 2005), [Online]. Available: <http://www.highgames.com/?set=hardwareview&view=8>.
- [10] B. P. Mille, M. Zhang, and E. R. Heymann, "The relevance of classic fuzz testing: Have we solved this one?," Jan. 2021, [accessed 12.05.2021]. [Online]. Available: <https://arxiv.org/pdf/2008.06537.pdf>.

Characterization of Object Detection Performance in an Edge Environment

Ruben Prokscha
 OTH Amberg-Weiden
 Amberg, Germany
 Email: r.prokscha@oth-aw.de

Abstract—Artificial Intelligence (AI) progresses to become ubiquitous in our day to day life. New models are able to solve ever more complex tasks. Simultaneously, new strategies and optimized hardware enable sophisticated machine learning (ML) algorithms to be performed on mobile devices. A new challenge arises by allowing these heterogeneous smart edges to interact with each other. The subsequent, highly adaptive edge clusters could anticipate problems before they even come up. A smart city approach would benefit immensely from this development. Each part of the infrastructure could be mapped to one or multiple smart nodes. This would enable precise traffic density estimations, which could in turn efficiently circumvent bottlenecks. Cars can be rerouted in a timely fashion, and the switching times of traffic lights could be optimized for the momentary demand. Necessary algorithms are directly processed on the edge by distributing them as micro tasks to available smart devices in the near vicinity. This in turn reduces latency and computational overhead compared to conventional solutions that utilize cloud servers. Realizing such an endeavour requires a high degree of considerations and groundwork to be build upon. In particular performance metrics, necessary for a smart task distribution, must be aquired.

I. INTRODUCTION

This paper considers the deployment and performance of Deep Learning (DL) tasks for different types of smart nodes. First of all, traffic density estimation is proposed as a practical example for a decentralized AI task. The following section provides background information on how modern object detection models are being structured. This in turn provides the inside for the subsequent section where different state-of-the-art (SOTA) object detection models are being introduced regarding their origins and attributes. A benchmark was performed for each object detector on different edge accelerators in terms of loading time, inference speed and energy consumption. The results are visualized and put into perspective. Finally, a summary is drawn to point out the key insights from this research.

II. TRAFFIC DENSITY ESTIMATION

Technology is constantly evolving and the amount of data generated is increasing rapidly. The missing link is how this data can be directly processed at the source. This section considers a data stream generated by traffic cameras. Ideas are proposed on how the image sequence can be processed. Furthermore, what insight can be

gained from the data and how this information can be used for real time traffic optimization.

The data used in the following examples originates from traffic cameras in Tampere City, Finland [1]. The images were continuously scraped over a period of several months from 2019 and 2020. A You Only Look Once (YOLO) version three [2] model was used to detect traffic specific objects within the images. The network was used with the default weights and classes from the Common Objects in Context (COCO) dataset [3].

Traffic density has to be derived by analyzing a camera stream frame by frame. The number of objects of interest divided by a time interval (e.g. sampling frequency) can be used as an estimate on how crowded an intersection, such as seen in Figure 1, is. Simply counting objects can be misleading though, depending on the scenario, additional post processing filters and case distinctions could help to make the predictions more robust. Such filters could sort out cars which are parking by defining regions of interest and ignoring objects that are static for a predefined time interval. Furthermore, the number of cars could be set into context, depending on which lane they are on. Such could be the rush hour traffic, having cars moving city inwards in the morning and outwards in the evening.

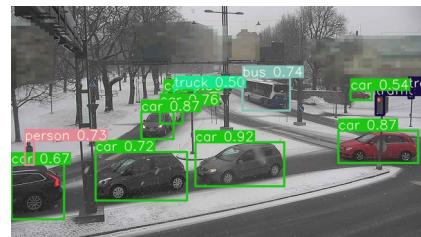


Figure 1: Detecting traffic specific objects inside a camera frame.

Figure 2 shows the development of the car density for the previously introduced intersection. A clear trend can be deduced that shows few cars in the night hours and a peak at around 14 o'clock for all graphs. Due to the central position, a rush our trend is not visible. Another phenomenon is the steep drop of cars between February and March 2020. This can be traced back to

the first Covid-19 counter measures (home office, contact restrictions, etc.) which in turn caused people to use their car less frequently overall.

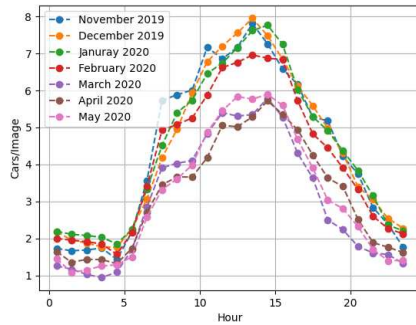


Figure 2: Rolling average of car density over the time of day for different months.

The number of vehicles alone is not a good indicator on how well traffic is flowing. Here the dynamic behavior in terms of time and space has to be taken into account. This can be done by taking the position of the detected objects in each frame and building a weighted average over a predefined time interval. This was done for Figure 3 in form of a heat map. The deep red regions indicate stagnant traffic or parking cars, while dark blue implicate the absence of vehicles. Analyzing this heat map suggests that the traffic lights causing waiting periods, which could be reduced by optimizing switching times or considering roundabouts.

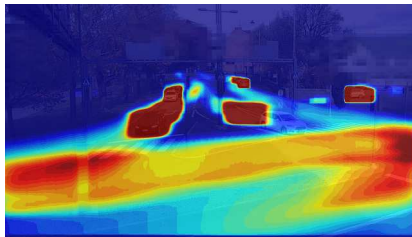


Figure 3: Traffic flow heat map.

The quality of such a dynamic analysis could be further increased by utilizing object tracking algorithms such as Deep Simple Online and Realtime Tracking (SORT) [4]. Provided, that the sample rate of the image stream is high enough to trace the movement of individual objects, a gradient analysis can be applied. By observing how the center of a moving object moves between frames, it can be determined how fast and in which direction it is moving. Such an analysis can be especially interesting for highways to quickly detect a traffic jam or dynamically regulating the speed ratings. This in turn would improve safety and traffic flow.

All these practical examples serve the purpose to demonstrate, how AI could be used to analyze and optimize existing infrastructure in a smart way. The proposed models and algorithms are fast enough to run

in real time on embedded hardware. Hence, cameras can be cheaply upgraded with computing units, which self-sufficiently evaluate the situation and only pass the result to a central server or other parts of the infrastructure.

III. OBJECT DETECTION MODELS

Developing an object detection model can be considered a challenging task. A naive approach would be to use an established Convolutional Neural Networks (CNN) for image classification like ResNet [5] and utilize a sliding window approach to detect possible object within the frame. Additionally, thresholding and Non Maximum Suppression (NMS) [6] can be used to find the optimal boxes for each object. While this would work in theory, the computational load would be very high and the inference time particularly slow.

A more promising concept is the usage of a region proposal algorithm such as selective search [7]. This limits the processing load to the proposed regions of the image. Region Based Convolutional Neural Networks (R-CNN) [8] incorporates this so called two stage network design. Further improvements were made by Fast-R-CNN [9], by using a CNN network as backbone to create a feature map of the image. Faster-R-CNN [10] introduced an even more significant speedup by replacing the region proposal algorithm with a trainable Region Proposal Network (RPN).

While Faster-R-CNN surpasses its predecessors in speed and accuracy, it is still too large and slow for real time application on embedded devices. Here, single stage detectors come into play. Instead of dividing the detection task into region proposal and classification, a single network is used. Similar to modern two stage detectors, a backbone network is used to generate a feature map of the input image. Instead of region proposals, the feature map is divided into a grid. The network has a defined number of default anchor boxes, which are applied to each grid segment. The rest of the network is then responsible to calculate a class, confidence score and offset parameter for the anchor boxes. Finally, thresholding and NMS is used to determine the end result.

Most object detection models are based of Single Shot Detector (SSD) [11] or You Only Look Once (YOLO) [12]. Both networks use the aforementioned structure. The difference lies in the detail. SSD networks use common CNN networks as backbone, while YOLO utilizes its own Darknet architecture [13]. The second core distinction is the classification part itself. SSD only uses convolutional layers to determine its output while YOLO uses both convolutional and dense layers.

IV. BENCHMARK CANDIDATES

Obtaining object detection models which work together with all edge accelerators proved to be a challenging task. Most models from the Open Neural Network

Exchange (ONNX) model zoo had an issue running with TensorRT (TRT), OpenVino or both. Adding compatibility for Google Coral products introduces additional concerns. To alleviate the matter, models were manually transferred from different repositories to the ONNX and Tensorflow (TF) Lite format according to Figure 4.

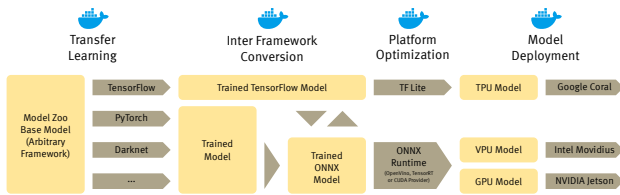


Figure 4: Deployment pipeline for benchmark execution.

The following subsection describes the different models, where they originate from and which alterations had to be performed. Table I shows the different models, which were tested in regard of their size.

Table I: Size in bytes for tested models.

	SSD MobileNetv2	TinyYolov4	Yolov4	Yolov5s	Yolov5l
ONNX	70.30MB	24.28MB	257.48MB	29.90MB	189.72MB
TFLite	6.95MB	6.92MB	65.65MB	10.68MB	53.57MB

Obtaining a SSD model which is compatible with all providers was not possible. For the benchmark a MobileNetv2-SSD was used. As the name suggests MobileNetv2 [14] serves as the lightweight backbone for the object detector. The base model for the ONNX model was taken from the TF1 object detection model zoo [15]. Running the model with the TRT provider was not possible. Furthermore, a conversion to TFLite did not work as well. Therefore, a model with the same label was taken from the Coral Edge Tensor Processing Unit (TPU) model zoo [16]. Both models have their input size set to 300 pixels times 300 pixels.

YOLOv4 [17] is the newest model from the original YOLO developers. It uses various micro optimizations in the model design and the training process to outperform existing models in both speed and accuracy. The benchmark considers both the full implementation, which is taken from "PINTO0309/PINTO_model_zoo", and the tiny version from "hkh7734/tensorflow-yolov4" (version 3.2). It is worth mentioning that the tiny model repository made additional modifications to the model to perform better on the Edge TPU. The models have perception field of 300 pixels squared for the full model and 608 pixels squared for the tiny variant.

Contrary to the name, YOLOv5 is not related to original YOLO project. It was published by the Ultralytics LLC company which as of now has not released a paper disclosing the architecture and performance [18]. Hence YOLOv4 can be considered SOTA, instead of being a predecessor. YOLOv5 comes in four different version (s,m,l,x) were each one is a compromise between size and

accuracy. The models are provided in PyTorch format. Scripts for transfer to ONNX and TFLite can be found in the official repository [19]. Version "x", was not executable on the Edge TPU. The benchmark evaluates the "s" and "l" model. Both using an input size of 640 pixels squared.

V. BENCHMARK METHODOLOGY

All measurements were executed on a NVIDIA Jetson Xavier AGX platform. As energy mode 30W with all cores enabled was chosen. An Intel Movidius Neural Compute Stick 2 (NCS2) and a Google Coral Edge TPU were added via Universal Serial Bus (USB) port. The benchmark itself ran inside a docker container. As base image "l4t-base:r32.4.3" was used for the Nvidia Jetson platforms. This sets the GPU library versions to Compute Unified Device Architecture (CUDA) 10.2, TensorRT 7.1.3 and CUDA Deep Neural Network Library (cuDNN) 8.0. Intel OpenVino 2020.4 was installed for VPU support. A custom ONNX runtime (v1.5.3) was compiled to enable multi provider support. Google's Coral TPU can be utilized with the tflite runtime in version 2.5 and the libedgetpu-15.0-std driver.

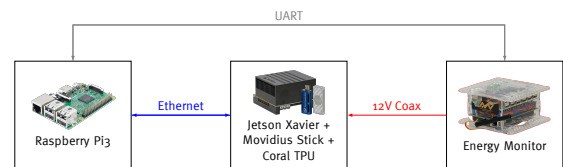


Figure 5: Test setup for benchmark measurements.

The benchmark considers time and energy measurements. Python's perf_counter was used to determine the execution time. Current and supply voltage were recorded by a custom energy monitor. Figure 5 shows how the measurement takes place. The energy monitor is used as power supply for the Jetson Xavier. It constantly measures current and voltage with a frequency of 20 Hz. The data is transferred via Universal Asynchronous Receiver Transmitter (UART) to a Raspberry Pi 4, where it is processed and cached. The Xavier can trigger the Pi to start and stop the evaluation process. Once a measurement is concluded, the data is retrieved from the Pi and stored together with the timing data.

VI. WARMUP EVALUATION

The warmup period describes the time delay required to load a model and run an inference for the first time. In a deployment scenario, it can be considered the latency to switch from one ML task to another. Hence, a lower time is necessary to realize a responsive system. During the warmup, memory has to be allocated and hardware is initialized. Therefore, it can take significant longer than subsequent loads and inferences that are executed within the same process. The benchmark script executes

exactly one model load and one single inference. To get a significant amount of measurements, the script was called 250 times for each model provider combination. Figure 6 depicts the warmup time in ascending order.

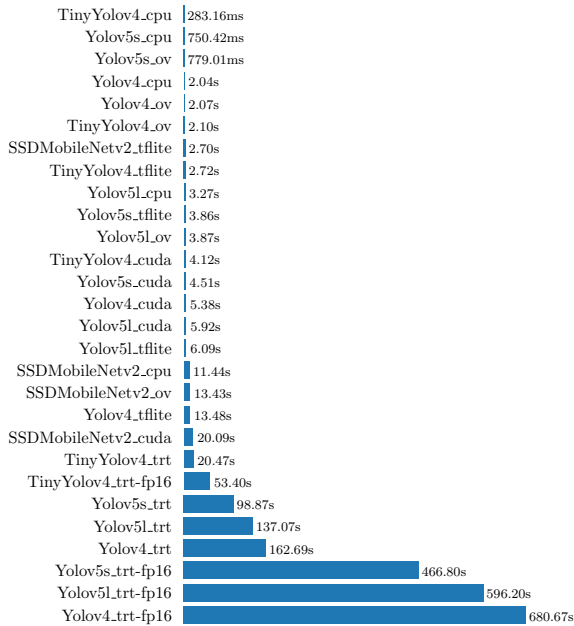


Figure 6: Warmup time for different model and provider combinations.

Small models profit from CPU inference due to memory locality. TFLite models have quick loading times since they are roughly four times smaller than their ONNX counterparts due to quantization. Additionally, they were precompiled during creation which avoids optimizations at runtime. TensorRT is the only provider which modifies the model at loading. This leads to a significantly increased warmup. Using 16bit floating point mode increases the delay even more. If a model has to be load frequently, engine caching could be used to alleviate this issue.

The SSDMobileNetv2 ONNX model has significant longer load times for all providers compared to the YOLO models. This could be an issue of the inter framework conversion from TF1 to ONNX. Most model-provider combinations spend the most warmup time with the model load. However, some others perform additional work during the first inference. This behavior does not appear to follow any obvious pattern regarding model type, size or provider.

VII. INFERENCE TIME EVALUATION

The inference process is usually executed periodically after a model is loaded. In case of a camera stream, the inference time is directly related to the processing frequency. A processing period of 33 ms would translate

to a frame rate of 30Hz which would be ideal for real time video stream processing.

The benchmark was executed by running a warmup at the beginning and after that repeating the inference process for a thousand times. The object detection was performed on two images of the intesection depicted on Figure 1. They significantly differed regarding the number of depicted objects. The camera shots were chosen to determine if the number of objects in an image has an impact on the models performance. However, such an effect was not detectable. This is most likely justified by the lack of an region proposal algorithm in one stage detectors.

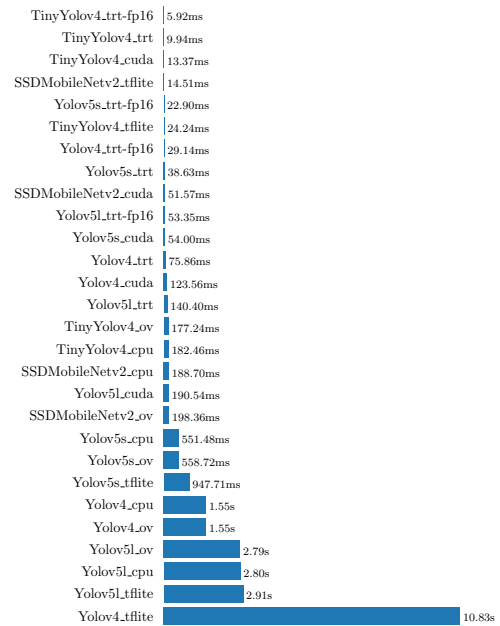


Figure 7: Averaged inference time for different model and provider combinations.

Figure 7 shows how the individual models perform on image inference. The long warmup interval of TensorRT pays off. TinyYOLO version four can achieve frame rates of over 100 Hz and all models perform significantly better than with all other providers. Reducing the parameter precision from 32 bit to 16 bit provides an additional speedup due to the Xavier's tensor cores. Larger models with more parameters like YOLOv4 profit even more than the smaller ones. CUDA is not as fast as TRT since the models are not optimized. However the load time is significantly faster (ref. Figure 6). In a scenario were a model is only required a few times, this provider could be worth preferring. OpenVino performs similar to CPU, this could suggest that most operation are not executed on the Movidius NCS2. It can be assumed, that OpenVino provider is not yet ideally integrated into the ONNX Runtime. It needs to be seen if future updates

can improve the performance. The inference time of TFLite depends on the size and optimization level of the individual model. The Edge TPU has a memory of roughly 8 MB. Therefore only TinyYOLOv4 and SSDMobileNetv2 can be mapped entirely to the device RAM. Each incompatible instruction has to be run on CPU. This requires the intermediate result to be moved from the device to the system memory. Additionally, quantization layer are being added to the model to allow the transition between TPU int8 and CPU floating point operations. The additional workload introduced by quantization and memory transference results in a performance drop of YOLOv4. A similar behavior can be observed for the YOLOv5 models.

VIII. ENERGY CONSUMPTION EVALUATION

Measuring the power consumption for a single inference was not possible for the fastest model because the sampling rate of the energy monitor was too slow. The issue was circumvented by continuously repeating the inference process and sampling over a time interval of about 250s (5000 points). In theory, the signal is not evenly sampled if the sampling rate and the inference time are integer multiples of each other. However, the Linux scheduler should introduce enough random delays that the collected data points are distributed evenly.

The average power consumption for each model provider combination was determined by removing the idle power from the measurements according to Equation (1). P_{raw} is the value which was directly measured. ΔP_{both} is the idle power consumption of both USB accelerators. The value was removed since both devices were connected during all measurements. At last ΔP_{dev} was added which is 0.362 W for TPU inference 0.684 W for VPU measurements and 0 W for everything else.

$$\Delta P_{inf} = P_{raw} - \Delta P_{both} + \Delta P_{dev} \quad (1)$$

From the inference time and power consumption the energy demand can be calculated according to Equation (2).

$$E_{inf} = \Delta P_{inf} \cdot t_{inf} \quad (2)$$

The results in Figure 8 enable an estimation on battery runtime as well as operating costs. GPU inference with small models benefits the most from short inference times. Generally, CUDA and TRT (especially with Tensor Cores) execute models more efficient than the CPU and OpenVino provider. TFLite performs well on small optimized models.

IX. BENCHMARK SYNOPSIS

There are four parameters which have to be considered when deciding on the execution provider for an inference task. These are loading time, inference time, energy consumption and model accuracy. The last point was not explicitly analyzed in this report. However,

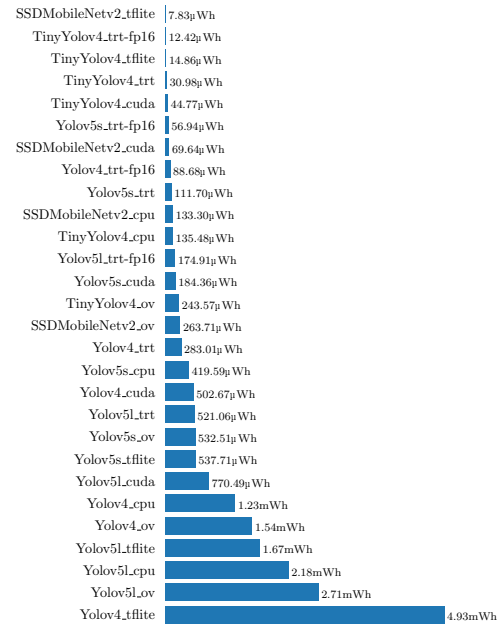


Figure 8: Average energy demand for one inference of different model and provider combinations.

when reducing the model parameters to 16 bit floating point (TensorRT Tensor Cores) or 8 bit integers (TFLite quantization) the accuracy will inevitably drop. How significant this reduction is must be evaluated in a future report. Regarding the other three points, TFLite performs best. However, this only applies for small model that are optimized to use TPU compatible operations. TensorRT performs best in terms of speed especially when using the devices Tensor Cores. This factor is bought by long loading times. The only benefit from using the CUDA provider over TRT is the quicker model load. Both CPU and OpenVino are too slow for object detection tasks. Whether the ONNX runtime is not optimized for VPU inference can not be said with certainty.

Considering the model performance, (Tiny)YOLOv4 has the best overall solution. The models execute well on all providers. Depending on the requirement, the same pipeline can be used to switch between speed (TinyYOLOv4) and accuracy (YOLOv4). Moreover, an accessible API is available to integrate transfer learning into a deployment pipeline. YOLOv5 has similar benefits however, the inference speed is significantly slower. If the "m" models would achieve a better accuracy than the YOLOv4 it could be considered an alternative. SSDMobileNetv2 ONNX has an average performance but the lack of TRT support is a big downside. The TF object detection API can be used for transfer learning. An other drawback is that the TFLite model uses custom modifications to run that well on the TPU. This could lead to issues when transfer learning is required.

Combining the insights of provider and model performance, the following combinations are worth considering for an object detection application. TinyYOLOv4 with TFLite should be ideal for a real time application where accuracy can be neglected. This could be the case, when a platform (e.g. Raspberry Pi) should be upgraded to perform vision tasks. This would only require adding an Edge TPU to the device. The low energy footprint would not require any modifications on the existing power supply. For professional tasks that require both accuracy and speed YOLOv4 with TensorRT would be the optimal solution. Additional weighting between precision and frame rate can be achieved by the enabling or disabling Tensor Core execution.

X. SUMMARY AND FUTURE WORK

Deploying object detections models on an edge environment entails a variety of different pitfalls. Both deployment frameworks come with issues one has to be aware of. ONNX suffers from incompatibility problems regarding instructions from other frameworks. This can in particular be problematic with networks that incorporate new methods or use algorithms that are based on the fourier transform. Additionally, the provider support for TensorRT and OpenVino is still experimental. Therefore, not all models will be executed properly. This includes the ONNX model zoo where one would expect full compatibility. TFLite on the other hand suffers from a convoluted pipeline with a proprietary edge compiler. Model conversion fails with meaningless error codes and debugging is not possible due to the closed source nature of the compiler. To actually benefit from the Edge TPU the model has to conform with the device instruction set and should be small enough to fit in the memory. Otherwise the performance suffers immensely.

Of all the devices proposed only GPU and with restrictions TPU inference was usefully applicable with regards to real time object detection. Similarly, only (Tiny)YOLOv4 can be considered as the only universal model solution and under certain circumstances YOLOv5 could be considered.

In a future report, additional benchmark results from different edge platforms are going to be generated. These empirical key figures are than be used to setup a container based deployment pipeline. The goal of this undertaking will be to determine how Deep Learning task could be efficiently distributed and processed on heterogeneous edge clusters.

REFERENCES

- [1] *Open Data License*. Publisher: Tampereen kaupunki. Oct. 20, 2015. URL: <https://www.tampere.fi/tampereen-kaupunki/tietoa-tampereesta/avoin-data/avoin-data-lisenssi.html>.
- [2] Joseph Redmon and Ali Farhadi. *YOLOv3: An Incremental Improvement*. Tech. rep. 2018.
- [3] Tsung-Yi Lin et al. "Microsoft COCO: Common Objects in Context". In: *ECCV*. 2014.
- [4] Nicolai Wojke et al. "Simple online and realtime tracking with a deep association metric". In: *IEEE*. 2017.
- [5] Kaiming He et al. "Deep Residual Learning for Image Recognition". In: *IEEE*. 2016.
- [6] Jan Hosang et al. "Learning Non-maximum Suppression". In: *IEEE*. 2017.
- [7] J. R. R. Uijlings et al. "Selective Search for Object Recognition". In: *IJCV*. 2013.
- [8] Ross Girshick et al. "Rich Feature Hierarchies for Accurate Object Detection and Semantic Segmentation". In: *IEEE*. 2015.
- [9] Ross Girshick. "Fast R-CNN". In: *IEEE*. 2015.
- [10] Shaoqing Ren et al. "Faster R-CNN: Towards Real-Time Object Detection with Region Proposal Networks". In: *IEEE*. 2017.
- [11] Wei Liu et al. "SSD: Single Shot MultiBox Detector". In: *ECCV*. 2016.
- [12] Joseph Redmon et al. "You Only Look Once: Unified, Real-Time Object Detection". In: *IEEE*. 2016.
- [13] Joseph Redmon. *Darknet: Open Source Neural Networks in C*. 2013. URL: <http://pjreddie.com/darknet/>.
- [14] Mark Sandler et al. "MobileNetV2: Inverted Residuals and Linear Bottlenecks". In: *IEEE*. 2018.
- [15] *Tensorflow 1 Model Zoo*. URL: <https://github.com/tensorflow/models>.
- [16] *Coral Edge TPU Model Zoo*. Coral. URL: <https://coral.ai/models/>.
- [17] Alexey Bochkovskiy et al. *YOLOv4: Optimal Speed and Accuracy of Object Detection*. 2020.
- [18] Ritesh Kanjee. *YOLOv5 Controversy — Is YOLOv5 Real?* 2020. URL: <https://medium.com/swlh/yolov5-controversy-is-yolov5-real-20e048bebb08>.
- [19] Glenn Jocher et al. *ultralytics/yolov5: v4.0 - nn.SiLU() activations, Weights & Biases logging, PyTorch Hub integration*. 2021.

Free Electric Vehicle Charging - A Practical Attack on Charging Systems

Jonas Schmidt

University of Applied Sciences Regensburg
Regensburg, Germany

Email: jonas.schmidt@st.oth-regensburg.de

Abstract—The change of mobility to the electric vehicle is ongoing. A critical aspect of it is to develop secure options to recharge the battery after driving. This paper investigates the security of the communication of charging systems while a user is authenticating for billing. This includes using RFID cards to communicate to the charging station and the backend communication from the charging station to a backend server over OCPP. It is partly a revisit to findings researchers made in 2017 and aims to look at the progress done till the end of 2020 by the manufacturers in terms of security.

I. INTRODUCTION

Climate change forced people and countries to develop and use new technologies to produce fewer emissions. One of the first ideas was to change mobility to the Electric Vehicle (EV). In EVs, a powerful battery is used to move the car, replacing the need for burning fuel.

Because a battery does not have the energy capacity of regular fuel, it needs to be charged after each drive. Charging a battery currently takes hours, giving the need to develop new technologies that can charge more quickly. If a battery is charged rapidly, heat is produced that needs to be controlled not to endanger the battery. Therefore different modes of charging were standardized to ensure the safety of the user and protect the battery. In these modes, the Electric Vehicle Supply Equipment (EVSE) can communicate with the EV during the charging process [1].

The long waiting time makes recharging a battery different from getting fuel. Gas stations need to be replaced by places with a charging station and with the possibility for the user to charge for a longer time. Because the cars need more refuel-time with a battery, this also leads to more people charging simultaneously, so the number of charging places needs to increase.

This development also influences billing. In a gas station, one person could take charge from all customers, but with a more distributed offer of charging stations, this is no longer possible.

This led to the introduction of charging cards. A customer can link his bank account to a provider's user account and then gets an RFID card linked to his user account. Before a charging station of the provider charges a car, an RFID card needs to be read out by the charging station and validated by the provider's backend system. No human cashier is required with this approach.

The security of such payment systems is fundamental since fraud of any kind can lead to financial impact for the provider or the customer. This paper aims to present the results of a security investigation that targeted the communication of a 2020 manufactured charging station while such a billing authentication process took place.

II. IMPORTANT TECHNOLOGIES

Radio-frequency identification (RFID) is a technology that uses electromagnetic fields to transfer data. The transponder can be built into cards or chips and carry authentication data that allow the user access to different services, like open a lock or starting the charging from a charging station [2]. Various technologies and protocols are used internally to read and write data, so some chips may not be compatible. NFC is a branch of High-Frequency RFID and can be found implemented on most smartphones. Today's mainly used card type of charging stations is the MIFARE classic RFID card, also operating in High-Frequency. The MIFARE Classic card-type is a relatively old but very cheap RFID card that uses the ISO 14443 Type-A protocol [3]. It was introduced in 1994 by NXP [4].

The Open Charge Point Protocol (OCPP) is a protocol that defines the communication between the charging station and the backend server. It is maintained and promoted by the OPEN CHARGE ALLIANCE, a global consortium with members from OEMs like BMW, energy providers like E.ON, and charging station manufacturers [5]. Many services are defined that can be communicated from/to the charging stations. One of them is the authentication of a user. There are two different Versions of OCPP used today:

- OCPP 1.5/1.6
- OCPP 2.0

OCPP 1.5 (release 2012) was the first widely used protocol for charging stations. After more different functions were needed for Smart Charging, OCPP 1.6 (release 2015) was built as an extension with the same basic functions. After many findings that decrease Cybersecurity, OCPP 2.0 (release 2018) was introduced to address the issues.

III. RELATED WORK

RFID cards are the source of many publications from security researchers. The MIFARE Classic RFID card was the headline of multiple publications. In 2007 Karsten Nohl and Henryk Plötz presented at the Chaos Computer Club (CCC)

that the primary security feature of MIFARE classic was the secret of the used algorithm [6]. This technique is called security by obscurity because it is only a security feature as long as an attacker does not know how it is implemented. If the algorithm gets publicly available, the security of the chip is no longer given. In March 2008, a research group from Radboud University completely reverse-engineered and published the used algorithm [7]. Since then, many tools have become available to read out, write and even clone a MIFARE Classic card. In 2014, Márcio Almeida held a talk about Hacking Mifare Classic Cards at the Blackhat Conference, with a detailed description of how to use the tools. It got so much public attention that it is the search result #1 on googling "Mifare Classic hack" [8].

In 2017 Mathias Dalheimer, a security specialist for charging stations, presented his findings on the CCC [9]. He researched both the RFID and the OCPP protocol used by public charging stations. For RFID, the MIFARE Classic cards of 1994 are used to authenticate the user, which is vulnerable to all the findings above. The OCPP protocol, which communicates the RFID authentication to the back-end server, was transferred unencrypted, sniffing the correct user data or using a Man-in-the-middle attack (MITM) attack the hole authentication was possible. Further, the update and maintenance process of the charging stations was working over USB-Sticks, which contained unencrypted files, and therefore was also attackable.

IV. CHARGING AUTHENTICATION

In picture 1 the whole communication of a charging process with RFID and OCPP authentication is shown. The process takes three steps to charge a car:

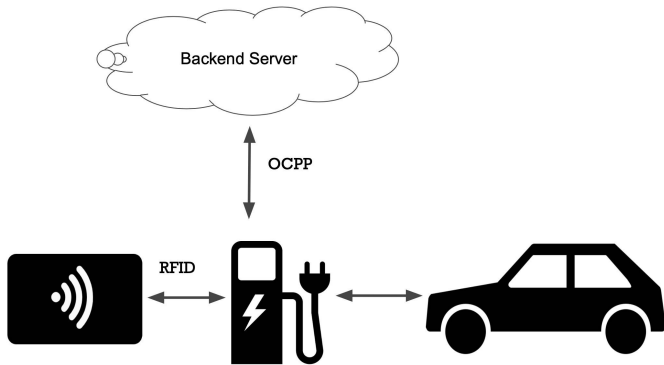


Fig. 1. Charging an electric Vehicle

1. Plugin the car
2. Authenticate over a RFID-card
3. Charging Station asks backend over OCPP if the authentication is valid

For the billing authentication, only the reading of the RFID card and the backend communication are relevant.

V. RFID CARDS

The RFID authentication of the charging station in 2020 also works over RFID cards. At the start of the investigation, the used card type had to be determined. This was done with a smartphone with an NFC chip. Today most smartphones are supporting RFID communication. The app stores feature a lot of different tools to read or write data over RFID. On Android, the "NFC Tools"-app [10] can be installed to read out the basic RFID card information.



Fig. 2. NFC Tool Result

As seen in figure 2, the old MIFARE Classic card-type is still used. The 1k stands for how much data can be written on the card and ranges between 1k-4k-bytes, 1k in this case. The usage of this card allows for an attack on all the public finding of the MIFARE Classic card type.

The data on the RFID card is saved in sectors. A sector contains four blocks of data. Each block has 16 Bytes. In block 3 of each sector (The last block since counting starts at 0), the read and write access of the block is secured by keys, KeyA and KeyB. The settings of which key is for reading or writing can differ, but usually, one key is reading only, and the other can read and write on the card. After an RFID card is produced, the keys have a factory default value. It depends on the manufacturer which value is given, but the list of possible factory defaults is also available online (see [11]). It is in the responsibility of the provider to change this defaults to a real values.



Fig. 3. NFC Tool Dump

As shown in figure 3, the RFID cards of the investigated charging station do not have a key set. Instead, the factory default 0xFFFFFFFF key is used for both KeyA and KeyB.

That has as a consequence that the data is basically not encrypted at all. With the default key used, anyone can read out the card's data or even write new data on it. This means the public attacks on MIFARE Classic are not even needed.

VI. RFID CARD DATA THEFT

Despite the RFID card being already broken 13 years ago and the card's insecure key settings, there is a more significant flaw in the RFID authentication for charging. The charging station does not read the RFID-cards data for authentication. Instead, only the so-called Unique Identifier (UID) is read out. The UID is an identifier used to differentiate the communication between two or more RFID cards. Every RFID card has a unique UID that is sent at the start of the communication. After that, the UID is used to identify the communication, so the receiver knows which message is from which RFID card.

Since the UID must be read out by the charging station and no other data is used to authenticate, a cloned card with the same UID is sufficient to get the same access as the original. All MIFARE Classic RFID cards have their UID written hardcoded in the factory, so it is impossible to change a UID in an RFID card's lifetime.

This makes it impossible to clone a MIFARE Classic card with another MIFARE Classic card. A special card is needed that allows to change the UID afterwards. Since it is not permitted on the western market to produce a MIFARE Classic card with such a design due to copyright, the cards are invented and made in China. That gave the changeable UID cards the official name "Chinese Magic Card". The magic of that card allows sending a custom command to the card that can change the UID. For 1-2\$, the cards can be bought at a low price and shipped to Europe.

Like mentioned before, many smartphones support NFC communication, and many tools are available in the app stores. The only limitation is that apple, despite supporting NFC communication, does not support the MIFARE Classic protocol, so an android phone is needed.

The challenge to clone an RFID card is to get the UID of the victim's card. The MIFARE Classic is a High-Frequency RFID card that operates in a frequency range from 3 to 30 MHz (13.56 MHz for MIFARE Classic). The read distance ranges from 10 centimeters to 1 meter with no obstacle in the way.

In the scenario that an attacker tries to steal the RFID card's data from a victim, the card is likely to be in a wallet. In our case we also assumed, that the attacker will not have expensive RFID reading equipment, which can extend the range and instead uses a phone for the attack. This makes the practical range of the attack significantly smaller.

There is also a difference in how filled the wallet is, especially how much different cards and coin money is in the way. By testing with an empty wallet, the attacker's phone had a range of 2cm to catch the data. With a full wallet, the range got down to only 1cm. Figure 4 shows how close an attacker (left) has to be to the victim (right) to get the data out of a full wallet. It is still possible without direct contact

but hard to get. The reading takes around half a second, so a fast run-by is insufficient to get the needed UID.



Fig. 4. Data Theft Progress

VII. RFID CARD CLONING

After the UID is stolen from the victim, the process of making an exact clone on a Chinese Magic Card is rather easy. There are many different apps can clone an RFID card's UID, too. To clone our RFID card, the app "MIFARE Classic Tool" [12] was chosen. It requires only three steps to clone a card:

1. Typing the UID to write or input it from the recently read list (Convenient usage for an attacker)
2. Press the Clone UID button
3. Hold the Chinese Magic Card on the Phone

After that, the Chinese Magic Card is an exact clone of the victim's RFID card in terms of authentication with UID. No reader can tell the difference between them. This allows the attacker to make purchases on the victim's account and get personal information.

Concluded everything needed to clone an RFID charging card is:

- Proximity access to original card (1cm-5cm)
- Smartphone with NFC Chip (Android needed, Apple does not support MIFARE Classic communication)
- Chinese Magic Card (Will be exact Clone of Alfen Card)

Since the proximity access is rather hard to get, a second way of obtaining the required UID will be presented in the following.

VIII. OCPP 1.5/1.6. AUTHENTICATION

After a charging station reads the RFID card, the data is transferred to a backend server to validate if the user is allowed to have access to the charging site. This is done with the OCPP. There are different versions of the protocol (newest 2.0.1). Therefore it is essential to know which version is used. The handbook of the charging station shows the following supported versions: OCPP 1.5/1.6. These versions use the same authentication with the central system.

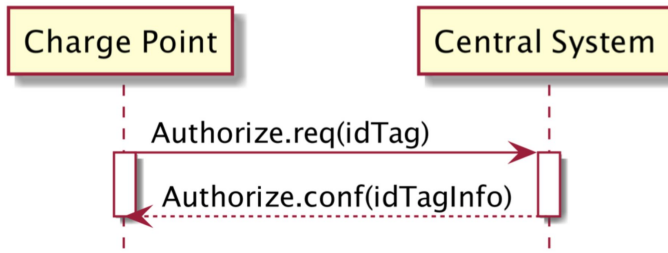


Fig. 5. OCPP 1.5/1.6 Authentication

The charging station sends an idTag to the central system (see figure 5). The idTag has up to 20 bytes. In the central system, every user is saved combined with the corresponding idTag. If the idTag is present in the database (no further check if it is the correct user), the central system sends the authorize command back to the charging station. After that, the power transfer to the car is unlocked by the charging station. The whole process uses the internet for communication. It can be over a direct ethernet connection or Global System for Mobile Communications (GSM) connectivity. The underlying protocol is Hypertext Transfer Protocol (HTTP) or Hypertext Transfer Protocol Secure (HTTPS).

HTTPS (HTTP wit TLS) would not be a problem if it is appropriately used. The problem with the used charging station is that HTTP is used by standard configuration. If a user does not change this manually by flashing the software, the communication relies on an insecure, unencrypted protocol. That allows an attacker to read out all messages used to communicate.

To set up the charging station with a central system, the open-source server SteckdosenVerwaltung (SteVe) was used. SteVe was developed at the RWTH Aachen University and provides essential functions for the administration of charge points, user data, and RFID cards for user authentication [13].

After the backend server was set up, the communication was sniffed with a third computer on the same network. For this, the free network protocol analyzer "Wireshark" [14] was used. By filtering the IP address of the charging station, the whole communication could be seen.

```

306 64.119298 172.16.25.63 172.16.25.64 WebSo... 108 WebSocket Text
308 64.143143 172.16.25.64 172.16.25.63 WebSo... 101 WebSocket Text
319 107.404109 172.16.25.63 172.16.25.64 WebSo... 108 WebSocket Text
320 107.417101 172.16.25.64 172.16.25.63 WebSo... 100 WebSocket Text
324 116.948287 172.16.25.63 172.16.25.64 WebSo... 84 WebSocket Text
325 116.962817 172.16.25.64 172.16.25.63 WebSo... 108 WebSocket Text
> Frame 306: 108 bytes on wire (864 bits), 108 bytes captured (864 bits) on interface en7, id
> Ethernet II, Src: 32:69:4f:14:73:42 (32:69:4f:14:73:42), Dst: Raspberr_bd:3e:db (dc:a6:32:b
> Internet Protocol Version 4, Src: 172.16.25.63, Dst: 172.16.25.64
> Transmission Control Protocol, Src Port: 57124, Dst Port: 8080, Seq: 663, Ack: 275, Len: 54
> WebSocket
Line-based text data (1 lines)
[2,"185","Authorize",{"idTag":"0411F26A8E6781"}]
  
```

Fig. 6. OCPP 1.5/1.6 Authorize Request

Figure 6 shows a authorize request by the charging station after reading an RFID card. The idTag, that the central system is verifying, is the UID of the RFID card. The Man-in-the-middle attack (MITM) attack of 2017 would still be possible if the direct channel between the two communication partners is accessed.

If you combine this with the weak RFID cards, sniffing alone is also sufficient. It is possible to read out all pairs of authorize requests, and authorize confirms that end up with a "valid" answer by the backend system. A list can be built that includes all recent users of the charging station with their UID. To clone a valid card, one of the UIDs has to be written on a Chinese Magic Card. The proximity access to the original card is not needed if you can sniff on the communication.

IX. CONCLUSION

Concluded, the charging station from 2020 also has substantial security issues like the presented by security specialists three years ago. In this case, by using the factory default keys on the RFID cards, an attack can be made even more accessible.

It is possible to steal the identity of a victim and make purchases in his name. Personal data will be displayed on some charging stations after holding an RFID card on it, which an attacker can also steal. This could be easily prevented by using more expensive but secure RFID cards and using OCPP 2.0, which has a secure version of the authentication process.

Seeing no change in nearly four years of development is a bad sign from the manufacturers. Multiple points need attention and fixing. It is only to hope that this developing attitude will change in the upcoming years.

REFERENCES

- [1] International Electrotechnical Commission (IEC). IEC 61851 - electric vehicle conductive charging system, 2017
- [2] smart-TEC. RFID-Technology. <https://www.smart-tec.com/en/auto-id-world/rfid-technology>, 2021. [Online; accessed 10-May-2021].
- [3] International Organization for Standardization (ISO). ISO/IEC 14443-4:2016.
- [4] NXP Semiconductors. MIFARE Classic@. https://www.nxp.com/products/rfid-nfc/mifare-hf/mifare-classic:MC_41863, 2021. [Online; accessed 10-May-2021].
- [5] OPEN CHARGE ALLIANCE. GLOBAL PLATFORM FOR OPEN PROTOCOLS. <https://www.openchargealliance.org>, 2021. [Online; accessed 10-May-2021].
- [6] Chaos Computer Club (CCC), Karsten Nohl and Henryk Plötz. Mifare Little Security, Despite Obscurity. https://media.ccc.de/v/24c3-2378-en-mifare_security, 2007. [Online; accessed 10-May-2021].
- [7] Flavio D. Garcia. Dismantling MIFARE Classic. <http://www.cs.ru.nl/~flaviog/publications/Talk.Mifare.pdf>, 2008. [Online; accessed 10-May-2021].
- [8] Blackhat, Márcio Almeida. Hacking Mifare Classic Cards. <https://www.blackhat.com/docs/sp-14/materials/arsenal/sp-14-Almeida-Hacking-MIFARE-Classic-Cards-Slides.pdf>, 2014. [Online; accessed 10-May-2021].
- [9] Mathias Dalheimer. Ladeinfrastruktur für Elektroautos: Ausbau statt Sicherheit. https://media.ccc.de/v/34c3-9092-ladeinfrastruktur_fur_elektroautos_ausbaustatt_sicherheit#t=309, 2017. [Online; accessed 10-May-2021].
- [10] Google Play. NFC Tools. <https://play.google.com/store/apps/details?id=com.wakdev.wdnfc&hl=en&gl=US>, 2021. [Online; accessed 10-May-2021].
- [11] Awesome Open Source. Mifare Classic Toolkit. <https://awesomeopensource.com/project/XaviTorello/mifare-classic-toolkit>, 2017. [Online; accessed 10-May-2021].
- [12] Google Play. MIFARE Classic Tool. <https://play.google.com/store/apps/details?id=de.syss.MifareClassicTool&hl=en&gl=US>, 2021. [Online; accessed 10-May-2021].
- [13] RWTH Aachen University. SteVe. Steve. <https://github.com/RWTH-i5-IDSG/steve>, 2021. [Online; accessed 10-May-2021].
- [14] Wireshark. Wireshark. <https://www.wireshark.org>, 2021. [Online; accessed 10-May-2021].

Concept & requirements for an AI-based automotive HiL-testing system

Roland Schöniger

Institute ProtectIT
Deggendorf Institute of Technology
94469 Deggendorf, Germany
roland.schoeniger@th-deg.de

Karl Leidl

Technology Campus Teisnach
Deggendorf Institute of Technology
94469 Deggendorf, Germany
karl.leidl@th-deg.de

Martin Schramm

Institute ProtectIT
Deggendorf Institute of Technology
94469 Deggendorf, Germany
martin.schramm@th-deg.de

Abstract— Today, cars and other vehicles have become much more than only a way to transport people and goods from one place to another destination. After beginning to aim for more road-vehicle safety in the early 60s with the crumple-zone, the passengers demanded for more comfort and luxury: While today there is touch-screen navigation and driver assisting systems, in the near future, the cars will become more and more automated, with implementation of autonomous or teleoperated driving. But those new features also require more and more interconnected electric control units, communicating not only to each other, but also wirelessly to the outer world. Testing those systems is usually done by hand, script-based or semi-automated, but the complexity leads to an inability for the human to cover all necessary tests, mandatory resulting in a security-issue with risk for the passenger's safety.

This paper provides a requirements analysis and a basic concept for a new hardware in the loop (HiL) testing system to finally help vehicle developers in reducing security issues in their product under development. This product is achieved by using a HiL as an approved automotive testing system, and combining it with a suitable test method, which is improved and automated by implementation of an artificial intelligence system. It is focused for an initial test with a real world teleoperated driving demonstrator, where attacks on the external and internal communication can be tested. Therefore, an analysis of a secure development process based on current standards is an integral part of this concept. An exemplary system of the concept is given.

Keywords— *Artificial intelligence, Automotive Safety, Automotive Security, Automotive, Autonomous Driving, Device under test, DuT, Fuzzing, Hardware in the loop, HiL, ISO 21434, ISO 26262, Penetration Testing, SAE J3061, SOTIF, Standards, SuT, System under Test, Teleoperated driving, Testing, Vulnerability Scanning, deep learning, machine learning;*

I. INTRODUCTION

Current and future road vehicle features, like comfort systems or driver assistance systems up to automation, like teleoperated or autonomous driving, require more and more connectivity of the embedded systems inside and outside of the vehicles. This development from a simple vehicle for transportation, to a convenient, fully interconnected entertainment transport system comes with a strong threat:

The car2x communication, necessary for all kinds of interconnected features, also is a welcome gateway for a new kind of cybersecurity threats to road vehicles. The attacks on the outer communication of cars are increasing rapidly [1].

While attacks on computer systems more often come with a financial risk, the loss or abuse of critical data or technical damages, the impact on road vehicles is the same as in the medicine. In both cases, security weaknesses can cause severe human damage, when safety-relevant systems malfunction. Fortunately, the first alleged death involving a cyberattack on a German hospital turned Germany's health policy awake to increase cybersecurity standards in the health system [2]. The automotive industry has to act similarly, since attacks and tests show the influence towards human safety, like the famous Jeep hack of 2015 [3]. The gear box of an electric Renault Twizy seems unable to prevent i.a. bruteforce attacks, as shown in [4, p. 5].

To keep road vehicles safe, several test methods and processes have been implemented over time. The importance of HiL testing is already described in [5, p. 3] in 2006. The author also demonstrates the difficulty to test every single scenario of applicable variants in the example Scania truck with only 21 electronic control units (ECU) [5, p. 8]. Today's cars offer up to 150 interconnected ECUs [6]. Another influence on driver's safety is the implementation of AI to all kinds of driver assistance systems: [7] shows new safety hazards due to advanced machine learning functions.

Yet, the introduction of AI to modern car functions may not only be a security threat, but also a security chance. To help engineers during the development of new vehicles, this approach aims to introduce a new concept for a HiL testing system. Therefore, a common test method shall be investigated, that is suitable for expansion with AI methods. Also, a secure development process for implementing this concept is investigated, based on modern automotive safety and security standards. An exemplary system, based on a teleoperated driving demonstrator, shows the requirements for implementing this concept inside a HiL.

This paper is structured as follows: Section II outlines the methodology to develop a requirements analysis and a concept for the testing system. Section III describes basic background information as well as other approaches towards automotive testing improvement. In Section IV the different test methods are evaluated. Section V shows a development process based on the current standards in automotive safety and security. In Section VI the technical concept of the HiL testing system will be drawn based on previously gained knowledge with an example setup based on the concept. Finally, Section VII

concludes this paper by evaluating its results with and a short outlook to upcoming research.

Although the example shows a possible implementation of this concept, it is not a target of this paper to define technical details in software or hardware, as those are influenced by details on the tested system. For example, the choice of a specific AI is based on the used protocols in the tested system or the hardware possibilities of the testing system and vice versa.

II. METHODOLOGY

The concept requires a gradual approach, where the focus is laid on three important topics: First, the technical setup of the HiL with this test system inside and the connection to the demonstrator. Second, the most suitable test method in combination with AI and third, the current safety and security standards for a secure development process of the system. To reach this approach, the gradual plan is presented in figure 1 and described in the following:



Fig. 1. Procedure for the concept design

The process shown in figure 1 can be described as follows:

1. Literature Research:

First, a literature research and analysis is necessary to gain basic overview of test methods, development processes, HiL testing and different approaches of automotive testing improvements.

2. (AI-based) Test method evaluation:

Second, based on previous research, a decision matrix is created, where special characteristics in regard to AI-improvability for the test methods can be evaluated. The evaluation results in the final test method for this concept.

3. Automotive safety & security standards analysis:

Third, for investigation of a secure development process for the implementation of this concept, current standards for industrial and automotive safety and security are analyzed. The focus is set to recency (towards new hazards of teleoperated driving) and completeness (in terms of the development process and the coverage of hardware and software components). This shall fill gaps, that classical software-based development processes cannot satisfy.

4. Expert interview:

Fourth, interviews with two suitable automotive suppliers will be given. First, the basics for the teleoperated driving demonstrator have to be set, based on proven and accessible components, providing the necessary protocols for communication that will be attacked.

Second, the integration into a HiL testing system has to be planned, that matches with the demonstrator and provides interchangeable access for either the testing system (with the test method), as well as the demonstrator.

5. Conclusion of HiL testing concept:

Finally, the previous steps will collectively result in a concept for the testing system with an exemplary setup of the components. Since this is a concept, it allows interchangeability of all components and further research and performance comparison.

III. RELATED WORK

To achieve this concept, general information about addressed topics, as well as current research on similar fields need to be explained. Therefore, scientific literature is analyzed.

To meet the requirements for testing the hazards of new automotive features, like autonomous and teleoperated driving, new AI-based driver assistance systems or just comfort systems, an overview over automotive testing in general is necessary. Next, an insight on the teleoperated system to be tested is essential for planning a testing system. Afterwards, the different approved testing methods will be explained and new ideas of combining them with AI methods investigated. Finally, an overview over development processes is given. At the end of each of these topics, the current related work in the automotive sector will be mentioned, to allow a comparison to this work.

A. Hardware in the loop (HiL) testing

HiL testing is a proven concept for testing new hardware components during their development. After its first application in the military for flight simulation and missile guidance system testing 55 years ago [8, p. 3194, 9, 10], it became, among others, a common standard in testing new automotive ECUs. Figure 2 shows the basic structure of a HiL:

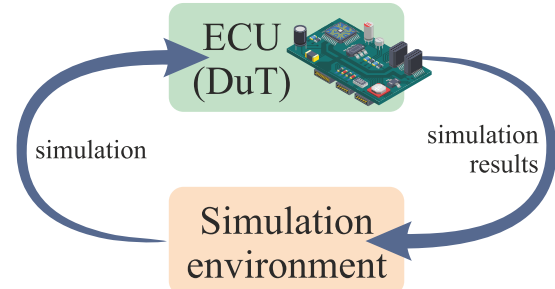


Fig. 2. Classic hardware-in-the-loop setup [11]

The advantage is, that device under development is not tested on mathematical models, but as a real device with its sensors and actors. Therefore, the HiL simulates the outside world of which the device-under-test (DuT) is placed in the final product. The output of the device is also captured by the HiL system, which, in turn, – adapts the simulation output to its new input from the DuT, what resembles the “loop” [8, p. 3194]. The HiL also executes predefined test scripts, usually from a control system outside this HiL. The reaction (output) of the DuT is then examined by the testing system for any anomalies, e.g., producing unwanted output, revealing information or just breaking down. Yet, teleoperated driving reveals additional hazards due to their communication setup.

B. Teleoperated Driving

Although the new concept is planned to be integrated or used for different kinds of vehicles and automatization systems, like autonomous cars, the implementation and evaluation of the concept shall be based on a teleoperated

driving simulator. Teleoperated vehicles are remotely operated by a human. Therefore, a stable, highly encrypted wireless network connection with low latency is necessary [12, p. 18]. Those entities represent three possible attack targets of this system, that need to be tested: Indifferently from the implemented software or hardware basis, delaying [12, p. 18], dropping or manipulating the sent packets of the communication between driver and vehicle, in both directions, needs to be handled properly to avoid safety hazards or comfort issues [13, p. 165]. One solution of reducing safety hazards is through the implementation of minimized autonomous driving functions [13, p. 172], demonstrating the connection between teleoperated and fully autonomous driving. Yet, testing those hazard-avoidance-systems is still a challenge when using common test methods.

C. (Automotive) Testing methods

Before car2x communication for more comfort became important, testing offline vehicles mainly meant testing for vehicle safety. Therefore, each ECU is i.a. integrated in a HiL with an adapted environment and tested accordingly. As test method, a mixture between two testing methods is usual and implemented either by hand, script-based or semi-automated [14]:

With vulnerability scanning, the ECU is tested automatically for known vulnerabilities, or weaknesses, from an existing database, like Mitre CVE for classic IT. The success is influenced by the scope of the database used, whereby specific automotive databases are still in development [15, p. 50]. Yet, even usual databases and tools find vulnerabilities, e.g. in the vehicles WiFi connection [16, p. 246].

Penetration testing is usually executed by a professional security engineer, who knows the weaknesses of the specific system, software, hardware or the used protocols. Yet, it is a predefined and continuous way of testing, divided in the four states of planning, discovery, attack and report [17, p. 37].

Another test method is fuzzing. The testing system sends intentionally invalid or manipulated data to the DuT, so that it takes invalid states, crashes or reveals information unwillingly [18]. In the automotive industry, fuzz testing still is seldomly used, according to a survey [14, p. 4]. This is understandable, since fuzzing is either time-consuming or requires targeted input. [19] automates fuzzing of ECUs with oracle functions.

D. Artificial Intelligence improved testing

Improving test methods with AI becomes more relevant in many fields. Especially the medicine benefits of it, as it reduces costs and enables targeted diagnostic of illnesses [20].

For automotive, ZF developed a so-called AI-in-the-loop HiL system, that allows testing of AI-based ECUs for autonomous vehicles [21]. Also, [22] shows that AI can also be used to improve security of wireless car connections by learning from attacks.

E. Development Processes

There are several development processes available. They all have in common to define a strategy for the development of a product of any kind, while every process has its advantages and drawbacks. In software engineering, examples are, among others, the “Software development life cycle”, the “waterfall model”, or the “V-model”, as well as “SCRUM” or “Prince2” for general project management.

Yet, as most of them are classic software or project management development processes, a security focused development process for the needs of modern automotive features is necessary for this concept. The SAE J3061 [23] from 2016 may be outdated, but introduced a security development process based on the classic V-model, which benefits of risk treatment are discussed in [24]. This encourages to find the answer for this target in current, or newly developed standards.

IV. TEST METHOD EVALUATION

After gaining basic knowledge about HiL testing and test methods in general, as well as the current progress of other studies, one test method has to be chosen. For an evaluation of the test methods towards the planned HiL and the combination with AI, several characteristics have been defined and selected:

A. Comparison Features

- Enhancement:
Can the general deficit of the test method be improved or eliminated by AI?
- Exposure:
Will the usage of AI help to expose new weaknesses?
- Implementability:
How can the AI be added to the test method? How can the test method be implemented in the HiL or adapted to other environments?
- Effectiveness:
How effective is the test method in general for exposing new weaknesses or vulnerabilities?
- Efficiency:
How efficient, in terms of computational time or hardware resources, is the method in general?

B. Test method comparison result

Characteristic	Test method		
	Penetration testing	Vulnerability scanning	Fuzzing
Enhancement	Project-dependent enhancement	Less to none enhancement through AI	Strong enhancement in efficiency
Exposure	Project-dependent exposure	Research shows less chance of exposing new vulnerabilities	Exposure of vulnerabilities in shorter (i.e., realistic) time
Implementability	Project-dependent implementation and AI adaption	Only protocol adaption; less research on AI-combination	Only protocol adaption; many researches on AI-combination
Effectiveness (without AI)	Effective to known & new vulnerabilities & weaknesses	Effective only towards known vulnerabilities	Effective towards new vulnerabilities
Efficiency (without AI)	Project-dependent efficiency	Efficient, working targeted by database input	Time-consuming due to brute-force-like procedure

Fig. 3. Decision matrix for evaluation of test methods

The comparison of all three common test methods in figure 3 shows, that the most benefits are generated by the enhancement of fuzzing with AI. New vulnerabilities can be discovered at a higher rate with the effectivity of fuzzing. The biggest weakness of this method – its efficiency - is reduced by decrease of the test vector and AI-targeted attacks. Fuzzing is comparably simple to implement and to adapt as e.g. penetration testing.

V. SECURE DEVELOPMENT PROCESS

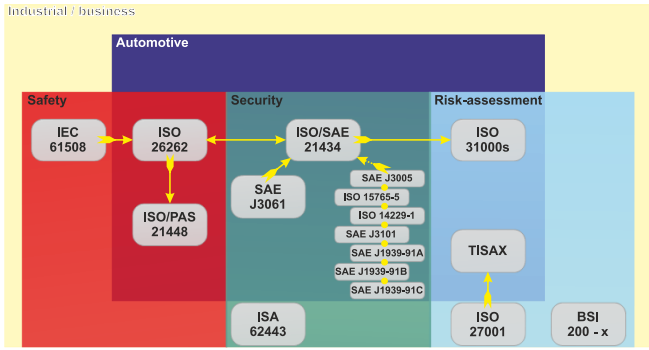


Fig. 4. Relationship of safety and security standards including risk assessment

After evaluation of the test method, the next step is to define a development process, that the implementation of this concept can be realized on. Although most processes are not described by them usually, the solution has been found by analyzing current standards, based on the focus of automotive safety and security during the development process. Figure 4 illustrates an (incomplete) overview of those standards that were analyzed, including the relationship to risk-assessment standards. The arrows illustrate the directions, from where new standards evolved.

The result shows an interaction of one current standard for automotive safety and a still under development standard for automotive security:

A. Automotive Safety

For vehicles, the still up-to-date standard for automotive electric system safety is the ISO 26262:2018 series, which defines functional safety as “the absence of unreasonable risk [...] due to hazards [...] caused by malfunctioning behaviour [...] of E/E systems [...]” [25, p. 14]. An example for this risk is personal damage (hazard) caused by an unintentional explosion (malfunctioning behaviour) of an airbag (E/E system). It is the adapted version of the industrial safety standard IEC 61508 [25, p. vi]. Its distinctive feature is the double-‘V’ development process, which allows parallel development of the system in hardware and software.

However, the conclusions of [7] have to be reconsidered when implementing this model, since machine learning of tested components may negatively influence the possibility to specify the function of those components. This again justifies the implementation of fuzzing, as it reduces the drawbacks of the rigid ISO26262 V-model.

Another remedy for this drawback is the additional usage of the ISO/PAS 21448:2019, currently being converted into the “Standard of the intended functionality” (SOTIF). This standard treats hazards complementary, which result from deviations of the intended function, generated by insufficient performance, misuse, or intended security attacks [26].

B. Automotive Security

Since automotive safety is directly influenced by security [23, p. 17], this concept concentrates more on the security of the vehicle to human interface communication. A still under development standard, the ISO 21434, offers not only the necessary security guidance, but several other benefits. As the direct successor of the SAE J3061, a toolset for modern automotive security, it inherits several features from its predecessor.

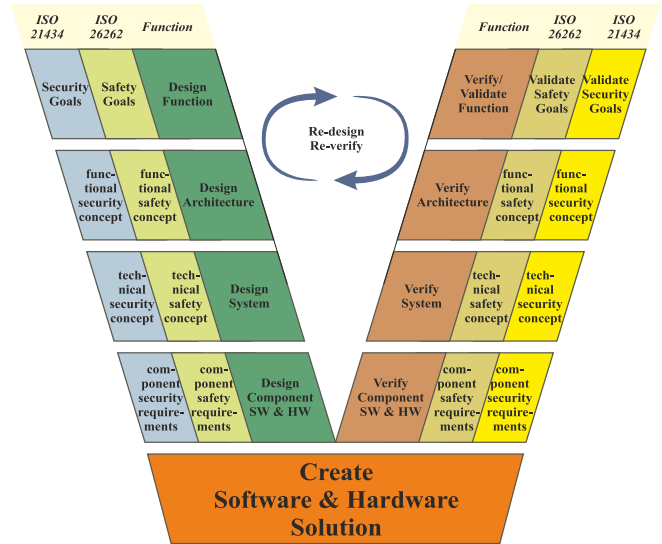


Fig. 5. Cooperation of ISO26262 and ISO21434 development process [27, p. 6]

The most characteristic feature is the retention of the automotive V-development-process of the SAE J3061. The advantage of this model is the strong cooperation through parallel design of the safety and security, as described in [27][28], by a parallel and similar development process of the ISO 21434:2020-2 and the ISO 26262:2018, as shown in figure 5.

The current draft of the ISO 21434:2020-2 closes gaps, that are not considered to this extend by other standards, especially its predecessor. Apart from treating the problems evolving from new autonomous and teleoperated features, as described in A), its development process starts from specifying security standards in the company before project planning and covers the full process to decommissioning. This also includes security requirements towards external suppliers of hardware and software, as needed in this concept. Additionally, continuous verifications of the security requirements and agile adaption to the development, solve the problem of a rigid V-model and ensure up-to-date security at the product finalization.

VI. CONCEPT AND EXAMPLE OF HiL TESTING SYSTEM

With the previous results of the fuzz-testing system and the development according to the ISO 21434:2020-2, the technical specifications can be defined. For the communication with the to-be-examined teleoperated demonstrator and the technical integration of the testing system in the HiL testing environment, interviews with two experts of experienced automotive suppliers result in the following technical concept.

A. Teleoperated driving demonstrator (communication)

For evaluation of the test method, figure 6 shows the basic components of an exemplary demonstrator system. The teleoperation (TeleOp) client is the control unit with monitor, steering and pedals for the human driver. The TeleOp module is inside the vehicle, controlling sensors and actuators. Both are managed through the TeleOp server.

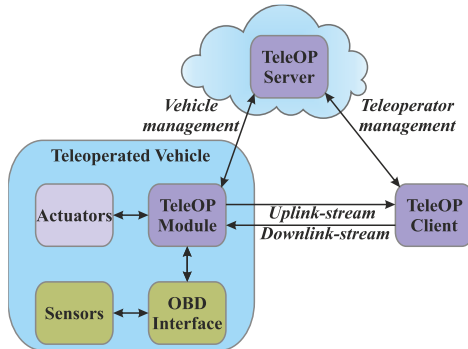


Fig. 6. Teleoperated vehicle demonstration system [29, 30]

As main protocol, the demonstrator communicates using MQTT, as a lightweight protocol for open m2m communication. Furthermore, for video streaming, UDP, TCP and RTP is used. Still, those protocols are sufficient for full demonstration and the MQTT provides fast integration in the HiL.

B. HiL testing platform integration

Setting the HiL-test system up as a system under test (SuT) allows the fuzzer to attack the whole system communication. The possible HiL setup is shown in figure 7. The concept is designed as a man-in-the-middle attack to manipulate communication between TeleOp server and client. Note, that other HiL-typical components, like sensor- and actuator-controls or voltage controls are not pictured for simplification.

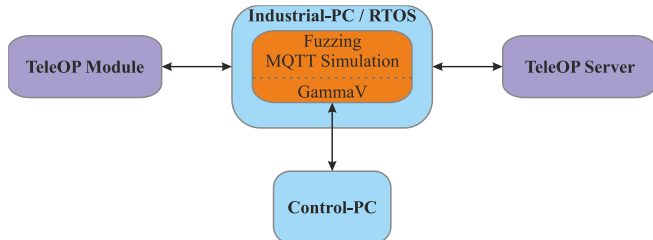


Fig. 7. HiL communication inside SuT [31]

To allow the concept system to be adaptable to other HiL setups or hardware, a middleware is implemented. For this concept, due to further existing integration of external software, like SimuLink [32] for visual preparation, the GammaV middleware is used in the example. On the one hand, it allows different testing systems on the HiL side, on the other, the existing adaption to a tool for designing network simulations is beneficial:

C. Network & protocol simulation

Omnet++, together with its framework inet, allows the reproduction of protocols used in this concept. As a simulation framework for designing networks and network protocols, the simulation or emulation of hardware responses can be implemented, as well as the integration of the GammaV middleware. This allows the fuzzer to be developed or adapted to the requested protocols modularly, without being inside the HiL system.

While figure 7 describes the concept of connecting the testing system (industrial PC) with the HiL, controlled by the control system, figure 8 visualizes the internal flow between GammaV and Omnet++. Information is exchanged through the use of commonly used process variables (PV).

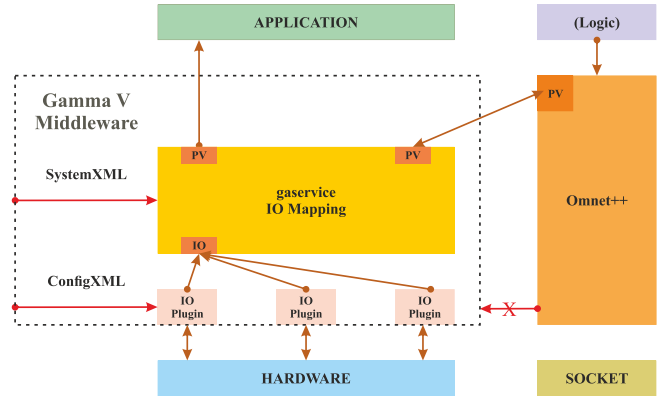


Fig. 8. GammaV communication with HiL and Omnet

D. Fuzzing tool

For the fuzzing tool itself, there are several applications accessible to build on. After research and tests, BooFuzz [33] was selected for satisfying several requirements, that are:

- Extensibility, for integrating and comparing miscellaneous AI-methods and protocol-adaption;
- Network protocol orientation;
- Monitoring features;
- Operational sequences, for building a defined flow of (MQTT) packages and to target the communication of the components in the SuT;
- Logging, for gathering output information;
- Failure detection and failure features, like DuT reset;

For implementation of the fuzzing tool on a hardware, two main aspects have to be kept in mind. Most importantly, the tool has to be installed on a real time operating system (RTOS). Otherwise, the processing of the packets would always have an unpredictable delay, resulting in falsifying the results. Although there are several RTOS available, even some Linux distributions offer real time (RT) features [34]. An example is Debian10 with a RT kernel, allowing a greater bandwidth of existing testing tools to integrate. Second, depending on the choice of the AI, the OS, the testing tool and the output generation of the SuT, the hardware basis for the testing system has to be selected accordingly.

VII. CONCLUSION

This paper treats three of the main consideration factors for defining a new concept of an AI-based HiL testing system. In summary:

- The paper proposes a methodology to design a concept for an AI-improved HiL testing system;
- The systematic comparison of test methods through AI reveals great benefits for fuzzing;
- ISO 21434:2020-2, together with ISO 26262:2018 implements a secure development process for this concept;

- An example of this concept shows a possible implementation for testing of a teleoperated driving demonstrator;

Further work will have to demonstrate the effectiveness of this concept by implementation. Therefore, a selection of one or more AI techniques is necessary, based on the respective protocols, the possible outputs of the demonstration system and the actual performance of the testing system. Another part is the test vector coverage and the risk assessment analysis or final risk evaluation, former especially influenced by the AI decision, which is also treated in the ISO 21434:2020-2.

ACKNOWLEDGMENT

This research work is supported by the research project 16KIS0967 of the funding measure “KMU-innovativ: Informations- und Kommunikationstechnologie (IKT)” of the ministry of education and research.

REFERENCES

- [1] Bundesministerium für Wirtschaft und Energie (BMWi), “Weißbuch Digitale Plattformen: Digitale Ordnungspolitik für Wachstum, Innovation, Wettbewerb und Teilhabe,” 2017. [Online]. Available: <https://www.bmwi.de/Redaktion/DE/Publikationen/Digitale-Welt/weissbuch-digitale-plattformen.html>
- [2] Ärztenachrichtendienst, *Bundestag winkt Digitalgesetz durch*. [Online]. Available: <https://www.aend.de/article/212068> (accessed: May 17 2021).
- [3] A. Greenberg, “Hackers Remotely Kill a Jeep on the Highway—With Me in It,” *WIRED*, 21 Jul., 2015. <https://www.wired.com/2015/07/hackers-remotely-kill-jeep-highway/> (accessed: Dec. 15 2020).
- [4] S. Jafarnejad, L. Codeca, W. Bronzi, R. Frank, and T. Engel, “A Car Hacking Experiment: When Connectivity Meets Vulnerability,” in *2015 IEEE Globecom workshops (GC wkshps): Proceedings : 6-10 December 2015, San Diego, CA, San Diego, CA, USA, 2015*, pp. 1–6.
- [5] M. Adenmark, M. Deter, and T. Schulte, “Testing Networked ECUs in a HiL Based Integration Lab,” in *SAE Technical Paper Series*, 2006.
- [6] Electronic Manufacturing Services - Syrma Technology, *Automotive ECU: The Core Component for Connected Cars*. [Online]. Available: <https://www.syrma.com/ecu/> (accessed: May 16 2021).
- [7] R. Salay, R. Queiroz, and K. Czarniecki, “An Analysis of ISO 26262: Using Machine Learning Safely in Automotive Software,” Sep. 2017. [Online]. Available: <http://arxiv.org/pdf/1709.02435v1>
- [8] M. Bacic, “On hardware-in-the-loop simulation,” in *2005 44th IEEE Conference on Decision and Control & European Control Conference: Seville, Spain, 12 - 15 December 2005*, Seville, Spain, 2005, pp. 3194–3198.
- [9] J.J. S. Cole, “Hardware-in-the-loop simulation at the U.S. Army Missile Command,” in *Proceedings of SPIE*, Orlando, FL, USA, Tuesday Apr. 1996, pp. 14–19.
- [10] M. E. Sisle and E. D. McCarthy, “Hardware-in-the-loop simulation for an active missile,” *SIMULATION*, vol. 39, no. 5, pp. 159–167, 1982, doi: 10.1177/003754978203900503.
- [11] Freepik - macrovector, *Circuit board isometric concept*. [Online]. Available: https://www.freepik.com/free-vector/circuit-board-isometric-concept_4027496.htm#page=1&query=hardware&position=17 (accessed: May 17 2021).
- [12] T. Tang, F. Chucholowski, and M. Lienkamp, “Teleoperated driving basics and system design,” *ATZ Worldw.*, vol. 116, no. 2, pp. 16–19, 2014, doi: 10.1007/s38311-014-0018-1.
- [13] A. Hosseini and M. Lienkamp, “Predictive safety based on track-before-detect for teleoperated driving through communication time delay,” in *2016 IEEE Intelligent Vehicles Symposium (IV): 19-22 June 2016, Gotenburg, Sweden, 2016*, pp. 165–172.
- [14] H. Altinger, F. Wotawa, and M. Schurius, “Testing methods used in the automotive industry: results from a survey,” in *Proceedings of the 2014 Workshop on Joining AcadeMiA and Industry Contributions to Test Automation and Model-Based Testing*, San Jose, CA, USA, 2014, pp. 1–6.
- [15] T. Brennich and M. Moser, “Putting Automotive Security to the Test,” *ATZ Electron Worldw.*, vol. 15, 1-2, pp. 46–51, 2020, doi: 10.1007/s38314-019-0155-9.
- [16] E. F. M. Josephlal and S. Adepu, “Vulnerability Analysis of an Automotive Infotainment System's WiFi Capability,” in *2019 IEEE 19th International Symposium on High Assurance Systems Engineering (HASE)*, Hangzhou, China, Jan. 2019 - Jan. 2019, pp. 241–246.
- [17] Murugiah Souppaya and Karen Scarfone, *Technical Guide to Information Security Testing and Assessment*: Special Publication (NIST SP), National Institute of Standards and Technology, Gaithersburg, MD. [Online]. Available: https://tsapps.nist.gov/publication/get_pdf.cfm?pub_id=152164
- [18] M. Sutton, A. Greene, and P. Amini, *Fuzzing: Brute Force Vulnerability Discovery*: Pearson Education, 2007.
- [19] T. Werquin, M. Hubrechtsen, A. Thangarajan, F. Piessens, and J. T. Muehlberg, “Automated Fuzzing of Automotive Control Units,” Feb. 2021. [Online]. Available: <https://arxiv.org/pdf/2102.12345>
- [20] F. Cismondi *et al.*, “Reducing unnecessary lab testing in the ICU with artificial intelligence,” *International journal of medical informatics*, vol. 82, no. 5, pp. 345–358, 2013, doi: 10.1016/j.ijmedinf.2012.11.017.
- [21] Oliver Maschmann, “AI-in-the-Loop: Neues Testsystem zur Validierung eines autonomen, KI-basierten Fahrzeugs mittels realistischer Sensorsimulation,” ZF Friedrichshafen AG, 2019. [Online]. Available: <https://www.dspace.com/de/gmb/home/applicationfields/stories/zf-ai-in-the-loop.cfm>
- [22] P. Sharma, H. Liu, H. Wang, and S. Zhang, “Securing wireless communications of connected vehicles with artificial intelligence,” in *2017 IEEE International Symposium on Technologies for Homeland Security (HST): The Westin-Hotel Waltham-Boston, Waltham, MA, April 25-26, 2017*, Waltham, MA, USA, 2017, pp. 1–7.
- [23] C. Inman, “SAE J3061 - Surface Vehicle Recommended Practice 2016-01 2414921,” 2016.
- [24] C. Schmittner, Z. Ma, C. Reyes, O. Dillinger, and P. Puschner, “Using SAE J3061 for Automotive Security Requirement Engineering,” in *Lecture notes in computer science Programming and software engineering*, vol. 9923, *Computer safety, reliability, and security: SAFECOMP 2016 Workshops, ASSURE, DECSoS, SASSUR, and TIPS, Trondheim, Norway, September 20, 2016: proceedings*, A. Skavhaug, Ed., Cham, Heidelberg: Springer, 2016, pp. 157–170.
- [25] *ISO 26262-01:2018: Vocabulary*, 1, Internationale Organisation für Normung, 2018.
- [26] Heicon Ulm, *ISO 21448 – SOTIF! Wo ist der Mehrwert? - Heicon Ulm*. [Online]. Available: <https://heicon-ulm.de/iso-21448-safety-of-the-intended-functionality-sotif-wo-ist-der-mehrwert/> (accessed: May 15 2021).
- [27] M. Skoglund, F. Warg, and B. Sangchoolie, *In Search of Synergies in a Multi-concern Development Lifecycle: Safety and Cybersecurity*: Springer International Publishing, 2018.
- [28] Barbara Galina, Muhammad Atif Javed, Helmut Martin, and Robert Bramberger, “Co-engineering of security and safety life-cycles for engineering security-informed safety-critical automotive systems in compliance with SAE J3061 and ISO 26262,” *24th International Conference on Reliable Software Technologies*, 2019. [Online]. Available: <https://graz.pure.elsevier.com/de/publications/co-engineering-of-security-and-safety-life-cycles-for-engineering>
- [29] Freepik - alliesinteractive, *Download Set Of Twelve Different Clouds On Blue Background. for free*. [Online]. Available: https://www.freepik.com/free-vector/set-twelve-different-clouds-blue-background_1149278.htm (accessed: May 16 2021).
- [30] Nicolas Gay, Burhan Yenidede, and Hatice Genc, “Teleoperated System Specification,” Luxoft, 2021. Accessed: May 16 2021.
- [31] iSyst GmbH, Ed., “Zwischenbericht SHORT: Security-Centered HiL-Plattform Offering Risk-aware Testing,” iSyst GmbH, 2021.
- [32] iSyst GmbH, *iSyst GmbH: GammaV-Blockset*. [Online]. Available: <https://www.isyst.de/de/produkte/testkomponenten/gammav-blockset/> (accessed: May 12 2021).
- [33] *boofuzz: Network Protocol Fuzzing for Humans — boofuzz 0.3.0 documentation*. [Online]. Available: <https://boofuzz.readthedocs.io/en/stable/> (accessed: May 15 2021).
- [34] J. Altenberg, “Echtzeit mit Linux,” *Embedded Software Engineering*, 18 Apr., 2019. <https://www.embedded-software-engineering.de/echtzeit-mit-linux-a-632464/> (accessed: May 15 2021).

A Calibration Workflow for 3D Beamforming Radar for Integrated Vehicle Safety Systems

Fatih Sezgin

CARISSMA Institute of Safety in Future Mobility

Technische Hochschule Ingolstadt

Germany, Ingolstadt

Email: Fatih.Sezgin@carissma.eu

Abstract—To increase the safety of road users, robust environment perception is essential. Radar plays an important role in this. Recent developments enable radars to provide high-resolution detection and height estimation. To ensure proper environment perception, the antennas must be calibrated. This paper presents an accuracy analysis focusing on azimuth and elevation estimation, a calibration method based on 16 measurements, and a method for observing accuracy over time. On the calibration side, the aim is to improve an existing simple calibration. Using the proposed method, systematic errors resulting from the calibration parameters were reduced by an average of 68.5% for azimuth angle estimation and 51.1% for elevation estimation. A generalization test with two different targets was also performed. Finally, the position estimation was conducted with an extended object, a pedestrian, to evaluate whether the results are plausible and applicable to real objects.

I. INTRODUCTION

According to the World Health Organization, traffic accidents are the number one cause of death for people between the ages of 5 and 29, with approximately 1.35 million deaths per year [1]. The goal of automotive safety systems is to reduce these numbers until Vision Zero is achieved. To accomplish this, these systems must evolve and new approaches must be found to successfully improve vehicle safety. Here we consider three categories in automotive safety. The first are active safety systems, which try to avoid the accident [2]. The second are passive safety systems. Here, after an accident, attempts are made to minimize the severity of the accident [2]. The final category is integrated vehicle safety, which combines the two previously mentioned. In a pre-crash scenario, these systems predict whether an accident is avoidable or not. If not, passive safety systems are activated at the optimal time to maximize the protection of vehicle occupants and vulnerable road users (VRUs) [2]. Robust environmental awareness is necessary to ensure fully functional prediction. Cameras, LiDAR, and RADAR are commonly used in these systems. These sensors have different advantages and disadvantages. To take advantage of each, a fusion of all three would be beneficial. Radars play an important role in such systems because they operate on a physical principle that leads, among other aspects, to robustness in adverse weather conditions [3]. Recent developments in radar technology enable high-resolution perception and even height estimation [4]. For proper operation, radars, like other sensors, require calibration of their antennas. Due

to manufacturing tolerances, they are calibrated before use. If calibration is not performed, inaccuracies or errors in detection can occur. Besides manufacturing tolerances, aging, hardware errors and temperature drift must also be compensated [5]. This means that it is possible that a radar may need to be calibrated more than once in its lifetime. In [5], a self-calibration method is proposed. The authors used a T-array radar. After a fast Fourier Transform of each transmitter (TX) receiver (RX) combination the unknown target is extracted from the Range spectrum. Then the mean over all signal amplitudes is calculated to estimate the incorrect amplitude gain of each RX-TX combination. Then the error-free phases are estimated with the help of least squares. In [6], the realization of direction of arrival is described and a calibration method is presented. The calibration is performed with a point like calibration object, which circles around the radar, so that a angle dependent measurement is conducted to determine the phase term. In [7] the calibration is done using a reference measurement with a corner reflector and a measurement with more targets. In [8] a method for array calibration is shown. As target, a corner reflector is used. It is placed at an azimuth angle of zero degrees and the calibration parameters are determined. In this article a two step calibration workflow using a Levenberg-Marquardt optimization method is presented. This workflow uses a total of 16 measurements with known positions to estimate and optimize the calibration parameters. The first step is the initial calibration based on the approach of [8] and the second step is the optimization to achieve the final calibration. A test protocol with a smaller number of measurements to observe how the accuracy of a radar sensor changes over time and to check if a new calibration is needed is also presented. This paper is organized as follows. In the second chapter, the materials and methods are presented. Here is shown how the measurements were done, how the signal processing is carried out, which steps are involved in the calibration, and how the results are collected. In the third chapter the results are presented, interpreted and discussed. In the last chapter a short conclusion and an outlook is given.

II. MATERIALS AND METHODS

A. Measurement Setup

The measurements were performed with three sensors simultaneously, a radar, a LiDAR and a camera. The radar is

a RadarLog from the manufacturer INRAS. The front end used has 2 differently polarized transmit antennas and 16 receive antennas. These are vertically polarized, serially fed patch antennas set up as a Uniform Linear Array (ULA). In our measurements, we used only the vertically polarized transmit antenna. The antennas are shown schematically in Figure 1. The first 12 receiving elements are used for azimuth angle estimation and the last 5 for height estimation. The 12th antenna is used in both cases. The configuration of the radar can be seen in Table I. The LiDAR is an Ouster OS1 with 128 lines. The camera used is a Chameleon 3 from FLIR and has a resolution of 1080 x 720 pixels, 8 bits and 45 fps. In the first series of measurements, ground truth data was obtained using a total station with millimeter accuracy. In the second, LiDAR was used for this purpose.

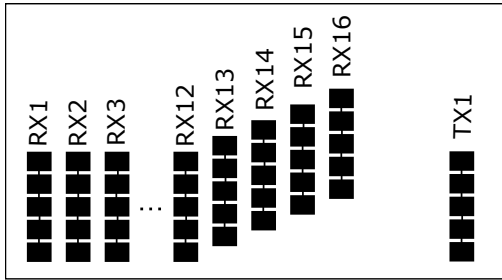


Figure 1. Schematic representation of the antennas

Table I
CONFIGURATION OF THE RADAR

Parameter	Value
Center frequency	77 GHz
Bandwidth	3 GHz
Range resolution	0.05 m
Sampling frequency	10 MHz
Chirp duration	51.2 μ s
Samples per chirp	512
Chirp repetition interval	60 μ s
Sensor height	0.35 m
Azimuth 3 dB beam width (TX)	51°
Azimuth 3 dB beam width (RX)	76.5°
Elevation 3 dB beam width (TX)	13.2°
Elevation 3 dB beam width (RX)	12.8°

B. Measurements

All measurements were conducted at the test and measurement center CARISSMA of the Technische Hochschule Ingolstadt. Two series of measurements were carried out with two triple reflectors of different sizes and different methods of ground truth determination. The height of the targets was 50 cm and remained the same. The target positions can be seen in Figure 2. The target was positioned on the circles for each measurement. In addition, a measurement was made with 0 degrees in azimuth and elevation, preferably at a known distance, resulting in a total of 16 measurements. A known distance gives the opportunity to check if the correct target is used for calibration in environments with other objects. The reason for two different sized targets and different methods of

determining ground truth was that this creates the opportunity for comparison and also a generalization test. The first test was performed with a 3D-printed triple reflector with a side length of 8 cm and sprayed with copper spray, and a ground truth determination with the total station. The second was done with a triple reflector, which has a side length of 12 cm and the LiDAR was used to get the ground truth data.

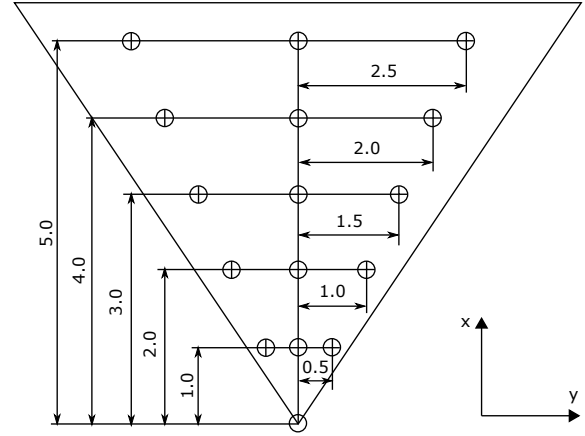


Figure 2. Positions of the Target. Values are in meters

C. Signal Processing

1) Radar

After receiving, mixing and filtering the reflected signals with a low-pass filter, the intermediate frequency (IF) signal is obtained. Since the target and sensors are static, only range processing with fast Fourier transform (FFT) is performed. Then the Burg algorithm is used to calculate the azimuth and elevation angles. The Burg algorithm results in improved spectral resolution in comparison to a discrete Fourier Transform (DFT) [9], [10]. This step results in two power spectral densities from which the positions with maximum intensities are extracted. The first spectrum is obtained from the first 12 antennas and the second with the last 5. With them the data point originating from the triple reflector with its Cartesian coordinates is calculated.

2) LiDAR and Camera

The LiDAR and camera data are recorded using Robot Operating System (ROS). After the measurements are taken, the data are stored in rosbag files. During signal processing, these are replayed and the LiDAR point clouds and camera images are generated. The LiDAR point clouds are then filtered with an intensity threshold to obtain only the data points that are reflected from the actual target. To simplify this, circular reflectors were attached to the corners of the target to make them appear distinct from the other objects in the environment due to their high reflectivity. The camera images are used in the event that unwanted radar detections occur to verify where they originated.

D. Accuracy Analysis

After the data was processed and all positions were estimated, an accuracy analysis was performed. The error between

the radar detections and the ground truth data was determined. This analysis showed a systematic error in our radar data. The data points were shifted to the right in azimuth. The error increased with increasing distance. Large errors in elevation estimation were also observed in this analysis. These radar detections and ground truth data are shown in Fig. 3 and 4 using the data from the first series of measurements. Similar observations were made with other radar sensors. The explanation is an outdated or an inaccurate calibration of the antennas. In addition, it is important to mention that the parameters used in the calibration must be the same as those used in the subsequent measurements.

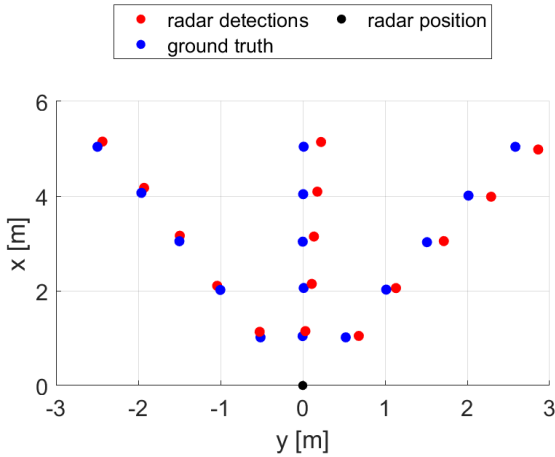


Figure 3. Estimated x-y positions of the target with the original calibration

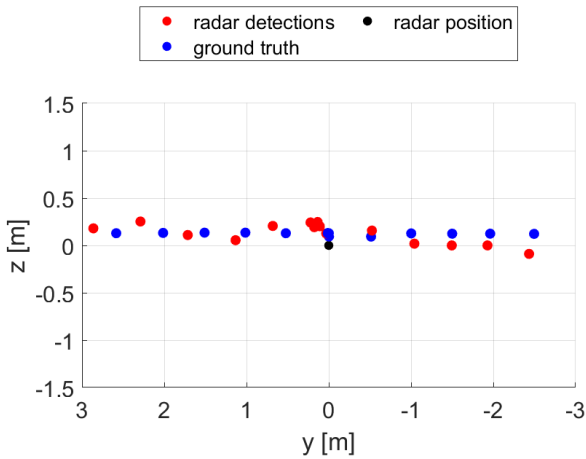


Figure 4. Estimated z-y positions of the target with the original calibration

E. Calibration Workflow

To improve the calibration a workflow (Fig. 5) was developed based on the 16 measurements mentioned in the previous chapters.

Due to the different length of the conduction paths, the gain and phase of the antennas have to be corrected. This

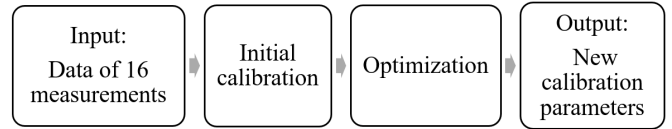


Figure 5. The calibration workflow

is done by estimating a parameter for each receiving antenna. These parameters have complex values. The first step is to make an initial calibration estimate based on the measurement where the target has zero azimuth and elevation angle and a known distance. The known radial distance is used to verify that the correct target is used in the optimization since there may be other objects in the environment. This step is based on [8]. The second step is to optimize the estimated parameters using a Levenberg-Marquardt optimization algorithm. The optimization settings used can be found in Table II. The entire radar signal processing is used as the objective function. The radar points are generated from the 15 measurements and the average deviation from the ground truth data is calculated. The last calculated value is the error to be optimized. This step is performed at each iteration of the optimization algorithm. To fully optimize the calibration parameters, the real and imaginary units were split before they were entered into the objective function. The reason for this is that the objective function only outputs a real value and therefore without this separation only the real units are optimized. In the last step, the accuracy is analyzed and the calibration file and the errors with their standard deviations are saved.

Table II
OPTIMIZATION SETTING

Parameter	Value
finite difference step size	0.2
step tolerance	0.2
function tolerance	0.2

F. Test Protocol

To check if the radar needs a new calibration at a later stage, a test protocol was developed (Fig. 6). Four new measurements are required for this. Therefore, the target is positioned at the 3 positions at a distance of 5 m as shown in Fig. 2 and on the middle position with an x-distance of 4 m. The error to the ground truth data is determined and the results are compared to the errors stored after calibration. High deviations indicate that a new calibration is necessary.

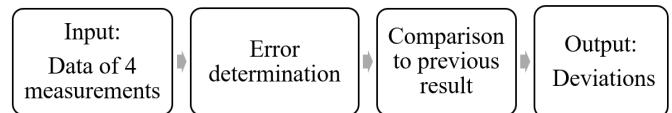


Figure 6. Test protocol

III. RESULTS AND DISCUSSION

In this chapter the results of the initial estimates and final optimizations of the calibration are presented and interpreted. After the initial estimation of the calibration parameters, the shift of the azimuth angle of the target positions is largely corrected. This can be seen in Fig. 7. The data visualized here is from the first measurement series. The positions of the data points on the left side show a shift to the left. The data points directly in front of the radar and on the right side are more aligned with the ground truth data. Fig. 8 shows the result of the first estimation from a perspective where the elevation information of the data points can be seen. Although the errors have become smaller here, there are still differences to the ground truth data. To improve the first estimate, a refinement of the calibration parameters is performed in the next step.

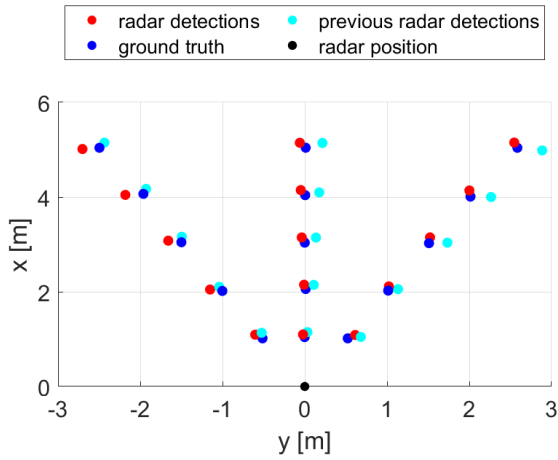


Figure 7. Estimated x-y positions with the initial calibration

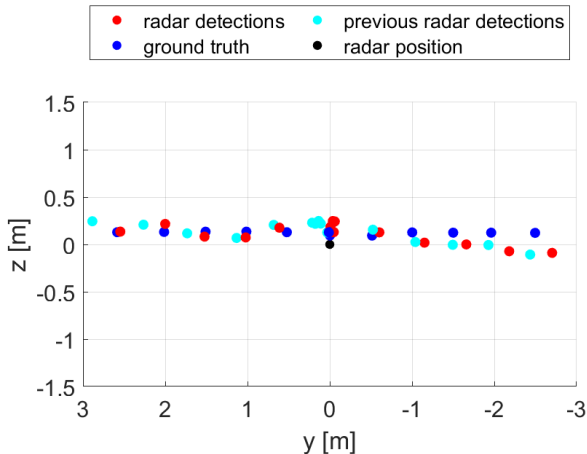


Figure 8. Estimated z-y positions with the initial calibration

After performing the optimization, Fig. 9 shows that the deviation of the data points from the ground truth data has decreased again and that there is no longer a significant shift.

The error in the height estimate has also been reduced, as shown in Fig. 10.

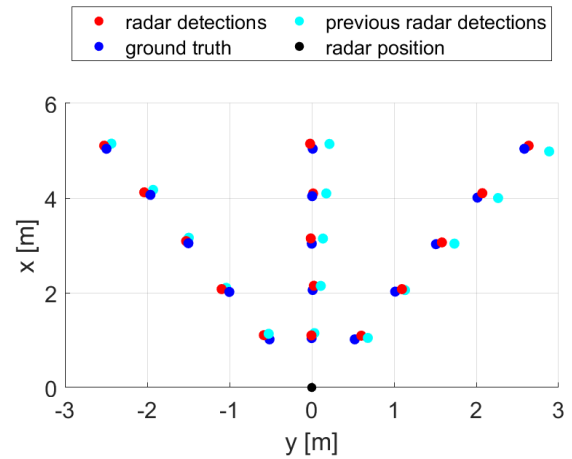


Figure 9. Estimated x-y positions of the target with optimized calibration

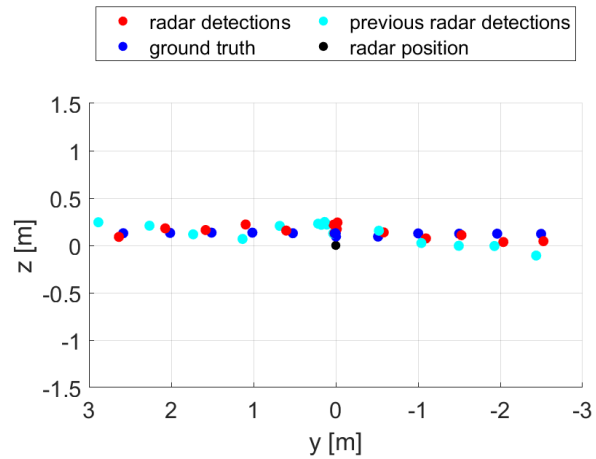


Figure 10. Estimated z-y positions of the target with optimized calibration

In Fig. 11 the errors and standard deviations of the individual steps are visualized for both series of measurements. The data annotated with "Original" originated from the processing with the calibration data received from the manufacturer, the data labeled with "Initial" was received after the initial estimation and "Optimized" is the final result. For comparison, the results obtained with the two different triple reflectors are shown. It can be seen that similar results were obtained with the data from the second series of measurements. After performing the presented workflow, the error was reduced by an average of 68.5% in azimuth and 51.1% in elevation. Table III shows the mean absolute errors and standard deviations obtained after each step of the workflow for both targets.

A. Generalization Test

To test the generalizability of the optimized calibration parameters, the calibration performed with the first target was

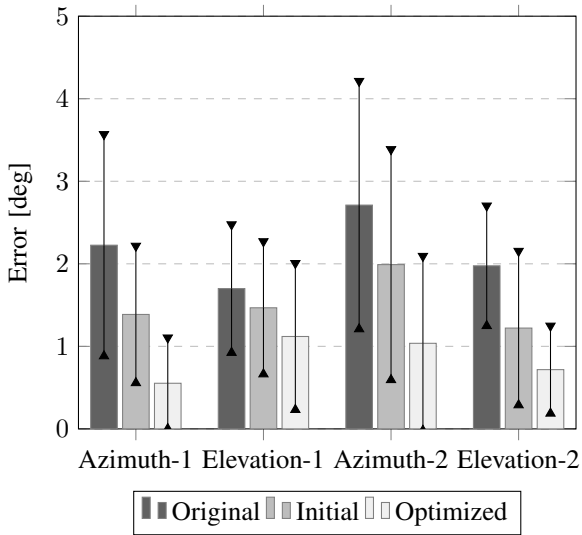


Figure 11. Comparison of the results achieved with both measurement series

Table III
ERRORS AND STANDARD DEVIATIONS RECEIVED AFTER THE INDIVIDUAL STEPS FOR BOTH TESTS

Parameter [deg]	Original	First Estimation	Optimized
Azimuth-1	2.2 ± 1.3	1.4 ± 0.8	0.6 ± 0.5
Elevation-1	1.7 ± 0.8	1.5 ± 0.8	1.1 ± 0.9
Azimuth-2	2.7 ± 1.5	2.0 ± 1.4	1.0 ± 1.0
Elevation-2	2.0 ± 0.7	1.2 ± 0.9	0.7 ± 0.5

tested with the second. In Fig. 12 and Fig. 13, the final position estimate, the ground truth data, and the estimate with the original calibration can be seen. Again, the rightward shift in the azimuth angle estimate was corrected. The elevation error was also reduced.

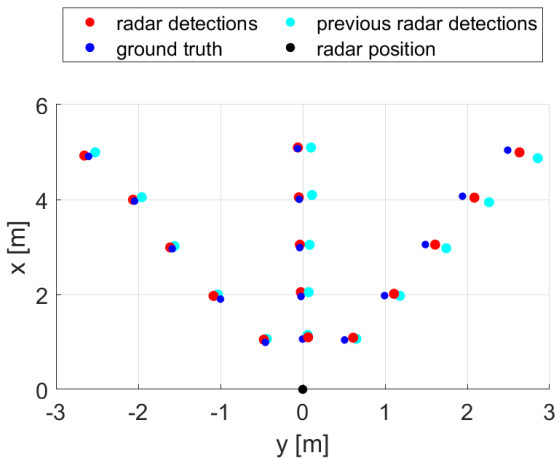


Figure 12. Estimated x-y positions of target 2 with the calibration done with target 1

The errors and standard deviations of the individual steps of the calibration and the test result with the other target are shown in Fig. 14. The error of azimuth angle estimation

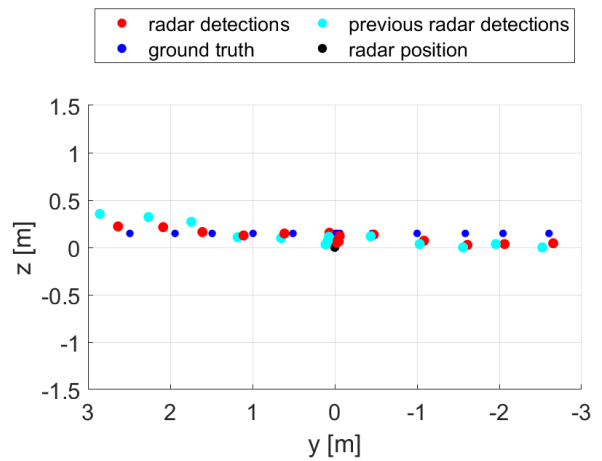


Figure 13. Estimated z-y positions of target 2 with the calibration done with target 1

remained stable in the test after optimization with a difference of 0.05 degrees which is a difference of 4.6%, but the error of elevation estimation increased by 0.4 degrees (56.6%). The result in numbers for both angles is shown in Table IV. Certain inaccuracies in the height estimation are to be expected due to the small number of elevation antennas.

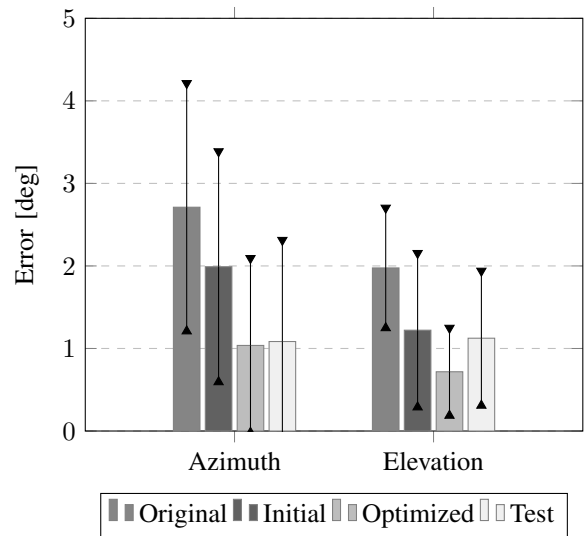


Figure 14. Comparison of the estimations of the generalization test

Table IV
ERRORS AND STANDARD DEVIATIONS RECEIVED AFTER THE GENERALIZATION TEST

Parameter [deg]	Error
Azimuth	1.1 ± 1.2
Elevation	1.1 ± 0.8

B. Test with an Extended Object

The last test was performed with an extended target, a pedestrian. Since the calibration is performed with point targets, it was necessary to evaluate the results with a target that is an actual road user. Figure 15 shows two point clouds obtained from the test object. The one on the left was generated using the radar manufacturer's original calibration and the one on the right was generated using the optimized calibration parameters. It can be seen that there are no anomalies in the shape of the resulting point cloud and that the pedestrian remains recognizable and the information plausible after applying the presented calibration method.

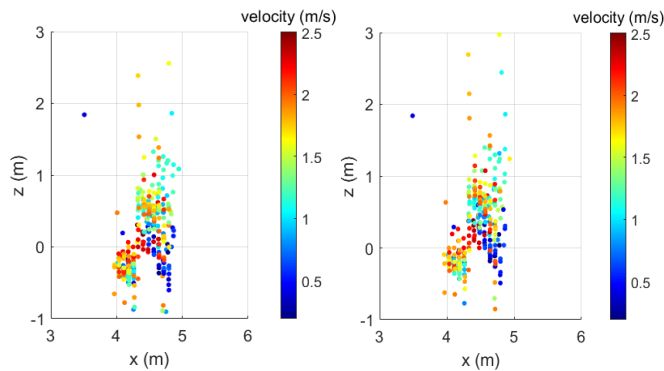


Figure 15. radar point cloud originated from a walking pedestrian with both feet on the ground estimated with the original calibration (left) and with the new optimized calibration (right)

IV. CONCLUSION

In this work a calibration workflow that requires a total of 16 measurements was presented and was tested with two different point targets. Generalizability was also investigated with two different sized triple reflectors for optimization and testing. The final test was performed with an extended target, a pedestrian, which shows that the calibration results are plausible. To show how the individual steps of the workflow impacted the data, the results of each step were also presented. In addition, a test protocol was also shown to help monitor the calibration over time to see if a new calibration is needed. The accuracy analysis and the calibration of the radar is an important step towards a radar-camera sensor fusion. Tests with different heights and targets, for example with cars, will also be performed in future.

ACKNOWLEDGMENT

The author would like to thank the test engineers of CARISSMA for their help in conducting the measurements and the Bavarian Research Foundation (Bayerische Forschungsstiftung) for funding of the SAVE ROAD research project under the grant number AZ-1355-18.

REFERENCES

- [1] *Road traffic injuries*, <https://www.who.int/news-room/fact-sheets/detail/road-traffic-injuries>, Accessed: 2021-04-11.

- [2] M. Botsch and W. Utschick, *Fahrzeugsicherheit und automatisiertes Fahren: Methoden der Signalverarbeitung und des maschinellen Lernens*. Carl Hanser Verlag GmbH & Co. KG, 2020.
- [3] Z. Wang, Y. Wu, and Q. Niu, "Multi-sensor fusion in automated driving: A survey," *IEEE Access*, vol. 8, pp. 2847–2868, 2020. DOI: 10.1109/ACCESS.2019.2962554.
- [4] J. Gamba, *Radar Signal Processing for Autonomous Driving*. Springer Nature Switzerland AG, 2020.
- [5] M. Harter, J. Hildebrandt, A. Ziroff, and T. Zwick, "Self-calibration of a 3-d-digital beamforming radar system for automotive applications with installation behind automotive covers," *IEEE Transactions on Microwave Theory and Techniques*, vol. 64, no. 9, pp. 2994–3000, 2016. DOI: 10.1109/TMTT.2016.2593731.
- [6] C. Vasanelli, F. Roos, A. Durr, J. Schlichenmaier, P. Hugler, B. Meinecke, M. Steiner, and C. Waldschmidt, "Calibration and direction-of-arrival estimation of millimeter-wave radars: A practical introduction," *IEEE Antennas and Propagation Magazine*, vol. 62, no. 6, pp. 34–45, 2020. DOI: 10.1109/MAP.2020.2988528.
- [7] J. Guetlein, A. Kirschner, and J. Detlefsen, "Calibration strategy for a tdm fmcw mimo radar system," in *2013 IEEE International Conference on Microwaves, Communications, Antennas and Electronic Systems (COMCAS 2013)*, 2013, pp. 1–5. DOI: 10.1109/COMCAS.2013.6685266.
- [8] R. Feger, C. Wagner, S. Schuster, S. Scheiblhofer, H. Jager, and A. Stelzer, "A 77-ghz fmcw mimo radar based on an sige single-chip transceiver," *IEEE Transactions on Microwave Theory and Techniques*, vol. 57, no. 5, pp. 1020–1035, 2009. DOI: 10.1109/TMTT.2009.2017254.
- [9] S. de Waele and P. M. T. Broersen, "The burg algorithm for segments," *IEEE Transactions on Signal Processing*, vol. 48, no. 10, pp. 2876–2880, 2000. DOI: 10.1109/78.869039.
- [10] P. Held, D. Steinhauser, A. Koch, T. Brandmeier, and U. T. Schwarz, "A novel approach for model-based pedestrian tracking using automotive radar," *IEEE Transactions on Intelligent Transportation Systems*, pp. 1–14, 2021. DOI: 10.1109/TITS.2021.3066680.

Development and commissioning of a component test bench for the operation of electrical machines used in EPS Applications

Okan Tunc
Munich University of Applied Science
Faculty of mechanical engineering
Munich, Germany
okan.tunc@hm.edu

Abstract—In this paper a brief overview of the acoustic behavior of permanent magnet synchronous motors and different test bench configurations will be given. This overview is followed by a test bench design approach for the operation of electrical machines, used in electric power steering applications. The test bench design will be investigated in terms of natural frequencies, to prepare the test bench for later acoustic measurements. After that the findings from the first test runs of the test bench are presented.

Keywords—NVH, acoustics, PMSM, EPS, power steering, structure-borne sound, natural frequency, active noise cancellation, test bench

I. INTRODUCTION

The increasing number of electrified or partial electrified powertrains of modern passenger cars is leading to new acoustic challenges. Operation without an internal combustion engine or an operation with the combustion engine switched off results in quieter passenger compartments, so that smaller sound sources from auxiliary units come to the foreground or noise from auxiliary units that were previously masked by the sound of the combustion engine become audible. Usually these noise sources were not part of an acoustic sound design process, resulting in a rather poor sound experience for the passengers. Auxiliary units such as the electric power steering system – EPS – use permanent magnet synchronous motors – PMSM – to deliver the needed assistance ratio for the steering system and thus contribute to the problem. In order to be able to analyze electrical machines in a laboratory environment, a test bench is required for operation. In this paper a brief overview of the acoustic behavior of electrical machines will be given, followed by a summary of different possible test bench configurations. After that the design and construction of a new test bench for use in laboratory environments will be presented. Finally, the results will be discussed and an overview of future work will be given.

II. CONTEXT

A. Acoustic behavior of electrical machines

Based on their generation mechanisms, the noises of electric motors can be divided into three groups: mechanical, aerodynamic and magnetic. The dynamic magnetic field forces, which are supported in the air gap between the rotor and the stator and are radiated as structure-borne noise via the motor housing, are decisive for the generation of noise, regardless of the motor design. In PMSM, a rotating field is generated by the winding in the stator of the motor. The induction of this magnetic field causes the previously mentioned dynamic forces in the air gap of the motor, which

are radiated as structure-borne noise via the motor housing. The alternating forces can generate dynamic torque components which cause vibration excitation of the structures coupled to the rotor [1].

B. Test bench configurations

Simple test stand configurations consist of a drive machine or the test specimen, a sensor system for measured quantity acquisition, and a resistance machine for generating counter torques. Shafts of electrical machines and measuring devices are connected via couplings. As an alternative to the resistance machine, hysteresis brakes or rotational impedances can be used to apply counter or resistance torques. Figure 1 shows a typical configuration of a component test bench.

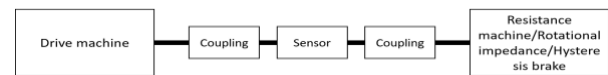


Fig. 1. Simple test bench configurations

Resistance machines have established themselves due to their good controllability. Additional advantages are the possible operation in positive and negative direction of rotation, as well as the possible drive operation of the test specimen in addition to the braking operation. The advantage of generator operation of the resistance machine is the generation of electrical energy, which can be fed into the power grid. Thus, a smaller amount of thermal energy must be dissipated [1][2].

III. TEST BENCH DESIGN

In order to be able to investigate the acoustic properties of the PMSM, a test bench for operating the motor is required. For this configuration with a drive and resistance machine, to deliver the needed resistance torque, was chosen. Figure 2 shows the schematic view of the planned test bench.



Fig. 2. Schematic view of the test bench

The test bench requires mountings for the machines and sensors for the measurement of parameters that are of interest. The test bench to be developed is to be commissioned in the laboratory for electrical machines at Munich University of Applied Sciences. It will be operated on the machine bed that is available there. The sensor that should be used is a two-range torque sensor type 4503A from Kistler mounted on a prefabricated mounting. Since the maximum torque of the

electric machine is 9.9 Nm, a sensor with a measuring range of up to 10 Nm is selected [1]. The distance of the rotation axis of the torque sensor, on the mounting, to the floor measures approximately 113 mm. The rotation axis of the electric motor must be aligned with the rotation axis of the sensor. Therefore the distance of the rotation axis of the PMSM to the floor is chosen with 115 mm to create tolerances. If the rotation axis of the sensor is too low, the distance between the axes can be readjusted with spacers under the sensor mounting. Clamping irons are used to hold the mountings of the two PMSM and the torque sensor in place. The motor mounting needs a base plate with sufficient surface for the clamps to secure the mounting on the machine bed. At the same time, a mounting plate on which the motor is attached is required. In order to reduce the use of materials and costs, the components are made of separate steel plates and connected by screw joints. To ensure stability, side plates are also required to connect the base plate and the mounting plate. To enable torque transmission from the shaft of the motor to the torque measuring shaft, couplings are used. In this case, balanced bellows couplings of type BKC15 from R+W were installed. The high torsional spring stiffness of the couplings results in higher natural frequencies of the test bench [1]. The torque measurement shaft can be used to measure the static and dynamic torque of the PMSM. Figure 3 shows the complete test bench as a 3D model.

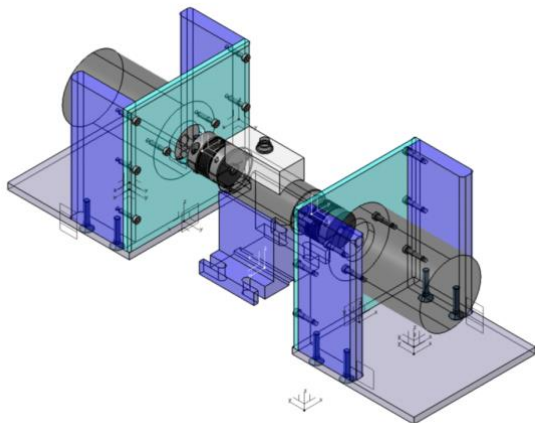


Fig. 3. Overview of the test bench as a .CATproduct

To minimize the influence of the test bench on future measurements, it is essential that the excitation frequencies during operation do not meet the natural frequencies of the overall test bench to avoid resonance effects. Otherwise resonance effects might falsify the results, making them unusable, or could prevent meaningful measurements from being made in the first place [3][4]. The natural frequencies will be simulated in the first step. In the second step, after the manufacturing process, the natural frequencies will be measured with an impulse hammer and evaluated with a special evaluation software.

IV. DETERMINATION OF THE NATURAL FREQUENCIES

A. Simulation

The simulated modal analysis is executed with Ansys. A fixed bearing is selected as the bearing condition. Since the motor holder fixes the base plate to the machine bed via clamps, the base plate is defined as a fixed bearing in Ansys. The calculation results are shown in tabular form and as a diagram, as shown in Figure 4.



Fig. 4. Calculation results

Figure 5 below shows the total deformation of the motor mount at the first two natural frequencies. Areas marked in red represent areas with particularly large deformation, while areas marked in blue represent areas with particularly small deformation. The darker the color, the larger or smaller, depending on the color, is the deformation. As the base plate was defined as a fixed bearing in the bearing conditions, there is no deformation at the natural frequencies at that point, as

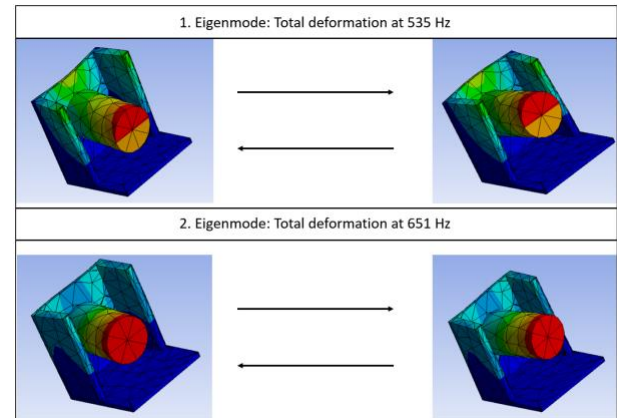


Fig. 5. Total deformation

expected. Figure 5 illustrates that the greatest deformation is to be expected primarily at the non-bearing end of the electrical motor and the side plates, as well as the middle of the mounting plate.

In order to identify optimization potentials and to be able to assess their effects on the natural frequencies, various experimental additional components were designed. These are then assembled with the motor mount as a “CATproduct” and simulated with respect to the natural frequencies with the aid of Ansys. Following components were designed and subsequently simulated:

- Straight crossbars with tubular profile
- Uneven crossbars with tubular profile
- Second support for the electric motor

A solid profile was initially used in the initial design of the cross bars. However, the simulations showed a reduction in the natural frequencies, which could be due to the additional masses that were added as a result. Subsequently, the solid profiles were replaced by tubular profiles, which brought about the desired change, i.e. an increase in the natural

frequencies. The design with the second support achieved the best improvement in the simulation, as shown in Figure 6.

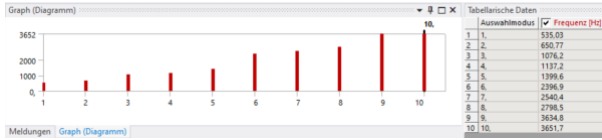


Fig. 6. Calculation results with second support

B. Measurement

An impulse hammer with a metal tip and several 1-axis accelerometers were used for the measurement. The sensor measures the acceleration perpendicular to the surface of the structure. Therefore the most significant wave type, the bending wave, is taken into account. The transfer function, phase and coherence were recorded during the measurement. A maximum in the transfer function is an indication of a natural frequency. The structural response of the motor holder is of particular interest. Since changes for future optimization are only possible on the motor mount or test bench, the focus was directed to the motor mount when placing the accelerometers. The measurement was performed with different structural configurations, regarding the motor holder with and without the electrical machine and the total test bench. Several measuring positions were equipped with accelerometers, e.g. to avoid measurements in vibration nodes where the result could be distorted. The acceleration sensors were first attached to the side plate. The side plate was then excited with the impulse hammer. This was carried out on the right and left sides in succession. The accelerometers were then attached to the mounting plate with subsequent excitation of the mounting plate by the pulse hammer. This was done first on the coupling side and then on the motor side. The frequency-dependent position of the maxima of the transfer function differs between the side plate and mounting plate. Therefore the results of the side plate and mounting plate will be portrayed separately. Table 1 shows the data of the peaks of the transfer function at a measuring point located at the side plate. There is no difference between the left and the right side. The peaks can be seen at the same frequency for each measuring point.

TABLE I. Peaks of the transfer function (total bench, side plate left)

	Frequency [Hz]	Phase [deg]	Magnitude [$\frac{m}{Ns^2}$]
Peak 1	52,5	-116,2	2,53
Peak 2	179,5	-91,4	1,94
Peak 3	339	-145	1,39
Peak 4	1551,5	-166,7	1,04

Table 2 shows the data of the peaks of the transfer function at a measuring point located at the mounting plate. The peaks can be seen at the same frequency for each measuring point, while the magnitude and phase differs.

TABLE II. Peaks of the transfer function (total bench, mounting plate, coupling side | motor side)

	Frequency [Hz]	Phase [deg]	Magnitude [$\frac{m}{Ns^2}$]
Peak 1	93,5	-116,8 -87	2,99 2,1
Peak 2	174	149 -111,8	0,4 1,3

Figure 7 and Figure 8 show the transfer function and phase of a measurement point located at the side plate and mounting plate respectively.

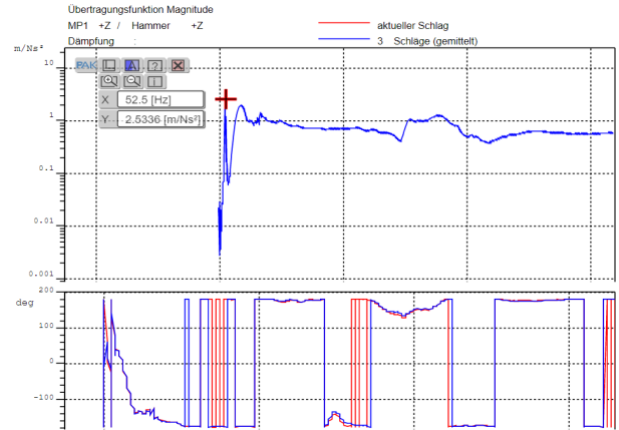


Fig. 7. Transfer function and phase (side plate left)

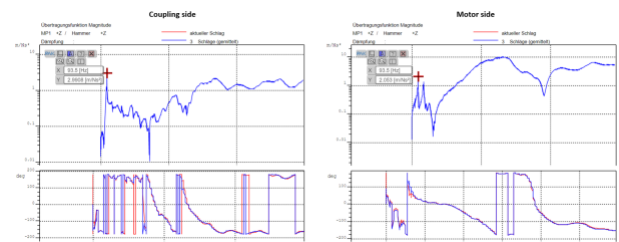


Fig. 8. Transfer function and phase (mounting plate)

V. INITIAL OPERATION

A. Preparation

First, the assembly of motor holders, electrical machines, couplings and torque measuring shaft took place. The rotational axis of the torque measuring shaft was 1.5 mm too low to be aligned with the rotational axis of the machines when mounted. For this purpose, spacers were placed under the holder of the torque measuring shaft to compensate for this distance. Then the entire test bench was clamped to the machine bed by iron clamps. A bidirectional voltage supply is selected as the grid connection, since current can flow back during generator operation. The system should supply the machines with voltage, but also be able to receive voltage. The control and regulation of the machine was carried out with the real-time capable system "LabBox" from the company dSpace, a self-developed motor control and power electronics. A field-oriented control is applied. The current is detected highly dynamically in the power electronics via the shunt resistors. An incremental encoder is used to detect rotor position and speed. For this purpose, phase A of the machine is aligned by pulling the magnet towards phase A. This is defined as the zero reference point. To minimize or completely avoid effects due to misalignment, the components were correctly aligned using a laser shaft alignment system prior to commissioning.

B. Operation

Figure 9 shows the test bench ready for operation.

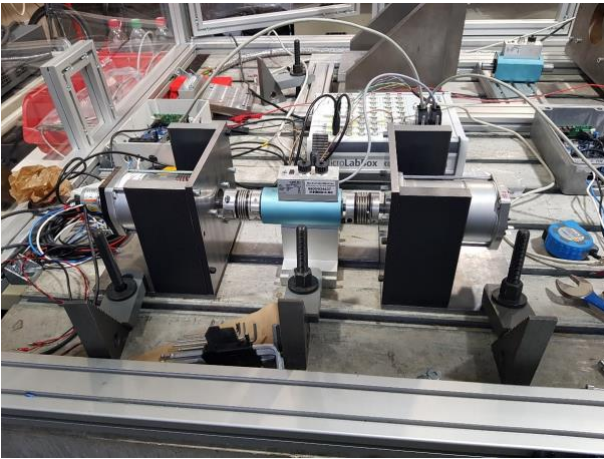


Fig. 9. Test bench ready for operation

In the first test the drive motor is governed to 1000 rpm. The test program foresees that for a given current in the q-direction, the entire range of currents in the d-direction is swept. Then the current in q-direction is increased and the entire range of current in d-direction is swept again. The current in the d-direction should have little or no influence on the moment, but a slight increase of torque can be seen when the current in d-direction is increasing, which can be explained by the reluctance moment. It is noticeable that at about 1100 rpm, abruptly higher amplitude fluctuations of the current in the q direction can be observed. The operating noise from the test bench increases at this rotational speed. If the rotational speed is increased further, the observed effects decrease again. The mechanical frequency at 1100 rpm is 18,33 Hz. Due to the number of pole pairs, the electrical frequency is 5 times greater than the mechanical frequency. The electrical frequency is therefore 92 Hz. The natural frequency measurement of the total test bench showed that the transfer function of the mounting plate has a maximum with a large magnitude at 93.5 Hz. Thus, the observed effects could represent a natural frequency excitation of the test bench, which would explain the increased operating noise at this rotational speed. At the same time, the increase of the current in q-direction could be favored by the test bench. However, this would have to be investigated in more detail.

VI. CONCLUSION AND FUTURE WORK

Within the scope of this work, a test bench for the operation of a PMSM was designed and put into service. The test bench

was designed as a 3D model and was then manufactured. In addition, a simulative modal analysis of the test bench was carried out in Ansys and, based on the simulation results, possible optimization measures were designed and simulated again. Subsequently, a natural frequency measurement was performed. Afterwards, the test bench was put into operation and the observations that could be made were documented. It turned out that the results from the simulative natural frequency analysis and the natural frequency measurement with the impulse hammer show strong discrepancies. Even though it was possible to operate the electrical machine on the test bench, it was noticed during initial operation that a natural frequency of the test bench was possibly excited at a rotational speed of 1100 rpm. This had a noticeable acoustic effect on the operating noise. Electrical measurements were also affected.

Future work includes an error analysis in order to be able to explain the discrepancy between measurement and simulation and to optimize the test bench acoustically. Since in the future, an active chain analysis concerning active noise cancellation with electrical machines is to take place, no additional excitation by resonance effects of the test bench should take place. As for now the test bench is suboptimal for this assignment. In addition, a force sensor is required for this task. For this purpose, a construction for the integration of a force sensor at the test bench should be made.

VII. ACKNOWLEDGEMENT

A special thanks to Prof. Dr.-Ing. Stefan Sentpali and M.Sc. Michael Schreiber from Munich University of Applied Sciences for their help and support with this work.

VIII. REFERENCES

- [1] F. Ebner, "Aufbau und Inbetriebnahme eines Komponentenprüfstandes für die akustische Verzielung der Momentenwelligkeit, dynamischen Momente und Strukturanbindungskräfte sowie der Körperschallabstrahlung eines E-Motors", March 2019.
- [2] K. Borgeest, „Messtechnik und Prüfstände für Verbrennungsmotoren“, Wiesbaden: Springer Fachmedien Wiesbaden, 2016.
- [3] M. Paulweber, "Mess- und Prüfstandstechnik", Wiesbaden: Springer Vieweg, pp.115-116, 2014.
- [4] R. Sinambari, S. Sentpali, "Ingenieurakustik", Springer Vieweg, pp.77-78, 2020.

Analysis of the influence of gear blank geometry on the transmission error of cylindrical gears

Alois Andreas Wenig
 Deggendorf Institute of Technology
 94469 Deggendorf, Germany
 Email: alois.wenig@stud.th-deg.de

Abstract—The gear noise problem that widely occurs in power transmission systems is typically characterised by one or more high amplitude acoustic signals. The noise originates from the vibration of the gear pair system caused by transmission error excitation that arises from tooth profile errors, misalignment tooth deflections and gear blank deflections. The measures to reduce noise emissions are divided into primary and secondary factors. In this work, the secondary factors are analyzed in more detail. In particular, the focus is on the geometric gear blank design. The gear blank geometry can have a considerable influence on the load-carrying capacity of cylindrical gears. This is evident from the fact that spur gears have greater elasticity of the face areas of the gearing, thus reducing the effect of contact line deviation. However, in the case of helical gears, both the web stress and the skewing of the gearing due to the acting axial force must be taken into account. The investigated gear blank geometries differ in the tooth rim thickness and in the web thickness. One parameter are the focus of the work, firstly the acoustically relevant transmission error. In addition to the various gears, their design and influences on the transmission error, the structure and settings of the calculation models are also described in detail. Within the scope of this paper the influence of different gear blank geometries on the transmission error were analyzed. The gear blank geometries differ in the rim thickness and the web thickness.

I. INTRODUCTION

August 26, 2015

Due to constantly increasing competitive pressure in the development of modern gearboxes, increasingly higher demands are being placed on the load capacity and noise behavior of the gearing [1]. In the course of the continuously targeted CO₂ reduction, these characteristic gearing objectives are already in the foreground in the design phase [2]. This is particularly true for electromobility, where the electrification of drive technology is steadily advancing. The desire for sustainability is reinforcing the trend towards electrification, also because the environmental aspect is becoming increasingly important to the public [3]. In the case of passenger cars powered by internal combustion engines, many noise sources are masked by broadband acoustic excitation from the internal combustion engine. This masking of noise sources does not occur with the significantly quieter electric motors. Consequently, the optimization of the acoustic behavior of a powertrain and the associated transmission faces new challenges [4].

Fig. 1 shows the effect of the lack of masking due to the absence of an internal combustion engine. It is noticeable that

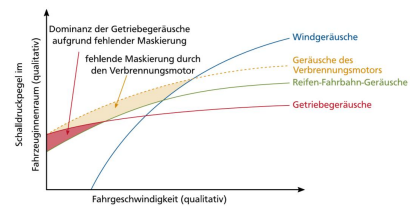


Fig. 1. Lack of masking by the combustion engine leads to increased perceptibility of transmission noise [5]

in the lower speed ranges, the transmission noise in the vehicle interior dominates. Due to the aforementioned targeted CO₂ reduction, spur gears should on the one hand be as light as possible and on the other hand still be able to transmit the required power. However, it must be mentioned at this point that lightweight construction has not only found its way into transmission design and thus also into gear design since the energy turnaround [3].

II. STATIC TRANSMISSION ERROR

Studies on the influence of the gear blank geometry on tooth root stress and on acoustic excitation behavior can be found in numerous scientific papers. In addition to numerical analyses, empirical studies also exist. Factors to reduce noise emissions are divided into primary and secondary measures. Primary factors reduce excitation at the source while secondary factors affect the transmission of sound [6]. Primary factors include changing the involute tooth flank shape by means of gear tooth corrections. In this process, the transmission error and thus also the acoustically relevant excitation behavior of a spur gear stage are specifically influenced. The general purpose is to equalize the transmission error, i.e. to optimize the peak-to-peak characteristic to the lowest possible level [7]. In contrast to the optimization of the actual gearing, which is assigned to the primary factors [8], the geometric optimization of the gear blank belongs to the secondary measures, since the gear blank contributes to the vibration excitation and transmission of the signals. The design of the gear blank geometry can also have significant influences on the load-carrying capacity of cylindrical gears [9]. This is noticeable in the fact that

ridge gears have greater elasticity of the face regions of the gearing, thus reducing the effect of contact line deviation. A common way of assessing the excitation behavior of gears is to calculate the rotational path behavior. To determine this, the deformation of the gearing is calculated for different rolling positions or meshing positions under load and the non-uniform portion of the motion transmission is evaluated at the resulting angular positions. This proportion is referred to as the rotary path deviation under load at the corresponding meshing position or as the loaded transmission error [10]. This consequently describes the difference between the actual position and the ideal position with perfect meshing conditions. The transmission error is due to several effects. Firstly, due to the force transmission and the resulting bending, there is a geometrical deviation of the flank. On the other hand, the manufacturing inaccuracies of the flank geometry are still relevant, even with negligible deformation of the gearing. Further effects are the assembly errors, which can be reduced but can never be neglected. In addition, shaft and housing deformations also have a relevant influence on the transmission error. If the flanks of the gearing are ideal, i.e. manufactured without any deviations, and also roll off each other without load, the transmission error is zero [11]. The transmission error can be described mathematically with the following equations, depending on the reference gear.

$$TE = \theta_2 - \frac{z_1}{z_2} * \theta_1 \tag{1}$$

$$TE = \theta_1 - \frac{z_2}{z_1} * \theta_2 \tag{2}$$

θ_1 and θ_2 describe the angular position of the respective gear and z_1 and z_2 are the corresponding numbers of teeth. To describe the excitation behavior, Gregory et al [12] recommended the transmission error, the same suggestion was made by [14]. For the evaluation of the excitation ratio not a single value of the transmission error is used, but the fluctuation range. Based on the course of the rotational deviation as a function of the rolling position, the difference between the maximum and the minimum value is formed. This difference is called the fluctuation width of the rotational displacement difference, rotational displacement deviation or peak-to-peak transmission error and is used to assess the excitation behavior [14]. Baethge compared measurements of the airborne sound level with measurements of the rotational displacement deviation and was thus able to establish a correlation [14]. Similar investigations were carried out by Harris [13] with the aid of experimental or computational considerations, which represent a confirmation of Baethge. In the context of an optimization study, in which mass reduction, gear efficiency and noise behavior were the variables to be optimized, it was found that no ideal gear blank geometry could be found between these optimization variables and a compromise was always the result. When the gearing was designed for mass and efficiency, the peak-to-peak transmission error was very large. As early as 1999, Chung, Steyer, Abe, Clapper, and Shah [16] found

out in a research project, that the design of the gear blank has an equally relevant influence on the transmission error as the profile modifications of the running gearing. With the optimum design of the gear blank, the noise level could be reduced. This order of magnitude alone shows the potential that this field of research holds. Due to the complex interrelationships and the sensitive overall system, optimum solutions cannot usually be determined by linear calculation approaches.

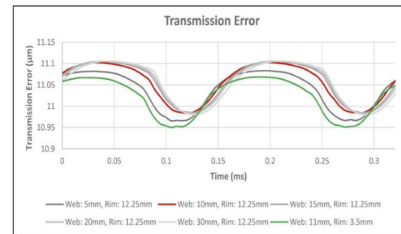


Fig. 2. ransmission error for different gear blank dimensions[15].

This is shown in Fig. 2, where the course of the static transmission error is plotted as a function of the meshing time. It is striking that the optimum results (green graph) were achieved with a gear blank geometry that was specifically optimized with the gear rim thickness and the web thickness. In comparison, the red graph represents the original gear blank geometry, and the graphs with a gray background are the geometric iteration steps for an optimum gear blank geometry. This is also reflected in the sound power curve, as can be seen in Fig. 3. Here, the optimized geometry (green graph) leads to significantly lower resonance as a function of frequency.

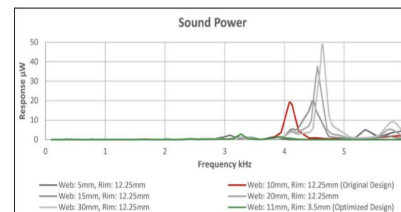


Fig. 3. Casing sound power in a logarithmic scale. Original design (red), optimized design (green) [15].

It can be seen clearly that the optimization of the web thickness in 5 mm steps leads to a serious deterioration [15]. An apparent special geometry offers the best results. Due to the many transverse influences, there are also differentiation possibilities for the rotary displacement deviation or the transmission error, so in the context of this work, the dynamic forces are not considered, so the static consideration of the rotary displacement deviation, consequently the static transmission error is in the foreground.

III. BOUNDARY CONDITIONS AND SIMULATION MODEL

A. Gearing parameters and load cases

In order to obtain a meaningful and reliable assessment, several calculation models are set up and examined. Thus, in the first step of this phase, the macro geometrie is defined. Depending on the application, the transverse concact ratio and the overlap ratio remain the same. This means that macro geometries, which are typical for input stages, have a transverse concact ratio of 2. and a overlap ratio of 2. By fixing these two parameters, the practical relevance is also given in this investigation, since these are typical parameters of a macro geometry of a transmission, which is installed in a purely electric-driven passenger car. The most important geometry parameters of the macrogeometry, in addition to the transverse concact ratio and the step overlap ratio, can be seen in Fig. 4.

Geometry			Diameters					
Name	Pinion	Wheel	Tip Diameter (mm)	d_a	80 (Specified)	112.2 (Specified)		
Number of Teeth	z	23	47	d_f	48.214	80.992		
Normal Module (mm)	m_n	2.05		Reference Diameter (mm)	d	50.521	107.325	
Transverse Module (mm)	m_t	2.284		Base Diameter (mm)	d_b	49.283	100.768	
Center Distance (mm)	a_w	80		Tip Form Diameter (mm)	$d_{f,2}$	56.1	112	
Face Width (mm)	b	30	30	Root Form Diameter (mm)	$d_{f,1}$	49.349	101.87	
Transverse Base Pitch (mm)	p_w	6.732						
Normal Pitch (mm)	p_n	6.44		Profile Shift				
Transverse Pitch (mm)	p_t	7.174		Nominal	x	0.506	-0.681	
Working Normal Pressure Angle (°)	α_w	18.4346	18.4346	Profile Shift Coefficient	Average	x_n	0.4918 (Calculated)	-0.5424 (Calculated)
Working Transverse Pressure Angle (°)	α_{wt}	20.3751	20.3751	Sum of Profile Shift Coefficient	Σx_n	0.03788	0.03788	
Normal Pressure Angle (°)	α_n	18.3		Profile Factors				
Transverse Pressure Angle (°)	α_t	20.2332		Basic Rack Addendum Factor	y_{Fa}	1.2882	1.6872	
Effective Face Width (mm)	b_w	30	30	Basic Rack Dedendum Factor	y_{Fd}	1.8864 (Auto)	1.5425 (Auto)	
Hand		Left	Right	Basic Rack Profile		ISO 53 Profile B	ISO 53 Profile B	
Helix Angle (°)	β	26.137						

Fig. 4. Macro geometry parameters

In the second step, sub-variants of the gear, previously defined by the macro geometry, are generated. These sub-variants differ only in the design of the gear blank. The microgeometry of the gear is identical for all sub-variants, so that all anomalies occurring during the analysis can be attributed exclusively to the gear blank geometry. In the design of the gear blank, there are essentially two parameters that can be varied. One is the thickness of the gear rim and the other is the web thickness. Fig. 5 shows the definitin of the web thickness b_s and the rim thickness S_R .

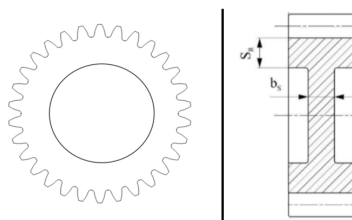


Fig. 5. Representation of gear blank geometries

These two geometry parameters are varied in the different sub-variants. Fig. 6 gives an overview of the sub-variants.

rim thickness S_R	web thickness b_s	calculation models
$3 * m_n$	$1 * b$	20
$2,75 * m_n$	$0,75 * b$	
$2,5 * m_n$	$0,5 * b$	
$2,25 * m_n$	$0,25 * b$	
$2 * m_n$		

Fig. 6. Overview of the geometry versions to be analyzed

Thus, a total of 20 calculation models were built and analyzed with respect to transmission error. When defining the load cases, the maximum load case was defined first. Starting from the defined macro geometry according to ISO 6336, backward calculations were performed in order not to exceed a tooth root stress $\sigma_F = 860 \frac{N}{mm^2}$. It should be noted, however, that the application factor and the dynamic factor were defined with the value 1. According to this procedure, a drive torque of 320 Nm was calculated.

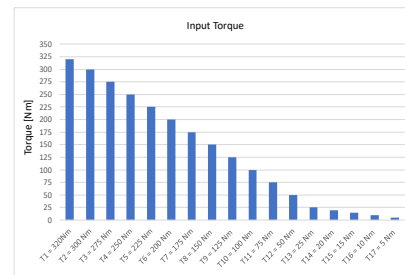


Fig. 7. Used torque steps

Fig. 7 shows the torque levels used. A total of 17 drive torques were used. Since lower drive torques result in lower deformations and therefore the influence of the microgeometry is increased, the torque steps are smaller than with the higher torques.

B. Setup of the simulation model

The model structure and the framework conditions are identical for all calculation models, which is why this chapter deals with the structure and settings of the calculation models. In addition to the meshing, the bearing arrangement of the cylindrical gears is one of the most important framework conditions, as these absorb the acting forces and torques.

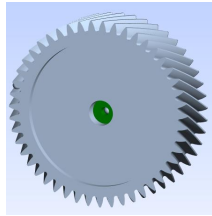


Fig. 8. Concept bearing of the spur gear

Each spur gear of the stage is realized by a concept bearing which can be seen as a green ring in Fig. 8. This bearing allows rotation around the axis of rotation and has a radial and axial stiffness of $1 * e^{12} Nmm$. This high stiffness value is intended to ensure an ideally stiff connection of the spur gear to the environment. In this way, the influences of shaft and housing deformations can be filtered out. In addition to the bearing, an input load is also attached to the pinion, which serves to introduce torque. In contrast, an output load is attached to the gear, which serves as a power output and from which the output torque is taken. For meshing, a quadratic approach function is used, since here nodes are not only at the corners and ends of an element, as is the case with linear approach functions, but also in the middle. These centrally located nodes are called intermediate nodes. The degrees of freedom of the additional intermediate nodes result in additional parameters for the higher order of the approach function. In this way, deformations can be calculated with greater numerical accuracy. Furthermore, hexahedra are used for the element shape, which have a size of 2 mm. Macrogeometry was also taken into account in the meshing of the gear blank. Fifteen elements were selected for the gear width, 10 elements for the profile, 8 elements for the root fillet and 8 elements for the tooth tip.

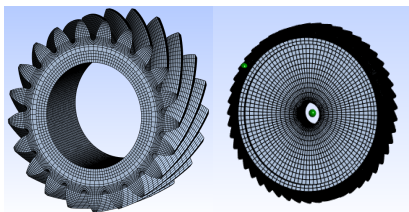


Fig. 9. FE-mesh of the pinion (left) and the wheel (right).

Fig. 9 shows the final meshed gear blank. The symmetrically evenly distributed elements should be emphasized. With the computer program MASTA, it is often necessary to mesh the gearing separately. MASTA then combines the stiffnesses of the FE gear blank with those of the gearing.

IV. RESULTS

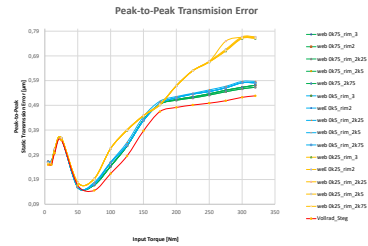


Fig. 10. Results of the peak-to-peak transmission error of the different gear blank geometries for the defined load cases

Fig. 10 shows the influence of the gear blank geometry on the peak-to-peak static transmission error. The input torque is shown on the abscissa and the peak-to-peak transmission error on the ordinate. A clear trend can be seen. The red graph shows the values of the peak-to-peak transmission error of a solid wheel, which serves as the reference geometry. It can be seen that the reference geometry shows the lowest values. Furthermore, a clear tendency for the web thickness can be seen. It can be stated that a thinner web thickness leads to a higher peak-to-peak static transmission error. The gear blank geometry variants with a web thickness of $b_s = 0.25 * b$ (yellow graphs) show the greatest peculiarity, since with these variants the peak-to-peak transmission error from 200 Nm input torque is significantly higher than the other variants. The TE values of the gear blank variants with $b_s = 0.5 * b$ (blue graphs) and $b_s = 0.75 * b$ (green graphs) are very close to each other, relative to the other variants. For further analysis, the gear blank variants with a web thickness of $b_s = 0.25 * b$ are not considered because the peak-to-peak static transmission error values are too high. This can only be compensated by relatively large values of the micro geometry. However, this complicates the optimal design of the micro geometry. This is because a compromise must always be made between high loads and low loads when designing the optimum micro geometry. With high loads, there is then a risk that the slope will be overcorrected. As a result, the peak-to-peak static transmission error is not uniform over the entire torque bandwidth, which can lead to acoustic conspicuities in certain torque ranges. In addition to noise, weight is also a significant factor that must be taken into account in the general design of a gear unit, since the gear blank variants with a web thickness of $b_s = 0.5*b$ entail a weight reduction of 59.6% and 60.5% (compared to the corresponding gear rim thickness), as shown in Fig. 11. The solid gear geometry was used as the reference geometry for determining the weight reduction.

Geometriertyp	Faktoren und Maße		Gewichtreduktion in Prozent
web0k5 rim2k75	Web Thickness [mm]	15	59,6
	Rim Thickness Factor	2,75	
web0k5 rim3	Web Thickness [mm]	15	60,5
	Rim Thickness Factor	3	
web0k75 rim2k75	Web Thickness [mm]	22,5	39,3
	Rim Thickness Factor	2,75	
web0k75 rim3	Web Thickness [mm]	22,5	40,7
	Rim Thickness Factor	3	

Fig. 11. Weight reduction for each version

For both acoustic and weight reasons, the gear blank variant $b_s = 0.5 * b$ is the preferred gear blank geometry in terms of web thickness.

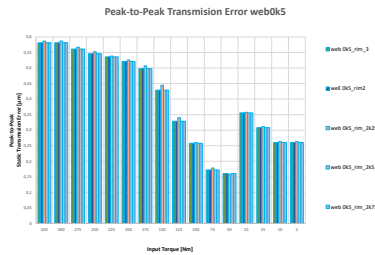


Fig. 12. Comparison of the peak-to-peak static transmission error of the respective rim thicknesses for different input torques at a web thickness of $b_s = 0.5 * b$

Fig. 12 shows the peak-to-peak static transmission error values for the respective gear rim thickness. It is noticeable that the gear rim thickness plays a subordinate role, since the values differ only minimally. A closer look reveals that at higher drive torques, the smaller rim thickness leads to higher values. Thus, Fig. 13 shows the thicker rim thicknesses and their values. A close look shows that a rim thickness of $S_R = 2.5 * m_n$ and $S_R = 2.75 * m_n$ has no significant influence. Thus, the maximum absolute deviation amounts to for the torque 275 Nm, in contrast to the minimum deviation of for the input torque of 25 Nm.

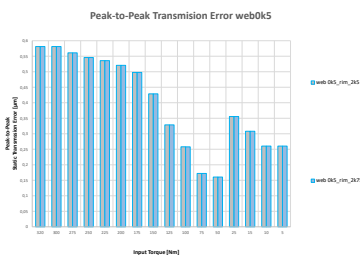


Fig. 13. Comparison of the peak-to-peak static transmission error of the respective rim thicknesses for different input torques at a web thickness of $b_s = 0.5 * b$ for rim thicknesses of $S_R = 2.5 * m_n$ and $S_R = 2.75 * m_n$

This is also confirmed by the examination of the gear rim thicknesses for the gear blank variant with a web thickness of $b_s = 0.75 * b$, as can be seen in Fig. 14. The maximum absolute deviation is $8.8 * e^{-6} Nmm \mu m$ at a torque of 250

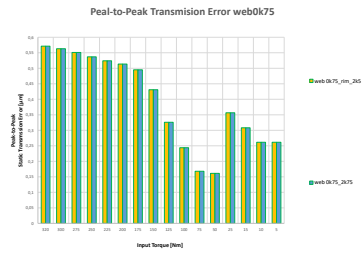


Fig. 14. Comparison of the peak-to-peak static transmission error of the respective rim thicknesses for different input torques at a web thickness of $b_s = 0.75 * b$ for rim thicknesses of $S_R = 2.5 * m_n$ and $S_R = 2.75 * m_n$

Nm and the minimum absolute deviation is $2.4 * e^{-6} Nmm \mu m$ at a torque of 150 Nm.

V. CONCLUSION

It can be noted that for the analyzed input stage, a web thickness $b_s = 0.75 * b$ and $b_s = 0.5 * b$ provide almost the same results for the static transmission error. A web thickness of $b_s = 0.25 * b$ leads to relatively high values of the static transmission error at the higher torques, which makes it more difficult to design the optimum microgeometry. This is because there is a risk that the tooth flank will be overcorrected for a certain torque range. The gear rim thickness has a negligible influence on the static transmission error. The findings resulting from this work show that a gear blank geometry with a web thickness of $b_s = 0.5 * b$ and a rim thickness of $S_R = 2.25 * m_n$ contains the optimum geometry parameters or design parameters in terms of load capacity, static transmission error and weight optimization.

In order to further substantiate the findings, further parameter studies are useful. The most relevant parameters would be the gear ratio and the center distance, as these have the greatest influence on the tooth forces. Furthermore, it would make sense to consider a more detailed differentiation or categorization of the gear rim thickness. One possibility would be to distinguish between geometries with an internal bore and ratchet gears. For example, geometries with an internal bore are pinion shafts or planets of an epicyclic gear. With more profound knowledge of the gear rim thickness and the web thickness, it will be possible in the future to realize gear blank geometries that are even more optimally adapted to the loads.

REFERENCES

- [1] A. Gacka and T. Griggel, *Kennwerte Anregungsverhalten*, Garching, Germany: FVA Forschungsvereinigung Antriebstechnik, 2006.
- [2] M. Zimmer, M. Otto and K. Stahl, *Berechnung und Optimierung von Geometrie und Eingriffsverhalten von Zahnformen beliebiger Achslage*, Garching, Germany: Springer, 2016.
- [3] P. Gwinner, *Schwingungsarme Achsgetriebe elektromechanischer Antriebsstränge*, Garching, Germany: Dr. Hut, 2017.
- [4] K. Genuit, *Sound-Engineering im Automobilbereich - Methoden zur Messung und Auswertung von Geräuschen und Schwingungen*, Herzogenrath, Germany: Springer, 2010.
- [5] P. Neubauer, *Konzeption und Auslegung von geräuschoptimierten in-äquidistanten Verzahnungen*, Darmstadt, Germany: CC BY-SA 4.0 International, 2019.
- [6] R. Lerch, S. Gerd and D. Wolf, *Technische Akustik - Grundlagen und Anwendungen*, Harlow, Germany: Springer, 2009.
- [7] T. Griggel, *Einfluss von Korrekturen und Fertigungsabweichungen auf die Schwingungsanregung von Stirnrädern*, Garching, Germany: Shaker Verlag, 2010.
- [8] S. Sanzenbacher, *Reduzierung von Getriebegeräuschen durch Körperschallminderungsmaßnahmen*, Stuttgart, Germany: Universität Stuttgart, 2016.
- [9] H. K. Linke, *Stirradverzahnung - Berechnung - Werkstoffe - Fertigung*, Dresden, Germany: Hanser Verlag, 2010.
- [10] M. K. Heider, *Schwingungsverhalten von Zahnradgetrieben - Beurteilung und Optimierung des Schwingungsverhaltens von Stirnrad und Planetengetrieben*, Garching, Germany: Dr. Hut, 2012.
- [11] P. Davoli, C. Gorla, F. Rosa, R. Rossi and G. Boni, *Transmission Error and Noise Emission of Spur Gears*, Las Vegas, USA: Proceedings of the ASME 2007 10th ASME International Power Transmission and Gearing Conference, 2007.
- [12] R. Gregory, S. Harris and R. Munro, *Dynamic behaviour of spur gears*, Proc. Inst. Mech. Eng., Nr. Vol. 178 Pt I No 8, pp. 207-226, 1963-64.
- [13] S. Harris, *Dynamic loads on the teeth of spur gears*, Proc. Inst., Bd. Inst. Mech. Eng., Nr. Vol. 172, pp. 87-112, 1958.
- [14] J. Baethge, *Drehwegfehler, Zahnfederhärte und Geräusche bei Stirnrädern*, München, Germany: 1958.
- [15] O. Harris, P. Langlois and A. Gale, *Electric Vehicle Whine Noise - Gear Blank Tuning as an Optimization Option*, GEARTECHNOLOGY, pp. 64-73, 2019.
- [16] J. Chung, G. Steyer, T. Abe, M. Clapper and C. Shah, *Gear Noise Reduction through Transmission Error Control and Gear Blank Dynamic Tuning*, Noise and Vibration Conference and Exposition, Michigan, USA: 1999.

Analysis of the required sensor range for an automated bus operating in rural areas based on a simulation

Fabian Zeitler

Technical University of Applied Sciences Amberg-Weiden
Amberg, 92224
f.zeitler@oth-aw.de

Abstract—In this paper the required sensor range for an automated bus should be analyzed. The frame conditions are an operation in rural areas including driving on country roads and considerations regarding two official guidelines. The first one is the ISO 15622 in which acceleration limits for automated controlled vehicles can be found. The second guideline is the RAL used because of its definition of the minimum visibility ranges on country roads. In order to perform the analysis and comparison between the two guidelines an iterative simulation was programmed in Python.

I. INTRODUCTION

In the last years there were many research projects regarding automated vehicles. Most of them focused either on highway scenarios or urban areas. Given that the infrastructure in cities is mainly well developed and the biggest percentage of the population is residing there it is a comprehensible trend. On the other hand there are arguments to research the possible usage of automated vehicles in a rural context. Average travel distances to locations for the daily businesses, as shopping, going to school or participating in cultural events, are wider in areas with lower population density. For example the typical travel time by car to the next doctor, which is in villages about six minutes, while in urban resident areas just half of the time is needed [1]. Another argument would be the provision of an economical solution for the local passenger transport in rural regions compared to line bus traffic. This can be accomplished with the savings for the labor costs of drivers in a fully automated vehicle of level four according to SAE J3016, a better utilization rate due to on demand distribution of passengers on the available vehicles and cost reduction by using production vehicles, which are upgraded to operate automated [2]. Because of these points the required sensor ranges, as one challenge, regarding an automated bus operating in rural areas should be examined. The comparison between the two official guidelines RAL for the construction of country roads and ISO 15622 for among other things FSR-ACC (Full Speed Range Adaptive Cruise Control) represents the framework of this paper [3], [4]. The RAL contains minimum required visibility ranges for country roads. The ISO 15622 includes the definition of longitudinal and lateral acceleration limits for vehicles controlled by a FSR-ACC. To

show if these two prerequisites are harmonizable is the main goal of this work.

The further structure of the paper is shown in the following paragraph. At first the section II will give an overview about the chosen traffic scenarios for the simulation. The section III explains the function of the written iterative simulation. The following section IV will show the results of the simulation, which are the necessary sensor ranges for the operation in rural areas. At the end the paper will be concluded.

II. CHOSEN TRAFFIC SCENARIOS

The area of operation of the fictive automated bus includes country roads as well as driving in town. In order to define the requirements for the sensor platform the different circumstances in both contexts have to be considered. Because of the higher speed limits the country roads are the environment, which provides more new challenges to the vehicle. These routes combine higher driving speeds, than in urban scenarios, with less structured roadway layouts, than seen on highways. Since a research regarding other projects showed none of them has considered such conditions yet, to the best of our knowledge neither a off the shelf sensor platform can be purchased nor a development focused on the requirements in these scenarios could be found [5], [6], [7].



Figure 1. Example intersection with speed limit $80 \frac{km}{h}$, $20 m$ radius and flat branching street [8]

To make well-founded statements different traffic scenarios should be analyzed, but at first they have to be defined.

In order to accomplish this the first step is to abstract the driveway of the vehicle when crossing an intersection. As a simplified assumption the bus drives a circular arc, if it is necessary to turn, and then the rest of the driveway is a straight line. The scenarios can be described with the help of three parameters: The maximum permissible speed, the radius of the curve and the angle that the vehicle passes during the curve. Table I shows all the values considered for the variables. The curve radii are intended to model, on the one hand, small intersections in towns, such as the exit from a parking lot onto a road, and, on the other hand, larger junctions on country roads. The curve angles are intended for roads at right angles to each other and for roads with shallow junctions. The scenarios considered always assumed a turn to the left, since this case is the one with the most right-of-way regulations to be observed. A distinction is made between three operations:

- **Driving onto a priority road without getting into the traffic:** Here, the vehicle turns onto a priority road and the distance of road users on the left side or from the front is considered. In this case, only the turn must be completed in order to be out of the way of other vehicles.
- **Driving onto a priority road with getting into traffic:** In this case, other vehicles are observed from the right and after the turn, it is still necessary to accelerate to the final speed without obstructing anyone.
- **Driving from a priority road:** This scenario intends a turn from the priority road. Here, only traffic approaching from the front must be observed and the situation ends with the turn.

Table I
LIST OF PARAMETERS FOR THE TRAFFIC SCENARIOS

v_{max} [km/h]	30	50	70	80	100
r_{curve} [m]	2	5	10	20	
α_{curve} [°]	45	90	135		

III. SIMULATION

For analysis, a simulation was written in Python that assumes constant values for the physical quantities in discrete time steps and calculates their change for the next iteration with the help of Newton's laws. For the individual scenarios, the distance is searched in which another road user must be located so that the automated vehicle can perform the maneuver without obstructing it. The programming was carried out taking into account the maximum longitudinal and lateral accelerations according to ISO 15622 for vehicles operated by an assistant for FSR-ACC [4]. In the following, the further framework conditions and assumptions for the simulation will be explained:

- **Safety factor:** The human driver in the other vehicle is expected to be traveling at a speed twenty percent above the speed limit.
- **Get into traffic:** A distinction is made as to whether acceleration to the final speed in the same lane must be taken into account for the considered encounter of road

users or whether the lane of the other vehicle has only to be crossed.

- **Safety distance:** Since the position of the vehicles refers in each case to the front, different distances must also be considered for the two cases distinguished above. If it is necessary to get into the traffic, the distance is half the numerical value of the speed limit in meters plus the length of the own vehicle according to the rule of thumb "half speedometer". If only a crossing of the other lane is simulated, the distance is again calculated with the rule of thumb, but at this point the safety factor is taken into account and the vehicle length does not have to be considered.
- **Termination conditions:** If a lane change is to perform, the entire distance of the curve must be covered and the speed limit must be reached. When crossing the lane of the other vehicle, it is sufficient to cover the distance of the curve.

For the start conditions some considerations had to be made. On the one hand the signs for the start speed and position must correspond to the scenario, thereby the zero point is always set for the own vehicle, but for the values of the other vehicle it plays a role whether the two vehicles drive towards each other or in the same direction. On the other hand, one of the three following values must be used for the starting speed of the automated bus:

- **Standstill:** When turning into a priority road, a complete standstill is always assumed as a precaution.
- **Maximum curve speed:** If you want to change from a priority road to a lower priority road, you must select the maximum curve speed corresponding to the permissible lateral acceleration as the starting value if this is lower than the speed limit.
- **Speed limit:** If the speed limit is lower than the curve speed, this can be used as the starting speed when leaving a priority road.

In order to be able to determine the required value, a small starting value for the distance between the vehicles is used and whenever the distance falls below the safety distance before the stop conditions corresponding to the scenario have been met, a premature stop is made because the other road user would be obstructed. Then the starting distance is increased until the stopping conditions can be fulfilled without falling below the safety distance. To save computing time, interval nesting was implemented at this point. This starts with 64 m steps at 64 m distance. If the simulation with these parameters is successful for the first time, it must be assumed that the searched value lies between the last and the penultimate distance value. Then the step size is quartered and the same procedure is performed for the relevant interval. This process is continued until a step size of one is used.

The result for the required distance, accurate to the meter, is then output and three additional diagrams are generated, one for the acceleration, one for the speed and one for the distance traveled. The diagrams for two different scenarios will now

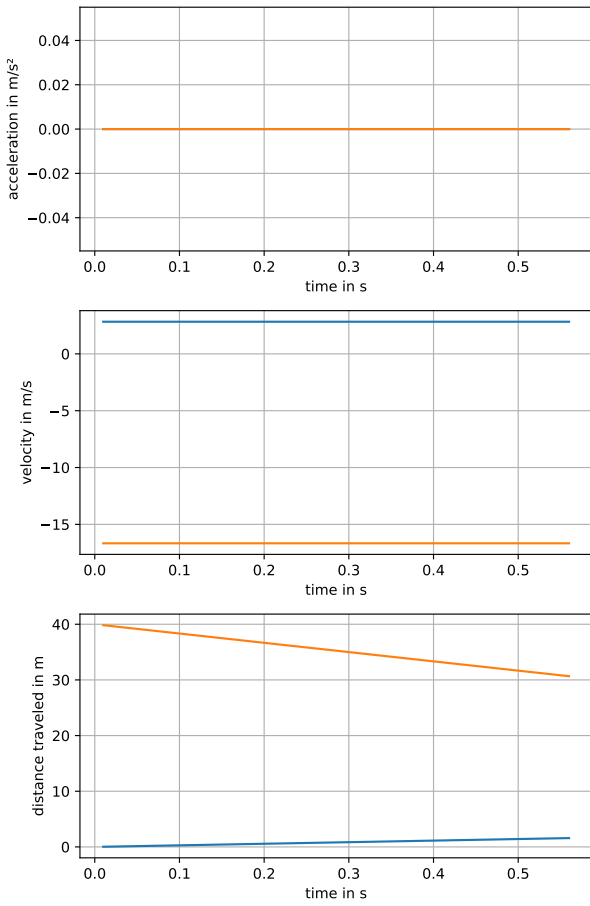


Figure 2. First example of a simulation result. The used parameters were: A speed limit of $50 \frac{km}{h}$, an angle of 45° and $2m$ as the curve radius.

be briefly examined and explained. The first traffic situation considered is leaving a priority road at a permitted speed of $50 \frac{km}{h}$. In this case, the other road users are expected head-on. The junction is located at an angle of 45° to the initial road and the radius is only $2m$, which is very small. Using $4 \frac{m}{s^2}$ as the maximum accepted lateral acceleration a_l and formula 1, the maximum permissible curve velocity v_c can be calculated to be $2.83 \frac{m}{s}$. Here r_c denotes the curve radius under consideration.

$$v_c = \sqrt{a_l \cdot r_c} \quad (1)$$

This speed is also clearly visible in the corresponding graph in Figure 2, since this value is used as the starting value if it is below the speed limit. The speed does not change during the simulation, because the termination condition is reached when leaving a priority road at the end of the curve.

The second scenario is the entry into a priority road with a speed limit of $80 \frac{km}{h}$. The radius of the curve to be driven is $10m$ and the intersecting roads are perpendicular to each other. In this case, the acceleration to the final speed must be taken into account. The correct behavior of the simulation according to ISO 15622 with respect to the longitudinal acceleration can be observed in the diagram of acceleration in Figure 3 [4].

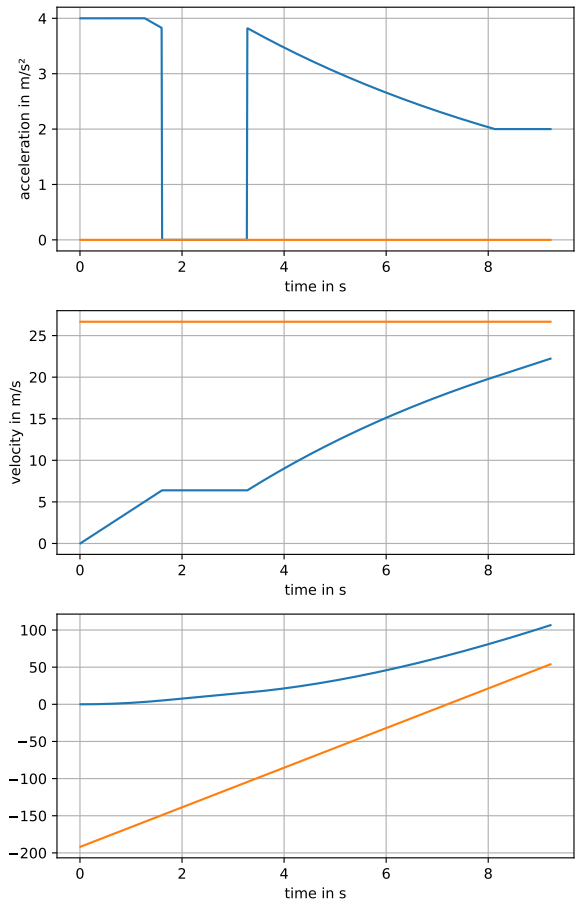


Figure 3. Second example of a simulation result. The used parameters were: A speed limit of $80 \frac{km}{h}$, an angle of 90° and $10m$ as the curve radius.

At velocities below $5 \frac{m}{s}$, $4 \frac{m}{s^2}$ are allowed, then the linear relationship becomes visible at velocities up to $20 \frac{m}{s}$. This continuous decrease in acceleration is interrupted when v_c is reached. After the turn is completed, the acceleration is further decreased until $20 \frac{m}{s}$ is reached and the constant permissible value of $2 \frac{m}{s^2}$ is maintained until the $80 \frac{km}{h}$ speed is reached.

This two examples with both textual and visual sources to explain the function of the simulation should be sufficient. The following section will show the resulting requirements for the sensor ranges.

IV. SENSOR RANGES

The simulation determined in total 180 ranges. This amount is derived from the values defined in table I, which allow 60 different combinations, and the three various operations simulated for each set of parameters. These results were stored and processed in order to increase the usability of the output data. Firstly statistical parameters for the results were derived, which can be seen in table II.

Subsequently two graphical representations of the sensor ranges were created. On the one hand the portion of ranges in a certain interval in figure 4 was generated in order to provide

Table II
STATISTIC PARAMETERS OF SIMULATION RESULTS

parameter	value [m]
minimum	24
maximum	348
mean	119
median	104

a good impression of the distribution of the results. On the other hand the aggregated share of ranges beneath an upper limit in figure 5 is shown, because this representation enables a better grasp on how many scenarios are covered with a certain sensor range.

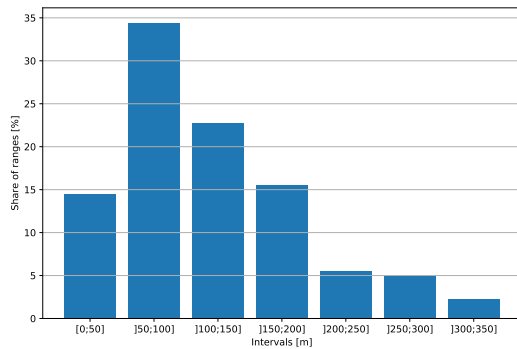


Figure 4. Portion of ranges as percentage calculated with the simulation against 50 meters wide intervals

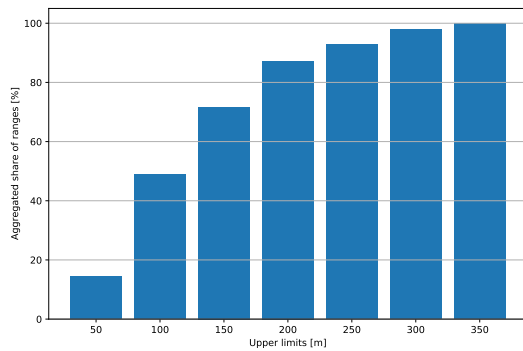


Figure 5. Aggregated share of ranges as percentage calculated with the simulation against the upper limit in meter

The results show that the two considered guidelines apparently use different acceleration limits, because 12.8% of the based on the ISO 15622 determined sensor ranges are higher than the necessary visibility range defined in the RAL as 200m in the cases of all speed limits above $70 \frac{km}{h}$.

V. CONCLUSION

An iterative simulation based on the possible traffic scenarios found in rural areas, the acceleration limits defined in the ISO 15622 for FSR-ACC controlled vehicles and the precondition that other traffic participants must not be obstructed, was programmed in Python to determine necessary sensor ranges. The comparison of the simulation results and the minimum visibility ranges specified by the RAL showed that the necessary ranges are partly higher.

The reason for this is most likely that human drivers are allowed to accelerate with higher rates compared to a vehicle controlled by an FSR-ACC. A further conclusion of this insight is that the automated bus operating in rural areas will probably need some kind of support beside his own sensor platform. This could be in the form of road side units equipped with suitable sensors, which communicate with the vehicle in order to extend its sensor range.

ACKNOWLEDGMENT

As this work was developed in the framework of the research project AUTBUS –Entwicklung eines autonomen Kleinbusses für den ländlichen Raum (engl. Development of an autonomous bus for the rural area) funded by the Bavarian State Ministry for Economic Affairs, Regional Development and Energy (funding code DIK-2006-0016//DIK0233/02), the author would like to thank the funder. Also we appreciate the cooperation with our project partner AVL Software and Functions GmbH.

REFERENCES

- [1] Bundesministerium für Ernährung und Landwirtschaft (BMEL), 'https://www.landatlas.de/daten.html', 2018. [Online]. Available: <https://www.landatlas.de/daten.html> [Accessed: May 6th 2021]
- [2] wikipedia.org, 'SAE J3016', 2021. [Online]. Available: https://de.wikipedia.org/wiki/SAE_J3016 [Accessed: May 6th 2021]
- [3] Forschungsgesellschaft für Straßen- und Verkehrswesen e.V., *Richtlinien für die Anlage von Landstraßen (RAL)*, Köln, Germany: Forschungsgesellschaft für Straßen- und Verkehrswesen e.V., 2012.
- [4] H. Winner and S. Hakuli, '32 Adaptive Cruise Control,' in *Handbuch Fahrerassistenzsysteme*, 2nd Edition. Wiesbaden, Germany: Springer Vieweg, 2012.
- [5] Berliner Verkehrsbetriebe (BVG), 'Autonomes Fahren in Berlin-Tegel | Projekt See-Meile', 2021. [Online]. Available: <https://www.see-meile.com/> [Accessed: May 6th 2021]
- [6] Stadtwerke Osnabrück AG, 'Flexible Mobilität / HUB CHAIN', 2021. [Online]. Available: <https://www.hubchain.de/> [Accessed: May 6th 2021]
- [7] FZI Forschungszentrum Informatik, 'EVA-Shuttle', 2021. [Online]. Available: <http://www.eva-shuttle.de/> [Accessed: May 6th 2021]
- [8] geoportal.bayern.de, Bayerische Vermessungsverwaltung, EuroGeographics 'BayernAtlas - der Kartenvierer des Freistaates Bayern', 2021. [Online]. Available: https://geoportal.bayern.de/bayernatlas/index.html?lang=de&topic=bvv&bgLayer=atkis&zoom=12&mobile=false&catalogNodes=11&E=749299.24&N=5459499.29&layers=luftbild,KML%7C%7Chttps:%2F%2Fgeoportal.bayern.de%2Fba-backend%2Ffiles%2Ff_76492ff0-7112-11eb-89dd-677f9628b0a0_780_c6c3e-c66d-432a-ad1d-1cacb5193eaa%7C%7Ctrue [Accessed: May 7th 2021]

Chapter 7

Papers: Logistics and Organization

Contents

7.1	Application of Lean Construction Management to sustainably increase of productivity in the construction industry	368
7.2	Structural Differences in the Higher Education Research in Germany between Universities and Universities of Applied Sciences	374
7.3	Use of Digital Assistance Systems in Production	380

Application of Lean Construction Management to sustainably increase of productivity in the construction industry

Identification of potentials to increase productivity in the construction industry by reducing types of waste through the application of lean management and analysis of possible applications in housing construction

Lena Kempf, B.Eng.
University of Applied Sciences Augsburg
An der Hochschule 1
86161 Augsburg, Germany
lena.kempf@hs-augsburg.de

Abstract – The construction industry still suffers from comparatively low productivity compared to other industries. The reasons for this are numerous. On the one hand, there is unsatisfactory reliability with regard to deadlines, and on the other hand, the value-added activities in the construction industry are in the very low range in terms of the total output and are characterised by waste. Waste in this context refers to the inefficient use of resources of any kind, such as money, material or energy. The deficiency in the organisation of the different work processes also often results in long waiting times and, in turn, non-value-added rework. At the same time, the construction industry is facing the challenges of our time, like climate change and global competition, and has to meet increasingly high demands in terms of energy and resource efficiency.

Lean construction management could be a promising approach to mastering these challenges. The basis for this, is the analysis and standardisation of processes as well as a cooperative partnership between all project participants. In order to be able to identify the disruptions and problems that occur within construction projects, it is important to analyse reference projects and thus be able to identify weak points and starting points for improvements. Using the methods and tools of lean construction management, this is possible so that problem points are ideally identified at an early enough stage to avoid waste, costs and delays.

This research paper will first give an overview of the origin, definition and basic idea of lean management. Secondly, lean management will be discussed in relation to its application in the construction industry. Furthermore, the standardisation of process chains will be examined so that a starting point for further research can be created.

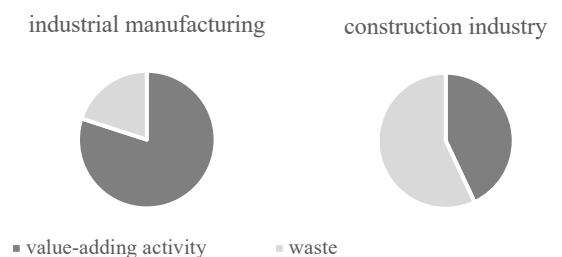
Keywords – lean construction, lean management in the construction process, optimization of the construction process, avoidance of waste

I. INTRODUCTION

Increasingly high demands on energy efficiency and functionality place constantly rising demands on the quality of buildings. At the same time, buildings are becoming more and more complex, which means that an increasing number of project participants are involved in their construction. While productivity per working hour has increased by about 42% on average in all sectors of the economy over the last 25 years, it has stagnated at the same level in the construction industry for years. This indicates that the development in terms of productivity in the construction sector is problematic and requires fundamental changes. [1] If the direct comparison is made with other industries, the high proportion of waste in the value-creating process becomes clearly visible.

Lean construction has the objective of eliminating any kind of waste in the construction process and significantly increasing value creation. In addition to focusing on the value chain, lean aims to improve cooperation by making processes more transparent and thus establishing orderly and stable processes on the construction site. For the successful application of Lean Construction, it is first important to know the necessary requirements and assumptions. Only in this way can the greatest possible added value and optimization potential be achieved.

Fig. 1 Comparison of waste in industrial manufacturing and in construction. Own representation based on [1]



II. LEAN MANAGEMENT

Origins of lean management and the lean philosophy

The beginnings of lean management can be traced back to assembly line production in the automotive industry at the beginning of the 20th century. Within this framework, Henry Ford introduced the division of labour in assembly line production. [2] The idea was that each employee carried out a limited sequence of work steps in order to achieve the greatest possible degree of optimization. After the end of the Second World War, some of the most important principles of lean management that are still valid today developed in Japan from Toyota's production system. The different elements of the Toyota production principle are shown in the "Lean House" according to Fuji Cho. The elements interact with each other in complex ways and have a decisive impact on the production flow. At the centre are the humans, who through their knowledge and commitment contribute to the continuous improvement of the system's processes. Through collective action and learning, they should identify waste and in this way contribute to improving quality. Fundamental principles are also stable and standardised processes as well as clear, visual management. In this context, the system can be understood on the one hand as a management system and on the other hand as a philosophy that needs to be lived. [3] Some of the main methodologies and tools resulting from the Toyota Production Principle are:

- Continuous Improvement (Kaizen)
- Elimination of waste (Muda)
- Just-in-Time (JIT)
- Continual quality control (Jidoka)
- Employee involvement
- Visual management

In 1985, the Massachusetts Institute of Technology started a research project comparing car production systems worldwide. In particular, the Toyota production concept described above was investigated. The researchers summarised the results and called the concept Lean Management for the first time. [2][12][13]

III. LEAN IN CONSTRUCTION MANAGEMENT

A. Origin of Lean Construction Management

In the 1990s, the term lean management was used to describe the experience gained in improving production processes in the automotive industry. The successful approaches were subsequently adopted in many other sectors of

the economy. The adaptation to the construction execution process is called Lean Construction. [7] In 1993, the International Group for Lean Construction (IGLC) was founded to exchange knowledge on theoretical principles in the field of lean construction management. In yearly conferences, knowledge and practical experience is exchanged in this context. [8] The topic of lean construction can be divided into three main areas: cooperative work planning, production systems and contract design. Cooperative work planning is particularly characterized by the Last Planner System. This is one of the most popular lean construction methods, which relies on collaborative scheduling. The common creation of a schedule with all project participants is intended to create commitment and achieve greater reliability. Production systems deal with the development of new methods for planning and controlling construction processes. One example of this is the method of takt planning, in which each building trade must complete defined work packages at a fixed takt time in a locally limited takt area. The contract design options are based on partnership contracts between the client, planners and construction companies. The division of responsibility among all project participants is intended to promote solution-oriented thinking. [9]

B. Problems with transferability/ differences stationary industry and construction industry

In the past, efficiency on construction sites has been improved through the use of new machines, the development of more efficient construction methods or the increase of the degree of prefabrication. In view of this, today, the point has increasingly been reached at which no further major improvement is possible in these areas. In contrast, lean management focuses on the analysis and optimization of work processes and procedures. By adapting and adjusting lean methods as they are applied in the stationary industry, lean management approaches can also be transferred to the construction industry. Nevertheless, the transfer encounters some difficulties. The reasons are that the stationary manufacturing industry and the construction industry differ in the following respects:

- Changing workplace

For example, while automobiles are produced entirely in stationary factories, a large part of the construction process takes place on site. This results in different local conditions for each new construction project, which can vary enormously. Therefore, it is necessary to prepare individual plans for logistics processes and construction site equipment for each project.

- Changing workers

While in the stationary industry every employee usually belongs to a fixed team, it can happen that workers on the construction site only stay on one construction project for days at a time and are also deployed on other projects, depending on

staffing needs. For capacity reasons, subcontractors may have to be commissioned, who in turn first have to be trained in processes. This can lead to a loss of the so-called training effect and thus to a reduction in the efficiency of the work.

- Changing processes

It frequently happens that building owners' decisions are made late and have to be flexibly incorporated into the construction process. In addition, different conditions, such as different terrain, require different measures and workflows. For each construction project, it is therefore necessary to react individually to the existing conditions and adapt the work processes accordingly.

- Outdoor manufacturing

With the exception of prefabrication, production in the construction industry takes place outdoors and is therefore heavily exposed to the weather. Not only wind, rain, snow and frost, but also above-average temperatures in summer reduce the performance of workers and prevent them from carrying out certain types of work.

- High degree of manual production

In contrast to the stationary industry, a lot of work in the construction industry continues to be done by hand, with only minor use of machinery.

- Planning and execution of the work by various companies

The execution of the construction work is usually awarded when the planning is already at an advanced stage, although the early involvement of the executing companies could considerably improve the quality of the planning. As a result of the low level of cooperation among the companies involved, there is a high loss of information. In the stationary industry, on the other hand, planning, production and delivery have been standardised at the highest level to prevent information losses.

- Individual production

Because of the common opinion that buildings have a unique character, construction processes are not sufficiently documented to make the knowledge acquired usable for later productions. Series production, though, will continue to increase in the future. With regard to this, it is therefore important that similar processes are documented in the best possible way in order to be able to standardise and optimise them later. [4][5][6]

C. Main types of lean construction management

The unique character of the projects, however, is no reason not to apply the lean philosophy in a modified form. This is possible because the processes carried out in different projects are repeated again and again. Lean construction can be divided into a total of three main types of manifestation:

- Cooperative work planning

Cooperative work planning is decisively shaped by the so-called Last Planner System®. This is one of the best-known methods of lean construction management. The focus is on collaborative scheduling of all project participants to generate a solid workflow. [8]

- Production systems

The design and control of production systems deals with the development of new methods for planning and controlling construction processes based on lean thinking. One of the best-known examples of this is takt planning, in which each trade performs defined work packages at fixed takt times in a locally limited takt range. [9]

- Contract design

The third type deals with new contract design options. The content of these contracts is based on partnership between the client, planner and general contractor. This should happen at an early phase of the project if is possible. Responsibility is distributed among all project participants, so that individual interests should play a subordinate role. [9]

IV. IDENTIFICATION OF DISRUPTIONS AND CLASSIFICATION IN THE LEAN PHILOSOPHY USING THE EXAMPLE OF A STANDARD WORKFLOW

The conventional way of construction is characterised by unsatisfactory reliability. Within the framework of the master's thesis "Identifikation von Anwendungsfeldern für Lean Management im Wohnungsbau", a standard procedure for the extension of a multi-family building was developed on the basis of literature research and empirical values. In this research paper, the approach and the most important findings have been summarised. The objective was to identify all possible disruptions in the construction process and to compare these with the types of waste according to the lean philosophy in order to identify solutions from the field of lean management that can be used to support the value creation process in the construction industry. The development and implementation of standard workflows could be facilitated in the future through the professional documentation of construction processes and the disruptions they involve. On a significantly larger data basis, it would therefore be possible to identify disruptions at an early stage and avoid them in the future. [10]

A. Approach to the development of a process workflow

First, a standard process workflow was determined, as it is common for residential construction. The basis for this was formed by six different example projects from which common construction processes were filtered out. As a data basis for this, schedules were compared, and recurring processes identified. In addition, process steps described in the literature were used. [9] Secondly, the process flows were illustrated by breaking down the process into areas. The areas were divided into roof,

balconies, façade, standard floor, outdoor area. By using this classification, the processes were structured and an order was created for them. Special dates were marked with milestones. For clarity, different colours have been assigned to the different crafts and a legend has been created for them. Processes running consecutively are illustrated one after the other and processes running simultaneously are arranged one below the other. Following this, a timeline was developed for the designed processes. An example building was generated for this purpose. In order to determine the duration of the processes, various sources were used. On the one hand, the times from sample schedules of projects of the size of the study project were analysed, and on the other hand, time requirement values from the literature were used. In addition, assumptions from other projects were used to complete the results. In order to determine the operation durations, time requirement values were multiplied by the quantities to be produced and divided by the number of workers and their daily working time.[10]

B Identification of disruptions in the construction process

In a next step, typical disruptions within the construction process were analysed and identified. Problems that can result in disruptions to the construction process can have a variety of origins. Disruptions are especially critical when they result in schedule deviations. In general, two main reasons can be identified for this. These are, on the one hand, changes in the framework conditions and, on the other hand, incorrect scheduling. Changed framework conditions can result, for example, if the client has subsequent change requests or fails to give approval for the execution of certain processes. Delays can be caused by inadequate or missing planning, but also by insufficient capacity on the part of the construction companies carrying out the work. In interviews, various construction participants were first asked about their understanding of lean management and then asked to describe disruptions on the basis of a submitted process structure. In this context, the processes were to be checked for their useful arrangement and possible faults were to be identified. In addition, general disturbances and problems should be named. Afterwards, the interviews were evaluated by clustering the statements of the interviewees. Categories were formed from this. In the table shown, the frequency of the disruptions named in the interviews is listed from top to bottom. [10]

C. Discussion of the problem categories in the context of lean waste types

After the recorded problems had been assigned to the different types of use of lean management, the next step was to start finding methods and techniques from lean management for their elimination. All the categories listed belong to avoidable activities and are therefore classified as waste. Waste can also be subdivided. These different types of waste can then be assigned to the types of disruption. According to the Lean

philosophy, a total of seven/eight types of waste can be identified:

- **Waiting times**
Planned and unplanned waiting times
- **Defective products**
Waste, post-processing and corrections
- **Unnecessary movements**
Unnecessary movements of people and machines
- **Transportation**
Unnecessary transport of materials
- **Over-processing**
Unnecessary processes
- **Overproduction**
Products without customer requirements
- **Inventory**
Unnecessary stocks of intermediate and end products
- **Unused creativity potentials**
Unused knowledge of employees or lack of support [11]

Category		Description	Type of waste according to the lean principle
1	Low capacity	Insufficient available labour force	<ul style="list-style-type: none"> ▪ Waiting times ▪ Over processing
2	Missing planning	Delay in the production of the planning documents	<ul style="list-style-type: none"> ▪ Waiting times ▪ Defective products ▪ Inventory
		Lack of sharp details	
3	Missing or insufficient advance delivery	Continuous control of stock levels in buffer	<ul style="list-style-type: none"> ▪ Waiting times ▪ Defective products ▪ unnecessary movements ▪ Inventory
		Continuous control of material consumption data	
4	Defective performance of the subcontractor	Coordination problems of the stakeholders	<ul style="list-style-type: none"> ▪ Waiting times ▪ unnecessary movements

		Missing coordination	<ul style="list-style-type: none"> Defective products unused creativity potentials
5	Logistics problems	Problems with the delivery	<ul style="list-style-type: none"> Waiting times Transportation unnecessary movements inventory
		lack of storage space	
6	incorrect cost calculation	incorrect calculation of the costs	<ul style="list-style-type: none"> Defective products
7	Decisions of the client	Omission of the client's obligation to cooperate	<ul style="list-style-type: none"> Waiting times Overprocessing
		Change requests of the client	
8	Time pressure	Deadlines that cannot be kept	<ul style="list-style-type: none"> Waiting times Defective products unnecessary movements
9	Insolvency	Solvency is no longer guaranteed	<ul style="list-style-type: none"> Waiting times Overproduction
10	Building permission	Lack of planning permission	<ul style="list-style-type: none"> Waiting times

Fig. 3: Disruptions and problems in the construction process and types of waste. Own representation based on [10]

V. MEASURES TO AVOID WASTE ACCORDING TO THE LEAN PRINCIPLES

After the categories have been assigned to the types of waste, the next step is to use the appropriate methods from lean management to eliminate the problems.

- Ident value**
 the definition of value depends on the client
- Map value stream**
 The value stream is determined on the basis of the value creation principle
- Create flow**
 This flow does not include interruptions such as storage
- Establish Pull**
 The flow is guided by the customer's needs according to the so-called pull principle. This means that a process only starts when the customer's demand is received
- Pursuit perfection**
 The constant improvement of the realisation of the principles is aimed at [11]

After the categorised problems were assigned to the different types of waste according to Lean Management, it was possible to identify tools from Lean Management to eliminate the problems. These are not explained in more detail in this paper, but can be found in the literature. Other possible tools are not excluded

Category	Lean principles	Lean tools
1	Low capacity <ul style="list-style-type: none"> Create flow Establish Pull 	<ul style="list-style-type: none"> Kaizen Levelling of production Hansei Jidoka
2	Missing planning <ul style="list-style-type: none"> Create flow 	<ul style="list-style-type: none"> Kaizen 5 whys 5S (methodology) Poka yoke
3	Missing or insufficient advance delivery <ul style="list-style-type: none"> Create flow Establish Pull Pursuit perfection 	<ul style="list-style-type: none"> Kaizen Just-in-time Visual management Genchi genbutsi Jidoka
4	Defective performance of the subcontractor <ul style="list-style-type: none"> Create flow 	<ul style="list-style-type: none"> Kaizen Visual management
5	Logistics problems <ul style="list-style-type: none"> Map value stream Create flow 	<ul style="list-style-type: none"> Kaizen Just-in-time Visual management (Kanban)
6	incorrect cost calculation <ul style="list-style-type: none"> Pursuit perfection 	<ul style="list-style-type: none"> Kaizen Poka yoke Jidoka
7	Decisions of the client <ul style="list-style-type: none"> Ident value Map value stream Create flow Establish Pull 	<ul style="list-style-type: none"> Kaizen Visual management
8	Time pressure <ul style="list-style-type: none"> Map value stream Create flow Establish Pull 	<ul style="list-style-type: none"> Kaizen Visual management (Kanban) SMED
9	Insolvency	Well-planned foresight for timely identification of liquidity bottlenecks and control of cash flows
10	Building permission <ul style="list-style-type: none"> Create flow 	<ul style="list-style-type: none"> Kaizen Visual management

Fig. 4: Disruptions and problems in the construction process, lean principles and tools. Own representation based on [10]

VI. FURTHER RESEARCH TOPICS

The demand for building products continues to rise. The construction industry therefore faces the challenge of significantly increasing its productivity in the coming years. This requires in particular a sharpening of the process thinking of those involved in construction and significantly higher planning qualities. In the continuation of the project, it would therefore be interesting and promising to confirm the results of the first research work by means of representative results. This should be done using a holistic model. In addition, synergies between methods of process optimisation, such as Lean Management, in combination with planning methods, such as Building Information Modelling principles, should be investigated. In this context, suitable interfaces could be identified and valuable synergy potentials highlighted. Since the construction industry is still very far from recognising the value creation potential in the individual construction processes, an implementation of process management thinking on the one hand and information-based planning on the other could be promising. A closer look reveals that the approaches of both methods are similar: Value management in Lean Construction focuses on identifying the processes that create value for the client and eliminating processes that do not. In the use of Building Information Modelling, value creation potentials are also specifically supported by different process steps and predefined requirement profiles to query the fit of process steps and delivery results. Both approaches are therefore based on similar principles, so that it should be examined where there is potential for sensible dovetailing of the two methodologies.

ACKNOWLEDGMENT

This research is generally supported by our colleagues from HSA_ops - the operational research team of our university of applied research in Augsburg - who provided expertise that greatly assisted the research, although they may not agree with all of the interpretations of this paper.

REFERENCES

- [1] M. Christoph; Schwahn Florian: Bauwirtschaft – konjunkturelle Entwicklungen der letzten 25 Jahre im Fokus der Statistik in: Jahressausgabe VDI Bautechnik 2017/2018, Springer-VDI-Verlag GmbH & Co KG, Düsseldorf 2017
- [2] P. Gorecki; P. Pautsch: Praxisbuch Lean Management – Der Weg zur operativen Excellence, 3. Auflage, Carl Hanser Verlag GmbH & Co. KG, München 2018
- [3] Liker J.: Der Toyota Weg. 14 Managementprinzipien des weltweit erfolgreichsten Automobilkonzerns, 8. Auflage, FBV Finanz Buch Verlag, München 2013
- [4] Helmus M.; Offergeld B (Bundesanstalt für Arbeitsschutz und Arbeitsmedizin): Qualität des Bauens – Eine Studie über den Begriff und die Wahrnehmung der Bauqualität bei privaten und öffentlichen Bauherren und Bauunternehmen, Bonifatius Druckerei, Paderborn 2012, S.18-21

- [5] Stark K.: Baubetriebslehre – Grundlagen, 1. Auflage, Friedr. Vieweg & Sohn Verlag, Wiesbaden 2006, pp. 22-24
- [6] BWI-Bau: Ökonomie des Baumarktes – Grundlagen und Handlungsoptionen: Zwischen Leistungsversprecher und Produktanbieter, Springer Fachmedien Wiesbaden, 2013, pp.17-19
- [7] Heidemann A.: Kooperative Projektabwicklung im Bauwesen unter der Berücksichtigung von Lean Prinzipien – Entwicklung eines Lean-Produktionssystems, KIT Scientific Publishing, 2011, pp. 12
- [8] International Group for Lean Construction: <https://www.leanconstruction.org/about-us/> access source: 20.01.2020
- [9] Fiedler M.: Lean Construction – Das Managementhandbuch. Agile Methoden und Lean Management im Bauwesen, Springer Gabler, Berlin 2018
- [10] Wierer L.: Identifikation von Anwendungsfeldern für Lean Construction Management im Wohnungsbau, Augsburg 2019
- [11] German Lean Construction Institute: Lean Construction – Begriffe und Methoden, KIT Institut für Technologie und Management im Baubetrieb, Karlsruhe 2019
- [12] Ohno, T.: Das Toyota Produktionssystem. Unter Mitarbeit von Wilfried Hof, Campus-Verlag, 3., erweiterte und aktualisierte Aufl, Frankfurt a. Main 2013
- [13] Womack J. P. et al.: The Machine That Changed the World: The Story of Lean Production, Westview Press Inc; Reprint Edition, 1991

Structural Differences in the Higher Education Research in Germany between Universities and Universities of Applied Sciences

Felix Kluger

University of Applied Sciences Augsburg
 Faculty for Mechanical Engineering
 An der Hochschule 1, 86161 Augsburg, Germany
 Email: felix.kluger@hs-augsburg.de

Abstract—Research at higher education institutions has undergone a structural change in Germany in recent decades. While for a long time it had been the exclusive preserve of universities to conduct research, it might be observed that in recent years universities of applied sciences have also become increasingly research-intensive. Even before the Bologna Process universities of applied sciences had actively expanded their research activities. Therefore, they were increasingly claiming what was previously the unique selling point of universities. This development is confirmed by the current amendment to the Bavarian Higher Education Act. It provides further expansions of research at universities of applied sciences.

This article shows the most striking structural differences in the research sector between the two higher education systems in Germany. Both types of higher education institutions are analysed in terms of digitalisation, research output, study focus as well as financial and human resources. In summary, it can be stated that there are still major differences in terms of resources and developments in the research areas between those systems.

Keywords: UAS, university of applied sciences, university, research, development, differences, Germany

I. INTRODUCTION

The development of higher education research at universities and universities of applied sciences (UAS) is characterised by their respective histories. The first universities in Germany were founded in the 14th century. At this time, they were geared towards administering and preserving knowledge. The establishment of research at German universities can be traced back to Wilhelm von Humboldt in the 19th century. His idea of universities that focus on research is still considered to be a landmark in the development of universities today. Thus, universities were the only type of higher education institution in Germany intending to conduct education through science in the areas of teaching and research for a long time. As a result of the expansion of student numbers in the 1960s, universities of applied sciences were introduced nationwide in the early 1970s as a further type of higher education institution [1]. Providing students with an application-oriented academic education was the aim of founding universities of applied sciences [2]. In the following decades, the individual federal

states introduced several federalist higher education reforms. It ensured both the strengthening of practice-oriented teaching at the UAS and the establishment of application-oriented research [3]. This development was reinforced by the decision of the European Ministers of Education on the Bologna Process in 1999. Not only did the policy reform envisage creating a more unified higher education system in Europe, but also achieving a higher output of highly skilled workers. In general, the Bologna Process was designed to ensure the harmonisation of the two higher education systems across Europe. Application-oriented research at the universities of applied sciences has received a significant boost from this reform. In contrast, the reform intended to invest in a significant strengthening of the area of study and teaching at the universities [4].

The plans for the implementation of the reform in the period from 2000 to 2010 were perceived as an educational revolution by many higher professionals across Europe [5]. Especially the strengthening of higher education research at universities of applied sciences caused debates throughout Europe about orientation and alignment between the two higher education systems. At the state level, some of these discussions have been continued to this day. Two different philosophies emerged between the two higher education systems in Europe. While many countries focused on the convergence of both systems, different ways of implementing the reform have been observed, as in Switzerland or Finland. In these countries, the specialisation of the UAS research profiles was defined. This targeted definition created an explicit characteristic distinction between the two types of higher education institutions and their activity profile in the field of research [6]. However, in Germany, there has been a politically desired convergence between universities and universities of applied sciences in recent years. This convergence had been generated by state-specific higher education reforms in the individual federal states. Higher education institutions were also given more autonomy to better obtain their "freedom of science, research and teaching" [7]. The guideline of the Bavarian Higher Education Act confirms the expansion of research at the UAS. The reinforcement of the research mandate should be ensured

without equating it with the obligatory university research mandate. Bavarian universities of applied sciences have to be given the task of performing research and development related to specific applications as a new assignment. In order to maintain differentiation between the two types of higher education institutions, application-oriented teaching should remain the primary task of the UAS [8].

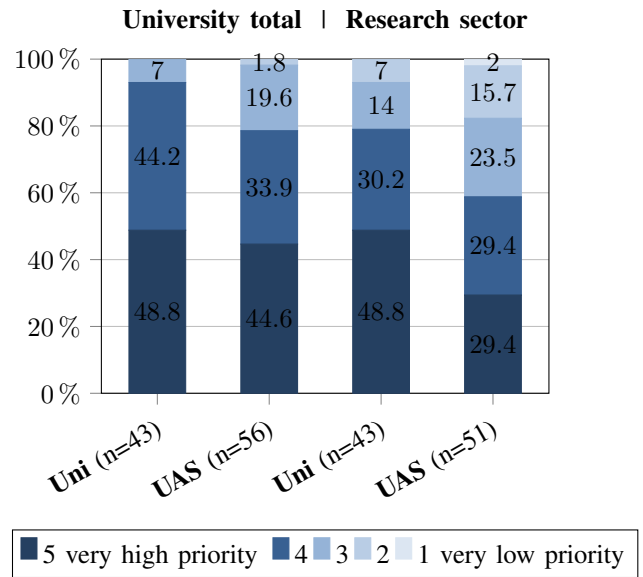
Developments in recent decades show an increasing convergence between the two higher education systems in Germany. Higher education research is being increasingly expanded at the UAS. Thus, it is catching up more and more with university research. This paper analyses and highlights the existing elementary differences in higher education research between universities and universities of applied sciences in Germany. To illustrate those differences, the following categories have been analysed and compared between UAS and universities: the research output, the study focus, the financial and human resources as well as the level of digitalization as an indicator for a modern research structure.

A. Digitalisation

Currently, the structural change towards an information and knowledge society shapes all parts of society [9]. Digitalisation is an elementary tool that guarantees this conversion. This change also effects higher education research. Digitalisation creates new forms of gaining knowledge in science. Moreover, digital knowledge transfer promotes and opens up new areas of research. In addition, digitalisation also establishes a platform for the global transfer of knowledge and information [10]. Digitalisation is very important because it provides a contemporary and modern form of interdisciplinary and resource-efficient research. This enables higher education institutions to respond more quickly in case of new challenges and changes in the fast-moving field of research. Also, it permits them to act in a more fact-based way. Digitalisation of German higher education institutions is progressing very slowly compared to other countries. Particularly bureaucratic and complex processes lead to a protracted implementation of digitalisation in Germany. Further, there is a persistently sceptical and pessimistic attitude among higher education staff towards digitalisation at institutions in Germany. This development is primarily due to the technically premature and conceptually immature implementation of projects in the past [11]. The digitalisation of research at German higher education institutions, therefore, has a certain “shadowy existence“ among a great number of employees [12]. Nevertheless, according to a study, digitalisation has a high priority among higher education leaders in Germany. In a comparison between the two higher education systems, digitalisation is given a slightly higher priority at universities than at UAS. The research sector shows a significantly higher difference between the two systems. While 48.8 % of the universities surveyed assign a very high priority to digitalisation, the rate at the university of applied sciences is merely 29.4 %. The complete breakdown according

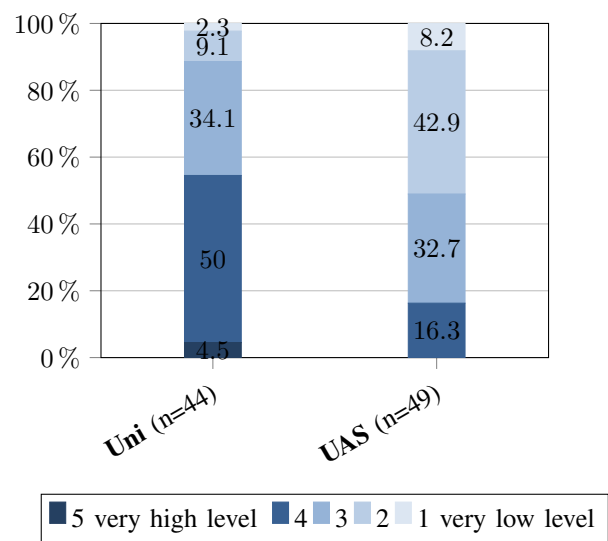
to the entire higher education sector and the research sector is shown below by type of higher education institution in figure 1 [13].

Figure 1. Importance of digitalisation at German higher education institutions by type of institution and sector. All data in percent. (Source: [13])



Moreover, this development is evident in the implementation of digitalisation at higher education institutions. While the surveyed university administrations of universities assessed the status of digitalisation at their institution with 29.5 % as high or very high in the areas of study & teaching, research, and administration, the rate at UAS is merely 14.3 % [13]. The large difference in the implementation of digitalisation between universities and universities of applied sciences in the research sector becomes apparent in figure 2.

Figure 2. Status of digitalisation in the research sector by type of higher education institution. All data in percent. (Source: [13])



The status of digitalisation is rated as high or very high by 54.5 % of university managers in the research sector at universities. In comparison, only 16.3 % of the executives at the UAS surveyed assessed the status at their research institution as high. It is particularly striking that no management at the UAS evaluates the implementation of digitalisation as very high.

Digitalisation in research helps to generate contemporary processes and to automate tedious administrative steps. Digital research is divided into core tasks and supporting procedures for research processes [12]. The supporting processes can be implemented through Research Data Management (RDM), Current Research Information Systems (CRIS), or Virtual Research Environment (VRE), among others. According to the study on digitalisation at higher education institutions in Germany, research information systems are the most widespread. More than 30.6 % of the higher education institutions surveyed stated that they had implemented a CRIS. In addition, 18.8 % of the participants declared that they had realized a virtual research environment in their higher education research. Of the respondents, 18.2 % indicated that they had installed a research data management system at their institution. The survey also revealed that universities have more IT systems for their research infrastructure than UAS [13].

B. Research Output

Digitalisation of research forms the basis for higher education institutions to be able to make a contemporary assessment of research output. Publications are a significant factor for the output. Publication management is necessary to promote the creation and management of scientific contributions. This can be implemented, for example, through a digital Current Research Information System. Despite some possibilities for software-based support of authors, a sobering result can be observed at higher education institutions in connection with the use of publication management. There are a number of tasks associated with this management, which many authors find organisational and time-consuming. In many cases, this includes not only the reporting of bibliographic data, but also clarification with the Open Access policy of the respective institution [14]. In Germany, around half of all specialist articles can be accessed via the higher education institutions' Open Access standards. Every second an institution of higher education in Germany has a corresponding publication strategy. The big difference between universities and UAS is striking. While more than half of all German universities have an Open Access strategy (51.3 %), only 15.8 % of universities of applied sciences have one. Moreover, it is obvious, that this ratio will continue for the foreseeable future. Regarding universities, 28.2 % plan to establish a strategy. This contrasts with 33.3 % of UAS that want to integrate an Open Access policy into their operations [15]. In order to be able to measure research output, it is necessary to define indicators and key figures. It should be noted that many indicators established in the higher education

landscape were conceived from a university perspective. These include the listing of publications in international databases, the amount of third-party funding acquired or the number of doctorates. The UAS lack uniform standards for indicators in the area of applied research. Therefore, a comparison of scientific output between UAS is often only subjectively measurable [16]. The following table I demonstrates that research output at UAS should not be purely publication-based as it is usually the case at universities. The table illustrates the distribution of scientific publications worldwide by discipline.

Table I
WORLDWIDE PUBLICATIONS BY DISCIPLINE IN PERCENTAGE TERMS.
PERCENTAGES MAY NOT ADD TO 100 % BECAUSE OF ROUNDING.
(WITH DATA FROM:[17])

Discipline	%	Discipline	%
Medical sciences	21.13	Geosciences	5.77
Engineering	18.49	Social sciences	5.73
Biological sciences	15.00	Mathematics	2.47
Computer sciences	9.05	Agricultural sciences	2.34
Physics	8.75	Psychology	1.74
Chemistry	7.88	Other life sciences	1.17

NOTE: Contributions refer to publications from a selection of peer-reviewed journals, books, and conference proceedings in science and engineering fields from Scopus.

When looking at the distribution, it becomes clear that many subject groups with strong publications are mainly located at universities. Subject groups with strong publications, such as medical sciences or biological sciences, are partly not located at all or only to a very small extent at universities of applied sciences [17]. The UAS have a higher proportion of creative and design subject groups than the universities. In these disciplines, research performance is often marked by awards and prizes. This confirms that research output differs between basic and applied research. Purely publication-based research output cannot take this development into account.

C. Study focus

Since the area of study & teaching is firmly coupled with the area of research, some indicators from this area also allow conclusions to be drawn about the research mode. A strong application-oriented research is evident at the UAS. The research mode at universities is more oriented towards basic research [18]. This different orientation with regard to research disciplines between universities and universities of applied sciences is reflected, among other things, in the distribution of students by course of study [19].

In the following table II, the subject groups and the respective number of enrolled students are broken down by type of higher education institution. It is remarkable that especially in the subject groups with a very high proportion of basic research, such as Mathematics & Natural Sciences, Humanities and Human Medicine & Health Sciences, significantly more students are enrolled in universities than at UAS. In contrast, in

Table II
NUMBER OF ENROLLED STUDENTS IN THE WINTER SEMESTER 19/20 IN GERMANY BY TYPE OF HIGHER EDUCATION INSTITUTION AND SUBJECT GROUPS. (WITH DATA FROM: [19])

Subject group	Uni	UAS
Humanities	311.306	8.952
Sport	26.735	1.285
Law, Economics and Social Sciences	561.095	460.863
Mathematics, Natural Sciences	295.156	20.776
Human Medicine, Health Sciences	127.446	58.258
Agricultural, Forestry, Food Sciences and Veterinary Medicine	38.125	24.530
Engineering	356.372	416.813
Arts, Arts Sciences	29.504	31.105

the application-oriented research area of Engineering, conspicuously more students are enrolled at UAS than at universities. This confirms that the orientation of universities is more geared towards subject groups with strong basic research as UAS are increasingly home to degree programmes with applied research.

The study quality monitor of the Federal Ministry of Education and Research demonstrates in a study how many students are connected with research. In this regard, the ministry determined in a survey that almost one in two students can be provided with research-related courses at universities. However, the study also shows that only 16 % of universities and only 11 % of UAS provide students with very intensive research-related study opportunities. It is particularly apparent that research-related offers are mostly integrated into Master’s degree programmes. In the Bachelor’s and state exam’s degree programmes, the research-related offerings are very low [20].

D. Financial resources

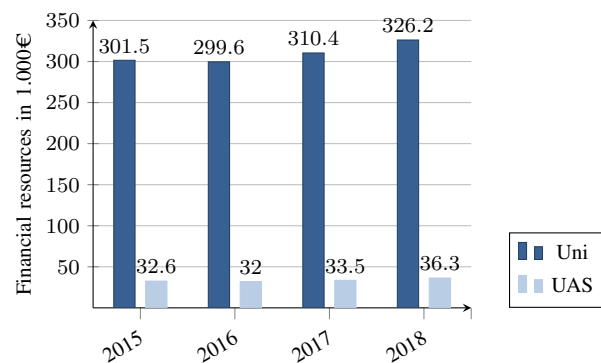
In order to be able to better compare research and development expenditure between universities, the Federal Ministry of Research and Education has introduced the “R&D coefficient”. The coefficient indicates how large the share of research expenditure is in relation to total expenditure [21]. Table III lists the R&D coefficients by type of higher education institution. In the case of universities, more precise data is available for several subject groups.

Table III
R&D-COEFFICIENT IN 2018 ACCORDING TO TYPE OF HIGHER EDUCATION INSTITUTION AND SUBJECT GROUP. (WITH DATA FROM: [21])

Subject group	R&D-coefficient
<i>Universities</i>	
- Humanities, Arts, Arts Science, Sport	29,2%
- Law, economics and social sciences	36,0%
- Mathematics, Natural Sciences	44,2%
- Agricultural, Forestry and Nutritional Sciences	36,8%
- Engineering sciences	39,5%
<i>Universities of Applied Sciences</i>	
- Average	15,0%

By contrast, only an average value is available for the universities of applied sciences, which was determined by the ministry through several expert interviews. A comparison between the two higher education systems clearly demonstrates that the coefficient at the universities with a range of 29.2 % to 44.2 % is significantly higher than the average value at the UAS with 15.0 %. The R&D coefficient can also be used to reach a conclusion about the basic equipment in the research and development sector. Since the coefficient is significantly higher at universities than at UAS, it is much easier for universities to provide an improved equipment infrastructure for research. The infrastructure includes, among other things, research buildings but also large-scale equipment. The equipment is mainly financed through subsidies from the university sponsor or through third-party funding within the framework of cooperations. It is apparent that many of the University of Applied Sciences’ cooperation partners tend to be regionally anchored and more often belong to the group of small and medium-sized enterprises. As a result, the size of the projects and the financial strength of the cooperation partners are often significantly smaller than the cooperations of the universities, most of which cooperate with large, supraregional, and international companies [18]. The distribution of research funding with companies for 2018 is as described below, according to a report by the Federal Statistical Office from 2020. According to this, universities receive around 90.1 % of all funding, while universities of applied sciences receive only 9.9 % of cooperation funding from companies [21]. The difference in financial resources between the types of higher education institutions becomes particularly apparent when one looks at the third-party funding per professor. Figure 3 shows the third-party funding income by type of higher education institution. It becomes obvious that the acquisition of third-party funding per professor is significantly higher at the universities than at the UAS.

Figure 3. Third-party funding per professor by type of higher education institution. (Own illustration with data from: [21], [22], [23])



Taking into account the different staff structures at the two higher education systems, the difference is partly relativised. The universities are able to raise significantly more third-party funding than the UAS because the professors have significantly more academic staff to support them [18].

E. Human resources

In order to achieve a good reputation in research, it is important to have well educated and sufficient scientific staff at the research institution. Considering the scientific personnel structure as a total in Table IV, it is evident how great the differences are between universities and universities of applied sciences.

Table IV
NUMBER OF EMPLOYEES IN STAFF GROUPS BY TYPE OF HIGHER EDUCATION INSTITUTION. (WITH DATA FROM: [24])

Occupational group	Uni	UAS
Full-time professors	24.683	20.035
Scientific and artistic staff	298.306	101.013

The number of professors is higher at universities than at the UAS. Taking into account the number of higher education institutions with 108 universities and 211 universities of applied sciences for the winter semester 2020/2021, it is obvious that there are significantly more professors available at universities on average than at universities of applied sciences. From this, it can be deduced that on average 229 professors are employed per university, while at the UAS there are only 95 professors per institution [24].

Furthermore, universities are not only entitled to more professors, but they also have more working time to devote to research. While on average most professors at universities have to teach eight semester hours per week, many UAS professors have up to 18 semester hours per week. The regulation of teaching duties is determined by the individual laws of the federal states [25], [26]. Moreover, there are also great differences in the employment relationships of academic staff. Student assistants are neglected in the statistics. For each university professor, there are on average twelve research assistants. At universities of applied sciences, there are only five research assistants for every professorial position [24]. In the process, the research assistants carry out many elementary supporting activities in research. Among others, that includes the preparation and collaboration in research projects and research institutions of the higher education institutions, but also the preparation of publications [27]. Besides other issues, the large difference in the number of academic staff is due to the right to award doctorates in the respective state higher education laws. Most of the higher education laws stipulate that only universities have full doctoral rights. At most UAS in Germany, therefore, only a cooperative doctoral procedure together with a university is possible. Only the state higher education laws in the states of Hesse and Saxony-Anhalt temporarily allow universities of applied sciences to already exercise the right to award doctorates under certain conditions. Some federal states see good opportunities to further expand research at universities of applied sciences by establishing the right to award doctorates [28].

Recently, this is demonstrated by the plans to amend the State University Act in Bavaria. In this way, research-strong areas of the UAS have to receive the right to award doctorates

temporarily from the State Ministry in order to be able to expand research activities at the universities of applied sciences in the long term [8].

II. CONCLUSION

Over the last few years the expansion of higher education research at universities of applied sciences in Germany has been progressing steadily. This study confirms that German universities of applied sciences are more focused on application-oriented research and the universities are more geared towards basic research. Despite the expansion of research activities at the UAS, there are still major differences between the two systems in terms of their research structure.

Digitalisation in the research sector at universities is better advanced than at universities of applied sciences. The UAS has to act urgently on this issue in order not to lose touch with other research institutions, nationally as well as internationally. In terms of research output, UAS need to collect data more systematically in order to measure and compare their research performance. In addition, corresponding UAS-specific key figures should be more effectively taken into account in the “Kerndatensatz Forschung“. Especially large differences in research occur between the two systems in terms of financial and human resources. The responsible bodies of higher education institutions must ensure that the research infrastructure at the universities of applied sciences is better developed and more extensively financed. This might lead to a significant improvement in the R&D coefficient at UAS as well. Another fundamental issue is the expansion of academic staff at the UAS and the comprehensive introduction of the right to award doctorates in research-intensive disciplines. In addition, more research professorships should be promoted. Alternatively, professors at UAS should be relieved of their teaching load, which is very high compared to universities. This would enable professors to do more research.

High quality of application-oriented research at the universities of applied sciences can only be guaranteed in the long term if better financial and personnel resources are ensured by the responsible bodies of higher education institutions. Nevertheless, it is obvious that despite great differences, UAS can already offer some profitable unique selling points in applied research. The facilities and institutes at the universities of applied sciences are significantly smaller than at universities. This makes them much more agile and flexible regarding their focus on new areas of research. In addition, research at UAS can be conducted more cost-effectively, which is particularly interesting in cooperation with start-up companies. These companies benefit particularly from the industry- and practice-oriented research direction of the universities of applied sciences.

The UAS have great potential to optimise their research structures. Especially in the area of digitalisation, there are many internal and external advantages for the UAS. In the internal administrative area of higher education research,

digitalisation can contribute to a significant increase in efficiency with regard to the cost and personnel structure. By contrast, in the external area, digital systems can improve the visibility of research output to the outside world and ensure a transparent presentation of research activities to the public. The special feature of digitalisation in the structures of higher education research is that the respective management of the UAS can specifically influence the degree of digitalisation. In this context, the UAS are politically more independent than in the other structural areas of higher education research.

In summary, the expansion of research at the universities of applied sciences is a profitable success for the entire higher education landscape in Germany. It enables universities to concentrate fully on basic research. In contrast, the universities of applied sciences can completely serve applied research. Higher education institutions in Germany are administered by the federal states, therefore more detailed research should be conducted at the federal state level in the future. As a result, it would be possible to show the respective structural differences in higher education research in even greater detail.

REFERENCES

- [1] HÜTHER, Otto: *Von der Kollegialität zur Hierarchie? - Eine Analyse des New Managerialism in den Landeshochschulgesetzen*. Berlin Heidelberg New York : Springer-Verlag, 2010. – ISBN 978–3–531–92538–7
- [2] *Kapitel "Vor uns liegt ein Bildungszeitalter", Umbau und Expansion - das bayerische Bildungssystem 1950 bis 1975*. In: MÜLLER, Winfried ; SCHRÖDER, Ingo ; MÖSSLANG, Markus: *Bayern im Bund. 1. Band: Die Erschließung des Landes 1949 bis 1973 (Quellen und Darstellungen zur Zeitgeschichte 52)*. Thomas Schlemmer/Hans Woller (Hg.), 2001, S. 273–355
- [3] KONDRATJUK, Maria ; POHLENZ, Philipp: *Die Organisation von Hochschulen in Theorie und Praxis - Forschungen zur Reform des Wissenschaftsbetriebes*. Berlin : Verlag Barbara Budrich, 2019. – ISBN 978–3–847–41338–7
- [4] NICKEL, Sigrun: Zwischen Kritik und Empirie – Wie wirksam ist der Bologna-Prozess? (2011), S. 8–17. – ISBN 978–3–941927–18–6
- [5] WINTER, Martin: Die Revolution blieb aus: Überblick über empirische Befunde zur Bologna-Reform in Deutschland. (2011), S. 20–35. – ISBN 978–3–941927–18–6
- [6] LEPORIA, Benedetto ; KYVIK, Svein: The Research Mission of Universities of Applied Sciences and the Future Configuration of Higher Education Systems in Europe. In: *Higher Education Policy* (2010), Nr. 23, S. 295 – 316. <http://dx.doi.org/doi:10.1057/hep.2010.11>. – DOI doi:10.1057/hep.2010.11
- [7] DOHMEN, Dieter ; KREMPKOW, Rene: Hochschulautonomie im Ländervergleich-Bestandsaufnahme und Ausblick auf künftige Entwicklungen / Konrad-Adenauer-Stiftung. Sankt Augustin, 2015. – Forschungsbericht
- [8] BAYERISCHES STAATSMINISTERIUM FÜR WISSENSCHAFT UND KUNST: Eckpunkte zur Novellierung des Bayerischen Hochschulrechts. 2020. – Forschungsbericht
- [9] NORTH, Klaus: *Wissensorientierte Unternehmensführung - Wissensmanagement gestalten*. Berlin Heidelberg New York : Springer-Verlag, 2016. – ISBN 978–3–658–11643–9
- [10] *Digitalisierung: Zeitenwende für die Forschung*. Bundesministerium für Bildung und Forschung. <https://www.bmbf.de/de/digitalisierung-zeitenwende-fuer-die-forschung-3854.html>. Version: Februar 2017. – Last accessed 06 May 21
- [11] DEMANTOWSKY, Marko ; LAUER, Gerhard ; SCHMIDT, Robin ; WILDT, Bert t.: *Was macht die Digitalisierung mit den Hochschulen? - Einwürfe und Provokationen*. Berlin : De Gruyter, 2020. – ISBN 978–3–110–67331–9
- [12] HEYDE, Markus von d. ; HARTMANN, Andreas ; AUTH, Gunnar ; ERFURTH, Christian: Zur disruptiven Digitalisierung von Hochschulforschung-Faktoren der Skalierung und ein Zukunftsszenario. In: *Informatik Spektrum* (2018), S. 359–368. <http://dx.doi.org/https://doi.org/10.1007/s00287-018-01126-1>. – DOI <https://doi.org/10.1007/s00287-018-01126-1>
- [13] GILCH, Harald ; BEISE, Anna S. ; KREMPKOW, René ; MÜLLER, Marko ; STRATMANN, Friedrich ; WANNEMACHER, Klaus: *Digitalisierung der Hochschulen - Ergebnisse einer Schwerpunktstudie für die Expertenkommission Forschung und Innovation*. Expertenkommission Forschung und Innovation (EFI), 2019
- [14] *Kapitel Publikationsmanagement an Hochschulen. Wie erreiche ich mehr durch weniger?* In: STEENWEG, Helge: *Die neue Bibliothek - Anspruch und Wirklichkeit: 31. Österreichischer Bibliothekartag*. Innsbruck, 18. - 21.10.2011, S. 89–95
- [15] HOCHSCHULBAROMETER - STIFTERVERBAND: Lage und Entwicklung der Hochschulen aus Sicht ihrer Leitungen, Ausgabe 2018 - Open Science - Welche Chancen sehen Hochschulen in der Zusammenarbeit mit unüblichen Akteuren? 2017. – Forschungsbericht. – 31–37 S.
- [16] DUONG, Sindy: *Facetten und Indikatoren für angewandte Forschung und Third Mission an HAW -*. HoF Wittenberg, Institut für Hochschulforschung an der Martin-Luther-Universität Halle-Wittenberg, 2016
- [17] WHITE, Karen E.: Science and Engineering Publication Output Trends: 2017 Shows U.S. Output Level Slightly Below That of China but the United States Maintains Lead with Highly Cited Publications. In: *Info Brief - National Center for Science and Engineering Statistics* (2019), Mai, Nr. NSF 19-317, S. 1–6
- [18] In: HACHMEISTER, Cort-Denis ; DUONG, Sindy ; ROESSLER, Isabel: *Forschung an Fachhochschulen aus der Innen- und Außenperspektive: Rolle der Forschung, Art und Umfang*. 2015. – ISBN 978–3–941927–61–2, S. 30
- [19] STATISTISCHES BUNDESAMT (DESTATIS): Bildung und Kultur - Studierende an Hochschulen - Wintersemester 2019/2020. 2020 (: 2110410207004). – Forschungsbericht
- [20] MULTRUS, Frank: Forschung und Praxis im Studium-Befunde aus Studierendensurvey und Studienqualitätsmonitor / Bundesministerium für Bildung und Forschung. Berlin, 2012. – Forschungsbericht
- [21] STATISTISCHES BUNDESAMT (DESTATIS): Bildung und Kultur - Monetäre hochschulstatistische Kennzahlen 2018. 2020 (2110432187004). – Forschungsbericht
- [22] STATISTISCHES BUNDESAMT (DESTATIS): Bildung und Kultur - Monetäre hochschulstatistische Kennzahlen 2017. 2019 (2110432177004). – Forschungsbericht
- [23] STATISTISCHES BUNDESAMT (DESTATIS): Bildung und Kultur - Monetäre hochschulstatistische Kennzahlen 2016. 2018 (2110432167004). – Forschungsbericht
- [24] STATISTISCHES BUNDESAMT (DESTATIS): Bildung und Kultur - Personal an Hochschulen 2019. 2020 (2110440197004). – Forschungsbericht
- [25] WISSENSCHAFTSRAT: Empfehlungen zu einer lehrorientierten Reform der Personalstruktur an Universitäten. Berlin, Januar 2007 (7721-07). – Forschungsbericht
- [26] LEHRE, Forschung und: *Klage gegen hohes Lehrdeputat an Fachhochschulen*. <https://www.forschung-und-lehre.de/recht/klage-gegen-hohes-lehrdeputat-an-fachhochschulen-2090/>. Version: September 2019. – Last accessed 06 May 21
- [27] TECHNISCHE UNIVERSITÄT BERLIN: Leitfaden zum Aufgabenbereich wissenschaftliche(r) Mitarbeiter/innen an der Fakultät VII (Wirtschaft und Management) der TU Berlin. Berlin, Juli 2008. – techreport
- [28] PAUTSCH, Arne: Warum das FH-Promotionsrecht ein Irrweg ist. In: *Forschung und Lehre* (2020), August. <https://www.forschung-und-lehre.de/warum-das-fh-promotionsrecht-ein-irrweg-ist-3027/>. – Last accessed 06 May 21

Use of Digital Assistance Systems in Production

Anina Rembold
 Fakultät für Maschinenbau,
 Fahrzeugtechnik, Flugzeugtechnik
 Hochschule für angewandte Wissenschaften München
 München, Deutschland
 Email: Rembold@hm.edu

Abstract—The paper presents a progress report of the ongoing research project “use of digital assistance systems in production”. This project is made in cooperation with the company MTU Aero Engines AG. The structure of the research project is divided into three subsequent theses. The first one covers the state of technology and differentiation of digital assistance systems. The second thesis focuses on the selection of digital assistance devices depending on a use case. Therefore, the norm DIN EN ISO 9241-210 is used as a guideline. In the third thesis the implementation and resulting experiences will be discussed. With these three topics ‘state of technology’, ‘selection’ and ‘implementation’ the skeletal structure of a promising usage of digital assistance systems is made. The aim of this research project is to create a structured process model for the implementation of digital assistance systems that fits to different use cases and companies. In this paper, the classification of digital assistance systems is discussed. Furthermore, the approach of selecting an assistance device is mentioned briefly.

I. INTRODUCTION

Since the 18th century there have been three big industrial revolutions. The steam engine by James Watt was the first one, followed by the assembly line from Henry Ford and thirdly, the electronic data processing. Today’s revolution is characterised by the digitalization of processes and Industry 4.0. [1] Industry 4.0 stands for a production that is no longer statically automated but instead intelligent. Companies worldwide are faced with that topic. They have to rethink their manufacturing and development processes. A part of the digitalization are digital assistance systems. In production, they can be used to support the worker in complex situations. The aim of the systems is to counteract the increasing complexity, skill short-age and higher quality standards. Many companies find it challenging to allocate the right amount of time and resources for the implementation of digital assistance systems. The cost factor and the lack of experience is a barrier to them. Especially medium-sized companies have a problem to get an overview of all different assistance technologies. [2]

The aim of this research project is to simplify the decision of an assistance system by the classification of the different technologies and a structured procedure model for the selection.

II. STATE OF TECHNOLOGY

A. Classification of digital assistance systems

Assistance systems in general are devices which support the user in his operations. Digital assistance systems are able

to use computer based information, additionally. They can be differentiated into physical, sensorial and cognitive assistance systems (cf. Fig. 1). Furthermore, sensorial and cognitive assistance devices subclassify into optical, acoustic, haptic and other systems.

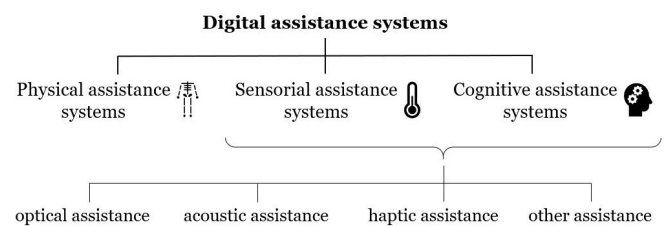


Figure 1. Differentiation of digital assistance systems.

- Physical assistance systems are used to support demanding physical work. They often enable an improvement of ergonomics at the working place. Furthermore, they can be a support for physically decreasing capabilities or a step to prevent injury. The assistance systems can support by force or speed, for example at the installation working place. [3]

These digital assistance systems will not be discussed any further in this research project.

- Sensorial assistance systems are particularly suitable for employees with limited functionality of the sensory organs or with age-related weaknesses [3]. Another application can be the use for measurements and collection of data. Therewith, processes can be optimized.
- Cognitive assistance systems offer selective support with real time and process-orientated information [3]. The systems can be differentiated into helping systems, instruction systems and tutorial systems. Thereby, the differences are the level of support and the field of application. [4]

The differentiation between optical, acoustic, haptic and other assistance systems is the variation of information output. The optical assistance devices show visual information like texts or pictures. The acoustic ones have an output of auditory signals and tones. The haptic systems transmit the information by vibration. At last, there are the other assistance systems which do not have a defined optical, acoustic or haptic information output. [5] [6] [7] [8]

B. Digital assistance devices

There are numerous different opportunities of digital assistance systems to support the worker in production. The devices can be differentiated according to their provision of information. As mentioned in the previous chapter, there are four different categories of information output.

- As a first category, there are devices that present the information on a display or in the view field of the user. These devices are classified as optical assistance systems. Examples are tablets, smartwatches or computer monitors. They are used for presenting process documents and drawings or instruction sheets. Furthermore, smart glasses for virtual or augmented reality are optical systems, too. They can be used exemplarily for generating a virtual world. This is a method that is mostly used for trainings and for the product development.
- Secondly, there are acoustic assistance devices such as headphones and headsets. These systems are beneficial for communication and service operations. The user wears the headphones and can pursue his work without movement restrictions.
- The third category are the haptic assistance devices. They are limited to the information output by vibration. Often, this technology is used like a feedback module to give brief directions to the user. Examples are sensor bracelets or gloves for collection data or identification processes. These devices give a feedback if the task was not executed correctly.
- At last, the other assistance devices usually do not have an information output. They can be used for processes that do not need a feedback signal for the user. Exemplary processes are collecting data or identification. Devices can be RFID tools for identification or smart clothes to control the healthiness of the wearer. Furthermore, a movement sensor can be used to improve ergonomics by analysing the data.

III. APPROACH OF SELECTING A DIGITAL ASSISTANCE SYSTEM

Based on the norm DIN EN ISO 9241-210, a procedure model is developed as a part of the research project. The model enables a structured approach of selecting a digital assistance system depending on an application. It consists of four subsequent steps.

1. Analyse current state
2. Define usage requirements
3. Solution design
4. System implementation and evaluation

The procedure model consists of continuous improvement to get the best fitting assistance device.

A. Analyse current state

The first step is to analyze the current process and usage context which should be improved by the new system. Thereby, the user and its attributes should be defined. Moreover, the objectives and tasks of the user and the process

environment must be clarified. This is necessary to uncover deficiencies, problems or limitations of the process. A detailed specification of the usage context is the base for a detailed list of requirements. [4] [9]

B. Define usage requirements

After the recorded usage context, the usage requirements can be identified. Several requirements can be derived from the usage context and the environmental conditions directly. Furthermore, ergonomics and norms are included in this step. The existing interfaces at the company and internal or customer-related guidelines have to be considered. Likewise, safety rules have to be abided. Furthermore, in this step, the usability requirements and goals are defined which should be achieved by the assistance system. At last, the organizational requirements of a process have to be identified. Those can be cycle times or provided user qualifications. [9]

With this information, a structured list of requirements can be developed that fits to the specific application of an assistance system.

C. Solution design

The third step is the selection of a digital assistance device that fits best to the pre-defined requirements. The solutions can base on different creative ideas and former experiences or knowledge. The ideas should be developed for each application individually. [9] The solution process is divided into three consecutive steps. The aim is to compare the specific requirements of an application with the capabilities of the assistance devices. This should follow along a structured and methodical approach. [10] The subsequent steps are:

1. Creating ideas for the realization of the requirements
2. Comparing the ideas with the capabilities of digital assistance devices
3. Including norms and guidelines

At first, ideas should be developed how to realize the requirements with a digital device. Thereby the functions and possibilities of the different technologies have to be regarded. [9] An example could be that the system has to present information visually in form of texts and pictures. That would be the requirement. Ideas to realize this is a display or a projection unit. That means for the following step, the assistance device should have one of these technologies integrated. This is just one example covering the information output. Other requirements depend on the information input, the energy supply or the investment costs. Not to forget are wireless and tethered data transfers that also belong to the information input and output. In this way, every pre-defined requirement should be related to a technology that realizes it.

Secondly, the ideas have to be compared to the capabilities of the assistance devices. The aim of this step is to select the most suitable assistance system to the application. For that reason, different assistance devices have to be analysed. This can be done with a capability model. Fig. 2 shows a structured

approach of analysing the assistance devices. The devices are described by their technology and components. Every device consists of different components which use different technologies. These technologies enable the capabilities of the system that are demanded for the application. [10]

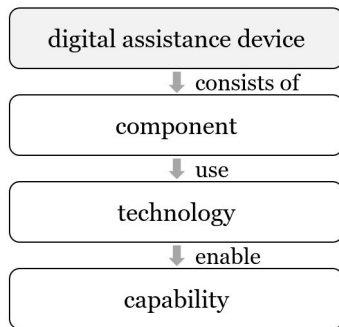


Figure 2. Approach of analysing digital assistance systems. Based on [10].

For this method of analyzing the assistance devices, a structured separation of components and technologies is necessary. Components are always physical objects like displays, microphones or Bluetooth transmitter. The related technologies are for example the information input or output. [10]

The relation between technology and capabilities is multifaceted. One technology area can have several different capabilities. The assignment of technologies and capabilities can be identified with a matrix. [10] An exemplary matrix is shown in Fig. 3. In the first line is the technology 'information output' listed as an example for the different technologies that are possible. At the second line are the related components mentioned which use the different technologies. Furthermore, at the left side are the resulting capabilities listed. With that structure it is easy to specify the different digital assistance systems and compare them to the implementation possibilities from the first point.

The continuation of the previous example is marked with crosshatching (cf. Fig. 3). The requirement was an information output in form of texts and pictures. As an exemplary assistance system the capabilities of a tablet are marked with small cross. The overlap of the requirements and capabilities can be compiled by the display of the tablet.

The third step is to include guidelines and norms. Especially internal guidelines or customer given requirements have to be considered. An example would be the data transfer. Sometimes it is not possible to transmit the information wirelessly due to safety reasons. In that case it must be guaranteed that the data transfer is tethered. Also important are guidelines about the duration of use.

When all norms and requirements are regarded, a final assistance device can be chosen. For a structured selection of one system, an evaluation matrix can be consulted. Furthermore, to get a first impression of the assistance devices, prototypes can be modelled. Possible are different

		information output						
		display	speaker	signal light	projection unit	cable connection	WLAN transmitter	BT transmitter
capabilities of information output	visual	binary signal			x			
		text	crosshatched			crosshatched		
		pictures	crosshatched			crosshatched		
		videos	x					
	acoustic	signal		x				
		speech		x				
	wireless	data transfer					x	x

Figure 3. Exemplary matrix of a capability model. Based on [10]

types of prototypes. For a haptic impression, the models can be created out of paperboard. For a handling impression, a simplified software solution achieves good results. [4]

D. System implementation and evaluation

After the selection of a digital assistance device, it can be implemented and evaluated. The first step should consist of testing prototypes. This can be carried out in a differentiated development laboratory or in a small number of working places at the real usage environment. At this stage, the usability can be tested at a manageable dimension and final problems can be easily detected and resolved. [4] After successful prototyping, the system can be implemented in production. Otherwise, further improvement has to be achieved to eliminate the issues. The procedure of selecting a digital assistance system aims at continuous improvement to steadily meet a greater goal.

IV. FUTURE APPLICATIONS OF DIGITAL ASSISTANCE SYSTEMS

There are many prospective challenges and chances with digital assistance systems. Companies worldwide are working on the integration of assistance devices to support the daily work of their employees. Topics like health and ergonomics can be optimized with digital sensors. Two other important applications are the qualification and the conservation of knowledge.

The training of the worker is an omnipresent topic. Thereby, digital assistance systems support with virtual settings or in a playful manner. Especially for practicing dangerous situations, virtual reality enables a safe environment. Furthermore, it is possible to train on virtual machines without needing access to the actual machine. That saves costs, time and materials. Besides, the conservation of knowledge is another important application. The knowledge of the personnel is one of the most important resources of a company. There will always be

a fraction of employees that will leave for retirement or other reasons. If the knowledge and experience of these people is not documented, it will be lost. Thereby, digital assistance systems can support the documentation and the safeguarding generation.

V. CONCLUSION

Nowadays, digitalization is a big topic for various companies worldwide. Some of them do already use digital systems like assistance devices and achieve great success with them. They facilitate the daily work routine and minimize mistakes. Additionally, a lot more projects are already planned to optimize the process. On the other side, there are companies, especially medium-sized ones, which have problems implementing such devices into their production [2]. There are several challenges, like the different environmental conditions and individual applications which causes that it is not possible to have one solution that fits all. The companies have to invest a lot of resources to implement digital assistance systems. The aim of this research project is to create a guideline for implementing digital assistance systems. The classification of the different assistance systems and the procedure model are the main aspects to simplifying and structure the selection of a digital assistance system. Moreover, this guideline can be easily adapted to different companies and conditions. In the future, topics like education, ergonomics and conservation of knowledge will be important. Different assistance systems have the potential to support with these topics. Thereby, it is important to choose the best fitting assistance devices to get the best results.

REFERENCES

- [1] Stefan Kühner. *Neue Technik, Neue Wirtschaft, Neue Arbeit? - Digitalisierung, Künstliche Intelligenz, Industrie 4.0*. PapyRossa Verlag, Köln, 2020.
- [2] *Presseinformation - Digitale Assistenzsysteme in der Produktion*. Fraunhofer IAO, 19. September 2019
- [3] Wenke Apt, Marc Bovenschulte, Kai Priesack, Christine Weiß, Ernst Andreas Hartmann. *Forschungsbericht 502 - Einsatz von digitalen Assistenzsystemen im Betrieb*. Institut für Innovation und Technik, Januar 2018
- [4] Wenke Apt, Michael Schubert, Steffen Wischmann. *Digitale Assistenzsysteme - Perspektiven und Herausforderungen für den Einsatz von Industrie und Dienstleistungen*. Institut für Innovation und Technik, Berlin, Januar 2018
- [5] Mandy Tawalbeh. *Optische interaktive Assistenzsysteme - Ein Überblick*. Mittelstand 4.0 - Kompetenzzentrum Chemnitz, n.d.
- [6] Mandy Tawalbeh. *Akustische interaktive Assistenzsysteme - Ein Überblick*. Mittelstand 4.0 - Kompetenzzentrum Chemnitz, n.d.
- [7] Mandy Tawalbeh. *Haptische interaktive Assistenzsysteme - Ein Überblick*. Mittelstand 4.0 - Kompetenzzentrum Chemnitz, n.d.
- [8] Sebastian Grogger, Nissrin Arbesun Perez, Phil Hermanski, Christian Fimmers, Dr. Michael Wächter. *Digitale Produktionstechnologie - Einsatz mobiler Endgeräte in der Produktion kleiner und mittlerer Unternehmen*. Werkzeugmaschinenlabor WZL der RWTH Aachen, Aachen, März 2018
- [9] DIN Deutsches Institut für Normen e. V. *Ergonomie der Mensch-System-Interaktion - Teil 210: Menschzentrierte Gestaltung interaktiver Systeme (ISO 9241-210:2019)*. Beuth Verlag GmbH, Berlin, März 2020
- [10] L. Merkel, J. Starz, C. Schulz, S. Braunreuther, G. Reinhart. *Digitale Assistenzsysteme in der Produktion - Fähigkeitenmodell zur Auswahl der digitalen Assistenzsysteme in der Produktion*. wt Werkstattstechnik online, Jahrgang 107 (2017) H.3, Springer-VID-Verlag, Düsseldorf, März 2017

Chapter 8

Papers: Machine Learning

Contents

8.1	Applications of Robust Dynamical Component Analysis (DyCA) on simulated Data	386
8.2	Embedded Development of an Artificial Neural Network for Range Estimation on Infrared Images	392
8.3	Simulative data generation and labeling for autonomous driving specific AI models using MATLAB/Simulink, ROS and Gazebo	396
8.4	Applications and Limitations of Dynamical Component Analysis (DyCA)	401
8.5	Parameter choice for the short-time Fourier transformation in frequency-domain Blind Source Separation	407
8.6	AI-based control-algorithm for stationary batteries with regards to load-management	412

Applications of Robust Dynamical Component Analysis (DyCA) on simulated Data

Fabienne Anselstetter, Patricia Schell, Monika Warmuth and Christian Uhl

*Faculty of Engineering Sciences
Ansbach University of Applied Sciences
Ansbach, Germany*

{Fabienn.Anselstetter, Patricia.Schell, Monika.Warmuth, Christian.Uhl}@hs-ansbach.de

Abstract—Dynamical Component Analysis (DyCA) allows the analysis of multivariate time series. Research results showed that the DyCA is well suited for signals disturbed with component noise and low additive noise. However, DyCA is not suited for signals with additive noise below 40dB. The method called joint regularized L^p -denoising DyCA or Robust DyCA combines denoising of the data with the application of DyCA, allowing the reconstruction of signals with additive noise. In the present analysis, it is investigated how denoising affects the result of dimensional reduction. For this analysis, the Rössler attractor, the Lorenz attractor and the Blue-Sky catastrophe are used. The signal is perturbed with high additive noise and high additive and component noise. The performance of dimension reduction is analyzed based on the generalized eigenvalues, the deviation of the original signal from the reconstructed signal and the relative reconstruction error. It is shown that the combination of the two methods reconstructs the noisy signals better than only using DyCA.

I. INTRODUCTION

Dimensionality reduction of multivariate time series are used for the purpose of extracting the underlying low-dimensional features from a given high-dimensional signal, which enables a more appropriate representation of the data. Some of the best-known methods for dimensionality reduction are the Principal Component Analysis (PCA) [1] and the Independence Analysis (ICA) [2] [3], each based on a statistical model assumption. When examining time series that follow certain deterministic dynamics, however, the Dynamic Component Analysis (DyCA) has a more beneficial effect in preserving important signal features [4] [5] [6].

DyCA is a recent data-driven dimension reduction and subspace detection method for multivariate time series that preserves the underlying dynamics of the data. Assuming that these dynamics follow a system of m linear and n non-linear differential equations, where $m \geq \frac{n}{2}$ is assumed, DyCA projects the data onto a low-dimensional subspace and searches for a best-fit solution to the system of differential equations with respect to the linear differential equations. In addition to dimensionality reduction, however, an important task in multivariate signal processing is the removal of Gaussian white noise, which is usually measured unintentionally in real applications.

In previous work, it has already been shown that DyCA can be applied well to simulated and noisy data if the data meet the requirements of DyCA [7]. In order to extend the usability

as well as the efficiency in terms of quality of DyCA in a next approach, a variational method widely used in image analysis is implemented in precedence of DyCA by a combination of data terms, regularisation term and DyCA term and using the discrete L^p norm [8], the so-called Joint L^2 -Denoising [9]. The underlying dynamics improve the signal reconstruction as well as the calculation of the DyCA components.

In order to investigate if this combination, further called L^p -denoising DyCA, is more efficient in terms of quality than the pure application of DyCA, a modified method from the previous work by Schell et al. [7] is used in this analysis. For this purpose, three signals that were used in the previous work are simulated. In this context, the differential equation system of one signal fulfils the requirements of DyCA, the Rössler attractor [10]. The differential equation systems of the other signals, the Lorenz attractor [11] and the Blue-Sky Catastrophe [12], do not fulfil the requirements of DyCA.

In order to evaluate the efficiency of the combination of the DyCA and the Joint L^2 -Denoising according to the pure use of the DyCA, a variation of the mentioned method from Schell et al. [9] is thus performed in this paper. Therefore, the signals are perturbed with two different noise variations, additive noise and a combination of additive noise and component noise, in a range from 0dB to 50dB. For the evaluation, the eigenvalues of the DyCA and the calculation of two different error types for all three signals are analysed.

In the following, the methodology is first explained in more detail. An overview of the dimension reduction method of DyCA and L^p -denoising is given. Next, the simulated basic signals, the Rössler attractor, the Lorenz attractor and the Blue-Sky catastrophe as well as the noise method are being presented. This is followed by the presentation of the results with subsequent discussion and the conclusion.

II. DYNAMICAL COMPONENT ANALYSIS (DYCA)

The section briefly provides an overview of DyCA, which is discussed in more detail in [4]. Let $q(t) \in \mathbb{R}^N$ be a multivariate time series with $t = t_1, t_2, \dots, t_T$, $T \geq N$. Under ideal circumstances, it is assumed, that the signal $q(t)$ can be decomposed into components

$$q(t) = \sum_{i=1}^n x_i(t)w_i \quad (1)$$

with linearly independent vectors $n \leq N$ and $w_i \in \mathbb{R}^N$, whilst the deterministic amplitudes $x_i(t)$ belong to a set of linear (2) and nonlinear (3) ordinary differential equations (ODE)

$$\dot{x}_i(t) = \sum_{k=1}^n a_{i,k} x_k(t) \quad \text{for } i = 1, \dots, m \quad (2)$$

$$\dot{x}_i(t) = f_i(x_1(t), \dots, x_n(t)) \quad \text{for } i = m + 1, \dots, n \quad (3)$$

with $m \geq \frac{n}{2}$. This can be transcribed in matrix notation as

$$Q = WX, \quad (4)$$

with $Q \in \mathbb{R}^{N \times T}$, $W \in \mathbb{R}^{N \times n}$, and $X \in \mathbb{R}^{n \times T}$. In addition, it must be assumed that the data matrix Q and its time derivative \dot{Q} are of full rank N . Since the data in practice often have at least a small amount of noise, the full rank is usually the case. DyCA aims to calculate a generalised left inverse $W^{-} \in \mathbb{R}^{n/N}$ of W , which results in $W^{-}W = I_n$ and

$$X = W^{-}Q. \quad (5)$$

Assuming linearly independent vectors w_i leads to the fact that the lines $\{u_1^{\top}, \dots, u_n^{\top}\}$ of W^{-} are also linearly independent. Therefore, the amplitudes $x_i(t)$ can be calculated by the scalar product

$$x_i(t) = u_i^{\top} q(t) = q(t)^{\top} u_i \quad (6)$$

with time derivative $\dot{x}_i(t) = \dot{q}(t)^{\top} u_i$. DyCA estimates these vectors u_i first and then approximates the corresponding modes w_i in a further step. Herefore one can define $v_i := \sum_{k=1}^n a_{i,k} u_k$ for $i = 1, \dots, m$ and write (2) as follows:

$$\dot{q}(t)^{\top} u_i = \sum_{k=1}^n a_{i,k} q(t)^{\top} u_k = q(t)^{\top} v_i \quad (7)$$

In order to obtain the estimations for the vectors u_i , v_i , the error functions

$$D(u_i, v_i) := \frac{\frac{1}{T} \sum_{j=1}^T \|\dot{q}(t_j)^{\top} u_i - q(t_j)^{\top} v_i\|^2}{\frac{1}{T} \sum_{j=1}^T \|\dot{q}(t_j)^{\top} u_i\|^2} \quad (8)$$

were defined and the approximation vectors \tilde{u}_i , \tilde{v}_i , $i = 1, \dots, m$ as solutions to the least squares problem $\arg \min_{u_i, v_i} \sum_{i=1}^m D(u_i, v_i)$ were calculated under the assumption that u_1, \dots, u_m are linearly independent. According to some basic calculations which can be found in [4] and defining $C_0 := \frac{1}{T} Q Q^{\top}$, $C_1 := \frac{1}{T} \dot{Q} Q^{\top}$, and $C_2 := \frac{1}{T} \dot{Q} \dot{Q}^{\top}$, (7) reduces to the solution of a generalized eigenvalue problem

$$C_1 C_0^{-1} C_1^{\top} u = \lambda C_2 u \quad (9)$$

with $\tilde{v}_i = C_0^{-1} C_1^{\top} \tilde{u}_i$ for the corresponding eigenvectors \tilde{u}_i . Thus, for the generalised eigenvalues λ_i obtaining

$$\min_{u_i, v_i \in \mathbb{R}^N} D(u_i, v_i) = 1 - \lambda_i \quad (10)$$

i.e. the linear approximation of (7) is suitable well for $\lambda_i \approx 1$. Consider a minimal subset of vectors \tilde{u}_i , \tilde{v}_i such that $\tilde{n} = \dim(\{\tilde{u}_1, \dots, \tilde{u}_{\tilde{m}}, \tilde{v}_1, \dots, \tilde{v}_{\tilde{m}}\})$ then gives an estimate \tilde{W}^{-} for the matrix W^{-} . An estimate \tilde{W} of W can be calculated

as $\tilde{W} = \frac{1}{T} Q \tilde{X}^{\top} C_{\tilde{X}}^{-1}$ with $C_{\tilde{X}} = \frac{1}{T} \tilde{X} \tilde{X}^{\top}$. Altogether, the complete DyCA algorithm is available in [4]. By taking a closer look at the equation (2) here, one could notice that applying a linear transformation to the linear part of the ODE system has the effect of keeping the structure of the data invariant. As a consequence, this degree of freedom leads to ambiguity in the choice of estimates for the matrix W and the amplitudes $x_i(t)$, resulting in rotated DyCA trajectories compared to the original data.

III. JOINT SIGNAL DENOISING AND DIMENSIONALITY REDUCTION MODEL

In the following section, the method of joint regularized L^p -denoising DyCA [9] will briefly discussed. It is assumed that random additive noise $n(t)$ is added to the original signal q_{org}

$$q(t) = q_{org}(t) + n(t). \quad (11)$$

Since currently the application of DyCA to signals with high additive noise is not successful, a variational minimization problem of the general form is used for noise reduction.

$$\hat{q}_{org}, \tilde{u}, \tilde{v} = \arg \min_{q_{org}, u, v} \mathcal{D}(q_{org}, q) + \beta \mathcal{R}(q_{org}) + \gamma \mathcal{S}(q_{org}, u, v) \quad (12)$$

Thereby the data term $\mathcal{D}(q_{org}, q)$

$$\mathcal{D}(q_{org}, q) = \frac{1}{p} \|q_{org} - q\|_p^p, \quad (13)$$

with $p = 1, 2$ links the measured data q with q_{org} . Here $\|\cdot\|_p$ denotes the L^p Norm. While the data term $\mathcal{D}(q_{org}, q)$ describes the deviation of q_{org} from the initial data set q , the regularization term $\mathcal{R}(q_{org})$

$$\mathcal{R}(q_{org}) = \frac{1}{r} \|\Delta q_{org}\|_r^r, \quad (14)$$

with $r = 1, 2$ offers the possibility to prioritize desired signal properties. The terms are weighted by the regularization parameter β and γ . In addition, the DyCA minimization problem is taken into account by the DyCA data term $\mathcal{S}(q_{org}, u, v)$

$$\mathcal{S}(q_{org}, u, v) = \frac{1}{2} \|\dot{q}_{org}^{\top} u - q_{org}^{\top} v\|_2^2, \quad (15)$$

where u and v are the projection vectors that provide a suitable approximation of the signal.

The alternating minimization approach leads to one iteration statement for q_{org}^{k+1} and one for u^{k+1} , v^{k+1} .

$$q^{k+1} = \arg \min_q \frac{1}{T} \sum_{j=1}^T \frac{1}{2} \|q(t_j) - s(t_j)\|_2^2 + \frac{\beta}{2} \|\partial_t q(t_j)\|_2^2 + \frac{\gamma}{2} \|(u^k)^{\top} \partial_t q(t_j) - (v^k)^{\top} q(t_j)\|_2^2 \quad (16)$$

$$u^{k+1}, v^{k+1} = \arg \min_{u, v} \frac{\gamma}{2T} \sum_{j=1}^T \|u^{\top} \partial_t q^{k+1}(t_j) - v^{\top} q^{k+1}(t_j)\|_2^2 \quad (17)$$

The Chambolle-Pock algorithm [13] is used to solve q_{org}^{k+1} and the standard DyCA method is used for u^{k+1}, v^{k+1} .

IV. APPLICATION AND RESULTS

Previous research results have already demonstrated the successful application of DyCA to simulated and real data. Thereby simulated data such as the Rössler attractor as well as real electroencephalographic (EEG) data, electrocardiographic (ECG) data and motion data were considered [5] [6] [4]. However, limitations of DyCA could also be identified in a past research work [7]. It showed that DyCA is not suited for signals with additive noise below 40dB. Based on this, it will be investigated how denoising affects the result of dimensional reduction.

Our aim in this work is to systematically investigate the applicability of joint regularized L^p -denoising DyCA examining its performance on three different simulated signals $q_{org}(t)$ and noise $d(t)$

$$q(t) = q_{org}(t) + d(t), \quad (18)$$

whereby $d(t)$ corresponds to a combination of additive noise $n(t)$ and component noise $n_c(t)$

$$d(t) = n_c(t) + n(t) = \sum_{j=1}^p \xi_j(t)\psi_j + n(t). \quad (19)$$

It is specified that the underlying components w_i are simulated randomly with $N = 20$ and are linearly independent of each other. Furthermore, disturbances due to component noise $n_c(t)$ and additive noise $n(t)$ are simulated. In addition to w_i , the time-dependent amplitudes $\xi_j(t)$ and the components ψ_j are also chosen randomly with ψ_j linearly independent to the components w_i . The number of added noise components p is chosen as large as possible with $p = N - 3$. First, the additive noise is varied from 0dB to 50dB in 5dB steps. Then the component noise is added to the additive noise. For this, both noise components are set simultaneously from 0dB to 50dB in 5dB steps.

The models chosen for analysis consist of three differential equations, each differing in the number of linear and non-linear differential equations. The systems are integrated numerically using a Runge-Kutta(4,5) method. The signals selected for analysis are the Rössler attractor [10], the Lorenz attractor [11] and the Blue-Sky catastrophe [12].

For each variation, we perform 10 runs and then the mean values of the different parameters are calculated. Thereby the parameters are plotted analogously to the method described in [7], where they were plotted as a function of the different noise variations. Plotted alongside the first three eigenvalues λ_i are the results of $1 - \eta$ as well as the data calculated from $1 - \epsilon$. Whereby the parameter ϵ describes an error function which investigates the reconstruction performance by representing the deviation of the original model from the reconstructed signal

$$\epsilon(\tilde{x}_i, \tilde{w}_i) = \frac{\langle \|q_0(t) - \sum_{i=1}^{\tilde{n}} \tilde{x}_i(t)\tilde{w}_i\|^2 \rangle}{\langle \|q_0(t)\|^2 \rangle}. \quad (20)$$

Through minimisation of a least squares error η , described by

$$\eta(w_i) = \frac{\langle \|q(t) - \sum_{i=1}^{\tilde{n}} \tilde{x}_i(t)w_i\|^2 \rangle}{\langle \|q(t)\|^2 \rangle}, \quad (21)$$

the estimation of the accuracy of the DyCA components \tilde{w}_i is done.

Furthermore, $m = 2$ and $\tilde{n} = \dim(\text{span}\{\tilde{u}_1, \tilde{u}_2, \tilde{v}_1, \tilde{v}_2\}) = 3$ are assumed for all cases examined. For a better comparison, we further included the reconstruction results of the two different projection matrices $\tilde{W}_1^- = (\tilde{u}_1, \tilde{u}_2, \tilde{v}_1)^\top$ and $\tilde{W}_2^- = (\tilde{u}_1, \tilde{u}_2, \tilde{v}_2)^\top$ which can be used. For a better differentiation, the error functions η and ϵ with their corresponding indices 1 and 2 were included accordingly: $\eta_1, \eta_2, \epsilon_1$ and ϵ_2 .

Regarding the method of joint regularized L^p -denoising DyCA, different parameters can be set. The regularization parameters β and γ can be varied, as well as the Lebesgue norms p and r of the data and regularization terms. In addition, the step sizes τ and σ , resulting from solving the minimization problem with the Chambolle-Pock algorithm can be modified. It is always assumed that $\tau = \sigma$. The implemented algorithm also provides the possibility to set the number of iteration steps, which we always set to three. Furthermore, if known, the number of eigenvalues close to one can be set via the parameter *NumEV*. Alternatively, if the number of linear components of the ODE system is unknown or the system has no linear components, *NumEV* is set to zero and the threshold parameter α has to be defined instead. In this case, all eigenvalues $\lambda_i > \alpha$ are considered to be close enough to one and therefore the associated vectors u_i and v_i are taken along.

The respective settings for the different signals are identified as suitable parameters in preliminary tests. For the analysis, the parameters p and r are set to two and γ is set to one. In addition, a step size of 0.0004 is chosen for τ .

A. Rössler attractor

The Rössler attractor [10] is described by the following differential equation system:

$$\begin{aligned} \dot{x}_1 &= -(x_2 + x_3) \\ \dot{x}_2 &= x_1 + ax_2 \\ \dot{x}_3 &= b + (x_1 - c)x_3 \end{aligned} \quad (22)$$

with $a = 0.15, b = 0.2$ and $c = 10$. In the case of this simulated signal, two linear and one non-linear differential equation is included. For this reason, the requirement $m \geq \frac{n}{2}$ is met. Therefore, the value two is selected for *NumEV* and 0.015 is used for β . The corresponding trajectory in phase space is shown in figure 1. Figure 2 summarizes the results of performance of the variation of the different noise components. In the case of additive noise, the linear components of the system could be correctly detected over the entire variation of the noise component (two generalized eigenvalues, λ_1 and λ_2 close to one, hidden by the green and red lines). Moreover a good signal reconstruction is achieved since the parameters $1 - \eta_1, 1 - \eta_2, 1 - \epsilon_1$ and $1 - \epsilon_2$ have the same course close to one. Both projection matrices seem to be suitable as well.

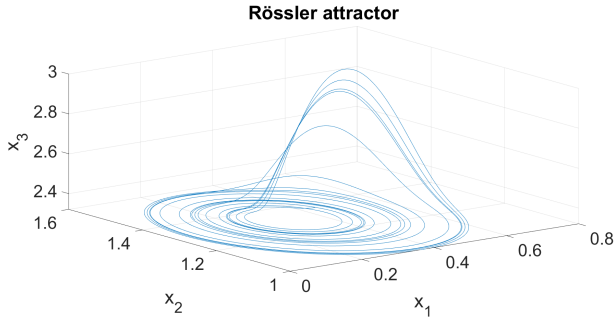


Figure 1. Trajectory of the Rössler attractor

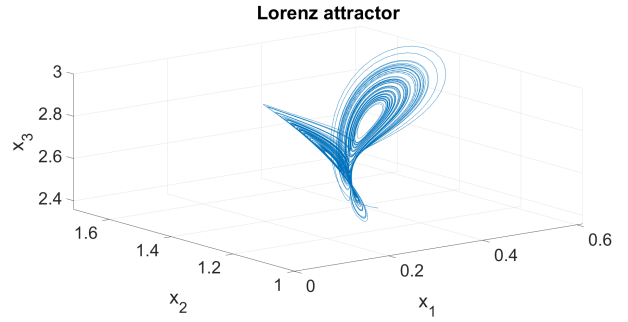


Figure 3. Trajectory of the Lorenz attractor

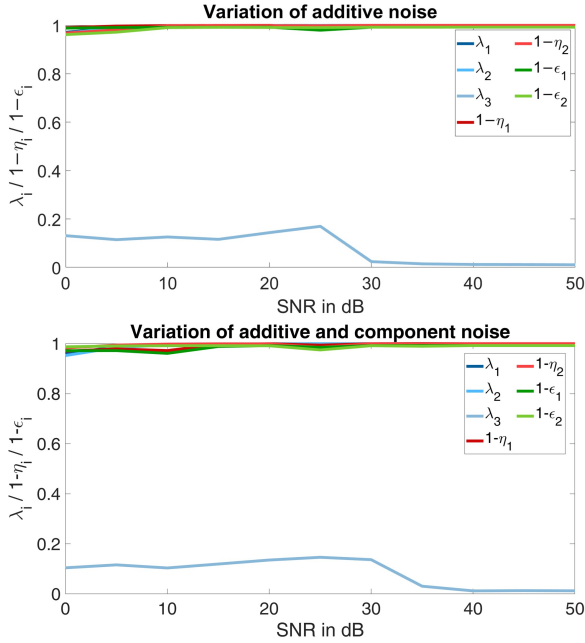


Figure 2. Rössler attractor – variation of noise components

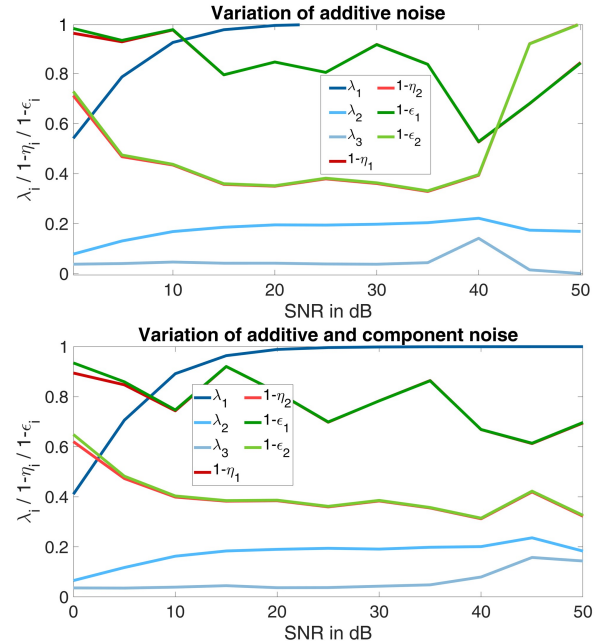


Figure 4. Lorenz attractor – variation of noise components

B. Lorenz attractor

For the simulation of the Lorenz attractor [11] the following differential equation system which contains only one linear differential equation, is thereby used and results in the trajectory shown in figure 3.

$$\begin{aligned} \dot{x}_1 &= \delta(x_2 - x_1) \\ \dot{x}_2 &= x_1(\theta - x_3) - x_2 \\ \dot{x}_3 &= x_1x_2 - \iota x_3 \end{aligned} \quad (23)$$

with $\delta = 10$, $\theta = 28$, $\iota = \frac{8}{3}$. Consequently, the value one is chosen for *NumEV* and 0.01 is used for β . Figure 4 summarizes the results of the different noise variations tested on the Lorenz attractor. The variation of the noise component shows that the first eigenvalue is close to one for noise levels greater 20dB. Above this signal to noise ratio, the linear component of the system is detected successfully. When we use projection matrix W_1^- , $1 - \eta_1$ and $1 - \epsilon_1$ are near to one from 0dB to 35dB. Afterwards, there is a dip before the graph again has a value above 0.8 at 50dB. In the case of

reconstruction with W_2^- , the graphs $1 - \eta_2$ and $1 - \epsilon_2$ are in a rather low range up to 35dB and at 50dB they are close to one.

C. Blue-Sky catastrophe

The Blue-Sky catastrophe [12] is governed by the following ODE system:

$$\begin{aligned} \dot{x}_1 &= x_1(2 + \mu - 10(x_1^2 + x_2^2)) + x_3^2 + x_2^2 + 2x_2 \\ \dot{x}_2 &= -x_3^3 - (1 + x_2)(x_3^2 + x_2^2 + 2x_2) - 4x_1 + \mu x_2 \\ \dot{x}_3 &= (1 + x_2)x_3^2 + x_1^2 - \kappa, \end{aligned} \quad (24)$$

with $\kappa = 0.0357$ and $\mu = 0.456$. Since the ODE system does not have any linear differential equation, *NumEV* was set to zero and α is defined by a threshold value of 0.292. Note that the threshold is very low and actually not close to one. Tests show that it is still working in practice, even if the threshold is actually rather unsuitable. The parameter β is set to 0.015. The corresponding trajectory in phase space is shown in figure 5. Figure 6 shows the results for the noise variation in case of

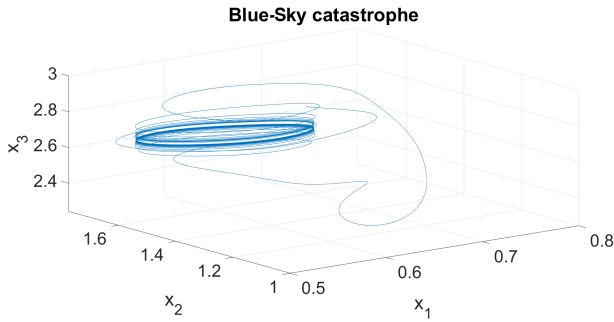


Figure 5. Trajectory of the Blue-Sky catastrophe

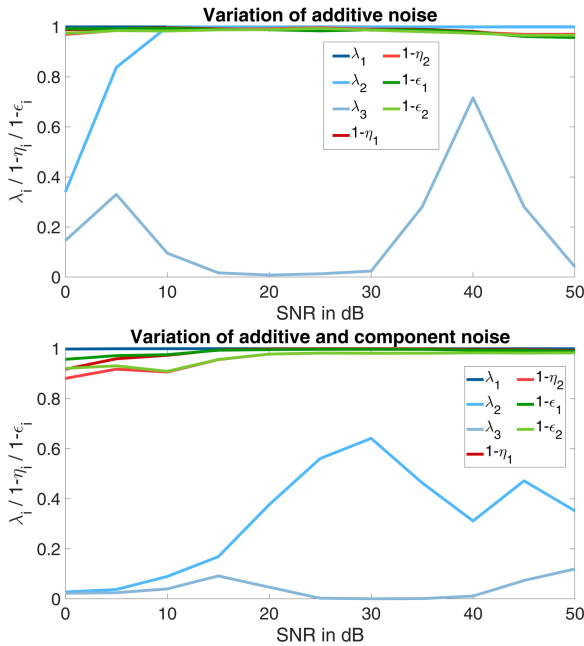


Figure 6. Blue-Sky catastrophe – variation of noise components

the Blue-Sky catastrophe.

Although no eigenvalue should be close to one, the first eigenvalue λ_1 is close to one. The courses of the error functions show that the reconstruction of the signal was successful from the beginning. $1 - \eta_1$, $1 - \eta_2$, $1 - \epsilon_1$ and $1 - \epsilon_2$ are close to one. In case of projection by means of W_1^- , minimally better results were shown for $1 - \eta_1$ and $1 - \epsilon_1$ since they are closer to one by up to 20dB. Above 20dB, both projection matrices seem to be equally suitable.

V. CONCLUSION

In case of the Rössler attractor and the Lorenz attractor, the method analysed the correct number of eigenvalues. For the Blue-Sky catastrophe, however, all eigenvalues above the threshold α along with corresponding vectors u_i , v_i are chosen for further computations. By definition, the vectors u_i , v_i represent the linear part of the ODE system, which is nonexistent in case of the Blue-Sky catastrophe. Therefore, the assumptions of DyCA are not fulfilled and the value for α

is set low enough to still find eigenvalues above this threshold. Note that in consequence, in the course of the iterations the calculated values are increasingly linearised as they are fitted more and more to a system of linear ODE. In principle, this is what the algorithm is intended to do to find an estimation for the linear and finally the nonlinear ODE. Nevertheless, for the Blue-Sky catastrophe as well as for other types of data that do not meet the requirements for DyCA, some kind of forced linearisation occurs. This is due to the fact that the algorithm does not know that the threshold α is poorly chosen and hence, adapts the values more and more to linear ODE that do not actually exist. Therefore, we cannot make any statement about the successful detection of the linear parts of the system. Even though the analysed eigenvalues are not representative for the Blue-Sky catastrophe, the Robust DyCA still works in practice. We assume that the ODE system of Blue-Sky exhibits some kind of underlying linear features that are captured well enough by Robust DyCA. One could also conclude that the ODE system can be sufficiently well approximated by a combination of linear (and nonlinear) differential equations. However, this interpretation has to be treated with caution, as there is no guarantee that this also holds true for other kinds of data sets, see for example the Lorenz attractor.

Based on the two errors, it was also shown that the DyCA in combination with the L^p -denoising reconstructed the signals very effectively in terms of quality. This is also shown by the comparison with the analysis preceding the paper using DyCA without L^p -denoising [7]. The reconstruction using the L^p -denoising DyCA is successful for amplitude noise as well as for component and amplitude noise in combination.

With regard to the results, the Robust DyCA can now be used in the further steps for a more effective analysis and reconstruction of different simulated signals. Furthermore, original signals without a known system of differential equations like an EEG-Signal could be reconstructed to get to know more about the possible applications of this method.

ACKNOWLEDGEMENT

This work was supported by the German Federal Ministry of Education and Research (BMBF, Funding number: 05M20WBA).

REFERENCES

- [1] K. Pearson, "On lines and planes of closest fit to a system of points in space," *The London, Edinburgh and Dublin Philosophical Magazine and Journal of Science*, 1901.
- [2] A. Hyvärinen and E. Oja, "Independent component analysis: algorithms and applications," *Neural Networks*, 2000.
- [3] A. Hyvärinen, J. Karhunen, E. Oja, and S. Haykin, *Independent Component Analysis*, JOHN WILEY & SONS INC, 2001.
- [4] C. Uhl, M. Kern, M. Warmuth, and B. Seifert, "Subspace Detection and Blind Source Separation of Multivariate Signals by Dynamical Component Analysis (DyCA)," *IEEE Open Journal of Signal Processing*, 2020.
- [5] B. Seifert, K. Korn, S. Hartmann, and C. Uhl, "Dynamical component analysis (DyCA): Dimensionality reduction for high-dimensional deterministic timeseries," *IEEE 28th International Workshop on Machine Learning for Signal Processing (MLSP)*, 2018.

- [6] K. Korn, B. Seifert, and C. Uhl, "Dynamical component analysis (DyCA) and its application on epileptic eeg," *ICASSP 2019 - 2019 IEEE International Conference on Acoustics, Speech and Signal Processing (ICASSP)*, 2019.
- [7] P. Schell, F. Anselsteter, M. Warmuth, and C. Uhl, "Applications and Limitations of Dynamical Component Analysis (DyCA)," *ARC 2021 Applied Research Conference*, 2021.
- [8] M. Burger, H. Dirks, and C.-B. Schönlieb, "A variational model for joint motion estimation and image reconstruction," *SIAM Journal on Imaging Sciences*, 2018.
- [9] M. Warmuth, P. Romberger, and C. Uhl, "Robust dynamical component analysis via multivariate variational denoising," *2021 29th European Signal Processing Conference (EUSIPCO) (accepted)*, 2021.
- [10] S. Gerlach, *Computerphysik: Einführung, Beispiele und Anwendungen*, chapter Der Rössler Attraktor, Springer Spektrum Berlin Heidelberg, 2016.
- [11] D. Viswanath, "The fractal property of the lorenz attractor," *Physica D: Nonlinear Phenomena*, 2004.
- [12] N. Gavrilov and A. Shilnikov, "Example of a blue sky catastrophe," *Methods of Qualitative Theory of Differential Equations and Related Topics - American Mathematical Society*, 2000.
- [13] A. Chambolle and T. Pock, "A first-order primal-dual algorithm for convex problems with applications to imaging," *Journal of Mathematical Imaging and Vision*, 2011.

Embedded Development of an Artificial Neural Network for Range Estimation on Infrared Images

Julia Kornatzki

Technische Hochschule Nürnberg

Keßlerplatz 12, 90489 Nuremberg

Email: kornatzkiju81898@th-nuernberg.de

Abstract—This paper describes a neural network architecture for range estimation on infrared images, that is suitable for usage in an embedded environment. The range triangulation is based on three network parts, designed for pixel-wise segmentation, classification and 3D pose estimation of a depicted object. While orientated on the structure of two-stage detectors, the modules in this network are more flexibly coupled. This difference allows easier training and individual optimization of every network part on its own. It is evaluated against the I.MX 8M Mini microcontroller and several efficiency benchmarks.

I. INTRODUCTION

The determination of range towards a specific object is an important piece of information in many areas of application. Depending on the intended usage, such as autonomous driving or robot navigation, technical requirements and resources may vary. While many range estimation methods rely on images as a data source, machine learning has achieved remarkable results in the fields of image understanding [1]. However, the current state of the art networks require high computational resources, excluding most target devices of everyday life [2]. This paper describes range estimation with a neural network that is specifically built for environments with resource constraints. It aims for infrared images as a data source to support most conceivable scenarios, regardless of illuminance and weather situation. The key challenge is to determine a network architecture that is lean enough, but yet able to solve the different subtasks between input image and computed range. Therefore, a comparable thermal view camera environment is described as well as the processing pipeline. Every network part is built dedicated to one single task such as object segmentation or classification. At last, the range estimation network is validated against several efficiency benchmarks and the described embedded environment.

II. RELATED WORK

Object detection is a fundamental problem in computer vision. It becomes even more challenging, if an objects three dimensional spatial shape should be reconstructed from the two dimensional image. In order to solve this task, researchers have developed a broad range of methodical approaches varying in detection granularity and processing complexity. The Region-based CNN (RCNN) [3] is an important representative of two-stage detectors. In this structure the type and location of an object is predicted in two separate steps: Category-independent region proposals are generated from an image,

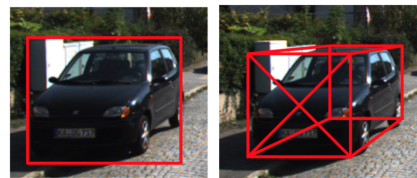


Figure 1. 2D bounding box, which serves as basis for estimated 3D bounding box. While the 2D bounding box locates the object, the 3D bounding box also allows spatial pose estimation [5].

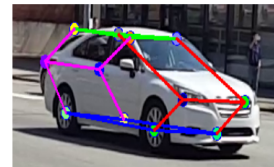


Figure 2. Annotated car with keypoints from CarFusion data set. Every keypoint represents a certain position, e.g. right front tire [6].

before object classification and bounding box regression takes place for each region of interest. Accordingly, the training of a RCNN is a multistage pipeline where each subnetwork requires separate training and specific data must be pre-processed for each step [4]. The specialization of network parts towards one specific subtask is a remarkable milestone in deep learning[1]. But the modules of the RCNN are still coupled together very tight and completely rely on the previous output, thus making development and optimization very complicated [4]. Further developed versions of the RCNN architecture show leading results on popular benchmark datasets, but the structure is computationally expensive and therefore not suitable for embedded usage [1].

Mousavian et al. [5] propose to locate objects as 3D bounding boxes from a single image. This can be classified as a single-stage detector, where the whole prediction is solved in one unified step. While previous work takes the point of view into account and requires complicated preprocessing or synthetic data sampling for training [7], the concept of this network is a lot simpler: The 3D bounding box is based on the correspondence between 2D keypoints on the image and a 3D model of the object. As a prerequisite the 3D bounding box is assumed to fit tightly into a 2D detection window [5]. Both bounding boxes in figure 1 illustrate this relationship.

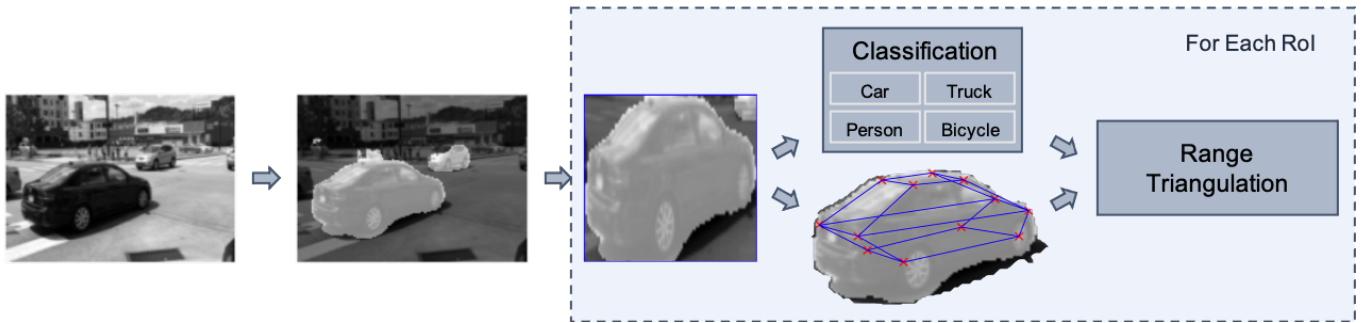


Figure 3. Illustration of the Range Estimation Pipeline (from left to right): Input image, binary map with region proposals, single cropped region proposal, classification/keypoint regression and range triangulation.

This constraint requires that each side of the 2D bounding box is touched by at least one corner of the 3D box [5]. This is clearly a very smart approach because it makes use of a simple visual correlation, but the quality of the pose estimation is also limited: The 3D bounding box does not fit tight to the actual appearance of an object. No specific context is provided in relation to the object type or any detailed outline information. It is rather a 2D bounding box enriched with some depth information than a complete 3D pose regression.

Keypoints are the most exact form of object segmentation in the three dimensional space. They provide detailed information about an objects location, pose and context [8]. Different object types may have an individual set of keypoints associated, where the number of points and relative position matches an objects general shape. The CarFusion [6] and ApolloCar3D [8] datasets both provide a large number of 3D car instances. Figure 2 illustrates a car annotated with keypoints from CarFusion.

III. EMBEDDED ENVIRONMENT

As a versatile usage of the range estimation network is intended, it must work regardless of the available technical components. Although machine learning applications in embedded context often rely on server-side processing [9], this design makes the application dependent from a permanent network connection and potentially unstable. Therefore, instead of bypassing computation limits, they serve as a target specification. The range estimation network is designed as a closed system consisting of a thermal view camera, which delivers the image stream, and a microprocessor for the inference of the neural network.

The thermal camera operates in long wave infrared spectrum (LWIR) at a wavelength of $8 - 14 \mu\text{m}$ [10]. Images are generated by a sensor with thermal sensitivity $< 60 \text{ mK}$ at a resolution of 320×240 pixels and 60 Hz. The image is processed in grayscale values. The camera is portable and has a battery capacity of 4.2 Wh with an estimated power consumption of 1 W/TFLOP [11]. Central processing unit (CPU) for the image data in the camera is the IMX 8M Mini microprocessor [12]. Therefore, it is intended as primary integration target for the range estimation network. It is equipped with four Cortex-A53 cores with ARM architecture

at 1.8 Ghz clock rate each. The IMX 8M Mini is designed for video processing at 1080p and 60 Hz [11]. An interesting alternative is the IMX 8M Plus [13]. Coming from the same model series it shares many features with the IMX 8M Mini such as the described CPU, but it is additionally equipped with a neural processing unit (NPU). This AI accelerator is specialized towards the inference of neural networks: NPUs lift the common separation between computation and data storage. Their design physically encourages typical computations such as matrix multiplications or convolutions [13].

IV. RANGE ESTIMATION

The distance to an object is calculated on the basis of a depicted object whose dimensions are brought into relation with the focal length of the camera. Therefore, it is necessary to know where an object is located on the image and what type it is. Localization in this context means not only position location but also pose estimation. As objects can be rotated along the axes, they may visually appear larger and taller than the real dimensions. Measuring the front width of a car on basis of figure 1 visualizes this effect. In this approach, classification is limited to the common types: Car, person, truck and bike. They give hint on the objects measurements, which are assumed and serve as reference in the scale of object to image dimensions.

A. Triangulation Pipeline

As illustrated in detail in figure 3, several tasks are performed to calculate the range: When an image is put into the pipeline, some category-independent regions of interest (RoI) are generated first. They highlight everything that appears to be one of the four target object types. The complete map gets disassembled into several patches: Every RoI is cut out and cropped into a standard size of 64×64 pixels. Then each highlighted object undergoes classification and gets annotated with keypoints. In order to maintain proportions, the position of the keypoints must be scaled back from the cropped patch to the original image size. Based on the provided standard dimensions for each object type and the proportion of the object in the image, the height and width of the scene can be calculated. In combination with the focal length of the camera these measurements allow to triangulate the range

between camera and depicted object. Along the pipeline the tasks of region proposal, object classification and keypoint regression are performed by three different neural networks, while RoI cropping and range triangulation are computed without machine learning.

B. Model Architecture

The architecture of the range estimation pipeline is inspired by two-stage detectors, mainly the RCNN [3]. As described in the previous section the first neural subnetwork detects regions of interest on the image. It takes the whole image with a resolution of $320 \times 240 \times 1$ as input. The architecture consists of several compression blocks, increasing the number of channels with a constant compression rate of the layer size. They are followed by the same number of decompression blocks for linear expansion back to initial layer size, all connected by multiple residual bypasses. This results in an hourglass shape with relative high complexity but few parameters. The output tensor is a binary mask in the size of the input image with pixel values either $[0,1]$, indicating a negative or positive detection.

The second network classifies the cropped objects. It receives the RoI patch as $64 \times 64 \times 1$ input vector. The first block consists of several convolutions with linear expansion rate. It is followed by four identical linear bottleneck modules in parallel arrangement. These are designed to specialize on the detection of a single object type. Each one is connected linear to the previous expansion block and receives the same tensor output. The activation layer outputs a one hot encoded array with four values between $[0,1]$ that can be interpreted as detection probability for each class.

The third network finally performs keypoint regression on the same cropped RoI patch as the previous network. While every object type requires an individual set of keypoints and thus a separate network, the current proof of concept is restricted to the class 'car'. It consists of several residual blocks, followed by regression blocks in linear arrangement that reduce the number of channels. The output is an array of twelve pixel coordinates, which identify e.g. the tires.

Although the processing through the subnetworks seems quite similar to the RCNN, there are remarkable differences between both models: The RCNN regresses bounding boxes while the region proposal network performs pixel-wise object segmentation. The region proposals of RCNN are not the final localization output and serve as input for the actual bounding box regression [3], whereas the RoI output for range estimation is considered to represent ground truth right away. An interesting property of the range estimation architecture is that it provides a clear separation between the individual tasks. In- and output of the subnetworks serve as interface, their design has a great impact on reusability of the modules and training difficulty. The network parts in the RCNN widely rely on detailed features from previous subsections and therefore they are hard to train and optimize [3]. In contrast, the three subnetworks are loose coupled and allow individual inference and training.

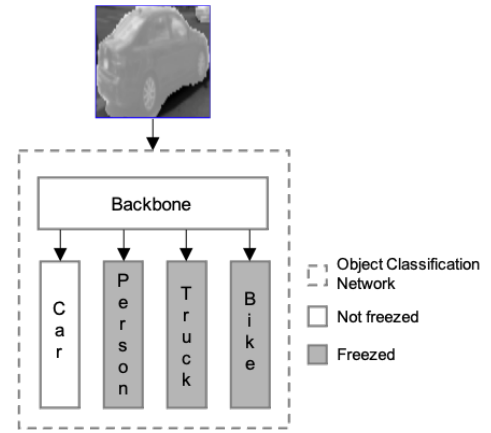


Figure 4. Control of the custom callback function over the weights in the object classification network during the training. For the object type associated with a region proposal sample the corresponding linear bottleneck is set to trainable, while weights of other columns are frozen. This forces the active layers to focus on features of a specific classification.

Table I
TRAINING PARAMETERS OF THE RANGE ESTIMATION SUBNETWORKS.

Neural Network	Data Set	Epochs	Batch Size
Region Proposal	COCO [15]	2.000	16
Object Classification	COCO [15]	2.000	20
Keypoint Regression	CarFusion [6]	10.000	32

C. Training

The training was performed for each subnetwork in separate with the parameters summarized in table I. Because the tasks are very divergent, two different data sets were used. According to the outlined architecture, the required training data could be prepared with low effort. Images were grayscaled and cropped to imitate region proposal input for classification and keypoint regression. For all networks dropout and batch normalization were utilized. During training of the object classification network a custom callback function was used: It controls the learning process of dedicated network parts to ensure specialization of each linear bottleneck column towards the features of one specific object type [14]. As illustrated in figure 4 the function dynamically freezes the weights in other columns, so a linear bottleneck module is trained only with data of a single classification layer type. In the validation phase and for backpropagation all layers are unfrozen again.

V. EVALUATION

The range estimation network is evaluated against several efficiency benchmarks and tested on the IMX 8M Mini [12]. Table II summarizes the number of parameters and computations for all three subnetworks. Except for the number of computations for range estimation, all three networks have a very small size and low complexity. This is confirmed for the object classification and keypoint regression networks by a fast inference on the target microcontroller (see Table III). Measurement of the inference time of the region proposal

Table II

COMPUTATION COST OF THE RANGE ESTIMATION NETWORKS.

Neural Network	Params	Computations
Region Proposal	5.986.996	104.53 GFLOPS
Object Classification	2.349.370	0.26 GFLOPS
Keypoint Regression	2.159.100	15.52 GFLOPS

Table III

SIZE AND PERFORMANCE OF THE RANGE ESTIMATION NETWORKS.
INFERENCE TIME WAS MEASURED ON CPU [12]

Neural Network	Memory Size	Inference Time
Region Proposal	28.16 MB	-
Object Classification	9.14 MB	10.54 ms
Keypoint Regression	26.66 MB	46.60 ms

network could not yet be carried out. According to the large amount of computations it will probably take much more time than the other two networks, but is still expected to be operable in an embedded environment. Other networks aimed for embedded deployment often have an even higher complexity, e.g. the MobileNetV1 [16]. With 3.2 million parameters and 568 million multiply-adds it took 40.32 ms to classify an image on the I.MX 8M Mini [16]. For optimization of the computational workload, the pipeline does not always have to be run through entirely. If no region of interest is detected on the image, processing can be terminated prematurely without passing classification, keypoint annotation and range triangulation steps. The redundant check of a recognized object also increases result quality: Both the region proposal and classification networks must recognize an object separately in order to triangulate the distance to it.

VI. CONCLUSION

This paper described a simple network architecture that allows to estimate the range towards a certain object based on a single image. It was possible to adapt the concept of two-stage detectors for an embedded environment by tailoring the architecture tight to the use case. The loose coupled structure has several advantages such as easier training and adjustment. It also allows a simple extension of the pipeline for other purposes by forwarding the output of a subnetwork into other applications (e.g. for visual highlighting of detected objects).

REFERENCES

- [1] L. Liu, W. Ouyang, X. Wang, P. Fieguth, J. Chen, X. Liu, and M. Pietikäinen, "Deep learning for generic object detection: A survey," *International journal of computer vision*, vol. 128, no. 2, pp. 261–318, 2020.
- [2] M. Sandler, A. Howard, M. Zhu, A. Zhmoginov, and L.-C. Chen, "Mobilenetv2: Inverted residuals and linear bottlenecks," in *Proceedings of the IEEE conference on computer vision and pattern recognition*, 2018, pp. 4510–4520.
- [3] R. Girshick, J. Donahue, T. Darrell, and J. Malik, "Rich feature hierarchies for accurate object detection and semantic segmentation," in *Proceedings of the IEEE conference on computer vision and pattern recognition*, 2014, pp. 580–587.
- [4] R. Girshick, "Fast r-cnn," in *Proceedings of the IEEE international conference on computer vision*, 2015, pp. 1440–1448.
- [5] A. Mousavian, D. Anguelov, J. Flynn, and J. Kosecka, "3d bounding box estimation using deep learning and geometry," in *Proceedings of the IEEE Conference on Computer Vision and Pattern Recognition*, 2017, pp. 7074–7082.
- [6] N. Dinesh Reddy, M. Vo, and S. G. Narasimhan, "Carfusion: Combining point tracking and part detection for dynamic 3d reconstruction of vehicles," in *The IEEE Conference on Computer Vision and Pattern Recognition (CVPR)*, June 2018.
- [7] Y. Xiang, W. Choi, Y. Lin, and S. Savarese, "Subcategory-aware convolutional neural networks for object proposals and detection," in *2017 IEEE winter conference on applications of computer vision (WACV)*. IEEE, 2017, pp. 924–933.
- [8] X. Song, P. Wang, D. Zhou, R. Zhu, C. Guan, Y. Dai, H. Su, H. Li, and R. Yang, "Apollocar3d: A large 3d car instance understanding benchmark for autonomous driving," in *Proceedings of the IEEE/CVF Conference on Computer Vision and Pattern Recognition*, 2019, pp. 5452–5462.
- [9] S. Greengard, "Ai on edge," *Communications of the ACM*, vol. 63, no. 9, pp. 18–20, 2020.
- [10] J. Byrnes, *Unexploded ordnance detection and mitigation*. Springer Science & Business Media, 2008.
- [11] J. Kornatzki, "Architecture and deployment scenario of an artificial neural network for range estimation on infrared images," 2021.
- [12] N. Semiconductors, "I.mx 8m mini fact sheet," Accessed on: Jan. 9, 2020. [Online]. Available: <https://www.nxp.com/docs/en/fact-sheet/IMX8MMINIFS.pdf>, 2020.
- [13] —, "I.mx 8m plus fact sheet," Accessed on: Jan. 9, 2020. [Online]. Available: <https://www.nxp.com/docs/en/fact-sheet/IMX8MPLUSFS.pdf>, 2020.
- [14] M. Abadi, A. Agarwal, P. Barham, E. Brevdo, Z. Chen, C. Citro, G. S. Corrado, A. Davis, J. Dean, M. Devin, S. Ghemawat, I. Goodfellow, A. Harp, G. Irving, M. Isard, Y. Jia, R. Jozefowicz, L. Kaiser, M. Kudlur, J. Levenberg, D. Mané, R. Monga, S. Moore, D. Murray, C. Olah, M. Schuster, J. Shlens, B. Steiner, I. Sutskever, K. Talwar, P. Tucker, V. Vanhoucke, V. Vasudevan, F. Viégas, O. Vinyals, P. Warden, M. Wattenberg, M. Wicke, Y. Yu, and X. Zheng, "TensorFlow: Large-scale machine learning on heterogeneous systems," 2015, software available from tensorflow.org. [Online]. Available: <https://www.tensorflow.org/>
- [15] T.-Y. Lin, M. Maire, S. Belongie, J. Hays, P. Perona, D. Ramanan, P. Dollár, and C. L. Zitnick, "Microsoft coco: Common objects in context," in *European conference on computer vision*. Springer, 2014, pp. 740–755.
- [16] A. G. Howard, M. Zhu, B. Chen, D. Kalenichenko, W. Wang, T. Weyand, M. Andreetto, and H. Adam, "Mobilenets: Efficient convolutional neural networks for mobile vision applications," *arXiv preprint arXiv:1704.04861*, 2017.

Simulative data generation and labeling for autonomous driving specific AI models using MATLAB/Simulink, ROS and Gazebo

Ahmet Sahin

DEPARTMENT OF MECHANICAL, AUTOMOTIVE
AND AERONAUTICAL ENGINEERING
Munich University of Applied Sciences
Munich, Germany
Email: asahin@hm.edu

Abstract—This paper focuses on the automated labeling of simulatively generated data for AI models. The application for this is a students' competition for autonomous driving functions on the model vehicle level, the VDI Cup. It is investigated whether camera data from the open source application ROS and its simulation environment Gazebo in combination with MATLAB and Simulink can be automatically labeled according to the targeted machine learning architecture on the one hand, and on the other hand whether the quality of the data is sufficient for the real world application.

I. INTRODUCTION

Many automobile manufacturers offer their vehicles with Advanced Driver Assistance Systems (ADAS) and autonomous driving functions such as lane keeping assist, adaptive cruise control and traffic sign recognition. As a result, developers are moving closer to fully automated driving. For many camera-based systems such as object or lane detection, it is possible to use artificial intelligence (AI), or more precisely machine learning, instead of traditional image processing techniques. In terms of performance and generalization, such models are often superior to classical methods. However, training and validation of such models requires the use of data that is both high quality and sufficiently quantitative. This data must not only be obtained, but also labeled. This means that in the example of lane detection, for each image available, it is also necessary to specify where the lane is located. This process is often tedious and human errors can occur during labeling.

In the automotive industry, it is now common practice for components such as ADAS to be implemented and tested in simulations first. The advantage of this is that testing assistance systems in simulations is cheaper and safer, since adjustments can be made more quickly and without physical effort, and nothing can break in simulations. In addition, it can be generally claimed that if a system does not work in a simulation, it will not work in reality regardless. Due to the fact that simulations play a major role in the development of ADAS, the question is whether the systems can not only be tested, but also data for AI models can be generated and



Figure 1. Picture taken from the VDI-Cup 2020 [2]

automatically labeled.

The application area of this project is the VDI Cup. In this competition, teams of students from various Bavarian universities compete with 1:8 scale model vehicles in autonomous driving disciplines such as lap times or pursuit races. In the process, a race track with given characteristics that is unknown to the students is provided, on which the competition takes place [1].

This paper addresses the question of whether data can be generated for different models related to autonomous driving using simple resources. The focus is not on comparing suitable architectures. Rather, it is about using the tools available to students in the form of MATLAB/Simulink and the open-source program ROS. Thus, it should be determined whether an efficient generation of data is possible with the said tools and whether the quality of the data is sufficient.

II. RELATED WORK

The field of autonomous driving by means of artificial intelligence is not a new topic and therefore there are many publications concerning it. For example, the authors of [3], two developers from the company Valeo, have asked themselves whether AI is the solution to all common problems in the field of autonomous driving. In doing so, they looked at the entire chain of operation, i.e. the recognition of the environment and its own position by sensors, interpretation of this information, prediction of possible events, planning

of the next actions and operation of the vehicle. They have come to the conclusion that AI techniques are superior to the respective traditional methods. However, they mention that an over engineered AI model based on weak sensors cannot be the solution for autonomous driving. The said problem has to be addressed for this project as well. The vehicle in the competition will only be equipped with one camera (Intel RealSense D435i). This camera must be located inside the vehicle, which means that the field of view is not ideal for detecting lane, objects and racing line. Therefore, it must be taken into account that on the one hand the camera in the simulation corresponds to the real counterpart and on the other hand that the representation in the simulation, especially with regard to light interference or disturbances such as people standing around the track, may not completely correspond to reality.

In [4], the authors provide an overview of AI and machine learning in terms of autonomous driving. They conclude that continuously improved neural networks will be able to perform autonomous driving functions increasingly effectively and safely in the future. Like many other papers, they divide the overall task of autonomous driving into the sub-problems of sensing, planning, and acting. Sensing describes the detection of the vehicle's environment, i.e. the recognition of other traffic participants, the lane and other important objects which can affect the vehicle. Planning further processes this information to determine upcoming actions. It is important here that prediction is also performed. This must estimate where dynamic objects will be in the upcoming instants. The keyword for this is anticipatory driving. The last step, the acting, describes the execution of the planned actions. The authors of [5] make a similar division of the problem. They name the areas recognition, prediction and planning. This order is more detailed compared to the previously mentioned paper, but this does not mean that it is more precise, because ultimately the same tasks have to be performed. This division also makes a lot of sense for this project, as it allows complex problems to be divided into less complex sub-problems. Especially with such a division into different sub-problems and thus into models, the data gathering becomes a tedious task. This intensifies the question whether a generation of data from simulations is reasonable.

An alternative for the realization of autonomous driving is described with behavioral cloning in [6]. As the name suggests, the AI tries to copy the behavior of a user. This works by linking the input data (camera image) with the driving inputs given at that moment (throttle and brake position, steering angle). According to the publication, the advantage of the process is that the data is easy to obtain and first acceptable results are achievable with just a small amount of data. A disadvantage is that all data must be generated by the user himself. So the user has to drive perfectly on these race tracks himself, so that the AI learns this perfect behavior. The AI is not capable of labeling bad decision as bad. It is also more difficult to learn more complex maneuvers like overtaking and finding and keeping the ideal racing line.

Simulative data generation is ideally suited for behavioral cloning because it allows driving maneuvers to be either determined in advance or to ensure controlled driving while the vehicle is in motion. Either way, the generated data can be taken directly from the simulation.

[7] describes the problem that existing datasets are mostly based on static scenarios, but in traffic a dynamic interaction, i.e. a prediction as already mentioned, is needed. The authors use the CARLA simulator to represent such dynamic scenarios. Thereby they hope to narrow the gap between reality and simulative data. This indicates that the interest in simulatively generated data is high and many efforts are being made to use such data as beneficially as possible.

III. METHOD

A. Simulation environment

As a simulation platform, the open-source environment Robot Operating System (ROS) was chosen. ROS consists of many tools, libraries and conventions that help to program the software of robots. The advantage for this project is that ROS provides its own 3D simulation environment, Gazebo. In addition to the robot and its degrees of freedom of movement, other objects for the surrounding area can also be simulated in this environment. Sensors such as cameras can be attached to the robot, and the sensor data can be published in so-called topics, where they can be subscribed to by other components. This creates a robot ecosystem in which data and commands can be published and subscribed from and to different instances.

In addition, MATLAB/Simulink is used in this project. For MATLAB, the so-called ROS Toolbox is provided, which creates an interface between MATLAB and ROS. This offers the advantage that the vehicle dynamics can be modeled in Simulink and the necessary parameters, translational velocity and yaw rate, can be passed on to ROS and thus also to Gazebo. In addition, the vehicle's camera and odometry data can be brought into Simulink, where they are further processed after simulation. Thus, data can be processed and labeled using the wide range of tools that MATLAB offers. Even a direct use of these for training in neural networks is conceivable.

Since this project is related to a competition with race tracks, Gazebo must be able to use race tracks as ground. For this purpose, a tool was developed that can generate black and white images of race tracks. The track sections are read from a spreadsheet document and converted. If the user input does not lead to a closed loop, the track is closed with a cubic spline.

These images are first converted to Scaleable Vector Graphics (SVG), where a smoothed path of the file is created. Programs such as Blender can convert these files into 3D objects. However, Gazebo offers its own model editor where SVG files can be extruded. In addition, the position, color and geometry of the track can also be specified in the same instance. The resulting 3D models are saved and can be reused. Figure 2

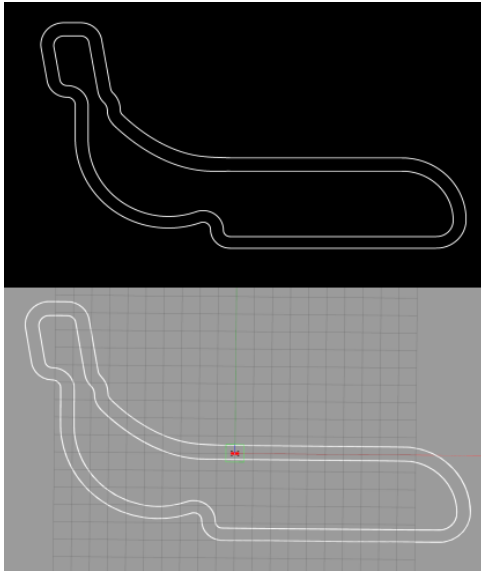


Figure 2. Conversion of the race track in pixel format into a 3D simulation

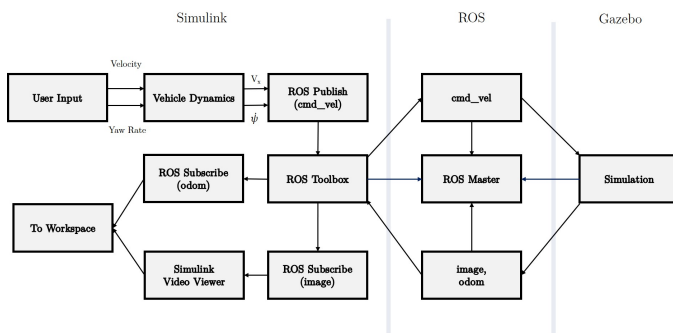


Figure 3. Interaction of ROS, Gazebo and Simulink

shows the comparison of the race track in pixel format and as a 3D object in Gazebo.

As shown in figure 3, a constant data exchange is maintained between Simulink and ROS during simulation. While in Simulink user inputs are converted into motion quantities via a vehicle dynamics simulation and sent to ROS/Gazebo, Simulink receives the camera images and odometry data from the ROS environment. This data is then submitted to the MATLAB workspace. The advantage of this system is that all the resources provided in Simulink are available. For example, blocks from the Vehicle Dynamics Toolbox, the Automated Driving Toolbox, and the Robotics System Toolbox can be used to calculate the speeds.

B. Data generation and labeling

The race tracks are generated with a known ratio, usually 1 pixel per cm. By placing the track in Gazebo in its original form and in the center of the simulation and by knowing the odometry data, i.e. position and direction angle, it is possible to calculate where the vehicle is located on the image and in which direction it is looking. First, a square with an side length

that is twice the length of the field of view is placed around the vehicle. Then, each pixel in this square is checked to see if it is in the field of view. This field of view depends on the angle at which the vehicle is looking. This sorting method has proven to be better and more efficient than a direct calculation of the pixels. This method can be used to determine which lane markers the camera can currently observe and where they are located on the image. This works by transforming the 2D image coordinates into the 3D camera image. This allows data for lane detections to be generated and labeled.

Data for object recognition can be obtained by the same principle. From objects like signs, 3D objects can be created and also placed in the simulation. With the information about where signs are located and how tall they are, they can be marked on images. Through such further processing, the data for established image recognition algorithms can be generated in the next step.

In addition to object and track detections, data for the previously mentioned behavioral cloning can also be obtained. The drawback with the actual data acquisition is that driving errors are included. This can be avoided by a controlled driving process. There are several possibilities for this. One of the possibilities is Model Predictive Control, in which the most ideal route and driving commands are selected on the basis of the route and known driving dynamics. For this, however, the driving dynamics of the competition vehicle are still unknown and the control used should be largely generally valid and occur in real time, a different method of control is chosen for this project.

In the first and second step of this method a point in front of the vehicle is determined, which represents a future position of the vehicle. In the third step, it is calculated how far away said point is from the center of the track. This basically calculates how far the vehicle will be from the target "lane center" at a future time. Step four calculates a vector pointing from the current position to the calculated lane center. In the fifth step, the angle between the current and the target viewing direction is calculated. Depending on this angle, it is determined whether and in which direction the vehicle should steer. The steering angle depends on the distance between steps two and three, so that once the vehicle has reached the center of the lane, driving is achieved with only small corrections. This concept is visualized in figure 4. The speed of the vehicle is still determined by a user, although automation is conceivable here as well. Meanwhile, the driving signals are stored in the MATLAB workspace by simout blocks after the simulation, which allows them to be filtered, processed, and stored in the correct format afterwards.

IV. RESULTS

A. Lane and object labeling

Lane markings and objects can basically be detected reliably and accurately. Due to the fact that all important information is known, the data can be generated after several calculations. It makes sense not to perform real-time marking, but to store the data and then process it. This way the data can be reused

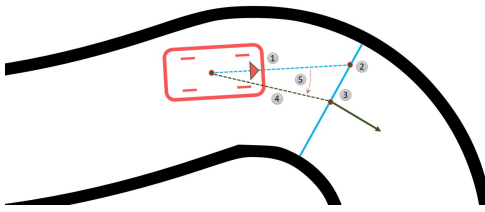


Figure 4. Control of the vehicle to keep the center of the lane

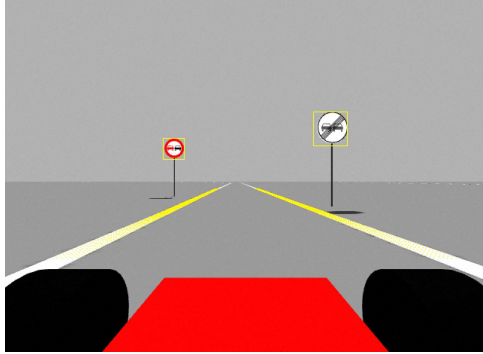


Figure 5. Marked shields and lanes

if new functions are to be implemented.

For the lane detection, race tracks with curves with different radii and shapes (U-curves, chicanes, ...) are used, so that the data are as varied as possible to avoid overfitting and to train different track situations.

For the test of the generation of object recognitions, signs were created which can also occur in the VDI Cup. These are "No Passing" and "Passing Allowed" signs and mark places on the track where it is allowed to overtake opponents. Depending on the desired algorithm, the coordinates of the sign must be stored. For example, in the You Only Look Once (YOLO) algorithm, the position of the upper left corner and the size of the bounding box must be stored, with all four values divided by the image width or height. This data must then be stored in text documents, after which it can be used for training. The training itself has a very low loss. However, this does not necessarily mean that a very good model has been created. It is very likely that because the data is very similar, overfitting has occurred and thus the model is merely handling the simulation data well.

B. Behavioral cloning

The control method described above allows the vehicle to maneuver autonomously through the track. By always looking at future points, the vehicle reacts early to curves or deviations. Because the steering angle is selected depending on the distance to the center of the track, there is little oscillation during steady-state driving. Since the data is not stored in real time but processed after the simulation, driving situations in which the vehicle did not drive as desired can be sorted out or adjusted. For example, steering angles that are too high or

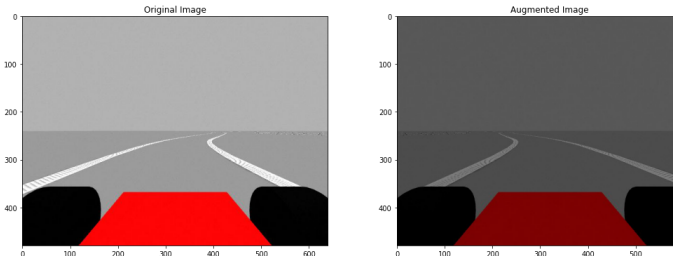


Figure 6. Data Augmentation
Left: Original Image, Right: Augmented (Mirrored and darkened image)

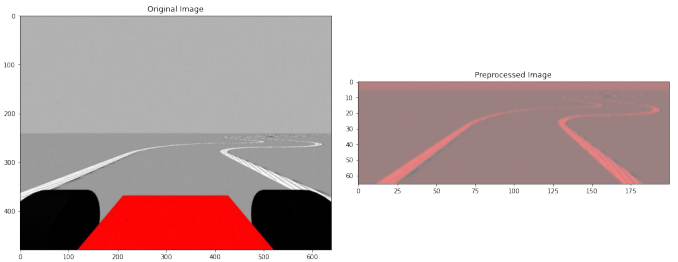


Figure 7. Image Preprocessing
Left: Original Image, Right: Preprocessed Image

too low can be regulated, thus avoiding inappropriate values during training. Data augmentation, i.e. artificial extension of the data by image processing methods such as adjusting the brightness, zooming, shifting or mirroring the images (see figure 6), can significantly extend the number and variety of the data. The image is thereby cut to the essentials. Visible vehicle parts and irrelevant zones are removed, as can be seen in figure 7, so that only the track is visible. Because this is also done in reality, along with the artificially augmented images, data is created that is realistic and suitable for training.

A model trained for the test purpose was able to produce useful results with only a small amount of data from just one track in Gazebo. By generating further data from different tracks and thus driving scenarios and complicating the data by placing irrelevant objects in the simulation, the model can be prepared for real-world use. However, it must be noted that a realistic vehicle dynamics model should be available so that the learned driving commands relate to the real vehicle.

C. Computing power and technological limitations

One problem with the whole procedure is the required computing power. With the realtime factor, Gazebo displays a value that describes how close the simulation is to the real time. If there is a track and the vehicle controlled via MATLAB in the simulation, this factor is 1, which means that the simulation takes place in real time. However, if additional complex objects such as signs are placed, the real time factor drops below 1. As a result, a real time simulation with multiple objects is not possible. This is obviously also dependent on the device on which the simulation is running.

There is also another issue with the labeling of the data. Simulink processes all blocks one by one, which means that

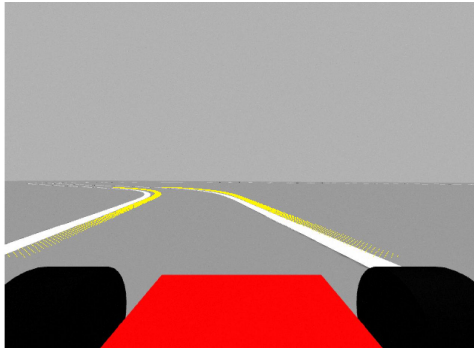


Figure 8. Missed lane detection due to delay in the simulation process

different functions are not called at the same time. As a result, as can be seen in figure 8, it happens that the odometry data does not match the position on the camera data, which can cause a slight offset. This data must be filtered out for training a neural network.

V. DISCUSSION

It was determined that data can be generated quickly and in large quantities. This validates the motivation of this project. However, it cannot be universally stated that the generated data is of high quality. In sign detection, the problem is that the data tends to be very similar. As a result, there is a high risk of overfitting the model, i.e., fitting the model too closely to the training data. Although the data could be designed more effectively by placing additional objects that are not to be recognized, the realtime factor is affected, as already mentioned. Although this problem could be partially solved by using a more powerful PC, it would violate the basic idea of the project, which is to use the resources available to the students. In addition, the creation of more 3D objects, which could actually occur in the real application, would be tedious. This raises the question whether a time saving of a simulative approach for object recognitions exists at all, because labeling tools for object recognition help to label data quickly. For example, the image labeler [8] in MATLAB can be used to label all region of interests of an image. Thus, all that would be needed is to obtain real data.

The problem of an unrealistically empty environment does not apply to lane detection and behavioral cloning because the camera images are cropped to the essentials. Due to the fact that the lane in the simulation as well as in reality are just white lines on a dark background, the data generated from the simulation could actually extend the real data at least. For the use in the VDI Cup, which is simple in contrast to the real road traffic, a complete use of this data would be conceivable. However, different color and light effects should be used to make the simulation more realistic. The training of the behavioral cloning using generated data and its use in Gazebo has confirmed that the models do work in the simulation at least. This leaves the question open whether a deployment in reality would work as well.

VI. CONCLUSION

With the VDI Cup in mind, the goal of this project was to simulatively generate and automatically label data from ROS and Gazebo using aids from MATLAB and Simulink. While the data for track recognition and behavioral cloning are worthy of consideration for training and real-world application, it is unlikely that reliable models can be trained for object recognition due to the similarity of the data.

To check exactly which data and algorithms work best and how well, an implementation in a real system would be conceivable. In principle, however, it can be concluded that the currently available simulation environments, due to their graphics and simplicity, are suitable for the aforementioned competition, but by no means should be used for real road traffic. Rather, a testing process could be established in which, before real data is tediously obtained, labeled, and used for training, simulatively generated and labeled data can be used to test the model and its utility within the simulation. This allows a developer to determine if an idea for an AI is worth implementing in reality.

ACKNOWLEDGMENT

The author would like to thank Prof. Dr. rer. nat. Markus Krug for his help and support with this work.

REFERENCES

- [1] F. Seufert, "Technical and sporting regulations of the vdi autonomous driving challenge." [Online]. Available: <https://bit.ly/3i53NKg>
- [2] "Vdi autonomous driving challenge." [Online]. Available: <https://www.vdi-adc.de/>
- [3] S. Milz and J. Schrepfer, "Is artificial intelligence the solution to all our problems? exploring the applications of ai for automated driving," in *Automatisiertes Fahren 2019*, ser. Proceedings, T. Bertram, Ed. Wiesbaden: Springer Fachmedien Wiesbaden, 2020, pp. 95–115.
- [4] A. Jungmann, C. Lang, and M. Pelz, "Artificial intelligence for automated driving - quo vadis?" *ATZelectronics worldwide*, vol. 15, no. 3, pp. 8–13, 2020.
- [5] A. E. Sallab, M. Abdou, E. Perot, and S. Yogamani, "Deep reinforcement learning framework for autonomous driving," *Electronic Imaging*, vol. 2017, no. 19, pp. 70–76, 2017. [Online]. Available: <https://bit.ly/38wbGFk>
- [6] R. Tripathi, S. Vyas, and A. Tewari, "Behavioral cloning for self-driving cars using deep learning," in *Proceedings of International Conference on Big Data, Machine Learning and their Applications*, S. Tiwari, E. Suryani, A. K. Ng, K. K. Mishra, and N. Singh, Eds. Singapore: Springer Singapore, 2021, pp. 197–209.
- [7] J. Shenoy, E. Kim, X. Yue, T. Park, D. Fremont, A. Sangiovanni-Vincentelli, and S. Seshia, "A customizable dynamic scenario modeling and data generation platform for autonomous driving," 2020.
- [8] "Get started with the image labeler." [Online]. Available: <https://de.mathworks.com/help/vision/ug/get-started-with-the-image-labeler.html>

Applications and Limitations of Dynamical Component Analysis (DyCA)

Patricia Schell, Fabienne Anselstetter, Monika Warmuth, Christian Uhl

Faculty of Engineering Sciences
Ansbach University of Applied Sciences
Ansbach, Germany

Email: {Patricia.Schell, Fabienn.Anselstetter, Monika.Warmuth, Christian.Uhl}@hs-ansbach.de

Abstract—Dynamical component analysis (DyCA) is a recently introduced dimensionality reduction method for high-dimensional time series with a certain type of underlying low-dimensional dynamics. While the method has already been successfully applied to various simulated and real world data sets, the limitations of DyCA have not yet been thoroughly investigated. To test these limits by evaluating characteristic DyCA parameters, different influencing parameters like component noise and additive noise are varied for simulated data of the Rössler and Lorenz attractors, blue-sky catastrophe, and ECG-type data. The computation of those parameters reduces to the solution of a generalized eigenvalue problem, whereas the corresponding generalized eigenvalues provide information about the successful detection of linear components. Furthermore, the deviation of the original signal from the reconstructed signal as well as the relative reconstruction error are considered for the evaluations.

I. INTRODUCTION

Dimensionality reduction methods allow the analysis of multivariate time series and particularly the detection and subsequent elimination of multicollinearities in high-dimensional signals. Therefore, these methods offer a way to extract relevant information from a large data set without losing important signal components. Examples in the medical field are electroencephalogram (EEG) [1], electrocardiogram (ECG) [2] and electromyogram (EMG) [3] recordings. Additionally, it is possible to apply dimensionality reduction methods to human gait data [4] and to applications in the technical field, such as motion sequence data of wind turbines [5] or the diagnosis of bearing faults [6].

There is a wide range of different dimensionality reduction methods. Typical examples are principal component analysis (PCA) [7] and independent component analysis (ICA) [8]. Forecastable component analysis [9] and canonical correlation analysis [10] can be mentioned as further methods. Yet, the disadvantage of many dimensionality reduction methods is that they are based on the assumption of a stochastic signal and are therefore not optimally suited for the analysis of dynamic signals [11]. The method of dynamical component analysis (DyCA), which was introduced in 2018 by Seifert et al. [11], is an approach to describe the underlying dynamics of the signal in a more suitable way. DyCA is based on the assumption that the underlying dynamics are governed by a system of linear and nonlinear ordinary differential equations (ODE). The projection of the signal onto a low-dimensional

subspace is carried out by solving a generalized eigenvalue problem. By the solution of this problem, projection vectors can be determined which provide a suitable low-dimensional approximation of the signal while capturing the most important dynamic features. On the basis of different datasets, Korn et al. [12] and Uhl et al. [13] already showed that the analysis by DyCA outperforms more stochastic methods like PCA and ICA for describing the underlying dynamics of deterministic time series.

Currently, however, the limits of the applicability of DyCA are still unknown. The recorded signals can be affected by a variety of parameters that may have an impact on whether or not the extraction of the important signal features is successful. Interference factors are typically different types of noise such as component noise and additive noise, which can be caused by the 50Hz mains hum, a patient's muscle tremor, or loose contacts at the sensors [14]. The use of simulated data with varying noise types and levels provides the basis for the following analysis. After applying DyCA to noisy Rössler and Lorenz attractor data as well as to the blue-sky catastrophe and synthetic ECG data, the generalized eigenvalues, the relative reconstruction error and the deviation of the reconstructed signal from the original signal are taken into account for determining the limits of DyCA.

The paper is structured as follows. In section II we provide the basic concept of DyCA. The analysis of the reconstructed signal characteristics are presented in section III. Finally, the results are discussed and concluded in section IV.

II. DYNAMICAL COMPONENT ANALYSIS

In this subsection, DyCA is briefly summarized. The complete derivation can be found in [13]. Starting point is a model of a multivariate time series $q(t) \in \mathbb{R}^N$, where N describes the number of channels. The model is assumed to be decomposable into time-dependent amplitudes $x_i(t)$ and linear independent vectors $w_i \in \mathbb{R}^N$:

$$q(t) = \sum_{i=1}^n x_i(t)w_i \quad (1)$$

The dynamic of the signal $q(t)$ is assumed to be driven by a system of m linear differential equations (2) with $m \geq \frac{n}{2}$ and

$n - m$ nonlinear (3) differential equations:

$$\dot{x}_i(t) = \sum_{k=1}^n a_{i,k} x_k(t) \quad \text{for } i = 1, \dots, m \quad (2)$$

$$\dot{x}_i(t) = f_i(x_1(t), \dots, x_n(t)) \quad \text{for } i = m + 1, \dots, n \quad (3)$$

The coupling of the linear equations, given by the coefficient matrix $a_{i,k}$, is assumed to be such that the block matrix $a_{i,k}, i = 1, \dots, m, k = m + 1, \dots, n$ has full rank. The vectors w_i , the amplitudes $x_i(t)$, the coefficients $a_{m,k}$, and the smooth functions f_n are unknown. The aim of DyCA is to estimate the model from a measurement $q(t) \in \mathbb{R}^N$ by estimating projection vectors $\tilde{u}_i, \tilde{v}_i \in \mathbb{R}^N$ minimizing the least-square error functions

$$D(u_i, v_i) = \frac{\langle \|\dot{q}(t)^\top u_i - q(t)^\top v_i\|^2 \rangle}{\langle \|\dot{q}(t)^\top u_i\|^2 \rangle} \quad (4)$$

subject to the u_i being linearly independent with $i = 1, \dots, m$ and $\langle \dots \rangle$ denoting the time average. Defining

$$C_0 = \langle q(t)q(t)^\top \rangle, C_1 = \langle \dot{q}(t)q(t)^\top \rangle, C_2 = \langle \dot{q}(t)\dot{q}(t)^\top \rangle, \quad (5)$$

the minimization of $D(u_i, v_i)$, yields the vectors \tilde{u}_i by solving the generalized eigenvalue problem

$$C_1 C_0^{-1} C_1^\top u = \lambda C_2 u, \quad (6)$$

and the vectors \tilde{v}_i by calculating $\tilde{v}_i = C_0^{-1} C_1^\top \tilde{u}_i$. For the generalized eigenvalues λ_i we obtain

$$\min_{\substack{u_1, \dots, u_m \in \mathbb{R}^N \\ v_1, \dots, v_m \in \mathbb{R}^N}} \sum_{i=1}^m D(u_i, v_i) = \sum_{i=1}^m (1 - \lambda_i). \quad (7)$$

To identify the m candidates $(\tilde{u}_i, \tilde{v}_i)$ minimizing the error functions $D(u_i, v_i)$, the generalized eigenvalues λ_i are sorted in descending order in accordance with the vectors \tilde{u}_i and \tilde{v}_i . Introducing a threshold $\alpha > 0$, the vectors \tilde{u}_k ($k = 1, \dots, \tilde{m}$) corresponding to generalized eigenvalues $1 \geq \lambda_k \geq \alpha$ yield the estimated amplitudes $\tilde{x}_k(t)$ obeying the linear differential equation (2) with an estimation of its right-hand side by the projection of the measured signal onto \tilde{v}_k . The linear hull of these vectors \tilde{u}_k and \tilde{v}_k span an \tilde{n} -dimensional subspace \mathbb{R}^N and yield an estimate of n :

$$\tilde{n} := \dim(\text{span}\{\tilde{u}_1, \dots, \tilde{u}_{\tilde{m}}, \tilde{v}_1, \dots, \tilde{v}_{\tilde{m}}\}) \quad (8)$$

The estimation of the DyCA components \tilde{w}_i is achieved by minimizing a second least-squares error,

$$\eta(w_i) = \frac{\langle \|q(t) - \sum_{i=1}^{\tilde{n}} \tilde{x}_i(t) w_i\|^2 \rangle}{\langle \|q(t)\|^2 \rangle}, \quad (9)$$

leading to \tilde{n} DyCA components \tilde{w}_i whose solution reads $\tilde{w}_i = \sum_{j=1}^{\tilde{n}} (C_{\tilde{X}}^{-1})_{ij} \langle \tilde{x}_j(t) q(t) \rangle$ with $(C_{\tilde{X}})_{ij} = \langle \tilde{x}_i(t) \tilde{x}_j(t) \rangle$.

III. APPLICATION AND RESULTS

The potential of applying DyCA to simulated and real world data has already been shown for several examples in [11]–[13]. In this work, we want to study systematically the applicability and limitations of DyCA by investigating its performance on four different simulated models $q_0(t) \in \mathbb{R}^N$ and different superimposed disturbances $d(t) \in \mathbb{R}^N$:

$$q(t) = q_0(t) + d(t), \quad (10)$$

Each model consists of a set of three differential equations numerically integrated by a Runge-Kutta (4,5) method. The systems differ in their number of linear and nonlinear differential equations and their mutual coupling. The underlying original simulated components w_i are chosen randomly with $N = 20$, and linearly independent to each other. The disturbances are simulated by component noise $n_c(t) = \sum_{j=1}^p \xi_j(t) \psi_j$ and additive white noise $n(t) \in \mathbb{R}^N$,

$$d(t) = n_c(t) + n(t) = \sum_{j=1}^p \xi_j(t) \psi_j + n(t), \quad (11)$$

with time-dependent random amplitudes $\xi_j(t)$ and components $\psi_j \in \mathbb{R}^N$ also being chosen randomly, but linearly independent of the model components w_i . The number of added noise components p is chosen as large as possible by $p = N - 3$. The noise types are varied for both additive noise and component noise from 0dB to 100dB in steps of 10dB. We perform 100 runs per variation and subsequently calculate the mean values of the respective parameters. The data to be analyzed is then plotted as a function of the above-mentioned noise variation. The first three generalized eigenvalues $\lambda_i, i = 1, \dots, 3$ representing $\lambda_i = 1 - D(\tilde{u}_i, \tilde{v}_i)$ and $1 - \eta(\tilde{w}_i)$ are illustrated as well. To investigate the reconstruction performance we introduce another error function

$$\epsilon(\tilde{x}_i, \tilde{w}_i) = \frac{\langle \|q_0(t) - \sum_{i=1}^{\tilde{n}} \tilde{x}_i(t) \tilde{w}_i\|^2 \rangle}{\langle \|q_0(t)\|^2 \rangle}, \quad (12)$$

representing the deviation of the original model $q_0(t)$ from the reconstructed signal $\sum_{i=1}^{\tilde{n}} \tilde{x}_i(t) \tilde{w}_i$ computed from the noisy data $q(t)$ and show $1 - \epsilon(\tilde{x}_i, \tilde{w}_i)$ in the following graphs. For better comparison of all investigated cases we assume $\tilde{m} = 2$ and $\tilde{n} = \dim(\text{span}\{\tilde{u}_1, \tilde{u}_2, \tilde{v}_1, \tilde{v}_2\}) = 3$. Therefore we discuss and compare the projection matrices $\tilde{W}_1^- = (\tilde{u}_1, \tilde{u}_2, \tilde{v}_1)^\top$ and $\tilde{W}_2^- = (\tilde{u}_1, \tilde{u}_2, \tilde{v}_2)^\top$ and denote the error functions η and ϵ with the indices 1 and 2 accordingly: $\eta_1, \eta_2, \epsilon_1, \epsilon_2$.

A. Rössler attractor

The Rössler attractor [15] is described by the following system of differential equations:

$$\begin{aligned} \dot{x}_1 &= -(x_2 + x_3) \\ \dot{x}_2 &= x_1 + ax_2 \\ \dot{x}_3 &= b + (x_1 - c)x_3 \end{aligned} \quad (13)$$

with $a = 0.15, b = 0.2$ and $c = 10$. As this ODE system consists of two linear and one nonlinear differential equations, the requirement $m \geq \frac{n}{2}$ for model reconstruction by DyCA

is fulfilled. The representation of the Rössler attractor in the three-dimensional space is shown in figure 1.

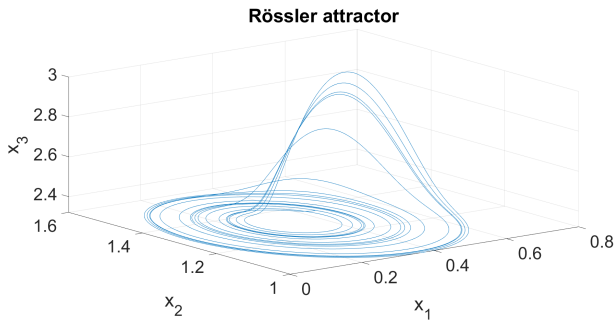


Figure 1. Trajectory of the Rössler attractor

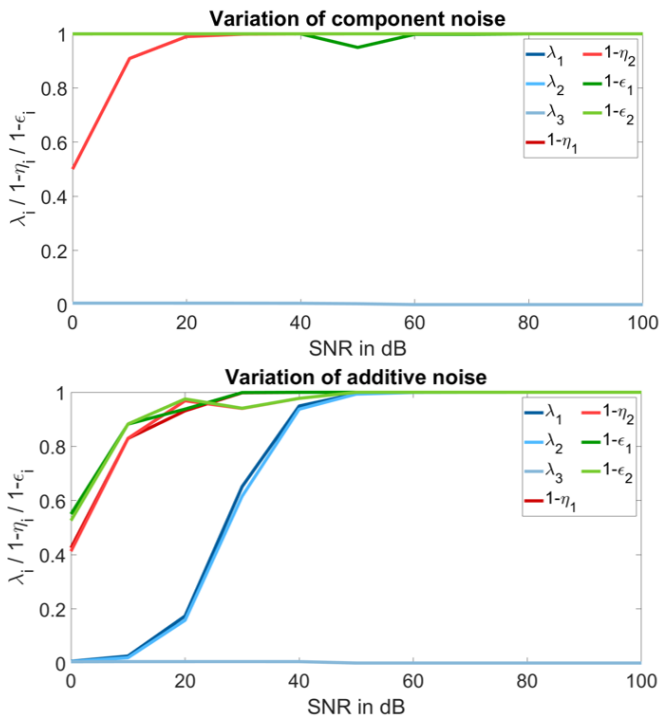


Figure 2. Rössler attractor – variation of noise components

Figure 2 summarizes the different noise and DyCA component variations tested on the Rössler attractor. Considering the component noise variations, the linear part is constantly detected correctly (two generalized eigenvalues, λ_1 and λ_2 close to one, hidden by the green lines), which is further approved by the values of $1 - \epsilon_1$ and $1 - \epsilon_2$ being close to one. Since the course of $1 - \epsilon_1$ is more constant, we conclude that \widetilde{W}_1^- yields a suitable projection matrix. It is visible that from 30dB, $1 - \epsilon_1$, $1 - \epsilon_2$, $1 - \eta_1$, and $1 - \eta_2$ have the same course close to one. The variation of the additive noise shows that the first two generalized eigenvalues are close to one for noise levels greater than 50dB. Above this SNR, the linear components are detected successfully. When reconstructing with the projection matrix \widetilde{W}_1^- , $1 - \epsilon_1$ and $1 - \eta_1$ are already

close to one from 30dB on, whereas for \widetilde{W}_2^- this is only the case for noise levels greater than 50dB. This indicates that the projection matrix \widetilde{W}_1^- is the better choice.

B. Lorenz attractor

The well-known Lorenz attractor [16] is governed by the following ODE system:

$$\begin{aligned} \dot{x}_1 &= \delta(x_2 - x_1) \\ \dot{x}_2 &= x_1(\beta - x_3) - x_2 \\ \dot{x}_3 &= x_1x_2 - \gamma x_3 \end{aligned} \tag{14}$$

with $\delta = 10$, $\beta = 28$, $\gamma = \frac{8}{3}$. This system, which leads to the trajectory shown in figure 3, contains only one linear differential equation.

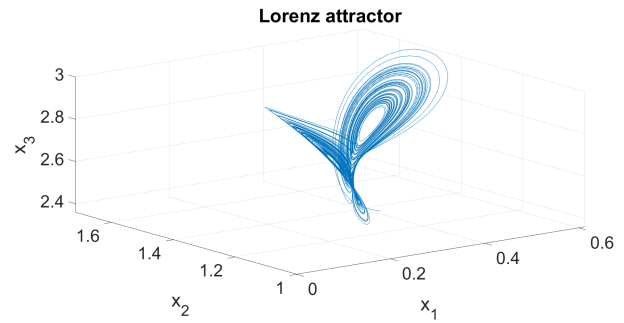


Figure 3. Trajectory of the Lorenz attractor

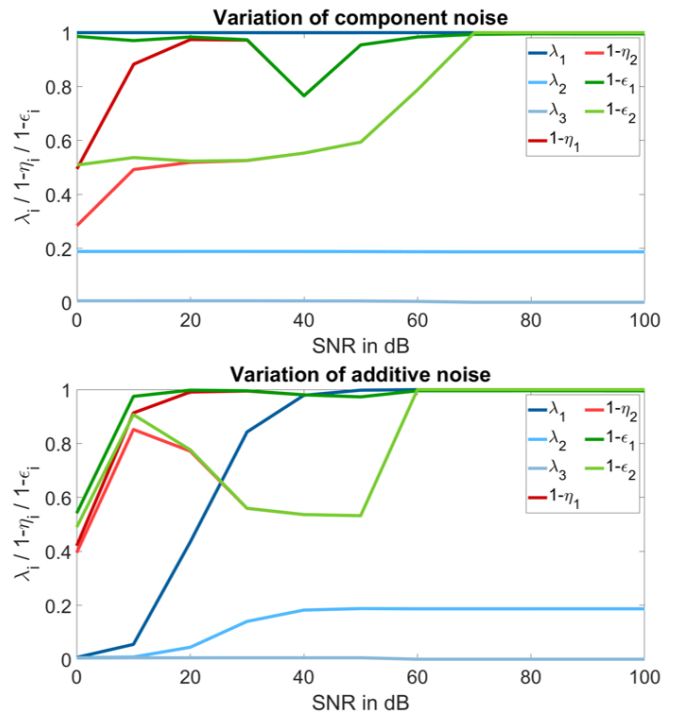


Figure 4. Lorenz attractor – variation of noise components

Figure 4 shows the results of the noise variations for the Lorenz attractor. Concerning the component noise, the first

generalized eigenvalue is close to one right from the beginning, which indicates that the linear parts of the ODE system are recognized correctly. The results show that a reconstruction using \widetilde{W}_1^- leads to better results, as $1 - \epsilon_1$ and $1 - \eta_1$ are closer to one than $1 - \epsilon_2$ and $1 - \eta_2$, despite a dip at 40dB. In case of additive noise, the linear components of the system are detected correctly from a noise level of greater than 50dB. For a reconstruction using \widetilde{W}_1^- it can be seen that from 10dB on, the values of $1 - \epsilon_1$ and $1 - \eta_1$ are one. In both cases the projection matrices \widetilde{W}_1^- seems to be the proper choice.

C. Blue-sky catastrophe

The blue-sky catastrophe [17] can be described by the following system of differential equations,

$$\begin{aligned} \dot{x}_1 &= x_1(2 + \mu - 10(x_1^2 + x_2^2)) + x_3^2 + x_2^2 + 2x_2 \\ \dot{x}_2 &= -x_3^3 - (1 + x_2)(x_3^2 + x_2^2 + 2x_2) - 4x_1 + \mu x_2 \\ \dot{x}_3 &= (1 + x_2)x_3^2 + x_1^2 - \kappa, \end{aligned} \quad (15)$$

with $\kappa = 0.0357$ and $\mu = 0.456$, leading to a trajectory shown in figure 5. Note, that all three differential equations are nonlinear in this case.

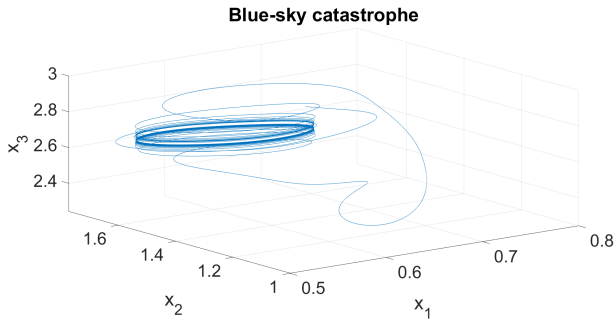


Figure 5. Trajectory of the blue-sky catastrophe

Figure 6 summarizes the variation of the noise components for the blue-sky catastrophe. The variation of the component noise reveals that the linear components are correctly detected from the beginning (no generalized eigenvalue is close to one) and a good signal reconstruction is achieved using DyCA. Both matrices \widetilde{W}_1^- and \widetilde{W}_2^- seem to be a proper choice. In case of additive noise, the linear components are correctly detected from an SNR of 50dB and a consistently good signal reconstruction is achieved from 30dB. Both projection matrices seem to be suitable as well.

D. ECG Data

The dynamical model for generating a synthetic ECG signal [18] can be described by the following system of differential equations:

$$\begin{aligned} \dot{x}_1 &= \alpha x_1 - \omega x_2 \\ \dot{x}_2 &= \omega x_1 + \alpha x_2 \\ \dot{x}_3 &= - \sum_{i \in \{P, Q, R, S, T\}} a_i \Delta \theta_i \exp\left(-\frac{\Delta \theta_i^2}{2b_i^2}\right) - (x_3 - x_3^{(0)}) \end{aligned} \quad (16)$$

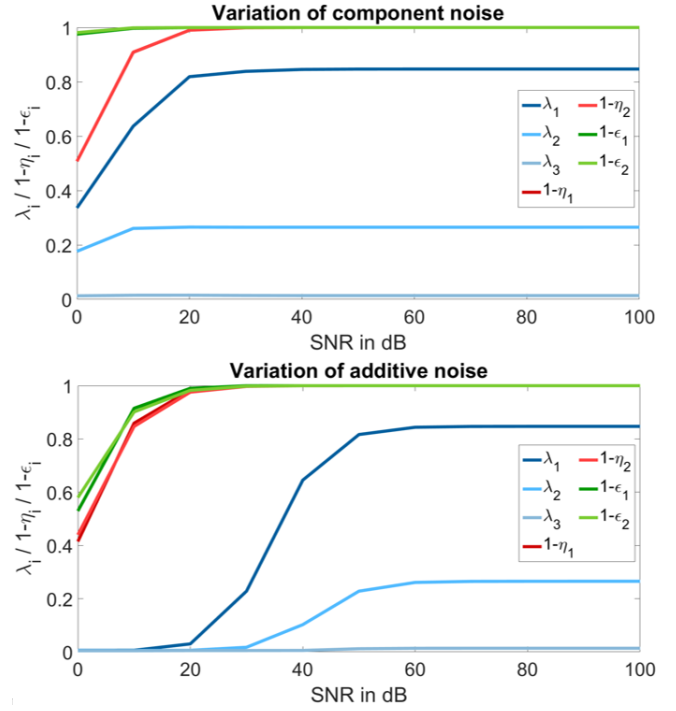


Figure 6. Blue-sky catastrophe – variation of noise components

with $\alpha = 1 - \sqrt{x_1^2 + x_2^2}$, $\Delta \theta_i = \theta - \theta_i$ and $\theta = \text{atan2}(x_2, x_1)$. The corresponding trajectory in phase space is shown in figure 7.

The first two differential equations characterize an attracting limit cycle of unit radius in the x_1 - x_2 -plane, independent of the variable x_3 . This corresponds to two linear differential equations decoupled from x_3 in the limit cycle neighborhood. The third differential equation specifies deflections associated with the ECG complexes described by the letters P, Q, R, S, and T. For further details, we refer the reader to [18]. For our simulations we rescaled the amplitude $x_3(t)$ to deal with comparable magnitudes of amplitudes $x_i(t)$.

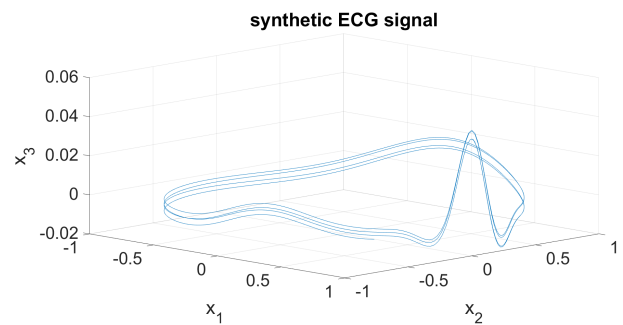


Figure 7. Trajectory of the synthetic ECG signal

Figure 8 summarizes the noise component variations for the synthetic ECG signal. As expected there are two generalized eigenvalues close to one (two blue lines one above the other) describing the two linear equations for all investigated component noise levels. In the case of additive noise the two

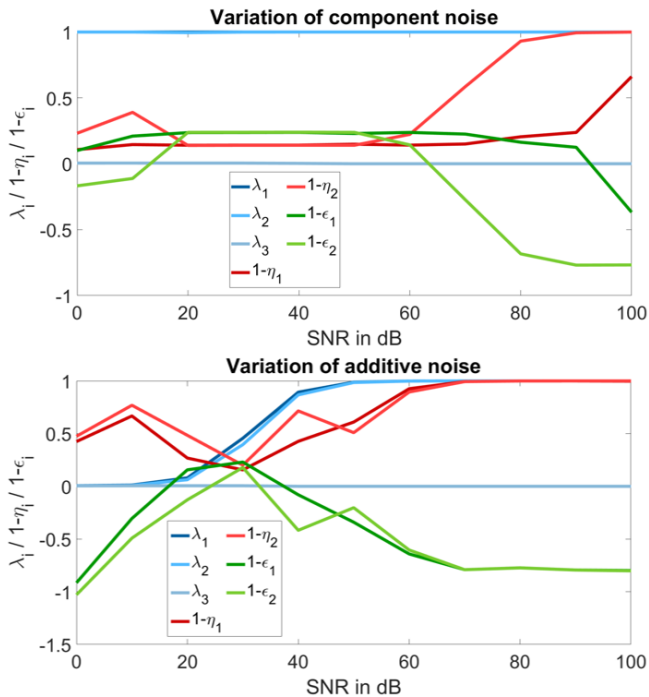


Figure 8. ECG signal – variation of noise components

generalized eigenvalues close to one only appear for low noise levels (above 40dB) with decreasing value as the additive noise level increases. For very low noise levels (above 80dB) the reconstruction of the signal quantified by $1 - \eta_{1,2}$ is still possible, but fails for higher noise levels. The reconstruction of the model given by $1 - \epsilon_{1,2}$ completely fails as shown by the green lines. This is due to the missing coupling of the linear differential equations with the nonlinear equations.

IV. CONCLUSION

In summary, the results of section III show that DyCA is well-suited for signals with component noise. Even from a noise level of 0dB, the linear signal components can be correctly detected. Reconstruction of the model from the signals perturbed by component noise is well possible if the linear equations are coupled with all nonlinear equations – for both the cases: condition $m \geq n/2$ is fulfilled (example III-A) and not satisfied (examples III-B, III-C). This is probably due to least-square-error function (4) acting as a “smooth function detector” by approximating linear differential equations. In the case of missing coupling (example III-D), DyCA still enables the detection of the linear components of the signal, but fails to reconstruct the underlying model. In the case of additive noise, reconstruction of the model is still reasonably possible to some extent at noise levels above about 15dB, while detection of linear signal components is only possible at low noise levels above approx. 35dB.

To achieve a successful reconstruction even with higher additive noise, the noise must be removed before performing a dimensionality reduction via DyCA. A pre-filtering should provide the ability to apply DyCA on highly noisy data, thus

extending its range of applications. In [19] the authors linked the DyCA minimization problem of (4) with a regularized variational L^2 -denoising approach. An iterative procedure is created, whereby both processes, the denoising process and the dimensionality reduction, improve each other. Initial tests with the Rössler attractor show that this method can handle both high additive noise values of 1dB and missing data entries. Future research will be done testing this approach on more data sets and thus, further testing the potential and limitations of dynamical component analysis.

ACKNOWLEDGMENT

This work was supported by the German Federal Ministry of Education and Research (BMBF, Funding number: 05M20WBA).

REFERENCES

- [1] P. Boonme, P. Thongserm, P. Arunsuriyasak, and P. Phasukkit, “Hand Movement Classification Base on EEG Signals using Deep Learning and Dimensional Reduction Technique,” *2019 12th Biomedical Engineering International Conference (BMEICON)*, pp. 1–4, 2019.
- [2] C. Bakir, “Classification of ECG Signals By the Neighborhood Feature Extraction Method,” *Balkan Journal of Electrical and Computer Engineering*, vol. 3, pp. 353–363, 2015.
- [3] R. Chowdhury, M. B. I. Reaz, M. Mohd Ali, A. A. A Bakar, K. Chellappan, and T.-G. Chang, “Surface Electromyography Signal Processing and Classification Techniques,” *Sensors (Basel, Switzerland)*, vol. 13, pp. 12 431–12 466, 2013.
- [4] C.-W. Cho, W.-H. Chao, S.-H. Lin, and Y.-Y. Chen, “A vision-based analysis system for gait recognition in patients with Parkinson’s disease,” *Expert Systems with Applications*, vol. 36, pp. 7033–7039, 2009.
- [5] Y. Wang, X. Ma, and P. Qian, “Wind Turbine Fault Detection and Identification Through PCA-Based Optimal Variable Selection,” *IEEE Transactions on Sustainable Energy*, vol. 9, no. 4, pp. 1627–1635, 2018.
- [6] S. Agrawal, V. Giri, and A. Tiwari, “Induction motor bearing fault classification using WPT, PCA and DSVM,” *Journal of Intelligent & Fuzzy Systems*, vol. 35, pp. 1–12, 2018.
- [7] K. Pearson, “LIII. On lines and planes of closest fit to systems of points in space,” *The London, Edinburgh, and Dublin Philosophical Magazine and Journal of Science*, vol. 2, no. 11, pp. 559–572, 1901.
- [8] A. Hyvärinen and E. Oja, “Independent component analysis: algorithms and applications,” *Neural Networks*, vol. 13, no. 4, pp. 411–430, 2000.
- [9] G. Georg, “Forecastable Component Analysis,” *Proceedings of the 30th International Conference on Machine Learning*, vol. 28, no. 2, pp. 64–72, 2013.
- [10] J. Bortz, *Statistik*. Springer Berlin Heidelberg, 1999, ch. Kanonische Korrelationsanalyse.
- [11] B. Seifert, K. Korn, S. Hartmann, and C. Uhl, “Dynamical Component Analysis (DyCA): Dimensionality Reduction for High-Dimensional Deterministic Time-Series,” in *2018 IEEE 28th International Workshop on Machine Learning for Signal Processing (MLSP)*. IEEE, 2018, pp. 1–6.
- [12] K. Korn, B. Seifert, and C. Uhl, “Dynamical Component Analysis (DyCA) and Its Application on Epileptic EEG,” in *ICASSP 2019 - 2019 IEEE International Conference on Acoustics, Speech and Signal Processing (ICASSP)*. IEEE, 2019, pp. 1100–1104.
- [13] C. Uhl, M. Kern, M. Warmuth, and B. Seifert, “Subspace Detection and Blind Source Separation of Multivariate Signals by Dynamical Component Analysis (DyCA),” *IEEE Open Journal of Signal Processing*, vol. 1, pp. 230–241, 2020.
- [14] G. Haufe, *Medizintechnik in der Intensivmedizin: diagnostische und therapeutische Verfahren; Grundlagen, Gerätetechnik, Anwendung, Sicherheit*. expert-Verlag, 1998.
- [15] O. Rössler, “An equation for continuous chaos,” *Physics Letters A*, vol. 57, no. 5, pp. 397–398, 1976.
- [16] D. Viswanath, “The fractal property of the Lorenz attractor,” *Physica D: Nonlinear Phenomena*, vol. 190, no. 1, pp. 115–128, 2004.
- [17] N. Gavrilov and A. Shilnikov, “Example of a blue sky catastrophe,” *Am. Math. Soc. Transl.*, vol. 200, pp. 99–105, 2000.

- [18] P. McSharry, G. Clifford, L. Tarassenko, and L. Smith, "A dynamical model for generating synthetic electrocardiogram signals," *IEEE transactions on biomedical engineering*, vol. 50, no. 3, pp. 289–294, 2003.
- [19] M. Warmuth, P. Romberger, and C. Uhl, "Robust Dynamical Component Analysis via Multivariate Variational Denoising," in *2021 29th European Signal Processing Conference (EUSIPCO) (accepted)*, 2021.

Parameter choice for the short-time Fourier transformation in frequency-domain Blind Source Separation

Tobias Vorderobermeier

Faculty of Electrical Engineering and Information Technology

OTH Regensburg

Regensburg, Germany

tobias.vorderobermeier@st.oth-regensburg.de

Abstract—This paper discusses the impact of the short-time Fourier transformation, particularly the choice of its parameters on the solution-finding process of frequency-domain blind source separation. It points out and is motivated by the lack of consistency regarding the parameter choice of previous publications. The work highlights the issues that arise from modeling the linear convolution in the short-time Fourier domain and how to circumvent or at least mitigate them with an optimal synthesis window and manipulation of the parameters. It further discusses how increasing the length of the discrete Fourier transformation has drawbacks on the feasibility of the permutation problem, the estimation, and the model assumptions of independent component analysis. It finally demonstrates how a decreased shift could help in restoring the latter.

I. INTRODUCTION

A common problem in signal processing is that specific signals of interest can only be observed indirectly, as part of mixtures and hence need to be estimated from such. There are numerous methods to tackle this issue, gathering under the name of source separation. Their way of achieving this separation crucially depends on the amount of information available on the respective source signals. Problems where little to no information is known beforehand are called blind source separation (BSS) problems. One of the major statistical tools applicable under these circumstances is independent component analysis, abbreviated as ICA, whose applications span from the medical field [1] across the financial sector [2] over to audio signal processing, which this paper will put its focus on. One of the most commonly used examples to motivate audio source separation is the so-called "Cocktail party Problem" [3]. It seeks to replicate the humans remarkable ability to focus on a single speaker in the presence of many, proficiently extracting the chosen source.

A. Problem Formulation

Even after restricting oneself to audio signals, there remain significant differences in how certain scenarios need to be dealt with. Depending on the given application, it first needs to be specified to which degree acoustic effects should be modeled. Table I offers three different models with growing complexity. The instantaneous case assumes the signals to be superimposed

with no delay and no reverberation. It hence only accounts for different amplitudes of the source signals, while the anechoic setting allows for delays but no reverberations, which are also part of the echoic model. Judging by the model alone, the

Table I
MIXING MODEL SPECIFIC LINEAR OPERATORS AND MIXING PARAMETERS. [4]

Mixing Model	Generative Model	Parameter (\mathbf{A}) _{ij}
Instantaneous	$\mathbf{x}(t) = \mathbf{A}\mathbf{s}(t)$	c_{ij}
Anechoic	$\mathbf{x}(t) = \mathbf{A} * \mathbf{s}(t)$	$c_{ij}\delta(t - \delta_{ij})$
Echoic	$\mathbf{x}(t) = \mathbf{A} * \mathbf{s}(t)$	$\sum_{k=1}^T c_{ij}^{(k)}\delta(t - \delta_{ij}^{(k)})$

instantaneous case, due to its simple matrix multiplication, fits most naturally with the generative model of ICA as given in [5]. However, since it cannot account for those highly relevant aspects of real-life recordings, it bears next to no relevance in most practical scenarios. The echoic, or often called convolutive mixture model, on the other hand, can consider these peculiarities but, due to its more complex structure induced by the convolution, can't be directly addressed by ICA. The key difference is that while (\mathbf{A})_{ij} in the instantaneous case is a mere constant, it becomes a discrete function of time in the convolutive model, specifically the impulse response between the i -th recording microphone and the j -th source. As the sum limit in table I makes clear, these impulse responses are bound in length by the same constant T . This shows that the convolutive model increases the number of parameters to estimate per source and microphone from 1 to T , which underlines the giant leap in difficulty.

B. Methodology

ICA assumes the M microphones and I sources to be connected via a linear mapping expressed by the $M \times I$ mixing matrix \mathbf{A} . This obviously isn't the case for convolutive mixtures. Hence the method is not applicable unless the problem can be transformed to take this shape. There are various methods to achieve this transformation, which can be

categorized by the domain they are based in. Time-domain approaches [6]–[8] aim at finding subspaces of the observations space –spanned by the microphone recordings and time-lagged copies of such– that correspond to the separated signals. Therefore, they try to construct data vectors or matrices of special structure, through which the convolution is translated into a vector/matrix product [8]. Due to the convolution being the core issue, the second, arguably more natural way of analyzing the problem, lies in the frequency-domain since the Fourier transformation reduces the convolution to a mere multiplication. Approaches that exploit this property [9]–[19] apply the ICA algorithm for instantaneous mixtures to each frequency bin separately and are the focus of the discussion to follow. For ICA to be applicable in a frequency bin, there have to be multiple observations for each such bin, which makes it clear that it is not the Fourier transform directly, but its short-time version that is being analyzed. In such a representation, the amplitude of a sound is given as a function of both time and frequency, and it is, therefore, able to jointly account for its temporal and spectral characteristics [20]. What motivates this discussion is that there seems to be no clear consent on how to set the parameters of this transformation. For example, some publications suggest that the optimal length of the discrete Fourier transform (DFT) is given by $L = 2T$ [10], where T is the maximum length of the impulse responses, while others argue that it is not good to be constrained by $L \geq T$ [21]. This lack of agreement is also manifested in the wide range of values actually used, with the DFT-length spanning from as little as 8ms [14], past 32ms [15], and 46ms [9] all the way up to 256ms [10], [22]. Some publications even consider extremely large DFT sizes reaching up to 1 second [19]. Similarly, the shift also varies greatly between the publications, from as little as 3% in [15] and 15% in [14] up to the more commonly used 50% [9], [10]. The only thing the mentioned publications manage to agree upon is using a Hamming window in the synthesis process. In light of these observations, this work wants to discuss the benefits and drawbacks that increasing or decreasing these parameters has on the solution-finding process.

II. SHORT-TIME FOURIER TRANSFORMATION

The very first step in all frequency-domain BSS approaches is the transformation into the time-frequency-domain, that is, in most cases, achieved via the short-time Fourier transformation (STFT). This transformation has a number of parameters to choose, the notation for which is defined as follows:

- L The length of the discrete Fourier transform (DFT) in samples, demanded to be a multiple of 2.
- h_a The real-valued analysis window with compact support of length $W = L$, i.e., $h_a(n) = 0$ for $n \notin \{0, \dots, W - 1\}$.
- h_s The real-valued synthesis window, which is demanded to have the same length as $h_a(n)$.
- S The number of samples the analysis window gets shifted.

Since this work only considers windows whose length is equal to the number of samples the DFT considers, the terms window size and DFT-length are interchangeable for all intents and purposes in the frame of this discussion. The time-frequency representation of a real-valued time signal, in this case a microphone recording $x(n)$, is now given as the collection of the shifted, windowed segments to which the discrete L -point Fourier transformation is applied, giving:

$$\hat{x}(m, k) := \sum_{n=-\infty}^{+\infty} h_a(n - Sm)x(n)e^{-2\pi j \frac{(n-Sm)k}{L}} \quad (1)$$

where m is the discrete time index and $k \in \{0, \dots, \frac{L}{2}\}$ is the discrete frequency. Although k is properly defined on the whole set $\{0, \dots, L - 1\}$, it is sufficient to consider only the selection of frequencies since the recording $x(n)$ and the window function $h_a(n)$ are real-valued and hence is their product. In addition to which, the following property:

$$e^{2\pi j \frac{nk}{L}} = e^{2\pi j \frac{n(L-L+k)}{L}} = e^{2\pi j \frac{n(k-L)}{L}} = \overline{e^{2\pi j \frac{n(L-k)}{L}}} \quad (2)$$

where the line denotes the complex conjugate, holds for all $k \in \{0, \dots, \frac{L}{2}\}$ and $n \in \mathbb{Z}$. Combining these gives:

$$\hat{x}(m, k) = \overline{\hat{x}(m, L - k)} \quad k \in \left\{0, \dots, \frac{L}{2}\right\}, m \in \mathbb{Z} \quad (3)$$

which states that the selected set of discrete frequencies carries all the relevant information. These frequencies translate to the Hz frequency through:

$$f_k = \frac{k}{L} F_s \quad (4)$$

with F_s denoting the sampling frequency of the microphone recording.

Just as important as the way into the time-frequency domain is the way back, which is achieved by applying the inverse L -point discrete Fourier transformation to each of the time bins and summing the resulting segments up, while applying a synthesis window to compensate for the initial windowing and the shift.

$$\begin{aligned} x(n) &= \sum_m h_s(n - Sm) \frac{1}{L} \sum_{k=0}^{L-1} \hat{x}(k, m) e^{2\pi j \frac{(n-Sm)k}{L}} \\ &= x(n) \sum_m h_s(n - Sm) h_a(n - Sm) \end{aligned} \quad (5)$$

For this to return the original signal the synthesis window has to meet the condition:

$$\sum_m h_s(n - Sm) h_a(n - Sm) \stackrel{!}{=} 1 \quad (6)$$

for all $n \in \mathbb{N}$. It should be stressed that there are multiple synthesis windows that fulfill (6) as is shown in [23]. This is important as there is in fact an optimal choice which will be derived in the next section.

III. PARAMETER CHOICE

Using this representation one now seeks to describe the echoic model in table I through:

$$\hat{\mathbf{x}}(m, k) = \mathbf{A}(k)\hat{\mathbf{s}}(m, k) \quad (7)$$

where $\hat{\mathbf{x}}(m, k)$ denotes the collection of the k -th frequency bin across the STFT-representations of all the recording microphones and analogously $\hat{\mathbf{s}}(m, k)$ means the collection of these frequency components across the sources. $\mathbf{A}(k)$ now denotes the frequency dependent mixing matrix, in particular the element $(\mathbf{A}(k))_{ij}$ represents the k -th frequency component of the L -point discrete Fourier transform of the room impulse response between j -th source and the i -th recording microphone. As the index suggests, for each k there is a different matrix. The great merit this description has, is if (7) is valid or at least a good approximation, the demixing matrices $\mathbf{A}(k)^{-1}$ can be directly estimated using any (complex-valued) ICA algorithm since the connection between the sources and observations is given via a matrix product. This doesn't mean that the frequency-domain BSS problem is solved once this description holds since there are more challenges to overcome such as the permutation and scaling problem. It is nonetheless crucial to ask when, that is to say for which choice of the STFT parameters, (7) is reasonable.

The first thing to note hereby is that the mixing matrices, unlike $\hat{\mathbf{x}}$ and $\hat{\mathbf{s}}$, are *not* dependent on the time index m . This means that, on one hand, $\mathbf{A}(k)$ does not change over time, which was presupposed since the convolution is only a valid description of linear *time-invariant* systems and, on the other hand, every room impulse response can be fully described by the L -point Fourier transform.

This already suggests that, if T , as in table I, denotes the maximum length of all impulse responses, the DFT length needs to be chosen at least as big, i.e., $L \geq T$. This already highlights the first issue, T is generally unknown. The impulse response represents the system that needs to be identified, the parameters that need to be estimated by ICA. Although there can be made reasonable assumptions based on the type of room the mixture has been recorded in and hence the reverberation time that can be expected, there is no way outside of actually measuring the room beforehand, to precisely determine T . This makes it even more important to choose L big enough, especially in high reverberant environments, where short DFT lengths are destined to lead to bad results since the room impulse responses can't be sufficiently modeled.

A. The linear convolution in the STFT-domain

One way to understand the problems that arise from describing the linear convolution through (7) is by examining what a multiplication under the L -point Fourier transformation really describes. For that reason consider a signal segment $x_s(n)$ of length N , a room impulse response $h(n)$ of length

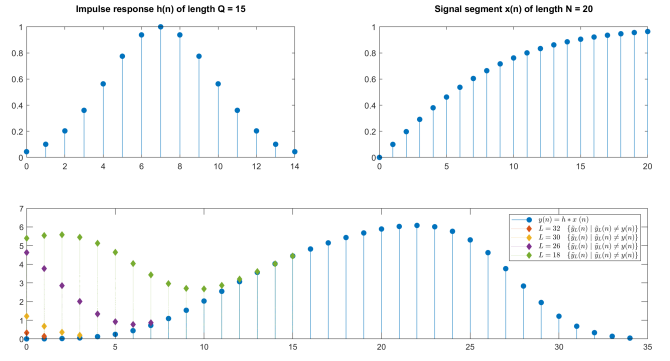


Figure 1. Cyclic convolution artefact for different choices of the DFT length.

Q and let $\hat{x}_s(k)$, $\hat{h}(k)$ denote their L -point Fourier transforms with $L \geq \max\{N, Q\}$. By considering the inverse Fourier transform of the element-wise product, it can be shown that it is equal to [23]

$$\begin{aligned} \tilde{y}(n) &= \frac{1}{L} \sum_{k=0}^{L-1} \hat{h}(k) \hat{x}_s(k) e^{2\pi j \frac{nk}{L}} \quad (8) \\ &= \sum_{l=1}^{L-1} h(l) x((n-l)_L) \quad (9) \end{aligned}$$

where $(\cdot)_L$ means modulo L and which shows that it is not equal to a linear convolution but a cyclic convolution of period L . The result of a linear and a cyclic convolution can only coincide on the interval $\{0, \dots, L-1\}$ if the DFT-length is chosen to be big enough, precisely $L \geq N + Q - 1$. The further L falls below this threshold, the more so called cyclic artefacts distort the result, as is illustrated in figure 1. The figure also suggests, which can be proven mathematically, that these artefacts always sit on the front of the segment.

To see where this comes into play, assume now that ICA is capable of perfectly separating, scaling and permuting all sources, meaning that for every k it finds a demixing matrix $\mathbf{W}(k)$ such that:

$$\hat{\mathbf{s}}(m, k) = \mathbf{W}(k)\hat{\mathbf{x}}(m, k) \quad (10)$$

Focusing now on a single source $j \in \{1, \dots, I\}$ at one specific time index $m = m_0$, this gives:

$$\hat{s}_j(m_0, k) = \sum_{i=1}^M \mathbf{W}_{ji}(k) \hat{x}_i(m_0, k) \quad (11)$$

for which the corresponding time-domain segment is calculated through the inverse (windowed) L -point DFT:

$$\begin{aligned} s_j(n + Sm_0) &= h_s(n - Sm_0) \frac{1}{L} \sum_{k=0}^{L-1} \sum_{i=1}^M \mathbf{W}_{ji}(k) \hat{x}_i(m_0, k) \\ &= \sum_{i=1}^M h_s(n - Sm_0) \frac{1}{L} \sum_{k=0}^{L-1} \mathbf{W}_{ji}(k) \hat{x}_i(m_0, k) \end{aligned}$$

This rearrangement ties back into the earlier discussion as element-wise products have to be transformed back into the time-domain and it is hence here, where cyclic convolution artefacts can occur. In fact they must occur since the (analysis) window length has been set to be of the same length as the DFT, which implies: $L \leq N + Q - 1 = L + Q - 1$ and thus $(Q - 1)$ -cyclic artefacts. Note that Q here does not denote the maximum length of the impulse responses, but rather that of the respective inverse filters. The effect of these artefacts can be mitigated in two ways, first by choosing $L \gg T$ and using a sufficiently smooth analysis window function (see the appendix of [24] for further insight) and secondly by choosing the synthesis window in a specific way. It has been mentioned that there are multiple solutions to (6), which can now be exploited. In light of the fact, that the artefacts occur at the beginning of the frame first and then spread towards its end, the optimal choice for the synthesis window is given by:

$$h_s(n) = \begin{cases} h_a(n)^{-1} & \text{for } L - S \leq n \leq L - 1 \\ 0 & \text{otherwise} \end{cases} \quad (12)$$

So a synthesis window that, for every segment, only reconstructs the last S values, where S as mentioned, denotes the number of samples the synthesis window gets shifted, when creating the STFT representation. To see that this window actually fulfills (6) see [23]. This now gives meaning to the shift, as reducing it also reduces the number of cyclic artefacts.

B. The permutation problem

The discussion so far suggests that increasing the DFT length always leads to a better result. To put this in perspective, this section and the next want to offer a number of arguments against an increase of the DFT length. The heading references arguably the most critical task in solving the frequency-domain blind source separation problem. The so-called permutation problem arises from an inherent indeterminacy of ICA, that is, ICA is not capable of correctly recovering the order of the separated signals. This is no problem for instantaneous mixtures, it becomes, however, a big issue in the convolutive case. As described, the source separation problem is solved independently for every discrete frequency. Since the signals found at each k are unordered, they need to be assigned to the proper sources. Increasing the DFT-length means increasing the number of frequency bins. It is, therefore, self-explanatory that having to link 65 bins at $L = 128$ is easier, than it is to correctly link 1025 bins at $L = 2048$. Note that the number of frequency bins can be reduced for real-valued signals as explained through (3).

Furthermore, the approaches themselves suffer from a too long window. For example, methods that cluster the activity of sources such as proposed here [25], rely on sources not being mutually active. Since the time resolution degrades by increasing L , this of course becomes less likely. This is especially unfortunate since, compared to approaches that evaluate time differences of arrival, these are more robust to

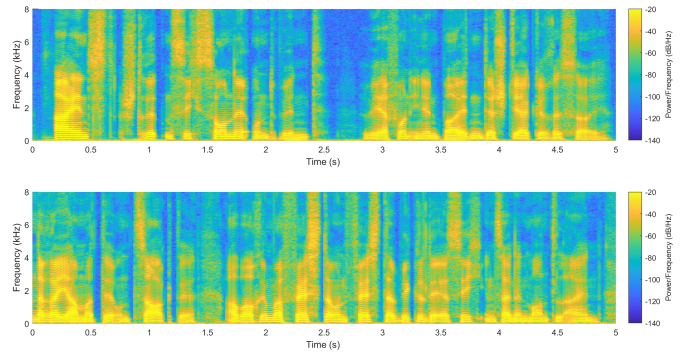


Figure 2. Spectrograms \hat{s}_1 , \hat{s}_2 for $F_s = 48\text{kHz}$, $L = 2048$, $olp = 0, 75\%$ and a hanning window.

reverberation [26], the modeling of which demands a longer DFT size.

C. Estimation and Model assumptions

Another very obvious drawback of a long DFT-length is, that increasing L increases the number of parameters to estimate, while at the same time reducing the samples available, since the time-resolution gets degraded. But not only does it make the estimation difficult, it also endangers the prerequisites of ICA. As [21] points out the assumption on statistical independence of the sources, especially when considering short time signals, does no longer hold. One proposed measure to demonstrate the loss of independence is the average of the correlation coefficient over all frequency bins:

$$J(L) = \frac{1}{\frac{L}{2} + 1} \sum_{k=0}^{\frac{L}{2}+1} |r_w| \quad (13)$$

where

$$r_w = \frac{\sum_k (\hat{s}_1(m, k) - \mu_1(k)) (\hat{s}_2(m, k) - \mu_2(k))}{\sqrt{\sum_k [\hat{s}_1(m, k) - \mu_1(k)]^2} \sqrt{\sum_k [\hat{s}_2(m, k) - \mu_2(k)]^2}}$$

μ_1 represents the mean value with respect to the time index of the STFT representation of the source signal s_1 . Of course uncorrelatedness does not imply statistical independence, since the latter is much stronger, but independent signals can never be correlated. This implies that an increase in correlation represents a decrease in independence.

This measure is applied to two clean speech signals from a single male speaker of 5 seconds length, whose spectrograms are shown in figure 2. The result shown in figure 3 confirms that an increase in the DFT-length from a millisecond to over half a second is accompanied by a big increase in correlation. However, the figure, in particular the lower plot, hints at a potential way to at least mitigate this problem. It could be demonstrated for this particular example, that increasing the overlap and thus decreasing the shift, leads to a noticeable drop of the correlation coefficient. This suggests that it could be beneficial to use a small shift when applying large L , especially for short time signals.

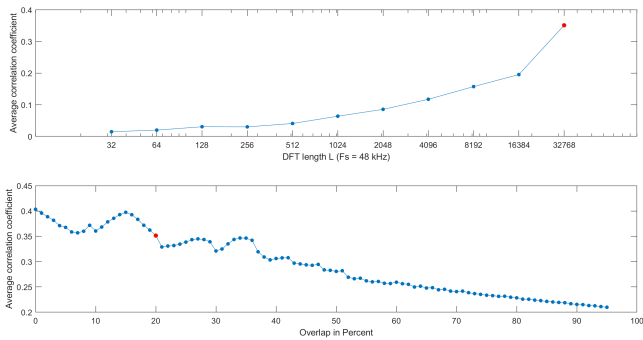


Figure 3. The upper plot illustrates the relationship between L and the correlation coefficient for a fixed overlap of 20%. The lower plot fixes $L = 32768$ and shifts the overlap from 0% to 95%.

IV. CONCLUSION AND OUTLOOK

This paper discussed the influence of the various parameters of the short-time Fourier transform on the solution-finding process of frequency-domain blind source separation. It has been shown that the choice of the DFT-length is a balancing act between setting it big enough to account for the rooms impulse response, especially in high reverberant environments, and keeping it small enough to not hurt the model assumptions of ICA, while also keeping the difficulty of the permutation problem feasible. It was further shown, that out of the many possible synthesis windows, there exists an optimal choice (12) with respect to minimizing the number of cyclic artefacts in the reconstruction of the time-domain source signals. Another tool to minimize these distortions is the shift as it determines how many values the synthesis window has to recreate from every segment. Since these values sit at the end of the frame and are thus, as has been shown, less prone to distortions, a decrease of the shift is beneficial. A small shift has also been advocated for in section III-C where it helped to restore the endangered model assumption in the case of a long DFT and comparably short time signal.

However, since the shift introduces no new information from a mathematical standpoint, it has to be wondered if there are any drawbacks to decreasing it arbitrarily, especially in view of the ICA algorithms separation performance. With respect to the algorithm, there is another interesting point to be investigated. Complex-valued ICA algorithms demand the real and imaginary parts of every frequency bin in the sources STFT-representations to be uncorrelated and of equal variance [27]. It isn't obvious why this should be the case for speech signals, let alone arbitrary acoustic signals. Neither is it clear how the parameters can affect this.

Since there are many more interesting questions to discuss, the author wants to expand on this discussion in future works and back up these theoretical findings with practical measurements and results.

REFERENCES

[1] R. N. Vigário, "Extraction of ocular artefacts from EEG using independent component analysis," *Electroencephalography and Clinical Neurophysiology*, vol.

103, no. 3, pp. 395–404, 1997.

[2] A. D. Back und A. S. Weigend, "A first application of independent component analysis to extracting structure from stock returns," *International journal of neural systems*, vol. 8, no. 4, pp. 473–484, 1997.

[3] E. C. Cherry, "Some Experiments on the Recognition of Speech, with One and with Two Ears," *The Journal of the Acoustical Society of America*, vol. 25, no. 5, pp. 975–979, 1953.

[4] P. O'Grady, B. Pearlmutter and S. Rickard, "Survey of sparse and non-sparse methods in source separation", *International Journal of Imaging Systems and Technology*, vol. 15, no. 1, pp. 18–33, 2005.

[5] A. Hyvärinen und E. Oja, "Independent component analysis: algorithms and applications," *Neural Networks*, vol. 13, no. 4, pp. 411–430, 2000.

[6] H. Buchner, R. Aichner, and W. Kellermann, "A generalization of blind source separation algorithms for convolutive mixtures based on second-order statistics," *IEEE Transactions on Speech and Audio Processing*, vol. 13, no. 1, pp. 120–134, 2005. Systems, vol. 10, pp. 273–279, 1997.

[7] J. Bourgeois and W. Minker, *Time-Domain Beamforming and Blind Source Separation*. Dordrecht: Springer, 2009.

[8] Z. Koldovsky and P. Tichavsky, "Time-Domain Blind Separation of Audio Sources on the Basis of a Complete ICA Decomposition of an Observation Space," *IEEE Transactions on Audio, Speech, and Language Processing*, vol. 19, no. 2, pp. 406–416, 2011.

[9] P. Smaragdís, "Blind separation of convolved mixtures in the frequency domain," *Neurocomputing*, vol. 22, no. 1-3, pp. 21–34, 1998.

[10] M. Ikram and D. Morgan, "A beamforming approach to permutation alignment for multichannel frequency-domain blind speech separation", *IEEE International Conference on Acoustics Speech and Signal Processing*, 2002.

[11] S. Kurita, H. Saruwatari, S. Kajita, K. Takeda and F. Itakura, "Evaluation of blind signal separation method using directivity pattern under reverberant conditions," *2000 IEEE International Conference on Acoustics, Speech, and Signal Processing*, pp. 3140–3143 vol. 5, 2000.

[12] S. Araki, S. Makino, Y. Hinamoto, R. Mukai, T. Nishikawa, and H. Saruwatari, "Equivalence between Frequency-Domain Blind Source Separation and Frequency-Domain Adaptive Beamforming for Convolutive Mixtures," *EURASIP Journal on Advances in Signal Processing*, 2003.

[13] J. Anemüller and B. Kollmeier, "Amplitude Modulation Decorrelation For Convolutive Blind Source Separation," *International conference on Independent Component Analysis and Blind Source Separation*, 2000.

[14] N. Murata, S. Ikeda, and A. Ziehe, "An approach to blind source separation based on temporal structure of speech signals," *Neurocomputing*, vol. 41, no. 1-4, pp. 1–24, 2001.

[15] F. Asano, S. Ikeda, M. Ogawa, H. Asoh, and N. Kitawaki, "Combined approach of array processing and independent component analysis for blind separation of acoustic signals," *IEEE Transactions on Speech and Audio Processing*, vol. 11, no. 3, pp. 204–215, 2003.

[16] H. Sawada, R. Mukai, S. Araki and S. Makino, "Polar coordinate based nonlinear function for frequency-domain blind source separation," *IEEE International Conference on Acoustics, Speech, and Signal Processing*, 2002, pp. 1-1001-1-1004.

[17] L. Parra and C. Spence, "Convolutive blind separation of non-stationary sources," *IEEE Transactions on Speech and Audio Processing*, vol. 8, no. 3, pp. 320–327, 2000.

[18] D. Schobben and P. W. Sommen, "A frequency domain blind signal separation method based on decorrelation," *IEEE Transactions on Signal Processing*, vol. 50, no. 8, pp. 1855–1865, 2002.

[19] F. Nesta, P. Svaizer, and M. Omologo, "Convolutive BSS of Short Mixtures by ICA Recursively Regularized Across Frequencies," *IEEE Transactions on Audio, Speech, and Language Processing*, vol. 19, pp. 624–639, 2011.

[20] K. Gröchenig, *Foundations of time-frequency analysis*, 1. ed., ser. Applied and numerical harmonic analysis. New York, NY: Springer Science + Business Media, 2001.

[21] S. Araki, R. Mukai, S. Makino, T. Nishikawa, and H. Saruwatari, "The fundamental limitation of frequency domain blind source separation for convolutive mixtures of speech," *IEEE Transactions on Speech and Audio Processing*, vol. 11, no. 2, pp. 109–116, 2003.

[22] H. Sawada, R. Mukai, S. Araki, and S. Makino, "A Robust and Precise Method for Solving the Permutation Problem of Frequency-Domain Blind Source Separation," *IEEE Transactions on Speech and Audio Processing*, vol. 12, no. 5, pp. 530–538, 2004.

[23] T. Vorderbermeier, *Frequency Domain Blind Source Separation For Convolutive Audio Mixtures*. OTH Regensburg, 2021.

[24] M. Kowalski, E. Vincent and R. Gribonval, "Beyond the Narrowband Approximation: Wideband Convex Methods for Under-Determined Reverberant Audio Source Separation," *IEEE Transactions on Audio, Speech, and Language Processing*, vol. 18, no. 7, pp. 1818–1829, 2010.

[25] H. Sawada, S. Araki and S. Makino, "Measuring Dependence of Bin-wise Separated Signals for Permutation Alignment in Frequency-domain BSS," *IEEE International Symposium on Circuits and Systems*, 2007, pp. 3247–3250.

[26] E. Vincent, S. Gannot, and T. Virtanen, *Audio source separation and speech enhancement*. Hoboken, NJ: John Wiley & Sons, 2018.

[27] E. Bingham and A. Hyvärinen, "A fast fixed-point algorithm for independent component analysis of complex valued signals," *International journal of neural systems*, vol. 10, no. 1, pp. 1–8, 2000.

AI-based Control-Algorithm for Stationary Batteries with Regards to Load-Management

Georg Weber

University of Applied Sciences Augsburg
Augsburg, Germany
georg.weber@hs-augsburg.de

Philipp Theumer

Fraunhofer IGCV
Augsburg, Germany
philipp.theumer@igcv.fraunhofer.de

Prof. Dr. Stefan Braunreuther

University of Applied Sciences Augsburg
Augsburg, Germany
stefan.braunreuther@hs-augsburg.de

Abstract—Stationary battery storage systems can significantly reduce the energy costs of manufacturing companies in Germany and at the same time reduce stress on the electric grid. So far stationary batteries are operating with simple rule-based controls, aiming to avoid load peaks. This paper presents an approach for the training of an intelligent control system utilizing reinforcement learning (RL) to achieve better battery utilization and overall cost-effectiveness by considering influencing factors such as battery aging and seasonal fluctuations in energy consumption.

I. INTRODUCTION

As a consequence of the energy turnaround, manufacturing companies are confronted with high electricity costs (compare to [1], [2], [3]), especially for peak loads [4]. In contrast, the costs of generating their own electricity, for example by using photo-voltaic modules, and the cost for battery storage fell sharply in recent years. Battery storage facilities can thus be increasingly used economically to smoothen costly peak loads and to increase company's own consumption of electricity through intermediate storage [5]. Given of limited storage capacity, battery aging effects, as well as fluctuating load and generation, the operating strategy of the storage system represents a central challenge.

II. STATE OF THE ART CONTROL SYSTEMS

Currently installed control systems are based on rules that specify when the battery should be charged and discharged. These rules are based on the time of day and the current power consumption. In the simplest case, such rules describe a load following operation: the battery is discharged/charged according to a given profile. To operate peak shaving with respect to a given load limit, this profile P_F is calculated from the difference between the peak limit to be maintained P_{max} and the given consumption profile P_V :

$$P_F = P_{max} - P_V$$

In this case, the battery would always be discharged (negative sign) when $P_V > P_{max}$ and charged accordingly when $P_V < P_{max}$. The total load profile P_G is composed of P_V and P_F :

$$P_G = P_V + P_F$$

More complex rules can also include the consumption balance in the current billing period (15 min), since any short-time load peaks do not cause any costs if the average value in the billing

period is below a specific target value.

Both a simple load-following strategy and an advanced strategy that considers the 15-minute average were implemented in experiments to obtain comparative values for the developed AI-based operating strategies.

III. RESEARCH GOAL

The aim of the research project is the development of a self-learning operation strategy for electricity storage in manufacturing companies to reduce electricity costs and stress on the electric grid (compare to [1], [6]). The intelligent control system should focus on increasing internal consumption and avoiding costly load peaks. Furthermore the control system has to take into account battery aging effects, since they can strongly influence the long term cost and profitability of the storage system [7]. The performance of the AI-based operating strategy will be compared with established operating strategies and advantages, disadvantages and opportunities will be identified in this regard.

IV. APPROACH

For the implementation of an agile battery controller, that is able to learn how to react dynamically to a wide variety of input variables, RL methods are used, whose potentials seem very promising due to the numerous influencing factors and stochastic events occurring in the production environment, such as unscheduled shutdown or startup of power heavy systems. To achieve this, the first step is to gather all necessary information and to set up an environment, that simulates the behavior of the battery and an exemplary energy system of a production system. This is the basis for the development and testing of the AI-based operation strategy. To consider all real occurring influences, a prototypical implementation for the validation of the developed operation strategy is planned for a later stage of the research project [8].

A. RL Framework

The implementation of the RL-agent is using Tensorflow and RLlib [9] as they deliver an abstract interface to a variety of RL-agents [10] and therefore a variety of RL Algorithms can be tested with little to no adjustment effort and the most promising implementation can be identified by trial and error. Furthermore, RLlib uses the Ray framework, which allows

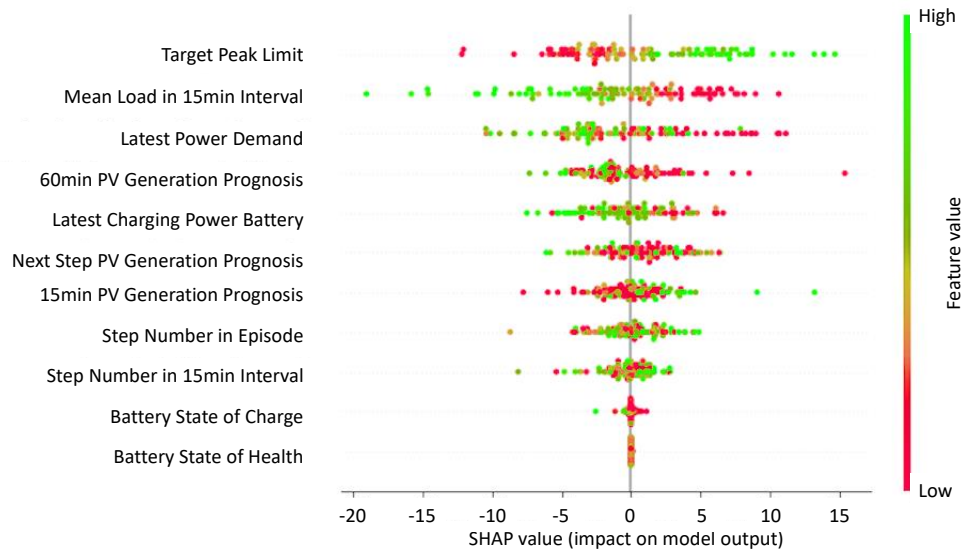


Figure 1. shap values for a trained agent - each dot represents a simulation step and corresponding agent action

multi-threaded and cluster-training and thus significantly reduces the training time.

B. Simulation Design

Although there are approaches to train RL agents in parallel with the conventional operation of systems, it is more purposeful, especially for an exploratory approach, to create a simulation of the environment and thus get the opportunity to try different training approaches in a fraction of the simulated time. A simulation adequate for the research objective must meet the following requirements:

- a representation of all physical values and information relevant for the training of a control system
- a calculation of the costs resulting from chosen actions and the agent reward that can be calculated from these costs
- an implementation of a normalized interface, which allows the call by RLlib
- a short run-time to perform as many training trial runs as possible

In order to make the simulation as flexible as possible and to avoid limitations due to the use of a simulation framework, the simulation is developed from scratch in Python. To represent the different elements of an energy system in the simulation, performance measurements exported from existing energy management systems of industry partners in the research project are used. These measurements are read and processed in the simulation so that a suitable representation of the state of the energy system is available for each simulation step. Since the state of the battery storage is dependent on the selected actions of the agent, it is not represented by historical data, but by a physical model. The battery model used is the open-source application "SimSES" developed by

Faculty for Electrical Energy Systems (EES) of TUM [11]. The SimSES model is executed every simulation step and calculates resulting charging states, battery degradation and power losses from the requested charging power.

C. RL Algorithms

RLlib provides a variety of state of the art Reinforcement Learning Algorithms as agents with a unified interface. Several agents were tested with their respective standard parameterization. The agents heavily differ in suitability for the given challenge in terms of resulting runtime, convergence behavior in training and performance in validation runs. Best results were achieved with the Proximal Policy Optimization (PPO) [12] agent. The Soft Actor Critic (SAC) agent [13], while also promising in convergence behavior, has disadvantages due to longer training run-time.

The Policy of a the PPO algorithm is a Deep Neural Network, that has environment states as an input, and a discrete set of output actions. In this case the output actions are percentages of the battery's maximum charging/discharging power between -1 and 1 in steps of 0.04. Policy Optimization means, that this policy is to be optimized in terms that the output action generates a maximized reward. This is done by iterating over the training data and adjusting the weights of the Neural Network, so that the sum over all chosen actions and their estimated rewards are maximized. Proximal in this context means, that the adjustment of the weights is clipped by a value ϵ , so that changes on the policy can only occur gradually to prevent big policy changes in the wrong direction induced e.g. by outlier data from which the policy can possibly not recover. The Objective function $L^{CLIP}(\theta)$ can be differentiated resulting in the policy gradient estimator \hat{g} that can then be optimized for example with a Stochastic Gradient Descent (SGD).



Figure 2. comparison of load-management performance: rule-based and reinforcement-agent

$$L^{CLIP}(\theta) = \hat{\mathbb{E}}_t[\min(r_t(\theta)\hat{A}_t, \text{clip}(r_t(\theta), 1 - \epsilon, 1 + \epsilon)\hat{A}_t)]$$

The Estimation Operator $\hat{\mathbb{E}}_t$ is applied on a batch of samples with timestamps t , resulting in the average expected value. The ratio r_t represents the changes in probability due to updated θ values, and \hat{A}_t are the value estimations for the actions. The core improvements of the Proximal PO are the clipping and min operations: even if updated θ values lead to big increases/decrease of $r_t\hat{A}_t$, the clipping/min operations limit those changes to an interval defined by ϵ , so that updated policies are still in the proximity of the old policy. Typical values for ϵ are around 0.2 [12].

D. Sparse Reward and Reward Shaping

A key challenge of this reinforcement learning application is the fact that only the highest annual overrun of the targeted performance limit results in costs for billing. Exceeding this limit a second time is irrelevant for billing as long as the exceedance is not even higher than the previous one. Since training an RL agent requires a more continuous punishment/reward, the real cost cannot be used for reward allocation: Instead of once a year, a peak-shaving reward is given for every 15-minute billing interval. That is, for 1-minute simulation steps, the agent receives reward every 15th simulation step. Even this is still at the limit of trainability, with respect to the sparseness of the reward signal.

E. Feature Sets and Shap Values

As mentioned above, the representation of relevant information (features) by the simulation is a requirement for the simulation. In order to find out which data are useful for training an RL-based control system, a multi-stage series of experiments has been carried out.

First, all available information is collected and a selection to feature sets is made manually, to test which combination

of features lead to the best results. Different representations of data selected for the feature sets are tested as well. For example, a time stamp for each simulation step in unixtime can be used to infer a daily periodicity less easily than if the time of day is represented by a consecutive numbering of the simulation steps in the course of the day. A simulation step that represents the time of day, e.g. 12:00 o' clock, therefore also passes a corresponding number to the agent, which assumes the same value for each day. Another example for the importance of data representation is seasons: spring through winter can be represented with numbers from one to four. However, if one wants to choose a representation that contains information about the similarity of seasons, a vector can be used that encodes winter with $(1, 0)$, summer with $(-1, 0)$ and spring and autumn with $(0, 1)$ $(0, -1)$, respectively to take into account the circular reoccurrence of seasons. Since outdoor temperatures can have an impact on energy consumption and photo voltaic (PV) generation, a representation that makes the similarities of the seasons recognizable enables a potentially better training result.

In addition to the manual selection of plausible features, a shap value analysis is performed [14], that shows the impact of different features on the outcome of the RL-agent decision. In order to determine the weight of an input features in combination with other features, the shap explainer uses a large number of feature-value permutations on the trained agent and analyses the outcome. Once the shap explainer is trained with those permutations, the actions selected in a validation episode can be explained. In figure 1 the result of such a shap value analysis for an episode is displayed. In this "bee plot" a feature set is displayed in rows on the y-axis and the shap values are plotted for each of these rows on the x-axis. Additionally each plot point is colored corresponding to the specific feature value, i.e. the value that was delivered to the agent for this particular agent action. The rows are sorted according to the

average absolute shap value. Features contribute proportionally to their shap values to the selection of a corresponding action value. Negative or positive signs correspond to a tendency towards an discharge or charging action. In this particular example the RL-agent was not taking into account the batteries SoH (state of health), because optimizing battery degradation was a secondary objective to peak shaving in the scaling of this training runs reward.

F. Curriculum Learning

As indicated in the previous section, it is not always possible to train a RL-agent in respect to every goal in just one training run. To account for this, training runs with different reward designs were performed consecutively on the same agent. This is a known as curriculum learning [15]. To further improve the performance of the RL-agent, imitation learning is used in the first training run. Imitation learning is RL training in which the agent is rewarded for selecting actions that are similar to actions resulting from a given target logic that is to be imitated. The logic to be imitated is the rule based state of the art control system that was foremost implemented as a benchmark for the RL-Training.

V. RESULTS

With a series of optimizations applied to feature sets and reward allocation and using state-of-the-art curriculum training, the developed RL-agent is able to beat simple control strategies and almost reaches the performance of optimized control strategies (see fig. 2) in terms of peak-shaving performance (ca. 10% difference in summed up peak-limit exceedance). In some validation episodes the RL-agent is performing better than the optimized control strategies. A comparison in real operation is still pending, due to smaller control intervals of established controllers, a slightly worse relative performance than in simulation operation is to be expected. Looking at battery degradation the RL-agent even outperforms conventional control strategies. Along the validation, the difference in SoH between the best rule and RL strategies was 0.3%, meaning 0.3% less capacity is lost over the course of 40 days due to cyclic degradation effects. Overall these values have to be verified in the upcoming prototypical implementation, at least in a simulation that runs parallel to a real battery operation, to be able to make safe predictions on whether AI-based control systems are a worthwhile improvement.

VI. OUTLOOK

To further improve the agent and generate an advantage over conventional controls, the model is being further improved. The following features are already being worked on:

- additional phases in the curriculum training that focus solely on the improvement of battery health loss
- cooperative multi-agent training to combine battery control and operation of adjustable electrical loads
- multi-agent training to control additional power generation sources and heat grid

With these improvements and further development, the training of an RL-agent that exceeds the performance of optimized control strategies is potentially possible.

REFERENCES

- [1] L. Bank, M. Rösch, E. Unterberger, S. Roth, A. Rohrer, J. Köberlein, S. Braunreuther, and J. Schilp, "Comparison of simulation-based and optimization-based energy flexible production planning," *Procedia CIRP*, vol. 81, pp. 294–299, 2019.
- [2] M. Roesch, C. Linder, C. Bruckdorfer, A. Hohmann, and G. Reinhart, "Industrial load management using multi-agent reinforcement learning for rescheduling," 2019.
- [3] M. Roesch, C. Berger, S. Braunreuther, and G. Reinhart, "Cost-model for energy-oriented production control," in *IEEE IEEM2018*. [Piscataway, New Jersey]: IEEE, 2018, pp. 158–162.
- [4] C. Schultz, S. Braun, S. Braunreuther, and G. Reinhart, "Integration of load management into an energy-oriented production control," *Procedia Manufacturing*, vol. 8, pp. 144–151, 2017.
- [5] T. Bruendlinger, E. J. Koenig, O. Frank, and D. Gruendig, "dena-leitstudie integrierte energiewende: Impulse für die gestaltung des energiesystems bis 2050: Ergebnisbericht und handlungsempfehlungen," 2018.
- [6] S. Roth, M. Thimmel, J. Fischer, M. Schöpf, E. Unterberger, S. Braunreuther, H. U. Buhl, and G. Reinhart, "Simulation-based analysis of energy flexible factories in a regional energy supply system," *Procedia Manufacturing*, vol. 33, pp. 75–82, 2019. [Online]. Available: <https://www.sciencedirect.com/science/article/pii/S2351978919304883>
- [7] A. Zeh, M. Müller, M. Naumann, H. Hesse, A. Jossen, and R. Witzmann, "Fundamentals of using battery energy storage systems to provide primary control reserves in germany," *Batteries*, vol. 2, no. 3, p. 29, 2016.
- [8] Maik Naumann, Cong Nam Truong, Michael Schimpe, Daniel Kucevic, Andreas Jossen, "Simses: Software for techno-economic simulation of stationary energy storage systems," in *International ETG Congress*, Bonn, 2017, pp. 442–447.
- [9] E. Liang, R. Liaw, P. Moritz, R. Nishihara, R. Fox, K. Goldberg, J. E. Gonzalez, M. I. Jordan, and I. Stoica, "Rllib: Abstractions for distributed reinforcement learning." [Online]. Available: <https://arxiv.org/pdf/1712.09381>
- [10] —, "Rllib: Abstractions for distributed reinforcement learning." [Online]. Available: <https://arxiv.org/pdf/1712.09381>
- [11] M. Naumann and C. N. Truong, "Simses - software for techno-economic simulation of stationary energy storage systems."
- [12] J. Schulman, F. Wolski, P. Dhariwal, A. Radford, and O. Klimov, "Proximal policy optimization algorithms." [Online]. Available: <https://arxiv.org/pdf/1707.06347>
- [13] T. Haarnoja, A. Zhou, K. Hartikainen, G. Tucker, S. Ha, J. Tan, V. Kumar, H. Zhu, A. Gupta, P. Abbeel, and S. Levine, "Soft actor-critic algorithms and applications." [Online]. Available: <https://arxiv.org/pdf/1812.05905>
- [14] S. Lundberg and S.-I. Lee, "A unified approach to interpreting model predictions." [Online]. Available: <https://arxiv.org/pdf/1705.07874>
- [15] Y. Bengio, J. Louradour, R. Collobert, and J. Weston, "Curriculum learning," in *Proceedings of the 26th Annual International Conference on Machine Learning*, A. Danyluk, Ed. New York, NY: ACM, 2009, pp. 1–8.

Chapter 9

Papers: Robotics

Contents

9.1	Preliminary work on determining the global and local pose of a mobile robot in outdoor environments using proprioceptive and exteroceptive sensor technology . .	418
9.2	Development and construction of a Hand Exoskeleton for Virtual Reality	423
9.3	An Enhancement of Common Rail Track Detection Methods for Automatic Train Operation in Shunting Services	426
9.4	System Architecture of Autonomous Mobile Robots	431

Preliminary work on determining the global and local pose of a mobile robot in outdoor environments using proprioceptive and exteroceptive sensor technology

Markus Fenn

Faculty of Electrical Engineering, Precision Engineering, Information Technology
University of Technology Georg Simon Ohm Nuernberg
Nuernberg, Germany
Email: fennma67764@th-nuernberg.de

Abstract—Autonomous robot missions are not only in demand on production floors and warehouses, but are increasingly finding application in outdoor areas. They help humans to execute long lasting monotonous tasks as well as supporting them in carrying equipment or operate in areas that are not safe for humans. All of them have to face the issue of global positioning in fast changing rough areas that are sometimes not easy to pass. That is why they need different sensor types to estimate their global and local pose for accurate navigation tasks as well as data storage and labelling. This is why proprioceptive, for inner robot state, as well as exteroceptive, for global positioning, sensor types are used. This paper gives a introduction about the preparation work using this different sensor systems to fuse them afterwards in order to get an discrete and accurate robot pose.

I. INTRODUCTION

A. Project description

The mobile robot platform used for the validation and data collection described in this paper is part of a project founded from the German Ministry for Economy and Energy (BMWi). There are several small and medium sized companies as well as the University of Würzburg and the University of Technology Nürnberg working together. The aim of the project is to develop an autonomous driving robot that is capable to maintain a photovoltaic field power plant through weeding and infrared inspection from below the panels. The environment the platform should operate in is a former hill of garbage which is now covered by grass and photovoltaic modules. The project aims to make energy generation from photovoltaic more efficient to compete in the future against relatively cheap energy sources like nuclear and coal burning power plants. This is not just about saving money for the energy companies but also to help protect the earth from climate change.

B. Robot description

The basic chassis of the robot is a platform called VolksBot[®] RT6 developed by the Fraunhofer IAIS. The kinematic model is skid steering and in this special case six wheeled. The drive shafts of the wheels on each side are connected via a chain and driven by one 150 W motor

per side. In basic configuration the weight is around 19 kg [1] the robot at the projects end will have around 65 kg to 75 kg. To navigate autonomously, the robot needs to know it's current position in the global map and the relative direction it is heading to. The sensors used for this will be described on the following pages. A rendering of the current robot can be seen in Figure 1. The red cone displays the Field of View (FOV) from the infrared inspection camera that is used to spot thermal hotspots on the photovoltaic panel. The DGNSS antennas as well as the obstacle avoidance systems are missing in this model.

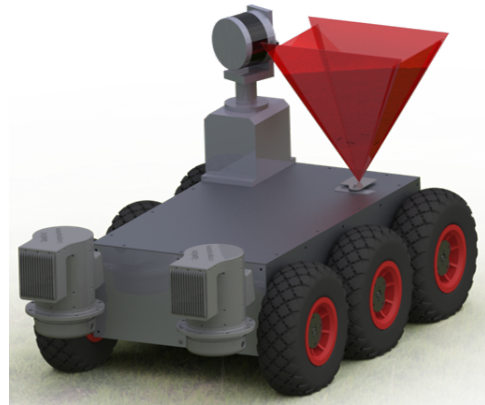


Figure 1. Rendering of VolksBot[®] RT6 with current project configuration

C. Problem description

In an two dimensional indoor area like an office or shop floor there are sharp edges that never or rarely change. This is why most times LIDAR (Light Detection And Ranging) scanners are enough for the global and local positioning. When moving a robot outside, the environment changes more often for example through seasons, weather conditions or vegetation. Especially when the robot changes its environment like for example through mowing in this case, there are no or less

sharp edges where the scan matching or slam algorithm can rely on. Also through hills and slopes the surrounding area is three-dimensional. This why the robot needs sensors that give it information about how far it has moved and its global position on the map or world. The pose needs to be precisely determined to prevent small sections of grass from remaining unmown. Another reason that calls for precision in this project is the comprehensive and accurate recording of infrared images under the solar panels.

II. SENSOR SYSTEMS

As described in Chapter I-C, using only LIDAR scanners is not enough to get an exact pose. This is why the robot needs to carry more proprioceptive and exteroceptive sensor systems. To get an discrete, precise and continuous robot pose several different types of sensors need to be fused using for example the `robot_localization` package provided in ROS (Robot Operating System) [2]. To use this package or the data in general the sensors need to be mounted and implemented. The three different sensor types used for the pose estimation are described in the following subsections of this Chapter.

A. Global Navigation Satellite System

For world wide positioning different GNSS (Global Navigation Satellite System) providers are available. The most common include for example Americas GPS (Global Positioning System), Russians Glonass or European Unions Galileo. Modern GNSS modules are capable of determining their position via all the above mentioned representatives. GNSS systems in general are influenced by some effects that cause the measurement with those sensors to be not mathematically perfect. Those are for example relativistic effects or drifts in the satellites clock, atmospheric influences in the Ionosphere and Troposphere as well as the multipath effect which is caused through reflection on buildings [3]. Shading of the sky, for example in this case through photovoltaic modules, cause a total or nearly loss of signal. Another problem using GNSS systems on mobile robots is the fact that they are moving. The average accuracy of those positioning systems that can be found on different sources like books and the internet is around 1 m to 10 m. If they would stand on the same point the measurement errors could be summed up and averaged. Through this the precision could be increased. Exactly this method is the basis of DGNSS, the "Differential Global Navigation Satellite System" also commonly known as RTK GPS (Real Time Kinematic GPS). Those systems consist of at least two GNSS receiving modules with at least two antennas per module. One for the GNSS signal and the other for a offset radio connection. In the basic configuration there is one "Base Station" that always stands still and is able to average the measurement error (Figure 2). The other module, known as "Rover", is the moving part of the system. If each systems measure their position with the same satellites the base is able to calculate an offset, because it knows the value and direction of the error. This offset or correction factor is

now send to Rover and internally used to determine its exact position. With systems like this it is possible to bring the accuracy down to <1 cm [4]. The Rover Base set used in this project is called `simpleRTK2B` from the Spanish company `Ardusimple`. It provides a accuracy down to <1 cm in RTK-Mode and 1.5 m in stand alone mode (for example only Rover) [4].



Figure 2. DGNSS Base Station with GNSS antenna and radio transmitting antenna

To use the data for pose estimation a package called `nmea_navsat_driver` is available for ROS that uses the informations from the GNSS module and publishes a standard Topic called `sensor_msgs/NavSatFix` which can be used for many programs. GNSS systems are exteroceptive sensors and the only sensor type used on the projects robot that is able to estimate the position referring to the world. The outcome of the DGNSS-node is indiscrete.

B. Inertial Measurement Unit

An IMU (Inertial Measurement Unit) belongs to the family of proprioceptive sensor types as it senses an internal robot state. It is a spatial combination of different inertial sensors like gyroscopes and accelerometers. Sometimes but not in this use case the data of magnetic field sensors are used as well to improve the sensor arrays outcome. This wouldn't make sense in this project because of the strong magnetic fields the power cables of the photovoltaic modules generate as well as disruptions through metal mount frames. The gyroscope measures rotating rates around linear axes. In former times mechanical gyros have been used to determinate for example the tilt angle of planes. Modern gyroscopes use MEMS (Micro Electro Mechanical Systems). The angles are called roll (around x-axis), pitch (around y-axis) and yaw (around z-axis) [5]. Accelerometers detect the acceleration in a linear direction. Three

of them cover all three dimensional axes x, y and z. The task of the IMU is to validate the pose that comes from the odometry calculation of the drive (Chapter II-C). There normally is a drift around the pitch axis which could be erased using more than one IMU. The inertial measurement unit used in this project is an validation and learning board for different sensor types called X-NUCLEO-IKS01A3 developed and marked by the company ST Microelectronics. To compute the sensors information and transmit them to a computer, Prof. Dr. Stefan May from the Technical University of Nürnberg wrote code that fuses the accelerometers and gyroscopes information and provides the data in ROS using the standard message type `sensor_msgs/Imu`.

C. Wheel odometry

The wheel odometry describes the odometry that is calculated using the rotation rates of the wheels and the kinematic model of the platform. For drive configurations like mecanum or differential drive on a flat floor like industrial cement or office carpet the calculation is precise. The arrangement of wheels in this project does not follow a easy to express kinematic. The name of it is six wheeled skid steering. To calculate the platforms linear and angular velocity two inputs are required. The rotation rates of the wheels on the left and right side. All wheels each side rotate with the same speed as they are mechanically linked by a chain. To get the current rotation rates of the wheels each side, the encoders inside the motors are used. The projects configuration for this is an 216 counts per turn encoder, directly connected to the motors shaft followed by a 66:1 gear. The standard way to describe the platforms movement is to give as an output, for subsequent pose estimation, the current velocity in x and y direction and the angular speed around the z-axis called ω . This results to the expression:

$$\dot{x} = \begin{bmatrix} v \\ \omega \end{bmatrix} = \begin{bmatrix} v_x \\ v_y \\ \omega \end{bmatrix} = j(\omega_l, \omega_r) \quad (1)$$

This leads to the estimated velocities \hat{x} .

$$\hat{x} = J(k)y \quad (2)$$

The y in Equation 2 stands for $y = (\omega_l, \omega_r)^T$. $J(k)$ is called Jakobian Matrix of the kinematic model and the part of the calculation that is difficult to define. With reference to a publication of Laval University in Canada, which deals with the subject of pose estimation of skid locomoted platforms, there are four more or less suitable approaches of the matrix. As they are all based on experimental search for parameters and four wheel skid steering the decision has been made use the model of perfect differential drive and add an factor that is determined by experimental trail and error. The reason the other models are not suitable is that the the configuration of a six wheeled skid steering robot is an overlay of differential drive (wheels in the middle) and four wheeled skit steering (outer wheels). The wheels located in the middle

would only drive around the centre point without appreciable losses in friction. The outer four wheels cause dynamical friction losses as they get pulled sideways when turning. The standard Jakobian Matrix J for differential drive robots is described as following:

$$J = r \begin{bmatrix} \frac{1}{2} & \frac{1}{2} \\ 0 & 0 \\ -\frac{1}{b} & \frac{1}{b} \end{bmatrix} \quad (3)$$

To describe the friction losses through the ground another matrix called Ground Matrix needs to be defined as following:

$$G = \begin{bmatrix} 1 & 0 & 0 \\ 0 & 0 & 0 \\ 0 & 0 & \beta \end{bmatrix} \quad (4)$$

To combine those two for further calculations Equation 4 needs to be multiplied from left to Equation 3 resulting to the Jakobian Matrix J_s for this special six wheeled skid steering robot:

$$J_s = rGJ = r \begin{bmatrix} 1 & 0 & 0 \\ 0 & 0 & 0 \\ 0 & 0 & \beta \end{bmatrix} \begin{bmatrix} \frac{1}{2} & \frac{1}{2} \\ 0 & 0 \\ -\frac{1}{b} & \frac{1}{b} \end{bmatrix} = \quad (5)$$

$$r \begin{bmatrix} \frac{1}{2} & \frac{1}{2} \\ 0 & 0 \\ -\frac{1}{b} \cdot \beta & \frac{1}{b} \cdot \beta \end{bmatrix}$$

To use Equation 2, 3 and 4 note that r is the wheels diameter, ω_l and ω_r are the rotation rates for left and right side while all three tires rotate with the same angular velocity. b is the track-base. β is the factor that affects only the platforms rotation rate and can be every rational number between 0 and 1. The higher the value of β the less friction affects the turning rate (for example on wet grass the value is higher than on asphalt). To calculate the current velocities, J_s of Equation 5 needs to be set for $J(k)$ in Equation 2. The implementation following this thoughts has been done by an employee of the project partner Evocortex GmbH, a robot development company from Nürnberg. The output of the software package is a ROS standard message called `nav_msgs/Odometry`. To identify the factors β value a test path has been driven, using a wireless game controller, with predefined end pose in rotation like 180° or -45° . After a few experiments the perfect value for the laboratories floor has been found.

III. SINGLE DATA VALIDATION

This chapter will describe how the data, that has been collected using the systems described in Chapter II, is validated in order to ensure parametrisation and programming error-free application in future sensor fusion. Due to Coronavirus it hasn't been possible to test the whole system until now. That is why only parts of the robot have been tested together. The chapter will start with single validations followed by data recordings with different sensor types together.

A. DGNSS

For the validation a test track has been set up in an outdoor environment. First three test models (done several times each time) have been straight movements of exactly 15 m with different velocities. Data logging has been done using `rosviz` and converting to `.csv` for postprocessing using the Google Service `my.maps` where you can measure distances between points and have a map overlay to see the movement in the real world. The result can be seen in Figure 3. The image only shows three lines all taken with different unmeasured velocities. As you can see the point line itself is straight but they vary in their position. This shows that the DGNSS hasn't been very accurate due to buildings and trees around the antennas. This has not been done on a free field because in the real scenario the robot has to face these interference sources.



Figure 3. Movement of test skid displayed with my.maps using DGNSS data

Measurements between start and end position, using Google's service, showed the distance measurement of 15 m has been accurate. The configuration that has been used to record the data can be seen in Figure 4 and will be described in Chapter III-D.

B. IMU

A negative aspect in using an inertial measurement unit is that they have a temperature dependent drift around at least one axis. That is why the test that has been done for the validation of the IMU was mainly about finding out the value of the drift. To validate this error the sensor system needs to lay on a flat surface. After starting up, it is possible to display the IMUs frame in ROS package called `rviz` which is used to display for example sensor data. If there would be a big drift, it would be possible to visualize and detect it without any data analysing. The result of this test has been that the drift is negligibly small and for short term movements, like turning rate of the platform, irrelevant.

C. Wheel Odometry

There are three different movement states the robot can enter. Those are straight, turning or straight with an turning overlay. For the straight movement the robot needs to drive a certain length followed by a manual evaluation of the real driven and the calculated distance. The real and calculated distance can be different if the robot is stuck or on slippery ground for example after rain. The fact that the turning rate varies not only from the surface ground but also from the distribution of centre of mass, tire condition and slope angle the robot tries to turn leads to the conclusion that the turning rate outputted by the wheel odometry node is only suitable for stuck detection comparing these values to the IMU outputs. That is why for the fusion using a Kalman Filter or something similar the information of the turning rate needs a high value of covariance.

D. IMU and DGNSS together

The IMU and DGNSS Rover module has been mounted on a sledge which simulates a skid steering model at least in straight movement very good. Also it simulates while turning a centre point that does not lay in the middle of the "robot". The configuration can be seen in Figure 4. To validate if the movement the IMU and DGNSS outputs is in the same direction. The recorded data has been used to display the movements in `mapviz` which is a ROS-package to visualise map relevant data as well as sensor data. The heading of the IMU was indicated using an arrow and the DGNSS points have been displayed as points. In order to validate the interaction of the two sensor systems another random movement has been recorded. The outcome of this validation process has been that the heading the IMU is sensing and the direction of movement, the GNSS is displaying indirectly via points, fit together.

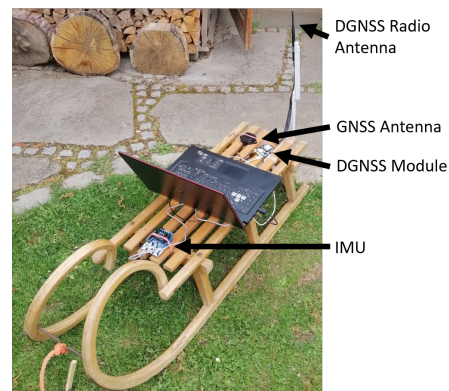


Figure 4. Test skid with IMU and DGNSS System

E. IMU and Wheel Odometry together

As already mentioned in Chapter III-C the odometry output of the wheel-node is only suitable for linear movements. That is why the most trust for the rotation part of the pose estimation lays on the IMU. To simulate the rough

environment at the projects mission side mecanum wheels have been mounted to a small test robot as they produce strong rattling while driving over flat hard ground. The reason is to test the effect the rattling has to the IMU. The test configuration used can be seen in Figure 5.

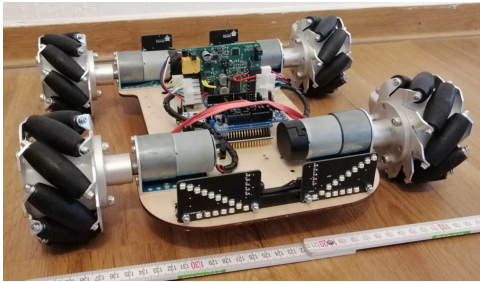


Figure 5. Test robot equipped with an IMU and motors with encoders

As this test has shown the rattling does not affect the Inertial Measurement Units output, but it detects the vibrations on the platform. The effect of this to the sensor fusion needs to be validated and if necessary a filter has to be implemented that filters fast angular movements.

IV. CONCLUSION

The sensor systems DGNSS, Inertial Measurement Unit and wheel odometry using motor encoders described in this paper should be good enough for pose estimation in rough environments. The estimation could be improved using a second IMU as well as another DGNSS module to get the heading of the robot as an output of the DGNSS-node. The odometry calculated through the wheel encoders can hardly be trusted as it varies very much from the ground. In future work the sensor data collected and validated will be used to test and validate a fusion node to get one discrete pose.

ACKNOWLEDGMENT

At the end of this work I would like to express special thanks to the Laboratory of mobile Robotics at the Technical University Georg Simon Ohm in Nürnberg under the lead of Prof. Dr. Stefan May. It provided me with information and code and has been my employer for the duration of the project. I would also like to thank the company Evocortex GmbH for advising me, writing the code for the wheel odometry and employing me as a student trainee.

REFERENCES

- [1] Fraunhofer IAIS. "Volksbot RT 6". Accessed: May 06th, 2021. [Online]. Available: <https://www.volksbot.de/rt6-de.php>.
- [2] More, Tom. "robot_localization wiki". Accessed: May 06th, 2021. [Online]. Available: http://docs.ros.org/en/melodic/api/robot_localization/html/index.html.
- [3] B. Bhatta, "Chapter 5 - Errors and Accuracy Issues", in *Insights into GPS, GLONASS, Galileo, Compass, and others*, Hyderabad, India: BS Publications, 2010.
- [4] ardusimple. "simpleRTK2B". Accessed: May 07th, 2021. [Online]. Available <https://www.ardusimple.com/simplertk2b/>.

- [5] T. Foote, M. Purvis. "ROS REP 103". Accessed: May 09th, 2021. [Online]. Available <https://www.ros.org/reps/rep-0103.html#rotation-representation>.
- [6] D. Baril, V. Grondin, S. Deschênes, J. Laconte, M. Vaidis, V. Kubelka, A. Gallant, P. Giguère, F. Pomerleau. (April 2020) "Evaluation of Skid-Steering Kinematic Models for Subarctic Environments". [Online]. Available: https://www.researchgate.net/publication/340560421_Evaluation_of_Skid-Steering_Kinematic_Models_for_Subarctic_Environments.

Development and construction of a Hand Exoskeleton for Virtual Reality

1st Dennis Gerdts
 Deggendorf Institute of Technology
 Deggendorf, Germany
 dennis.gerdts@th-deg.de

Abstract— Virtual reality (VR) is being used in more and more industries and is a steadily growing market. The main function of VR is to fully immerse the user into the virtual world. In order to do this all senses must be tricked into thinking that what is Infront of them is real. Sight is being controlled by VR goggles which sit in front of the users' eyes showing them the virtual world. Hearing is done by using 360° headphones. The only senses missing are touch and smell, in this paper we will be focusing on how to trick the touch sense into “feeling” the virtual world. To do this we will be building an exoskeleton for the hand which will act as a controller in the 3D world while giving the user direct feedback about the object they are touching. We will be exploring the use of piezo actuators to stop the bending of the fingers to simulate objects. We start off by designing various prototypes of joints to experiment with the correct placement of piezos to achieve the best braking force. The different designs end up showing various pros and cons which lead us to the final design which includes a piezo stack and a metal band. The piezo stack is housed inside of a tower which allows the piezo to only expand in one direction. When a voltage is applied to it, it will expand and push down on the metal band stopping it from moving, thereby the user thinks there is something in his hand. (*Abstract*)

I. INTRODUCTION

Virtual reality is a steadily growing and future oriented market. It covers a wide variety of fields ranging from gaming to manufacturing. The Cambridge Dictionary defines the term virtual reality as “A set of images and sound, produced by a computer, that seem to represent a place or situation that a person can take part in” (Dictionary, 2014). In order to immerse in this virtual reality, the user wears a set of VR goggles. These goggles are made up of two screens, one for each eye, and a set of lenses to focus the images on the eyes. By covering the full range of sight of the user, the user feels immersed in the virtual world. By adding headtracking either with cameras or sensors integrated in the headset the users head movements are directly translated into the 3D world. To interact with this 3D environment, the user has two controllers which act as the user's virtual hands. The controllers however are the one part of the system that stops the user from fully immersing in the Virtual world, since they do not receive any feedback of the object they are holding. We are going to fix this problem by turning the controller into an exoskeleton which can give direct feedback to the hand of the user.

II. THE HAND

A. The Mechanics

The exoskeleton will be a mixture between static and powered since the movement will come from the users' hands. In order to simulate the feeling of the user holding something all we must do is create a resistance that the user can feel. We are going to do this by using small piezo actuators which will expand to create friction and thereby stopping the finger joint from bending. This will give the user the impression that the hand is holding something.

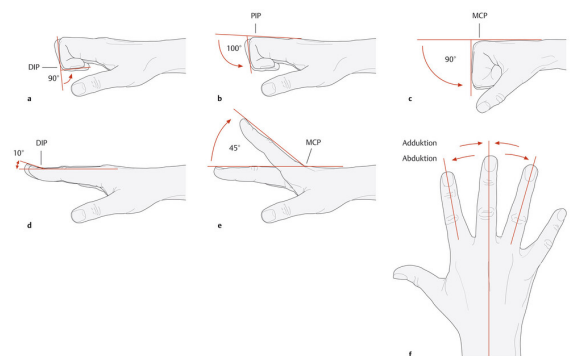


Fig. 1. (Schünke, 2011)

Before we can start designing the exoskeleton, we need to have a look at the Human Hand. Each finger has three joints, each with its own range of motion. These three joints are called Metacarpophalangeal joint (MCP), Interphalangeal Joint (PIP), and Distal interphalangeal joint (DIP).

III. CAD DESIGN

The complete skeleton was designed using the CAD software Solidworks. This was chosen due to its ease of use and availability from the university. First a basic model of a hand was designed in order to simplify the design of the skeleton. This hand model has the dimensions and diameters of all of the fingers on a hand. Using this the skeleton could be built around it.

First, we have to decide on the positioning and shape of piezo actuators we will be using. Piezo actuators come in various shapes and sizes which gives is a few options of where to place the actuators. The smallest actuators would allow us to place them in the rotational axis on each finger

joint, this would be the simplest option. Two round piezo discs would be used and would work like a drum brake.

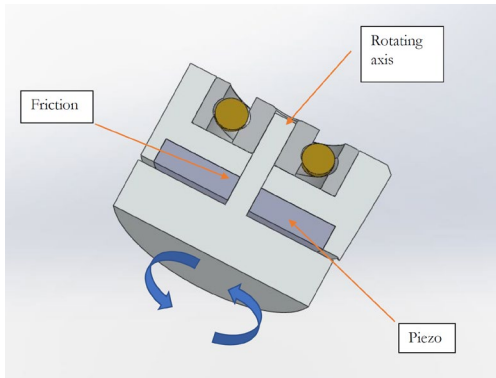


Fig. 2. Drum brake

This design however would need to be very thin in order to fit between the fingers and would not achieve enough friction to stop the fingers from moving.

The next piezos that were tested were piezo stacks. Piezo stacks are layers of piezo materials, the more layers there are the larger the expansion of the piezo and thereby the greater the braking force. These however are too long to be fitted between the finger joints and must therefore be placed on top of each finger. To be able to stop the finger from bending we will be attaching a thin metal band to each of the finger joints which will run underneath the piezo stack. By applying a voltage to the piezo, the piezo expands pushing down on the metal band and thereby stopping it from moving.

We start by designing a shell for each of the finger joints, these will be where the piezos and the metal band gets connected to. Each part first gets designed in CAD and then 3D printed for quick testing.



Fig. 2. Fist tests on finger

Fig. 2 shows the basic setup of the exoskeleton for one finger. Each joint has its own shell which allows us to control each joint separately. The towers house the piezo actuator which when a voltage is applied to expands creating friction between the metal band, stopping the bending motion.

The largest range of motion comes from the MCP joint, which requires a different solution to keeping the



Fig. 3. Finger joints with hand shell

exoskeleton in one piece. As seen in Fig. 3 we use two external rods to achieve the desired range of motion. Fig. 3 also shows the first prototype of the hand shell, this is where each of the finger joints will be connected to. Testing this on the hand showed that the stiff connectors between the fingers and the hand can limit the range of motion and can make moving the hand feel unnatural. This is why in the next version connectors were printed out of elastic material as seen in Fig. 5. These elastic joints keep the glove together without limiting the motion of the fingers.



Fig. 4. Completed skeleton without thumb

Next, we need to design a way of controlling the thumb. This is the most complex part of the exoskeleton since the thumb has a very large range of motion in different axis. As seen in Fig. 5 a separate wrist shell was designed in order to achieve the correct angle to stop the thumbs movement.

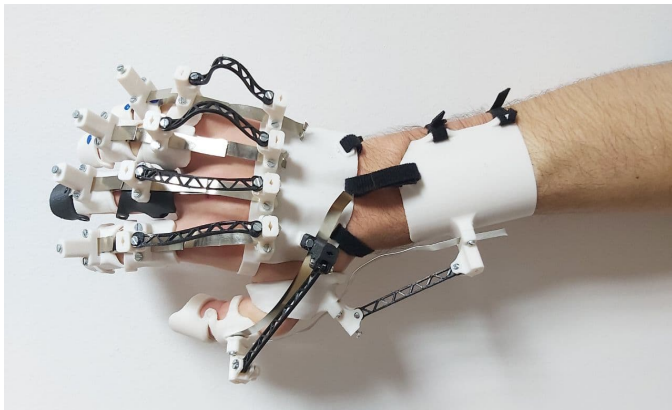


Fig. 5. Completed hand skeleton

IV. ELECTRONICS

To create the braking force we will be using small piezo actuators. Piezo function can be split up into two categories: the direct piezoelectric effect and the inverse piezoelectric effect. “The direct piezoelectric effect, also called generator or sensor effect, converts mechanical energy into electrical energy.” (*Fundamentals of Piezo Technology*, 2021). Whereas the inverse piezoelectric effect “causes a change in length in this type of materials when an electrical voltage is applied. This actuator converts electrical energy into mechanical energy.” (*Fundamentals of Piezo Technology*, 2021). We will be using the inverse piezoelectric effect to create friction between the piezo and a metal band. There will be a pair of piezo and metal band for each finger joint allowing for a very precise control and simulation of objects. Piezo actuators can create force of up to 120N however the travel range is in the micrometer range. This travel range can be increased by stacking piezos on top of each other. Each piezo requires a piezo driver which can then be controlled by a program. For now these drivers require a lot of power and we would require a total of 18 in order to control each joint individually. Testing will show if one piezo can be enough to control the whole finger. This would greatly reduce the amount of power needed to control the exoskeleton. Piezos are very delicate parts which means any damage done to the housing can become hazardous to the user or stop the piezo from functioning correctly. This means we cannot have the piezo be in direct contact with the metal band, since the friction and forces caused by this would brake the piezo. To solve this problem a small piston is inserted between the piezo and the metal band. When the piezo expands it pushes the piston against

the metal band which creates friction without putting too much stress on the piezo.

V. MANUFACTURABILITY

For prototyping, the parts of the exoskeleton have been made using a 3D printer. This allows us to quickly make adjustments to parts and test out how they fit together. 3D printing however has its limitations, which include very low tolerances which in this case makes testing difficult since we are dealing with such small parts. The final version should be made out of injection molded plastic. This would allow us to manufacture the exoskeletons very cheaply and out of good quality, while still keeping the weight to a minimum. Only certain parts like hinges will be made out of metal to ensure a good fit and a long lifetime.

VI. CONCLUSION

In conclusion further testing will have to show if the piezo actuators can produce enough force to completely stop a finger from moving, which would be required to achieve the desired effect. The exoskeleton will also be integrated into a glove which will make applying and removing the skeleton a lot easier. A simpler way of driving the piezos must be found since the current system requires too much power.

REFERENCE

VII. REFERENCES

- Fundamentals of Piezo Technology*. (2021). Retrieved from PI:
<https://www.physikinstrumente.com/en/technology/piezo-technology/fundamentals/>
 Schünke, M. (2011). *Bewegungsausmaß der Fingergelenke*. Thieme.

An Enhancement of Common Rail Track Detection Methods for Automatic Train Operation in Shunting Services

Johanna Heuser

Institute of Vehicle Technology
Nuremberg Institute of Technology
Nuremberg, Germany

Email: heuserjo64489@th-nuernberg.de

Abstract—The development of rail track detection is an important task on the way to autonomous driving trains. Trains that drive autonomously offer the possibility to elevate transport capacity and to deploy manpower more efficiently. For the development of autonomous trains, hazard assessment is mandatory. Therefore, trains need to determine whether objects interfere with the railway loading gauge. This again requires knowledge of the rail track course. This article gives an overview of current rail track detection methods. It opposes the advantages and disadvantages of rail track detection techniques as well as their suitability for autonomous trains. Furthermore, this article introduces an enhanced method of rail track detection based on previous track detection methods. This new method includes techniques such as image masking, Inverse Perspective Mapping, edge detection and rail identification.

I. INTRODUCTION

The development of automatic and autonomous vehicles is currently discussed by many researchers. The main advantages of automatic and autonomous driving are cost reduction and safety increase as well as an increase in transport capacity and time table accuracy. The development of automatic and autonomous driving is complex. One essential feature for autonomous driving is hazard assessment. That means especially in driving mode 'on sight', as it is always the case in shunting service, the vehicle must be able to determine whether objects interfere with the vehicle's track and autonomously take action if necessary. This requires knowledge about the vehicle's track including its hazard area.

The Institute for Vehicle Technology at the Nuremberg Institute of Technology is engaged in developing an automatic shunting locomotive. This article presents an approach for determining rail tracks by combining map-provided rail track data with optical detected rail tracks. The rail network of shunting yards is usually documented in a digital rail network map. In combination with a GNSS sensor, the vehicle's position can be located in the rail network map. The course of the shunting locomotive is given by the shunting order. This means that the course of the shunting locomotive can be extracted from the digital rail network map. Next, the digital course needs to be transformed to a representation relative to the vehicle's orientation so that the hazard area

can be determined. Although the vehicle is lead by the rail, the locomotive's orientation is not fully determined because of clearance between wheel frames and the rail track. A small variation in the orientation of the rail track relative to the locomotive leads to high deviations in a calculated point of interest in large distances as object detection and localization is computed in relative position to the sensor located on the locomotive body. Therefore, the orientation of the track provided by map data is matched with track data originated by the sensors, enabling sensor and map fusion. This demands an accurate and robust detection to the rail track.

This article focuses on the optical rail track detection for trains in order to adjust map provided track data relative to the orientation of the vehicle. It firstly points out the current state of research by opposing previous works related to track detection for cars and trains (Section II). In this context, advantages and limits of different methods are exposed. In Section III, a concept suited to the requirements of rail map adjustment is introduced. Special focus is set on the design of an appropriate image mask in order to reduce data. Furthermore, a method for initial segment detection and curve modulation is described. The concept finishes with an Inverse Perspective Mapping (IPM) and rail track identification in order to fit the rail track representation of the rail network map.

II. RELATED WORK

The automotive industry already uses efficient lane detection algorithms for cars. Automotive lane detection is usually based on lane markings with high visual contrast. A real-time generic obstacle and lane detection (GOLD) is presented in [1]. This work models a lane boundary as a plane curve with a constant lane marking width and high visual contrast between the lane marking and the roadbed. The lane detection is based on a black-white-black pattern matching that characterizes the contrast of the lane marking. For computational efficiency, an IPM is performed first. This is followed by an iterative geodesic morphological dilation to detect lane markings. The

adaptive threshold of pixel differences makes the detection robust against shadows and illuminations.

The high visual contrast that is required for this method, is not given between rails and the rail bed. Therefore, this method is not transferable to trains. In addition, track switches emit higher disturbance which sets different requirements to the detection. Also, the breaking distance of a train is much longer than the breaking distance of a car. While road vehicles can drive obstacle avoidance maneuvers, the rail track is a boundary for the train's course without any degree of freedom in lateral direction. Therefore, the detection range of a train's track must be much higher than for a car.

Approaches for rail track detection are introduced in [2], [3], [4]. These works are based on lane detection for cars.

In [2] an approach for rail track and obstacle detection is introduced. This work uses a combination of the Canny algorithm [5] and Hough transform [6] based on straight lines to detect rails. The method fails for curved rail tracks and is dependent on illumination. The exact procedure in this work is poorly documented and therefore hardly traceable.

In [3] a concept for rail detection is described. The concept is based on the parallelism of rails. Therefore, an IPM is performed first. Edges are then detected using a Difference of Gaussian filter. The detected edges are then sliced and proven for parallelism.

In [4] rail and obstacle detection methods based on clothoid (also called Euler spiral) [7] segments with smooth transition are described. This work gives no details about the used track detection. The exact method for the rail track detection is therefore untraceable.

One of the promising methods is introduced in [8]. This approach features automatic self-calibration. For this, the intersection point of two rails is determined. Rails are identified using gradient computation and the knowledge of rail head width, rail head distance d and distance of the sleepers. Then, all lines intersecting with this point and the bottom row of the image are determined. Along those lines, the mean of the intensity values of the bottom third of the image are calculated. Comparing the similarity of those intensity means of two lines with distance d , the initial rail segment is considered. A 3D model of the rail is built using piecewise quadratic functions with continuity constraints. The results of this approach shows rail detection up to more than 100m. It is robust against shadows and reliable even in bad illumination conditions. The approach is stated to be real-time capable, but the computational configuration used is not specified in the article.

In further research, approach [8] shows unreliable results for sudden changes in exposure [9]. In [9] a new rail detection approach was derived using Canny algorithm and Hough transform. The camera calibration in this work is more complex than in [8]. In return, the detection is more robust against lighting conditions. However, to reach this robustness, strong manual help is required for camera calibration, for threshold setting for the Canny algorithm and for track initializing.

Additionally, it is unpredictable which track the algorithm follows at switches.

Another approach for rail track detection is given by [10]. This approach first performs an IPM transforming the original image into a top view. Subsequently, the image is smoothed using a Gaussian filter. Edges in the image are detected using the Canny algorithm. Some erroneous edges are eroded applying a binary mask to the image. Erroneous edges are once again eliminated using morphological operators. From the remaining edges, rails are identified using RANSAC. This approach shows a high detection range for the analyzed images. Results for rail detection at different weather and lighting conditions are not given.

An approach similar to [10] is given in [11]. The analysis of different edge detection methods showed best results using the Canny algorithm. Edges that belong to actual rails are identified setting regions of interest iteratively under the constraints of continuity and maximum curvature for rails. The approach delivers robust results as long as a sufficient image quality is given. The IPM and edge detection with different filters turn out to take high computation time.

The most recent track detection method at the Institute for Vehicle Technology is given by [12]. This method first performs a projection of acquired images into the top view. Secondly, possible areas of the rail's appearance on the bottom of the image are manually defined. Next, edges in the image are detected using the Canny algorithm. In order to determine the rail track, the RANSAC algorithm [13] based on third degree polynomials is used. For the RANSAC algorithm the condition is set that one of the selected points lies in the appearance area that was defined in advance. The results in this work were satisfying for adequate illumination and the method was also robust when the image contains switches. The computation time does not meet real-time capability.

In general, image processing often uses methods based on artificial intelligence. The problem using artificial intelligence is that its decision making is not completely traceable. In addition, the legal use of artificial intelligence is not given yet in European traffic as given by the European standard EN50128:2011 [14]. Therefore, this article focuses on classic detection methods.

III. METHODOLOGY

The method introduced in this section is based on the method introduced in [12], but enhanced by further image processing techniques. The overall procedure of the method is visualized in Figure 1. The techniques framed by continuous lines are common techniques in the development of rail detection. The techniques framed by dashed lines are refinements derived in this article.

The structure of the algorithm may vary in order but must contain the following steps for robust track detection. The challenge in the development of automatic and autonomous

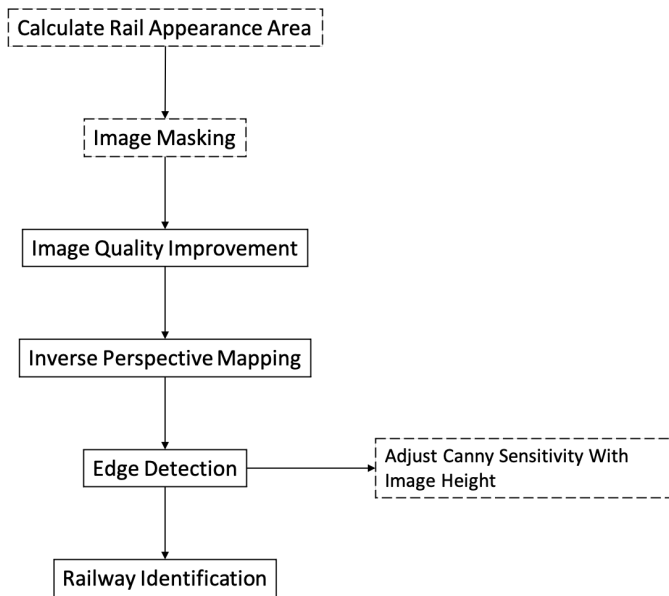


Figure 1. Overall structure for the rail track detection algorithm. Continuous frames represent common rail track detection techniques. Dashed frames represent techniques of improvement.

trains is real-time operation. Therefore, the run-time is an important factor when analyzing different methods. The amount of data has a significant influence on the run-time of noise reduction methods as well as on the IPM. In order to reduce the amount of data, it is beneficial to use a binary image mask. This image mask removes sections from the picture where the track is impossible to appear in the image by setting the corresponding pixels to zero. Real images are usually afflicted with noise. This can be reduced by noise reduction methods. Common noise reduction methods are the Sigma filter, Gaussian filter and Median filter. In addition, a method for contrast enhancement may be necessary to enhance edge detection. The rail can be found in the image using edge detection. The Laplace operator, Sobel operator, Hough transform as well as the Canny algorithm are commonly used methods for edge detection in images. An IPM offers the possibility to use the knowledge of parallelism of the rails. Additionally, approaches for edge detection and rail identification are introduced and analyzed. Last, two suited curve representations are described.

A. Image Quality Improvement

Sometimes, images are afflicted with bad quality. Quality can be impaired by fuzziness or bad illumination which leads to low contrasts. Several proven methods exist that enhance image quality. Noise reduction as well as contrast enhancement methods significantly improve the image quality.

Typical methods for noise reduction are the average filter, Gaussian filter, Median filter and Sigma filter. The average filter, Gaussian filter and Median filter are very efficient in run-time and noise reduction. Nevertheless, the average filter and Gaussian filter intensify blurring which can lead to problems when edges shall be detected. The Median filter may distort

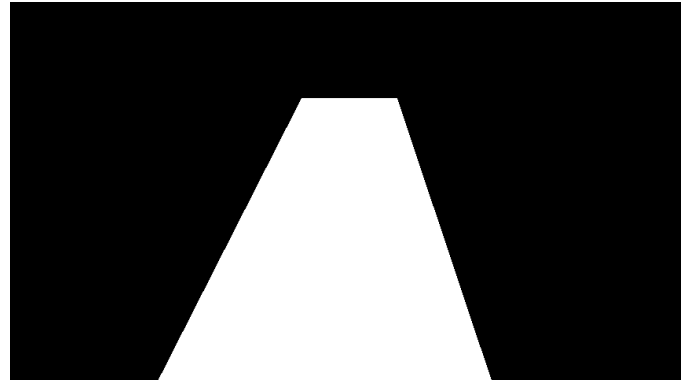


Figure 2. One possible image mask for a straight rail track in vanishing point perspective.

the image and may delete thin lines. The major advantage of the Sigma filter is that it retains the sharpness of the image, but it is slower than the above mentioned filters.

Contrast can be intensified using linear contrast enhancement or histogram adaption.

In order to test the suitability of those methods for rail images, the test of different image scenarios is beneficial. This points out the strengths and weaknesses of the specific methods. It may also be beneficial, to apply more than one method to an image. In this case, the influence of different application orders needs to be analyzed. Once, influences and suitability of different quality improvement techniques are pointed out, an extension for an automatic quality improvement may be considered. Its task is to automatically choose appropriate quality improvement techniques for scenarios at shunting yards.

B. Image Masking

This work focuses on the vehicle's own track. That means all areas apart from the rail track do not need to be taken into account and can be ignored. This can be done using a binary image mask that fits the possible rail course. Ignoring as many image points as possible, holds the advantage to reduce erroneous rail track detection. At the same time, it significantly reduces the amount of data that needs to be processed and therefore saves computing time.

Due to the fix position of the camera on the locomotive, the appearance range of the rail in the bottom part of the image is limited. Instead of defining this area manually as executed in [12], this area can be calculated. In order to reduce the amount of remaining pixels even more, the maximum curvature of rails can be regarded. A rail's curvature is restricted by norms. These restrictions are static. Information about the track is given by the shunting order. Combined with the network information of the rail map, rail appearance in the image can be pursued.

One possible image mask for an image of a straight rail track in vanishing point perspective is shown in Figure 2.



Figure 3. Example of an image taken from the locomotive's front.

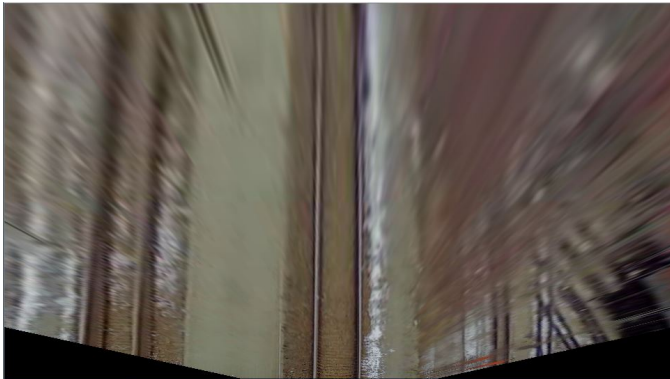


Figure 4. Figure 3 in top view after performing IPM.

C. Inverse Perspective Mapping

The available images from the locomotive's front are afflicted with perspective effects. That means that although two corresponding rails proceed parallel from top view, the rails taper in the image with increasing distance from the camera. On the other hand, the use of the rail's parallelism is beneficial for the rail identification.

Perspective effects of an image can be eliminated using an IPM. Knowing the camera's intrinsic and extrinsic parameters, each point of an image can be transformed into an image that results in a top view and the rails appear parallel. The result of an image after performing IPM is shown in Figure 4.

Many previous works applied the IPM at the very beginning of the method. In order to save computation time, it may be beneficial to perform the IPM at a later point of the method, e.g. after the edge detection. On the other hand, this may distort the detected edges. The best suited point for the performance of the IPM therefore needs further investigation.

D. Edge Detection

Rails in an image can be located by identifying their edges. Edges in an image can be identified by the contrast of neighboring pixels. There are many methods to detect edges in images, e.g. the Laplace operator, Sobel operator, Prewitt algorithm or Canny algorithm. The Canny algorithm

has proven to be a robust edge detection method for rail detection [11][8].

IPM results in increasing blur for rails at large distances. The sensitivity of the Canny algorithm can be adjusted to the sharpness of the image. Therefore, it may be beneficial to adjust the sensitivity of the Canny algorithm to different parts of the image. In this case it might be adjusted with the height of the image.

E. Rail Identification

The edge detection likely delivers several detected edges. The task is now to identify the actual rail course. Therefore, we combine the detected edges with the knowledge of parallelism, distance and curvature constraints.

The rail identification in [9] requires manual help, but the approach presented in [10] is able to identify rails automatically. This work therefore follows the rail identification as in [10] that first identifies edge detected pixels that are parallel to each other within a specific distance and regards restrictions of curvature changes to following pixels. After those are identified, the RANSAC method is performed to estimate the rail's layout.

F. Curve Representation

The choice of a suited curve representation to the actual rail curve significantly influences the accuracy and robustness of the rail detection. Suitable representations for rails are clothoid segments, piecewise quadratic functions with continuity constraints and third degree polynomials.

In newer rail design, clothoids are often used to design the geometry of rails [15]. This is especially beneficial when used for trains at high velocity. Clothoids are characterized by a continuous change in curvature (see Figure 5). This eliminates jerks and reduces erosion at the same time. On the other hand, clothoids can not be evaluated in closed form. The trade-off between computational cost and accuracy needs to be investigated separately.

However, in reality, rails do not always follow the clothoid design. Deviations from clothoid construction especially appear in transition curves. In those cases, the layout of the line likely follows the geometry of circular arcs. The calculation of Cartesian coordinates, requires solving Fresnel integrals. Therefore, clothoids can not be solved in closed form. Cartesian coordinates of clothoids are commonly calculated using approximation methods. The calculation is always a trade-off between accuracy and computational cost.

Clothoids with small curvature can be approximated using polynomials. Common approximation methods use polynomials of second or third degree. In this case, the instant use of polynomials saves computation time. As in shunting yards rails usually are not constructed after clothoids, the use of polynomials make the rail identification more versatile.

IV. SUMMARY

This article discussed the advantages and disadvantages of techniques necessary for rail detection for automated trains.

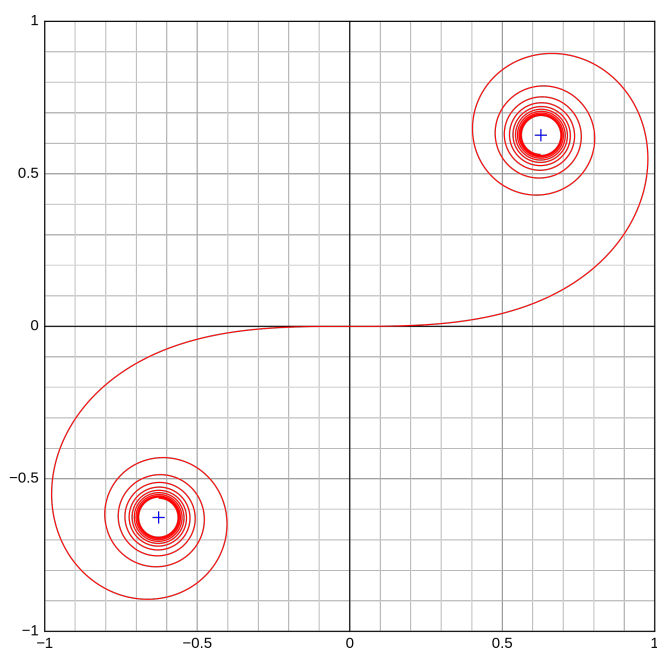


Figure 5. A double-end Euler spiral [16]

The main difficulty in rail detection is set by low contrast between rails and the rail bed. This disadvantage might be compensated by the use of image processing techniques and the use of geometrical constraints given by norms.

The results of previous works on rail detection show the difficulty of a real-time capable and fully automatic rail track detection method. Previous investigations delivered satisfying results for rail detection for a selection of scenarios but still need improvement. This article introduced enhancements for rail track detection containing the calculation of rail appearance areas on the bottom of the acquired images. Those ranges can be used for the construction of the binary image mask but also for rail identification. The binary image mask shall reduce the computation time significantly by eliminating irrelevant image points. Thereafter, techniques for image quality improvement shall increase edge detection. An IPM enables the use of geometrical constraints of the rails. The following edge detection, using the Canny algorithm, is expanded by sensitivity adjustment according to the change in sharpness due to the IPM. Finally, the rails are identified using the RANSAC algorithm. For the rail identification, the calculated appearance ranges are considered.

V. FUTURE WORK

The further task of this work lies in implementing, testing and evaluating the introduced techniques. In comparison to previous works, the introduced method shall be tested to a wide range of different scenarios that show strengths, weaknesses and limits of the method. The scenarios shall contain different requirement aspects such as alternating weather conditions, shade effects, disturbances through light reflection,

vegetation and others. Further inspection lies in testing the reaction of the individual techniques to possible occurrences in real train operations.

REFERENCES

- [1] M. Bertozzi and A. Broggi, "Gold: A parallel real-time stereo vision system for generic obstacle and lane detection," *IEEE transactions on image processing*, vol. 7, no. 1, pp. 62–81, 1998.
- [2] L. F. Rodriguez, J. A. Uribe, and J. V. Bonilla, "Obstacle detection over rails using hough transform," in *2012 XVII Symposium of Image, Signal Processing, and Artificial Vision (STSIVA)*. IEEE, 2012, pp. 317–322.
- [3] M. Gschwandtner, W. Pree, and A. Uhl, "Track detection for autonomous trains," in *International Symposium on Visual Computing*. Springer, 2010, pp. 19–28.
- [4] M. Ruder, N. Mohler, and F. Ahmed, "An obstacle detection system for automated trains," in *IEEE IV2003 Intelligent Vehicles Symposium. Proceedings (Cat. No. 03TH8683)*. IEEE, 2003, pp. 180–185.
- [5] J. Canny, "A computational approach to edge detection," *IEEE Transactions on pattern analysis and machine intelligence*, no. 6, pp. 679–698, 1986.
- [6] P. V. Hough, "Method and means for recognizing complex patterns," Dec. 18 1962, uS Patent 3,069,654.
- [7] "Euler's integrals and euler's spiral," *American Mathematical Monthly*, vol. 25, no. 8, pp. 276 – 282, 1918.
- [8] F. Maire, "Vision based anti-collision system for rail track maintenance vehicles," in *2007 IEEE Conference on Advanced Video and Signal Based Surveillance*. IEEE, 2007, pp. 170–175.
- [9] F. Maire and A. Bigdeli, "Obstacle-free range determination for rail track maintenance vehicles," in *2010 11th International Conference on Control Automation Robotics & Vision*. IEEE, 2010, pp. 2172–2178.
- [10] P. Kugler, "Fahrwegerkennung von Schienenstrecken mit OpenCV für autonomes Fahren," IFZN Technische Hochschule Nürnberg, 2018.
- [11] E. Hankin, "Entwicklung einer Methodik zur Matlab basierten Standalone-Anwendung für Bild- und Datenverarbeitung der Schienen-erkennung im Rangierbetrieb," IFZN Technische Hochschule Nürnberg, 2020.
- [12] S.-L. Zäch, "Kamerabasierte Gleiserkennung mittels RANSAC für eine automatische Rangierlok," IFZN Technische Hochschule Nürnberg, 2021.
- [13] M. A. Fischler and R. C. Bolles, "Random sample consensus: a paradigm for model fitting with applications to image analysis and automated cartography," *Communications of the ACM*, vol. 24, no. 6, pp. 381–395, 1981.
- [14] D. Trentesaux, R. Dahyot, A. Ouedraogo, D. Arenas, S. Lefebvre, W. Schön, B. Lussier, and H. Cheritel, "The autonomous train," in *2018 13th Annual Conference on System of Systems Engineering (SoSE)*. IEEE, 2018, pp. 514–520.
- [15] R. Menius and V. Matthews, *Bahnbau und Bahninfrastruktur*. Springer, 2020, vol. 10.
- [16] Wikipedia, the free encyclopedia, "Euler spiral," 2021, [Online; accessed May 17, 2021]. [Online]. Available: https://en.wikipedia.org/wiki/Euler_spiral#/media/File:Euler_spiral.svg

System Architecture of Autonomous Mobile Robots

Lennard Römmelt

Faculty of Electrical Engineering, Precision Engineering, Information Technology
Nuremberg University of Technology Georg Simon Ohm

Nuremberg, Germany

Email: roemmeltle85628@th-nuernberg.de

Abstract—Automating transportation tasks and enabling mobile robots requires a robotics base platform. These complex systems consist of many components and subsystems on a software and hardware level. To work out a suitable structure on both system levels, an iterative process is used: After analyzing the current system state and comparing it to the requirements, the system’s structure is extended, modified and tested before the process repeats. Covered aspects include the choice of a GPU-enabled embedded PC as well as the decision on a software packaging solution for industrial applications.

Index Terms – robot, autonomous, AMR, structure, systems engineering, architecture

I. INTRODUCTION

Automating simple and repetitive tasks is common practice in the industry today. Mostly, these are tasks that require a certain set of motions executed sequentially by a robot in a fixed workstation. As automation advances, it is logical to also automate tasks that require robots to move within a certain environment. Intralogistic transportation tasks on a shop floor are usually done by human workers using forklifts or tuggers. Using this personnel capacity elsewhere can be possible by designing a robotic application that carries out these tasks without needing instructions or steering commands by a human. The system needs to percept its environment and react to it appropriately. The transportation tasks can be generated by a shopfloor management system and sent to the robot. There they are carried out autonomously, increasing effectivity by keeping interaction time with humans at a minimum.

Various task-specific components have to communicate to other parts of the robotics system. The components themselves and their physical connections form a certain structure as do the flows of information on a software level. Combining the physical and the information-based part they form a “system architecture” or “core structure”. The goal is to find suitable key components, analyse physical and informational layer of connections in between them and design, refine and optimize a core structure that is sufficient for autonomous mobile robots (AMRs) in industrial applications. This will require modifying, adding or extending components and subsystems on a hardware- and software level.

II. STATE OF THE ART

A. Robots

Using mobile robots to move trolleys or workpieces is already being done in industrial scenarios. Robots that are



Figure 1. System of interest: EvoCarrier; Image: [3]

already in use doing transportation tasks autonomously include MiR’s *MiR200* [1] and Metralabs’ *Cary* [2]. They compete with the *EvoCarrier* by Evocortex shown in Fig. 1. It features omnidirectional movement using mecanum drives, autonomous navigation without external markers and fine positioning with an accuracy of less than 1 mm. This robot is used to evaluate and further enhance internal structure and interaction with and within the system.

B. Software for Robots

Controlling a robot’s behavior and interaction with its environment is done with software, but there are differences on how the code is distributed and organized. One widely known open source solution is the Robot Operating System (ROS) [4] that can be used for all kinds of robots. The idea is to divide a system and its code into functional units or modules that can be easily combined in a different way, enabling the developers to use existing code snippets. A similar yet proprietary framework is Nvidia ISAAC SDK [5] that specializes in GPU-powered computing to enable autonomous robots to percept their surroundings.

III. METHODS

To start, a basic analysis of other current systems beside the EvoCarrier is done, focusing on the different systems, their use cases and applications as well as on their functionality. A systems engineering approach is used to identify the types of components required for the desired robotics system. Comparing these results to the components of the existing system ensures covering all necessary parts. After this, there should be an overview showing core components and their connections which is the basis of the requirement analysis.

A robotics system design process includes a variety of stake holders like the customer, investor, developer and the user. As they all have different relations to the system, their requirements differ in certain criteria, e.g. the user's main requirement is an easy-to-use system while the investor wants maximum profit of the project. To gather and categorize all requirements the Volere Template [6] is used as a guideline of the analysis. These requirements are the basis for designing and modifying the existing system as they explicitly state the expectations of the stakeholders.

To improve and refine the system, components are modified, added or replaced to meet the described requirements. This is an iterative process and is therefore expected to be executed continuously or at least multiple times. Within this process a separate overview of the software structure is added and refined as some of the requirements will cover software or noncomponent aspects. The iterations also include tests of the subsystems and components to ensure everything works as expected. This also provides a decision basis which component fits a certain use case or environment best. Developing and optimizing the architecture is done with focus on particular aspects like application in industrial environment, usability or modularity, depending on the stakeholders' needs that are most important at a given time.

IV. RESULTS

A. Core Structure

After the basic analysis of the existing robot there is a system overview diagram that shows the main components as well as their connections. This includes a computing and control unit, motors and their driver circuit boards, sensors for perception and safety, an information transfer interface as well as a power supply. A simplified diagram is shown in Fig. 2.

B. Integrating an Embedded Computer

To drive autonomously, the robot needs to localize itself within its environment using optical sensors. It then needs to plan its route and calculate the control commands to follow this route autonomously. For both of these aspects, the sensor data evaluation and the computation of autonomous movements, a suitable computing unit is needed. As the sensor evaluation process is GPU-accelerated, an embedded PC with a GPU is chosen and implemented into the EvoCarrier. The code for behavior runs on a Linux-based operating system.

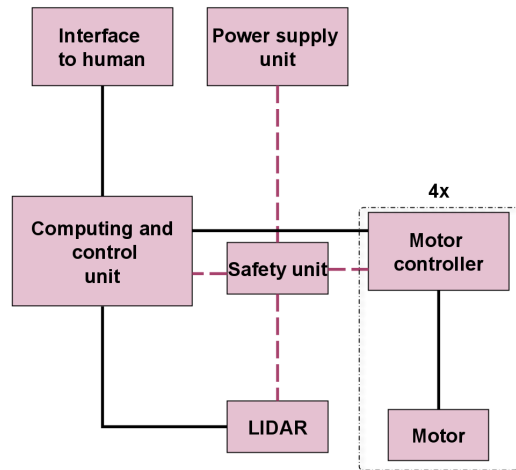


Figure 2. Simplified system architecture of the EvoCarrier

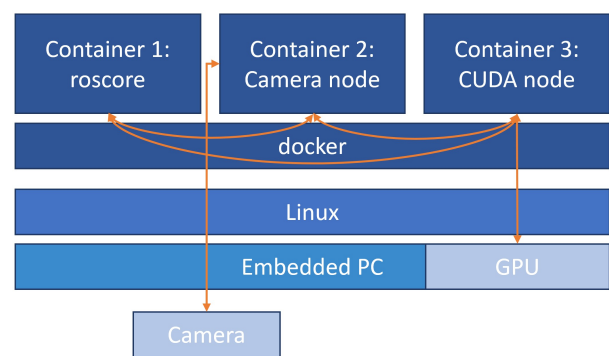


Figure 3. Example container structure with hardware access using Docker Compose

C. Assembling Software into Packages

The robot's software is updated regularly to extend functionality and to fix bugs. These updates should be done remotely and ideally with minimum interaction required by the customer. To simplify the process and to protect the know-how, the software is bundled into packages. For the developer it is also important to maintain an overview of what version of which package is currently deployed in a certain robot. Using "Choosing by Advantages" [7] for deciding on a technology, Docker prevails over OpenVz and Linux Containers as it is widely used, works with the existing system and provides device passthrough. This was successfully tested by running an example environment as shown in Fig. 3. One container runs roscore, another one runs a ROS camera node with access to a USB-camera and a third node executes GPU-accelerated computations in its own container. The application uses Docker Compose for handling setup and network.

D. Refined Architecture Diagram

At the end of the first phase, the previously introduced core structure in Fig. 2 is extended and refined as is its representation that is displayed in Fig. 4. It now shows the division into a

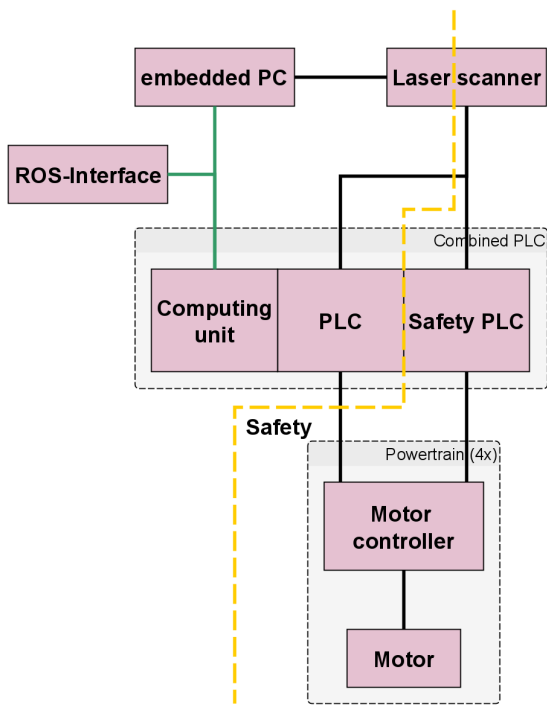


Figure 4. Refined system architecture diagram with added embedded PC

safety-monitored side and a non-monitored side more clearly. This structure enables the system to do computations on tasks and navigation on a nonsafety-certified high power system (Fig. 4 left) featuring the added embedded PC connected via ROS to a combined PLC. The software receives the required data from a laser scanner, whose protective field outputs are connected to a Safety PLC. This enables safe operation at all times in combination with the advantages of GPU-accelerated sensor data evaluation.

V. NEXT STEPS

A. Safety Improvements

The robot is already equipped with basic safety mechanisms. However, additional measures have to be taken to make the robot fulfil the needs of the applicable standards. This could include 360° coverage of laser scanners or modifications in the powertrain. Additional sensors could widen the application spectrum if they are able to safely detect partly transparent obstacles like grids or glass. This makes the robot more interesting für a wider range of customers.

B. Software Rollout and Management

While software packages have already been covered, the next issue is to deliver them to the robots at the customer's site. Different software rollout solutions and fleet management systems have to be compared and evaluated.

C. Usability

Currently, human workers can interact with the robot using a PS4-controller or an app. These only provide immediate control but no option to program simple transportation tasks or more advanced functionality. In the future, a web-based interface should be developed, providing intuitive control of the robot as well as block-based programming tools to easily program logistics tasks without the need of programming skills or external hardware.

VI. CONCLUSION

Robots are advancing to do more complex tasks in the industry. Carrying out these tasks require safe perception of and autonomous reaction to a robot's surroundings. Analysing the existing system and the project around it brings up the optimization potentials. Extending the system by choosing a powerful computer for autonomous tasks was the first aspect covered. Further, the software updating process was reviewed and tests executed using Docker with Docker Compose as a packaging and managing system with repeatable results. The architecture diagram is extended and refined to depict the core structure more clearly.

Whereas these aspects certainly help the robot to advance, there are still more tasks to come: further research concerning automatic update and rollout processes of software packages, maybe including optional packages in a modular way still offers potential for convenient maintenance softwarewise. Programming the robot to do certain tasks is currently difficult and can hardly be done by the user. For an easy setup process an intuitive interface has to be created, allowing programming and configuration of robots as well as creating, modifying and execution of transportation tasks.

ACKNOWLEDGMENT

This research is supported by Evocortex as the company provides the author with test systems and parts as well as a workplace. The author thanks his colleagues at Evocortex as well as his supervisor Prof. Dr. May for general support and patiently answering questions.

REFERENCES

- [1] Mobile Industrial Robots A/S. "Robots." [mobile-industrial-robots.com](https://www.mobile-industrial-robots.com/en/solutions/robots/). (accessed Apr. 28, 2021).
- [2] MetraLabs GmbH. "Cary." [metralabs.com](https://www.metralabs.com/transport-roboter-cary/). (accessed May 3rd, 2021).
- [3] Evocortex GmbH. "EvoCarrier mit Rollstapel," internal rendering.
- [4] Open Robotics. "About ROS." [ros.org](https://www.ros.org/about-ros/). (accessed Apr. 28, 2021).
- [5] NVIDIA Corporation. "NVIDIA Isaac SDK." [nvidia.com](https://developer.nvidia.com/isaac-sdk). (accessed Apr. 28, 2021).
- [6] *Volere Requirements Specification Template*, 16th. ed., Atlantic Systems Guild Limited, London, UK, 2012.
- [7] J. Suhr, *The Choosing by Advantages Decisionmaking System*, Westport, CT, USA: Quorum Books, 1999.

Chapter 10

Papers: Measurement Technologies

Contents

10.1	Hardware Setup for Three-Dimensional Acoustic Source Localization	436
10.2	Ultra Low Noise Amplifier for a Noise Measurement System	441
10.3	“Applied error analysis on a research ORC Plant at the University of Bayreuth” .	445
10.4	High-speed ADC Data Acquisition with an FPGA for OTDR-based Fiber Sensors .	450
10.5	Development of measuring methods for condition monitoring, fault detection and optimization of a medical angiography floor stand	454
10.6	Miniaturisation of a Sensor System Using Reflectivity Based Surface Plasmon Resonance Imaging (SPRi)	459
10.7	Investigation of the Float Current Analysis and the Float Current Settling Process via DVA on 18650 Li(NiCoAl)O ₂ /Graphite Cells	463
10.8	Theoretical and experimental investigation of code correlation methods for optical time domain reflectometry in POF	469
10.9	Method Development for the detection of filmic contaminations in additive manufacturing	474

Hardware Setup for Three-Dimensional Acoustic Source Localization

Benedikt Bugl
 Faculty of Electrical Engineering and
 Information Technology
 Ostbayerische Technische Hochschule
 Regensburg
 Regensburg, Germany
 benedikt.bugl@st.oth-regensburg.de

Abstract—This paper aims to discuss basic hardware and software implementations for research on three-dimensional acoustic localization. Hereby particular attention is paid to the design and construction of a highly variable microphone array and a recording system, as well as a special testing speaker. The whole setup should be flexible enough to be configured for various applications as well as different localization and tracking algorithms, while causing minimal disturbance of the test or measurement it is used for. For the evaluation of the hardware setup a simple implementation of a Time Difference Of Arrival (TDOA) localization algorithm is discussed. To show the capabilities of acoustic localization simple tests are done under ideal conditions.

Keywords—Acoustics, Signal Processing, Localization, TDOA, Microphone Array.

I. INTRODUCTION

The human hearing is able, to localize sound with astonishing precision. For sound coming from the front the angle resolution can be as precise as 1° [6]. In an evolutionary sense acoustic localization has been highly important for survival. Hearing a predator or an enemy approaching in the dark is hardly useful without the ability to localize, where that sound is coming from. While we may no longer have to escape from predators, for communication, robust acoustic localization is also important. In a situation like it would be found at a cocktail party, with many people talking, music playing, possibly in a reverberant room, a listener is able to focus very well upon one speaker. This situation, posing a huge challenge for signal processing and speech recognition, is often referred to as the “cocktail party problem” [5]. While humans get along fine with just two ears, most approaches upon acoustic localization use microphone arrays. The following contribution describes a hardware solution for acoustic localization and shows how good a basic localization algorithm can work under ideal conditions.

II. TESTING HARDWARE

A. A Cartesian Array

The array discussed here is specifically designed to meet the requirements for research on three-dimensional acoustic localization. One of the key requirements for the array was upgradability and variability for microphone positioning. A large part of future research will focus upon comparing SRP- (Steered Response Power-) methods to TDOA (Time Difference Of Arrival) methods. In beamforming, which is the base of the SRP methods, the spacing between the microphones has large influence upon the results. Depending on the frequencies to be captured, as well as the number of sensors available, they can be spaced further apart, closer together, equidistant or with a logarithmic increase of distance towards the outside of the array [4]. For TDOA methods these requirements may vary. Another part of future research will be applications of the localization system. For indoor use, a small array, that can easily fit through doors and be repositioned is needed. For localizing acoustic sources that are further away from the array, a bigger geometry will deliver more precise results. Although a planar array can localize sound in three dimensions, a three-dimensional array should give some advantages, especially for near-field localization.

The basic geometry of the array is a cartesian array. As the name states the microphones are located on three rods, arranged like the x, y and z axis of three-dimensional cartesian coordinates. The idea behind this geometry is to make exact (re-)positioning of the microphones easier. A slight deviation from the position fed into the localization algorithm compared to the actual microphone position will have substantial influence on the systems results. Figure 1 shows the construction. In the making of the array great attention is paid on precise geometry. The center of the array is an aluminum cube milled to a side length of 76 mm. For the microphone in the coordinate origin a hole is drilled diagonally from corner to opposing corner.

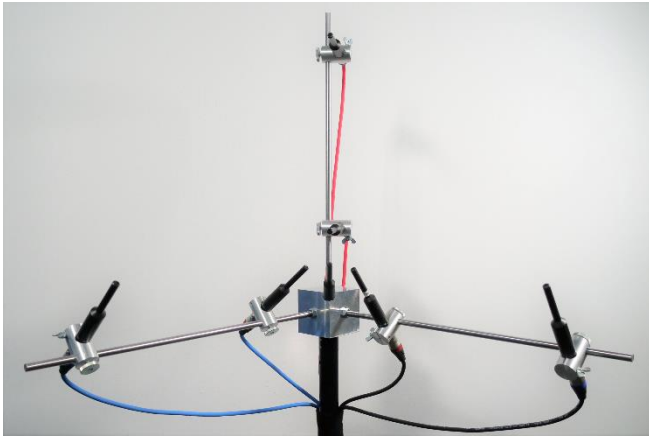


Fig. 1. A Cartesian Array

Interestingly the angle α at which the cube has to be clamped (the angle between the space diagonal of the cube and the bottom) for that hole is quite unusual:

$$\alpha = \sin^{-1}\left(\frac{1}{\sqrt{3}}\right) = 35.26^\circ \quad (1)$$

The holes for the axis-rods are drilled on a lathe, to make sure they are centered in the cube. The rods can be swapped between 500 mm and 1000 mm. The microphones are attached to the rods using custom made aluminum clamps that allow the microphones to be rigidly fixed in place. To minimize reflections, wherever possible all dimensions were kept small and round material was used. Round rods and clamps disperse sound rather than making noticeable reflections in some specific directions. For the cube this was not possible, but assuming the array is mostly used for sources located in front of it, reflections from the cube will be directed away from the microphones. In spite of the effort put into the low-reflective design, reflections will still occur, as very sophisticated support rod designs still cause some reflections [9]. For future projects the array can easily be upgraded to feature 16 microphones or more. Therefore 3D-printed plastic clamps will replace the aluminum design, as they are easier to produce in high quantities (figure 2).

For setting up the array, a cross-line laser level is employed. Using the laser from different directions, all microphones can be aligned vertically and horizontally, after being spaced, with a caliper. All in all, the microphones can be placed with a maximum deviation of about 2 mm, mainly caused by the inability of the operator to position the microphones any more precisely.

The array is equipped with Beyerdynamic MM1 measurement microphones. Important for the choice of the microphone was its size. With a head diameter of just 9 mm and a very small membrane the microphone is highly omnidirectional and reflections are minimal. The smaller head dimensions also make positioning easier. With a flat frequency response, low harmonic distortion and barely any deviation between actual microphones the influence of the

microphones can be neglected for most measurements. If the need shall arise, the array can be equipped with any microphone with a shaft diameter of 19-20 mm, like the AKG SE300/CK92, which is also available for future tests.



Fig. 2. Beyerdynamic MM1 microphones in the two clamp versions

B. The Recording System

For all tests, a RME Octamic XTC 8-channel preamp connected to a PC via a RME MADiface 128-channel USB interface is used. This setup is very capable, achieving a Signal-to-Noise-Ratio (SNR) of up to 117 dBA and Total Harmonic Distortion (THD) of up to 110 dB on its microphone inputs [8]. Another important aspect is, that the setup can do full-duplex transmission, in order to play and record simultaneously. For future upgrades that recording system can be extended by plugging in more Octamic devices. To minimize the chances of mixing up the wiring, all microphone cables are color coded. If the array has to be placed further away from the interface, the symmetric XLR cables can easily be extended with a multicore. On the PC the recording is done by a MATLAB® script, using the *audioPlayerRecorder* system object, provided by the *Audio Toolbox*. Sampling rates can be set depending on the requirements in the post processing.

C. A Special Loudspeaker for Localization testing

A crucial point in the process of evaluating the localization system is a suitable acoustic source. This loudspeaker has to be small enough to deliver unambiguous results for localization tests. The frequency response is required to be as flat as possible and the range close to the one of human hearing. Another important aspect is the directivity of the speaker, especially when moving the source very close to the array. For better spatial resolution it is keys, that the sound emitting part of the speaker is as small as possible. The most significant influence on the directivity of a speaker membrane or rather of the whole box, are its dimensions in the plane of the membrane. As [2] states, the directivity effect starts coming into play when $k \cdot a = 1$, with the wavenumber $k = 2 \cdot \pi / \lambda$, the wavelength λ and the radius of the membrane a . For a frequency of 20 kHz, $k = 366 \text{ 1/m}$, so the membrane radius would have to be about 2.7 mm. Though one

could buy a speaker with such a small membrane, it would be impossible to get enough output volume for a sufficient SNR (not even considering distortion), especially at low frequencies. The driver chosen is the Visaton BF 45/8. The radius of the speaker is about 22mm, $k \cdot a = 1$ being the case at a frequency of 2.5 kHz. So undeniably some compromise has to be made between a flat frequency response, directivity and SNR. While the directivity, as well as the output volume are hard to fix, the frequency response can be flattened on the electrical side of the speaker. The speaker is built into a tube-shaped box to keep the diameter of the front as small as possible. It can be mounted on any microphone stand.



Fig. 3. Special loudspeaker used for Localization testing

III. TIME DIFFERENCE OF ARRIVAL (TDOA) LOCALIZATION

A. Determining Arrival Time Differences

Acoustic waves travel at the speed of sound $c = 343$ m/s (room conditions) which depends upon temperature, humidity and on the gas within which the waves propagate. Depending on the spacing of the microphones, the sound from a source will arrive at different times at the microphones. From the delay Δt , the detour the sound has to make to the microphones Δs can be calculated [10]:

$$\Delta s = \Delta t \cdot c \quad (2)$$

In a microphone array, the position of every microphone is known. This can be used to localize sound from the recordings of the microphones. Under ideal acoustic conditions (no reverberation, no noise), the signals arriving at the microphones are identical apart from a varying delay and a slight difference in amplitude. The crosscorrelation of the measured sound at the microphones will peak at a value that corresponds exactly to their time difference of arrival.

For tests, the *xcorr* function in MATLAB® was used. Note that the result will only be an estimation, as the signals are not infinitely long. It is defined as follows [7]:

$$xcorr(M_0, M_X) = \hat{C}_{0X}[m] \quad (3)$$

$$\hat{C}_{0X}[m] = \begin{cases} \frac{\sum_{n=0}^{N-m-1} \overline{M_0[n]} \cdot M_X[n+m]}{\hat{C}_{0X}[-m]} & m \geq 0, \\ \hat{C}_{0X}[-m] & m < 0. \end{cases} \quad (4)$$

Figure 4 shows the estimated crosscorrelation \hat{C}_{0X} of the microphone in the origin of the array (M_0) to all other microphones (M_1 - M_6). The testing signal is 1 s of music, played in the anechoic chamber at a distance of about 1.5 m from the array origin. For more possible values for the delay (which makes the localization more accurate), the signal was upsampled by factor 4, from $F_s = 96$ kHz to $F_s = 384$ kHz. The peaks can easily be found by applying the *max* function in MATLAB® and the delay times can be calculated from position of the peaks.

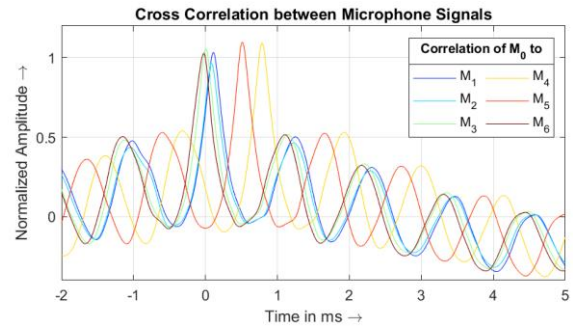


Fig. 4. Correlation of the microphone signals in ideal conditions

B. Multilateration

For localization there are basically two geometric approaches: The first one being Triangulation, where angles of imaginary lines from three known sensor positions towards a target are measured and a location is estimated by their point of intersection. Though this method is often mentioned in crime or action movies, in most applications Trilateration or rather Multilateration, if there are more than three sensors, is used for localization. Here the distances between the sensors and the target are used to estimate the position. An example for Multilateration is GPS [3]. In case of GPS or acoustic source localization, the actual distances are not known, but differences in distance can be calculated. In most applications, these differences are derived from arrival times (for example from arrival times of characteristic radio signals), so these techniques are referred to as Time Difference Of Arrival (TDOA) techniques. The Multilateration problem faced in acoustic localization is quite similar to the one in GPS. In GPS there is just one sensor (e. g. a smartphone), but many sources (satellites) and the sent signals are known. In case of acoustic localization using a microphone array, there are several sensors (microphones), and one (or more) sources (e. g. a loudspeaker), playing unknown sound. Though in GPS, the sensor's position is unknown and in case of three-dimensional acoustic localization it's the source position, that is unknown, the actual problem stays the same: estimating the smartphones (or loudspeaker's) position from the various delays for various satellites (or microphones). In both cases the satellites (microphones) positions are known. An algebraic solution for

this problem is presented in [1], stating the base for the following technique:

- One microphone is selected as the reference point (in case of the cartesian array, the one in the coordinate origin was the obvious choice). Its position is saved in a N-by-one matrix $R(n,1)$, where N is the number of dimensions.
- The other microphones positions are gathered in a N-by-M matrix $P(n,m)$, where N is the number of dimensions and M is the number of these sensors.
- A matrix $D(1,m)$ with 1 by M elements, consisting of all the delays between the microphones in P and the reference microphone multiplied with the speed of sound.
- A matrix $A(m,n)$ is calculated as follows:

$$A = 2 \begin{bmatrix} R(1,1) - P(1,1) & \dots & R(1,N) - P(1,N) & -D(1,1) \\ \dots & \dots & \dots & \dots \\ R(1,1) - P(M,N) & \dots & R(1,N) - P(M,N) & -D(1,M) \end{bmatrix} \quad (3)$$

- A scaling matrix B is calculated as follows (elementwise square of matrix is written \blacksquare^2):

$$B = D^{-2} + \|R\|^2 + \sum_{n=1}^N P(n,m)^{-2} \quad (4)$$

- The result is captured in a 1-by-4 matrix L that is calculated as follows (\blacksquare^+ is the Moore-Penrose inverse):

$$L = A^+ \cdot B \quad (5)$$

The results are found in L, consisting of the three coordinates on the x, y and z axis, as well as the distance from the origin.

IV. TESTS

To evaluate the hardware setup, the first tests are done under ideal conditions. An anechoic chamber provides free field conditions, meaning very low noise (no wind either), minimal reflections. This is very important, because noise or reflections could result in localization errors, when instead of the source the noise or reflections of the source cause a peak in the cross correlation of the microphones.

The test setup consists of the hardware mentioned above. An important challenge for future development is a method of precisely placing the array and the testing speaker. Using a laser-level, a laser rangefinder, a measuring rod, some rope and a tape measure it is still a challenge to place the test setup even close to where it was supposed to be. The fact that the floor of the anechoic chamber is just a steel wire net that is not even and the walls are not straight either, does not help. All in all, the precision of the acoustic localization system might be way better than the placement of the test setup. The

testing speaker was arranged at the position $x = 1.5 m$, $y = 1 m$, $z = 0.15 m$ with tolerances of about 2.5 cm in either direction. The most exact value was the distance from the origin, that was measured at $r = 1.8 m$, with a maximum deviation of 1 cm. As a test signal 1 s of speech was played through the loudspeaker. The results of the TDOA Multilateration were $\hat{x} = 1.450 m$, $\hat{y} = 1.032 m$, $\hat{z} = 0.133 m$, $\hat{r} = 1.791 m$. The result can be seen in figure 5.

It is hard to tell, how much the errors in these numbers are caused by the placement of the test setup, but all values are within the tolerances. Tests in different positions showed similar results.

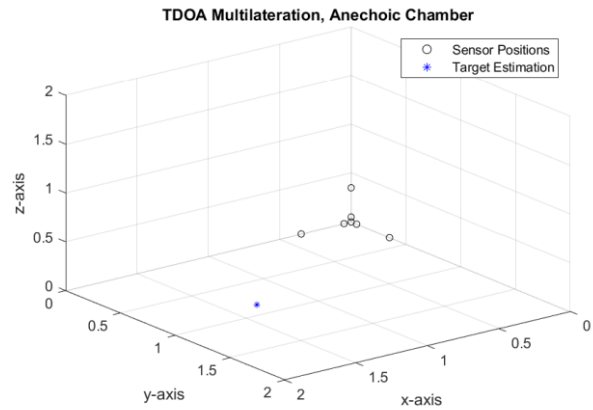


Fig. 5. Result of TDOA Multilateration in ideal conditions (stationary source)

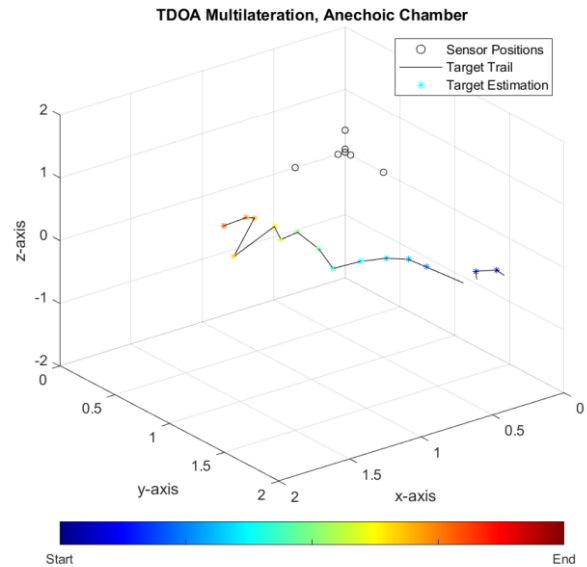


Fig. 6. Result of TDOA Multilateration in ideal conditions (moving source)

Another test was done, where the source was moved in front of the array by hand while playing music. The whole measurement took about 5 s and the target position was estimated every 0.25 s. Figure 6 shows the result. The colored points are the estimated positions for every timeslot. The color of the points turns from blue to red as time progresses. Note that some points are outside of the range of the plot. Although this test is not a representative in a quantitative sense, it shows how well moving objects can be tracked as long as they emit sound.

V. CONCLUSION AND OUTLOOK

All in all, a capable setup for future tests has been implemented. The array can be set up precisely for the actual array geometry that is required, while causing only minimal reflections. The small loudspeaker also works good enough for qualitative tests. Furthermore, tests showed that the array can localize stationary, as well as a moving sound sources. A big challenge that will have to be faced in future tests is exact placement of the sound source relative to the array. That problem will require more hardware, that is not available yet. A solution for the moving source is a turntable, that is still being developed. This low-noise and low-reflection device can then be used to rotate the array. A stationary sound source will then be tracked in a circle, that is as exact as the measurement. The main focus of future research will be upon implementing, testing and possibly improving localization algorithms that are more robust to noise and reflections. While the algorithm presented above performs well in free-field conditions, more advanced methods like SRP-PHAT or GCC-PHAT are expected to outperform it in reverberant or noisy conditions [4].

REFERENCES

- [1] S. Bancroft, "An Algebraic Solution of the GPS Equations," *IEEE Trans. Aerosp. Electron. Syst.*, AES-21, no. 1, pp. 56–59, 1985, doi: 10.1109/TAES.1985.310538.
- [2] L. L. Beranek and T. J. Mellow, *Acoustics: Sound fields and transducers*. Oxford: Academic Press, 2012. [Online]. Available: <http://gbv.ebib.com/patron/FullRecord.aspx?p=1000318>
- [3] A. Born, *Algorithmen zur Positionsbestimmung sowie deren Genauigkeiten in drahtlosen Sensornetzwerken*. München: Beck, 2011.
- [4] M. Brandstein and D. Ward, *Microphone Arrays: Signal Processing Techniques and Applications*. Heidelberg: Springer, 2001.
- [5] E. C. Cherry, "Some Experiments on the Recognition of Speech, with One and with Two Ears," *The Journal of the Acoustical Society of America*, vol. 25, no. 5, pp. 975–979, 1953, doi: 10.1121/1.1907229.
- [6] T. Görne, *Tontechnik: Schwingungen und Wellen, Hören, Schallwandler, Impulsantwort, Faltung, Sigma-Delta-Wandler, Stereo, Surround, WFS, Regiegeräte, tontechnische Praxis*, 1st ed. München: Hanser, Carl, 2011. [Online]. Available: <http://www.hanser-elibrary.com/action/showBook?doi=10.3139/9783446427402>
- [7] MATLAB, *xcorr: Cross-correlation*. [Online]. Available: https://www.mathworks.com/help/releases/R2020b/matlab/ref/xcorr.html#mw_01b546db-b642-4f02-8625-16078810d80f (accessed: Apr. 27 2021).
- [8] RME, *Octamic XTC: User's Guide*. [Online]. Available: https://www.rme-audio.de/downloads/octamicxtc_e.pdf (accessed: May 14 2021).
- [9] M. Zollner, "Einfluß von Stativen und Halterungen auf den Mikrofonfrequenzgang," Institut für Elektroakustik, Technische Universität München, München, 1982.
- [10] M. Zollner and E. Zwicker, *Elektroakustik: Mit 13 Tabellen*, 3rd ed. Berlin: Springer, 2003.

Ultra Low Noise Amplifier for a Noise Measurement System

Raphael Lukas

Deggendorf Institute of Technology
94469 Deggendorf
Email: raphael.lukas2@stud.th-deg.de

Josef Kölbl

Deggendorf Institute of Technology
94469 Deggendorf
Email: josef.koelbl@th-deg.de

Michael Kufner

Deggendorf Institute of Technology
94469 Deggendorf
Email: michael.kufner@th-deg.de

Abstract—This paper shows a ultra-low-noise amplifier for low frequency measurement applications. Due to its ultra low noise density of $0.42 \frac{nV}{\sqrt{Hz}}$ in a bandwidth up to 500 kHz it is capable to measure even the lowest noise opamps like the AD797 from Analog Devices [1]. It is a modification and optimization of the amplifier introduced by Charles Wenzel [2], which had a voltage noise density of $<1 \frac{nV}{\sqrt{Hz}}$. To display the measurement results a high quality USB sound card and the software from Prof. Thomas Baier "AudioMeter" [3] is needed.

I. INTRODUCTION

Low noise amplifiers are employed in many applications where signal and noise can hardly be distinguished. Examples include applications like non contact capacitive sensors to measure displacement, distance and position, as well as thickness, optical receivers in laser range finder applications, sensitive microphones to detect high frequency audio signals and many more. Hence amplifiers with low noise densities are required. An example for an amplifier in the regime we are talking about is the AD797 from Analog Devices with a voltage noise density of $0.9 \frac{nV}{\sqrt{Hz}}$ at $f = 1 \text{ kHz}$ [1]. This setup is specifically designed to measure these kind of amplifiers voltage noise density.

II. SETUP

To measure amplifiers with this low voltage noise densities, the setup needs a even smaller voltage noise density in the desired frequency bandwidth.

This setup is capable of measurements up to 500 kHz. In Fig. 1 the block diagram of the measurement setup is shown. This topology is an amplifier introduced from Charles Wenzel and modified by Bernd Kaa [4]. The peculiarity here is, the use of four low noise JFETs in parallel which will lead to a reduced voltage noise density given by eq. 1. This shows, that the number of parallel JFET's n will reduce the voltage noise density by the reciprocal square root of n in theory.

$$e_n = \frac{1}{\sqrt{n}} \cdot \sqrt{\frac{8 \cdot k_B \cdot T}{3 \cdot g_m}} \quad (1)$$

Where k_B is the Boltzmann constant, g_m is the transconductance of the transistor and T the absolute temperature in Kelvin. The JFETs are cascaded with an opamp, the already mentioned AD797, this will reduce the noise of the opamp drastically. With a feedback resistor to the source of the JFETs,

a gain of 30 dB is set. A second opamp with 30 dB gain works as driver for the output to the high Z input of a sound card or even the 50Ω input of a spectrum analyzer. Important here is to use an opamp with an adequate gain-bandwidth-product (GBP), like the NE5534A, to get the bandwidth up to 500 kHz. The second opamp needs no special requirements regarding low noise. Important is also the resistor technology, metal-thin-film resistors generate lower voltage noise than normal thick-film resistors. For the power supply a regular laboratory power supply is not suitable, because it's way to noisy. Instead we use rechargeable lithium batteries for the $\pm 9 \text{ V}$ supply voltage, here it is not very important, that the voltages of the two batteries are identical. As a sound card the 0204 USB Audio Interface from E-MU is used, because this has no internal low pass filter at 20 kHz as most of the modern sound cards have. Hence signals up to $f_s = \frac{f_{s\text{max}}}{2} = 96 \text{ kHz}$ can be measured and displayed via the software DG8SAQ AudioMeter [3].

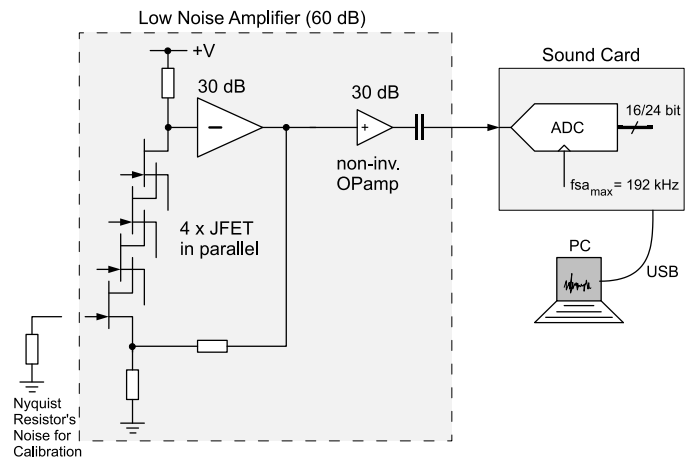


Figure 1. Block diagram of the measurement setup; on the left side the amplifier circuit inside an extra case, on the right side the connected sound card

III. SETUP ANALYSIS

The Gain curve in Fig.2 was measured with a vector-network-analyzer (VNA) from Rohde & Schwarz, the ZNB8. The gain has a mean value of 60.5 dB up to 100 kHz. The 3-dB-bandwidth is somewhere between 500 kHz and 600 kHz, which is sufficient for most measurements in this topic. Figure

3 shows the short-circuit input RMS noise voltage spectral density, the mean value up to 100 kHz is about $0.42 \frac{\text{nV}}{\sqrt{\text{Hz}}}$. This was measured with the Rohde & Schwarz spectrum analyzer FSP on the output and a short circuit plug on the input of the amplifier. Unfortunately the measurement devices start to work from a few kHz which is too high to see phenomena like the $1/f$ noise (flicker noise).

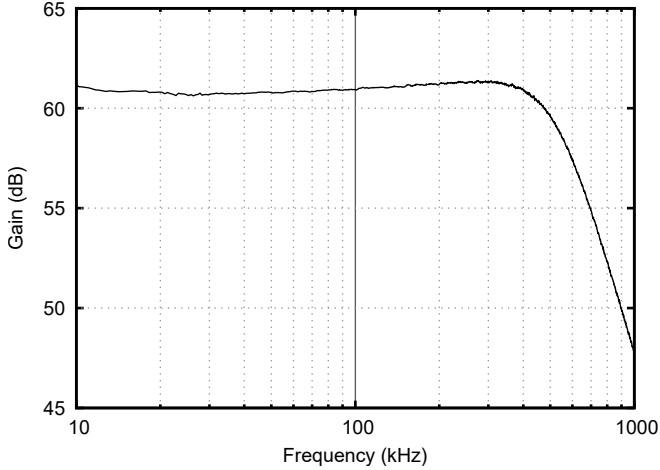


Figure 2. Determined gain curve of the low noise amplifier, measured with the ZNB8 vector-network-analyzer from Rohde & Schwarz.

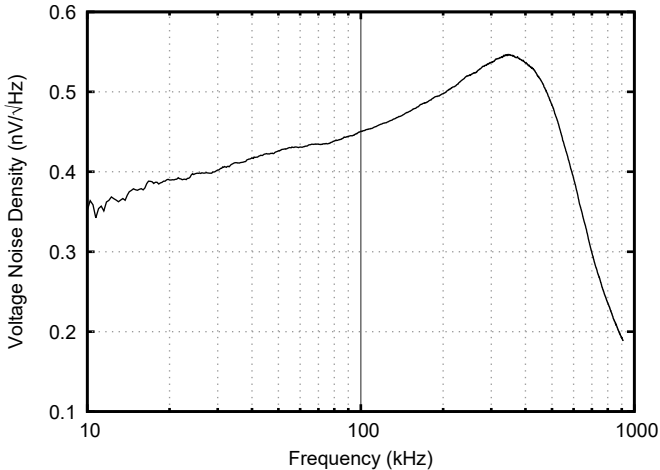


Figure 3. Equivalent short-circuit input RMS noise voltage spectral density, determined with a short circuit on the input of the amplifier and measured with the FSP spectrum analyzer from Rohde & Schwarz

IV. 1/F NOISE

The $1/f$ noise phenomenon is not only a serious problem in audio products. It is also of importance in RF circuit applications like in amplifiers and especially in oscillators where it gives rise to single sideband phase noise in signal sources. Although the $1/f$ noise is low frequency in nature, the process in nonlinear semiconductor devices like transistors and diodes is such, that the $1/f$ low frequency shape is inherently mixed-upwards (ie. up-converted) onto the high frequency carrier at,

say, GHz regime. Ultimately, it appears as phase noise skirt equally folded two-sided around the carrier as sidebands, even though it was low-frequency in origin. The $1/f$ power spectral density is due to tiny fluctuations of DC current observed in electronic semiconductor devices at low frequencies, known as $1/f$ flicker noise. These fluctuations of the number of carriers and mobility fluctuation in the semiconductor material are due to trapping/de-trapping of carriers in semiconductor devices. Hence, charge trapping and de-trapping is the main physical reasoning for $1/f$ noise. In general, one can think of small on/off current flowing pulses due to impurities in the semiconductor generation/recombination process. Now, when transforming an impulse shape from time domain into the Fourier domain, a spectral envelope of $1/f$ shape is obtained. Upscaling many pulses, a pronounced $1/f$ rise is seen, merging with a flat $1/f^0$ white noise region. On an oscilloscope, however, the flat white noise appears as smooth and Gaussian distributed, whereas the $1/f$ noise is rather jumpy (recall the comparison with making popcorn)[5]. In many cases the $1/f$ noise has some kind of pronounced bulge in the frequency plot which transforms into random noise pulses in the time domain, so-called random telegraph noise (RTN) or random telegraph signal (RTS) [6]. Hence, $1/f$ noise is also a quite effective indicator of material process quality. Hence we measure with a sound card, instead of the spectrum analyzer, which can measure up from a few Hz.

V. SETUP VERIFICATION

The sound card is not able to measure any absolute values, hence it has to be determined with calibration measurements. This is done with two different measurements, one with a short circuit and one with a 50Ω resistor on the input. As seen in Fig. 4 the floor of the short circuit is at around -104 dB and for the 50Ω around -96.5 dB. Hence the 50Ω resistor adds 7.5 dB of thermal noise which is calculated in eq. 2 for a 1 Hz measurement bandwidth.

$$E_{n_{50}} = \sqrt{4 \cdot k_B \cdot T \cdot R} \quad (2)$$

$$E_{n_{50}} = \sqrt{4 \cdot k_B \cdot 295 \text{ K} \cdot 50 \Omega} = 0.90 \frac{\text{nV}}{\sqrt{\text{Hz}}}$$

With the value from eq. 2, the voltage noise density E_{ni} of the amplifier can be verified, see eq. 3. This is because the measured value of -96.5 dB, with the 50Ω resistor, is the RMS noise of the actual resistor noise and the noise of the amplifier itself at 0Ω input is

$$E_{ni} \cdot 10^{\frac{7.5}{20}} = \sqrt{\left(0.90 \frac{\text{nV}}{\sqrt{\text{Hz}}}\right)^2 + E_{ni}^2} \quad (3)$$

$$E_{ni} = 0.42 \frac{\text{nV}}{\sqrt{\text{Hz}}}$$

Further evaluation of the system was done with several resistors, the voltage noise densities shown in Table I are the RMS values of the actual resistor noise and the noise of the amplifier itself at 0Ω . With this calibration the setup is completely determined and ready for measurements.

Resistance	Plateau	Diff. to 0Ω	RMS Voltage Noise Density
0Ω	-104 dB	0 dB	0.42 $\frac{nV}{\sqrt{Hz}}$
50Ω	-96.5 dB	7.5 dB	0.99 $\frac{nV}{\sqrt{Hz}}$
75Ω	-95 dB	9 dB	1.18 $\frac{nV}{\sqrt{Hz}}$
90Ω	-94.3 dB	9.7 dB	1.28 $\frac{nV}{\sqrt{Hz}}$
200Ω	-91.1 dB	12.9 dB	1.85 $\frac{nV}{\sqrt{Hz}}$

Table I

MEASUREMENT RESULTS FOR MULTIPLE RESISTORS ON THE INPUT OF THE SETUP

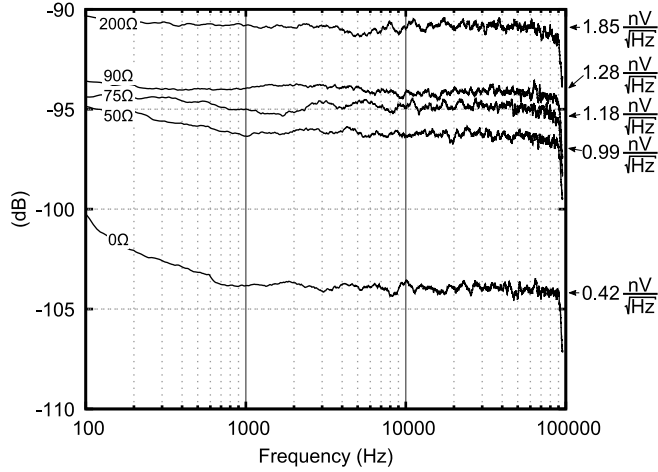


Figure 4. Relative voltage noise densities of multiple measured resistors, absolute values are determined by calculating.

VI. MEASUREMENTS

To start the measurement, the calibration has to be done with the 0Ω and the 50Ω resistors, Fig. 5. The different scale compared to Fig. 4 comes from slightly different settings, like averaging, internal gain, etc., of the sound card. The JFET was measured in a biased condition as a common source amplifier. To get the input voltage noise density of the JFET the measured data has to be corrected by the gain of the common source amplifier. Figure 5 shows the measured data (Noise JFET) and the corrected data (gain corrected Noise JFET), whilst the input of the transistor is shorted.

With the calibration, the gain corrected voltage noise density at 100 kHz of the JFET can be calculated to

$$E_{JFET} = \sqrt{\left(10^{\frac{10}{20}} \cdot E_{ni}\right)^2 - E_{ni}^2} \quad (4)$$

$$E_{JFET} = 3 \cdot E_{ni} = 1.26 \frac{nV}{\sqrt{Hz}}$$

and at 10 kHz to

$$E_{JFET} = \sqrt{\left(10^{\frac{13}{20}} \cdot E_{ni}\right)^2 - E_{ni}^2} \quad (5)$$

$$E_{JFET} = 1.83 \frac{nV}{\sqrt{Hz}}$$

As seen in eq. 4 and 5 the input noise voltage densities of the transistor need to be corrected by the internal noise $E_{ni} = 0.42 \frac{nV}{\sqrt{Hz}}$ of the system. This leads to a new y-axis in Fig. 5, which starts at $0.0 \frac{nV}{\sqrt{Hz}}$ for the 0Ω measurement. This is done to see directly the absolute voltage noise density of the transistor, without any influence of the measurement system. The flicker corner frequency of this JFET is estimated to be between 3 kHz and 4 kHz.

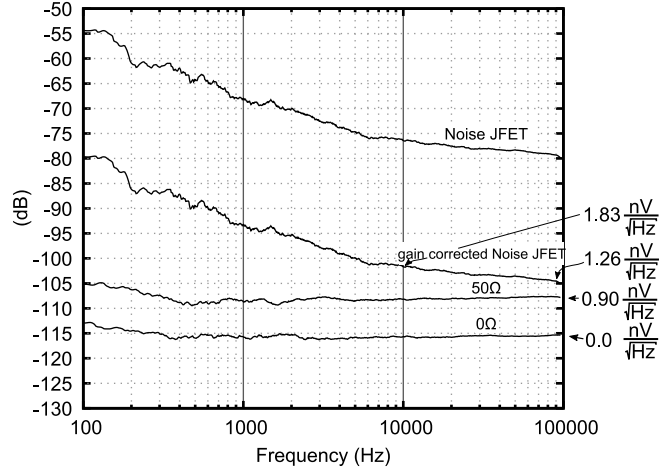


Figure 5. Measurement of the voltage noise density of the calibration resistors 0Ω and 50Ω to determine the voltage noise density of the JFET. Only the curve "Noise JFET" was measured, the "gain corrected Noise JFET" was added after correction.

VII. MEASUREMENT SETUP

In Fig. 6 the measurement setup with the sound card and the used resistors is shown.

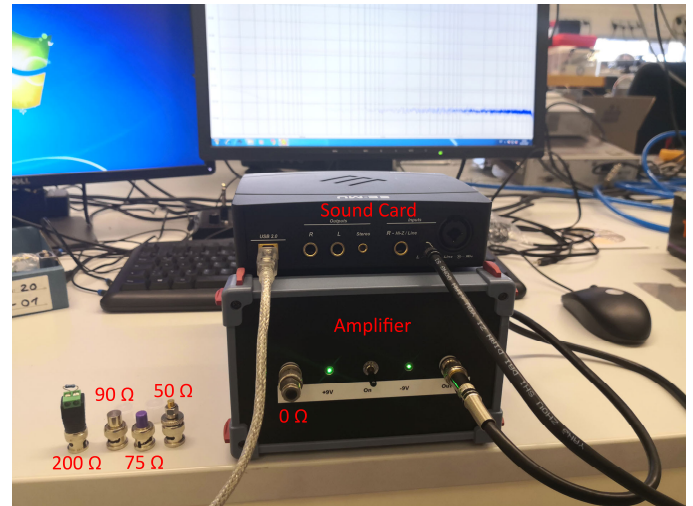


Figure 6. Measurement setup, on the front panel is a switch to power the amp, two LED's to indicate that the system is on and the batteries provide plus and minus 9 V and two BNC connectors for the input and output. The amplifier and the sound card are connected together via a BNC to 3.5 mm Jack plug, additionally the sound card is connected to a PC via USB.

	This Work	[1]	[7]	[8]	[9]	[10]
Topology	JFET	OpAmp	-	-	JFET	Bipolar
Input voltage noise density ($\frac{nV}{\sqrt{Hz}}$)	0.42	0.90	0.67	0.90	< 1	0.70
Gain (dB)	60	adjustable	-	-	30 or 60	40 - 100
Bandwidth	0.1 Hz - 500 kHz	DC - 110 MHz	0.03 Hz - 1 MHz	0.1 Hz - 10 MHz	10 Hz - 1 MHz	DC - 100 kHz
Input Impedance	50 Ω or 1 M Ω	100 M Ω common	-	-	50 Ω or High-Z	1 M Ω

Table II

COMPARISON TABLE OF DIFFERENT LOW NOISE AMPLIFIER AND NOISE ANALYZER. DATA IS EXTRACTED FROM THE PRODUCT DATASHEETS

VIII. CONCLUSION

This work shows a very cost efficient measurement setup to determine ultra low voltage noise densities at frequencies from less than 1 Hz up to 500 kHz, see table II to compare it with other low noise amplifiers and noise analyzer. The used setup can be improved by selecting JFET's with the same Pinch-Off voltage, unfortunately this was not possible due to the poor availability of this JFET type.

REFERENCES

- [1] Product Datasheet AD797, Analog Devices, Inc.
- [2] C. Wenzel, "Low Noise Amplifier for Phase Noise Measurements," Wenzel Associates, Inc., Austin, Texas, USA, Date. Accessed: May 2021 [Online]. Available: <https://wenzel.com/wp-content/uploads/lowamp.pdf>
- [3] T. Baier, "DG8SAQ: AudioMeter-Software zum Messen mit der Soundkarte," (in German), FUNKAMATEUR, vol. 64, 10/2014, Germany, pp. 1078-1080
- [4] B. Kaa, "Sehr rauscharmer 60-dB-Verstärker - bis 500 kHz linear," (in German), FUNKAMATEUR, vol. 65, 10/2015, Germany, pp. 1076-1079
- [5] C. D. Motchenbacher and J. A. Connelly, "Kapitel," *Low-Noise Electronic System Design*, New York, NY, USA: John Wiley & Sons, Inc., 1993
- [6] G. Ghibaudo, T. Boutchacha, "Electrical noise and RTS fluctuations in advanced CMOS devices," *Microelectronics Reliability*, Volume 42, Issues 4-5, 2002, Pages 573-582, ISSN 0026-2714, doi: 10.1016/S0026-2714(02)00025-2
- [7] Product Datasheet E4727A(K03) LNA1, Keysight Technologies, Inc.
- [8] Product Datasheet 3002A, AdMOS GmbH
- [9] Product Datasheet LNAA, Wenzel Associates, Inc.
- [10] Product Datasheet DLPVA-100-BLN-S, FEMTO Messtechnik GmbH

“Applied error analysis on a research ORC Plant at the University of Bayreuth”

Jan Mišák

Faculty of electrical engineering, information technology and media technology
OTH Amberg-Weiden, Amberg, Germany
j.misak@oth-aw.de

Abstract—The errors in the measurement chains/technology while experiments are unavoidable. If errors are known, they can either be minimalized or be mathematically considered. The only possible way of measuring with no error is the hypothetical way by considering infinite number of tests. This paper shows the methods of error analysis and error calculation as well as the hypothesis test on the example of the ORC (Organic Rankine Cycle) research plant. Also, the criticisms on the existing methods will be presented. ORC systems are a widespread technology for recovering the (waste) heat in the form of residual heat from manufacturing processes or from renewable energy sources, such as geothermal energy. In this publication, the main point of interest lies on the efficiency of the ORC Turbine.

Keywords—error analysis, measurement technology, Gaussian error calculation, Design of Experiments

I. THE AIM OF THE RESEARCH PLANT

The experimental ORC (Organic Rankine Cycle) research plant was built in the year 2011 in scope of the common BFS (Bayerische Forschungsstiftung) project “Mini ORC-Kraftwerk” of the OTH Amberg-Weiden, the University of Bayreuth and the DEPRAG SCHULZ GMBH u. CO company. The research plant has been involved in many research projects. Currently, the aim of the plant is the examination of ORC-micro turbines with special focus on turbines with automatic mass flow adjustment. Those ORC turbines are being used for the utilization of the residual heat, for instance from manufacturing processes or as a second-grade turbine in the steam power plant for converting heat energy into electric energy. The micro-organic vapor cantilever turbine as the expansion machine achieves power up to about 12 kW at the design point. The working medium of the research plant is the MM – Hexamethyldisiloxane [1].

II. THE TECHNICAL PRINCIPLE OF ORC

A. Technical Basics

Organic Rankine Cycles (ORC) basically work on the same principles as steam Rankine cycles. The difference is the used organic working medium instead of steam. Those organic mediums have lower boiling temperatures than water (at the same pressures), which makes the exploitation of “cold” residual heat sources possible. For generating electricity, the sources with a temperature of 80°C and more can be used. Colder sources can only be used for heating purposes.

B. Applications of ORC

ORC power plants represent an alternative to steam power plants. The application of ORC power plants is combined with decentralized energy supply, which also means that the achievable amount of energy is much smaller compared to a central steam powered power plant. ORC plants will then be used when the disposal heat is not sufficient for driving a steam turbine. Besides the residual heat from manufactures, the ORC will be used combined with geothermal heat or solar heat for the generation of electricity [1].

III. COMPOSITION OF THE RESEARCH PLANT

The ORC research plant basically consists of four main sectors shown in the figure 1. Every sector is equipped with sensors for determination of physical quantities.

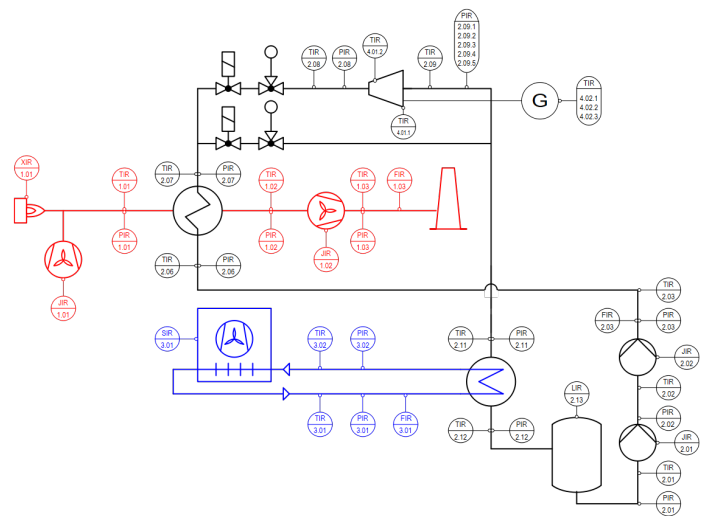


Figure 1. The scheme of the ORC research plant

A. Heat generation (in red)

Firstly, the red colored heating line includes a propane gas burner for the generation of heat for the evaporator supported by one draft fan and one suction fan.

B. The main process circuit (in black)

The main circuit is filled with MM which will be pumped around by two in series arranged pumps. After the evaporator (Plate & Shell type heat exchanger), the vapor state MM with 6 bar pressure drives the experimental Quasi-Impulse Cantilever turbine with a generator and its power feedback unit. After that, MM will be condensed to the liquid state and the circular process starts again.

C. Working medium cooling circuit (in blue)

The blue line is the cooling circuit. This should cool the working medium (air cooling) downstream the turbine through a plate heat exchanger and bring it to the liquid state again. The residual heat is rejected to the environment.

D. Other components

To be able to ensure constant conditions of the mechanical parts of the turbine, the bearings of the turbine will be kept at constant temperature of around 140°C. This is performed by an external heating/cooling unit.

IV. THE ERROR ANALYSIS

A. Error Sources

The error analysis starts with the analysis of the system and its possible sources of errors. The most important points are errors caused by the deviations of the measurement technology. Those errors cannot be avoided – they can only be minimized by more accurate sensors and evaluation units. The deviations of the measurement technology are basing on the random physical-natural effects. The manufacturer always specifies the accuracy of the technology. This is the maximum deviation that can occur. If we can determinate the real deviation which is always smaller, for instance by calibration with more accurate test device, we can use this real deviation for the error calculation. Furthermore, it is necessary to ensure that the research plant is free from systematic errors, for instance errors in the constructions as leakages or sensors with insufficient measuring range. If systematic errors occur, the generated data is unusable. Systematic errors can only be discovered when the testing parameters change. The last possible issue is the wear of mechanical parts or even of the measurement technology. Those issues can be solved if they are known by renewed calibration or by replacement of the worn part. One of the greatest additional impacts is in fact the user/operating staff [2].

B. The aim of the error analysis

The error analysis always has a goal. Besides the fact that there are no systematic errors, the main goal is specification of the deviation of the turbine efficiency. The focus is aligned on the maximum possible deviation called the Gaussian uncertainty as well as the real deviation which is given by the standard deviation of the measured values. Secondly, the deviations of all other parts will be determined.

C. Acquisition of the measurement data

If it is assured that there are no systematic errors and that the measurement technology is properly calibrated and in good condition, the generation of data can be performed. If possible, there should always be the same number of tests in every setting performed. This is advantageous, because especially the variance and the standard deviation can be directly compared. Even the subsequent analysis of variance can be performed with lower effort. The aim should be to eliminate all of the above-mentioned disruptive factors. Occurring events are always to be noted. The most interesting data are the measurements on the turbine itself. Those will be performed by the technology listed in the table I.

Table I
MEASUREMENT TECHNOLOGY

Function	Name	Accuracy	Range
Pressure bef. Turbine	Omega PAA23 SY-C-10-M12	1.5% of end-value	0-10 bar
Pressure aft. Turbine	Omega PAA23 SY-C-2-M12	1.5% of end-value	0-2 bar
Temperature bef. Turbine	Omega M8M	0.2% of measured value ±0.05% of end-value	0-350°C
Temperature aft. Turbine	Omega M8M	0.2% of measured value ±0.05% of end-value	0-350°C
MM Massflow	ABB FCB 350	0.4% of measured value	0-417 g/s
Turbine Power	Electricity Gegerator	0.45% of measured value	0-20 kW

Deviations always have reference points around which they vary naturally, called the true value. True values can either be defined as a constant or as average value of several test runs. The more values are taken into account for the average value the lower the uncertainty will be. The smaller the uncertainty the more credible is the true value [3]. The pressure behind the turbine is determined by three pressure tapings: two of them placed in the wall of the tube and a third in its centre. At this point, the Gaussian error calculation must already be applied, because the final pressure value downstream of the turbine is an average value of several sensors, each of which including a deviation. The final value will be calculated according to the formula:

$$p_{final} = \frac{p_1 + p_2}{2} + p_3 \quad (1)$$

According to the Gaussian error calculation the deviation of every sensor adds. In this case the total deviation is even smaller than the deviation of one sensor itself and amounts to 0.92% of the end of range-value of 2 bar. The turbine power will be determined by the generated electric power. The evaluation of the turbine power depends on a calibration curve of the generator and its frequency converter which

was performed by a third-party company. The measurement deviation of the generator was retrospectively calculated according to the permissible deviation of the technology which was used for the determination of the calibration curve. The result of this calculation is the maximal deviation of 0.45% of the measured value. The experimental turbine will be tested at speeds between 15,000 and 29,000 RPM and mass flows between 152 to 336 g/s. Every point of setting will be tested for approximately 15 minutes with a settling time of 5 minutes. The last field of errors is the calculation of thermodynamical quantities using REFPROP 9.1 [8] database. The deposited material values have an average deviation of about 0.75% [4]. This error factor will be taken out from the calculation because it cannot be precisely quantified. The error of the electrical evaluation parts like PC interface is negligible small and will even not be taken into account.

D. Using of Design of Experiments

The methods of Design of Experiments (DoE) considering the influences of factors on the target value are basically not suitable to the error calculation but can be very helpful during the error analysis. The challenge in using DoE in the error calculation is the fact that one of the most important requirements cannot be given: to be able to adjust the factors. The deviation varies naturally without adjustment options. On the other side DoE is helpful while determining the significant factors, which means factors that influence the result the most. Even the method of randomizing is helpful by driving test runs. Randomizing means that the order of the runs with different settings will be defined randomly. This method reduces the risk of random effects [2]. The measurements on the research plant were not performed corresponding to any DoE test plan. In this case it will be called a random test plan which depends on the user. Even on those plans the control procedures which will be introduced in the following chapter of DoE can be performed.

V. THE ERROR CALCULATION

A. Evaluation of measured data

The first point of the data evaluation is the check of the distribution of data in MS Excel. The requirement for proceeding the error calculation is that the data is distributed naturally. This means that every value occurs with the same probability. If this requirement is met, the error calculation can begin. If not, there are a couple of alternative methods:

- The addition of not normally distributed value series leads to normal distributed results.
- Also, an approximation of normal distribution leads to useful results.

A one-sided distribution of values means there are non-random effects which impact the result [5]. Another reason can be that the number of test runs is too small, which means that some values have not occurred yet, but they will when being measured with the same settings [3]. There are two issues concerning the normal distribution. Firstly, there is no exact

rule for the number of values. Strictly speaking, the infinite amount of data must be tested. In the real-world it will only be calculated with samples. Samples should depict the whole population [6]. There is no exact method of proving how accurate this depicting happens. Reliable results will usually be reached through tests with 200 runs or more. Secondly, the distribution test counts as hypothesis test. Hypothesis tests always need a definition of permissible risk. This definition is mostly 5% and is defined as an experience value. There are no calculations behind this value, only a hypothesis [5]. The last important rule during the evaluation of data is that it is forbidden to take out certain values, for instance those that do not fit the expectations. When the scope of the samples that are to be evaluated has to be reduced, it can only be done following the random principle [2]. In the case of this research plant always 10 to 20 measuring points are made. An exact number of values for a run cannot be adjusted because of the evaluating software. The number of measurements must always be considered. It also means that every point of settings has another uncertainty of the average value.

B. The Gaussian error calculation

The Gaussian error analysis considers the addition of single errors of calculated values. It is also known as the Gaussian uncertainty of values. If the maximum deviations (given by the manufacturer) of the single factors will be used, the result is the maximum deviation that can occur. If the average value and standard deviation of every factor will be used, the result is the real Gaussian uncertainty. This value is mostly similar in magnitude with the standard deviation of the calculated value [6]. If the real deviation is bigger than the maximum, there is an systematic error. To be able to perform the Gaussian error calculation it is necessary to know the physical relationship – the formula. This will be derived and worked up according to:

$$\Delta Y = \sqrt{\left(\left(\frac{\delta y}{\delta x_1}\right) + \Delta X_1\right)^2 + \dots + \left(\left(\frac{\delta y}{\delta x_k}\right) + \Delta X_k\right)^2} \quad (2)$$

The formula for the calculation of the turbine efficiency is:

$$\eta = \frac{P}{\dot{m} * \Delta h} \quad (3)$$

The turbine power P and the mass flow m are directly provided by the generator, respective mass flow sensor. The enthalpy drop Δh will be calculated based on temperatures and pressures in the REFPROP software version 9.1. The measurement is also burdened with four sources of error ΔX which must be considered:

- power measurement (0.45% of measured value)
- mass flow measurement (0.4% of measured value)
- temperature and pressure sensors (1 – 2.5% of measured value depending on the measuring point)
- error of REFPROP's fluid properties (up to 0.75%, will be left off)

After the derivation and deployment, the result is a maximum deviation ΔY of around 1.05 percentage points of the turbine efficiency in the design point. Figure 2 shows that the extreme deviations as well as the real measurements represented by blue triangles.

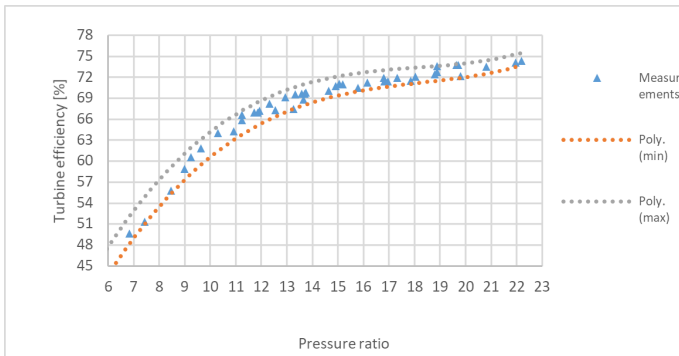


Figure 2. The error limits of the turbine efficiency compared to the real measured data

C. The real error

As described in the previous chapter, the maximal error has to be compared with the real error. To keep the evaluation simple, the real error will be represented with the standard deviation of the turbine efficiency. This presumption can be made if there is a significant difference between the real and the maximum error. In case that it does not, the Gaussian error for the real measurements has to be performed, because it is the more accurate method. The average real error represented by the standard deviation is 0.13 percentage points. The maximum is about 0.41 percentage points. That means the calculation of the real Gaussian uncertainty is not necessary. The difference between the standard deviation and the real Gaussian uncertainty is around 5 – 10%. The figure 3 shows the trend of the standard deviations depending on the rotational speed for different days. The standard deviation is given with the accuracy of 2σ , which means a probability of 95%. It can be seen that the maximum deviation is much smaller than the acceptable one. There was a presumption that the speed of the feed pumps has an impact on the trend and causes the fluctuations on January 14th and January 28th. The analysis of regression has shown that there is no ascertainable connection.

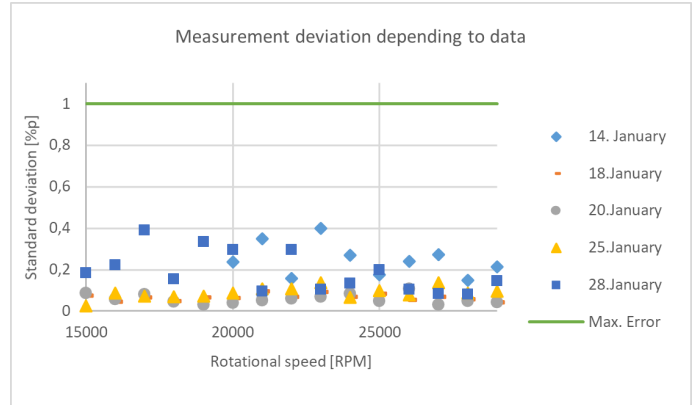


Figure 3. The standard deviations of turbine efficiency per measuring day

As can be seen, the measurement technology is performing much more accurate as it have to. Even the deviation of the single sensors is fortunately much smaller than acceptable. This presents the figure 4.

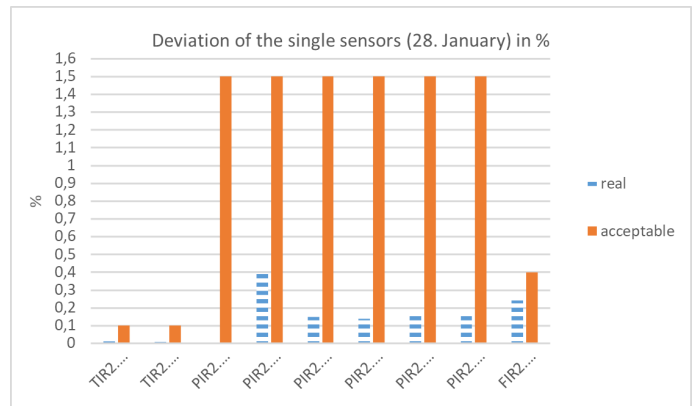


Figure 4. The deviation of the measurement technology

The same investigation was performed for the evaporator. Its real error is about 1 percentage point while the maximum one is 2,5 percentage points of the efficiency. A necessary part of every result is the definition of the uncertainty u which depends on the standard deviation σ , the number of measurements N and the Student factor t , which can be found in tables or automatized in MS Excel.

$$u = \frac{\sigma}{\sqrt{N}} * t \tag{4}$$

The average uncertainty of measurement is 0.034 percentage points of the measured turbine efficiency.

D. Validation of the results

During the evaluation of data, there is always a possibility of the certain results arising only randomly. MS Excel offers several tools like the T-test, F-Test or ANOVA that can be used for simply data analysis. Basically, the function of those proceeds is making a statement about the existence of any correlations behind those values or a random appearing [7]. All of these methods base on the hypothesis test which implies a probability that values came up randomly with a risk of fail of 5%. This means that all statements are valid with a probability of 95%. The data analysis has shown that there are no significant differences between the measuring days apart from January 14th and January 28th. In the case of these two days there are significant differences as well between the date as the rotational speed. Because of the deviation, which is much smaller than the acceptable one, even those values are valid. Analysis of variance basically checks if the measured values from one run with the same setting are significantly different. The presumption is that when the data comes from the same measurement, in fact they should have the same standard deviation, respectively variance which is defined as square of the standard deviation [5]. The advantage of the variance compared to standard deviation is the lack of unity.

VI. CRITICISM ON THE ERROR CALCULATION

Basically, the error calculation is contestable because of the fact that all performed calculations are associated with a risk. Even the average value of several measurements is an estimated value as well as the uncertainty. Even the uncertainties or standard deviations are uncertain as well [7]. To solve this problem, it must be calculated with infinite number of values, which cannot be performed in the real-world usage. The error calculation is not an exact science. The next point of criticism are the controlling methods like analysis of variance. All the hypothesis test basing methods are using a manually chosen risk [7]. That means it is relative what is significant and what is not. Despite criticism of the method, there are still no more precise procedures.

VII. SUMMARY OF THE MEASUREMENT RESULTS

It has been proven that the ORC research plant enables high quality measurements on experimental turbines. With the probability of 95% the measurements will be performed with an average deviation of turbine efficiency of 0.13 percentage points and the uncertainty of the average value of 0.034 percentage points.

REFERENCES

- [1] T. Popp, F. Heberle, A. P. Weiß, D. Brüggemann, "THERMODYNAMIC EVALUATION OF AN ORC TEST RIG - FROM COMPREHENSIVE EXPERIMENTAL RESULTS TO A SIMULATION MODEL UNDER CONSIDERATION OF PART-LOAD CHARACTERISTICS: Paper submitted for publication at the:"currently under review", ZET Bayreuth, Bayreuth, 2021.
- [2] K. Siebertz, D. van Bebber, and T. Hochkirchen, *Statistische Versuchsplanung*. Berlin, Heidelberg: Springer Berlin Heidelberg, 2017.
- [3] H. Schmid, "Stochastische Prozesse," Amberg, 2019
- [4] P. Colonna, N. R. Nannan, A. Guardone, and E. W. Lemmon, "Multiparameter equations of state for selected siloxanes," *Fluid Phase Equilibria*, vol. 244, no. 2, pp. 193–211, 2006, doi: 10.1016/j.fluid.2006.04.015.
- [5] T. Cleff, *Deskriptive Statistik und moderne Datenanalyse*, 2. Auflage: Gabler, 2012.
- [6] M. Grabe, *Grundriss der Generalisierten Gauß'schen Fehlerrechnung*. Berlin, Heidelberg: Springer Berlin Heidelberg, 2011
- [7] J. Puhani, *Statistik*. Wiesbaden: Springer Fachmedien Wiesbaden, 2020
- [8] E. W. Lemmon, M. L. Huber and M. O. McLinden, "NIST Standard Reference Database 23: Reference Fluid Thermodynamic and Transport Properties-REFPROP, Version 9.1," [online], <https://www.nist.gov/publications/nist-standard-reference-database-23-reference-fluid-thermodynamic-and-transport>.

High-speed ADC Data Acquisition with an FPGA for OTDR-based Fiber Sensors

Fabian Morf, Juri Vinogradov, Flaviu Nopp-Nowak, Rainer Engelbrecht
 Polymer Optical Fiber Application Center,
 Technische Hochschule Nürnberg Georg Simon Ohm
 Wassertorstraße 10, 90489 Nuremberg, Germany.
 Corresponding author: morffa69345@th-nuernberg.de

Abstract—Polymer optical fibers (POF) are to be used as strain sensors in geogrids in structural health monitoring. For this purpose, special OTDR measurement devices are needed that cost less than 3000 €. These devices provide a measurement result in less than 5 seconds and have a good spatial resolution. For this application, OTDR measurement values are acquired with a high-speed analog-digital-converter (ADC) and processed with an FPGA. In this paper the concept is shown, and the first steps of the development are presented. For the first step an evaluation board from Analog Devices Inc. and a development board from Intel Corporation are used.

Keywords—FPGA, OTDR, analog-to-digital converter, optical sensor, high-speed measurement data acquisition

I. INTRODUCTION

Geogrids (Fig. 1) are used for stabilizing structures in buildings and earthworks, for example against sinkholes. Here, the geogrid is a static load-bearing member. Since it is not completely predictable how the soil will behave or change, it may be important from an engineering point of view to perform a structural health monitoring. A polymer optical fiber (POF) can be used for monitoring. The POF is woven into a geogrid and installed in the soil.[1]



Fig. 1. Geogrid and sinkholes [1]

To evaluate along the POF the strain distribution or damage, a measurement device injects a light pulse into it and the backscatter is measured. The geogrid is stretched into varying degrees depending on the soil movement. This causes the light to be backscattered differently, depending on the intensity of the stretching. For structural monitoring, it is important to perform a spatially resolved strain measurement to locate critical areas. For this purpose, the optical time-domain reflectometry (OTDR) measurement method is used. As a basis for a field application, a special adapted OTDR hardware is required that significantly reduces the costs and the measurement time for fiber optic strain sensors. For this purpose, the hardware or the measuring device should have a high measurement rate. In addition, for critical areas of railroads or dikes, many OTDR devices are needed as the length of one fiber is limited to 300 m due to high attenuation. Commercially available OTDR measurement devices for POF are usually based on the effective photon-counting technique but cost

more than 30000 € and the measurement time takes longer than 10 minutes. Therefore, this project will develop a measurement device that evaluates a POF sensor under 5 seconds and costs under 3000 €.

II. BASICS OF OTDR

OTDR is used as a standard measurement method to examine the optical fiber. A short light pulse is generated by a laser and injected into the fiber.

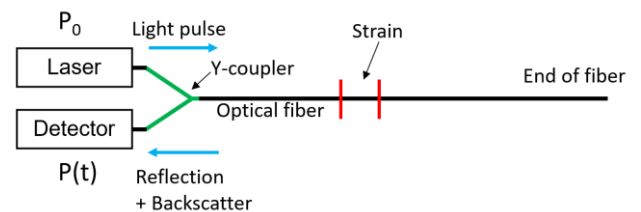


Fig. 2. OTDR-setup

Due to inhomogeneous material, a part of the light is backscattered to each point of the fiber. This is the so-called Rayleigh backscatter. The power of the backscatter is measured as a function of time. To apply the backscatter along the fiber as sketched in Fig. 3, the time stamps are halved and multiplied by the group velocity. The group velocity is the speed of light c_0 divided by the effective refractive index n_{eff} of the POF.

$$z = \frac{t}{2} \cdot \frac{c_0}{n_{eff}} \quad (1)$$

Usually, the backscattered power $P(t)$ is plotted in dB_{OTDR} , defined as:

$$\text{dB}_{OTDR} = \frac{1}{2} \cdot 10 \cdot \log\left(\frac{P(t)}{P_0}\right) \quad (2)$$

To measure the strain, the backscatter is measured, which is marked in red in Figs. 2 and 3. The intensity of the strain can be inferred from the height of the backscatter.

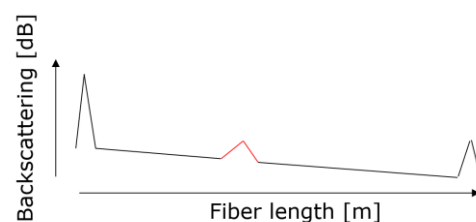


Fig. 3. OTDR-signal

In Fig. 3 the first peak is caused by the Y-coupler, the last peak is caused by the Fresnel reflection at the end of the fiber. The spatial resolution depends on duration t_p of the light pulse:

$$z = t_p \cdot \frac{c_0}{2n_{eff}} \quad (3)$$

A problem of the OTDR method is that the backscatter power is very low. The shorter the pulse, the less backscatter power arrives. [2]

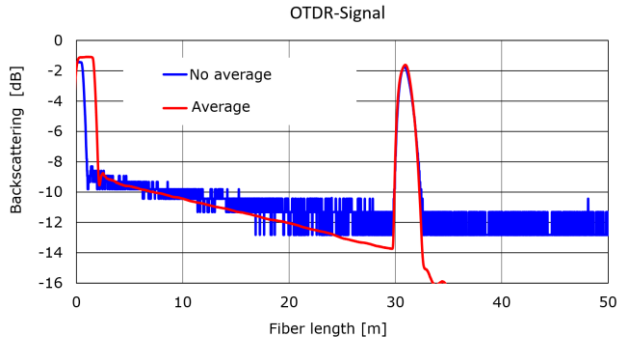


Fig. 4. OTDR-signal [3]

In Fig. 4 the blue graph shows a single shot measurement. Here the signal-to-noise ratio is very low. The red graph has been averaged with 2^{20} measurements, which is about one million measurements. This is necessary to detect strains by the end of the fiber.

III. MEASUREMENT DEVICE

The aim of this project is to measure the optical backscatter of a POF strain sensor (Fig. 5). The POF is connected to the laser diode and the avalanche photodiode (APD) via a Y-coupler. The laser diode converts the electrical pulse from the FPGA into an optical pulse. The APD is a fast and sensitive detector and contains an internal amplifier. It detects the power of the optical backscatter which takes place with an analog-to-digital converter with a sample rate of 1 GS/s and 14-bit word width. The large dynamic range is needed to capture the large power differences between discrete reflections at the fiber beginning and distributed backscatter at the fiber end due to attenuation. The samples of backscatters are read into an FPGA at high speed for storage and averaging.

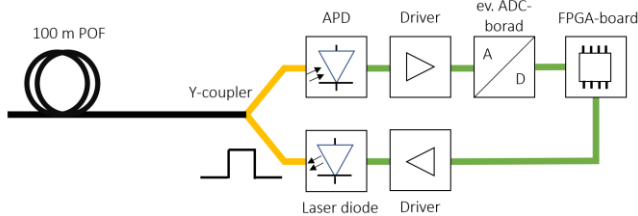


Fig. 5. Measurement setup

As shown in chapter II Fig. 4, single shots are very noisy. To get a good signal-to-noise ratio, 2^{20} single shots are averaged. The acquisition as well as the processing of the single shots should be under 5 seconds. For a 100 m POF, about one billion measurement values are processed. Furthermore, the pulse width is adjustable from 1 to 10 ns and the POF with a length of up to 300 meters can be evaluated.

The ADP and laser diode modules are already developed. Evaluation/development boards are used for data acquisition and processing. When the FPGA is configured and optimized, a PCB for an ADC and FPGA will be developed in the later development phase. For the acquisition of the analog backscatter the AD-FMCDAQ2-EBZ evaluation board (ADC-board) from Analog Devices Inc [4]. is used. The ADC-board includes an AD9680 [5] analog-to-digital converter (ADC) and an AD9144 [6] digital-to-analog converter (DAC). The AD9680 sample rate at 1 GS/s with a 14-bit word width has two inputs. The AD9144 has a maximum sample rate of 2.8 GS/s with a 16-bit word width and two outputs. The ADC inputs and DAC outputs are differential and are led out of the evaluation board as single-ended. For the high-speed measurement value processing the Arria 10 SoC Development Kit [7] (DevKit) from Intel Corporation is used. In this case, system on a chip (SoC) means that an Arria 10 FPGA and a microcontroller dual-core ARM Cortex-A9 MPCore Hard Processor System (HPS) are integrated on one chip.

IV. ARRIA 10 SOC DEVKIT

The FPGA is configured by Quartus Prime Pro 19.3 from Intel Corporation. It has to perform three main tasks: measurement configuration, pulse generation and processing the measurement values. The hardware project [8] is based on the project provided by Analog Devices Inc. The project of Analog Device Inc. stores the sampled data from ADC for the Cortex-A9. The modified Linux [9] operating system from Analog Device Inc. runs from it. In order to control ADC and acquire data Analog Devices Inc. provides software programs such as Libii [10] or IIO Oscilloscope [11]. Libii is a library that eases the development of software for interfacing Linux Industrial I/O (IIO) devices. It streams ADC data in the default settings. The Cortex-A9 is too slow for averaging about one million measurements. Therefore, the project from Analog Devices Inc. has to be modified so that it still configures the ADC, but the measurement values are captured on the FPGA side.

V. MEASUREMENT CONTROL UNIT

The measurement control unit links all modules such as processing of the measurement value or measurement configuration. The FPGA workflow algorithm is shown in Fig. 6. The start command is power on. The measurement configuration is organized like in a microcontroller via registers. In the register with the address 0x0002 for example the pulse width can be set. The register can be written and read via the protocol UART. The interface is designed to be used later by a microcontroller to set the measurement and query measurement results. This microcontroller is also responsible for evaluating the measurement. It is also possible to connect a PC. After power on the registers are set with their default values.

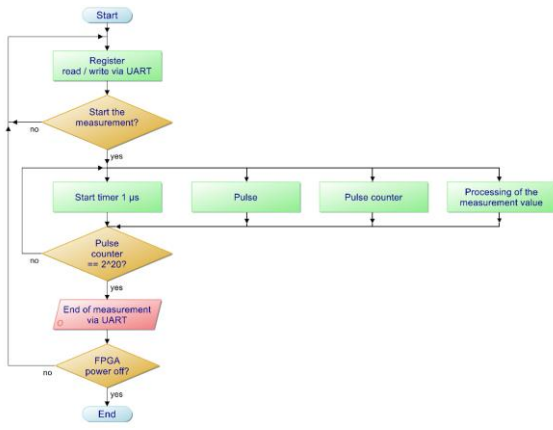


Fig. 6. Architecture of the FPGA algorithm

The measurement can also be started via the register. If the measurement is started, all 2^{20} single shots are cyclically acquired and processed. All blocks horizontal to each other in Fig. 6 are processed parallelly. There is a timer that counts $1 \mu s$ for the 100 m fiber. At the same time a light pulse is given to the fiber. The pulse counter is incremented. The measurement value processing unit receives the digitized power of the optical backscatter from the ADC and processes them. Afterwards it is checked whether the pulse counter contains the desired value, here for example it is 2^{20} . The number of the pulse counter corresponds to the number of single shots. If this number is reached, an end of measurement is sent via UART and the result can be queried via the register. If the number is not reached, the next single shot starts. The measurement device can be terminated with power off.

VI. MEASUREMENT VALUE PROCESSING UNIT

The measurement value processing algorithm calculates the arithmetic average of the single measurements. The FPGA works with whole numbers N_0 , therefore only the sum is formed in the FPGA and the word size is adjusted at the end.

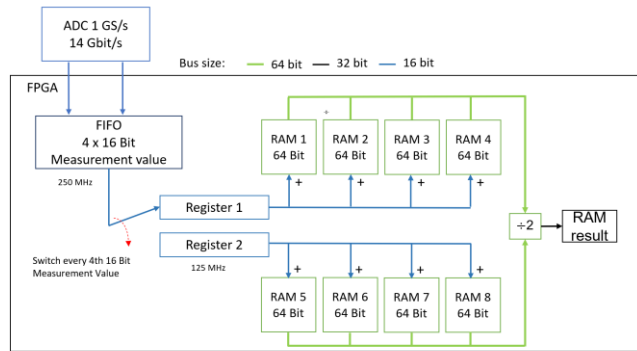


Fig. 7. Measurement value processing algorithm

The 14-bit measurement values of the ADC are transmitted to the FPGA. There, four measurement values are buffered and stored into the FIFO. The 14-bit measurement values are stored here in a 16-bit word size because the memory word size is always settable in two power sizes. Since four measurement values are always stored next to each other in the FIFO, the clock is halved. Thus, 1 GHz becomes 250 MHz. Now the measurement values are divided between register 1 and register 2. By splitting the clock can be halved again because while for example register 1 receives new data,

register 2 can pass on its data. Blocks are memories. In these all single shots are added and stored, that means the sum of all digitized power of the optical backscatter is calculated. With 2^{20} single shots (N) and an initial measurement size of 14-bits (w_{ADC}), the memory word size is 34-bits (w_r). The required word width should be 32-bits.

$$w_r = ld(N) + w_{ADC} \tag{4}$$

Therefore, the word width at the end is adjusted. Here the last two LSB are lost, mathematically the measurement result is divided by 2 without rest. By shifting a very small part of the accuracy of the measurement is lost, however, but it is possible to use a 32-bit bus size.

VII. MODIFICATION OF THE ANLAOG DEVICES INC. HARDWARE PROJECT

As discussed in chapter IV, the ADC is configured via Libiiio, and the ADC transmits the measurement values to the FPGA. Here, measurement values are buffered, processed in parallel and transferred to Linux. FPGA configuration is closely linked to the software. To further configure the ADC via software, it is important that the operation of the original project from Analog Devices Inc. is maintained. In the following, only the modification will be explained. Analog Devices Inc. has created their configuration in IPs. These are managed in Quartus Prime by the Platform Designer. The connection to Linux and FPGA is also configured via this tool. Three signals are needed to tap the measured values: data clock, data signal, write enabel. The util_ad9680_cpack IP gets the measurement values from both ADC channels and provides FIFO control signals for further processing of the measurement values (Fig. 8).

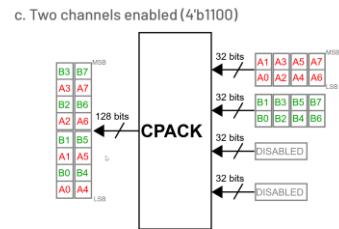


Fig. 8. CPACP IP [12]

It uses the signals `if_packed_fifo_wr_en` and `if_packed_fifo_wr_data`. Fig. 9 shows a cutout of the original Platform Designer. Inside the Platform Designer it is possible to export the signals to the FPGA side, but when a signal is exported it is no further possible to connect it to other IPs in the Platform Designer.

Name	Description	Export
util_ad9680_cpack	Channel Pack Utility v2	
clk	Clock Input	Double-click to export
reset	Reset Input	Double-click to export
if_packed_fifo_wr_en	Conduit	Double-click to export
if_packed_fifo_wr_sync	Conduit	Double-click to export
if_packed_fifo_wr_data	Conduit	Double-click to export
if_packed_fifo_wr_overflow	Conduit	Double-click to export
if_fifo_wr_overflow	Conduit	Double-click to export
adc_ch_0	Conduit	Double-click to export
adc_ch_1	Conduit	Double-click to export
ad9680_adciffo	UTIL ADC FIFO IP core	
if_adc_clk	Clock Input	Double-click to export
if_adc_rst	Reset Input	Double-click to export
if_adc_wr	Conduit	Double-click to export
if_adc_wdata	Conduit	Double-click to export
if_adc_worf	Conduit	Double-click to export
if_dma_clk	Clock Input	Double-click to export
if_dma_wr_req	Conduit	Double-click to export
if_dma_wr_status	Conduit	Double-click to export
m_axis	AXI 4 Stream Master	Double-click to export

Fig. 9. Platform Designer – original ADC-board project

In the original hardware project of Analog Devices Inc., `if_packed_fifo_wr_en` is connected to `if_adc_wr`, as well as `if_packed_fifo_wr_data` to `if_adc_data`. To maintain the connection, all these signals must be exported to the FPGA side and reconnected (Fig. 10).

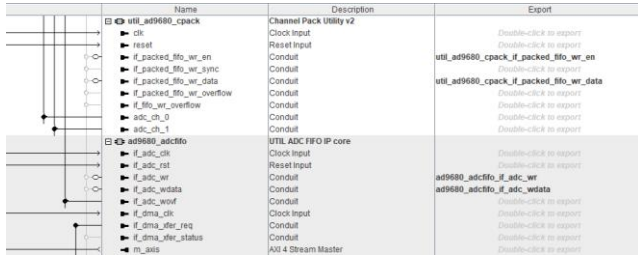


Fig. 10. Platform Designer – modified ADC-board project

The data clock `link_clk` is generated by the IP `ad9680_jesd204`. To export it towards the FPGA side there is a special Clock Bridge Intel FPGA IP (Fig. 11). The `link_clk` is 250 MHz.

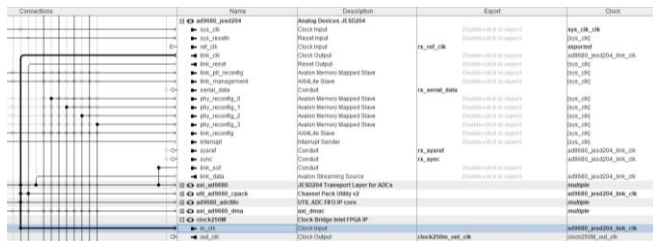


Fig. 11. Data clock to FPGA

VIII. PULSE GENERATION

The laser diode driver needs an SMA low-voltage differential signaling (LVDS) input. Therefore, the pulse generator (FPGA) requires an LVDS output. The Arria 10 Soc DevKit has two FPGA Mezzanine Card (FMC) connectors. These connect numerous pins of the FPGA. One FMC connector has 400 pins. The first FMC connector is used by ADC-board. The second one is used for pulse output. For a quick solution, a male FMC connector (ASP-134486-01) is soldered by 2 wires (red, Fig. 12) which each have an SMA socket at the end. For future handling, an adapter PCB has to be developed.

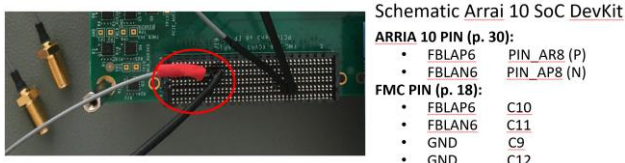


Fig. 12. FMC connector – schematic [13]

The pulse generation is done by LVDS SERDES intel FPGA IP. Quartus Prime intellectual property (IP) files are components that are ideally fully portable within a Quartus Prime version. They can be written by oneself or purchased. The LVDS SERDES intel FPGA IP fetches a 10-bit array every 10 ns and sends the data serially at 1 GHz. The bits must be set low or high depending on the pulse width.

IX. CONCLUSION AND OUTLOOK

The current project status is that pulses with adjustable widths can be generated by the FPGA. Furthermore, the measurement values can be processed on the FPGA side and an external device - PC or microcontroller - can read out the measurement values via UART. This allows to capture single OTDR backscatter curves. The next step is to synchronize the data acquisition by the pulse generation and implement the averaging algorithm. Further steps are integrating an external microcontroller, testing the FPGA plus the ADC with the optical electronics in the laboratory to measure the power of the optical backscatter and evaluating the sensor.

ACKNOWLEDGMENT

This work has been sponsored by the Federal Ministry of Education and Research, funding program Forschung an Fachhochschulen (FHprofUnt) under contract number 13FH137PX6, "Optische Sensoren zur Überwachung von Erdstrukturen (SmartOSE)".

REFERENCES

- [1] R. Engelbrecht, Project outline „Optische Sensoren zur Überwachung von Erdstrukturen (Smart-OSE)” POF-AC, Nuremberg University Georg Simon Ohm.
- [2] S. Geckeler, "Monomodefasern", Nachrichtentechnik Vol. 16, Springer Verlag, DOI 10.1007/978-3-642-83951-1
- [3] J. Vinogradov, et al, "FPGA and APD based optical time domain reflectometry in sensor applications", conference proceedings, 28th Int. Conf. on Plastic Optical Fibers, 20.-22.11.2019, Yokohama, Japan, ISBN 978-112-27-5128-5.
- [4] Analog Devices Inc., AD-FMCDQA2-EBZ User Guide, <https://wiki.analog.com/resources/eval/user-guides/ad-fmcdqa2-ebz>, call 15.05.2021
- [5] Analog Devices Inc., AD9680 data-sheet, <https://www.analog.com/media/en/technical-documentation/data-sheets/AD9680.pdf>, call 15.05.2021
- [6] Analog Devices Inc., AD9144 data-sheet, <https://www.analog.com/media/en/technical-documentation/data-sheets/AD9144.pdf>, call 15.05.2021
- [7] Intel Corporation, Arria 10 SoC development kit, <https://www.intel.com/content/www/us/en/programmable/documentation/iga1434736665480.html>, call 15.05.2021
- [8] Analog Devices Inc., Hardware Project, GitHub, <https://github.com/analogdevicesinc/hdl>, call 15.05.2021
- [9] Analog Devices Inc., Linux, GitHub, <https://github.com/analogdevicesinc/linux>, call 15.05.2021
- [10] Analog Devices Inc., Library Industrial I/O (Libio), GitHub, <https://github.com/analogdevicesinc/libio>, call 15.05.2021
- [11] Analog Devices Inc., IIO Oscilloscope, GitHub, <https://github.com/analogdevicesinc/iio-oscilloscope>, call 15.05.2021
- [12] Analog Devices Inc., "Channel CPACK Utiliy Core", https://wiki.analog.com/resources/fpga/docs/util_cpacak, call 04.05.2021
- [13] Intel Corporation, Arria 10 Soc development kit schematic, https://www.intel.com/content/dam/altera-www/global/en_US/support/boards-kits/arrria10/soc/Production_files/a10_soc_devkit_03_31_2016.pdf, call 04.05.2021

Development of measuring methods for condition monitoring, fault detection and optimization of a medical angiography floor stand

Thorsten Riedl

University of Applied Sciences Amberg-Weiden
Faculty of electrical engineering, media and computer science
Amberg, Germany
Email: t.riedl1@oth-aw

Abstract—In this research work, measurement techniques for machine diagnosis on a medical device are presented. These methods should make it possible to create a mechatronic reference model of a drive train and draw conclusions about its mechanical properties. The foundation of the data collection and the extraction of reliable information is realised with the help of electrical and mechanical state variables, which are obtained directly as physical signal curves from internal drive and control circuit parameters. control loop parameters. The collection of the data is collected with the help of a quantitative approach, the analysis procedure of the the measurement procedure, as well as the graphical realisation user interface are presented in the following as part of this presented as part of this work.

I. INTRODUCTION

The advance of the digital age brings with it a significant increase in the automation of information and decision-making processes. With their help, process flows can be optimised and their quality increased and considerably improved. However, a large collection of resilient information is required as the foundation of the survey. Crucial for this are measurement data that provide information on the current state, experience with certain behaviours and the planned use of the components used. This leads to immense benefits in the field of predictive maintenance [1]. In modern industry, condition monitoring of physical machine data and signals has become particularly well established [2]. However, the use of such a service and its application in an industrial environment, especially to a specific piece of equipment, still poses a great challenge to the user. In order to answer the resulting questions and to gain initial experience with the realisation of such a measurement system, the Ostbayerische Technische Hochschule Amberg-Weiden, in cooperation with the medical technology manufacturer Siemens Healthineers, is addressing this topic.

II. PROBLEM DESCRIPTION AND STATE OF RESEARCH

The main task of a monitoring and diagnostic system is to assess the behaviour of an object. The systems and methods used for this purpose usually monitor a system through continuous and periodic recordings of measured values. The measured values used for this purpose are usually physical variables as well as process data, which are obtained directly

from the control system and placed in the context of the machine status. In this way, one benefits from the fact that malfunctions in mechanical and electrical components become noticeable in the form of certain symptoms over a defined period of time [3].

The requirements for these measurement methods are largely determined by their monitorability. This means that the recording and evaluation of the system status must be well-founded or error-free and adapted to the existing mechatronic system [4]. This results in the requirement that no additional external sensors are installed for the diagnosis, but that the existing control system can be used. The focus of the work is therefore on the creation of measurement procedures that can be realised through indirect signal recording. Signals internal to the control system and system variables from the already available control units serve as the data basis for this.

In recent decades, the monitoring and diagnosis of processes, as well as the collection of data of any kind, has become increasingly important in the industrial environment [5]. As a result, a large number of different approaches to the analysis and diagnosis of process and machine states have already been published. Based on selected examples of research work and the findings from the previous project phases, the methodologies described below were developed with regard to the techniques for signal acquisition, processing and evaluation.

III. METHODOLOGY AND APPROACH

As described in the problem definition section, the measurement methods are to be realised with the help of internal control and drive signals. In order to achieve this, knowledge about the control system and the properties of the mechatronic axis is necessary. For this purpose, a prototype of an angiography floor stand with the corresponding control units was used for the investigations. The prototype is shown in figure 1. The control of a mechatronic axis, consisting of a servo motor with a motor measuring system and coupled mechanics, is carried out by means of a numerical control. In order to keep the complexity of the mechanics low, we limited ourselves to a partial section of the first mechatronic axis. In order to better illustrate the recorded data and the

analysis methods, a graphical interface is to be created using the numerical calculation programme Matlab.

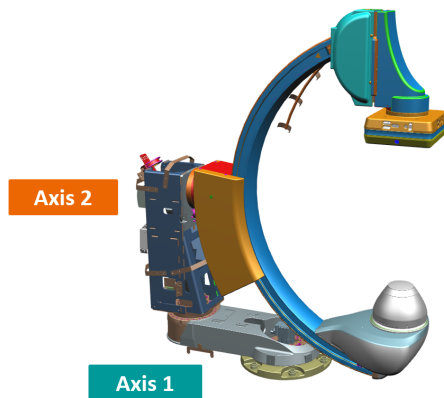


Figure 1. Prototype Angiography Floor Stand

A. Data acquisition and information consistency

Since the control unit for the individual axes is a platform concept from one manufacturer, data acquisition is relatively simple. The data is collected by means of a trace and logic analyser function, with which access to the internal status variables of the control and feedback control system, as well as the drive variables, is possible. The measured variables are collected directly via the control unit's operating panel and can be retrieved as text format from the control unit's internal memory. The bandwidth of the signals is band-limited to 250 Hz within the trace function. In the previous project phases, the information continuity of the hardware used, as well as the process-related information content of the signals available from the cascaded control loop, were already examined. In particular, the influence of the control parameters and the cycle times of the digital controls on the available signals was considered. The investigations showed that the cycle time of the signal acquisition of 2 ms is sufficient to obtain usable signal information [5].

B. Development of the measurement methods

Solutions for function and quality monitoring require extensive knowledge of the possible factors influencing the functionality and quality of the mechatronic axis. Such faults usually arise as a result of dissipation effects, which occur as undesirable changes in system elements or system parameters. Susceptible components include the electrical and mechanical components of a drive train. Such irregularities can be clearly identified by certain symptoms which provide information on a specific signal frequency or signal form. [6][7]

1) *Vibration spectrum by means of order analysis:* Damage and irregularities in elements of a mechatronic drive train can be reliably detected by measuring and analysing vibrations [8]. For axes that are moved with the help of an electric motor, it is obvious that the signal frequency is dependent on the excitation speed [9]. A possible solution is therefore

to compare the occurring vibrations with calculated theoretical natural frequencies of the components used. A further time-frequency analysis method is the order analysis. This is a common evaluation method in vibration engineering to investigate speed-dependent noise mechanisms or imbalances in mechanics [9]. The use of frequency-dependent spectrograms is unsuitable for fluctuating speeds, as the noise mechanisms also vary with the frequency, making evaluation difficult [9]. In order to create an appropriate measurement methodology, various physical signals from the control loop were considered in the preliminary investigations and examined for their information content with an additional vibration transducer. The following error was extracted as a meaningful variable for the project. This is the difference between the setpoint and actual position of the controlled system. The advantage of this signal variable is that the actual position of the mechanical system comes directly from the absolute measurement system of the drive and thus has a low quantisation noise. The influence of the time delay due to the two inner control loop cascades is also negligible. Assuming that the control parameters of the system are optimally designed, the following error reflects the absolute positioning error of the mechanics used [5].

For the realisation of the measurement methodology, a corresponding travel profile with speed-dependent interpolation points was created for the numerical control. The two position signals were recorded during the measurement run and have a constant time offset due to the structure of the position controller. However, this has a disadvantageous effect on the formation of the following error and the spectral representation conceived from it, since the instantaneous values of the time signal would be shifted by the time offset. To avoid smearing in the spectral range due to the equidistant time axis, the temporal offset of the position controller was determined by measurement and the actual position was corrected by this value. In order to ensure a constant sampling of the signal, the constant travel range per speed was considered for the spectral representation. The corrected following error was transferred into the frequency spectrum by means of a Fast Fourier Transformation and processed representatively by signal processing, as can be seen in the second illustration.

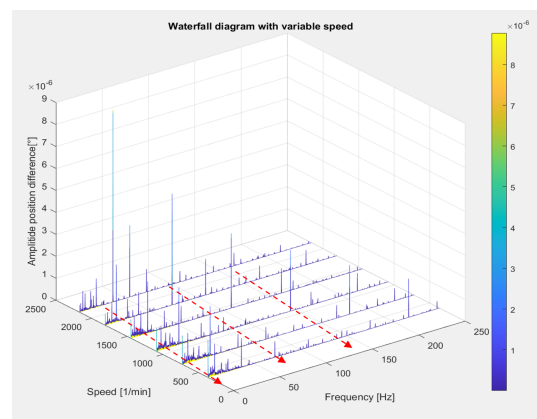


Figure 2. Waterfall diagram with variable speed - Spectral representation

The waterfall diagram shows a shift of the spectral components depending on the rotational speed. To compensate for this dependence, the equidistant frequency axis can be normalised using a frequency-dependent quantity and converted into an equidistant order axis. For this purpose, the speed of the drive or a quantity normalised with it can often be found in the literature [9]. Thus, the frequency axis can be redefined for each individual spectrum $A_T(t_i)$ recorded at the measurement time t_i [9]. The normalisation procedure is shown in the third figure.

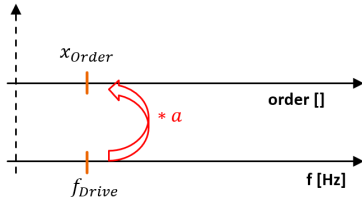


Figure 3. Procedure normalisation frequency axis

The normalisation factor a can be determined from the ratio of the desired ordinal number and the drive frequency, as shown in formula (1).

$$a = \frac{x_{Order}}{f_{Drive}} \left[\frac{1}{Hz} \right] \quad (1)$$

In order to quickly and specifically identify the location of irregularities in the complex drive train with our measurement method, the transmission ratio of the mechanical axis was chosen as the order. This makes it possible to assign the resulting peaks of the order spectrum to a fixed mechanical system and to compare them with calculated theoretical kinematic frequencies or orders. The order of the fastest component, i.e. the drive, would be found exactly at the value of the transmission ratio. Thus, the resulting order spectrum can be analysed independently of the speed. For example, the rotor order corresponds to the x th order of the drive at x poles.

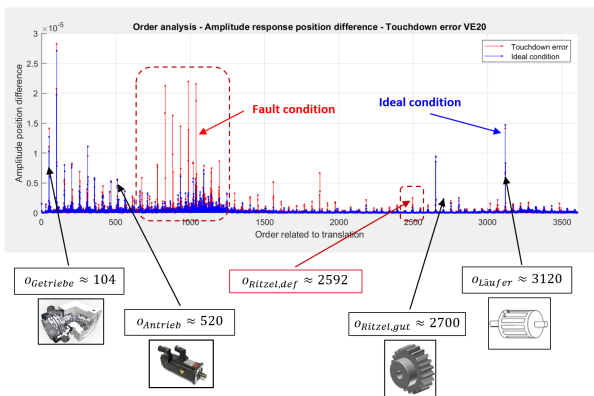


Figure 4. Order analysis with error detection

Figure 3 shows an order spectrum of the first mechatronic axis (blue spectrum) for a travel speed of 2167 1/min and mirrored against a fault case (red spectrum). The resulting

amplitudes were assigned to individual components from the mechanics, which were calculated theoretically in advance.

2) *Non-linear friction behaviour using the Stribeck curve:* Another meaningful indicator for the behaviour of a mechatronic axis is the friction behaviour. Friction usually occurs where two components are in mutual contact with their surfaces and are moved against each other [10]. As can be seen from the literature [10], friction effects can be described relatively well by linear models and from this the three types of friction known to us, which are presented in the following section, can be determined. For simplification, the assumption is made that friction always acts in the opposite direction to the direction of movement.

$$\text{Sliding friction : } F_{Slide} = F_N \cdot \mu_{Slide} \cdot \text{sign}(v) \quad (2)$$

$$\text{Viscose friction : } F_{Visco} = F_v \cdot v \quad (3)$$

$$\text{Static friction : } F_{Static} = F_N \cdot \mu_{Static} \quad (4)$$

It is easy to see from the first two types of friction that they are dependent on speed. In reality, however, a combination of the described types of friction always occurs in complex systems. In order to be able to record these metrologically, the reproduction of the speed-dependent friction in the form of a Stribeck curve is predominantly used in the literature [10]. This describes the behaviour of the friction or the force values over the speed. The following mathematical description is often used for the function of the Stribeck curve:

$$F_{Stribeck} = \text{sign}(v) \cdot F_{Speed} + F_{Visco} \quad (5)$$

$$F_{Speed} = \left(F_{Slide} + (F_{Static} - F_{Slide}) \cdot e^{-| \frac{v}{v_s} |^\delta} \right) \quad (6)$$

In order to determine the two speed-dependent friction values with the presented approach, the internal control parameters of the actual speed value and the actual torque value were used. Likewise, a corresponding positive and negative, speed-dependent travel profile was again designed for the measurement process that utilises the maximum speed range of the drive. For the realisation of the supporting points of the Stribeck curve, we restricted ourselves to the constant areas of the profile and this was generated by the arithmetic mean. By means of a regression line describing the linear part of the curve, the two velocity-dependent types of friction could be determined. On the one hand, this is viscous friction, which corresponds to the increase in the linear curve simplification with speed. Secondly, the sliding friction corresponds to the value of the linear curve simplification at velocity $v(t=0)$ or speed $n(t=0)$ zero [10]. For gravity-loaded axes, an additional compensation of this value must be carried out. A reference curve (weak graph) of the axis resulting from the measurement procedure with the corresponding compensation line can be

seen in Figure 5. The friction values determined from the curve are also given.

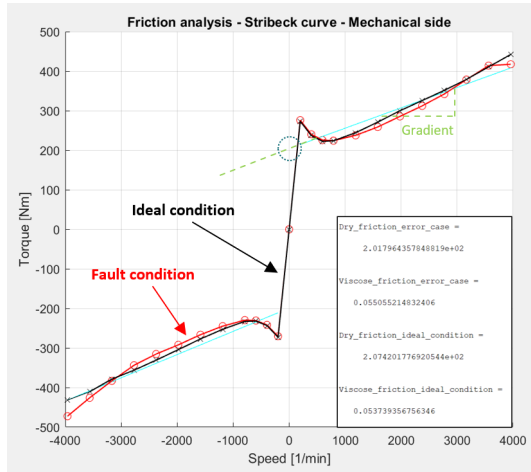


Figure 5. Stribeck curve with error detection

To make a change in the mechanical behaviour visible, the reference curve is mirrored against a fault case (red graph) during evaluation. On the basis of the curve progression and the output values of the friction, corresponding deviations can then be determined and tolerances defined. In the example shown, a change in the friction behaviour can be seen at high travel speeds.

3) *Synchronization consideration and signal deviations due to signal conditioning:* As known from the previous description of signal acquisition, the internal state variables and parameters are recorded as time-continuous signal characteristics with the help of the trace and logic analyser function.

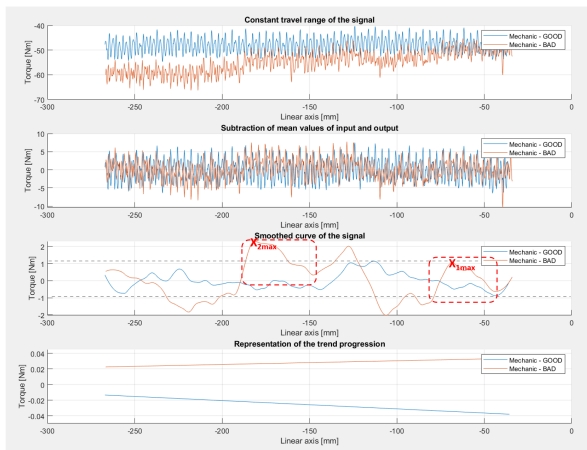


Figure 6. Synchronous operation torque with error detection

It is also possible to draw conclusions about the mechatronic behaviour and changes in the machine state variables of the drive train by means of such time sequences [6]. These changes or effects are contained as information in the recorded signal, which can be detected, for example, in the

form of changes in force, acceleration or vibration or in quantities such as current or speed [6]. In order to be able to use these measurable effects for fault diagnosis, the time courses must be pre-treated by signal processing methods. This makes it possible to extract certain characteristics from the curves and use them to make statements about the behaviour of the system [6]. Such processing is necessary because there is a transmission path between the source of the signal and the measuring system and the detected signals always represent a sum of differently acting sources [6]. In order to be able to use the signals obtained from the control system for initial analysis purposes, a measurement method was created with whose pre-processing it is possible to obtain an initial characteristic description of the signal. This method is shown in Figure 6 on the basis of the actual torque value and again mirrored against an error image (red graph). In order to additionally relate to the mechanics, the constant travel range of the physical signal is plotted against the mechanical position, as can be seen in the upper graph. It can also be seen that the signal has a high noise component, a clear tendency and a discontinuity. For better analysis procedures, this linear trend or offset value is corrected in the second graph. For feature extraction, the noise component is also removed from the signal using filters, as can be seen in the third graph. In the last section, a trend graph of the signal in relation to the position is also shown. [6][11]

As can be seen from the filtered curves in Figure 6, the faulty torque signal (red graph) has a periodic disturbance in contrast to the reference signal (blue graph). Thus, it is possible to already perform a feature calculation of the signal and a fault localisation by pre-processing the signal.

4) *Graphical realization of a user interface:* In order to make the developed measurement methods usable in the event of an error or application, a graphical user interface was created.

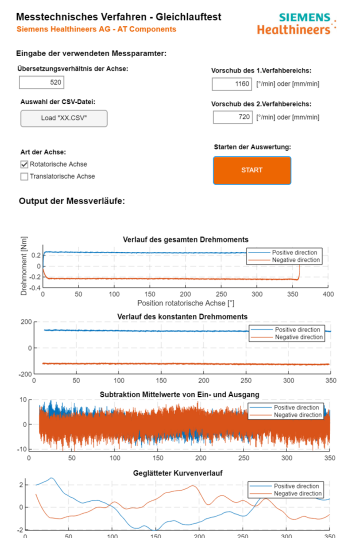


Figure 7. Graphical user interface of the synchronisation observation

In order to make the developed measurement methods usable in the event of an error or application, a graphical user interface was created. The interface was realised as an app with the help of Matlab App Designer. The visual components, the behaviour of the interface and the design of the GUI could be easily created and the code used for the measurement methods implemented. Using the Matlab compiler, the resulting measurement tools can be used as independent executable desktop applications. Figure 7 below shows the graphical user interface of the signal processing methodology. The user input is adapted in such a way that the framework conditions of the measurement can be matched to the travel profile used.

IV. CONCLUSION AND OUTLOOK

The measurement methods presented in this research work are intended to help interpret the mechanical quality and mechatronic behaviour of a medical angiography floor stand. As a prerequisite for the under-interpretation of the results, sound mechatronic knowledge of the axes and the system must be available. The data acquisition for the measuring systems is carried out exclusively by indirect signals, which originate from the control and converter system, as well as the absolute measuring system of the drive. The methods developed have already been used for real fault analysis and with their help the first fault cases could be detected and verified very well. In addition, reference models can be created and limit values defined for the mechatronic axes to be examined. With the help of a co-simulation, a simulative accompaniment of possible error patterns and their resulting patterns can take place. It would also be conceivable to extend the axes with an additional absolute measuring system to expand the method module.

ACKNOWLEDGMENT

The author would like to thank the supervising professor as well as the responsible persons and employees from the AT Components development department at the Kemnath site of the medical manufacturer Siemens Healthineers for their support in the preparation of this thesis.

REFERENCES

- [1] B. Leidinger, *Digitalisierung*, In: *Wertorientierte Instandhaltung*, 2nd ed., pp. 121-129 Springer Gabler, Wiesbaden, 2017, ISBN: 978-3-658-17855-0.
- [2] N. Wunderlich, J. Schumann and F. Wangenheim, *Management und Marketing ferngesteuerter Dienstleistungen: Konzeptionelle Verortung, betriebswirtschaftliche Herausforderungen und künftige Forschungsaufgaben*, In: *Zeitschrift für Betriebswirtschaft*, Band 81, pp. 977-1001 2011, DOI 10.1007/s11573-011-0500-9.
- [3] J. Kolerus and J. Wassermann, *Zustandsüberwachung von Maschinen - Das Lehr- und Arbeitsbuch für den Praktiker*, 7th ed. Expert-Verlag, Renningen, 2017, ISBN: 978-3-8169-3377-9.
- [4] M. Walther, *Antriebsbasierte Zustandsdiagnose von Vorschubantrieben*, In: *ISW/IPA Forschung und Praxis*, Nr. 183 Josef-Jetter Verlag, Heimsheim, 2017, ISBN: 978-3-939890-77-5.
- [5] R. Brügel, *Prozessanalyse an spanenden Werkzeugmaschinen mit digital geregelten Antrieben*, In: *iwb Forschungsberichte*, Band 151, Herbert Utz Verlag GmbH, München, 2001, ISBN: 3-8316-0021-X.

- [6] C. Brecher and M. Weck, *Werkzeugmaschinen Fertigungssysteme 3 - Mechatronische Systeme, Steuerungstechnik und Automatisierung*, 9th ed. Springer Vieweg, Berlin, 2021, ISBN: 978-3-662-46569-1.
- [7] A. Fiel, *Machine specific Sensor Map for Condition Monitoring Systems*, Diplomarbeit Technische Universität Wien, Österreich.
- [8] K. Uchtmann and R. Wirth, *Maschinendiagnose an drehzahlveränderlichen Antrieben mittels Ordnungsanalyse* Abteilung Messtechnik und Maschinendiagnose der Flender Engineering und Service Antriebstechnik GmbH, Herne.
- [9] B. Käferstein, *Ordnungsanalyse-Toolbox für Matlab*, In: *Maschinenaustik - Mitteilungen aus dem Institut für Maschinenwesen*, Nr. 27 Technische Universität Clausthal, 2002, ISSN: 0947-2274
- [10] A. Krämer and J. Kempkes, *Modellierung und Simulation von nicht-linearen Reibungseffekten bei der Lageregelung von Servomotoren*, In: *FHWS Science Journal*, Jg. 1, Nr. 2 Hochschule für angewandte Wissenschaften Würzburg-Schweinfurt, 2013.
- [11] H.-G. Natke, *Einführung in Theorie und Praxis der Zeitreihen- und Modalanalyse - Identifikation schwingungsfähiger elastomechan. Systeme* Springer Fachmedien Wiesbaden GmbH, 1983, ISBN: 978-3-322-96178-5.

Miniaturisation of a Sensor System Using Reflectivity Based Surface Plasmon Resonance Imaging (SPRi)

Benedikt Schloder

Deggendorf Institute of Technology
Deggendorf, Germany
benedikt.schloder@th-deg.de

Abstract— Insulating oil is an essential medium in power transformers as it provides cooling and insulation of the windings. The interest of knowing the oil quality in realtime is rising since load cycles caused by renewable energies reduce the lifetime of the oil. Currently, the oil quality is determined by an extraction and a subsequent analysis of the sample in the laboratory which is time consuming and only a snapshot in time that shows no trends. Surface Plasmon Resonance Imaging (SPRi) is a common application for biological and chemical sensors. It is non destructive and highly sensitive and suitable for detecting small changes in the refractive index close to a gold surface. The gold surface requires spots with recognition elements to become sensitive to the molecules of interest. Most setups are limited in the number of sensing spots and require operation in a controlled environment. With a homogeneous illumination of a large sensor surface arrays with different receptors, the simultaneous detection of many analytes is possible. Furthermore, a simple and robust system setup that allows easy manufacturing and handling by operators is searched. Providing a suitable illumination makes this setup more efficient and more sensitive. The main focus lies on improving the setup together with a smart evaluation of the images by artificial intelligence and a self calibration that allows the use on real power transformers.

Keywords—surface plasmon resonance spectroscopy, miniaturisation, SPR-imaging, micro-opto-electromechanical system

I. INTRODUCTION

Surface Plasmon Resonance (SPR) sensors are important tools often used for biological and chemical sensors. The SPR approach offers unique advantages regarding its real-time and label-free sensing capabilities [1]. A high throughput can be reached by using 2D sensor arrays, the so called SPR imaging (SPRi). SPRi uses a reflectivity based configuration. Compared to other configurations like angle-, wavelength-, polarization- or phase-resolved it allows parallel measurements with several sensing spots. Therefore a 2D intensity contrast image of the sensing surface is created and evaluated. The setup has no moving parts and thus a high potential for miniaturisation.

The instrumentation of SPRi however is quite challenging. Many sensor setups are used in laboratories and require operation by trained personal that makes the use quite expensive. The system is highly temperature sensitive and shows a trade off

either from missing transportability or from low sensitivity. Motivated by the potential of supplying an efficient and low cost sensor, further optimisations need to be done and are part of this work.

II. SENSING PRINCIPLE

Surface Plasmon Resonance is a charge-density oscillation that may exist at the interface of two media with opposite signs [1]. A common method for the excitation of surface plasmons (SP) is the attenuated total reflection (ATR) by a prism coupler in Kretschmann geometry as shown in figure 1. In the Kretschmann geometry of the ATR method, a high refractive index prism with refractive index n_p is interfaced with a metal-dielectric waveguide consisting of a thin metal film permittivity ϵ_m and thickness q , and a semi-infinite dielectric with a refractive index n_d ($n_d < n_p$) [2].

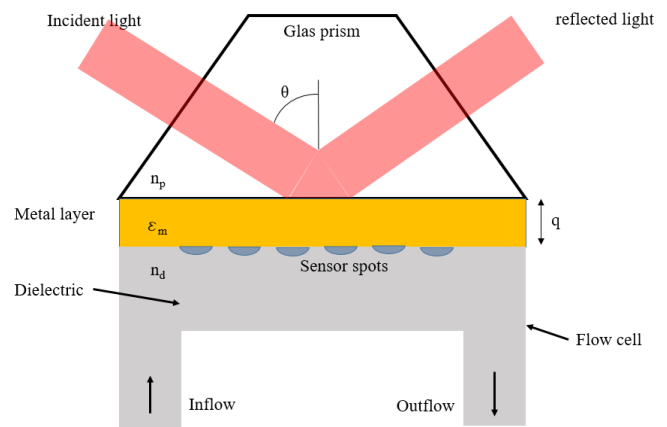


Figure 1: Kretschmann geometry using the attenuated total reflection (ATR). The dielectric represents the insulating oil. Selective sensor spots are located at the sensor surface and surrounded by the flow cell. Note: Metal layer not true to scale.

If the incident light is p-polarized and the angle of incidence θ is altered, a typical SPR curve can be seen (figure 2). Characteristic of this curve is the narrow dip in the intensity of the reflected light. Surface plasmons are then excited at the interface gold/dielectric and the oscillation is in resonance. At reflectivity-based SPRi an angle in the linear region is chosen for highest sensitivity. Collimation is required to ensure the same angle of incidence over the complete sensor surface. The

SPR curve depends on the refractive index of the dielectric close to the gold layer which is in this configuration the insulating oil. Variations in the chemical composition and therefore in the dielectric function shift the SPR curve and the detector recognizes an intensity shift since the angle of incidence remains constant.

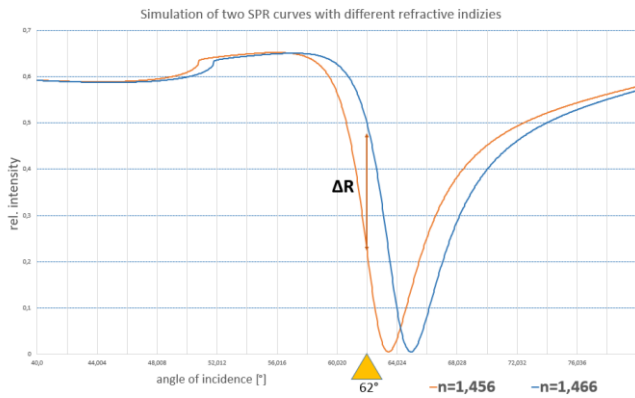


Figure 2: Simulated SPR curves with a change in refractive index of 0.01 and the shift in reflectivity ΔR .

Selectivity to a special molecule of interest is generated by a chemical functionalization of the gold film by recognition elements [3]. Figure 3 shows the principle of the sensor array with different receptors. Here, the concentration of the target molecules from receptor 2 and 3 are changing from time t_0 to t_1 that leads to an intensity shift. At time t_1 the ROI's have become darker. The reason for this intensity shift is the presence of the target molecule close to the surface and therefore a changed dielectric function. Due to the dispersion relation the wave vector of the SP depends on the dielectric function of the medium. Thus the SPR curve is shifting. Each sensor spot is represented by ROI's (region of interest). They enable evaluation via image processing.

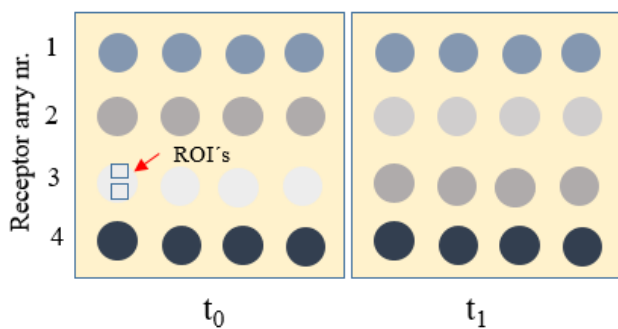


Figure 3: Illustration of receptor arrays and the intensity shift in a ROI (region of interest).

III. SETUP

The developed sensor system must fulfill the requirements of a reflectivity based SPR instrumentation. All components of this optical setup must fit together from a technical point of

view, taking into account the costs and availability of the systems components.

The schematic setup in Figure 4 shows the sensor components. Beginning with the detector, the CMOS Camera BFS-U3-63S4M-C with a 10-bit resolution and 3072x2048 pixel was used. The 10-bit resolution divides each pixel into $2^{10} = 1024$ gray scales. This camera is a compromise between price and size which offers a basis for a first miniaturisation. The sensitivity of the CMOS camera has its maximum at 600 nm and decreases with increasing wavelength. The radiative losses of the plasmon wave decrease with longer wavelength resulting in a narrowing of the SPR response curve, and the propagation length of the surface plasmon wave is longer in the NIR range than in the visible region [1]. As a tradeoff the LED from OSRAM (GH CSSRM2.24) with 660 nm was used, due to the low costs and market availability. Moreover visible light facilitates operation and adjustments. Since the SPR curve slightly depends on the wavelength, a 10nm FWHM filter narrows the spectrum of the LED. S-polarization must be attenuated to avoid overexposure and a failing SPR at the detector. A linear polarizer with an extinction ratio of 9000:1 ensures p-polarization. This enables the detection of excited surface plasmons. The position of polarizer and bandpass was defined to be on the illumination side, but can also be located in front of the camera.

The prism made of Schott F6 glass is the main component of the sensor and carries the sensor surface. The refractive index of F6 at 660 nm is relatively high with $n=1.79$ which makes the use as SPR-coupler appropriate. Insulating oil has a refractive index of approximately $n=1.456$ at room temperature. For the metallic sensor surface silver or gold layers are used. Silver has a higher conductivity compared to gold which leads to a more narrow resonance dip on the SPR curve and a higher sensitivity [4]. However in most applications gold is applied because of its chemically inert properties. A thin layer of 2 nm chromium acts as an adhesion layer between the glass substrate and the 48 nm gold layer. There is only a small influence of the chromium layer on the SPR curve [4]. The quality of the gold surface determines the sensitivity of the system. It is mainly influenced by the deposition process and the quality of the glass substrate. Surface roughnesses of 1 nm representing a P4 polishing according to DIN ISO 10110-8 are feasible in production without much effort. Before deposition, a smooth and clean glass surface is required. The cleaning process can be improved by using an atmospheric plasma treatment of the glass surface [4].

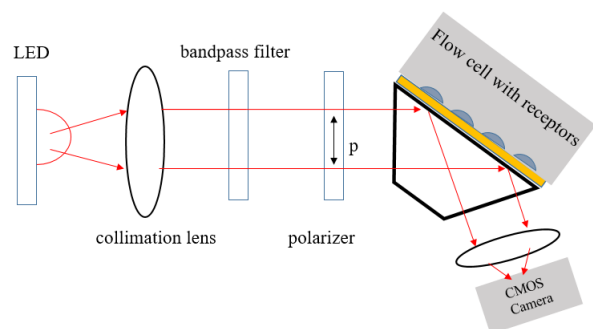


Figure 4: Schematic system setup of the SPR sensor with reflectivity based operation.

A LED cannot be collimated punctually such as a laser source. A small divergence will always remain that slightly varies the angle of incidence in proximity to the optical axis i.e. over the sensor surface. This divergence shall be considered when placing the receptors. Target molecules show different SPR angle since the refractive indices of the molecules vary. However, if a divergent light source is used, the angle of incidence is splayed and every receptor can be placed at its most sensitive angle of incidence [3]. This effect needs to be considered for the development of receptors.

IV. RESULTS

In order to design the sensor probe some theoretical aspects were observed.

A. SPR Simulation

Knowing the SPR angle is essential for developing the sensor system. Simulations give an estimation of the SPR angle that is necessary for operation. This angle is affected by various parameters and very sensitive to fluctuations, especially in the layer thickness. In simulations the parameters were adjusted to get a relatively broad linear region. This reduces slightly the sensitivity but makes rapid prototyping of the sensor much easier and lowers the demanded tolerances. The simulations were done with Winspall. This is a program used for simulating the reflectivity of optical multi layer systems as well as Surface Plasmons. Either the complex values ϵ' or ϵ'' of the permittivity or the refractive index n with the extinction coefficient k can describe the optical properties of the layer. These values are connected with following equations (1) and (2):

$$\epsilon' = n^2 - k^2 \quad (1)$$

$$\epsilon'' = 2nk \quad (2)$$

SPR simulation parameter					
Thickness [nm]	ϵ'	ϵ''	n	k	material
0	3,22	0	1,794	0	Glass F6
2	-1,62	20,6	3,085	3,338	Chrom
48	-14,99	1,31	0,169	3,875	Gold
0	2,12	0	1,456	0	Transformer oil

Table 1: SPR simulation parameters for the layersystem used for insulating oil.

The parameters from table 1 result in a SPR curve shown in figure 2 (orange curve). As can be seen, the linear region is at an angle of incidence of 62° . The values from the literature are either in permittivity or in refractive index, but can easily be transferred by equation (1) and (2).

The 48 nm gold layer can only be deposited within a certain range, assumed within ± 5 nm. To verify variations in the layer thickness at the deposition process two more SPR curves were

simulated showing the effect (see figure 5). The reflectivity decreases by 15% at 43 nm and increases by 29% at 53 nm compared to the original layer thickness of 48 nm. The system still operates in the linear region but shows changes in reflectivity among each prism which are only caused by a variation of the layer thickness.



Figure 5: Simulated SPR curves with thickness variation of ± 5 nm Au at the deposition process. Orange curve shows the aspired curve.

Due to the high sensitivity of SPRi, each prism can not directly be compared and needs a calibration or an initial measurement.

B. Homogenous illumination and collimation

To improve illumination of the sensor surface the system LED in combination with the collimation lens was simulated. The distance between lens and LED was altered and the collimation of the light source as well as a homogenous radiation were examined. The simulated rays from figure 6 show very low divergence and thus a good collimation. The orange plain is situated at the position of the detector. Cross sections were made to check for a homogeneous illumination profile which can be seen in figure 7.

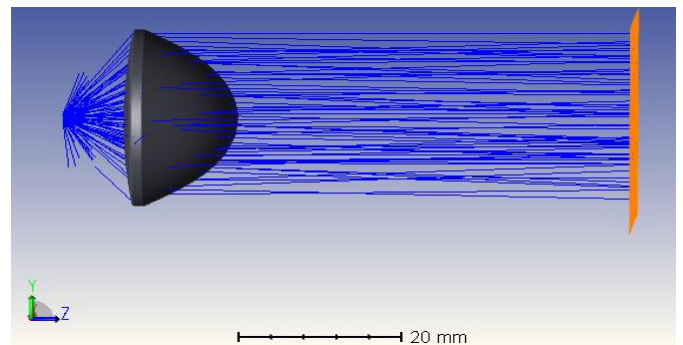


Figure 6: Simulated aspheric lens with detector plain on the right side.

At the position of the detector, a „TopHat“ beam profile can be seen in figure 7. The rectangle in the x-y plot and the two vertical lines of the cross section illustrate the detector size.

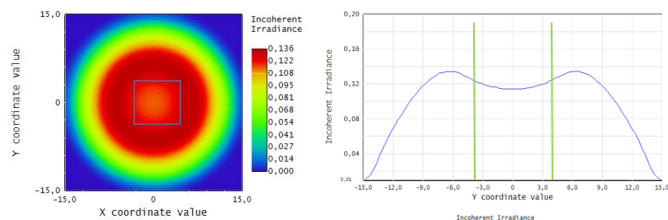


Figure 7: Simulated illumination at the detector plain with a cross section showing a „TopHat“ profile.

C. Miniaturisation

The simulation of the SPR angle and the geometrics of the optical components were the starting point for designing the sensor probe. The main issue was to fix all components in consideration of the systems flexibility. During the construction process, the possibility of rapid prototyping was taken into account, as this offers the advantage of a faster production of the components and allows flexibility of the design. Furthermore complex geometries like holes and cavities of the flow cell can be printed into the housing by using a stereolithography (SLA) printer.

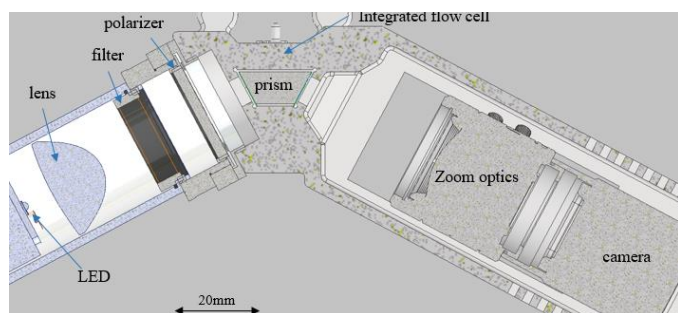


Figure 8: Cross section view of the first miniaturisation of the SPRi sensor with an integrated flow cell

A cross section view of the final sensor probe is shown in figure 8. The design allows easy adjustments while being a first miniaturisation of conventional probes. SLA printing allows manufacturing of features inside like channels of the micro fluidic. Usually the resolution of SLA printers is in the range of approximately 0.1 mm. Functional features or surfaces with low geometric tolerances need a post process after printing. This process can be done via 5-axis milling which allows treatment from all sides. The sensor probe was printed with extensions for clamping on a 3R pallet as illustrated in figure 9. The pallet can be clamped onto the milling machine. The extensions allow an easy installation on a plate or mounting on a real transformer.

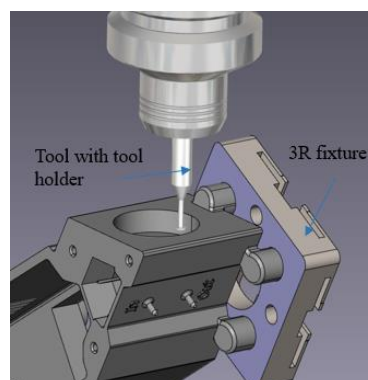


Figure 9: Tool path simulation with CAM software for thread milling.

The LED, lens and filter are clamped by standard lens tubes. Collimation was adjusted by retaining rings and the beam was projected on a screen to check for collimation.

V. OUTLOOK

The development of the setup shows a high potential because of its simplified setup as well as low costs and availability of the components. Towards higher integration and resistivity against external influences, the system must become more reliable. The LED must be operated with a constant current source. Without a low noise source the system will detect variations in the intensity. One possible solution could be the use of reference marks as mirrors at the gold layer. According to the experiences from the sensor probe, the design can be further improved with a spherical surface onto the entrance side of the prism for collimation. This should make the collimation lens obsolete. In general, the aim is to avoid discrete elements for future setups if possible.

REFERENCES

- [1] D. Wang, "Recent Advances in Surface Plasmon Resonance Imaging Sensors," *Sensors* 2019, 19, p. 1-4, 1266, doi:10.3390/s19061266
- [2] J. Homola p.107 "Surface Plasmon Resonance Based Sensors," Springer, p.63 Vol.4, 2006
- [3] P. Hausler, R. Bierl, "Homogeneous Light Source for Surface Plasmon Resonance Imaging," In *Proceedings of the 8th International Conference on Photonics, Optics and Laser Technology- PHOTONICS*, 2020, p 1-5
- [4] S. Horstmeier, "Aufbau eines Oberflächenplasmonenresonanz-Biosensors," *Universität Bielefeld*, 31.03.2008, p 65-70

Investigation of the Float Current Analysis and the Float Current Settling Process via DVA on 18650 Li(NiCoAl)O₂/Graphite Cells

Michael Theiler

Electromobility and learning systems
Technisch Hochschule Ingolstadt
Ingolstadt, Germany
Email: mit7713@thi.de

Meinert Lewerenz

Electromobility and learning systems
Technisch Hochschule Ingolstadt
Ingolstadt, Germany
Email: meinert.lewerenz@thi.de

Michael Schmid

Electromobility and learning systems
Technisch Hochschule Ingolstadt
Ingolstadt, Germany
Email: michael.schmid@thi.de

Abstract—The float current observation is a promising method to characterize the capacity loss by calendar aging of a lithium-ion battery. For the measurement, the cell voltage is kept constant in potentiostatic mode, while the required current (float current) is recorded with high resolution. The float currents of cylindrical 2.5Ah NCA/graphite+silicon cells (Samsung 25R) show the known behavioral patterns of calendrical aging with respect to temperature and state of charge. With increasing temperature as well as with increasing state of charge, the float current increases in a quasi-state of equilibrium. This is validated for five cells with the cell voltages 4.1V, 3.85V, 3.7V, 3.52V, and 3.4V in a temperature range between 5°C and 60°C where the float current increases from 1 μ A up to 315 μ A. The loss of capacity, calculated from the float currents and determined by the check-ups, shows the same trend. Changes of the float current during a temperature step is successfully assigned to the entropy effect and correspond qualitatively to an entropy effect. Furthermore, the ever-slower equalization processes for high SOC are assigned to increasing internal resistance and inhomogeneities within the cell.

I. INTRODUCTION

Lithium-ion batteries have long been part of mobile devices such as laptops and cell phones. Thanks to their high efficiency and sustainability, they are increasingly used in hybrid and purely electric vehicles. In addition to high energy density and longer lifespan, lithium-ion cells also have a low self-discharge rate compared to other battery technologies. The battery system of electric vehicles represents a large part of the purchase price and has increased life expectancy requirements. For these reasons, an optimization of the aging behavior and long-term stable operation is of great importance. To achieve this, a precise understanding of the cells' aging behavior and suitable methods for aging diagnostics are essential.

Aging is usually divided into calendrical and cyclical aging. The calendrical aging is analyzed in more detail in this paper and reflects the change of cell parameters without load. Calendrical aging is mainly dependent on the two parameters state of charge (SOC) and temperature [1], [2]. For static calendrical aging tests, the cells are usually charged to a defined SOC and then stored at a defined temperature for a certain period of time. In general, these two factors are kept constant during

the aging period to determine the influence of SOC or OCV and temperature. Such classical calendar aging determination methods with capacity tests are very costly and usually take months or years for a reliable lifetime prediction. Rumberg et al. [3] and Hoog et al. [4] reported the dependency of the aging rate on temperature and SOC in 3D representations. However, a high effort in time or necessary test cells and test equipment is apparent. In addition, classical tests are periodically interrupted by so-called check-ups and are thus superimposed with cyclic aging effects. Also, this method is overlaid with reversible effects of the anode overhang [5], [6] and polarization [7].

In contrast, the method investigated in this paper is diagnosing the aging rate by evaluating float currents. Here, the cell is charged to a defined SOC with a corresponding OCV and then kept in a potentiostatic mode [8]. Since the OCV change depends on the aging and the applied temperature [9], the battery must usually be permanently recharged with a float current. To avoid measuring side effects, the float current is only evaluated in the steady-state. Since the float current compensates self-discharge and side reactions [10], a correlation is assumed between the float current and the loss of capacity or the aging rate of the lithium-ion cell. The advantage of this method is that the calendrical aging with respect to the available cell capacity does not require charging and discharging processes (check-ups), and thus, the overlapping of cyclical and calendrical aging is avoided [8]. However, it is not possible to determine the internal resistance of the cell directly using this method. To evaluate the resistance, an additional electrochemical impedance spectroscopy can be performed without major changes in the measurement procedure. This is evaluated at test temperature and test voltage and cannot be measured at a reference voltage and temperature for several cells, as otherwise, the cell voltage and the cell temperature must be changed during the measurement procedure.

M. Lewerenz et al. investigated in [11] by means of float currents the calendrical aging of nine 8Ah cells with a cathode made of lithium iron phosphate (LFP), graphite

as anode and (EC-DMC-DEC-EMC)-LiPF₆ as electrolyte at the temperatures 25°C, 40°C and 60°C with a nominal cell voltage of 3.6V. It was shown that this method is a promising measurement as the float current in the μA range correlates with the capacity loss rate. At temperatures above 45°C, a temperature path dependence of the float current was also demonstrated. However, a state of charge dependence of the float current was not shown in this paper.

In this contribution, not only the float current itself is analyzed, but also the influence of temperature changes and the equalization process towards the steady-state current. Therefore, the float currents are analyzed at five different cell voltages. Additionally, several temperatures between 5°C and 60°C are applied. The work is structured as follows. First, the used cells, the measurement setup and the measurement procedure are described. Then the check-ups are evaluated, including internal resistance, capacity loss and differential voltage analysis (DVA). Afterwards, the equalization processes leading to a steady-state float current are investigated. At the end, the obtained float current and the influence of temperature changes are shown and the results are compared to the classical method.

II. EXPERIMENTAL

Cylindrical cells with a capacity of 2.5Ah from the manufacturer Samsung of the type INR18650-25R are investigated for the calendar aging test using an LBT21084 test system from Arbin. According to the datasheet, this cell type has a positive electrode made of $\text{LiNi}_y\text{Co}_z\text{Al}_{1-y-z}\text{O}_2$ (NCA) and a negative electrode made of graphite. However, energy dispersive X-ray spectroscopy (EDS) revealed that the anode of these cells contains silicon and the cathode has an NMC portion in addition to the NCA [12]. Table I shows the specifications of the manufacturer of this cell type. All investigated cells are stored in the DY110 climate chamber from ATT to control and vary the temperature.

Five cells with different float voltages are investigated and documented in table II including their corresponding SOC. To investigate the anode overhang effect one voltage is chosen to correspond to the delivery voltage 3.52V. During the first period of 165 days, the cells were stored at 30°C to reach a steady-state of the float current. It is assumed that after this long period of time the anode overhang effect and equalization process are concluded and can be, therefore, neglected. Because of problems keeping the appropriate measurement range of the float current, it was impossible to make a reasonable evaluation of the float current prior to day 165. Periodically check-ups are performed to measure the cell capacity and the internal resistance at a reference temperature of 30°C. Firstly, the cells were fully charged with CCCV to the cut-off voltage of 4.2V until the current drops below 0.25A. A subsequently 15-minute break is followed by a 1C and 0.1C charge and discharge cycle to the corresponding cut-off voltage. The 1C charge step is followed by a CV-phase according to the first fully charge cycle. After all charge and discharge steps, a 15-minute rest period is performed. Afterwards 40-seconds pulse

TABLE I
CELL SPECIFICATIONS

Manufacturer	Samsung
Type	INR18650-25R
Chemistry	LiNiCoAlO_2
Nominal Capacity	2.5Ah
Charge cut-off-voltage	4.2 V
Discharge cut-off-voltage	2.5V
Max. charge current	4A
Max. discharge current	20A
Voltage (SOC) at test begin	3.52V

TABLE II
TESTMATRIX

Cell number	Float Voltage	SOC
1	4.1V	90%
2	3.85V	62%
3	3.7V	47%
4	3.52V	19%
5	3.4V	8%

tests with 1C at 4.2V and 3.7V are carried out before the check-up ends with a fully 0.1C discharge step to 2.5V. The cells are charged to the corresponding float voltage (SOC) after the check-up process according to table II.

After 165 days, the float current has reached a steady state. At this point, different temperatures are applied to the cells. Fig. 1 depicts the complete temperature course. In the first part, a low temperature cycle is executed for approximately 36 days. Therefore, the temperature is decreased from 30°C to 5°C and afterward increased to 30°C step-by-step with $\Delta T=5\text{K}$. This is followed by a high temperature cycle in which the temperature is increased from 30°C up to 60°C by 5°C steps. In contrast to the low temperature cycle, the float current is measured at the reference temperature of 30°C after each temperature increase. By means of returning to 30°C reference temperature in the high temperature cycle, we are able to investigate temperature path-dependency. After a temperature change was made, we waited until the float current had reached a constant value before making another change. To compare the measured float current with the capacity loss at the beginning and at the end of both cycles, check-ups are performed.

III. RESULTS AND DISCUSSION

At the beginning of this chapter, the internal resistance and the DVA obtained by the check-ups are evaluated. Afterward, the equalization processes after the check-ups and the float current with the entropy influence are discussed. In the end, the float current results are compared to the results of the check-ups.

A. Check-up

1) *Internal resistance and capacity:* Both pulse tests, performed at 3.7V and 4.2V, show similar results. The internal resistance in Fig. 2 a) is calculated using the pulse test data at 4.2V. Data for the 3.7V and 4.1V cells are missing at the beginning of the test due to erroneous check-ups. The internal

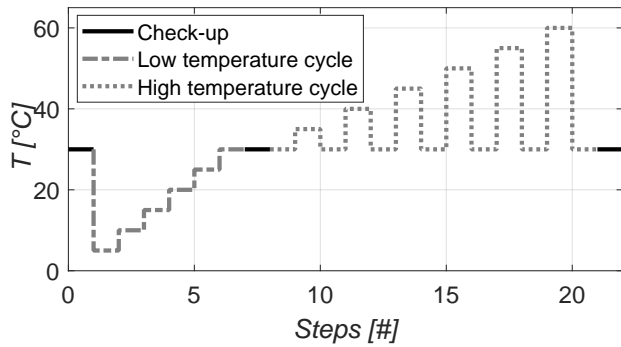


Fig. 1. Illustration of the temperature sequence. Check-ups are black, the low temperature cycle and the high temperature cycle are in grey, emphasized in different line styles.

resistance rises over time for all cells. However, the cell aged at 4.1V shows the strongest increase and the cell aged at 3.85V, reveals a slightly higher slope than the cells stored at 3.4V, 3.52V and 3.7V. Hence, the cell at 4.1V might suffer from other and stronger aging processes compared to all other cells. During the low temperature cycle, only low aging is measured for the higher test potentials. An opposite trend with a greater slope is observable during the high temperature cycle as now additional aging mechanisms are triggered.

Fig. 2 b) shows the normalized charged capacity with 0.1C. As expected, the capacity loss rises with increasing SOC. The disorientation at the beginning is explainable by the erroneous check-ups. Until day 50, the impact of the anode overhang is observable. Hence, for cells that are not close to the delivery SOC of 3.52V, it is more pronounced, leading to a higher capacity loss. Moreover, the effects of the temperature cycles are visible for cells with higher SOC resulting in higher or lower slopes. All cells show the typically calendrical aging trend over temperature and SOC as expected.

2) *Differential voltage analysis*: Fig. 3 a)-e) depicts the differential voltage analysis for all cells. With the increasing degree of blackness of the curves, aging increases. Additionally, Fig. 3 e) shows peaks, which are characteristic for the anode (dashed cycles) and the cathode (solid cycle). Fig. 3 f) shows the relative difference in the shift of the two cathodes characteristics. In accordance with the internal resistance, the DVA reveals a different aging pattern for the 4.1V cell. In contrast to all other cells, the 4.1V cell suffers from a strong loss of cathode material (Fig. 3 f)). In addition, there is no significant loss of anode material, which can be seen from the absence of peak shift in the anode characteristics. Therefore, the main aging process in cells with a high SOC is driven by processes on the cathode side besides lithium loss due to solid electrolyte interphase (SEI) formation. The decreasing peak height at approximately 2.2Ah-2.4Ah of the 4.1V cell (Fig. 3 a)) can be associated with an increase of inhomogeneities within the cell [13]. The superposition of several half cells with different SOC leads to a decrease of the peak height and further flattens if the SOC distribution increases. Therefore the cathode might suffer from inhomogeneities over aging.

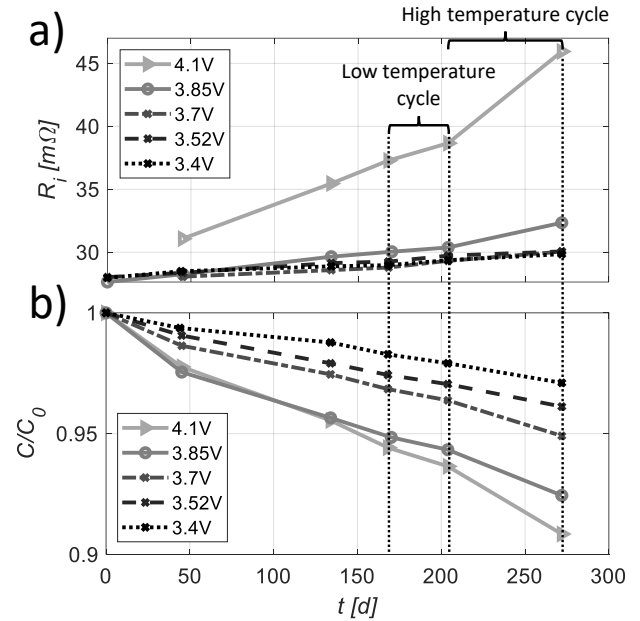


Fig. 2. Graph of a) the internal resistance and b) normalized capacity over time for all cell potentials. With dashed lines the low and high temperature cycle are highlighted.

B. Equalization process after check-up

The equalization process after a check-up and the 0.1C CC phase to the corresponding voltage is shown in Fig. 4. The speed of these processes depends on the target float voltages. The equalization process of cells at 3.4V and 3.85V are the fastest immediately followed by 3.52V and 3.7V cells. Significantly longer takes the process at 4.1V. The DVA, shown in Fig. 5, can explain this SOC depending behavior within a cell. For the very first check-up, the DVA is depicted in black. In grey with a solid and a dashed line, the DVAs of the corresponding half-cells (cathode and anode) are given. The anode shows the two typical characteristics of graphite and the flat course at higher SOC. These curves are obtained using a self-written Matlab-model by fitting half-cell curves of the anode and the cathode to the full cell curve. The rectangles mark the places which belong to the float voltages used in the test. By comparing Fig. 4 and Fig. 5, it becomes clear that higher values in the DVA at the operating point lead to an acceleration of the equalization speed due to a greater voltage difference within a cell.

Another effect at the highest float voltage (4.1V) is observable in Fig. 4. With increasing aging, the equalization process takes longer to settle. Since the aging is mainly caused on the cathode side and the anode has no big influence on high SOC on the DVA, this might be originated from by the cathode. The increasing inhomogeneity and the increasing internal resistance for this cell, especially on the cathode side, could lead to this ever-slower equalization process within a cell with increasing aging.

It took at least 11 days before the float current settled to a steady-state value at 30°C after a check-up. With two check-

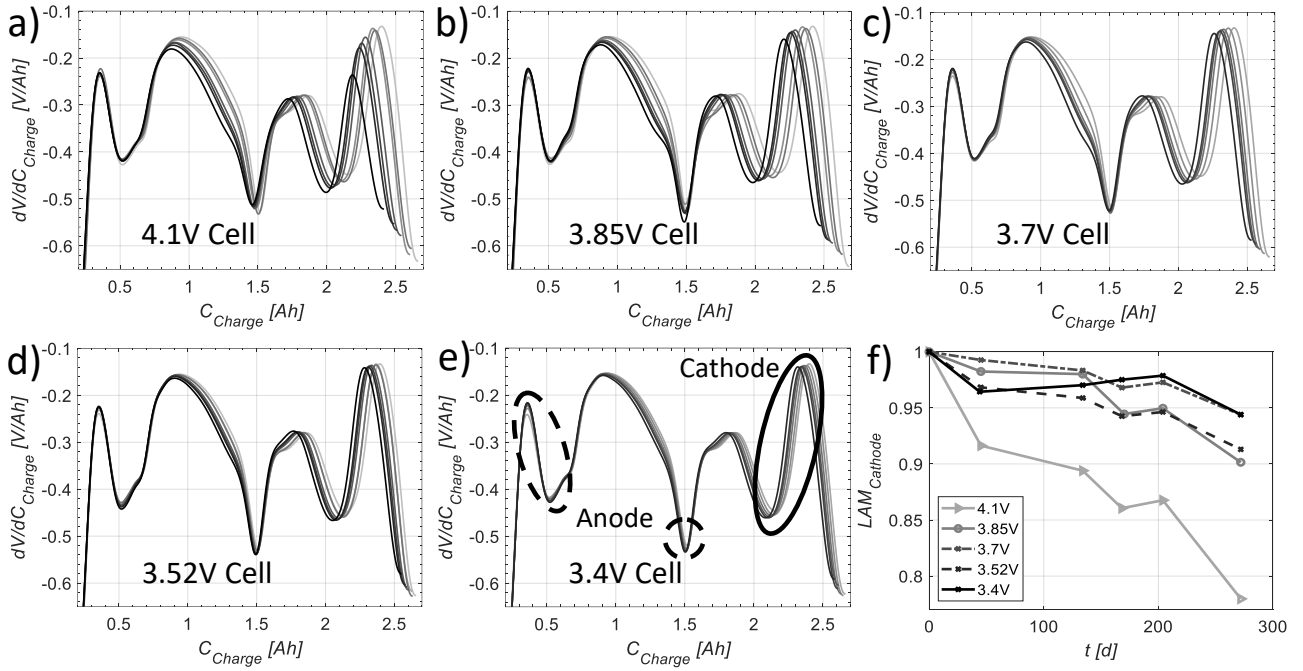


Fig. 3. a) – e) DVA of all cells for all performed check-ups by using the 0.1C charge sequence and f) calculation via DVAs of the loss of active material on the cathode side. e) emphasizes also the characteristic peaks for the anode (dashed cycles) and cathode (solid cycle).

ups and a test period of about 104 days, this takes more than 20% of the total test duration. One of the float current's main goals is the very short test time compared to other aging investigating technics. As the equalization processes are a considerable delay of the test, it would be desirable to shorten them.

C. Float currents

Due to measured current jumping between ± 1 mA with the highest possible current measurement resolution of $\pm 1 \mu$ A the floating current was evaluated through the floating capacity.

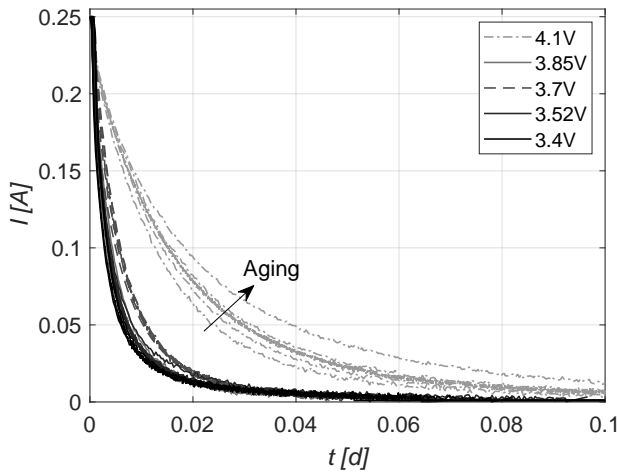


Fig. 4. Illustration of the CV-phase after the 0.1C CC charge to the corresponding float voltage for all cells. Due to a good view, only the process up to 0.1 days are included.

The floating capacity C_{Float} is the difference between the charged C_{Charge} and discharged capacity $C_{Discharge}$ (1).

$$C_{Float} = C_{Charge} - C_{Discharge} \quad (1)$$

As can be seen in (2), the floating current I_{Float} results from the derivative of the capacity after time.

$$I_{Float} = \frac{dC_{Float}}{dt} \quad (2)$$

For all cells, the float currents are shown in Fig. 6. They are treated with a moving average filter with a width of 2000 samples. Approximately between day 29 and 42, a check-up

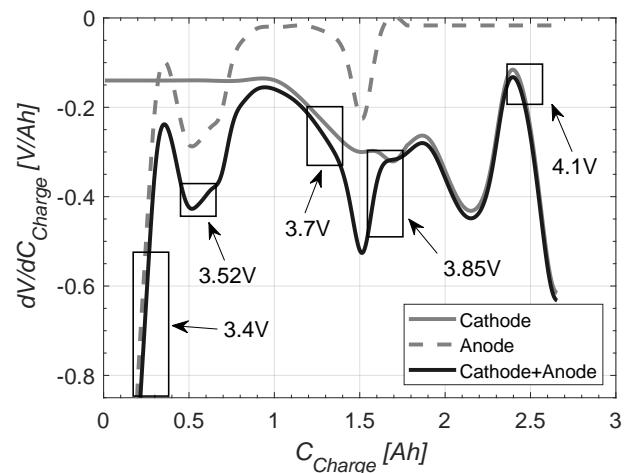


Fig. 5. Illustration of the half-cell DVA for the cathode (grey solid), the Anode (grey dashed) and combined (black) of the charged capacity.

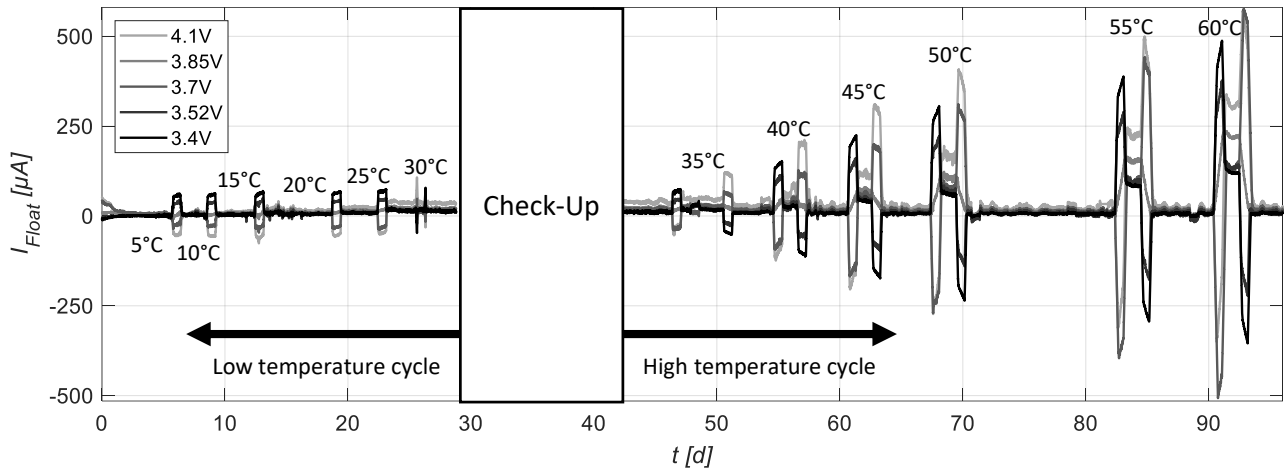


Fig. 6. Float current over time for five different cell voltages for the low and high temperature cyclus. Due to a good view, the transient path after a check-up and the check-up itself are excluded.

with the subsequent equalization process is performed. Before this check-up, the low temperature cycle is conducted and after the check-up, the high temperature cycle follows. Due to the calendrical aging behavior, the float current increases as expected with both the floating voltage and the temperature. The highest value of approximately $315\mu\text{A}$ is obtained at 60°C for the 4.1V cell and the lowest at 5°C and 3.4V with approximately $1\mu\text{A}$. Furthermore, due to the Arrhenius relation, an exponential trend between float current and temperature is expected. A more detailed investigation of the float current, including the Arrhenius relation, the activation energy, temperature path-dependency, voltage, and temperature behavior, is discussed in another work [14]. At each temperature rise or decrease, current peaks are observable due to the entropy effect, which is discussed in the following section. This effect is also visible between day 27 and 28 due to a climate chamber error with accompanied temperature changes. Additionally, a small current fluctuation occurred over the entire measurement time. The same direction of fluctuation for all cells with different entropy coefficients cannot be caused by entropy. Instead, they are assigned to the temperature fluctuation in the surrounding test container of typical $\pm 2\text{K}$. Due to these temperature fluctuations, the test station's voltage output and thus the float current are affected. Therefore, these tests should be performed under a very constant temperature condition. In our case, during summer, the sun heats the test container during the daytime, leading to a high temperature fluctuation. A room with better temperature control or measurement in winter will increase the measurement accuracy significantly.

D. Influence of entropy

The influence of entropy is recognizable at each temperature change leading to a float current peak due to some mV shifting open-circuit potential. The entropy coefficient ΔS according (3) defines the sign and the strength of the float current peak during a temperature step. With n is the number of electrons

involved, F the Faraday constant, T the temperature and E the electromotive force.

$$\Delta S = nF \frac{dE}{dT} \quad (3)$$

The entropy coefficient $c = \Delta V/\Delta T$ over the depth-of-discharge (DOD) of an aged cell of the same type is depicted in Fig. 7. Furthermore, the cell voltage was not measured in an equalized state but under charge or discharge conditions. This does not correspond to the usual determination of entropy and is therefore subjected to deviations. For this reason, the curve is considered only qualitatively. Fig. 8 revealed a positive entropy coefficient for the 4.1V and 3.7V cell, with $c_{3.7V} < c_{4.1V}$. Hence, a temperature rise results in a higher open-circuit voltage and a drop in the floating current. Furthermore, $c_{3.52V}$ and $c_{3.4V}$ are both negative and correlating with the float current behavior of the corresponding cells ($|c_{3.4V}| > |c_{3.52V}|$). The 3.85V has a $c_{3.85V} = 0$ leading to hardly any visible current peak in Fig. 6. The same behavior for all cells is visible at approximately day 27 and 28, where a climate chamber error leads to a drop following by a rise of the temperature.

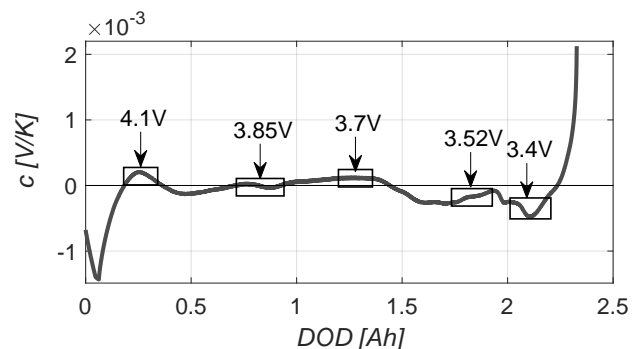


Fig. 7. The entropy coefficient over DOD for an aged cell of the same cell type. The rectangles emphasize the parts of the corresponding float voltages.

E. Check-up vs. floating current

In Fig. 8 the loss of capacity C_{Loss} is obtained by both check-ups at the beginning and the end of the test is depicted in a solid grey line. The capacity loss calculated through the obtained float current is shown in the black dashed line. Therefore a self-developed fitting strategy is used to determine the float current for each temperature step. Then the floating capacity can be calculated with the duration of the respective temperature steps. Since the temperatures in the check-ups are 30°C, the float current of a 30°C step is used for the check-ups. As expected, the capacity loss rises with increasing float voltage. Both curves show a high correlation in trend and absolute value. Therefore, the results obtained from float current and check-ups are in good agreement over a very complex temperature sequence. A small deviation is observable at very high and very small voltages. This is explainable by the errors of the check-ups and the float current measurement.

IV. CONCLUSION

Measurements and evaluations of the float current provide valuable information about the capacity loss of cells during calendar aging. The float current was successfully measured for different cell voltages and different temperatures between 5°C and 60°C. The float current rises with increasing temperature as well as with increasing voltage. Validation of the float current analysis with the classical method shows a high correlation between the two measuring methods. The entropy trend for certain SOCs could be determined and was successfully compared to an entropy measurement. The results obtained from the DVAs and the check-up revealed a particular increasing internal resistance and inhomogeneities on the cathode side leading to ever-slower equalization processes for the cell stored at 4.1V. Therefore, we assumed that this cell suffers from an additional aging mechanism due to strong aging at very high SOC of 90%. Testing and validation of the floating current analysis on further cell types is the subject of future work.

ACKNOWLEDGMENT

The results from this paper are generated during the project “Research on fast and high-precision float current technology

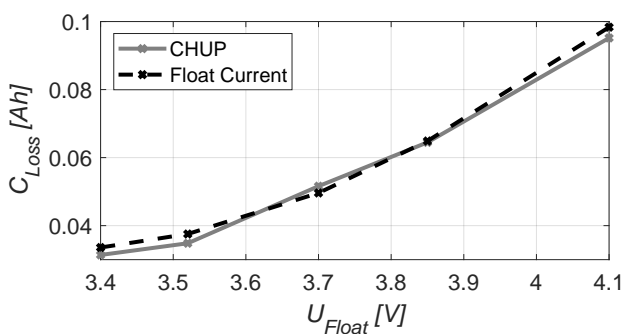


Fig. 8. Capacity loss obtained from capacity tests (solid grey) and from float tests (dashed black) over the float voltage of the cells for the low and high temperature cycle.

as an alternative to conventional calendar aging tests on lithium ion cells and research on fast parameterizable aging prognosis simulations” (LE 4469/1). We like to thank the Deutsche Forschungsgemeinschaft (DFG) for funding. Special thanks to the support by Sascha Speer and Lidiya Komsiyyska.

REFERENCES

- [1] M. Ecker et al., “Calendar and cycle life study of Li(NiMnCo)O₂-based 18650 lithium-ion batteries,” *Journal of Power Sources*, vol. 248, pp. 839–851, 2014, doi: 10.1016/j.jpowsour.2013.09.143.
- [2] S. Käbitz et al., “Cycle and calendar life study of a graphite/LiNi_{1/3}Mn_{1/3}Co_{1/3}O₂ Li-ion high energy system. Part A: Full cell characterization,” *Journal of Power Sources*, vol. 239, pp. 572–583, 2013, doi: 10.1016/j.jpowsour.2013.03.045.
- [3] B. Rumberg, B. Epping, I. Stradtman, M. Schleder, and A. Kwade, “Holistic calendar aging model parametrization concept for lifetime prediction of graphite/NMC lithium-ion cells,” *Journal of Energy Storage*, vol. 30, p. 101510, 2020, doi: 10.1016/j.est.2020.101510.
- [4] J. de Hoog et al., “Combined cycling and calendar capacity fade modeling of a Nickel-Manganese-Cobalt Oxide Cell with real-life profile validation,” *Applied Energy*, vol. 200, pp. 47–61, 2017, doi: 10.1016/j.apenergy.2017.05.018.
- [5] M. Lewerenz, P. Dechent, D. U. Sauer, “Investigation of capacity recovery during rest period at different states-of-charge after cycle life test for prismatic Li(Ni 1/3 Mn 1/3 Co 1/3)O₂-graphite cells,” *Journal of Energy Storage*, vol. 21, pp. 680–690, 2019, doi: 10.1016/j.est.2019.01.004.
- [6] M. Lewerenz, G. Fuchs, L. Becker, and D. U. Sauer, “Irreversible calendar aging and quantification of the reversible capacity loss caused by anode overhang,” *Journal of Energy Storage*, vol. 18, pp. 149–159, 2018, doi: 10.1016/j.est.2018.04.029.
- [7] F. An, H. Zhao, and P. Li, “Self-discharge rates in cells have a critical effect on the cycle life of parallel lithium-ion batteries,” *RSC Adv.*, vol. 8, no. 54, pp. 30802–30812, 2018, doi: 10.1039/C8RA05403G.
- [8] M. Lewerenz, Dissection and quantitative description of aging of lithium-ion batteries using non-destructive methods validated by postmortem-analyses: RWTH Aachen University, 2018.
- [9] A. Farmann and D. U. Sauer, “A study on the dependency of the open-circuit voltage on temperature and actual aging state of lithium-ion batteries,” *Journal of Power Sources*, vol. 347, pp. 1–13, 2017, doi: 10.1016/j.jpowsour.2017.01.098.
- [10] B. Gyenes, D.A. Stevens, V.L. Chevrier, J.R. Dahn, “Understanding anomalous behavior in coulombic efficiency measurements on Li-Ion batteries,” *J. Electrochem. Soc.* 162 (2015) 278e283, <http://dx.doi.org/10.1149/2.0191503jes>.
- [11] M. Lewerenz et al., “New method evaluating currents keeping the voltage constant for fast and highly resolved measurement of Arrhenius relation and capacity fade,” *Journal of Power Sources*, vol. 353, pp. 144–151, 2017, doi: 10.1016/j.jpowsour.2017.03.136.
- [12] Lain, Brandon, and Kendrick, “Design Strategies for High Power vs. High Energy Lithium Ion Cells,” *Batteries*, vol. 5, no. 4, p. 64, 2019, doi: 10.3390/batteries5040064.
- [13] M. Lewerenz and D. U. Sauer, “Evaluation of cyclic aging tests of prismatic automotive LiNiMnCoO₂-Graphite cells considering influence of homogeneity and anode overhang,” *Journal of Energy Storage*, vol. 18, pp. 421–434, 2018, doi: 10.1016/j.est.2018.06.003.
- [14] Theiler, M.; Endisch, C.; Lewerenz, M. Float Current Analysis for Fast Calendar Aging Assessment of 18650 Li(NiCoAl)O₂/Graphite Cells. *Batteries* 2021, 7, 22. <https://doi.org/10.3390/batteries7020022>.

Theoretical and experimental investigation of code correlation methods for optical time domain reflectometry in POF

Denis Unruh, Rainer Engelbrecht, Simon Dengler

Polymer Optical Fiber Application Center, Technische Hochschule Nürnberg Georg Simon Ohm
Wassertorstraße 10 Nürnberg, Germany
Email: unruhde67163@th-nuernberg.de

Abstract—For structural health monitoring in geotechnical engineering, the use of different modulation techniques for the optical time domain reflectometry (OTDR) offer an alternative method to the conventional monopulse method. Due to a higher average optical power in polymer optical fibers (POF), the new modulation methods (Simplex-, Golay) deliver a higher signal-to-noise ratio compared to the monopulse-OTDR. The theoretical basics, simulation models and experimental results are presented for the new methods.

I. INTRODUCTION

The use of coarse-meshed plastic textiles (so-called geogrids) with integrated optical fibers enables the condition of structures to be monitored for impermissible loads due to vibration or strain. This type of condition monitoring is known as structural health monitoring (structural health monitoring (SHM)). The geogrids used to serve to reinforce earthworks against landslides, while the optical fibers (glass optical fiber, polymer optical fibers) are used as optical sensors. Standard PMMA-POF can be strained to more than 40% while fully maintaining their light guiding and sensing properties. These sensors provide information about the location of the local structural damage. [1]

A well known method of using fiber optical sensors is the time-resolved analysis of the optical backscatter of a short incident light pulse. This measurement method is known as optical time domain reflectometry (OTDR). A disadvantage of OTDR methods is the low average optical power along the fiber due to the short light pulse that is required for good spatial resolution. For this reason, many individual measurements must be averaged for precise results, which requires a long measurement time in the range of minutes, which arises from the required pulse intervals due to the pulse transit time. An alternative method therefore uses longer pulse sequences and a mathematical correlation in signal processing (code-correlation OTDR). This could theoretically lead to a greater reproducibility of the strain measurement in a shorter measurement time.

II. OTDR FUNDAMENTALS

A. Polymer optical fibers (POF)

A typical structure of a POF consists of two coaxial layers of homogeneous and optical transparent polymers as shown in Fig. 1. The central part is the core and the outer part is the cladding of the fiber. In order to keep the light in the core, the refractive index of core (n_K) is designed to be lower than that of the cladding (n_M). In order to have total internal reflection at the interface of core and cladding without leaking to cladding, the reflection angle Θ at the interface of core and cladding is required to be smaller or equal to the critical angle:

$$\Theta_{max} = \arcsin\left(\frac{n_K}{n_M}\right) \quad (1)$$

This effect causes the fiber to act as an waveguide and keep the light in the core. [2, S.4]

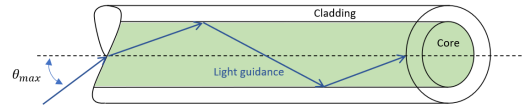


Figure 1. Example of a cross section of an optical fiber

In the event that a light wave hits a flat interface between two media with different refractive indices (e.g. polymer-air), this light is transmitted and scattered back. This effect is known as Fresnel reflection. A fundamental parameter that must be considered for OTDR-measurements is the attenuation along the fiber, which is caused by the fiber material. The attenuation coefficient α (depending on the wavelength) is defined as [3]:

$$P_{out}(z) = P_{in} \cdot e^{-\alpha(\lambda)z} \quad (2)$$

where $P_{out}(z)$ is the output power and P_{in} is the optical power of the input light, as it travels through the fiber $z = v_g \cdot t$ with the group velocity $v_g = \frac{c_0}{n_g}$ of the fiber, which is described by the speed of light c_0 and the effective refractive index n_g . Furthermore, scattering has usually a very strong influence on the attenuation characteristics of optical fibres. Scattering is caused by local changes of the refractive-index. The actual effect of these local variations depends strongly on their size

with respect to the wavelength, the light is scattered into all directions, which can be described by the Rayleigh scattering coefficient α_s . With the backscatter coefficient S , the Rayleigh scattering can be described in the backward direction by [4]:

$$\eta_S = \alpha_s \cdot S \left[\frac{1}{\text{m}} \right] \quad (3)$$

The gradient η_S corresponds to the attenuation coefficient of the fiber.

B. Optical time domain reflectometry (OTDR)

OTDR is the principle of backscatter measurement. A short light pulse P_{in} is coupled into one end of an optical fiber via a coupler and the reflected light is received over time at the same fiber end. Due to the effects in the POF (e.g. Fresnel reflection, Rayleigh scattering), an OTDR backscatter diagram is created, which shows the characteristics of the fiber. Fig. 2 shows the structure of an OTDR-setup and a example for a corresponding backscatter-diagram in a logarithmic scaling. Since the light

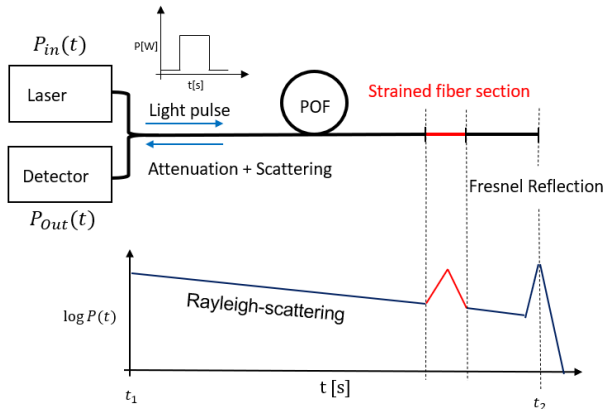


Figure 2. Basic structure of the OTDR method & OTDR Diagram

pulse in this structure has to traverse the fiber in the forwards and backwards direction and thus has a double fiber path, the factor $\frac{1}{2}$ must be taken into account when calculating the position of a peak or for the logarithmic scaling, as shown in equation 5. Due to this prefactor, the calculation is realized for the logarithmic scaling with the factor $5 = 10 \cdot \frac{1}{2}$, so the slope in the OTDR diagram represents the attenuation in $[\frac{\text{dB}}{\text{km}}]$:

$$P_{OTDR}(t) = 5 \cdot \log \left(\frac{P_{out}(t)}{P_{in}(t)} \right) \text{ [dB]} \quad (4)$$

For the conversion from the time domain to the spatial domain:

$$z(t) = \frac{1}{2} \cdot v_g \cdot t \text{ [m]} \quad (5)$$

The OTDR backscatter profile $P_{out}(t)$ is generally described by the convolution (*) of the impulse response $H_{IR}(t)$ [3]:

$$H_{IR}(t) = \frac{v_g}{2} \cdot \eta_S \cdot e^{-\alpha(\lambda)v_g t} \quad (6)$$

of a optical system and the light pulse $P_{in}(t)$ [5]:

$$P_{out}(t) = P_{in}(t) * H_{IR}(t) \quad (7)$$

III. MODULATION TECHNIQUES

The approach to use modulation techniques of the light source for the OTDR-measurement has already been published in innumerable studies [5] - [10]. Various modulation methods were investigated for this, such as the Barker-code or PRBS-sequences [7]. Since these have not been found to be suitable for such measurements, the Golay- and Simplex-codes are considered for further investigation. All these investigations relate to the experimental implementation of the respective modulations in single-mode fibers, whereby the present work deals with the new approach to implement these methods in multi-mode fibers such as POF.

A. Golay-Code (GC)

To investigate code methods with correlation-based signal processing, the use of bipolar code types with ideal autocorrelation properties is essential. These code-sequences must provide autocorrelation properties that have no other side lobes, apart from the main peak at $t = 0$. In this case, the use of complementary code pairs with an appropriate signal processing turned out to be ideal for the OTDR method. A complementary code sequence is defined as a pair of finite sequences of two kinds of elements that have the property of having the same number of elements. [5]

The Golay-Code method always has two code sequences that are of the same length and can be extended infinitely. Two sequences are complementary if the sum of the autocorrelations of the two sequences is zero for all nonzero shifts. Assuming a Golay-Code delivers two sequences A_L and B_L with $(i = 1, 2, 4, \dots, 2^N)$ of two L -long complementary series, the respective discrete autocorrelation (*) terms of each sequence can be described as [8]:

$$R_{aa} = A_L * A_L = \sum_{i=-L}^L A[i] \cdot A[i+n] \quad (8a)$$

$$R_{bb} = B_L * B_L = \sum_{i=-L}^L B[i] \cdot B[i+n] \quad (8b)$$

where the sum of the autocorrelation terms, delivers the following equitation.

$$R_{aa} + R_{bb} = 2L\delta_i \quad (9)$$

with

$$\delta_n = \begin{cases} 1, & \text{for } n=0 \\ 0 & \text{otherwise} \end{cases}$$

The calculation of the complementary Golay-Code pair is known as 'appending'. This designation becomes clear when the two codes A_L and B_L are considered, which are formed by adding the sequences A and B and the sequences A and \bar{B} [8]. These procedure can be described as:

$$\begin{pmatrix} A \\ B \end{pmatrix} \rightarrow \begin{pmatrix} A & | & B \\ A & | & \bar{B} \end{pmatrix} \quad (10)$$

Starting with a 2-element code pair with the initial values $A=1$ & $B=1$ and length 1, Golay-Codes of lengths $L = 2, 4, 8, 16, \dots, 2^N$ can be calculated. \bar{B} is the complement of variable B and swaps the value 1 to -1.

$$\begin{pmatrix} 1 \\ 1 \end{pmatrix} \rightarrow \underbrace{\begin{pmatrix} 1 & 1 \\ 1 & -1 \end{pmatrix}}_{L=2} \rightarrow \underbrace{\begin{pmatrix} 1 & 1 & \dots & 1 \\ 1 & 1 & \dots & -1 \end{pmatrix}}_{L=2^N}$$

This process will always produce bipolar sequences. The first line forms the bit sequence of the first sequence A_L , correspondingly the second line forms the second sequence B_L . To illustrate the theoretical basis, a Golay-Code of length $2^7 = 128$ is calculated below. The shape of the respective sequences is visualized in the figure 3. By calculating the autocorrelation of the respective sequences and by finally adding the autocorrelation functions, a result is obtained with a main lobe of height

$$2 \cdot L \cdot \delta_0 = 2 \cdot 128 \cdot 1 = 256$$

and the complete cancellation of the noise-like, but deterministic side lobes is achieved, as shown in figure 4.

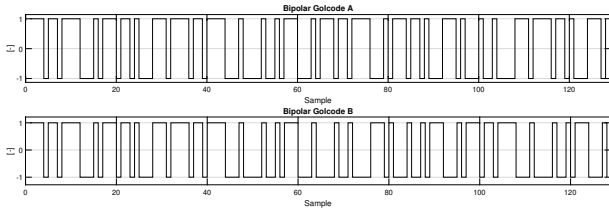


Figure 3. Golay-Codes of length $2^7 = 128$

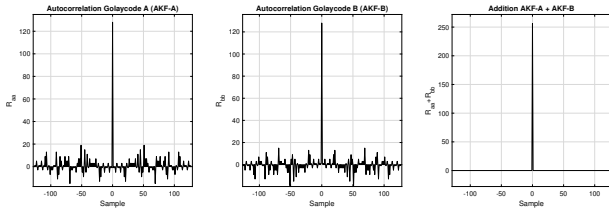


Figure 4. Autocorrelation of the Golay-Codes of length $2^7 = 128$

1) *Signal processing of the Golay-Code:* As shown in equation (7), the result of an OTDR measurement $P_{out}(t)$ can be described by the convolution ($*$) of the coupled light pulse $P_{in}(t)$ with the transfer function $H_{IR}(t)$ of a corresponding system. If one looks at the identical system using two complementary Golay code sequences, the result of an OTDR measurement can be described as:

$$P_{out}^A(t) = H_{IR}(t) * A_L(t) \quad (10a)$$

$$P_{out}^B(t) = H_{IR}(t) * B_L(t) \quad (10b)$$

In the next step, it is necessary to calculate the correlation described above. Since two different signals are correlated with

one another here, this process can be referred to as cross-correlation ($*$) in the present case.

$$y_A(t) = A_L * P_{out}^A(t) \quad (11a)$$

$$y_B(t) = B_L * P_{out}^B(t) \quad (11b)$$

Finally, in order to obtain the monopulse equivalent OTDR-trace, the sum of the cross-correlations is formed.

$$P_{out}(t) = y_A(t) + y_B(t) \quad (12)$$

The entire algorithm for the Golay-Code signal processing can be described by:

$$P_{out}(t) = A_L * P_{out}^A(t) + B_L * P_{out}^B(t) \quad (13a)$$

$$= (A_L * A_L + B_L * B_L) * H_{IR}(t) \quad (13b)$$

$$= 2L\delta_k * H_{IR}(t) \quad (13c)$$

$$\rightarrow P_{out}(t) = 2LH_{IR}(t) \quad (13)$$

The result obtained in equation (13) corresponds to the monopulse OTDR-signal, based on a code sequence with a much higher average power.

2) *Conversion of bipolar codes to unipolar codes:* In order to convert this process into a real optical system, it must be noted that an optical system has unipolar properties. This means that a light source can only be modulated with a value of 0 (light off) and a value of 1 (light on). However, a calculated bipolar sequence cannot simply be converted by replacing the -1 with 0, since such a function would no longer correspond to the properties of the complete subtraction of the sidelobes of the autocorrelation. For this reason, each bipolar code word must be split into further unipolar sequences, which in total correspond to the original sequence. In general, the bipolar sequence A can be described by the unipolar sequence A_1 & A_2 and the sequence B by B_1 & B_2 [9].

$$A = A_1 - A_2 = \underbrace{\frac{1+A}{2}}_{A_1} - \underbrace{\frac{1-A}{2}}_{A_2} \quad (14)$$

$$B = B_1 - B_2 = \underbrace{\frac{1+B}{2}}_{B_1} - \underbrace{\frac{1-B}{2}}_{B_2} \quad (15)$$

The respective bipolar sequences are converted into a unipolar code by adding or subtracting from 1 and divided by 2 for normalization. By subtracting the unipolar code A_2 from A_1 we get the original bipolar sequence A. Correspondingly, the same procedure takes place with the sequence B. For use in a real system, the respective four sequences must now be coupled into the fiber and its backscatter profiles subtracted from one another. Correspondingly, the backscatter profile of sequence A_2 has to be subtracted from that of A_1 and that of B_2 has to be subtracted from B_1 . Finally, the correlations of the backscatter profiles with the bipolar sequences A and B are carried out and the backscatter profile of the fiber is obtained by adding the correlation results.

B. Simplex-Code (SC)

The simplex code is a further coding option for an OTDR-measurement. No correlation techniques are used with the simplex code and the number of the respective sequences depends on the length of the code and, accordingly, on the matrix size, because the simplex code is derived from the bipolar Hadamard matrix. It is possible to calculate code lengths of ($i = 3, 7, \dots, 2^N - 1$) and extend them infinitely accordingly. Unlike the Golay code, you will always get an odd number of the code length. The values for a simplex code are derived from the so-called S matrix, which is calculated from the transformation of a Silvester - Hadamard matrix. The Sylvester Hadamard matrix of order N is constructed by the Kronecker tensor product \otimes of an initial matrix [10]:

$$H_2 = \begin{pmatrix} 1 & 1 \\ 1 & -1 \end{pmatrix} \quad (16)$$

leading to:

$$H_{2^N} = H_2 \otimes H_{2^{N-1}} = \begin{pmatrix} \mathbf{H}_{2^{N-1}} & \mathbf{H}_{2^{N-1}} \\ \mathbf{H}_{2^{N-1}} & -\mathbf{H}_{2^{N-1}} \end{pmatrix} \quad (17)$$

When the desired matrix size has been calculated, the first column and the first row must be removed, as these will always consist of the value 1. Finally, the complement of the calculated matrix is formed and by replacing the values -1 with 0, a unipolar matrix is formed from the bipolar matrix. The result obtained is called the S-matrix. The individual rows form the bit pattern of the respective sequences of the simplex code. For example, if a second-order matrix $2^{N=2} = 4$ is calculated, this would result in an S-matrix with the size $2^2 - 1 = 3$ after the conversion:

$$H_4 = \begin{pmatrix} 1 & 1 & 1 & 1 \\ 1 & -1 & 1 & -1 \\ 1 & 1 & -1 & -1 \\ 1 & -1 & -1 & 1 \end{pmatrix} \rightarrow S_3 = \begin{pmatrix} 1 & 0 & 1 \\ 0 & 1 & 1 \\ 1 & 1 & 0 \end{pmatrix}$$

The individual rows of the S matrix form the respective codewords. In the present case, an S-matrix S_3 supplies the code words: CW1=[1 0 1]; CW2=[0 1 1]; CW3=[1 1 0]. It can thus be seen that the number of code words depends on the respective matrix size. Each of these codewords are then fed into an optical system and, after appropriate signal processing, an OTDR-backscatter profile is obtained.

1) *Signal processing of the Simplex-Code:* The convolution operation according to equation 7 can also here be used to describe the respective backscatter profiles $\eta_k(t)$ of the individual code words [6]:

$$\begin{pmatrix} \eta_1(t) \\ \eta_2(t) \\ \dots \\ \eta_{2^N-1}(t) \end{pmatrix} = S_L * H_{IR}(t) \quad (18)$$

In order to restore the conventional OTDR-backscatter profile ψ , the respective backscatter profiles are processed with the inverse S-matrix S^{-1} .

$$\begin{pmatrix} \hat{\psi}_1(t) \\ \hat{\psi}_2(t) \\ \dots \\ \hat{\psi}_{2^k-1}(t) \end{pmatrix} = S_L^{-1} \begin{pmatrix} \eta_1(t) \\ \eta_2(t) \\ \dots \\ \eta_{2^k-1}(t) \end{pmatrix} \quad (19)$$

Finally summed up using a pulse-width τ dependent shift and averaged over the number of code words, we obtain the final OTDR-trace:

$$P_{out}(t) = \frac{1}{L} \sum_{i=1}^L \hat{\psi}_k(t + (i-1)\tau) \quad (20)$$

IV. THEORETICAL INVESTIGATION

For the theoretical investigation of the properties of a OTDR-method, a simulation is created by using the software MATrix LABoratory (MATLAB). This simulation enables to investigate monopulse OTDR-methods depending on the properties of optical components (e.g. bandwidth, noise) or polymer optical fibers (e.g. length, attenuation). The simulation consists of a central control-program that combines all methods and calculation steps and delivers the corresponding backscatter traces for the respective modulation method (Monopuls, Simplex, Golay). The figure 5 shows the result of a simulation taking into account a 5ns puls width and a fiber length of 50m.

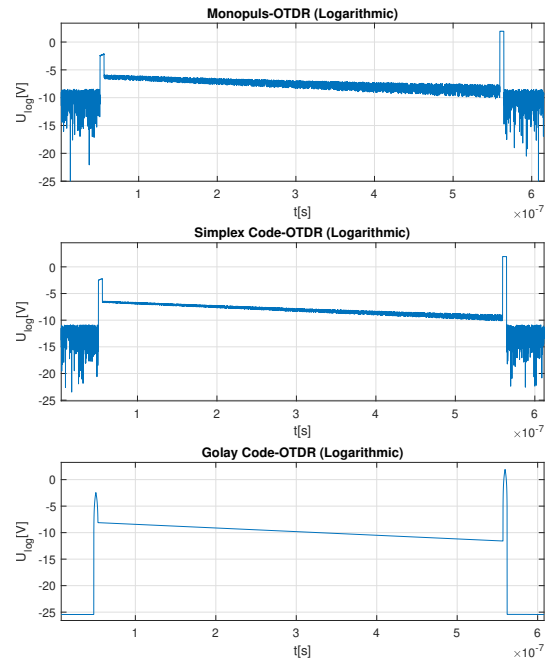


Figure 5. Representation of the simulation results in logarithmic scaling

The result of the simulation clearly shows that, on the one hand, the theoretical models of the modulation techniques can be implemented in the simulation and function correctly. It can also be observed that the use of modulation techniques leads to an improvement in the SNR compared to

the conventional monopulse method. The simulation makes it possible to examine a wide variety of pulse modulations, taking into account the characteristics of optical components, without having to create complex laboratory set-ups. This simplifies the investigation of different modulation functions and makes an important contribution to the project SmartOSE for monitoring of geogrids.

V. EXPERIMENTAL INVESTIGATION

To carry out the experimental investigation, a monopuls-OTDR should be realized in the first step with the existing laboratory equipment in order to show that the test set-up works correctly. In the next steps, the modulation methods of the Simplex and Golay codes should then be examined with the properly working test set-up. The same laboratory equipment/fibers should be used for all methods and measurements. The signal processing, the modulation and the entire test set-up should be controlled centrally by MATLAB. The figure 6 shows the laboratory test set-up.

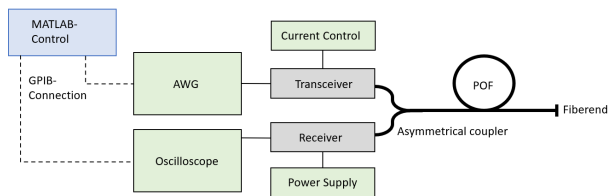


Figure 6. OTDR-investigation test configuration

To evaluate the respective methods, the results of the experimental investigations should be presented in a OTDR-logarithmic scale (figure 7). The experimental results have shown, that the coding methods (Simplex, Golay) produce results similar to those of the monopulse-OTDR. The present study has proven that the methods works correctly. The plausibility checks have shown that all coding methods work correctly and deliver correct results.

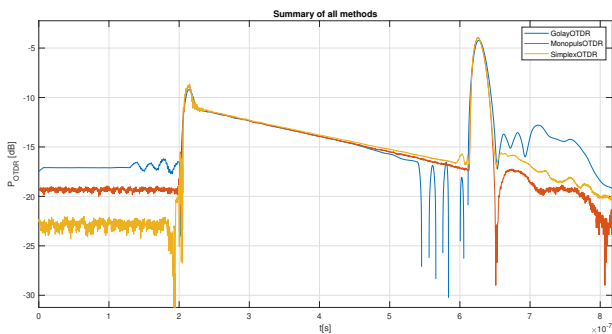


Figure 7. Summary of preliminary OTDR-experiments (Monopuls, Simplex, Golay)

VI. CONCLUSION

To investigate code methods for the optical time domain reflectometry, a simulation was initially created using the MATLAB software. In the first step, the monopuls-method was

implemented in the simulation to ensure that it works correctly and that it can be compared with known results. In the next step, the theoretical knowledge of the Simplex and Golay-Code was implemented in the simulation. The simulation clearly showed that the algorithms were correctly implemented in MATLAB and that the new methods lead to an SNR improvement in the same measurement time. The simulation outputs results for various OTDR-modulations and offers the possibility of comparing them. The simulation can be used to examine different code lengths, pulse widths, fiber properties or properties of the optical components. Initial investigations also provide OTDR curves that are experimentally similar to those of monopulse. In this way, a fundamentally correct implementation in the measurement setup was achieved experimentally and the data evaluation algorithms were realized correctly. Both the theoretical and experimental investigations have shown that the modulation methods can be used for an OTDR-setup and provide a typical OTDR-backscatter trace, further investigations to optimize the method are being carried out.

ACKNOWLEDGMENT

This work has been funded by the Federal Ministry of Education and Research, funding program Forschung an Fachhochschulen (FHprofUnt) under contract number 13FH137PX6, "Optische Sensoren zur Überwachung von Erdstrukturen (SmartOSE)".

REFERENCES

- [1] LIEHR, Philipp; Krebber Katerina; Seeger Monika; Thiele Elke; Metschies Heike; Gebreselassie Berhane; Muenich Johannes; Stempniewski L. Sascha; Lenke L. Sascha; Lenke: Distributed Strain Measurement With Polymer Optical Fibers Integrated into Multifunctional Geotextiles. In: *Proceedings of SPIE - The International Society for Optical Engineering 7003* (2008), April
- [2] DING, Desheng; Wang Wenyu; Luo Yanhua; Peng Gang-Ding Mingjie; F. Mingjie; Fan ; PENG, Gang-Ding (Hrsg.): *Basics of Optical Fiber Measurements*. Springer Singapore, 2018
- [3] HARTOG, Martin Arthur; G. Arthur; Gold: On the theory of backscattering in single-mode optical fibers. In: *Journal of Lightwave Technology* 2 (1984), April, Nr. 2, S. 76 – 82
- [4] VARSHNEYA, Stefan Mohr; Luis Figueroa; Mototaka Kitazawa; Norris E. Lewis; Robert E. Steele; D.: Characterization of plastic optical fibers by optical time-domain reflectometry. In: *Specialty Fiber Optic Systems for Mobile Platforms and Plastic Optical Fibers* Bd. 1799 International Society for Optics and Photonics, SPIE, 1993, S. 38 – 47
- [5] NAZARATHY, S.A.; Giffard R.P.; Moberly D.S.; Sischka F.; Trutna W.R.; Foster S. M.; Newton N. M.; Newton: Real-time long range complementary correlation optical time domain reflectometer. In: *Journal of Lightwave Technology* 7 (1989), Nr. 1, S. 24–38
- [6] LEE, Hosung; Kim Pilhan; Park Jonghan; Park N. Duckey; Yoon Y. Duckey; Yoon: Optimization of SNR improvement in the noncoherent OTDR based on simplex codes. In: *Lightwave Technology, Journal of* 24 (2006), Februar, S. 322– 328
- [7] WANG, Chang Yan; S. Yan; Sun: The Application of Pseudo-Random Sequence in the Properties Measurement of Polymer Optical Fiber. In: *Applied Mechanics and Materials* (2013), März, Nr. 313, S. 653–657
- [8] GOLAY, M.: Complementary series. In: *IRE Transactions on Information Theory* 7 (1961), Nr. 2, S. 82–87
- [9] MUHAMMAD, Haleema; Naseem Anwar; Abbas S. Sajid; Mehmood M. Sajid; Mehmood: Hybrid Coding Technique for Pulse Detection in an Optical Time Domain Reflectometer. In: *Radioengineering* 21 (2012), Juni
- [10] JONES, M.D.: Using simplex codes to improve OTDR sensitivity. In: *IEEE Photonics Technology Letters* 5 (1993), Nr. 7, S. 822–824

Method development for the detection of filmic contaminations in additive manufacturing

Steffen Weinmann
 Department of Mechanical, Automotive
 and Aeronautical Engineering
 Munich University of Applied Sciences
 Munich, Germany
 weinmann@hm.edu

Abstract — Filmic contaminations on component surfaces cause a wide variety of negative influences over the entire process chain in additively manufactured components. In order to remove these contaminations and later ensure the proper functionality of subsequent processes, a comprehensive knowledge of type, composition and amount of the contamination is indispensable. For this reason, the development of methods for rapid and spatially resolved detection of filmic contaminants is required to produce sufficient component quality and thus remain competitively. In this paper, previously selected methods that are capable of analyzing filmic contamination for various criteria are presented. Impulse Thermography and laser-induced fluorescence measurement were used for the imaging of filmic contaminations on a reference component made of polyamide 12. By outputting dimensionless intensities of the measured heat or fluorescence, calibration lines were generated to quantify the contamination. Furthermore, fluorescence spectroscopy was found to be suitable for the identification of the contamination against references due to characteristic excitation and emission wavelengths. Infrared spectroscopy can likewise be used to detect characteristic absorption bands that can be utilized to draw conclusions about the origin of the contamination. A quantification can also be performed via calibration lines. Since the contaminations must be present in solution for spectroscopies, a method for extracting the contaminations from the component surface was developed in parallel. Using a sampler followed by extraction in suitable solvent, selected reference contaminations were analyzed.

Keywords — *technical cleanliness, filmic, contaminations, additive manufacturing, inspection*

I. INTRODUCTION

A growing market for additively manufactured components with simultaneous increasing demands on technical cleanliness results in the need to detect contaminants and remove them to a predefined degree [1, 2]. Additive manufacturing allows a high degree of design freedom for components in order to create complex structures such as cavities, undercuts or cooling channels. At the same time, process-related accumulations of particular (particles, fibres) and filmic contaminants (oils, fingerprints) occur, which can impair the functionality of the component and are difficult to remove due to the geometries just mentioned [3]. Especially in post-processes, such as eroding the component from the building platform or various surface post-treatments, for instance polishing, undesirable production aids can remain on the component. The results for subsequent processes are a reduction the quality and a shortened service life, as even the slightest contaminations can influence the sufficient adhesion behavior during gluing, welding or coating [4].

To be able to remove these residues, it is particularly important to design a cleaning process chain according to requirements. In order to fulfil this task, it is essential to have a broad knowledge of the contamination at hand. Polarity, chemical composition as well as quantity and location of the contamination are examples of information that have direct influence on the selection of parameters such as cleaning chemistry, mechanics, time and temperature [5].

The aim of the work is therefore to develop methods for analyzing filmic contaminations, as these have received less attention in the past than particular contamination, which were addressed early on in the VDA19 [6]. In cooperation with research projects of the Fraunhofer Institute for Casting, Composite and Processing Technology, components are researched that were manufactured from polyamide 12 using the selective laser sintering process. In addition to the development of methods for the analysis of filmic contaminations, an extraction method is also developed for indirect (spectroscopic/chromatographic) methods that can convert contaminations quickly and efficiently into solution.

II. METHOD

Available analysis methods were selected based on an utility value analysis according to VDI 2225 [7]. The most important criteria were weighted via a survey with a pairwise comparison in order to evaluate the analysis methods subsequently. For the former, this work covers laser-induced fluorescence and active thermography, and for the latter, ATR infrared spectroscopy and fluorescence spectroscopy.

A. Reference components and contaminations

Reference components and contaminants representative of additive manufacturing are used to develop the analysis method. With regard to the research at Fraunhofer IGCV and the state of the art, the selective laser sintering process (SLS) is chosen as one of the most common used representatives of 3D printing technology [8]. As a characteristic example, the most frequently used material in SLS is polyamide 12 [9].

Aiming to be able to examine complex structures such as lettering, grid structures, channels and QR codes, a sample component, which has the required microstructures on one side and is flat on the other side, was created (see figure 1).

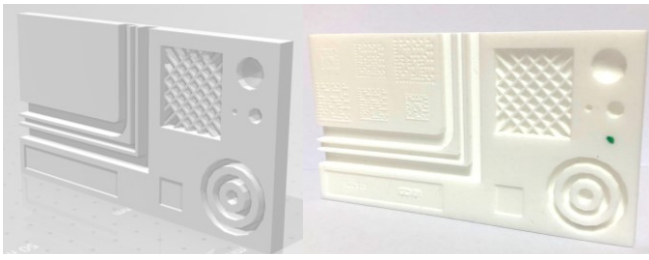


Fig. 1: Reference component as CAD blank (left) and additively manufactured (right)

Since the laser sintering process itself evaporates all possibly occurring filmic contaminants (e.g. from the powder or from the roller) due to heat input, none of them should be present after manufacturing. Mainly post-processes, like surface finishing, are of interest, because they leave manufacturing aids behind. Similarly cross and environmental contamination, such as fingerprints, oily vapors or dirt in shipping crates, must be observed [10]. Using studies of the most commonly used post-processing methods in additive manufacturing and determining the largest intersection of commonly occurring filmic contaminants, cooling lubricants and lubricating oils are identified [3, 11, 12]. Because the studies refer to all materials in 3D printing, the statements cannot be applied to plastic components alone, but also contamination with lubricating oil from the compressed air used for blowing off the powder is often found. However, reproducible method development can take place via the lubricants mentioned. Based on these contaminants, the methods can then be applied to application examples from industry. In the attempt of being able to consider different polar substances, the water-soluble (polar) cooling lubricant Syntixol 6.5 from Tribol Chemie GmbH and the non-polar lubricating oil Wicoil 754 from Wilke Kühlschmiertechnik GmbH are selected as application examples.

B. Extraction method

In order to analyze filmic contaminations with indirect measuring instruments, it is necessary to transfer the residues into a solution. The research of a fast and efficient extraction method should enable an analysis coupled to the production. The large-scale rinsing of the component surface with solvent, which is evaporated subsequently in order to measure non-volatile residues (short: nvr), is currently

standard [13]. This method is not only costly and time-consuming, but information about the location of the contamination is also lost.

Local sampling can be performed using various samplers. These are swept in a specific pattern over a defined area of the components surface in the first step. Secondly, the sampler with the contamination on it is put into an extraction vessel filled with a suitable solvent. Swabs, cloths and sponges have proven their worth as samplers in biology and pharmacy [14]. These are able to soak themselves with solvent in order to remove residues from the surface and to release them later. It is also important that the samplers themselves have a sufficiently low level of contamination (e.g. total organic carbon (TOC) limits) and do not tend to abrasion during sampling. In the third step, various mechanisms of action (shaking, ultrasound...) can be used to improve the extraction of contaminations from the sampler. A detailed procedure on how to extract a contaminant from a flat surface with a swab is described in Figure 2.

For a successful extraction method, a suitable solvent that can dissolve both polar and non-polar impurities and is compatible with the material of the component and the sampler must be selected. Solvents that lead to little distortion of the spectrum in infrared spectroscopy and have a UV cutoff in the low UV-C range in fluorescence spectroscopy are advantageous. For this reason, isopropanol has been chosen for all further experiments, since both reference contaminations can be dissolved in it. Moreover, the porosity of the component comes into play as this factor binds the contamination in the component and makes extraction more difficult.

C. Sample Preparation

Since the selected analytical methods each involve two imaging and spectroscopic evaluations, the samples must be prepared differently. Due to the absence of concrete parameters and measured values, geometric dilution series of the selected reference contaminations are prepared using isopropanol. Thus, concentrations from 10,000 ppm to 1 ppm were set up for the spectroscopic procedures.

In order to contaminate the plane surface of the component with the lubricants via a squeegee system, a 20% solution of the references were prepared with isopropanol.

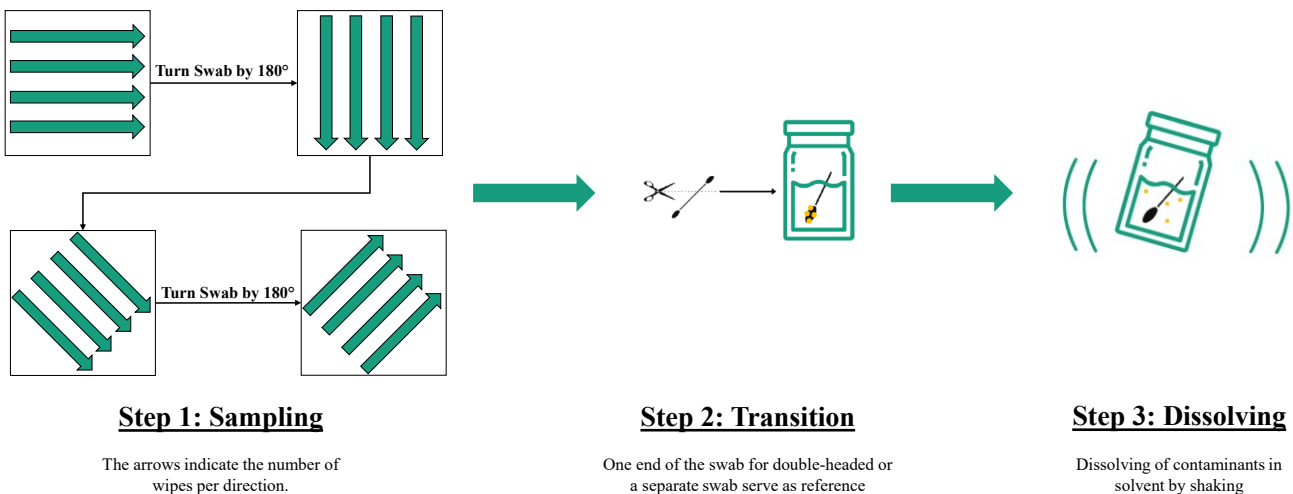


Fig. 2: Extraction Method using the example of Swab Sampling on a plane surface

In order to create a calibration line for imaging methods, wet layer thicknesses of 10 μm, 25 μm, 50 μm and 100 μm were squeegeed and the solvent was then evaporated on air for at least one hour.

The required squeegee volume can be calculated from the fact that a layer geometrically resembles a cuboid. The volume is calculated as the product of the desired layer depth d and the squeegee area A , which is composed of the length l and width w of the area.

$$(1) V_s = l * w * d$$

Due to the clamping of the component in the squeegee device, the entire surface of the component cannot be coated, which is why the area to be coated for the sample plastic parts is

$$A = 10 \text{ cm} * 6.5 \text{ cm} = 65 \text{ cm}^2.$$

In order to ensure a continuous layer, an excess of 0.1 ml squeegee volume is applied since excess application material is removed anyway.

For further calculations, the dry layer thickness is relevant since the solvents evaporate from the wet layer thickness. This is evidenced by measurements in infrared spectroscopy, where no peak appears in the O-H bonds after evaporation of the isopropanol. Thus, the layer thickness d of the filmic contamination is changed, but not the squeegee area A . For the calculations, the mass of the film is required, which is why it is exemplary listed in Table 1 and can be calculated via

$$(2) \rho = \frac{m}{V}$$

and

$$(3) \rho_{\text{solution}} = \frac{1}{V} \sum_i m_i = \frac{\sum_i \rho_i * V_i}{V}.$$

Table 1: Calculations for dry layer thickness with d_w as wet layer thickness, V_s as Squeegee volume, m as mass of the contamination, d_{td} as theoretical dry layer thickness, d_{gd} as gravimetrically measured dry layer thickness and Δ as deviation.

d_w [μm]	V_s [μl]	m [g]	d_{td} [μm]	d_{gd} [μm]	Δ [%]
100	0,6500	2,0740	20	19,6	4,0
50	0,3250	1,0372	10	9,80	2,0
25	0,1625	0,5186	5	4,76	4,8
10	0,0650	0,2074	2	1,96	2,0

Table 1 was filled in for the cooling lubricant with 20% dilution in isopropanol. The theoretical dry film thickness can be calculated via the squeegee volume and the mass of the contamination, which was checked by gravimetric measurement before and after drying. The difference between the theoretical and gravimetric film thickness provides information on the validity of the method used. In the following, only the wet layer thickness will be considered since the dry layer thickness can be easily calculated if required.

In order to subject complex geometries to the extraction method, the QR codes are each prepared by pipetting 50 μl of the 20% dilution. Theoretically, this results in a contamination of 10 μl or 9,63 mg of the reference impurities.

III. RESULTS

A. Laser induced fluorescence

In particular, fats and oils tend to fluoresce after excitation with certain wavelengths [16]. The emitted light can be detected unambiguously after spectral filtering of the excitation wavelength, because the emission wavelength shifts into the longer wavelength range due to the Stokes shift. The F-scanner makes use of this property and scans the surface of the sample component point by point with a laser in order to process the signals obtained in real time by means of imaging [17].

Using non-fluorescent components the contamination can be detected down to minute amounts. Due to the presence of a π-bond, the polyamide 12 tends to self-fluoresce, which already creates a signal originating from the material of the component and complicates the measurement. If the scale is manipulated by setting the lower limit to the value of a blank measurement of a clean sample, the background signal will be masked largely.

The four layer thicknesses were each squeegeed and examined on four components and then an average was taken for each film thickness. The resulting calibration curves can be viewed in Figure 4 and later used to quantify contamination on components.

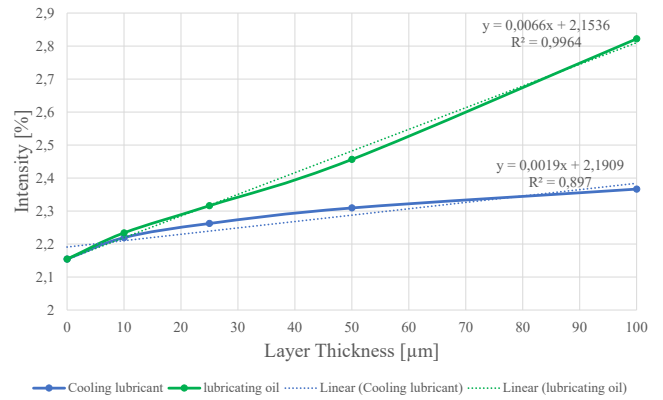


Fig. 3: Calibration curves for Syntixol 6.5 and Wicoil 754 on polyamide 12 with different wet layer thicknesses

For sufficient accuracy, compensation lines with associated straight-line equations were created to be able to rearrange them according to the coating thickness. With the values for the coefficient of determination, the compensation line describes the measured values very well and it confirms that the fluorescence intensity increases linearly with the layer thickness.

If the general equation of the straight line is transferred to the layer thickness and fluorescence intensity, the following will be obtained.

$$(4) I(d) = m * d + c$$

With I as fluorescence intensity, d as wet layer thickness, m as straight-line slope and c as y-axis intercept.

The straight-line equations for Wicoil 754 (5) and Syntixol 6.5 (6) are as follows:

$$(5) y = 0,0066x + 2,1536$$

$$(6) y = 0,0019x + 2,1909.$$

If these equations are converted according to the layer thickness, the calibration line for the lubricating oil Wicoil 754 is obtained:

$$(7) d(I) = \frac{I}{0,006} - 358,90 \mu\text{m}$$

and for the cooling lubricant Syntixol 6.5

$$(8) d(I) = \frac{I}{0,0019} - 1153,11 \mu\text{m}.$$

The influence of porosity and the associated entrainment of the contamination into the component is to be taken into account in all measurements. Fluorescence images differ significantly when comparing a measurement taken directly after application of the contamination and a sample first viewed 180 minutes later since the average intensity decreases by approximately 15%. This behavior can be observed for both impurities. Similarly, repeated irradiation of the contaminated component appears to have an effect on the fluorescence intensity, which was found to decrease by approximately 0.0005% after each measurement. Since the decrease also occurs on components without contamination, it is reasonable to assume that the laser changes the structure of the component. Due to the high power of the laser ($P = 300 \text{ mW}$), it is possible that the specific surface area decreases due to re-sintering and thus the fluorescence intensity decreases. This effect is not observed on metallic components.

Since the contaminations to verify the extraction method were only pipetted onto the QR codes of the sample component, the layer thickness is unknown. After measuring the fluorescence intensity for Wicoil 754 and Syntixol 6.5, a coating thickness of $17 \mu\text{m}$ and $12 \mu\text{m}$ can be determined via the calibration lines.

B. Fluorescence Spectroscopy

In fluorescence spectroscopy, some considerations must be made before the first measurements. Attention must be paid to the correct selection of a solvent as well as the recognition of a range in which linear correlations of the measurement are recognizable. Furthermore, the so-called artifacts, device-specific deflections in the spectrum due to the diffraction of the laser waves by the monochromator, must be taken into account. These artifacts can be observed along with a 10% dilution of the lubricating oil in isopropanol in Figure 4, where the ordinate is the excitation wavelength and the abscissa is the fluorescence wavelength. The color scale describes the dimensionless digital intensity of the fluorescent light.

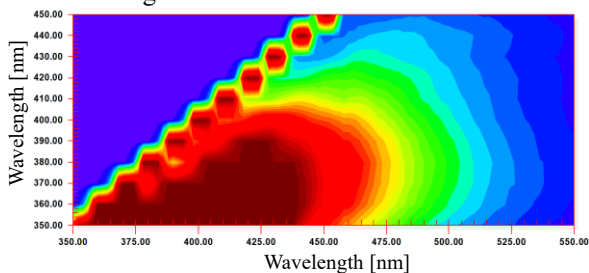


Fig. 4: Fluorescence spectrum of a 10% dilution of the lubricating oil with isopropanol

The precise consideration of a suitable solvent is due to their property to have a UV cutoff wavelength. Below this specific wavelength, solvents absorb all light, which means that no signal can be perceived in the spectrum below it. After weighing this and other requirements (solubility of various polar impurities, health risks, etc.) for the solvent, isopropanol (UV cutoff: 205 nm) and hexane (UV cutoff: 195 nm) are particularly suitable; acetone is excluded due to its UV cutoff at 330 nm.

In addition, the shift in the spectrum due to the solvent must be considered. The internal conversion of excitation energy leads to dissipation of energy by vibrational modes and collisions with the solvent molecules, resulting in a decrease in fluorescence intensity and a shift of the curve to higher concentrations. If the individual dilutions are measured, individual coordinates will be selected to calculate an average value for each sample. In order to obtain a statement about the linearity, the intensities are entered in a coordinate system in figure 5, whereby the application of the concentration is logarithmic.

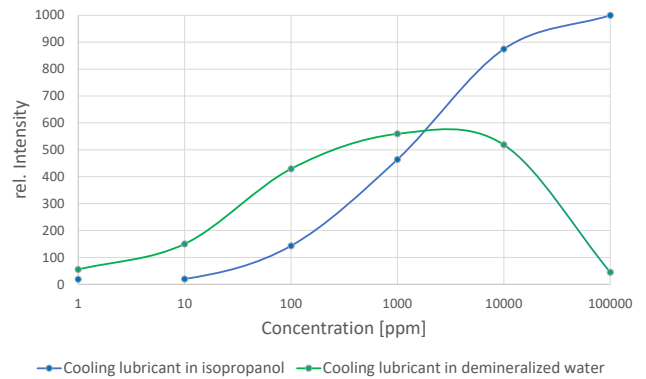


Fig. 5: Fluorescence spectroscopic measurements of dilution series of cooling lubricant in deionized water and isopropanol

A decrease in fluorescence intensity can be seen from about 5000 ppm in water. Various physical effects lead to this observation at higher concentrations, such as clouding of the sample, which leads to reduced transmission and various scattering phenomena, like Mie and Raman scattering. Because the cooling lubricant turns milky in water, but not in isopropanol, the fluorescence intensity is generally lower in water. However, as soon as a certain concentration is exceeded, depending on the solvent, the spectra are no longer meaningful. This behavior is described by the internal filter effect: Most of the fluorescence light is absorbed by the sample itself. The flattening of the Syntixol-isopropanol curve between 10^4 and 10^5 ppm indicates that this phenomenon already occurs there. Since the extracted concentrations (down to 10 ppm) are much lower in practice, fluorescence spectroscopy is suitable for even the minimal contamination.

C. Active Thermography

Because filmic contaminants have a thermal conductivity that differs from that of polyamide 12, thermography can provide an image by measuring infrared radiation, which, according to Plank's theory, is emitted by all bodies with a temperature above absolute zero. By exciting the contaminated component with a high-energy flash, the component is homogeneously heated to record the cooling subsequently. If

several hundred images per second are recorded the filmic contaminants will be detected in some of these images [18]. Parallel to the laser-induced fluorescence measurement, calibration lines can be plotted with the prepared samples by marking a region for each layer (region of interest, ROI for short) and displaying the horizontal profile of the dimensionless intensity (see figure 6).

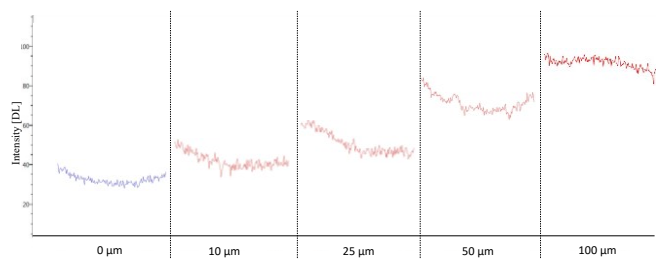


Fig. 6: Images of the QR code with suitable parameters clean (left), contaminated (middle) and extracted (right).

Because the intensities are already very close to the theoretically measurable minimum, the Fourier transform with the resulting phase of the signal provides further information content to interpret the differences of the origin of the signal.

The phase distinguishes different properties of the component and the contamination from each other, which often results in a more differentiable image depending on the difference in thermal conductivity, as shown in figure 7. Shown is a contaminated hole of the sample component with 2 mg of the cooling lubricant.

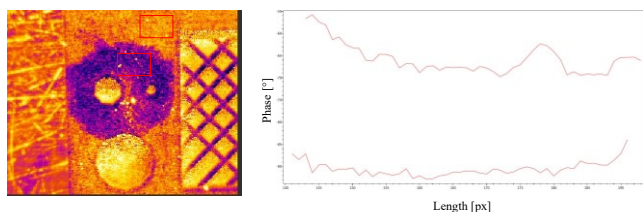


Fig. 7: Thermographic image of contamination around a hole (left) and the phase diagram of cleaned component surface and contaminated component surface (right).

The Fourier transform reveals distinct differences between contaminated and clean surfaces visually. The phase diagram over the length of the ROI also shows clear differences of the signal. If both the intensity and the phase of the signal are evaluated, contamination can be displayed clearly and quantified.

The overall experimental setup is of particular interest, too. The best results are obtained in darkened rooms since ambient light reduces the sensitivity. Furthermore, the energy input of the flash should be as uniform as possible, which means that the flash lamp must be arranged vertically above the component. The camera can therefore no longer be positioned vertically and must measure at a 45° angle.

D. Infrared spectroscopy by ATR

The applied dilution series can be analyzed by means of infrared spectroscopy by ATR. The absorbance is measured in a wavenumber range from 500 to 4000 cm^{-1} in order to

conclude the identity of the impurity on the basis of characteristic bands in the spectrum subsequently.

Due to the commonality of the reference impurities and the solvents to consist mainly of hydrocarbons, an unambiguous determination is not possible. However, the possibility of heating the ATR crystal and allowing the solvent to evaporate offers the possibility of looking at the residual contamination alone.

One way of quantification derives from the decrease in the peak of the O-H group at 3600 to 3200 cm^{-1} due to the isopropanol, see Figure 8. The more impurity in the solution, the lower the peak compared to pure isopropanol. The absorption bands of the C-H bonds behave in the opposite way at 3000 to 2800 cm^{-1} since the absorption is increased by the contamination.

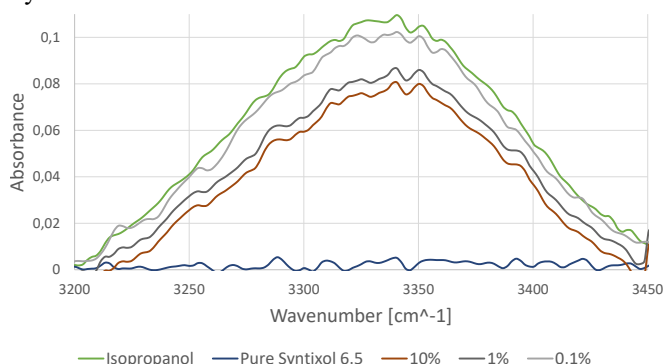


Fig. 8: Quantification of different dilutions using the absorbance of specific alcohol bonds from solutions of Syntixol 6.5 in isopropanol

In order to make a statement about the concentration of the solution, the concentration should not be less than 0.1%.

Since many industrial process aids contain additives that reveal specific bands in the infrared spectrum, it is still possible to make a statement about the identity of other contaminants.

E. Extraction Method

In order to examine the extraction procedure presented, the sample components were contaminated as described. For verifying the functionality, the detached contamination is quantified by using gravimetry and the F-scanner, see Table 2.

Table 2: Determination of the extracted contamination of the QR code (theoretical extraction maximum: 9,63 mg).

Sampler	Contamination	$m_{Fluo}[mg]$	$m_{grav}[mg]$
Texwipe Alpha Low TOC Swab	Syntixol 6.5	6,84	5,64
Texwipe Alpha Low TOC Swab	Wicoil 754	4,99	4,81
Texwipe AlphaSat Swipe	Syntixol 6.5	7,39	6,64
Texwipe AlphaSat Swipe	Wicoil 754	6,35	5,97

As an example, Figure 9 shows the result for an extraction of the lubricating oil with a swab in the F-scanner.

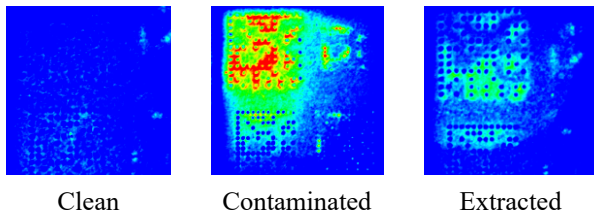


Fig. 9: Results of the extraction method on the QR-Code after the swab procedure

Due to the chemical and mechanical action of the samplers, even surface adhering contaminants can be removed. Comparisons on metal show that a simple rinse cannot loosen all types of contaminants, such as fingerprints.

Since, in principle, not all contaminations can be carried along at two points in the extraction process, namely during the detachment itself and the transfer into solution, this must be taken into account in possible quantifications. However, the method shows that spatially resolved identification is certainly possible.

Besides, further tests demonstrate that the swipe method is more suitable for large, flat components due to the large area of the swipes, and that the swab method is relevant for small, even complex surfaces.

IV. CONCLUSION

The selected analytical methods are all suitable for the qualification about the presence of contaminations; the spectroscopic methods can further contribute to the identification against references. Moreover, each method is also applicable to quantify contaminations via calibration lines, which can be used, for instance, in the industry defining and checking limit values.

Fluorescence spectroscopy can determine accurately whether the contamination is similar to the reference based on characteristic peaks of the impurity versus a reference. Together with the developed extraction method, this ensures a fast and efficient analysis that can identify and quantify contaminants.

A combination of fluorescence spectroscopy with the F-scanner also offers potential. For example, if unavoidable contamination is known from manufacturing, fluorescence spectroscopy will determine the optimal excitation wavelength at which the F-scanner should operate. In addition, the area to be detected can be directly adjusted since the spectrum reveals the wavelengths of fluorescence.

Thanks to the structure elucidating properties of the infrared spectrum, it is possible to make direct statements about the identity of the sample in FTIR spectroscopy. Evaporation of the solvent eliminates its influence and the impurity can be analyzed separately. Since many different additives are generally used in filmic contaminations, characteristic peaks are formed in many spectra that allow conclusions to be drawn about the identity of the impurity.

V. REFERENCES

- [1] T. Wohlers, R. I. Campbell, O. Diegel, R. Huff, and J. Kowen, *Wohlers report 2020: 3D printing and additive manufacturing state of the industry*. Fort Collins, Colo.: Wohlers Associates, 2020.
- [2] T. Zachmann and J. Krusche, "Filmische Verunreinigungen als Qualitätskriterium," *J Oberfl Techn*, vol. 56, S1, pp. 58–59, 2016, doi: 10.1007/s35144-016-0047-1.
- [3] S. Krottil, "Technische Sauberkeit in der additiven Fertigung," *J Oberfl Techn*, vol. 59, no. 11, pp. 52–55, 2019, doi: 10.1007/s35144-019-0402-0.
- [4] M. Rochowicz, "Neue Anforderungen an die filmische Sauberkeit," *J Oberfl Techn*, vol. 56, no. 3, pp. 52–55, 2016, doi: 10.1007/s35144-016-0028-4.
- [5] S. Schweinstig, *Technische Sauberkeit in der Refabrikation*. Zugl.: Bayreuth, Univ., Diss., 2012. Aachen: Shaker, 2012.
- [6] Verband der Automobilindustrie e.V. (VDA), Ed., *Qualitätsmanagement in der Automobilindustrie: Prüfung der Technischen Sauberkeit. Partikelverunreinigungen funktionsrelevanter Automobilteile*, 2nd ed. Berlin, 2014.
- [7] *VDI 2225 - Konstruktionsmethodik - Technisch-wirtschaftliches Konstruieren - Technisch-wirtschaftliche Bewertung: Blatt 3*, Verein Deutscher Ingenieure, 1998.
- [8] Sophian Beyerlein and M. Aboushama, "Evaluation of Continuous Fiber Reinforcement Desktop 3D Printers Desktop 3D Printers Overview," Unpublished, 2020.
- [9] A. Gebhardt, *Additive Fertigungsverfahren: Additive Manufacturing und 3D-Drucken für Prototyping - Tooling - Produktion*, 5th ed. München: Hanser, 2016.
- [10] Fachverband industrielle teilereinigung e.V., "Filmische Verunreinigung beherrschen: FiT-Richtlinie," Hilden, 2018.
- [11] N. N. Kumbhar and A. V. Mulay, "Post Processing Methods used to Improve Surface Finish of Products which are Manufactured by Additive Manufacturing Technologies: A Review," *J. Inst. Eng. India Ser. C*, vol. 99, no. 4, pp. 481–487, 2018, doi: 10.1007/s40032-016-0340-z.
- [12] S. Schweda and S. Ellenrieder, "Reinigung und Restschmutzanalyse in der additiven Fertigung," *J Oberfl Techn*, vol. 56, S1, pp. 12–13, 2016, doi: 10.1007/s35144-016-0038-2.
- [13] M. Rochowicz and M. Keller, "Prüfung von filmischen Verunreinigungen," *J Oberfl Techn*, vol. 60, no. 3, pp. 64–67, 2020, doi: 10.1007/s35144-020-0485-7.
- [14] P. L. Pluta, *Cleaning and Cleaning Validation: Volume 2: PDA-DHI*, 2013.
- [15] S. Kelekar, "Why the swab matters in cleaning validation," Dec. 2010.
- [16] D. Schulz, "Filmische Verunreinigungen zuverlässig detektieren," *J Oberfl Techn*, vol. 58, no. 1, pp. 30–31, 2018, doi: 10.1007/s35144-017-0391-9.
- [17] A. Brandenburg, "F-Scanner: Grossflächige Inline-Prüfung von Oberflächenreinheit und Beschichtungen," Fraunhofer-Institut für Physikalische Messtechnik, 2016.
- [18] M. Sackewitz, "Leitfaden zur Wärmefluss-Thermografie: Zerstörungsfreie Prüfung mit Bildverarbeitung," Stuttgart, 2011. Accessed: May 4 2021. [Online]. Available: <https://shop.vision.fraunhofer.de/artikel/leitfaden-12-waermefluss-thermographie>

Author's index

- Acikgöz, Yunus Ahmet, 13, 288
Agacdeviren, Deniz, 23
Agchar, Ismael, 15
Albert, Martin, 15, 30
Aleshin, Nikita, 23
Aleynikov, Danil, 20, 163
Allrich, Vincent, 23
Anselstetter, Fabienne, 16, 386, 401
Anzenhofer, Alexander, 23
Arndt, Lorin, 16
Arnold, Fabian, 23
Aydogdu, Seda, 14
- Bär, Katharina, 22, 258
Bäumel, Benedikt, 20, 169
Böhmisch, Markus, 20
Babl, Roman, 13, 292
Bader, Luca, 23
Baldauf, Tobias, 23
Barth, Tobias, 23
Bastl, Daniel, 18, 122
Baur, Sebastien, 20, 172
Beloschapkin, Igor, 15, 34
Benke, Lukas, 20, 177
Bentz, Jörg, 15, 54
Beringer, Jakob, 20, 183
Bier, Tobias, 18
Bischoff, Sarah, 18
Bröll, Lukas, 23
Braunreuther Stefan, 16, 412
Briechele, Maximilian, 21, 189
Bruckschloegl, Jonas, 23
Bugl, Benedikt, 17, 436
Burger, Simon, 18
- Cameron, Emily, 23
Cevallos, Gabriel, 16
Czerwek, Florian, 21
- Dawoud, Belal, 21, 22, 202, 238, 253
Dendorfer, Sebastian, 17
Dengler, Simon, 17, 469
Detling, Michael, 23
Diewald, Maximilian, 23
Durak, Eren, 15, 38
- Egeler, Jonas, 16
Ehrenwirth, Mathias, 20–22, 183, 216
Elias, Jörg, 21, 207
Engelbrecht, Rainer, 17, 450, 469
Eursch, Andreas, 13, 303
- Förster, Florian, 23
Falk, Maximilian, 15
Faust, Moritz, 23
Fenn, Markus, 14, 418
Fiechtl-Otter, Georg, 23
Fischer, Maximilian Dominik, 21, 193
Fitznar, Dennis, 15, 44
Flach, Charley Michelle, 23
Frey, Lars, 23
Friedrich, Sissy, 16
Fuxen, Philipp, 24
- Göttling, Federica, 24
Götz, Rebekka, 21
Gegaj, Lumbardh, 21, 199
Gerdtts, Dennis, 14, 423
Glashauser, Michael, 24
Gleichauf, Johanna, 17
Goldmann, Daniel, 21, 193
Goller, Ralf, 18, 135
Goltz, Jonas, 16
Grabinger, Lisa, 24
Graml, Johanna, 18, 110
Gremer, Michaela, 24
Greve, Alina, 24
Gronau, Maximilian, 13, 297
Guidolin, Michele, 18
Guidolin, Michele, 18
Guillermo, Luis, 24
- Högl, Christina, 18
Hümmer, Benedikt, 17
Hanisch, Patrick, 18
Hansen, Philipp, 24
Hanser, Andreas, 21, 202
Hausmann, Philip Andrew, 24
Heberl, Michael, 22, 253
Heberl, Michael, 21, 238
Heckel, Robert, 17

- Heidacher, Konstantin, 18, 116
Heindl, Melanie, 24
Heinzl, Alexandra, 13, 303
Hennemann, Lukas, 24
Henze, Diane, 20, 21, 172, 232
Herrmann, Sven, 17
Heuser, Johanna, 14, 426
Heusgen, Valentin, 24
Heyder, Susanne, 18
Hildebrand, Jan Sebastian, 19, 144
Hoang, Van Danny, 24
Hofmann, Christoph, 24
Huber, Lea, 21, 22, 238, 253
Huber, Robert, 18
Hupfeld, Alexander, 13, 309
Husser, Evelyn, 24
- Iberl, Andreas, 24
Ilter, Ahmet, 24
Izycki, Thomas, 24
- Jäck, Christian, 24
Jaeger, Magnus, 20, 22, 169, 279
Jamakatel, Prakash, 14
Joerg, Kilian, 25
Joop, Dominik, 25
- Köck, Hannah, 25
Kögler, Michael, 17
Kölbl, Josef, 17, 441
König, Gabriel, 25
Kaiser, Markus, 21, 207
Kempf, Lena, 20, 368
Kern, Annabelle, 25
Kern, Tobias, 21, 212
Ketterle, Andreas, 25
Khan, Farrak, 13, 316
Kluger, Felix, 20, 374
Knepper, Karoline, 21, 216
Kokorsch, Marcel, 25
Kornatzki, Julia, 16, 392
Kottre, Andreas, 25
Kraupner, Johannes, 25
Kraus, Andreas, 25
Krause, Julia, 15, 49
Krause, Robert, 13, 320
Krcmar, Wolfgang, 19, 144
Kroiß, Tobias, 18
Krug, Niklas, 25
Kuffer, Alexander, 21, 221
Kufner, Michael, 17, 441
Kullmann, Manuel, 25
- Lamert, Sergej, 25
Lamprecht, Robert, 15
Lasow, Alexander, 13, 325
Lehle, Karla, 19
- Leibold, Christoph, 17
Leidl, Karl, 14, 340
Leuze, Nico, 25
Lewerenz, Meinert, 17, 463
Lichtenstern, Isabella, 18
Limbeck, Simon, 20, 21, 172, 232
Loretschk, Michael, 18, 122
Ludwig, Korbinian, 13
Lukas, Raphael, 17, 441
Lukas, Sibö, 21, 227
- Mück, Jochen, 25
Mülbredt, Natalie, 15, 58
Münch, Andreas, 15
Maierhofer, Michael, 13
May, Fabio, 25
Mayer, Florian, 15, 54
Mehta, Kedar, 20, 183
Meiser, Joshua, 18, 126
Meisinger, Alexander, 25
Menne, Valentina, 21, 232
Mišák, Jan, 17, 445
Miedaner, Marco, 25
Mikschl, Manuel, 25
Morf, Fabian, 17, 450
Mottok, Jürgen, 15, 20
Mutzhas Dominic, 21
- Naulin, Janine, 26
Neudecker, Christine, 26
Niebler, Christine, 17
Nopp-Nowak, Flaviu, 17, 450
- Ott, Jonas, 26
Oumard, Christina, 15, 64
- Pace, Dominik, 21, 238
Paglia, Chiara, 26
Palme, Frank, 21, 227
Pastore, Antonello, 26
Pellert, Nico, 22, 243
Pettinger, Karl-Heinz, 21, 227
Pfeffer, Peter E., 14
Preis, Michael, 22, 248
Probst, Florian, 18
Prokscha, Ruben, 13, 330
- Römmelt, Lennard, 14, 431
Rückerl, Alexander, 22, 264
Raab, Daniel, 21, 189
Rampl, David, 26
Rauchheld, Sarah, 18, 132
Rechenauer, Christian, 22, 248
Reichstein, Simon, 18, 132
Reidl, Tobias, 22, 253
Reindl, Thomas, 26
Reineck, Marcel, 16

- Reischl Thomas, 22
Reitenberger, Johannes, 18, 135
Rembold, Anina, 20, 380
Reum, Tobias, 22
Riedl, Thorsten, 17, 454
Riedmaier, Thomas, 22, 258
Rosner, Florian, 26
Rudolph, Matthias, 18, 122
- Sahin, Ahmet, 16, 396
Salg, Manuel, 19, 141
Salzberger, Stefan, 26
Schäufele, Thomas, 26
Schönhärl, Stefan, 15, 73
Schöniger, Roland, 14, 340
Schaeffer, Leon, 26
Schaller, Timo, 22, 269
Scharnagl, Tassilo, 26
Scharold, Franziska, 15, 70
Scheck, Korbinian, 14
Schell, Patricia, 16, 386, 401
Scheuerer, Ralph, 26
Schick, Bernhard, 14
Schidek, Anna, 26
Schlereth, Benedikt, 26
Schloder, Benedikt, 17, 459
Schmid, Michael, 17, 463
Schmid, Stefanie, 19
Schmidt, Jonas, 14, 336
Schmidt, Manuel, 26
Schoplocher, Paul, 26
Schrag, Tobias, 22
Schramm, Martin, 14, 340
Schramm, Simon, 21, 193
Schratzenstaller, Thomas, 19
Schubaur, Philipp, 20, 76
Schulitschenko, Andreas, 13, 92
Schwarz, Sascha, 18, 122
Schweiberer, Philipp, 22, 271
Schweigler, Christian, 15, 54
Seibold, Joshua, 19, 144
Seidel, Felix, 19
Sequeira, Gerald Joy Alphonso, 13, 320
Sezgin, Fatih, 14, 346
Shigailow, Markus, 26
Sieg Müller, Anna, 20
Simon, Marvin, 26
Sparrer, Lisa Marie, 27
Spellauge, Tillmann, 13, 98
Stapff, Veronika, 27
Starost, Veit, 22, 276
Steffens, Oliver, 20, 22, 87, 264
Straller, Armin, 27
- Sturm, Elisabeth Christine, 20, 81
Sudhop, Stefanie, 18, 122
Swierkot, David, 27
- Theen, Johannes, 27
Theil, Markus, 13, 103
Theiler, Michael, 17, 463
Theumer, Philipp, 16, 412
Timur, Issayenko, 27
Toutouly, Lovis, 20, 87
Tröger, Johannes, 19, 148
Tunc, Okan, 14, 352
Tworek, Anton, 14
- Uhl, Christian, 16, 386, 401
Unruh, Denis, 17, 469
Urlhart, David, 27
Utz, Elisabeth, 19, 151
- Veitl, Jakob, 27
Vinogradov, Juri, 17, 450
Vollenbröcker, Julia, 27
von Wilcken, Jean-Luc, 27
Vorderobermeier, Tobias, 16, 407
- Wachter, Sarah Maria, 20
Wagner, Felix, 27
Warmuth, Monika, 16, 386, 401
Weber, Georg, 16, 412
Weber, Julia, 27
Weber, Lukas, 22, 279
Weber, Robert, 27
Weidlich, Johanna, 22
Weigelt, Samuel, 27
Weindler, Jeremy, 27
Weinmann, Steffen, 17, 474
Weinzierl, Manuel, 27
Wendt, Thilo, 27
Wenig, Alois Andreas, 14, 356
Werner, Patrick, 27
Werther, Martin, 20, 177
Whittlesey, Niklas, 19, 156
Wieser, Helmut, 18
Wolf, Martin, 14
Wopper, Christoph, 22, 282
Wrana, Christian, 19
Wucherer, Stefanie, 18
- Zörner, Wilfried, 20–22, 183, 216, 258
Zeitler, Fabian, 14, 362
Zeitler, Sally, 16
Zeyer, Klaus Peter, 20, 21, 172, 232
Zinnel, Laura, 27